AGARD-CP-93

AGARD-CP-93

AGARD

ADVISORY GROUP FOR AEROSPACE RESEARCH & DEVELOPMENT

AGARD CONFERENCE PROCEEDINGS No. 93

on

Turbulent Shear Flows
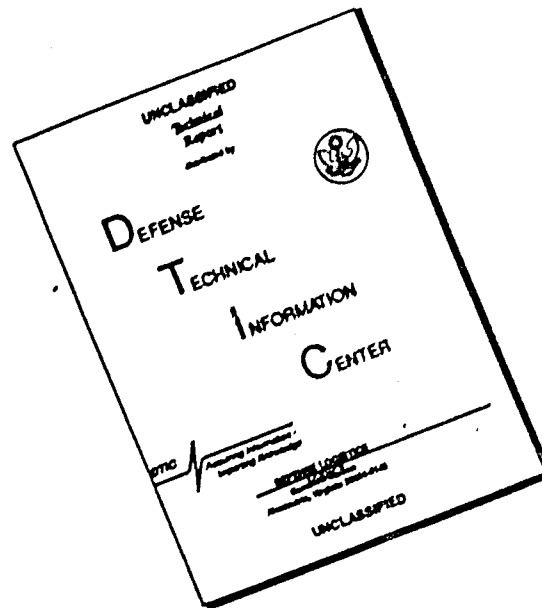
D D C
RECEIVED
MAR. 2 1972

NORTH ATLANTIC TREATY ORGANIZATION

**DISTRIBUTION AND AVAILABILITY
ON BACK COVER**

DISCLAIMER NOTICE

THIS DOCUMENT IS BEST
QUALITY AVAILABLE. THE COPY
FURNISHED TO DTIC CONTAINED
A SIGNIFICANT NUMBER OF
PAGES WHICH DO NOT
REPRODUCE LEGIBLY.

NORTH ATLANTIC TREATY ORGANIZATION

ADVISORY GROUP FOR AEROSPACE RESEARCH AND DEVELOPMENT

(ORGANISATION DU TRAITE DE L'ATLANTIQUE NORD)

TURBULENT SHEAR FLOWS
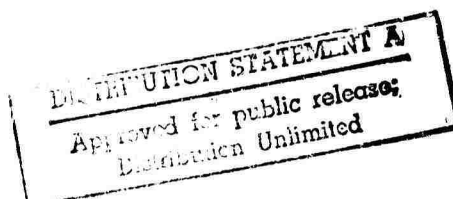
Papers presented at the Fluid Dynamics Panel Specialists' Meeting, held in
London, U.K., 13–15 September 1971

THE MISSION OF AGARD

The mission of AGARD is to bring together the leading personalities of the NATO nations in the fields of science and technology relating to aerospace for the following purposes.

– Exchanging of scientific and technical information;

– Continuously stimulating advances in the aerospace sciences relevant to strengthening the common defence posture;

– Improving the co-operation among member nations in aerospace research and development;

–– Providing scientific and technical advice and assistance to the North Atlantic Military Committee in the field of aerospace research and development;

– Rendering scientific and technical assistance, as requested, to other NATO bodies and to member nations in connection with research and development problems in the aerospace field.

– Providing assistance to member nations for the purpose of increasing their scientific and technical potential;

– Recommending effective ways for the member nations to use their research and development capabilities for the common benefit of the NATO community.

The highest authority within AGARD is the National Delegates Board consisting of officially appointed senior representatives from each Member Nation. The mission of AGARD is carried out through the Panels which are composed for experts appointed by the National Delegates, the Consultant and Exchange Program and the Aerospace Applications Studies Program. The results of AGARD work are reported to the Member Nations and the NATO Authorities through the AGARD series of publications of which this is one.

Participation in AGARD activities is by invitation only and is normally limited to citizens of the NATO nations.

AGARD FLUID DYNAMICS PANEL OFFICERS

CHAIRMAN: Professor W.R.Sears
DEPUTY CHAIRMAN: Professor L.G.Napolitano

PROGRAMME COMMITTEE MEMBERS

Professor S.M.Bogdonoff (Chairman)
Mr L'Ing Général A.Auriol
Professor K.Gersten
Dr R.H.Korkegi
Professor L.G.Napolitano
Professor A.D.Young

PANEL EXECUTIVE

Dr L.H.Townend

FOREWORD

The Meeting was held in order to clarify understanding of the basic physical structure of turbulent shear flows such as boundary layers, jets and wakes, in non-reacting flows of gas. Factors considered were the basic structure of "equilibrium" shear flows and the influence of compressibility, pressure gradients, surface curvature, three-dimensional flows, noise, density and/or temperature gradients.

Thirty-four papers were presented, four being invited from internationally known authors to present an overview of the field of turbulent shear flows. Papers in Session I present new information on the structure of the boundary layer. Session II covers theoretical treatments. Papers in Sessions III and V are particularly concerned with new experimental boundary layer results, and in Session IV with jets and wakes. Papers in Session VI cover a series of special areas in turbulent shear flows.

By invitation of the British National Delegates to AGARD, the Specialists' Meeting recorded in this document was held at the Royal Zoological Society of London, during 13–15 September 1971.

CONTENTS

VARIATIONS ON A THEME OF PRANDTL

Peter Bradshaw
Department of Aeronautics, Imperial College, London

SUMMARY

Because Reynolds stress gradients are usually significant only in fairly thin shear layers, many of the complex turbulent flows that are important in engineering are recognizable as perturbations of the classical thin shear layers to which Prandtl's approximation applies. We distinguish (i) interacting shear layers (ii) shear layers perturbed by small extra rates of strain, which can nevertheless produce appreciable changes in the turbulence (iii) shear layers perturbed by large extra rates of strain. Examples are (i) aerofoil boundary layers merging into a wake (ii) boundary layers on curved surfaces (iii) reattaching shear layers. In this paper we discuss the essential phenomena that appear in these complex turbulent flows and show that they are not excessively numerous, so that a moderate programme of turbulence measurements should enable calculation methods to be extended to a wide range of complex flows. A short discussion of the general types of calculation method suitable for complex flows is included.

1. INTRODUCTION

Prandtl's boundary layer approximation was first developed for two-dimensional laminar boundary layers. It has since been applied to flows that are three-dimensional, or turbulent, and to free shear layers: let us therefore call it the "thin-shear-layer approximation". It can be expressed in several ways: in the present context the essential feature of a thin shear layer is that the only stress gradients that affect the mean motion are shear-stress gradients in the direction normal to the plane of the layer. In laminar flow this is just a mathematical simplification, since we know what the neglected stress gradients are - simply the viscosity times the appropriate rate of strain. In turbulent flow, where we have no exact expressions for the stress gradients, it is a useful physical simplification to be able to neglect most of them. Melville Jones' concept of the "streamlined aeroplane" was an aeroplane entirely covered by a thin shear layer: real aeroplanes are near enough to this ideal for the study of thin shear layers to have been popular and profitable. Moreover, it was not possible, until the advent of computers, to make more than very limited calculations of viscous flows other than thin shear layers - that is, flows described by the full Navier Stokes equations. However, the importance of thin shear layers in research work has perhaps exceeded their importance in real life.

Recently, numerical analysts have successfully attacked laminar flows other than thin shear layers (which I shall call "complex" laminar flows - see Fig. 1) and have turned their attention to complex turbulent flows also. Now the calculation of complex laminar flows is purely a numerical problem - which is not to say an easy problem - but to calculate complex turbulent flows we need a great deal of empirical information about the behaviour of the Reynolds stresses. Not only may normal stress gradients become important, but the behaviour of the shear stresses is likely to be more complicated than in a thin shear layer. Furthermore, extra rates of strain (such as accelerations) which are small compared to the mean shear, and which would therefore produce only small extra stresses in a laminar flow, may produce large effects on turbulence: thus even within the thin-shear-layer approximation there are many flows whose turbulence structure must be regarded as complex.

Complex turbulent flows like those shown in Fig. 1 are important: engineers want to calculate them, numerical analysts try to calculate them, but, for the most part, basic research workers do not try to measure them (by a basic research worker I mean someone who is trying to understand a general phenomenon rather than solve a particular engineering problem). There are of course exceptions, groups like those at McGill[1], Queen Mary College and Rutgers[2] which have long-standing programmes of research on the subject, and some individual workers referenced below. In general, however, there is surprisingly little information on turbulence in complex flows that is of any real use in developing engineering calculation methods (which is surely the main justification for studying turbulence). As a result the development of prediction methods for complex turbulent flows amounts to making bricks without straw. What seems to be lacking is a point of view from which to study these flows experimentally: the point of view that I offer in this paper is that quite a wide range of complex flows can be explained in terms of only a few extra phenomena, and progress is more likely to result from basic research on a small number of phenomena than from disconnected work on a large number of flows. Furthermore, basic research is more likely to produce results of practical use if it is broadly motivated by the needs of calculation methods than if the stimulus is pure scientific curiosity - though it would be a mistake to tie a research programme too closely to a particular calculation method. Therefore, I want to discuss both the dominant phenomena of complex turbulent flows and the kind of empirical information one needs to calculate them: neither part of the discussion is exhaustive, but I hope to convince at least some readers that progress can and should be made with complex flows of engineering importance.

As my title implies, most of the complex turbulent flows of engineering importance are not too different from Prandtl's thin shear layer. Typical Reynolds stresses in a turbulent flow are of the order of 0.01 of a typical dynamic pressure, whereas typical static pressure differences are of the order of the dynamic pressure; therefore, Reynolds stress gradients will in general be negligible compared to longitudinal pressure gradients unless the typical transverse scale of the turbulent flow is small compared to a typical longitudinal scale. We are therefore interested in shear layers that are perturbed, for instance by interaction with another shear layer or by accelerations imposed by the boundary conditions: the "extra phenomena" mentioned above are perturbations of various sorts. A wide range of complex flows, steady or unsteady, can be classified as either

    (i) interacting shear layers

    (ii) perturbed shear layers with small extra rates of strain

    (iii) perturbed shear layers with large extra rates of strain or other strong perturbations.

Fig. 1 shows examples of each (mainly two-dimensional, for ease of drawing). Type (iii) alone necessarily disobeys the thin-shear-layer approximation although some examples of type (i), such as flows along a streamwise corner, may not fully obey it. It is, of course, important to recognize that these flows do differ significantly from simple thin shear layers - in the past, theoreticians have tended to minimise these differences, for instance by assuming that a reattaching shear layer immediately obeys all the empirical formulae derived for well-behaved boundary layers.

Section 2 of the paper is a brief outline of the type of calculation method needed for complex turbulent flows: this shows that measurements of fairly complicated turbulence quantities are desirable. Sections 3 to 5 are discussions of topics (i) to (iii) above. In general I have included only references actually needed in the discussion, with a few pioneering papers or recent reviews. A "Bibliography of complex turbulent flows" containing about 600 references, selected for their relative usefulness from a rather larger number, will be available - probably at a price - from the Aeronautics Department, Imperial College: these references are mainly studies of particular engineering problems without the sort of turbulence measurements that would contribute to a more general understanding of the subject, but they are the only available background to the kind of study that I am proposing.

2. CALCULATION METHODS FOR COMPLEX TURBULENT FLOWS

The essential problem is to find empirical expressions for the Reynolds stresses. From the instantaneous Navier Stokes equations one can derive exact "transport" equations for the rate of change, along a mean streamline, of any of the components of the Reynolds stress (Ref. 3, pp 25-26). The right hand sides of these equations contain

(i) "source" terms representing generation of Reynolds stress by the action of the mean rates of strain on the turbulence;

(ii) "sink" terms representing destruction of Reynolds stress, or exchange between one stress component and another, by the action of pressure fluctuations. The Poisson equation for the pressure contains the mean rates of strain and it has been shown (Ref. 4) that they may affect these "sink" terms as well as the "source" terms (i), though there is still some controversy about this;

(iii) "sink" terms representing destruction of Reynolds stress by the action of viscosity after its transfer from large eddies to small;

(iv) "transport" terms (expressible in divergence form) representing spatial transport by the action of velocity fluctuations, pressure fluctuations or (usually negligibly) viscosity.

To make the equations soluble one must represent the terms (i) to (iv) by empirical functions of the Reynolds stresses for which equations are being considered: since the terms in the equations have dimensions $[\rho \times \text{velocity}^3/\text{length}]$ some sort of length scale must be inserted, in addition to the velocity scales provided by the Reynolds stresses themselves. Possible approaches are discussed in the other invited lectures: it is worth making the general point that since these are equations for rate of change of Reynolds stress, temporal rates of change (unsteady flow) can be accommodated in the same way as spatial rates of change.

In simple shear layers, the only significant Reynolds stress gradients are $\partial(-\rho\overline{uv})/\partial y$ and - in three-dimensional flow - $\partial(-\rho\overline{vw})/\partial y$; the only significant rates of strain are, correspondingly, $\partial U/\partial y$ and $\partial W/\partial y$; the rates of change of Reynolds stress along a mean streamline are small; and the eddy length scale is closely related to the thickness of the shear layer. Thus some of the "transport" equations can be neglected altogether, and some of the terms in the remaining ones neglected according to taste (even to the point of neglecting the transport terms and rate-of-change terms altogether and thus converting a differential equation for Reynolds stress into an algebraic formula of the "eddy viscosity" type).

In complex turbulent flows some or all of these simplifications disappear: very roughly speaking, we expect shear-layer interactions to be dominated by transport terms, while in strongly-perturbed flows the rate of change of Reynolds stress will be large and, of course, more Reynolds stresses have to be considered, especially in three-dimensional flows. It is difficult to see how eddy viscosity concepts can be used even as a rough approximation except in very restricted cases, and one is faced with the problem of finding empirical representations of many terms in many equations, including equations for eddy length scales. Some people hope that this can be done by trial-and-error adjustment of a moderate number of "universal" constants or functions to optimise mean-flow predictions; whether or not this is true in principle it is certainly impossible to do it by using thin-shear-layer data alone because some of the terms do not even appear in thin shear layers. Both this approach, and the more reliable approach of deriving empirical functions from actual turbulence measurements, will remain futile until we have more experimental data, either to improve our knowledge of phenomena or to act as test cases. It seems likely that we shall not in the near future devise a calculation method, based on a single set of empirical functions, capable of treating all of the complex turbulent flows in Fig. 1: almost certainly we shall have to use different empirical functions for different regions (strictly, for different phenomena). This is analogous to the finite-element techniques used in structural analysis, where it has been found more efficient to devise complicated elements, a few of which will cover the field, rather than to use many simple elements and ignore regional peculiarities. In structural analysis, where the equations are simple, this is a matter of economy; in turbulent flow it is likely to be a necessity.

Up to the present, engineers concerned with complex flows have predicted them by using direct correlations (of the eddy viscosity type but not necessarily so explicit) between the mean flow and the Reynolds stresses or other turbulence quantities. The choice is between a single eddy viscosity formula to cover the whole flow or a more rational approach of applying different formulae in different regions: unfortunately the reliability of the results is not likely to increase with the number of formulae because it is difficult to establish the range of validity of a formula that is not based on a realistic physical model, unless one has a vast quantity of data. The advantage of an approach based on the Reynolds-stress transport equations is that, since it is based on an exact turbulence equation rather than a hypothetical

connection between turbulence and mean flow, it requires fewer different experimental cases to provide the empirical information, while the range of validity can be estimated, for the most part, by examination of the assumptions rather than exhaustive comparisons with experiment. Against this, however, one requires more detailed information from each experiment.

Having dismissed the eddy viscosity concept as a means of calculating complex turbulent flows (and noting with satisfaction the crumbling of two of the remaining bastions of eddy viscosity, at Los Alamos (Ref. 5) and the Mechanical Engineering Department of Imperial College (Ref. 6)) I must now excuse myself for using eddy viscosity in discussing the effect of small extra strain rates on turbulent flow (section 4)! At present our experimental and theoretical knowledge of this subject relates mainly to self-preserving flows, in which, purely for dimensional reasons, the eddy viscosity for the dominating shear stress obeys simple rules and is therefore a suitable measure of changes in turbulence structure (it is for the same reason that a simple eddy viscosity formula gives good results in thin shear layers that are not too far from self-preservation). I do not suggest that the apparent eddy viscosity is the same for all the Reynolds stresses in complex flows: it is known (Refs. 7-9) that it is not even the same for the two components of shear stress in a thin or slender shear layer in three-dimensional flow.

3. INTERACTING SHEAR LAYERS

In this section we suppose that the thin-shear-layer or slender-shear-layer approximation applies throughout the flow, except for minor regions ("Navier Stokes regions") near trailing edges or other discontinuities in boundary conditions. The interaction between two shear layers can be classified according to the relative orientation of the shear stresses in the two layers. If the two shear stresses are in the same plane and in the same direction we call the smaller layer an "internal shear layer"; an example is the internal boundary layer growing from a step change of surface roughness into a pre-existing boundary layer. If the two shear stresses are in planes inclined at an angle we have a "corner flow". If the two shear stresses are in the same plane but have opposite sign we have the most familiar form of interaction, found in a duct, plane jet, wake or wall jet.

3.1 Internal shear layers

The internal shear layer has been studied by many authors, generally however in its simplest manifestation, the internal boundary layer following a roughness change. If the internal boundary layer lies within the inner layer of the main boundary layer the flow depends on comparatively few variables, similarity can be invoked, and if the roughness change is not too large the turbulence is not too far from local energy equilibrium. Ref. 10 gives a good discussion. In other cases, only weak interactions are amenable to treatment because a strong interaction produces what is in effect a single new shear layer which must be treated as such. Eskinazi (Ref. 11) performed a pioneering experiment which has not been followed up.

3.2 Corner and edge flows

A flow along a streamwise corner can be more usefully regarded as an interaction because at large distances from the corner each shear layer is unaffected, except for any lateral component of velocity resulting from the displacement thickness of the other shear layer. If the corner angle approaches 180 deg. the interaction is again difficult to treat as such, but, since it is certain to be weak, rules developed for sharper corners may suffice. External edges (angles significantly larger than 180 deg.) produce flows with some features in common with concave corners. In all cases, Reynolds stress gradients in the plane normal to the primary flow direction produce "secondary flows" of Prandtl's second kind, partly opposed by pressure gradients in the same plane. The most common cases of a 90 deg. corner and a 360 deg. corner (i.e. a streamwise edge) have been studied experimentally by quite a large number of workers (Refs 12-16: see also the paper by Mojola and Young in these Proceedings).

These secondary flows are of course quite weak (the maximum yaw angle in a 90 deg. corner is about 3 deg.) and I feel that in many practical cases they are likely to be overwhelmed by asymmetry of the flow about the bisector of the corner (it is really difficult to set up a symmetrical corner flow). A typical corner boundary layer flow is that in the junction between an aerofoil (wing, turbomachine blade) and the body (fuselage, hub) supporting it: when the body boundary layer meets the leading edge of the aerofoil longitudinal vorticity is generated and fed into the corner, and in general there will be a static pressure difference between the aerofoil and the body so that even the external streamlines will not be parallel to the corner. The flow round the tip of a turbomachine blade, moving relative to the outer casing, will be even more asymmetrical, and the flow round the tip of a wing will be complicated by spanwise flow. It might be thought that duct flows are more likely to be symmetrical about the corner but this is strictly true only of a straight, square duct. Surface shear stress measurements in rectangular ducts show appreciable asymmetry (e.g. Ref. 17). Moreover, commercial ducts are often curved, or preceded by a bend, again leading to net longitudinal vorticity. I feel that we need measurements on an asymmetrical corner flow to see whether the work on idealized corners is relevant. Work on longitudinal vortices imbedded in plane boundary layers (Ref. 18) may be at least as useful.

The maintenance of secondary flows of Prandtl's second kind, and the diffusion of extraneous longitudinal vorticity, both rest on delicate balances of Reynolds stress gradients: for instance the main stress terms in the longitudinal vorticity equation (e.g. Ref. 16) are the second derivatives of the difference of two stresses. It appears that rather accurate representations of the Reynolds stresses is needed if the vorticity is to be predicted, as it must be even if the practical interest is only in the streamwise velocity component. Therefore corner and edge flows must be treated via separate equations for each stress: local-equilibrium assumptions (mixing length, eddy viscosity) will be particularly inappropriate since turbulent transport of Reynolds stress in both the y and z directions will occur.

3.3 Opposing shear layers

The simplest kind of shear-layer interaction is that between two layers with shears of opposite sign, such as the two halves of a wake flow. Because the mean shear changes sign, any shear-stress-bearing eddies that cross the line of zero mean shear tend to be damped out as the rates of production of turbulent

energy or of shear stress ($-\overline{\rho uv} \, \partial U/\partial y$ or $\rho \overline{v^2} \, \partial U/\partial y$) become negative (this is a slightly loose statement; one has to consider averages over the intruding eddies rather than conventional averages, but the qualitative conclusion is valid). This means that the effect of the interaction on the turbulence structure will not extend very far either side of the line of zero mean shear. Of course, the profiles of velocity, shear stress, turbulent intensity and so on will be affected by what amounts to a change in boundary condition. Some work we have done at Imperial College shows that even in the interaction region the turbulence structure of each shear layer is not grossly altered, almost as if the two turbulence fields could be superposed. This is consistent with the idea that spreading of turbulent flow is effected by the large eddies, carrying the small-scale eddies with them. Near the line of zero mean shear the large eddies will arrive, more or less alternately, from either shear layer, displacing fluid belonging to the other shear layer; a true interaction between the random vorticity fields of the two layers will occur only when a particularly intense eddy from one side entrains weaker turbulence from the other.

The practical value of these observations is that interactions between oppositely-sheared layers can be predicted to good accuracy by superposing calculations of shear stress for the separate shear layers (but of course using a common velocity profile). Clearly this is possible only with calculation methods that do not relate the shear stress directly to the velocity profile but allow for turbulent transport of stress from elsewhere; if the flow is symmetrical, the line of zero shear stress coincides with the line of zero mean shear, but in general the eddy viscosity ($-\overline{uv}$)/($\partial U/\partial y$) becomes in turn zero, negative and infinite. Important examples of asymmetrical interactions include the wake of a lifting aerofoil, the flow in an annular duct and the wall jet, but it is necessary to realise that the interaction mechanism is much the same in a symmetrical flow as an asymmetrical one; symmetry just disguises the more striking results of the interaction. More complicated multiple interactions occur on aerofoils with slotted flaps and in the rolling up of spanwise or longitudinal vortices.

Our own calculation method has so far been programmed only for a symmetrical duct flow (Ref. 19) which requires relatively little alteration to the basic boundary layer program, except that the shear layer thickness, which provides a length scale for the turbulence functions, is now obtained (more logically) from the shear stress profile rather than the velocity profile. The asymmetrical case requires more computing but no more empirical information; we can calculate duct flows quite well enough using data obtained solely from boundary layers. Hanjalic (Ref. 6) has produced a more elaborate calculation method using a differential equation for length scale; the main point of this is to incorporate turbulent transport effects on the length scale but because the interaction region is fairly thin this refinement may not be necessary except in extreme cases.

A problem related to shear-layer interaction is the spread of a shear layer into a non-turbulent but rotational stream. The problem appears exactly in this form in the boundary layer on a body carrying a curved detached shock wave, where it appears (Ref.20) that the rate of growth of the boundary layer can be considerably increased. An internal shear layer growing into a weaker external shear layer may behave similarly but if the mean vorticity in the external layer is significant the fluctuating vorticity (i.e. the turbulence) may be significant also, at least when the two shear layers have the same sign of mean shear.

Of course the spreading of a turbulent stream into irrotational flow still takes place via a non-turbulent but rotational region, the viscous superlayer. At low Reynolds numbers where the superlayer is thick it may be necessary to treat its interaction with the fully turbulent flow explicitly: apparently the turbulence structure in the whole intermittent region is affected.

The true interaction of a turbulent shear layer with surface waves or internal waves has been little studied, in contrast with the popular problem of the effect of turbulence on waves. If the wavelength is long compared to a typical eddy size the flow can be treated as an unsteady turbulent flow (the turbulence structure being the same as in a steady flow if $\partial(-\overline{uv})/\partial t$ is fairly small compared to the rate of generation of $-\overline{uv}$, $\overline{v^2} \, \partial U/\partial y$), but if the wavelength is of the same order as the eddy size (as when the turbulence produces the waves) strong interaction is to be expected (Ref. 21). It seems to be established that sound waves generated by turbulence do not affect the turbulence greatly, at least at non-hypersonic Mach numbers. Paradoxically, shock-wave/boundary-layer interaction is better regarded as a perturbed flow than an interaction in the present sense, and we postpone discussion to the next section.

4. PERTURBED SHEAR LAYERS WITH SMALL EXTRA RATES OF STRAIN

Only recently has it been realized how frequently small extra rates of strain (in different directions from the initial simple shear) can cause large differences in shear stress. If one represents the effect on the eddy viscosity - say - by a factor of the form

$$1 + \frac{C(\text{extra rate of strain})}{\partial U/\partial y}$$

the constant C is commonly of order ± 10. This implies that the fractional changes in $\overline{uv}$ are of the order of 10 times as large as the fractional change in the generation terms ((i) in the list at the beginning of Section 2). There is even evidence that shear stress can be increased by an extra rate of strain $\partial W/\partial z$ (normal to the plane of the shear stress)! If the "Poisson's ratio" of turbulent fluid is really of order 10 it is truly ein ganz besonder Saft. We proceed to discuss the effects of various types of strain rate separately. In all cases we suppose that the extra strain rates are small enough for the letter of the thin-shear-layer approximation to apply.

4.1 Normal acceleration (rotation, surface curvature or streamline curvature)

In this case the extra rate-of-strain component is $\partial V/\partial x$, or U/R where R is the radius of curvature of a mean streamline in the x,y plane. Direct experiments and empirical adjustment of calculation methods both suggest that the fractional change in apparent mixing length, $\sqrt{(\tau/\rho)}/(\partial U/\partial y)$, in a curved flow is roughly $-10(U/R)/(\partial U/\partial y)$ ($\beta = 5$ in the notation of Ref. 22). This is of the order of $30\delta/R$ in the outer layer of a boundary layer and produces significant effects even on a moderately-

cambered aerofoil. In impinging jets, wall jets on curved surfaces, turbomachine blades or highly-curved or rotating ducts spectacular changes can be seen; curvature in a stabilizing sense (angular momentum increasing outwards, as on the top surface of an aerofoil) can induce reverse transition, and destabilizing curvature can generate longitudinal vortex rolls. In all cases the effects of curvature on the turbulent eddies far exceed the effect of the extra terms in the mean-motion equation r even the extra rate-of-strain terms in the Reynolds-stress transport equations.

There are still large gaps in our knowledge, even at the empirical level: for instance it seems likely that curvature effects in the outer layer of a boundary layer will depend more on integrated properties of the outer layer than on the turbulence at the point considered, but we have no data. The problem is of the same order of difficulty as the problem of buoyancy effects in meteorology and more measurements of turbulence structure would be very valuable.

One important general point is that if small values of $\partial V/\partial x$ have a large effect, we cannot assume, as Townsend did, that the turbulence depends solely on the rate of strain $\partial V/\partial x + \partial U/\partial y$ and not on the vorticity $\partial V/\partial x - \partial U/\partial y$. In a thin shear layer the two are equal and opposite, but evidently small differences between the numerical values of the two appreciably change the turbulence structure. This casts doubt on the immediate relevance of experiments on irrotational plane strain (Ref. 23) to the behaviour of shear layer turbulence.

4.2 Lateral divergence or convergence

There is evidence that here, too, the effect on properties of the turbulence is of greater order than the rate-of-strain ratio $(\partial W/\partial z)/(\partial U/\partial y)$. The rate of growth of a radial wall jet is about the same as that of a plane wall jet which implies that the entrainment rate or typical shear stress is about twice as large although $(\partial W/\partial z)/(\partial U/\partial y)$ is roughly equal to $d\delta/dx$, about $0\cdot1$: again the fractional change in "eddy viscosity" is ten times the rate-of-strain ratio.

Keffer (Refs 24, 25) has reported large changes in a diverging wake but negligible changes in a converging one: it appeared that large divergence greatly augmented the z-component vorticity of the larger eddies whereas the effect of contraction of spanwise vortex lines in the converging flow was small compared to other sources of vorticity fluctuation. This implies that simple linear formulae like that in the last section are not to be trusted for large total strains, just as linear formulae for buoyancy effects break down at large Richardson number.

It is probable that divergence was among the miscellany of special influences affecting the waisted-body flow of Winter, Rotta and Smith (Ref. 26): the increase in surface shear stress near the rear of the body in the subsonic tests is larger than expected due to pressure gradient alone.

4.3 Longitudinal acceleration

In two-dimensional flow a longitudinal rate of strain $\partial U/\partial x$ is accompanied by an equal and opposite value of $\partial V/\partial y$ and it is difficult to say which is the first cause of any changes in turbulence structure. The change in the generation terms in the transport equation for $\overline{uv}$ is exactly zero and the change in the turbulent energy equation for $\overline{u^2} + \overline{v^2} + \overline{w^2}$ is small. It is therefore not surprising that positive $\partial U/\partial x$ has not so far been found to affect the turbulence structure until reverse transition occurs (probably due to secondary causes rather than the direct effect of $\partial U/\partial x$ on the turbulence). I shall not discuss reverse transition because there are enough labourers in that particular vineyard already.

Prolonged application of appreciable negative values of $\partial U/\partial x$ to a boundary layer produces separation. In separation from the rear of a body (as opposed to separation induced by a shock or a forward-facing step) the ratio of $\partial U/\partial x$ or $\partial V/\partial x$ (sic) to $\partial U/\partial y$ is not necessarily large even though the thin-shear-layer approximation may be technically violated, but it is more convenient to discuss separation in Section 5.

It is not certain how strongly turbulence is affected by moderate negative ratios of $\partial U/\partial x$ to $\partial U/\partial y$. A ciné film by Head of Cambridge clearly shows distortion of the eddies in a smoke-filled separating boundary layer, and Gartshore (Ref. 27) has suggested that the fractional change in eddy viscosity is (once more) about $-10(\partial U/\partial x)/(\partial U/\partial y)$. Gartshore's result is based, in effect, on comparing the growth rates of pairs of self-preserving flows and assuming that changes are all due to $\partial U/\partial x$ (or $\partial V/\partial y$). However dubious this process may be, the results are certainly credible in view of the discussion in the last two sub-sections.

Further work is needed to decide whether $\partial U/\partial x$ or $\partial V/\partial y$ is the first cause. Since turbulent mixing is the result of the eruption of large eddies in the positive y direction it is plausible that $\partial V/\partial y$ should be the sensitive strain rate. Obviously one cannot decide except by considering a range of flows with - say - the same value of $\partial V/\partial y$ and different values of $\partial U/\partial x$. But this requires variations of $\partial W/\partial z$ which is known to produce effects of its own on the turbulence....... clearly a coherent programme of research work will be needed to give us even an empirical understanding of the large effects of small extra strain rates.

5. PERTURBED SHEAR LAYERS WITH LARGE EXTRA RATES OF STRAIN OR OTHER STRONG PERTURBATIONS

We now turn to flows which are so strongly influenced by extra strain rates or other outside agencies that they violate the thin-shear-layer approximation of slow streamwise change so that normal-stress gradients, as well as shear stress gradients, affect the flow. Not only does the need to predict the normal stresses complicate a calculation method but, if the phenomena mentioned in the last section are anything to go by, the behaviour of both the shear stresses and normal stresses will differ greatly from that in a thin shear layer. It is unlikely that simple linear formulae like those of the last section will be valid for large rates of strain (in the atmosphere, for instance, the linear formulae for change of turbulence structure with buoyancy forces fail, and the extreme states are free convection on the one hand

and complete damping of turbulence on the other).

Strong perturbations of a shear layer in the plane of the mean shear (i.e. large values of $\partial V/\partial x$ or of $\partial U/\partial x \equiv -\partial V/\partial y$) usually involve solid surfaces and separation or reattachment of the shear layer: an exception is perturbation by a shock wave, considered separately. We therefore concentrate on perturbations involving separation and/or reattachment.

5.1 Separation and reattachment

If separation is followed quickly by reattachment, as in the flow over a narrow spanwise cavity, the shear layer is recognizable throughout as a (perturbed) boundary layer. If separation or reattachment are permanent, as in the flow from a nozzle or the impingement of a jet, the shear layer changes eventually to another species of thin shear layer (respectively a mixing layer or a wall jet in these two examples). The main classification of perturbations of an initially thin shear layer is therefore into those that cause a change of species, called "overwhelming" perturbations by Bradshaw and Wong (Ref. 28) and those that do not. Overwhelming perturbations do not necessarily involve more spectacular violations of the thin shear layer approximation than other types of perturbation but they do produce larger changes in turbulence structure. For instance, flow over a narrow spanwise cavity or step can be treated as a perturbation of the boundary layer, using the same inner-layer similarity arguments as a change in surface roughness, but permanent separation at the lip of a nozzle can be so treated only in its early stages where the perturbation is confined to the inner layer. Further downstream it is no longer profitable to regard the shear layer as a perturbed boundary layer; it is a perturbed mixing layer. If the region where the flow is recognizably a perturbed boundary layer overlaps the region where it is recognizably a perturbed mixing layer, then we can use a technique analogous to that of matched expansions to continue a calculation from one to the other, <u>providing</u> that we have rules for including perturbations in calculations of each type of shear layer. Paradoxically, perturbations which do not produce a change of species may be more difficult to treat than overwhelming ones. Consider the case of flow over a downstream-facing step of height h. If $h/\delta \ll 1$ the perturbation of the boundary layer can be treated by a roughness analysis. If $h/\delta \sim 1$, the flow at reattachment is a boundary layer with its inner layer - at least - in the process of changing into the low-speed side of a mixing layer. After reattachment, the flow nearest the surface starts to change back into a boundary layer so that <u>three</u> shear layers - outer boundary layer, quasi-mixing-layer and inner quasi-boundary-layer - are all interacting. Bearing in mind the difficulties of dealing with interactions of shear layers with the same sign of mean shear we can see that the reattached flow, in which the shear layers are not even well-developed, is highly intractable. By contrast, if $h/\delta \gg 1$ the shear layer at reattachment is recognizably a well-developed mixing layer, perhaps weakly perturbed by streamline curvature and re-entrainment from the recirculating flow region. There is at least some hope of calculating the interaction between this and the inner boundary layer in a rational fashion.

Separation does not necessarily involve such large extra rates of strain as reattachment, and in permanent separation from a bluff body, the boundary layer thickness at separation is usually small compared with the size of the recirculating-flow region: therefore, the entrainment of fluid from the recirculating flow (the key factor in the wake behaviour) will not be greatly affected by extra strain rates near separation. It remains to discuss whether the extra strain rates influence the turbulence structure upstream of separation enough to affect the separation point. Undoubtedly we must expect large effects in the outer layer of the boundary layer; but in the inner layer $\partial U/\partial y$ is large and U is small so that $(\partial U/\partial x)/(\partial U/\partial y)$ - or any other rate-of-strain ratio - is small. On the other hand, the stress gradients in the outer layer are too small, compared with the pressure gradient that induces separation, to have any appreciable effect on the flow: therefore, only the inner-layer turbulence matters and we have just seen that this is not likely to be affected by extra strain rates. Therefore, perhaps surprisingly, bluff-body separation is <u>not</u> primarily a strongly-perturbed flow (for a fuller discussion, see Ref. 29).

5.2 Splitting of a turbulent flow

Large changes must occur in turbulent flows which are split by contact with a solid body. The random vortex lines which are forced to wrap around the body are stretched out in the stream direction and it is not immediately clear whether or not the extra turbulent energy thus created appears only very close to the solid surface. The larger eddies split by the body probably tend to <u>lose</u> shear stress (if any) and turbulent energy. The most important cases are the flow round an obstacle, such as a turbomachine blade in a turbulent oncoming flow or a building in the atmospheric boundary layer, the impingement of a jet, and the reattachment of a shear layer, in which part of the mass flow is deflected upstream to supply the entrainment from the separated-flow region. The flow of an unsheared turbulence field round an obstacle has been studied theoretically by Hunt and experimentally by Bearman (both unpublished) in the region near the leading edge where classical rapid-distortion theory is expected to apply, but little seems to be known of the flow further downstream. Turbulence measurements near reattachment have been made by Arie and Rouse (Ref. 30), Tani et al. (Ref. 31), and others (for a review, see Ref. 28): among the curious features are the rapid decrease of uv along the reattaching streamline prior to reattachment and the apparent decrease of turbulent length scale after reattachment. Thin-shear-layer calculation methods fail to represent the flow accurately for a long distance downstream of reattachment.

5.3 Passage of turbulence through shock waves

A normal shock wave produces a very large negative value of $\partial U/\partial x$ for a very short time, without significant values of $\partial V/\partial y$ or $\partial W/\partial z$; thus the density of a fluid element increases. The compression does work against the Reynolds normal stress $-\bar{\rho}\overline{u^2}$, increasing the turbulent energy per unit mass; the shear stress $-\bar{\rho}\overline{uv}$ is increased both immediately via the term $\bar{\rho}\overline{uv}\,\partial U/\partial x$ and eventually, following the increase in $\overline{v^2}$, via $\bar{\rho}\overline{v^2}\,\partial U/\partial y$. An oblique shock wave, which shears a fluid element as well as compressing it, causes a larger immediate change in $-\bar{\rho}\overline{uv}$. As far as I am aware, most of the work on passage of turbulence through a shock wave relates to the emission of noise (a recent example is Ref. 32) rather than the effects on the Reynolds stresses and the phenomena mentioned above have been ignored in calculation methods. It is easy enough to include the extra terms in the Reynolds-stress transport equations but the actual change in Reynolds stress may be smaller than predicted because of the effects of

the extra rates of strain on terms involving the pressure fluctuation, as in the analysis of Crow (Ref. 4) for a step change in $\partial U/\partial y$. Alternatively the fractional change in Reynolds stress might be larger than predicted solely from the extra terms, as seems to be the case with prolonged extra rates of strain (Section 4).

6. CONCLUSIONS AND SUGGESTIONS FOR FUTURE WORK

In many complex turbulent flows, such as those shown in Fig. 1, the flow is recognizably a perturbation of one of the classical thin shear layers to which Prandtl's approximation applies. Nevertheless the three phenomena represented in Fig. 1, namely

(i) interaction between shear layers,

(ii) significant changes in turbulence structure, due to small extra rates of strain,

(iii) large changes in turbulence structure and appearance of more significant stress gradients, due to large extra rates of strain,

cannot be adequately treated by calculation methods developed for simple thin shear layers. Further experimental work is needed before we can develop the more refined calculation methods required for complex turbulent flows. It seems probable that the only calculation methods with a worthwhile range of validity are those based explicitly on empirical closures of the exact "transport" equations for Reynolds stress and turbulence length scale. These calculation methods are supposed to model turbulence phenomena without being too closely linked to particular flow configurations or boundary conditions: therefore, the kind of experimental work indicated is a detailed study of turbulence quantities in a few simple flows exhibiting phenomena like (i) to (iii), above, rather than a large number of unconnected mean-flow measurements (with a few hot wire readings thrown in) in many different engineering situations, as in the past. Briefly, since we can now attempt the development of calculation methods which are oriented towards general phenomena rather than particular hardware, we should do experiments that are phenomenon-oriented rather than hardware-oriented.

A personal choice of the most important tasks for experimenters on the above three phenomena, representing three types of complex turbulent flow, is

(i) Study of turbulent transport of energy or Reynolds stress across a velocity extremum or into another field of turbulence. Conditional sampling ("eddy chasing") is a powerful test for such studies.

(ii) Improvement of current techniques which crudely represent the effects of small extra strain rates by multiplying the eddy viscosity by $[1 + \beta(\text{extra strain rate})/(\partial U/\partial y)]$ where β is a constant of order 10.

(iii) Studies of the effect of extra strain rates (in the xy plane at least) which are too large for linear formulae like the above to be acceptable; also, studies of bifurcation of impinging shear layers. Since separated flows are very easily disturbed by inserting probes, the Doppler (laser) anemometer may be preferable to the hot wire in some cases.

REFERENCES

1. ————— . Annual progress report Oct. 1969-Oct. 1970 "Research in basic aerodynamics", McGill Univ. M.E.R.L. Memo. 70-5, 1970

2. Page, R.H. "Annual report - separated flows 1969-1970", Rutgers Univ., Dept. of Mech. and Aerospace Engg., RU-TR 135-MAE-F, 1970

3. Townsend, A.A. *The Structure of Turbulent Shear Flow*, University Press, Cambridge, 1956

4. Crow, S.C. "Viscoelastic properties of fine-grained incompressible turbulence", J. Fluid Mech., **33**, 1, 1968

5. Daly, B.J. and Harlow, F.H. "Transport equations in turbulence", Phys. Fluids **13**, 2634, 1970

6. Hanjalic, K. "Two-dimensional asymmetric flow in ducts", Ph.D. Thesis, Imperial College, Mech. Engg. Dept., 1970

7. Roberts, L.W. "The prediction of turbulent swirling pipe flow", Imperial College, Mech. Engg. Dept., EF/TN/A/37, 1971

8. Lilley, D.G. and Chigier, N.A. Nonisotropic turbulent stress distribution in swirling flow from mean value distributions. Int. J Heat Mass Transf. **14**, 573, 1971

9. Bradshaw, P. and Terrell, M.G. "Response of a turbulent boundary layer on an infinite swept wing to the sudden removal of pressure gradient", NPL Aero Rep. 1305, 1969

10. Peterson, E.W. "A numerical model of the mean wind and turbulent energy downstream of a change in surface roughness", Penn. State Univ., Center for Air Environment Studies, Pub. 102-69, 1969

11. Eskinazi, S. "Mixing of wakes in a turbulent shear flow", NASA TND-83, 1959

12. Davies, E.B. and Young, A.D. "Streamwise edge effects in the turbulent boundary layer on a flat plate of finite aspect ratio", ARC R. & M. 3367, 1963

13. Gessner, F.2. and Jones, J.B. "Fully-developed turbulent flow in 1   gular channels", J. Fluid Mech. **23**, 689, 1965

14. Bragg, G.M. "The turbulent boundary layer in a corner", J. Fluid Mech. **36**, 485, 1969

C-8

15. Krajewski, B. "Determination of turbulent velocity field in a rectilinear duct with non-circular cross-section", Int. J. Heat Mass Transf. *13*, 1819, 1970

16. Perkins, H.J. "The formation of streamwise vorticity in turbulent flow", J. Fluid Mech. *44*, 721, 1970

17. Staff of the Aerodynamics Division, NPL "On the measurement of local surface friction on a flat plate by means of Preston tubes", ARC R & M, 3185, 1961

18. Spangler, J.G. and Wells, C.S. "Effects of spiral longitudinal vortices on turbulent boundary layer skin friction", NASA CR-145, 1964

19. Bradshaw, P., Dean, R.B. and McEligot, D.M. "Calculation of interacting turbulent shear layers: duct flow", Imperial College, Aero. Dept., Rep. 71-14 ,1971

20. Watson, R.C., Rose, W.C., Morris, S.J. and Gallo, W.F. "Studies of the interaction of a turbulent boundary layer and a shock wave at Mach numbers between 2 and 10", NASA SP-216, 1969

21. Hussain, A.K.M.F. and Reynolds, W.C. "The mechanics of a perturbation wave in turbulent shear flow", Stanford Univ. Thermosciences Divn., Rept FM-6, 1970

22. Bradshaw, P. "The analogy between streamline curvature and buoyancy in turbulent shear flow", J. Fluid Mech. *36*, 177, 1969

23. Tucker, H.J. "The distortion of turbulence by irrotational strain", McGill Univ., Mech. Engg. Dept. Rep. 70-7, 1970

24. Keffer, J.F. "The uniform distortion of a turbulent wake", J. Fluid Mech. *22*, 135, 1965

25. Keffer, J.F. "A note on the expansion of turbulent wakes", J. Fluid Mech. *28*, 183, 1967

26. Winter, K.G., Rotta, J.C. and Smith, K.G. "Studies of the turbulent boundary layer on a waisted body of revolution in subsonic and supersonic flow", A.R.C. R. & M. 3633, 1968

27. Gartshore, I.S. "The streamwise development of two-dimensional wall jets and other two-dimensional turbulent shear flows". Ph.D. Thesis, McGill Univ., Dept. of Mech. Engg., 1965

28. Bradshaw, P. and Wong, F.Y.F. "The relaxation of a turbulent shear layer after reattachment", Imperial College, Aero. Dept. Rep. 71-05, 1971

29. Bradshaw, P. "Note on conditions near a separation line in two-dimensional turbulent flow", N.P.L. Aero Rep. 1232, 1967

30. Arie, M. and Rouse, H. "Experiments on two-dimensional flow over a normal wall", J. Fluid Mech. 1, 129, 1956

31. Tani, I., Iuchi, M. and Komoda, H. "Experimental investigation of flow separation associated with a step or groove", Univ. Tokyo, Aero. Res. Inst. Rep. 364, 1961

32. Arnoldi, R.A. "Aerodynamic broadband noise mechanisms applicable to axial compressors", NASA CR-1743, 1971
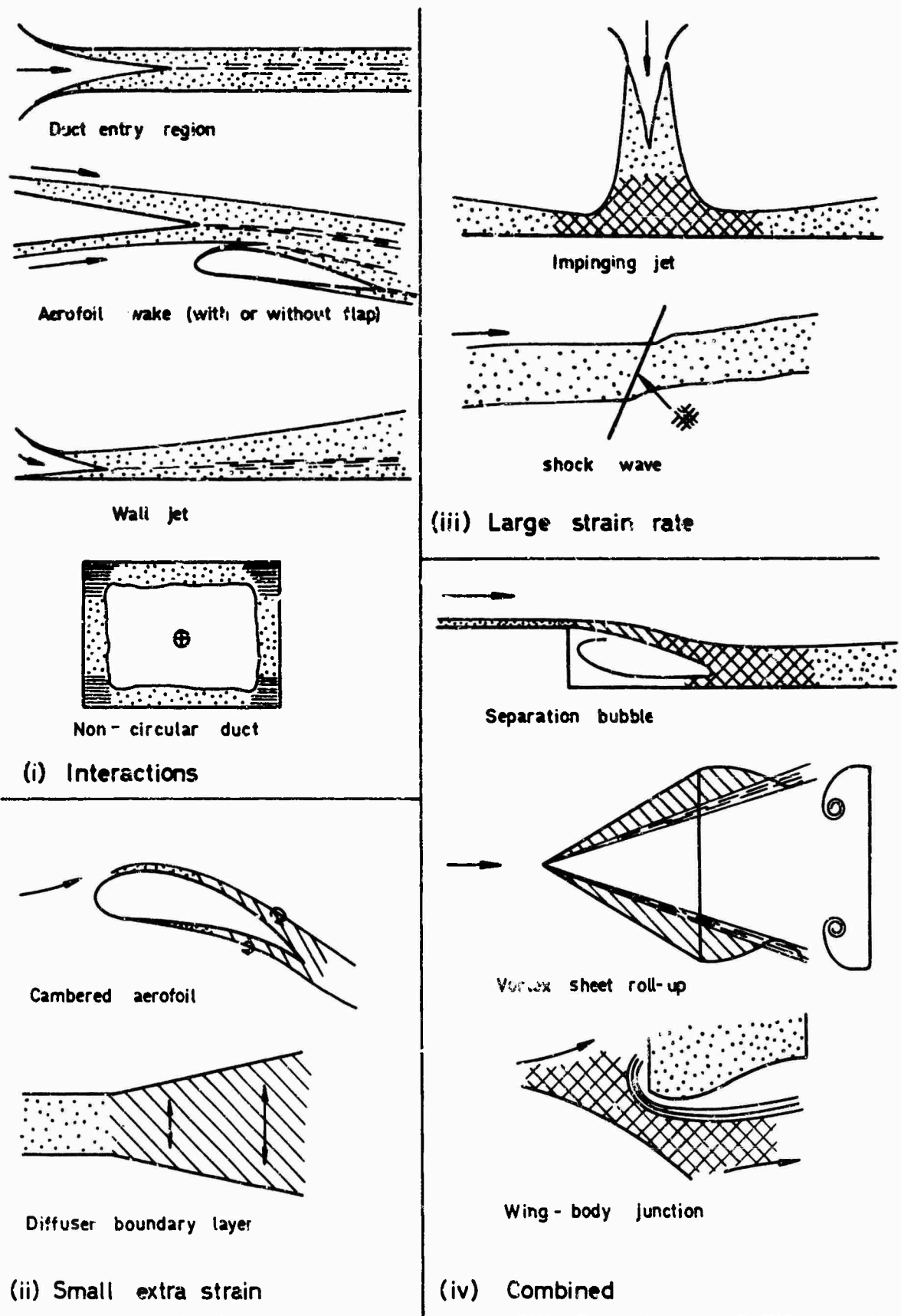
FIG. 1 EXAMPLES OF COMPLEX TURBULENT FLOWS.

Solid surface: ——————

Interaction: ⌐⌐⌐⌐⌐⌐

Thin shear layer: ▬▬▬▬▬▬

Small strain: ///////////

Large strain: ▨▨▨▨▨▨

Approaching
velocity profile

⌐C

Trailing vortices

Sense of rotation
depends on height/
diameter ratio.

⌐
B

B

Projection of
streamlines in
this plane

A

A
Lc

Streamlines in
plane of symmetry

SECTION C-C

"Horseshoe"
vortex core

The flow round the rear
is unsteady and lightly
complicated.

SECTION A-A

Incipient vortex street.

SECTION B-B

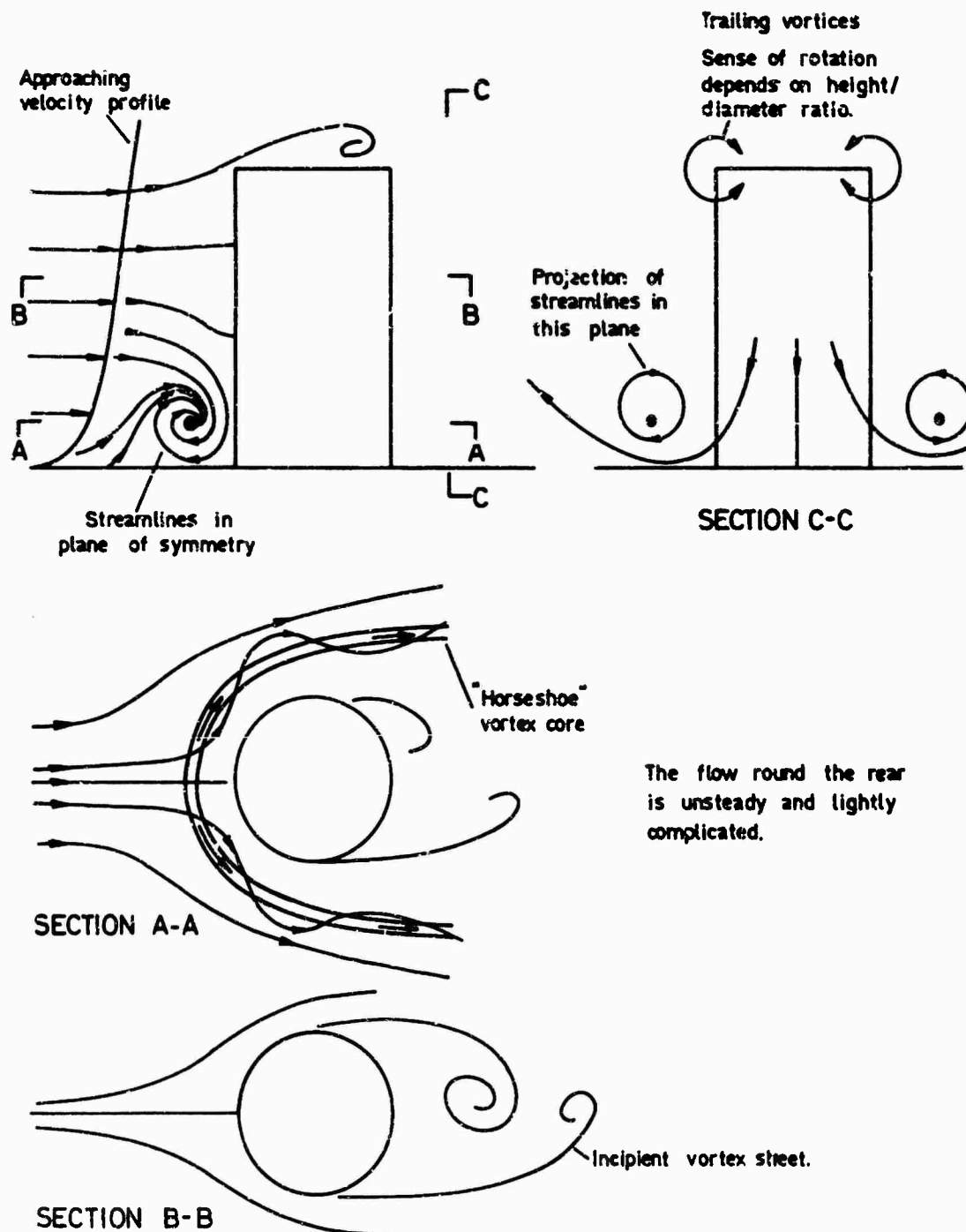FIG. 2 Much simplified sketch of flow past an obstacle
in a boundary layer (building in a wind).

STRUCTURE OF THE REYNOLDS STRESS NEAR THE WALL

by

W. W. Willmarth and S. S. Lu
Department of Aerospace Engineering
The University of Michigan
Ann Arbor, Michigan 48104
USA

SUMMARY

Experimental studies of the flow field near the wall in a turbulent boundary layer using hot wire probes are reported. Measurements of the product uv are studied using the technique of conditional sampling with a large digital computer to single out special events, bursting, when large contributions to turbulent energy and Reynolds stress occur. The criteria used to determine when the product uv is sampled are that the streamwise velocity at the edge of the sublayer has attained a certain value. With this simple criteria we find that 60 percent of the contribution to $\overline{uv}$ is produced when the sublayer velocity is lower than the mean. This result is true at both low, $R_\theta = 4230$, and high, $R_\theta = 38,000$, Reynolds number. With more strict sampling criteria, that the filtered sublayer velocity at two side-by-side points is simultaneously low and decreasing, individual contributions to $\overline{uv}$ as large as $62 \ uv$ have been identified. Additional measurements using correlations between truncated u and v signals reveal that the largest contributions to Reynolds stress and turbulent energy occur when $u < 0$, $v > 0$ or during an intense bursting process and the remainder of the contributions occur during a less intense recovery process. Thus, contributions to the turbulent production and Reynolds stress at a point near the wall are of relatively large magnitude, short duration, and occur intermittently. A rough measure of the intermittency factor for uv at a point near the wall is 0.55 since 99 percent of the contribution to $\overline{uv}$ is made during only 55 percent of the total time.

1.0 INTRODUCTION

This paper is a report of an experimental study of the nature of the unsteady flow near the wall that is responsible for the Reynolds stress developed in the boundary layer on a smooth flat plate. Information about the flow field in the region near the wall is of great importance for a proper understanding of the structure of turbulence in the boundary layer. Just outside the sublayer in the region $20 < y^+ < 200$ the Reynolds stress and the turbulent kinetic energy are a maximum. Somewhat nearer the wall, $y^+ \simeq 10$, the production and dissipation of turbulent kinetic energy are a maximum. Based upon local mean values the turbulent kinetic energy is a maximum of roughly 20 percent of the local mean kinetic energy at approximately $y^+ = 15$ and maintains a high value, greater than 60 percent of the maximum value all the way to the wall within the sublayer.

In the past fifteen years, there have been numerous studies of the turbulent flow field near the wall. We do not have the space for a comprehensive review of all the literature and will confine our discussion to the papers and results pertinent to the present investigation of the structure of the Reynolds stress The primary motivation for the present work on turbulent structure was provided by the studies of Kim, Kline & Reynolds {1}, the work of Corino and Brodkey, {2}, and by our interest in a model for the turbulent structure near the wall, {3}.

The recent studies by Kim, et al., {1}, show that the low speed fluid in the region near the wall occasionally erupts violently into the high speed outer region of the boundary layer. Following Kim, et al. this process is called bursting. During the bursting process Kim et al. measured (from the trajectories of small hydrogen bubbles) the rate of production of turbulent energy. They concluded that "essentially all the turbulent production occurs during bursting periods in the zone $0 < y^+ < 90$." The bursting process, as described in {1}, began with a lifting motion of a streak or filament of low speed fluid within the sublayer. The streaks of low speed fluid were identified by filamentary concentrations of tracer particles introduced into the fluid very near the wall. When the rising filament of low speed fluid reached a height in the range $8 < y^+ < 12$, an oscillatory motion of marked fluid lines (streak lines) within the parcel was observed. The oscillatory motions, which were of various types, appeared to be associated with a swirling motion of the fluid. As the amplitude of the swirling motion of the rising fluid became larger, the pattern "broke up" at a distance from the wall in the range $10 < y^+ < 40$. During the break-up process, a significantly more random chaotic motion occurred in which marked lines of fluid were obliterated owing to the sudden increase in turbulent mixing.

The detailed observations of Kim, et al. were obtained by marking the fluid (water) passing over a slender wire normal and/or parallel to the wall. A succession of current pulses passing from the water into the wire caused electrolysis of the water and subsequent deposition of the lines of small hydrogen bubbles in the water moving past the wire. The motion of the lines of bubbles could be observed until the break-up process occurred. In this way, a significantly greater amount of qualitative information about the flow field near the wall was obtained than had ever been available before.

Corino and Brodkey, {2}, used a high speed motion picture camera to photograph the trajectories of very small particles suspended in the flow. The camera was mounted on a traversing mechanism so that the motions within the convected flow structure responsible for the bursting phenomena could be kept in view as the pattern was swept downstream. The observations of the bursting phenomena reported by Corino and Brodkey are in essential agreement with the observations reported by Kim, et al. Corino and

Brodkey observed the motion of all the fluid particles passing through the field of view of the camera. They were able to identify additional features of the break-up process that could not be observed by marking only the fluid elements that passed over the upstream bubble generating wire used by Kim, et al.

The sequence of events before and after chaotic breakdown during the bursting process, that Corino and Brodkey reported, began with the formation of a low speed parcel of fluid near the wall, $0 < y^+ < 30$. The velocity of the low speed region was often as low as 50 percent of the local mean velocity with very little streamwise velocity gradient within the low speed region. After a low speed region had formed within the view of the camera, the next step occurred, called acceleration by Corino and Brodkey. During acceleration a much larger scale high speed parcel of fluid came into view and by "interaction" began to accelerate the fluid. The high speed fluid often entered almost parallel to the wall or moving slightly downward toward the wall. Occasionally, the high speed fluid entered with larger vertical velocity, 20 percent of the streamwise component, and moved towards the wall at an angle of 5° to 15°

At various times the entering high speed fluid appeared to occupy the same region on the photograph as the low speed fluid. The explanation is that the high speed region was within the field of view but at a different spanwise station to one side or the other of the low speed parcel of fluid. It appears that the spanwise variation revealed by the above observation may be related to the observation of a streaky structure of spanwise variation within the sublayer reported by Kline, Reynolds, Schraub & Runstadler, {4}. This is supported by the fact that the field of view was of the right order of magnitude $z^+ \sim 18$ to allow observation of a single transverse shear layer formed by adjacent high and low speed regions near the wall where the streaks have a typical spanwise spacing of $z^+ = 100$. On the other hand, one must be cautious because the Reynolds number of Corino and Brodkey's flow was considerably higher than that of the flow studied by Kim, et al. Laufer, {5}, has reported that as the Reynolds number increases, the length scale of the spanwise variation within the sublayer is changed.

Continuing with the description of the acceleration phase, if the high and low speed fluid met at the same spanwise station, the interaction was often immediate and the low speed fluid above a particular y^+ location was accelerated and often a very sharp interface or shear layer between accelerated and retarded fluid was formed. If the high and low speed fluid were at different spanwise stations, acceleration of the low speed fluid took a longer time and gradually the spanwise velocity variation began to disappear. The next step in the process was called ejection by Corino and Brodkey. During ejection one or more correlated (in time) or sometimes uncorrelated (in time) eruptions of low speed fluid occurred immediately or shortly after the start of the acceleration process. The ejections of low speed fluid were of rather small scale, the maximum dimension (streamwise length) of the field of view was only $x^+ = 62$. Once ejection began, the process proceeded rapidly to a fully developed stage during which a continuing ejection of low speed fluid persisted for varying periods of time and then gradually ceased. The length scale of ejected fluid elements was small, of the order of $7 < z^+ < 2v$ and $20 < x^+ < 40$. Most of the ejections occurred at distances from the wall in the range $5 < y^+ < 15$. When the ejected low speed fluid encountered the interface between high and low speed fluid, at the high shear layer, a violent interaction occurred with intense abrupt, and chaotic movements. The entire interaction structure was of very small scale and destroyed the identity of individual fluid elements. The intense interaction continued as more fluid was ejected. The end result was the creation of a relatively large scale region of turbulent motion reaching into the sublayer as the violent interaction region spread out in all directions and disrupted the ejected fluid parcels.

The ejection or bursting phase ended with the entry from upstream of fluid directed primarily in the stream direction with a velocity approximating the normal mean velocity profile. The entering high speed fluid carried away the retarded fluid remaining from the ejection process and was called the sweep event by Corino and Brodkey.

Both Corino and Brodkey and Kim, et al. agree that the bursting phenomena is an important process for turbulent energy production. Corino and Brodkey conclude that: "the results do indicate that the ejections are very energetic and well correlated so as to be a major contributor to the Reynolds stress and thus the production of turbulent energy." Their rough estimates of the Reynolds stress contribution during bursting from a small sample of bursting events indicated that 70 percent of the Reynolds stress was produced during ejections.

Using the above information as a background we have designed a number of experiments using hot wire anemometers to make quantitative measurements of the flow field near the wall. The experiments are designed to provide additional information about the turbulent velocity field that is difficult to obtain with flow visualization methods. It should be noted that fluid velocity measurements at a given point in the flow cannot be made using photographs of bubble trajectories downstream of the bubble generating wire unless the bubbles happen to pass through the given point. Also, fluid velocity measurements at a given point in the flow cannot be made using the motion picture photographs of numerous small suspended particles unless the field of view can be made very small relative to the flow field in question. In Corino and Brodkey's photographs the depth of field was of the order $z^+ = 20$ which is as large as the typical size of an ejected region of low speed fluid near the wall.

The experiments that are discussed in the body of this report consist primarily of various fluid velocity measurements near the wall that we have made at random times during the past few years. The measurements show substantial agreement with the process of bursting as observed and described by Kim, et al. and by Corino and Brodkey. We are able to give quantitative support to the idea that the bursting process is important for the production of turbulent energy. In addition, the above flow visualization results for the bursting process; the results of our present measurements and of our previous pressure-velocity correlation measurements, {6}, all agree with a simplified model that we have proposed, Willmarth and Tu, {3}, for the turbulent structure near the wall.

2.0 EXPERIMENTAL APPARATUS AND METHODS

The experiments were conducted in a thick turbulent boundary layer developed on the smooth floor of the 5 x 7 ft. low speed wind tunnel of the Department of Aerospace Engineering at The University of Michigan. Some pertinent characteristics of this facility are discussed in {7}

2.1 Mean Boundary Layer Characteristics

Most of the detailed measurements were done in a boundary layer with a thick sublayer that is produced at low free stream speeds, $U_\infty \simeq$ 20 ft./sec. Some measurements were also made at higher free stream speeds, $U_\infty \simeq$ 200 ft./sec., in this case the sublayer is much thinner. Owing to the small scale of the bursting phenomena near the wall, we preferred to use the boundary layer with as large a sublayer thickness as possible but found that at very low speeds $5 < U_\infty < 10$ ft./sec., with natural transition, the turbulent boundary layer was not fully developed at the rearmost station, x = 35 ft. of the test section. The lowest possible speed was 20 ft/sec.

Typical mean velocity profiles measured with an impact pressure tube and with a hot wire are displayed in fig. 1 and Table 1 lists the pertinent parameters for the two fully developed flat plate boundary layers. We emphasize here that artificial tripping and roughness were not used because we did not desire to introduce additional unnatural flow disturbances which might not die out before reaching the measurement station. We believe that flow structure measurements and/or measurements of fluctuating quantities are more sensitive to artificial upstream disturbances than are measurements of mean quantities.

Table 1

Properties of the Actual and Ideal Turbulent Boundary Layer
(as tabulated by Coles, {13})

U_∞ ft./sec.	R_θ	δ ft.	$\delta*$ ft.	θ ft.	$\delta*/\theta$	u_τ/u_∞	R_x	Remarks
19.7	4230	0.405	0.494	0.0363	1.365	.0386	---	Transition Location Not Known
---	3800	---	---	---	1.383	.0387	2.1×10^6	Cole's ideal boundary layer
204	38,000	0.42	0.041	0.0315	1.30	0.0326	3.1×10^7	See reference {3}
---	39,000	---	---	---	1.30	0.0318	3.2×10^7	Cole's ideal boundary layer

2.2 Hot Wire Anemometer Probes

The bulk of the measurements were made with hot wire anemometer probes of various types. The measurements of streamwise velocity very near the wall were made with platinum wires of diameter 1.5×10^{-4} in. The wires were glued directly on the wall 0.002 in. from the surface and were .032 in. long for the high speed measurements. The technique has been described by Tu and Willmarth, {3}. For low speed measurements the wires were soldered to the tips of needles protruding through the wall. The dimensions of the wires used at low speeds were .037 in. from the wall with lengths of 0.10 in. and 0.045 in. These wires were made by etching the silver away from the platinum wire, soldering the wire to one needle tip and letting it hang, with a small weight on the end, near the lower needle tip. Then the hanging wire was soldered to the lower needle tip. The surface tension of the molten solder was very effective in pulling the wire onto the needle tip.

The streamwise vorticity component was measured using a probe construction described by Kovasznay {8}. The probe was constructed by Dr. Bo Jang Tu in 1968 using four 2×10^{-4} in. diameter tungsten wires that were copper plated before soldering to the four needle probe. Careful matching of the resistance of the four wires using a process of individual etching of copper from individual wires made the probe insensitive to velocity fluctuations of a scale larger than the probe. The etching process was accomplished using a tiny bubble of copper sulfate solution suspended in a loop of thin platinum wire. The wires were matched so that the difference in the resistance of the four wires was less than three percent of the nominal wire resistance. The probe was calibrated using a specially constructed oscillating mechanism and gave a linear response to the imposed vorticity caused by rotating the probe about its streamwise axis.

The Reynolds stress was measured using the usual x wire configuration of 2×10^{-4} in. diameter copper plated tungsten wires. Each wire was soldered on needles 0.07 in. apart at angles of $\pm 45^\circ$ to the flow. The distance between the wire centers was 0.04 in. and the wires were 0.035 in. long. The wire resistance was approximately three ohms when cold and the difference in resistance between a pair of wires was less than three percent of the nominal wire resistance.

2.3 Hot Wire Anemometer Equipment

The hot wire signals were processed using both constant current and constant temperature equipment. The electrical signals from the vorticity probes and the x wire probes were obtained when the wires were heated using constant current operation. The signals were amplified and compensated using techniques as described by Kovasznay. {8}.

In the case of the streamwise vorticity probe the four wires were connected in a Wheatstone bridge configuration with a constant current supply across two arms of the bridge and the input of a differential amplifier across the other two arms. In our system we used a Shapiro and Edwards amplifier and compensator which has one side of the input grounded. The constant current supply was obtained from a pack of batteries isolated from ground.

Each wire of the x wire probe was separately heated at constant current and a separate channel of amplification and compensation was used for each wire. The wires, amplifier gain, and amount of

compensation in each channel were carefully matched so that they were identical within a few percent. Each wire was separately calibrated in a steady laminar flow at various velocities. The calibrations differed by less than three percent and obeyed King's law with good accuracy. The wires were operated at an overheating ratio of one-half. The time constant of each wire was approximately 9.5×10^{-4} sec. near the wall in the low speed boundary layer and 5×10^{-4} sec. in the high speed boundary layer. The above values represent the maximum amount of compensation necessary near the wall. We carefully compared the gain and phase shift of each channel with compensation network operating over the entire frequency band, $1 < f < 20,000$ Hz., using a Lissajous figure displayed on matched x and y channels of a Hewlett Packard oscilloscope. The gain and phase shift did not differ by more than three percent over the entire bandwidth.

The streamwise velocity signal at the edge of the sublayer that was used for conditional sampling measurements was produced with a Miller constant temperature hot wire set or occasionally with a DISA Model 55 D05 constant temperature hot wire set. The Miller hot wire set is based on a design reported by Kovasznay, et al. (9). We did not use linearizers for the hot wire signals from the wires in the sublayer. We know that some error in the signal u_w is introduced on this account. However, the signal representing streamwise sublayer velocity, u_w, was only used to determine the condition of the sublayer in the conditional sampling measurements. The actual values of the vorticity and Reynolds stress in the sampled measurements are not affected.

2.4 Other Electronic Equipment

The signals obtained from the hot wires were recorded on magnetic tape using a frequency modulated system installed in a three-channel Ampex Model FR-1100 tape recorder. We also used a six-channel Ampex Model 300A recorder with the same frequency modulated electronic system. The analog data were stored on reels of magnetic tape and could be played back later at faster or slower speed.

The initial data reduction was accomplished using an analog scheme. We constructed a small analog computer to compute the Reynolds stress from the signals produced by the two wires on the x probe. The scheme is outlined in fig. 2. The summing amplifier was a Fairchild ADO-25 and the multiplier was an Intronics Model M502 wide-band analog multiplier. The analog computation was accurate within one percent in amplitude and phase in the range $0 < f < 20,000$ Hz.

The Reynolds stress signal from the multiplier was detected by a Princeton Applied Research Model TDH-9 Wave Form Eductor. The sampling cycle of the Wave Form Eductor was triggered by a signal derived from a comparitor and pulse shaping circuit made up from Fairchild 2N2422 and 2N3904 transistors. We gratefully acknowledge the assistance of Professor V. Kibens who showed us how to design the circuit. The circuit was designed to produce an output pulse when the input signal, the velocity at the sublayer edge, reached a certain level (which could be adjusted) with either positive or negative slope. Details of the circuit are available by writing to the authors. The stored samples in the wave form eductor were plotted out on a Mosley x-y plotter.

Figure 3 is a sketch of the scheme for the conditional sampling. The trigger level circuit produces a pulse which accuates a single sampling cycle of the wave form Eductor. The wave form Eductor consists of a bank of 100 capacitors with appropriate switching transistors that sequentially store samples of the Reynolds stress signal, uv. Figure 3 is a simplified version of the actual procedure because the triggering signal in fig. 3 occurs too late (in the middle of the desired sample) if the Reynolds stress signal uv is sent to the eductor at the same time as the triggering signal. What was done to eliminate this problem was to introduce a time advance equal to one-half the sampling time into the channel carrying the signal, u_w, representing the velocity at the wall. This was accomplished with a movable playback head on the FR-1100 tape recorder.

Numerous samples of Reynolds stress data were required to obtain stable average values. We did completely reduce the data from a single high speed run. However, it required a great deal of time and careful work owing to the long averaging time required by the wave form Eductor. So much time was required for the single run (about two man-weeks of continuous running of the tape recorder) that the magnetic tape finally began to wear out. If the data had been reduced without a tape recorder the wind tunnel running charge would have been prohibitive. Further details about the analog data reduction process are given in the next section where the actual experimental measurements are discussed.

We were forced to find a better way to reduce the data. We decided to use the large IBM 360/67 digital computer at The University of Michigan. To obtain efficient usage of the computer, it was necessary to convert the analog data to digital form and record it on magnetic tape. The only analog-to-digital converter available for our use was a Redcor Model 632 A/D Converter which was a part of a Control Data Corporation Model 160A digital computer which controlled a Control Data Corporation Model 164 digital magnetic tape system. The A/D converter and multiplexer could operate with three or four-channel input at a rate of 1000 conversions per second for each channel. This conversion rate was deemed adequate for a 100 Hz. signal (i.e., one would have ten data points per cycle). It was therefore necessary to reduce the speed of the magnetic tape recorder when playing back data. The speed was reduced by a factor of eight by recording data at 60 in./sec. and playing it back at 7.5 in./sec. In this way, our digitized data were accurate to frequencies of the order of 1000 Hz. Fortunately, the signals from the hot wires in the low speed, $U_\infty = 20$ ft./sec., boundary layer contain very little energy above 1000 Hz.

After converting the raw data to digital form, the rest of the data reduction—including plotting in some cases—was done by the IBM 360/67 computer using simple FORTRAN programs.

Further details of the data reduction are given later when the experiments are discussed. We would like to point out at this time that digital data reduction for conditional sampling measurements has definite advantages over analog sampling methods using capacitor storage devices. The advantage takes the form of flexibility in that various operations like comparison of signals, integration over short intervals, single

samples or samples of clipped (i. e., truncated signals), are very simple to program. Also, another very important advantage is that less raw data is required for digital conditional sampling measurements because none of the data is lost or used to charge up capacitors as in the wave form Eductor where each capacitor starts out with zero charge and is provided with a finite "leak" or time constant. It turned out that the amount of raw data required to obtain stable averages of digital data was about one-twentieth the amount required using analog methods.

3.0 EXPERIMENTAL MEASUREMENTS

The measurements described below were made over a considerable time span. For example, the velocity measurements at the wall using a ladder array of hot wires were made in 1968 by Dr. Bo Jang Tu in the high speed boundary layer as well as the measurements of $\overline{u \, v}_x$ which were made at approximately the same time. During the last year, 1970, we made most of the measurements in the low speed boundary layer.

3.1 Measurements of the Velocity in the Sublayer

The instantaneous streamwise velocity distribution in the sublayer was measured using four hot wires arranged in a "ladder" array as shown in fig. 4. The hot wire array was constructed by Dr. Bo Jang Tu. One will note that the wires are rather long, being about $z^+ = 265$, when immersed in the sublayer of the high speed boundary layer. Note that the spanwise variation represented by the low speed streaks in the sublayer at low Reynolds number reported by Kline. et al., {14}, had a spanwise separation of $z^+ = 100$.

The data obtained from the wires is displayed in fig. 5. The data shows that the large scale streamwise velocity fluctuations that occur in the sublayer can be thought of as a time varying mean shear. This indicates that the streamwise velocity above a given point on the wall can be represented approximately by the formula

$$u_w = const. \; y \; f(t) \tag{1}$$

There are obviously transverse and vertical velocity fluctuations occurring also in and near the sublayer; however, these are of much smaller magnitude. For example, the root-mean-square fluctuating velocity u' (here and elsewhere in this paper a prime denotes a root-mean-square value) is about three times and six times as large as w' and v', respectively at $y^+ = 10$, see Laufer, {10}. As one approaches the wall, the ratio of w'/y and v'/y approach zero; however, u'/y approaches a constant value. This means that the transverse velocity field from the streamwise vorticity responsible for the low speed streaks observed by Kline, et al., {1, 4}, in the sublayer must be considerably less energetic than the streamwise velocity fluctuations. The primary result of the above measurements of streamwise velocity is that the large scale energetic fluctuating streamwise velocity in the sublayer $y^+ < 5$ varies linearly with distance from the wall. Therefore, a single wire at $y^+ < 5$ can be used to deduce the streamwise fluctuating velocity field all the way to the wall. Note that the above measurements were made at high Reynolds number when the sublayer is very thin. No one has yet shown that the streaky structure in the sublayer exists at high Reynolds number. It is conjectured by the authors that the low speed streaks may not be very important for boundary layers at large Reynolds number because the ratio of sublayer thickness to boundary layer thickness becomes very small. For example, in our tests, the ratio is 3×10^{-3} at $R_\theta = 4230$ but becomes 3×10^{-4} at $R_\theta \sim 38,000$. The turbulence is so much more energetic at large Reynolds number relative to viscous forces that it may continually disturb the sublayer, thus preventing low speed streak formation.

3.2 General Considerations about the Conditionally Sampled Measurements of Reynolds Stress

We were introduced to the concepts and methods of conditional sampling (using analog methods) by V. Kibens. See Kovasznay, Kibens & Blackwelder, {11}, for an explanation of various concepts and methods that they developed. Our first conditionally sampled measurements of Reynolds stress were made in the high speed boundary layer, $R_\theta = 38,000$, using analog methods and a wave form Eductor as described in Section 2. As explained in Section 2, the data averaging process during the analog sampling measurements was very time-consuming. These first measurements were exploratory in nature, but will be reported below (see Section 3.2.3). We found that the measurements were possible but the spatial resolution of the flow field near the wall was poor because the sublayer thickness was very small, $y^+ = 7.5$ corresponded to y = 0.002 in. For this reason, we altered the experiment and used a lower stream speed (approximately 20 ft./sec.) to reduce the friction velocity and thus increase the sublayer thickness. The distance between test section entrance and measuring station was approximately 35 ft. This gave a thick turbulent boundary layer of approximately the same thickness as at high speed but with a much thicker sublayer, at $y^+ = 7.5$, y = 0.019 in., see also Table 1 and fig. 1.

Another change in the experiment was the use of the large digital computer to perform the conditionally sampled measurements. The details about the hardware have been discussed in Section 2. The program for conditional sampling was simple in concept. A block of digitized data from the velocity at the wall, u_w, and from the velocity components at the two wires on the x probe, u_{1n} and u_{2n}, (see fig. 2) was read into the computer memory from the magnetic tape. The computer than compared each digitized value of the velocity at the wall, u_w, with the desired constant level of the velocity u_w representing the sampling criteria. This level is proportional to the trigger level, labeled T.L., on the plots. When the value u_w was equal to T.L. u'_w, within a certain small error, the computer was told to store the product of the sum and difference of u_{1n} and u_{2n} for each digitized data point in a certain time interval before and after the sampling criteria were met. Actually, the sampling procedure was simple. The program was required to detect the change in sign of the difference, u_w/u'_w - T.L. Note also that the sign of the slope of u_w can also be determined from the change in sign of the difference, u_w/u'_w - T.L., and this was also part of the sampling procedure.

The sampled data were digitized samples of the product uv where for two crossed wires at 90°, see fig. 2.

$$uv = [(u_{1n} + u_{2n})/\sqrt{2}][(u_{1n} - u_{2n})/\sqrt{2}] = (u_{1n}^2 - u_{2n}^2)/2 \qquad (2)$$

It should be noted that the product uv represents only turbulent transport across a line y = const. of streamwise momentum fluctuations. Thus, uv is not the entire fluctuating stress caused by turbulence on a surface, y = const. because the mean streamwise momentum is also transported by v fluctuations and the mean V velocity also transports fluctuations in streamwise momentum. The true fluctuating stress is, (U + u)(V + v) - UV. We are indebted to S. Corrsin for reminding us of this fact. In the boundary layer, $V = (9/U_\infty \delta/L)$ so that the most important terms in the fluctuating stress are Uv and uv. We have not studied the term Uv in detail. A few measurements show that contributions from this term are appreciable but the interpretation became quite complicated and a discussion of these results will be included in a report at a later date. For the present, we will confine our discussion to the term uv which is the only term ultimately contributing to the average of the fluctuating stress, i.e., the Reynolds stress $= \overline{uv}$.

Returning to the discussion of the computerized data reduction process, we found that to avoid excessive computing time and expense it was necessary to read the data from the tape into the computer as infrequently as possible. Therefore, the program was designed to perform the conditional sampling for all values of T.L. and for both positive and negative slope of u_w in one pass or reading of the tape. Files were set up for storage of sampled data for each trigger level and slope. After the program was run, the stored data was plotted in final form using a CalComp plotting system. It was not feasible to use a printed digital output because the sheer mass of data was too great for efficient comprehension.

Our first analog conditionally sampled data was obtained using the full bandwidth of the signal, u_w. We found that numerous extraneous samples were obtained compared to conditionally sampled data obtained when high frequencies were removed from the signal, u_w. We therefore conditionally sampled the low speed contributions to the Reynolds stress using both filtered and unfiltered u_w signals. The analog filter was a low pass Butterworth filter of third order with half power point at 10 Hz. The filter was constructed using an Applied Dynamics PB-64 Analog Computer. The signal, u_w, was filtered before the recorded analog data were digitized. Since the analog data were played back from magnetic tape at 1/8 the recording speed before A/D conversion, the filter half power point was actually 80 Hz. in real time.

3.2.1 Conditionally Sampled Measurements of Reynolds Stress at a Single Point near the Wall

The plots of sampled data that we obtained are very numerous. In order to conserve space we show in fig. 6 only a few examples of plots of sampled Reynolds stress for the low speed boundary layer when the signal u_w was filtered to remove high frequencies. The hot wire producing the signal u_w is located at a distance y = 0.037 in. from the wall or $y^+ = 16.2$. This location was chosen based on Corino and Brodkey's (2) observation that the approximate center of the low speed region near the wall was at $y^+ = 15$. The data of fig. 6 show sampled contributions to uv for various trigger levels, $u_w/u_w' = \pm 2.15, \pm 1.07, \pm 0.54$ and 0. The quantity uv was measured with the x wire located directly above the point where u_w was measured. The center of the x wire was located at y = 0.07 in. or $y^+ = 30$. Again, Corino and Brodkey, (2), indicate that this is the approximate location of the region of violent interaction.

In fig. 6 the ordinate labeled Reynolds stress (uv) is the ratio of the average value of the samples of uv to the overall average value of uv, i.e., $\overline{uv}$. Thus, the ordinate is

$$\text{Reynolds stress (uv)} = 1/N \sum_{i=1}^{N} (uv)_i/\overline{uv} = \widetilde{uv}/\overline{uv} \qquad (3)$$

In Eq. (3) N is the number of stored samples that have accumulated in each storage file when the data reduction is complete. The abscissa of the plots in fig. 6 labeled time (dimensionless) is the dimensionless time tU_∞/δ^*, where time is zero at the beginning of the sample. Note that the sampling criteria $u_w/u_w' = $ T.L. with negative slope occurs at the midpoint of the sampled data.

Finally, one should note that in fig. 6, see Eq. (3), the ratio $\widetilde{uv}/\overline{uv}$ should be one if the N samples are selected at random times or if the sampling criteria are unrelated to the data that is being sampled. Accordingly, it is clear that the large significant contributions to $\overline{uv}$, uv $\simeq 5 \overline{uv}$, are made with T.L. $= -2.15$ (see fig. 6a) at dimensionless time $tU_\infty/\delta^* = 7.0$. At T.L. = 0, fig. 6d the contribution is uv $\simeq 1.4 \overline{uv}$ at the center of the interval. For positive T.L., the contribution to $\overline{uv}$ is somewhat less than one at the center of the sampling interval, see figs. 6c,f,g.

The data of fig. 6 are typical of all the sampled data for uv that we have collected except that the data of fig. 6 show the largest values of $\widetilde{uv}$ because the sampling criteria have been improved by filtering out high frequency noise from the signal u_w.

We will now consider how one can obtain a quantitative assessment of the total contribution of $\widetilde{uv}$ to $\overline{uv}$ as a function of T.L. The data of fig. 6 do not contain enough information to assess the relative contribution made by uv at each T.L. We need information about the frequency of occurrence, or the relative number, of samples obtained at each T.L. This information can be obtained from the probability density of the signal u_w. A program was written to generate an indicator function (see Lumley, (12), for a complete explanation) $\phi(T.L.; t)$ for many closely spaced values of T.L. Here the indicator function is defined as

$$\phi(T.L.; t) = \begin{cases} 1 & u_w/u_w' < T.L. \\ 0 & u_w/u_w' \geq T.L. \end{cases} \qquad (4)$$

From time averages of the indicator function, the probability distribution of u_w was obtained. By differentiation with respect to u_w, β_{u_w}, the probability density of u_w, was obtained and is shown in fig. 7. The

probability density for a Gaussian distribution is also shown for reference in fig. 7.

With the data of fig. 7 at hand, one can now obtain a qualitative measure of the contribution to uv to $\overline{uv}$ as a function of T. L. This measure is obtained by multiplying the value of $uv/\overline{uv}$ at the time the triggering criteria, u_w/u'_w = T. L., was met by the probability density at that T. L. The result is shown in fig. 8. The ordinate in fig. 8, $\Delta\widetilde{uv}/\overline{uv}$ is

$$\Delta\widetilde{uv}/\overline{uv} = \widetilde{uv}/\overline{uv}\,\beta_{u_w} \tag{5}$$

Note that the integral,

$$1/2 \int_{-\infty}^{\infty} [(\Delta\widetilde{uv}/\overline{uv})_{-slope} + (\Delta\widetilde{uv}/\overline{uv})_{+slope}]d(T.L.) = 1 \tag{6}$$

so that the ordinate in fig. 8 is a measure of the contribution per unit T. L. of sampled uv data to the value of $\overline{uv}$. The ordinate (5) for negative slope is not symmetric about the origin T. L. = 0 and has a maximum value at T. L. $\simeq$ - 0.7. The data for positive slope is also shown in fig. 8 and is much more symmetrical about the origin T. L. = 0. This indicates that greater contributions to Reynolds stress occur when the velocity at the wall u_w is less than the mean value and decreasing. This result adds additional information to what is known from the visual studies of Kim, et al., [1], and Corino and Brodkey, [2]. In the visual studies the velocity at the wall was not measured but it was determined in both [1] and [2] that u_w was low during bursting. Kim, et al. also state that the velocity profile was inflectional. We can now add that from the present data the bursts occur when the velocity profile first becomes inflectional, i.e., when the wall velocity is low and decreasing. It will be recalled, from the result of fig. 5, that when the sublayer velocity decreases at a given point it also decreases at every point in the sublayer above or below the given point, the decrease being proportional to distance from the wall.

When the slope of u_w is positive, a low value of u_w is not related to unusually large contributions at that time, to $\overline{uv}$. As a matter of fact, the conditionally sampled data for positive slope (analogous to the data of fig. 6) show that for T. L. < 0 unusually large contributions to uv are made but at times prior to the time when u_w/u'_w = T. L. with positive slope. This indicates that when u_w/u'_w = T. L. with positive slope the burst occurred earlier (when u_w/u'_w = T. L. with negative slope) and now when u_w is increasing the bursting event is over.

Figure 9 shows the contributions to the Reynolds stress from samples of the signal uv that are obtained at various values, T. L., of the unfiltered velocity u_w, at the wall. The results of fig. 9 should be compared with those of fig. 8. Note that in fig. 9 the curve for negative slope is again unsymmetrical about the origin T. L. = 0 but the difference between the curves for positive and negative slope is much smaller than in fig. 8. This shows that the filtered signal, u_w, provides better criteria for the identification of samples of uv that contribute to the Reynolds stress when u_w decreases. We also should emphasize the fact that in the digital data reduction program a sample of uv was taken whenever u_w/u'_w = T. L. Therefore, if u_w had many rapid changes in value while a burst was occurring the signal u_w might pass through the trigger level more than once during the burst. This would cause the same burst in uv to be stored on top of itself but shifted in time. Therefore, the large contributions to uv would in effect be smeared out and reduced over the sampling interval.

3. 2. 2 Spatial Distribution and Decay of Sampled Reynolds Stress

We have made conditionally sampled measurements of Reynolds stress at various distances from the wall when the x wire is at various locations transverse and downstream from the u_w wire which is located at the point y^+ = 16. 2. The results of these measurements have not yet been fully analyzed. However, we can state that the measurements show that the largest contribution to $\overline{uv}$ from the sampled signal uv, occur when u_w < 0 with negative slope and are confined to a narrow (in the spanwise direction) region near the wall and downstream of the u_w wire. The approximate dimensions of the narrow region are x < 2. 5 in., y < 0. 35 in. and z < 0. 35 in. or x^+ < 1110, y^+ < 154 and z^+ < 154. There is also evidence that the spanwise extent of the region in which appreciable contributions to the sampled Reynolds stress occur increases in width downstream of the point where u_w is measured. For example, no contribution, $\widetilde{uv}/\overline{uv}$ = 1, was obtained at x = .2 in., y = .07 in., z = .08 in., but an appreciable contribution was obtained at x = .5 in., y = .08 in., z = 0. 1 in. The angle θ, between the stream direction and edge of the region of contributions to $\overline{uv}$ (i. e., $\widetilde{uv} > \overline{uv}$) is therefore in the range $12^\circ < \theta < 23.5^\circ$. The disturbance is also convected downstream. An approximate convection velocity was measured from the change in the location (in time) of the maximum contribution from the conditional samples uv (for T. L. < 0 with negative slope) at a succession of points downstream of the point where u_w was measured. The convection velocity was approximately the local mean speed at the distance from the wall where uv was measured.

3. 2. 3 Effect of Reynolds Number on Conditionally Sampled Reynolds Stress Measurements

We have not yet investigated in any detail the contributions to $\overline{uv}$ from sampled measurements of uv at high Reynolds number. We have one set of measurements made at R_θ = 38, 000 with analog data reduction. The signal u_w was not filtered to remove extraneous high frequency signals. Nevertheless, appreciable contributions to $\overline{uv}$ were made near the wall when u_w was negative and decreasing. The measurements are in qualitative agreement with the results already described in Section 3. 2. 1, see fig. 9, for a boundary layer at lower Reynolds number R_θ = 4230. The results of the low and high Reynolds number measurements at points downstream from the point where u_w was measured are shown in fig. 10. The ordinate in fig. 10 is

$$<\Delta\widetilde{uv}/\overline{uv}> = 1/2\{(\widetilde{uv}/\overline{uv})_{+slope} + (\widetilde{uv}/\overline{uv})_{-slope}\}\beta \tag{7}$$

which is the average of the contribution from uv for positive and negative slope. As noted in Eq. (6), the area under each curve in fig. 10 should be unity. From the similarity between these two sets of data at widely different Reynolds number and points which correspond, within a factor of 2. 5, in wall variables

x^*, y^* and z^* we can conclude that the burst phenomena still occur when $u_w < 0$ at high R_θ. Note that from the area under each curve for T.L. < 0 we can state that 60 percent of the Reynolds stress at the given downstream location is produced when the upstream velocity near the wall is lower than the mean. We add that for the data in fig. 10 the hot wire near the wall is located at $y = .002$ in. or $y^* = 7.5$ for $R_\theta = 38,000$ and at $y = .019$ in. or $y^* = 8.3$ for $R_\theta = 4230$. This location is nearer the wall than for the data of fig. 8 and fig. 9.

3.2.4 Conditionally Sampled Reynolds Stress Measurements with an Improved Detection Scheme

The use of a low pass filter for the signal u_w resulted in improved detection of contributions to $\overline{uv}$. We then realized that still greater improvement in our detection criteria might result if we used a crude spanwise spatial filter for the detector signal, u_w. To accomplish this, we installed two hot wires side by side at $y = .037$ in. or $y^+ = 16.5$. The wire length was $l = .045$ in. or $l^+ = 20$. The wires were soldered on the tips of three needles at the same streamwise station. The center needle was common to both wires. The distance between the center of each wire was therefore $l = .045$ in. or $l^+ = 20$. This distance is approximately one-fifth of the wavelength of the low speed streak structure observed in the sublayer by Kim, et al., [1].

The sampling criteria that we used with the two velocity signals u_{w_1} and u_{w_2} from the wires side by side near the wall was based on the idea that if a burst event occurred directly above them, both u_{w_1} and u_{w_2} would be decreasing and less than the mean. In other words, the plane between the two wires that is normal to the wall and is parallel to the free stream would be a plane of symmetry for the burst event if $u_{w_1} = u_{w_2}$ when both decreased.

We digitized four channels of data obtained at $U_\infty = 20$ ft./sec. with the x wire slightly downstream from and centered between the wires producing the signals u_{w_1} and u_{w_2}. The x wire was located at $y = 0.07$ in. from the wall (or $y^+ = 30.5$) and was $x = 0.18$ in. (or $x^+ = 78.5$) downstream from the wires u_{w_1} and u_{w_2}. Upon examining the data, we could observe that there were a number of occasions when, for negative T.L., $u_{w_1}/u'_w < $ T.L. with negative slope at the same time that $u_{w_2}/u'_w < $ T.L. with negative slope. However, in many instances, even when high frequencies were removed from both u_{w_1} and u_{w_2} (as described in Section 3.2.1), the two signals did not both remain less than T.L. for the same length of time. It was clear that some kind of an integral condition over time had to be added to the sampling criteria. This was accomplished by writing a computer program that summed all the digitized data values for u_{w_1} and u_{w_2} during the time that both signals were below a specified negative trigger level, provided that both signals simultaneously (within a small error) fell below the specified trigger level. The sum of digitized data values for both u_{w_1} and u_{w_2} were then compared and if the sums were both greater in magnitude than a specified value, and if both the signals u_{w_1} and u_{w_2} simultaneously (within a small error) rose above the specified trigger level, a burst event was presumed to have occurred. In operation, the program caused the computer to search the digitized data recorded on magnetic tape for special events meeting the above criteria. As one might perhaps expect, events meeting the above criteria were not numerous. In 13 seconds of data or 1.05×10^5 digitized data points we found only ten events meeting the above criteria.

For each event the computer then plotted the signal uv. In each case when T.L. $= -1$ (i.e., $u_{w_1} = u_{w_2} = -u'_w$) and the slope of u_w was negative, large contributions to $\overline{uv}$, uv > 20 $\overline{uv}$, occurred at some time within the sampling interval which included 300 digitized data points or was 0.0375 sec in duration. In some samples a number of contributions occurred, each of the order of 10 to 20 $\overline{uv}$. In other samples, single or double contributions occurred which were twice as large. In one case, two large contributions, uv ~ 60 $\overline{uv}$, occurred. An example of a single large contribution to $\overline{uv}$ is shown in fig. 11. The contribution is uv $= 62$ $\overline{uv}$ at the peak. These results represent truly sizeable contributions to Reynolds stress during bursting events. This is qualitatively in accord with results and conclusions of Kim, et al., [1], and Corino and Brodkey, [2]. However, neither [1] or [2] could accurately measure the magnitude of the contributions to $\overline{uv}$ during a burst, but both investigators agreed that the bursting events were very energetic. We have also applied the above specialized detection criteria to our data for positive T.L. (T.L. $= 1.0$) with positive slope in an attempt to observe the sweep event described by Corino and Brodkey, [2]. Recall from the introduction that the sweep was observed after the burst when higher speed fluid enters the field of view. We found approximately 12 events meeting the detection criteria and in all these events appreciable contributions to $\overline{uv}$ occurred. The signal uv was not as peaked as it was during bursting, but appeared to be relatively constant and large, uv ~ 7 $\overline{uv}$, for longer times than during bursting. This was our first strong indication that not all the contributions to Reynolds stress near the wall are associated with outflow of low speed fluid. Note that Kim, et al., [1] state that essentially all the contributions to $\overline{uv}$ occur during bursting. Corino and Brodkey estimate that 70 percent of the average contribution to $\overline{uv}$ occurs during bursting.

3.3 Streamwise Vorticity Measurements

As mentioned earlier, we have also made measurements of streamwise vorticity fluctuations, ω_x, and found that the streamwise vorticity fluctuations near the wall are correlated with the velocity, u_w, at the edge of the sublayer. The measurements were made by Dr. Bo Jang Tu and the senior author in 1968 in the high speed boundary layer. The correlation between u_w and ω_x

$$R_{u_w \omega_x} = \overline{u_w \omega_x} / u'_w \omega'_x \tag{8}$$

was found to be a maximum along a highly swept back line passing through the point on the wall where u_w is measured and proceeding downstream and away from the wall at an angle to the wall and to the stream of approximately $10°$. The maximum correlation coefficient that was measured was $R_{u_w \omega_x} = -0.095$.

The arrangement of the vorticity probe for the above measurement is shown in fig. 12. The location of the probe when maximum negative correlation was found is shown in fig. 12 where the distances are $x = 1.0$ in. (or $x^+ = 1250$), $y = 0.149$ (or $y^+ = 185$) and $z = 0.203$ (or $z^+ = 250$) relative to the upstream point where u_w was measured

We have measured the contributions to the correction $R_{u_w \omega_x}$ in four quadrants of the u_w, ω_x plane. The results are displayed in fig. 12. Note that the bulk of the negative correlation occurs in the fourth quadrant $u_w < 0$, $\omega_x > 0$. Here the correlation in the first quadrant (for example) is simply given by Eq. (8) but with $u_w > 0$, $\omega_x > 0$ in the numerator only. The quarter correlation was measured using an analog method (a diode in the feedback loop of an operation amplifier). The results of fig. 12 show that when $u_w < 0$, positive values of ω_x are more likely than negative values. This suggests that the positive streamwise vorticity component may be associated with the burst phenomena which occurs when $u_w < 0$.

To examine this possibility in more detail, we made conditionally sampled measurements of ω_x for the above data. The results of the measurements show that when u_w passes below a given negative value (with negative slope) the sampled data for ω_x representing contributions to $\omega_x = 0$ were all positive when $u_w < 0$. The positive contributions were appreciable. We can therefore conclude that during a burst event there is an appreciable antisymmetric pattern of streamwise vorticity present in the region near the wall on either side of the point where u_w is measured. Note that the positive sign of the vorticity component, ω_x, at the probe location shown in fig. 12 is consistent with upwelling of low speed fluid from the wall into the outer flow downstream of the point where u_w is measured.

The sampled data for ω_x representing contributions to $\omega_x = 0$ when $u_w > 0$ with positive slope were all negative. This result may be consistent with the idea that just before or during the sweep event (u_w increasing) high speed fluid approaches the wall in a jet-like flow with a pattern of downstream vorticity whose rotation is opposite to that of the bursting pattern. Additional study of this phenomena should be undertaken.

3.4 Direct Observations and Measurements of the Signal uv and of the Reynolds Stress $\overline{uv}$

The flexibility and relative simplicity of digital computation methods were exploited in a study of the signal uv from the x hot wire probe.

3.4.1 Nature of the Signal uv

Figure 13 displays the signal uv as a function of time. The signal was obtained from the x wire when it was located at a distance $y = 0.07$ in. or $y^+ = 30.5$ from the wall in the low speed boundary layer, $R_\theta = 4230$. The signal very definitely contains large short duration negative spikes and much smaller positive contributions of considerably longer duration than the negative spikes. For a considerable fraction of the time, the signal uv is approximately zero. This suggests that the signal, uv, from the region in the boundary layer where turbulent kinetic energy is a maximum is rather highly intermittent.

3.4.2 Probability Density of uv

We measured the probability density of uv, β_{uv}, using the same computer program developed to find the probability density of u_w, see Section 3.2 and Eq. (4). The result is shown in fig. 14. Note that for this unusual random signal the maximum value of β_{uv} occurs at zero but the mean value is located at $uv/\overline{uv} = 1$ at which point $\beta_{uv} \sim 1/6 (\beta_{uv\,max})$. Furthermore, the probability density has a long "tail" for positive $uv/\overline{uv}$ and rapidly vanishing values of β_{uv} for $uv/\overline{uv} < 0$. These features of the probability density of uv are consistent with the behavior of uv as shown in fig. 13. The peak in β_{uv} at uv = 0 corresponds to the fact that uv is relatively quiescent or nearly zero much of the time. The long "tail" of β_{uv} for $uv/\overline{uv} > 0$ is a result of the spiky nature of Reynolds stress contributions during bursting events.

3.4.3 Four Quadrant Correlation Map of Contributions to $\overline{uv}$

To obtain a quantitative measure of the intermittency of the uv signal and to better understand the nature of contributions to $\overline{uv}$ from the burst and sweep processes, we have computed contributions to $\overline{uv}$ in four quadrants of the u-v plane. The measurements of uv were made with the x wire at a distance from the wall where $y = 0.07$ in. or $y^+ = 30.5$. The contributions of the correlation $\overline{uv}$ in each quadrant were computed for each pair of digitized data values for u and v. The product uv was added to previous values of uv in each of four storage files depending upon the signs of u and v. Also, a count of the number of samples contained in each of the four storage locations was made. From this data we computed the relative contributions to $\overline{uv}$ from each quadrant, the time spent by the signal uv in each quadrant and the number of uninterrupted individual contributions to $\overline{uv}$ made by the signal uv in each quadrant. The individual contributions are called samples in fig. 15.

Figure 15 is a copy of the computer printout of this data reduction procedure. Note that the largest contribution to Reynolds stress, $uv/\overline{uv} = 0.805$, occurs in the fourth quadrant $u < 0$, $v > 0$, and this represents violent upwellings of low speed fluid. There is, however, also a large contribution (0.435) to Reynolds stress in the second quadrant where $u > 0$, $v < 0$. This contribution may be the result of the sweep event described by Corino and Brodkey, [2], or can occur as a result of the swirling motion during a burst event that has often been observed by Kim, et al., [1]. In the swirling motion, high speed fluid must pass the measuring station and enter the wall region. However, during bursting u_w is lower than the mean and our data for sampled Reynolds stress in figs. 8, 9 and 10 all show that considerable contributions to Reynolds stress are made when u_w is greater than the mean value. This indicates that the contribution to Reynolds stress in the second quadrant $u > 0$, $v < 0$ is caused by the sweep event and not during bursting. This important conclusion will be discussed again below.

3.4.4 Four Quadrant Correlation Maps of the Contribution to $\overline{uv}$ Above a Certain Value of $|\overline{uv}|$

Contributions to the correlation $\overline{uv}$ were also measured in four quadrants of the u-v plane when the signal uv was greater than a certain value of $|uv| = $ const. The purpose of these measurements, which were easily done by a slight alteration of the computer program, was to single out the large contributions to $\overline{uv}$ which occur in the fourth quadrant $u < 0$, $v > 0$. The program alteration consisted of the creation of a fifth storage location into which a digitized value of uv was thrown if for that sample $|uv| < $ const. The correlation contributions that remain in the u-v plane are contributions which occur in each quadrant outside of a central cross-thatched region bounded by four hyperbolas called the "hole" shown in the sketch below.
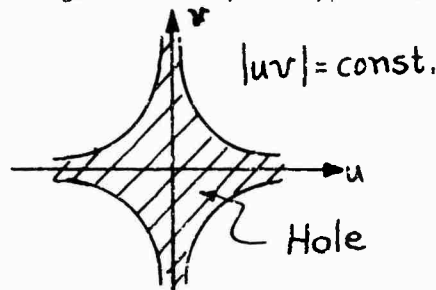

Figure 16 shows a plot of the results of the measurements of contributions to $\overline{uv}$ with hyperbolic central region omitted for various values of the size of the "hole." From fig. 16, it is clear that the contributions to $\overline{uv}$ from the fourth quadrant are larger than from any of the others. Furthermore, above the value $|uv| = 5|\overline{uv}|$ essentially all the remaining contributions to $\overline{uv}$ come from the fourth quadrant. Also shown on fig. 16 is a curve representing the percentage of time that the signal uv remains in the hyperbolic "hole" $|uv| < $ constant. Clearly, for a large fraction of the time $|uv|$ is very small relative to shorter intervals of intense activity. Roughly speaking, the intermittency factor for uv (at $y^+ = 30.5$) is 0.55 since 55 percent of the time the signal uv is in the "hole" yet during this time the contribution to $\overline{uv}$ that is made by the signal uv while in the "hole" is small $(uv/\overline{uv})_{"hole"} = 0.01$. The size of the "hole" for this estimate is $|uv| < 0.5\,\overline{uv}$, see fig. 16.

4.0 SUMMARY OF THE RESULTS OF THE MEASUREMENTS

In this section the results of the measurements will be discussed and a model for the flow structure of the bursting event that was first presented in {3} will be discussed in light of the present measurements.

4.1 Discussion of Measurements

The key to an understanding of the results appears to us to be the fact that when u_w becomes negative with negative slope, a burst occurs which makes large contributions to Reynolds stress and production of turbulent energy. The sampled Reynolds stress contributions uv like those of fig. 6 for $u_w < 0$ and negative slope are convected downstream with the local mean speed as our numerous measurements reveal (these measurements are not yet in final form and are not included in this paper). The region occupied by the burst event is long and narrow and appears to grow as it is convected downstream. Furthermore, when $u_w < 0$ with negative slope, sampled measurements of the streamwise component of vorticity were made. The measurements showed that an anti-symmetric pattern (in the spanwise direction) of streamwise vorticity was present. This is strong evidence that appreciable vorticity is present during the bursting event. The sign of the vorticity is such that an upwelling $v > 0$ of fluid would be expected when $u_w < 0$ with negative slope and it is shown from the measurements that intense bursts do squirt low speed fluid from the region near the wall upward into the higher speed outer flow.

The spatial and temporal scale of the upward ejections of low speed fluid is less than $l \sim 0.5$ in. $\sim \delta^*$ or $l^+ \sim 250$ for the low speed boundary layer. Our earlier measurements, {3} and {14}, of the correlation of the pressure field at the wall with velocity components near the wall led us to propose, in {3}, that a swept back pattern of streamwise vorticity in the shape of a hairpin with legs pointing upstream could be responsible for the wall pressure disturbances.

We now propose that the same model for the flow structure near the wall is also responsible for the intense bursting events that have been studied by Kim, et al. {1}, Corino and Brodkey, {2}, and here with sampled measurements of uv. Another reason for proposing the model of the hairpin shaped vorticity is that this configuration of vorticity appears to be the only way an intermittent, very intense small scale ejection of fluid could occur. We recall that the onset of the ejection is very abrupt and believe that it must be the result of vortex stretching on at first a very small scale in the wall region. Furthermore, it does not seem likely that anything other than an intense local convected pattern of vorticity could be responsible for the highly intermittent signal uv, see fig. 13.

Numerous interesting questions remain to be investigated. For example, the question of the nature of the flow disturbance that initiates the bursting event is still in doubt. Also, the nature of the chaotic interaction observed after the ejection process is well developed is not understood. Unfortunately, we do not have space here to survey a number of computational results from simplified models of possible flow structures near the wall. We also would like to suggest that the localized flow structure during the bursting event is similar to the organized flow structure that occurs during the creation of a turbulent spot in the transition from laminar to turbulent flow. The initial instability mechanism that initiates the first stages of the process leading to a concentrated localized flow structure during transition may not be the same as it is in the fully developed turbulent boundary layer. However, we propose that the basic flow structure and vorticity pattern that is developed at later stages and the results (creation of Reynolds stress and turbulence) are similar when intermittent and intense contributions to $\overline{uv}$ occur near the wall in the fully developed turbulent boundary layer.

REFERENCES

{1} Kim, H T., Kline, S. J. & Reynolds, W. C., An Experimental Study of Turbulence Production Near a Smooth Wall in a Turbulent Boundary Layer with Zero Pressure-Gradient, Report MD-20, Thermosciences Division. Department of Mechanical Engineering, Stanford University. January 1965.

{2} Corino, E. R. & Brodkey, R. S., A Visual Investigation of the Wall Region in Turbulent Flow, J. Fluid Mech., vol. 37, no. 1, pp. 1-30, 1969.

{3} Willmarth, W. W. & Tu, B. J., Structure of Turbulence in the Boundary Layer Near the Wall, Phys. Fluids, Supplement 1967, pp. 134-137. More extensive results available in University of Michigan Technical Report ORA 02920-3-T, 1966.

{4} Kline, S. J., Reynolds, W. C., Schraub, F. A. & Runstadler, F. W., The Structure of Turbulent Boundary Layers, J. Fluid Mech., vol. 30, no. 4, pp. 741-773, 1967.

{5} Laufer, J., New Techniques in Boundary Layer Research. Paper presented at Symposium on Experimental Turbulent Boundary Layers, Purdue University, March 27, 1970. Also published as Gupta. A. K., Dissertation, University of Southern California, January 1970.

{6} Willmarth, W. W. & Wooldridge, C. E., Measurements of the Correlation between the Fluctuating Velocities and Wall Pressure in a Thick Turbulent Boundary Layer, AGARD-NATO. Report 456, April 1963.

{7} Willmarth, W. W. & Wooldridge, C. E., Measurements of the Fluctuating Pressure at the Wall Beneath a Thick Turbulent Boundary Layer, J. Fluid Mech., vol. 14, no. 2, pp. 187-210, 1962.

{8} Kovasznay, L. S. G., Hot Wire Method, Art. F.2, pp. 227-228 in Physical Measurements in Gas Dynamics and Combustion, vol. IX, High Speed Aerodynamics and Jet Propulsion. Princeton University Press, 1954.

{9} Kovasznay, L. S. G., Miller, L. T. & Vasudeva, B. R., A Simple Hot Wire Anemometer, Project SQUID Technical Report JHU-22-P, July 1963.

{10} Laufer, J., The Structure of Turbulence in Fully Developed Pipe Flow, NACA Technical Report 1174, 1954.

{11} Kovasznay, L. S. G., Kibens, V & Blackwelder, R. F., Large-Scale Motion in the Intermittent Region of a Turbulent Boundary Layer, J. Fluid Mech., vol. 41, no. 2, pp. 283-325, 1970.

{12} Lumley, J., Stochastic Tools in Turbulence, volume 12, Monographs in Applied Mathematics and Mechanics, Academic Press, New York, p. 4, 1970.

{13} Coles, D. E., The Problem of the Turbulent Boundary Layer, Z. A. M. P., vol. 5, p. 181, 1954.

{14} Willmarth, W. W. & Wooldridge, C. E., Measurements of the Correlation between the Fluctuating Velocities and the Fluctuating Wall Pressure in a Thick Turbulent Boundary Layer, AGARD-NATO Technical Report 456, April 1963.
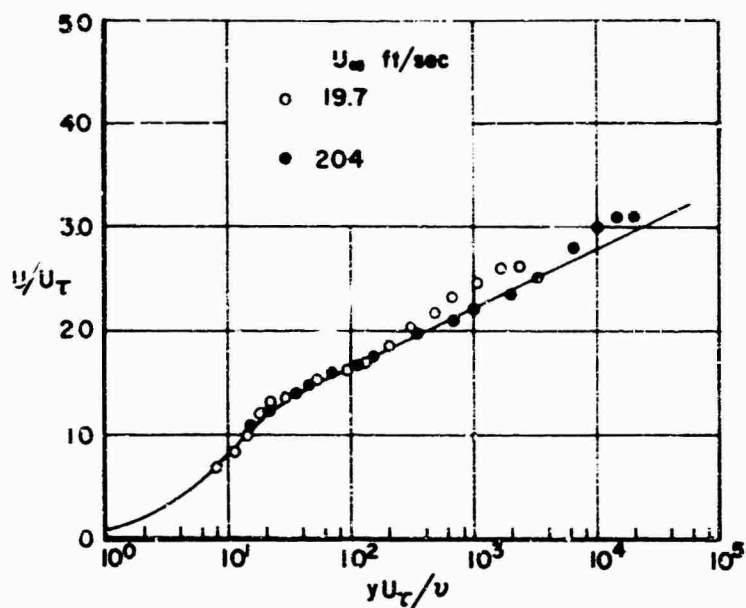
Fig.1 Mean velocity profiles (also see Table 1)
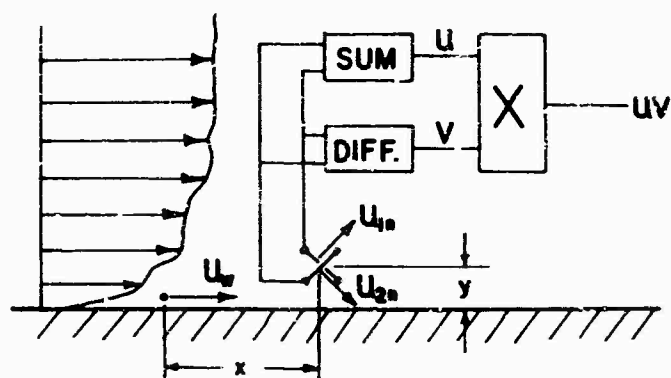
Fig.2 Sketch of arrangement of hot wires for measurement of u_w and uv
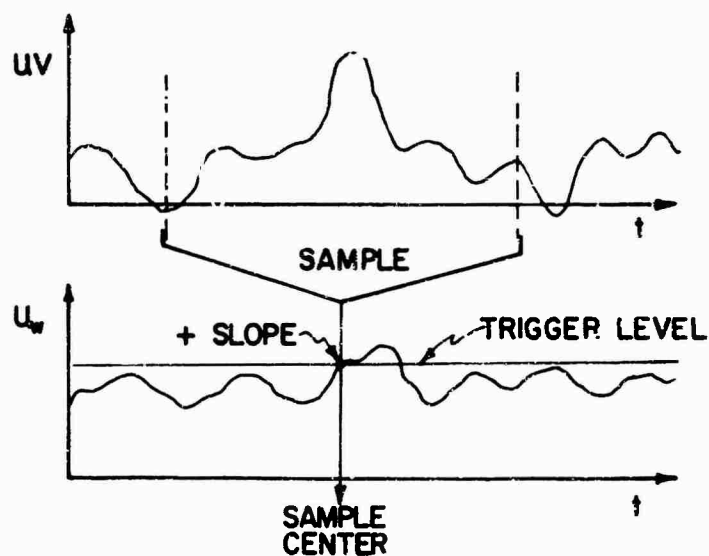
Fig.3 Sketch of conditional sampling method

STREAMLINED SUPPORTS
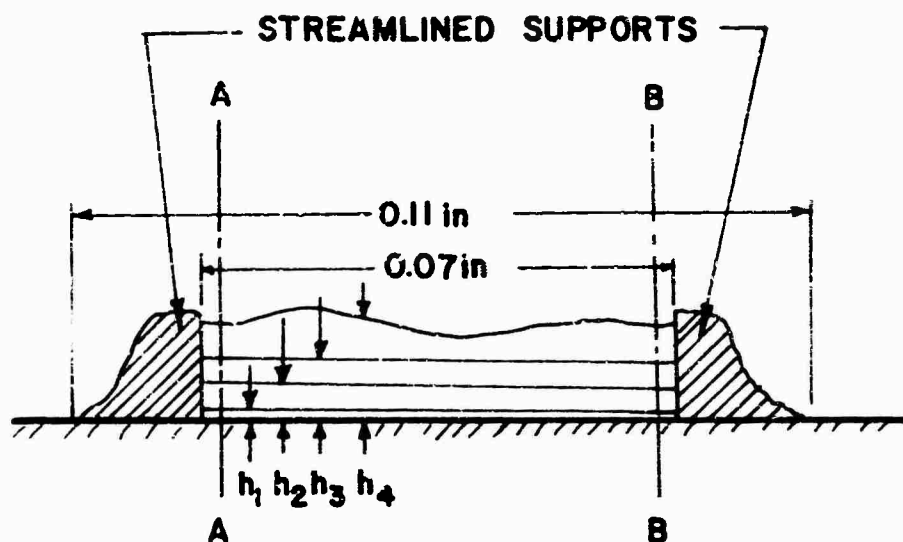
Fig.4 Downstream view of "ladder" array of four hot wires for sublayer velocity measurements
1.5 x 10⁻⁴ in. dia. platinum wires.
At Station A-A: h_1 = 1.4 x 10⁻³, h_2 = 5.5 x 10⁻³, h_3 = 8.8 x 10⁻³, h_4 = 13.4 x 10⁻³ in.
At Station B-B: h_1 = 0.4 x 10⁻³, h_2 = 4.4 x 10⁻³, h_3 = 7.9 x 10⁻³, h_4 = 13.4 x 10⁻³ in.
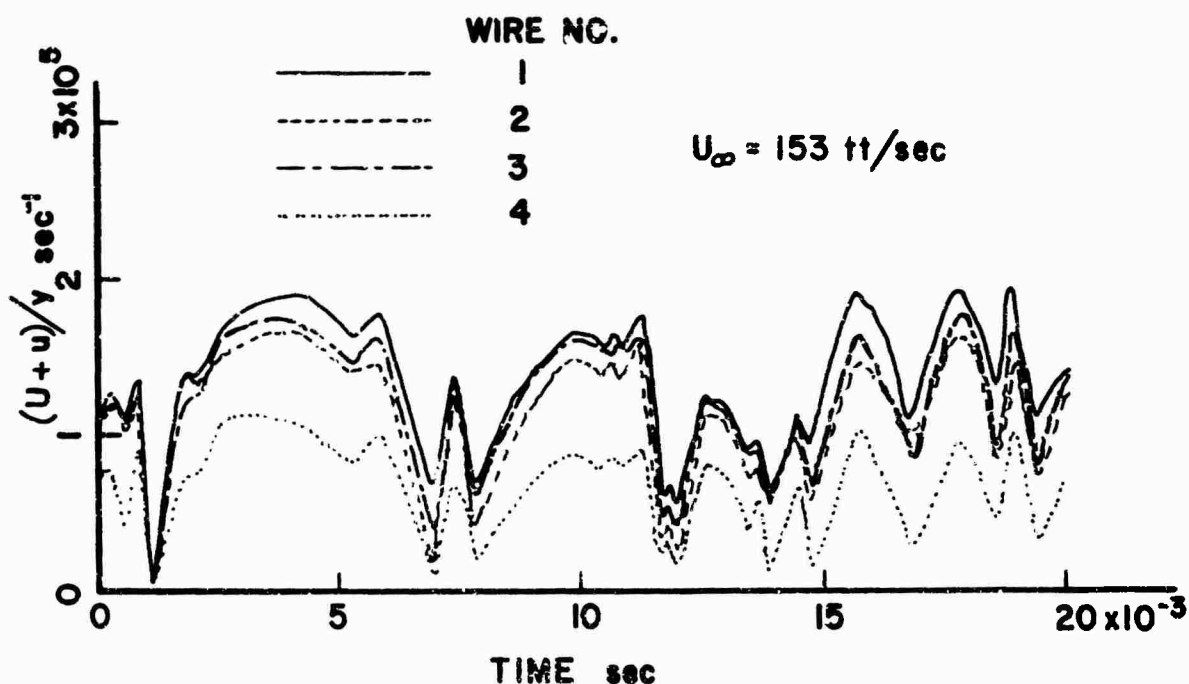
Fig.5 Velocity fluctuations measured in sublayer using "ladder" array of Figure 4. Miller hot wire
anemometers with linearization were used for these measurements
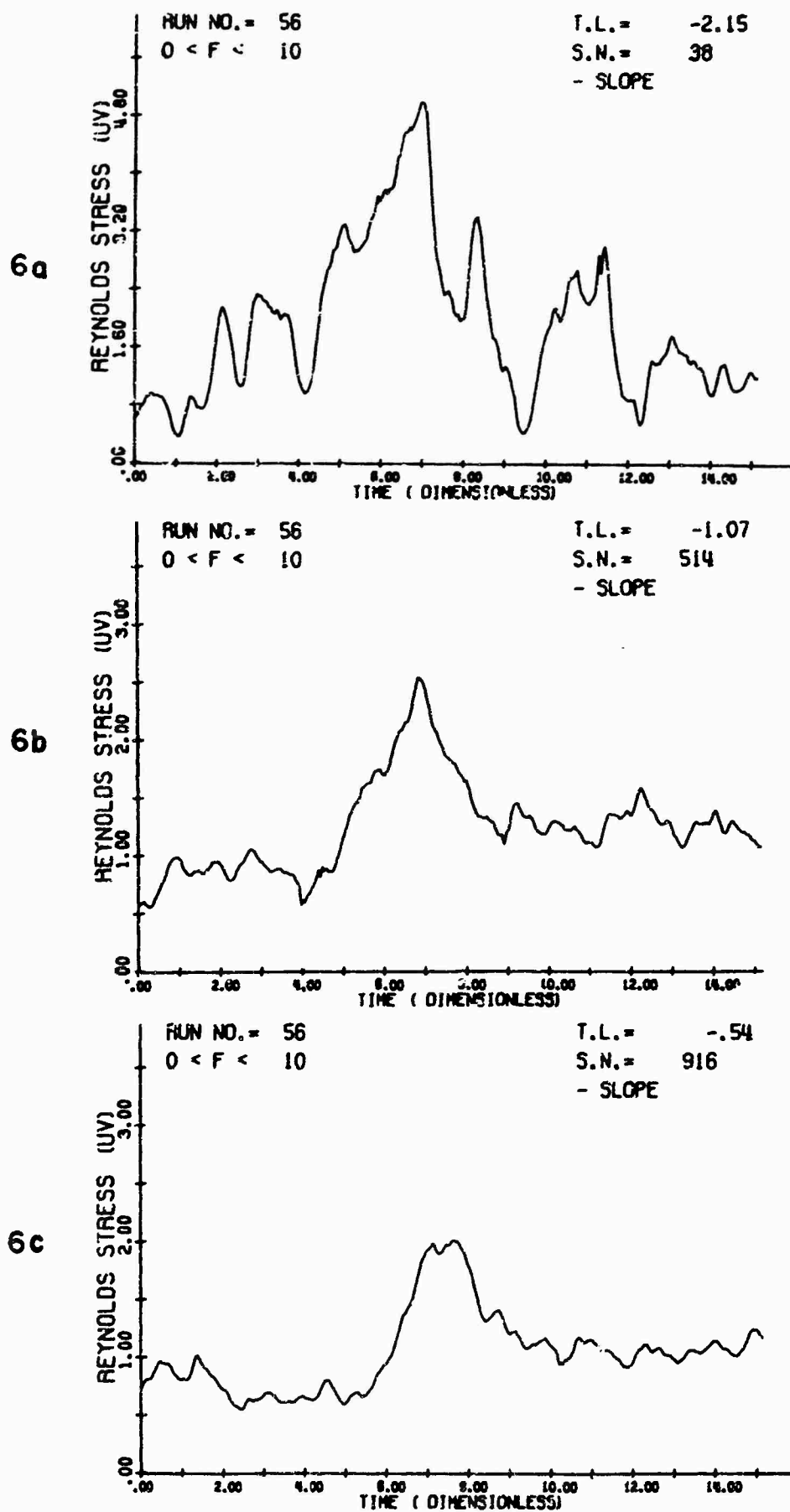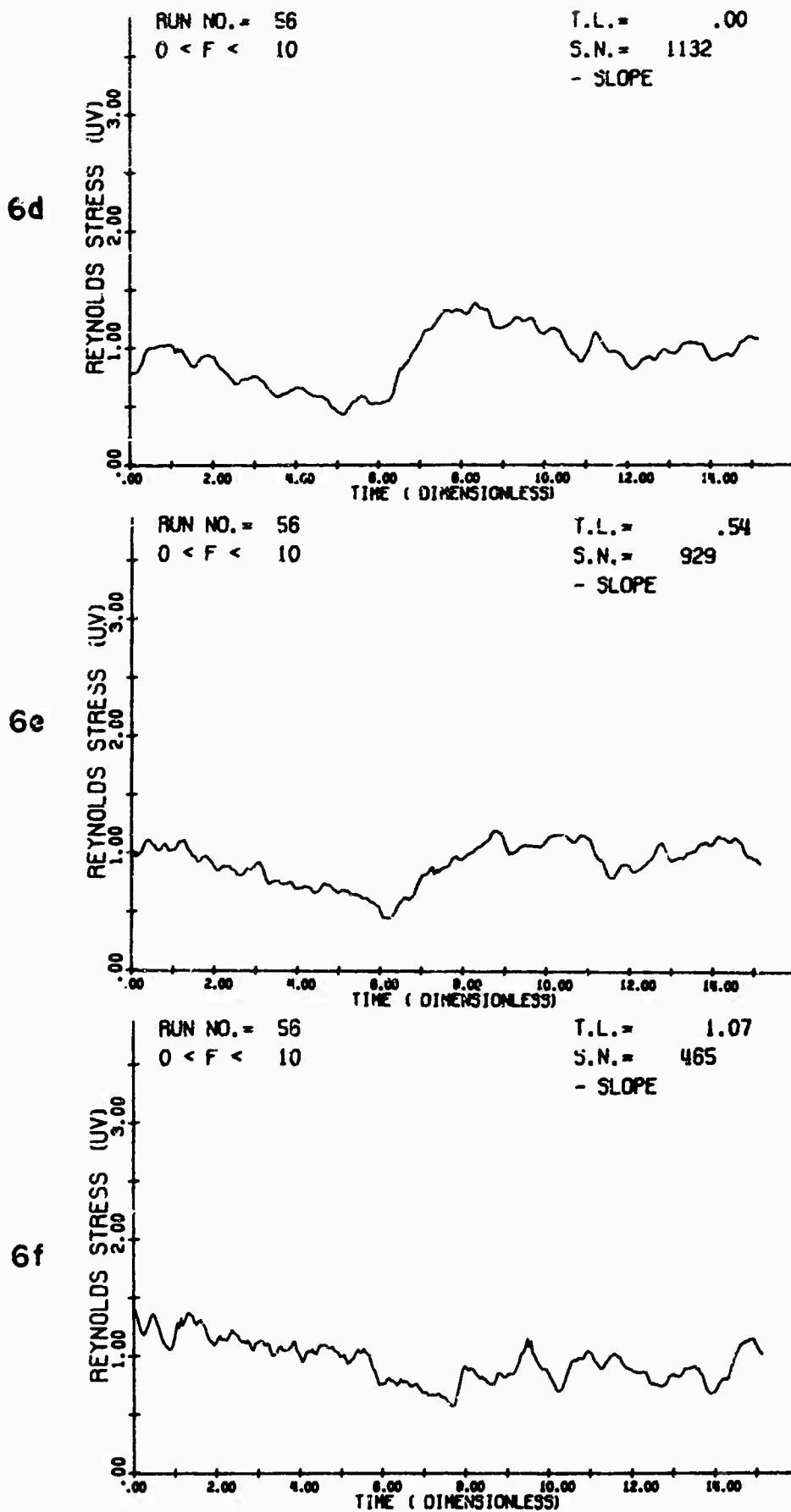
Fig.6   Conditionally sampled measurements of contributions to the Reynolds stress, see text for definition of
Abscissa, Ordinate and T.L.   S.N. is the number of samples of uv that were
obtained at each value of T.L.

Fig.6 Conditionally sampled measurements of contributions to the Reynolds stress, see text for definition of Abscissa, Ordinate and T.L. S.N. is the number of samples of uv that were obtained at each value of T.L.

RUN NO. = 56   T.L. =   2.15
0 < F <   10   S.N. =   7
                      - SLOPE

REYNOLDS STRESS (UV)

TIME (DIMENSIONLESS)

Fig.6   Conditionally sampled measurements of contributions to the Reynolds stress, see text for definition of
Abscissa, Ordinate and T.L.   S.N. is the number of samples of uv that were
obtained at each value of T.L.

β_{u_w}

GAUSSIAN

u_w / u'_w
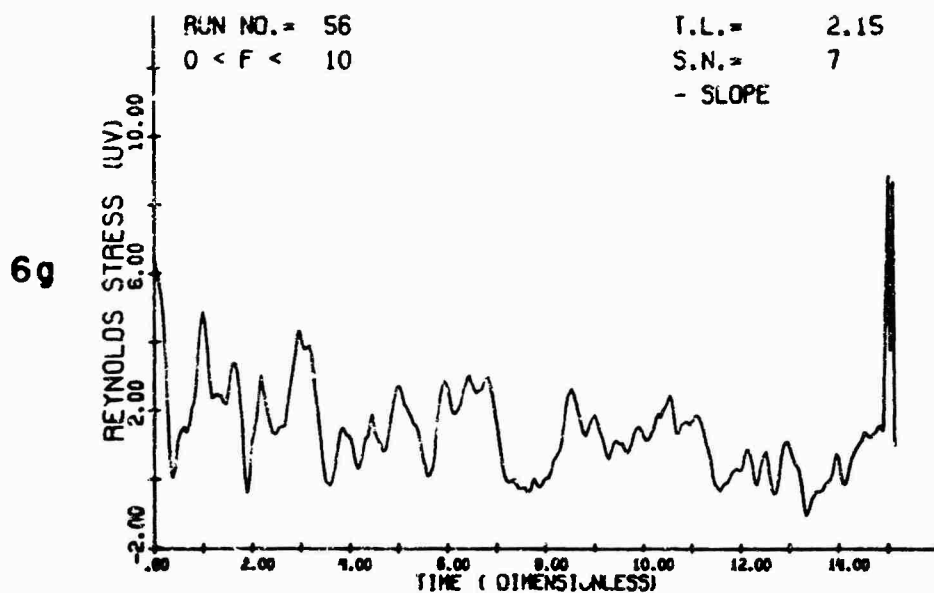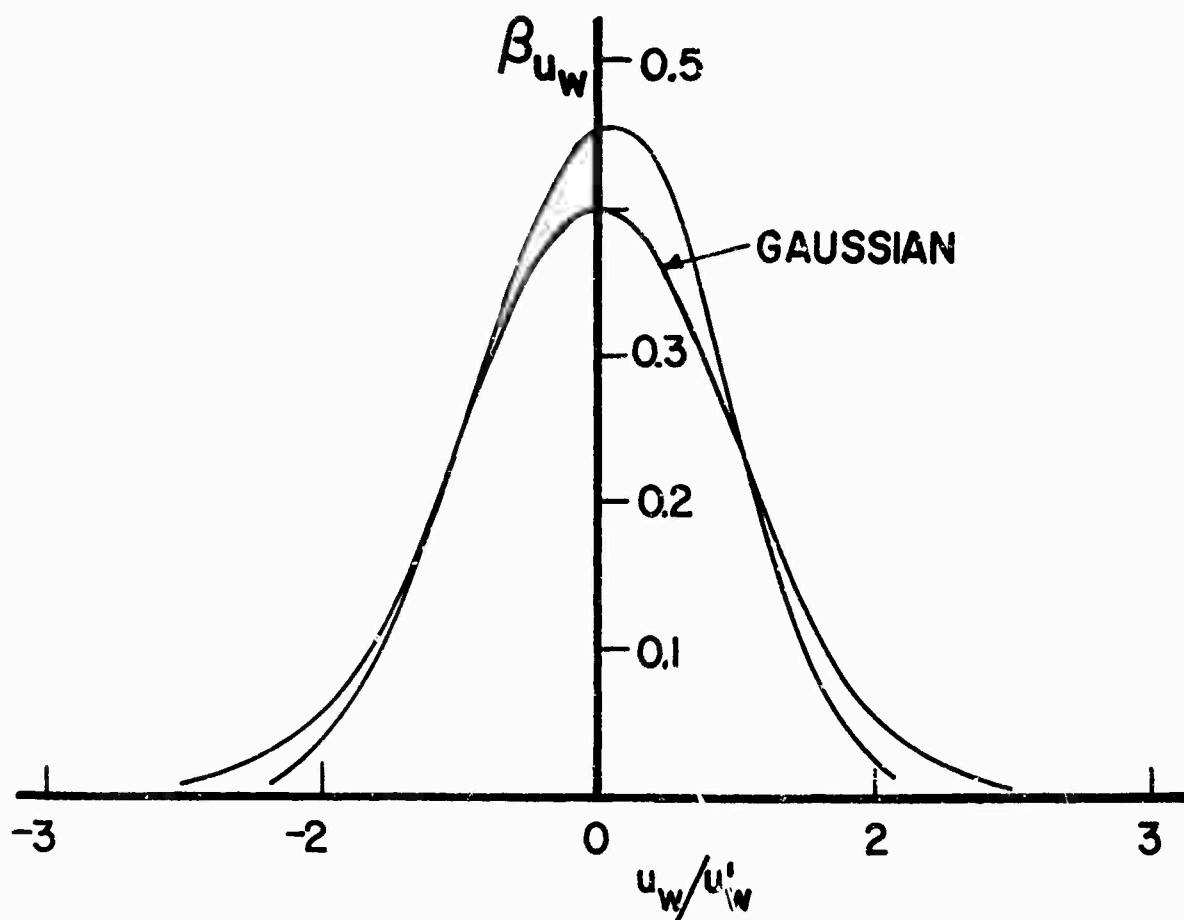
Fig.7   Probability density of u_w after passing the signal u_w through a low pass Butterworth filter of third
order with half power point at 80 Hz. The velocity u_w was measured at
y^+ = 16.2 and the stream speed was 19.7 ft/sec.

$1.0 \; \Delta \widetilde{UV}/\overline{UV}$ PER UNIT T.L.

.8

.6

.2

o — SLOPE

● + SLOPE

-3 $\quad -2$ $\quad -1$ $\quad 0$ $\quad 1$ $\quad 2$ $\quad 3$

TRIGGER LEVEL u_w/u'_w
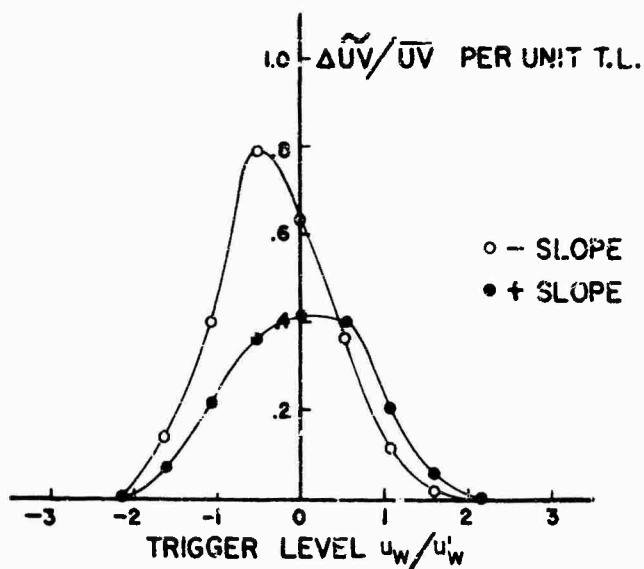
Fig.8 Conditionally sampled contributions to uv as a function of T.L. A low pass filter was used for u_w frequency band $0.26 < f < 80$ Hz. Signal uv sampled when $u_w = $ T.L. u'_w, x wire location $x^+ = 0$, $y^+ = 30$, $U_\infty = 19.7$ ft per sec.

$1.0 \; \Delta \widetilde{UV}/\overline{UV}$ PER UNIT T.L..

.8

.6

.4

.2

o — SLOPE

● + SLOPE

-3 $\quad -2$ $\quad -1$ $\quad 0$ $\quad 1$ $\quad 2$ $\quad 3$

TRIGGER LEVEL u_w/u'_w

Fig.9 Conditionally sampled contributions to uv as a function of T.L. Frequency band for u_w was $0.26 < f < 8000$ Hz. Signal uv sampled when $u_w = $ T.L. u'_w, x wire location $x^+ = 0$, $y^+ = 30$, $U_\infty = 19.7$ ft per sec.

$1.0 \; \langle \Delta \widetilde{UV}/\overline{UV} \rangle$ PER UNIT T.L.

.8

.6

.4

.2

R_θ

——— 38,000

- - - 4700

-3 $\quad -2$ $\quad -1$ $\quad 0$ $\quad 1$ $\quad 2$ $\quad 3$

TRIGGER LEVEL u_w/u'_w
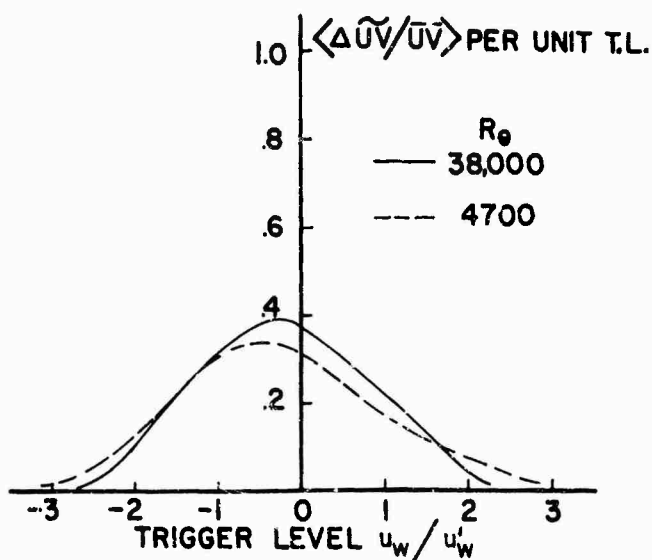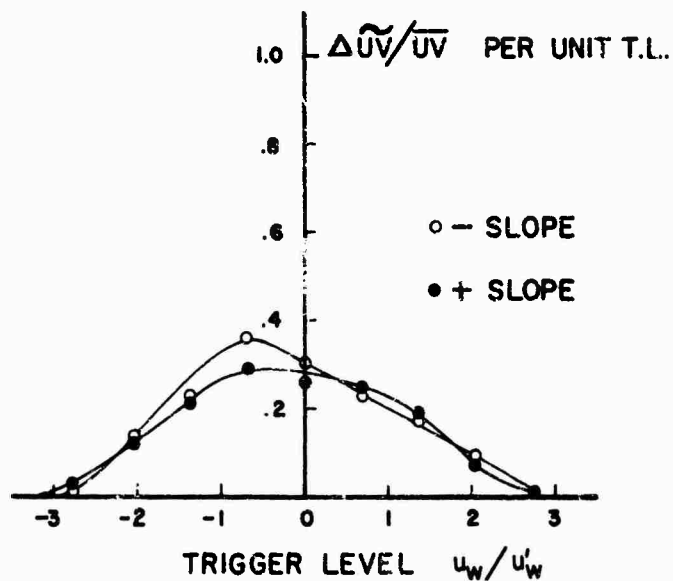
Fig.10 Average of sampled contributions to uv for + and − slope as a function of T.L. at low and high Reynolds number. No filter was used for u_w. Hot wire locations were:
high Re: u_w, $y^+ = 7.5$ uv, $x^+ = 1690$, $y^+ = 263$
low Re: u_w, $y^+ = 8.3$ uv, $x^+ = 762$, $y^+ = 116$

RUN NO. = 70   T.L. =   -1.00
0 < F <   10   S.N. =   1
                      - SLOPE

UV/UVAVG

VEL X TIME/DISP
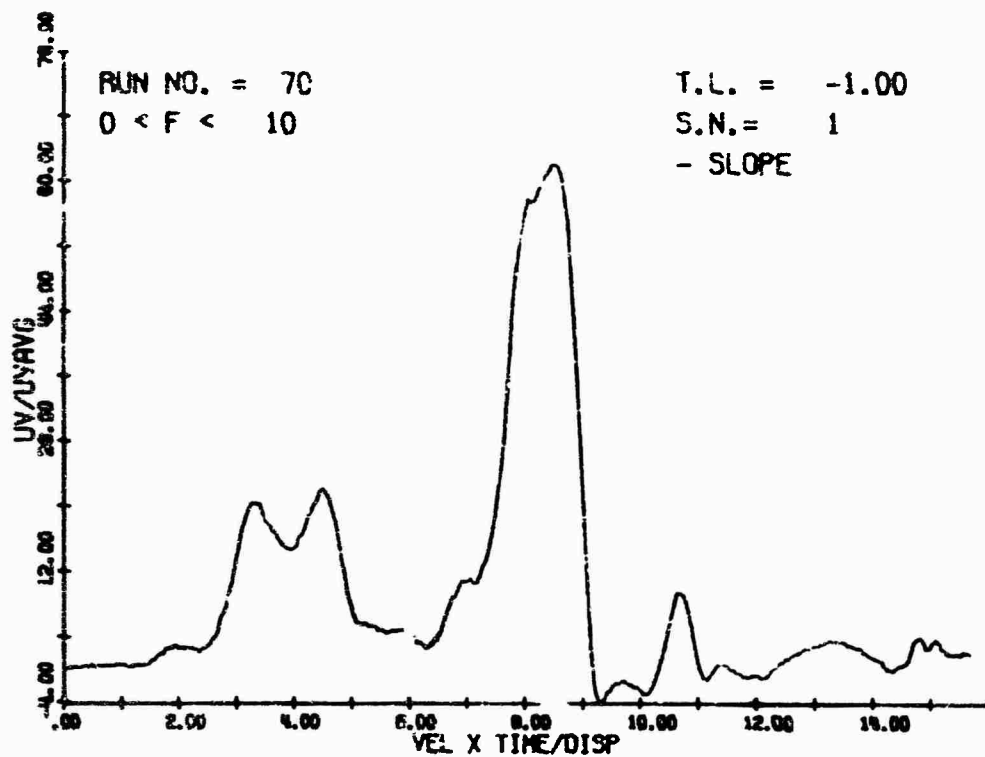
Fig.11 Example of a very large single contribution to Reynolds stress. Sample found using special spatial and temporal filtering criteria, see Section 3.2.4.

$R = -0.095$

ω_x

y/δ^*

x/δ^*

-0.208 $R_{1/4} = +0.130$

$\omega_x(1.0, 0.149, 0.203)$

u'

$u_w(0, 0.004, 0)$

$+0.150$ -0.167

z/δ^*
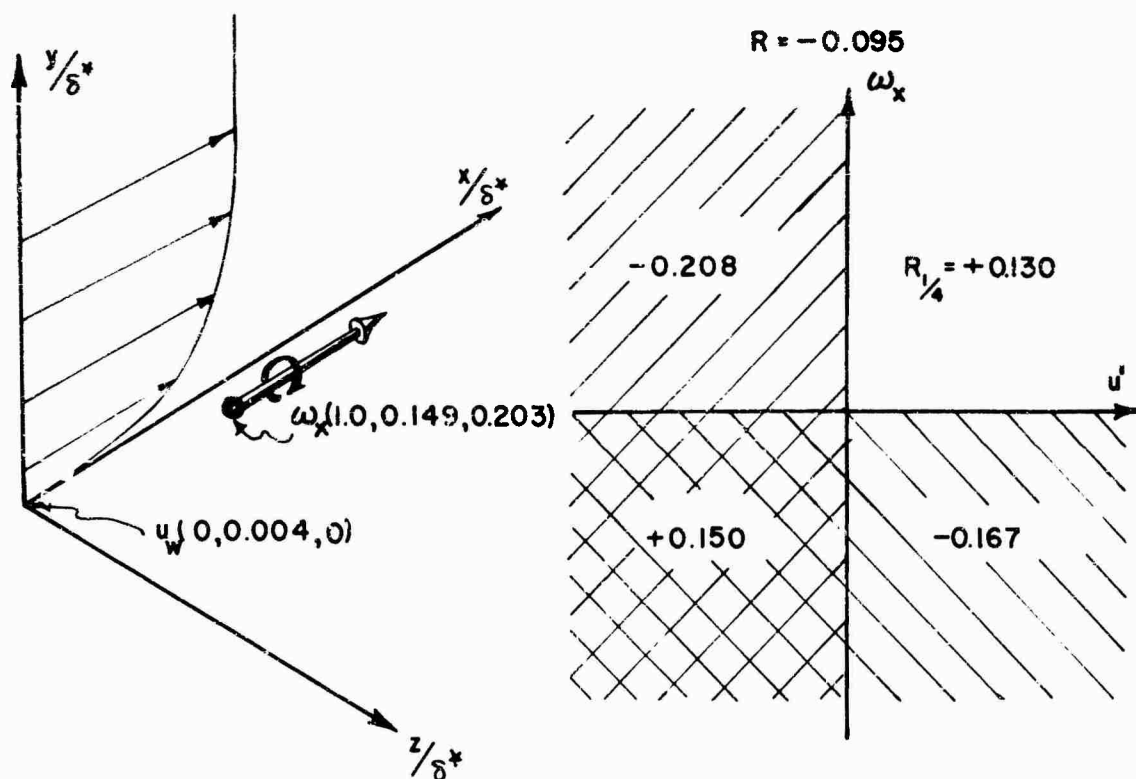
note: $R_{1/4} = 1/2\pi \pm 0.159$ for two
       independent (uncorrelated)
       gaussion random variables.

Fig.12 Contributions to correlation between streamwise vorticity and velocity in the sublayer from four quadrants in the u, ω_x plane. $U_\infty = 204$ ft/sec.

Fig. 13 The signal uv as a function of time at $y^+ = 30$ in low speed boundary layer, $U_\infty = 19.7$ ft/sec.
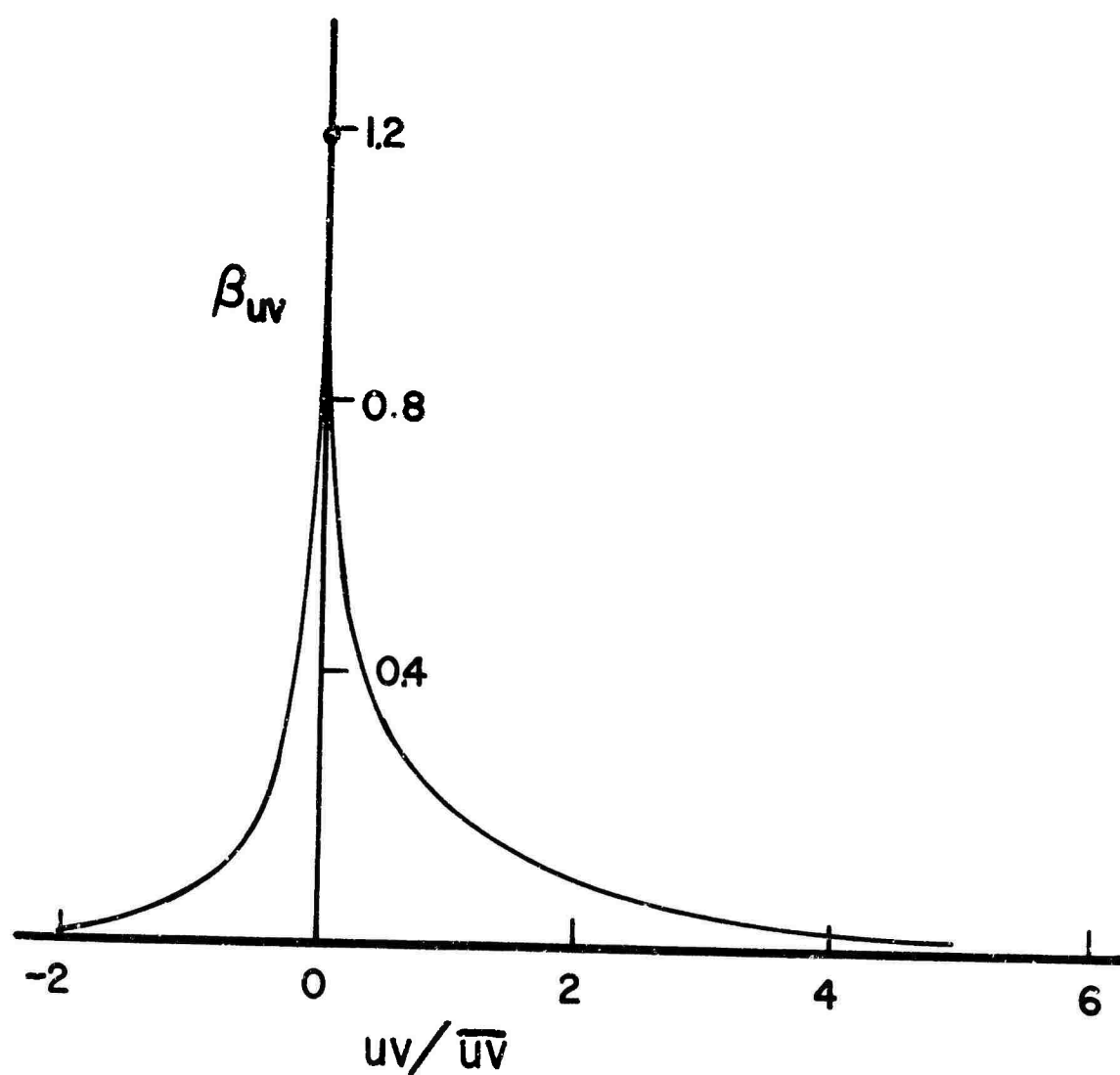
Fig. 14 Probability density of uv measured at $y^+ = 30$ in low speed boundary layer, $U_\infty = 19.7$ ft/sec.

```
                                          I
                                          I
                                          I
         U < 0, V > 0                      I          U > 0, V > 0
                                          I
    UV SUM    =    0.35647E 10            I     UV SUM    =   -0.51697E 09
    TIME      =    36902                  I     TIME      =    21933
    SAMPLE    =    2555                   I     SAMPLE    =    3122
                                          I
    UV/UVAVG  =    2.747                  I     UV/UVAVG  =   -0.603
    % TIME    =    29.29 %               I     % TIME    =    17.41 %
    TIME/S.N.=    14.44                   I     TIME/S.N.=    7.03
    UV/S.N.   =    39.68                  I     UV/S.N.   =   -4.23
                                          I
    CONTRIBUTION TO UV/UVAVG              I     CONTRIBUTION TO UV/UVAVG
              =    0.805                  I              =   -0.105
                                          I
                                          I
----------------------------------------+------------------------------------------
                                          I
         U < 0, V < 0                      I          U > 0, V < 0
                                          I
    UV SUM    =   -0.66439E 09            I     UV SUM    =    0.21444E 10
    TIME      =    22033                  I     TIME      =    45132
    SAMPLE    =    2656                   I     SAMPLE    =    3223
                                          I
    UV/UVAVG  =   -0.771                  I     UV/UVAVG  =    1.215
    % TIME    =    17.49 %               I     % TIME    =    35.82 %
    TIME/S.N.=    8.30                    I     TIME/S.N.=    14.00
    UV/S.N.   =   -6.40                   I     UV/S.N.   =    17.01
                                          I
    CONTRIBUTION TO UV/UVAVG              I     CONTRIBUTION TO UV/UVAVG
              =   -0.135                  I              =    0.435
                                          I
                                          I
                                          I
```

Fig.15 Computer printout of contributions to Reynolds stress in four quadrants of the u, v plane. Signal uv measured at y^+ = 30 in low speed boundary layer, U_∞ = 19.7 ft/sec.

σ u > 0 , v > 0
Q u > 0 , v < 0
ρ u < 0 , v < 0
℧ u < 0 , v > 0
● HOLE

Fig.16 Contributions to Reynolds stress from truncated quadrants of u, v plane and percentage time spent in hole as a function of hole size. uv measured at y^+ = 30 in low speed boundary layer, U_∞ = 19.7 ft/sec.

REPARTITIONS SPECTRALES DES FLUCTUATIONS THERMIQUES

DANS UNE COUCHE LIMITE TURBULENTE

par

L. FULACHIER[x] et R. DUMAS[xx]
Institut de Mécanique Statistique de la Turbulence
Laboratoire Associé au C.N.R.S.
Université de Provence, Marseille.

-o-o-o-o-o-o-

RESUME.-

Les spectres des fluctuations de température et les répartitions spectrales des corrélations température-vitesse ont été mesurés dans la couche limite turbulente d'une plaque plane chauffée. Dans les conditions de ces expériences, la température se comporte comme un contaminant passif.

La méthode du diagramme des fluctuations a été appliquée aux signaux filtrés en fréquence, notamment pour la détermination des répartitions spectrales des corrélations.

Une comparsison systématique des spectres des fluctuations de température et de ceux des trois composantes de vitesse est présentée, depuis la zone interne jusqu'à la frontière de la couche limite. On constate une forte analogie entre le spectre des fluctuations thermiques et celui formé par la somme $Q(n)$ des spectres des trois composantes de vitesse pondérées par leurs moyennes quadratiques. Si on appliquait les formules de turbulence isotrope, ceci reviendrait à admettre une similitude des fonctions spectrales totales relatives aux fluctuations de température et de vitesse. Toutefois près de la paroi $(y^+ \sim 15)$ le spectre des fluctuations thermiques et celui de la composante longitudinale de vitesse diffèrent assez peu car cette composante est prépondérante devant les deux autres, ce qui est mis en évidence par l'estimation de $Q(n)$ qui demeure en forte analogie avec le spectre thermique.

Les équations de bilan des répartitions spectrales relatives à la température et à $Q(n)$ sont données. Certaines remarques sont faites compte-tenu des répartitions spectrales des termes de production, qui diffèrent pour la température et la vitesse, et des termes de dissipation par les effets moléculaires.

SUMMARY.-

The temperature fluctuation spectra and spectral distributions of temperature-velocity correlations have been measured in a turbulent boundary layer on a heated flat plate. In experimental conditions temperature acts like a passive contaminant.

The method of fluctuation diagram has been use for frequency filtered signals especially in order to measure spectral distributions of correlations.

A systematic comparison of thermal spectra and those of three components of velocity is presented from internal zone as far as the edge of boundary layer. It appears to be a strong analogy between thermal spectra and spectra equal to the sum $Q(n)$ of the spectra of the three velocity components, weighted by their mean square values. If one uses isotropic turbulence formula the above analogy would be equivalent to assume a similarity of total spectral function for temperature and velocity. However near the wall $(y^+ \sim 15)$ thermal spectrum and longitudinal velocity spectrum are little different, because the value of this component is very large in ratio of the two others ; this result is explained by computation of $Q(n)$ which remains in close analogy with thermal spectrum.

Balance equations of spectral distributions concerning temperature and $Q(n)$ are given. Some remarks are pointed taking in account spectral distributions of production terms, which differ for temperature and velocity, and molecular dissipation terms.

1.- INTRODUCTION

Les résultats présentés ici concernent une partie des études sur la structure des couches limites turbulentes subsoniques avec transfert thermique à la paroi, qui sont poursuivies à l'I.M.S.T. (1, 2, 3, 4, 5, 6). Les écarts entre la température Θ_p de la paroi et celle de l'air Θ_e extérieur étant faibles, de l'ordre de 22°C, le champ des vitesses n'est pratiquement pas modifié par l'échauffement.

En ce qui concerne les grandeurs moyennes, les comparaisons portent sur la vitesse relative longitudinale U/U_e et les écarts relatifs de température $\Theta_p - \Theta/\Theta_p - \Theta_e$ l'indice e étant relatif aux conditions à l'extérieur. En particulier lorsque les conditions aux frontières sont

.../...

semblables les profils de vitesse et de température sont analogues (7, 8).

On remarque que les composantes normale à la paroi V et transversale W , sont faibles ou nulles et ne jouent pas un rôle direct dans la comparaison. Par contre lorsque l'on considère les fluctuations turbulentes de température θ' et les composantes longitudinale u' , normale v' et transversale w' de la vitesse turbulente, $\overline{q'}$, on sait que les variances $\overline{u'^2}$ ne sont pas en général très prépondérantes devant les variances $\overline{v'^2}$ et $\overline{w'^2}$. On constate d'ailleurs que les spectres définis par TAYLOR de la composante longitudinale u' et de la température θ' sont en général différents dans la couche limite (8), dans un jet (9) et dans un écoulement cylindrique (10).

C'est pourquoi, nous avons entrepris une étude détaillée des répartitions spectrales des fluctuations de température, des trois composantes de vitesse, ainsi que des corrélations température-vitesse et vitesse-vitesse, dans une couche limite turbulente, où à notre connaissance ces mesures n'ont pas été effectuées systématiquement.

Les théories spectrales développées pour le cas des grands nombres de Reynolds et concernant les échelles petites vis à vis de celles contenant l'énergie, permettent de prévoir pour les vitesses les lois de décroissance des fonctions spectrales à trois dimensions dans l'espace. On suppose la turbulence localement homogène et isotrope. En fait les résultats expérimentaux montrent que les lois de décroissance spectrales (11) sont en général applicables même en turbulence anisotrope si le nombre de Reynolds est fort, ainsi il en est de la loi en $k^{-5/3}$ (12, 13, 14). En ce qui concerne le champ de température, on le considère comme passif et sous la dépendance du champ de vitesse ; CORRSIN (15) notamment définit pour les nombres de Péclet élevés une zone d'équilibre de convection qui joue le rôle de la zone d'équilibre dynamique de KOLMOGOROV (11) lorsque le nombre de Reynolds est élevé ; l'analyse dimensionnelle montre que dans cette zone la fonction spectrale à trois dimensions de température est proportionnelle à $\varepsilon_\theta \, \varepsilon^{-1/3} \, k^{-5/3}$ ε étant la dissipation par viscosité de la turbulence de vitesse et ε_θ la dissipation par la conductivité moléculaire des fluctuations turbulentes de température. Toutefois BATCHELOR (16) a montré que les zones d'inertie et de convection, où les lois spectrales seraient en $k^{-5/3}$ ne sont d'étendue comparable que si le nombre de Prandlt est voisin de l'unité, ce qui est d'ailleurs le cas des présentes mesures. PLATE et ARYA (17) semblent avoir vérifié dans une couche limite à grand nombre de Reynolds, avec effet de stratification, la décroissance spectrale en $k^{-5/3}$ pour la température. De plus, la loi de décroissance spectrale en k^{-4} ,établie par TCHEN pour les vitesses (18) lorsque le taux de production de turbulence est élevé, serait vérifiée expérimentalement pour les températures par PLATE et ARYA dans l'expérience précitée, ainsi que par BREMHORST et BULLOCK dans un conduit cylindrique (10).

En ce qui concerne les présents résultats, on s'est surtout attaché à effectuer une comparaison entre les énergies spectrales des fluctuations de température et des fluctuations de vitesse. Cependant des considérations ont été faites sur les lois de variation spectrale. Ainsi, nous avons comparé le spectre de température $F_{\theta\theta}$ (n) de TAYLOR, n étant la fréquence, au spectre Q (n) défini par l'expression :

$$\overline{q'^2} \, Q(n) = \overline{u'^2} \, F_{uu}(n) + \overline{v'^2} \, F_{vv}(n) + \overline{w'^2} \, F_{ww}(n) \qquad (1)$$

$$\overline{q'^2} = \overline{u'^2} + \overline{v'^2} + \overline{w'^2} \qquad F_{uu} \; , \; F_{vv} \; , \; F_{ww} \quad \text{spectres}$$

de TAYLOR des composantes u' , v' , w' . En effet les équations conduisent à faire une analogie entre le scalaire $\overline{\theta'\theta'_o}$

et le produit scalaire : $\overline{q'.q'_o} = \overline{u'u'_o} + \overline{v'v'_o} + \overline{w'w'_o}$

Les valeurs sont considérées en deux points de l'espace et du temps. En un point fixe de l'espace, avec un décalage dans le temps τ , on compare les autocorrélations dans le temps :

$$\overline{\theta'(t)\,\theta'(t+\tau)} \quad \text{et} \quad \overline{u'(t)\,u'(t+\tau)} + \overline{v'(t)\,v'(t+\tau)} + \overline{w'(t)\,w'(t+\tau)}$$

ce qui conduit par transformation de Fourier aux spectres $F_{\theta\theta}(n)$ et $Q(n)$ précités.

L'expérience confirme l'intérêt du choix de $Q(n)$ comme critère de comparaison.

2.- DISPOSITIF EXPERIMENTAL

Les mesures ont été effectuées au-dessus de la plaque plane chauffée disposée dans le plancher de la soufflerie S.2 de l'I.M.S.T. (3). La longueur de la maquette est de 4850 mm, la largeur de 560 mm. Deux cas d'expériences sont à distinguer. Dans le premier cas, le début du chauffage était à 3050 mm en aval de la transition à la turbulence , transition obtenue par un réglet. Dans le deuxième cas, le chauffage ne débutait qu'à 250 mm en aval de la transition. Compte-tenu de la position de mesure habituelle située à une distance X = 3690 mm de la transition, la couche limite dynamique est à cette position entièrement chauffée. Dans le premier cas la distance X_θ en aval du début du chauffage était habituellement de 640 mm et dans le deuxième cas de 3440 mm. A la position X = 3690 mm, les conditions aérodynamiques sont les suivantes : vitesse extérieure U_e = 12 m sec^{-1} ; épaisseur de la couche limite à $U=U_e$ $\delta \approx 62$ mm ; vitesse de frottement V^* = 0,46 m sec^{-1} ; coefficient de frottement C_f = 30.10^{-4}. Les écarts de température entre la paroi et l'air de la veine d'expériences sont $\Theta_n - \Theta_e \approx 22°C$. Dans le premier cas d'expérience, le nombre de Stanton est S_t = 21.10^{-4}, dans le deuxième cas S_t = 17.10^{-4}. Des mesures de contrôle ont été effectuées en dessous de la maquette à plaque plane chauffée disposée dans la soufflerie S.1 de l'I.M.S.T. (8). Les mesures de profil de vitesse avec et sans chauffage sur les deux maquettes, dans lesquelles la gravité joue en sens opposé, montrent que les chauffages n'ont pratiquement pas d'effet, à la précision près des mesures, sur les

grandeurs moyennes.

En ce qui concerne l'appareillage de mesure, des fils chauds droits et croisés en X ont été utilisés. Le diamètre des fils, en platine rhodié, était en général de 2,5 μ . Les anémomètres sont à intensité de courant de chauffage constante (19). La bande passante de ces appareils est de 1 Hz à 6000 Hz (à 3db). D'autres appareils ont été utilisés pour des contrôles, dont la bande passante est de 1, Hz à 6 000 Hz (à 3 db). La gamme de mesure de l'analyseur spectral (14) s'étend de 1 à 6 000 Hz. Les courbes de sélectivité pour les diverses fréquences utilisées ont été déterminées avec précision ; la largeur de bande passante du filtre est égale à 5 % de la fréquence d'accord. Toutefois, pour les fréquences supérieures à environ 3 000 Hz, la sélectivité de ce genre d'appareil est mal adaptée aux mesures des spectres de turbulence, qui décroissent très fortement lorsque la fréquence augmente. Par contre,aux fréquences basses son fonctionnement est satisfaisant (14).

La constante de temps due à l'inertie thermique des fils chauds est déterminée par la méthode des signaux hautes fréquences (19).

3.- METHODE DE MESURE DES REPARTITIONS SPECTRALES EN PRESENCE DE FLUCTUATIONS DE VITESSE ET DE TEMPERATURE

Des mesures de $\overline{u'^2}$, $\overline{\theta'^2}$ et $\overline{\theta'u'}$ ont été effectuées avec deux fils chauds parallèles, ou mis bout à bout, afin de séparer les variables u' et θ' . Les résultats ont été plus incertains que ceux obtenus avec un seul fil et la méthode du diagramme de fluctuations (1).

Les répartitions spectrales de $\overline{\theta'^2}$, $\overline{u'^2}$,des corrélations $\overline{\theta'u'}$ et $\overline{\theta'v'}$ ont donc été mesurées par la méthode des diagrammes de fluctuations appliquée aux signaux filtrés en fréquence (6).

Dans le cas d'un seul fil perpendiculaire à la vitesse moyenne, on a la relation (6) :

$$e^{*2} = \left(\frac{\sqrt{(\hat{e})^2}}{\beta}\right)^2 = r^2 \frac{\widehat{(u)^2}}{U^2} - 2 r \frac{\widehat{u'\theta'}}{U\Theta} + \frac{\widehat{(\theta')^2}}{\Theta^2} \qquad (2)$$

le symbole $(\wedge)$ indique que le signal est obtenu à la sortie d'un filtre linéaire de largeur de bande Δn ; e^*est le signal fluctuant aux bornes du fil chaud ; $r = \alpha/\beta$ où α est le coefficient de sensibilité à la vitesse et β à la température. Le coefficient r est fonction du courant de chauffage du fil. Le diagramme obtenu, qui est une hyperbole dans la représentation fonction de r , donne les valeurs de $\widehat{(u)^2}, \widehat{(\theta)^2}$ et $\widehat{u'\theta'}$, soit un point correspondant à la fréquence d'accord n pour les spectres $F_{uu}(n), F_{\theta\theta}(n)$ et $F_{\theta u}(n)$ respectivement (cf. 5.1.).

Dans le cas de deux fils (notés 1 et 2) croisés en X (1) on a la relation, avec application d'un filtre linéaire (6) :

$$e^{*2} = \frac{\widehat{(e_1)^2} - \widehat{(e_2)^2}}{2 \mathcal{E}'(\beta_1+\beta_2)} = - r \frac{\widehat{u'v'}}{U^2} + \frac{\widehat{\theta'v'}}{\Theta U} \qquad (3)$$

$\mathcal{E}'$étant le coefficient de sensibilité à v' . Le diagramme tracé qui est une droite dans la représentation e^* en fonction de r permet donc d'obtenir un point des spectres $F_{uv}(n)$ et $F_{\theta v}(n)$ correspondants aux corrélations $\overline{u'v'}$ et $\overline{\theta'v'}$.

La Figure 8 présente un exemple de mesures effectuées à une distance de la paroi $y = 7$ mm par la méthode précitée. Les grandeurs spectrales F sont normées à l'unité, et les grandeurs spectrales E aux valeurs des coefficients de corrélation R correspondant. En abscisse sont portés les logarithmes des nombres d'onde $k_1 = 2\pi n/U$, en ordonnée les valeurs $k_1 F(k_1)$ ou $k_1 E(k_1)$; les conditions de normalisation sont donc :

$$\int_0^\infty k_1 F(k_1) d(Log\, k_1) = 1 \quad \text{et} \quad \int_0^\infty k_1 E(k_1) d(Log\, k_1) = R \qquad (4)$$

Cette representation a l'avantage de mettre en évidence les zones spectrales qui renferment une énergie notable, en considérant simplement les aires.

Dans le cas des spectres $F_{\theta\theta}$, F_{uu} , $E_{\theta u}$, $E_{\theta v}$ les points correspondent aux mesures faites par la méthode des diagrammes. La courbe tracée pour F_{uu} a été obtenue en écoulement isotherme, la concordance avec les résultats déduits des diagrammes est satisfaisante. Ceci confirme que le chauffage ne semble pas modifier le champ des vitesses fluctuantes. La courbe tracée pour $F_{\theta\theta}$ a été obtenue avec un fil chaud très peu chauffé ($r \sim 0,009$), après correction de la contamination due surtout à $\overline{\theta'u'}$ (Equa. 2); l'accord avec les points déduits des diagrammes est aussi satisfaisant, ce qui justifie l'utilisation d'un fil peu chauffé pour la mesure des spectres de température. Notons que sur la Figure 8 les spectres $F_{\theta\theta}$ et $E_{\theta u}$ ont été mesurés dans le premier cas d'expérience ($X_\theta = 640$ mm). Si on ne corrige pas les mesures faites avec un fil peu chauffé ($r \sim 0,009$) de la contamination, les spectres ont la même forme mais sont décalés vers les basses fréquences. A titre d'exemple dans le cas de la Figure 8, l'énergie non corrigée est en excès de 18 % à $k_1 = 11$ m^{-1} et en défaut de 19 % à $k_1 = 1485$ m^{-1} , ce qui équivaut pratiquement à un décalage d'ensemble du spectre non corrigé de 20 % vers les bas nombres d'ondes. Toutefois près de la paroi ($y \sim 0,5$ mm) les spectres de θ' et de u' étant voisins (Fig. 1) les corrections sont négligeables.

Malgré l'utilisation de fil chaud de diamètre faible 2,5 μ , dont la constante de temps reste inférieure à 0,40 millisec., une erreur dans la mesure de la constante de temps peut entraîner une modification des spectres importante, principalement pour les températures qui ont un spectre étendu aux fréquences élevées. La détermination des constantes de temps a donc été effectuée soigneusement et nous estimons que l'incertitude sur la valeur spectrale est à 1 000 Hz de l'ordre de 1 % et à 4 000 Hz de 13 %.

A titre d'exemple une partie des mesures spectrales effectuées à des distances qui sont représentatives des différentes zones de la couche limite sont présentées dans les figures 1 à 6. Ces exemples ont été choisis parmi les mesures effectuées lorsque le début du chauffage est voisin de la transition à la turbulence (X_θ = 440 mm). Les points expérimentaux de $F_{\theta\theta}$ ne sont pas corrigés d'effets possibles de contamination (Cf. Parag. 5). L'intérêt de la représentation utilisée, avec une échelle logarithmique en abscisse, a été commenté paragraphe 3.

Les spectres de température $F_{\theta\theta}$ et les spectres des trois composantes de vitesse pondérées par leur énergie relative $\overline{u'^2}/\overline{q'^2} F_{uu}$, $\overline{v'^2}/\overline{q'^2} F_{vv}$, $\overline{w'^2}/\overline{q'^2} F_{ww}$ sont donnés. Le spectre $Q(k_4)$ calculé par la formule (1) est indiqué en traits tirets courts, le spectre F_{uu} est aussi mentionné en tirets fins. Pour chaque cas de figure, on a déterminé, en faisant l'hypothèse de Taylor, les longueurs suivantes (13) :
- la longueur intégrale $L_u \approx \pi/2\, F_{uu}$ (5) pour les plus petits k_4 ;
- les longueurs de dissipation relatives aux trois composantes de la vitesse par les relations :
$$\lambda \approx U/2\pi N \quad \text{avec} \quad N^2 = \int_0^\infty n^2 F(n)\, dn \qquad (6)$$

On définit d'une façon similaire une longueur* λ_θ pour la température ; λ_θ est liée à la dissipation de $\overline{\theta'^2}$ par la conduction moléculaire (Cf. Parag. 5.4.). Nous avons défini aussi λ_Q à partir de l'équation (1) :
$$\overline{q'^2}\, \lambda_Q^{-2} = \overline{u'^2}\lambda_U^{-2} + \overline{v'^2}\lambda_V^{-2} + \overline{w'^2}\lambda_W^{-2} \qquad (7)$$

Les valeurs L_u, λ_u, λ_Q et λ_θ données ci-après sont lues sur des courbes moyennes tracées à partir de 10 à 13 positions de mesure. Les valeurs de λ_θ correspondent aux spectres $F_{\theta\theta}$ non corrigés d'effets de contamination. Le nombre de Reynolds $\mathcal{R}_\lambda = \sqrt{\overline{u'^2}}\,\lambda_u/\nu$ est voisin de 135 dans la région centrale de la couche limite.

La Figure 1 présente les résultats à la distance y = 0,5 mm de la paroi, le nombre de Reynolds correspondant $y^+ = v^* y/\nu$ = 15,5. Les valeurs des autres paramètres sont L_u = 12,5mm, λ_u = 2,0 mm, λ_Q = 1,8 mm, λ_θ = 1,8 mm, la vitesse U = 5,26 m sec^{-1}. Les spectres F_{vv} et F_{ww} n'ont pu être mesurés à cette position à cause des dimensions du fil en X, les courbes tracées ont été estimées avec une marge d'incertitude faible, car elles sont peu évolutives en nombre d'onde lorsque la distance y varie. Les valeurs de $\overline{u'^2}$ et $\overline{v'^2}$ ont été déterminées compte tenu des valeurs proposées par KLEBANOFF (12). A cette position, où la production de turbulence est proche de son maximum, on constate que F_{uu} diffère assez peu de $F_{\theta\theta}$, mais le spectre $Q(k_4)$ calculé en est encore plus voisin.

La Figure 2 présente les résultats pour y = 2,5 mm, y^+ = 77, L_u = 24,4 mm, λ_u = 2,1 mm, λ_Q = 1,5 mm, λ_θ = 1,3 mm, U = 7,38 m sec^{-1}. Cette position est située dans la zone où le profil de vitesse est logarithmique. Le spectre F_{uu} diffère plus du spectre de $F_{\theta\theta}$ qu'à la position y = 0,5 mm, par contre le spectre Q en reste voisin, ceci est dû à ce que les composantes v' et w' prennent de l'importance vis à vis de u'. De plus il apparaît dans le spectre $F_{\theta\theta}$ un palier accentué que l'on retrouve, quoique moins accusé, dans le spectre calculé Q.

La Figure 3 est relative à y = 7 mm position correspondant encore à la zone de la loi logarithmique de la vitesse. Les valeurs des paramètres sont y^+ = 215, L_u = 30,7 mm, λ_u = 2,4 mm, λ_Q = 1,7 mm, λ_θ = 1,4 mm (valeur corrigée 1,3 mm), U = 8,54 m/sec. Les mêmes remarques peuvent être faites que dans le cas de la figure 2.

La Figure 4 correspond à y = 15 mm, y^+ = 460, L_u = 31,4 mm, λ_u = 2,9 mm, λ_Q = 2,2mm, λ_θ = 1,7 mm (valeur corrigée 1,6 mm), U = 9,64 m/sec. Cette position est située au début de la zone dite de sillage. Le palier du spectre $F_{\theta\theta}$ a disparu, le spectre Q reste voisin de $F_{\theta\theta}$, toutefois il lui est inférieur pour les nombres d'onde élevés, ce qui est mis en évidence par les valeurs de λ_Q et λ_θ.

La Figure 5 présente les résultats à y = 30 mm pour y^+ = 930, L_u = 31,4 mm, λ_u = 3,8 mm, λ_Q = 2,7 mm, λ_θ = 2,2 mm, U = 10,94 m/sec. Cette distance correspond à la zone de sillage, l'intermittence est d'environ 98 %. Les spectres de v' et w' continuent de prendre de l'importance relative ; le spectre Q demeure voisin du spectre $F_{\theta\theta}$ et le spectre F_{uu} est nettement décalé vers les grandes échelles.

La Figure 6 donne les résultats pour y = 50 mm, y^+ = 1550, L_u = 24,0 mm, λ_u = 4,8mm, λ_Q = 3,4 mm, λ_θ = 3,0 mm, U = 11,90 m sec^{-1}. L'intermittence est d'environ 45 %. Les mêmes constatations peuvent être faites que pour la figure 5.

Etant donné que la pondération des spectres de vitesse est capitale dans le calcul de Q, la figure 7 présente les écarts types relatifs des fluctuations turbulentes de vitesse et de température dans la couche limite. Il semble que les rapports $\dfrac{\sqrt{\overline{q'^2}}\,(\partial\theta/\partial y)}{\sqrt{\overline{\theta'^2}}\,(\partial U/\partial y)}$ soient peu variables,

pour $y > 0,5$ mm, restant voisin de -1,5.

5.- DISCUSSIONS DES RESULTATS

Il est nécessaire pour interpréter les résultats d'expériences d'établir les équations de bilan des répartitions spectrales au sens de Taylor.

---

* HINZE (13) définit une longueur $\lambda'_\theta = \sqrt{2}\,\lambda_\theta$
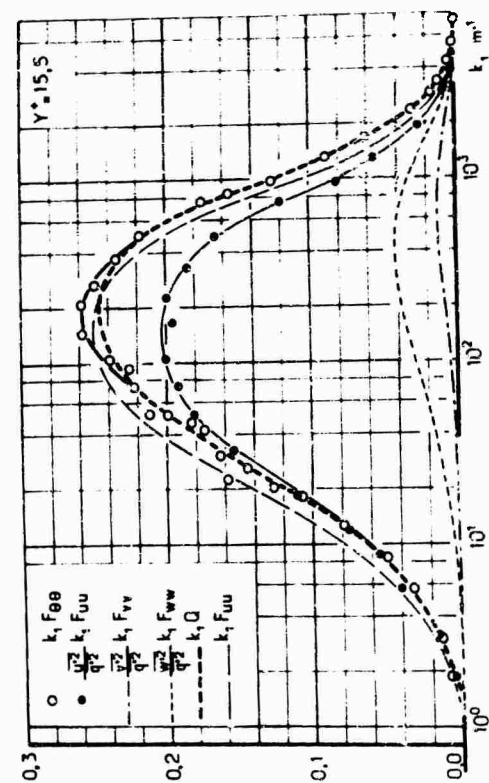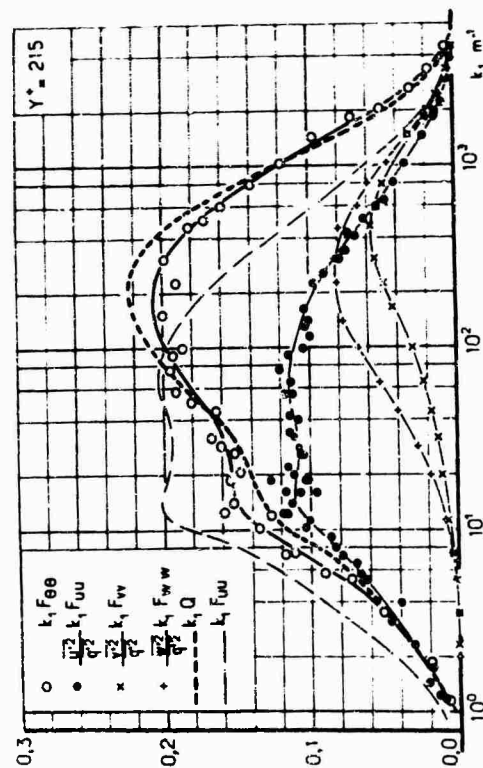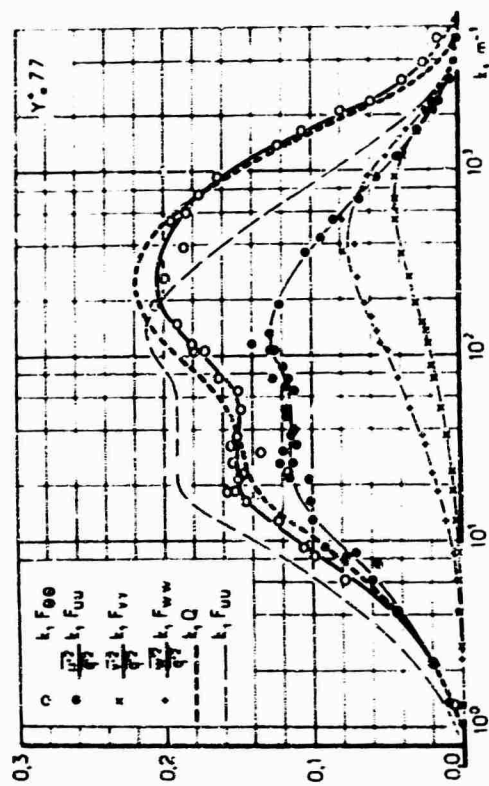
Figure.2.

Figure.4.

Figure.1.
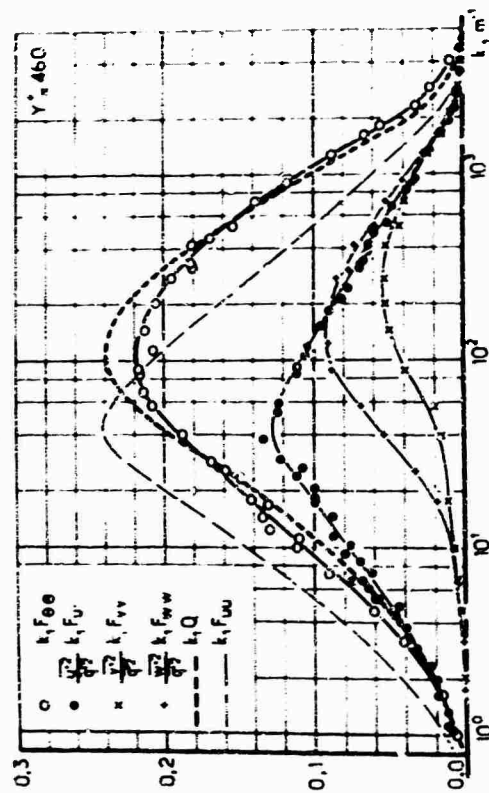
Figure.3.

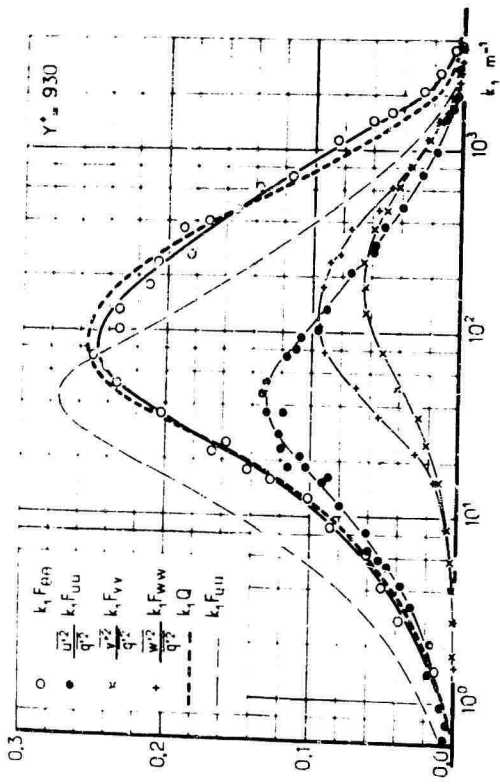REPARTITIONS SPECTRALES DES FLUCTUATIONS DE TEMPERATURE ET DE VITESSE

Figure.5.

Figure.6.

REPARTITIONS SPECTRALES DES FLUCTUATIONS DE TEMPERATURE ET DE VITESSE
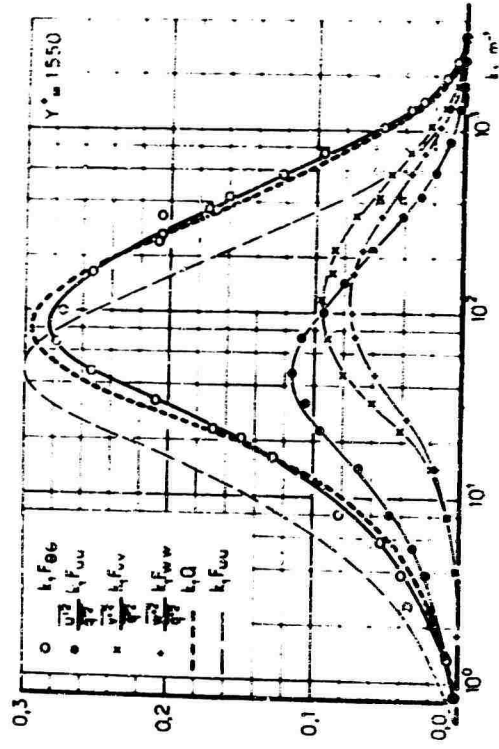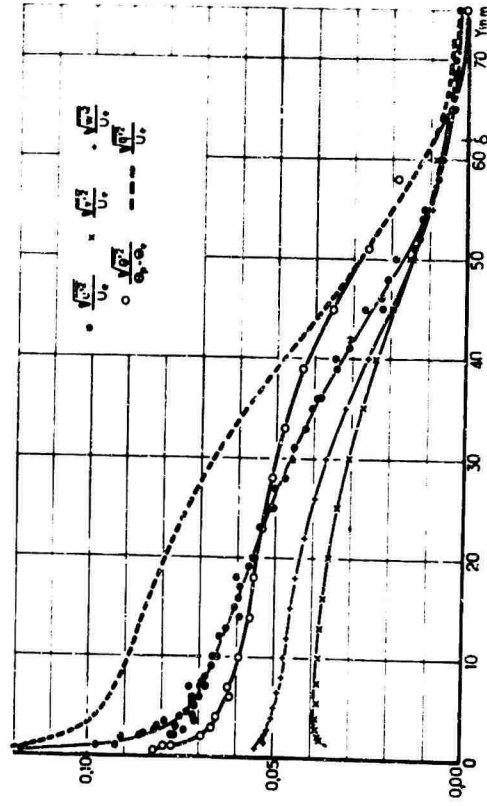
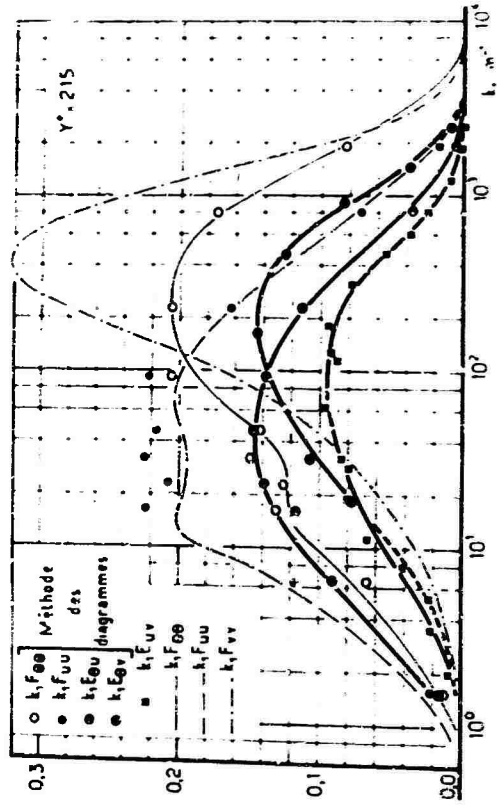Figure.7. ECARTS TYPES RELATIFS DES FLUCTUATIONS

Figure.8. REPARTITIONS SPECTRALES DES CORRELATIONS

5.1. Équations de bilan spectral.

Les équations aux fluctuations, en notation tensorielle, pour les composantes de vitesse sont (20 , 8) :

$$\frac{\partial v'_\alpha}{\partial t} + V_\gamma \frac{\partial v'_\alpha}{\partial X_\gamma} + v'_\gamma \frac{\partial V_\alpha}{\partial X_\gamma} = - \frac{\partial v'_\gamma v'_\alpha}{\partial X_\gamma} + \frac{\partial \overline{v'_\gamma v'_\alpha}}{\partial X_\gamma} - \frac{1}{\rho} \frac{\partial p'}{\partial X_\alpha} + \frac{1}{\rho} \frac{\partial f'_{\alpha\gamma}}{\partial X_\gamma} \qquad (8)$$

le symbole $\overline{(\ )}$ indique une moyenne statistique, $f'_{\alpha\gamma}$ fluctuation des tensions moléculaires.

Pour la température, dans les conditions de ces expériences, l'équation s'écrit (8) :

$$\frac{\partial \theta'}{\partial t} + V_\gamma \frac{\partial \theta'}{\partial X_\gamma} + v'_\gamma \frac{\partial \Theta}{\partial X_\gamma} = - \frac{\partial v'_\gamma \theta'}{\partial X_\gamma} + \frac{\partial \overline{v'_\gamma \theta'}}{\partial X_\gamma} + \frac{1}{\rho C_p} \frac{\partial h'_\gamma}{\partial X_\gamma} \qquad (9)$$

h'_γ représentant les fluctuations de la conduction moléculaire. On pourrait obtenir les équations de bilan spectral par transformée de Fourier des équations de bilan des corrélations dans le temps (22). Au point de vue physique la technique expérimentale est mieux suivie en considérant un filtre linéaire passif (21) noté $\widehat{(\ )}$. Appliquons cet opérateur $\widehat{(\ )}$ aux équations (8) et (9) . Multiplions alors l'équation des vitesses par $\widehat{v'_\alpha}$ et celle des températures par $\widehat{\theta'}$. On a $\frac{\widehat{\partial(\ )}}{\partial t} = \frac{\partial\widehat{(\ )}}{\partial t}$ (8) . Ceci entraîne que $\widehat{v'_\alpha}\widehat{\left(\frac{\partial v'_\alpha}{\partial t}\right)} = \frac{1}{2}\frac{\partial}{\partial t}\widehat{v'_\alpha}\widehat{v'_\alpha} = 0$ et de même $\widehat{\theta'}\widehat{\left(\frac{\partial\theta'}{\partial t}\right)} = 0$. Les équations moyennées relatives aux vitesses avec sommation des indices α et γ sont, compte tenu de l'équation de continuité :

$$V_\gamma \frac{\partial \overline{\widehat{v'_\alpha}\widehat{v'_\alpha}}/2}{\partial X_\gamma} + \overline{\widehat{v'_\alpha}\widehat{v'_\gamma}} \frac{\partial V_\alpha}{\partial X_\gamma} = - \overline{\widehat{v'_\alpha}\frac{\partial \widehat{v'_\alpha v'_\gamma}}{\partial X_\gamma}} - \frac{1}{\rho}\frac{\partial\overline{\widehat{v'_\alpha}\widehat{p'}}}{\partial X_\alpha} + \frac{1}{\rho}\overline{\widehat{v'_\alpha}\frac{\partial\widehat{f'_{\alpha\gamma}}}{\partial X_\gamma}} \qquad (10)$$

avec $\overline{\widehat{v'_\alpha}\widehat{v'_\alpha}} = \overline{\widehat{q'}\,\widehat{q'}}$, $\widehat{q'}$ vecteur de composante $\widehat{v'_\alpha}$.

Pour la température, l'équation s'écrit de même

$$V_\gamma \frac{\partial \overline{\widehat{\theta'}\widehat{\theta'}}/2}{\partial X_\gamma} + \overline{\widehat{\theta'}\widehat{v'_\gamma}} \frac{\partial \Theta}{\partial X_\gamma} = - \overline{\widehat{\theta'}\frac{\partial(\widehat{\theta'v'_\gamma})}{\partial X_\gamma}} + \frac{1}{\rho C_p}\overline{\widehat{\theta'}\frac{\partial\widehat{h'_\gamma}}{\partial X_\gamma}} \qquad (11)$$

Introduisons alors les spectres et les co-spectres (22) supposés continus ; si le filtre est idéal et de largeur infiniment étroite, Δn , on a :

$$\overline{\widehat{v'_\alpha}\widehat{v'_\alpha}} = \overline{q'^2}\,Q(n)\Delta n \quad , \quad \overline{\widehat{v'_\alpha}\widehat{v'_\gamma}} = \overline{v'_\alpha v'_\gamma}\,F_{\alpha\gamma}(n)\,\Delta n \quad , \quad \overline{\widehat{v'_\alpha}\frac{\partial\widehat{v'_\alpha v'_\gamma}}{\partial X_\gamma}} = \overline{v'_\alpha\frac{\partial v'_\alpha v'_\gamma}{\partial X_\gamma}}\,S_{\alpha\gamma}(n)\,\Delta n \,,$$

$$\overline{\widehat{v'_\alpha}\widehat{p'}} = \overline{v'_\alpha p'}\,\pi_\alpha(n)\,\Delta n \quad , \quad \overline{\widehat{v'_\alpha}\frac{\partial\widehat{f'_{\alpha\gamma}}}{\partial X_\gamma}} = \overline{v'_\alpha\frac{\partial f'_{\alpha\gamma}}{\partial X_\gamma}}\,D_{\alpha\gamma}(n)\Delta n, \quad \overline{\widehat{\theta'}\widehat{\theta'}} = \overline{\theta'^2}\,F_{\theta\theta}(n)\,\Delta n \quad , \qquad (12)$$

$$\overline{\widehat{\theta'}\widehat{v'_\gamma}} = \overline{\theta'v'_\gamma}\,F_{\theta,\gamma}(n)\,\Delta n \quad , \quad \overline{\widehat{\theta'}\frac{\partial\widehat{\theta'v'_\gamma}}{\partial X_\gamma}} = \overline{\theta'\frac{\partial\theta'v'_\gamma}{\partial X_\gamma}}\,S_{\theta,\gamma}(n)\Delta n, \quad \overline{\widehat{\theta'}\frac{\partial\widehat{h'_\gamma}}{\partial X_\gamma}} = \overline{\theta'\frac{\partial h'_\gamma}{\partial X_\gamma}}\,D_{\theta,\gamma}(n)\Delta n \,,$$

les équations s'écrivent alors :

$$V_\gamma\frac{\partial\overline{q'^2}/2\,Q(n)}{\partial X_\gamma} + F_{\alpha\gamma}(n)\overline{v'_\alpha v'_\gamma}\frac{\partial V_\alpha}{\partial X_\gamma} = -S_{\alpha\gamma}(n)\overline{\frac{\partial v'_\alpha v'_\gamma}{\partial X_\gamma}/2v'_\gamma} - \frac{1}{\rho}\frac{\partial(\overline{v'_\alpha p'}\,\pi_\alpha(n))}{\partial X_\alpha} + \frac{1}{\rho}D_{\alpha\gamma}(n)\overline{v'_\alpha\frac{\partial f'_{\alpha\gamma}}{\partial X_\gamma}}$$
$$\qquad (13)$$
$$V_\gamma\frac{\partial\overline{\theta'^2}/2\,F_{\theta\theta}}{\partial X_\gamma} + F_{\theta,\gamma}(n)\overline{\theta'v'_\gamma}\frac{\partial\Theta}{\partial X_\gamma} = -S_{\theta,\gamma}(n)\overline{\frac{\partial\theta'^2}{\partial X_\gamma}/2v'_\gamma} + \frac{1}{\rho C_p}D_{\theta,\gamma}(n)\overline{\theta'\frac{\partial h'_\gamma}{\partial X_\gamma}}$$

Si l'on intègre pour toutes les fréquences de 0 à l'infini, on retrouve bien les équations de bilan classiques; pour une fréquence donnée les termes moyens habituels sont à pondérer par les fonctions spectrales, qui peuvent modifier les rapports de grandeur de ces termes.

5.2. Validité de la comparaison proposée entre $Q(k_1)$ et $F_{\theta\theta}(k_1)$.

Il ressort des six exemples présentés, ainsi que de cinq autres mesures effectuées à des positions intermédiaires et non données ici, que le spectre $Q(k_1)$ est voisin du spectre $F_{\theta\theta}(k_1)$. Néanmoins, aux nombres d'ondes élevés, il apparaît d'après la comparaison des valeurs de λ_q qui sont supérieures à λ_θ , et d'après les figures 1 à 6 et 9, que Q renferme moins d'énergie que $F_{\theta\theta}$. Cette différence se situe environ au delà des nombres d'onde $1/\lambda_Q$, c'est à dire lorsque la viscosité et la conductivité se manifestent. Toutefois, à la position $y = 0,5mm$, la concordance semblerait se vérifier à tous les nombres d'ondes, mais les spectres des composantes V' et W' , dont l'influence est déterminante aux fréquences élevées, ayant été estimés, rendent ce résultat sujet à caution aux grands nombres d'ondes.

Notons de plus que les points expérimentaux présentés pour $F_{\theta\theta}$ ne sont pas ici corrigés de la contamination due à la composante u' ; en fait cette correction améliorerait la comparaison effectuée entre Q et $F_{\theta\theta}$ pour les nombres inférieurs à $1/\lambda_Q$, et accentuerait légèrement la différence aux nombres d'ondes plus élevés.

Par ailleurs, les mesures qui ont été effectuées dans le cas où le chauffage est situé loin en aval de la transition ($X_\theta = 640$ mm) montrent que les spectres $F_{\theta\theta}$ ne subissent pas de modifications significatives; les considérations précédentes sont donc aussi valables. Ceci confirme, en outre, que le champ fluctuant de température est bien sous la dépendance du champ turbulent de vitesse. CORRSIN et UBEROI (9) dans un jet cylindrique chauffé étaient arrivés à la conclusion que les spectres à trois dimensions de la vitesse et de la température, sur l'axe du jet, semblaient approximativement semblables ("roughly alike"). Cette conclusion est en faveur de l'introduction de la fonction $Q(k_1)$. En effet, en turbulence homogène et isotrope, on a :

$$\overline{u'^2}F_{uu}(k_1) = \int_{k_1}^\infty \frac{E(k)}{k}\left(1 - \frac{k_1^2}{k^2}\right)dk \quad , \quad \overline{v'^2}F_{vv}(k_1) = \frac{1}{2}\int_{k_1}^\infty \frac{E(k)}{k}\left(1 + \frac{k_1^2}{k^2}\right)dk \qquad (14)$$

$E(k)$ fonction spectrale à trois dimensions (13) avec $\overline{q'^2} = 2 \int_o^\infty E(k) \, dk$ (15)

En ce qui concerne la température, on définit de même (13) : $\overline{\theta'^2} = \int_o^\infty E_\theta(k) \, dk$ (16)

et on a la relation $\overline{\theta'^2} F_{\theta\theta}(k_4) = \int_{k_4}^\infty \frac{E_\theta(k)}{k} \, dk$ (17) qui est à rapprocher de celle

déduite de (14) et (15) pour $Q(k_4)$: $\overline{q'^2} Q(k_4) = 2 \int_{k_4}^\infty \frac{E(k)}{k} \, dk$ (18)

L'analogie proposée entre $F_{\theta\theta}$ et Q reviendrait, en turbulence isotrope, à supposer une simili-tude entre les fonctions spectrales à trois dimensions $E(k)$ et $E_\theta(k)$, tout au moins en ce qui concerne les nombres d'ondes inférieurs à $1/\lambda_\theta$. Cette hypothèse avait été avancée en 1949 par KOVASZNAY, UBEROI et CORRSIN (23) ; il ne semble pas qu'elle ait été reprise par la suite, car les mesures de MILLS, KISTLER, O'BRIEN et CORRSIN (24) en aval d'une grille de turbulence chauf-fée montreraient   plutôt que les spectres F_{UU} et $F_{\theta\theta}$ sont comparables.

5.5. Répartitions spectrales des termes de production et spectre de température.

La figure 8 présente avec le même système de coordonnées que les figures 1 à 6, un exemple des co-spectres $E_{\theta U}$, $E_{\theta V}$ et E_{UV} à la distance $y = 7$ mm ($y^+ = 215$). Ces répartitions spectrales sont représentatives pour la région centrale de la couche limite où le profil des vitesses est logarithmique. Les coefficients de corrélation correspondants sont nettement différents pour la température et la vitesse :

$$R_{\theta u} = \int_o^\infty E_{\theta U}(k_4) \, dk_4 \# 0,65 \quad , \quad R_{\theta v} = \int_o^\infty E_{\theta V}(k_4) \, dk_4 \# 0,60 \quad , \quad R_{uv} = \int_o^\infty E_{UV}(k_4) \, dk \# 0,40$$

De plus, les co-spectres $E_{\theta V}$ et E_{UV} , qui interviennent dans les termes principaux de produc-tion (Equs. 13) avec les simplifications habituelles p   couche limite, montrent un décalage de $E_{\theta V}$ par rapport à E_{UV} vers les nombres d'ondes élevés. Si l'on considère le rapport des productions relatives correspondantes, à savoir : $\dfrac{\overline{q'^2}}{\overline{\theta'^2}} \dfrac{\overline{\theta v}}{\overline{u'v'}} \dfrac{\partial \Theta/\partial y}{\partial U/\partial y} \approx \dfrac{2,2}{Pr_t} \approx 2,7$

(Pr_t nombre de Prandtl turbulent voisin de 0,85 pour $y = 7$ mm) on voit que globalement la production relative est nettement plus forte pour la température que pour la vitesse, et ceci s'accentue très fortement aux nombres d'onde élevés.

Dans les figures 2 et 3 on a vu que le spectre de $F_{\theta\theta}$ présentait un palier accentué. Sur la Figure 8 on constate que ce palier correspond au maximum de $E_{\theta U}$ et à une variation en k_4^{-1} de F_{UU} . Dans ce domaine de nombre d'onde le coefficient de corrélation entre θ' et u' est encore élevé, voisin de 0,8 dans le cas de cet exemple. D'une façon générale aux faibles nombres d'onde la température est en forte corrélation avec la composante longitudinale de vitesse et aux nombres d'ondes plus élevés, de l'ordre de $1/\lambda_\theta$, en forte corrélation avec la composante normale V' . La composante W' , par suite de l'homogénéité spatiale, n'intervient pas dans les termes de production, par contre elle intervient notamment dans les termes moléculaires explicitement ou implicitement.

La Figure 9 donne, dans la représentation classique (échelles logarithmiques), $F_{\theta\theta}$, F_{UU} et Q en fonction de k_4 . Les pentes correspondant aux lois en k_4^{-1} et $k_4^{-5/3}$ sont tracées afin que l'on puisse, dans le cas de ces expériences, constater le domaine de validité de ces lois. La loi de Tchen est mieux vérifiée pour F_{UU} que pour $F_{\theta\theta}$ par suite notamment du palier précité (Cf. Fig. 2 et 3).

5.4. Répartitions spectrales aux nombres d'onde élevés.

La Figure 9 notamment permet de comparer les décroissances de $\overline{F}_{UU}$, $F_{\theta\theta}$ et Q aux valeurs élevées de k_4 , où l'on vérifie (Cf. Parag. 5.2.) que $Q(k_4)$ devient inférieur à $F_{\theta\theta}(k_4)$.

On admet que (16, 25), dans cette zone, le spectre $F_{\theta\theta}$ n'est fonction que de la dissipation de l'énergie cinétique ε, de la viscosité cinématique ν , de la dissipation des fluctuations thermiques ε_θ , et de la diffusivité α . A partir des équations (13) , prises globalement pour toutes les fréquences, on peut expliciter les termes correspon-dant aux effets moléculaires avec les hypothèses habituelles (13) :

$$\frac{1}{\rho} \overline{v'_\alpha \frac{\partial \sigma'_{\alpha\gamma}}{\partial X_\gamma}} = \nu \frac{\partial}{\partial X_\gamma} \overline{v'_\alpha \left| \frac{\partial v'_\alpha}{\partial X_\gamma} + \frac{\partial v'_\gamma}{\partial X_\alpha} \right|} - \nu \overline{\left| \frac{\partial v'_\alpha}{\partial X_\gamma} + \frac{\partial v'_\gamma}{\partial X_\alpha} \right| \frac{\partial v'_\alpha}{\partial X_\gamma}} \quad (19)$$

$$\underbrace{}_{\text{I}} \qquad \underbrace{}_{\text{II}}$$

$$\frac{1}{\rho C_p} \overline{\theta' \frac{\partial h'_\gamma}{\partial X_\gamma}} = \alpha \frac{\partial}{\partial X_\gamma} \overline{\left| \theta' \frac{\partial \theta'}{\partial X_\gamma} \right|} - \alpha \overline{\frac{\partial \theta'}{\partial X_\gamma} \frac{\partial \theta'}{\partial X_\gamma}} \quad (20)$$

$$\underbrace{}_{\text{I}} \qquad \underbrace{}_{\text{II}}$$

Les termes I sont les termes de diffu-sion ; les termes II représentent la dissi-pation des fluctuations de l'échelle turbulente à l'échelle moléculaire . On définit habituellement ε par le terme II de (19) ce qui conduit en turbulence (dans notre cas $\lambda_g = \lambda_u$) ou encore, avec la

FIGURE 9 - SPECTRES DE VITESSE ET DE TEMPERATURE.

nomogène isotrope (13) à : $\varepsilon = 15 \, \nu \dfrac{\overline{u'^2}}{\lambda^2_g}$

valeur de λ_Q , définie au paragraphe 4, en turbulence isotrope :

$$\varepsilon = \frac{3 \nu \overline{q'^2}}{\lambda^2_Q} \quad (21)$$

A partir du terme II de l'équation (20), on obtient de même pour la température, en turbulence homogène et isotrope, par un calcul similaire à celui effectué pour la vitesse (13) :

$$\varepsilon_\theta = \frac{3\alpha \overline{\theta'^2}}{\lambda_\theta^2} \qquad (22)$$

En général il intervient un coefficient 12 (13 p. 229 Equ. 3-203) ; mais ici ε_θ est relatif à $\overline{\theta'^2}/2$ et non à $\overline{\theta'^2}$ et λ_θ défini comme λ_θ , est égal à $1/\sqrt{2}$ fois la longueur habituellement considérée. GIBSON (25), s'appuyant sur des travaux de BATCHELOR (16), propose de rechercher les lois universelles en portant pour un scalaire l'expression adimensionnelle :

$$\frac{\overline{\theta'^2} F_{\theta\theta}. k_s^3 \nu \sqrt{Pr}}{\varepsilon_\theta} \qquad \text{en fonction de} \quad \frac{1}{\sqrt{Pr}} \frac{k_1}{k_s} \qquad (23)$$

Quant aux vitesses, en considérant la fonction $Q(k_1)$ on porte l'expression :

$$\frac{\overline{q'^2} Q. k_s^3 \nu}{\varepsilon} \qquad \text{en fonction de} \quad \frac{k_1}{k_s} \qquad (24)$$

$k_s = \left(\frac{\varepsilon}{\nu^3}\right)^{1/4}$ est l'inverse de la longueur de KOLMOGOROV.

Pour les spectres Q et $F_{\theta\theta}$ on est donc conduit, d'après (21, 22, 24) à comparer $Q(k_1) \lambda_Q^2$ en fonction de k_1 à $F_{\theta\theta}(k_1) \lambda_\theta^2 (Pr)^{1/2}$ en fonction de $\frac{k_1}{\sqrt{Pr}}$.

Pour $y^+ = 15,5$ comme $\lambda_Q \neq \lambda_\theta$ à la précision des mesures et que $\sqrt{Pr} = 0,855$, les deux spectres Q et $F_{\theta\theta}$ restent dans cette nouvelle représentation encore très voisins. A $y^+ = 215$ ($k_s \approx 8600$ m^{-1}) et $y^+ = 460$ ($k_s \approx 7400$ m^{-1}), où $F_{\theta\theta}$ avait pu être corrigé de la contamination, le calcul montre un regroupement acceptable de Q et $F_{\theta\theta}$ pour $k_1 > 0,1$ k_s , dans la représentation proposée. Toutefois, les mesures ayant été faites surtout en vue d'une étude détaillée des régions spectrales renfermant l'énergie, les conclusions précédentes seraient à vérifier. Par ailleurs, a l'aide des expressions (21) et (22), on a calculé le rapport de la production de $\overline{q'^2}$ divisé par la dissipation ε à la production de $\overline{\theta'^2}$ divisée par la dissipation ε_θ , soit :

$$H = Pr \frac{\overline{q'^2}}{\overline{\theta'^2}} \frac{\lambda_\theta^2}{\lambda_Q^2} \frac{\overline{\theta'v'}}{\overline{u'v'}} \frac{\partial\Theta/\partial Y}{\partial U/\partial Y}$$

A la précision près des mesures pour $y^+ > 62$ le rapport H reste très voisin de 1 ; plus près de la paroi les résultats sont incertains. Ceci conduirait à penser que, sauf peut être au voisinage de la paroi, les termes de production et de dissipation sont d'importance relative comparable dans les équations de bilan de $\overline{q'^2}$ et $\overline{\theta'^2}$.

6.- CONCLUSION.

Les mesures des spectres des trois composantes de la vitesse ont permis de calculer une fonction spectrale $Q(k_1)$ dont la répartition d'énergie est pratiquement la même que celle du spectre des fluctuations de température $F_{\theta\theta}(k_1)$, lorsque les dissipations par effets moléculaires n'interviennent pas notablement.

La signification de $Q(k_1)$ a été précisée dans l'introduction et dans le chapitre 5.1. qui donne les équations de bilan spectral de $Q(k_1)$ et de $F_{\theta\theta}(k_1)$ dans lesquelles interviennent comparativement $\overline{q'^2}/2$ et $\overline{\theta'^2}/2$.

En faisant des hypothèses de turbulence homogène et isotrope, la comparaison entre Q et $F_{\theta\theta}$ entraînerait une similitude des fonctions spectrales à trois dimensions, tout au moins pour les nombres d'onde les plus bas, correspondant à environ 80 % de l'énergie dans les conditions de ces expériences.

Dans la région de la couche limite où les spectres de vitesse de la composante longitudinale varient selon une loi en k_1^{-1} , les spectres $F_{\theta\theta}$ correspondants suivent cette loi sur un intervalle plus restreint ; ceci correspond à l'influence des deux autres composantes dont l'effet devient prépondérant lorsque k_1 augmente. La variation en k_1^{-1} de $F_{\theta\theta}$ correspond d'ailleurs à la zone du co-spectre $E_{\theta u}$ qui renferme le maximum d'énergie.

En ce qui concerne les termes principaux de production de l'énergie spectrale, le terme relatif à la température $E_{\theta v}$ est nettement plus décalé vers les nombres d'ondes plus élevés que celui relatif au cas des vitesses E_{uv} .

Il faut s'attendre donc à ce que les spectres $F_{\theta\theta}$ et Q diffèrent tout au moins aux nombres d'ondes élevés.

En effet, il apparaît que, pour les grandes valeurs de k_1 , pour lesquelles les effets moléculaires sont importants, les spectres $F_{\theta\theta}$ ont une énergie relative plus élevée que celle correspondant à Q . Il semble que l'on pourrait prendre en compte les effets moléculaires par l'introduction de paramètres de similitudes basés sur les dissipations par la viscosité et la conductivité de $\overline{q'^2}/2$ et $\overline{\theta'^2}/2$ respectivement, et le nombre de Prandtl.

Ainsi, dans le cas de ces expériences, on a établi une correspondance entre le spectre de température et celui formé à partir des trois composantes de vitesse.

REFERENCES

(1) - E. VEROLLET : Contribution aux méthodes de mesures de turbulence de vitesse et de tempéra-
         ture par l'anémomètre à fils chauds.
         Thèse de 3e Cycle Fac. Sc. Marseille (1962). P.S.T. Minist. Air N°449 (1969).

(2) - L. FULACHIER : Contribution à l'étude des analogies de Reynolds. Ecoulement turbulent
         avec aspiration sur paroi chauffée.
         Thèse Dr.-Ing. Fac. Sc. Marseille (Juin 1965).

(3) - E. VEROLLET, L. FULACHIER, R.DUMAS, A. FAVRE : Etude d'une couche limite turbulente avec
         aspiration et chauffage à la paroi.
         Communication Ecole d'Eté Inte. . Inst. Boris Kidric Herceg-Novi,Yougoslavie
         (Sept. 1968).

(4) - E. VEROLLET, L. FULACHIER : Mesures de densités de flux de chaleur et de tensions de
         Reynolds dans une couche limite turbulente avec aspiration à la paroi.
         C.R. Acad. Sc. Paris, t. 268 p. 1577-1580 (Juin 1969).

(5) - E. VEROLLET, L. FULACHIER : Résultats expérimentaux concernant les spectres de fluctua-
         tions de température dans une couche limite turbulente.
         C.R. Acad. Sc. Paris, t. 270 p. 1342-1345 (Mai 1970).

(6) - L. FULACHIER : Répartitions spectrales des fluctuations de flux de chaleur dans une couche
         limite turbulente.
         C.R. Acad. Sc. Paris, t. 272 p. 1022-1025 (Avril 1971).

(7) - J. KESTIN, P.D. RICHARDSON : Heat Transfer across turbulent incompressible boundary layers.
         Int. J. Heat Transfer, Vol. 6 p. 147-189 (1963).

(8) - A. FAVRE, R. DUMAS, E. VEROLLET : Célérités de fluctuations turbulentes de température et
         de vitesse dans une couche limite.
         Proc. 20th Int. Cong. Appl. Mech. p. 132-208 (August 1968).

(9) - S. CORRSIN, M.S. UBEROI : Spectrums and diffusion in a round turbulent jet.
         NACA T.N. 2124, Washington (July 1950).

(10) - K. BREMHORST, K.J. BULLOCK : Spectral measurements of temperature and longitudinal velocity
         fluctuations in fully developed pipe flow.
         Int. J. Heat Transfer Vol. 13 p. 1313-1329 (August 1970)

(11) - G.K. BATCHELOR : The theory of homogeneous turbulence.
         Cambridge Univer. Press (1967).

(12) - P.S. KLEBANOFF : Characteristics of turbulence in a boundary layer with zero pressure
         gradient.   N.B.S. NACA T.N. 3178 (1954).

(13) - J.O. HINZE : Turbulence .   Mc Graw Hill (1959)

(14) - R. DUMAS : Contribution à l'étude des spectres de turbulence.
         Thèse Univ. Aix-Marseille (1962) - P.S.T. Minit. Air, Paris N° 404 (1964).

(15) - S. CORRSIN : On the spectrum of isotropic temperature fluctuations in an isotropic turbu-
         lence. Dt. of Aero. The Johns Hopkins Univ. (August 1950).

(16) - G.K. BATCHELOR : Small-scale variation of convected quantities like temperature in
         turbulent fluid. J. Fl. Mech. Vol. 5 Part 1 p. 113-133 (Jan. 1959).

(17) - E.J. PLATE, S.P. ARYA : Turbulence spectra in a stably stratified boundary layer.
         Radio Science Vol. 4 N° 4 p. 1163-1168 (Dec. 1969).

(18) - C.M. TCHEN : On the spectrum of energy in turbulent shear flow.
         J. Research N.B.S. Vol. 50 N° 1 (Jan. 1953).

(19) - J. GAVIGLIO : Sur quelques problèmes de mesures de turbulence effectuées à l'aide de
         l'anémomètre à fils chauds parcourus par un courant d'intensité constante.
         Thèse Doctorat. Fac. Sc. Marseille (1958). P.S.T. Minist. Air N° 385 (1962).

(20) - A. FAVRE : Equations des gaz turbulents compressibles.
         Journal de Mécanique, Vol. 4 N° 3 (Sept. 1965) et N° 4 (Déc. 1965).

(21) - A. BLANC-LAPIERRE, B.PICINBONO : Propriétés statistiques du bruit de fond. Masson (1961).

(22) - J.L. LUMLEY, H.A. PANOFSKY : The structure of atmospheric turbulence. John Wiley et S.(1964).

(23) - L.S. KOVASZNAY, M.S. UBEROI, S. CORRSIN : The transformation between one and three dimen-
         sional power spectra for an isotropic scalar fluctuation field.
         Physics of Fluids (1949).

(24) - R.R. MILLS, A.L. KISTLER, O'BRIEN, S. CORRSIN : Turbulence and temperature fluctuations
         behind a heated grid. NACA T.N. 4288, Washington (Aug. 1958).

(25) - C.H. GIBSON, W.H. SCHWARZ : The universal equilibrium spectra of turbulent velocity and
         scalar fields. J.F.M. Vol. 16, Part 3 (Jul. 1963).

INTERMITTENT STRUCTURES IN TURBULENT BOUNDARY LAYERS

by

R. F. Blackwelder and R. E. Kaplan
Department of Aerospace Engineering
University of Southern California
Los Angeles, California 90007, U.S.A.

SUMMARY

The intermittent structure in the outer region and the occurrence or intermittent bursts near the wall that have been observed by many investigators are inspected in detail. The extent of these structures is characterized by the existence of substantial streamwise momentum defects that have been detected by correlation techniques. These correlations suggest a connection between the now well-established bursting that occurs in the wall region and the intermittent bulges of turbulence that protrude from the outer reaches of the turbulent boundary layer. A scheme was found and presented which detected the turbulent bursts near the wall. Conditional averaging showed that during the burst there was a substantial streamwise momentum defect followed by an extremely rapid acceleration. The measurements suggest that perhaps a local instability is the source of the break up of the wall flow.

INTRODUCTION

In recent years, the turbulent boundary layer has been the subject of several intensive investigations which have explored its detailed structure. These investigations have utilized visual techniques, space-time correlations, and more sophisticated and different types of averaging techniques. The main emphasis of these studies has been to analyse the outer intermittent region and the intensive production region near the wall.

In the outer region, Kaplan and Laufer (Ref. 1) used a digital computer to analyse hot-wire signals to form an intermittency function, I(t), which distinguished between the turbulent and non-turbulent regions. Using conditional averaging, they were able to find the mean velocity defect in the turbulent bulges and other statistics relating to the shape of the bulges. Kovasznay, Kibens and Blackwelder (Ref. 2) used analogous analogue techniques and were able to conditionally average both the streamwise and normal velocity components in this outer region. In addition they used space-time auto- and cross-correlations of u, v and I to ascertain the average structure of the large eddies in the outer flow field. The tangential Reynolds stress in the outer intermittent region was conditionally averaged in the turbulent and non-turbulent regions by Blackwelder and Kovasznay (Ref. 3). All three of these studies have supported the hypothesis that entrainment of irrotational fluid into the turbulent boundary layer occurs primarily on the backside of the turbulent bulges.

Using dye injection near the wall, Hama (see Ref. 4) observed the presence of streamwise streaks in the sublayer. Kline et al. (Ref. 5) and Kim, Kline and Reynolds (Ref. 6) used a hydrogen bubble technique to explore this region in more detail. They observed that the streaks break up near $y^+ = 30$ and eject parcels of low speed momentum away from the wall. Corino and Brodkey (Ref. 7) found this bursting phenomenon in the buffer layer of a turbulent pipe flow by observing particle trajectories in another visualization study. These investigations found that the bursting phenomenon occurs at random and on the basis of some qualitative estimates suggested that it accounts for a large percentage of the turbulent production. The recurrence of these events has commonly been called "internal intermittency" to distinguish it from the intermittency of the outer turbulent-non-turbulent region.

Another study in the sublayer was undertaken by Bakewell and Lumley (Ref. 8) who obtained correlations in the sublayer and buffer layer of a turbulent pipe flow. By using the proper orthogonal decomposition theorem, their experimental data revealed pairs of contrarotating eddies occurring at random. These eddies were aligned approximately in the streamwise direction suggesting that they are responsible for the streaks observed in the visualization studies. By analysing cross-correlations between the wall pressure and all three velocity components, Willmarth and Tu (Ref. 9) suggested that the streamwise vortex pair is produced by the stretching and distortion of a lateral vortex by the mean velocity gradient near the wall.

Morrison and Kronauer (Ref. 10) analyzed data from a turbulent pipe flow in the frequency-wave number space in order to obtain the spectral form of the existing structure. They obtained a similarity function which collapsed their cross spectral data into a universal cross-spectrum at different Reynolds number from the buffer layer and logarithm region. The ability to collapse this data implies that a similar type structure is also present in the logarithmic region but it is probably obscured by the small scale background turbulence.

In a study devoted to the bursting phenomenon near the wall, Narahari et al. (Ref. 11) have shown that the mean frequency of the bursts scales with the outer flow variables instead of the inner variables and that the probability distribution of the time between the bursts is log-normal. Laufer and Badri Narayanan (Ref. 12) also noted the scaling with the outer parameters and showed that the mean frequency of the inner burst was of the same order as the mean frequency of the turbulent bulges in the outer intermittent region.

All of these studies have yielded quantitative data on the outer intermittent region and have established that there is a recurring eddy structure near the wall. One might ask if there is any relationship between these two structures. In particular it can be conjectured that the bursting phenomenon near the wall moves outward and influences or ultimately forms the bulges in the outer region. Thus far, quanti-

tative data supporting this hypothesis is lacking, primarily because it is very difficult to detect the eddy structure near the wall and follow it as it decays. The present study proposes a means of detecting these inner bursts and gives quantitative data on their structure. Also space-time correlations indicate that the turbulent structure near the wall can influence the outer intermittent region.

EQUIPMENT

To obtain the space-time correlations much of the basic electronic equipment and the open return wind tunnel described by Kovasznay, Kibens and Blackwelder (Ref. 2) was used. The x co-ordinate was aligned with the free stream velocity, U_{∞}, y was the coordinate perpendicular to the wall and z was the spanwise co-ordinate. The velocity fluctuations in the x,y and z directions are u,v and w respectively. The boundary layer thickness, δ, was 10 cm. and the corresponding Reynolds number based upon the momentum thickness was $U_{\infty}\theta/\nu = 2950$.

The conditional averages were taken in the wind tunnel described by Kaplan and Laufer (Ref. 1) and the above co-ordinate system was used. The hot wire data were recorded on a 14 channel FM Hewlett Packard tape recorder with a frequency response from D. C. to 20 kc. The data were analysed on an IBM 360/44 digital computer.

To obtain all of the data, the inner probe protruded through the wall and the outer probe entered the boundary layer from the free stream. For the $R_{uv}(0,Y,0,T')$ correlation map, a special x-probe was constructed consisting of four needles projecting through the wall onto which four jeweler's broaches were soldered. The jeweler's broaches extended 2.5 cm. upstream from the needles. Tungsten wires of 3.8 micron diameter were spot welded onto the thin ends of the broaches. The final configuration was two 1.5 mm. long wires forming the x-probe.

SPACE-TIME CORRELATIONS

The studies mentioned in the introduction have shown that the predominate streamwise streaks lift upward from the wall and break up into parcels of turbulence around $y^+ = 30$. These parcels of fluid are swept outward from the wall along a mean trajectory. This general motion is indicated by the space-time correlation map of the streamwise velocity component shown in Fig. 1. The lines of constant correlation are given by

$$R_{uu}(0,Y,0,T') = \frac{\overline{u(x_0,y_0,z_0,t_0)\, u(x_0,y,z_0,t)}}{\left[\overline{u(x_0,y_0,z_0,t_0)^2}\,\overline{u(x_0,y,z_0,t)^2}\right]^{\frac{1}{2}}} = \text{constant} \tag{1}$$

where $(\ )_0$ denotes the position and time of the fixed probe location at $y_0/\delta = 0.03$ ($y^+ = 24$) and $(\ )$ is the position and time of the moveable probe. The nondimensional co-ordinates are $Y = (y-y_0)/\delta$ and $T' = (t-t_0)\,U_{\infty}/\delta$ where U_{∞} is the free stream velocity and δ is the boundary layer thickness.
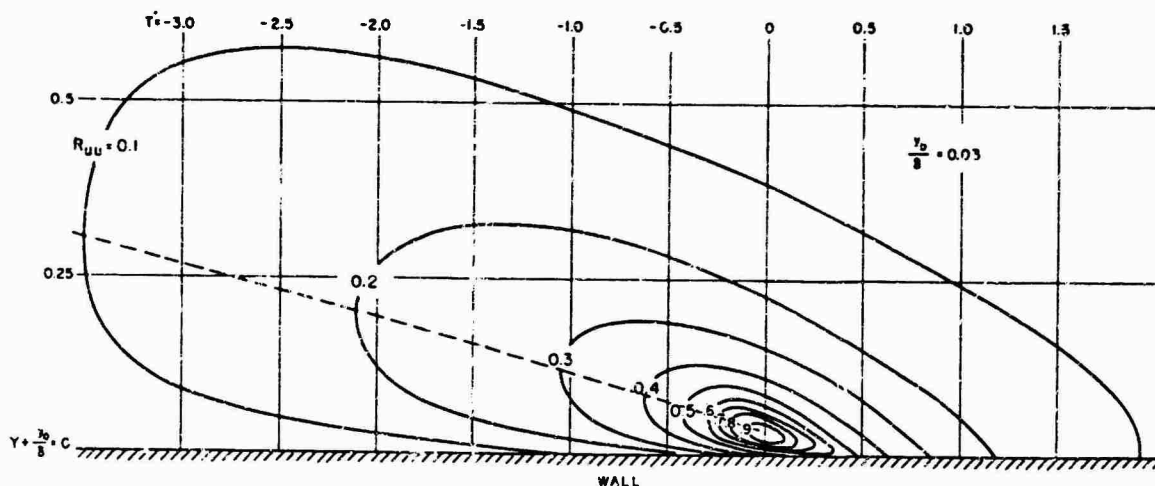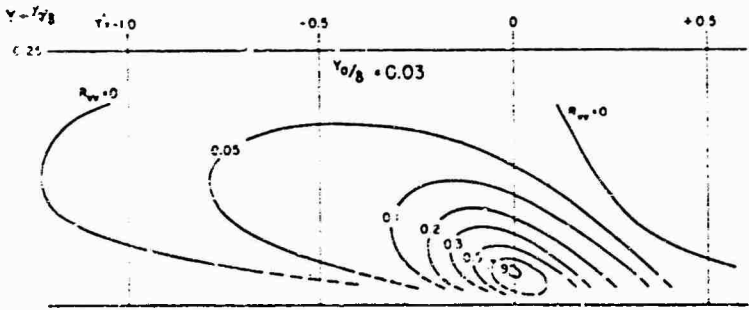

Figure 1. Space-time auto-correlation map of u deep in the boundary layer, $R_{uu}(0,Y,0,T')$ at $y_0/\delta = 0.03$. The dashed line gives the position of the maximum correlation as a function of the time delay.

Ideally one would wish to have a streamwise separation between the two probes. Then the characteristics of the turbulence recorded at the upstream probe would be correlated with those obtained from the downstream probe at a fixed later time, T_0, corresponding to the spatial separation and the convection velocity. For experimental convenience, a variable time delay was used instead of a streamwise separation. If the turbulence were convected as a strictly "frozen pattern" (Taylor's hypothesis) with a convection velocity, U_c, then the two methods would yield equivalent results. Since Taylor's hypothesis is only approximately valid in a turbulent boundary layer, the correlations obtained with a variable time delay are only qualitatively equivalent to those that would have been obtained with a variable streamwise spatial separation. Corresponding to the variable time delay shown in Figs. 1 and 2, the free stream velocity is from right to left.

The value of the correlation decreases with increasing temporal and spatial separation as expected. In Fig. 1 the maximum correlation at each fixed time delay (fixed streamwise spatial separation if Taylor's

hypothesis is used) is given by the dashed line. This line then defines an average trajectory of the turbulence which passed the fixed probe at $y^+ = 24$. After allowing for the difference between the free stream velocity used in the normalization and the mean velocity at each y position, this trajectory agrees quite well 1th that reported by Kline et al. (Ref. 5).

Another significant feature of Fig. 1 is that there is still 10% correlation beyond $y/\delta = 0.5$ which is in fact already in the outer intermittent region. This suggests that the turbulence which originates near the wall must ultimately effect the outer intermittent flow field.

The corresponding auto-correlation of the normal velocity components is shown in Fig. 2. Since the individual wires of the stationary probe at $y^+ = 24$ were located across a region of considerable shear, some error was probably introduced into the resulting v signal. This error was assumed to be small because the u signal from this x-probe gave the same u' intensity and correlation patterns as a single wire at the same location aligned in the spanwise direction. Thus the v correlation data were accepted and presented since no acceptable means are presently available for correcting the errors caused by a shear on x-probes.

Figure 2 (above). Space-time auto-correlation map of v deep in the boundary layer, $R_{vv}(0,Y,0,T')$ at $y_o/\delta = 0.03$.

Figure 3 (to the right). Schematic of the turbulent signal, the VITA averages and the intermittency function.
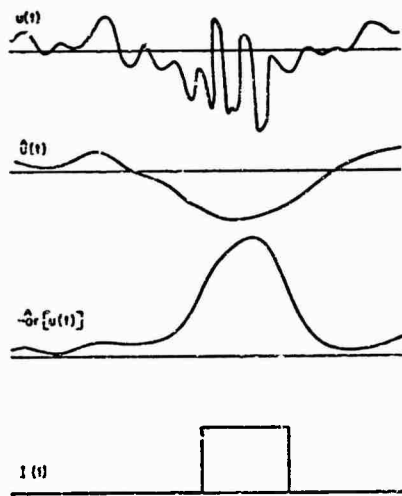
It is immediately evident from Fig. 2 that the extent of the correlation of the normal velocity component is much less than that of the streamwise velocity component although the orientation of the patterns are similar. If these correlations do indeed represent the evolution of eddies ejected from near the wall then these eddies seem to be more easily identifiable by their characteristic streamwise momentum than by their outward motion. However, it must be realized that these correlations were taken continuously in time and no attempt was made to identify and isolate the particular eddies; thus their structure remains unrevealed. To proceed further in the study of the bursting phenomenon near the wall, some means of detecting these events had to be found.

DETECTION SCHEME AND DEFINITION OF THE CONDITIONAL AVERAGES

While it is relatively straightforward to decide on a criterion for the presence of turbulence in the outer portion of the turbulent boundary layer, the detection of the bursting phenomenon near the wall is more difficult. Observations that were made led to the selection of a conditioned variance of the u velocity as a criterion for detection of the turbulent bursts. These observations were based on an inspection of the signals from a pair of hot wires aligned in the spanwise direction and separated by a distance of $y^+ = 3.5$. As these wires were traversed across the boundary layer it was observed that their difference signal yielded almost no low frequency signals, which is to be expected. However, when there was an exceptionally high fluctuation level on a single u recording, the low frequency velocity fluctuation was always negative.

Hence it was decided to use a technique almost identical to that used by Kaplan and Laufer (Ref. 1). To explain and to briefly review this technique which has been called Variable Interval Time Averaging (VITA) in the past, the following definition is introduced

$$\hat{u}(y,t) = \frac{1}{T} \int_{t-T/2}^{t-T/2} u(y,s)ds \qquad (2)$$

where T is the length of the averaging window, $u(y,t)$ is the unaveraged signal and $\hat{u}(y,t)$ is the VITA average as shown in Fig. 3. Obviously, for a stationary flow

$$\lim_{T \to \infty} \hat{u}(y,t) = \bar{u}(y) \quad \text{(independent of t)}. \qquad (3)$$

where $\bar{u}(y)$ is the conventional mean velocity.

In this framework, the variance is generalized to

$$\hat{var}\left[u(y,t)\right] = \hat{u^2}(y) - \hat{u}(y)^2 \qquad (4)$$

and is a positive definite quantity, which is time dependent. As T becomes large,

$$\lim_{T \to \infty} \widehat{\text{var}} \left[u(y,t)\right] = \overline{u^2}(y) - \bar{u}(y)^2 \tag{5}$$

which equals the mean square of the velocity fluctuations.

The $\widehat{\text{var}}$ signal is interpreted as a measure of the fluctuations in a localized region and it scales with the convential variance. This variance is heavily biased on fluctuations which are completed in time T, so in a sense it is a measure only of the high frequency fluctuations, with $1/T$ representing a cut-off frequency. Hence the VITA process may be regarded as a process for selecting out a portion of the low frequency part of the spectrum, while $\widehat{\text{var}}$ selects a positive definite measure of the high frequency part of the spectrum.

The internal intermittency function $I(y,t)$ is defined by

$$I(y,t) = H\left\{\widehat{\text{var}}\left[u(y,t)\right] - k \ \overline{\left[u(y) - \bar{u}(y)\right]^2}\right\} \tag{6}$$

where H is the Heaviside function which is zero for negative argument and +1 for positive values, $\overline{(u-\bar{u})^2}$ is the mean square of the velocity fluctuations and k is a constant corresponding to a set discriminator level. The intermittency function is dependent on two parameters, T (the decision time) and k (the decision level).

The conditional average of a quantity Q is defined as

$$\langle Q(y)\rangle_{y^+} = \int I(y^+,t) \ \hat{Q}(y,t) \ dt \tag{7}$$

where the independent variable y denotes the position at which the sampling occurred and the subscript y^+ denotes the position of the detector probe giving the $I(y^+,t)$ signal. In effect, the average is over an ensemble of events determined by $I(y^+,t)$.

The delayed conditional average was generated differently. The detector probe was used to generate a random sequence of delta functions located at t_1 where t_1 are the points in time at which $\frac{\partial I}{\partial t} > 0$. The signal probe was located at another position and its signal was averaged according to

$$\langle Q(\underset{\sim}{x}, \tau)\rangle_{y^+} = \frac{1}{N} \sum_{i=1}^{N} Q(\underset{\sim}{x}, \ t_i + \tau) \tag{8}$$

where N is the number of samples and τ is the time delay applied to the signal $Q(x,t)$.

CONDITIONAL AVERAGES

Initially the hot-wire was traversed across the boundary layer and the detection and sampling both occurred simultaneously at the same location, which is indicated by the notation $\langle u(y)\rangle_y$. An example of the results of this type of averaging are shown in Fig. 4. The points summarize two Reynolds numbers (2500 and 5500, based on momentum thickness), 3 sets of decision times varying by a factor of two, and a set of thresholds varying by a factor of two. It is readily observed that there is a substantial non-trivial average when conditional sampling is used. Furthermore, the conditional averages were found to scale with the inner flow variables, u_* and γ, and not with the outer variables, U_∞ and δ.

The results and the peak magnitude of approximately 22% of the local mean velocity is not very surprising, considering that the result agrees with the observation that when the turbulent activity was high, the velocities were low. There seems to be quite a distinct and easily detected relationship between a measure of the local intensity, $\widehat{\text{var}}$, and the local "unsteady" mean velocity. These departures are all of the order of the convential root mean square of the velocity and have to be regarded as an intensely strong effect.

There was a trend that was evident as the decision time, T, and discriminator level, k, were changed. Shorter times and higher discriminator levels generated stronger effects. The fact that the predominant defect strengthened with inspection of high frequencies and thresholds was consistent with the observations that changing these variables enabled us to "center" on the bursts.

Each data point is based on a set of approximately 100 samples detected during a 20 second run. The small number of samples required to yield such consistent results also gave an indication that such a phenomenon is of basic importance to the dynamics of the buffer layer and sublayer. While not shown in the figure, these defects were still detectable out to y^+ of 500.

For y^+ less than 100 and $k = 1.2$, typical values of the internal intermittency were 1% and the non-dimensional frequency $\frac{f\delta}{U_\infty}$ was approximately 0.10 . In the outer intermittent region the frequency $\frac{f\delta}{U_\infty}$ was approximately 0.6 at the half intermittency level. These two different values are still not inconsistent with the idea that the parcels of turbulence ejected from the buffer layer may ultimately form the bulges in the outer region. The interface measurements include many crossings encountered on the edges of the large bulges. The turbulent bursts near the wall have a smaller size than the interfacial bulges and the present measurements were able to center more directly on a burst by varying the threshold level, k. Thus one expects a higher frequency in the outer region than near the wall.

Since the largest effect in $\langle u(y)\rangle_y$ is observed at $y^+ = 15$, another hot-wire was used as a stationary detector probe at $y^+ = 15$, while the sampling probe was traversed above and below the fixed probe. The results are shown in Fig. 5 which is the velocity profile when the burst occurred at $y^+ = 15$. The conditional profile shows that the defect region is confined near the wall and that there is a local
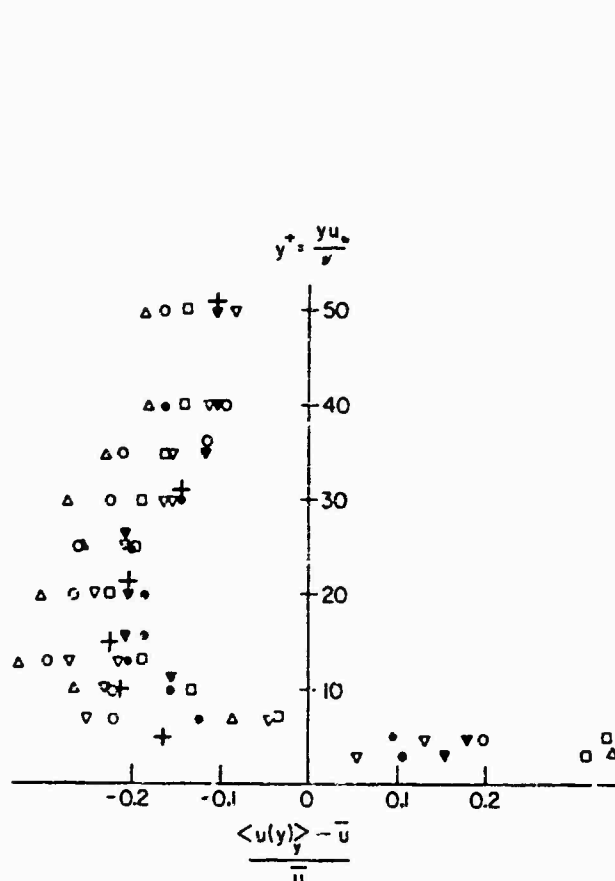
Figure 4. Conditional average of the
streamwise velocity with
triggering and averaging
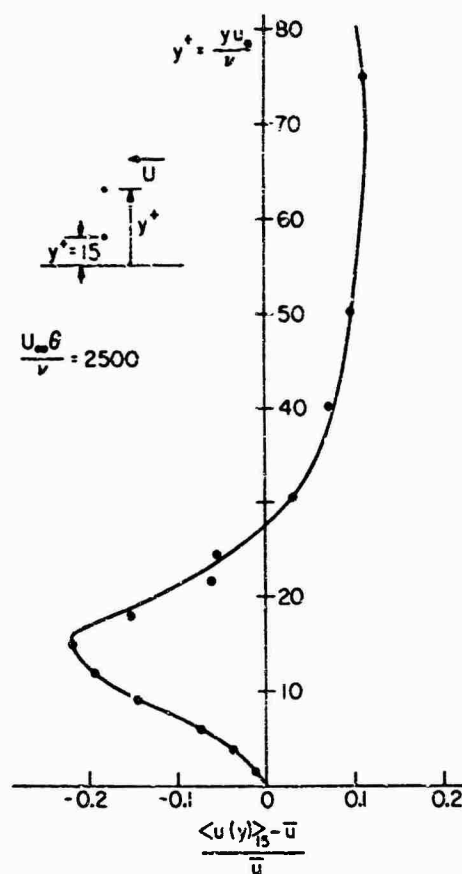occurring at the same location.

Figure 5. Conditional average of the
streamwise velocity with the
triggering at $y^+ = 15$.

excess of velocity for $y^+ > 30$. When combined with the steady mean velocity profile, the resultant velocity distribution may have an inflection point close to the wall which is of interest if some type of hydrodynamic instability is important in the generation of the bursts.

DELAYED CONDITIONAL AVERAGES

Since the above conditional velocity defect is so strong, then it should be possible to detect the bursts for a considerable time after they are formed. Thus the sampling probe was placed one boundary layer thickness downstream of the detector probe which was still located at $y^+ = 15$. The data were ensemble averaged according to Eq. 8 and the results are shown on Fig. 6 as a function of the time delay, $T = \bar{U}\tau/\delta$, and the location in the boundary layer, y. The ordinate is given by the spacing between the horizontal lines which is 2/3 u_{rms}. The results show that there is a detectable correlation of approximately 60% of the rms fluctuation. Several features were quite surprising however; first there was no descernible relationship between the conditioned averages at various locations, i.e., the profiles at a fixed time delay had considerable scatter. This is not completely unexpected since there were few bursts detected and the signal probe was so far from the controlling event. What was disturbing is that these profiles indicated a positive velocity perturbation, while all of the other measurements showed a negative perturbation. Since these positive values at $\bar{U}\tau/\delta = 1$ were not consistent with the momentum defects shown in the previous figures, it was decided to use a smaller spacing between the sampling and detector probes in order to understand how this momentum defect evolved into a momentum excess.

The results are shown in Fig. 7 for zero streamwise separation between the two probes. The abscissa is the non-dimensional time delay, $\bar{U}\tau/\delta$, and the ordinate is given by the spacing between the horizontal lines which is now 4/3 u_{rms}. The results are quite dramatic. Immediately prior to the occurrence of a burst (negative $\bar{U}\tau/\delta$) and during the detection there is a defect of momentum at the lower values of y/δ as also seen in Fig. 5. However immediately after the occurrence of the burst, there is an extremely rapid acceleration of the fluid at the sampling probe's location which persists for a substantial period thereafter. Evidently this excess of momentum predominates downstream and was found in Fig. 6 near $\bar{U}\tau/\delta = 1$. If these parcels of fluid maintain approximately the same momentum as they move toward the outer intermittent region, they will be characterized by a momentum defect again because of the higher mean velocity in the outer regions.

CONCLUSION

Space-time correlation of the streamwise and normal velocity components taken across the boundary layer indicate that there is a definite outward motion of fluid from the buffer layer toward the inter-
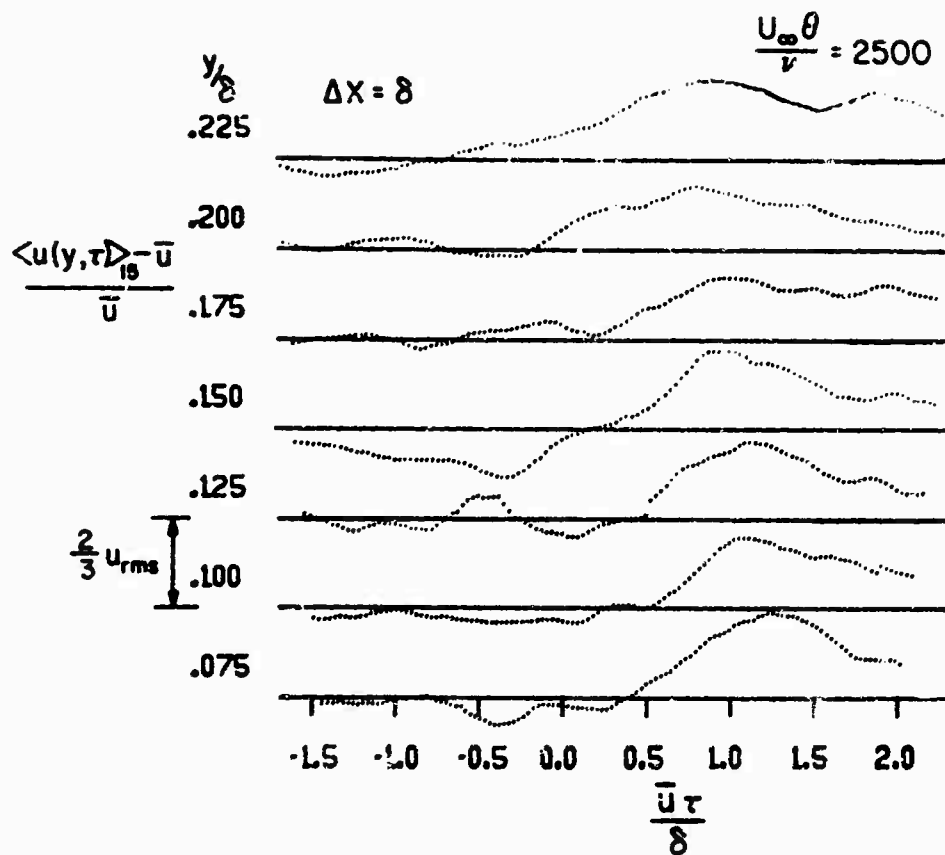
Figure 6. Conditional average of the streamwise velocity. Detector probe is located at $y^+ = 15$ and sampling probe is $\Delta X = \delta$ downstream.
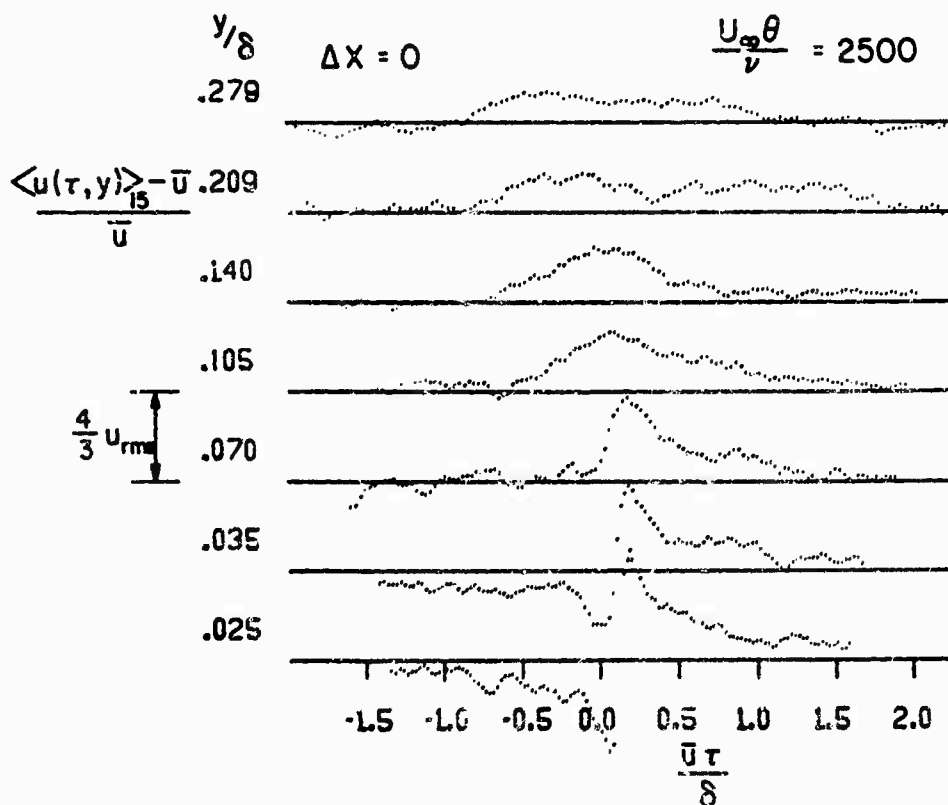
Figure 7. Conditional average of the streamwise velocity. Detector probe is located at $y^+ = 15$ and both the detector and sampling probes are at the same ΔX position.

facial region. The 10% correlation beyond $y/\delta = 0.5$ suggests that the events occurring in the buffer layer do influence the structure of the outer intermittent region.

In order to examine the bursting phenomenon near the wall, it was obvious that data was needed of a more quantitative nature than that which had been obtained previously. Thus a scheme was developed and presented for detecting these turbulent bursts in the buffer layer. The instantaneous velocity profile at the time of bursting scaled with the inner flow variables and agreed with the qualitative data of Kline et al. (Ref. 5) and Corino and Brodkey (Ref. 7). The data showed that there is a strong momentum defect greater than $0.20\ \bar{U}$ at $y^+ = 15$ during the bursting event. However this velocity profile exists only momentarily because immediately after the bursting, there is a strong acceleration of the fluid in the region $y^+ = 15$ to 100. This accelerated fluid is still detectable at least one boundary layer thickness downstream.

REFERENCES

1. Kaplan, R. E. and Laufer, John, Proc. <u>12th Int. Cong. Appl. Mech.</u>, Springer, 1969, p. 236.

2. Kovasznay, Leslie S. G., Kibens, Valdis and Blackwelder, Ron F., J. Fluid Mech., <u>41</u>, 1970, p. 283.

3. Blackwelder, Ron F. and Kovasznay, Leslie S. G., to be published.

4. Corrsin, S., <u>Proc. 1st Naval Hydro-Symp</u>, Pub. 515, Natn. Acad. Sci./Natn. Res. Counc, 1957, p. 373.

5. Kline, S. J., Reynolds, W. C., Schraub, F. A. and Runstadler, P. W., J. Fluid Mech., <u>30</u>, 1967, p. 741.

6. Kim, H. T., Kline, S. J., and Reynolds, W. C., Report MD-20, Stanford University, 1968.

7. Corino, E. R. and Brodkey, R. S., J. Fluid Mech. <u>37</u>, 1969, p. 1.

8. Bakewell, Henry and Lumley, John L., Phys. Fluids, <u>10</u>, 1967, p. 1880.

9. Willmarth, W. W. and Tu, Bo Jang, Phys. Fluids Supplement, 1967, p. S134.

10. Morrison, W. R. B. and Kronauer, R. E., J. Fluid Mech., <u>39</u>, 1969, p. 117.

11. Narahari, Rao, K., Narashima, R. and Badri Narayanan, M. A., J. Fluid Mech., <u>48</u>, 1971, p.339.

12. Laufer, John and Badri Narayanan, M. A., Phys. Fluids, <u>14</u>, 1971, p. 182.

ACKNOWLEDGEMENT

AN INTEGRAL METHOD FOR APPROXIMATE CALCULATION OF COMPRESSIBLE TURBULENT BOUNDARY LAYERS WITH STREAMWISE PRESSURE GRADIENT

by

H.-J. Küster

wissenschaftlicher Mitarbeiter [+]
Institut für Oberschalltechnik
Technische Universität Berlin
1 Berlin 10
Franklinstraße 29
Deutschland

SUMMARY

By a compressibility transformation of the COLES-type the integral equations for compressible turbulent boundary layers are converted into those at low speed. In contrary to earlier investigations a new approach to the transformation function $\sigma_{(x)}$ is presented which avoids both the sublayer and the substructure hypothesis. The coupling of σ with the relative skin friction coefficient $c_f/\bar{c}_f$ is used to close the set of equations. The best agreement between theory and experiment has been obtained by a modified version of the skin friction law of KUTATELADSE & LEONTEV. The thermodynamic behaviour is approximately described by a modification of the VAN DRIEST version of the CROCCO-integral, which accounts for non-unit Prandtl number and variable pressure and/or wall temperature. The boundary layer parameters of the transformed constant property flow are calculated by the method of WALZ, which is based on the integral equations for momentum and mechanical energy. The calculation method is applied to a variety of turbulent boundary layers with and without pressure gradient and is compared with published experiments.

SYMBOLS

c_f	total skin friction coefficient	
$c_{j(x)}$	correction function Eq (15)	
h; T; p	enthalpy, temperature, pressure	
H_{12}; H_{32}	form parameter δ_1/δ_2; δ_2/δ_3	
$\bar{I}$ $\bar{I}'$	parameter Eq (30)	
M_δ	external Mach number	
m_δ	Mach parameter $(\kappa - 1)/2 \, M_\delta^2$	
Pr	Prandtl number	
Re_{δ_2}; Re_x	Reynolds number $\dfrac{\rho_\delta u_\delta \delta_2}{\mu_w}$; $\dfrac{\rho_\infty u_\infty x}{\mu_\infty}$	
r	radius of body of revolution Eq (1)	
...	recovery factor	
u, v	velocities respectively along and normal to body	
x, y	space coordinates respectively along and normal to body	

$$\delta_1 = \int_0^\delta (1 - \frac{\rho u}{\rho_\delta u_\delta})dy \quad \text{displacement thickness}$$

$$\delta_2 = \int_0^\delta (\frac{\rho u}{\rho_\delta u_\delta})(1 - \frac{u}{u_\delta})dy \quad \text{momentum thickness}$$

$$\delta_3 = \int_0^\delta \frac{\rho u}{\rho_\delta u_\delta}[1 - (\frac{u}{u_\delta})^2]dy \quad \text{mech. energy thickness}$$

$$\delta_4 = \int_0^\delta \frac{\rho u}{\rho_\delta u_\delta}(\frac{\rho_\delta}{\rho} - 1)dy \quad \text{density thickness}$$

ε	flow index Eq (1)
...	error [%]
μ	molecular viscosity
σ, ξ, η	COLES scaling functions Eq (3)
σ', ξ'	modified scaling functions Eq (19)
$\bar{\pi}_1, \bar{x}, \bar{\zeta}$	boundary layer parameter Eq (26)
ρ	density
τ	shear stress
$\psi = r^\varepsilon \int_0^y \rho u \, dy$	stream function

SUBSCRIPTS

t	turbulent flow
w	wall condition
δ	external condition
∞	free-stream condition (initial starting point)

SUPERSCRIPTS

$(\bar{\ })$	transformed value (CP plane)
$(\ )^0$	stagnation value
$(\ )^*$	normalized value Eq (20)
< >	time mean value

[+]) wissenschaftlicher Assistent since 15-4-1971
Hermann-Föttinger-Institut für Strömungstechnik
Technische Universität Berlin
1 Berlin 12 (Deutschland)
Müller-Breslau-Straße 8

INTRODUCTION

The idea of relating a variable property (VP) boundary layer to a constant property (CP) counterpart is not new. On firm physical grounds it has first been developed for laminar boundary layers. The extension to turbulent flows, however, contains a certain element of arbitrariness, because of our incomplete knowledge of the turbulence mechanism in shear flows. Nevertheless all known prediction methods for compressible turbulent boundary layers are based on such a transformation concept in the sence that they need a functional correspondence between some characteristic boundary layer parameters for high and low speed flow. This is mainly due to the existence of a substantical body of low speed experimental data which allows the formulation of quite accurate semi-empirical theories for the CP case. (This aspect will be discussed in some detail below.)

The reader is referred to COLES [1] for an excellent review of the early approaches to a compressibility transformation (CT) and to ECONOMOS [2] for a comparison of the main hypotheses and the basic literature about CTs which has been published after the work of COLES. From these references it is evident that at present the COLES-CROCCO [3] compressibility transformation is one of the most succesfull approaches to compressible turbulent boundary layers and it is still in a developing stage.

This investigation shows that boundary layers with streamwise pressure gradients can be calculated without applying the commonly used sublayerand substructure hypotheses which postulate the invariance of a characteristic sublayer Reynolds number against the transformation.

DEVELOPMENT OF ANALYSIS [+]

Prandtl's boundary layer equations describing the mean properties of steady two-dimensional and axisymmetric compressible turbulent flows can be expressed in coordinates normal and parallel to the body contour by:

Conservation of mass[++]

$$\frac{\partial}{\partial x}\left(r^{\varepsilon}\rho\,u\right) + \frac{\partial}{\partial y}\left(r^{\varepsilon}\,\rho\,v\right) = 0 \qquad \text{with } \varepsilon = \begin{cases} 0 & \text{plane case} \\ 1 & \text{axisymmetric case} \end{cases} \qquad (1)$$

Conservation of momentum

$$\rho u\,\frac{\partial u}{\partial x} + <\rho v>\frac{\partial u}{\partial y} \qquad = \qquad -\frac{dp}{dx} + \frac{\partial \tau}{\partial y} \qquad (2)$$

and a suitable formulation for the energy equation.

Supposed a compressibility transformation of the COLES type [1] exists then three initially unspecified scaling functions may be defined by:

$$\sigma_{(x)} = \left(\frac{r}{\bar{r}}\right)^{\varepsilon}\frac{\bar{\eta}(\bar{x}\ \bar{y})}{\psi(x\ y)} \qquad \qquad \xi_{(x)} = \frac{d\bar{x}}{dx} \qquad \qquad \eta_{(x)} = \frac{\bar{\rho}}{\rho}\frac{\partial\bar{y}}{\partial y} \qquad (3)$$

If this transformation represents the true mapping of one high speed flow field into its low speed equivalent and not only a mathematical manipulation then the corresponding constant property flow may be described by

$$\frac{\partial}{\partial \bar{x}}\left(\bar{r}^{\varepsilon}\ \bar{\rho}\bar{u}\right) + \frac{\partial}{\partial \bar{y}}\left(\bar{r}^{\varepsilon}\bar{\rho}\ \bar{v}\right) = 0 \qquad (4)$$

$$\bar{\rho}\ \bar{u}\ \frac{\partial \bar{u}}{\partial \bar{x}} + \bar{\rho}\bar{v}\ \frac{\partial \bar{u}}{\partial \bar{y}} = -\frac{d\bar{p}}{d\bar{x}} + \frac{\partial \bar{\tau}}{\partial \bar{y}} \qquad (5)$$

with the immediate implications for the velocity profiles and the pressure gradients of the two flows

$$\frac{u}{u_{\delta}} = \frac{\bar{u}}{\bar{u}_{\delta}} \qquad (6)$$

$$\frac{\sigma^2}{\xi\eta^2}\frac{\bar{\rho}_{\delta}}{\rho_{\delta}}\left[\frac{dp}{dx} + \rho_{\delta}\ u_{\delta}^2\ \frac{d}{dx}\left(\ln\frac{\eta}{\sigma}\right)\right] = \frac{d\bar{p}}{d\bar{x}} \qquad (7)$$

According to CROCCO [3] it is somewhat doubtful whether COLES' transformation can give a unique point to point mapping of the two flows. No doubts, however, exist about the validity of the transformation if the integral equations for the whole boundary layer are transformed.

[+]
Only a brief outline of the transformation concept is presented here. For more detailed derivations see Refs [1] ; [3] ; [4]

[++]With the boundary layer thickness considered to be much smaller than the body radius i.e. both the lateral and longitudinal radii of curvature.

The integral relations for momentum and mechanical energy are:

$$\frac{d\delta_2}{dx} + \frac{\delta_2}{u_\delta} \frac{du_\delta}{dx}\left[2 + \frac{\delta_1}{\delta_2} - M_\delta^2\right] + \frac{\delta_2}{r^\epsilon}\frac{dr^\epsilon}{dx} = \frac{\tau_w}{\rho_\delta u_\delta^2} \tag{8}$$

$$\frac{d\delta_3}{dx} + \frac{\delta_3}{u_\delta}\frac{du_\delta}{dx}\left[3 + 2\frac{\delta_4}{\delta_3} - M_\delta^2\right] + \frac{\delta_3}{r^\epsilon}\frac{dr^\epsilon}{dx} = \frac{2}{\rho_\delta u_\delta^3}\int_0^{u_\delta}\tau\, du \tag{9}$$

Applying the transformation (3) to Eq (8) gives the following correspondence between the skin friction in the physical and the transformed plane:

$$\frac{\sigma^2}{\xi\eta}\left[\frac{\tau_w}{\bar\tau_w} + \frac{\rho_\delta u_\delta^2}{\bar\tau_w}\left[\delta_2\frac{d\,\ln\sigma}{dx} - (\delta_1 + \delta_2 - \int_0^\delta(1 - \frac{\bar\rho_\delta}{\bar\rho}\frac{\rho}{\rho_\delta})dy)\frac{d}{dx}(\ln\frac{\eta}{\sigma}) + \right.\right.$$
$$\left.\left. + \frac{1}{\rho_\delta u_\delta^2}\frac{dp}{dx}\int_0^\delta(1 - \frac{\bar\rho_\delta}{\bar\rho}\frac{\rho}{\rho_\delta})dy\right]\right] = 1 \tag{10}$$

Furthermore from the definition of the skin friction coefficient follows, since Newtonian shear is assumed to apply at the wall:

$$\frac{c_f}{\bar c_f} = \frac{\sigma}{\bar\mu_w}\frac{\mu_w}{\bar\rho_w}\frac{\rho_w}{\rho_\delta}\frac{\bar\rho_\delta}{\rho_\delta} \tag{11}$$

The relations (7) (10) (11) form the system of three equations which is required to determine the scaling functions σ, ξ, η. However, additional information is needed because

1. Eq (7) involves both $d\bar p/d\xi$ and dp/dx one of which is unkown a priori

2. The evaluation of the integrals over the density profiles in Eq (10) requires a specification of the temperature field and

3. Eq (11) serves as a determining equation for σ only if the relative skin friction law $c_f/\bar c_f$ is known.

LEWIS [5] investigated the behaviour of the velocity profile in the vicinity of the wall and found that the pressure gradients are linked by the following relationship

$$\frac{\rho_\delta}{\rho_w}\frac{\delta_2}{\tau_w}\frac{dp}{dx} = \frac{\bar\rho_\delta}{\bar\rho_w}\frac{\bar\delta_2}{\bar\tau_w}\frac{d\bar p}{d\bar x} \tag{12}$$

which serves here to relate the pressure gradients of both flows and hence the velocities at the edge of the boundary layer.

Since the integral approach is used for the flow field it seemed somewhat contradictory to describe the thermodynamic behaviour by means of a finite-difference solution of the energy equation. Therefore the following approximation has been applied.

THE THERMODYNAMIC BEHAVIOUR

There are two well known exact solutions of the energy equation which are, however, restricted both to rather specialised cases. The CROCCO-relationship between total enthalpy (h^0) and velocity (u) which is valid for unit Prandtl number, zero pressure gradient, and isothermal wall

$$\frac{h^0}{h_\delta^0} = \frac{h_w}{h_\delta^0} + (1 - \frac{h_w}{h_\delta^0})\frac{u}{u_\delta} \tag{13}$$

and the particular integral of the energy equation which is restricted to Prandtl number unity and zero heat transfer buch which is valid for arbitrary pressure gradients

$$\frac{h^0}{h_\delta^0} = \frac{h_w}{h_\delta^0} = 1 \tag{14}$$

The lack of a closed-form solution of the energy equation for arbitrary external and wall conditions can be overcome by using an approximate procedure suggested by COHEN [6] and WALZ [7]. The idea consists of introducing a relationship for h^0/h_δ^0 which contains equations (13) and (14) and takes account of the effects of Prandtl number, pressure gradient and variable wall temperature by extending the linear relationship in u to a polynomial of higher order in u [8]:

$$\frac{h^0}{h_\delta^0} = \frac{h_w}{h_\delta^0} + (1 - \frac{h_w}{h_\delta^0})\left[\frac{u}{u_\delta} + \sum_{j=1}^n c_j(x)\left(\frac{u}{u_\delta}\right)^j\left(\frac{u}{u_\delta} - 1\right)\right] - \frac{m_\delta(1-r)}{1+m_\delta}\left[\frac{u}{u_\delta} - \left(\frac{u}{u_\delta}\right)^2\right] \tag{15}$$

where $c_{j(x)}$ are coefficients vanishing for $Pr = 1$, constant pressure and constant wall-temperature. The additional term represents the VAN DRIEST [9] correction where the recovery factor r accounts for small deviations from $Pr = 1$. The unknown functions $c_{j(x)}$ require further equations.

The following possibilities have been suggested:

1. The integral form of the total energy equation, WALZ [7] .

2. A modified Reynolds analogy containing momentum and energy equation, COHEN [6] .

3. One or more compatibility conditions of the energy equation, DIENEMANN [10] , WALZ [7] , CROCCO [3] .

For a first approximation two compatibility conditions have been used to determine $c_{1(x)}$ and $c_{2(x)}$.

Together with the perfect gas assumption this equation is necessary to relate the temperature T and the density ρ to the velocity distribution as well as to the external and wall conditions.

THE SKIN FRICTION LAW

SPALDING and CHI [11] compared 491 zero pressure gradient experimental points for supersonic friction and heat transfer measurements with nineteen different theories. They found that the best results are given by theories of SPALDING & CHI, VAN DRIEST, WILSON and KUTATELADSE & LEONTEV . The later derived from the Prandtl mixing length theory for the limiting case $Re_{\delta_2} \to \infty$ what they called the limiting relative law of friction [12]

$$\frac{c_f}{\bar{c}_f} = \left[\int_0^1 (\frac{\rho}{\rho_\delta} \frac{\bar{\tau}_t/\bar{\tau}_w}{\tau_t/\tau_w})^{1/2} d \frac{u}{u_\delta} \right]^2 \tag{16}$$

Supposed the shear stress distribution is independent of compressibility effects then the integral can be evaluated if the relation between density and velocity is known. Hence this formula can easily be expended to flows with streamwise pressure gradients. The great advantage of this limiting law is that it does not contain any empirical constants depending on the mechanism of the turbulence.

For zero transverse pressure gradient one finds

$$\frac{T}{T_\delta} = \frac{\rho_\delta}{\rho} \tag{17}$$

hence Eq (15) may be used, together with the perfect gas assumption, to compute the relative skin friction from Eq (16).

For the special case of zero streamwise pressure gradient follows

$$\frac{c_f}{\bar{c}_f} = \frac{1}{T_e^+ - 1} \left[arc \sin \frac{2(T_e^+ - 1) + (T_w^+ - T_e^+)}{[4(T_e^+ - 1)T_w^+ + (T_w^+ - T_e^+)^2]^{1/2}} - arc \sin \frac{T_w^+ - T_e^+}{[4(T_e^+ - 1)T_w^+ + (T_w^+ - T_e^+)^2]^{1/2}} \right]^2$$

$$\text{with } T^+ = \frac{T}{T_\delta} , \quad T_e^+ = T_{adiabatic}^+ \tag{18}$$

For nonzero pressure and wall temperature gradient no closed solution can be obtained. Therefore the evaluation has been carried out numerically on the basis of Eqs (15) and (16).

THE TRANSFORMATION EQUATIONS

The transformation equations still depend on the density $\bar{\rho}$ and the viscosity $\bar{u}$ of the transformed flow. Both quantities are unknown a priori. Therefore they are eliminated by redefining the scaling functions

$$\sigma' = \frac{\mu_\infty}{\bar{\mu}_0} \sigma \qquad \xi' = \frac{\bar{\rho}_\infty \bar{u}_\infty/\bar{u}_\infty}{\rho_\infty u_\infty/\mu_\infty} \xi = \frac{Re_{\bar{x}}}{Re_x} \qquad \eta' = \frac{\bar{u}_\infty}{u_\infty} \frac{\mu_\infty}{\bar{\mu}_\infty} \eta \tag{19}$$

Hence one finds after some conversions [4] if CP flow is assumed in the transformed plane and if normalized quantities with respect to free-stream condition at the starting point are introduced, i. e.

$$u_\delta^* = \frac{u_\delta}{u_\infty} \qquad \rho_\delta^* = \rho_\delta/\rho_\infty \qquad \mu_w^* = \mu_w/\mu_\infty \quad \ldots$$

1. The coupling relationship for the edge conditions of both CF and VP flow from Eq (12)

$$\frac{d\bar{u}_\delta^*}{d\overline{Re}_{\bar{x}}} = \rho_w^* \frac{\lambda}{\rho_w^* u_w^*} \frac{1}{\eta^2} \frac{du_\delta^*}{d\overline{Re}_x} \tag{20}$$

2. Three equations for the redefined scaling function σ', ξ', η':
   2.1 from Eqs (17) and (12)

$$\frac{1}{\eta'} \frac{d\eta'}{d\overline{Re}_{\bar{x}}} = \frac{1}{\xi'\eta'} \frac{d\sigma'}{d Re_x} + \frac{\bar{\zeta}}{\bar{H}_{12}} \frac{\bar{\pi}_1}{\overline{Re}_{\bar{\delta}_2}} \left[1 - \frac{\rho_w^*}{\rho_\delta^*} \sigma_w^* u_w^* \frac{\sigma'\eta'}{\zeta'} \right] \tag{21}$$

$$\left[\text{for definition of } \bar{\pi}_1, \bar{\zeta} \text{ see Eq (26)} \right]$$

   2.2 from Eq (10)

$$\frac{1}{\zeta'} = \frac{d Re_x}{d \overline{Re}_{\bar{x}}} = \left[1 + \frac{\bar{H}_{12} + 1}{\bar{H}_{12}} \bar{\pi}_1 \right] \left[\sigma'\eta' \rho_w^* u_w^* (1 < \frac{\bar{H}_{12}+1}{\bar{H}_{12}} \bar{\pi}_1 \frac{h_\delta^0}{h_w^0}) + \frac{\overline{Re}_{\bar{\delta}_2}}{\bar{\zeta}} \frac{1}{\sigma'} \frac{d \sigma'}{d Re_x} \right]^{-1} \tag{22}$$

   2.3 from Eq (11)

$$\sigma' = \frac{\rho_\delta^*}{\rho_w^* u_w^*} \frac{c_f}{\bar{c}_f} \qquad \text{with } c_f/\bar{c}_f \text{ from Eqs (15) and (16).} \tag{23}$$

Hence the problem has been shifted from the computation of the compressible turbulent high speed flow to the computation of the low speed CP case. Or in other words, given a low speed flow which is completely specified these relationships can be used to construct an equivalent supersonic flow for a given Mach number and given external and wall conditions.

THE CP CALCULATION METHOD

The success of this calculation method based on a transformation technique depends to a high degree upon a suitable constant property formulation. Since only the integral properties of the low speed flow are required for the present, an integral calculation method is sufficient. In recent years the available procedures have been reviewd several times, see e. g. ROTTA [13] and THOMPSON [14] . Form the most extensive comparison at AFOSR-IFP Conference at Stanford [15] it is evident that there are many procedures which lead to quite accurate predictions of the incompressible two-dimensional turbulent boundary layer. One of these is the "integral dissipation" method of FELSCH, GEROPP and WALZ [16] , which is used in a slightly modified version here [4] .

Eqs (8) and (9) are written in the dimensionless variables $\overline{Re}_{\bar{\delta}_2}$, $\bar{H}_{32}$ and $\overline{Re}_{\bar{x}}$:

$$\frac{d \overline{Re}_{\bar{\delta}_2}}{d \overline{Re}_{\bar{x}}} = \zeta \left[1 + \bar{\pi}_1 \frac{\bar{H}_{12} + 1}{\bar{H}_{12}} + \bar{x} \right] \tag{24}$$

$$\frac{d\bar{H}_{32}}{d\overline{Re}_{\bar{x}}} = \frac{1}{\overline{Re}_{\bar{\delta}_2}} \frac{d \bar{H}_{32}}{d\ln \overline{Re}_{\bar{\delta}_2}} \bar{\zeta}\left[1 + \bar{\pi}_1 \frac{\bar{H}_{12} + 1}{\bar{H}_{12}} + \bar{x}\right] \tag{25}$$

where the following parameters were introduced:

$$\bar{\pi}_1 = -\frac{\bar{H}_{12}}{\bar{\zeta}} \frac{\overline{Re}_{\bar{\delta}_2}}{\bar{u}_\delta^*} \frac{d \bar{u}_\delta^*}{d\overline{Re}_{\bar{x}}}$$

$$\bar{x} = \frac{\overline{Re}_{\bar{\delta}_2}}{\bar{\zeta} \bar{r}^\epsilon} \frac{d \bar{r}_\delta^\epsilon}{d\overline{Re}_{\bar{x}}} \tag{26}$$

$$\bar{\zeta} = \bar{u}_\delta^* \frac{\bar{c}_f}{2}$$

The pressure gradient parameter $\bar{\pi}_1$ is based on $\bar{\delta}_1$ instead of $\bar{\delta}_2$. For empirical information have been used:

1. The skin friction law of LUDWIEG & TILLMANN in a modified version of FERNHOLZ [17]

$$\frac{\bar{c}_f}{2} = 0,029 \left[0,07775 (4 - \bar{H}_{12})^{2,241} \right]^{1,705} \overline{Re}_{\bar{\delta}_2}^{-0,268} \tag{27}$$

2. The form parameter coupling law of FERNHOLZ [17]

$$\bar{H}_{12} = 1 + 1,48 (2 - \bar{H}_{32}) + 104 (2 - \bar{H}_{32})^{6,7} \tag{28}$$

3. The law for the dissipation parameter of FELSCH [18]

$$\frac{d \overline{H}_{32}}{d \ln \overline{Re}_{\delta_2}} = (\overline{T}' - 0.134 \ \overline{T}) \left[\overline{Re}_{\delta_2}^{0.134} \ \frac{\partial^2}{\partial \overline{H}_{32}} \ (\overline{T} \ \overline{Re}_{\delta_2}^{-0.134}) \right]^{-1} \qquad (29)$$

with $\quad \overline{T}_{(\overline{H}_{32})} = \dfrac{\overline{H}_{12} - 1}{\overline{H}_{12}} \ (\dfrac{\overline{c}_f}{2})^{-1/2}$

$$\overline{T}_{(\overline{T}, \overline{\tau}_1)} = \left[- \frac{\overline{T} + 1.36827796 - 6.09172363 \ (\overline{\tau}_1 + 1.7)^{1/2}}{-0.12156796(\overline{\tau}_1+1.7)^{1/2}-0.05222203(\overline{\tau}_1+1.7)-7.200671_{10}^{-5}(\overline{\tau}_1+1.7)^2} \ e^{0.05\overline{\tau}_1} \right]^{5/3} \qquad (30)$$

which has been approximated by PETERS (private communication).

THE FINAL SYSTEM OF EQUATIONS AND THE STARTING CONDITIONS

The above discussed set of equations is composed of five ordinary differential equations (20) (21) (22) (24) (25) with the dependent variables $\overline{Re}_{\delta_2}$, $\overline{H}_{32}$, $\overline{u}_\delta^\bullet$, Re_x, n' and with $\overline{Re}_x$ as the independent variable. In addition four algebraic equations (23) (27) (28) (30) for σ', $\overline{c}_f$, $\overline{H}_{12}$, $\overline{T}$ which represent the empirical information have been used. The molecular viscosity of air μ has been computed by the KEYES [19] formula

$$\mu = \frac{1.515 \ T^{1/2}}{1 + \dfrac{1.221}{T \ 10^{5/T}}} \cdot 10^{-7} \quad \left[\frac{kps}{m^2} \right]$$

This set of equations is well defined provided the external, wall and initial conditions are specified.

EXTERNAL CONDITIONS. In connection with the perfect gas assumption and negligible lateral pressure gradients, specification of total pressure p^o, total temperature T^o, and the external velocity distribution $u_\delta(Re_x)$ suffice for the determination of all external flow properties provided the external flow field is isentropic.

WALL CONDITIONS. If the wall temperature distribution $T_w(Re_x)$ is given, the wall conditions are completely specified. Although the CROCCO relation is valid for constant wall temperature only it has been shown that variable wall temperatures can be accounted for via a set of correction functions.

INITIAL CONDITIONS. An investigation of the transformation relationships shows that they are neither explicitly dependent on Re_x nor on $\overline{Re}_x$. Accordingly the initial value for Re_x is arbitrary and may be assumed to be $\xi_0' = \overline{Re}_x/Re_x = 1$ From Eqs (19) and (6) one finds $\sigma_0' = n_0'$ with σ_0 known from Eq (23). The initial value of $\overline{u}_\delta^\bullet$ is unity by definition. Finally $\overline{Re}_{\delta_2}$ and $\overline{H}_{32}$ are related to Re_{δ_2} and H_{32} by the transformation [4] . Hence the computation has been started with the initial values for Re_{δ_2} and H_{32} of the particular high speed experiment of interest.

COMPARISON OF THEORY WITH EXPERIMENT

There are very few entirely reliable experiments for compressible turbulent boundary layers. In particular, there are no reliable experiments in prolonged adverse pressure gradient. A further complication is that in several sets of data in strong favourable pressure gradient reverse transition occured presumably. And last not least there is a number of measurements with initially small Re_{δ_2} numbers, which seem to be still laminar or transitional [20] .

Hence a comparison between theory and experiment is rather difficult at present.

Preliminary results have been obtained for the following experiments:
HASTINGS & SAWYER [21] published local skin friction coefficients and boundary layer profiles measured in adiabatic flow on a flat plate at Mach numbers of about 5.0. A comparison between theory and experiment is shown in Fig. 1 for momentum thickness Reynolds number, form parameter and skin friction coefficient. The agreement is good and it can be expected that it becomes even better if the experiments had been performed at higher Reynolds numbers. FERNHOLZ [20] could show that the boundary layer at low values of x is still transitional, a fact which explains the high skin friction values given by the theory.

LEE, YANTA & LEONAS [22] measured zero pressure gradient velocity and temperature profiles as well as skin friction coefficients on a flat cooled nozzle wall at $M_\delta = 4$. In Fig. 2 momentum thickness Reynolds number, skin friction and form parameter are compared with theory. The theory predicts Re_{δ_2} and c_f fairly well. Discrepancies at low values of x can again be explained by the transitional state of the boundary layer. [20] .
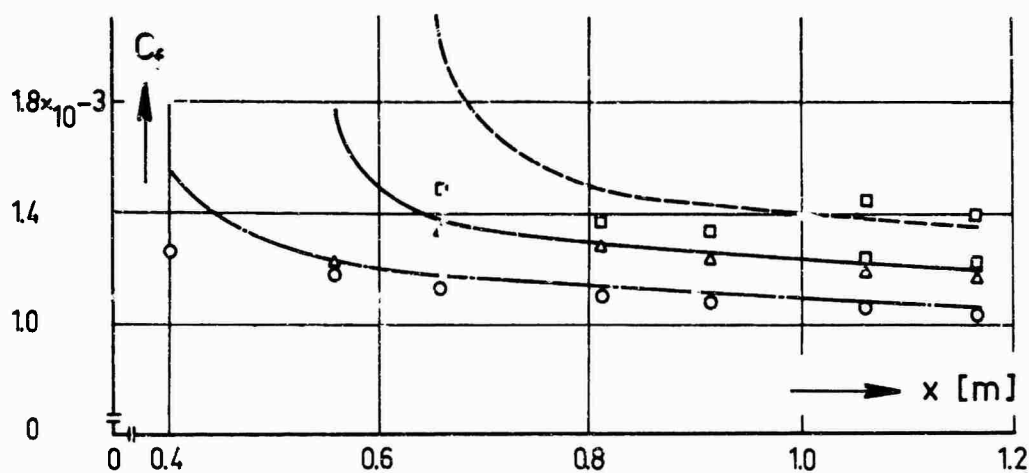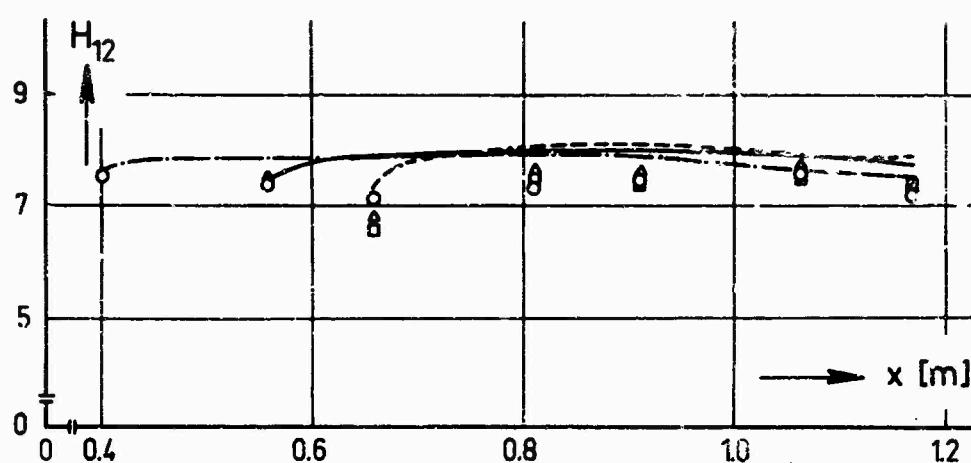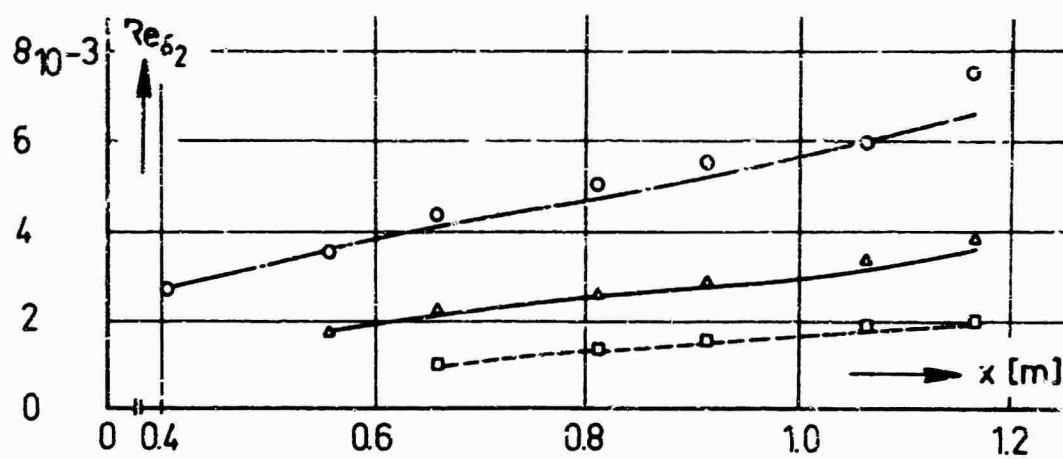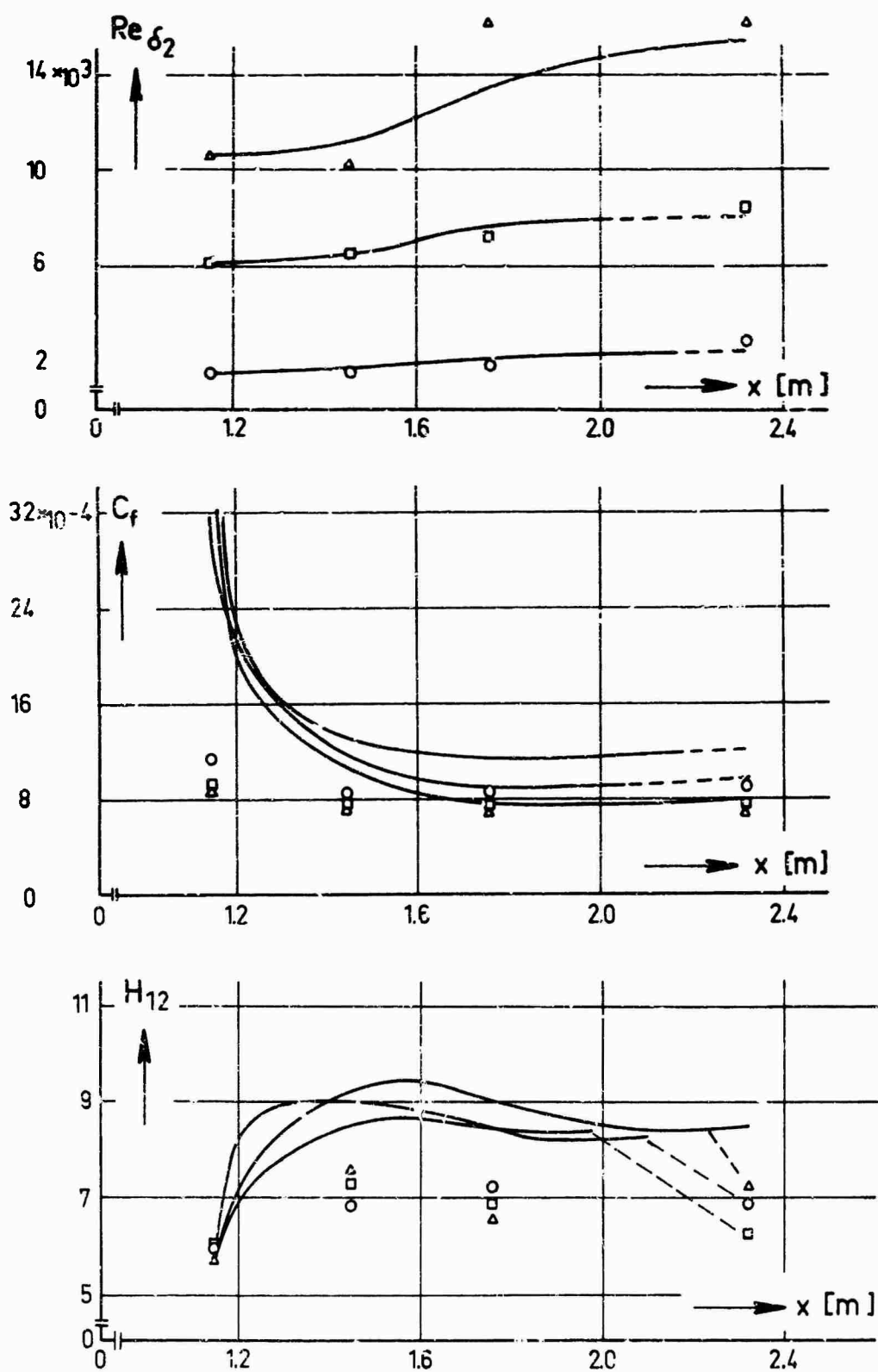
Fig. 1 - Comparison between theory and measurements of Ref. 21
For momentum thickness Reynolds number, form parameter
and skin friction . ($\frac{dp}{dx}$ = 0, adiabatic wall)

$$
\begin{array}{llll}
\text{———·——·} & \circ & p^0 = 6.9063 \text{ kp/cm}^2 & \\
\text{————} & \triangle & p^0 = 3.4531 \text{ kp/cm}^2 & T^0 = 313 \ ^0\text{K} \\
\text{— — — —} & \square & p^0 = 1.7265 \text{ kp/cm}^2 &
\end{array}
$$

Fig. 2 - Comparison between theory and measurements of Ref. 22
For momentum thickness Reynolds number, skin friction
and form parameter ($\frac{dp}{dx} = 0$, cooled wall)

	p^o kp/cm^2	T^o ^oK
o	1.032	429.5
□	5.278	433.9
Δ	10.546	413.3

No explanation can be given for the discrepancy between measured and computed form parameters.

PASIUK, HASTINGS & CHATHAM [23] have measured the development of the velocity and temperature profiles on a flat plate in an expanding supersonic nozzle with an exit Mach number of 3.0. Fig. 3 shows the comparison with experimental values of δ_1 and δ_2 (c_f has not been measured). The agreement between theory and experiment is satisfactory.

JONES & FELLER [24] presented total-temperature and total-pressure distributions measured in the boundary layer on the wall of a straight cooled pipe with small adverse pressure gradient at four different locations. The free-stream Mach number was approximately 5.0. Fig. 4 shows the theoretical prediction of displacement thickness δ_1 compared with the experiments for four different runs. Agreement is good. The variation of Re_{δ_2} with Re_x is shown in Fig. 5. Five different computations have been performed, one for each of the four different runs and one for the total range of Re_x where the first measured profile was used to compute the initial value for H_{32} and Re_{δ_2} (dotted line).

The overall agreement between theory and measurements is good but it could still be better. Hence from these preliminary tests of the theory the conclusion can be drawn that theory and experiment both have to be improved.
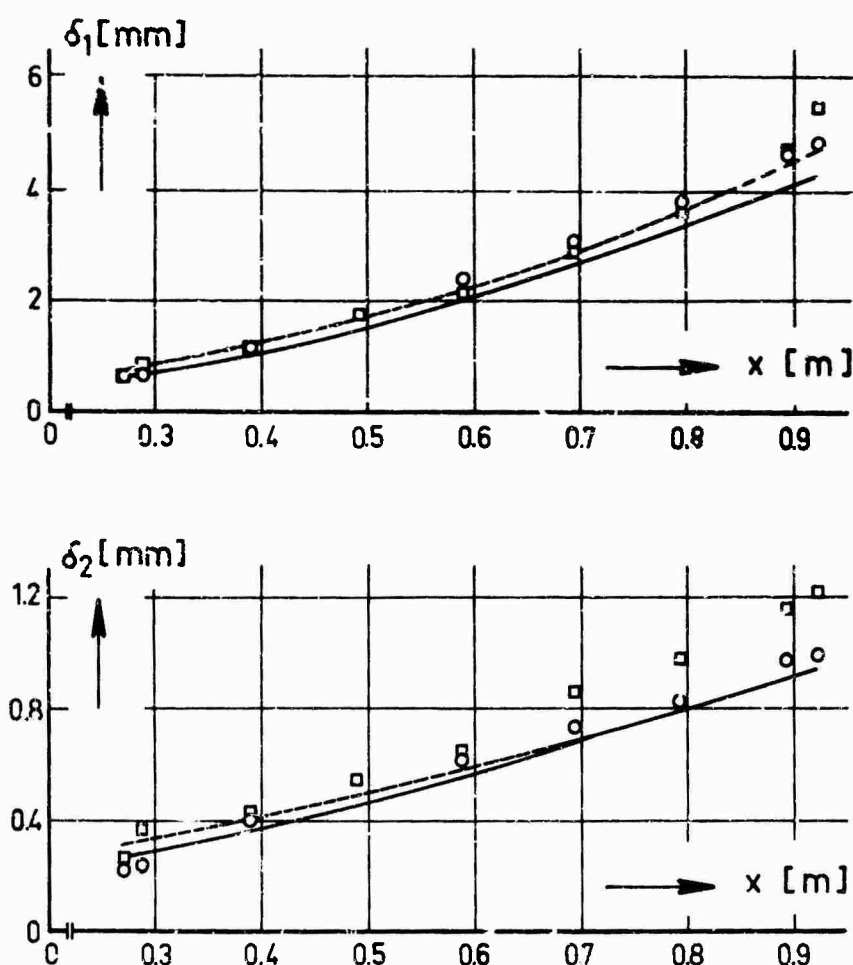
Fig. 3 - Comparison between theory and measurements of Ref. 23.
For displacement thickness and momentum thickness (favourable pressure gradient).

  o zero heat transfer ---
  □ high heat transfer ——
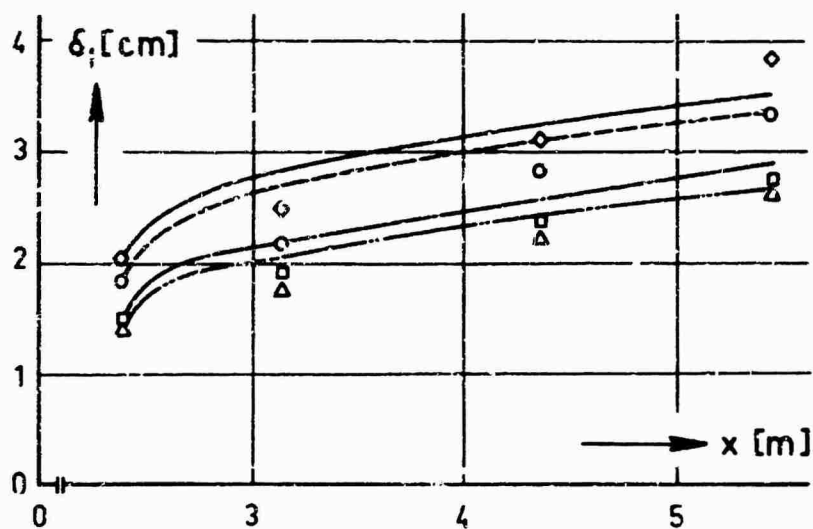
Fig. 4 - Comparison between theory and measurements
of Ref. 24.
For displacement thickness

p^o [kp/cm^2]		T^o [^oK]
◇	4.590 ———	457.1
○	8.058 —————	462.8
□	22.134 —·—·—	491.3
▵	40.316 —··—··—	500.4
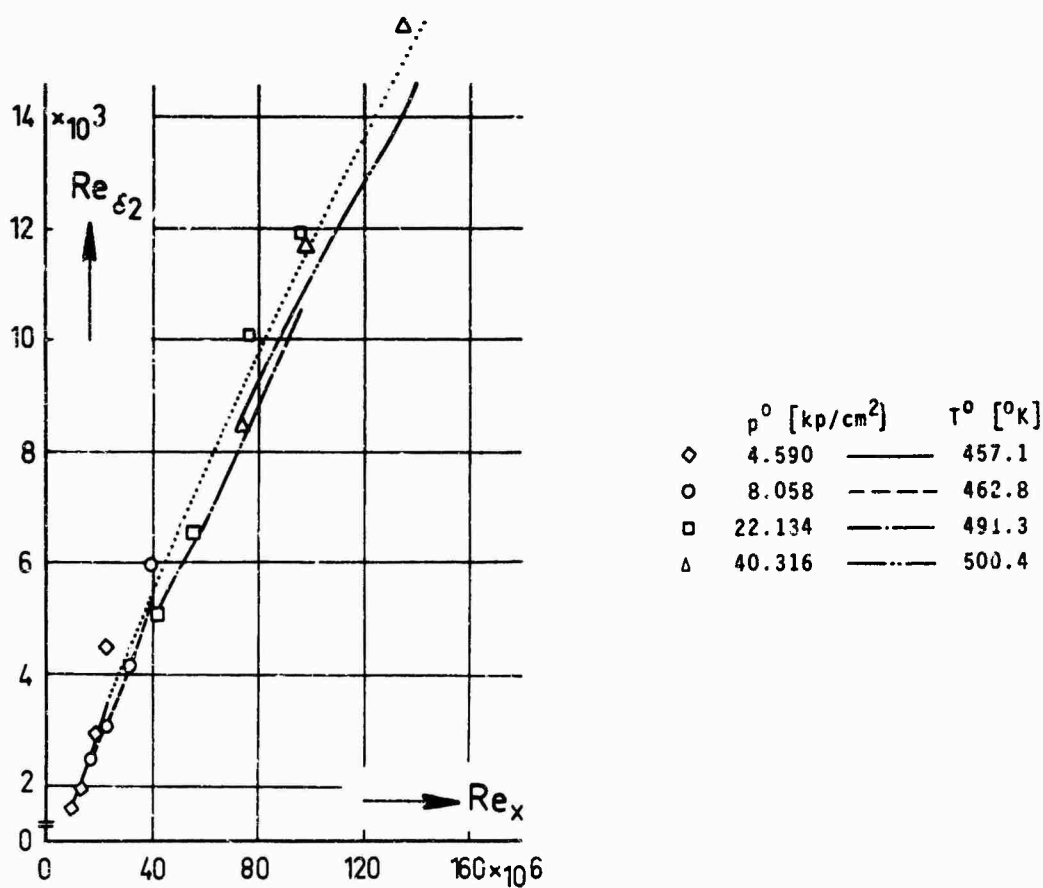
Fig. 5 - Comparison between theory and
measurements of Ref. 24.
For momentum thickness Reynolds
number (small adverse pressure
gradient, cooled wall).

REFERENCES

1. COLES, D. The turbulent boundary layer in a compressible fluid, Phys. Fluids. Vol. 7, No. 9, (1964), pp. 1403 - 1423

2. ECONOMOS, C., BOCCIO, J. An investigation of the high speed turbulent boundary layer with heat transfer and arbitrary pressure gradient, NASA CR-1679, Dec. 1970

3. CROCCO, L. Transformations of the compressible turbulent boundary layer with heat exchange, AIAA J. Vol. 1 No. 12, (1963) pp. 2723-2731

4. KOSTER, H. J. Näherungsweise Berechnung kompressibler turbulenter Grenzschichten mit Druckgradient und Wärmeübergang mittels einer Kompressioilitätstransformation, Interner Bericht T.U.Berlin 1971

5. LEWIS, J. E. Compressible boundary layer and its low speed equivalent, AIAA J. Vol. 6 No. 6, (1968) pp. 1185 - 1187

6. COHEN, N. B. A method for computing turubulent heat transfer in the presense of a streamwise pressure gradient for bodies in high-speed flow, NASA memo.1-2-59L

7. WALZ, A. Compressible turbulent boundary layers, Mécanique de la Turbulence, Marseille (1961)

8. KOSTER, H. J. Effect of streamwise pressure gradient and wall temperature gradient on the temperature-velocity relationship in turbulent boundary layers. Presented at EUROMECH 21-Colloquium Toulouse, Sept. 1970

9. van DRIEST, E. R. Turbulent flows and heat transfer. Published in High Speed Aerodynamics and Jet Propulsion Sect. F., Princeton Univ. Press 1959, ed. by C.C.Lin

10. DIENEMANN, W. Berechnungsverfahren des Wärmeübergangs an laminar umströmten Körpern mit konstanter und ortsveränderlicher Wandtemperatur, Diss. TH Braunschweig 1951; ZAMM 33 (1953) S. 89 - 109

11. SPALDING, D. B., CHI, S. W. The drag of a compressible turbulent boundary layer on a smooth plate with and without heat transfer, JFM Vol.18, part 1, pp. 117-143

12. KUTATELADSE,S.S., LEONTEV, A.I. Turbulent boundary layers in compressible gases, Edward Arnold Publishers London (1964) p. 1 - 170

13. ROTTA, J. C. Critical review of existing methods for calculating the development of turbulent boundary layers, published in Fluid Mechanics of Internal Flow, ed. by G. Sovran, Elsevier Publishing Co. (1967)

14. THOMPSON,B.G.J. A critical review of existing methods of calculating the turbulent boundary layer, Aeronautical Research Council 26, 109 (1964)

15. KLINE, S.J., MORKOVIN, M.W., SOVRAN, G., COCKRELL, D.J. Computation of turbulent boundary layers, Vol. 1 (1968), Proceedings of AFOSR-IFP, Stanford 1968 Conference, Publ. Stanford University

16. FELSCH, K.-O., GEROPP, D., WALZ, A. Method for turbulent boundary layer prediction. Proceedings of AFOSR-IPF, Stanford 1968, Conference Vol. 1, ed. by Kline, Morkovin, Sovran, Cockrell, Publ. Stanford University

17. FERNHOLZ, H. Halbempirische Gesetze zur Berechnung turbulenter Grenzschichten nach der Methode der Integralbedingungen. Ing.Archiv. Bd. 33, Heft 6, S.384-395

18. FELSCH, K.-O. Beitrag zur Berechnung turbulenter Grenzschichten in zweidimensionaler inkompressibler Strömung. Dissertation T.U. Karlsruhe 1965

19. KEYES, F.G. The heat conductivity, viscosity, specific heat and Prandtl numbers for thirteen gases. Techn.Rep. No.37, Project SQUID, MIT Cambridge, Mass.

20. FERNHOLZ, H. Departures from a fully developed turbulent velocity profile on a flat plate in compressible boundary layers. To be presented at Symposium on "Advanced Problems and Methods in Fluid Mechanics" at Warschau Sept.1971

21. HASTINGS, R.C., SAWYER, W.G. Turbulent boundary layers on a large flat plate at $M = 4$, Royal Aircraft Establishment TR 70040 (1970)

22. LEE, R.E., YANTA, W.J., LEONAS, A.C. Velocity profile,skin-friction balance and heat transfer measurements of the turbulent boundary layer of Mach 5 and zero pressure gradient, NOL TR 69-106 (1969)

23. PASIUK, L., HASTINGS, S.M., CHATHAM, R. Experimental Reynolds analogy factor for a compressible turbulent boundary layer with a pressure gradient, NOL TR 64-200 (1964)

24. JONES, R.A., FELLER, W.V. Preliminary suvey of the wall boundary layer in a Mach 6 axisymmetric tunnel, NASA TN D - 5620 (1970)

Equation (19), which is the basic relation derived in this paper, is valid only for negligibly small wall temperature variations. More specifically, it does not account for variations with x of the ratios (T_w/T_e), (μ_w/μ_e), and (T_{aw}/T_e). When this is done, three extra terms are added to the basic relation, Equation (19), and the function G from Equation (17) breaks down into four separate pieces:

$$G_0 = \int_0^{\delta^+} \frac{1}{2} u^{+2} \, dy^+ \; ;$$

$$G_1 = \int_0^{\delta^+} \frac{\rho}{\rho_w} u^{+2} \, dy^+ \, , \text{ where } (\rho_w/\rho) = 1 + \beta u^+ - \gamma u^{+2} \; ;$$

$$G_2 = \int_0^{\delta^+} \frac{\rho}{\rho_w} \left[u^+ \frac{\partial u^+}{\partial \beta} - \frac{1}{\rho \nu_w} \frac{\partial u^+}{\partial y^+} \frac{\partial \psi}{\partial \beta} \right] dy^+ \; ;$$

$$G_3 = \int_0^{\delta^+} \frac{\rho}{\rho_w} \left[u^+ \frac{\partial u^+}{\partial \gamma} - \frac{1}{\rho \nu_w} \frac{\partial u^+}{\partial y^+} \frac{\partial \psi}{\partial \gamma} \right] dy^+ \; .$$

Note that the original function $G = (G_1 + \beta G_2 + 2\gamma G_3)$. The revised version of Equation (19) which accounts for wall temperature variations is as follows:

$$\left(G - 3\alpha H - \frac{F}{\lambda} B \sqrt{\frac{T_w}{T_e}} \right) \frac{d\lambda}{dx^*} + \frac{V'}{V} \lambda(\lambda^2 \delta^+ - G_1) - \lambda^4 H \frac{(1/V)''}{R_L} = R_L V(1 + B) +$$

$$+ F\lambda^2 \frac{d}{dx^*}(\nu_w/U_e) + \frac{d}{dx^*} \left(\frac{T_w}{T_e} \right) \left[\lambda G_0 + \frac{\lambda^4 (1/V)'}{2R_L T_w/T_e} + \frac{T_{aw}}{T_w} \frac{G_3}{\lambda} - \frac{1}{2} \beta \lambda G_2 \right] +$$

$$+ \frac{\lambda^4 (1/V)'}{R_L} \frac{d}{dx^*} [\ln(\mu_w/\mu_e)] + \frac{d}{dx^*} \left(\frac{T_{aw}}{T_w} \right) \left[\frac{T_w}{T_e} \frac{G_3}{\lambda} - G_2 \sqrt{(T_w/T_e)} \right] \; .$$

Terms which are new or different from the printed paper are underlined. By assuming a specific viscosity/temperature law, one could combine the two terms involving the derivatives of wall temperature and viscosity ratio.

Having just discovered this omission of temperature variations, we have not yet evaluated how significant the effect will be on our basic theory. We are hopeful that the simplifications of our graphical theory (Eq. 24 and Fig. 2) will still be valid unless temperature gradients are very large.

In the meantime, one should be alert to the possibility that our original method may be inaccurate for strongly varying wall or recovery temperature.

"A SIMPLE ANALYSIS OF TWO-DIMENSIONAL TURBULENT SKIN FRICTION WITH ARBITRARY WALL AND FREESTREAM CONDITIONS" [3]

by

Frank M. White[1]

and

George H. Christoph[2]

University of Rhode Island, Kingston, Rhode Island, USA

SUMMARY

A new approach is proposed for an approximate analysis of the two-dimensional turbulen. boundary layer under a wide variety of arbitrary conditions. The initial step is to discard entirely the celebrated Karman momentum integral relation and to ignore completely any consideration of integral thicknesses, shape factors, or moment relations. The second step is to develop an effective formula for the law-of-the-wall which accounts for all of the different parameters considered. The final step is to combine the wall law with the differential momentum equation into a single first-order ordinary differential equation for the skin friction coefficient, suitable for computer or graphical solution and, in special cases, closed form solutions.

Examples are given covering combinations of eight different effects: pressure gradient, heat transfer, compressibility, roughness, wall transpiration, transverse curvature, longitudinal curvature, and aqueous polymer solutions. The results indicate that the new theory is not only the simplest existing analysis of the turbulent boundary layer but also is apparently one of the most accurate.

NOTATION

English Symbols:

a = speed of sound

A = compressibility factor, Eq.(22)

B = transpiration factor, = $2\rho_w v_w/(\rho_e U_e C_f)$

C_f = friction coefficient, = $2\tau_w/(\rho_e U_e^2)$

C_{f_o} = value of C_f for an impermeable wall

c_p = specific heat at constant pressure

f^*, g^* = graphical functions, Eq.(24), Fig.2

F, G, H = functions defined by Eq.(17)

F_c, F_{R_x} = flat plate factors, Eq.(29)

h = transpiration parameter, Eq.(32)

k = thermal conductivity

L = reference length

M = Mach number

p = static pressure

q = heat flux

r = wall recovery factor (≈ 0.89)

r_o = transverse radius of curvature

r_o^+ = $r_o v^*/v_w$

R = longitudinal radius of curvature

R_x = $U_e x/v_e$

R_L = parameter defined by Eq.(19)

R^* = $R_L/(1/V)'$, Eq.(23)

T = static absolute temperature

u, v = streamwise and normal velocities

u^+ = u/v^*

U_e = freestream velocity

U_o = reference velocity

V = U_e/U_o

v^* = friction velocity, = $(\tau_w/\rho_w)^{\frac{1}{2}}$

v_w = wall normal velocity (positive for blowing)

v_w^+ = v_w/v^*

v_o = polymer solution onset velocity

v_o^+ = v_o/v^*

x, y = streamwise and normal coordinate

x^* = x/L

y^+ = yv^*/v_w

Greek Symbols:

α = pressure gradient parameter, Eq.(3)

β = heat transfer parameter, Eq.(3)

γ = compressibility parameter, Eq.(3)

δ = boundary layer thickness

δ^+ = $\delta v^*/v_w$

ϵ = wall roughness height

κ = Karman's constant, ≈ 0.4

λ = basic dependent variable, Eq.(19), = $(2/C_f)^{\frac{1}{2}}$

ρ = density

μ = viscosity

ν = kinematic viscosity

θ = momentum thickness

τ = shear stress

ψ = stream function, Eq.(13)

Subscripts and Superscripts:

$(\ )_e$ = freestream

$(\ )_w$ = wall

$(\ )_{aw}$ = adiabatic wall

$(\ )_{inc}$ = computed by an incompressible formula

$(\ )'$ = derivative with respect to x^*

---

[1] Professor of Mechanical and Ocean Engineering.

[2] Graduate Research Assistant, Department of Mechanical Engineering and Applied Mechanics.

1. INTRODUCTION

The fact that seven or more methods at the 1968 Stanford Conference (1) were judged to be satisfactory in accuracy has caused a well deserved decline in publication of incompressible turbulent boundary layer analyses. Interest has now centered on the next two most viable flow conditions: a) the compressible turbulent boundary layer, as reviewed by Beckwith (2) and b) turbulent flow with wall transpiration, as reviewed by Jeromin (3).

For analysis of compressible turbulent flow with, say, pressure gradient or wall blowing, there are at least four different types of computational schemes now in use: a) correlation techniques based on limiting case theories (4-8); b) methods using the Karman momentum integral relation (9-12); c) compressibility transformations (3,13-15); and d) finite difference computations (16-21). The present falls into an intriguing new category: an integral relation based upon inner or "wall" variables.

The correlation techniques are usually flat plate formulas, mostly using reference temperature concepts, which are extended, hopefully, to modest variations in pressure gradient or wall transpiration. But in fact "modest" means very small indeed, and these formulas are not usually reliable except for rough estimates. Often they predict the wrong trend (26).

The Karman integral methods are extensions of the low-speed methods of reference 1. The high speed Karman relation contains at least three unknowns - momentum thickness, shape factor, and skin friction coefficient - and two important parameters: the wall transpiration rate and the longitudinal curvature. Considerable empiricism is needed to obtain extra relations for closure of Karman methods. The recent method of Alber and Coats (11) contains seven different auxiliary relations, yet is valid only for adiabatic nontranspired flow. The method of Thompson (12) requires an extensive set of wall blowing charts, yet is valid only for "moderate" pressure gradients. The Karman method of Sasman and Cresci (10) is so complex that a recent FORTRAN program for this method (23) contains nearly one thousand instructions, yet wall transpiration is not allowed. Also, longitudinal curvature has such a striking effect that most Karman methods are essentially invalid for supersonic flow along curved walls(22,26).

The compressibility transformations are of particular interest because of their analogy with the well established laminar flow transformations (24). The turbulent transformations are definitely valid for flat plate flow but become progressively inaccurate with increases in Mach number, heat transfer, or pressure gradient. No current transformation is accurate in hypersonic flow under any conditions (25) but the inner law used here seems valid at Mach numbers approaching fifty. Beckwith (2) criticizes turbulent transformations for several reasons, and the transformation theorists themselves (13) admit to discrepancies in their equations, which, incidentally, are quite complex, even for integral methods.

Finally, finite difference computations on a digital computer are now well established for compressible turbulent flows, often including wall transpiration, and a few program listings are available (16,21). A large computer is a necessity, with run times of the order of five minutes for a given boundary layer. The individual must of course be prepared to accept and use the existing programs, which probably took years to construct. The finite difference methods have the potential of handling arbitrarily difficult boundary conditions, but their performance to date has been spotty, as seen for example in Figure 5 of this paper. Also, longitudinal curvature has a profound effect on turbulence structure, so that, for example, Bradshaw and Ferriss (21) frankly decline to compare their much admired computations with flow over curved surfaces.

Since the correlation techniques are so limited, there is presently no compressible turbulent method which a person could sit down and use effectively with a piece of paper or a small computer program. It is the purpose of this paper to present just such a simple method, useful for a wide variety of parametric conditions. There seems to be some serendipity involved, for the new method, although based on a single simple approximation, appears to be surprisingly accurate, even exceeding the authors' own expectations.

The new method has also spawned certain psychological problems. It is so simple that it is difficult to take seriously. It invites instinctive distaste by pointedly ignoring fifty years of conventional approaches to turbulent boundary layer analysis. Further, if the approach is taken seriously, it more or less threatens the very existence of all other methods in the literature. In short, the proposed method is controversial - revolutionary, even - and the authors sense that its acceptance, if any, will probably grow from the user end, rather than from the research end, of the turbulent boundary layer analysis spectrum.

2. THE LAW-OF-THE-WALL WITH EIGHT PARAMETERS

Basic to the development of any approximate analysis of the boundary layer is a detailed knowledge of the velocity profile and its dependence upon flow parameters. We will consider eight different parameters in this paper, all assumed to be known functions of streamwise direction x:

1. Pressure gradient: dp_e/dx
2. Heat transfer: q_w or T_w
3. Compressibility: a_e

5. Wall roughness height: ϵ
6. Transverse radius of curvature: r_0
7. Longitudinal radius of curvature: R

4. Wall transpiration: $\rho_w v_w$ 8. Polymer solution onset velocity: v_o

Traditionally, one plans to use these parameters in the Karman momentum integral relation, now celebrating its fiftieth anniversary. For a perfect gas, we have:

$$\frac{d\theta}{dx} + \frac{\theta}{r_0}\frac{dr_0}{dx} + \frac{\theta}{U_e}\frac{dU_e}{dx}(2 + H - M_e^2) + \frac{1}{\rho_e U_e^2}\frac{d}{dx}\left(\int_0^\delta (p_e - p)\,dy\right) = \tfrac{1}{2}C_f(1 + B) \quad, \tag{1}$$

where θ is the compressible momentum thickness, $H = \delta*/\theta$ is the shape factor, and $C_f = 2\tau_w/\rho_e U_e^2$ is the local skin friction coefficient. The quantity $B = 2\rho_w v_w/(\rho_e U_e C_f)$ is the wall transpiration parameter and is positive for blowing. Notice the seldom seen lateral pressure gradient term, which is usually a correction for longitudinal curvature. This effect, though usually neglected, can be painfully large. In the supersonic curved ramp experiment of Sturek and Danberg (26), this term, measured experimentally, is even larger than $(d\theta/dx)$ itself.

If we nondimensionalize our stream wise velocity profile with an eye toward the Karman relation, our eight parameters above would typically arrange themselves as follows:

$$\frac{u}{U_e} = fcn\left\{ \frac{y}{\delta} , \frac{\delta}{\tau_w}\frac{dp_e}{dx} , \frac{T_w}{T_e} , \frac{U_e}{a_e} , \frac{\epsilon U_e}{\nu_e} , \frac{r_0}{\delta} , \frac{\rho_w v_w}{\rho_e U_e} , \frac{R}{\delta} , \frac{v_0}{U_e} \right\} , \tag{2}$$

from which we could compute θ and H. This provides one of the <u>two</u> equations needed to close the Karman relation, Eq.(1). We are left to search for a third relation(s), hopefully one which employs good physics and accounts for a goodly number of our eight parameters.

Now in fact analytic relations such as Eq.(2) do not abound in the literature. This lack of a suitable profile expression led the writers to select an inner or "wall" law as an alternative approximation. The inner law is scaled by the friction velocity $v* = \sqrt{(\tau_w/\rho_w)}$ and studiously avoids any use of outer parameters such as U_e, θ, δ, or T_e. Thus the nondimensional inner law selected is of the following form:

$$\frac{u}{v*} = fcn\left\{ \frac{yv*}{\nu_w} , \frac{\nu_w}{\tau_w v*}\frac{dp_e}{dx} , \frac{q_w \nu_w}{T_w k_w v*} , \frac{r v*^2}{2c_p T_w} , \frac{v_w}{v*} , \frac{\epsilon v*}{\nu_w} , \frac{v* r_0}{\nu_w} , --- , \frac{v_0}{v*} \right\} ,$$

$$\text{OR:} \quad u^+ = fcn\left(y^+ , \alpha , \beta , \gamma , v_w^+ , \epsilon^+ , r_0^+ , --- , v_0^+ \right) , \tag{3}$$

where r is the recovery factor, assumed known (≈ 0.89). We have indicated three dashes (---) in the place where a longitudinal curvature parameter should appear. This was an unexpected bonus: to the authors' knowledge, there is no significant effect of longitudinal curvature on the law-of-the-wall, as evident from, e.g. reference 26. Thus longitudinal curvature is a non-issue from the present point of view. We can and will compute skin friction in supersonic turbulent flow over curved walls (see Figures 4 and 5-a).

Most of the parameters in Eq.(3) are obvious and well known, with the possible exception of β and γ, which were suggested by writing the Crocco approximation in terms of inner variables:

Thus: $T \approx T_w + C_1 u + C_2 u^2$

becomes: $T/T_w \approx \rho_w/\rho \approx 1 + \beta u^+ - \gamma u^{+2}$ (4)

for a perfect gas with constant specific heats. When written in terms of stagnation temperature, the Crocco law can be a very poor approximation to air flow measurements, as pointed out by many investigators (see ref. 27). However, Eq.(4) is an excellent approximation to the static temperature distribution, being matched directly to the actual wall heat flux and recovery factor. We will use the Crocco law in what follows, but it is not essential to the basic development.

The effect of each of the seven parameters in Eq.(3) on the law-of-the-wall is sketched in Figure 1, where each curve represents the specific effect and no other. We see that cold walls, adverse gradients, blowing, and polymer solutions all tend to raise the inner law above the usual logarithmic profile, whereas hot walls, favorable gradients, suction, compressibility, and convex transverse curvature all push the profile downward. As mentioned, longitudinal curvature has no significant effect, nor does concave transverse curvature (pipe flow, for example). The effect of favorable pressure gradient, as sketched, is small but not always negligible.

To derive a simple but adequate analytic formula for Eq.(3), we make the usual Couette-flow approximation at the wall, plus a mixing length expression for turbulent shear. The boundary layer momentum equation reduces to:
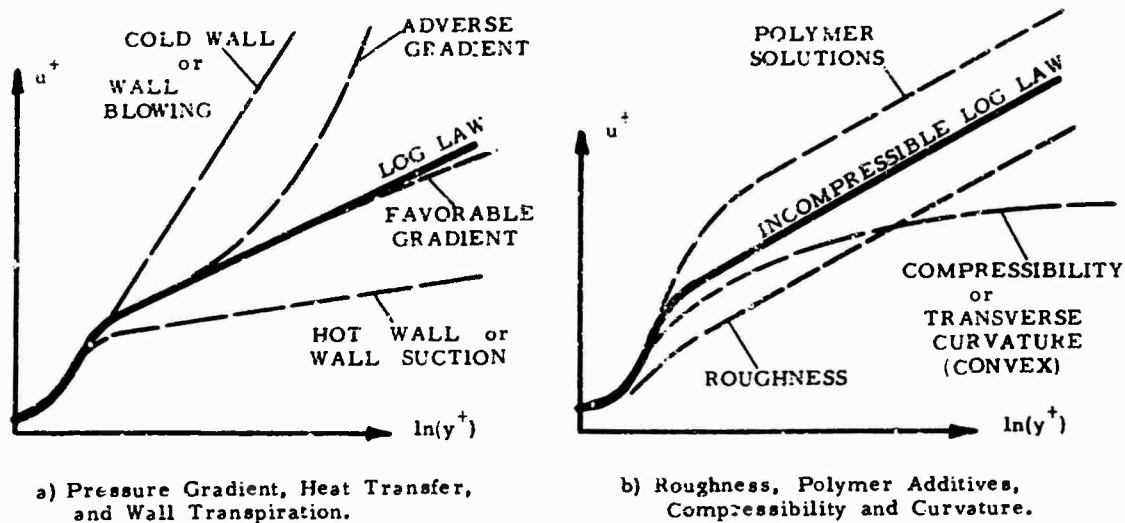
a) Pressure Gradient, Heat Transfer, and Wall Transpiration.

b) Roughness, Polymer Additives, Compressibility and Curvature.

Figure 1. PARAMETRIC EFFECTS ON THE INCOMPRESSIBLE LAW-OF-THE-WALL.

$$\rho_w \, v_w \, \frac{du}{dy} \approx - \frac{dp_e}{dx} + \frac{d}{dy} \{ \, \rho \, \kappa^2 \, y^2 \, | \, \frac{du}{dy} \, | \, \frac{du}{dy} \, \} \tag{5}$$

We have neglected viscous shear and will match our integrated result to a point in the sublayer. It turns out that an accurate formula for the sublayer is not needed for any of our eight parameters except strong transverse curvature (ref. 28). We may integrate Eq.(5) once and substitute for ρ from Eq.(4), rewriting the velocity gradient in terms of inner variables:

$$\frac{du^+}{dy^+} = \frac{1}{\kappa y^+} (1 + \beta u^+ - \gamma u^{+2})^{\frac{1}{2}} (1 + \alpha y^+ + v_w^+ u^+)^{\frac{1}{2}} + \text{constant} \tag{6}$$

Although the variables are not separable unless either pressure gradient (α) or transpiration (v_w^+) vanishes, Eq.(6) may readily be integrated numerically. The initial value (u_o^+, y_o^+) should be close to the wall and consistent in the limit with the ordinary low speed logarithmic law:

$$u^+(y^+, 0, 0, 0, 0, 0, 0, 0) \approx \frac{1}{\kappa} \ln y^+ + b \qquad (\kappa \approx 0.4, \ b \approx 5.5) \tag{7}$$

The simplest possible initial value is the point of apparent no-slip:

$$u_o^+ = 0 \quad \text{at} \quad y_o^+ = e^{-\kappa b} \quad (\approx 0.1108) \tag{8}$$

We shall adopt Eq.(8) in all our calculations, although Simpson et al (29) suggest that a better match-point for wall blowing problems is obtained at the "two-layer" intersection point (u_o^+, y_o^+) = (11.0, 11.0). Closed form integrals of Eq.(6) are possible for two important cases, the first of which is when transpiration is zero:

$$u^+(y^+, \alpha, \beta, \gamma, 0, 0, 0, 0) = \frac{1}{2\gamma} [\, \beta + Q \sin\{ \varphi + \frac{\gamma^{\frac{1}{2}}}{\kappa} [2(S - S_o) + \ln(\frac{S-1}{S+1} \frac{S_o +1}{S_o -1})] \} \,] \tag{9}$$

where $\varphi = \sin^{-1}[(2\gamma u_o^+ - \beta)/Q]$, $Q = \sqrt{(\beta^2 + 4\gamma)}$, $S = \sqrt{(1 + \alpha y^+)}$.

This is a cumbersome formula but can be adapted to simple expressions in the new theory. The second special case of Eq.(6) is for wall transpiration only, with no other effects present:

$$\frac{2}{v_w^+} [(1 + v_w^+ u^+)^{\frac{1}{2}} - 1] = \frac{1}{\kappa} \ln y^+ + b \tag{10}$$

This is Stevenson's law-of-the-wall (30) for transpired incompressible boundary layers.

The remaining three effects in Eq.(3) may be easily accounted for as follows:

a) Wall roughness (sand grains): take $b \approx 5.5 - \frac{1}{\kappa} \ell n(1 + 0.3 \, \epsilon v^*/v_w)$

b) Polymer solutions (ref. 31): take $b \approx 5.5 + W \ell n(v^*/v_o^*)$, where $W = W(\begin{smallmatrix} \text{polymer} \\ \text{concentration} \end{smallmatrix})$.

(11)

c) Transverse curvature (ref. 32): replace y^+ by $Y = r_o^+ \ell n(1 + y^+/r_o^+)$.

All three of these effects are apparently valid even in the presence of other multiple effects, such as heat transfer and pressure gradient. Thus it is not out of the question to consider six or seven effects together analytically, although data is lacking for comparison. The polymer solutions are liquids, where compressibility would not be a factor. Also, the constant 0.3 in Eq.(11-a) would need to be modified for roughness elements other than sand grains.

3. DERIVATION OF THE BASIC DIFFERENTIAL EQUATION

The analysis which follows is a generalization of the incompressible flow method presented in reference 33. It is desired to solve, approximately, the boundary layer continuity and momentum equations for two-dimensional compressible turbulent flow:

a)
$$\frac{\partial}{\partial x}(\rho u) + \frac{\partial}{\partial y}(\rho v) = 0$$

(12)

b)
$$\rho u \frac{\partial u}{\partial x} + \rho v \frac{\partial u}{\partial y} = -\frac{dp_e}{dx} + \frac{\partial \tau}{\partial y}$$

The energy equation is not needed because of the use of the Crocco approximation, Eq.(4). The following three steps complete the analysis:

1) We assume that our law-of-the-wall, Eq.(3) or (6), is valid across the entire boundary layer at any local streamwise position. The chief source of error lies with "relaxing" flows, where a real boundary layer may "lag" somewhat behind this local-wall-law assumption.

2) We resist the temptation to use the Karman relation, Eq.(1). This step requires some courage.

3) We substitute the wall-law directly into Eq.(12-b) and integrate with respect to y^+ across the entire boundary layer. This gives the desired first-order differential equation, Eq.(19).

The vertical velocity may be eliminated by the stream function ψ and the law-of-the-wall:

$$\rho v = -\frac{\partial \psi}{\partial x} = \rho_w v_w - \mu_w \int_0^{y^+} \frac{u^+ \, dy^+}{1 + \beta u^+ - \gamma u^{+2}} \}$$

(13)

Now combine Eqs.(3), (12-b) and (13), using the Bernoulli relation to rewrite the pressure gradient. The result is:

$$\rho v^* u^+ \frac{\partial}{\partial x}(v^* u^+) - \frac{\partial \psi}{\partial x} \frac{v^*}{v_w} \frac{\partial}{\partial y^+}(v^* u^+) = \rho_e U_e \frac{dU_e}{dx} + \frac{v^*}{v_w} \frac{\partial \tau}{\partial y^+}$$

(14)

Leaving y-derivatives untouched, we carry out x-derivatives with the chain rule. For brevity, we account here only for pressure gradient, heat transfer, compressibility, and transpiration effects:

$$\frac{\partial}{\partial x} = \frac{\partial y^+}{\partial x}\frac{\partial}{\partial y^+} + \frac{\partial \alpha}{\partial x}\frac{\partial}{\partial \alpha} + \frac{\partial \beta}{\partial x}\frac{\partial}{\partial \beta} + \frac{\partial \gamma}{\partial x}\frac{\partial}{\partial \gamma} + \frac{\partial v_w^+}{\partial x}\frac{\partial}{\partial v_w^+}$$

(15)

Combine Eqs.(14) and (15) and integrate the entire result with respect to y^+ (not y) from the wall ($\tau = \tau_w$) to the freestream ($y^+ = \delta^+$, $\tau = 0$). The result is:

$$v^* \frac{dv^*}{dx} G + v^{*2} \frac{d\alpha}{dx} H + F(v^* \frac{dv_w}{dx} - v_w \frac{dv^*}{dx}) + \frac{v_w U_e v^*}{v_w} = \rho_e \frac{U_e}{\rho_w}\frac{dU_e}{dx} - \frac{v^* \tau_w}{v_w}$$

(16)

where the functions F, G, and H result from the integration:

$$F = \int_0^{\delta^+} \frac{\rho}{\rho_w}(u^+ \frac{\partial u^+}{\partial v_w^+} - \frac{1}{\mu_w}\frac{\partial \psi}{\partial v_w^+}\frac{\partial u^+}{\partial y^+}) \, dy^+ \quad ; \quad H = \int_0^{\delta^+} \frac{\rho}{\rho_w}(u^+ \frac{\partial u^+}{\partial \alpha} - \frac{1}{\mu_w}\frac{\partial \psi}{\partial \alpha}\frac{\partial u^+}{\partial y^+}) \, dy^+$$

(17)

$$G = \int_0^{\delta^+} \frac{\rho}{\rho_w}(u^{+2} - \mu u^+ \frac{\partial u^+}{\partial \beta} + 2\gamma u^+ \frac{\partial u^+}{\partial \gamma} + \frac{\beta}{\mu_w}\frac{\partial \psi}{\partial \beta}\frac{\partial u^+}{\partial y^+} - \frac{\gamma}{\mu_w}\frac{\partial \psi}{\partial \gamma}\frac{\partial u^+}{\partial y^+}) \, dy^+$$

Since every quantity in Eq.(16) can be expressed in terms of v^* and known flow conditions - U_e, T_w, v_w, etc - it follows that Eq.(16) is the desired result: a single differential equation for computing $v^*(x)$. It is convenient to non-dimensionalize everything with respect to reference values U_0 and L. Define:

$$\lambda = (2/C_f)^{\frac{1}{2}} \quad ; \qquad x^+ = x/L \quad ; \qquad V = U_e(x)/U_o = V(x^*) \tag{18}$$

In terms of these variables. Eq. (16) becomes:

$$(G - \alpha H - \frac{F}{\lambda} B \sqrt{\frac{T_w}{T_e}}) \frac{d\lambda}{dx^*} + \frac{V'}{V} \lambda (\lambda^2 \delta^+ - G) - \lambda^4 H \frac{(1/V)''}{R_L} = R_L V (1 + B) + F \lambda^2 \frac{d}{dx^*}(\frac{v_w}{U_e}) \quad , \tag{19}$$

where $R_L = (U_o L/\nu_e)(\mu_e/\mu_w)(T_e/T_w)^{\frac{1}{2}}$ and $B = 2\rho_w v_w/(\rho_e U_2 C_f) = \lambda^2 v_w/U_e$.

Equation (19) is in final form and similar to the incompressible relation of ref. 33, except that now heat transfer, compressibility and transpiration are included with pressure gradient. Each of the four functions (F, G, H, δ^+) varies with the five quantities $(\lambda, \alpha, \beta, \gamma, v_w/U_e)$, with δ^+ being computed from the wall law, Eq. (6), and (F, G, H) from Eqs. (17). We have not yet correlated our computations for all four parameters simultaneously, but we offer the following curve-fit expressions for no transpiration, where F and v_w vanish and:

$$G \approx 8.0 \ (\delta^+/.1108)^{1.2} + 1.2 \ \alpha H \quad ; \qquad H \approx 0.5 \ \delta^{+2}[\lambda (T_e/T_w)^{\frac{1}{2}} - 0.4 \ \alpha \delta^+] \tag{20}$$

These are not particularly accurate curve-fits, and the graphical method of Section 4 is more highly recommended for general usage in impermeable wall cases. The three parameters (α, β, γ) are computed as functions of λ and x^* by rewriting their definitions:

$$\alpha = \lambda^3 (1/V)'/R_L \quad ; \qquad \beta = \frac{(T_{aw}/T_w - 1)}{\lambda (T_e/T_w)^{1/2}} \quad ; \qquad \gamma = (T_{aw}/T_e - 1)/\lambda^2 \quad . \tag{21}$$

Separation occurs when the coefficient of $(d\lambda/dx^*)$ in Eq. (19) vanishes, which causes $C_f = 2/\lambda^2$ to approach zero. Thus separation is explicit and does not require any artificial correlation.

4. GRAPHICAL METHOD FOR IMPERMEABLE WALLS

For impermeable walls $(v_w = F = 0)$, it turns out that the graphical scheme of ref. 33 is still valid, if the coefficients are scaled by the van Driest (6) parameter A, defined as:

$$A = \frac{(T_{aw}/T_e - 1)^{\frac{1}{2}}}{\sin^{-1}(\frac{a}{c}) + \sin^{-1}(\frac{b}{c})} \quad , \text{ where } a = \frac{T_{aw} + T_w}{T_e} - 2 \ ; \ b = \frac{T_{aw} - T_w}{T_e} \ ; \ c = [(\frac{T_{aw} + T_w}{T_e})^2 - 4 \frac{T_w}{T_e}]^{\frac{1}{2}} . \tag{22}$$

Numerical values of A are shown in Figure 2-a for various Mach numbers and wall temperatures. For any given local conditions, the "separation" friction coefficient, λ_{max}, is approximated by:

$$\lambda_{max} \approx 3.7 A \log_{10}(R^*) \quad , \qquad \text{where} \qquad R^* = R_L/(1/V)' . \tag{23}$$

One computes the value of (λ/λ_{max}) and enters Figure 2-b (taken from ref. 33) to obtain the two functions f^* and g^* for use in the following generalized approximation of Eq. (19):

$$\frac{d\lambda}{dx^*} \approx \frac{\frac{(1/V)'}{(1/V)}[1 + 9 A^{-2} g^* R^{*0.07}] + \frac{(1/V)''}{(1/V)'} [3 A^2 g^* R^{*0.07}]}{0.16 \ f^* A^3} \tag{24}$$

With Figure 2 and Eq. (24), an entire compressible boundary layer can be hand computed in about twenty minutes, or the procedure can be computerized by stuffing Figure 2 into the computer memory, as was recently done by two of our colleagues. If (λ/λ_{max}) is less than 0.4 or if R^* is negative (favorable gradient), Eq. (24) is unnecessary and one proceeds with the following "small pressure gradient" approximation:

$$\frac{d\lambda}{dx^*} \approx \frac{1}{8} R_L V \exp(-0.48 \lambda/A) - 5.5 V'/V \tag{25}$$

All of the computations for impermeable walls in the next section were performed using this hand computation method. Tabulated values of f^* and g^* are given in reference 33. One interesting note: for supersonic flow, A is typically greater than one (Fig. 2-a), which tends to reduce both the "pressure gradient" and the "relaxation" terms in the numerator of Eq. (24). Thus a supersonic boundary layer is resistant to strong adverse pressure gradients. In other words, it will probably not be necessary to hold a "compressible" version of the 1968 Stanford Conference (1).

5. COMPARISON OF THEORY AND EXPERIMENT

There are several experiments which consider two or more of the eight parameters listed at

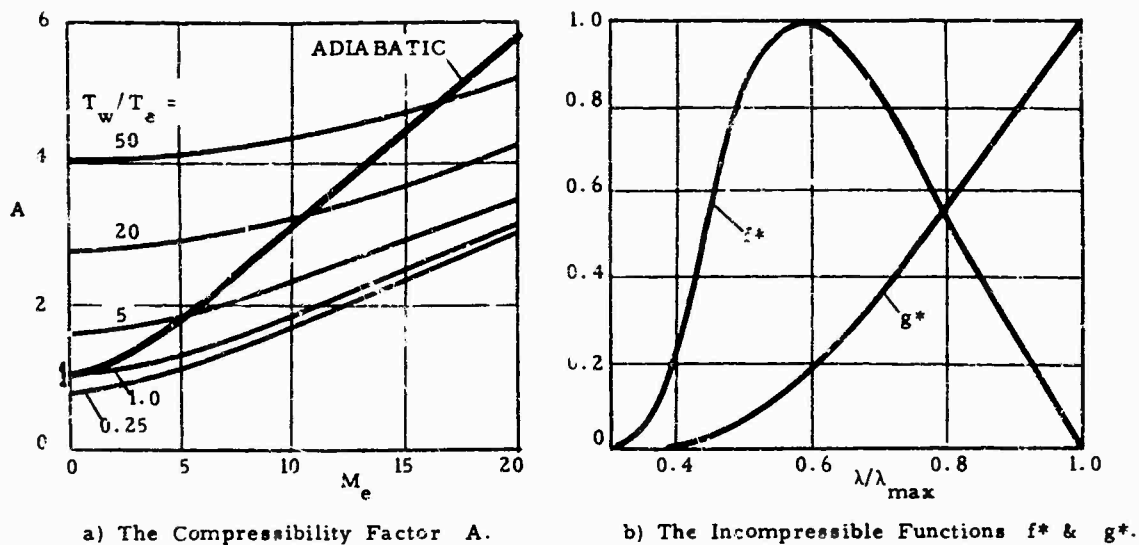a) The Compressibility Factor A.   b) The Incompressible Functions f* & g*.

Figure 2. FUNCTIONS NEEDED FOR THE GRAPHICAL ANALYSIS, EQ.(24).

the beginning of Section 2. Let us consider some of these in a brief resume'.

5. Compressible Flow past an Impermeable Flat Plate

For this, the most heavily analyzed problem in the literature, $\alpha = 0$ and, if the wall is isothermal, β and γ depend only upon A, which is constant. Equation (19) reduces to:

$$G \frac{d\lambda}{dx^*} = R_L , \quad \text{or:} \quad R_x = U_e x / \nu_e = \frac{\mu_e}{\mu_w} \sqrt{\frac{T_e}{T_w}} \int_0^\lambda G \, d\lambda , \tag{26}$$

where, in the limit as $\alpha = 0$, $\quad G = 8.0 \exp(0.48 \lambda / A)$. $\tag{27}$

Combining Eqs.(26) and (27) and integrating, we obtain:

$$C_f(\text{flat plate}) \approx 0.455 / \{A^2 \ell n^2 [0.06 R_x (\mu_e/\mu_w)(T_e/T_w)^{\frac{1}{2}} / A] \} , \tag{28}$$

which is an accurate formula over the entire range of flat plate Mach numbers, wall temperatures, and turbulent Reynolds numbers. It also demonstrates (once again) the existence of a flat plate compressibility transformation. As expressed in the generic notation of Spalding and Chi(5), we have:

$$C_{f_{comp}} = \frac{1}{F_c} C_{f_{incomp}} (R_x F_{R_x}) , \quad \text{where we propose: } F_c = A^2 \text{ and } F_{R_x} = \frac{1}{A} \frac{\mu_e}{\mu_w} (T_e/T_w)^{\frac{1}{2}}. \tag{29}$$

The particular F_c and F_{R_x} in Eq.(29) differ significantly from other theories in the literature. Table 1 compares Eq.(29) with five other theories, selected because they are either very popular or very accurate or both. The 427 adiabatic and 230 heat transfer points constitute the most extensive

Table 1. COMPRESSIBLE FLAT PLATE SKIN FRICTION BY SIX THEORIES

METHOD:	ADIABATIC: 427 Points		HEAT FLUX: 230 Points	
	RMS Error	ABS. Error	RMS Error	ABS. Error
Eckert (7)	12.44 %	9.06 %	29.45 %	25.56 %
Moore (36)	8.87	6.54	17.69	13.08
Sommer & Short (4)	9.40	7.77	23.55	20.14
Spalding and Chi (5)	7.59	5.46	21.13	16.94
Van Driest II (6)	7.55	5.46	17.49	13.81
Equation (29)	7.80	5.26	14.31	11.28

list of flat plate data ever compiled, most of which is tabulated in ref. 34, but some of which is new since that date, e.g. refs. 25 and 35. We have computed both the RMS and mean absolute error:

$$\text{RMS Error} = [\frac{1}{N} \sum_1^N e_i^2]^{\frac{1}{2}} ; \quad \text{Mean Absolute Error} = \frac{1}{N} \sum_1^N | e_i | . \tag{30}$$

We prefer the latter criterion, for reasons which may be evident from Table 1. We feel that the RMS error has a tendency to accentuate bad data points. It would appear that the present theory is the most accurate of all flat plate analyses in existence. It is also the only one of the six

theories in Table 1 which is readily applicable to pressure gradient effects.

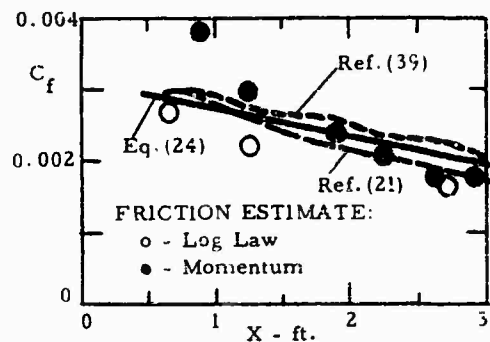### 5.2 Incompressible Nontranspired Flow with Pressure Gradient

For this case, Eq. (19) reduces to the method of ref. 23. This single parameter, pressure gradient, was the subject of the 1968 Stanford Conference (1), in which we did not compete. It seems that our method has since been applied to the Stanford data. According to a letter received from a professor at another university, the sixteen students in his class, as a homework problem, each applied Eq. (24) to one of the sixteen "mandatory" Stanford flows. The reader may join us in speculating as to whether Eq. (24) fell into the upper, middle, or lower third. It is also interesting to speculate as to what alternate method could have been assigned as a homework problem.

5.3 Compressible Nontranspired Flow with Favorable Gradient

Equation (25) is valid for this case and was applied to two relatively strong favorable gradient experiments by Brott et al (37), for Mach 3.7 to Mach 5, and by Pasiuk et al (38), for Mach 1.7 to Mach 3 acceleration. The results are shown in Figure 3. The Brott flow was for a cold wall, $T_w \approx 0.82\, T_{aw}$, while the Pasiuk flow was approximately adiabatic walls. Pasiuk did not measure skin friction, which has been estimated by overlap (21) and by momentum (39) considerations. The theory is in good agreement, as are the finite difference computations of refs. (21) and (39) for Pasiuk's flow. Favorable gradients are really not a very stern test for a computation method.
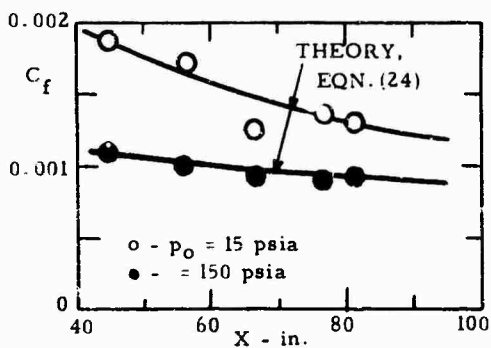
a) The Experiment of Brott et al (39). b) The Experiment of Pasiuk et al (38).

Figure 3. COMPARISON OF THEORY AND EXPERIMENT FOR SUPERSONIC NONTRANSPIRED FLOW WITH FAVORABLE PRESSURE GRADIENT.

5.4 Supersonic Adverse Gradient with Longitudinal Curvature

The experiment of Sturek and Danberg (26) generated an adverse pressure gradient by compression along a curved ramp. The average ratio (R/δ) was about forty, which means, according to ref. 21, that curvature should have a strong effect on turbulence structure. But, as seen in Fig. 4, the wall law appears insensitive to curvature, and Eq. (24) is in good agreement with the measured skin friction, especially since it was necessary to estimate $(1/V)'$ and $(1/V)''$ from sketchy velocity data. To our knowledge, no other theory has yet been applied to this experiment.
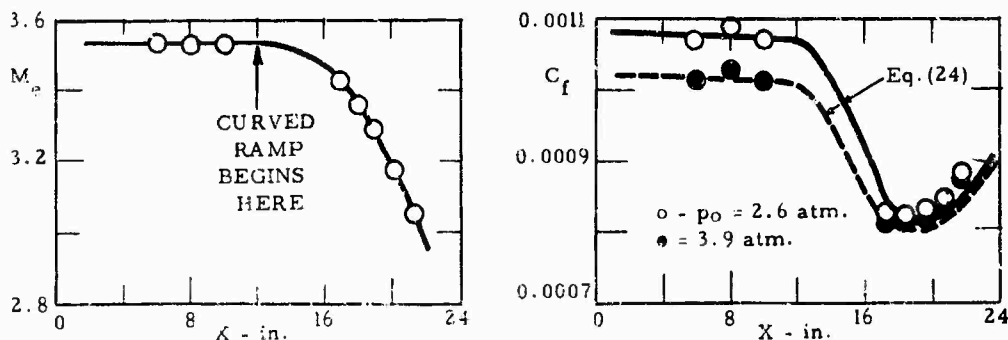
Figure 4. THE ADVERSE PRESSURE GRADIENT EXPERIMENT OF STUREK AND DANBERG(26).

5.5 Supersonic "Relaxing" Flows with Impermeable Walls

The discrepancy in the theory for "relaxing" flows, where the pressure gradient is suddenly removed, was noted in ref. 33 and tends to vanish at supersonic speeds. Figure 5 compares the theory with the flow of Winter et al (40), which decelerates from Mach 3.3 to 2.5, and for the flow of Zwarts (unpublished, reported in ref. 21), which decelerates from Mach 4 to Mach 3. Equation (24) is in good agreement with both experiments, perhaps too good to be realistic. The Winter experiment (40)

a) The Experiment of Winter et al (40).($M_\infty = 2.8$)

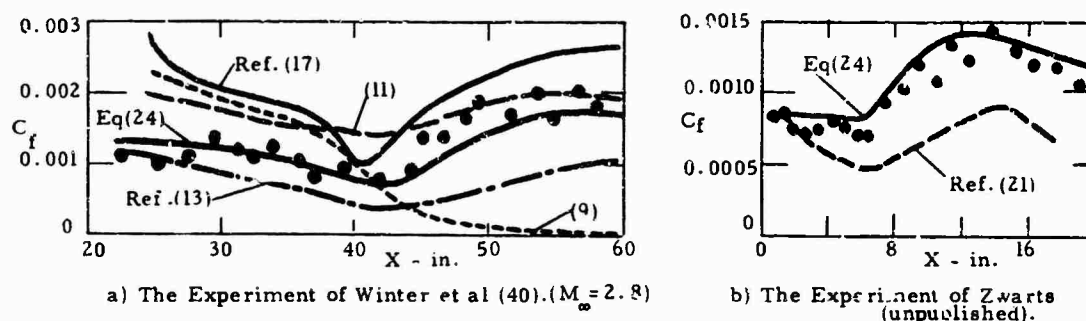b) The Experiment of Zwarts (unpublished).

Figure 5. THEORY AND EXPERIMENT FOR RELAXING SUPERSONIC BOUNDARY LAYERS.

is rather controversial, being complicated by both transverse and longitudinal curvature and possibly by relaminarization also. Transverse curvature only slightly influences C_f for Winter's flow but has a strong effect on momentum thickness and shape factor - but this is of no concern to our method. The finite difference theory of Bradshaw and Ferriss (21), for which we have a very high regard, shows an unexplained discrepancy for the flow of Zwarts (Figure 5-b).

5.6 Flat Plate Flow with Uniform Wall Transpiration

For a flat plate with constant v_w, U_e, and T_w, $\alpha = 0$ and Eq.(19) reduces to a quadrature:

$$R_x = \int_0^\lambda \{\frac{G - F\lambda(v_w/U_e)(T_w/T_e)^{\frac{1}{2}}}{1 + \lambda^2(v_w/U_e)}\} d\lambda \tag{31}$$

By curve-fitting G and F, we were able to obtain a closed form expression for the skin friction, which is usually expressed as a ratio of transpired to nontranspired flow:

$$C_i = (h/A)^2 C_{f_o}[\frac{h^{1.8}}{A} \frac{\mu_e}{\mu_w} (T_e/T_w)^{\frac{1}{2}} R_x] , \text{ where } h = \frac{2}{B}[(1 + B)^{\frac{1}{2}} - 1]. \tag{32}$$

This is an extension of Eq.(29) for nontranspired flow and is valid for either blowing ($h < 1$, $B > 0$) or suction ($h > 1$, $-1 < B < 0$). For incompressible flow, if we assume smooth wall flow and a one-seventh power law for the skin friction, we obtain the following simple approximations:

INCOMPRESSIBLE PLATE FLOW:

$$\frac{C_f}{C_{f_o}}\Big|_{\substack{const \\ R_x}} \approx h^{1.74} \quad ; \quad \frac{C_f}{C_{f_o}}\Big|_{\substack{const \\ R_\theta}} \approx h^{1.33} \tag{33}$$

Equations (33) are in nearly perfect agreement with the recent data of Simpson et al (41) for both suction and blowing and also agree with the interesting recent theory of Weber (15). Equation (32) predicts only a slight compressibility effect, with (C_f/C_{f_o}) increasingly slowly with Mach number; this is in rough agreement with experiment and with ref. 15 but quite contrary to the conclusion of Jeromin (3).

5.7 Flat Plate Flow with Varying and Discontinuous Wall Blowing

For incompressible flat plate flow with variable $v_w(x)$, Eq.(19) reduces to:

$$(G - F\lambda v_w/U_e)\frac{d\lambda}{dx^*} = R_L(1 + \lambda^2 v_w/U_e) + F\lambda^2\frac{d}{dx^*}(v_w/U_e) , \tag{34}$$

which may easily be solved by hand or otherwise for variable or even discontinuous changes in v_w.

a) For Continuously Variable Blowing (41).
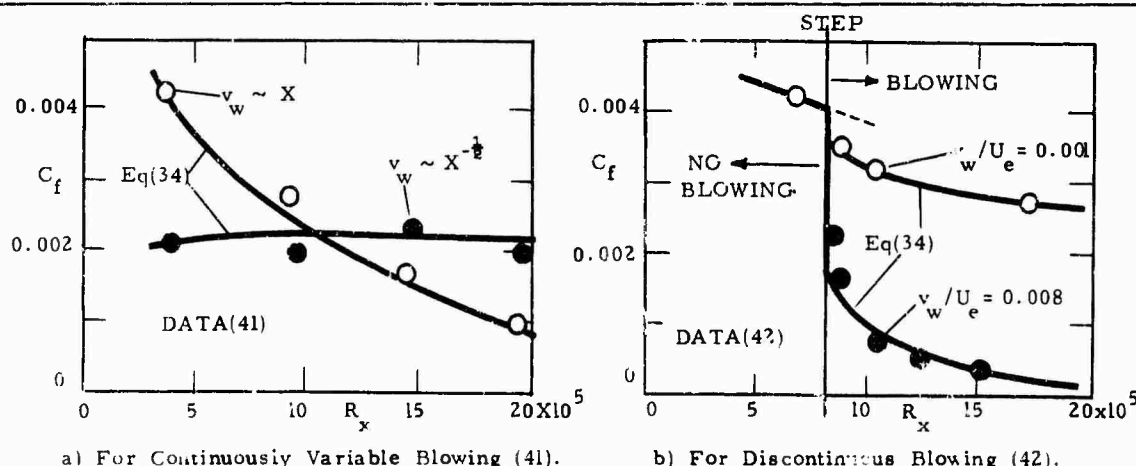
b) For Discontinuous Blowing (42).

Figure 6. COMPARISON OF EQ(34) FOR VARIABLE AND DISCONTINUOUS WALL BLOWING.

Figure 6 shows the comparison of Eq.(34) with experimental data for both variable blowing (41) and discontinuous blowing (42). The agreement is good in all cases. Note that the theory predicts a discontinuous change in C_f (or λ) in Fig. 6-b, which is approximated by the sharp drop in the data.

5.8 Other Cases: Transverse Curvature, Polymer Additives, and Roughness

Space does not permit an extensive discussion of other parametric cases. The solution of Eq(19) for the transverse curvature effect on a long cylinder (using Eq.11-c) is given in ref. 28, and the analysis for flat plate flow of a polymer solution (using Eq.11-b) is given in ref. 43. Finally, we give here, without proof, the solution of Eqs.(19) and (11-a) for incompressible flat plate flow with uniform sand-grain roughness:

$$R_x(\text{rough plate}) = 1.73125 (1 + 0.3 \epsilon^+) e^{\kappa\lambda}[\kappa^2\lambda^2 - 4\kappa\lambda + 6 - \frac{0.3\epsilon^+}{1+0.3\epsilon^+}(\kappa\lambda-1)], \text{ where } \epsilon^+ = \frac{R_x}{\lambda}\frac{\epsilon}{x}. \quad (35)$$

This formula, which is not a curve-fit but rather a closed form solution of the present theory, is valid for smooth wall, intermediate, or fully rough flows past a flat plate. We have not yet made the calculation for compressible rough-plate flow, but an interesting Karman-type analysis of compressible rough-wall flows was recently presented by Chen (44).

CONCLUSIONS

It has been shown that a single, rather crude assumption - that the law-of-the-wall (eq.3) is valid across the entire boundary layer - leads to a simple differential equation (Eq19) for the compressible turbulent boundary layer which predicts remarkably accurate skin friction values for a wide variety of parametric freestream and wall conditions. With further extension and improvement, it is postulated that this method may someday supplant the classic Karman integral approach.

REFERENCES

1. S.J. Kline et al, Proc. 1968 Stanford Turbulent Boundary Layer Conference, 2 Vols., 1968.
2. I. E. Beckwith, NASA SP-228, October 1969, pp 355-416.
3. L. O. F. Jeromin, Progress in Aeronautical Sciences, Vol. 10, 1970, pp 65-189.
4. S. C. Sommer & B. J. Short, NACA Technical Note No. 3391, 1955.
5. D. B. Spalding & S. W. Chi, Jour. Fluid Mechanics, Vol. 18, part 1, 1964, pp 117-143.
6. E.R. van Driest, Aeronautical Engineering Review, Vol. 15, No. 10, October 1956, pp 26-41.
7. E. R.G. Eckert, Jour. Aero. Sciences, Vol. 22, 1955, pp 585-587.
8. D. B. Spalding, D.M. Auslander, & T.R. Sundaram, Supersonic Flow, Chemical Processes and Radiative Transfer, Pergamon Press, 1964, pp 211-276.
9. E. Reshotko & M. Tucker, NACA Technical Note No. 4154, 1957.
10. P. K. Sasman & R. J. Cresci, AIAA Journal, Vol. 4, No. 1, January 1966, pp 19-25.
11. I. E. Alber & D. E. Coats, A.I.A.A. Paper Number 69-689, 1969.
12. B.G.J. Thompson, Aeronautical Research Council, London, RM-3622, 1970.
13. J.E. Lewis, T. Kubota, & W.H. Webb, AIAA Journal, Vol. 8, No. 9, Sept. 1970, pp 1644-1651.
14. C. Economos, A.I.A.A. Journal, Vol. 8, No. 4, 1970, pp 758-764.
15. H. E. Weber, A.S.M.E. Paper Number 71-FE-1, May 1971.
16. S. V. Patankar & D. B. Spalding, Heat & Mass Transfer in Boundary Layers, London, 1967.
17. J. H. Herring & G.L. Mellor, NASA CR-1144, Sept. 1968 (see also reference 27).
18. D. M. Bushnell & I. E. Beckwith, AIAA Journal, Vol. 8, No. 8, August 1970, pp 1462-1469.
19. T. Cebeci & A.M.O. Smith, A.S.M. E. Paper No. 70-FE-A, 1970.
20. R. H. Pletcher, A.I.A.A. Paper Number 71-165, January 1971.
21. P. Bradshaw & D. H. Ferriss, Jour. Fluid Mechanics, Vol. 46, part 1, 1971, pp 83-110.
22. H. McDonald, N.A.S.A. SP-216, 1968, pp 181-230.
23. W. D. McNally, N.A.S.A. Technical Note D-5681, May 1970.
24. W. H. Dorrance, Viscous Hypersonic Flow, McGraw-Hill Book Company, 1962.
25. J.H. Kemp & F.K. Owen, AIAA Paper Number 71-161, January 1971.
26. W. B. Sturek & J.E. Danberg, AIAA Paper Number 71-162, January 1971.
27. M.H. Bertram, "Symposium on Compressible Turbulent Boundary Layers", NASA SP-216, 1968.
28. F. M. White, A.S.M.E. Paper Number 71-FE-25, May 1971.
29. R. L. Simpson, Jour. Fluid Mechanics, Vol. 42, part 4, 1970, pp 769-802.
30. T.N. Stevenson, College of Aeronautics, Cranfield, England, Aero. Rept. No. 166, 1963.
31. W. A. Meyer, A.I.Ch.E. Journal, Vol. 12, No. 3, May 1966, p 522.
32. G.N. Rao, Journal of Applied Mechanics, Vol. 34, March 1967, pp 237-238.
33. F.M. White, Jour. of Basic Engineering, September 1969, pp 371-378.
34. F.M. White & G.H. Christoph, Air Force Flight Dynamics Lab. Rept. AFFDL-TR-70-133, 1970.
35. E.J. Hopkins & E. R. Keener, AIAA Paper Number 71-167, January 1971.
36. D.L. Moore, Defense Research Lab., Univ. of Texas, Report DRL-480, CM-1014, 1962.
37. D. L. Brott et al, AIAA Paper No. 69-685, June 1969 (see also NOLTR 69-143, Aug. 1969).
38. L. Pasiuk, S. M. Hastings, & R Chatham, Naval Ordnance Laboratory, Report NOLTR-64-200,1965.
39. T. Cebeci, A. M.O. Smith, & G. Mosinskis, AIAA Journal, Nov. 1970, pp 1974-1982.
40. K. G. Winter, K. G. Smith, & J.C. Rotta, AGARDograph #97, Part II, 1965, pp 933-962.
41. R. L. Simpson, R.J. Moffat, & W.M.Kays, Intl. J. Heat Mass Tr., Vol. 12, 1969, pp 771-789.
42. R. L. Simpson, "The Effect of a Discontinuity in Wall Blowing on the Turbulent Incompressible Boundary Layer", to appear in Intl. Jour. Heat Mass Transfer, 1971.
43. F. M. White, Jour. Hydronautics, Vol. 2, No. 4, Oct. 1968, pp 181-186.
44. K. K. Chen, A.I.A.A. Paper Number 71-166, January 1971.
45. R. L. Simpson, D.G. Whitten, & R.J. Moffat, Intl. J. Heat Mass Tr., Vol.13, 1970, pp 125-143.

AN EDDY VISCOSITY BASED ON THE SECOND PRINCIPAL
INVARIANT OF THE DEFORMATION TENSOR

Willi Schönauer

Rechenzentrum der Universität Karlsruhe

SUMMARY

The aim of this paper is to derive equations for the time mean values of incompressible turbulent flow. The stress tensor is considered to be a function of the deformation tensor. The assumption of spatial homogenity and isotropy leads to an eddy viscosity depending on the second principal invariant of the deformation tensor. The eddy viscosity function contains empirical coefficients which must be determined from measurements of turbulent equilibrium flows. Nonequilibrium flows then are described by relaxation equations. For internal fluid mechanics the empirical coefficients of the viscosity function are determined from measurements of equilibrium pipe flow. Equations for the turbulent boundary layer are derived. Similar solutions of these equations define equilibrium boundary layer flows. The empirical coefficients of the eddy viscosity function are determined for a flat plate flow.

1. INTRODUCTION

The laminar motion of a fluid is a macro motion which is superposed by the micro motion of the molecules. The transport of momentum by the micro motion results in the laminar viscosity of the fluid. When the mean free path of the molecules is small in comparison to the dimensions of the flow problem, the laminar viscosity is a function of the fluid and it is independent of the boundary conditions of the flow problem. The micro motion is described by the Boltzmann equation. The laminar viscosity and the equations for laminar flow can be derived from this equation in those cases, where an approximate solution is possible. When such a solution is not possible, for example in the case of a liquid, the equations for laminar flow may only be derived by phenomenological methods and the viscosity must be taken from measurements.

Similarly the time mean values of incompressible turbulent flow are considered to be a macro motion which is superposed by the unsteady turbulent oscillations about these mean values. The oscillations are described by the unsteady Navier-Stokes equations and we may write down the equations for the mean values in terms of the oscillations and thus may define a turbulent or eddy viscosity. But the solution of the Navier-Stokes equations being not possible until nowadays, this is useless for practical application. Most calculations of turbulent flow are based on Prandtl's mixing length concept, which is between an exact theory of the micro motion and a phenomenological approach. In this paper we try to develop a phenomenological theory of the turbulent motion. Consequently the eddy viscosity must be determined by measurements.

2. THE EDDY VISCOSITY FUNCTION

We postulate the conservation of mass and momentum for the time mean values of the flow. The balance of mass yields the continuity equation

(2.1) $$\nabla^T \mathcal{W} = 0.$$

We use a matrix notation and consider vectors as one column matrices or transposed as one row matrices. The velocity vector for the time mean value is

$$\mathcal{v} = \begin{vmatrix} u \\ v \\ w \end{vmatrix} ; \qquad \mathcal{v}^T = (u,v,w) \ .$$

The nabla operator is

$$\nabla = \begin{vmatrix} \partial/\partial x \\ \partial/\partial y \\ \partial/\partial z \end{vmatrix} ; \qquad \nabla^T = (\partial/\partial x, \partial/\partial y, \partial/\partial z) \ .$$

The result of (2.1) is a scalar. Therefore transposition of (2.1) yields $\mathcal{v}^T \nabla = 0$, thus showing that in this notation the elements of ∇ are directly applied to the elements to which they are connected by the ordinary multiplication.

The balance of momentum yields the momentum equation (all quantities are time mean values):

(2.2) $$\rho \mathcal{v}_t + \rho (\mathcal{v}\nabla^T)\mathcal{v} - T\nabla = 0 \ ,$$

with the density ρ and the stress tensor

(2.3) $$T = \begin{vmatrix} -p+\tau_{xx} & \tau_{yx} & \tau_{zx} \\ \tau_{xy} & -p+\tau_{yy} & \tau_{zy} \\ \tau_{xz} & \tau_{yz} & -p+\tau_{zz} \end{vmatrix} \ .$$

The static pressure is p and τ_{xy} is a stress acting in the y-direction on a surface with normal in x-direction. The problem is now to find a constitutive equation relating T to $\mathcal{v}$, that is a stress strain relation. The relative change per unit time of the length of an infinitesimal fluid element is described by the deformation tensor

(2.4) $$D = \begin{vmatrix} u_x & \frac{1}{2}(u_y+v_x) & \frac{1}{2}(u_z+w_x) \\ \frac{1}{2}(v_x+u_y) & v_y & \frac{1}{2}(v_z+w_y) \\ \frac{1}{2}(w_x+u_z) & \frac{1}{2}(w_y+v_z) & w_z \end{vmatrix} \ .$$

It is assumed that the change of length is responsible for the stress in the fluid. Stokes used a linear relation

(2.5) $$T = -pE + \beta D \ ,$$

with $\beta=2\eta$, η=dynamic viscosity, E=unit matrix.
This relation is accepted as constitutive equation for the laminar motion of a newtonian fluid. Therefore(2.5) cannot describe the behaviour of a turbulent motion.

We desire a momentum equation which is independent of the location of the origin and of the orientation of the coordinate system. Therefore we postulate spatial homogenity and isotropy of the fluid. This is expressed by the relation (2.5), but SERRIN [12] shows, that β need not be constant. It may be a function of the principal invariants of the deformation tensor. These are the coefficients h_i of the characteristic equation for D.

$$\det(\lambda E - D) = \lambda^3 - h_1 \lambda^2 - h_2 \lambda - h_3 = 0.$$

The calculation yields $h_1 = 0$ because of (2.1). The first (and simplest) nonvanishing principal invariant is h_2. For simple writing we use the expression

$$(2.6) \qquad h = 4h_2 = 2(u_x^2 + v_y^2 + w_z^2) + (u_y + v_x)^2 + (u_z + w_x)^2 + (v_z + w_y)^2 .$$

The main idea of this paper is to use the constitutive equation

$$(2.7) \qquad T = -pE + \beta(h)D .$$

This stress strain relation is not linear.

The general theory cannot give further information about the function $\beta(h)$. We assume a turbulent shear layer along a fixed wall. Then in the immediate vicinity of the wall the velocity goes to zero and the turbulent oscillations, which cause the additional viscosity go to zero, too. Therefore at the wall β must be equal to the laminar value 2η. In the center of a tube with circular cross section for axisymmetric turbulent flow vanishes h, but nevertheless there is additional turbulent viscosity. These "boundary conditions" for $\beta(h)$ led to the relation

$$(2.8) \qquad \beta(h) = 2\eta^* = 2\eta + 2\rho(w^2)^q (c_0 + c_1 h^s) ,$$

thus defining an eddy viscosity η^*. The equations (2.2),(2.4),(2.7),(2.8) then lead to momentum equations which we call generalized Navier-Stokes equations for the time mean values of a turbulent flow.

The four coefficients q, s, c_0, c_1 must be determined by measurements. They are the result of the oscillations and therefore an expression for a solution of the laminar Navier-Stokes equations. Such a solution will depend on the Reynolds number and on the boundary conditions of the flow problem. Therefore the four coefficients will depend on these parameters too. If the reference Reynolds number is properly defined, we may expect that the coefficients are the same for flows with similar boundary conditions. For the derivation of (2.7) the fluid was assumed to be isotropic. The turbulent flow in its micro structure is surely not isotropic. This micro structure could only be described by a matrix $\beta(h)$. Taking $\beta(h)$ as a skalar function, we take the mean value of the eddy viscosity matrix. The formation of the mean value is effected by the determination of the coefficients from measurements. The measurements must be done for equilibrium flows, that is for flows with a "constant" turbulence structure. Nonequilibrium flows then will be described by relaxation equations for the coefficients by means of a measured relaxation time.

3. INTERNAL FLUID MECHANICS

The simplest flow which may be used for the determination of the coefficients is the axisymmetric flow in a tube with circular cross section. From the generalized Navier-Stokes equations, putting $u = u(y,z)$, $v \equiv w \equiv 0$, follows $p_y = p_z = 0$. We transform the resulting equation to cylindrical coordinates $(x,y,z) \longrightarrow (x,r)$. With reference values for length L, velocity U and kinematic viscosity ν the following dimensionless quantities are defined

$$\bar{x} = \frac{x}{L} \; ; \quad \bar{r} = \frac{r}{L} \; ; \quad \bar{p} = \frac{p}{\rho U^2} \; ; \quad \bar{u} = \frac{u}{U} \; ;$$

(3.1)

$$\bar{c}_0 = \frac{c_0 U^{2q}}{\nu} \; ; \quad \bar{c}_1 = \frac{c_1 U^{2q+2s}}{\nu L^{2s}} \; ; \quad Re = \frac{UL}{\nu} \; .$$

Then from (2.8) we get with $\bar{u} = \bar{u}(\bar{r})$

(3.2) $$\frac{\nu^*}{\nu} = 1 + \bar{u}^{2q}(\bar{c}_0 + \bar{c}_1 \bar{u}_{\bar{r}}^{2s}) \; .$$

Comparing (3.2) with Prandtl's mixing length theory, see SCHLICHTING [6] page 539, we find (3.2) to be a generalisation of the mixing length concept. But (3.2) is the special case of a three dimensional theory and we may expect that the coefficients taken from one dimensional experiments may be generalized to two or three dimensional flows.

The differential equation for the flow in the tube is

(3.3) $$Re \, \bar{p}_{\bar{x}} = \left[1 + \bar{u}^{2q}(\bar{c}_0 + \bar{c}_1 \bar{u}_{\bar{r}}^{2s}) \right] (\bar{u}_{\bar{r}\bar{r}} + \frac{1}{\bar{r}} \bar{u}_{\bar{r}}) +$$

$$+ 2q\bar{u}^{2q-1} \bar{u}_{\bar{r}}^2 (\bar{c}_0 + \bar{c}_1 \bar{u}_{\bar{r}}^{2s}) + 2s\bar{c}_1 \bar{u}^{2q} \bar{u}_{\bar{r}}^{2s} \bar{u}_{\bar{r}\bar{r}} \; .$$

Taking $L=d=$diameter of the tube and $U=u(0)$ the velocity in the center of the tube, the boundary conditions are

(3.4) $$\bar{u}(0.5) = 0 \; ; \quad \bar{u}(0) = 1 \; ; \quad \bar{u}_{\bar{r}}(0) = 0 \; .$$

The equations (3.3),(3.4) form a boundary value problem for $\bar{u}(\bar{r})$ and $\bar{p}_{\bar{x}}$.

The determination of the coefficients $q, s, \bar{c}_0, \bar{c}_1$ in (3.2) was done by comparing solutions of (3.3),(3.4) with measurements. The coefficients are altered until the numerical solution agrees with the measured values. Details are given in [7], [8]. The boundary conditions (3.4) beeing the same for all flows, the coefficients are functions of the Reynolds number alone. In accordance with this conclusion, in (3.3) Re is the only parameter. From measurements of NIKURADSE [4] followed, that s is a constant and $q, \bar{c}_0, \bar{c}_1$ depend linearly on Re in double logarithmic scale. The values then have been determined from measurements of LAUFER [3], which seem to be more accurate than the values of NIKURADSE. In the range of $0.5 \stackrel{<}{=} s \stackrel{<}{=} 3$ all values of s could be chosen. But once s is fixed, the other coefficients are depending on the value of s. For $s=1$ the following values were determined which may be linearly interpolated for other values of Re in double logarithmic scale:

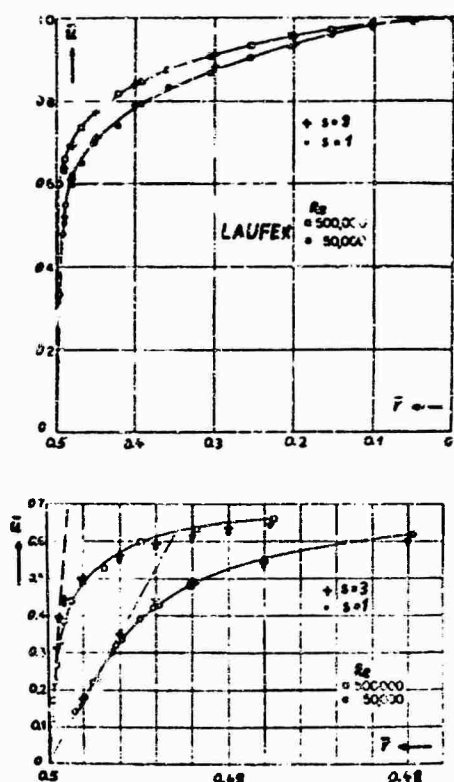|	Re	q	$\bar{c}_0$	$\bar{c}_1$
(3.5)	$5 \cdot 10^4$	7.8	1.8	1160
	$5 \cdot 10^5$	10.3	78.3	15500

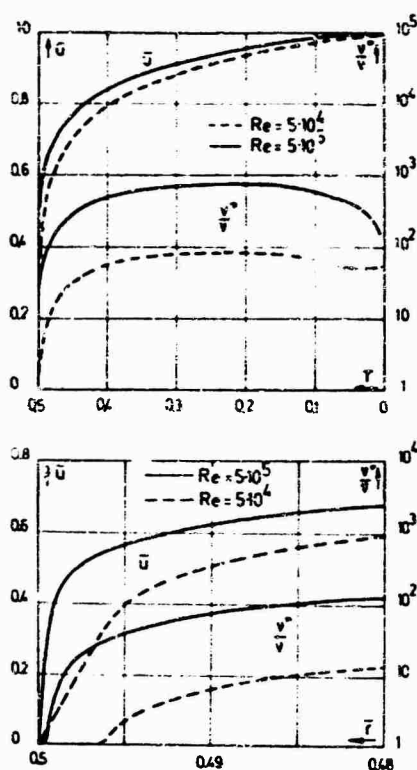Fig.1. Measured values from LAUFER [3]
and computed values for s=1 and 3.

Fig.2. Computed velocity and eddy
viscosity profiles for s=1.

Fig. 1 shows the comparison of LAUFER's measurements with the computed values for
s=1, corresponding to the coefficients (3.5); further computed values for s=3 are shown.
In fig. 2 the computed velocity profiles for s=1 are shown together with the
corresponding ratio of turbulent to laminar viscosity, equation (3.2). The dotted
line for v^*/v in the lower fig. 2 clearly shows, that in the laminar sublayer the
computed value of v^* is equal to v.

If we want to use the coefficients determined from (3.5) for internal fluid dynamic
problems other than circular cross section but constant reference Reynolds number, we
may expect to get the same values, if the Reynolds number is based on the hydraulic
diameter. This is the ratio of the wetted surface (in which the turbulence is initiated
by the steep wallgradients) and the flow volume (in which the turbulent energy is
dissipated). If the reference Reynolds number changes, for example if the diameter in
a tube increases or decreases, the coefficients will not abruptly follow the change
in the turbulence structure (this is the reason for the initiaton length of pipe flow).
This is a relaxation process which may be described by relaxation equations for the
coefficients. With a dimensionless relaxation time $\bar{\tau}$ (determined from measurements as
a function of Re) for example the behaviour of $\bar{c}_1$ would follow the equation

(3.6)
$$\frac{d\bar{c}_1}{dt} = \frac{\bar{c}_{1\ equil} - \bar{c}_1}{\bar{\tau}} ,$$

with $\bar{c}_{1\ equil}$ as given function of Re and with $\bar{c}_1$ as actual value; d/dt is the total
derivative along the streamline where the maximum velocity occurs, which is used as
reference velocity. By such a relaxation equation the whole history of the turbulent
flow is described in a natural way. Some basic remarks for the treatment of com-
pressible turbulent motion are given in [8].

4. THE TURBULENT BOUNDARY LAYER

From the two dimensional generalized Navier-Stokes equations we may try to derive equations for the turbulent boundary layer. The laminar boundary layer transformation $\bar{y} = y\sqrt{Re}$, with Re=UL/ν (fixed reference vaulues U,L,ν) yields equations for the laminar sublayer only. Boundary layer equations which are valid in the laminar and turbulent part of the boundary layer, result by a transformation which depends on the coefficient s und which is given below. Using the experience of former papers [9], [10], instead of (2.8) a generalized relation for the eddy viscosity with dimensionless coefficients $\hat{c}_o,\hat{c}_1$ is used

$$(4.1) \qquad \frac{\nu^*}{\nu} = 1 + F(\frac{\upsilon}{\upsilon_a}) \left[\hat{c}_c + \hat{c}_1 \left(\frac{hL^2\kappa^2}{\upsilon_a^2}\right)^s \right] .$$

The functions υ_a, δ depend on x/L; h is the two dimensional form of (2.6) and F is a function of the variable υ/υ_a, with υ_a as the velocity at the outer edge of the boundary layer. F must obey the conditions F→0 for υ→0 and F→1 for υ→υ_a.

We introduce the following dimensionless quantities

$$\bar{x} = \frac{x}{L} ; \quad \bar{\bar{y}} = \frac{y}{L} Re^{\frac{1}{2(s+1)}} ; \quad \bar{u} = \frac{u}{U} ; \quad \bar{u}_a = \frac{u_a}{U} ;$$

$$(4.2)$$

$$\bar{v} = \frac{v}{U} Re^{\frac{1}{2(s+1)}} ; \quad \bar{v}_a = 0 ; \quad \bar{p} = \frac{p}{\rho U^2}$$

Then for Re→∞ eliminating all terms which are small in comparison to other terms, we deduce from the two dimensional generalized Navier-Stokes equations and the continuity equation the following system of boundary layer equations, with F' as derivative of F to its argument:

$$\bar{u}\bar{u}_{\bar{x}} + \bar{v}\bar{u}_{\bar{y}} = -\bar{p}_{\bar{x}} + \left\{ -\frac{1}{Re^{\frac{s}{s+1}}} + F(\frac{\bar{u}}{\bar{u}_a}) \left[\frac{\hat{c}_o}{Re^{\frac{1}{s+1}}} + \right. \right.$$

$$(4.3a)$$

$$\left. \left. (1+2s) \hat{c}_1 \frac{\delta^{2s}\bar{u}_{\bar{y}}^{2s}}{\bar{u}_a^{2s}} \right] \right\} \bar{u}_{\bar{y}\bar{y}} + F'(\frac{\bar{u}}{\bar{u}_a}) \frac{\bar{u}_{\bar{y}}^2}{\bar{u}_a} \left[\frac{\hat{c}_o}{Re^{\frac{s}{s+1}}} + \hat{c}_1 \frac{\delta^{2s}\bar{u}_{\bar{y}}^{2s}}{\bar{u}_a^{2s}} \right] ;$$

$$(4.3b) \qquad \bar{p}_{\bar{y}} = 0 ;$$

$$(4.3c) \qquad \bar{u}_{\bar{x}} + \bar{v}_{\bar{y}} = 0 .$$

In (4.3a) there are terms with Re in the denominator. These terms cannot be omitted in comparison to the other terms in the curved brackets: at the wall F=0 and the first term describes the laminar sublayer; at the outer edge $\bar{u}_y$=0 and the $\hat{c}_o$-terms describe the turbulent viscosity at the outer edge, which may be larger than the laminar viscosity. The ratio of the laminar sublayer to the turbulent zone is a function of the Reynolds number. Therefore logically Re must appear as parameter in (4.3a).

In order to determine the coefficients in (4.1) from measurements, we must use an equilibrium boundary layer with constant turbulence structure. For example the flat plate boundary layer is growing with $\bar{x}$ and seems to have not a constant structure. There is the same problem in the laminar case. There we get a velocity profile independent of $\bar{x}$ if we apply a similarity transformation: the Falkner-Skan transformation. We apply this transformation to the equations (4.3a,c). With the dimensionless velocity $\bar{u}_a(\bar{x})$ at the outer edge of the boundary layer we define a function $A(\bar{x})$, a boundary layer thickness $\delta(\bar{x})$ and the Pohlhausen or similarity parameter $\lambda(\bar{x})$ by

(4.4)
$$A = \bar{u}_a \delta^2 = 2 \int_0^{\bar{x}} \bar{u}_a(\xi) d\xi / \bar{u}_a(\bar{x}) \; ; \quad \lambda = A\bar{u}_a' / \bar{u}_a = \delta^2 \bar{u}_a' \; .$$

With the following similarity variables

(4.5)
$$Y = \bar{y}/\delta \; ; \quad f(\bar{x},Y) = \bar{u}/\bar{u}_a \; ; \quad g(\bar{x},Y) = \bar{v}\delta$$

and with the condition for inviscid flow at the outside of the boundary layer

(4.6)
$$\bar{u}_a \bar{u}_a' = -\bar{p}_{\bar{x}}$$

we get from (4.3a,c)

(4.7)
$$A f f_{\bar{x}} + \left[(\lambda-1) \, Yf + g \right] f_Y + \lambda(f^2-1) -$$

$$\left\{ \frac{1}{Re^{\frac{s}{s+1}}} + F(f) \left[\frac{\hat{c}_0}{Re^{\frac{s}{s+1}}} + (1+2s) \, \hat{c}_1 f_Y^{2s} \right] \right\} f_{YY} - F'(f) f_Y^2 \left[\frac{\hat{c}_0}{Re^{\frac{s}{s+1}}} + \hat{c}_1 f_Y^{2s} \right] = 0 \; ;$$

(4.8)
$$A f_{\bar{x}} + (\lambda-1) \, Yf_Y + \lambda f + g_Y = 0 \; .$$

Because $\bar{x}$ does not appear explicitly in the transformed equations, in the laminar case this system contains similar solutions, if the only parameter λ is constant. In the turbulent equations additional parameters appear: the constants Re, s and the coefficients $\hat{c}_0, \hat{c}_1$ which may depend on $\bar{x}$. The function $F(f)$ is supposed to be a function of f with coefficients $q_1, q_2, \ldots$ which may depend on $\bar{x}$, too. If all these coefficients are determined as functions of λ, then for λ=constant we get similar solutions as solutions of the system (4.7), (4.8) with $f_{\bar{x}} \equiv 0$. These solutions form a two parameter family with parameters λ and Re. The condition λ=constant implies for the outside velocity the wedge flow. But this flow has no characteristic length and velocity. Therefore we choose as reference length $L=1 \, [cm]$ and as reference velocity $U=u_a(L) \, [cm/sec]$. For nonsimilar solutions L and U are taken on the tangent wedge of the flow contour. With these prescriptions for similar solutions the outside velocity is

(4.9)
$$\bar{u}_{a \, sim} = \bar{x}^{\frac{\lambda}{2-\lambda}} \; .$$

The two parameter family of similar solutions are the boundary layers which we call equilibrium boundary layers. From these flows the coefficients in the eddy viscosity function (4.1) must be determined. This may be done by comparing numerical solutions of the similar boundary layer equations with measurements and changing the coefficients, until computation and measurements agree sufficiently, see [10]. Only for the flat

plate flow, $\lambda=0$, measurements with sufficiently constant value of λ exist. Now the question arises: are these measured flat plate flows similar solutions? For flat plate flow all profiles for f or $\bar{u}$ or u over $y/\sqrt{x}$, measured along a flat plate for the same constant reference Reynolds number, must coincide into one profile.
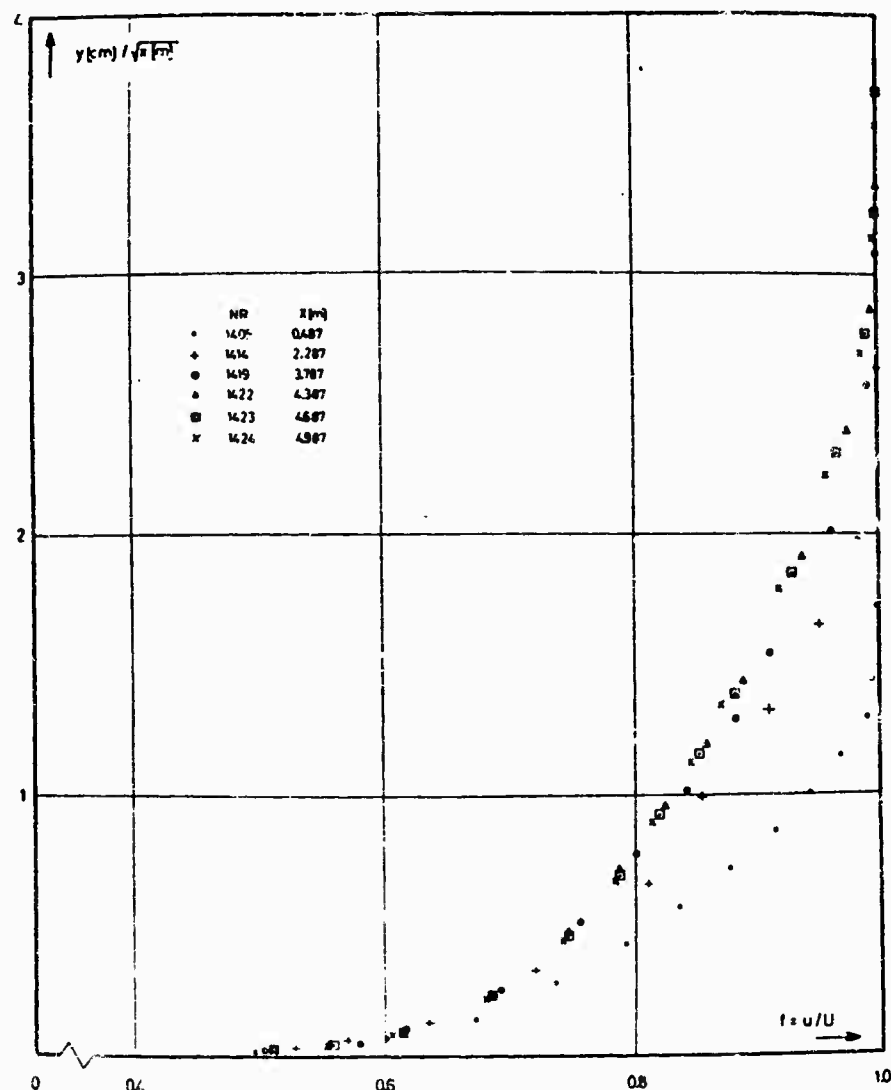

Fig. 3. Velocity profiles measured by WIEGHARDT [1] on a flat plate,
$Re_{1cm} = 2.2 \cdot 10^4$.

In fig. 3 velocity profiles measured by WIEGHARDT [1] on a flat plate show, that the profiles for small values of x do not coincide. For large values of x the profiles nearly coincide and it seems that they tend to a similar profile. The nonsimilar profiles for small values of x may be interpreted as an initiation part of the boundary layer, in which the turbulence structure develops as in the initiation part of a turbulent pipe flow. This part of the measurements could be used to determine a relaxation time.

Measurements of SCHULTZ-GRUNOW [11] show the same behavior as fig. 3. In fig. 4 velocity profiles measured by SMITH and WALKER [13] on a flat plate are shown. Here the profiles coincide only in the wall region. Nevertheless, with the same x-increment, the distance between the velocity profiles dimini   es. In comparison to fig. 3 we may conclude, that these measurements are still in   initiation process and tend to a similar solution profile with increasing value of   These results are not in

contradiction neither with the law of the wall nor with the velocity defect law, see ROTTA [5], fig. 13.3, 13.4. If the velocity profiles approach a similar profile, all profiles u/u_τ over $\log{(yu_\tau/(v\delta))}$, with u_τ as friction velocity and δ from (4.4), will coincide for x large enough at the same values of Re und λ, but they will not coincide for different values of Re and λ.

From measurements of KLEBANOFF [2], which include values in the laminar sublayer, the coefficients of the eddy viscosity relation (4.1) with

$$(4.10) \qquad F(\frac{v}{v_a}) = F(f) = f^{2q} \; ; \quad F'(f) = 2qf^{2q-1}$$

have been determined. In the solutions of (4.7), (4.8) with $f_x \equiv 0$ the coefficients have been altered, until the computed values approached best the measured values, fig. 5.
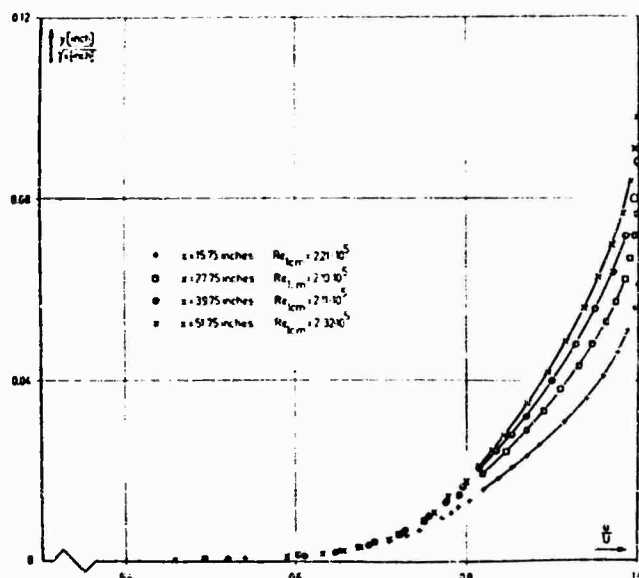
Fig. 4. Measurements of SMITH and WALKER [13], velocity profiles on a flat plate.

In the laminar sublayer, the transition regime and the inner part of the turbulent zone the measured profile is well met by the computed values. But for values $u/U > 0.8$ the agreement is not satisfactory. This part of the boundary layer is characterized by the intermittency. Here the eddy viscosity function (4.1), (4.10) furnishes too large values. Therefore an additional factor in the $\hat{c}_1$-term in (4.1) has been introduced, but the computed profile did not coincide with the measurements, for details see [10]. Now the research is continued with functions F in (4.1) which are composed of two different functions.

The values in fig. 5 have been computed with the following coefficients

$$(4.11) \quad s=1; \quad \hat{c}_0 \; 20; \quad \hat{c}_1 = 10^4; \quad q=10.$$

The value $\hat{c}_0$ has only a week influence on the result. The Reynolds number is $Re_{1cm} = 9.7 \cdot 10^3$. The values s, $\hat{c}_1$, q are the same as the values s, $\bar{c}_1$, q for pipe flow, interpolated from (3.5) for $Re = 3.5 \cdot 10^5$. From this result we may conclude that the turbulence structure of the similar solution for flat plate flow at $Re_{1cm} = 9.7 \cdot 10^3$ corresponds to that of pipe flow at $Re = 3.5 \cdot 10^5$.

Fig. 5. Comparison of computed velocity profile (+) with measurements of KLEBANOFF [2], $Re_{1cm} = 9.7 \cdot 10^3$.

The main problem now is to obtain measurements with an outside velocity (4.9) with sufficiently con-

stant value of λ and sufficiently large x, so that the velocity profiles approach the similar solution profile. Such measurements must be furnished for different values of Re_{1cm}. Then the coefficients for the eddy viscosity function (4.1) form the equilibrium values. Together with a relaxation time and with relaxation equations like (3.6), nonequilibrium boundary layers may be computed from the system (4.7),(4.8).

REFERENCES

1 D.E.COLES, E.A.HIRST, Proceedings Computation of Turbulent Boundary Layers, 1968 AFOSR-IFP-Stanford Conference, Vol II, Compiled Data, series 1400, measurements from WIECHARDT

2 P.S. KLEBANOFF, Characteristics of Turbulence in a Boundary Layer with zero Pressure Gradient, NACA Report 1247 (1955)

3 J.LAUFER, The Structure of Turbulence in Fully Developed Pipe Flow, NACA Report 1174 (1954)

4 J.NIKUPADSE, Gesetzmässigkeit der turbulenten Strömung in glatten Rohren, Forsch.-Arb. Ing.-Wes., Heft 356, 1932

5 J.C.ROTTA, Turbulent Boundary Layers in Incompressible Flow, Progress in Aeronautical Science, vol 2, edited by A.FERRI, D.KÜCHEMANN, L.H.G.STERNE, Pergamon, London 1962

6 H.SCHLICHTING, Grenzschicht-Theorie, Braun, Karlsruhe 1962

7 W.SCHÖNAUER, Die Beschreibung der turbulenten Rohrströmung mit Hilfe einer "turbulenten Zähigkeit", to appear in ZAMM, Sonderheft GAMM-Tagung 1970

8 W.SCHÖNAUER, Die Beschreibung der turbulenten Strömung durch die zeitlichen Mittelwerte, to appear in Ing.Arch.

9 W.SCHÖNAUER, Zur Definition einer Gleichgewichtsgrenzschicht bei turbulenter Strömung, to appear in ZAMM, Sonderheft GAMM-Tagung 1971

10 W.SCHÖNAUER, Numerische Experimente mit einem Ansatz für die turbulente Zähigkeit am Beispiel der Plattengrenzschicht, to appear in conference proceedings on "Laminare und turbulente Grenzschichten", edited by F.W.RIEGELS

11 F.SCHULTZ-GRUNOW, Neues Reibungswiderstandsgesetz für glatte Platten, Luft-fahrtforschung 17, 239-246 (1940)

12 J.SERRIN, Mathematical Principles of Classical Fluid Mechanics, page 125-263, Encyclopedia of Physics, vol VIII/1, Springer, Berlin 1959

13 D.W.SMITH, J.H.WALKER, Skin-Friction Measurements in Incompressible Flow, NASA Technical Report R-26 (1959)

EFFECTS OF STRONG AXIAL PRESSURE GRADIENTS ON TURBULENT BOUNDARY-LAYER FLOWS

by

Clark H. Lewis, Professor, E. W. Miner, Instructor and
E. C. Anderson, Graduate Student
Aerospace Engineering Department
Virginia Polytechnic Institute and State University
Blacksburg, Virginia USA 24060

SUMMARY

The effects of strong axial pressure gradients on nonreacting turbulent boundary-layer flows through nozzles are presented. Both rocket and hypersonic aerodynamic wind-tunnel nozzles are considered. Comparisons are made between present predictions using a finite-difference method and previous integral methods used to predict compressible turbulent flows with pressure gradient and wall heat transfer. Both cooled and heated walls were studied. Comparison with available experimental data on wall heat transfer and skin friction showed good agreement with present predictions. Van Driest and Reichardt's models were considered in a two-layer eddy viscosity model. Small differences in wall-measurable quantities were found between the two models. Under heated wall conditions (i.e. wall temperature greater than the adiabatic wall temperature), strong coupling effects were found between wall heating and axial pressure gradients. For cooled wall conditions, predictions of velocity and temperature profiles downstream of regions of strong favorable pressure gradients were in good agreement with limited experimental profile data. Limitations in the use of boundary-layer transformations for heated-wall flows are presented. This research, a portion of which is presented in this paper, led to the development of a computer program to predict nonreacting and equilibrium chemically reacting laminar and/or turbulent boundary-layer flows for internal (nozzle) and external two-dimensional and axisymmetric flows. A fully documented computer program is available for interested users.

NOTATION

A^+	= damping constant	T	= T^*/T^*_{ref}, nondimensional temperature
a^*	= reference length	T^*_t	= local stagnation temperature, °R
C	= $\rho\nu/(\rho_e\mu_e)$, density-viscosity product ratio	u^*, v^*	= tangential and normal velocity, ft/sec
C_1	= $1 - 1/Pr$, constant for perfect gas	u^*_f	= $(\tau^*_w/\rho^*)^{1/2}$, friction velocity, ft/sec
C_{f_∞}, C_{f_e}	= $2\tau_w/\rho u^2$, skin-friction coefficient based on free-stream and edge conditions	u^*_τ	= $(\tau^*_w/\rho^*_w)^{1/2}$, friction velocity, ft/sec
$\hat{C}_{f_\infty}$	= $C_{f_\infty}/\epsilon_{VD}$	U^*_{ref}	= U^*_∞
		u	= u^*/U^*_{ref}
C_{h_∞}, C_{h_e}	= $q_w/\rho u(H_{aw}-H_w)$, heat-transfer coefficient based on free-stream and edge conditions	V	= transformed normal velocity
		u', v'	= u'^*/u^*_{ref} and $v'^*/(u^*_{ref}\epsilon_{VD})$, nondimensional fluctuating velocity components
c^*_p	= constant pressure specific heat ft^2/(sec^2-R)	
$\bar{r}$	= u/u_e or f', normalized tangential velocity component	v^+_w	= v^*_w/u^*_f
f	= stream function	x,y	= x^*/a^* and $y^*/(\epsilon_{VD} a^*)$, nondimensional distances along and normal to surface
g	= H/H_e, stagnation enthalpy ratio	y^+	= $y^*u^*_f/\nu^*$
H^*	= total enthalpy, ft^2/sec^2	z	= z^*/a^*, nondimensional axial distance
k_1, k_2	= 0.4 and 0.0168, constants in eddy-viscosity expression	β	= pressure gradient parameter
		γ	= ratio of specific heats
L_T	= tube length upstream initial probe, in.	δ, δ^*	= boundary-layer and displacement thicknesses
M	= Mach number	
P^*_{ref}	= $\rho^*_{ref}u^{*2}_{ref}$, reference pressure, lb/ft^2	δ^*_k	= incompressible displacement thickness
P	= P^*/P^*_{ref}, nondimensionalized pressure	$\epsilon^+_i, \epsilon^+_o, \epsilon^+$	= inner, outer and local eddy viscosity, ϵ^*/μ^*
P'_o	= stagnation pressure behind a normal shock	
p^+	= pressure gradient parameter	ϵ^*_k	= eddy thermal conductivity, lb/(sec-°R)
Pr	= $c^*_p \mu^*/K^*$, Prandtl number of mixture	ϵ_{VD}	= $[\nu^*_{ref}/(\rho^*_{ref} u^*_{ref} a^*)]^{1/2}$, Van Dyke parameter
Pr_t	= $c^*_p\epsilon^{+*}/\epsilon^*_k$, turbulent Prandtl number	θ	= momentum thickness
q_w	= $q^*_w/(\rho^*_{ref}u^{*3}_{ref})$	μ^*	= viscosity, lb-sec/ft^2
r^*	= body radius, dimensional	μ^*_{ref}	= $\mu^*(T^*_{ref})$
St_∞, St_e	= $q_w/\rho u(H_o-H_w)$, Stanton number based on free-stream and edge conditions	μ	= μ^*/μ^*_{ref}
T^*_{ref}	= u^{*2}_{ref}/c^*_p, °R, reference temperature	ν	= $\nu^* \rho^*_{ref}/\mu^*_{ref}$, nondimensional kinematic viscosity

ζ, η	= Levy-Lees variables		**Subscripts and Superscripts**		
ρ^*	= density, slugs/ft^3		e, w	= outer edge and wall conditions	
τ	$= \dfrac{\tau^* \epsilon_{VD} a^*}{\mu^*_{ref} u^*_{ref}}$, nondimensional shear stress		ref	= reference condition	
			∞, o	= free-stream and stagnation conditions	
			( )'	= differentiation with respect to η	
ϕ	= energy layer thickness, in.		( )*	= dimensional quantity	

1. INTRODUCTION

The existing literature on numerical solutions of the laminar boundary-layer equations for two-dimensional and axisymmetric flows is extensive. A recent review of the most commonly used techniques for solving the laminar boundary layer equations for nonequilibrium, equilibrium, and chemically non-reacting flows is given by Blottner [1]. Kline et al. [2] presented a similar review of the prediction methods used for the solution of the incompressible turbulent boundary-layer equations. Examples of recent solutions of the nonreacting turbulent boundary-layer equations are the papers by Cebeci [3-5] and Pletcher [6].

The implicit finite-difference scheme of the Crank-Nicholson type has been developed extensively by Blottner [1,7,8] and by Davis [9-11] for a wide range of laminar viscous-layer flows. This method of solution has been demonstrated to be accurate and stable and does not require an excessive amount of computing time. This type of finite-difference scheme was used by Harris [12] to solve the turbulent boundary-layer equations for nonreacting gases. Harris also considered mass transfer at the wall and the laminar-to-turbulent transitional regime. Cebeci et al. [3-5] used an implicit finite-difference scheme to obtain solutions of the turbulent boundary-layer equations. However, the numerical procedure used by Cebeci differed considerably from the Crank-Nicholson type scheme. Pletcher used an explicit finite-difference calculation procedure based on the DuFort-Frankel scheme. The turbulent boundary-layer solutions of Cebeci and Pletcher also considered only nonreacting gas chemistry.

In the references cited above, the authors considered only external flows. Elliott, Bartz, and Silver [13] developed an integral method of solution for predicting turbulent boundary-layer flows in rocket nozzles. Boldman et al. [14] applied the method to predict turbulent flows in supersonic nozzles. Edenfield [15] extended the method to predict turbulent flows in hypervelocity nozzles in which the gas was considered to be in chemical equilibrium.

For the lower Mach number perfect gas cases considered by Elliott, Bartz, and Silver and by Boldman et al., relatively good agreement between the predictions and the experimental data for the heat-transfer distribution was obtained. Edenfield found that the method did not predict the boundary-layer displacement thickness accurately downstream of the nozzle throat and failed to converge for local Mach numbers of about 16. Thus, for hypersonic nozzle flows, a limit existed in the use of the integral method. Other disadvantages of the integral method are the amount of empirical data needed and the number of adjustable parameters which strongly influence the results of the predictions.

As a result of the excellent agreement between experiment and theory which has been obtained by Blottner and Davis for laminar boundary-layer flows of both reacting and nonreacting gases and by Harris for nonreacting turbulent flows using the Crank-Nicholson type implicit finite-difference scheme, this method of solution was selected for the present investigation. The two-layer eddy viscosity model originally proposed by Cebeci for turbulent boundary-layer flows was used. Both laminar and turbulent flows of perfect gases and mixtures of perfect gases in chemical equilibrium were considered over flat plates, wedges, two-dimensional and axisymmetric blunt bodies, and in axisymmetric nozzles. Mass transfer was considered for the case where the injected gas was the same as that of the external flow. The primary emphasis has been to obtain solutions for high Mach number flows having strongly favorable pressure gradients and highly cooled walls.

Recently Back and Cuffel [16,17] measured velocity and temperature profiles through turbulent boundary layers at several locations in a nozzle with cooled and heated walls. Measurements were made at one location in the inlet section, four locations in the convergent section and one location in the divergent section of a Mach 3.6 nozzle. The upstream end of the nozzle was attached to a long circular tube which was cooled or heated to the same temperature level of the nozzle. Comparisons were made with the integral method of Elliott, Bartz and Silver [13]. These experimental and numerical data are compared with results from the present study. Predicted wall skin-friction and heat-transfer data and velocity, temperature and mass flux profiles are compared with the available experimental data. The effects of tube length and wall heating on the predictions are considered in some detail. Limiting effects of wall heating on convergent numerical solutions are presented.

The research presented here is discussed in more detail by Lewis, Anderson and Miner [18], and the computer program is described in detail including necessary instruction for its use by Miner, Anderson, and Lewis [19]. Transition models for laminar-to-turbulent flow are also described in the report on the computer program. Those interested in obtaining copies of the computer program and the two reports noted above should contact the first author on this paper.

2. ANALYSIS

The equations of motion for laminar or turbulent flow of perfect gases and equilibrium gas mixtures were developed in Levy-Lees variable and expressed in the general parabolic form necessary for the implicit finite-difference solution procedure employed by Blottner [1].

Several turbulent eddy viscosity models were investigated and the effects of strongly favorable pressure gradients on the eddy viscosity models were considered. In this section the governing equations and eddy viscosity models are given.

2.1 Governing equations.--The governing equations for laminar or turbulent boundary-layer flow of an arbitrary gas in thermodynamic equilibrium or of a perfect gas are presented in transformed Levy-Lees variables. The rate of mass transfer at the wall boundary for porous walls is assumed small in comparison to the boundary-layer mass flow and normal gradients are negligible. The boundary-layer thickness is

assumed to be small in comparison to the body radius of curvature and centrifugal forces are neglected.

2.2 **Turbulent boundary-layer equations in Levy-Lees variables.**--The boundary-layer equations in physical variables were nondimensionalized as proposed by Van Dyke [20] as follows:

$x = x^*/a^*$, $y = y^*/a^*\epsilon_{VD}$, $p = p^*/\rho_\infty^* U_\infty^{*2}$, $\rho = \rho^*/\rho_\infty^*$, $T = T^*/T_{ref}^* = T^*/(U_\infty^{*2}/c_p^*)$, $u = u^*/U_\infty^*$, $v = v^*/U_\infty^*\epsilon_{VD}$ and

$\mu = \mu^*/\mu_{ref}^* = \mu^*/\mu(T_{ref}^*)$ where $\epsilon_{VD}^2 = \mu_{ref}^*/\rho_\infty^* U_\infty^* a^*$. The resulting equations were transformed using the Levy-Lees variables

$$d\xi = \rho_e u_e \mu_e r_w^{2j} \, dx \quad \text{and} \quad d\eta = \rho u_e r_w^j/(2\xi)^{1/2} \, dy$$

The resulting turbulent boundary-layer equations are:

Continuity: $2\xi F_\xi + V' + F = 0$ (2.1)

Momentum: $2\xi F F_\xi + V F' = \beta (\rho_e/\rho - F^2) + (C(1 + \epsilon^+) F')'$ (2.2)

Energy: $2\xi Fg_\xi + Vg' = \dfrac{C}{Pr} (1 + \epsilon^+ Pr/Pr_t) + [(C/Pr)(1+\epsilon^+ Pr/Pr_t)]' \, g'$

$+ u_e^2/H_e(1-1/Pr)[C' FF' + CF'^2 + CF''] + CFF' (1-1/Pr)'$ (2.3)

where $V = \dfrac{2\xi}{\rho_e u_e \mu_e r_w^{2j}} \left[F \eta_x + \dfrac{(\rho v + \overline{\rho'v'}) \, r_w^j}{(2\xi)^{1/2}} \right]$, $F = u/u_e$ and $g = H/H_e$ (2.4a)

and at the stagnation point $V = \dfrac{\rho v + \overline{\rho'v'}}{[(j+1)\rho_e \mu_e du_e/dx]^{1/2}}$ (2.4b)

The boundary conditions at the wall, $\eta = 0$, and at the outer edge of the boundary-layer, $\eta = \eta_e$, for Eq. (2.1) - (2.4) are:

at $\eta = 0$: $F = 0$; $g = H_w/H_e = h_w/H_e$, $V = V_w$ (2.5)

and

at $\eta = \eta_e$: $F = 1$; $g = 1$ (2.6)

2.3 **Eddy viscosity models.**--The eddy viscosity, ϵ^{+*}, was evaluated using the concept of a two-layer eddy viscosity model consisting of an inner law, ϵ_i^{+*}, valid near the wall boundary and an outer law, ϵ_o^{+*}, for the remainder of the boundary layer. This procedure has been employed successfully by a number of authors; for example, Cebeci, Smith and Mosinskis [4]. These authors use expressions for the inner eddy viscosity law which are based on Prandtl's mixing length concept stated as

$$\epsilon_I^{+*} = \rho^* \, \ell^{*2} \, |\partial u^*/\partial y^*|$$ (2.7)

where ℓ^* is the mixing-length. In the present study of the turbulent boundary-layer equations, a number of expressions based on Eq. (2.7) have been used, and in addition to these models, an eddy viscosity based on the Boussinesq relation

$$\tau^* = \mu^* \, (1+\epsilon_i^{+*}/\mu^*) \, \partial u/\partial y$$ (2.8)

has been used.

The eddy viscosity law based on Eq. (2.7) have been derived by analogy with Van Driest's [19] proposal for the mixing length where he considered Stokes' flow for an infinite flat plate with periodic oscillations in the plane parallel to the plate. A number of recently proposed eddy viscosity models based on Van Driest's model are given below:

Van Driest [21] $\epsilon_i^+ = X_1 \{1 - \exp [-X_2(\hat{C}_{f_\infty}/2)^{1/2}]\}^2 |F'|$ (2.9)

Cebeci, Smith and Mosinskis [4] $\epsilon_i^+ = X_1\{1-\exp[-X_2(|\hat{C}_{f_\infty}/2-\rho_e u_e y/\rho du_e/dx|)^{1/2}]\}^2|F'|$ (2.10)

Absolute Value of the Pressure Gradient $\epsilon_i^+ = X_1\{1-\exp[-X_2(\hat{C}_{f_\infty}/2+\rho_e u_e y/\rho|du_e/dx|)^{1/2}]\}^2|F'|$ (2.11)

Cebeci [5] $\epsilon_i^+ = X_1 [1 - \exp(-y^+/A^+)]^2|F'|$ (2.12)

where, as proposed by Cebeci [5], $A^+ = 26 [1 - 11.8 P^+]^{-1/2}$ without mass transfer (2.13)

and here $X_1 = \dfrac{k_1^2 \, y^2 \, \rho^2 u_e^2 \, r_w^j}{\epsilon_{VD} \, \mu \, (2\xi)^{1/2}}$, $X_2 = \dfrac{y\rho}{26 \, \mu \, (\epsilon_{VD})^{1/2}}$ (2.14)

Reichardt [22] considered the incompressible continuity equation for the fluctuating velocity components to demonstrate that ϵ_i^{+*} varied with y^{*3} and presented an expression obtained by curve fitting experimental data of flow in pipes. Richardt's expression for the inner eddy viscosity is

$$\epsilon_i^{+*} = 0.4 \, \mu^* \, \{y^* u^*_f/\nu^* - 11 \tanh [y^* u_f^*/(11 \, \nu^*)]\}$$ (2.15)

In transformed variables, Reichardt's law becomes

$$\epsilon_i^+ = 0.4 \, y \, u_t/\mu - 4.4 \tanh [y \, u_t/(11 \, \mu)]$$ (2.16a)

where $$u_t = [\hat{C}_{f_\infty} \, \rho/(2 \, \epsilon_{VD})]^{1/2}$$ (2.16b)

For wall mass transfer, Cebeci [5] proposed

$$\epsilon_i^+ = X_1 \left[1 - \exp\left(-y^+/A^+\right)^2 \right] |F'| \tag{2.17}$$

where

$$A^+ = 26 \left[-(p^+/v_w^+)[\exp(11.8 \, v_w^+) - 1] + \exp(11.8 \, v_w^+) \right]^{-1/2} \tag{2.18}$$

The Clauser-Klebanoff outer law

$$\epsilon_o^+ - k_2 u_e \, \delta_k^* \, \gamma/a^* \tag{2.19}$$

was used where δ_k^* is the two-dimensional incompressible boundary-layer displacement thickness and γ is Klebanoff's intermittancy factor.

2.4 Numerical solution procedure.--The conservation equations for laminar or turbulent flow were solved using an implicit finite-difference scheme employed by Blottner [2] and Davis [9-11] which requires that the governing equations be expressed in the general parabolic form

$$W'' + A_1 W' + A_2 W + A_3 + A_4 W_\xi = 0 \tag{2.20}$$

where W is the dependent variable F or g and the coefficients $A_i = A(\xi, \eta, W, W')$.

The governing equations were expressed in the form of Eq. (2.20) for a perfect gas or an equilibrium gas mixture as:

Momentum:

$$F'' + A_1 F' + A_2 F + A_3 + A_4 F_\xi = 0 \tag{2.21}$$

where $A_1 = \dfrac{C'}{C} + \dfrac{\overline{A}_o'}{\overline{A}_o} - \dfrac{V}{A_o}$, $A_2 = -\dfrac{\partial F}{A_o}$, $A_3 = \beta \dfrac{\rho_e}{\rho}/A_o$, $A_4 = -2\xi F/A_o$

$A_o = C$ for laminar flow, $A_o = C(1+\epsilon^+)$ for turbulent flow and where $\overline{A}_o = A_o/C$.

Energy:

$$g'' + A_1 g' + A_2 g + A_3 + A_4 g_\xi = 0 \tag{2.22}$$

where $A_1 = \dfrac{C'}{C} + \dfrac{\overline{A}_o'}{\overline{A}_o} - \dfrac{V}{A_o}$, $A_2 = 0$

For a perfect gas

$$A_3 = \frac{u_e^2}{H_e} \left(1 - \frac{1}{Pr} \right) \left[\frac{C'}{C\overline{A}_o} FF' + \frac{F'^2}{\overline{A}_o} + \frac{FF''}{\overline{A}_o} \right]$$

and for an equilibrium gas
$$A_3 = \frac{u_e^2}{H_e} \frac{C_1}{\overline{A}_o} \left[\left(\frac{C'}{C} + \frac{C_1'}{C_1} \right) FF' + F'^2 + FF'' \right], \quad A_4 = -2\xi F/A_o$$

for laminar flow
$$A_o = C/Pr$$

and for turbulent flow
$$A_o = C/(1+\epsilon^+ Pr/Pr_t)/Pr$$

again
$$\overline{A}_o = A_o/C \text{ and } C_1 = 1 - 1/Pr.$$

Continuity:

The continuity equation was computed by trapezoidal integration of the expression

$$V = V_w - \int_0^{\eta_e} (2\xi \, F_F + F) \, d\eta$$

after each iteration of the momentum and energy equations.

3. RESULTS AND DISCUSSION

Solutions of perfect gas turbulent flows using different expressions for the inner eddy viscosity law are compared with experimental data and/or other numerical solutions for cases where these data were available.

The numerical solutions presented assume fully developed turbulent flow; however, the boundary-layer computer program described by Miner, Anderson, and Lewis [19] provides options for either an instantaneous or a continuous transition from laminar to turbulent flow. The continuous transition model was based on the experimental results of Owen [20] and is discussed in the computer program users manual [19].

3.1 Perfect gas solutions for turbulent flows over flat plates.--For flat-plate flows the inner eddy viscosity laws expressed by Eq. (2.9) - (2.12) are identical and are referred to as the Van Driest model. The inner eddy viscosity law given by Eq. (2.16) is referred to as the Reichardt model.

The results of the present numerical method of solution are compared with Coles [24] experimental data and the solution of Dorrance [25].

The predicted skin-friction coefficients for the three cases are compared with the theory of Dorrance and Coles' experimental data in Fig. 1. The skin friction predictions for Cases 20 and 26 are in excellent agreement with both the experimental data and Dorrance's solutions. For case 62, the present method of solution is in good agreement with the experimental data for Reynolds numbers greater than 3×10^6, but for $Re_\infty = 1.7 \times 10^8$ the present numerical solution predicted a skin friction coefficient which was approximately 15% lower than the experimental value. The present method of solution is in better agreement with the experimental data for this case than the theory of Dorrance.

The above results are representative examples of turbulent flat-plate solutions, and in all cases considered the numerical results were not significantly influenced by the choice of the inner eddy viscosity law. However, the use of the Reichardt inner law reduced the computing time.

3.2 Turbulent flow of perfect gases in axisymmetric nozzles.--The present method of solution has been used to solve four axisymmetric nozzles, and the results are compared with the integral method of solution developed by Elliott, Bartz, and Silver [13] and available experimental data. The inner eddy viscosity laws of Van Driest Eq. (2.9), Cebeci and Smith Eq. (2.10), absolute value of the pressure gradient Eq. (2.11), and Reichardt Eq. (2.16) have been considered for the sample case given by Elliott, Bartz, and Silver.

3.2.a Elliott, Bartz, and Silver sample case.--The problem considered consisted of a 30° conical inlet section, a circular arc throat section with a throat radius of 0.885 in. and a 15° conical divergent section.

The profiles of velocity and temperature differed by less than 5% for the solutions obtained using the different viscosity laws. The boundary-layer parameters θ, δ^*, δ, c_f, etc. also agreed to within 5%. If the inner law of Cebeci and Smith Eq. (2.10) were excluded in the comparison, the resulting solutions differed by less than 3%. These results indicate that including the pressure gradient term in the inner law had little influence upon the eddy viscosity profiles and had essentially no influence upon the resulting solutions.

As a result of the above, and the formulations of expressions Eq. (2.10) and (2.11) for the inner law, these expressions were dropped from further consideration. The results which are discussed below were obtained using the Van Driest or Reichardt expression for the inner eddy viscosity law. However, as in the previous cases, use of the Reichardt inner law resulted in a substantial reduction of the computer time required. Since the differences in these solutions were insignificant, these data are shown as a single curve.

The heat-transfer coefficient predicted by the present numerical solutions is compared in Fig. 2 with the results obtained by Elliott, Bartz, and Silver using an integral method of solution. The solutions using the present numerical method and the integral method differ up to 30%; however, it should be noted, that the solutions using the integral method can be varied over a wide range by changing the assumptions for the nominal entrance conditions. Since the starting profiles for the present method were determined from the solution of the governing equations, direct comparison of the two methods was not possible; moreover, it is not clear what assumptions should be made for the initial conditions necessary for the integral method if experimental data were not available before the calculations were made. Because of the arbitrariness in the solutions using the integral method, the present finite-difference solutions are believed superior to the results from the integral method.

3.2.b NASA-Lewis rocket nozzle flows.--This nozzle consisted of a 30-degree half-angle convergent section and a 15-degree half-angle nozzle. In the calculations experimentally measured wall temperature and pressure distributions were used.

Solutions to this problem were obtained using the Van Driest Eq. (2.9) and the Reichardt Eq. (2.16) expressions for the inner eddy viscosity laws, and as in the previously discussed Elliott, Bartz, and Silver sample case, the differences in the solutions were insignificant. However, the solution using the Van Driest inner law required more computing time than was necessary using the Reichardt inner law.

The predicted heat-transfer coefficient using the present method of solution is compared with the experimental data and the solutions obtained using the Elliott, Bartz, and Silver integral method in Fig. 3. The present method of solution is in excellent agreement with the experimental data in the throat region and downstream. Differences of up to 20% between the predicted and experimentally determined heat-transfer coefficient are noted in the subsonic region of the nozzle. The nearly discontinuous change in the experimental value of the heat-transfer coefficient at $z = 1.97$ was the result of the experimental temperature distribution in this region; also the experimental pressure data were not smooth in this region. For the present calculations, these data were smoothed in the region $1.9 < z < 2.5$. The integral method of solution is seen to reflect a strong dependence upon the assumed starting conditions. The two solutions presented using the integral method differed from each other by as much as 50%.

3.2.c AEDC hotshot wind-tunnel nozzle.--The problem considered corresponds to the case referred to as "Hotshot 1" by Edenfield [15]. The nozzle geometry is shown in Fig. 4. The results presented assumed a one-dimensional expansion of equilibrium nitrogen. The experimental wall enthalpy distribution was used as Edenfield used in his calculations. The stagnation pressure and temperature were 11,500 psi and 5400°R.

Edenfield [15] considered the nozzle discussed in this section for preliminary investigations leading to the design of contoured nozzles for hypersonic hotshot wind tunnels with $M_\infty = 20$. Edenfield used a number of theories to predict the downstream boundary-layer displacement thickness, but the available methods of prediction either failed to give a complete solution for the nozzle or the results were found to be unacceptable. Attempts to solve the problem using the Elliott, Bartz, and Silver [13] integral method failed at $z/r^* = 1350$. This failure was attributed to the assumed power law total enthalpy profiles used in the integral method. All other attempts to predict the displacement thickness used the momentum equation only with the Crocco enthalpy distribution or correlation formulas.

It should also be noted that the total length of the nozzle was given as 92.087 inches (see Edenfield [15]). Using a throat radius of 0.055 inches results in a maximum value of z/r^* of approximately 1684. However, experimental pressure measurements were given for values of z/r^* up to approximately 1850. The pressure data employed upstream of $z/r^* = 100$ corresponded to an isentropic expansion of equilibrium nitrogen based on geometric area ratio. The transition from the one-dimensional expansion pressure data to the experimental data is particularly noticeable in large scale plots of the boundary-layer thicknesses computed using the present method of solution for z/r^* between 100 and 400. With reference to the above comments, it is not clear what conclusions should be made in the comparison of the predicted and experimental displacement thickness. However, the same conditions were used for all prediction methods and the results of the different solutions may be compared.

The heat-transfer rates are given in Fig. 5. The results presented for the integral method were obtained by solving both the momentum and energy integral equations with a power law for the velocity and total enthalpy profiles. The heat-transfer rates predicted by the integral method were from 30 to 50% lower than the rates predicted by the present method. The results obtained with the integral method do not appear to be realistic, and as noted previously, the method failed at $z/r^* = 1350$. The assumed power law total enthalpy profiles together with the assumed velocity profiles in the integral method resulted in solutions which predicted large densities near the outer edge of the boundary layer in the downstream region of the nozzle. The density profiles predicted by the integral method, the method of Enkenus and Maher [26] using the Crocco enthalpy distribution, and the present method are shown in Fig. 6 for $z/r^* = 984$. As noted by Edenfield [15], pitot pressure measurements would have detected the presence of these peaks in density if they had existed, but the measurements made indicated that such peaks did not exist. The density profile predicted with the present method showed a increase in density near the wall which is characteristic of boundary layers over highly cooled walls.

Fig. 7 shows δ^* predictions of the Elliott, Bartz, and Silver method for both an assumed power law and the Crocco enthalpy distribution. For the latter, only the momentum equation was solved by the integral method. Two solutions are given corresponding to different skin-friction laws using the method of Enkenhus and Maher. The present two-dimensional and asixymmetric solutions are in good agreement with the other solution procedures which used tne momentum equation only. Other than the comments made previously about the length of the nozzle and corresponding pressure distribution, it is not clear why the present predictions should be in good agreement with experimental data for z/r^* up to 1100 and overpredict the displacement thickness by a factor of two at the nozzle exit.

3.2.d **Back and Cuffel's cool wall nozzle flow**.--Calculations were also made with the present method to compare with the experimental data of Back and Cuffel [16]. The experimental pressure and wall temperature distributions were used in the calculations, and the nozzle calculation was preceded by an inlet tube ($L_T = 60$) the leading edge of which was assumed to be sharp and at the stagnation conditions. The experimental nozzle was preceded by a rounded edge inlet tube, $L_T = 45$. The present value of L_T was chosen to give the best match of the momentum thickness and the other boundary-layer parameters at probe 0 ($z = -2.14$ inches).

As will be discussed below, the present method using the previously discussed two-layer eddy viscosity model predicted temperature profiles which were in less than satisfactory agreement with the experimental data. Alternate calculations were made using the eddy viscosity law of Van Driest (1956) [21] throughout the entire boundary layer. An $L_T = 45$ was chosen to give the best match with the experimental value of θ and acceptable agreement with the other boundary-layer parameters at probe 0. Results of the calculations are presented using both the two-layer and the single-layer eddy viscosity models. As will be shown, some improvement was obtained in the temperature profiles caused by the change in the eddy viscosity models, but some adverse effects were obtained with the single-layer model, especially in the calculated heat transfer, which were primarily because of the shorter length of inlet tube.

The eddy viscosity profiles at probe 1 ($z = 1.42$ in.) are presented in Fig. 8. For y less than 0.14 in., the values of ϵ^+ did not differ by a plottable amount. For y greater than 0.14 inches, the values of ϵ^+ differed considerably. The two-layer model used the Clauser-Klebanoff outer law and ϵ^+ tended to 0 as $y \to \delta$. The single-layer model used the Van Driest (1956) law throughout the boundary layer, and ϵ^+ increased to a peak at $y/\delta = 0.75$ and went to zero at $y/\delta = 1.4$. The peak value of the single-layer model was four times the peak value of the two-layer model and occurred at a value of y greater than the boundary-layer thickness which was obtained with the two-layer model. Even though the values of δ differed by more than a factor of two, the values of δ^* and θ were nearly the same. The velocity profile data indicate δ is better predicted by the two-layer model than by the single-layer model of Van Driest, while the remaining boundary-layer parameters were in good agreement using both eddy viscosity models.

Fig. 9 shows the nozzle contour with probe positions noted and the edge Mach number as given as in [16]. In the present calculations, the experimental pressure distribution was used from which the experimental edge Mach number was obtained. Also given in Fig. 9 are the friction coefficient and Stanton number distributions for the experimental data [16], numerical results using the JPL method of Elliott, Bartz and Silver [13] as presented in [16], and numerical results from the present method using both eddy viscosity models. The predictions of the friction coefficient by the present method using the two models are in excellent agreement with each other from one inch upstream of the nozzle throat to the nozzle exit and in very good agreement in the region upstream of the throat. The differences in the present calculations from $z = -2$ to 8 inches were due primarily to the difference in the inlet tube length ($L_T = 60$ with the two-layer and $L_T = 45$ with the single-layer eddy viscosity model) and, as will be seen from the velocity profiles later, the differences exist only secondarily because of differences in the eddy viscosity models. The JPL method predicted a friction coefficient distribution which was in good agreement with the experimental data and the present predictions in the region of the inlet tube but in poor agreement throughout the nozzle. In fact, the JPL method predicted values for $C_f/2$ which were less than 50% of the present or experimental results.

Comparison of predicted and experimental Stanton number distributions are shown in Fig. 9. The present results using the two-layer eddy viscosity model predicted well the Stanton number in the convergent portion of the nozzle but overpredicted the heat transfer in the divergent portion of the nozzle. The JPL predictions are in excellent agreement with the experimental data in the throat region but are low in the divergent portion of the nozzle and are even lower in the convergent section of the nozzle. Over-all, the results of the present method do not compare quite as well with the experimental data as do the results of the JPL method. The present method with the single-layer eddy viscosity model yields results which are about 15% higher than the results with the two-layer model. At the inlet of the nozzle, the higher prediction is due primarily to the difference in tube length. Other calculations, which have been made with the present method and results of which are not included in this paper, indicate that differences in L_T have a more persistent effect on the Stanton-number distribution than on the skin-friction distribution. Thus, the calculation with the shorter inlet tube is expected to predict a higher Stanton number.

The justification for choosing different L_T can be seen in Fig. 10. The two calculations with the present method yield essentially identical results for the momentum thickness. The results for the displacement thickness are slightly different in the inlet and the first part of the convergent portion

of the nozzle but are nearly the same for the remainder of the nozzle. A comparison with the results of the JPL method and the experimental data show very good agreement except in the divergent portion of the nozzle. Another difference is that the JPL method predicted a more pronounced peak in both δ and δ* at the end of the inlet tube. Also, the JPL method and experimental data show δ* negative even as far downstream as probe 5, whereas the present method clearly predicted a positive value of δ* at probe 5. The edge Mach number distribution shown in Fig. 9 would require that the flow be positively displaced from the wall toward the nozzle centerline from z = 15 inches to the nozzle exit.

The energy thickness distribution (Fig. 10) predicted by the present method agrees very well with both the experimental data and the results of the JPL method. Again, the prediction with the shorter L_T was slightly higher.

The velocity profiles predicted by the present method using the two-layer eddy viscosity model shown in Fig. 11 are in excellent agreement with the experimental data even though the value of δ predicted by the present method is smaller than the experimental value. It is interesting to note that the two-layer eddy viscosity model yielded a much better prediction of the velocity ratio than did the single-layer model at probes 0, 1, and 5, but at probes 2, 3, and 4 the single-layer eddy viscosity model gave a slightly better prediction.

The velocity profiles are also shown in Fig. 12 in law-of-the-wall coordinates. The agreement between the present predictions and the experimental data is very good except at probe 5. The present calculations show much less difference than appeared in Fig. 11. The one exception is near the outer edge of the boundary layer at probe 0 where the difference appears much greater than in Fig. 11. In the law-of-the-wall coordinates, the two-layer eddy viscosity model consistently provided better agreement with the experimental data than did the single-layer eddy viscosity model. The lack of agreement between the present calculations and the experimental data at probe 5 is particularly noteworthy. In Fig. 11, the agreement was very good, yet in Fig. 12 the results from the present method were about 15% lower than the experimental data. As was shown in Fig. 9 at probe 5, the value of the friction coefficient from the present calculations was about 30% greater than the experimental value. Thus, the value of u_τ for the present calculations is 15% greater than the experimental value, and therefore the curves for u+(y+) from the present calculations are 15% lower and 15% to the right of what the curves would be if the experimental and present predictions of u_τ were the same. Since velocity profiles in law-of-the-wall coordinates are sensitive to changes in the measured or calculated skin friction, considerable care must be exercised in comparing velocity profiles presented in law-of-the-wall coordinates.

Temperature profiles are given in Figs. 13-15. In Fig. 13 the temperature data are given in the form of the temperature difference ratio $(T_t - T_w)/(T_0 - T_w)$. Fig. 14 presents the same data but using the ratio T/T_e. The results of the present method using the single-layer eddy viscosity model agree better with the experimental data near the wall and near the outer edge of the boundary layer while the two-layer model results agree better with the experimental data from $y/\phi = 1$ to $y/\phi = 3$ or 4.

While the temperature difference ratio of Fig. 13 is convenient in that the data are bounded by zero and unity, this choice of coordinates obscures an effect shown in Fig. 14.

At probe 5 the static temperature drops from the wall value to a value less than the edge value and remains below the edge value throughout the boundary layer. This effect occurs in both the experimental data and present prediction results. Further, the numerical results predicted a slight rise in temperature near the wall before the temperature dropped. This effect was expected but did not appear in Fig. 14 because it occurred so near the wall.

The temperature profiles presented in law-of-the-wall variables in Fig. 15 are not in as good agreement as the profiles in Fig. 13 and 14. In the law-of-the-wall variables, both T+ and y+ are affected by changes in u_τ and, in addition, T+ is strongly affected by changes in the wall heat transfer. Thus, at probes 2-4, where the experimental and predicted values of skin friction and heat transfer are in good agreement, the velocity profiles in law-of-the-wall variables are in good agreement. At probe 0 the present method underpredicted the heat transfer and the experimental velocity profile was lower than the calculated profiles. At probe 5 the present method overpredicted the heat transfer and skin friction and calculated velocity profiles were lower than the experimental profile by an amount equal to the over-prediction of the heat transfer less the overprediction of the friction velocity. Also, the calculated velocity profiles agree better in Fig. 15 than in Fig. 13 and 14 except near the outer edge of the boundary layer where the difference was greater. The caution advised in comparing velocity profiles in law-of-the-wall variables is more strongly advised when comparing temperature profiles in law-of-the-wall variables.

Mass flux ratio profiles are shown in Fig. 16. The good agreement between the numerical results and the experimental data is consistent with the agreement obtained for the velocity and temperature profiles except at probe 5. At this probe location in the divergent portion of the nozzle, the edge of the experimental boundary layer was at a value of $y/\theta = 37$ which is well off the figure. The maximum value of $y/\phi = 20$ shown in Fig. 16 corresponds to $y/\phi = 6.5$ in Fig. 14, and so the mass flux profiles at probe 5 are consistent with the velocity and temperature profiles presented in Figs. 11 and 14.

The present calculations discussed above were all made with $Pr_t = 0.9 = $ constant. Recent results of Simpson, Whitten, and Moffat [27] have strongly indicated that Pr_t should not be constant across the boundary layer. They suggest $Pr_t = 0.95 - 0.45 (y/\delta)^2$ in the outer portion of the boundary layer. Calculations were made with this variation in Pr_t and only small differences in the results occurred. The most noticiable effect was in the temperature profiles in which the results with the two-layer eddy viscosity model were shifted slightly to the right. The agreement with the experimental data was only slightly improved, and the velocity profiles were unaffected. Since only small changes in the numerical results were obtained with the variable Pr_t, those results are not shown.

If Pr_t were constant, the eddy conductivity would vary directly as the eddy viscosity; however, if Pr_t varies with y as given above, the values of the eddy conductivity would be greater than the values obtained with constant Pr_t. Thus, changes in Pr_t affect the solutions of the energy equation directly but affect the solutions of the momentum equation only through the coupling of the equations. The effect of variations in Pr_t therefore appears primarily in the temperature profiles.

The eddy conductivity is also affected by changes in the eddy viscosity. With Pr_t constant, the change in eddy viscosity using the single-layer model instead of the two-layer model produces a like change in the eddy conductivity. If the eddy conductivity used in numerical calculations of turbulent boundary-layer flows is obtained from ϵ^+ and Pr_t, then changes in ϵ^+ appear to affect ϵ_k^+ more than do changes in Pr_t.

3.2.e Back and Cuffel's heated wall nozzle flows.--By lowering the stagnation temperature and circulating heated water through the coolant passages of the inlet and nozzle, Back and Cuffel [.7] were able to obtain experimental data with slight wall heating ($T_w/T_0 = 1.1$). Calculations were made with the present two-layer eddy viscosity model using the experimental pressure distribution and a constant wall temperature. Three sets of predictions obtained with the present method are presented; $L_T = 60$ and $T_w/T_0 = 1.1$, $L_T = 20$ and $T_w/T_0 = 1.1$, and $L_T = 60$ and $T_w = T_{adw}$.

Distributions of θ, δ^* and c_f are given in Fig. 17. The present predictions of θ and δ^* (with $L_T = 60$) agree very well with the experimental data and the JPL results. As in the cool wall case, the JPL method predicted a sharper peak in θ and δ^* at the end of the inlet tube than did the present method. With $L_T = 20$, the present method underpredicted θ and δ^* in the convergent section of the nozzle but, from the nozzle throat downstream, predicted essentially the same distribution of θ and δ^* as with $L_T = 60$.

The present predictions of c_f are in good agreement with the experimental data and with the JPL results in the inlet and the diverget section of the nozzle. The JPL method underpredicted c_f in the convergent section of the nozzle and overpredicted c_f in the throat region. The present method with $L_T = 60$ and $T_w/T_0 = 1.1$ did not give a converged solution beyond $z = 9.4$ in., and the prediction of c_f began to deteriorate at $z = 8.5$ inches. The problem of obtaining predictions with wall heating and long inlet tubes is discussed in the next section.

Velocity profiles are presented in Figs. 18 and 19. The agreement between the experimental results and the present predictions with $L_T = 60$ is very good for all values of z. With $L_T = 20$ the present method underpredicted θ, and as shown in Fig. 18 the predicted velocity profiles are thus shifted to the right. This effect is most obvious at probe 5 but does appear at probes 2-4. Since the predicted boundary layer was correspondingly thinner at probes 0 and 1, the effect does not appear there.

The present method with $L_T = 20$ overpredicted u_τ at probes 0 and 1 and thus the values of u^+ (Fig. 19) are correspondingly smaller. Since the predicted boundary layer was also thinner, the maximum values of y^+ are smaller at probes 0 and 1. The other predicted velocity profiles agreed quite well with the experimental data in the law-of-the-wall coordinates.

3.2.f Coupling between tube length and wall heating.--In the present calculations for the heated wall case of Back and Cuffel [17], difficulties were encountered near the nozzle throat. With $L_T = 60$ and $T_w/T_0 = 1.1$, the prediction of c_f began to deteriorate at $z = 8.5$ in. and the solution failed to converge at $z = 9.4$ in. Calculations with other values of L_T and T_w/T_0 indicated that the failure was related in part to the very large values of the pressure gradient parameter β in the throat region. The value of β is a function dp/ds and ξ, and as L_T is changed, β is changed. Changes in T_w/T_0, with T_0 constant, had little effect on β but did affect the n-ξ coordinate transformation. Points at which solutions failed to converge together with pressure gradient distribution are shown in Fig. 20. The data points shown correspond to calculations made and faired curves were drawn through these points. Calculations were also made with $L_T = 45$ and 30, and the corresponding data points lay between the curves for $L_T = 60$ and 20.

With $T_w/T_0 = 2.5$, failure occured at a point where β was 1% of the peak throat value. The trend of the curve indicates that at sufficiently large values of T_w/T_0, failure would occur almost as soon as any pressure gradient was encountered.

The mechanism by which the amount of wall heating couples with the value of ξ (or β) to limit the region in which solutions can be obtained is not clearly understood. However, the Levy-Lees transformation is a similarity transformation for laminar flow and has been employed successfully by many investigators, particularly for flows over highly cooled walls. The transformation has in fact proved quite satisfactory for flows over insulated walls as shown above. The inclusion of the density in the transformation of the normal coordinate does indicate that the n-ξ coordinates are most useful in calculating flows over highly cooled walls. While other investigators may have encountered problems in using the Levy-Lees transformation, the authors believe this is the first documentation of an apparent upper limit on the applicability of the Levy-Lees transformation when used in turbulent boundary-layer theory with strong favorable pressure gradients.

4. CONCLUSIONS

A method has been developed and tested to predict turbulent boundary-layer flows of nonreacting and equilibrium chemically reacting gases through axisymmetric nozzles with strongly favorable pressure gradients and with wall cooling and heating. Some significant results of this study were as follows:

(i) For flat-plate flows, predictions using both the Van Driest and Reichardt inner eddy viscosity models, when used in a two-layer eddy viscosity model, gave identical results. The Reichardt law was found to be more efficient in computing time.

(ii) The present finite-difference predictions were in better agreement with available experimental wall heat-transfer and boundary-layer displacement data than integral methods for solving compressible turbulent boundary-layer flows in rocket nozzles and hypersonic aerodynamic wind-tunnel nozzles.

(iii) Predictions of velocity and temperature profiles, wall heat transfer and skin friction, and integral boundary-layer thicknesses were in excellent to good agreement with available experimental data for rocket nozzle flows.

(iv) Further refinements in eddy viscosity models and an independant expression for the eddy thermal conductivity are needed.

(v) Under the boundary-layer transformations used in the theory, strong coupling effects were found between wall heating and strong favorable pressure gradients. An upper limit was determined

for the applicability of the Levy-Lees transformation in calculation of boundary-layer flows over heated walls with favorable pressure gradients.

5. ACKNOWLEDGEMENTS

6. REFERENCES

[1] Blottner, F. G., "Finite Difference Solution of the First-Order Boun- ary Layer Equations," Non-reacting and Chemically Reacting Viscous Flows Over a Hyperboloid at Hypersonic Condition, Ed. by C. H. Lewis, AGARDograph No. 147, NATO, Paris, 1970, pp. 13-36.

[2] Kline, S. J., M. V. Morkovin, G. Sovran, and D. J. Cockrell eds., Computation of Turbulent Boundary Layers - 1968 AFOSR-IRP-Stanford Conference Vol. 1 - Methods, Predictions, Evaluation and Flow Structure, 1968.

[3] Cebeci, T., and A M. O. Smith, "A Finite-Difference Solution of the Incompressible Turbulent Boundary-Layer Equations by an Eddy-Viscosity Concept," Douglas Aircraft Co., Report No. DAC-67130, 1968.

[4] Cebeci, T., A. M. O. Smith, and G. Mosinskis, "Calculation of Compressible Adiabatic Turbulent Boundary Layers," AIAA Paper 69-687, 1969.

[5] Cebeci, T., "Behavior of Turbulent Flow Near a Porous Wall with Pressure Gradient," AIAA Journal, Vol. 8, No. 12, Dec. 1970, pp. 2152-2156.

[6] Pletcher, R. H., "On a Calculation Method for Compressible Turbulent Boundary Layer Flows with Heat Transfer," AIAA Paper 71-165, 1971.

[7] Blottner, F. G., and M. Lenard, "Finite Rate Plasma Generation in the Laminar Air Boundary Layer of Slender Reentry Bodies," Transactions of the Eight Symposium on Ballistic Missile and Space Technology, San Diego, California, 1963.

[8] Blottner, F. G., "Non-Equilibrium Laminar Boundary Flow of Ionized Air," General Electric Report R64SD56, 1964. Also AIAA Journal, Vol. 2, No. 11, Nov. 1964, pp. 1921-1927.

[9] Davis, R. T., and I. Flugge-Lotz, "Second-Order Boundary-Layer Effects in Hypersonic Flow Past Axisymmetric Blunt Bodies," J. Fluid Mechanics, Vol. 20, Part 4, pp. 593-623.

[10] Davis, R. T., "The Hypersonic Fully Viscous Shock-Layer Problem," Sandia Laboratories Report SC-RR-68-B40, 1968.

[11] Davis, R. T., "Solution of the Viscous Shock-Layer Equations for a Binary Mixture," Nonreacting and Chemically Reacting Viscous Flows Over a Hyperboloid at Hypersonic Condition, Ed. by C. H. Lewis. AGARDograph No. 147, NATO, Paris, 1970, pp. 55-69.

[12] Harris, J. E., "Numerical Solution of the Compressible Laminar, Transitional, and Turbulent Boundary Layer Equations," Ph.D. Dissertation, VPI & SU, Blacksburg, Virginia, 1970.

[13] Elliott, D. G., D. R. Bartz, and S. Silver, "Calculation of Turbulent Boundary Layer Growth and Heat Transfer in Axisymmetric Nozzles," JPL TR-32-387, 1963.

[14] Boldman, D. R., H. E. Newmann, and J. F. Schmidt, "Heat Transfer in 30° and 60° Half-Angle of Convergence Nozzles with Various Diameter Uncooled Pipe Inlets," NASA TN D-4177, 1967.

[15] Edenfield, E. E., "Contoured Nozzle Design and Evaluation for Hotshot Wind Tunnels," AIAA Paper 68-369, 1968.

[16] Back, L. H. and R. F. Cuffel "Turbulent Boundary Layer and Heat Transfer Measurements Along A Convergent-Divergent Nozzle," to be published in ASME J. Heat Transfer.

[17] Back, L. H. and R. F. Cuffel, private communications, May 1971.

[18] Lewis, C. H., E. C. Anderson, and E. W. Miner, "Nonreacting and Equilibrium Chemically Reacting Turbulent Boundary-Layer Flows," AIAA Paper 71-597, 4th Fluid and Plasma Dynamics Conference, June 1971.

[19] Miner, E. W., E. C. Anderson, and C. H. Lewis, "A Computer Program for 2-D and Axisymmetric Non-Reacting Perfect Gas and Equilibrium Chemically Reacting Laminar, Transitional, and Turbulent Boundary-Layer Flows," College of Engineering Report, VPI-E-71-8, May 1971, Blacksburg, Virginia.

[20] Van Dyke, M., "Second-Order Compressible Boundary-Layer Theory with Application to Blunt Bodies in Hypersonic Flow," Stanford University Report SUDAER No. 112, 1961.

[21] Van Driest, E. R., "On Turbulent Flow Near a Wall," J.A.S., Vol 23, No. 11, Nov. 1956, pp. 1007-1011, 1036.

[22] Reichardt, H., "Vollstandige Darstellung der turbulenten Geschwindigkeitsverteilung in glatten Lutungen," ZAMM, Vol. 31, No. 7, 1951, pp. 208-219.

[23] Owen, F. K., "Transitional Experiments on a Flat Plate at Subsonic and Supersonic Speeds," AIAA J., Vol. 8, No. 3, March 1970, pp. 518-523.

[24] Coles, D., "Measurements of Turbulent Friction on a Smooth Flat Plate in Supersonic Flow," J. Aero Sci. Vol. 21, No. 7, July 1954, pp. 443-448.

[25] Dorrance, W. H., Viscous Hypersonic Flow, McGraw-Hill, New York, 1962, Chapter 7.

[26] Enkenkus, K. R., and L. F. Maher, "The Aero
dynamic Design of Axisymmetric Nozzles for
High Temperature Air," NOL-R-7395, 1962.

[27] Simpson, R. L., D. G. Whitten and R. J.
Moffat, "An Experimental Study of the
Turbulent Prandtl Number of Air with
Injection and Suction," Int. J. Heat and
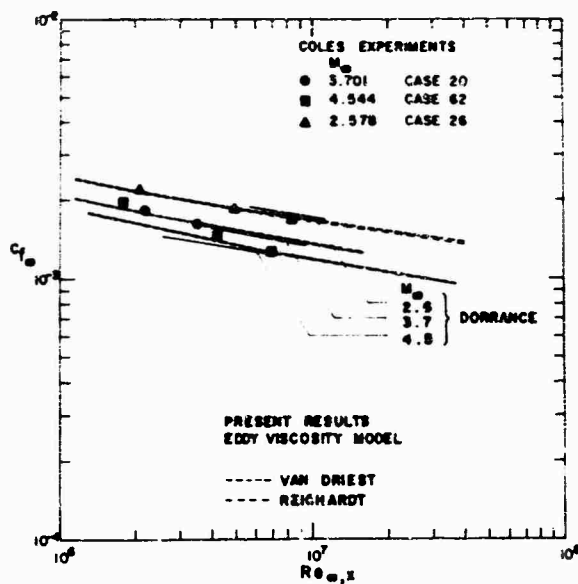Mass Transfer, Vol. 13, No. 1, Jan. 1970,
pp. 125-143.

Fig. 3 - NASA-Lewis Nozzle Heat Transfer
Distributions

Fig. 1 - Turbulent Flat-Plate Skin
Friction Distributions for
Coles Experimental Conditions
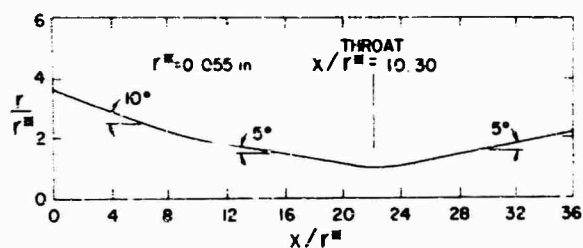
Fig. 4 - AEDC Hotshot Nozzle Geometry

Fig. 2 - Heat-Transfer Distributions for the
Elliott, Bartz and Silver Nozzle Flow
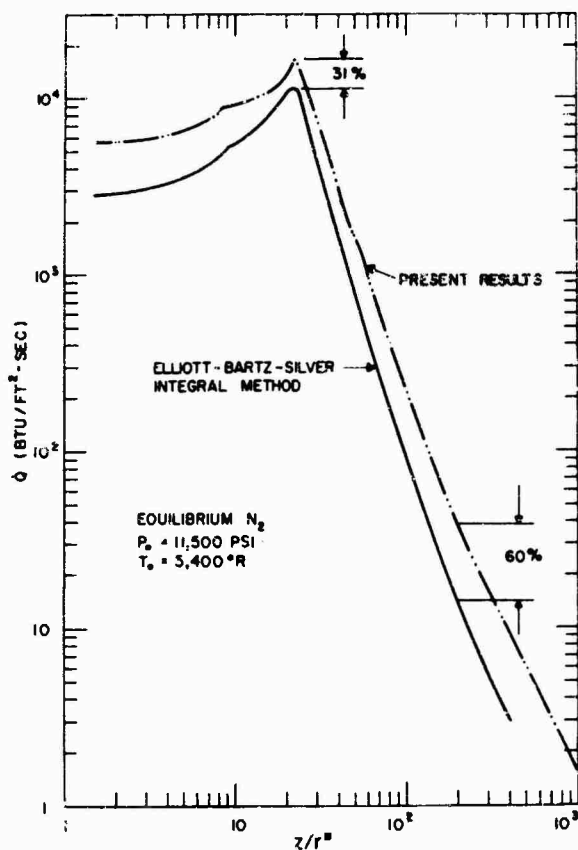
Fig. 5 - AEDC Hotshot Nozzle
Heat-Transfer Distributions
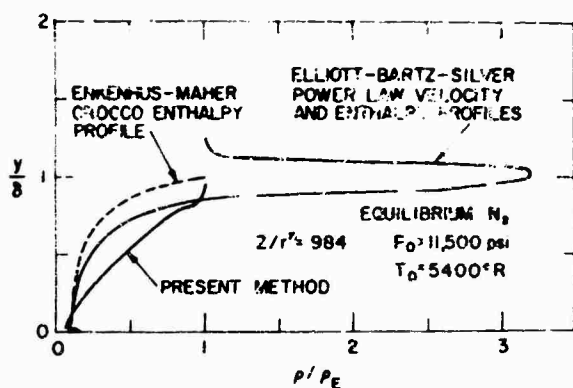
Fig. 6 - Density Profiles for the AEDC
Hotshot Nozzle Flow
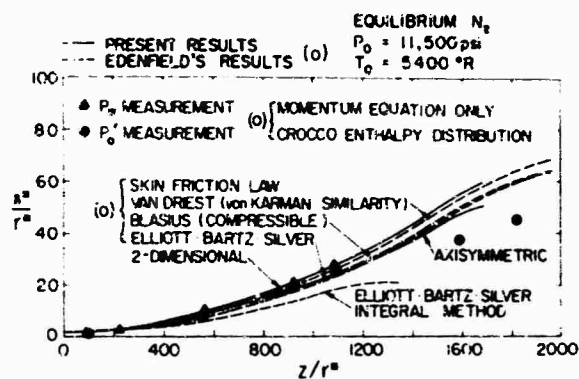
Fig. 7 - Comparison of Predicted Displacement
Thickness Distribution for the AEDC
Hotshot Nozzle
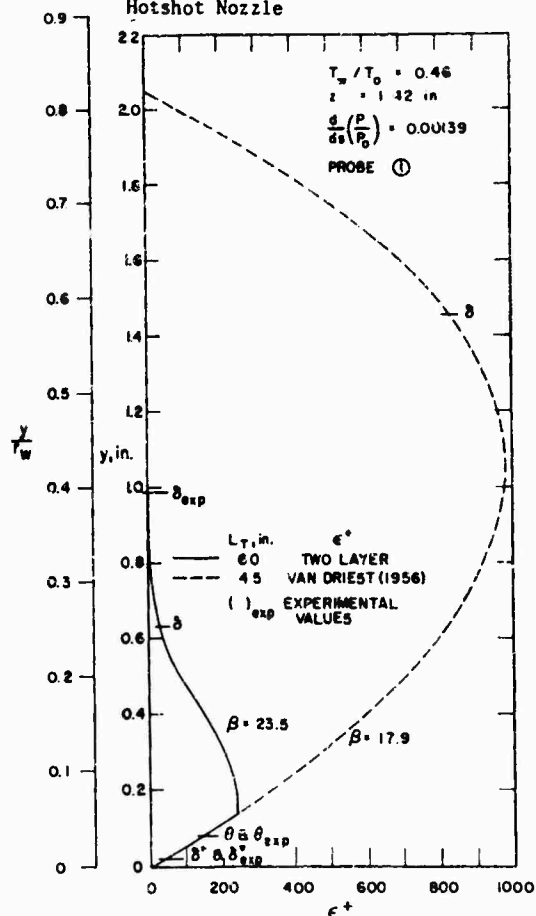
Fig. 8 - Eddy Viscosity Distributions Based
upon the Two-Layer and Van Driest
Single-Layer Models for the Back and
Cuffel Cooled Wall Nozzle Flow
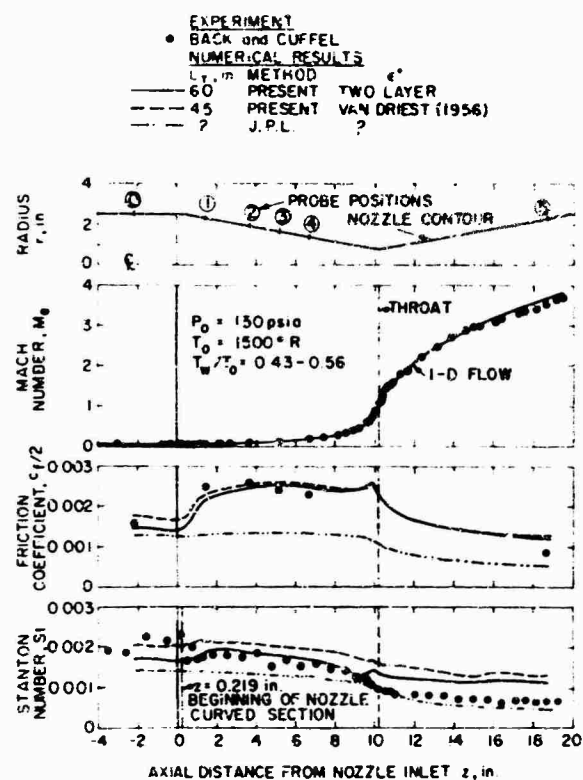
Fig. 9 - Skin-Friction, Stanton Number and
Mach Number Distributions for the Back
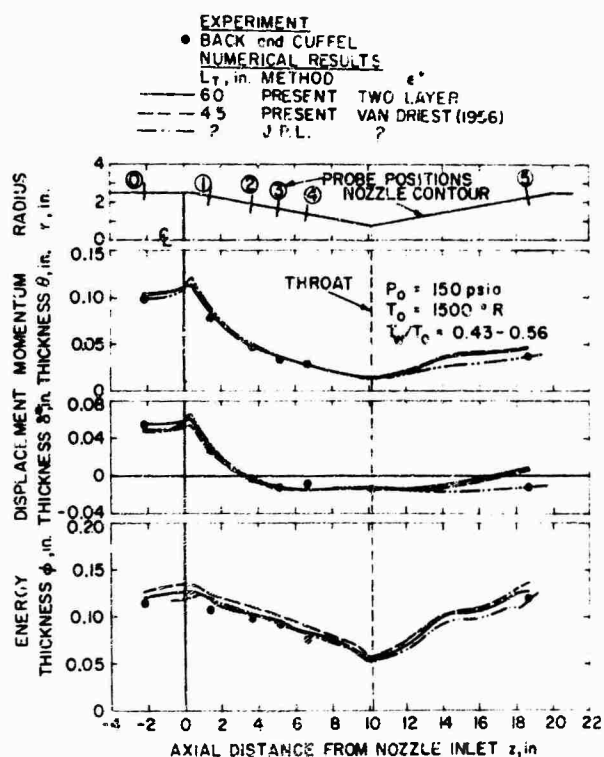and Cuffel Cooled Wall Nozzle Flow

Fig. 10 - Momentum, Displacement and
Energy Layer Thickness
Distributions for the Back and
Cuffel Cooled Wall Nozzle Flow
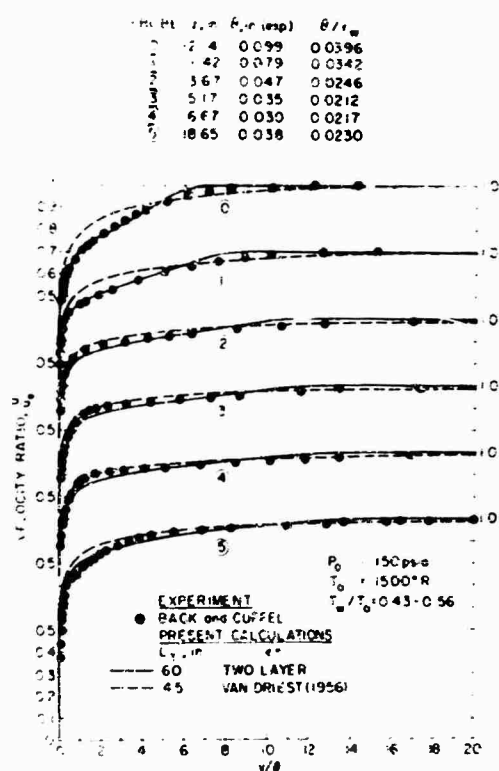
Fig. 11 - Velocity Profiles for the Back and
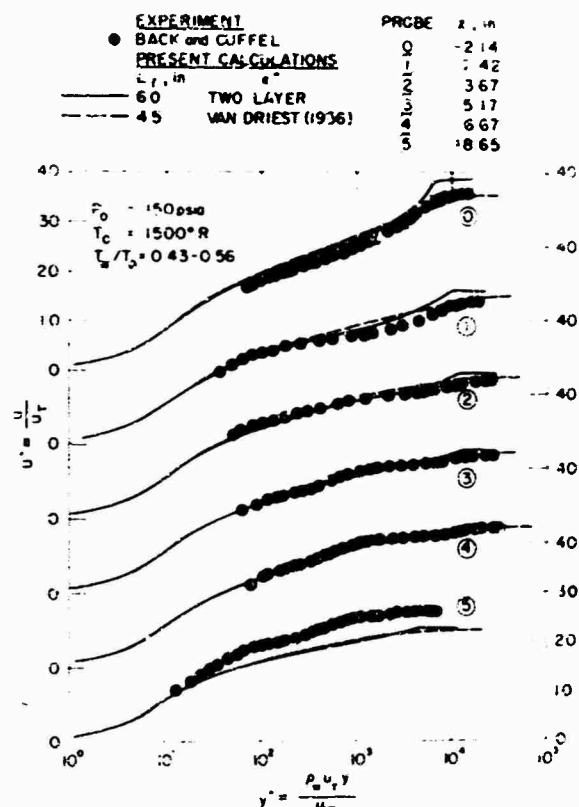Cuffel Cooled Wall Nozzle Flow

Fig. 12 - Velocity Profiles in
Law-of-the-Wall Coordinates
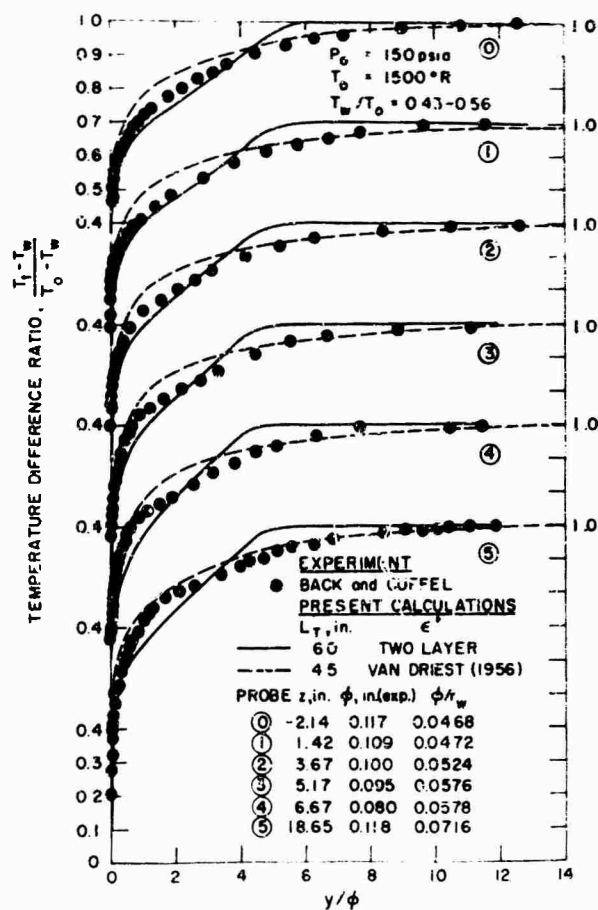for the Back and Cuffel Cooled
Wall Nozzle Flow

Fig. 13 - Temperature Difference Ratio
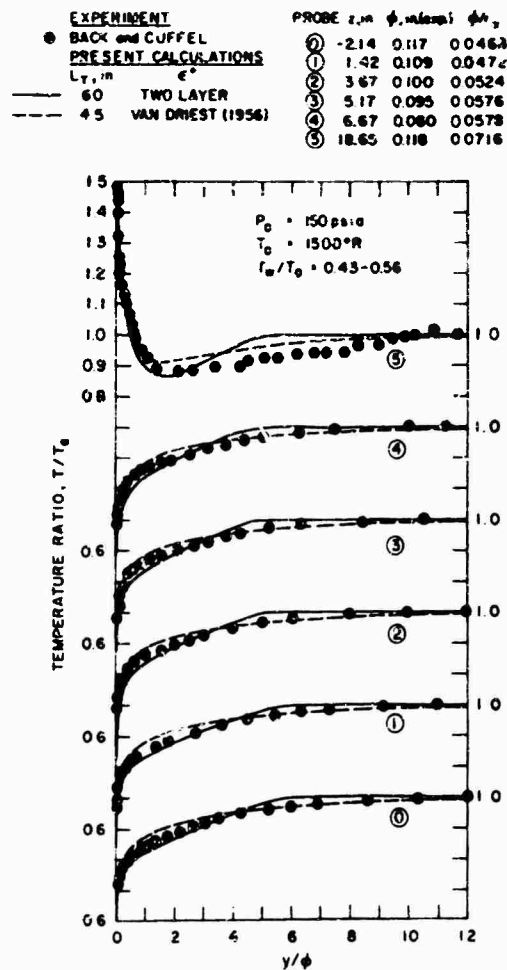Profiles for the Back and
Cuffel Cooled Wall Nozzle Flow

Fig. 14 - Static Temperature Ratio
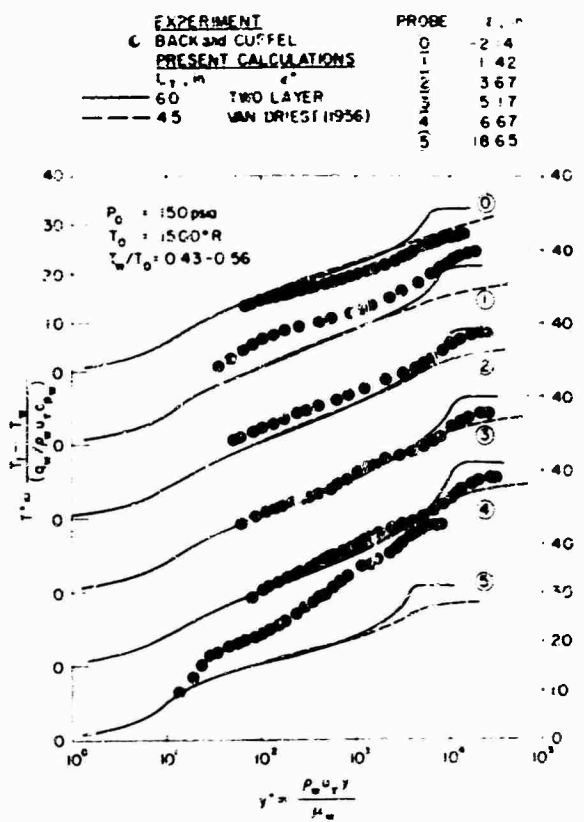Profiles for the Back and
Cuffel Cooled Wall Nozzle Flow

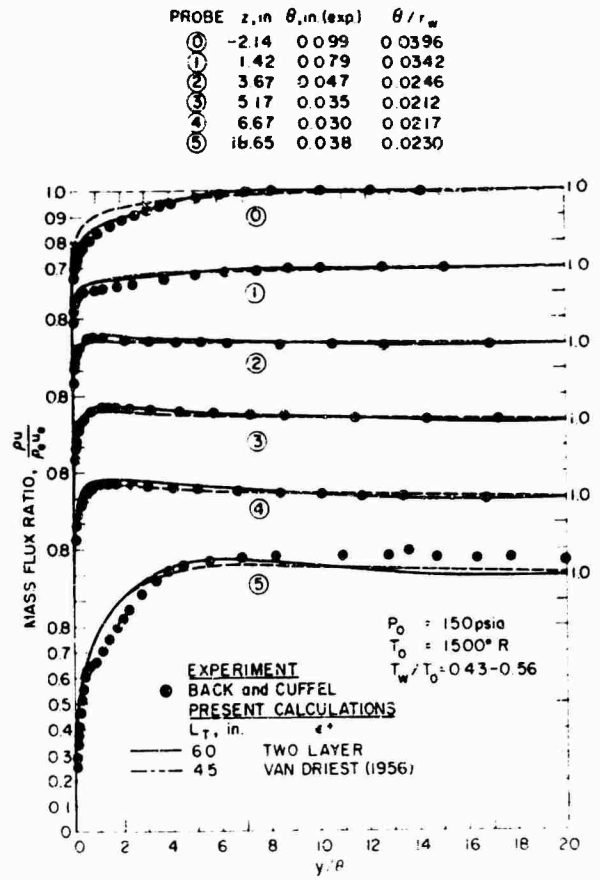Fig. 15 - Temperature Profiles in Law-of-the-Wall Coordinates for the Back and Cuffel Cooled Wall Nozzle Flow

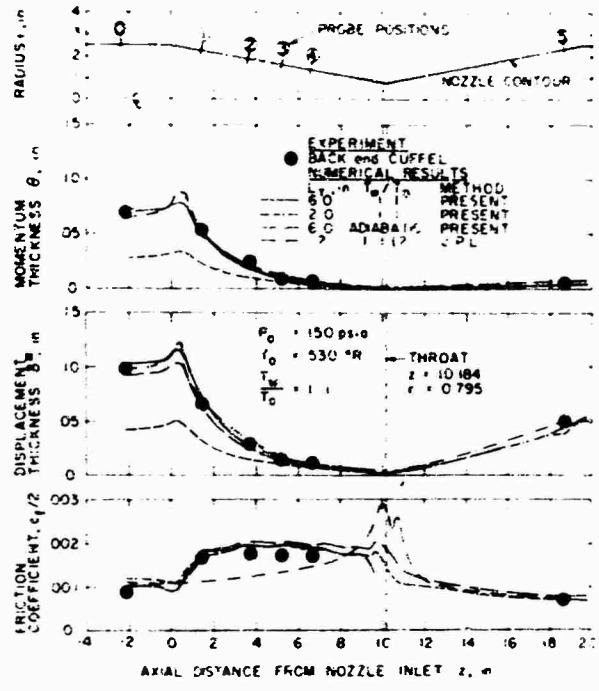

Fig. 17 - Momentum, Displacement and Friction Coefficient Distributions for the Back and Cuffel Heated Wall Nozzle Flow

PROBE	z, in	θ, in (exp)	θ/r_w
⓪	-2.14	0.099	0.0396
①	1.42	0.079	0.0342
②	3.67	0.047	0.0246
③	5.17	0.035	0.0212
④	6.67	0.030	0.0217
⑤	16.65	0.038	0.0230

PROBE	z, in	θ, in (exp)	θ/r_w
⓪	-2.14	0.0690	0.0276
①	1.42	0.0530	0.0229
②	3.67	0.0240	0.0126
③	5.17	0.0077	0.0047
④	8.67	0.0068	0.0049
⑤	16.65	0.0065	0.0039

Fig. 16 - Mass Flux Ratio Profiles for the Back and Cuffel Cooled Wall Nozzle Flow
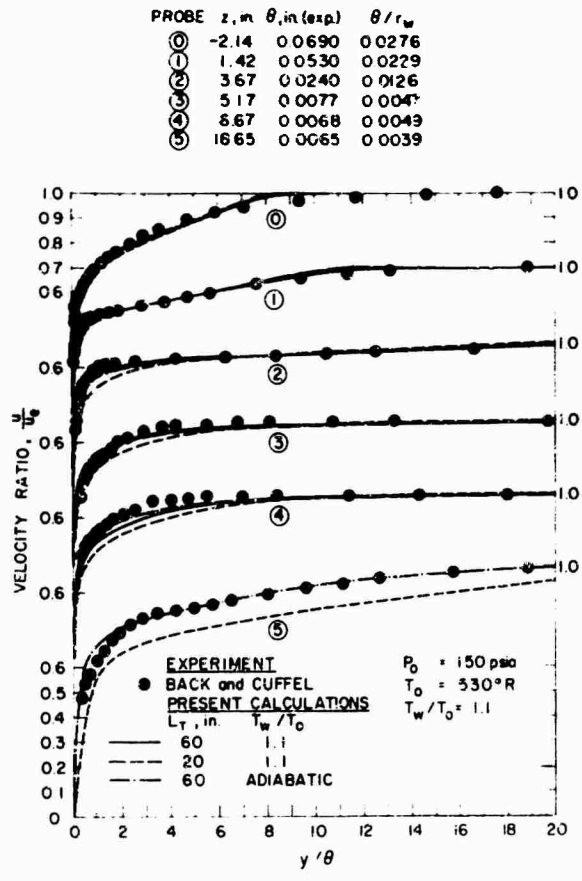

Fig. 18 - Velocity Profiles for the Back and Cuffel Heated Wall Nozzle Flow
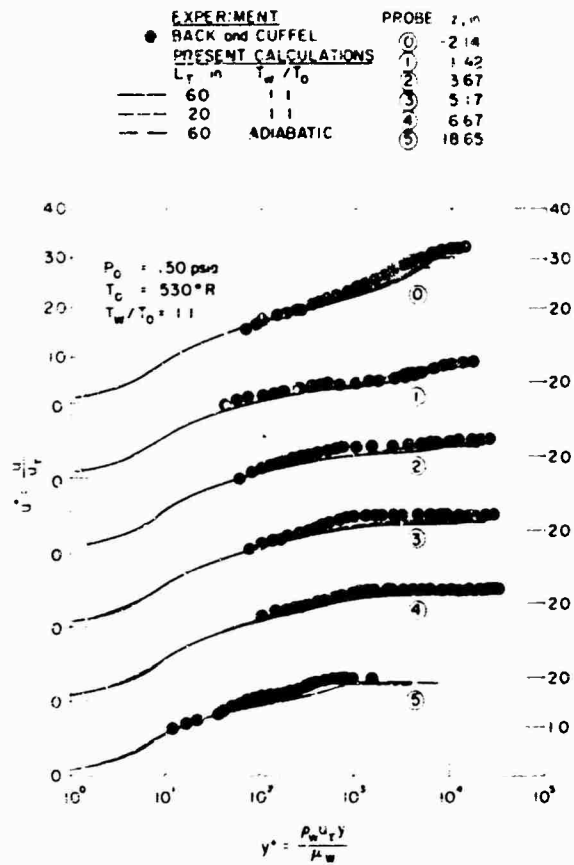
Fig. 19 - Velocity Profiles in Law-of-the-Wall
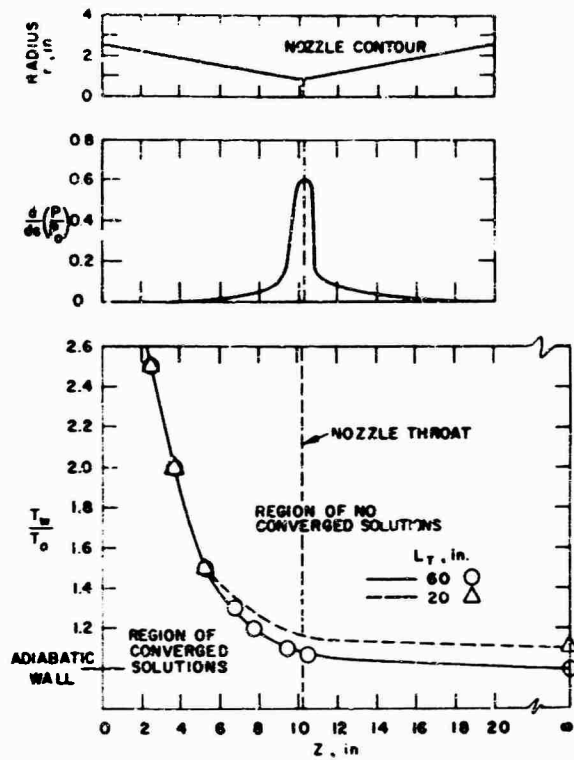Coordinates for the Back and Cuffel
Heated Wall Nozzle Flow

Fig. 20 - Effects of Wall Temperature
and Inlet Tube Length on
Numerical Results for the Back
and Cuffel Nozzle Flow
Conditions

MACH NUMBER EFFECTS IN TURBULENT FLOW

J.J.D. Domingos[*]
Instituto Superior Técnico, Lisboa 1, Portugal

Starting from-fundamental assumptions of microscopic Thermodynamics and continuum mechanics the existence of a velocity potential for the flow of viscous fluids was prooved as a general property. The implications are discussed and the role of compressibility as an esssencial feature of turbulence, either in subsonic or supersonic flows, is stressed. The apparently contradictory consequence of zero vorticity in flows which derive from a potential is clarified through a discussion of concepts implicitly assumed in the usual definitions of mean density, mean velocity and Thermodynamic equation of state.

Developing the basic assumptions, the general partial differential equation for the velocity potential is deduced. It contains as particular cases the usual equations of inviscid fluid mechanics. The fundamental equation is a third-order, quasi-linear-partial differential equation.

One of its approximations is a generalization to the three-dimensions of Burger's equation, whose general solution is presented. The meaning of the approximation is discussed and its precise physical meaning stressed. It is shown, as a mathematical consequence, that pressure coupling decreases with increasing Mach number. For $M^2 >> 2/(\gamma-1)$ which for air means $M >> 2,25$ the coupling practically disappears and the mathematical solution becomes exact.

The results are applicable to general supersonic viscous flows because the theory is concerned with instantaneous velocity fields, without separation into mean and turbulent quantities.

The solutions found are assimptotically exact solutions of the time dependent three dimensional Navier-Stokes equations for a viscous and compressible fluid which follows a polytropic evolution $P = C\rho'$.

NOMENCLATURE

a - local velocity of sound
C - constant in a polytropic evolution
c_p - specific heat per unit mass at constant volume
c_v^p - specific heat per unit mass at constant volume
$F = \int \frac{dP}{\rho} = \frac{C^{\gamma-1}}{\gamma-1}$ (see also formula 31)

G - mass velocity
i,j - running indices (i,j=1,2,3)
M - local Mach number
P - pressure
t - time
V - velocity (=G/ρ)
V* - velocity of incompressible fluid (=G/ρ*)
x_i, x_j - spacial coordinates
β - arbitrary function of time; also constant
γ = politropic exponent (usually $\gamma=c_p/c_v$)
ϵ -constant
ϕ - velocity potential
λ - constant
ρ - specific mass per unit volume
ρ*- conventional specific mass per unit volume in incompressible fluids
ω - vorticity associated with V. Also angular velocity
ω* - vorticity associated with V*
Ψ - external potential per unit mass
ν - kinematic viscosity
θ, θ* - solutions of heat equation
$\frac{d}{dt}$ = substantial derivative (following the motion)

Obs: repeated indices always means summation on that index

Also $(\frac{\partial\phi}{\partial x_j})^2 = \frac{\partial\phi}{\partial x_j} \frac{\partial\phi}{\partial x_j} = \sum_{j=1}^{3} (\frac{\partial\phi}{\partial x_j})^2$

_____ [*] Professor of Mechanical Engineering,
Division of Applied Thermodynamics
Director, Núcleo de Estudos de Engenharia Mecânica

1. INTRODUCTION

Any theoretical work concerned with turbulence invariably assumes incompressibility as a starting assumption. Besides, all known theories explain turbulence in terms of vorticity which is considered a distintive feature of viscous fluids, probably because vorticity is mostly a consequence of the aderence condition on solid walls. In a sense, incompressibility and vorticity are the basic stones of all known theories of turbulence. However, turbulence is yet an unsolved problem, which probably justifies a different approach. This paper is a first atempt in such direction. In it, compressibility is considered one of the basic features of turbulence and vorticity a matter of interpretation. In doing so, we are not pursuing contradiction with established ideas but logical reasoning from first principles, in a different way. If contradiction energes, it has always the rewarding aspects of clarifying concepts and ideas accepted by habitute and convenience.

1.1. Fundamental background

The problem of turbulence is largely a mathematical problem, which we try to solve by physical reasoning based on experimentation, assuming validity of the basic equations The role of experimentation is to find acceptable simplifications, or to find new fundamental equations if the known ones were unable to explain experimental facts. Presently, we can not reject the Navier-Stokes equations because they have not been solved, and by the same reason we do not know its range of validity.

The mathematical difficulty is due to non-linearity and vectorial character of the momentum equations. However, because in laminar flows the equations can be simplified for one or two dimensions on the assumption of symmetry;because an order of magnitude argument allows the heuristic simplification of incompressibility and turbulence apnears in subsonic ("incompressible flows")flows, we kept this simplification even knowing that, two dimensional incompressible fluids do not allow turbulence.At the same time, we kept most of the assumptions and results from the theory of inviscid incompressible fluids, to the point of using it as the most basic practical standard to measure fluid velocities (through Pitot tubes, or equivalent).

Inviscid fluid theory, uncontroversly known to be Thermodynamically untenable, owes much of its usefulness to the existence of a velocity potential which considerably simplifies the mathematical treatment. If this is so, we can justifiably ask why a mathematical theory for the flow of viscous fluids has not emerged based on such simplifying assumptions? This theory would benefit from the inclusion of viscous effects and the mathematical advantage of transforming the three momentum equations into only one scalar equation. The answer to this question, as long as we can interpret past work which discarded such an approach, is:

a) The flow of an incompressible fluid which follows a velocity potential is also an exact solution of the Navier-Stokes equations with the property that viscous effects automatically cancel; besides, their differential equation beeing only of second order does not allow the non slip-condition combined with zero normal component of velocity at a solid wall.

b) In turbulent flows, incompressibility and potential flow only gives rise to turbulent normal stresses on the Reynolds approximation, not shear stresses.

Incompressible and incompressibility have been underlined in the above statements because both objections have their roots there. In fact, if the velocity field derives from a potential and the fluid is incompressible, the motion is completely defined by the equation of continuity (conservation of mass). However, if the restriction of incompressibility is remooved, both of the objections above desappear, as will be shown.

Because of such obvious advantages in having a scalar equation instead of a vectorial one for general 3-D flows, we can ask if the existence of a velocity potential for a viscous fluid is just an accident or a general hiden fact. An answer to this question has been given elsewhere [1] . The main conclusion is based on the following hypoteses:

- The fluid can be considered as an isolated, homogenous,Thermodynamic system.

- The microscopic motion of elementary particules can be described by Newton's Mechanics.

- The typical assumptions of continuum theories are valid.

With these hypotesis, we have shown that a velocity potential always exist [1] .

Because we are mainly concerned with turbulence, the above assumptions seem to us much more basic than any others used until now in turbulence theories. They can give rise to different fundamental equations of motion or simplify the general Navier-Stokes equations.

The above conclusion (as any reasoning based in Thermodynamics) rejects incompressibility as physically untenable. Besides,incompressibility and viscosity are contradictory at a microscopic level,as we understand them. So, we reject incompressibility on the present approach not only on these physical arguments but specially for the mathematical simplification which it allows through the existence of a velocity potential.

The existence of a velocity potential can be accepted on the above basis or, as a fundamental axiom to accept or to reject on experimental evidence.

By a velocity potential we mean that the macroscopic velocity field (V) is the gradient of a scalar function (ϕ):

$$V = \cdot \text{grad} \phi$$

where $\cdot$ is some unspecified constant.

The first logical consequence is that:

$$\omega = \frac{1}{2} \text{ curl } V = 0$$

which means an identically zero vorticity field, or an irrotational flow.

Of course, to reject vorticity as non-existent in any viscous flows is probably too much for anyo e concerned with turbulence. However, vorticity can be looked just as a mat-ter of convenience in interpretation.

In fact, the macroscopic velocity field is not a uniquely defined concept unless we define the density, because the only quantity acessible for measurement is momentum or mass velocity.

Let G be mass velocity, ρ^* be the conventional density of an incompressible fluid, V^* its associated macroscopic velocity. We have

$$G = \rho^* V^* = \rho V$$

If $V = \cdot$ grad ϕ we have:

$$\text{curl } (\rho V) = 0 = \text{curl } (\frac{\rho^*}{\rho} V^*)$$

and by a vectorial identity (with $\wedge$ meaning vectorial product):

$$\text{curl } (\frac{\rho^*}{\rho} V^*) = \text{grad}(\frac{\rho^*}{\rho}) \wedge V^* + \frac{\rho^*}{\rho} \text{ curl } V^* = 0$$

and

$$\omega^* = \frac{1}{2} \text{ curl } V^* = \frac{1}{2} V^* \wedge \text{grad log } (\frac{\rho^*}{\rho})$$

which shows that the macroscopic velocity field V^* has vorticity provided ρ is not constant.

The question was discussed elsewhere [2] in detail. It emerges that the existence of vorticity in viscous fluids can be considered a consequence of the assumption of incompressibility.

The assumption of incompressibility devoids the pressure of its Thermodynamic meaning transforming it in a compatibility parameter between the momentum and the continuity equation. To our velocity potential is associated the Thermodynamic equation of state. So, both approaches are compatible and vorticity a matter of convenience.

Remark that, in a fluid at rest, $\rho^* = \rho$ and that, for a given ϕ, the vorticity can be considered a measure of departure from incompressibility.

1.2. - Outline of the main contribution

Because our interest (here) is turbulence, and because the basic assumptions of Navier-Stokes equations have not been rejected, our fundamental equations can be derived from them. As a first step, we will consider constant kinematic viscosity, and the general equation for the velocity potential of a viscous fluid with equation of state $P=C\rho^\gamma$ will be deduced. This equation is of third order, which allows the specification of the usual boundary conditions of non-slip and zero normal velocity on a solid boundary. The exact solution of this general equation is not known. However, one of its approximations is a 3-D generalization of Burger's model. We feel this to be one of the first interesting results because for the first time it is shown that the Burger's model has a precise physical meaning as an approximation to real turbulence. This gives a new interest to this widely studied equation in its one-dimensional version. This approximation gives support, as a mathematical consequence, to turbulence as a phenomena characterized by intermitency, a fact experimentally known but not explained by known theories.

The effect of the mathematical approximation beeing to neglect the instabilizing role of pressure coupling it does not account for production of turbulence energy. However, the dissipation mechanism is well described which as some important consequences in desagreement with widely accepted assumptions. Giving physical support to the mathematical study of the one-dimensional Burger's equation due to Saffman, we can plausibly accept its validity to the 3-D case in questioning the Kolmogorof assumptions. If these results can be extrapolated to 3-D is yet an open question whose definite answer is only dependent of working time, because the exact general solution will be shown.

From the intermitency or "shock-wave" behaviour of turbulence, emerges the unnatural character of Fourier analysis in describing turbulence, and an insight is gained into the

why of unsucessfull attempts to describe the turbulent field by truncated series or integral expansions.

Taking a less classical view of the equation it is shown that the same type of approximation has a particular solution of the damped travelling wave type which gives the proper form to the usual one and two point correlation curves.

2. FUNDAMENTAL EQUATIONS

- Assuming:

The validity of the Navier-Stokes equations in the form

$$\frac{\partial V_i}{\partial t} + V_j \frac{\partial V_i}{\partial x_j} = \nu \nabla^2 V_i - \frac{1}{\rho} \frac{\partial P}{\partial x_i} - \frac{\partial \Psi}{\partial x_i} \quad (i,j = 1,2,3)$$

- A Thermodynamic equation of state $P = C\rho^\gamma$

- A continuous velocity potential ϕ such that $V = \text{grad } \phi$

- $\nu, C,$ - physical constants

The momentum equations can be written as:

1) $$\frac{\partial}{\partial t}\frac{\partial \phi}{\partial x_i} + \frac{\partial \phi}{\partial x_j}\frac{\partial^2 \phi}{\partial x_j \partial x_i} = \nu \nabla^2 \frac{\partial \phi}{\partial x_i} - \frac{1}{\rho}\frac{\partial P}{\partial x_i} - \frac{\partial \Psi}{\partial x_i}$$

defining now:

2) $F = \int \frac{dP}{\rho}$ or, if $\gamma \neq 1$ $\quad F = \frac{C\gamma}{\gamma-1} \rho^{\gamma-1}$

Equation 1) can be put in the form

3) $$\frac{\partial}{\partial x_i}\left(\frac{\partial \phi}{\partial t} + \frac{1}{2}\frac{\partial \phi}{\partial x_j}\frac{\partial \phi}{\partial x_j} - \nu\nabla^2\phi + F + \Psi\right) = 0$$

and integrating in x_i

4) $$\frac{\partial \phi}{\partial t} + \frac{1}{2}\frac{\partial \phi}{\partial x_j}\frac{\partial \phi}{\partial x_j} - \nu\nabla^2\phi + F + \Psi = \beta(t)$$

where $\beta(t)$ is an arbitrary function of time (or a constant) to be defined.

Equation 4) is the first fundamental equation which we will write in a more compact form as

5) $$\frac{\partial \phi}{\partial t} + \frac{1}{2}(\frac{\partial \phi}{\partial x_j})^2 - \nu\nabla^2\phi = -F - \Psi + \beta$$

where $\quad (\frac{\partial \phi}{\partial x_j})^2 = \sum_{j=1}^{3}\frac{\partial \phi}{\partial x_j}\frac{\partial \phi}{\partial x_j}$

The second fundamental equation is the continuity equation

$$\frac{d\rho}{dt} = -\rho \frac{\partial V_j}{\partial x_j}$$

or

6) $$\frac{d}{dt}\log \rho = \nabla^2 \phi$$

where $\frac{d}{dt}$ is the substancial derivative. This equation is now written in terms of F through relation (2):

From (2) taking account that $F > 0$ if $\gamma > 1$

$$\log F = \log \frac{C\gamma}{\gamma-1} + (\gamma - 1)\log \rho$$

or

$$\log \rho = \frac{1}{\gamma-1}\log \frac{(\gamma-1)F}{C\gamma}$$

which transforms (6) into

7) $$\frac{d}{dt}\log \frac{F(\gamma-1)}{C\gamma} = -(\gamma-1)\nabla^2\phi$$

or, because $\frac{\gamma-1}{C\gamma}$ is a constant

8) $\frac{d}{dt} \log F = -(\gamma -1)\nabla^2\phi$

Multiplying now (5) by -1, and taking the log of both members

9) $\log -(\frac{\partial\phi}{\partial t} + \frac{1}{2}(\frac{\partial\phi}{\partial x_j})^2 - \nu\nabla^2\phi - \beta = \log F$

Taking the substantial derivative of both members of (9), log F can be eliminated using (7), resulting

10) $\frac{d}{dt} \log -\{(\frac{\partial\phi}{\partial t} + \frac{1}{2}(\frac{\partial\phi}{\partial x_j})^2 - \nu\nabla^2\phi)= -(\gamma-1)\nabla^2\phi$

Taking into account that the substantial derivative of a logaritm follows the rules of the usual derivative, (10) can also be written as

11) $\frac{d}{dt}\{\frac{\partial\phi}{\partial t} + \frac{1}{2}(\frac{\partial\phi}{\partial x_j})^2 - \nu\nabla^2\phi+\Psi-\beta\}=-(\gamma-1)\{\frac{\partial\phi}{\partial t} + \frac{1}{2}(\frac{\partial\phi}{\partial x_j})^2 - \nu\nabla^2\phi+\Psi-\beta\}\nabla^2\phi$

where, of course, it has been assumed that

12) $\frac{\partial\phi}{\partial t} + \frac{1}{2}(\frac{\partial\phi}{\partial x_j})^2 - \nu\nabla^2\phi+\Psi-\beta \neq 0$

Equation (11) is the fundamental equation for the velocity potential of a viscous fluid which follows a polytropic evolution of exponent $\gamma> 1$. We think that it is presented here for the first time.

Before its usual simplifications are discussed, we consider briefly the case of $\gamma=1$, which corresponds to an isothermal evolution.

If $\gamma=1$, $F = C \log \rho$, and the continuity equation becomes

13) $\frac{dF}{dt} = - C\nabla^2\phi$

and the fundamental equation for the velocity potential assumes the form:

14) $\frac{d}{dt}\{\frac{\partial\phi}{\partial t} + \frac{1}{2}(\frac{\partial\phi}{\partial x_j})^2 - \nu\nabla^2\phi+\Psi-\beta\} = C\nabla^2\phi$

2.2 - Particular cases

To show how the fundamental equations deduced contain the usual equations of inviscid fluid mechanics as particular cases, we briefly recall some of them.

For an incompressible fluid, $\rho=0$, $\nabla^2\phi = 0$, and equation (5) reduces to

15) $\frac{\partial\phi}{\partial t} + \frac{1}{2}(\frac{\partial\phi}{\partial x_j})^2+ \frac{P}{\rho} + \Psi = \beta$

If the flow is steady

16) $\frac{1}{2}(\frac{\partial\phi}{\partial x_j}) + \frac{P}{\rho} + \Psi = \beta$

which are the usual Bernoulli equations, with β a constant to be found from a known value of the l.h.s.

Usually, Ψ is the gravity potential.

Remark that β is the same constant for all streamlines.

For a compressible fluid, instead of $\frac{P}{\rho}$ we will have F, as usual.

If the fluid is inviscid, $\nu = 0$, and 11) reduces to

17) $\frac{d}{dt}\{\frac{\partial\phi}{\partial t} + \frac{1}{2}(\frac{\partial\phi}{\partial x_j})^2+\Psi-\beta\}=-(\gamma-1)\{\frac{\partial\phi}{\partial t} + \frac{1}{2}(\frac{\partial\phi}{\partial x_j})^2 +\Psi-\beta\}\nabla^2\phi$

The usual expression, however, uses generally as equation of state a linearization of $P = C\rho$ and the final expression is formally analogous to (14) with $\nu=0$, having instead of C a different constant, say c^*. Also, a different rearrangement of terms in (10) is usually presented which is got after expansion of

$\frac{d}{dt} = \frac{\partial}{\partial t} + \frac{\partial\phi}{\partial x_i} \frac{\partial}{\partial x_i}$

The acoustic approximation of (17) is got, linearizing P≈Cρ and neglecting convective terms:

$$\frac{d}{dt} = \frac{\partial}{\partial t}$$

$$(\frac{\partial \phi}{\partial x_j})^2 = 0$$

So:

18) $$\frac{\partial^2 \phi}{\partial t^2} = c'\nabla^2\phi$$

2.3 .- The generalized Burger's equation

-Let us assume

19) $$-\frac{\partial \zeta}{\partial t} + \frac{1}{2}(\frac{\partial \phi}{\partial x_j})^2 - \nu\nabla^2\phi + \Psi - \beta = \varepsilon$$

with ε an arbitrarily small constant.

In this case, we get from (11)

$$0 = -(\gamma-1)\varepsilon\nabla\phi$$

If $\varepsilon = 0$, (18) would be a particular solution of (11), if (11) did not implies $\varepsilon \neq 0$ for its validity. However, on a first approximation we can possibly infer that the limit term of the solutions of 18) when $\varepsilon\to 0$ would, in a sense, be very near a particular solution of (11). This, of course, is only an heuristic justification. Its physical implications are clearly seen from (5): They correspond to approximate F by ε, and so to eliminate the coupling do to P and ρ. This approximation originates a generalization to 3-D of Burger's equation. In fact with $\Psi = 0$.

20) $$\frac{\partial\phi}{\partial t} + \frac{1}{2}(\frac{\partial\phi}{\partial x_j})^2 - \nu\nabla^2\phi = \varepsilon$$

taking the derivative in x_i and noting that

$$\frac{\partial\phi}{\partial x_i} = V_i$$

we get

21) $$\frac{\partial V_i}{\partial t} + V_j \frac{\partial V_i}{\partial x_j} = \nu\nabla^2 V_i \qquad (i=1,2,3)$$

and for i=j=1

22) $$\frac{\partial V}{\partial t} + V \frac{\partial V}{\partial x} = \frac{\partial^2 V}{\partial x^2}$$

which is the equation proposed by Burger's as a mathematical model for turbulence more than twenty years ago. This equation has been the subject of much recent work related to turbulence, as a mathematical model for studying properties of the Navier-Stokes equations.

The exact solution of (22) was found by Hopf [3] and Cole [4] who show that the solution of (22) is related to the solution of the heat equation:

$$\frac{\partial\theta}{\partial t} = \nu \frac{\partial^2\theta}{\partial x^2}$$

through

23) $$V = -2\nu \frac{\partial}{\partial x_i} \log \theta$$

However, (22) as always been considered as mathematical model ilustrating some features of turbulence. Probably because Burger's proposed, not deduced it, a precise physical meaning regarding turbulence had not been given previously to the equation. The name of "Burgilence" used by Saffman [5] (who quotes Cole) in his study of the equation reflects this feeling. This probably justifies why no attempt is known to generalize the model to 3-D.

As can be shown [6], the generalized equation (20) has the general solution

24) $$\phi = -2\nu \log \phi$$

and θ is a solution of

25) $\dfrac{\partial \theta}{\partial t} - \nu \nabla^2 \theta = \epsilon \theta$

which in itself is related to the solution of

26) $-\dfrac{\partial \theta^*}{\partial t} = \nu \nabla^2 \theta$

by

27) $\theta = \theta^* \exp \epsilon t$

So, the value of ϵ does not affect the value of V_i, and the mathematical heuristic approximation appears with some support.

3. APPROXIMATE SOLUTIONS

3.1. General remarks

Retracing steps taken so far, equation (11) express mathematically the model which emerges from the basic assumptions and is compatible with the classical Navier-Stokes equations. It is a quasi-linear equation of third order. Equations of this type have not deserved, until now, any detailed study, regarding their properties and behaviour. So, for the time beeing, we can only state some general properties and guess the others.

Regarding the behaviour, and extrapolating from linear equations, the behaviour seems to be "intermediate" between classical parabolic and hyperbolic, as long as they allow solutions typical of both types according to the value of the coeficients. However, in the quasi-linear equation, the higher order derivatives have the form

28) $\nu \dfrac{\partial \phi}{\partial x_j} \dfrac{\partial^3 \phi}{\partial x_j \, \partial x_i^2}$

with $\dfrac{\partial \phi}{\partial x_1}$, $\dfrac{\partial \phi}{\partial x_2}$, $\dfrac{\partial \phi}{\partial x_3}$ having, generally speaking, positive or negative signs. So, we expect the equation to have a behaviour typical of a mixed type, with the increased complexity of a change in type probably associated with the time, besides the space.

In what concerns boundary conditions its third order nature allows the specification of a non-slip boundary condition, besides the normal component of the velocity field in a solid boundary (in a way similar to the boundary-layer equations expressed in terms of stream function). Because the equation is of the second order in time a specification of ϕ and $\dfrac{\partial \phi}{\partial t}$ would also be necessary.

If we could find exact solutions for ϕ, we would get ρ and F from the continuity equation. The complexity of the equation prevents such hope for the near future (though a numerical solution seems presently at reach), so approximate solutions must be thought. Burger's model is one of such approximations.

In order to master the consequences of approximations involved, we first remark that the third order derivatives are a consequence of the transport or convective terms in the continuity equation i.e. $V_j \dfrac{\partial \log \rho}{\partial x_j}$ or $\dfrac{\partial \phi}{\partial x_j} \cdot \dfrac{\partial \log \rho}{\partial x_j}$

Besides, the third order derivative is important for the specification of the non-slip condition in a solid wall. Like in the boundary-layer approximation we can possibly infer that, far from the wall, these terms can be neglected. The set of fundamental equations would then reduce to

29) $\dfrac{\partial \phi}{\partial t} + \dfrac{1}{2} (\dfrac{\partial \phi}{\partial x_j})^2 - \nu \nabla^2 \phi = -F + \beta$

30) $\dfrac{\partial \log F}{\partial t} = -(\gamma-1) \nabla^2 \phi$

or

31) $F = \exp\{ -(\gamma-1) \displaystyle\int_{t_0}^{t} \nabla^2 \phi \, dt \}$

and

32) $\dfrac{\partial \phi}{\partial t} + \dfrac{1}{2} (\dfrac{\partial \phi}{\partial x_j})^2 - \nu \nabla^2 \phi + \beta = -\exp\{-(\gamma-1) \displaystyle\int_{t_0}^{t} \nabla^2 \phi \, dt \}$

which can be solved step by step starting from a known value of ϕ. For this, we first reduce (32) to the linear heat equation

$$\frac{\partial \theta}{\partial t} - \nu \nabla^2 \theta + \beta \theta = H(x_j) \theta$$

through

33) $\phi = -2\nu \log \theta$

with

34) $H(x_j) = F(t_0, x_j)$

The equation can also be solved by iteration.

In this approximation, we stress, the coupling between equations is retained though disregarding the transport terms in the continuity equation.

3.2. Mach number effects

The fundamental equations can be expressed in a slightly different form if the local Mach number is explicitly taken into account. This allows a straighfoward interpretation and an assimptotically exact solution for very high Mach numbers.

Because we assumed $P = C\rho^\gamma$, the local velocity of sound is given by

35) $a = \sqrt{\frac{dP}{d\rho}} = \sqrt{\gamma C \rho^{\gamma-1}}$

So, the local Mach number is, by definition

36) $M = \frac{\sqrt{(-\frac{\partial \phi}{\partial x_j})^2}}{a}$

Taking into account (35), (36), and (2), F can be expressed as

37) $F = \frac{1}{(\gamma-1)M^2} (\frac{\partial \phi}{\partial x_j})^2$

which introduced in the fundamental equation for ϕ, without body forces gives:

38) $\frac{\partial \phi}{\partial t} + (\frac{1}{2} + \frac{1}{(\gamma-1)M^2}) (\frac{\partial \phi}{\partial x_j})^2 - \nu \nabla^2 \phi = \beta$

which is another exact form for ϕ, the coupling with the continuity equation appearing now through M.

If

39) $M^2 >> \frac{2}{\gamma - 1}$

The equation is approximated by

40) $\frac{\partial \phi}{\partial t} + \frac{1}{2} (\frac{\partial \phi}{\partial x_j})^2 - \nu \nabla^2 \phi = \beta$

which is, again, the generalized Burger's equation.

The above result is formally exact for $M \to \infty$. However, as long as variations in M do not affect to much the coeficient of $(\frac{\partial \phi}{\partial x_j})^2$ in (38) (or if M can be approximated

by a known function of ϕ the exact solution is known [6]) we can probably infer that $M = \frac{2}{\gamma-1}$ is the boundary where the structure of the flow begins to change due to the progressive uncoupling with the continuity equation through the pressure.

For air, $\gamma = 1,4$ so the "transition" Mach number would be around

$M = \sqrt{5} - 2,23$

Though exact solutions for the initial value problem are known, the boundary value problem must also be considered as the simultaneous solution of the continuity equation.

The last one can be solved by standard methods provided the velocity field is known. The boundary value problem is reduced to the problem of the heat equation with non--linear boundary conditions. However, if solid walls are present, in the wall we can not have, obviously, $M > \frac{2}{\gamma-1}$, because M=0 and the third order derivatives must be taken into account, unless its effects can be expressed by suitable source terms or artificial boundary conditions.

Though definite conclusions regarding this point can not be stated, it seems that the boundary region is the only source of turbulence. At least for very high Mach numbers, turbulence production due to mean flow gradients appears to be an artificial device of the averaging process. The previous analysis, we must stress, was concerned with the instantaneous velocity field without any separation between mean and flutuating quantities. And the fact that quantitative estimates and assimptotically exact solutions were found starting from basic postulates is obviously an interesting and quite uncommon result...

3.3 - Further results

Once the physical basis of Burger's equation is known, all the mathematical studies already published gain a new value. These studies are all concerned with the equation

$$41) \quad \frac{\partial V}{\partial t} + V \frac{\partial V}{\partial x} = \frac{\partial^2 V}{\partial x^2}$$

without any reference to a velocity potential. The general behaviour, of the one-dimensional solution will not change, probably, when general 3D flows are considered.

There are, in the literature, many results concerned with these behaviour and also some obviously wrong statements. Beeing out of scope to review them here we refer the basic works of Cole (4) and Saffman (5). Intermitency, inadequacies of Fourrier Analysis and the questioning of Kolmogorov assumptions are remarkably considered by Saffman though in the conte.:t of homogeneous turbulence. Cole (4) deals with the shock wave behaviour and general mathematical properties. In fact, the equation has been used as a model in both contexts, an interesting fact of the present contribution beeing, we think, the unifying approach.

Though in a stage of devellopment, we shall refer some further results. The generalized version of the equation for which an exact solution was found, is:

$$42) \quad \frac{\partial \phi}{\partial t} + f(\phi) (\frac{\partial \phi}{\partial x_j})^2 = \nu \nabla^2 \phi$$

withfan arbitrary function of ϕ.These contains, obviously, the Burger's equation as the particular case $f = 1/2$, and will represent (36) if M can be expressed in terms of ϕ, (Q is eliminated by a straigthfoward transformation).

The exact solution of 42) is related to the solution of

$$43) \quad \frac{\partial \theta}{\partial t} = \nu \nabla^2 \theta$$

by the implicit relation given by

$$44) \quad \theta = A \int_{\phi_0}^{\phi} \exp\{ - \frac{1}{\nu} \int_{\lambda_0}^{\lambda} f(\tau) d\tau \} d\lambda$$

as shown in (6), with A, ϕ_0, λ_0, arbitrary constants to be choosen.

Because the integrand in (44) is always positive, there is a one to one relation between θ and ϕ, and because the initial value problem for θ has only one solution it follows that ϕ has also only one solution, whatever f (ϕ), provided it is continuous.

So, given an initial velocity field V_i^0, the initial potential is given by

$$45) \quad \phi_0 = \int_{-\infty}^{\infty} V_i dx_i$$

to which corresponds a $\theta(x_i, 0)$ given by (44).

The exact solution of 43) is then

$$46) \quad \theta = \frac{1}{(8\pi\nu t)^{3/2}} \iiint_{-\infty}^{\infty} \theta(x_1', x_2', x_3', 0) \exp\{ [(x_1-x_1')^2+(x_2-x_2')^2+(x_3-x_3')^2]/4\nu t \} dx_1', dx_2', dx_3'$$

and ϕ follows from (44), from which $V_i = \frac{\partial \phi}{\partial x_i}$ is found.

The above results apply to the initial value problem. The boundary value problem for θ is usually non-linear, if a non zero value is specified for V_i or ρV_i, except for

some special forms of $f(\phi)$.

However, because any solution of (43) transforms into a solution of (42), a particularly interesting result is obtained for harmonic oscilation in the boundary or by distributed point sources.

Because (43) admits the solution

$$47) \quad \theta = 1 + A e^{-kx} \cos(wt - \alpha x)$$

The corresponding one dimensional velocity field is, for the Burger's equation

$$48) \quad V = \frac{1}{1+A\theta} \frac{d\theta}{dx} = \frac{Ae^{-kx}\{a\,sen(\omega t-\alpha x)-k\cos(\omega t-\alpha x)\}}{1+Ae^{-kx}\cos(\omega t-\alpha x)}$$

This expression shows that the energy spectrum of V has all the frequencies multiples of ω, giving the familiar experimental shape. Besides, the two-point correlation curves have the usual form, as is easily verified.

We also notice that V is represented by a superposition of damped travelling waves which gives the usual shape to the space-time correlations. In these respect, quantitative test is in progress with the extremely limited experimental data available.

In a prospective line we must refer that to each frequency in (47) we associate an amplitude A_n. Besides, k and α, which are equal for (43) are taken in a coordinate

system mooving with the mean velocity. Scarcity of filtered space time correlations prevents, for the time beeing, any reliable conclusion, though preliminary results are quite encouraging.

References

1 - J.J.D.DOMINGOS - Le potentiel instantané de vitesses d'un fluide visqueux - Comptes Rendus, de l'Acad. Sciences, séance 14 Juin 1971, Paris 1971 (Also D.T.A. Report RC/3, Division of Applied Thermodynamics, Instituto Superior Técnico, Lisbon 1, 1971)

2 - J.J.D.DOMINGOS - General remarks concerning a new approach to a theory of viscous fluids, D.T.A. report RC/1, Division of Applied Thermodynamics, Instituto Superior Técnico, Lisbon 1, 1971)

3 - E. HOPF - Commun. Pure Appl. Math, 3, 1950, 201

4 - J.D. COLE - Quart. of App. Math. 9, 1951, 225

5 - P.G.SAFFMAN - "Topics in Nonlinear Physics" ed N. Zabuski, Berlin, Springer-Verlag, 1968, p.485.

6 - J.J.D.DOMINGOS - The non-linear equation $-\frac{\partial\phi}{\partial t} + f(\phi)(\nabla\phi)^2 = \mu\nabla^2\phi$

D.T.A. Report RC/2, Division of Appl. Thermodynamics, Instituto Superior Técnico, Lisbon 1, 1971)

Aknowledgements:

A TWO-LAYER MODEL OF HIGH-SPEED, THREE-DIMENSIONAL TURBULENT BOUNDARY LAYERS AND SUPERCRITICAL BOUNDARY LAYER-INVISCID FLOW INTERACTIONS

by

Barry L. Reeves
Avco Systems Division
Wilmington, Massachusetts U.S.A.

SUMMARY

A two-layer model of the three-dimensional compressible turbulent boundary layer is developed which is applicable to flows with pressure gradient and surface mass transfer. The model is based on the small cross-flow approximation in which the spreading metric is determined by the inviscid streamline pattern. A modified Mangler transformation is employed which permits transformation of the boundary layer equations to a two-dimensional form without transforming the turbulent stress or heat flux. It turns out that the computational speed of the method is rapid enough to enable equations for the inviscid stream deflection to be coupled with the present method for calculations of strong (supercritical) interactions, such as in the region downstream of the critical point in reattaching flows or in regions of strong blowing.

Solution of the inner (wall) layer for the velocity, enthalpy, stress and heat flux is obtained using mixing length theory and the thin layer Couette model. This solution is obtained without using a compressibility transformation and leads to a generalized compressible law of the wall with mass injection. In the outer wake layer an integral moment method is used along with appropriate matching conditions with the inner layer.

Several solutions and experimental comparisons are presented. In particular the effect of positive and negative pressure gradients on the relative scale of the inner and outer layers is demonstrated as well as the effect on the stagnation enthalpy-velocity relationship. Results are also presented for relaxing flows where C_f and $(2C_H/C_f)$ initially are far from their equilibrium values.

LIST OF SYMBOLS

Symbols		Symbols	
a	sonic velocity	m_e	$[(\gamma-1)/2]\,M_e^2$
a^*	$(1-\bar{U}_m)$	m	mass flux in inner layer
A^2	parameter in Crocco integral for wall layer, Eq. (24)	M	surface mass injection parameter $\rho_w\,\tilde{v}_w/\rho_e\,\tilde{v}_e$.
A_i	coefficients defined in Appendix 2	n	exponent of velocity profiles in outer layer, Eq. (35)
B	parameter in Crocco integral for wall layer, Eq. (25)	p	static pressure
$\bar{B}$	empirical "constant" in law of the wall	Pr_L	molecular Prandtl number
B_i	coefficients defined in Appendix 2	Pr_T	turbulent Prandtl number
C_f	skin friction coefficient, Eq. (38), $\tilde{C}_f = 2C_f$	q	heat flux
		$r(\tilde{x})$	spreading metric of inviscid streamlines
C_f'	$(u_r/u_e)^2$ or $(h_w/h_e)\,C_f$	Re_y	$y^+/(u_r/u_e)$
C_H	Stanton number	St	modified Stanton number, Eq. (37)
C_p	specific heat at constant pressure	$\tilde{u}, \tilde{v}$	velocity components in physical coordinates $\tilde{x}, \tilde{y}$, respectively
E_i	coefficients defined in Appendix 2	u, v	velocity components in transformed, "two-dimensional" coordinates x, y, respectively
F	inverse turbulent Reynolds number in outer layer, Eq. (48)	U, V	velocity components in transformed, constant density coordinates X, Y, respectively
h	static enthalpy		
h^+	h/h_w	$\bar{U}$	U/U_e
H	stagnation enthalpy	$\tilde{u}^+$	$\tilde{u}/\tilde{u}_r$
$\bar{H}$	H/H_e	$\tilde{u}_r$	friction velocity, $(\tau_w/\rho_w)^{1/2}$
I_i	coefficients defined in Appendix 2	$y_m(x)$	thickness of inner layer (match point)
J_i	flux integrals in inner layer, Eqs. (30) and (33), (34)	$\tilde{y}^+$	$\tilde{u}_r\,\tilde{y}/\nu_w$
		γ	ratio of specific heats
K	empirical constant in law of the wall, $K = 0.41$	δ	thickness of outer layer in transformed, constant density coordinates X, Y
ℓ	mixing length	δ_e	thickness of boundary layer (two-dimensional)
L	reference length in coordinate transformation, Eq. (6)	δ_i^*	"incompressible" displacement thickness
		δ^*	displacement thickness (two-dimensional)
M_e	Mach number at edge of boundary layer	θ	momentum thickness (two-dimensional)
m	exponent of stagnation enthalpy profiles in outer layer, Eq. (36)		

Symbols (Cont'd)   Symbols (Concl'd)

$\widetilde{\delta}_e, \widetilde{\delta}^*$ thickness and displacement thickness in physical coordinates

ρ density

τ stress

ϵ turbulent eddy viscosity

ϕ dimensionless mixing length function, Eq. (56)

η normalized coordinate in outer layer, Eq. (39)

ψ stream function

θ momentum thickness (two-dimensional)

Subscripts

$\widetilde{\theta}$ momentum thickness in physical coordinates

e edge of boundary layer

m at match point y_m

μ viscosity

o stagnation conditions behind normal shock

ν kinematic viscosity

s local stagnation conditions at edge of layer

ζ $\widetilde{u}/\widetilde{u}_e$

w wall conditions

aw adiabatic wall conditions

1. INTRODUCTION

Accurate prediction of turbulent boundary layers about reentry bodies is of critical importance in calculating wall friction and heat transfer, observables (initial conditions for near wake calculations), communication (guidance, and telemetry), and reentry aerodynamics in general. Recently, interest in maneuvering and lifting reentry vehicles has placed added emphasis on developing methods for predicting three-dimensional turbulent boundary layers over bodies at angle of attack and for predicting turbulent boundary layer separation and reattachment. Separation occurring on control surfaces and on the leeward side of bodies at angle of attack are problems of much interest, but are flows for which current theories are either incomplete or inadequate. For example, the wake-like model of turbulent separation and reattachment[1] has yet to be extended to three-dimensional flows, and the model itself is incapable of treating the important region downstream of the critical point in two-dimensional reattaching flows.

This paper presents a progress report on work being carried out under Air Force (Space and Missile Systems Organization) Contract F04701. The goal of this work is to produce a method which will yield wall conditions and boundary layer profiles sufficiently accurate for subsequent calculations of electron concentration through a three-dimensional turbulent boundary layer. The work is aimed at computing flow fields around arbitrary bodies at angle of attack, with particular emphasis on calculating boundary layers in strong positive and negative pressure gradients with surface mass injection. Entropy layer swallowing in regions downstream of a blunted nose is also being considered.

A two-layer model has been developed for this purpose in which an analytical solution for the inner layer, based on a compressible law of the wall, is matched with a moment integral method in the outer layer. Solution of the inner layer is obtained without the use of a compressibility transformation. In the outer layer the explicit appearance of the density is removed from the convective terms in the conservation equations without transforming the turbulent stress and heat flux.

The relative scale in inner and outer layers (location of the match point $\widetilde{y}_m$) is computed as an integral property of the flow and depends on the upstream history of the layer. At separation, for example, which now can be predicted by the model if the pressure distribution is prescribed, $\widetilde{C}_f \to 0$, $\widetilde{y}_m/\widetilde{\delta}_e \to 0$ and $(u/u_e)_m \to 0$ so that the boundary layer is dominated by the outer layer (or dominated by the "wake component" in the terminology of Coles[2]). One of the unique features of the model is that the stability of the system of ordinary differential equations can be used to establish upper and lower bounds on the turbulent production integral

$\int \tau \, du$ in the outer layer. Stable solutions up to Mach 10 for a wide range of wall to free stream temperature ratios show that compressibility has little effect on the properly normalized lateral stress profiles, confirming the results of Maise and McDonald.[3]

The computational speed of the method is sufficiently rapid that the whole boundary layer flow field on bodies at angle of attack can be calculated (except, of course, the leeward side at large angles of attack). It also appears that the computational speed is rapid enough to permit calculations of supercritical boundary layer-inviscid stream interactions.

The model is based on the small cross-flow approximation in which the boundary layer equations are solved along inviscid streamlines. In this coordinate system the cross-flow component of velocity in the layer is uncoupled from the streamwise momentum and energy equations and can be ignored as long as the approximation is valid. For flow around bodies at angle of attack, inviscid streamline patterns and the spreading metric are computed by integrating the inviscid momentum equation normal to inviscid streamlines on the body using either experimental or calculated inviscid pressure distributions.[4]

2. TURBULENT BOUNDARY LAYER MODEL

2.1 Equations of Motion and Coordinate Systems

If the boundary layer equations are written following inviscid streamlines and the cross flow in the boundary layer normal to the local inviscid streamline direction can be assumed small, the mean flow equations are

$$\frac{\partial}{\partial \widetilde{x}} (\rho \widetilde{u} r) + \frac{\partial}{\partial y} (\rho \widetilde{v} r) = 0 \qquad (1)$$

$$\rho\tilde{u}\,\frac{\partial\tilde{u}}{\partial\tilde{x}} + \rho\tilde{v}\,\frac{\partial\tilde{u}}{\partial\tilde{y}} = -\frac{dp_e}{d\tilde{x}} \cdot \frac{\partial r}{\partial\tilde{y}} \tag{2}$$

$$\rho\tilde{u}\,\frac{\partial\tilde{H}}{\partial\tilde{x}} + \rho\tilde{v}\,\frac{\partial H}{\partial\tilde{y}} = \frac{\partial}{\partial\tilde{y}}\,(q + \tilde{u}\,r) \tag{3}$$

where $r(\tilde{v})$ is the spreading metric determined by the inviscid flow streamline geometry. Here, since the cross-flow component of velocity is assumed small, the uncoupled cross-flow momentum equation is ignored and we assume furthermore that the additional contributions to turbulent stress and heat flux resulting from fluctuations in the cross flow velocity are likewise small.

Thus,

$$r = \mu\,\frac{\partial\tilde{u}}{\partial\tilde{y}} - \rho\,\overline{u'v'} \tag{4}$$

and

$$q = k\,\frac{\partial h}{\partial\tilde{y}} - \rho\,\overline{v'h'} \tag{5}$$

Clearly, for a body at large angle of attack these stress and heat flux models will break down in a region on the leeward side because strong cross flows with additional contributions to the Reynolds stress would have to be included along with interaction with the outer flow.

The explicit appearance of the spreading metric in the equations of motion can be eliminated by means of a modified Mangler transformation. Although it turns out that $r(\tilde{x})$ later appears in a constant of integration in the compressible law of the wall, the transformation is convenient since it is possible to remove r from the continuity equation without transforming the stress or heat flux. Letting

$$dx = \frac{r(\tilde{x})}{L}\,d\tilde{x} \quad\text{and}\quad dy = \frac{r(\tilde{x})}{L}\,d\tilde{y} \tag{6}$$

with

$$u = \tilde{u}, \quad v = \tilde{v} + \frac{\tilde{u}\,\tilde{y}}{r}\,\frac{dr}{d\tilde{x}} \tag{7}$$

Eqs. (1) through (3) become

$$\frac{\partial(\rho u)}{\partial x} + \frac{\partial(\rho v)}{\partial y} = 0 \tag{8}$$

$$\rho u\,\frac{\partial u}{\partial x} + \rho v\,\frac{\partial u}{\partial y} = -\frac{dp_e}{dx} + \frac{\partial r}{\partial y} \tag{9}$$

$$\rho u\,\frac{\partial H}{\partial x} + \rho v\,\frac{\partial H}{\partial y} = \frac{\partial}{\partial y}\,(q + u\,r) \tag{10}$$

where r and q are still defined by Eqs. (4) and (5). Solution of the inner layer is obtained directly using Eqs. (8) - (10) without further transformation of the coordinates to remove the explicit appearance of the density. The reason for this is two fold. First, within the framework of the present model for the inner layer an analytic solution can be obtained without introducing a compressibility transformation. Thus, no useful simplification would be provided by such a transformation. Second, Maise and McDonald[3] have shown that a compressibility transformation leads to generally poor results for the turbulent stress distributions across the boundary layer even for constant pressure, adiabatic flows. They also showed poor correlation of experimental velocity profiles using the transformation for constant pressure flows with heat transfer. More recently, Lewis et al.[5] attempted to generalize Coles' transformation but they also found significant deviation between experimental velocity profiles and profiles predicted using the the transformation, especially in the wall layer. They showed that the discrepancy between profiles increased with increasing Mach number so that for flow on a flat plate at Mach 6, for example, a difference of 20 percent in velocity profiles can be expected. Although not all of this discrepancy should be attributed to the transformation, there appears to be little justification for using it in the wall layer particularly in flows with heat transfer and pressure gradient.

In the outer wake-like layer, however, where we use an integral moment method, a simple compressibility transformation is used to remove the explicit appearance of the density from Eqs. (8) through (10). This can be accomplished without transforming the stress and heat flux by letting

$$dX = dx, \quad dY = \frac{a_e}{a_o}\,\frac{\rho}{\rho_o}\,dy \tag{11}$$

$$Y = \dot{U}, \quad U = (a_o/a_e)u \tag{12}$$

$$V = \frac{\rho}{\rho_o} \; v + U \; \frac{\partial Y}{\partial x}$$

so that Eqs. (8) through (10) become

$$\frac{\partial U}{\partial X} + \frac{\partial V}{\partial Y} = 0 \tag{13}$$

$$U \; \frac{\partial U}{\partial X} + V \; \frac{\partial U}{\partial Y} = (H/H_e) \, U_e \; \frac{dU_e}{dX} + \frac{a_o}{a_e \, \rho_o} \; \frac{\partial r}{\partial Y} \tag{14}$$

$$U \; \frac{\partial H}{\partial X} + V \; \frac{\partial H}{\partial Y} = \frac{1}{\rho_o} \; \frac{\partial}{\partial Y} \left(q + \frac{a_e}{a_o} \, Ur \right) . \tag{15}$$

Here r and q are still the physical stress and heat flux defined by Eqs. (4) and (5). Eqs. (13) through (15) are used to develop the integral moment equations for the outer layer.

With the equations of motion and proper coordinate systems developed for the inner and outer layers, we now proceed to the turbulence model used in the two-layer model.

2.2 Turbulence Model

In order to develop a scheme for integrating Eqs. (1)-(3), or their transformed counterparts Eqs. (8)-(10), it is necessary to have some knowledge either of the relationships between r, q and the mean flow quantities p, u, H (provided such relationships exist) or have additional independent differential equations for r and q. Several model equations[6,7] for the stress and heat flux based on the latter approach have been developed recently and, hopefully these will provide new insight into the way the stress and heat flux respond to changes in boundary conditions as the flow proceeds downstream. To date, however, all these approaches using differential equations for r and q have had to invoke assumptions for closure of the unknown correlation functions which are either pure hypothesis or whose physical basis has only been demonstrated in incompressible flows. At moderate Mach numbers, however, say up to $M_e \cong 7$ there is considerable experimental evidence that the turbulent boundary layer may be divided into an inner wall layer and an outer wake layer, as in incompressible flow. In the wall layer the properly normalized experimental velocity and enthalpy profiles have been shown to be functions of the local wall stress, heat flux and injection rate and except for the streamwise variations of these quantities are more or less independent of the upstream history of the layer.[8,9] This is precisely the result predicted by mixing length theory and the thin layer, Couette model, which leads to a compressible law of the wall and a Crocco integral for the inner layer. For flows with surface mass injection Danberg and Squire have shown that this same model accurately predicts the velocity distribution in the wall layer. In fact, the experimental evidence for the Van Driest[10] form of the law of the wall for $M = 0$ and the Squire form of this law for $M \neq 0$ is now so strong that the model equations for the turbulent stress either "reduce" to this law near the wall or are matched to it.

In this paper a first approximation for the velocity and enthalpy profiles in the inner layer is used in which the laminar sublayer and transition layer is neglected and the flow is assumed to be fully turbulent to the wall. Maise and McDonald have shown that in this region the mixing length varies linearly away from the wall, i.e. $\ell = K \, \tilde{y}$ with $K = 0.41$, for Mach numbers up to about five. Thus, with the additional assumption that $Pr_t = 1$ in the first approximation, the stress and heat flux in the inner layer are

$$r \cong \rho \, K^2 \, \tilde{y}^2 \, (\partial \tilde{u} / \partial \tilde{y})^2 \tag{16}$$

$$q \cong \rho \, K^2 \, \tilde{y}^2 \, (\partial \tilde{u} / \partial \tilde{y}) \, (\partial h / \partial \tilde{y}) \tag{17}$$

The error incurred in computing integral properties such as θ and the wall stress by neglecting the sublayer is small, except, perhaps, in very strong negative pressure gradients. Second approximation profiles are subsequently computed which include the laminar contribution to the total stress and are not restricted to $Pr_t = 1$ or $Pr_L = 1$.

The evaluation of the stress and heat flux in the outer layer is much more questionable. Bradshaw concluded, from his measurements in relaxing incompressible boundary layers, that the stress in the outer layer depends on the whole history of the layer and cannot be found from local mean flow properties as in equilibrium layers. Thus, according to Bradshaw and others, the use of an eddy viscosity or mixing length theory in the outer layer of rapidly adjusting flows must be held suspect because for these flows there is no simple relationship between the turbulent stress and mean velocity gradient. If this is the case, then the relative scale of the inner and outer layers, $\tilde{y}_m$, likewise cannot be determined from the local velocity gradient, as is usually assumed in conventional finite difference methods,[11,12] for example, but must be found from the whole history of the flow. In the present theory we have attempted to avoid using a simple local relation for determining $\tilde{y}_m$. By taking a higher moment of the momentum equation, $\tilde{y}_m$ is found as one of the integral properties of flow.

In the present two-layer model it turns out that a relation for the stress along the match point $\widetilde{y}_m$ is required along with a relation for the "production" integral in the outer layer

$$\int (\tau/\tau_m)\,du$$

The stress along the match point is evaluated using an eddy viscosity normalized by the constant density displacement thickness, as was suggested by the calculations of Maise and McDonald. Thus along $\widetilde{y}_m$

$$\tau_m = \rho_m \epsilon_m \ (\partial\widetilde{u}/\partial\widetilde{y})_m \tag{18}$$

where

$$\epsilon = F\,u_e\,\widetilde{\delta}_i^* \ , \quad F = \text{constant} \tag{19}$$

Thus, while the evaluation of τ_m is subject to some of the objections of "localness," the location of the match point $\widetilde{y}_m$ where ϵ_m is evaluated depends on the upstream history of the layer.

It turns out the two-layer model provi.' ' upper and lower bound on the magnitude of the production integral. If estimates for this integral a: . ∶ which are too small or too large, integrations of the system of equations downstream develop instab. ∶s where $\overline{U}_m\to 1$ for the former and $n\to\infty$ for the latter. Thus, we find that the production integral over the outer layer cannot be assumed negligibly small nor can it be evaluated using a constant eddy viscosity across the outer, as was suggested by Clauser.[13] Both assumptions give unstable solutions, although the Clauser assumption is stable for Mach numbers below about 2.5.

By evaluating the production integral as though the density were constant across the outer layer and by using a cubic variation of ϵ between $\widetilde{y}_m$ and $\widetilde{\delta}_e$ with $\epsilon\to 0$ at the outer edge, stable solutions have been obtained up to Mach 10 for wall to free stream stagnation temperature ratios between 0.05 and 1.0. These results for the bounds on the production integral and the assumptions used to produce stable solutions verify to some extent the results of Maise and McDonald who showed that compressibility has little effect on the lateral stress profiles (when normalized by the wall stress) up to about Mach 5. A cubic variation of ϵ for $\widetilde{y}_m < \widetilde{y} < \widetilde{\delta}_e$ is also consistent with the ϵ variations inferred by Maise and McDonald and Bradshaw.[14]

3. SOLUTION OF INNER LAYER AND MATCHING CONDITIONS

Experiments in compressible turbulent boundary layers with moderate pressure gradients and surface mass injection have shown that even at hypersonic speeds there is an inner (wall) layer in which velocity and temperature gradients normal to the surface are so large that terms involving x derivatives in the conservation equations are generally negligible. The lateral extent of this inner layer $\widetilde{y}_m$ at any given point $\widetilde{x}$ is determined by previous history of the layer and by local conditions such as magnitude and sign of the pressure gradient or strength of injection. In large positive pressure gradients or with large blowing the extent of the inner layer may become vanishingly small, while in negative pressure gradients $\widetilde{y}_m$ may approach the edge of the layer.

With mixing length theory used to determine the stress and heat flux, and a thin layer Couette model of the flow near the wall, a generalized law of the wall for the velocity and enthalpy with surface mass injection is obtained. These velocity and enthalpy profiles are then inserted back into the full continuity, momentum and energy equations, which are integrated away from the surface to give the stress, heat flux and mass flux at the outer edge of the inner layer. The velocity, enthalpy, stress, heat flux and mass flux at the edge of the wall layer can be obtained analytically, and these expressions, along with certain auxiliary relations for normal and streamwise derivatives of the velocity and enthalpy, are used for matching with the integral method in the outer layer. One of the key features of the present two layer model is that the integral equations in the outer layer ultimately determine the lateral extent of the wall layer (or in Coles terminology the strength of the wake component); it is not specified implicitly in advance in terms of the eddy viscosity or mixing length as in most finite difference methods.

With the possible exception of boundary layers in very strong pressure gradients we assume that a wall layer exists in which $\ell = K\widetilde{y}$ and the velocity and enthalpy profiles are closely approximated by a Couette flow model. Neglecting the laminar sublayer (in the first approximation) and setting $Pr_t = 1$, the equations for the stress and heat flux obtained by integrating the momentum and energy equations away from the surface are

$$\tau(\widetilde{y}) = \tau_w + \rho_w\widetilde{v}_w\widetilde{u} \equiv \rho K^2 \widetilde{y}^2 \left(\frac{\partial\widetilde{u}}{\partial\widetilde{y}}\right)^2 \tag{20}$$

$$q(\widetilde{y}) = q_w - \widetilde{u}\,\tau(\widetilde{y}) + \rho_w\widetilde{v}_w(H - H_w) \equiv \rho K^2 \widetilde{y}^2 \left(\frac{\partial\widetilde{u}}{\partial\widetilde{y}}\right)\left(\frac{\partial b}{\partial\widetilde{y}}\right) \tag{21}$$

Dividing the second equation by the first and integrating the result gives a Crocco integral, which is always valid in the inner layer only, independent of pressure gradient or surface mass injection.

$$H/H_w = 1 + B\,(\widetilde{u}/\widetilde{u}_e) \tag{22}$$

or

$$b/h_w = 1 + B(\widetilde{u}/\widetilde{u}_e) - A^2(\widetilde{u}/\widetilde{u}_e)^2 \qquad (23)$$

where

$$A^2 = [m_e/(1 + m_e)](H_e/H_w) \qquad (24)$$

$$B = [2 m_e/(1 + m_e)](H_e/H_w)(St/C_f) \qquad (25)$$

Substituting for $\rho = \rho_w(h_w/h)$ in the expression for $r(\widetilde{y})$, defining $M = \rho_w \widetilde{v}_w/\rho_e \widetilde{u}_e$ and integrating from the edge of the laminar sublayer to any point $\widetilde{y}^+ = \widetilde{y} u_\tau/\nu_w$, with $\xi = \widetilde{u}/\widetilde{u}_e$, gives

$$\int_{\xi_s}^{\xi} \frac{d\xi}{[(b/h_w)(1 + B\xi - A^2\xi^2)]^{1/2}} = \left[(1 + m_e)\frac{H_w}{H_e}\right]^{1/2} \frac{1}{K} \ln \frac{\widetilde{y}^+}{\widetilde{y}_s^+}$$

which can be written, after changing the limits of integration

$$(h_w/h_e)^{-1/2} \int_0^{\xi} \frac{d\xi}{[(b/h_w)(1 + B\xi - A^2\xi^2)]^{1/2}} = \frac{1}{K} \ln \widetilde{y}^+ + \overline{B}$$

where B is the empirical "constant"

$$\overline{B} \equiv -\frac{1}{K} \ln \widetilde{y}_s^+ + (h_w/h_e)^{-1/2} \int_0^{\xi_s} \frac{d\xi}{[(b/h_w)(1 + B\xi - A^2\xi^2)]^{1/2}}$$

Whereas in incompressible flow $\overline{B} \simeq 5$, the experiments of Danberg and Squire have demonstrated that $\overline{B}$ is a function of M and H_w/H_e, which can be approximated by the curve fits:

$$0 < M_e < 3.5 : \overline{B}/\overline{B}_{M=0} = 1 - 0.6 \times 10^3 M (M_e/3.5)^{3/2}$$

$$M_e > 3.5 : \overline{B}/\overline{B}_{M=0} = 1 - 0.6 \times 10^3 M$$

with

$$\overline{B}_{M=0} = 5 + 8(1 - H_w/H_e), \quad \overline{B} \geq 0$$

Defining*

$$C_1 = (B - \sqrt{B^2 + 4A^2})/2A^2, \quad C_2 = (B + \sqrt{B^2 + 4A^2})/2A^2$$

$$C_3 \equiv C_f/M, \quad k^2 \equiv (C_2 - C_1)/(C_3 + C_2), \quad \sin^2\theta \equiv (C_2 - \xi)/(C_2 - C_1)$$

and since $\ln \widetilde{y}^+ = \ln \widetilde{y}^+ + \ln L/r$

the compressible law of the wall becomes

$$-2\left[\frac{h_w/h_e}{A^2 M(C_3 + C_2)}\right]^{1/2} [\mathcal{F}(\theta, k) - \mathcal{F}(\theta_{\xi=0})k)] = \frac{1}{K} \ln [(C_f')^{1/2} Re_y]$$

$$+ \frac{1}{K} \ln \frac{L}{R} + \overline{P} \qquad (26)$$

where

$$\mathcal{F}(\theta, k) \equiv \int_0^{\theta} \frac{d\theta}{(1 - k^2 \sin^2\theta)^{1/2}} \qquad (27)$$

---

*For large blowing, $\sin^2\theta$ and k^2 are redefined, i.e. $k^2 \equiv (C_3 + C_2)/(C_2 - C_1)$ and $\sin^2\theta \equiv (C_2 - \xi)/(C_2 + C_3)$ so that k^2 is always less than one.

$$y^* = y\,u_r/\nu_w = (C_f')^{1/2}\,Re_y \tag{28}$$

$$Re_y = \frac{\rho_s}{\rho_o}\left(\frac{\rho_o\,a_o}{\mu_o}\right)\left(\frac{H_e}{H_w}\right)^2\,(1+m_e)^{-\frac{(3\gamma-1)}{2(\gamma-1)}}\,M_e\,y \tag{29}$$

For $M = 0$, $k = 0$ and the elliptic integrals $\mathcal{F}(\theta,k)$ reduce to arcsin functions, and the law of the wall is given by the Van Driest "generalized" velocity distribution.[10] Evaluating the law of the wall at y_m gives the velocity ratio $(u/u_e)_m = \bar{U}_m$ along the match point. Actually, what we require for matching with the outer layer is the streamwise derivative of $(u/u_e)_m$, which is found by differentiating the law of the wall.

With the velocity profile given by the law of the wall and the enthalpy profile given by the Crocco integral in the inner layer, exact expressions for the stress and heat flux at y_m can be obtained by integrating the momentum and energy equations away from the surface, i.e.,

$$\tau_m - \tau_w = \frac{dp}{dx}\,y_m + \int_0^{y_m}\left(\rho u\,\frac{\partial u}{\partial x} + \rho v\,\frac{\partial u}{\partial y}\right)dy$$

$$= \frac{dp}{dx}\,y_m + \frac{d}{dx}\int_0^{y_m}\rho u\,(u-u_m)\,dy + \int_0^{y_m}\rho u\,dy\cdot\frac{du_m}{dx} + \rho_w\,v_w\,u_m$$

and

$$(q + u\,\tau)_m - q_w = \int_0^{y_m}\left(\rho u\,\frac{\partial H}{\partial x} + \rho v\,\frac{\partial H}{\partial y}\right)dy$$

$$- \frac{d}{dx}\left[\frac{H_w\,B}{u_e}\int_0^{y_m}\rho u\,(u-u_m)\,dy\right] + \int_0^{y_m}\rho u\,dy\cdot\frac{dH_m}{dx} + \left(\frac{H_w\,B}{u_e}\right)\rho_w\,v_w\,u_m$$

where the integrals in these expressions are evaluated using Eqs. (23) and (26). For example if

$$J_1 = \int_0^{y_m}\frac{\rho u}{\rho_w\,u_e}\,dy \quad\text{and}\quad J_2 = \int_0^{y_m}\frac{\rho u}{\rho_w\,u_e}\left(\frac{u}{u_e} - \frac{u_m}{u_e}\right)dy \tag{30}$$

then

$$J_i = \frac{K\,\nu_w}{u_r}\,\frac{u_e}{u_r}\,e^{-K\bar{B}}\int_0^{\bar{U}_m}\frac{i_i\,\exp\{a\,f(\xi)\}}{(h/h_w)^{3/2}\left(1+\frac{M}{C_f}\,\xi\right)^{1/2}}\,d\xi \tag{31}$$

which can be integrated repeatedly by parts if

$$a = K(u_e/u_r), \quad Z = \exp\{a\,f(\xi)\}$$

$$f(\xi) = \int_0^{\bar{U}_m}\frac{d\xi}{(h/h_w)^{1/2}\left(1+\frac{M}{C_f}\,\xi\right)^{1/2}}, \quad g(\xi) = \frac{i_i}{a(h/h_w)}$$

$$i_i = \xi \quad\text{for } J_1, \quad i_i = \xi(\xi - \bar{U}_m) \quad\text{for } J_2$$

to give

$$\int g(\zeta)\,d\gamma \quad \exp\{a f(\zeta)\} \Big|_f \; g(\zeta) \; \cdot \; \frac{g(\zeta)}{af'(\zeta)} \; \cdot \; \frac{1}{a^2 f'(\zeta)} \; \frac{d}{d\zeta}\left(\frac{g'}{f'}\right) \cdots \Big| \tag{32}$$

where $\frac{1}{a} \sim \mathcal{O}(C_f^{1/2}) \cdots 1$. By approximating $h\cdot h_e \simeq h_m/h_w$ in $f(\zeta)$ and $g(\zeta)$ and $\left(1 \cdot \frac{M}{C_f}\zeta\right) \simeq \left(1 \cdot \frac{M}{C_f}\bar{U}_m\right)$ in $f(\zeta)$ the above series truncates with the term $\mathcal{O}(a^{-1})$ for J_1, and $\mathcal{O}(a^{-2})$ for J_2 so that*

$$J_1 \quad \frac{\bar{U}_m y_m}{(h_m\cdot h_w)} \; - \; \frac{1}{K}\left(\frac{u_f}{u_e}\right)\frac{y_m}{(h_m/h_w)^{1/2}} \quad \left(1 \cdot \frac{M}{C_f}\,\bar{U}_m\right)^{1/2} \tag{33}$$

$$J_2 \quad - \frac{1}{K}\left(\frac{u_f}{u_e}\right)\frac{\bar{U}_m y_m}{(h_m/h_w)^{1/2}} \left(1 \cdot \frac{M}{C_f}\,\bar{U}_m\right)^{1/2} \cdot \frac{2}{K^2}\left(\frac{u_f}{u_e}\right)^2 y_m \left(1 \cdot \frac{M}{C_f}\,\bar{U}_m\right) \tag{34}$$

The expressions for J_1 and J_2 are the key results for the evaluation of the stress, heat flux and mass flux in the inner layer. With J_1 and J_2 given by Eqs. (33) and (34) the evaluation of r_m and $(q \cdot u\,r)_m$ is straightforward (although somewhat lengthy) and the results are given in Appendix 1.

Solution of wall layer for the velocity, enthalpy stress and heat flux has been obtained an. ytically in terms of the given wall and edge conditions ($M_e, H_w/H_e$ and M); three "parameters" (y_m, C_f and St), and two empirical "constants" (K and $\bar{B}$). By matching this liner solution with an integral moment method for the outer layer the three "parameters" y_m, C_f and St are determined. In addition to u/u_e, H/H_e, r and q, $\cdots$ ∂y and $\partial H \cdot \partial y$ are also matched and the expressions are given in Appendix 1 along with certain other auxiliary expressions (such as $d\bar{U}_m/dx$, $d\bar{H}_m/dx$, etc.) required for the matching.

4. MOMENT INTEGRAL METHOD FOR OUTER LAYER

In order to determine the relative scale of the inner and outer layers, y_m, and the quantities r_m and q_m, which are related to the quantities of interest, namely C_f and St, in the equations given in Appendix 1, a moment integral method is used in the outer layer. In this layer independent two-parameter families of profiles are chosen for u and H. The "free" parameters of the profiles are determined implicitly by matching with relations obtained for the inner layer (law of the wall and Crocco integral) for u and H and the lateral and streamwise derivatives of these quantities along the unknown match point y_m. The profiles selected are power-laws of the form

$$\bar{U} \; U/U_e \; = \; 1 - (1 - \bar{U}_m)(1 - \eta)^n, \quad n > 0 \tag{35}$$

$$\bar{H} \; H/H_e \; = \; 1 - (1 - \bar{H}_m)(1 - \eta)^m, \quad m > 0 \tag{36}$$

so that very "full" profiles without overshoot are possible with $n, m \gg 1$. In order for a Crocco integral to exist in the outer layer m must equal n but in general this will not be true. In fact, in terms of the more conventional definitions

$$C_H \quad - q_w/(H_w - H_e)\rho_e u_e \; - \; \frac{2 m_e \; St}{(1 \cdot m_e)(1 - H_w/H_e)} \tag{37}$$

$$\tilde{C}_f \; = \; 2\tau_w/\rho_e u_e^{2} \quad 2C_f \tag{38}$$

it is easy to show, using Eq. (A 1-2) and the definition of H that a Crocco integral ($m \; n$) exists in the outer layer only when the Reynolds analogy holds, i.e., when $C_H \; \tilde{C}_f/2$.

In the above profile families

$$\eta \; (Y - Y_m) \, \delta \tag{39}$$

where δ is the thickness of the outer layer in the transformed coordinate

$$Y - Y_m \quad \int_{Y_m}^{Y} \frac{a_e \rho}{a_0 \rho_0} \; dy \tag{40}$$

The momentum integral, first velocity moment and energy integral for the outer layer are obtained by integrating the transformed conservation equations from $Y = Y_m$ to $Y \;\;\; _m \cdot$

---

*These approximations yield identical results for the leading term of the series as the exact expressions for 1 and g, and are used here merely to simplify the task of differentiating J_2.

Momentum Integral – Outer Layer

$$
\left.
\begin{aligned}
&-\delta A_i \frac{d\bar{U}_m}{dx} \;+\; \delta A_2 \frac{dn}{dx} \;+\; I_5 \frac{d\delta}{dx} \;+\; (\rho_s/\rho_o)(1+m_e)^{\frac{-(\gamma+1)}{2(\gamma-1)}} \cdot M(1-\bar{U}_m) \\[2mm]
&-(1-\bar{U}_m)\left(\frac{1}{\rho_o U_e}\frac{d\dot m}{dx}\right) \;+\; (E_1 - I_4 - I_2)\frac{\delta}{M_e}\frac{dM_e}{dx} \;-\; \left(\frac{a_o}{U_e^2 \, a_e \, \rho_o}\right) r_m
\end{aligned}
\right\}
\tag{41}
$$

First Velocity Moment – Outer Layer

$$
\left.
\begin{aligned}
&-\delta A_3 \frac{d\bar{U}_m}{dx} \;+\; \delta A_4 \frac{dn}{dx} \;+\; I_6 \frac{d\delta}{dx} \;+\; (\rho_s/\rho_o)(1+m_e)^{\frac{-(\gamma+1)}{2(\gamma-1)}} \cdot M(1-\bar{U}_m^2) \\[2mm]
&-(1-\bar{U}_m^2)\left(\frac{1}{\rho_o U_e}\frac{d\dot m}{dx}\right) \;-\; (2E_2 - I_6 - 2 I_3)\frac{\delta}{M_e}\frac{dM_e}{dx} \\[2mm]
&\hspace{3cm} -2\left(\frac{a_o}{U_e^2 \, a_e \, \rho_o}\right) r_m \,(\bar{U}_m + a_o)
\end{aligned}
\right\}
\tag{42}
$$

Energy Integral – Outer Layer

$$
\begin{aligned}
&-\delta B_3 \frac{d\bar{U}_m}{dx} \;+\; \delta B_4 \frac{dn}{dx} \;+\; E_4 \frac{d\delta}{dx} \;+\; \delta B_1 \frac{d\bar{H}_m}{dx} \;+\; \delta B_2 \frac{dm}{dx} \\[2mm]
&+ (\rho_s/\rho_o)(1+m_e)^{\frac{-(\gamma+1)}{2(\gamma-1)}} \cdot M(1-\bar{H}_m) \;-\; (1-\bar{H}_m)\left(\frac{1}{\rho_o U_e}\frac{d\dot m}{dx}\right) \\[2mm]
&= -E_4 \frac{\delta}{M_e}\frac{dM_e}{dx} \;-\; \left(\frac{1}{\rho_o U_e H_e}\right) q_m \;-\; \left(\frac{a_e}{\rho_o a_o H_e}\right)\bar{U}_m r_m
\end{aligned}
\tag{43}
$$

where the integral functions A_i, B_i, E_i and I_i are given in Appendix 2. The equations for $\dot m/\rho_o U_e$ and the normalized stress and heat flux at y_m, obtained from the inner layer, are given in Appendix 1. The term involving the integral of the turbulent stress across the outer layer in the velocity moment (called the turbulent production by Townsend) is

$$
a_o = \int_0^1 \frac{r}{r_m}\left(\frac{\partial \bar{U}}{\partial \eta}\right) d\eta
\tag{44}
$$

According to the work of Maise and McDonald, there is virtually no effect of compressibility on the _normalized_ stress distribution, r/r_m, across the turbulent boundary layer. Thus, we can evaluate r/r_m as though the density is constant, i.e.,

$$
\frac{r}{r_m} = \left(\frac{\epsilon}{\epsilon_m}\right)\frac{(\partial \bar{U}/\partial \eta)}{(\partial \bar{U}/\partial \eta)_m}
\tag{45}
$$

Since $\epsilon \to 0$ at the edge of the layer, the lateral variation of ϵ in the outer layer can be approximated by

$$
\epsilon/\epsilon_m = 1 - \eta^\omega
\tag{46}
$$

where, according to measurements by Bradshaw and the analysis of data for supersonic layers by Maise and McDonald, ω has a value around 2 or 3. On the basis of stability of solutions over a wide range of Mach numbers we tentatively select the value $\omega = 3$ (see discussion in Sections 2 and 7).

Finally, a relation for r_m is obtained in terms of the eddy viscosity and velocity gradient at the matching point y_m. Following the suggestion of Herring and Mellor and the results of Maise and McDonald, the scale length for the eddy viscosity is the constant density displacement thickness

$$
\tilde{\delta}_i^* = \int_0^{\tilde{\delta}_e} (1 - u/u_e)\, dy
\tag{47}
$$

and

$$\tau_m \quad F u_e \, \widetilde{\delta}_i^* \qquad F \cong 0.018 \tag{48}$$

Then, since

$$\tau_m \quad \rho_m \, \tau_m \, (\partial \widetilde{u} \, / \partial \widetilde{y})_m$$

and $(\partial \widetilde{u} \, / \partial \widetilde{y})_m$ is known from the solution of the inner layer, the normalized stress along y_m is given by

$$\left(\frac{\tau_o}{U_e^2 \, a_e \, \rho_o} \right) \quad \tau_m \quad (\rho_s / \rho_o)^2 \, (1 + m_e)^{-\frac{(\gamma+1)}{\gamma-1}} \quad \frac{F \cdot (\delta_i^* / \delta) \, a^* \, n}{\left[\overline{H}_m \cdot m_e \, (\overline{H}_m - \overline{U}_m^2) \right]^2} \tag{49}$$

With the three integral equations for the outer layer, the above equation for τ_m, and the matching relations from the inner layer, the system of ordinary differential equations can be integrated downstream. Since the solution of the inner layer involves three "parameters" (C_f, S_t and y_m) and the unknown in the outer layer is δ, these four quantities must be specified at the initial station in order to form all other quantities (n, m, etc) and all the initial streamwise derivatives.

5. INITIAL CONDITIONS AND INTEGRAL THICKNESSES

Instead of having to specify y_m and δ along with C_f and S_t at the initial station $\widetilde{x} = 0$, it is more convenient to specify θ and δ_e, the momentum thickness and thickness of the layer. From the equations for J_1 and J_2 in the inner layer and the integral functions in the outer layer one obtains the following:

$$\delta_e \quad y_m \cdot (\rho_o / \rho_s)(1 + m_e)^{\frac{\gamma+1}{2(\gamma-1)}} \, \left[(1 + m_e) E_1 - m_e \, I_2 \right] \delta \tag{50}$$

$$\theta \quad \frac{\overline{U}_m (1 - \overline{U}_m) \, y_m}{(h_m / h_e)} \cdot \frac{C_f^{1/2} \, y_m}{K \, (h_m / h_e)^{1/2}} \quad (2 \overline{U}_m - 1) \, \beta_o - (2/K^2) \, C_f \, y_m \, \beta_o^2$$
$$\cdot (\rho_o / \rho_s)(1 + m_e)^{\frac{\gamma+1}{2(\gamma-1)}} \, [I_1 - I_2] \delta \tag{51}$$

$$\delta'' \quad \left[1 - \frac{\overline{U}_m}{(h_m / h_e)} \right] \, y_m \quad \frac{C_f^{1/2} \, y_m \, \beta_o}{K \, (h_m / h_e)^{1/2}}$$
$$\left. \cdot (\rho_o / \rho_s)(1 + m_e)^{\frac{\gamma+1}{2(\gamma-1)}} \, [(1 + m_e) E_1 - m_e \, I_2 - I_1] \delta \right\} \tag{52}$$

$$\delta_i^* \quad y_m (1 - \overline{U}_m) + (C_f \, h_m / h_e)^{1/2} \, (y_m \, \beta_o / K) \tag{53}$$

Also,

$$\delta_e \quad (\tau / L) \, \widetilde{\delta}_e, \quad \delta^* \quad (\tau / L) \, \widetilde{\delta^*}, \quad \theta \quad (\tau / L) \, \widetilde{\theta} \tag{54}$$

By specifying C_f, C_H, δ_e and θ at the initial station the above expressions and matching conditions are used to calculate the remaining unknowns: y_m, $\overline{U}_m$, δ, m, n, $\overline{H}_m$, and B.

6. FINAL VELOCITY AND ENTHALPY PROFILES

Since at hypersonic speeds the peak boundary layer temperature can occur well within the wall layer, accurate velocity and enthalpy profiles near the wall are required. In order to avoid the logarithmic singularity at the surface given by the law of the wall the laminar sublayer and transition layer are included in the determination of final profiles (as well as arbitrary laminar and turbulent Prandtl numbers) so that $\widetilde{u} \quad 0$ at $\widetilde{y} = 0$. This is accomplished by including the laminar contribution to the total stress and heat flux in the expressions for $\tau(\widetilde{y})$ and $q(\widetilde{y})$ in the wall layer and by using the Van Driest variation for the dimensionless mixing length Φ, i.e.,

$$\Phi \quad K \widetilde{y} \, [1 - \exp(-\widetilde{y} / a)] \tag{55}$$

where

$$\Phi(\widetilde{y}^\cdot, a) \quad \widetilde{u}, f \quad \iota_{\mathbf{w}} .$$ (56)

For adiabatic flows with M 0 , a is a constant and equals the incompressible value a 25. For cold walls and M $\neq$ 0 the experimental velocity profiles of Danberg and Squire (that is the shift in the value of $\bar{B}$) indicate large variations in a. The determination of a from these experimental profiles is discussed below.

Introducing the normalized wall layer variables

$$\widetilde{u}^\cdot \quad \widetilde{u}/\widetilde{u}_r, \quad h^\cdot \quad h/h_{\mathbf{w}}, \quad \widetilde{y}^\cdot \quad \widetilde{u}_r\, \widetilde{y}/\iota_{\mathbf{w}}$$

the differential equations for $\widetilde{u}^\cdot$ and $h^\cdot$ obtained from the equations for the total stress and heat flux become

$$\frac{\Phi^2}{h^\cdot}\left(\frac{d\widetilde{u}^\cdot}{d\widetilde{y}^\cdot}\right)^2 \cdot h^\cdot \frac{d\widetilde{u}^\cdot}{d\widetilde{y}^\cdot} = 1 \cdot (\widetilde{v}_{\mathbf{w}}/\widetilde{u}_r)\widetilde{u}^\cdot \tag{57}$$

$$\frac{\Phi^2}{h^\cdot\, Pr_t}\left(\frac{d\widetilde{u}^\cdot}{d\widetilde{y}^\cdot}\right)\left(\frac{dh^\cdot}{d\widetilde{y}^\cdot}\right) \cdot \frac{h^\cdot}{Pr_L}\frac{dh^\cdot}{d\widetilde{y}^\cdot} \quad - \quad \frac{(\widetilde{v}_{\mathbf{w}}/\widetilde{u}_r)}{M}\left(1 - \frac{H_e}{H_{\mathbf{w}}}\right)C_H$$

$$-\left(\frac{m_e}{1 \cdot m_e}\right)\left(\frac{\rho_e\, H_e}{\rho_{\mathbf{w}}\, H_{\mathbf{w}}}\right)\widetilde{C}_f\left(1 \cdot \frac{\widetilde{v}_{\mathbf{w}}\,\widetilde{u}^\cdot}{\widetilde{u}_r}\right)\widetilde{u}^\cdot \cdot (\widetilde{v}_{\mathbf{w}}/\widetilde{u}_r)\left(\frac{H}{H_{\mathbf{w}}} - 1\right) \tag{58}$$

with boundary conditions, $\widetilde{y}^\cdot$ 0 : $\widetilde{u}^\cdot = 0$; $h^\cdot = 1$.

The differential equations for $\widetilde{u}^\cdot$ and $h^\cdot$ need only be solved at selected points in the flow field where accurate profiles near the wall including the sublayer are required. Since both boundary conditions for the two first order equations are known at the wall the solution does not require iteration and is performed as an auxiliary calculation in the downstream integration of the two-layer equations.

The asymptotic integral of the equation for $\widetilde{u}^\cdot$ for $\widetilde{y}^+ \gg 1$ is

$$\int_0^{\widetilde{u}^\cdot}\frac{d\widetilde{u}^+}{\{h^+(1\cdot\widetilde{v}_{\mathbf{w}}\widetilde{u}^+/\widetilde{u}_r)\}^{1/2}} = \frac{1}{K}\,\ell n\,\widetilde{y}^+ + \bar{B} \tag{59}$$

which, for a given value of a and solution of the differential equations for $\widetilde{u}^+$ and h^+, can be solved for $\bar{B}$. By iterating on an assumed value of a and matching the computed $\bar{B}$ with the experimental values reported by Danberg and Squire the variation of a with $H_{\mathbf{w}}/H_e$ and M for various Mach numbers was obtained (see Figure 1).

7. COMPUTER RESULTS AND EXPERIMENTAL COMPARISONS

By specifying initial values for δ_e, θ, $\widetilde{C}_f$ and C_H, and also the unit stagnation Reynolds number, where for an isentropic external flow with $\mu \sim T$

$$\rho_0\, a_0\, /\mu_0 \quad (u_e/\iota_e)\,/\,M_e\,(1 \cdot m_e)^{\frac{\gamma-3}{2(\gamma-1)}}$$

Eqs. (23), (26), (50), (51), (A 1-1) and (A 1-2) are solved simultaneously to give all the necessary starting conditions. A set of nine nonlinear differential equations is then integrated to give the solution downstream of the initial station. These differential equations are the momentum, first moment and energy equations for the outer layer, the equation for r_m from the inner layer, and equations obtained by differentiating the relations for $\bar{U}_m, \bar{H}_m, m, n$ and B with respect to x. The method used to solve the system, which is linear when solving for the derivatives, uses Gauss elimination with partial pivoting, with an iterative routine to improve the solution.[15] A comparison of this method of solving systems of linear equations with other techniques is given in Reference 16.

For zero pressure gradient, nonadiabatic flows the average computing time on an IBM 360 machine is about 15 seconds for Re_{θ} to increase by a factor of 10^2. This is approximately the computing time required by finite difference methods to calculate a single station.[11] As of the date of completion of this paper (June 1971), computer runs have been made for adiabatic and cold walls ($0.05 < H_{\mathbf{w}}/H_e < 1$) up to Mach 10, relaxing flows where $\widetilde{C}_f$ and/or C_H are far from their equilibrium values initially, boundary layers in strong positive and negative pressure gradients and flows with a varying spreading metric. Comparisons have been made with several of the experiments for incompressible flows reported at the AFOSR-Stanford conference[17] and results for $\widetilde{C}_f$, θ and $\delta^{*\cdot\theta}$ compare quite well with most of these experiments. For example, Figure 2

shows a comparison with one of the more interesting experiments -- the relaxing flow from a positive pressure gradient reported by Bradshaw and Ferriss. Momentum balance considerations show that the first experimental value for θ (at x = 4.4 ft.) is probably too small. If the initial θ had been taken to be about 0.475 in. the theoretical curve would have just about passed through the five values of θ measured farther downstream.

Figure 3 shows that Eqs. (57) and (58) yield quite accurate results for the velocity profile in the wall layer with surface mass injection, provided that empirical values of the additive constant $\bar{B}$ are available. These results show that not only is the linear law of the wall, (Eq. (59)), still in evidence with blowing but that the value of y^+ where the profile deviates from a linear law can be represented reasonably well. Here $f(u^+)$ is the integral on the left hand side of Eq. (59).

The variation of the equilibrium flat plate $\tilde{C}_f$ with Re_θ and M_e is compared with several experiments in Figs. 4 and 5. These results (with the exception of the experiments by Lee, et al) are for adiabatic flow, however, the theory predicts a relatively weak effect of wall cooling on skin friction. At Mach 6 and $Re_\theta \approx 10^4$, for example, $\tilde{C}_f$ for $H_w/H_e = 0.05$ is only about 15 percent greater than the adiabatic value of $\tilde{C}_f$. At these same conditions the Reynolds number based on δ^* for the cold wall is about one-third the value for an adiabatic wall.

Figure 6 demonstrates the existence of an equilibrium $\tilde{C}_f$ variation with Re_θ and the approach to this equilibrium variation if the initial C_f is too large or too small. A similar type of relaxation for the heat transfer and total enthalpy profile is shown in Figure 7. For these solutions the initial $\tilde{C}_f$ was set equal to the equilibrium value but the initial value of the Reynolds analogy parameter $2 C_H/\tilde{C}_f$ was set at values other than one. This resulted in an initial H versus u profile which was nonlinear in the outer layer. The solutions shown in Figure 7 demonstrate the relaxation of the Reynolds analogy parameter back to one, and the relaxation of an initially perturbed H versus u profile back to a linear Crocco integral for the whole layer (see schematic inserts of profiles in Figure 7). Relaxing flows of this sort have been measured on wind tunnel walls downstream of the nozzle throat.

Figure 8 shows results for $\tilde{C}_f$, θ, $\bar{U}_m$, and the Reynolds analogy parameter for a boundary layer in a region where $dp/dx > 0$ followed by a region where $dp/dx < 0$. The edge Mach number decreases from 2.6 to 1.3 over the first 50 inches and then increases to 2.6 again at x = 100 inches. In each case the results are compared with a solution for M_e = constant = 2.6. In the region of positive pressure gradient the wall layer thickness decreases but then increases as $dp/dx < 0$. This behavior is reflected in the variation of $\bar{U}_m$, which shows that near x = 100 inches most of the velocity variation across the boundary layer occurs in the wall layer. Thus, the two-layer model is seen to predict the kind of behavior hypothesized by Coles[2] in his paper on the Law of the Wake.

Figures 9 and 10 show comparisons of the theory with data for two-dimensional flows in negative pressure gradients at initial Mach numbers of 1.5 and 3.9, respectively, while Figure 11 shows a comparison with the method of Bradshaw for a flow in zero pressure gradient at Mach 3, followed by a region of strong adverse pressure gradient. Both methods predict that the flow separates, i.e., $\tilde{C}_f \to 0$. For the two-layer model the solution was stopped when $\tilde{C}_f$ decreased to 2×10^{-5} at x = 67.8 cm. In this region $\bar{U}_m \to 0$ and the layer was composed almost entirely of the outer layer, again demonstrating the kind of behavior predicted by Coles.

Comparison with data obtained by Lewis[20] for a boundary layer in a positive and then negative pressure gradient is shown in Figure 12. The Mach number varied from 4 to 2.57 to 4.17 over a distance of 34 inches. The experiments were performed with an outer hollow cylinder and an inner axisymmetric pressure generating body with the boundary layer data taken on the inner surface of the cylinder. The local decrease in δ^* in the region of strong positive pressure gradient demonstrates the supercritical behavior of the turbulent boundary layer.[1] The theoretical distribution for θ also shows a local decrease. Both curves for δ^* and θ are compared with the predicted variations for zero pressure gradient.

Figure 13 shows several solutions (various initial values of $\tilde{C}_f$) for the experiments conducted by McLafferty and Barber,[21] which were performed on a two-dimensional curved compression ramp. The Mach number decreased from 3 to 1.8 in a distance of 3 inches, and the boundary layer was tripped upstream of the ramp by normal injection. Thus, $\tilde{C}_f$ initially was probably slightly less than the equilibrium value of 1.8×10^{-3}. Figure 13 shows that for an initial $C_f = 1.75 \times 10^{-3}$ the flow remains attached (McLafferty and Barber reported that the flow did not separate) but for an initial $\tilde{C}_f = 1.5 \times 10^{-3}$ the flow separates at x = 2.73 inches. In the latter case the strong pressure gradient did not permit relaxation back to the equilibrium $\tilde{C}_f$ so that flow separation on the ramp could have been produced if the injection upstream of the ramp had been stronger.

Comparison of the theory with data taken on an axisymmetric curved compression ramp is shown in Figures 14 and 15. In this case the Mach number decreased from 5.75 to 2.6 and the spreading metric increased by a factor of 1.7. Figure 15 shows that $\tilde{C}_f$ actually increases slightly due to the metric effect (the two-dimensional results show only a 40 percent decrease in $\tilde{C}_f$ at the trailing edge) and the layer does not even come close to separating. Both theory and experiment show a substantial increase in the wall heating (Figure 15).

Finally, comparisons with data on a waisted body of revolution at $M_\infty = 1.4$ and 2.4 are shown in Figure 16 and 17 which indicate large effects produced by the spreading metric, particularly on the momentum thickness variations.

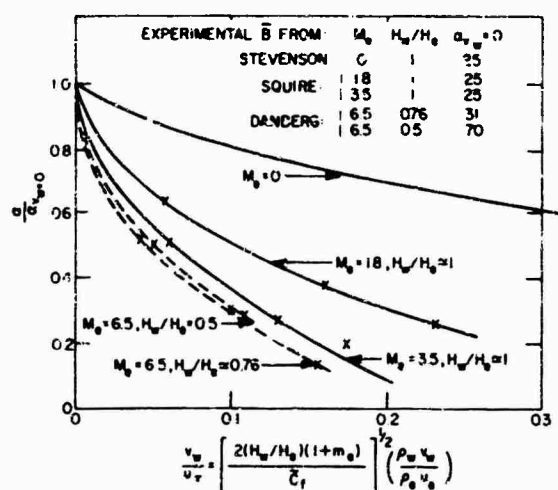Hopefully, results for flows with surface mass injection will be available at the time of the conference.

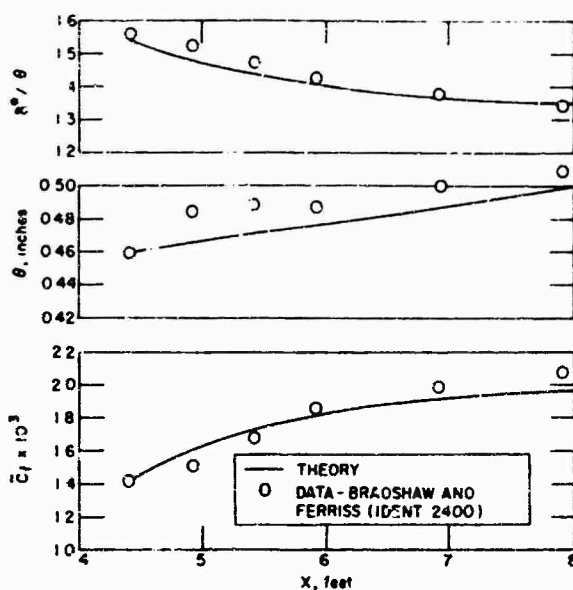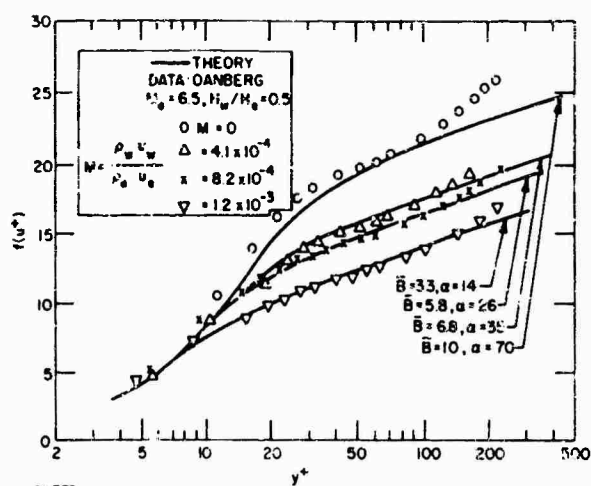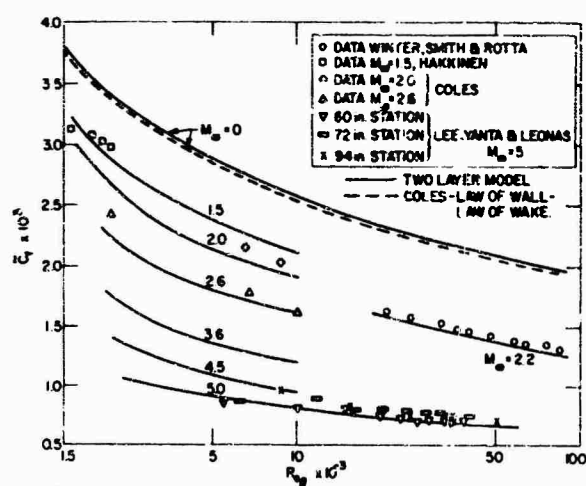Figure 1   α VARIATION WITH M_e, H_w, v_w OBTAINED FROM EXPERIMENTAL VALUES OF $\bar{B}$

Figure 2   RELAXING FLOW – ABRUPT REMOVAL OF POSITIVE PRESSURE GRADIENT, $M_e = 0$
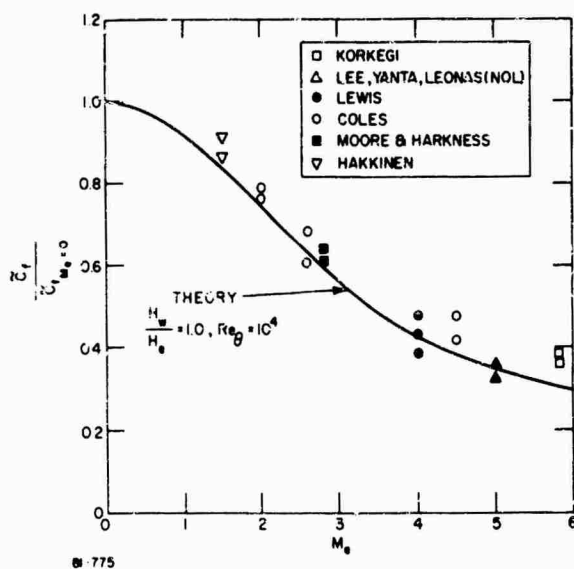

Figure 3   COMPARISON OF LAW OF THE WALL WITH DATA FOR SURFACE MASS INJECTION

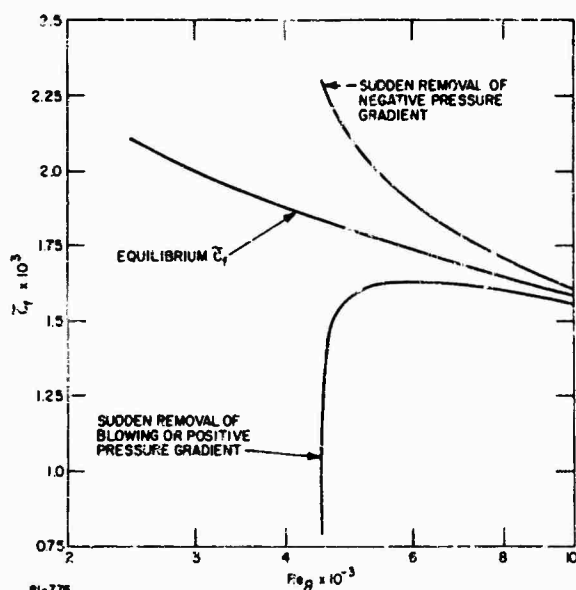

Figure 4 $\tilde{C}_f$ VERSUS Re_θ FOR EQUILIBRIUM $dP/dx = 0$

Figure 5   EFFECT OF M_e ON $\tilde{C}_f$

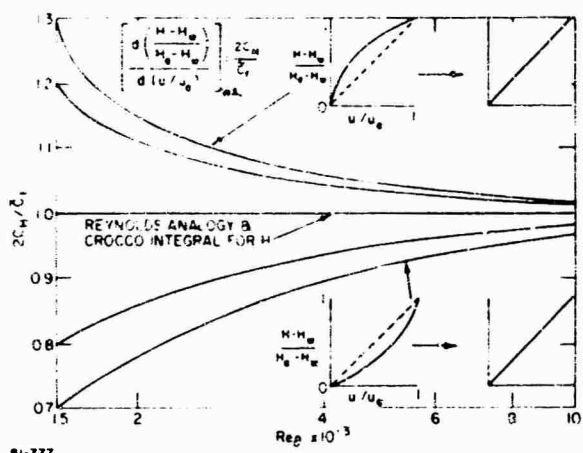Figure 6   RELAXING FLOWS AT M_e = CONSTANT = 2.6

Figure 7   RELAXING FLOW – INITIAL H ≠ A + BU,
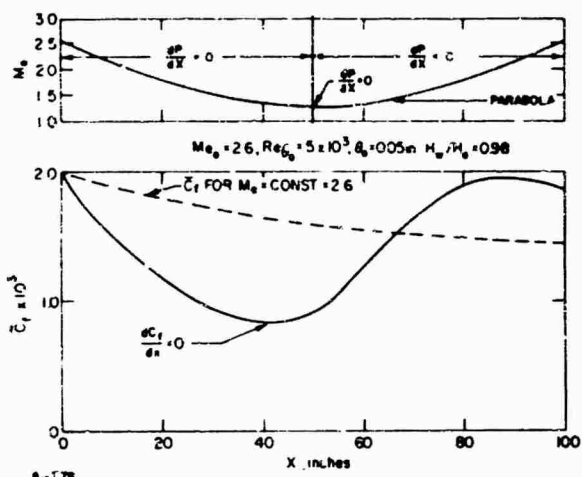$M_e = 3.6$, $H_w/H_e = 0.5$

81-778

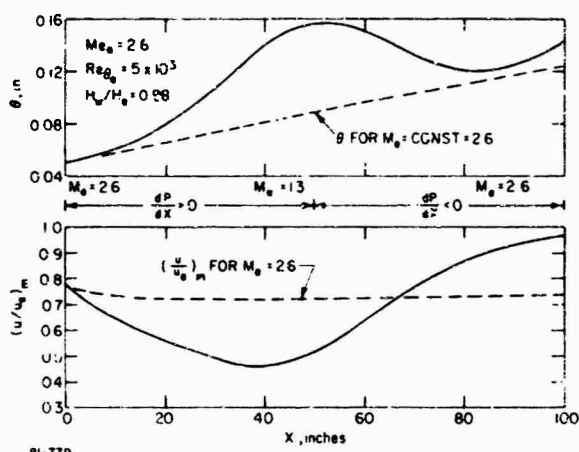Figure 8a   EFFECT OF dP/dx ON $\tilde{C}_f$

81-779

Figure 8b   EFFECT OF dP/dx ON θ AND VELOCITY RATIO AT
MATCH POINT

81-780

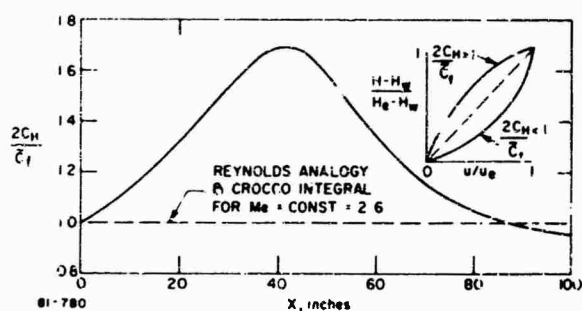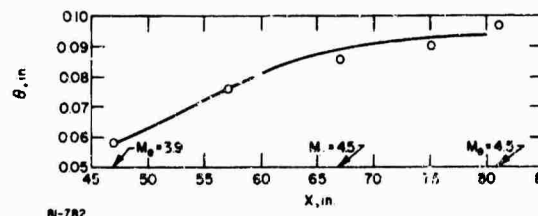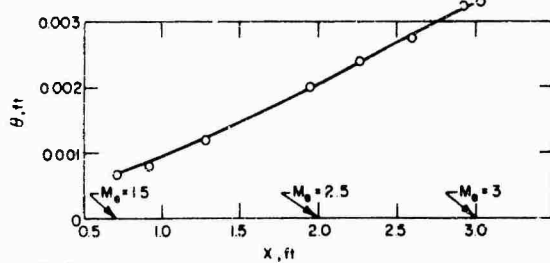Figure 8c   EFFECT OF dP/dx ON H VERSUS U PROFILE AND
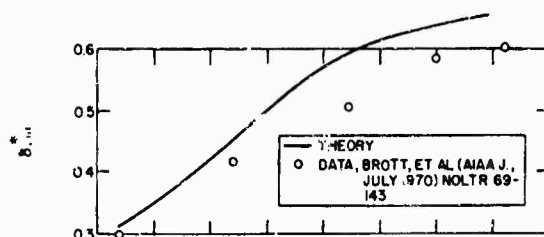ON REYNOLDS ANALOGY

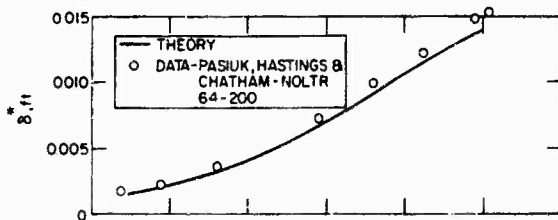81-781
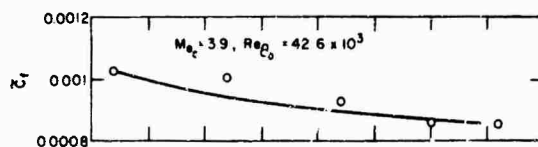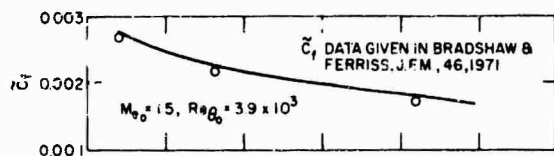
Figure 9   COMPARISON WITH DATA FOR dP/dx < 0

81-782

Figure 10   COMPARISON WITH DATA, dP/dx < 0

M_e

$\frac{dP}{dx} = 0$ $\frac{dP}{dx} > 0$

PRESENT METHOD
BRADSHAW AND FERRISS JFM 46, 1971

θ, cm

$\bar{U}_m = 0.74$

$\tilde{C}_f$

$\tilde{C}_f = 2 \times 10^{-5}$
$\bar{U}_m = 0.06$

X, cm

81-783
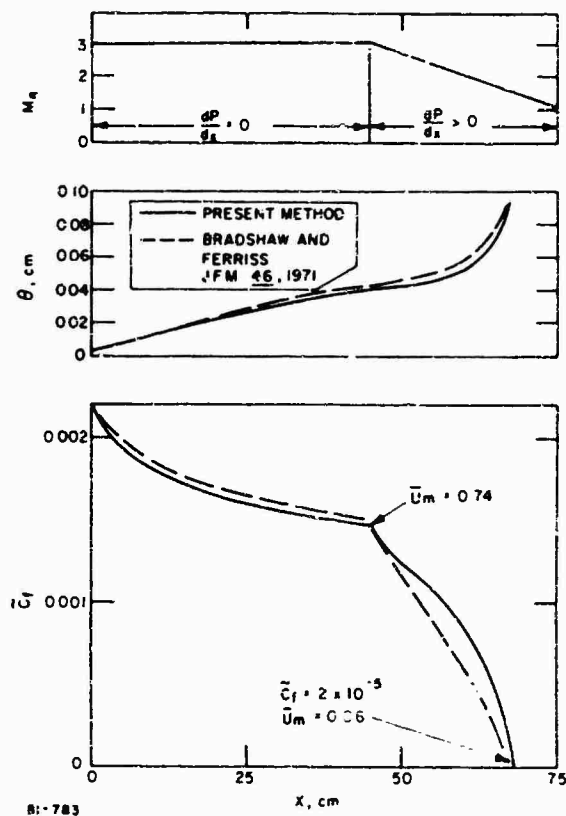
Figure 11   COMPARISON OF TWO-LAYER MODEL WITH
BRADSHAW METHOD, $H_w/H_e = 0.9$, $Re_{\theta_0} = 10^3$

$M_\infty = 4$, $\tilde{C}_{f_0} = 174 \times 10^{-3}$

DATA, LEWIS
THEORY
THEORY $dP/dx = 0$

δ^*, in

δ^*

θ, in

θ

$M_e = 4$ $M_e = 2.57$ $M_e = 4.17$

X, inches
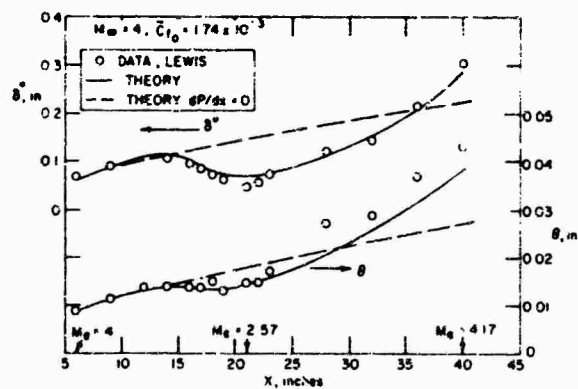
Figure 12   COMPARISON WITH LEWIS, STRONG POSITIVE AND
NEGATIVE PRESSURE GRADIENTS

DATA—McLAFFERTY & BARBER
THEORY $\tilde{C}_{f_0} = 175 \times 10^{-3}$ (NO SEPARATION)
THEORY $\tilde{C}_{f_0} = 1.5 \times 10^{-3}$ (SEPARATES $\times 273$)
THEORY $\tilde{C}_{f_0} = 1.3 \times 10^{-3}$ (SEPARATES $\times 2.66$)

FOR $dP/dX = 0$
EQUIL $C_{f_0} = 1.8 \times 10^{-3}$

$\tilde{C}_f$

LAST VALUES:
$\tilde{C}_f = 1.4 \times 10^{-7}$
$\bar{U}_m = 0.0019$
$y_m/\delta_e = 0.014$

$M_e = 3.0$ $M_e = 2.6$ $M_e = 2.1$ $M_e = 1.8$

$M_{e_0} = 3.0$, $Re_{\theta_0} = 2.54 \times 10^3$

θ, in

X, in

81-785

Figure 13   COMPARISON WITH DATA FOR $dP/dx > 0$

$M_{e_0} = 5.75$, $H_w/H_e = 0.63$, $Re_{\theta_0} = 3.8 \times 10^4$

DATA—HOYDYSH AND ZAKKAY
(AIAA NO 68-44)
THEORY (AXISYMMETRIC)
THEORY (TWO-DIMENSIONAL)

$\tilde{\delta}_0^* = 0.15$ in

$\frac{\tilde{\delta}^*}{\tilde{\delta}_0^*}$

$M_e = 5.75$ $M_e = 5.0$ $M_e = 4.0$ $M_e = 2.6$

$\tilde{\theta}_0 = 0.0123$ in

$\frac{\tilde{\theta}}{\tilde{\theta}_0}$

$\frac{r}{r_0} = 1.0$ $\frac{r}{r_0} = 1.07$ $\frac{r}{r_0} = 1.25$ $\frac{r}{r_0} = 1.7$

$\tilde{X}$, inches

81-786
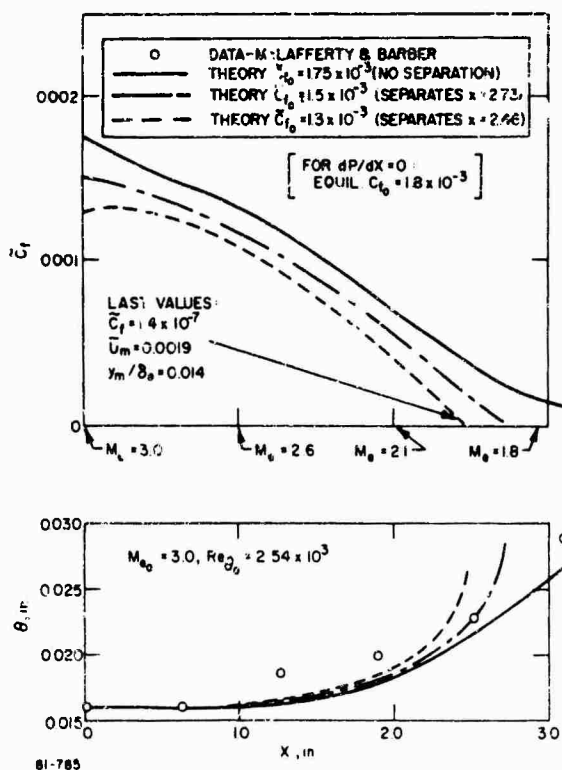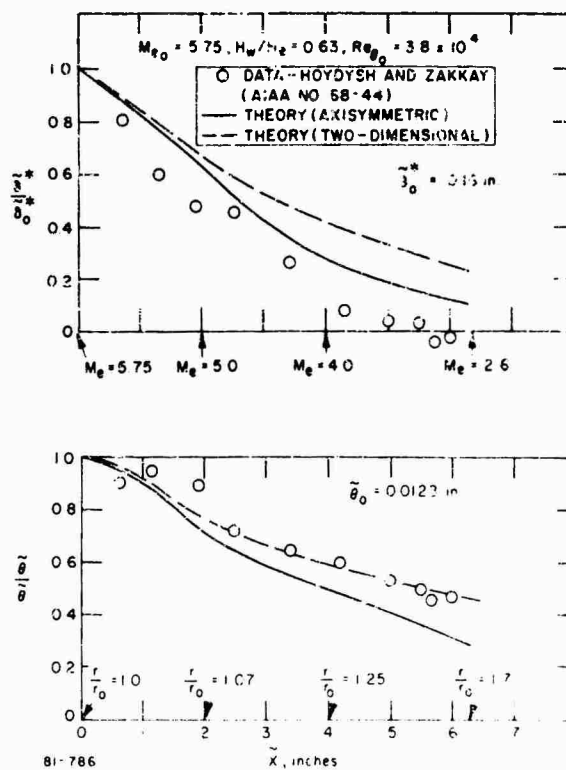
Figure 14   COMPARISON WITH DATA ON AN AXISYMMETRIC
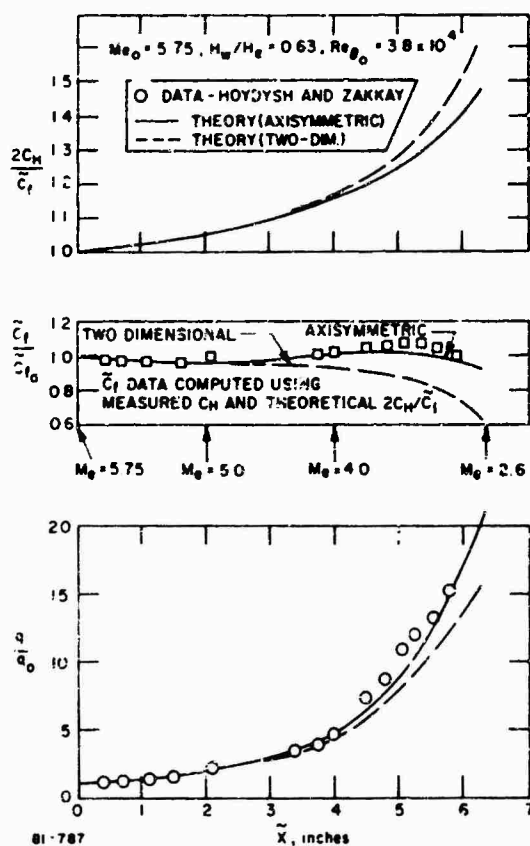COMPRESSION SURFACE

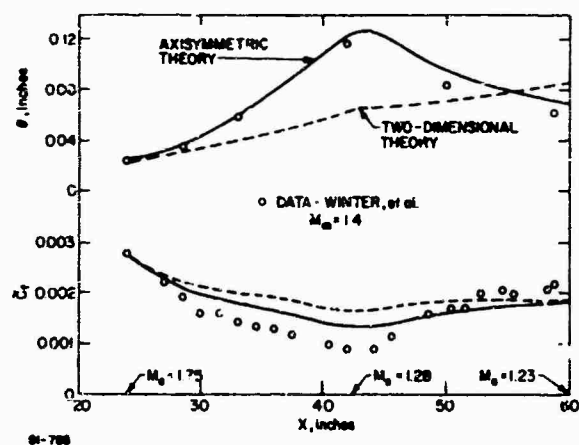Figure 15 COMPARISON WITH DATA ON AN AXISYMMETRIC COMPRESSION SURFACE
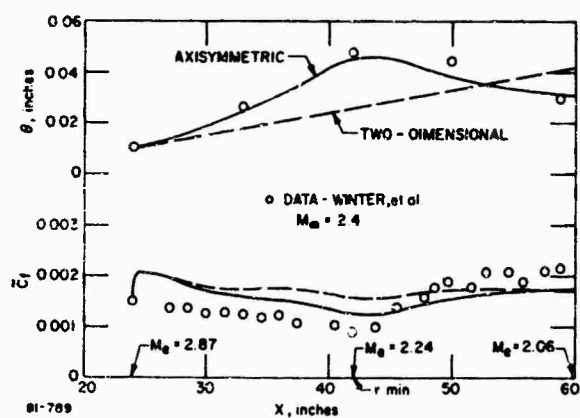

Figure 16 WAISTED BODY OF REVOLUTION

Figure 17 WAISTED BODY OF REVOLUTION

8. REFERENCES

1. Hunter, L. G. and Reeves, B. L. "Results of a Strong Interaction, Wake-Like Model of Supersonic SEparated and Reattaching Turbulent Flows," AIAA J., 9, 703-712 (1971).

2. Coles, D., "The Law of the Wake in the Turbulent Boundary Layer," JFM, 1, 191-226 (1956).

3. Maise, G. and H. McDonald, "Mixing Length and Kinematic Eddy Viscosity in a Compressible Boundary Layer," AIAA J. 6, 73-80 (1968).

4. Fannelop, T. K. and G. D. Waldman, "Displacement Interaction and Flow Separation on Cones at Incidence to a Hypersonic Stream," Paper presented at AGARD conference on "Hypersonic Boundary Layers and Flow Fields," at Royal Aeronautical Society, London (May 1968).

5. Lewis, J. E., T. Kubota, and W. Webb, "Transformation Theory for the Compressible Turbulent Boundary Layer with Arbitrary Pressure Gradient," SAMSO-TR-68-439 (September 1968).

6. Nee, V. and Kovasznay, L., "Simple Phenomenological Theory of Turbulent Shear Flows," Physics of Fluids, 12, 473-484 (1969).

7. Bradshaw, P. and D. Ferriss, "Calculation of Boundary Layer Development Using the Turbulent Energy Equation," J.F.M., 46, 83-110 (1971).

8. Squire, L. C., "A Law of the Wall for Compressible Turbulent Boundary Layers with Air Injection," JFM 37, 449-456 (1969).

9. Danberg, J. E., "Characteristics of the Turbulent Boundary Layer with Heat and Mass Transfer at M = 6.7", Naval Ordnance Laboratory, Report NOLTR 64-99 (October 1964).

10. Van Driest, E. R., "On Turbulent Flow Near a Wall," JAS 23, 1007-1011 (1956).

11. Smith. A. M. O. and T. Cebeci, "Numerical Solution of the Turbulent Boundary Layer Equations," McDonnell Douglas Report No. DAC 33735 (May 1967).

12. Herring, H. J. and G. L. Mellor, "A Method of Calculating Compressible Turbulent Boundary Layers", NASA CR-1144 (September 1968).

13. Clauser, F., "The Turbulent Boundary Layer", Adv. in Applied Mech. 4, Academic Press, 1-51 (1956).

14. Bradshaw, P. and Ferriss, D., "The Response of a Retarded Equilibrium Turbulent Boundary Layer to the Sudden Removal of Pressure Gradient", NPL Report 1145 (1965).

15. Forsythe, G. and C. Moler, "Computer Solution of Linear Algebraic Systems", Prentice Hall (1967).

16. Fitzgerald, K. E., "Error Estimates for the Solution of Linear Algebraic Systems", Journal of Research N.B.S., Math. Sci., 74B (1970).

17. Kline, S., Morkovin, M. Sovran, G. and D. Cockrell, AFOSR-IFP-Stanford Conference on Turbulent Boundary Layers, Stanford University Press (1968).

18. Pasiuk, L., S. Hastings and R. Chatham, "Experimental Reynolds Analogy Factor for a Compressible Turbulent Boundary Layer with a Pressure Gradient", NOL Report NOLTR 64-200 (1965).

19. Brott, D., W. Yanta, R. Voisinet and R. Lee, "Experiment of the Compressible Turbulent Boundary Layer with a Favorable Pressure Gradient", NOL Report 69-143 (1969).

20. Lewis, J., private communication, 1970, TRW Systems Division, Redondo Beach, California.

21. McLafferty, G. and R. Barber, "Effect of Adverse Pressure Gradients on Turbulent Boundary Layers in Supersonic Streams", J.A.S., 29, 1-10 (1962).

22. Hoydysh, W. and V. Zakkay, "An Experimental Investigation of Hypersonic Turbulent Boundary Layers in Adverse Pressure Gradient", AIAA Preprint No. 68-44 (1968).

23. Winter, K., K. Smith and J. Rotta, "Turbulent Boundary Layer Studies on a Waisted Body of Revolution in Subsonic and Supersonic Flow", AGARDOGRAPH 97 (1965).

APPENDIX 1

In addition to the law of the wall for U_m and the Crocco integral for H_m/H_w, matching relations for $(\partial u/\partial y)_m$ and $(\partial H/\partial y)_m$ are required to determine the exponents n and m of the power-law profiles in the outer layer. These are given below along with the expressions for r_m, $(q+u\tau)_m$ and $\dot{m}$ the mass flux in the inner layer. These expressions are applicable to a boundary layer growing into a rotational (variable entropy but constant stagnation temperature) inviscid flow.

From continuity of $(\partial u/\partial y)$ at y_m:

$$n = \frac{\rho_0}{\rho_s}\,(1 + m_e)^{\frac{\gamma+1}{2(\gamma-1)}} \cdot \frac{(h_m/h_e)^{3/2}\, C_f^{1/2}\, \delta\, \beta_o^{1/2}}{K\, s^*\, y_m} \tag{A 1-1}$$

From continuity of $(\partial H/\partial y)$ at y_m:

$$m = \frac{(H_w/H_e)\, B\, s^*\, n}{1 - \bar{H}_m} \tag{A 1-2}$$

where

$$\bar{H}_m = (H_w/H_e)(1 + B\,\bar{U}_m)\,, \quad h_m/h_e = \bar{H}_m + m_e\,(\bar{H}_m - \bar{U}_m^2)\,; \tag{A 1-3}$$

$$\beta_o = \left(1 + \frac{M}{C_f}\,\bar{U}_m\right)^{1/2} \tag{A 1-4}$$

Stress at y_m (obtained by differentiating J_2 and inserting result into relation for r_m:

$$
\begin{aligned}
&(\rho_0/\rho_s)(1 + m_e)^{\frac{\gamma+1}{2(\gamma-1)}} \left(\frac{s_o}{U_e^2\, s_e\, \rho_0}\, r_m\right) - C_f = \\
&a_{01}\,\frac{d\bar{U}_m}{dx} + a_{02}\,\frac{dy_m}{dx} + a_{03}\,\frac{dC_f}{dx} + a_{04}\,\frac{dB}{dx} + a_{05}\,\frac{dM}{dx} \\
&+ a_{06}\,\frac{dM_e}{dx} + a_{07}\,\frac{d}{dx}\left(\frac{\rho_s}{\rho_0}\right) + M\,\bar{U}_m
\end{aligned}
\tag{A 1-5}
$$

where

$$a_{01} = \frac{J_1}{(h_w/h_e)} - \frac{\beta_3\, C_f^{1/2}\, y_m}{(h_m/h_w)^{1/2}}\left[1 - \frac{\bar{U}_m\,(B - 2A^2\,\bar{U}_m)}{2(h_m/h_w)} + \frac{\bar{U}_m\, M}{2\,\beta_o^2\, C_f}\right] + \frac{2\, y_m\, M}{K^2}$$

$$a_{02} = -\frac{\beta_3\, C_f^{1/2}\, \bar{U}_m}{(h_m/h_w)^{1/2}} + \frac{2\,\beta_o^2\, C_f}{K^2}$$

$$a_{03} = -\frac{\beta_3\,\bar{U}_m\, y_m}{2(h_m/h_w)^{1/2}C_f^{1/2}}\left[1 - \frac{M\bar{U}_m}{\beta_o^2\, C_f}\right] + \frac{2\,\beta_o^2\, y_m}{K^2} - \frac{2\, y_m\, M\,\bar{U}_m}{K^2\, C_f}$$

$$a_{04} = \frac{\beta_3\, C_f^{1/2}\,\bar{U}_m^2\, y_m}{2\,(h_m/h_w)^{3/2}}$$

$$a_{05} = -\frac{\beta_3\,\bar{U}_m^2\, y_m}{2\,\beta_o^2\,(h_m/h_w)^{1/2}\, C_f^{1/2}} + \frac{2\, y_m\,\bar{U}_m}{K^2}$$

$$a_{06} = \frac{J_1 \bar{U}_m}{M_e (1 + m_e)(h_m/h_w)} - \frac{\gamma_m}{M_e (1 + m_e)} + \frac{4 C_f \gamma_m \beta_o^2}{K^2 M_e}\left[1 - \left(\frac{\gamma}{\gamma - 1}\right)\frac{m_e}{(1 + m_e)}\right]$$

$$- \frac{\bar{U}_m \gamma_m \beta_o}{K M_e}\left[\frac{(H_e/H_w) C_f}{(1 + m_e)(h_m/h_w)}\right]^{1/2}\left[2 - \frac{(3\gamma - 1)}{(\gamma - 1)}\frac{m_e}{(1 + m_e)} + \frac{m_e}{(1 + m_e)^2}\frac{(H_e/H_w)\bar{U}_m^2}{(h_m/h_w)}\right]$$

$$a_{07} = -\frac{\bar{U}_m \gamma_m \beta_o}{K}\left[\frac{(H_e/H_w) C_f}{(1 + m_e)(h_m/h_w)}\right]^{1/2} + (2/K^2) C_f \gamma_m \beta_o^2$$

$$\beta_3 = \frac{\beta_o}{K}\left[\frac{H_e/H_w}{1 + m_e}\right]^{1/2}$$

Heat flux at y_m (from equation for $(q + \alpha \tau)_m$):

$$\left(\frac{1}{\rho_o U_e H_e}\right) q_m + \left(\frac{a_e}{\rho_o u_o H_e}\right)\bar{U}_m \tau_m =$$

$$\left.\begin{array}{l} a_{11} \dfrac{d\bar{U}_m}{dx} + a_{12} \dfrac{d\gamma_m}{dx} + a_{13} \dfrac{dC_f}{dx} + a_{14} \dfrac{dB}{dx} + a_{15} \dfrac{dM}{dx} \\[2mm] + a_{16} \dfrac{dM_e}{dx} + a_{17} \dfrac{d}{dx}\left(\dfrac{\rho_s}{\rho_o}\right) + a_{18}\, St + a_{19}\, M\bar{U}_m \end{array}\right\}$$

$$(A\ 1\text{-}6)$$

where

$$a_{11} = \frac{\rho_s}{\rho_o}\left[-\frac{\beta_1 C_f^{1/2}\gamma_m}{(h_m/h_w)^{1/2}}\left\{1 - \frac{\bar{U}_m(B - 2A^2 \bar{U}_m)}{2(h_m/h_w)} + \frac{\bar{U}_m M}{2\beta_o^2 C_f}\right\} + \beta_2 \gamma_m M\right.$$

$$\left. + (1 + m_e)^{\frac{1 - 3\gamma}{2(\gamma - 1)}} J_1 B\right]$$

$$a_{12} = \frac{\rho_s}{\rho_o}\left[-\frac{\beta_1 C_f^{1/2}\bar{U}_m}{(h_m/h_w)^{1/2}} + \beta_2 \beta_o^2 C_f\right]$$

$$a_{13} = \frac{\rho_s}{\rho_o}\left[-\frac{\beta_1 \bar{U}_m \gamma_m}{2(h_m/h_w)^{1/2} C_f^{1/2}}\left(1 - \frac{\bar{U}_m M}{\beta_o^2 C_f}\right) + \beta_2 \beta_o^2 \gamma_m - \beta_2 \gamma_m M\bar{U}_m/C_f\right]$$

$$a_{14} = \frac{\rho_s}{\rho_o}\left[(1 + m_e)^{\frac{1 - 3\gamma}{2(\gamma - 1)}}(J_1 \bar{U}_m + J_2) + \frac{\beta_1 C_f^{1/2}\bar{U}_m^2 \gamma_m}{2(h_m/h_w)^{3/2}}\right]$$

$$a_{15} = \frac{\rho_s}{\rho_o}\left[\beta_2 \gamma_m \bar{U}_m - \frac{\beta_1 \bar{U}_m^2 \gamma_m}{2\beta_o^2 (h_m/h_w)^{1/2} C_f^{1/2}}\right]$$

$$a_{16} = \frac{\rho_s}{\rho_o}\left[\frac{\beta_2 C_f \gamma_m \beta_o^2}{M_e}\left\{1 - \left(\frac{\gamma + 1}{\gamma - 1}\right)\frac{m_e}{(1 + m_e)}\right\} - \frac{\beta_1 C_f^{1/2}\bar{U}_m^3 \gamma_m (H_e/H_w)(\gamma - 1) M_e}{2(h_m/h_w)^{3/2}(1 + m_e)^2}\right.$$

$$\left. - \frac{(\rho_s/\rho_o)(H_w/H_e)^{1/2} B C_f^{1/2}\bar{U}_m \gamma_m \beta_o}{K M_e (h_m/h_w)^{1/2}}(1 + m_e)^{-\frac{\gamma}{\gamma - 1}}\left\{1 - \left(\frac{2\gamma}{\gamma - 1}\right)\frac{m_e}{(1 + m_e)}\right\}\right]$$

$$a_{17} = -\frac{\beta_1 C_f^{1/2} \bar{U}_m y_m}{(h_m/h_w)^{1/2}} + \beta_2 C_f \beta_2^2$$

$$a_{18} = 2(\rho_s/\rho_o) m_e (1 + m_e)^{\frac{1 - 3\gamma}{2(\gamma - 1)}}$$

$$a_{19} = (\rho_s/\rho_o)(1 + m_e)^{\frac{-(\gamma + 1)}{2(\gamma - 1)}} (H_w/H_e) B$$

$$\beta_1 = (\rho_s/\rho_o)(H_w/H_e)^{1/2} (1 + m_e)^{\frac{-\gamma}{\gamma - 1}} (B \beta_o/K)$$

$$\beta_2 = 2(\rho_s/\rho_o)(H_w/H_e)(1 + m_e)^{\frac{-(\gamma + 1)}{2(\gamma - 1)}} (B/K^2)$$

The mass flux in the inner layer is

$$\dot{m}/\rho_o U_e = \frac{1}{\rho_o U_e} \int_0^{y_m} \rho u \, dy = (\rho_s/\rho_o)(1 + m_e)^{\frac{-(\gamma + 1)}{2(\gamma - 1)}} \left[\frac{\bar{U}_m}{(h_m/h_e)} - \frac{C_f^{1/2} \beta_o}{(h_m/h_e)^{1/2}} \right] y_m \qquad (A\ 1\text{-}7)$$

Also, from the definition of B

$$\frac{dB}{dx} = \left(\frac{H_e}{H_w}\right)\left(\frac{2 m_e}{1 + m_e}\right)\left[\frac{2 (St/C_f)}{M_e(1 + m_e)} \frac{dM_e}{dx} + \frac{d}{dx}\left(\frac{St}{C_f}\right)\right] \qquad (A\ 1\text{-}8)$$

Differential equations for dU_m/dx, dH_m/dx, dn/dx, dm/dx and $(1/\rho_o U_e)(d\dot{m}/dx)$ are also required as part of the system of equations to be solved along with the integral equations for the outer layer, and are obtained by differentiating the law of the wall, Crocco integral, and Eqs. (A 1-1), (A 1-2), (A 1-3) and (A 1-8) respectively.

APPENDIX 2

Integral functions for integral moment equations in outer layer:

$$A_1 = \frac{2a^*}{2n + 1} - \frac{1}{n + 1}$$

$$A_2 = \frac{a^*}{(n + 1)^2} - \frac{2 a^{*2}}{(2n + 1)^2}$$

$$A_3 = \frac{-3 a^{*2}}{3n + 1} + \frac{6 a^*}{2n + 1} - \frac{2}{n + 1}$$

$$A_4 = \frac{3 a^{*3}}{(3n + 1)^2} - \frac{6 a^{*2}}{(2n + 1)^2} + \frac{2 a^*}{(n + 1)^2}$$

$$B_1 = \frac{1}{m + 1} - \frac{a^*}{(m + n + 1)}$$

$$B_2 = \frac{(1 - \bar{H}_m)}{(m + 1)^2} - \frac{a^* (1 - \bar{H}_m)}{(m + n + 1)^2}$$

$$B_3 = \frac{(1 - \bar{H}_m)}{(m + n + 1)}$$

$$B_4 = \frac{-a^* (1 - \bar{H}_m)}{(m + n + 1)^2}$$

$$E_1 = \int_0^1 \bar{H} d\eta = 1 - \frac{(1 - \bar{H}_m)}{1 + m}$$

$$E_2 = \int_0^1 U \bar{H} d\eta = 1 - \frac{a^\bullet}{n+1} - \frac{(1 - \bar{H}_m)}{m+1} + \frac{a^\bullet (1 - \bar{H}_m)}{m+z+1}$$

$$E_3 = \int_0^1 U^2 \bar{H} d\eta =$$

$$1 - \frac{2 a^\bullet}{a+1} + \frac{a^{\bullet 2}}{2n+1} - \frac{(1 - \bar{H}_m)}{a+1} + \frac{2 a^\bullet (1 - \bar{H}_m)}{m+n+1} - \frac{a^{\bullet 2}(1 - \bar{H}_m)}{2n+m+1}$$

$$E_4 = \int_0^1 \bar{U}(\bar{H} - 1) d\eta = (1 - \bar{H}_m)\left(\frac{a^\bullet}{m+n+1} - \frac{1}{m+1}\right)$$

$$I_1 = \int_0^1 \bar{U} d\eta = 1 - \frac{a^\bullet}{n+1}$$

$$I_2 = \int_0^1 \bar{U}^2 d\eta = 1 - \frac{2a^\bullet}{n+1} + \frac{a^{\bullet 2}}{2n+1}$$

$$I_3 = \int_0^1 \bar{U}^3 d\eta = 1 - \frac{3a^\bullet}{n+1} + \frac{3a^{\bullet 2}}{2n+1} - \frac{a^{\bullet 3}}{3n+1}$$

$$I_4 = \int_0^1 \bar{U}^4 d\eta = 1 - \frac{4a^\bullet}{n+1} + \frac{6a^{\bullet 2}}{2n+1} + \frac{a^{\bullet 4}}{4n+1}$$

$$I_5 = \int_0^1 \bar{U}(\bar{U} - 1) d\eta = -\frac{a^\bullet}{n+1} + \frac{a^{\bullet 2}}{2n+1}$$

$$I_6 = \int_0^1 \bar{U}(\bar{U}^2 - 1) d\eta = -\frac{2a^\bullet}{n+1} + \frac{3a^{\bullet 2}}{2n+1} - \frac{a^{\bullet 3}}{3n+1}$$

APPLICATION D'UN SCHEMA AMELIORE DE LONGUEUR DE MELANGE

A L'ETUDE DES COUCHES LIMITES TURBULENTES TRIDIMENSIONNELLES

par J. COUSTEIX (*), C. QUEMARD (*) et R. MICHEL (**)

OFFICE NATIONAL D'ETUDES ET DE RECHERCHES AEROSPATIALES

92 - CHATILLON - FRANCE

SUMMARY -

An improved mixing-length model, previously applied to two-dimensional flow, is here extended to cover the three-dimensional case, relying on the assumption that the turbulent shear stress acts in the same direction as the laminar.

It is used to work out similar solutions to the local equations of a turbulent boundary layer with small cross-flow. In the general case of a compressible fluid with arbitrary pressure gradients, a digital routine enables the sets of transverse and longitudinal boundary-layer profiles and the wall skin-friction components to be determined as a function of two parameters expressing the influence of pressure gradients. A blow-by-blow comparison with available experimental results shows a fair measure of agreement. The model accordingly offers the requisite hypotheses on which to build an integral method of computing three-dimensional turbulent boundary layers.

NOTATIONS -

x,y,z directions longitudinale, normale et transversale

η distance réduite y/δ

u,v,w composantes de la vitesse

u_τ vitesse de frottement $(\tau_p/\rho_p)^{1/2}$

M nombre de Mach

p pression statique

ρ masse volumique

μ, ε viscosités laminaire et turbulente

$\mathcal{P}, \mathcal{P}_t$ nombres de PRANDTL laminaire et turbulent

τ frottement $(\tau_\ell + \tau_t)$

ϕ flux de chaleur $(\phi_\ell + \phi_t)$

ℓ longueur de mélange

F fonction correctrice de sous-couche visqueuse

C_{fx}, C_{fz} coefficient de frottement locaux

γ $\sqrt{C_{fx}/2}$

β_o angle limite

K_2 courbure des lignes de courant extérieures

K_1 courbure des lignes orthogonales

R_L nombre de Reynolds $\dfrac{\rho_e u_e L}{\mu_e}$

δ épaisseur conventionnelle ; $\delta_1 = \int_o^\delta \left(1 - \dfrac{\rho u}{\rho_e u_e}\right) dy$

$\theta_{11} = \int_o^\delta \dfrac{\rho u}{\rho_e u_e}\left(1 - \dfrac{u}{u_e}\right) dy$; $H = \dfrac{\delta_1}{\theta_{11}}$

$\delta_2 = \int_o^\delta -\dfrac{\rho w}{\rho_e u_e} dy$; $\theta_{21} = \int_o^\delta -\dfrac{\rho}{\rho_e}\dfrac{w}{u_e}\dfrac{u}{u_e} dy$

$\theta_{12} = \int_o^\delta \dfrac{\rho w}{\rho_e u_e}\left(1 - \dfrac{u}{u_e}\right) dy$; $\theta_{22} = \int_o^\delta -\dfrac{\rho}{\rho_e}\left(\dfrac{w}{u_e}\right)^2 dy$

Indices

e conditions à la frontière de la couche limite

p conditions à la paroi

l grandeurs laminaires

t grandeurs turbulentes

1 - INTRODUCTION

Le but de l'étude entreprise est d'obtenir pour une couche limite turbulente tridimensionnelle, des renseignements d'ordre théorique, apportant sur les caractéristiques de la couche limite et spécialement sur le profil des vitesses transversales des résultats moins empiriques que ceux dont il est généralement fait usage dans l'analyse des expériences ou dans l'établissement de méthodes de calcul.

Le traitement établi pour cela est basé sur l'extension au tridimensionnel d'un schéma de longueur de mélange déjà utilisé largement dans le cas des couches limites bidimensionnelles, et qui a conduit pour celles-ci à des résultats cohérents, bien confirmés par l'expérience dans un large domaine de conditions aux limites (Réf. [1] et [2]).

Ce schéma, qui fournit une expression du frottement dans toute la couche limite peut en principe être utilisé dans une résolution numérique des équations locales de la couche limite mettant en oeuvre, par exemple, une technique de différences finies avec des conditions aux limites quelconques. Pour aboutir plus simplement à des résultats qui permettent de juger de façon systématique de l'influence des facteurs agissants, il a semblé préférable de rechercher au préalable des solutions de similitude locale, en se plaçant dans des cas pour lesquels les dérivées longitudinales et transversales des profils de couche limite peuvent être négligées.

Ces solutions de similitude permettent de compléter les familles de profils longitudinaux établies pour le bidimensionnel, par des familles de profils transversaux et de déterminer l'influence des gradients de pression qui s'exercent dans les deux directions sur les caractéristiques de la couche limite et notamment sur le frottement de paroi.

(*) Ingénieur de Recherche, Direction d'Aérodynamique

(**) Chef de Division de Recherche, Direction d'Aérodynamique

2 - EQUATIONS GENERALES - PRINCIPE DE PREVALENCE -

Dans un système général de coordonnées curvilignes orthogonales les équations locales de la couche limite tridimensionnelle s'écrivent (voir par exemple la référence [3]) :

continuité
$$\frac{1}{h_1 h_2}\frac{\delta}{\delta x}(h_2 \rho u) + \frac{\delta}{\delta y}(\rho v) + \left[\frac{1}{h_1 h_2}\frac{\delta}{\delta z}(h_1 \rho w)\right] = 0 \qquad (1)$$

quantité de mouvement
suivant x
$$\frac{u}{h_1}\frac{\delta u}{\delta x} + v\frac{\delta u}{\delta y} + \left[\frac{w}{h_2}\frac{\delta u}{\delta z} - K_2 uw + K_1 w^2\right] = \frac{1}{\rho}\left(-\frac{1}{h_1}\frac{\delta p}{\delta x} + \frac{\delta \tau_x}{\delta y}\right) \qquad (2)$$

quantité de mouvement
suivant z
$$\frac{u}{h_1}\frac{\delta w}{\delta x} + v\frac{\delta w}{\delta y} + \left[\frac{w}{h_2}\frac{\delta w}{\delta z}\right] + K_2 u^2 - K_1 uw = \frac{1}{\rho}\left(-\frac{1}{h_2}\frac{\delta p}{\delta z} + \frac{\delta \tau_z}{\delta y}\right) \qquad (3)$$

conservation de l'énergie
$$\frac{u}{h_1}\frac{\delta h_i}{\delta x} + v\frac{\delta h_i}{\delta y} + \left[\frac{w}{h_2}\frac{\delta h_i}{\delta z}\right] = \frac{1}{\rho}\frac{\delta}{\delta y}\left(u\tau_x + \left[w\tau_z\right] - \phi\right) \qquad (4)$$

L'axe y est normal à la paroi sur laquelle se développe la couche limite. h_1 et h_2 sont les éléments suivant les axes x et z. K_1 et K_2, courbures géodésiques des lignes x = cte et z = cte, s'expriment par les relations :

$$K_1 = -\frac{1}{h_1 h_2}\frac{\delta h_2}{\delta x} \qquad\qquad K_2 = -\frac{1}{h_1 h_2}\frac{\delta h_1}{\delta z} = -\frac{1}{\rho u_e^2}\frac{1}{h_2}\frac{\delta p}{\delta z}$$

τ est le frottement total $(\tau_\ell + \tau_t)$, ϕ le flux de chaleur ($\phi_\ell + \phi_t$) dont les expressions seront discutées plus loin.
h_i est l'enthalpie totale $\left(h_i = h + \frac{u^2 + w^2}{2}\right)$

Il est commode de choisir un système d'axes lié à l'écoulement extérieur à la couche limite, les lignes z = cte étant alors formées par les lignes de courant de cet écoulement. Outre le fait que ce choix apporte une simplification des conditions aux limites ($w_e = 0$), il permet d'obtenir une grande simplification des équations elles-mêmes dans des cas où l'écoulement transversal ainsi défini peut être considéré comme faible devant l'écoulement longitudinal.

Les termes relatifs à l'écoulement transversal regroupés entre crochets dans les équations (1), (2), (3) et (4) disparaissent lorsqu'est appliqué ce principe de prévalence. Il est alors évident, comme il a été démontré à l'origine par EICHELBRENNER [réf. 4] que les équations longitudinales de quantité de mouvement et d'énergie ne contenant plus w sont découplées de l'équation de quantité de mouvement transversale (à condition toutefois que τ_x et ϕ soient aussi indépendants de w). Cette hypothèse de faible écoulement transversal et la simplification qu'elle apporte sont à la base du traitement de similitude qu'on va effectuer.

3 - SCHEMA DE TURBULENCE -- FROTTEMENT ET FLUX DE CHALEUR -

Rappelons qu'un schéma de longueur de mélange a été établi et appliqué (réf. 1 et 2) dans le cas d'une couche limite bidimensionnelle. Dans ce schéma, le terme turbulent du frottement est exprimé par la formule classique de longueur de mélange dans la partie extérieure de la couche limite. On a retenu pour cette longueur de mélange la formule universelle:

$$\frac{\ell}{\delta} = 0,085\, th\left(\frac{k}{0,085}\frac{y}{\delta}\right) \qquad (avec\ k = 0,41) \qquad (5)$$

Dans la sous-couche visqueuse, on a estimé nécessaire de tenir compte du fait que le frottement turbulent n'est plus proportionnel à l'intensité de turbulence et on a introduit une fonction correctrice F pour traduire l'influence de la viscosité sur le frottement turbulent. L'expression générale du frottement total a été mise ainsi sous la forme :

$$\tau = \mu\frac{\delta u}{\delta y} + \rho F^2 \ell^2 \left|\frac{\delta u}{\delta y}\right|\frac{\delta u}{\delta y}$$

Faisant appel aux résultats de Van DRIEST (réf. 5), relatifs à la plaque plane incompressible, on a supposé que F dépendait dans le cas général du rapport du frottement turbulent au frottement laminaire ; on a montré en fait (réf. 2), que la fonction correctrice s'exprimait également à partir du frottement total τ et de la longueur de mélange par la relation :

$$F = 1 - \exp\left[-\frac{\ell}{26 k\mu}(\tau\rho)^{1/2}\right] \qquad (avec\ k = 0,41) \qquad (6)$$

Nulle à la paroi, la fonction correctrice tend vers 1 en écoulement pleinement turbulent.

L'idée qui a permis d'étendre le schéma précédent au cas d'une couche limite tridimensionnelle, a été d'admettre qu'il existe une relation entre les directions du frottement turbulent et du frottement laminaire. L'hypothèse la plus simple, retenue également par NASH (réf. 6), est de supposer que ces directions sont confondues. Pour cela, il suffit que les composantes $\tau_{\ell y}$ et $\tau_{\ell z}$ du frottement laminaire soient dans le même rapport que les composantes τ_{tx} et τ_{tz} du frottement turbulent ; ceci implique que τ_{tx} et τ_{tz} peuvent se mettre sous la forme :

$$\tau_{tx} = \varepsilon\frac{\delta u}{\delta y} \qquad\qquad \tau_{tz} = \varepsilon\frac{\delta w}{\delta y}$$

ε apparaissant comme une viscosité turbulente commune aux deux directions.

ε devant de plus se ramener à la forme bidimensionnelle quand $w = 0$, on a été conduit à choisir l'expression :

$$\varepsilon = \rho F^2 \ell^2 \sqrt{\left(\frac{\delta u}{\delta y}\right)^2 + \left(\frac{\delta w}{\delta y}\right)^2}$$

dont la forme est d'ailleurs comparable à une formule proposée par PERRY et JOUBERT (réf. 7).

Le longueur de mélange est toujours donnée par la formule (5) ; la fonction correctrice s'exprime toujours en fonction de τ et ℓ par la formule (6).

Dans le cas d'un écoulement transversal faible les frottements totaux dans les deux directions se réduisent à :

$$\tau_x = \mu\ \frac{\partial u}{\partial y} + \rho F^2 \ell^2 \left|\frac{\partial u}{\partial y}\right| \frac{\partial u}{\partial y} \tag{7}$$

$$\tau_z = \mu\ \frac{\partial w}{\partial y} + \rho F^2 \ell^2 \left|\frac{\partial u}{\partial y}\right| \frac{\partial w}{\partial y} \tag{8}$$

On voit que τ_x ne dépend pas de w .

Le flux de chaleur, enfin, a été exprimé dans l'hypothèse d'un nombre de PRANDTL turbulent constant par :

$$\Phi = -\ \frac{\partial h}{\partial y} \left(\frac{\mu}{\mathcal{P}} + \frac{\varepsilon}{\mathcal{P}_t}\right) \tag{9}$$

On a choisi dans les calculs effectués jusqu'ici $\mathcal{P} = 0,725$ et $\mathcal{P}_t = 0,89$.

4 - SOLUTIONS DE SIMILITUDE -

4.1. - Hypothèses de similitude -

En vue de déterminer à partir du schéma précédent des familles de profils pour les vitesses longitudinale et transversale, et pour l'enthalpie dans le cas compressible, on s'est placé dans des conditions de similitude pour lesquelles les dérivées longitudinales de ces profils peuvent être négligées et pour lesquelles le système des équations (1), (2), (3) et (4) se réduit à un système d'équations différentielles ordinaires.

En ce qui concerne d'abord l'écoulement longitudinal, on a dit que l'hypothèse d'un écoulement transversal faible découple ses équations de l'équation transversale, et permet, compte-tenu des expressions de τ_x et Φ de traiter le problème comme pour un écoulement bidimensionnel. On rappellera qu'une solution asymptotique, valable pour un nombre de Reynolds tendant vers l'infini, a été établie (réf. 1 et 2) dans le cas du fluide incompressible. Basée sur l'observation expérimentale de couches limites d'équilibre, elle mettait en oeuvre une hypothèse de similitude qui portait sur le profil des vitesses déficitaires $(u_e-u)/u_\tau$, fonction de y/δ supposée indépendante de x .

Cette forme de similitude est beaucoup plus discutable dans le cas général compressible. On peut montrer d'autre part qu'aux grands nombres de Reynolds, elle est en fait identique à une similitude des u/u_e , puisque la dérivée suivant x de u_τ/u_e tend vers 0.

C'est donc plus simplement l'hypothèse de similitude locale, u/u_e = fonction de y/δ dont la dérivée suivant x est négligée, qui a été retenue dans le présent traitement. De la même manière une similitude locale a été supposée applicable aux profils d'enthalpie totale, sous la forme h_i/h_{ie} = fonction de y/δ

L'hypothèse de similitude à faire pour l'écoulement transversal est a priori plus délicate étant donné que l'équation transversale présente la particularité de dépendre non seulement du gradient de pression $\partial p/\partial z$, mais également, par K_1 et K_2, de la géométrie de la surface. Suivant une hypothèse utilisée pour la couche limite laminaire (réf. 8), on a posé que la vitesse transversale était le produit d'une fonction de x par une fonction de y/δ

$$\frac{w}{u_e} = \Theta(x)\cdot t'\left(\frac{y}{\delta}\right)$$

$\Theta(x)$ étant déterminée a posteriori pour satisfaire à la similitude.

4.2. - Solution et profils pour l'écoulement longitudinal -

L'hypothèse de similitude sur les vitesses et l'enthalpie totale réduite est donc de la forme :

$$\frac{u}{u_e} = f'\left(\frac{y}{\delta}\right) \text{ et } \frac{h_i}{h_{ie}} = g'\left(\frac{y}{\delta}\right)$$

Avec ces notations les formules (7) et (9) donnent pour le frottement et le flux de chaleur les relations :

$$\frac{\tau_x}{\rho_e u_e^2} = f''\left(\frac{\mu}{\mu_e}\ \frac{1}{R_\delta} + \frac{\rho}{\rho_e}F^2\left(\frac{\ell}{\delta}\right)^2 f''\right) \qquad \frac{-\Phi}{\rho_e u_e h_{ie}} = \left(g''-f'f''\ \frac{u_e^2}{h_{ie}}\right)\left(\frac{\mu}{\mu_e}\ \frac{1}{\mathcal{P}R_\delta} + \frac{\rho}{\rho_e}\ \frac{F^2}{\mathcal{P}_t}\left(\frac{\ell}{\delta}\right)^2 f''\right)$$

la dérivation de f et g étant effectuée par rapport à y/δ

L'hypothèse de similitude appliquée aux équations (2) et (4), écrites pour un écoulement transversal faible, conduit aux deux équations différentielles ordinaires

$$\left(\frac{\tau_x}{\rho_e u_e^2}\right)' = f''\left(\frac{\rho v}{\rho_e u_e} - \frac{\rho}{\rho_e}f'\ \frac{y}{\delta}\ \frac{\partial\delta}{\partial s}\right) + \frac{\delta}{u_e}\ \frac{\partial u_e}{\partial s}\left(\frac{\rho}{\rho_e}f'^2 - 1\right) \tag{10}$$

$$\left(\frac{\tau_x}{\rho_e u_e^2}f'\ \frac{u_e^2}{h_{ie}} - \frac{\Phi}{\rho_e u_e h_{ie}}\right)' = g''\left(\frac{\rho v}{\rho_e u_e} - \frac{\rho}{\rho_e}f'\ \frac{y}{\delta}\ \frac{\partial\delta}{\partial s}\right) \tag{11}$$

Les dérivées de f, g, τ_x et Φ sont prises par rapport à y/δ ; s est la longueur curviligne vraie ($ds = h_1 dx$).

La vitesse verticale $\rho v/\rho u_e$ s'exprime à partir de l'équation de continuité (1).

Les conditions aux limites utilisées pour résoudre ce système sont les conditions classiques d'adhérence à la paroi et d'écoulement extérieur sans frottement, à savoir :

en $\dfrac{y}{\delta}=0$: $f'=0$ et $\begin{cases} g'=h_p/h_{ie} \quad \text{(température imposée)} \\ \text{ou } g''=-\dfrac{\phi_p}{\rho_e u_e h_{ie}}\dfrac{\mu_e}{\mu_p}\, \varphi R_\delta \quad \text{(flux de chaleur imposé)}\end{cases}$

en $\dfrac{y}{\delta}=1$: $f'=1\,(u=u_e); \; g'=1\,(h_i=h_{ie}); \; f''=0\,(\tau_x=0)$

En ce qui concerne les paramètres, on notera d'abord que $f'(0)$, $g''(0)$ ou $g'(0)$, et $\delta\delta/\delta s$ qui apparaissent a priori sont en fait des résultats de la solution pour que les conditions aux limites soient satisfaites.

Les paramètres indépendants déterminant le famille des solutions sont ainsi les suivants :

Nombre de Reynolds $R_\delta=\dfrac{\rho_e u_e \delta}{\mu_e}$; nombre de Mach M_e

paramètre de gradient de pression $\beta=\dfrac{\delta}{u_e}\dfrac{\delta u_e}{\delta s}$; enthalpie ou flux de chaleur $\dfrac{h_p}{h_{ie}}$ ou ϕ_p

Un programme de résolution numérique du système des équations (10) et (11) a été établi, grâce auquel il est possible de déterminer dans le cas général d'un fluide compressible avec gradient de pression, température de paroi et nombre de Reynolds quelconques, les profils de vitesse et d'enthalpie, ainsi que les coefficients de frottement et de flux de chaleur à la paroi.

Un exemple de l'une des familles de profils ainsi établie est donné figure 1, pour un cas de nombre de Mach assez élevé, avec transfert de chaleur (on s'y est placé à un nombre de Reynolds assez grand pour qu'une solution réellement turbulente soit obtenue). Une variation systématique du paramètre β a permis de couvrir la gamme complète des gradients de pression positifs, de la plaque plane au profil de décollement. On notera l'influence essentielle de ce gradient de pression sur la forme des profils de vitesse et d'enthalpie. On observera spécialement la déformation considérable de la courbe enthalpie-vitesse (et en conséquence la variation du facteur d'analogie de Reynolds Ch/Cf) pour laquelle une relation linéaire tombe très évidemment en défaut dès que l'on s'écarte du cas de la plaque plane.

On donnera (réf. 9) les résultats obtenus lors d'une variation systématique du nombre de Mach, de la température de paroi et du paramètre de gradient de pression, en ce qui concerne les profils, le frottement, le flux de chaleur et les épaisseurs caractéristiques de la couche limite.

4.3. - Solution et profils pour l'écoulement transversal -

L'hypothèse de similitude sur la vitesse transversale est donc a priori de la forme $w/u_e=\Theta(s).t'(y/\ell)$ Cependant, pour clarifier la suite de l'exposé on dira dès maintenant que l'équation transversale de similitude écrite avec cette relation, fait apparaître un paramètre $K_2\delta/\Theta$; or celui-ci doit être constant pour que la similitude soit réalisée, la valeur de la constante étant d'ailleurs indifférente. On a ainsi été amené finalement à utiliser pour la similitude transversale un profil réduit défini par la formule :

$$\dfrac{w}{u_e}=-K_2\,\delta\cdot t'\!\left(\dfrac{y}{\delta}\right)$$

Avec cette relation, la formule (8) donne pour le frottement transversal :

$$\dfrac{-\tau_z}{\rho_e u_e^2 K_2 \delta}=t''\!\left(\dfrac{\mu}{\mu_e}\dfrac{1}{R_\delta}+\dfrac{\rho}{\rho_e}\,F^2\!\left(\dfrac{\ell}{\delta}\right)^2 f''\right)$$

L'hypothèse de similitude appliquée à l'équation (3) écrite pour un écoulement transversal faible, conduit à l'équation différentielle ordinaire :

$$\left(\dfrac{-\tau_z}{\rho_e u_e^2 K_2\delta}\right)'=t''\!\left(\dfrac{\rho v}{\rho_e u_e}-\dfrac{\rho}{\rho_e}f'\dfrac{y}{\delta}\dfrac{\delta\delta}{\delta s}\right)+\dfrac{\rho}{\rho_e}\left[\left(\dfrac{\delta}{K_2\delta}\dfrac{\delta K_2\delta}{\delta s}+\dfrac{\delta}{u_e}\dfrac{\delta u_e}{\delta s}-K_1\delta\right)f't'+\left(\dfrac{\rho_e}{\rho}-f'^2\right)\right] \quad (12)$$

Les dérivées de t' et τ_z sont prises par rapport à y/δ. La vitesse verticale $\rho v/\rho_e u_e$ s'exprime à partir de l'équation de continuité.

Les conditions aux limites sont encore dictées par la condition d'adhérence à la paroi et par celle d'une vitesse transversale extérieure nulle :

$$t'(0)=t'(1)=0$$

Pour des conditions R_δ, M_e, β et h_p fixées la distribution des vitesses longitudinales et des enthalpies qui apparaissent dans l'équation (12) est déterminée par la solution des équations longitudinales (10) et (11). L'équation (12) est ainsi linéaire en t' et fait apparaître un seul paramètre supplémentaire représentant l'influence du gradient de pression transversal et des courbures :

$$E=\dfrac{\delta}{K_2\delta}\dfrac{\delta K_2\delta}{\delta s}+\dfrac{\delta}{u_e}\dfrac{\delta u_e}{\delta s}-K_1\delta$$

Compte tenu des expressions données pour K_1 et K_2 (section 2) le paramètre de gradient de pression transversal peut encore s'écrire :

$$E=\delta\dfrac{\delta}{\delta s}\log\left|K_2\,\delta u_e h_2\right|$$

Un programme de résolution numérique de l'équation (12) a été établi et joint à celui qui permet de résoudre les équations longitudinales, de façon à obtenir également les profils de vitesse transversaux et le frottement correspondant, ceci pour des valeurs quelconques des cinq paramètres β, E, R_δ, M_e et h_p (ou ϕ_p). Appliqué intensivement dans une large gamme de ces paramètres, il a conduit à tout un ensemble de résultats, dont un
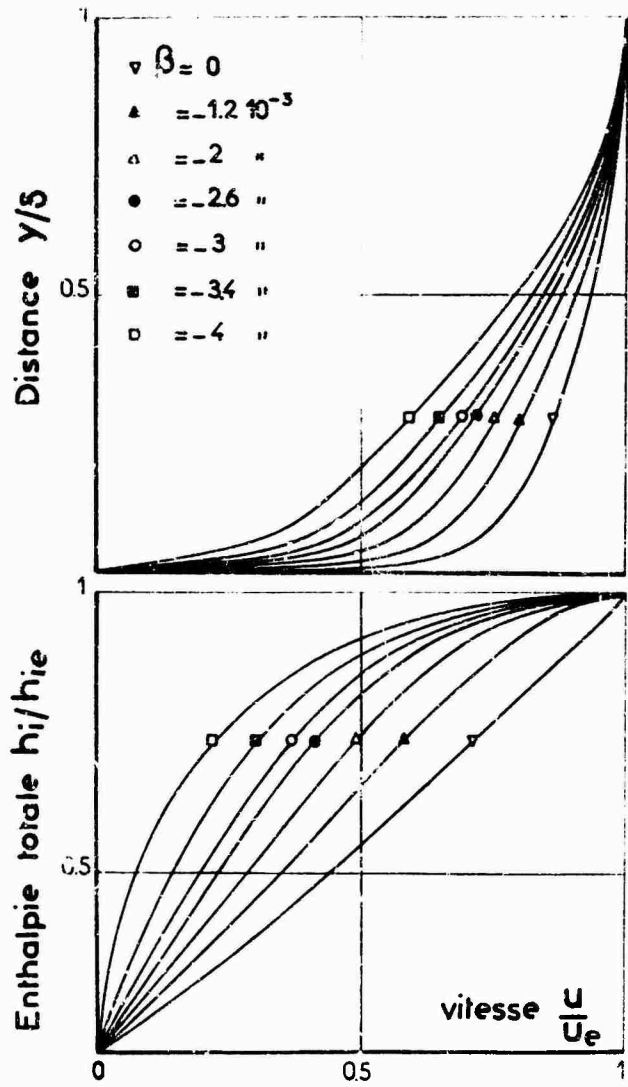
Fig. i – *Exemple de profils longitudinaux*
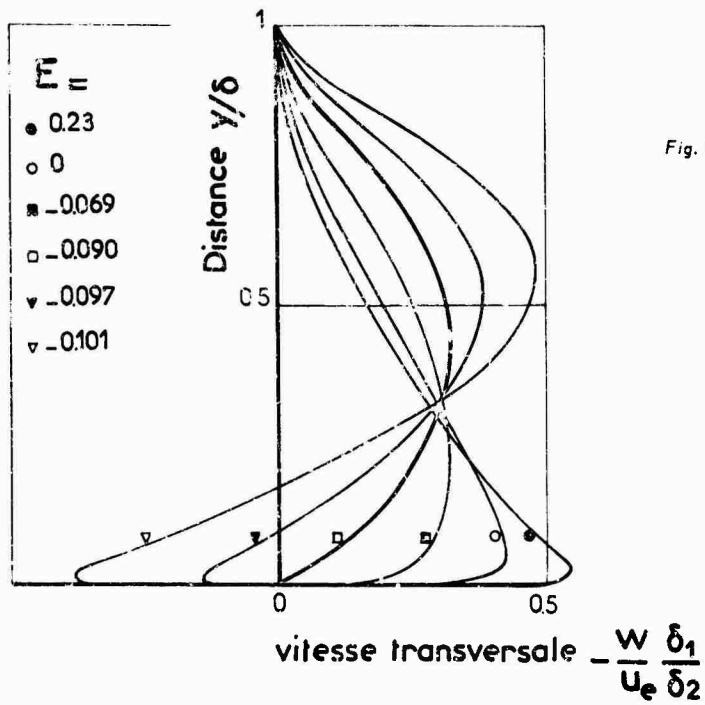
$(M_e = 7, h_p/h_{ie} \quad 0.17, R_\delta = 5.10^5)$.

Fig. 2 – *Exemple de profils transversaux*

(écoulement incompressible
$\beta = -0.015, R_\delta = 5.10^5)$.

exemple représenté figure 2 est relatif à un écoulement incompressible dans un gradient de pression longitudinal positif modéré.

Il est intéressant, en pratique de remplacer la variable $t' = \dfrac{w/u_{11}}{K_{2\delta}}$ par une variable dans laquelle $K_2 \delta$ n'intervient plus, en faisant intervenir les épaisseurs de déplacement longitudinale et transversale δ_1 et δ_2. La variable choisie est ainsi :

$$\frac{w}{u_e}\frac{\delta_1}{\delta_2} = -t' \int_o^1 \left(1 - \frac{\rho}{\rho_e} f'\right) d\left(\frac{y}{\delta}\right) \bigg/ \int_o^1 \frac{\rho}{\rho_e} t' d\left(\frac{y}{\delta}\right)$$

On a observé que t' tend vers 0 quand E tend vers $+\infty$ (écoulement transversal nul); par contre $\dfrac{w}{u_e}\dfrac{\delta_1}{\delta_2}$ tend vers un profil limite non nul.

On remarque également que l'on peut aboutir, quand E décroît, à des profils dont le sens s'inverse dans la partie intérieure de la couche limite, phénomène qui peut physiquement se produire le long d'une ligne de courant qui présente un point d'inflexion où le gradient de pression transversal change de signe.

5 – COMPARAISON DES PROFILS A L'EXPÉRIENCE –

5.1. – Mode de Comparaison –

On se propose maintenant, pour obtenir un premier contrôle de la validité de la solution proposée, de comparer les résultats auxquels elle conduit à ceux de l'expérience. Notons bien qu'il ne s'agit pas de calculer le développement de la couche limite, mais de contrôler que les profils expérimentaux sont bien représentables par la famille des profils théoriques.

La solution étant relative à des couches limites semblables, alors que l'expérience ne l'est pas a priori, il est préférable pour la comparaison envisagée de remplacer les paramètres β et E, directement liés aux propriétés de l'écoulement extérieur, par des paramètres de forme caractérisant les profils eux-mêmes.

Pour l'écoulement longitudinal, on a choisi ainsi comme paramètre de comparaison, le facteur de forme $H = \delta_1/\theta_{11}$. Le mode de comparaison consiste donc à donner à R_δ, M_e, h_p (ou ϕ_p) les valeurs expérimentales puis à rechercher la valeur de β qui permet d'obtenir dans la solution, le facteur de forme de l'expérience à laquelle on se compare.

Pour l'écoulement transversal, on a choisi le paramètre $\delta_1 \text{tg} \beta_0 / \delta_2$ qu'on peut former à partir de la solution ; on a en effet :

$$-\frac{\delta_1}{\delta_2} \text{tg} \beta_0 = \lim_{y \to 0} \left(\frac{t'}{f'}\right) \int_o^1 \left(1 - \frac{\rho}{\rho_e} f'\right) d\left(\frac{y}{\delta}\right) \bigg/ \int_o^1 \frac{\rho}{\rho_e} t' d\left(\frac{y}{\delta}\right)$$

Le mode de comparaison consiste alors, après avoir déterminé les profils longitudinaux, à rechercher la valeur de E qui permet d'obtenir dans la solution le paramètre $\dfrac{\delta_1}{\delta_2} \text{tg} \beta_0$ de l'expérience.

5.2. – Résultats de la comparaison –

Une première comparaison, relative à un écoulement incompressible, a été effectuée à propos des expériences de EAST et HOXEY [réf. 10]. Ces expériences avaient comporté une détermination détaillée des profils de vitesse longitudinaux et transversaux, pour la couche limite tridimensionnelle d'une plaque sur laquelle est posé un profil cylindrique ; la technique décrite précédemment a été appliquée de façon systématique à ces résultats expérimentaux.

Un exemple typique de la comparaison des profils transversaux est représenté figure 3 ; il est relatif à une série de quatre profils (notée 430 – 428 – 426 – 424 dans la référence [10]) montrant un écoulement transversal qui va en s'intensifiant à l'approche de la ligne de séparation. Après avoir déterminé, comme il a été décrit, les profils de $w\delta_1/u_e\delta_2$, les vitesses transversales ont été obtenues en prenant pour δ_1/δ_2 les valeurs expérimentales. Les profils sont donnés dans une représentation "polaire" $w(u)$. Mise à part une légère incertitude sur le maximum de w/u_e, qui provient d'une incertitude sur la valeur expérimentale de β_0, mais qui correspond en fait à une très faible distance y, l'accord peut être considéré comme satisfaisant. On soulignera que cet accord demeure satisfaisant même lorsque w/u atteint des valeurs importantes, bien que l'hypothèse d'un faible écoulement transversal soit à la base du résultat théorique.

La seconde comparaison, relative à un écoulement compressible, a porté sur les profils expérimentaux obtenus par HALL et DICKENS [réf. 11] à la paroi latérale d'une tuyère, donnant lieu à des lignes de courant qui présentent un point d'inflexion ($M_e = 1,92$, paroi adiabatique). La figure 4 montre la comparaison des profils transversaux aux stations notées B26, B28, B30, B32, B34, B35 dans la référence [11]. Il est intéressant d'observer notamment la déformation et le changement de signe des profils après le point d'inflexion ; ce comportement est effectivement indiqué par les profils déduits de la solution.

6 – EPAISSEURS CARACTERISTIQUES ET FROTTEMENT –

Sur un plan pratique, l'utilisation des solutions qui viennent d'être présentées doit tendre vers la détermination des caractéristiques principales de la couche limite, telles que les épaisseurs de déplacement et de quantité de mouvement et les coefficients de frottement longitudinaux et transversaux.

A priori ces caractéristiques sont déterminables dans le cas général au moyen du programme établi pour la résolution numérique des équations (10), (11) et (12) et dépendent des cinq paramètres énoncés. Il est évident, que pour un usage pratique, il convient de chercher à réduire, au moyen d'une représentation convenable, le nombre de ces paramètres ; il convient aussi de chercher à remplacer β et E par des paramètres plus commodément
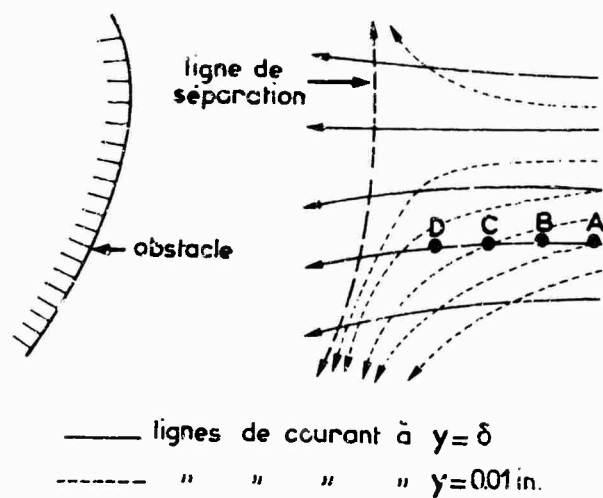
——— lignes de courant à $y = \delta$

- - - - - " " " " $y = 0.01$ in.

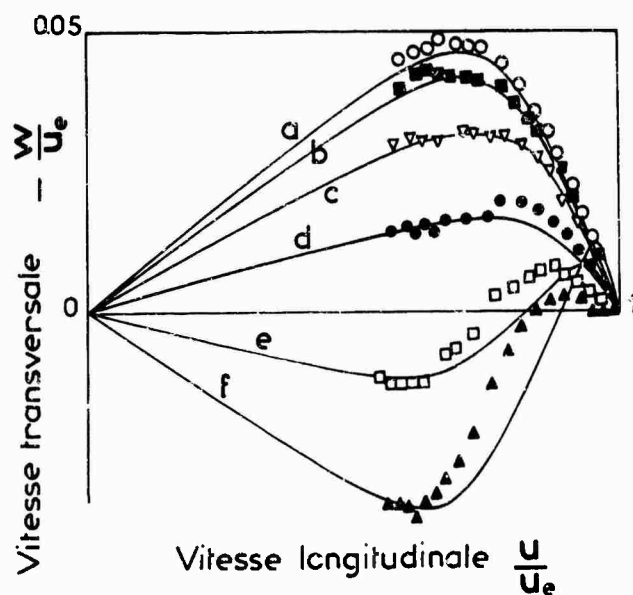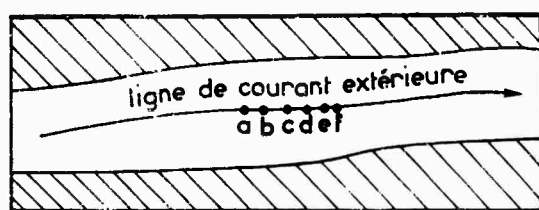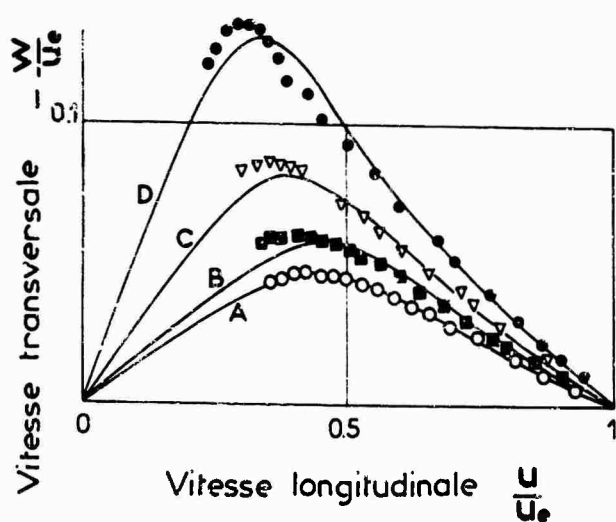*Fig. 3 – Comparaison aux profils*

de East et Haxey (incompressible .).

Fig. 4 – Comparaison aux profils

de Hall et Dickens (M≃2).

utilisables, par exemple dans une méthode intégrale.

Nous plaçant essentiellement pour ce qui suit dans le cas du fluide incompressible, les paramètres sont réduits à β, E et R_δ. On va chercher à utiliser les propriétés établies antérieurement par la solution asymptotique pour éliminer l'influence du nombre de Reynolds. On va voir apparaître en même temps des paramètres qui remplaceront commodément β et E.

6.1. - Ecoulement longitudinal -

Rappelons encore que dans le cas du fluide incompressible, une solution asymptotique a permis d'établir [réf. 1 et 2] la famille des profils de vitesse déficitaires, indépendante du nombre de Reynolds, sous la forme $(u_e - u)/u_\tau = F'(y/\delta)$ paramétrés a priori en fonction de $(\delta_1/\tau_p)\,dp/ds$. On a déjà montré [réf. 1] qu'il était commode de remplacer en pratique ce dernier paramètre par le facteur de forme du profil déficitaire (paramètre de CLAUSER) :

$$G = I_2/I_1 \quad \text{avec} \quad I_2 = \int_0^1 F'^2 d\eta \quad \text{et} \quad I_1 = \int_0^1 F' d\eta \quad (\eta = y/\delta)$$

On a vérifié enfin que les solutions obtenues dans la nouvelle hypothèse de similitude $u/u_e = f'(y/\delta)$ sont en très bon accord avec les relations déduites de la solution asymptotique ; celles-ci peuvent être utilisées pour obtenir les relations qui concernent les épaisseurs caractéristiques et le coefficient de frottement.

Désignant $\sqrt{Cf_x/2}$ par γ, les épaisseurs de déplacement et de quantité de mouvement sont alors données par les formules :

$$\frac{\delta_1}{\delta} = I_1 \gamma \qquad \frac{\delta_1}{\theta_{11}} = \frac{1}{1 - G\gamma}$$

La loi exprimant le coefficient de frottement s'écrit :

$$\frac{1}{\gamma} = \frac{1}{k} \log R_{\delta_1} + D^* \quad (k = 0,41)$$

I_1 et D^* sont des fonctions de G résultant de la solution asymptotique ; elles ont pu être représentées [réf. 1] par des formules qui sont rappelées section 6.3.

6.2. - Ecoulement transversal -

De la même manière que pour l'écoulement longitudinal, on a cherché à remplacer le paramètre E par un paramètre T plus commode et qui permette d'éliminer l'influence du nombre de Reynolds pour des fonctions appropriées. Le choix de ce paramètre T a été également dicté par l'établissement d'une solution asymptotique pour l'écoulement transversal ; dans cette solution la variable demeure $w/u_\tau K_1\delta$ qui est donc une fonction de y/δ indépendante de R_δ. Les profils asymptotiques ainsi obtenus, peuvent être paramétrés par leur intégrale c'est-à-dire par :

$$T = -\int_0^1 t' d\eta = -\frac{\delta_2/\delta}{K_1\delta}$$

T est ainsi le paramètre transversal choisi pour remplacer E.

On s'est limité dans les représentations qui suivent à utiliser les solutions dans la gamme $(0 < T < +\infty)$ des valeurs de T qui donnent des profils sans changement de signe. T = 0 représente l'écoulement transversal nul. T = $+\infty$ peut représenter un point d'inflexion.

On a vérifié par des solutions établies à différents nombres de Reynolds que le profil des vitesses transversales demeure très voisin du profil asymptotique, sauf à proximité de la paroi. En conséquence, les épaisseurs intégrales caractéristiques de la couche limite peuvent être exprimées au moyen des résultats de la solution asymptotique.

On donnera plus spécialement deux relations, intéressant les épaisseurs de déplacement et de quantité de mouvement transversales qui apparaissent dans les équations globales de la couche limite. On trouve immédiatement à partir de la solution asymptotique :

$$\frac{\delta_2}{\theta_{12}} = -\frac{\phi_1}{G\gamma} = -\phi_1 \frac{H}{H-1} \qquad \frac{\theta_{22}\delta_1}{\delta_2^2} = -\phi_2 G\gamma = \phi_2 \frac{H-1}{H}$$

$$\text{avec} \quad \phi_1 = -\frac{GT}{\int_0^1 F't' d\eta} \quad \text{et} \quad \phi_2 = \frac{I_1}{G} \frac{\int_0^1 t'^2 d\eta}{T^2}$$

Les fonctions ϕ_1 et ϕ_2 sont représentées figure 5. Observons qu'on aurait $\phi_1 = \phi_2 = 1$ pour un profil linéaire $w = C(u_e - u)$. Les fonctions s'écartent en fait assez peu de l'unité spécialement en gradient de pression positif et lorsque T tend vers 0 (écoulement transversal nul). Ces résultats rejoignent donc en pratique les observations expérimentales faites par JOHNSTON [réf. 12].

La validité des relations précédentes a été contrôlée au moyen d'une comparaison aux résultats expérimentaux de EAST et HOXEY (réf. 10) et de CUMPSTY et HEAD [réf. 13] ; la figure 6 montre ainsi un bon accord entre les valeurs mesurées de δ_2/θ_{12} et les valeurs calculées, ϕ_1 étant déterminé en fonction du G et du T qui résultent des valeurs expérimentales de $\delta_1, \theta_{11}, \delta_2, $ et γ. A titre comparatif on a également porté figure 6 la comparaison du δ_2/θ_{12} expérimental à celui qui résulterait d'un profil de MAGER $w/u = \text{tg}\,\beta_0(1 - y/\delta)^2$ [réf. 14]

Le problème se présente de façon plus délicate pour l'angle limite β_0 qui dépend évidemment du comportement à proximité de la paroi.
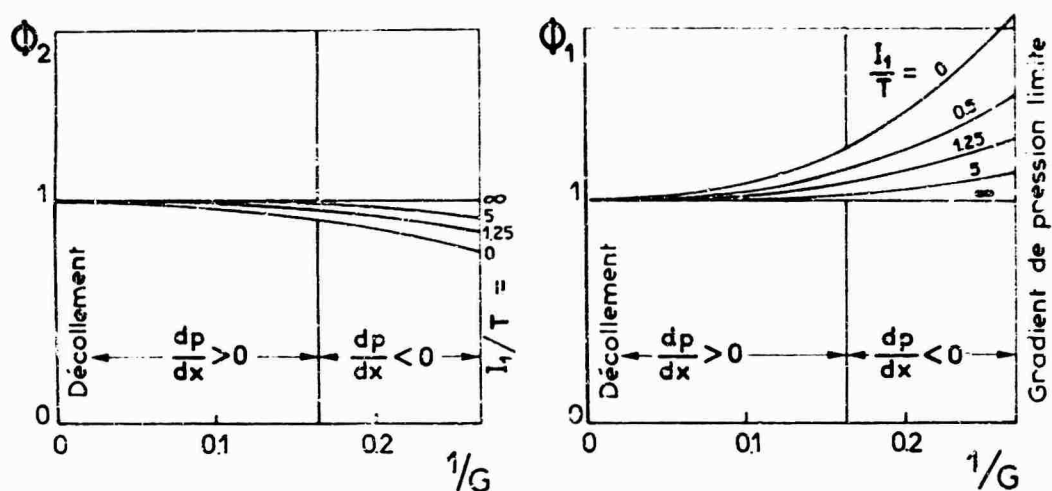
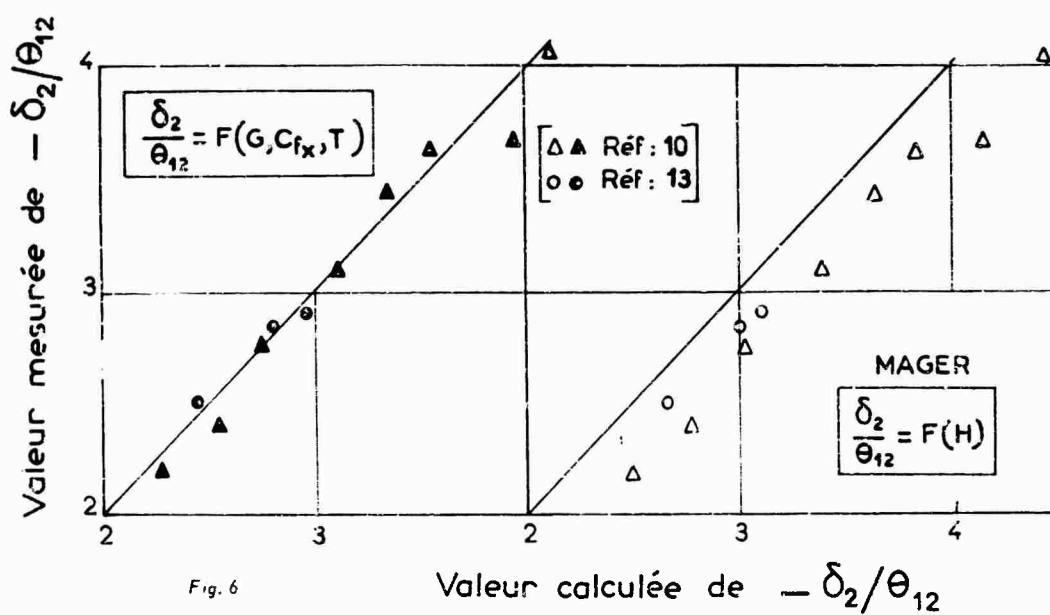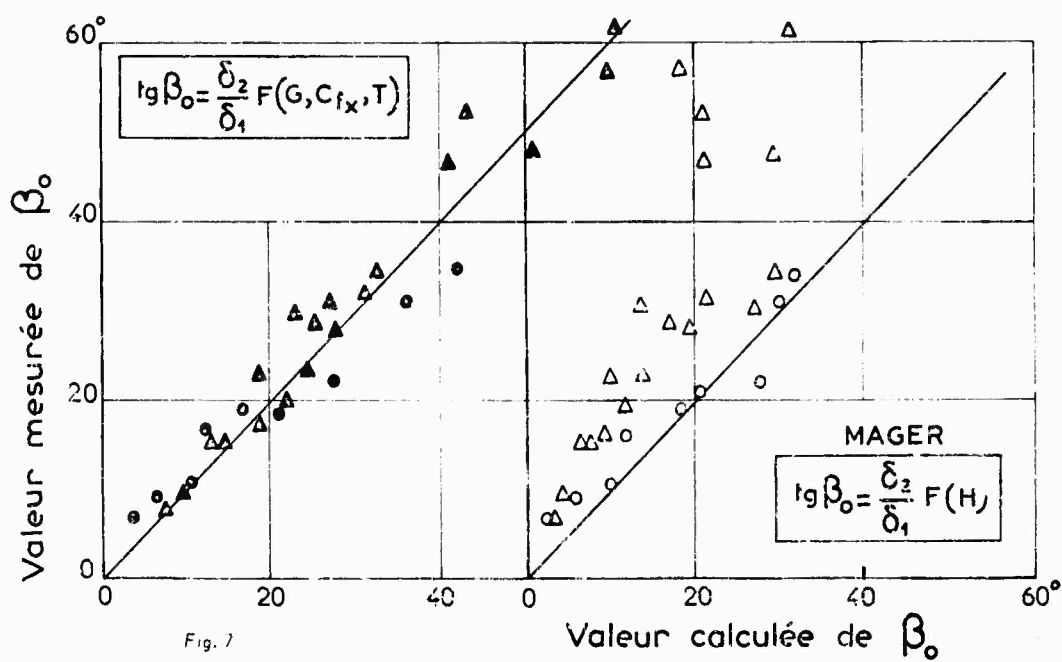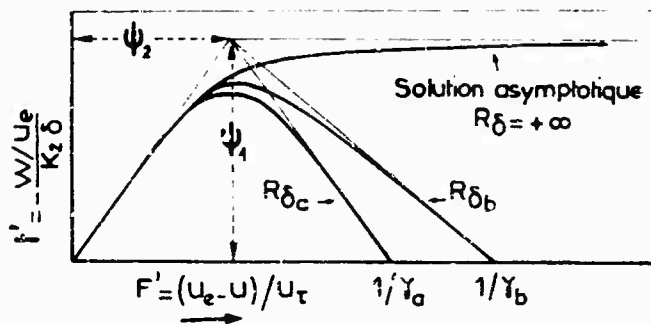Fig. 5 – Fonctions pour les rapports d'épaisseurs transversales.

Fig. 6

Fig. 7

Considérons ci-contre l'allure schématique des profils $t'(F')$ obtenus pour G et T fixés quand R_δ augmente vers l'infini. Les solutions montrent que leurs pentes à la paroi convergent pratiquement en un point de coordonnées ψ_1 et ψ_2 lesquelles sont fonctions seulement de G et T. On en déduit alors immédiatement que la loi pour l'angle limite est de la forme :

$$\frac{tg\beta_0}{K_2\delta} = \frac{-\psi_1(G,T)}{1 - \gamma\psi_2(G,T)}$$

On pourra préférer utiliser pour la comparaison à l'expérience ou dans une méthode intégrale une relation pour $tg\,\beta_0\,\delta_1/\delta_2$; celle-ci peut s'écrire finalement :

$$tg\,\beta_0 = \frac{-\delta_2/\delta_1}{\dfrac{\varepsilon_1}{I_1}\dfrac{GH}{H-1} - \varepsilon_2} \qquad (13)$$

$$\text{avec } \varepsilon_1 = \frac{T}{\psi_1} \quad \text{et} \quad \varepsilon_2 = \frac{\psi_2 T}{\psi_1 I_1}$$

ε_1 et ε_2 sont donc également deux fonctions de G et T fournies par les solutions asymptotiques. Des formules représentant les résultats obtenus pour ces deux fonctions sont données section 6.3.

La validité de cette relation pour le frottement transversal a également été contrôlée au moyen d'une comparaison aux résultats expérimentaux des références [10] et [13]. La figure 7 montre que les valeurs mesurées de β_0 sont en bon accord avec celles qui résultent d'une application de la relation (13) utilisant les valeurs expérimentales de δ_1, θ_{11}, δ_2 et γ. A titre comparatif on a également porté la comparaison du β_0 expérimental à celui qui résulterait de l'utilisation d'un profil de MAGER ; l'accord est assez bon avec les expériences de HEAD et COUSTEIX effectuées à un nombre de Reynolds $R_{\theta_{11}}$ de l'ordre de 5 000 ; le profil de MAGER donne par contre des β_0 très différents de ceux obtenus à un nombre Reynolds $R_{\theta_{11}}$ de l'ordre de 50 000 par EAST et HOXEY.

La formule que l'on propose, semble donc présenter l'avantage de tenir compte d'une influence importante du nombre de Reynolds sur l'angle limite β_0 .

6.3. - Revue des résultats pratiques -

En résumé on a vu que les épaisseurs caractéristiques de la couche limite et les coefficients de frottement peuvent être exprimés en fluide incompressible à partir des relations qui font intervenir des fonctions résultant des solutions asymptotiques.

Pour l'écoulement longitudinal, les épaisseurs caractéristiques et la loi de frottement s'écrivent :

$$\frac{\delta_1}{\delta} = I_1\gamma \quad ; \quad H = \frac{1}{1-G\gamma} \quad ; \quad \frac{1}{\gamma} = \frac{1}{k}\log R_{\delta_1} + D^* \quad \text{avec } \begin{cases} \gamma = \sqrt{Cf_x/2} \\ k = 0,41 \end{cases}$$

On a montré également [réf. 1] que l'entraînement du fluide extérieur par la couche limite est de la forme :

$$\frac{d\delta}{ds} - \frac{v_e}{u_e} = P\gamma$$

I_1, D^* et P sont des fonctions de G (paramètre de CLAUSER) pour lesquelles peuvent être utilisées les formules de représentation suivantes :

$$I_1 = 0,613\,G - (3,6 + 76,66\,(1/G - 0,154)^2)\,1/G$$
$$D^* = 2\,G - 4,25\,G^{\frac{1}{2}} + 2,12 \quad (\text{pour } G < 300)$$
$$P = 0,074\,G - 1,0957/G$$

Pour l'écoulement transversal, les rapports d'épaisseurs caractéristiques, et la loi de frottement ont été mises sous la forme :

$$\frac{\delta_2}{\theta_{12}} = -\phi_1\frac{H}{H-1} \;;\; \frac{\theta_{21}\delta_1}{\delta_2^2} = -\phi_2\frac{H-1}{H} \;;\; tg\beta_0 = \frac{-\delta_2/\delta_1}{\dfrac{\varepsilon_1}{I_1}\dfrac{GH}{H-1} - \varepsilon_2}$$

ϕ_1, ϕ_2, ε_1 et ε_2 sont des fonctions de G et de $T = -(\delta_2/\delta)/K_2\delta$ choisi comme paramètre transversal et dont on considère la variation dans la plage $0 < T < +\infty$.
Les fonctions ϕ_1 et ϕ_2 sont représentées figure 5.
Les fonctions ε_1 et ε_2 peuvent être représentées par les formules :

$$1/\varepsilon_1 = (\alpha_1(\alpha_2 - 1) + 1)\alpha_3 \qquad \alpha_1 = 20,6\,I_1^{1/2}/G^2$$

$$\varepsilon_2 = \varepsilon/(\varepsilon + 1/I_1) \qquad \alpha_2 = (\varepsilon + 0,317)/(2,21 + 0,423\,\varepsilon) + 0,856.10^{(-0,1175\,\varepsilon^{0,86})}$$

$$\varepsilon = 2\,I_1/T \qquad \alpha_3 = (2,28\,G^2 - 6,3\,G)/2\,I_1^2$$

7 - CONCLUSION -

L'utilisation du schéma de longueur de mélange proposé, dans la détermination de solutions semblables, a permis d'établir un ensemble de résultats relatifs aux couches limites turbulentes tridimensionnelles, résultats qui mettent en lumière l'influence des facteurs essentiels intervenant dans le développement de ces couches limites.

Une comparaison satisfaisante de ces résultats théoriques à ceux de l'expérience a été réalisée, notamment en ce qui concerne le profil des vitesses transversales. Il est à noter que les familles de profils déterminés par les solutions semblant en fait susceptibles de représenter correctement les profils expérimentaux, même dans des cas où l'écoulement transversal ne peut plus être considéré comme faible devant l'écoulement longitudinal.

Des lois pratiques pour les épaisseurs caractéristiques de la couche limite et pour les deux coefficients de frottement ont pu être déduites des solutions établies. Elles font intervenir deux paramètres représentant l'influence du gradient de pression longitudinal et du gradient transversal ; elles ont également l'avantage de tenir compte d'une influence appréciable du nombre de Reynolds sur l'angle limite β_0 ; données ici pour le fluide incompressible, leur extension au cas compressible est en cours.

On dispose en fin de compte de résultats qui semblent pouvoir fournir les hypothèses cohérentes et raisonnables souhaitées dans l'établissement d'une méthode intégrale de calcul des couches limites tridimensionnelles. Une telle méthode a en fait été mise au point et a déjà conduit à des résultats prometteurs dans différentes applications.

REFERENCES

1. MICHEL R.   Hypotheses on the mixing length and application to the calculation of the turbulent
   QUEMARD C.   boundary layer. - Computation of turbulent boundary layers 1968. AFOSR-IFP. STANFORD
   DURANT R.   Conference - Volume 1 - Methods, Predictions, Evaluation and Flow structure. pp 195-207.
                     Ed. S.J. KLINE, M.V. MORKOVIN, G. SOVRAN, D.J. COCKRELL (1968).

2. MICHEL R.   Application d'un schéma de longueur de mélange à l'étude des couches limites d'équilibre.
   QUEMARD C.   ONERA - N.T. 134 (1969).
   DURANT R.

3. MAGER A.   Three-dimensional laminar boundary layers. - High Speed Aerodynamics and Jet Propulsion
                     Vol. IV - Theory of laminar Flows - Section C pp. 286-394 - Ed. F.K. MOORE - Princeton
                     New-Jersey (1964).

4. EICHELBRENNER E.A. La couche limite laminaire à trois dimensions. - Publications Scientifiques et
                     Techniques du Ministère de l'Air. - n° N.T. 85 pp. 57-84 (1959)

5. VAN DRIEST E.R.   On turbulent flow near a wall - J.A.S., Vol. 23, Nov. (1956)

6. NASH J.F.   The calculation of three-dimensional turbulent boundary layers in incompressible flow.
                     J. Fluid. Mech. Vol. 37, Part. 4, pp. 625-642 (1969)

7. PERRY A.E.   A three-dimensional turbulent boundary layer. J. Fluid. Mech. Vol. 22, Part. 2
   JOUBERT P.N.   pp. 285-304 (1965)

8. TSEN LI FANG   Contribution à l'étude de la couche limite tridimensionnelle laminaire compressible
                     avec transfert de chaleur. - Thèse présentée à la Faculté des Sciences de l'Université
                     de POITIERS - n° d'ordre 55 (1965).

9. MICHEL R.   Solutions de similitude pour les couches limites turbulentes bidimensionnelles en
   QUEMARD C.   fluide compressible avec gradient de pression. - La Recherche Aérospatiale,
   COUSTEIX J.   ONERA - n° 1971-5.

10. EAST L.F.   Low-Speed three dimensional turbulent boundary layer data. Part. 1 - R.A.E. Technical
    HOXEY R.P.   Report 69 041 (1969).

11. HALL M.G.   Measurements in a three-dimensional turbulent boundary layer in supersonic flow -
    DICKENS H.B.   ARC. R&M n° 3537 (1968)

12. JOHNSTON J.P.   On the three dimensional turbulent boundary layer generated by secondary flow.
                     Journal of Basic Engineering - Series D, Trans. ASME - Vol. 82 pp. 233 (1960)

13. CUMPSTY N.A.   The calculation of three-dimensional turbulent boundary layers - Part. IV :
    HEAD M.R.   Comparison of Measurements with calculations on the rear of a swept wing.
                     ARC C.P. n° 1077 (1970)

14. MAGER A.   Generalisation of boundary layer momentum integral equations to three-dimensional
                     flows including those of rotating systems - NACA - Report 1067 (1952).

A CALCULATION METHOD
FOR THREE-DIMENSIONAL INCOMPRESSIBLE TURBULENT
BOUNDARY LAYERS

by

P. Wesseling and J.P.F. Lindhout
National Aerospace Laboratory NLR, Amsterdam, Netherlands

SUMMARY

A system of partial differential equations which can be used as a mathematical model for three-dimensional incompressible turbulent boundary layers is discussed. Certain mathematical properties of these equations are elucidated. The equations have a finite domain of dependence; this fact considerably simplifies the problem of calculating three-dimensional boundary layer flows.

The equations are solved numerically by means of a simple linear explicit finite difference scheme. The choice of an efficient difference scheme is guided by two well-known criteria for the stability of linear difference schemes with constant coefficients. The method is not restricted to small cross flow, or to flows under infinite swept wing conditions.

The method is used to calculate several experimental flows. The agreement between the computational and the experimental results is found to be encouraging, although there is room for improvement.

Computation times were found to be quite acceptable.

1. INTRODUCTION

As has been amply demonstrated at the 1968 Stanford Conference on Computation of Turbulent Boundary Layers (Ref. 1), the engineer who wishes to calculate a two-dimensional incompressible turbulent boundary layer has several methods of sufficient accuracy at his disposal. Some aspects require further attention, such as the effect of streamline curvature on the turbulence structure, but in most situations the remaining uncertainties do not seem to constitute a source of large inaccuracies. Because two-dimensional turbulent layers can now be calculated in a more or less satisfactory way, and because present-day computers possess sufficient computing capacity (as is shown by Refs. 2 and 3 and by the present paper), the time seems ripe for the development of methods to fulfill the practical need for three-dimensional turbulent boundary layer calculations on a routine basis.

Boundary layer calculation methods may be divided into two classes: differential and integral methods. Differential methods have the number of independent variables equal to the number of space dimensions, and enable the flow to be computed in detail. Integral methods have one independent variable less, and do not permit to predict the flow in detail, but give certain functionals of the solution, such as skin-friction and displacement thickness. In the two-dimensional case, there are differential as well as integral methods that give good results (Ref. 1). Leaving out of consideration methods for flows with small crossflow or flows with variations in two space-directions only (quasi-three-dimensional flows), a three-dimensional differential method (Ref. 2) and a three-dimensional integral method (Ref. 3) were recently published. It is generally held that in two dimensions differential methods are much more computer time consuming than integral methods, but in our opinion it is likely that further numerical analysis will make it possible to increase the efficiency of differential methods appreciably. At the present time it seems difficult to say whether in three dimensions the difference in computing time between differential and integral methods will be appreciable or not. Generalizing integral methods from two dimensions to three seems to require more additional empirical input than the extension of differential methods to three dimensions. At any rate, at the present stage of development of three-dimensional boundary layer calculation methods a discussion of advantages and disadvantages of integral as compared to differential methods seems premature.

The present paper presents a differential method, which, like the method of Nash (Ref. 2), is based on an extension to three dimensions of the two-dimensional Reynolds stress equation put forward by Bradshaw et al. (Ref. 4). No additional empirical input is necessary. The resulting equation is different from the Reynolds stress equation employed by Nash, but identical to the equation proposed by Bradshaw (Ref. 6). A numerical method for the solution of the resulting equations is described. The results are compared with several experiments, and with results obtained by Nash (Ref. 2) and, for quasi-three-dimensional flows, by Bradshaw (Ref. 6).

2. A SEMI-EMPIRICAL REYNOLDS STRESS EQUATION

For boundary layers on non-developable surfaces the equations have to be written down in curvilinear co-ordinates. This can be done most conveniently with the aid of tensor notation. The reader not familiar with tensor analysis may think of the equations as written in Cartesian co-ordinates by making no distinction between super- and subscripts, by interpreting the subscript $,j$ as $\partial/\partial x_j$ and the metric tensor g_{ij} as the Kronecker delta δ_{ij}, and by summing over indices that are repeated in a product. Cartesian co-ordinates can only be used for boundary layers on developable surfaces. The numerical scheme and the computational results to be described later in this paper will be restricted to such surfaces.

The co-ordinates x_i are chosen orthogonal and such that the surface to which the boundary layer is attached is given by $x_2 = 0$, and that normals to this surface are given by $x_1 = x_3 = 0$. Hence, x_2 measures distance along normals to the surface. Apart from the preceding conditions, the co-ordinate system does not need to be precisely defined at this stage. It may or may not be a streamline-co-ordinate system. The x_1-co-ordinate is chosen roughly but not necessarily precisely parallel to the inviscid streamlines at the edge of the boundary layer. Latin indices will have range $\{1,2,3\}$, Greek indices have range $\{1,3\}$.

In turbulent boundary layers the stress is dominated by the so-called Reynolds stress; except very close to the wall the viscous stress is negligible. From the Navier-Stokes equations the exact

equation for the Reynolds stress follows in a straightforward way (see e.g. Ref. 7). This exact equation should be distinguished from the semi-empirical approximations which will be discussed hereafter. The exact equation for the Reynolds stress $-\langle u_\alpha u_2 \rangle$ takes the following form in the boundary layer approximation:

$$U^j \langle u_\alpha u_2 \rangle_{,j} = -\langle u^2 u_2 \rangle U_{\alpha,2} - \langle u^2 u_\alpha u_2 + u_\alpha p \rangle_{,2} + \langle (u_{\alpha,2} + u_{2,\alpha}) p \rangle. \qquad (1)$$

The symbol $\langle \cdot \rangle$ denotes an average. Small letters denote turbulent fluctuations, capitals averaged quantities. The term at the left-handside represents advection of Reynolds stress, the first term at the right represents production, the second dissipation and the third interaction between rate of strain fluctuations and pressure fluctuations. The viscous dissipation term has been omitted because it is almost negligible. Eq. (1) cannot be used as it stands, because of the "closure-problem", which is at the heart of the difficulties connected with the understanding of turbulent flow: Eq. (1) contains unknown quantities $\langle u^2 u_2 \rangle$, $\langle u^2 u_\alpha u_2 \rangle$, etc. These unknown quantities will be replaced by expressions involving only $\langle u_\alpha u_2 \rangle$ and U_j by means of semi-empirical assumptions.

For the calculation of two-dimensional boundary layers, Bradshaw et al. (Ref. 4) have with good results made use of the following approximation to Eq. (1):

$$\frac{1}{a}\left(U_1 \frac{\partial}{\partial x_1} + U_2 \frac{\partial}{\partial x_2}\right) \langle u_1 u_2 \rangle = \langle u_1 u_2 \rangle \frac{\partial U_1}{\partial x_2} - M^{\frac{1}{2}} \frac{\partial}{\partial x_2} \left(G \langle u_1 u_2 \rangle \right) + \frac{\langle -u_1 u_2 \rangle^{3/2}}{L} \qquad (2)$$

where a, G and L are empirical functions, and M is the maximum of $\langle u_1 u_2 \rangle$ for a given value of x_1. It is assumed that $\langle u_1 u_2 \rangle$ is negative throughout the boundary layer. The first term at the right-handside of (2) is an approximation of part of the production term in (1), the second approximates the diffusion term and the third approximates the rate of strain-pressure interaction term and part of the production term. Because it tends to decrease $-\langle u_\alpha u_2 \rangle$ the last term will henceforth be referred to as the dissipation term. For a motivation of Eq. (2) the reader is referred to Ref. 4.

For three-dimensional boundary layers, Eq. (2) has to be replaced by two equations for the two equations for the two relevant components $\langle -u_\alpha u_2 \rangle$ of the Reynolds stress tensor. Since turbulence is inherently a three-dimensional phenomenon, the structure of the turbulence in two-dimensional boundary layers does not differ in an essential way from the structure in three-dimensional boundary layers, so that Eq. (2) may be taken as a point of departure for the derivation of a three-dimensional shear stress equation.

One way to generalize (2) to three-dimensions is to interpret this equation as an equation for the magnitude of the two-dimensional vector $\langle u_\alpha u_2 \rangle$. (Of course, the Reynolds stress is a tensor, but in the boundary layer approximation it behaves like a two-dimensional vector). Unfortunately, it is difficult to assign a direction to this vector. One is tempted to take the same direction as used in the eddy-viscosity methods, i.e.

$$\langle u_1 u_2 \rangle / \langle u_3 u_2 \rangle = U_{1,2} / U_{3,2} . \qquad (3)$$

This approach is followed by Naeh (Ref. 2). However, experiments show that (3) does not always hold. Another approach is to generalize Eq. (2) to a vector equation, assigning directions to the various terms. This strategy has been followed by Bradshaw (Ref. 6), and will also be followed here.

For a study of the pressure-strain rate interaction term it is useful to write down the equation for the pressure fluctuation:

$$p_{,ii} = -2 U^j_{,i} u^i_{,j} - u^i_{,j} u^j_{,i} + \langle u^i_{,j} u^j_{,i} \rangle \qquad (4)$$

The solution of this equation may be written as

$$
\left.
\begin{aligned}
p^{(1)}(x_R) &= -\iiint_D G(x_R, y_R) 2 U^i_{,i}(y_R) u^i_{,j}(y_R) \sqrt{g(y_R)}\, dy_1 dy_2 dy_3 , \\
p^{(2)}(x_R) &= -\iiint_D G(x_R, y_R) \left\{ u^i_{,j}(y_R) u^j_{,i}(y_R) - \langle u^i_{,j}(y_R) u^j_{,i}(y_R) \rangle \right\} \sqrt{g(y_R)}\, dy_1 dy_2 dy_3 \\
p &= p^{(1)} + p^{(2)}, \quad g = |g_{ij}| .
\end{aligned}
\right\} (5)
$$

Here G is the Green's function for the Laplace equation in the domain D, which is the boundary layer. In an infinite domain, G would be equal to $|x_R - y_R|/4\pi$. The pressure has been split up into two parts: $p^{(1)}$ is due to interaction between turbulence and mean flow, $p^{(2)}$ results from turbulence-turbulence interaction.

First, it will be tried to assign a direction to the pressure-strain rate interaction term in (1). For $\langle p^{(1)} u_{\ell,m} \rangle$ one finds

$$\langle p^{(1)}(x_R) u_{\ell,m}(x_R) \rangle = -2 \iiint_D G(x_R, y_R) U^i_{,i}(y_R) \langle u_{\ell,m}(x_R) u^i_{,j}(y_R) \rangle \sqrt{g(y_R)}\, dy_1 dy_2 dy_3 . \qquad (6)$$

The main contribution to the integral comes from eddies of which the length scale is the dissipation length parameter λ as defined by Townsend (Ref. 7, p.47). For high enough Reynolds number λ is much smaller than the scale of the energy containing eddies (i.e. the boundary layer thickness). This means that the eddies that dominate (6) are to a good approximation homogeneous. One then has

$$\langle u_{\ell,m}(x_k) u'_{,j}(y_k) \rangle = -\frac{\partial^2}{\partial y_m \partial y_j} \langle u_\ell(x_k) u^i(y_k) \rangle, \tag{7}$$

where for brevity the co-ordinate system has been assumed Cartesian, so that terms involving Christoffel symbols do not appear. Substitution of (7) in (6), repeated partial integration and application of the boundary layer approximation results in

$$\langle p^{(1)}(x_k) u_{\alpha,2}(x_k) \rangle = 2 \iiint_D \langle u_2(y_k) u_\alpha(x_k) \rangle U^\beta_{,2}(y_k) \left\{ G(x_k, y_k) \sqrt{g(y_k)} \right\}_{,\beta} dy_1 dy_2 dy_3 \tag{8}$$

$$\langle p^{(1)}(x_k) u_{2,\alpha}(x_k) \rangle = 2 \iiint_D \langle u_2(y_k) u_\alpha(x_k) \rangle U^\beta_{,2}(y_k) \left\{ G(x_k, y_k) \sqrt{g(y_k)} \right\}_{,\alpha\beta} dy_1 dy_2 dy_3 \tag{9}$$

The integrals are Cauchy principal value integrals. With the reasonable assumption that $\langle u_2(y_k) u_\kappa(x_k) \rangle$ is parallel to $\langle u_2(x_k) u_\kappa(x_k) \rangle$, the same is true for $\langle p^{(1)} u_{2,\alpha} \rangle$. The direction of $\langle p^{(1)} u_{2,\alpha} \rangle$ is not evident from (9). Because, as will be discussed shortly, there is evidence that part of the pressure-strain rate interaction term is in the direction of the velocity gradient, perhaps $\langle p^{(1)} u_{2,\alpha} \rangle$ is parallel to $U_{\alpha,2}$.

A detailed study of the pressure-strain rate interaction term has been made by Rotta (Ref. 8). He substitutes a Taylor-series for $U^i_{,i}(y_k)$ around the point $y_k = x_k$ and obtains a result of the following form:

$$\langle p^{(1)} u_{\ell,m} \rangle = a^{ij}_{\ell m} U_{i,j} + b^{ijk}_{\ell m} U_{i,jk} + \cdots \cdots \tag{10}$$

If the coefficients $a^{ij}_{\ell m}$ and $b^{ijk}_{\ell m}$ could be estimated, (10) would give information about the direction of $\langle p^{(1)} u_{\ell,m} \rangle$, but this does not seem easy for the non-isotropic eddy-structure of length scale λ, so that we will rely on (8) and (9), for guessing the direction of $\langle p^{(1)}(u_{\alpha,2} + u_{2,\alpha}) \rangle$. For $\langle p^{(2)}(u_{\alpha,2} + u_{2,\alpha}) \rangle$ Rotta obtains by physical reasoning the following result:

$$\langle p^{(2)}(u_{\alpha,2} + u_{2,\alpha}) \rangle = (\text{scalar}) \cdot \langle u_\alpha u_2 \rangle \tag{11}$$

The same reasoning that was used to obtain Eqs. (8) and (9) can be applied to $\langle p^{(2)}(u_{\alpha,2} + u_{2,\alpha}) \rangle$; one then finds this term to be parallel to a third-order moment of the velocity fluctuation. This result is not very useful. Assuming Eq. (11) to be accurate, $\langle p^{(2)}(u_{\alpha,2} + u_{2,\alpha}) \rangle$ is taken to be parallel to $\langle u_\alpha u_2 \rangle$.

According to the preceding discussion, the pressure-strain rate interaction term is for a large part parallel to $\langle u_\alpha u_2 \rangle$. Apart from the diffusion term, which is small, Eq. (1) then has a right-hand-side with a contribution parallel to the velocity gradient equal to $-\langle u^2 u_2 \rangle U_{\alpha,2} \cong -1.1 \langle u_\beta u_2 \rangle |U_{,2}$. In the two-dimensional case, this is equal to $1.1 \langle u_1 u_2 \rangle U_{1,2}$, instead of $0.3 \langle u_1 u_2 \rangle$, as in Eq. (2) with $a \approx 0.3$. This is one of the reasons for which Bradshaw (Ref. 6) postulates, that the pressure-strain rate interaction term consists of two parts, one of which is parallel to $\langle u_\alpha u_2 \rangle$, whereas the other equals $0.8 |\langle u_\beta u_2 \rangle| U_{\alpha,2}$. Bradshaw notes that some support for this assumption is provided by an exact solution for the asymptotic case of a large scale strain rate applied to a small scale isotropic turbulence field derived by Crow (Ref. 9). This point of view can be reconciled with the results just obtained, if it is hypothesized that $\langle p^{(1)} u_{2,\alpha} \rangle$ is parallel to $U_{\alpha,2}$. Because Rotta's study and the conclusion drawn here from Eq. (8) are not rigorous, and because Crow's solution is not strictly valid for boundary layers, there remains a considerable degree of uncertainty concerning the behaviour of the pressure-strain rate interaction term.

Fortunately, for the assignment of a direction to the dissipation term in (2) the knowledge that part of the pressure-strain rate interaction term is parallel to the shear stress is sufficient. The dissipation term in (2) must then be taken parallel to the shear stress, because there can be no doubt that the other term in (2) which represents part of the pressure-strain rate interaction, namely the production term, is not parallel to the shear stress, but parallel to the velocity gradient (see Eq. (1)). Hence, the dissipation term in (2) can be generalized to three dimensions as follows:

$$\text{Dissipation term} = \langle u_2 u_\alpha \rangle \cdot |\langle u_2 u_\beta \rangle|^{1/2}/L. \tag{12}$$

The diffusion term in (1) can also be transformed with the use of Eq. (5) and by partial integration. One obtains, in the boundary layer approximation,

$$\langle p^{(1)}(x_k) u_\alpha(x_k) \rangle = -2 \iiint_D \langle u_\alpha(x_k) u_2(y_k) \rangle U^\beta_{,2}(y_k) \frac{\partial}{\partial y_\beta} \left\{ G(x_k, y_k) \sqrt{g(y_k)} \right\} dy_1 dy_2 dy_3 \tag{13}$$

Again assuming $\langle u_\alpha(x_k) u_2(y_k) \rangle$ to be parallel to $\langle u_\alpha(x_k) u_2(x_k) \rangle$, $\langle p^{(1)} u_\alpha \rangle$ is also found to be parallel to this vector. Similarly, $\langle p^{(2)} u_\alpha \rangle$ is found to be parallel to a third order velocity fluctuation moment, which result cannot be used. For want of a better assumption, $\langle p^{(2)} u_\alpha \rangle$ is taken to be parallel to $\langle p^{(1)} u_\alpha \rangle$, which may be expected to dominate the diffusion term anyway. Thus, one has the following generalization of the diffusion term in (2):

$$\text{Diffusion term} = -M^{1/2}(G \langle u_\alpha u_2 \rangle)_{,2} \; ; \; M = \max_{\{x\}} |\langle u_2 u_\beta \rangle|. \tag{14}$$

The production term in (1) is obviously in the direction of $U_{\alpha,2}$.

It is now possible to write down the following three-dimensional generalization of (2), replacing $-\langle u_\lambda u_\mu \rangle$ by the symbol $\tau_{\lambda\mu}$:

$$\frac{1}{a} U^j \tau_{\alpha,j} = |\tau| U_{\alpha,2} - M^{1/2} (G\tau_\alpha)_{,2} - \tau_\alpha |\tau|^{1/2}/L , \tag{15}$$

where $|\tau| = \{\tau_\beta \tau^\beta\}^{1/2}$

The same shear stress equation has also been arrived at by Bradshaw (Ref. 6) by a different way of reasoning. Perhaps the fact that different trains of thought lead to (15) is encouraging.

3. DISCUSSION OF EQUATIONS AND BOUNDARY CONDITIONS

The equations to be used here as a mathematical model for three-dimensional turbulent boundary layers are:

$$U^j U_{\alpha,j} = Q_\alpha + \tau_{\alpha,2} , \tag{16}$$

$$\frac{1}{a} U^j \tau_{\alpha,j} = |\tau| U_{\alpha,2} - M^{1/2} (G\tau_\alpha)_{,2} - \tau_\alpha |\tau|^{1/2}/L , \tag{17}$$

$$U^j_{,j} = 0 , \tag{18}$$

where $Q_\alpha = U^\beta U_{\alpha,\beta}|_{y=\delta}$. Eqs. (16) and (17) may be combined such that the unknowns are differentiated in the same direction:

$$\mu_{1,2}\left(U_{\alpha,1} + \Upsilon_{1,2} U_{\alpha,2} + \frac{U_3}{U_1} U_{\alpha,3}\right) + \tau_{\alpha,1} + \Upsilon_{1,2}\tau_{\alpha,2} + \frac{U_3}{U_1}\tau_{\alpha,3} = \frac{1}{U_1}\left(\mu_{1,2} Q_\alpha - R\tau_\alpha\right) \tag{19}$$

where $\mu_{1,2} = p \pm (p^2 + a|\tau|)^{1/2}$, $p = aM\ell/2q_e$, $\Upsilon_{1,2} = U_2 + p \mp (p^2 + a|\tau|)^{1/2}$, $R = \frac{aM}{q_e}\frac{d\ell}{dy} + \frac{a|\tau|^{1/2}}{L}$, $q_e = |U_\beta|_{y=\delta}$.

From Eqs. (18) and (19) it is clear, that the equations are hyperbolic. There are three characteristics. Eq. (19) shows, that the bi-characteristics which together form one characteristic are tangent to the vector $(1, \Upsilon_{1,1}, U_3/U_1)$, and that the bi-characteristics of a second characteristic are tangent to the vector $(1, \Upsilon_2, U_3/U_1)$. Note that the orthogonal projections on the surface of these bi-characteristics coincide with the orthogonal projection of the velocity vector. The x- or the x-derivative may be eliminated from (18) with the use of (19), which shows that normals to the surface are also bi-characteristics.

It is of interest to investigate what the region of influence of a given point is. The foregoing hyperbolic system is not symmetric and the characteristics have points of contact; therefore a general theory concerning existence, uniqueness and domain of dependence of solutions is not available (Ref. 10, pp. 618, 676). One possibility is that a perturbation applied to a solution in a given point P propagates along the bi-characteristics through P without spreading to other bi-characteristics (Fig. 1(a)). Another possibility is that the perturbation spreads to all bi-characteristics that contain a point or intersect a region where the perturbation is present; as a consequence, the influence of a perturbation in P is present in the wedge which contains all bi-characteristics, or, equivalently, all velocity vectors through the normal on the body surface through P (see Fig. 1(b)). In the first case the region of influence of a given surface element is as depicted in Fig. 1(c), in the second case as drawn in Fig. 1(d). In the second case the domain of dependence is smaller, and is identical to the domain of dependence for the three-dimensional laminar boundary layer equations, as derived heuristically by Raetz (Ref. 11). As long as it is not known which of the two possibilities actually occurs it seems best to confine the calculations to the smaller one of these two domains, because one can then be sure that the initial data completely define the solution in this domain, and because one saves computational effort. Raetz's influence principle may be formulated as follows. Initial data given on an arbitrary surface S define the solution completely in a finite domain of dependence, which is bounded by S and by surfaces generated by normals to the body-surface, whose intersections with the body surface are in every point P tangent to the projection of that streamline through the normal in P, which makes either the largest or the smallest angle with the undisturbed stream of all streamlines through the normal in P. Fig. 2 may be helpful in understanding this definition. In Fig. 2, $\tan \beta = \max U_3/U_1$, $\tan \gamma = \min U_3/U_1$.

Intuitively, one expects the influence principle to be not just a property particular to the semi-empirical system of equations adopted here, but to have wider significance. For, whether a boundary layer be laminar or turbulent, one expects transport of the properties of the flow to be due to two effects only in the boundary layer approximation: (i) convection with the flow, and (ii) diffusion perpendicular to the surface. If this is admitted as fact, the influence principle immediately follows.

The influence principle is of great practical importance. Suppose for instance that one wishes to calculate the laminar boundary layer in a point P (Fig. 3) which is in the vicinity of a portion of the body for which boundary layer calculations are difficult to perform, such as the wing-fuselage junction, or a discontinuity due to a deflected control surface. According to the influence principle, the boundary layer in P can be calculated without computing the flow in the more difficult regions, as long as these are outside the domain of dependence of P. Furthermore, in experimental investigations the measurement of flow conditions in a given point P is only relevant if the flow is also measured in an upstream region of which the domain of dependence contains P. Otherwise, the flow in P cannot be predicted by calculation methods.

The initial and boundary conditions will now be considered. In order for the problem to be well-posed as a Cauchy initial value problem, U_α and τ_α should be given on a surface which is nowhere

tangent to the characteristic directions. Assuming this initial surface to be built up of normals to the body-surface, derivatives of U_α can be expressed in derivatives in the initial surface with Eq. (19). Then Eq. (18) gives U_2 on the initial surface, whereupon Eq. (19) gives the derivatives of U_α and τ_α, and the calculation can proceed. In contrast with laminar boundary layers, no boundary condition is to be applied at the outer edge of the boundary layer, a point which has been overlooked until now. The reason for this is, that near the outer edge, where $|\tau| \to 0$, all bi-characteristics point outwards, so that the unknowns are completely defined by the equations, and the application of boundary conditions results in non-existence of solutions, unless the boundary conditions are compatible with the equations, i.e. are such that they would also be satisfied by the solution if they were not imposed. This happens to be the case with the boundary conditions that are usually imposed on boundary layers:

$$U_\alpha \to U_\alpha\big|_{y=\delta} \,,\; \tau_\alpha \to 0 \quad \text{as } x_2 \to \infty \tag{20}$$

Near the wall one bi-characteristic points towards the wall, and two boundary conditions are needed here. Following Bradshaw et al. (Ref. 4), the law of the wall is imposed at a suitable distance from the wall, rather than imposing the no-slip condition and incorporating the hard to calculate viscous sublayer in the computational region. At present, there is still some uncertainty concerning the law of the wall in three dimensions. It seems best to assume, as Bradshaw (Ref. 6) and Nash (Ref. 2) also do, that in three dimensions the magnitudes of the velocity and shear stress vectors are related to each other in the same way as in two dimensions. In the calculations reported here the law was used in both its simple form:

$$|U_\alpha| = (\tau_w^{\frac{1}{2}}/K)(\ln(x_2 \tau_w^{\frac{1}{2}}/\nu) + A)\,, \tag{21}$$

with $K = 0.4$ and $A = 2$, and its extended form, as written down for example in Ref. 6.
A second boundary condition is obtained by prescribing the direction of the shear stress. In the region where the law of the wall is valid, mixing-length theory is a good approximation, so that the shear stress is in the direction of the velocity gradient. Numerical solutions of the equations with the method to be described shortly, showed that near the wall the velocity vector is almost parallel to the velocity gradient. Hence the shear stress may just as well be taken parallel to the velocity vector, and this assumption has been used, because it is computationally more convenient. Hence

$$\tau_1/\tau_3 = U_1/U_3 \tag{22}$$

Further boundary conditions need not be applied.

4. A FINITE DIFFERENCE SCHEME

In the region where the boundary layer is to be calculated a grid is constructed with nodes ($x_1 = l\Delta x_1, x_2 = m\Delta x_2, x_3 = n\Delta x_3$). After the solution has been found in grid-points in the plane $x_1 = l\Delta x_1$, it is calculated in the adjacent plane $x_1 = (l+1)\Delta x_1$, by means of a six-point one step explicit difference scheme. In order to calculate the solution in a typical point B in the plane $x_1 = (l+1)\Delta x_1$, use is made of the values of the solution in the points $A_1, \ldots A_5$ in the plane $x_1 = l\Delta x_1$ (see Fig. 4). The numerical solution will only converge to the exact solution as the computational grid is refined, if the difference scheme is consistent with the differential equations and is stable. The Courant-Friedrichs-Levy (CFL) condition (Ref. 12) is necessary for stability. The CFL condition says that for stability it is necessary that the characteristics through B intersect the plane $x_1 = l\Delta x_1$ within the quadrangle $A_2 A_3 A_4 A_5$. Because in Eq. (19) no derivatives of U_2 appear, it can be considered separately from Eq. (18). The characteristics of (19) have the following direction: $(1, \tau_{1,2}, U_3/U_1)$ The CFL condition takes the following form:

$$\Delta x_1 \leq \Delta x_2 \Delta x_3 / \max_{\{x_2, x_3\}} \left\{ \left|\frac{U_3}{U_1}\right| \Delta x_2 + \left|\tau_{1,2}\right| \Delta x_3 \right\} \tag{23}$$

Usually, $\tau_{1,2}$ is a small quantity (of the order of 0.05). Furthermore, for most boundary layers it is possible to choose the x_1-axis such that U_3/U_1 is also a small quantity over a large part of the flow. It turns out that the restriction placed on the step-size by (23) is not much more severe than the restriction imposed by the requirement of accuracy. In order for a scheme to be accurate the step-size should be so small that the variables change little over one step. Provided one can show that (23) is also sufficient for stability, there does not seem to be much reason to use more complicated difference schemes (e.g. implicit or two-step schemes), that are not subject to (23).

A condition that is usually sufficient for stability is the Neumann stability condition. This condition says that, if the coefficients in the difference scheme are taken to be constant and lateral boundaries (i.e. the wall and the edge of the boundary layer) are absent, the amplitude of a harmonic wave of arbitrary wave-length should not increase as it propagates through the computational grid. The Neumann condition is often more stringent than the CFL condition.

The difference scheme is constructed as follows. Use is made of the differential equations in the form (19) rather than (16) and (17). Assume that the solution has been calculated in the $x_1 = l\Delta x_1$ plane. A line is drawn through B (Fig. 4) parallel to one of the two characteristics $(1, \tau_{1,2}, U_3/U_1)$ in A_1. This line intersects the quadrangle $A_2 A_3 A_4 A_5$ in one of the four triangles that make up the quadrangle. The x_2- and x_3-derivatives are now discretized in such a way that use is only made of the vertices of the triangle just mentioned. This procedure for obtaining a difference approximation to quasi-linear hyperbolic systems was for the two-dimensional case first proposed by Courant, Isaacson and Rees (Ref. 13) For Eq. (19) one obtains:

$$\mu_{1,2}\left(U_{\alpha,\ell+1}^{m,n}-U_{\alpha,\ell}^{m,n}\right)+\mu_{1,2}\frac{\Delta x_1}{\Delta x_2}|T_{1,2}|\left(U_{\alpha,\ell}^{m,n}-U_{\alpha,\ell}^{m-\ell,n}\right)+\mu_{1,2}\frac{\Delta x_1}{\Delta x_3}\left|\frac{U_3}{U_1}\right|\left(U_{\alpha,\ell}^{m,n}-U_{\alpha,\ell}^{m,n-\ell}\right)$$

$$+\tau_{\alpha,\ell+1}^{m,n}-\tau_{\alpha,\ell}^{m,n}+\frac{\Delta x_1}{\Delta x_2}|T_{1,2}|\left(\tau_{\alpha,\ell}^{m,n}-\tau_{\alpha,\ell}^{m-\ell,n}\right)+\frac{\Delta x_1}{\Delta x_3}\left|\frac{U_3}{U_1}\right|\left(\tau_{\alpha,\ell}^{m,n}-\tau_{\alpha,\ell}^{m,n-\ell}\right)=\frac{1}{U_1}\left(\mu_{1,2}Q_\alpha-R\tau_\alpha\right),\quad(24)$$

where $\hat{R}=sgn\,T_{1,2}$, $\hat{J}=sgn\,(U_3/U_1)$. It has been assumed that the co-ordinates are Cartesian. After U_α and τ_α have been found from (24), any discretized version of Eq. (18) results in an ordinary difference equation for U_2, for which the stability properties are easy to investigate. It turns out that for Eq. (24) the Neumann condition is identical to the CFL condition (Eq. (23)). Hence, Eq. (24) is optimum in the sense that the stability condition is as weak as possible. It is noteworthy that this would not have been so if instead of (19) Eqs. (16) and (17) had been discretized, for instance such that the direction in which an unknown is differentiated is taken into account analogous to the way in which the direction of the characteristics is taken into account in (24). For the scheme obtained in this way, the Neumann condition was found to be much more severe than (23).

Eq. (24) contains the main body of the method. Special measures are necessary near the surface where the initial conditions are applied, and near the lateral boundaries of the computational region. In general, the initial surface is not a plane x_1 = constant. The lateral boundaries can be defined arbitrarily. In order to keep the computational work down to a minimum the lateral boundaries were made to coincide with the boundaries of the region of influence of the initial surface; obviously, calculations outside this region do not produce meaningful results. The orthogonal projection of the computational region typically looks like Fig. 5. In accord with the definition of the influence principle, $\tan\beta = \max U_3/U_1$, $\tan\gamma = \min U_3/U_1$. In order to treat cells that are not rectangular, the equations are transformed to non-orthogonal co-ordinates that coincide with the cell boundaries. As a result, along the lateral boundaries boundary conditions, which otherwise would have to be guessed, are not needed. The presence of lateral boundaries, which is not accounted for in the Neumann stability criterion, did no affect the stability of the calculations.

5. COMPARISON WITH EXPERIMENT

Four experiments have been selected to compare the present calculation method with; the results will be described successively. The computer program proved to be sufficiently flexible to accomodate the initial and boundary conditions for all test cases; no modifications in the program were necessary.

5.1 Relaxing constant pressure flow (Ref. 5)

The flow takes place over a flat plate under constant pressure, with three-dimensional initial conditions (Fig. 6). The flow at the trailing edge of a 45° "infinite" swept wing furnishes the initial profiles. As Fig. 6 shows, the initial profiles show almost no spanwise variation. Fig. 7 gives at three stations angles of velocity, shear stress and velocity gradient. The scatter in the direction of the velocity gradient is due to the fact, that the numerical evaluation of the velocity gradient is done very crudely, namely by first order differencing. Fig. 8 gives velocity and shear stress profiles, and Fig. 9 the magnitude of the skin-friction. The agreement between calculations and experiment is satisfactory. There is also good agreement between the present calculations and the calculations by Bradshaw (Ref. 6). This reflects favourably upon the soundness of the present numerical method. In Ref. 6 the same differential equations are solved as in the present paper, but with a more straightforward numerical technique, which uses the fact, that there are really only two independent variables in the present flow. A difference between the method of Ref. 6 and the present method is, that in Ref. 6 the law of the wall is employed in its extended form, i.e. assuming the shear stress magnitude to vary linearly in the wall region, whereas in the present calculations the law of the wall is used in its simple form, with the shear stress assumed constant. However, in the flow under discussion the pressure is constant, so that the difference between the two laws of the wall should be slight.

The calculation took 19 min., including compilation and printing, on a CDC-3300 computer. The number of grid-points in the x_2-direction (perpendicular to the wall) varied between 25 and 30. In the x_3-direction (perpendicular to the tunnel-axis) the number of grid-points was maximally 30; it decreased during the course of the computation because the width of the computational region decreased.

5.2 Forward facing step under 5° yaw (Ref. 14)

In this flow there were large pressure variations in the direction perpendicular to the surface. In the calculation the surface pressure has been used, therefore accuracy is to be expected only in the lower third or so of the boundary layer. The computational region is shown in Fig. 10. In the calculation separation occurred appreciably closer to the step than in the experiment. This corresponds to the fact that the wall-streamline angle is underestimated (Fig. 13). The calculation by Bradshaw (Ref. 6) also underestimates the wall streamline angle, but to a lesser extent. The difference between Bradshaw's and the present calculation is probably due to the difference in the law of the wall. Near the wall, the shear stress direction is predicted inaccurately by both methods. In Fig. 13, the scatter in the angle predicted by the present method is due to the fact that angles at different spanwise positions are presented. Because spanwise variations in initial and boundary conditions are absent, the scatter is a measure of the numerical truncation error of the present method. Figs. 11 (a) and (b) show, that the velocity magnitude is slightly overestimated, whereas the shear stress magnitude is predicted correctly. The prediction of the velocity and shear stress directions near the wall (Fig. 11 (c)) leaves something to be desired. The agreement with the calculations of Ref. 6 is satisfactory; the differences near the wall may be ascribed to the difference in the law of the wall. The skin-friction (Fig. 12) is slightly underestimated; again, improvement is to be expected from the extended law of the wall.

The computation time for this case was 50 min. The number of grid-points in the x_2-direction varied between 20 and 40; the number of grid-points in the x_3-direction was maximally 30.

5.3 "Infinite" swept wing boundary layer experiment (NLR, unpublished).

At NLR, an experiment is in preparation in which a pressure distribution qualitatively similar to the pressure distribution of an "infinite" 35° swept wing is imposed on a flat plate. Fig. 14 shows an oilflow pattern as observed during an exploratory run; the pattern approximately represents the surface streamline. The region of influence of a surface segment parallel to the leading edge is de-

picted in Fig. 15, together with a surface streamline. Two calculations were made, one with the simple and one with the extended law of the wall. Ideally, the left-hand boundary should coincide with this surface streamline. As in the previous test-case, the crossflow angle near the surface is underestimated, although the use of the extended law of the wall gives considerable improvement.

The calculation took 46 min. with the simple law of the wall and 37 min. with the extended law of the wall. The number of grid-points in the x_2-direction varied between 20 and 40; in the x_3-direction it was maximally 15.

5.4 Swept wing experiment by Cumpsty and Head (Ref. 15)

This experiment concerns the boundary layer flow on a 61.1° swept wing. Two calculations were made, both with the extended law of the wall but with different pressure distributions. One distribution (distribution (1)) was taken directly from the measurements; the pressure was assumed to vary linearly between the two chords where the pressure was measured. The second distribution (distribution (2)) is a tenth-degree polynomial fit to the(courteously to us supplied)pressure distribution used by Bradshaw (Ref. 6). Fig. 16 gives the resulting velocity distribution at the edge of the boundary layer at the locus where boundary layer measurements were made, together with the pressure gradient for Bradshaw's distribution and the polynomial approximation in the region where separation is predicted. Figs. 17 and 18 show that the agreement between the present calculation and that of Ref. 6 is reasonably close. The scatter in the present calculation is due to spanwise variations. With distribution (2), which has no spanwise variation, these should be absent. The scatter is a measure of the truncation error of the difference scheme. The large difference between the present calculations displayed in Fig. 18 shows, that relatively small pressure differences (see Fig. 16) can have a large effect on three-dimensional boundary layers. This fact has also been observed experimentally; introduction of the traverse gear into the flow caused the separation line to move appreciably in this experiment. The fact that Bradshaw's calculation predicts separation earlier than the present calculation corresponds probably to the fact that, as shown in Fig. 16, Bradshaw's calculation has a steeper pressure gradient in the region where separation is predicted. Fig. 19 gives a comparison between the present method, the method of Nash (Ref. 2) and experiment. The difference between the directions of shear stress and velocity gradient was found to be small, so that the present results should agree with those of Nash; this is indeed the case. Agreement with experiment is disappointing. Nash obtained much better agreement (Fig. 19) by imposing an additional spanwise pressure gradient, equal to twice that formed by dividing the maximum difference in pressure between the two spanwise measuring stations by the distance between them. Bradshaw also obtained better agreement with experiment than shown in the figures by correcting the mixing length for streamline curvature.

Both calculations took about 55 min. The number of grid-points in the x_2-direction was maximally 51, in the x_3-direction 27.

6. CONCLUSIONS

A method has been presented with which it is possible to compute three-dimensional incompressible turbulent boundary layers at reasonable cost. The method is not restricted to small-cross flows or "infinite" swept wing type flows, and is flexible enough to handle a variety of flow situations without modification.

Agreement with experiment is satisfactory, but can be improved. To this end, as has also been noted in Ref. 2, more and better experiments are needed. The pressure should be measured accurately and in many points, because small uncertainties in the pressure distribution or small deviations in the flow from a nominally "quasi-three-dimensional" state can have large effects.

REFERENCES

1. Kline, S.J., Morkovin, M.V., Sovran, G. and Cockrell, D.J., (eds), 1968, Proceedings Computation of Turbulent Boundary Layers - 1968 AFOSR-IFP Stanford Conference, Vol. 1.

2. Nash, J.F., 1969, The calculation of three-dimensional turbulent boundary layers in incompressible flow. J. Fluid Mech. 37, 625-642.

3. Myring, D.F., 1970, An integral prediction method for three-dimensional turbulent boundary layers in incompressible flow. RAE TR 70147.

4. Bradshaw, P., Ferriss, D.H. and Atwell, N.P., 1967, Calculation of boundary-layer development using the turbulent energy equation. J. Fluid Mech. 28, 593-616.

5. Bradshaw, P. and Terrell, M.G., 1969, The response of a turbulent boundary layer on an "infinite" swept wing to the sudden removal of pressure gradient. NPL Aero Rep. 1305.

6. Bradshaw, P., 1971, Calculation of three-dimensional turbulent boundary layers. J. Fluid Mech. 46, 417-445.

7. Townsend, A.A., The structure of turbulent shear flow. Cambridge 1956.

8. Rotta, J., 1951, Statistische Theorie nichthomogener Turbulenz. Z.f.Physik, 129, 547-572.

9. Crow, S.C., 1968, Viscoelastic properties of fine-grained incompressible turbulence. J. Fluid Mech. 33, 1-20.

10. Courant, R. and Hilbert, D., Methods of mathematical physics. Vol. II. New York 1962.

11. Raetz, G.S., 1957, A method of calculating three-dimensional laminar boundary layers of steady compressible flows. Northrop Rep. No. NAI-58-73. (also available as ARC 23, 634 F.M. 3170, 1962).

12. Courant, R., Friedrichs, K. und Lewy, H. 1928, Über die Partiellen Differenzengleichungen der Mathematischen Physik, Math. Ann. 100, 32-74.

13. Courant, R., Isaacson, E. and Rees, M., 1952, On the solution of nonlinear hyperbolic differential equations by finite differences. Comm. Pure Appl. Math. 5, 243-255.

14. Johnston, J.P., 1970, Measurements in a three-dimensional turbulent boundary layer induced by a swept, forward-facing step. J. Fluid Mech. 42, 823-844.

15. Cumpsty, N.A. and Head, M.R., 1970, The calculation of three-dimensional turbulent boundary layers. Part IV: Comparison of measurements with calculations on the rear of a swept wing. ARC C.P. No. 1077.
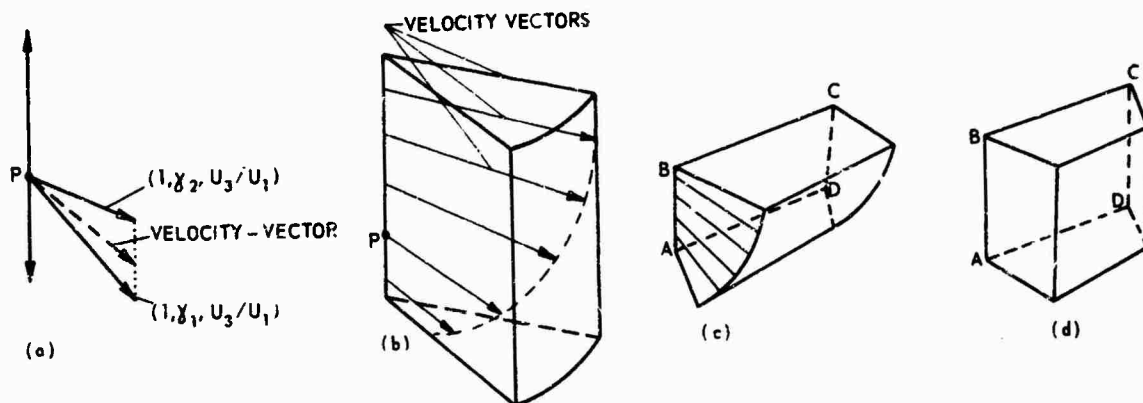
FIG. 1 (a) PERTURBATION CONFINED TO BI-CHARACTERISTICS THROUGH P.
   (b) PERTURBATION CONFINED TO WEDGE CONTAINING ALL VELOCITY VECTORS THROUGH THE NORMAL.
   (c) REGION OF INFLUENCE OF SURFACE ELEMENT ABCD.
   (d) REGION OF INFLUENCE OF SURFACE ELEMENT ABCD.
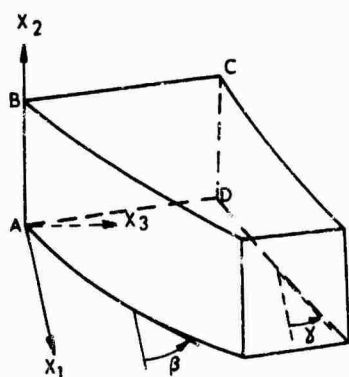
FIG. 2 DOMAIN OF INFLUENCE OF SURFACE SEGMENT ABCD ACCORDING TO RAETZ'S INFLUENCE PRINCIPLE.
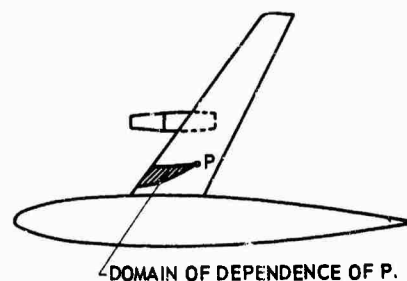
FIG. 3 TYPICAL SHAPE OF THE DOMAIN OF DEPENDENCE
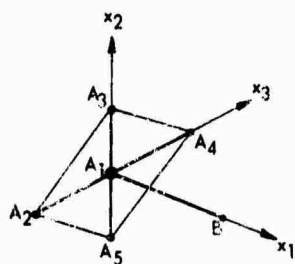
FIG. 4 THE SIX POINTS THAT OCCUR IN THE DIFFERENCE SCHEME
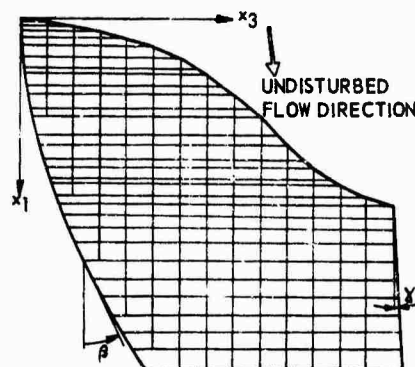
FIG. 5 ORTHOGONAL PROJECTION OF TYPICAL COMPUTATIONAL REGION.
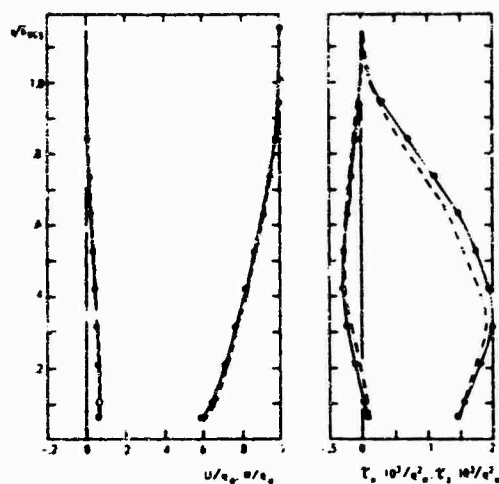
FIG. 6 INITIAL PROFILES FOR THE CALCULATION OF EXPERIMENT BY BRADSHAW AND TERRELL (REF. 5).
———, $z = 77$, $z = 2$, $\delta_{995} = .95$ (in.); ———, $z = 83$, $z = 0$, $\delta_{995} = .95$ (in.); o, EXPERIMENTAL RESULTS
AT $z = 77$, $z = 2$.

ANGLE FROM TUNNEL CENTERLINE, DEGREES
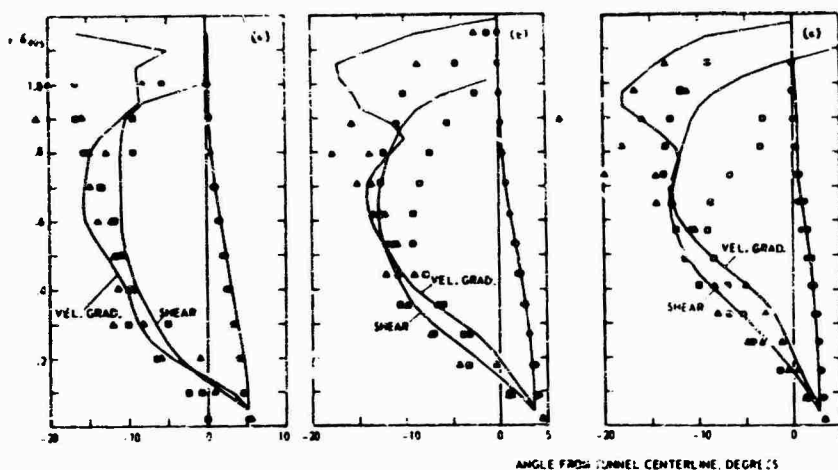
FIG. 7 CALCULATION OF VELOCITY, SHEAR STRESS AND VELOCITY GRADIENT ANGLES IN EXPERIMENT BY
BRADSHAW AND TERRELL (REF. 5). ———, CALCULATION. EXPERIMENTAL RESULTS o, VELOCITY,
□, SHEAR STRESS, △, VELOCITY GRADIENT. CALCULATION, REF. 6 : •, VELOCITY; ■, SHEAR STRESS,
▲, VELOCITY GRADIENT. (a), $x - z = 77$, $\delta_{995} = 1.00$ (in.), (b), $x - z = 83$, $\delta_{995} = 1.14$ (in.); (c), $x - z = 89$, $\delta_{995} = 1.23$ (in.)
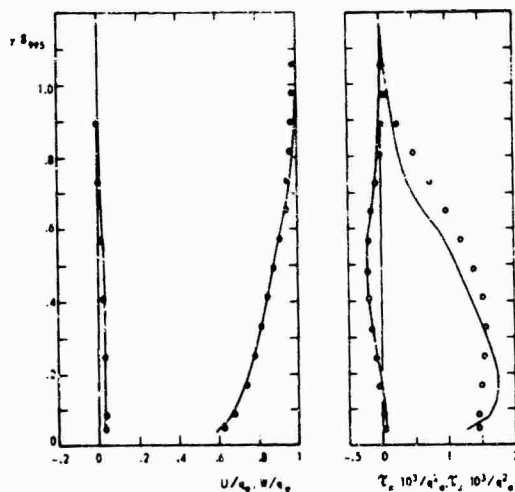
FIG. 8 MEASURED AND COMPUTED PROFILES, EXPERIMENT BY BRADSHAW AND TERRELL (REF. 5).
$x - z = 89$ (in.), $\delta_{995} = 1.23$ (in.) o, EXPERIMENT; ———, CALCULATION.
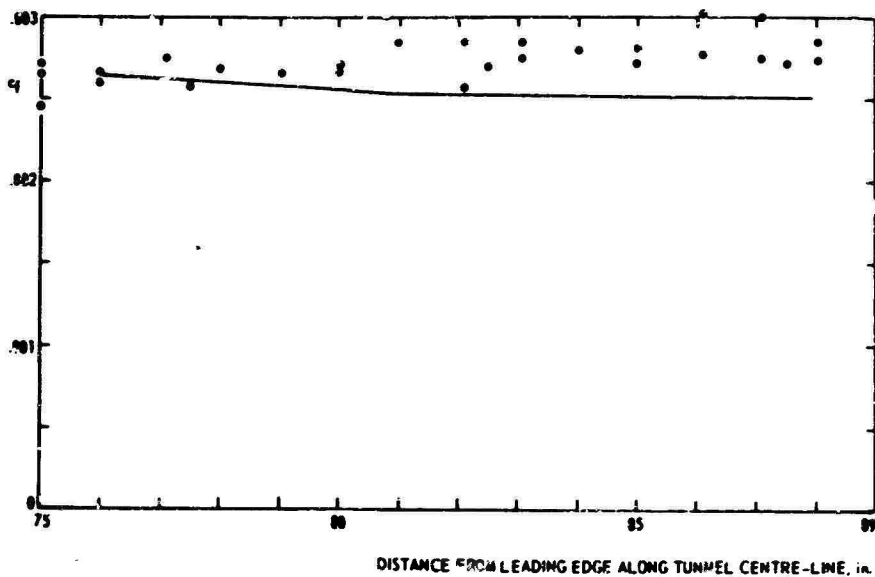
FIG. 9 MAGNITUDE OF SURFACE SHEAR STRESS. EXPERIMENT BY BRADSHAW AND TERRELL (REF. 5). ——, CALCULATION. ●, EXPERIMENT. ○, CALCULATION (REF. 6).
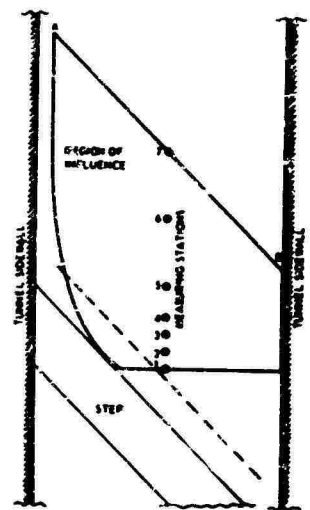
FIG. 10 REGION OF INFLUENCE OF SURFACE A B. ALSO COMPUTATIONAL REGION: JOHNSTON'S EXPERIMENT (REF. 14). ———, EXPERIMENTAL SEPARATION LINE.
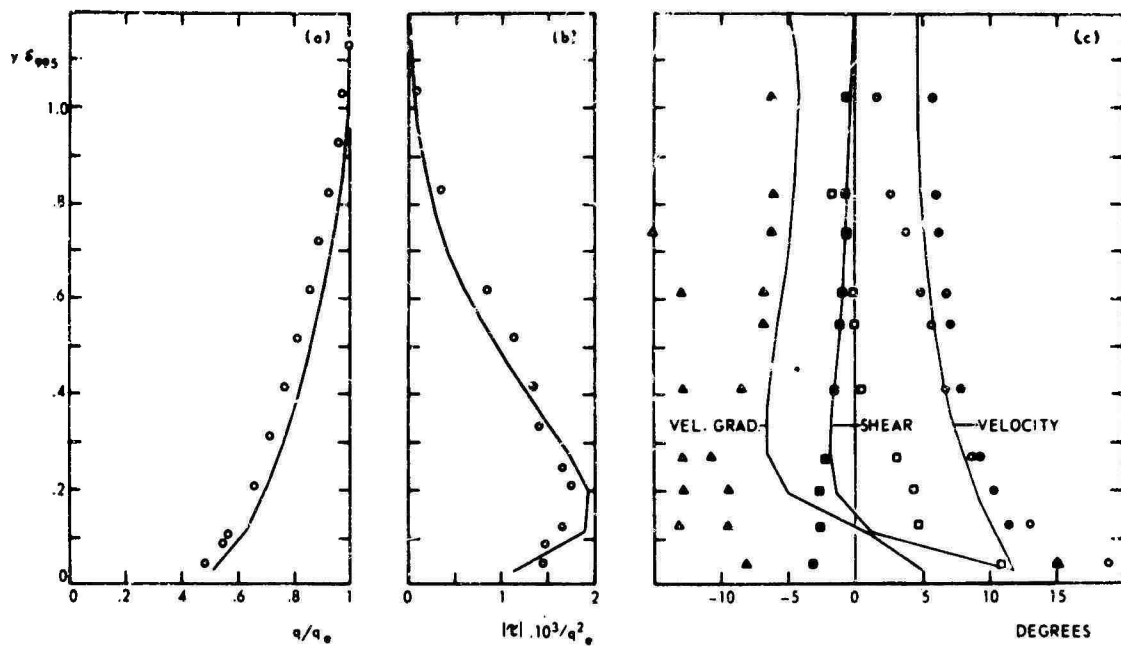
FIG. 11 COMPARISON WITH JOHNSTON'S EXPERIMENT (REF. 14). DISTANCE FROM STEP MEASURED ALONG TUNNEL CENTERLINE 4.3 in., δ_{995} = 2.43 in. (a) VELOCITY MAG-(a),(b),(c) NITUDE. ●, EXPERIMENT. ——, CALCULATION. (b) SHEAR STRESS MAGNITUDE. ○, EXPERIMENT. ——, CALCULATION. (c) VELOCITY, SHEAR STRESS AND VELOCITY GRADIENT ANGLES. ——, CALCULATION. EXPERIMENTAL RESULTS: ●, VELOCITY ; □, SHEAR STRESS. △, VELOCITY GRADIENT. CALCULATIONS OF REF. 6 : ●, VELO-CITY, ■, SHEAR STRESS, ▲, VELOCITY GRADIENT.
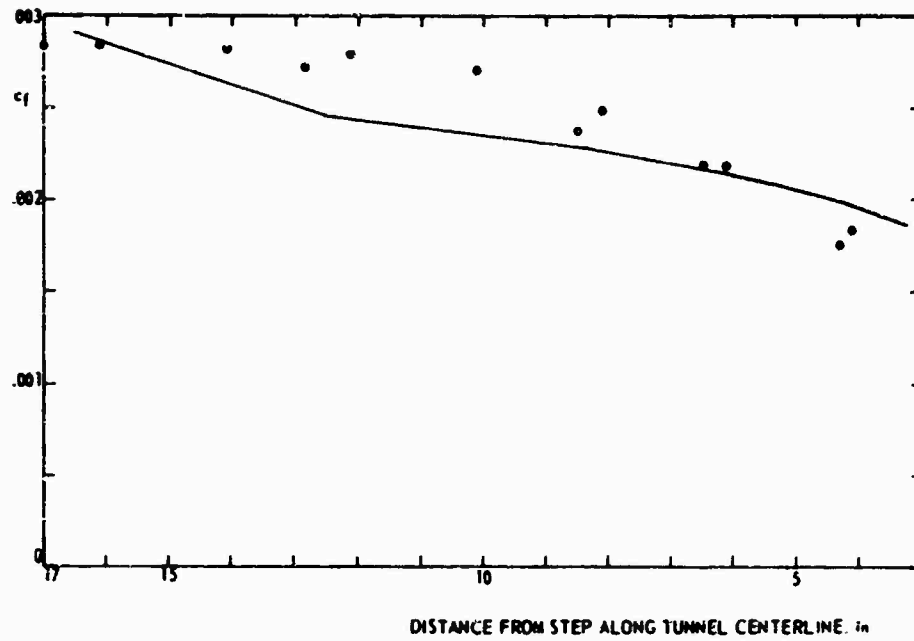
FIG. 12 JOHNSTON'S EXPERIMENT (REF. 14), c_f —————, CALCULATION, •, EXPERIMENT; ○, CALCULATION, REF. 6.

DISTANCE FROM STEP ALONG TUNNEL CENTERLINE, in

DISTANCE UPSTREAM FROM STEP, in
(MEASURED PARALLEL TO TUNNEL CENTERLINE)
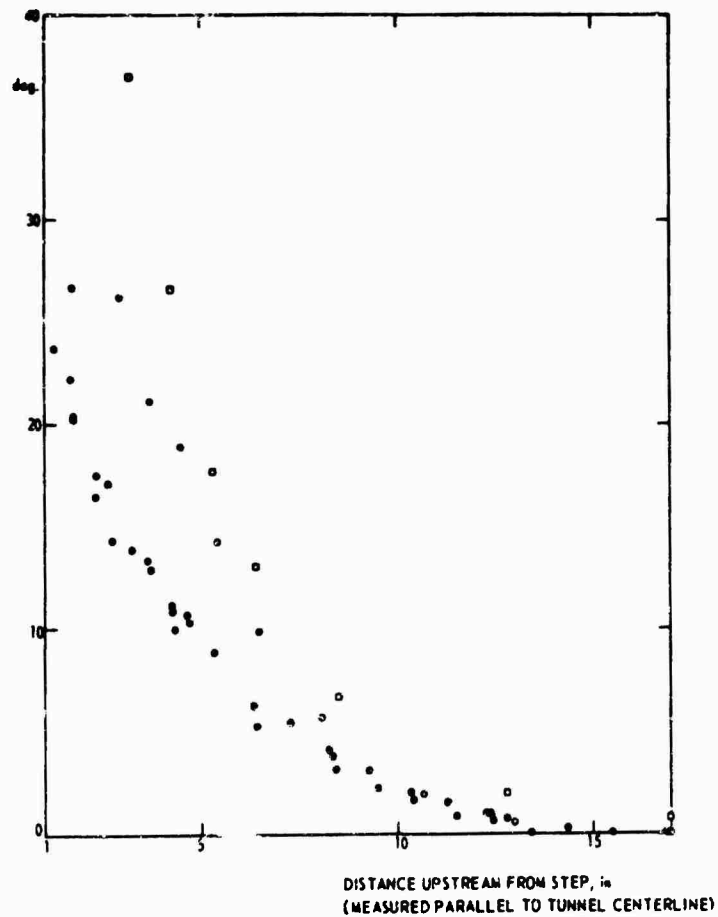
FIG. 13 ANGLE BETWEEN WALL STREAMLINE AND TUNNEL CENTERLINE, JOHNSTON'S EXPERIMENT (REF. 14).
•, PRESENT CALCULATION AT .074 in. FROM THE WALL; □, EXPERIMENT; ○, CALCULATION, REF. 6.
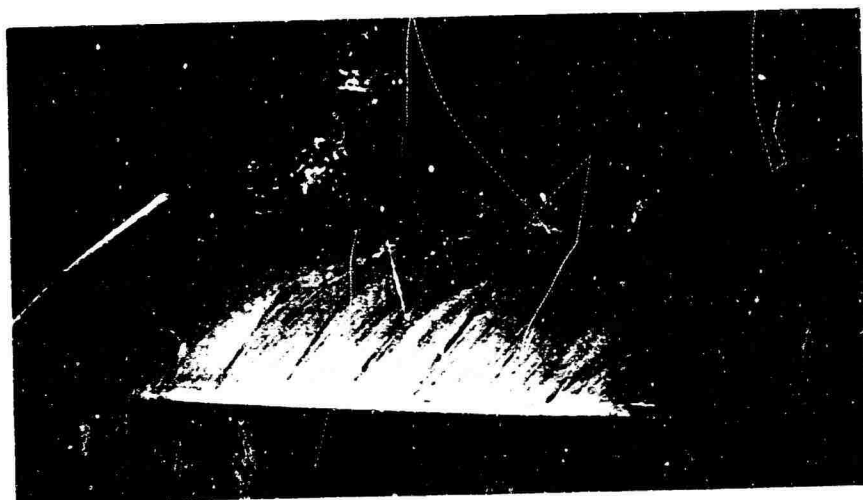
FIG. 14 OIL - FLOW PICTURE OF WALL - STREAMLINES IN NLR - EXPERIMENT
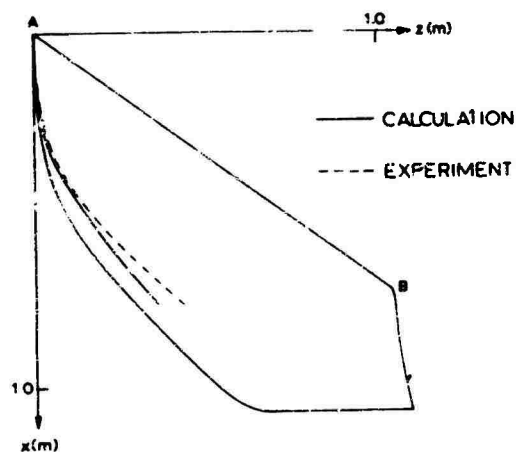
FIG. 15 REGION OF INFLUENCE, ALSO COMPUTATIONAL REGION, USING SIMPLE LAW OF THE WALL, NLR - EXPERIMENT. — — — —, EXPERIMENTAL WALL STREAMLINE. —————, COMPUTED WALL STREAMLINE USING EXTENDED LAW OF THE WALL
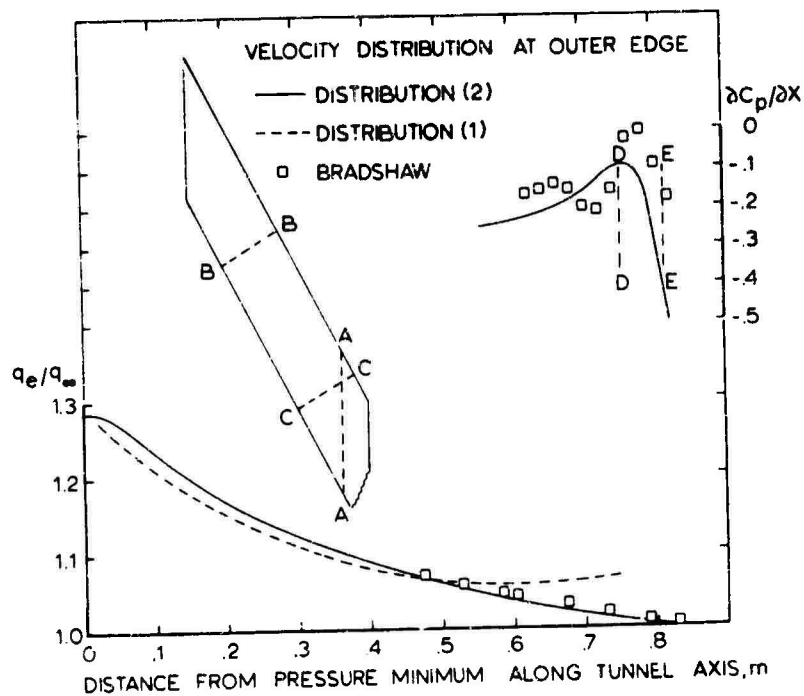
FIG. 16 THE TWO INVISCID VELOCITY DISTRIBUTIONS ALONG AA USED IN THE CALCULATIONS OF THE CUMPSTY AND HEAD FLOW. AA, LINE ALONG WHICH BOUNDARY LAYER MEASUREMENTS WERE MADE. BB AND CC, LINES ALONG WHICH THE PRESSURE WAS MEASURED. DD AND EE, BRADSHAW'S AND PRESENT SEPARATION PREDICTION, RESPECTIVELY
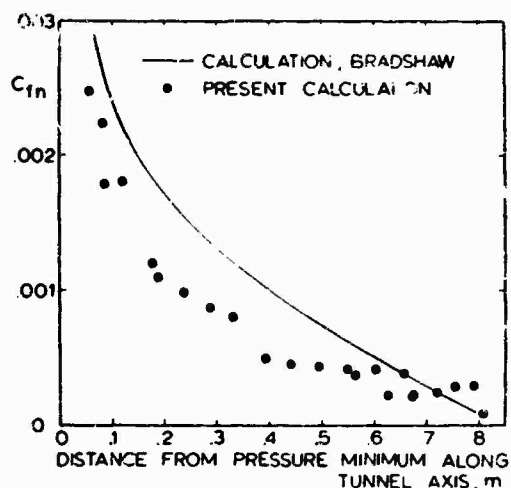
FIG. 17 CUMPSTY ANO HEAD EXPERIMENT. COMPARISON OF
CHOROWISE COMPONENT OF SKINFRICTION COEFFICIENT
IN CALCULATIQN OF REF. 6 AHO PRESENT CALC'ILATION,
USING EXTENDEO LAW OF THE WALL ANO PRESSURE
OISTRIBUTION (2).
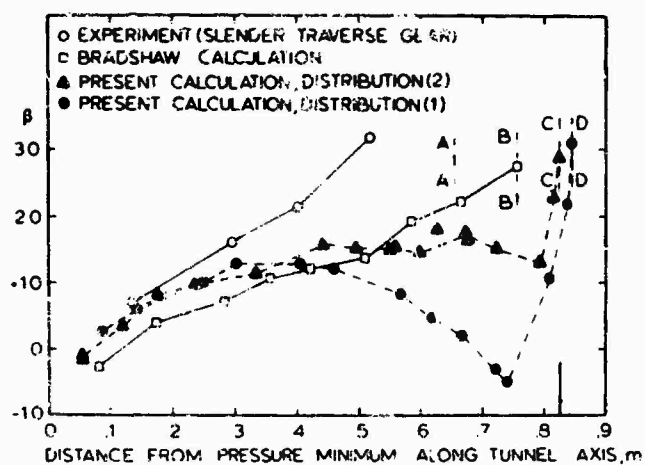
FIG. 18 CUMPSTY AHO HEAO EXPERIMENT, SURFACE CROSS—FLOW
ANGLE WITH RESPECT TO LOCAL FREE STREAM OIRECTION.
EXTENOEO LAW OF THE WALL USED IN THE CALCULATIONS.
AA, BB, CC, OO, SEPARATION POSITIONS, EXPERIMENTAL,
BRAOSHAW CALCULATION ANO PRESENT CALCULATIONS,
RESPECTIVELY.
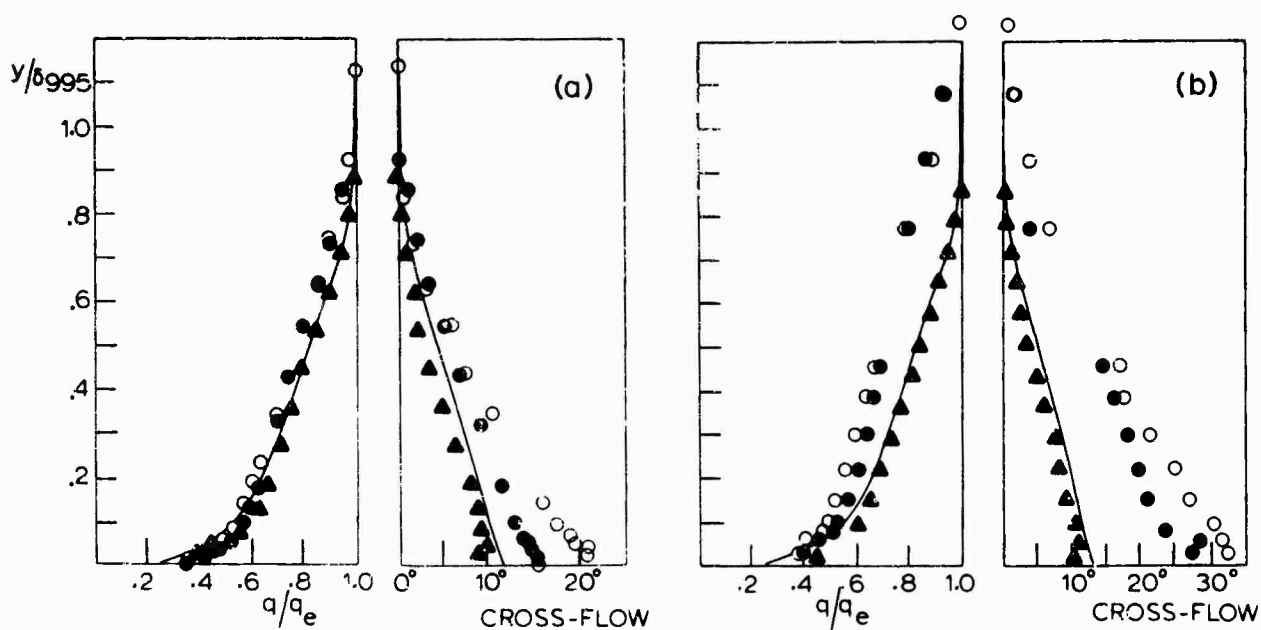
FIG. 19 CUMPSTY AND HEAO EXPERIMENT, MAGNITUOE ANO OIRECTION OF VELOCITY VECTOR.
————— , PRESENT CALCULATION WITH PRESSURE OISTRIBUTION (1); O , EXPERIMENT;
▲ , CALCULATION BY NASH (REF. 2); ● , CALCULATION BY NASH WITH AOOITIONAL
SPANWISE PRESSURE GRADIENT. (o), δ_{995} = 1S.4 mm., CHOROWISE DISTANCE FROM PRESSURE
MINIMUM 19S mm (b), δ_{995} = 19.0 mm., CHOROWISE DISTANCE FROM PRESSURE MINIMUM 249 mm.

A PROGRESS REPORT ON AN ATTEMPT TO CONSTRUCT AN INVARIANT MODEL OF TURBULENT SHEAR FLOWS

Coleman duP. Donaldson
President and Senior Consultant
Aeronautical Research Associates of Princeton, Inc.
50 Washington Road, Princeton, New Jersey 08540, USA

SUMMARY

Recent numerical studies carried out by the author and his colleagues in their attempt to develop an invariant model of turbulent shear flow are described. The results of comparing computations using a tentative model of such flows with experimental data for the axially symmetric free jet, the two-dimensional free shear layer, and the flat plate boundary layer are presented. The need for more carefully designed and documented free turbulent flow measurements is discussed in relation to the problem of selecting more refined models. Some observations are also made concerning the application of double correlation closure schemes, of which the present method is one, to the computation of turbulent flows other than classical incompressible shear layers. In particular, the possibility of more correct methods of calculating the behavior of chemically reacting turbulent flows is examined.

INTRODUCTION

It is certainly true that there is nothing new under the sun. The work in which my colleagues and I have been engaged for the past few years is certainly no exception to this rule. We have been attempting, as have a number of other groups, to construct a model of turbulent shear flows based on a closure of the equations of turbulent motion given by Reynolds (Ref. 1) almost a century ago. The method used to close the system of equations is a modeling of the appropriate terms in the equations for the second-order correlations of fluctuating quantities. This general approach was discussed in 1945 by Prandtl and Wieghardt (Ref. 2) and was pursued in some detail by Rotta (Ref. 3). Within the past few years, many investigators have turned their attention to such techniques.

The motivation for our own attempt to construct a new model of turbulent shear flows does not stem from a desire to calculate with greater accuracy or in more detail the characteristics of turbulent boundary layers or the classical free shear flows. The attempt is made because we wish to get some idea of the character of certain turbulent flows for which there is not sufficient empirical information available to permit the use of conventional computational techniques with any degree of confidence. The particular problems we were anxious to analyze were the decay of a turbulent vortex, the generation of turbulence by the atmosphere, and the dispersal of chemically active species in the earth's atmosphere. It has been our hope that, if we could develop a sufficiently general second-order closure model of turbulent shear flows that could handle with one invariant model the classical shear layer problems, we could then apply this model to the problems mentioned above.

This paper is an effort to bring to your attention some of the findings that have resulted from the detailed studies we have performed in our attempt to create an invariant model of turbulent shear flow.

DESCRIPTION OF AN INVARIANT MODEL OF TURBULENT SHEAR LAYERS

The equation for the time-independent mean velocity in an incompressible turbulent medium was given many years ago by Reynolds (Ref. 1). It is

$$\rho \bar{u}^j \bar{u}_{1,j} = -\bar{p}_{,1} + \left(\bar{\tau}_1^j - \rho \langle u^{j'} u_1' \rangle \right)_{,j} \tag{1}$$

In this paper, bars over a quantity or angular brackets around a quantity indicate average values of that quantity while primes indicate the instantaneous fluctuation of the quantity from its mean value. The mean molecular stress τ_1^j is given by

$$\bar{\tau}_1^j = g^{jk} \mu \left(\bar{u}_{1,k} + \bar{u}_{k,1} \right) \tag{2}$$

The second-order correlation of the velocity fluctuations that appears in Eq (1) represents the transport of momentum by turbulent eddies and is called the Reynolds stress. An equation for this second-order tensor was also given by Reynolds. It is, for steady flow,

$$\rho \bar{u}^j \langle u_1' u_k' \rangle_{,j} = -\rho \langle u^{j'} u_k' \rangle \bar{u}_{1,j} - \rho \langle u^{j'} u_1' \rangle \bar{u}_{k,j} - \rho \langle u^{j'} u_1' u_k' \rangle_{,j} - \langle u_1' p' \rangle_{,k} - \langle u_k' p' \rangle_{,1}$$

$$+ \langle p'(u_{1,k}' + u_{k,1}') \rangle + \mu g^{mn} \langle u_1' u_k' \rangle_{,mn} - 2\mu g^{mn} \langle u_{1,m}' u_{k,n}' \rangle \tag{3}$$

In the past, it has been customary to carry out investigations of turbulent shear flows by means of Eq (1). In these studies the unknown second-order velocity correlation term was modeled in terms of the mean velocity and a length. Computations made in this manner form the vast bulk of the literature on turbulent shear flow calculations to

the present time. The methods that are now in use employing this type of modeling, having evolved over a period of many years, are exceedingly useful and enough empirical data have been amassed to enable one to calculate solutions to a wide variety of engineering problems with a great deal of confidence. There are, however, a number of problems facing engineers today which require the calculation of turbulent shear flows for which there is no existing body of experimental data. Two flows which come readily to mind are the generation of turbulence and turbulent transport correlations by the earth's atmosphere and the decay of a turbulent vortex. In the case of these two flows, we may ask ourselves the following questions: "Is there not a somewhat more basic method of computing turbulent transport phenomena than the eddy viscosity or mixing length models presently in use?" "Can now such a method permit us to generalize the experimental results that presently exist so as to estimate the nature of turbulent flows that have not yet been investigated experimentally?" The answers to these two questions are not as straightforward as one would like. In answer to the question as to whether there is a more basic method, the reply must be: Yes, but the real difficulty comes when one tries to establish just how much more fundamental the proposed new method is to be. If a new method is truly more fundamental, then it will allow better estimates of unknown flows than can be made by older techniques. It is fair to say, at the present time, that there is considerable hope among those who practice the art of calculating turbulent shear flows that the new methods now being developed, of which the method to be described here is but one, take into account enough physics that is not contained in older models so that a technological advance can be made. It is as yet too early in the history of these new methods to make any strong statement as to just how much more powerful they are than the older methods.

If one wishes to make use of both Eqs (1) and (3) in computing turbulent shear flows, the first step must be a choice of models for those terms in Eq (3) which are not expressed in terms of the mean velocity or the second-order velocity correlation. The terms which must be modeled are

(1) the pressure-strain correlation in the tendency-towards-isotropy term, namely, $\langle p'(u'_{i,k} + u'_{k,i}) \rangle$;

(2) the third-order tensor in the velocity diffusion term, namely, $\langle u'_i u'_j u'_k \rangle$;

(3) the pressure velocity correlation in the pressure diffusion terms, namely, $\langle u'_i p' \rangle$;

(4) the general viscous dissipation term $2\mu g^{mn} \langle u'_{i,m} u'_{k,n} \rangle$.

There are many ways in which a modeling of the above-noted terms may be accomplished. We have tried, for our initial investigation, to take as simple a model as possible for each term. We have then attempted to determine by calculation the adequacy of the chosen model and the sensitivity of the calculated results to the particular choice of model.

To date the following models have been investigated to some extent.

(1) For the tendency-towards-isotropy term, we choose, following Rotta (Ref. 3), the following model:

$$\langle p'(u'_{i,k} + u'_{k,i}) \rangle = -\frac{\rho q}{\Lambda_1}\left(\langle u'_i u'_k \rangle - g_{ik}\frac{K}{3} \right) \qquad (4)$$

where

$$q^2 = K = \langle u^{m'} u'_m \rangle = \langle u'^2 \rangle + \langle v'^2 \rangle + \langle w'^2 \rangle \qquad (5)$$

and Λ_1 is a scalar length associated with the tendency towards isotropy and is to be identified. More complicated models of this term have been discussed by Chou (Ref. 4) and by Hanjalić and Launder (Ref. 5). To date, we have had considerable success using the simple Rotta model given above and, in line with our philosophy of using the simplest possible model that will give reliable results, we have confined the majority of our computational studies to the use of Eq (4).

(2) For the velocity diffusion term, we must model $\langle u'_i u'_j u'_k \rangle$. The simplest covariant tensor of rank three that is symmetric in all three indices that we can form out of the second-order correlations is

$$\langle u'_i u'_j \rangle_{,k} + \langle u'_j u'_k \rangle_{,i} + \langle u'_k u'_i \rangle_{,j}$$

This expression has all the tensor and symmetry characteristics required of our model. To make it dimensionally correct, the above expression must be multiplied by a scalar velocity and a scalar length. The simplest scalar velocity we can form from the second-order correlations is $\sqrt{\langle u^{m'} u'_m \rangle} = q$, so we model the tensor $\langle u'_i u'_j u'_k \rangle$ as

$$\langle u'_i u'_j u'_k \rangle = -\Lambda_2 q \left[\langle u'_i u'_j \rangle_{,k} + \langle u'_j u'_k \rangle_{,i} + \langle u'_k u'_i \rangle_{,j} \right] \qquad (6)$$

where Λ_2 is a scalar length associated with velocity diffusion and is also to be identified by matching experimental results.

(3) The pressure velocity correlation $\langle p'u'_k\rangle$ in the pressure diffusion term is modeled by analogy with the velocity diffusion term as

$$\langle p'u'_k\rangle = -\rho\Lambda_3 q\langle u^m u'_k\rangle_{,m} \tag{7}$$

In our work, in order to cut down the number of parameters in our turbulence model, we have considered only two special cases of Eq (7). We have considered the case $\Lambda_3 = \Lambda_2$ and the case where $\langle p'u'_k\rangle = 0$, i.e., the case $\Lambda_3 = 0$.

(4) We have considered two models for the expression $g^{mn}\langle u'_{i,m}u'_{k,n}\rangle$ appearing in the viscous dissipation term:

$$\text{(a)} \qquad g^{mn}\langle u'_{i,m}u'_{k,n}\rangle = \frac{\langle u'_i u'_k\rangle}{\lambda^2} \tag{8}$$

and

$$\text{(b)} \qquad g^{mn}\langle u'_{i,m}u'_{k,n}\rangle = \frac{K}{3\lambda^2} \tag{9}$$

In both these models, λ is a dissipative length scale. The argument for choosing the latter expression is that it is expected that the turbulence will be almost isotropic in that part of the spectrum responsible for dissipation of turbulent kinetic energy. Thus, one would expect the dissipation to be almost isotropic even if the turbulence itself is not. Further, there is experimental evidence that the loss of shear correlation by viscous action is relatively much smaller than the loss of kinetic energy by viscous action In our initial computations using Eq (9) as a model of dissipation, we experienced some difficulties in obtaining solutions. There was a tendency for solutions to develop with negative values for the mean square velocities when the turbulence became very nonisotropic. This tendency was overcome by the use of Eq (8) for the dissipation model. This model does not have a large effect on the development of the shear correlations because the primary contribution to loss of shear with this model is not the dissipation term but the tendency-towards-isotropy term. Although the whole question of modeling the dissipation term is still under investigation, the work reported here was carried out using Eq (8), for the reasons stated above.

In the models given above, we would expect that the scalar lengths Λ_1, Λ_2, and Λ_3 would all be related to the local integral scale of the turbulence. These lengths are, in turn, related to the local scale of the mean motion for the flows we shall investigate here, and we make the assumption in the computations we will discuss presently that Λ_1, Λ_2, and Λ_3 are all proportional to some local characteristic length δ_{char} of the mean motion under consideration.

We will expect the length appearing in the dissipation model to be related to the microscale of the turbulence which, in turn, must be related to the integral scale via a Reynolds number in such a way that production of turbulence is balanced to a large extent by dissipation.

If the models we have just discussed [Eqs (4) and (6) - (8)] are substituted in the basic equation for the second-order velocity correlations [Eq (3)], the resulting equation, taken together with the momentum and continuity equations, makes a closed set (see Appendix A). When this set is reduced to boundary layer form, it is found to form a parabolic system (see Appendix B).

This set of equations will admit similarity solutions at high Reynolds numbers as well as permit calculations of turbulent flows near walls, if one makes the following choice of the relation between the length scales:

$$\Lambda_1 = c_1\delta_{char} \tag{10}$$

$$\Lambda_2 = c_2\Lambda_1 = c'_2\delta_{char} \tag{11}$$

$$\Lambda_3 = c_3\Lambda_1 = c'_3\delta_{char} \tag{12}$$

and

$$\lambda = \Lambda_1/\sqrt{a + b\cdot Re_{\Lambda_1}} \tag{13}$$

where

$$Re_{\Lambda_1} = \rho q\Lambda_1/\mu \tag{14}$$

For self-similar free turbulent flows, the structure given above is all that is needed to compute a turbulent shear layer or a free jet, provided the five constants, c_1, c_2, c_3, a, and b are given. To find these constants, we must resort to the comparison of calculated flow fields with experimental results.

If we wish to compute a boundary layer flow, we must consider an additional problem. When a wall is present in a shear flow, we wish to apply the boundary condition at the wall that

$$\langle u_i' u_k' \rangle_{z=0} = 0$$

where z is measured normal to the surface. In addition, there should be no diffusion of $\langle u_i' u_k' \rangle$ through the surface, so that $\partial \langle u_i' u_k' \rangle / \partial z = 0$ at $z = 0$. Thus, it is reasonable to assume that near the wall

$$\langle u_i' u_k' \rangle = A_{ik} z^{1+\eta} \tag{15}$$

where A_{ik} is a constant and η is a positive constant. But if there is no diffusion through the wall, then all that is diffused towards the wall by viscosity at $z = \epsilon$ is dissipated in the region between $z = \epsilon$ and $z = 0$. (It is easily verified that all other terms in the model equation for $\langle u_i' u_k' \rangle$ are neglible if ϵ is small enough.) Thus,

$$2\mu \int_0^\epsilon \frac{\langle u_i' u_k' \rangle}{\lambda^2} \, dz = \mu \left(\frac{\partial \langle u_i' u_k' \rangle}{\partial z} \right)_{z=\epsilon}$$

or, using Eq (15),

$$2 \int_0^\epsilon \frac{z^{1+\eta}}{\lambda^2} dz = (1 + \eta)\epsilon^\eta$$

If this relation is to hold for all $\epsilon \to 0$, we must have

$$\lambda = \alpha z \tag{16}$$

where

$$\alpha^2 = 2/(1 + \eta)\eta$$

Thus, near a solid surface, we always assume, in applying our model, that Eq (16) holds in the region near the wall.

It is convenient to express this result in terms of Λ_1. Near a wall, Eq (13) becomes

$$\lambda = \Lambda_1/\sqrt{a} \tag{17}$$

Using Eq (16), we may write

$$\Lambda_1 = \alpha\sqrt{a}\, z \tag{18}$$

Thus, for boundary layer flows, α is another number which must be found from experimental results.

In our first attempts to construct a model of turbulent shear flows (Refs. 6 and 7), the following assumptions were made to construct the simplest possible model of boundary layer flows:

(1) It was assumed that all the large lambdas associated with inviscid modeling were equal, i.e., $\Lambda_1 = \Lambda_2 = \Lambda_3 = \Lambda$.

(2) It was assumed that α was equal to one.

(3) In the outer portion of a boundary layer, Λ was taken to be a constant c_1 times $\delta_{.99}$ ($\delta_{.99}$ is the value of z for which $\bar{u}$ is 99% of the free stream velocity). This value was assumed to hold, independent of z, as the wall was approached, until Λ became equal to $\sqrt{a}$ times z. For smaller values of z, Λ was taken equal to $\sqrt{a}\, z$.

With these assumptions, the boundary layer forms of Eqs (1) and (3) with appropriate modeling (Appendix B) were solved with various choices for the parameters a, b, and $c_1 = \Lambda/\delta_{.99}$ to produce a developing turbulent boundary layer on a flat plate. It was determined at that time that the following choice of parameters

$$c_1 = \Lambda/\delta_{.99} = 0.064$$
$$a = 2.5 \tag{19}$$
$$b = 0.125$$

yielded a fair representation of a turbulent boundary layer. The mean velocity profile and the behavior of skin friction with Reynolds number were adequately represented. The distributions of the second-order correlations within the boundary layer were reasonable.

The results of this original parameter search were used to compute a number of other turbulent flows in order to demonstrate the method (Refs. 8 and 9).

Before proceeding with further applications, it was considered necessary that a more detailed parameter search should be made. In particular, two free turbulent flows - the free jet and the free shear layer - should be calculated to determine the values of the parameters c_2, c_3, a, and b that would best fit the experimental results for both

flows. (The equations for the free shear layer are the same as those for the boundary layer given in Appendix B. The equations for the axially symmetric free jet are given in Appendix C.) The value of c_1 being the ratio of Λ_1 to some arbitrarily defined

characteristic length in each case is not an invariant of the problem and was to be chosen, with fixed values of the other parameters, to obtain best results in each case. Once these studies were complete, the model would be used to compute turbulent boundary layer flows so that, by comparison with experimental results, values for c_1 and α could be made for this flow. Hopefully, all flows could be described in a reasonable way by a single choice of the basic model parameters c_2, c_3, a, b, and (where appropriate) α.

The values of local Λ_1 determined from the values of c_1 in each case were then to be compared with the local magnitude of the integral scale L in each case. If it was found that the value of c_1 represented a choice that amounted to

$$\Lambda = \text{const } L = \beta L \tag{20}$$

then it would be assumed that a reasonable invariant model had been determined.

THE SEARCH FOR NEW MODEL PARAMETERS

Our search for a new model of turbulent shear layers began with an attempt to describe the axially symmetric free jet with the original turbulence model obtained for a boundary layer flow. This model, as mentioned in the previous section, was one for which $\Lambda_1 = \Lambda_2 = \Lambda_3 = \Lambda$. This choice leaves three parameters to be determined. They are $c_1 = \Lambda/\delta_{char}$ and the two constants a and b in the expression

$$\lambda = \Lambda/\sqrt{a + b \cdot Re_\Lambda}$$

The method of searching for values for these parameters was as follows. The equations for a free jet were programmed so as to solve the system of equations for a free jet developing in the axial direction. At an arbitrary initial station in the axial direction, a mean velocity profile and profiles of the pertinent second-order correlations were arbitrarily assumed. For a given choice of model parameters (in this case, a, b, and $c_1 = \Lambda/r_{.5}$,

where $r_{.5}$ is the radius for which $\bar{u}$ is one-half the centerline value), the free jet equations were solved for the development of the jet downstream of the initial distributions. In all cases, essentially self-similar solutions were obtained far downstream of the start of the calculation. If a set of parameters could be found so that the resulting self-similar flow agreed with experimental measurements with respect to the rate of spread, as well as with respect to mean velocity and correlation distributions, it would then be assumed that a reasonable turbulence model had been achieved.

Actually, such calculations were carried out for both free jets and two-dimensional free shear layers. With the single Λ model, it was found that no combination of parameters a, b, and c_1 could produce an adequate description of either a free jet or a free shear layer. In general, it was found that if the parameters were adjusted so as to give an adequate rate of spread of the mean profile (i.e., if the level of the turbulent shear correlation was large enough) the spread of the correlations $\langle u_i'u_j'\rangle$ by diffusion was always too large. This general result is illustrated in Figure 1 where it is seen that, if the general level of the shear correlation $\langle u'w'\rangle$ were to match the experimental data of Wygnanski and Fiedler (Ref. 10) in the region of maximum shear, it is clear that far too long a tail of $\langle u'w'\rangle$ at large r would result. This was a very general result for free shear flows and forces us to consider a more complicated model.

The difficulty that was experienced with the constant Λ model was the existence of too much diffusion relative to the rate of loss of correlations, either by dissipation or the tendency towards isotropy. To correct this difficulty in the studies reported here, the diffusion lengths Λ_2 and Λ_3 were made smaller than Λ_1. An idea of the

effect of reducing the diffusion lengths relative to the isotropy length can be seen from Figure 2. Here the rms value of the longitudinal velocity fluctuation w', that has been calculated for several choices of model parameters, is plotted versus radius in a self-similar free jet. Note that as the diffusion lengths Λ_2 and Λ_3 (which are c_2

times Λ_1) are reduced, the amount of diffusion is obviously reduced and the levels of turbulence on the jet centerline are appreciably increased.

The effect of the choice of the scale of the isotropy length Λ_1 can be seen from Figure 3. The distribution of longitudinal turbulence intensity is shown as a function of radius for two choices of Λ_1 relative to the local value of $r_{.5}$. It is seen that

the levels are much lower for the smaller Λ_1 than for the larger value. This is what one might expect because of the increased dissipation, as well as the increased loss of shear correlation by the tendency towards isotropy when the scale Λ_1 and, hence, λ is made smaller.

The effect of neglecting pressure diffusion can be seen in Figure 4; the longitudinal velocity fluctuations in a free jet are shown as a function of radial position for a given choice of model parameters a, b, c_1, and c_2 for two choices of c_3. One choice is $c_3 = c_2$ and the second is $c_3 = 0$, i.e., neglect of pressure diffusion. It is

seen that for this choice of the other parameters, the effect of neglecting pressure diffusion is not large.

Having given some idea of how some of the various parameters entering the model for turbulent shear layers affect the solutions, we must now discuss the selection of an actual set of parameters. If one considers only a single type of shear flow that one wishes to model, say, the free jet, it is possible to choose a whole spectrum of models which will give a good description of the mean spread of the free jet and the distribution of, say, the longitudinal turbulent velocity field. To illustrate this point, ie may refer to Figure 5. Here we see that two profiles of longitudinal velocity fluctuation can be obtained with radically different choices of b and Λ_1. It is observed that if one chooses small b one must also choose a small value of Λ_1 relative to a characteristic scale of the jet. What then is the basic difference between these two solutions? It is this. For the solution with small b and small Λ_1, the balance of the production of turbulence is more by dissipation and less by diffusion than for the other case. Also, for the case of small b and small Λ_1, the solutions are more isotropic on the jet centerline than for the other case.

The choice between the two models exhibited in Figure 5 must be made on the basis of the degree of diffusion and the degree of isotropy desired in the calculated result. This is a difficult decision to make, for existing experimental data do not agree as to how isotropic free jets are on their centerlines, as will be seen presently. There is another way that one can decide between two different models. If one uses the same model to compute two different turbulent flows having essentially different geometries, the model which gives the best results for both flows is, since we are seeking an invariant model, the one to choose.

As mentioned previously, we have computed self-similar solutions for a free shear layer as well as for an axially symmetric free jet. Actually a search for model parameters for each type of flow was carried out. As a result of these studies, it was determined that, insofar as the parameter studies have proceeded at this point, the following model for free turbulent shear flows gave the best results:

$$a = 2.5$$
$$b = 0.125$$
$$c_2 = 0.10 \tag{21}$$
$$c_3 = 0.10$$

Also, the value

$$c_1 = \Lambda_1/\delta_{char} = 0.50 \tag{22}$$

was found best for both flows, although it was not part of the plan to have a common value of c_1. As mentioned above, for the free jet,

$$\delta_{char} = r_{.5} \tag{23}$$

The characteristic length for the free shear layer was taken as

$$\delta_{char} = z_{.25} - z_{.75} \tag{24}$$

which is the distance normal to the flow in the shear layer from the point where the velocity is one-quarter the external driving velocity to where it is three-quarters this velocity.

In Figures 6 through 13, we show comparisons with experimental data of the velocity correlation profiles computed for both a free jet and a free shear layer, using the model parameters given above. The experimental results are taken from the work of Wygnanski and Fiedler (Refs. 10 and 11), Gibson (Ref. 12), and Donaldson, Snedeker, and Margolis (Ref. 13).

Figures 6 and 7 show the longitudinal fluctuations in a free jet and free shear layer, respectively. The agreement between model calculations and experiment is good in both cases. For the free jet in Figure 6, it would, perhaps, have been desirable to have a little more diffusion (larger Λ_1 and larger b) in the model in an attempt to reduce the overshoot in $\langle w'w' \rangle$ near the centerline of the jet.

Figures 8 and 9 show distributions of normal fluctuations in both the free jet and the free shear layer. Here we note the agreement with experimental data is not so good. There appears to be a little too much diffusion for these cases. Also, note the very large discrepancy between measured normal fluctuations on the centerline as reported in three separate experiments. The data of Gibson show the components of turbulent velocity to be essentially isotropic on the jet centerline, while those of Wygnanski and Fiedler and Donaldson, Snedeker and Margolis do not. From the results shown in Figure 8, it would appear that if one were to desire more isotropy, one would wish to choose a smaller value of Λ_1 and, hence, a smaller value of b. This is opposite to the conclusion drawn from Figure 6.

Figures 10 and 11 show the sidewise components of turbulence for the free jet and free shear layer, respectively. The agreement between experiment and computed results is better for the free jet than for the free shear layer. The reason for this behavior is

not known.

    In Figures 12 and 13, we show the shear correlations for the free jet and the free shear layer. The agreement in both cases is fair. It should be noted that the experimental values of shear correlation from Ref. 10 have been shown as reported (the open circles) in Figure 13 and also as corrected by us (the solid symbols) so as to agree with the measured rate of spread of the free shear layer. A comparison of the measured shear and that inferred from the mean velocity profile was reported by Wygnanski and Fiedler but apparently their computations contained an error. Also shown in Figure 13 is the level of shear that may be inferred from the mean spread of the free shear layer studied by Tollmien (Ref. 14) and Prandtl (Ref. 15) many years ago. It is seen from the results presented in Figures 12 and 13 that the model gives a fairly good representation of the shear in both the free jet and the free shear layer.

    A careful study of Figures 6 through 13 shows that it really is necessary to study further the problem of choice of model parameters. However, before this is done, it appears desirable to have at hand experimental data which one can rely on to be truly representative of the basic flow which is being calculated. It is difficult to choose a more sophisticated model until the question of the degree of isotropy on the centerline of a free jet is settled. In addition, one should, at this point, determine if the model just found for free shear layers can be used for a model of the outer regions of a boundary layer and give reasonable results.

    Before turning to the problem of the turbulent boundary layer, it will be instructive to find a relationship between the values of Λ_1 used in the free shear layer and the free jet calculations and the general magnitude of the integral scales measured for such flows. In the computations that have been made, it has been assumed that Λ_1 is constant across a free jet or a free shear layer at any given longitudinal position and, in magnitude, proportional to the local scale of the mean flow. It is well known that the integral scales of such flows are, in general, proportional to the local mean scale but the actual value of the integral scale varies across the layer.

    In Table 1, we present the values of integral scale within a free jet, as reported by Wygnanski and Fiedler. The integral scale tabulated is the longitudinal integral scale

$$L = \frac{1}{\langle w'w' \rangle (z_1)} \int_0^\infty \langle w'(z_1)w'(z_2) \rangle \, d(z_2 - z_1) \tag{25}$$

for the free jet.

Table 1. Integral Scales in a Free Jet after Wygnanski and Fiedler (Ref. 10)

Radial Position r/x	Dimensionless Scale $L/r_{.5}$	Scale Ratio Λ_1/L
0	0.448	1.12
.05	0.595	0.84
.10	0.726	0.69
.15	0.850	0.59
.20	0.855	0.58

Also presented in Table 1 is the ratio of the computational scale Λ_1 to the local integral scale L. Thus, a typical value for this ratio for the free jet is

$$\Lambda_1/L = 0.69 \tag{26}$$

    For the free shear layer, similar results are given in Table 2. These experimental values are also due to Wygnanski and Fiedler. The longitudinal integral scale is, in this case, defined by

$$L = \frac{1}{\langle u'u' \rangle (x_1)} \int_0^\infty \langle u'(x_1)u'(x_2) \rangle \, d(x_2 - x_1) \tag{27}$$

Table 2. Integral Scales in a Free Shear Layer after Wygnanski and Fiedler (Ref. 11)

Location in Jet	Dimensionless Scales		Scale Ratio
	L/x	$L/(z_{.25}-z_{.75})$	Λ_1/L
Inner Region	0.098	0.846	0.59
Center	0.103	0.883	0.57
Outer Region	0.147	1.27	0.39

A typical value of Λ_1/L for a free shear layer appears to be approximately

$$\Lambda_1/L = 0.55 \tag{28}$$

As mentioned previously, there is not much point in going further with studies of the present model until it has been applied to a boundary layer. Note should be made at this point, however, of other methods of calculating turbulent shear flows - methods that are similar to the methods being discussed here. As mentioned before, the idea behind the method is not new. It follows a trend suggested by Prandtl and Wieghardt (Ref. 2) and follows closely the general line of approach taken by Rotta (Ref. 3). Since these two pioneering papers, many more or less similar studies have been undertaken. Typical of many such studies are those of Glushko (Ref. 16), Bradshaw, Ferriss & Atwell (Ref. 17), Harlow & Romero (Ref. 18), Gawain & Pritchett (Ref. 19), and Beckwith & Bushnell (Ref. 20). The more sophisticated of these methods do not assume a local scale, as we have, but carry along with the computational scheme an equation for the required scale. Such an equation was derived by Rotta (Ref. 3) from the equation for the two-point correlation tensor $\langle u_i'(A)u_j'(B)\rangle$. There is no question but that, in the future, the method presented here should be enhanced by coupling the present set of model equations to an equation for the integral scale. To date, however, we have avoided making this connection in order to study the character of the model and its dependence on the scale Λ_1 without this dependence becoming inextricably mixed with the additional modeling that must be done in the equation that is used to compute a scale.

Before proceeding further, it must be demonstrated that, if the present model is applied to a boundary layer, useful results will be obtained for the same choice of model parameters that has been made for free turbulent shear flows.

APPLICATION OF MODEL TO BOUNDARY LAYERS

If the model of turbulent shear flows is to be applied to a boundary layer, the parameters c_2, c_3, a and b are known. But, since the characteristic length in a boundary layer is arbitrary (as it is in the free jet and the free shear layer), we are at liberty to choose c_1, i.e., the ratio between Λ_1 and the characteristic length (which, in this case, we take equal to $\delta_{.99}$, the thickness of the layer in which the velocity reaches 99% of its free stream value).

As discussed in a previous section of this paper, one other parameter enters the problem, namely, α, the coefficient appearing in Eq (16). We have, then,

$$\Lambda_1 = \alpha\sqrt{a}\,z \tag{29}$$

for $0 \leq z \leq c_1\delta_{.99}/(\alpha\sqrt{a})$ and

$$\Lambda_1 = c_1\delta_{.99} \tag{30}$$

for $z > c_1\delta_{.99}/(\alpha\sqrt{a})$

With only these two parameters α and c_1 to determine, the search is not difficult. The model that has been found is the following:

$$
\begin{aligned}
a &= 2.5 \\
b &= 0.125 \\
c_2 &= 0.1 \\
c_3 &= 0.1 \\
c_1 &= \Lambda_1/\delta_{.99} = 0.15 \\
\alpha &= 0.7/\sqrt{a} = 0.443
\end{aligned}
\tag{31}
$$

The ability of this model of a turbulent shear layer to predict the known mean properties of turbulent boundary layers is shown in Figures 14 through 16. In Figure 14, we show the skin friction developed by our model as it proceeds from a disturbed laminar layer to a fully turbulent layer. Also shown are the laminar skin friction law and the turbulent law proposed by Coles (Ref. 21) which is a good fit to experimental data. It is no great surprise that the general levels of skin friction we computed agree well with experimental findings inasmuch as the values of α and c_1 were chosen to get these levels correct. Of more importance is the nearly exact following of the trend of skin friction with Reynolds number by the model computations.

Figure 15 shows a comparison of the computed mean velocity profiles developed by the model in the vicinity of the wall and the well-known law of the wall as proposed by Coles (Ref. 21). It may be seen that the law of the wall is not quite achieved by the present selection of model parameters. The results, however, are sufficiently accurate to be encouraging.

In Figure 16 we compare the experimentally determined velocity defect law proposed by Coles (Ref. 21) with the results of our model computations. It is seen that, once the turbulent boundary layer is well established, the computational model gives a fairly good representation of the outer regions of the turbulent boundary layer.

With these results in hand, we must now consider the relationship of the computational scales used to the longitudinal integral scales that are found in the outer regions of turbulent boundary layers. For this purpose, we may use the measurements of Grant (Ref. 22). When the experimental correlations reported by Grant for $y/\delta_o = 0.66$ * in a turbulent boundary layer are integrated to give the longitudinal integral scale, one obtains $L/\delta_o \cong 0.3$. Since for our calculations, $\delta_o/\delta_{.99} \cong 0.83$, we find that $L/\delta_{.99} \cong 0.25$. Since the computational scale used was $\Lambda_1/\delta_{.99} = 0.15$, we find that

$$\Lambda_1/L \cong 0.6 \tag{32}$$

This is a most welcome result since it shows that, for all the turbulent flows we have investigated, the ratio of the proper computational scale to the longitudinal integral scale is approximately the same.

SOME COMMENTS ON SECOND-ORDER MODELING TECHNIQUES

The method of modeling turbulent shear flows which we have just described was developed, as we have previously pointed out, in order to attempt calculations of turbulent flows other than the classical shear layers that we . discussed in the previous sections. The author and his colleagues have applied the model to the calculation of the decay of a turbulent line vortex (Ref. 23), to the generation of turbulence in the earth's atmosphere (Refs. 7 and 9), and to the dispersal of pollutants by the atmosphere (Ref. 24). Since these computations were carried out with the original oversimplified constant Λ model discussed previously, one must not take the numerical values obtained too seriously; nevertheless, these computations did give some most interesting results and insights. Certainly the utility of the method was demonstrated and it appears that it, and others like it, should be carefully studied and refined in the next few years. The first order of business should be a continuance of the types of parameter studies that we have just described, for as large a spectrum of shear flows as can be reliably measured. In this way, we would hope to develop a model with the broadest capability possible.

It is here that one runs into the difficulties that were touched upon previously in connection with the free jet and the free shear layer. It would be very helpful indeed if the research community could agree on canonical free jet and free shear layer experiments which could be performed by several investigators. The purpose of these experiments would be to strive for agreement between experimentalists as to what the characteristics of such flows were and to explain any discrepancies that might exist. Before very much refinement of turbulent shear flow models can be accomplished, it appears that we are going to have to have a more precise definition of what the models must predict.

Assuming one had ideal experimental data with which to work in developing a second-order correlation model of turbulent flow, there is still the question of whether one really need go to all the trouble entailed. There are some who insist that such a model will not accomplish enough more than can be obtained from older methods to justify the effort and expense of such calculations. The author disagrees with this viewpoint and believes that the problem of computing chemically reacting turbulent flows is a case in point. For this reason, let us now turn to a brief discussion, for time does not permit a complete treatment, of some of the problems that are involved in the computation of chemically active, turbulent flows.

MODELING OF CHEMICALLY REACTING FLOWS

For most computations of chemically reacting turbulent flows, it has been customary for engineers to proceed with the calculation according to the following scheme. First, the engineer develops by some method (mixing length, eddy diffusivity, or other method) equations for the time-averaged or mean values of the concentrations of the reacting species of interest (say, species α and β) at each point in the turbulent flow under consideration. He also obtains an equation for the mean value of the temperature that is expected at each point in this flow. It is then customary, if the equations that generally govern the reaction between α and β, are

$$\frac{DC_\alpha}{Dt} = -k_1 C_\alpha C_\beta \tag{33}$$

$$\frac{DC_\beta}{Dt} = -k_2 C_\alpha^2 \beta \tag{34}$$

to assume that valid equations for the time rates of change of the mean values of the mass fractions of α and β are

$$\frac{D\overline{C}_\alpha}{Dt} = -\overline{k}_1 \overline{C}_\alpha \overline{C}_\beta \tag{35}$$

$$\frac{D\overline{C}_\beta}{Dt} = -\overline{k}_2 \overline{C}_\alpha \overline{C}_\beta \tag{36}$$

---

*Grant defined δ_o as that height in the boundary layer where the velocity defect was equal to the friction velocity.

In these equations, $\bar{c}_\alpha$ and $\bar{c}_\beta$ are the time-averaged mass fractions of the two species and $\bar{k}_1$ and $\bar{k}_2$ are the reaction rates k_1 and k_2 evaluated at the mean temperature $\bar{T}$, i.e., $\bar{k}_1 = k_1(\bar{T})$ and $\bar{k}_2 = k_2(\bar{T})$.

Although equations such as (35) and (36) are used extensively at the present time, it is not difficult to show that they are incorrect when reaction rates are fast and the scale of the turbulence is large. This may be done by considering the proper forms of Eqs (33) and (34) when they are averaged. The well-known results are*

$$\frac{D\bar{c}_\alpha}{Dt} = -\bar{k}_1\left(\bar{c}_\alpha\bar{c}_\beta + \langle c'_\alpha c'_\beta\rangle\right) - \left[\bar{c}_\alpha\langle k'_1 c'_\beta\rangle + \bar{c}_\beta\langle k'_1 c'_\alpha\rangle + \langle k'_1 c'_\alpha c'_\beta\rangle\right] \tag{37}$$

and

$$\frac{D\bar{c}_\beta}{Dt} = -\bar{k}_2\left(\bar{c}_\alpha\bar{c}_\beta + \langle c'_\alpha c'_\beta\rangle\right) - \left[\bar{c}_\alpha\langle k'_2 c'_\beta\rangle + \bar{c}_\beta\langle k'_2 c'_\alpha\rangle + \langle k'_2 c'_\alpha c'_\beta\rangle\right] \tag{38}$$

To demonstrate the character of these equations, let us discuss them under the assumption that $k'_1 = k'_2 = 0$. Equations (37) and (38) then reduce to

$$\frac{D\bar{c}_\alpha}{Dt} = -\bar{k}_1\left(\bar{c}_\alpha\bar{c}_\beta + \langle c'_\alpha c'_\beta\rangle\right) \tag{39}$$

and

$$\frac{D\bar{c}_\beta}{Dt} = -\bar{k}_2\left(\bar{c}_\alpha\bar{c}_\beta + \langle c'_\alpha c'_\beta\rangle\right) \tag{40}$$

It is clear from these equations that, if one wishes to calculate the reaction of α with β , it will be necessary to have an equation for the second-order correlation $\langle c'_\alpha c'_\beta\rangle$ unless one can show that $\langle c'_\alpha c'_\beta\rangle \ll \bar{c}_\alpha\bar{c}_\beta$ for the particular flow in question. The conditions required for $\langle c'_\alpha c'_\beta\rangle \ll \bar{c}_\alpha\bar{c}_\beta$ can be derived in the following way. First, by following the method used by Reynolds for the derivation of the equation for the turbulent stress tensor, one finds the following equation for the substantive derivative of the correlation $\langle c'_\alpha c'_\beta\rangle$:**

$$\frac{D\langle c'_\alpha c'_\beta\rangle}{Dt} = \left(\frac{D\langle c'_\alpha c'_\beta\rangle}{Dt}\right)_{chem} - \langle u^j{}' c'_\alpha\rangle\bar{c}_{\beta,j} - \langle u^j{}' c'_\beta\rangle\bar{c}_{\alpha,j} - \langle u^j{}' c'_\alpha c'_\beta\rangle_{,j}$$
$$+ \mathcal{D}g^{mn}\langle c'_\alpha c'_\beta\rangle_{,mn} - 2\mathcal{D}g^{mn}\langle c'_{\alpha,m} c'_{\beta,n}\rangle \tag{41}$$

where the term $(D\langle c'_\alpha c'_\beta\rangle/Dt)_{chem}$ is the contribution of chemical kinetics alone to the substantive derivative of $\langle c'_\alpha c'_\beta\rangle$. This expression can be found from Eqs (33) and (34) and is

$$\left(\frac{D\langle c'_\alpha c'_\beta\rangle}{Dt}\right)_{chem} = -k_1\left(\bar{c}_\alpha\langle c'^2_\beta\rangle + \bar{c}_\beta\langle c'_\alpha c'_\beta\rangle + \langle c'_\alpha c'^2_\beta\rangle\right)$$
$$-k_2\left(\bar{c}_\alpha\langle c'_\alpha c'_\beta\rangle + \bar{c}_\beta\langle c'^2_\alpha\rangle + \langle c'^2_\alpha c'_\beta\rangle\right) \tag{42}$$

It is instructive to discuss the behavior of the correlation $\langle c'_\alpha c'_\beta\rangle$ for the case of turbulent reactions in the absence of any appreciably large gradients. In this case, Eq (41) becomes

$$\frac{D\langle c'_\alpha c'_\beta\rangle}{Dt} = \left(\frac{D\langle c'_\alpha c'_\beta\rangle}{Dt}\right)_{chem} - 2\mathcal{D}g^{mn}\langle c'_{\alpha,m} c'_{\beta,n}\rangle \tag{43}$$

The second term on the right of Eq (43) is the destruction of the correlation $\langle c'_\alpha c'_\beta\rangle$ by the action of molecular diffusion. In line with our previous work, we will model this term by means of a diffusion scale length λ so that Eq (43) becomes

---

*For a discussion of these equations that is related to the present treatment, reference should be made to O'Brien (Ref. 25) which was published after this work on the modeling of chemically reacting turbulent flows was started.
**For the purposes of this illustrative discussion, the flow is treated as incompressible.

$$\frac{\partial \langle C'_\alpha C'_\beta \rangle}{\partial t} = \left(\frac{\partial \langle C'_\alpha C'_\beta \rangle}{\partial t}\right)_{chem} - 2\mathscr{D}\frac{\langle C'_\alpha C'_\beta \rangle}{\lambda^2} \tag{44}$$

The diffusion term in this equation is such that $\langle C'_\alpha C'_\beta \rangle$ tends to approach zero with a characteristic time that is

$$\tau_{diff} = \lambda^2/2\mathscr{D} \tag{45}$$

What is the overall effect of the first term on the right-hand side of Eq (44)? The effect is difficult to see from an inspection of Eq (42), but we may derive an expression for what this term accomplishes from Eqs (39) and (40). First, multiply (39) by $\bar{C}_\beta$ and (40) by $\bar{C}_\alpha$ and then add the resulting equations. The result is

$$\left(\frac{\partial \bar{C}_\alpha \bar{C}_\beta}{\partial t}\right)_{chem} = -\left(k_1 \bar{C}_\beta + k_2 \bar{C}_\alpha\right)\left(\bar{C}_\alpha \bar{C}_\beta + \langle C'_\alpha C'_\beta \rangle\right) \tag{46}$$

This equation can be interpreted by saying that the effect of chemistry alone is to drive $\bar{C}_\alpha \bar{C}_\beta$ to the negative of $\langle C'_\alpha C'_\beta \rangle$ (or $\langle C'_\alpha C'_\beta \rangle$ to the negative of $\bar{C}_\alpha \bar{C}_\beta$) with a characteristic time

$$\tau_{chem} = \frac{1}{k_1 \bar{C}_\beta + k_2 \bar{C}_\alpha} \tag{47}$$

Equation (46) states that the reaction between α and β will always stop, i.e., $\bar{C}_\alpha \bar{C}_\beta + \langle C'_\alpha C'_\beta \rangle$ will become zero, short of the exhaustion of α or β unless α and β are perfectly mixed wherever they occur in the turbulent flow under consideration. The physical reason for this is that, in the absence of diffusion, if α and β are not perfectly mixed to start with, the final state of the gas in any volume element will be α and products, β and products, α alone, or β alone, but never any region containing both α and β. It is easy to see that, no matter what the values taken on by C_α and C_β are as a function of time, if C_α is never nonzero when C_β is nonzero and vice versa so that no reaction is possible, it is mathematically true that $\bar{C}_\alpha \bar{C}_\beta + \langle C'_\alpha C'_\beta \rangle = 0$. Thus, Eqs (39) and (40) state that no reactions are possible as required by the physics of the problem.

An actual example may make the meaning of $\langle C'_\alpha C'_\beta \rangle$ more clear. Consider that the flow of material by a given point is such that alternate blobs of α and β pass the point. Let us suppose that half the time the flow is all α and half the time it is all β. The resulting concentrations are sketched in Figure 17. If this pattern keeps repeating, the average values of C_α and C_β are obviously $\bar{C}_\alpha = 1/2$ and $\bar{C}_\beta = 1/2$. Whenever the flow is all α, $C'_\alpha = +1/2$ and $C'_\beta = -1/2$. Whenever the flow is all β, $C'_\alpha = -1/2$ and $C'_\beta = +1/2$. We find then that the average value of $C'_\alpha C'_\beta$ must be $\langle C'_\alpha C'_\beta \rangle = -1/4$. Since $\langle C'_\alpha C'_\beta \rangle = -\bar{C}_\alpha \bar{C}_\beta$, no reaction is possible according to Eqs (39) and (40) and obviously no reaction should occur.

We may now return to Eq (44). If, in this equation, the scale λ is small enough and the reaction rates are slow enough, the second term on the right-hand side of the equation will be dominant and the flow will be such that $\langle C'_\alpha C'_\beta \rangle$ is always almost zero. This means that molecular diffusion is always fast enough to keep the two species well mixed. On the other hand, if the reaction rates are very fast and λ is very large, the first term on the right-hand side of Eq (44) will be dominant and $\langle C'_\alpha C'_\beta \rangle$ will tend to be approximately equal to $-\bar{C}_\alpha \bar{C}_\beta$ and the two species will be poorly mixed. The rate of removal from the flow of α and β by reaction will then not be governed by reaction rates but will be limited by molecular diffusion. To put these notions into quantitative form, let us consider the ratio of the two characteristic times

$$N = \frac{\tau_{diff}}{\tau_{chem}} = \frac{\lambda^2}{2\mathscr{D}}\left(k_1 \bar{C}_\beta + k_2 \bar{C}_\alpha\right) \tag{48}$$

and a contact index

$$I = \frac{\bar{C}_\alpha \bar{C}_\beta + \langle C'_\alpha C'_\beta \rangle}{\bar{C}_\alpha \bar{C}_\beta} = 1 + \frac{\langle C'_\alpha C'_\beta \rangle}{\bar{C}_\alpha \bar{C}_\beta} \tag{49}$$

We note that if N is much smaller than one, diffusion will be very rapid and the two species α and β will be in intimate contact with each other. In this case $\langle C'_\alpha C'_\beta \rangle / \bar{C}_\alpha \bar{C}_\beta$ will be small and the contact index will approach one. If, on the other hand, N is

much larger than one, mixing will be poor and $\langle C'_\alpha C'_\beta \rangle$ will approach $-\bar{C}_\alpha \bar{C}_\beta$. The contact index will then approach zero. In this case the reaction will be diffusion-limited.

In many laboratory flows, the dissipative or diffusive scale of turbulence is very small and N is, indeed, small so that the neglect of $\langle C'_\alpha C'_\beta \rangle$ in the kinetic equations is permissible. On the other hand, if the laboratory experiment is just increased in size, holding all other parameters such as velocity, temperature, etc., constant, one soon finds that the character of the flow changes. This may be seen by examining the expression for the dimensionless quantity N in more detail.

Let us assume the diffusive scale of a turbulent flow is of the order of the dissipative scale so that we may use the expression for λ given in a previous section, namely,

$$\lambda^2 = \Lambda_1^2 / (a + b\rho q \Lambda_1 / \mu) \tag{50}$$

Substituting this expression into Eq (48) gives

$$N = \frac{\Lambda_1^2}{2\mathcal{E}} \frac{k_1 \overline{r} + k_2 \bar{C}_\alpha}{a + b\rho q \Lambda_1 / \mu} \tag{51}$$

For relatively high Reynolds numbers, this expression becomes

$$N = \frac{1}{2b} \cdot \frac{\mu}{\rho \mathcal{E}} \cdot \frac{\Lambda_1}{q} \left(k_1 \bar{C}_\beta + k_2 \bar{C}_\alpha \right) \tag{52}$$

If an experiment is performed in the laboratory and a value of N for this experiment is determined or estimated and is found to be small compared to one, then we know that the diffusive mixing of the flow is such that the species α and β are in contact. The reaction rate of these species is then chemically controlled. Now if the apparatus is just scaled up in size, all other things being equal, N will increase linearly with size since the scale Λ_1 increases linearly with the size of the apparatus. When the scale has been increased sufficiently, so that N is no longer very small compared to one, the nature of the flow in the device must change, for the species α and β will no longer be in intimate contact at equivalent positions in the apparatus.

The turbulent atmospheric boundary layer is a good example of a flow in which it is essential to keep track of the correlation $\langle C'_\alpha C'_\beta \rangle$ if one is to be able to make sense of the reaction of species which are introduced into the flow. To demonstrate this, we list in Table 3 some of the second-order reactions responsible for the production of photochemical smog. We have also listed in this table the reaction rate recommended for each reaction (Ref. 26) and an estimate of the number N for each reaction if it occurs in the atmospheric boundary layer where a typical value for λ is 10 centimeters. It is interesting to note that it is, in general, those reactions listed in Table 3 for which N is greater than one that investigators have found to proceed more slowly than predicted by formulas such as Eqs (35) and (36) when the reaction rate determined from laboratory experiments is used. This difficulty has led some investigators to search for other chemical reactions that might be considered which would explain this discrepancy.

It certainly appears unwise to follow this course until such time as one has at least developed a viable scheme for properly computing turbulent reacting flows. It is the author's opinion that an acceptable method of computing such flows can be developed through the use of second-order correlation equations such as Eqs (41) and (42). Methods of modeling the third-order correlations that appear in these equations can be found that are similar to those used to study the generation of turbulence and turbulent transport that were discussed in previous sections of this paper. The development of a viable method for computing chemically reacting turbulent flows according to such a scheme is under active development by the author and his colleagues at the present time. It is important to note in this connection that it is essential in developing this general method to consider fluctuations in density and in the reaction rate constants when the chemical rate equations are considered.

SUMMARY

Recent numerical studies carried out by the author and his colleagues in their attempt to develop an invariant model of turbulent shear flow are described. The results of comparing computations using a tentative model of such flows with experimental data for the axially symmetric free jet, the two-dimensional free shear layer, and the flat plate boundary layer are presented. The need for more carefully designed and documented free turbulent flow measurements is discussed in relation to the problem of selecting more correlation closure schemes, of which the present method is one, to the computation of turbulent flows other than classical incompressible shear layers. In particular, the possibility of more correct methods of calculating the behavior of chemically reacting turbulent flows is examined.

Table 3. Some Second-Order Reactions Responsible for Photochemical Smog (Ref. 26)

Reaction	K $(ppm-sec)^{-1}$	N
$O_3 + NO = NO_2 + O_2$ *	3.3×10^{-4}	0.25 *
$NO_2 + O_3 = NO_3 + O_2$	1.7×10^{-5}	5.0×10^{-3}
$NO_3 + NO = 2NO_2$	4.8	1.4×10^{3}
$NO + HO_2 = NO_2 + OH$	1.7×10^{-1}	50.0
$OH + O_3 = HO_2 + O_2$	1.7	5.0×10^{2}
$OH + CO = H + CO_2$	5.0×10^{-2}	1.5×10^{2}
$CH_3O_2 + NO = CH_3O + NO_2$	1.7	5.0×10^{2}
$C_2H_3O_2 + NO = C_2H_3O + NO_2$	1.7	5.0×10^{2}
$C_2H_4O_2 + NO = CH_3CHO + NO_2$	1.7	5.0×10^{2}
$CH_3O + O_2 = HCHO + HO_2$	1.7	5.0×10^{2}
$C_3H_6 + O = CH_3 + C_2H_3O$	6.0×10^{-1}	1.8×10^{2}
$C_3H_6 + O_3 = HCHO + C_2H_4O_2$	6.3×10^{-3}	2.5
$C_3H_6 + O_2 = CH_3O + C_2H_3O$	1.7×10^{-2}	5.0
$C_3H_6 + HO_2 = CH_3O + CH_3CHO$	3.4×10^{-2}	10.0
$C_2H_3O + M = CH_3 + CO + M$	1.7×10^{-1}	50.0

*Those reactions for which N is small compared to one are those which can be treated using mean quantities in the basic equations of chemical change, i.e., correlations in fluctuating quantities may be neglected.

REFERENCES

1. Reynolds, O., "On the Dynamical Theory of Incompressible Viscous Fluids and the Determination of the Criterion," Phil. Trans. Royal Society, London, A 186, 1894, p. 123.

2. Prandtl, L. and Wieghardt, K., "Über ein neues Formelsystem für die ausgebildte Turbulenz," Nachr. Akad. Wiss. Goettingen 19, 6, 1945.

3. Rotta, J., "Statistische Theorie nichthomogener Turbulenz," Z. Physik, Vol. 129, 1951, p. 547.

4. Chou, P.Y., "Pressure Flow of a Turbulent Fluid between Two Infinite Parallel Planes,' Quarterly of Applied Math., Vol. 3, No. 3, 1949, pp. 198-209.

5. Hanjalić, K. and Launder, B.E., "A Reynolds Stress Model of Turbulence and its Application to Asymmetric Boundary Layers," Imperial College of Science & Technology, London, Report No. TM/TN/A/8, March 1971.

6. Donaldson, Coleman duP. and Rosenbaum, Harold, "Calculation of Turbulent Shear Flows Through Closure of the Reynolds Equations by Invariant Modeling," Hampton, Virginia, National Aeronautics and Space Administration Report No. NASA SP-216, December 1968, pp. 231-253.

7. Donaldson, Coleman duP., Sullivan, Roger D., and Rosenbaum, Harold, "Theoretical Study of the Generation of Atmospheric Clear Air Turbulence," AIAA Paper No. 70-55, New York, January 1970 (to be published in AIAA Journal).

8. Donaldson, Coleman duP., "Calculation of Turbulent Shear Flows for Atmospheric and Vortex Motions," AIAA Paper No. 71-217, New York, January 1971 (to be published in AIAA Journal, January 1972).

9. Donaldson, Coleman duP. and Conrad, Peter W., "Computations of the Generation of Turbulence in the Atmospheric Boundary Layer," Proceedings of the International Conference on Atmospheric Turbulence, London, The Royal Aeronautical Society, May 1971.

10. Wygnanski, I. and Fiedler, H., "Some Measurements in the Self-Preserving Jet," J. Fluid Mechanics, Vol. 38, Part 3, 1969, pp. 577-612.

11. Wygnanski, I. and Fiedler, H., "The Two-Dimensional Mixing Region," J. Fluid Mechanics, Vol. 41, Part 2, 1970, pp. 327-361.

12. Gibson, M.M., "Spectra of Turbulence in a Round Jet," J. Fluid Mechanics, Vol. 15, Part 2, 1963, pp. 161-173.

13. Donaldson, Coleman duP., Snedeker, Richard S., and Margolis, David P., "A Study of Free Jet Impingement. Part 2. Free Jet Turbulent Structure and Impingement Heat Transfer," J. Fluid Mechanics, Vol. 45, Part 3, 1971, pp. 477-512.

14. Tollmien, W., "Berechnung turbulenter Ausbreitungsvorgange," Zeitschrift für angewandte Mathematik und Mechanik, Vol. IV, 1926, p. 458.

15. Prandtl, L., "The Mechanics of Viscous Fluids," Aerodynamic Theory (W.Durand, editor), Stanford, California, Stanford University Press, 1934, pp. 34-208.

16. Glushko, G.S., "Turbulent Boundary Layer on a Flat Plate in an Incompressible Fluid," Bulletin of the Academy of Science, USSR, Mech. Series No. 4, 1965, pp. 13-23.

17. Bradshaw, P., Ferriss, D.H., and Atwell, N.P., "Calculations of Boundary Layer Development Using the Turbulent Energy Equation," J. Fluid Mechanics, Vol. 28, Part 3, 1967, pp. 593-616.

18. Harlow, F.H. and Romero, N.C., "Turbulence Distortion in a Nonuniform Tunnel," Los Alamos Scientific Lab. Report No. LA-4247, 1969.

19. Gawain, T.H. and Pritchett, J.W., "A Unified Heuristic Model of Fluid Turbulence," J. Computational Physics, Vol. 5, No. 3, 1970, pp. 383-405.

20. Beckwith, I.E. and Bushnell, D.M., "Detailed Description and Results of a Method for Computing Mean and Fluctuating Quantities in Turbulent Boundary Layers," National Aeronautics and Space Administration Report No. TN D-4815, 1968.

21. Coles, Donald, "Measurements in the Boundary Layer on a Smooth Flat Plate in Supersonic Flow. Part 1. The Problem of the Turbulent Boundary Layer," Jet Propulsion Laboratory Report No. 20-69, 1953.

22. Grant, H.L., "The Large Eddies of Turbulent Motion," J. Fluid Mechanics, Vol. 4, Part 2, 1958, pp. 149-190.

23. Donaldson, Coleman duP. and Sullivan, Roger D., "Decay of an Isolated Vortex," Aircraft Wake Turbulence and Its Detection (J. Olsen, A. Goldburg, and M. Rogers, editors), New York, Plenum Press, 1971, pp. 389-411.

24. Donaldson, Coleman duP. and Hilst, Glenn R., "An Initial Test of the Applicability of Invariant Modeling Methods to Atmospheric Boundary Layer Diffusion," Aeronautical Research Associates of Princeton Report No. 169, October 1971.

25. O'Brien, Edward E., "Turbulent Mixing of Two Rapidly Reacting Chemical Species," Physics of Fluids, Vol. 14, No. 7, 1971, pp. 1326-1331.

26. Worley, Frank W., "Report on Mathematical Modeling of Photochemical Smog," presented at Panel on Modeling, NATA/CCMS Pilot Project on Air Pollution, Paris, July 1971.
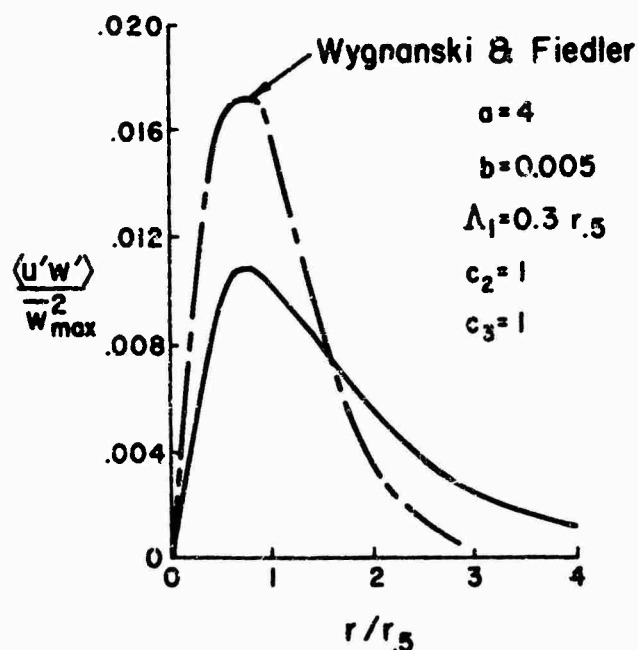
Figure 1. Result of a free jet computation with a single Λ model of turbulence
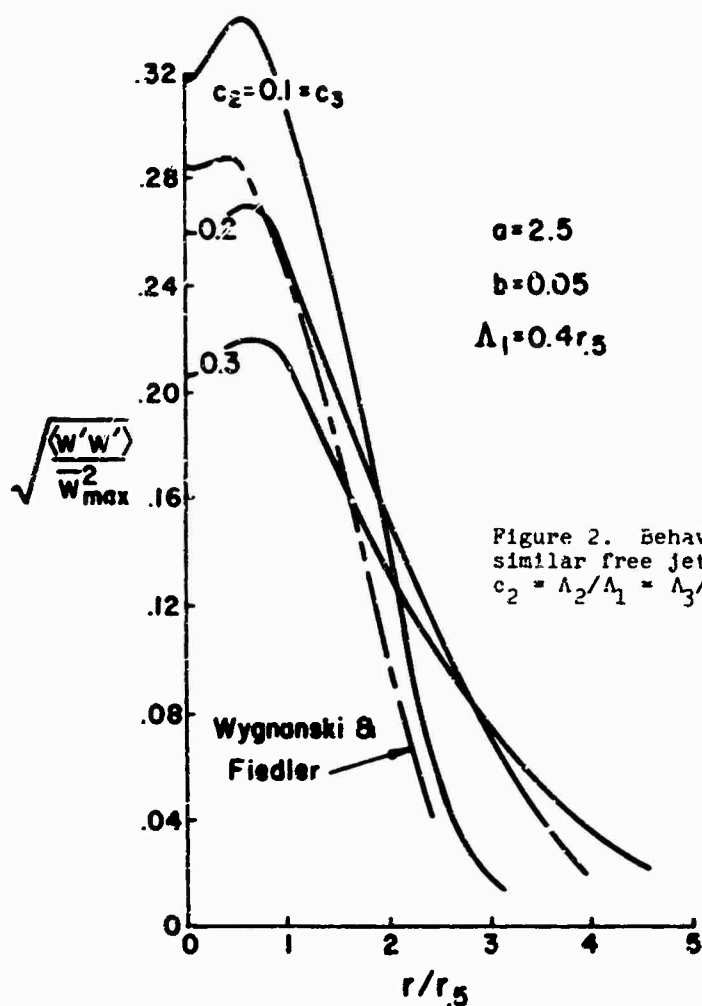
Figure 2. Behavior of solutions for a self-similar free jet when the parameter $c_2 = \Lambda_2/\Lambda_1 = \Lambda_3/\Lambda_1$ is varied

$a = 2.5$

$b = 0.05$

$\Lambda_1 = 0.4r_{.5}$
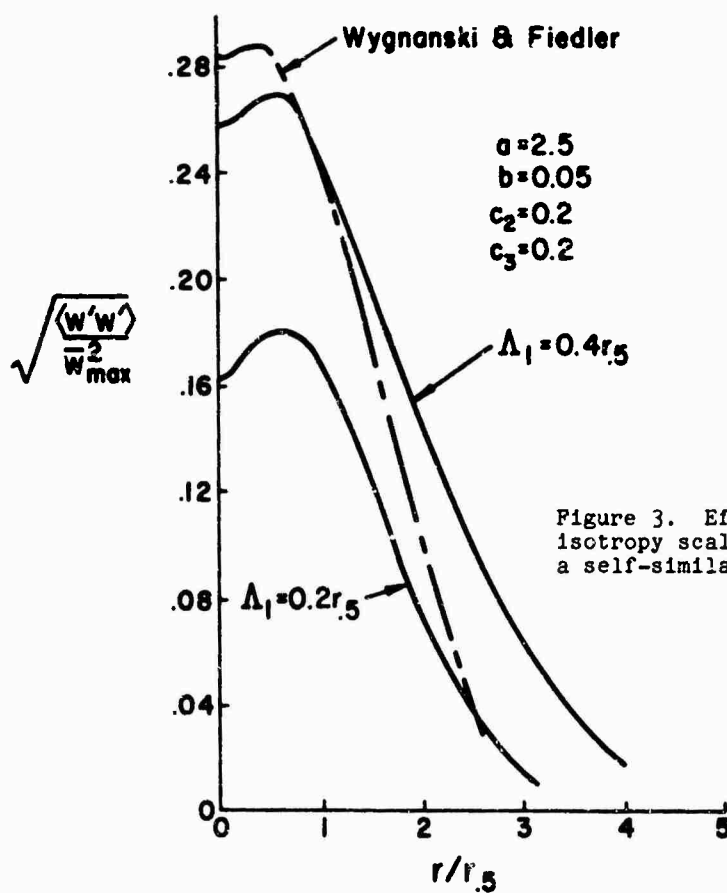
Figure 3. Effect of variation of the isotropy scale Λ_1 on characteristics of a self-similar free jet

$a = 2.5$
$b = 0.05$
$c_2 = 0.2$
$c_3 = 0.2$
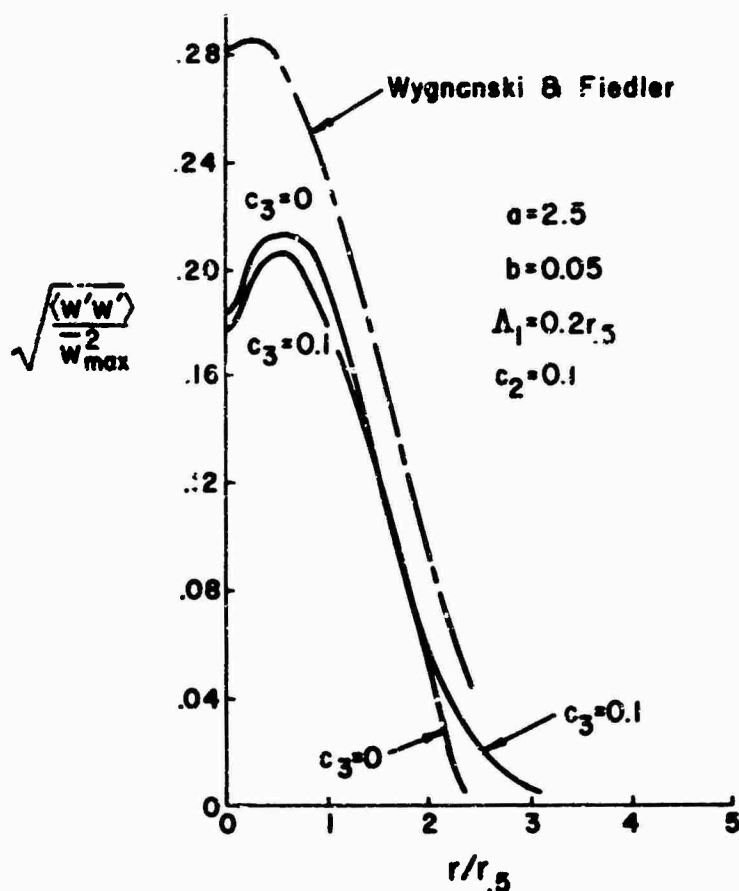
Figure 4. The effect of neglecting pressure diffusion when calculating a self-similar free jet
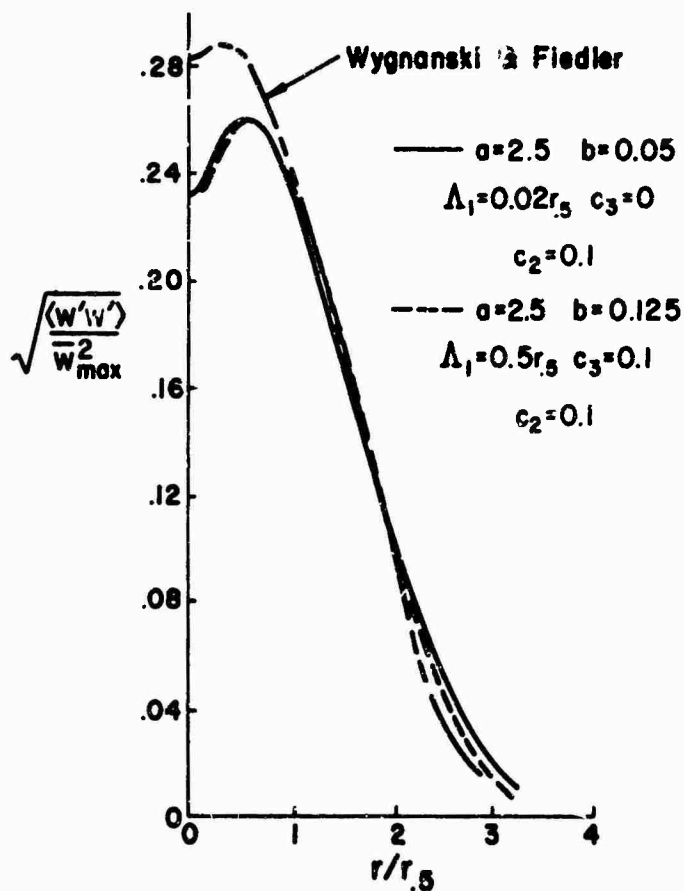
Figure 5. Two choices of model parameters that yield almost the same distributions of $\langle w'w' \rangle$ for a self-similar free jet
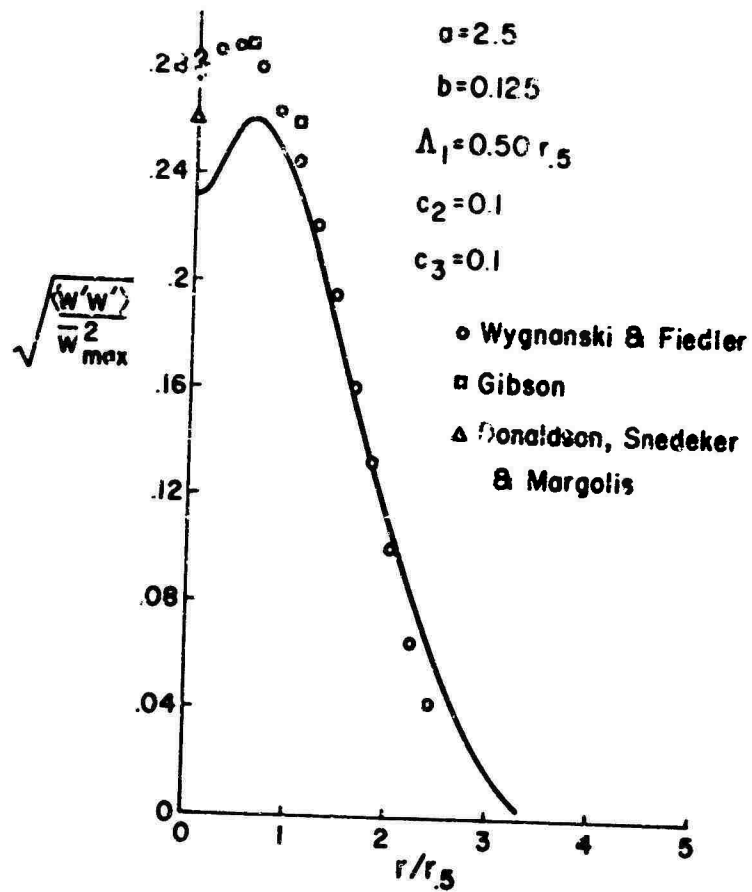
Figure 6. Comparison of experimental results and model predictions for the longitudinal velocity correlations in a free jet
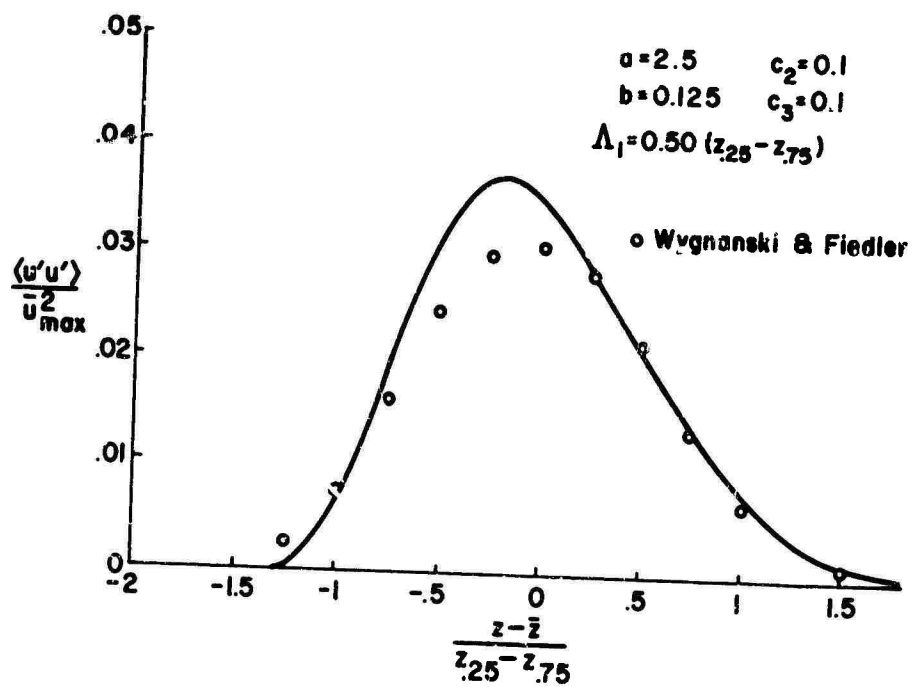
Figure 7. Comparison of experimental results and model predictions for the longitudinal velocity correlations in a free shear layer
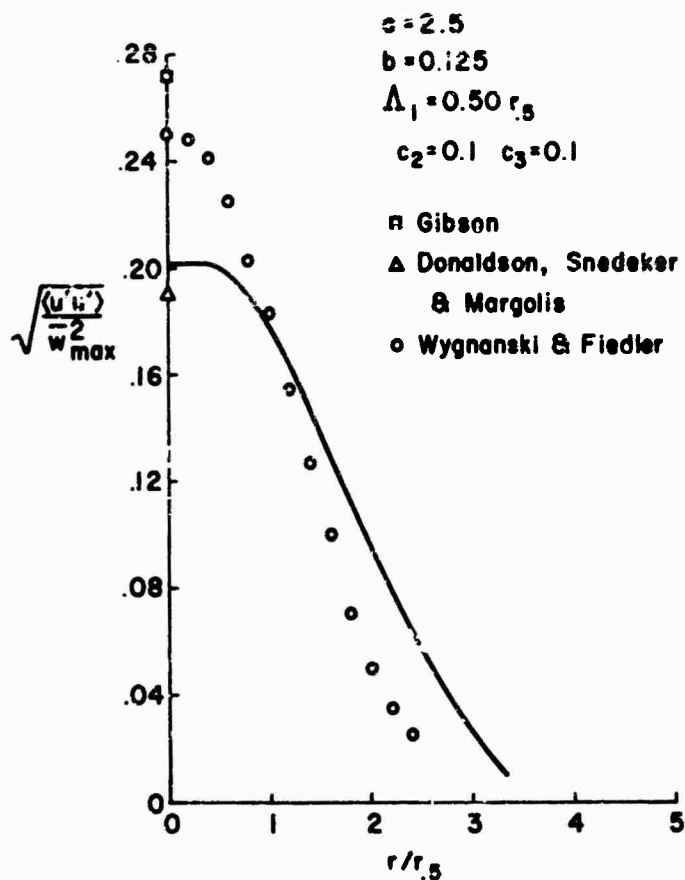
Figure 8. Comparison of experimental results and model predictions for the radial velocity fluctuations in a free jet
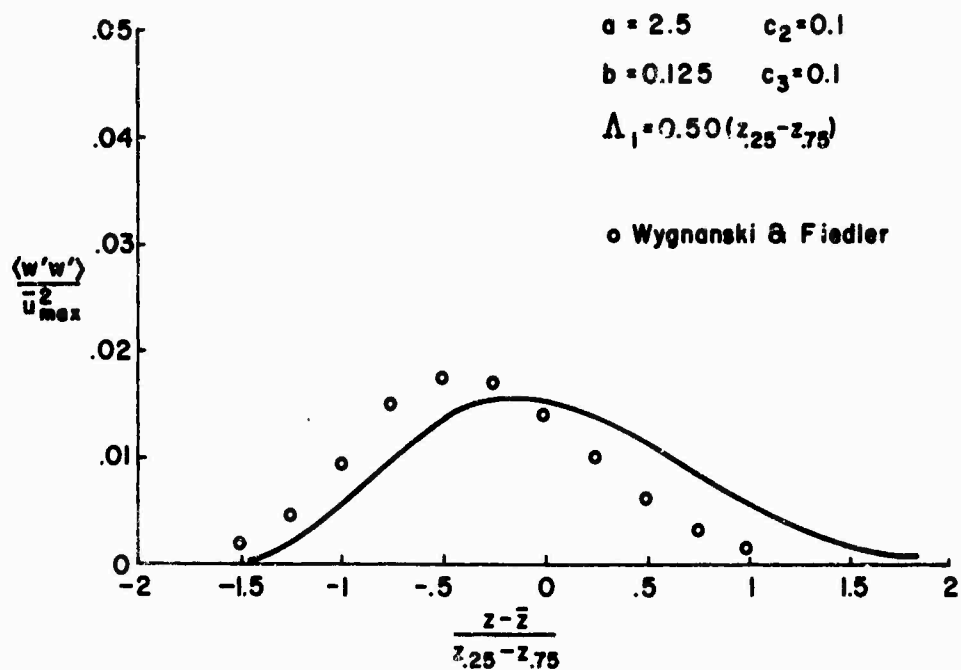
Figure 9. Comparison of experimental results and model predictions for the normal velocity fluctuations in a free shear layer
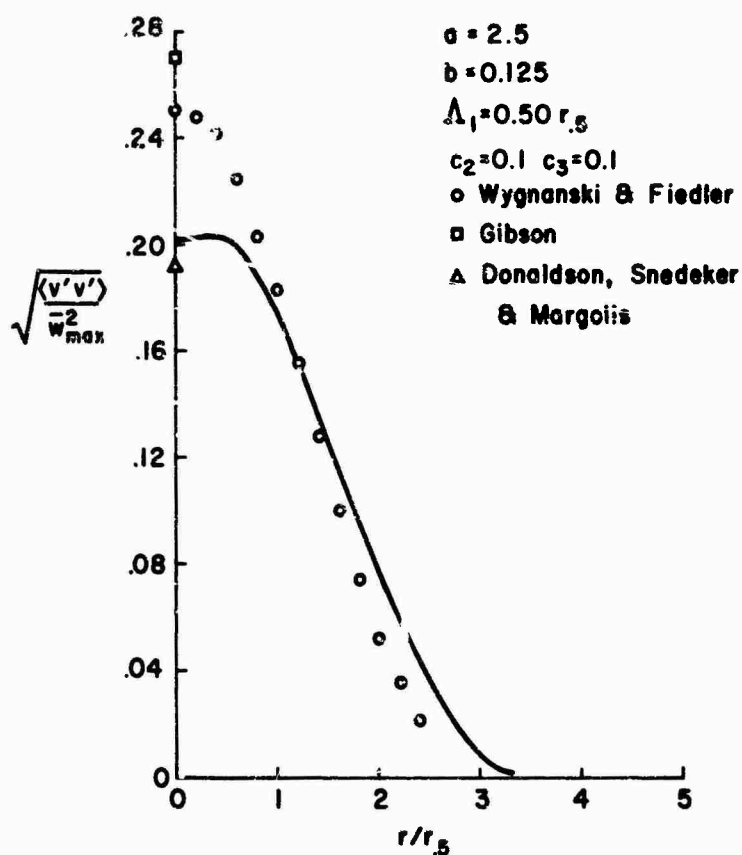
Figure 10. Comparison of experimental results and model predictions for the sidewise fluctuations in a free jet

Figure 11. Comparison of experimental results and model predictions for the sidewise fluctuations in a free shear layer
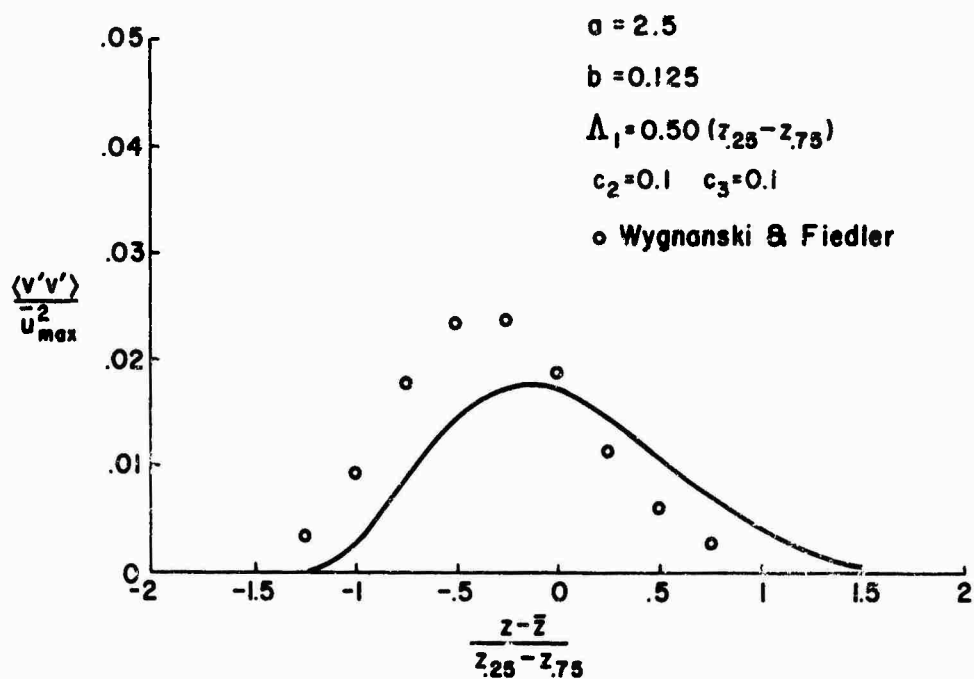
$$a = 2.5$$
$$b = 0.125$$
$$\Lambda_1 = 0.50 r_{.5}$$
$$c_2 = 0.1$$
$$c_3 = 0.1$$
○ Wygnanski & Fiedler
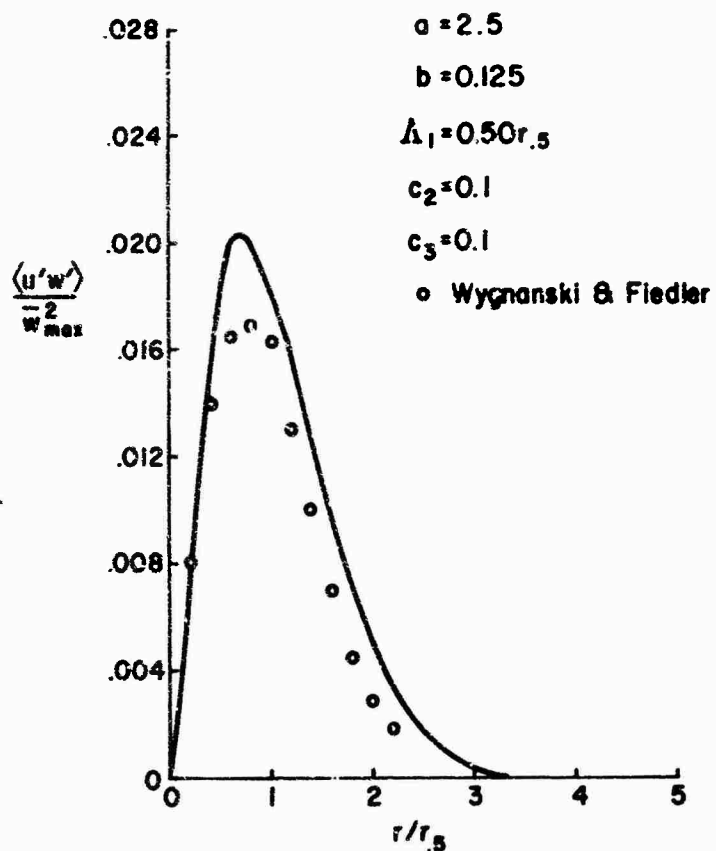
Figure 12. Comparison of experimental results and model predictions for the shear correlation in a free jet

○ Wygnanski & Fiedler as measured
● Corrected Wygnanski & Fiedler
$$a = 2.5 \quad c_2 = 0.1$$
$$b = 0.125 \quad c_3 = 0.1$$
$$\Lambda_1 = 0.50(z_{25} - z_{75})$$
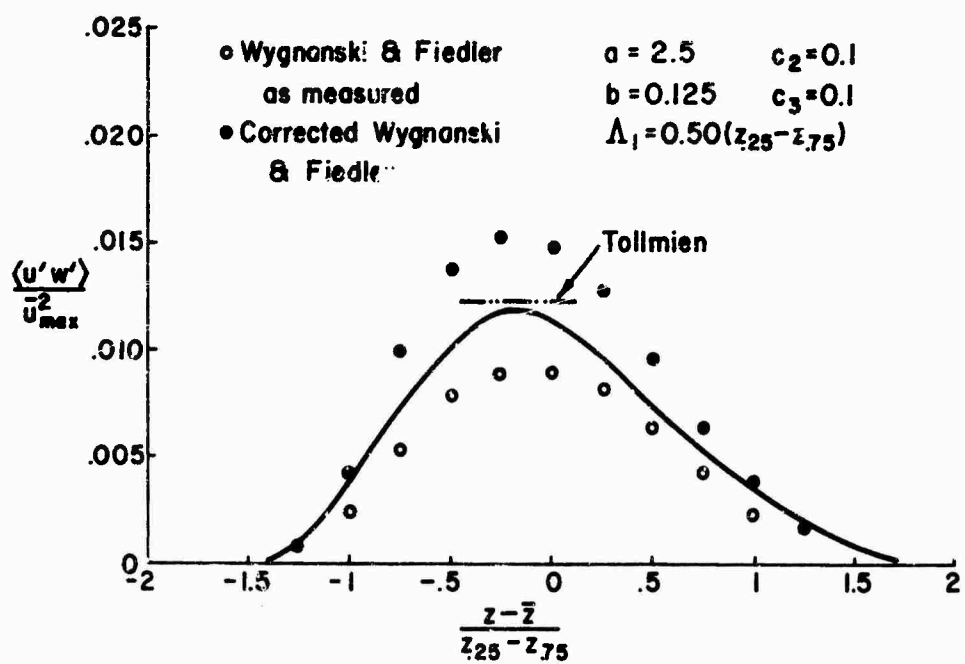
Figure 13. Comparison of experimental results and model computations for the shear correlation in a free shear layer

COMPUTED VALUES FOR
$a = 2.5$ $b = 0.125$ $\Lambda_1 = 0.15\delta_{99}$
$c_2 = 0.1$ $c_3 = 0.1$ $a = 0.443$

TABLE II OF COLES

LAMINAR

c_f

Re_x
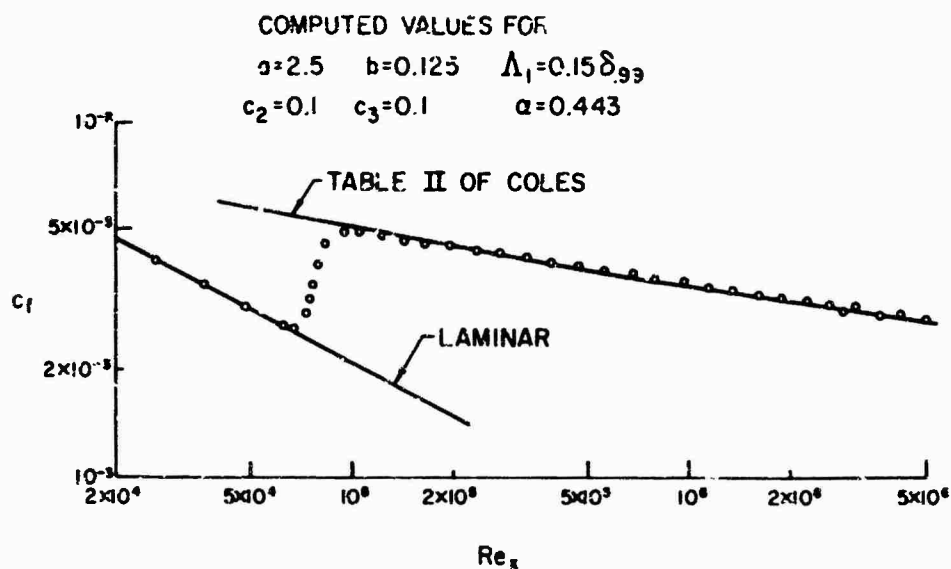
Figure 14. Computed variation of coefficient of friction with Reynolds number

COMPUTED VALUES FOR
$a = 2.5$ $b = 0.125$ $\Lambda_1 = 0.15\delta_{99}$
$c_2 = 0.1$ $c_3 = 0.1$ $a = 0.443$

$\circ$ $Re_x = 0.277 \times 10^6$
$\square$ $Re_x = 1.62 \times 10^6$
$\triangle$ $Re_x = 6.76 \times 10^6$

TABLE IV OF COLES

$\bar{u}/u_\tau$

zu_τ/ν
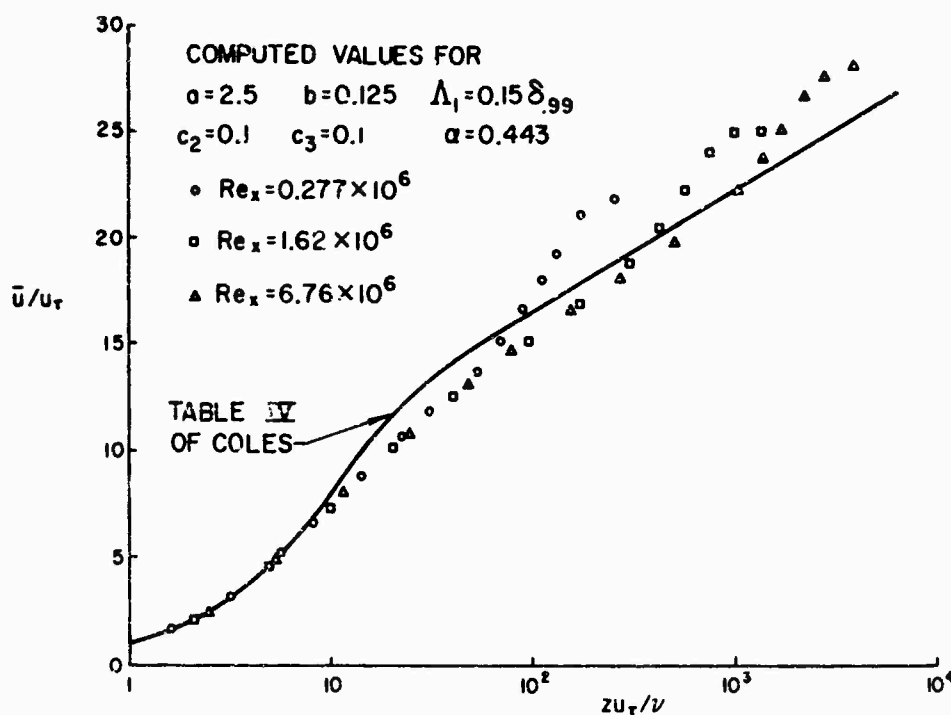
Figure 15. Computed velocity profiles for three Reynolds numbers.
Computation started at $Re_x = 20,000$. The reference velocity u_τ is
defined by $\tau_{wall} = \rho u_\tau^2$.

COMPUTED VALUES FOR

$\gamma = 2.5 \quad b = 0.125 \quad \Lambda_2 = 0.15\delta_{99}$

$c_2 = 0.1 \quad c_3 = 0.1 \quad a = 0.443$

○ $Re_x = 0.277 \times 10^6$

▫ $Re_x = 1.62 \times 10^6$

▲ $Re_x = 6.76 \times 10^6$

TABLE Ⅴ OF COLES
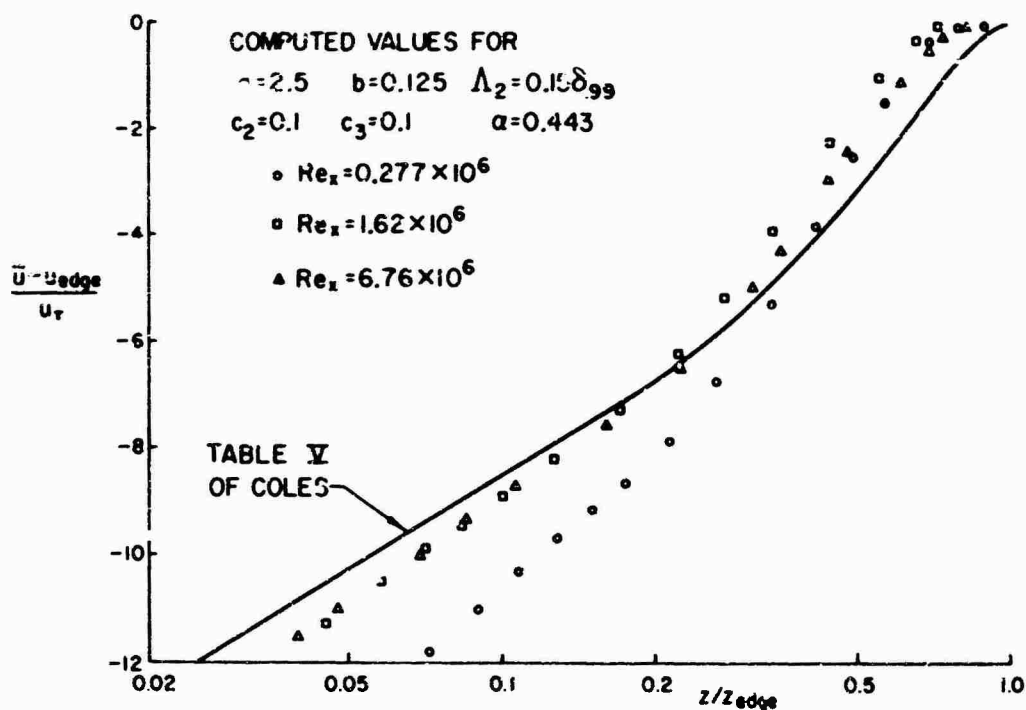
Figure 16. Computed velocity defects for three Reynolds numbers. Computation started at $Re_x = 20,000$. The reference velocity u_τ is defined by $\tau_{wall} = \rho u_\tau^2$.
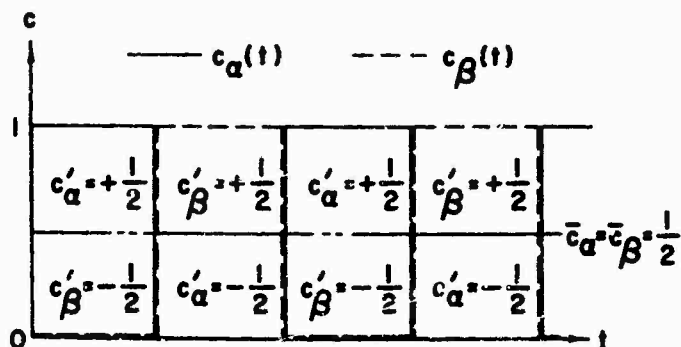
Figure 17. Simple problem illustrating $\langle c'_\alpha c'_\beta \rangle = -\bar{c}_\alpha \bar{c}_\beta$ when no reactions are possible

APPENDIX A. CONSTANT DENSITY MODEL EQUATIONS FOR STEADY FLOW

Continuity:

$$\bar{u}^j{}_{,j} = 0 \tag{A.1}$$

Momentum:

$$\bar{u}^j \bar{u}_{1,j} = -\frac{1}{\rho}\bar{p}_{,1} + \nu\left(g^{jk}\bar{u}_{1,k}\right)_{,j} - \langle u^{j'} u_1'\rangle_{,j} \tag{A.2}$$

Stress tensor:

$$\bar{u}^j \langle u_i' u_k'\rangle_{,j} = -\langle u^{j'} u_k'\rangle\,\bar{u}_{1,j} - \langle u^{j'} u_i'\rangle\,\bar{u}_{k,j}$$

$$+ g^{j\ell}\left[\Lambda_2 q\left(\langle u_i' u_\ell'\rangle_{,k} + \langle u_\ell' u_k'\rangle_{,1} + \langle u_i' u_k'\rangle_{,\ell}\right)\right]_{,j}$$

$$+ \left[\Lambda_3 q\,\langle u^{\ell'} u_i'\rangle_{,\ell}\right]_{,k} + \left[\Lambda_3 q\,\langle u^{\ell'} u_k'\rangle_{,\ell}\right]_{,1}$$

$$- \frac{q}{\Lambda_1}\left(\langle u_i' u_k'\rangle - \delta_{ik}\frac{K}{3}\right) + \nu\left[g^{j\ell}\langle u_i' u_k'\rangle_{,j\ell} - 2\frac{\langle u_i' u_k'\rangle}{\lambda^2}\right] \tag{A.3}$$

APPENDIX B. MODEL EQUATIONS FOR A BOUNDARY LAYER

We use a Cartesian coordinate system (x,y,z) with the free stream velocity in the x-direction and with z as the coordinate normal to the wall. The velocity components are denoted by (u,v,w). With the usual assumptions for a constant pressure boundary layer, Eqs (A.1) through (A.3) become

$$\frac{\partial \bar{u}}{\partial x} + \frac{\partial \bar{w}}{\partial z} = 0 \tag{B.1}$$

$$\bar{u}\frac{\partial \bar{u}}{\partial x} + \bar{w}\frac{\partial \bar{u}}{\partial z} = \nu\frac{\partial^2 \bar{u}}{\partial z^2} - \frac{\partial \langle u'w'\rangle}{\partial z} \tag{B.2}$$

$$\bar{u}\frac{\partial \langle u'u'\rangle}{\partial x} + \bar{w}\frac{\partial \langle u'u'\rangle}{\partial z} = -\langle u'w'\rangle\frac{\partial \bar{u}}{\partial z} + \frac{\partial}{\partial z}\left(\Lambda_2 q\frac{\partial \langle u'u'\rangle}{\partial z}\right) - \frac{q}{\Lambda_1}\left(\langle u'u'\rangle - \frac{K}{3}\right)$$
$$+ \nu\left(\frac{\partial^2 \langle u'u'\rangle}{\partial z^2} - \frac{2\langle u'u'\rangle}{\lambda^2}\right) \tag{B.3}$$

$$\bar{u}\frac{\partial \langle v'v'\rangle}{\partial x} + \bar{w}\frac{\partial \langle v'v'\rangle}{\partial z} = \frac{\partial}{\partial z}\left(\Lambda_2 q\frac{\partial \langle v'v'\rangle}{\partial z}\right) - \frac{q}{\Lambda_1}\left(\langle v'v'\rangle - \frac{K}{3}\right)$$
$$+ \nu\left(\frac{\partial^2 \langle v'v'\rangle}{\partial z^2} - \frac{2\langle v'v'\rangle}{\lambda^2}\right) \tag{B.4}$$

$$\bar{u}\frac{\partial \langle w'w'\rangle}{\partial x} + \bar{w}\frac{\partial \langle w'w'\rangle}{\partial z} = \frac{\partial}{\partial z}\left[(3\Lambda_2 + 2\Lambda_3)q\frac{\partial \langle w'w'\rangle}{\partial z}\right] - \frac{q}{\Lambda_1}\left(\langle w'w'\rangle - \frac{K}{3}\right)$$
$$+ \nu\left(\frac{\partial^2 \langle w'w'\rangle}{\partial z^2} - \frac{2\langle w'w'\rangle}{\lambda^2}\right) \tag{B.5}$$

$$\bar{u}\frac{\partial \langle u'w'\rangle}{\partial x} + \bar{w}\frac{\partial \langle u'w'\rangle}{\partial z} = -\langle w'w'\rangle\frac{\partial \bar{u}}{\partial z} + \frac{\partial}{\partial z}\left[(2\Lambda_2 + \Lambda_3)q\frac{\partial \langle u'w'\rangle}{\partial z}\right] - \frac{q}{\Lambda_1}\langle u'w'\rangle$$
$$+ \nu\left(\frac{\partial^2 \langle u'w'\rangle}{\partial z^2} - \frac{2\langle u'w'\rangle}{\lambda^2}\right) \tag{B.6}$$

APPENDIX C. MODEL EQUATIONS FOR A FREE JET

We use a cylindrical coordinate system (r,θ,z) with the velocity components denoted by (u,v,w), respectively. The assumptions for a constant pressure boundary layer are again applied to Eqs (A.1) through (A.3), along with the assumption of axial symmetry, giving

$$\frac{\partial \bar{u}}{\partial r} + \frac{\bar{u}}{r} + \frac{\partial \bar{w}}{\partial z} = 0 \tag{C.1}$$

$$\bar{u}\frac{\partial \bar{w}}{\partial r} + \bar{w}\frac{\partial \bar{w}}{\partial z} = \nu\left(\frac{\partial^2 \bar{w}}{\partial r^2} + \frac{1}{r}\frac{\partial \bar{w}}{\partial r}\right) - \frac{\partial \langle u'w'\rangle}{\partial r} - \frac{\langle u'w'\rangle}{r} \tag{C.2}$$

$$\bar{u}\frac{\partial \langle u'u'\rangle}{\partial r} + \bar{w}\frac{\partial \langle u'u'\rangle}{\partial z} = \frac{\partial}{\partial r}\left[(3\Lambda_2 + 2\Lambda_3)q\frac{\partial \langle u'u'\rangle}{\partial r}\right] + \frac{\Lambda_2 q}{r}\left(3\frac{\partial \langle u'u'\rangle}{\partial r} - 2\frac{\partial \langle v'v'\rangle}{\partial r}\right)$$
$$+ \frac{2}{r}\frac{\partial}{\partial r}\left[\Lambda_3 q(\langle u'u'\rangle - \langle v'v'\rangle)\right] - \frac{(4\Lambda_2 + 2\Lambda_3)q}{r^2}(\langle u'u'\rangle - \langle v'v'\rangle)$$
$$- \frac{q}{\Lambda_1}\left(\langle u'u'\rangle - \frac{K}{3}\right) + \nu\left[\frac{\partial^2 \langle u'u'\rangle}{\partial r^2} + \frac{1}{r}\frac{\partial \langle u'u'\rangle}{\partial r}\right.$$
$$\left. - \frac{2}{r^2}(\langle u'u'\rangle - \langle v'v'\rangle) - \frac{2\langle u'u'\rangle}{\lambda^2}\right] \tag{C.3}$$

$$\bar{u}\frac{\partial \langle v'v'\rangle}{\partial r} + \bar{w}\frac{\partial \langle v'v'\rangle}{\partial z} = \frac{\partial}{\partial r}\left(\Lambda_2 q\,\frac{\partial \langle v'v'\rangle}{\partial r}\right) + \frac{3\Lambda_2 q}{r}\frac{\partial \langle v'v'\rangle}{\partial r}$$

$$+ \frac{2}{r}\frac{\partial}{\partial r}\left[\Lambda_2 q(\langle u'u'\rangle - \langle v'v'\rangle)\right] + \frac{2\Lambda_3 q}{r}\frac{\partial \langle u'u'\rangle}{\partial r}$$

$$+ \frac{(4\Lambda_2 + 2\Lambda_3)q}{r^2}(\langle u'u'\rangle - \langle v'v'\rangle) - \frac{q}{\Lambda_1}\left(\langle v'v'\rangle - \frac{K}{3}\right)$$

$$+ \nu\left[\frac{\partial^2 \langle v'v'\rangle}{\partial r^2} + \frac{1}{r}\frac{\partial \langle v'v'\rangle}{\partial r} + \frac{2}{r^2}(\langle u'u'\rangle - \langle v'v'\rangle) - \frac{2\langle v'v'\rangle}{\lambda^2}\right] \quad (C.4)$$

$$\bar{u}\frac{\partial \langle w'w'\rangle}{\partial r} + \bar{w}\frac{\partial \langle w'w'\rangle}{\partial z} = -2\langle u'w'\rangle\frac{\partial \bar{w}}{\partial r} + \frac{\partial}{\partial r}\left(\Lambda_2 q\,\frac{\partial \langle w'w'\rangle}{\partial r}\right) + \frac{\Lambda_2 q}{r}\frac{\partial \langle w'w'\rangle}{\partial r}$$

$$- \frac{q}{\Lambda_1}\left(\langle w'w'\rangle - \frac{K}{3}\right) + \nu\left(\frac{\partial^2 \langle w'w'\rangle}{\partial r^2} + \frac{1}{r}\frac{\partial \langle w'w'\rangle}{\partial r} - \frac{2\langle w'w'\rangle}{\lambda^2}\right) \quad (C.5)$$

$$\bar{u}\frac{\partial \langle u'w'\rangle}{\partial r} + \bar{w}\frac{\partial \langle u'w'\rangle}{\partial z} = -\langle u'u'\rangle\frac{\partial \bar{w}}{\partial r} + \frac{\partial}{\partial r}\left[(2\Lambda_2 + \Lambda_3)q\,\frac{\partial \langle u'w'\rangle}{\partial r}\right]$$

$$+ \frac{2\Lambda_2 q}{r}\frac{\partial \langle u'w'\rangle}{\partial r} + \frac{1}{r}\frac{\partial}{\partial r}\left[\Lambda_3 q\,\langle u'w'\rangle\right] - \frac{(2\Lambda_2 + \Lambda_3)q}{r^2}\langle u'w'\rangle$$

$$- \frac{q}{\Lambda_1}\langle u'w'\rangle + \nu\left(\frac{\partial^2 \langle u'w'\rangle}{\partial r^2} + \frac{1}{r}\frac{\partial \langle u'w'\rangle}{\partial r} - \frac{\langle u'w'\rangle}{r^2} - \frac{2\langle u'w'\rangle}{\lambda^2}\right) \quad (C.6)$$

A RE-EVALUATION OF ZERO PRESSURE
GRADIENT COMPRESSIBLE TURBULENT BOUNDARY LAYER MEASUREMENTS

James E. Danberg*
University of Delaware, Newark, Delaware

SUMMARY

A number of compressible turbulent boundary layer velocity and temperature profiles with zero pressure gradient have been collected and prepared for computer analysis. An assumed equation for these profiles has been chosen allowing four constants to be adjusted by a nonlinear least squares technique to fit the experimental data. The four constants are: a velocity scale, boundary layer thickness, the constant of the semi-log region and the wake constant, Π. This equation is analogous to Cola's incompressible law of the wall and wake but uses a generalized velocity to account for compressibility. Measurements from 65 adiabatic wall tests have been analyzed covering a Mach number range from 2 to 6 and a momentum thickness Reynolds number range from 2.3×10^3 to 7.5×10^5. Of these profiles, 29 included skin friction balance data which allowed direct evaluation of the universal constant of turbulence (mean value of $k = .43$) through comparison between the shear velocity and the profile velocity scale. The constants of the semi-log and the wake region were found to be independent of Reynolds and Mach numbers. A similar analysis was carried out for the limited number of total temperature profiles.

NOTATION

C $\quad$ = Profile constant associated with semi-logarithmic region

H $\quad$ = Local total enthalpy = $C_p T_t$

H_s $\quad$ = Characteristic total enthalpy scale for the thermal boundary layer

H^{++} = Nondimensional total enthalpy = $\dfrac{1}{H_s} \int_0^H \sqrt{\dfrac{\rho}{\rho_w}} \, d(H-H_w)$

T $\quad$ = Temperature

u $\quad$ = Local mean velocity

u_s $\quad$ = Characteristic velocity scale for turbulent velocity profile

u^{++} = Nondimensional velocity = $\dfrac{1}{u_s} \int_0^u \sqrt{\dfrac{\rho}{\rho_w}} \, du$

u_τ $\quad$ = Shear velocity = $\sqrt{\tau_w/\rho_w}$

y $\quad$ = Distance normal to the surface

α $\quad$ = Thermal diffusivity

β $\quad$ = $(T_{aw}-T_w)/(T_{t\delta}-T_w)$

δ_s $\quad$ = Velocity boundary layer thickness

Δ $\quad$ = Thermal boundary layer thickness

κ $\quad$ = Universal constant of turbulence (mixing length constant)

ν $\quad$ = Kinematic viscosity

Π $\quad$ = Profile constant associated with the wake region

ρ $\quad$ = Density

τ $\quad$ = Shear stress

ω $\quad$ = Wake function

Subscripts

aw $\quad$ = Adiabatic wall conditions

s $\quad$ · Characteristic scale

t $\quad$ = Total

w $\quad$ = Wall conditions

δ $\quad$ = Edge of the boundary layer

*Associate Professor Department of Mechanical & Aerospace Engineering
and Consultant U.S. Army Ballistic Research Laboratories, Aberdeen, Maryland – U. S. A.

1. INTRODUCTION

Most experimentalists investigating some aspect of compressible turbulent boundary layers have attempted to measure the distribution of mean velocity and temperature through the layer. During the past 20 years, a considerable number of these profile measurements have been reported. It would appear that a sufficient body of data is now available to begin a more systematic correlation approach with the objective of trying to obtain more quantitative information from the boundary layer surveys themselves, rather than making comparison between theory and skin friction, heat transfer or other surface data. The approach of this study is an extension to compressible flow of some of the tests used by Coles and Hirst[1] to "classify and criticize" the available incompressible data for the AFOSR-1FP-Stanford Conference on Turbulent Boundary Layers.

2. APPROACH

In order to exploit the above proposal, the following approach was adopted:

(A) A considerable sample of the published compressible turbulent boundary layer survey data was collected and stored on IBM cards. The initial search turned up about 150 zero pressure gradient profiles where tabulated data where available or graphical data could be reasonably evaluated. These data cover a range of Mach numbers from 1.5 to 12 and momentum thickness Reynolds numbers from 10^2 to 10^6. Only perfect gas cases were considered with air or nitrogen as the test medium. The geometry of the test surfaces were mostly flat plates and nozzle walls where the pressure gradient effects are expected to be small. The main results reported here will be concerned with adiabatic wall conditions which limits the range of Mach numbers to approximately 2 to 6.

Obviously, not all of the surveys considered are equal in quality and part of the evaluation procedure must be concerned with determination of internal consistency and consistency between surveys. It is also evident where more experimental data are needed. In general, it may be concluded that none of the experimenters used all the techniques available to them - especially the investigators who concern themselves with skin friction balance measurements in zero pressure gradient adiabatic wall boundary layers. The most notable omission of these investigators was temperature profile measurements. Thus, their important measurements have to be interpreted using theory or correlations based on other temperature measurements.

(B) An analytical framework was assumed in order to reduce the mass of data points into a manageable set of numbers from which to draw some conclusions. The equations chosen to represent the velocity and temperature distribution are not final recommendations, but they do represent a first step, to which modifications may be introduced as required or alternative approaches adopted and then tested against the available experimental evidence. The initial approach is based on similarity concepts as extensions of the law of the wall - the law of the wake suggested by Millikan[2], Coles[3] and many others for incompressible turbulent boundary layers. The procedure makes the following assumptions:

1) The effects of compressibility are accounted for by forming a reduced velocity

$$u' = \int_0^y \sqrt{\rho/\rho_w}\, du \qquad (1)$$

This assumption is quite arbitrary in the present context although it is consistent with the Prandtl mixing length approach as applied to compressible flow by VanDriest[4], Moore[5], Spalding and Chi[6] among many others. The assumption can be tested to some extent by trying other alternative assumptions.

2) The boundary layer consists of two basic regions, a wall region and a wake or defect region describable by functions of two essentially independent variables. In the wall region, it is assumed that the velocity distribution can be described in terms of a velocity scale (u_s) and a length scale ν_w/u_s where u_s is to be determined from experimental velocity profile data. In the defect region, the same velocity scale is assumed to apply but a new length scale δ_s characteristic of the total boundary layer thickness is assumed and δ_s is also to be evaluated from experimental data. The specific definition of δ_s depends on the assumed form of the wake function.

3) The two regions of the boundary layer are connected by a region of overlap where formulas for both regions predict the same velocity distribution. Millikan[2] has shown that this implies that the velocity is a semi-logarithmic function of y in the overlap region.

$$\frac{u'}{u_s} = \ln\left(\frac{y}{\nu_w/u_s}\right) + C$$

or:
$$\qquad (2)$$

$$\frac{u'}{u_s} = \ln\left(\frac{y}{\delta_s}\right) + D$$

Note that the above semi-log equations are nearly identical with the usual turbulent boundary layer semi-log equations. The one difference is that the mixing length constant, κ, does not appear and may be considered to have been absorbed into the velocity scale, u_s. If u_s is replaced by u_τ/κ and C by $\kappa C + \ln\kappa$, then the usual form of this relation is recovered. The reason for this new definition of the velocity scale is because κ and u_s cannot be determined independently from experimental velocity profile data. Another reason for chosing this definition is that it clearly brings out that κ^2 is the slope of the non-dimensional velocity profile at y = 0;

that is, if the wall length scale is valid to $y = 0$, then:

$$u' = u_s\, f(u_s y/\delta_w)$$

and assuming Newtonian friction at the wall

$$\tau_w/\rho_w = \nu_w \left.\frac{du'}{dy}\right)_{y\,=\,0} = u_s^2 f'(0)$$

with the result that

$$\kappa^2 = f'(0) \tag{3}$$

Since the probe data is relatively poor near the wall in the laminar sub-layer, it is necessary to use skin friction balance measurements to obtain the relationship between u_s and u_τ and the ratio of u_s to u_τ provides a method of evaluating κ.

The equation which is used to describe the compressible turbulent velocity profile (neglecting the laminar sublayer) is obtained by analogy with incompressible flow equation proposed by Coles.

$$u^{++} = \frac{1}{u_s} \int_0^u \sqrt{\rho/\rho_w}\; du = \ln\left(\frac{u_s y}{\nu_w}\right) + C_u + 2\Pi_u\, w(y/\delta_s) \tag{4}$$

where approximately

$$w(y/\delta_s) = \sin^2\left(\frac{\pi}{2}\frac{y}{\delta_s}\right) \tag{5}$$

This equation is assumed valid except in the laminar sublayer and beyond the point where

$$\frac{du^{++}}{dy/\delta_s} = 0$$

The four profile constants u_s, δ_s, C_u and Π_u are determined by a least squares fit to each measured velocity profile.

3. TEMPERATURE PROFILE

The temperature distribution was calculated for many surveys where temperature measurements were not available by using a well known modification of the Crocco temperature-velocity relationship:

$$\frac{T_t - T_w}{T_{t\delta} - T_w} = \beta\frac{u}{u_\delta} + (1-\beta)\left(\frac{u}{u_\delta}\right)^2 \tag{6}$$

where

$$\beta = (T_{aw} - T_w)/(T_{t\delta} - T_w)$$

As has been noted by many investigators, almost any expression, similar to the above, gives adequate results for low Mach number data under adiabatic conditions. Across most of the layer, the total enthalpy is nearly constant in any case. However, for the high heat transfer or high Mach number situation, the deviation of experimental data from the Crocco relationship is known to be significant.

There appears to be a need to find better methods of correlating temperature profile data than the Crocco equation. In analogy to the above method of describing the velocity profile, two length scales $(\delta_H, \alpha_w/\sqrt{H_s})$ and a total enthalpy scale (H_s) are introduced in an attempt to find a more suitable correlation formula. The resulting equation is:

$$H^{++} = \frac{1}{H_S}\int_0^H \sqrt{\frac{\rho}{\rho_w}}\; d\,(H-H_w) = \ln\sqrt{\frac{H_s}{\alpha_w}}\,y + C_H + 2\Pi_H\,\omega_H \tag{7}$$

where $\omega_H \approx \sin^2\frac{\pi}{2}\frac{y}{\Delta}$

H_S = Characteristic enthalpy scale

Δ = Characteristic thermal boundary layer thickness
(Not necessarily equal to the thickness of the thermal layer)

The enthalpy scale and the thermal boundary layer thickness and the two profile constants (C_H and Π_H) are obtained from each profile where temperature data are reported by the same least squares method used for the velocity profile.

A related approach for the incompressible enthalpy profiles has been explored by Alber and Coats[7] in a recent paper. Their analys. is based on a mixing length analysis where it is assumed that H_s is proportional to the wall heat transfer rate and thus $H_s \approx 0$ for the adiabatic case. In the adiabatic compressible boundary layer there is a characteristic enthalpy distribution which has many of the same features of wall and wake regions as the velocity profile; thus, a finite enthalpy scale can be defined which is valid over a significant part of the enthalpy distribution although it does not appear that this similarity can extend to the wall as seems to be the case for the velocity profiles.

4. LEAST SQUARES METHOD

An initial computer program was written to determine u_s, δ_s, C_u and Π_u for the velocity profile and the corresponding quantities for the temperature profiles, where available, by an iteration procedure. The velocity profile equation (4) can be re-written as:

$$u' = a_1 \ln a_2 y + a_3 + a_4 \sin^2 a_2 y \qquad (8)$$

where a_1, a_2, a_3, and a_4 can be used to calculate the more meaningful profile quantities. Since δ_s (or a_2) is contained within the transcendental function, it cannot be evaluated by the usual methods and, therefore, its value was first estimated and the other three constants determined in a straight-forward way. The computer program calculated the standard deviation of the data points with respect to the resultant equation. A number of such calculations were required to bracket the minimum value of the standard deviation to a predetermined degree of accuracy. Later, a general weighted nonlinear least square fit sub-routine was obtained from the U. S. Naval Ordinance Laboratory which considerably shortened the iteration procedure with a higher degree of accuracy. This program computes the four constants from four initial estimates by assuming small perturbations to the a's which allows the equation to be expressed by the linear terms of a Taylor expansion whereby an improved estimate of the a's is obtained to start a new iteration. Again, a predetermined test is applied to terminate the calculation.

There are two problems that arise in the least square fitting procedure. First, the equation is quite nonlinear with a number of "local" maximums and minimums. This was a particularly troublesome problem with the first technique used. For example, if δ_s is overestimated, a_2 is small and the best fit equation tends toward the situation where the sine-squared term is eliminated. Trial and error changes of the initial values of the constants usually corrected the difficulty which was detected by finding absurd values for the a's or by the poor fit obtained when the data were graphed.

The second problem has to do with the a priori unknown range of validity of the basic equation. As already has been pointed out, the equation used here cannot be used to describe either the sublayer or the free stream. Unfortunately, it is often difficult to identify the data points which should be excluded from the calculation except by inspection of the plotted results. Ultimately, part of the problem can be eliminated by designing the form of the velocity profile which is valid across the entire boundary layer although there may still be a need to exercise judgment about those points effected by wall interference.

5. DISCUSSION OF RESULTS

Figures 1[19] and 2[9] show representative non-dimensional velocity profiles of u^{++} versus $u_s y/\nu_w$. The solid line drawn through the data is the best fit to equation 4. The standard deviation in u^{++} is .077 and .022, respectively, which can be interpreted as .6 and .25 percent of the free stream velocity. This shows that equation 4 describes the velocity data in the range where it has been applied to the same order of accuracy as that quoted for current pressure transducers.

Figure 3 shows an example of the quality of the fit of the $\sin^2$ term for the wake function of Coles. As pointed out earlier, no data beyond $y = \delta_s$ has been included in the fitting process.

5.1. Velocity Scale

As previously noted, if the similarity of the velocity profile is valid to $y = 0$ then the velocity scale obtained from the boundary layer profile is related to the shear velocity through Newton's law. This hypothesis is tested by a comparison between u_s and u_τ where values of u_τ have been obtained from skin friction measurements (references 8 to 11). Figure 4 shows the result in non-dimensional terms of u_δ/u_s versus u_δ/u_τ. The mean line through the data has a slope of .43 which is in reasonable agreement with the most frequently quoted values of .4 or .41 for the universal constant, κ.

5.2. Profile Constants

The computer evaluation of the constants C_u and Π_u are given in Figure 5 including results from 45 profiles obtained from 12 investigators (references 8 - 19). The constants are plotted versus the momentum thickness Reynolds number and no discernable trend is evident although there is considerable scatter in the data about the mean values of $C_u = 1.77$ and $\Pi_u = .81$. Also, there is no observable trend of C_u or Π_u with Mach number in the range of 2 to 6 or with the geometry of the test surface (flat plate and nozzle wall data are included).

5.3. Total Temperature Profile

Figure 6 and 7 illustrate the ability of the assumed equation to fit the total enthalpy distribution for one adiabatic wall case of Sturek[19]. The solid line through the data is best fit to equation 7 with the data points at both extremes omitted which obviously do not agree with the trend of the equation.

The wake function is approximated by the $\sin^2$ term equally as well as in the velocity case. A number of points beyond $y = \Delta$ fall on the computed line although there is a region at the outer edge of the profile where the transition to the constant free stream temperature occurs that cannot be included. Figure 6 also shows a sharp departure from equation 7 that occurs near the wall for these adiabatic heat transfer cases.

5.4. Temperature Profile Constants

Profile constants from only ten temperature surveys at near adiabatic wall conditions have been tested and eight are at essentially the same conditions for the present purposes. These preliminary results can thus be summarized in the following table where the eight profiles of Sturek[19] have been replaced by their average values.

Temperature Profile Constants
from Best Fit to Equation 7

Ref.	H_δ	Π_H	C_H	$Pr_w^2 H_s/u_s^2$	$\frac{\Delta}{\delta_s}$
12	2.49	.686	-3.74	.89	1.04
14	5.92	.902	-.82	.56	.68
19	3.5	.923	-5.32	.69	.83

These results represent such a small sample that the specific values should be considered highly preliminary; however, it is interesting that for the adiabatic wall conditions, H_s is approximately the same as $(u_s/Pr_w)^2$ and thus $\sqrt{H_s} y/\alpha_w \sim u_s y/\nu_w$. Some initial results which include the effects of heat transfer show that H_s is strongly affected by the heat transfer rate and increases with increasing heat transfer. The relatively large negative values of C_H can be associated with the size of the thermal sublayer in which the total enthalpy distribution is dominated by conditions at the wall. The thermal sublayer is an order of magnitude larger than the velocity sublayer as can be seen by comparing Figures 1 and 6. The wake constant Π_H is about the same magnitude as the velocity parameter. The thickness parameter Δ is generally smaller as might be expected although the total thermal boundary layer may be up to twice as large as Δ and therefore, larger than the velocity boundary layer.

6. CONCLUSIONS

A number of velocity and temperature profile measurements for compressible (Mach number 2 to 6) turbulent boundary layers (momentum thickness Reynolds numbers = 2.3×10^3 to 7.5×10^5) have been re-evaluated in terms of similarity concepts developed in incompressible flow. The velocity (or enthalpy) profile equation with four adjustable constants has been shown to adequately describe the velocity (or total enthalpy) with a high degree of accuracy except in the sublayer and in a transition region near the free stream. The velocity scale parameter (u_s) is shown to be proportional to the shear velocity (u_τ) and the constant of proportionality equals .43 which is in reasonable agreement with the incompressible values. The profile constants C_u and Π_u have been found to be independent of Reynolds number and Mach number although there is considerable scatter in the data. Preliminary data has shown that the total temperature profile can be described in a procedure analogous to that used for the velocity profile and that the enthalpy scale is approximately the same order as the square of the velocity scale. The thermal sublayer for the cases investigated was found to be considerably larger than the velocity sublayer.

REFERENCES

1. D. E. Coles and E. A. Hirst, "Proceedings AFOSR-IFP-Stanford Conference on Computation of Turbulent Boundary Layers - 1968" Vol. II, pp. 1-45

2. C. B. Millikan, "A Critical Discussion of the Turbulent Flows in Channels and Circular Tubes," Proceedings Fifth International Congress Appl. Mech., Cambridge, Mass., pp. 386-392 (1938)

3. D. E. Coles, "The Law of the Wake in Turbulent Boundary Layer" J. Fluid Mechanics, 1, Part 2, pp. 191-226 (1956)

4. E. R. VanDriest, "Turbulent Boundary Layer in Compressible Fluids," J. Aero. Sci., 18, 3, pp. 145 (1951)

5. D. R. Moore, "Velocity Similarity in the Compressible Turbulent Boundary Layer with Heat Transfer," Defense Research Laboratory Report DRL-480 CM-1014, The University of Texas (1962)

6. D. B. Spalding and S. W. Chi, "The Drag of a Compressible Turbulent Boundary Layer on a Smooth Flat Plate with and without Heat Transfer," J. Fluid Mech., 18, Part I, pp. 117-143 (1964)

7. I. E. Alber and D. E. Coats, "Equilibrium Enthalpy Profiles for the Incompressible Turbulent Boundary Layer with Heat Transfer," AIAA J. 9, 5, pp. 791-796 (1971)

8. F. W. Matting, D. R. Chapman, J. R. Nyholm and A. G. Thomas, "Turbulent Friction at High Mach Numbers in Air and Helium," NASA TR R-82 (1960)

9. D. R. Moore and J. Harkness, " Experimental Investigation of Compressible Turbulent Boundary Layers at Very High Reynolds Numbers," AIAA Journal, 3, pp. 631-638 (1965)

10. R. H. Korkegi, "Transition Studies and Skin Friction Measurements on an Insulated Flat Plate at a Mach Number of 5.8," Jour. of Aero. Sci., pp. 97-107, Feb. 1956

11. D. Coles, "Measurements in the Boundary Layer on a Smooth Flat Plate in Supersonic Flow: III Measurements in a Flat Plate Boundary Layer at the Jet Propulsion Laboratory," Report No. 20-71, Jet Propulsion Laboratory, California Institute of Technology, June 1, 1953

12. Unpublished Nozzle Wall data from NASA Langley

13. J. R. Sterrett and J. B. Barker, "A Theoretical and Experimental Investigation of Secondary Jets in a Mach 6 Free Stream with Emphasis on the Structure of the Jet and Separation Ahead of the Jet," Separated Flow Specialists Meeting, Fluid Dynamics Panel - AGARD, 1966

14. J. B. Adcock, J. B. Peterson, Jr., and D. I. McRee, "Experimental Investigation of a Turbulent Boundary Layer at Mach 6, High Reynolds Numbers and Zero Heat Transfer," NASA TN-D-2907 (1965)

15. R. E. Lee, W. J. Yanta and A. C. Leonas, "Velocity Profile, Skin Friction Balance and Heat Transfer Measurements of the Turbulent Boundary Layer at Mach 5 and Zero Pressure Gradient," NOL TR69-106 (1969)

16. R. M. O'Donnel and J. Harkness, " Experimental Investigations of the Turbulent Boundary Layer on a Flat Plate at High Reynolds Numbers, M = 2.8," Report O-7100/3R-23, Ling-Tempco-Vought Research Center (1963)

17. G. J. Nothwang, "An Evaluation of Four Experimental Methods for Measuring Mean Properties of a Supersonic Turbulent Boundary Layer," NACA Report 1320 (1957)

18. E. J. Hopkins and E. R. Keener, "Study of Surface Pitots for Measuring Turbulent Skin Friction at Supersonic Mach Numbers - Adiabatic Wall," NASA TN-D-3478 (1966)

19. W. B. Sturek, "An Experimental Investigation of the Supersonic Turbulent Boundary Layer in a Moderate Adverse Pressure Gradient. Part I. A Detailed Description of the Experiment and Data Tabulation," Ballistic Research Laboratories Report No. 1506, October 1970
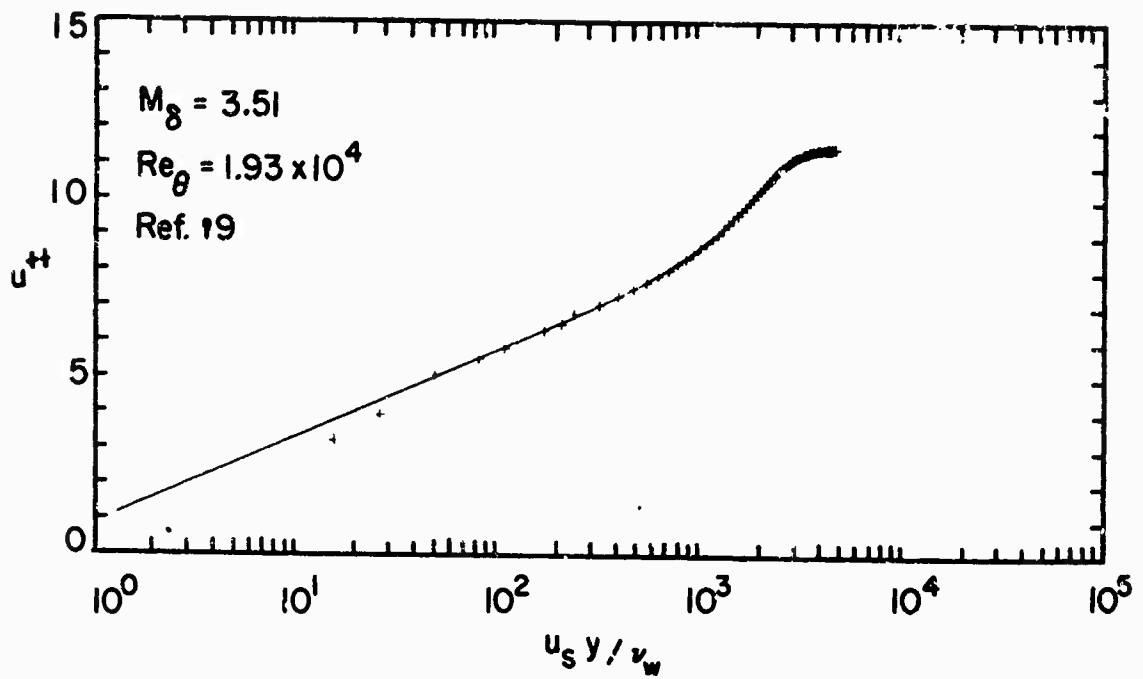
Figure 1. Non-dimensional Velocity Profile
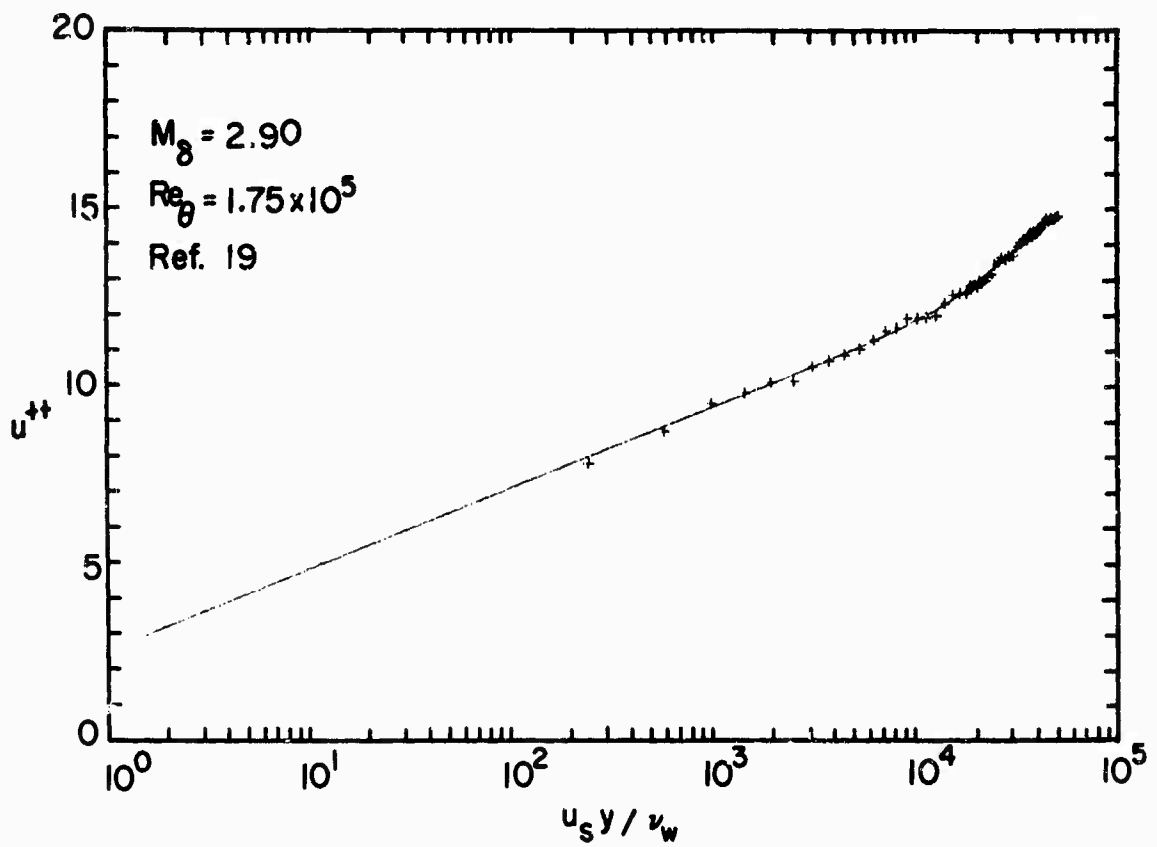
Figure 2. Non-dimensional Velocity Profile
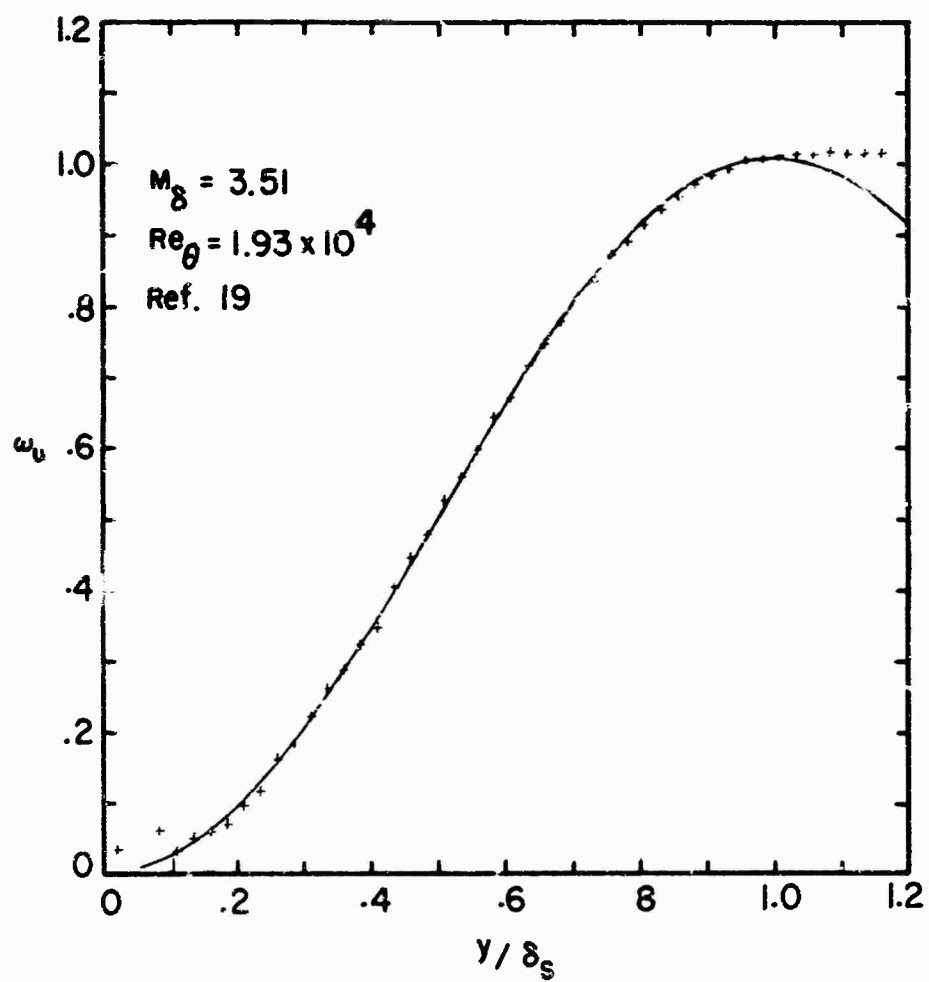
Figure 3. Wake Function for Velocity Profile
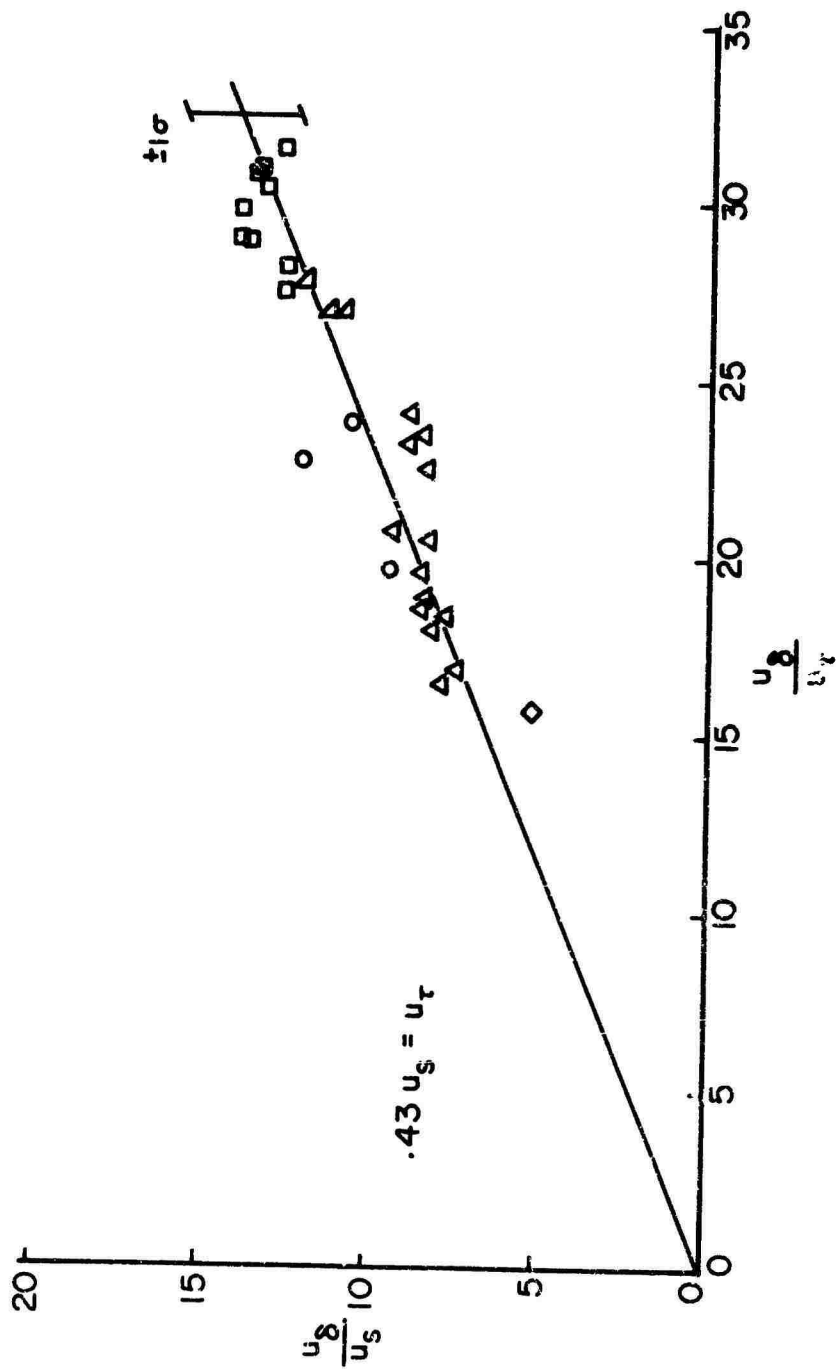
Figure 4. Velocity Scale Parameter versus Shear Velocity
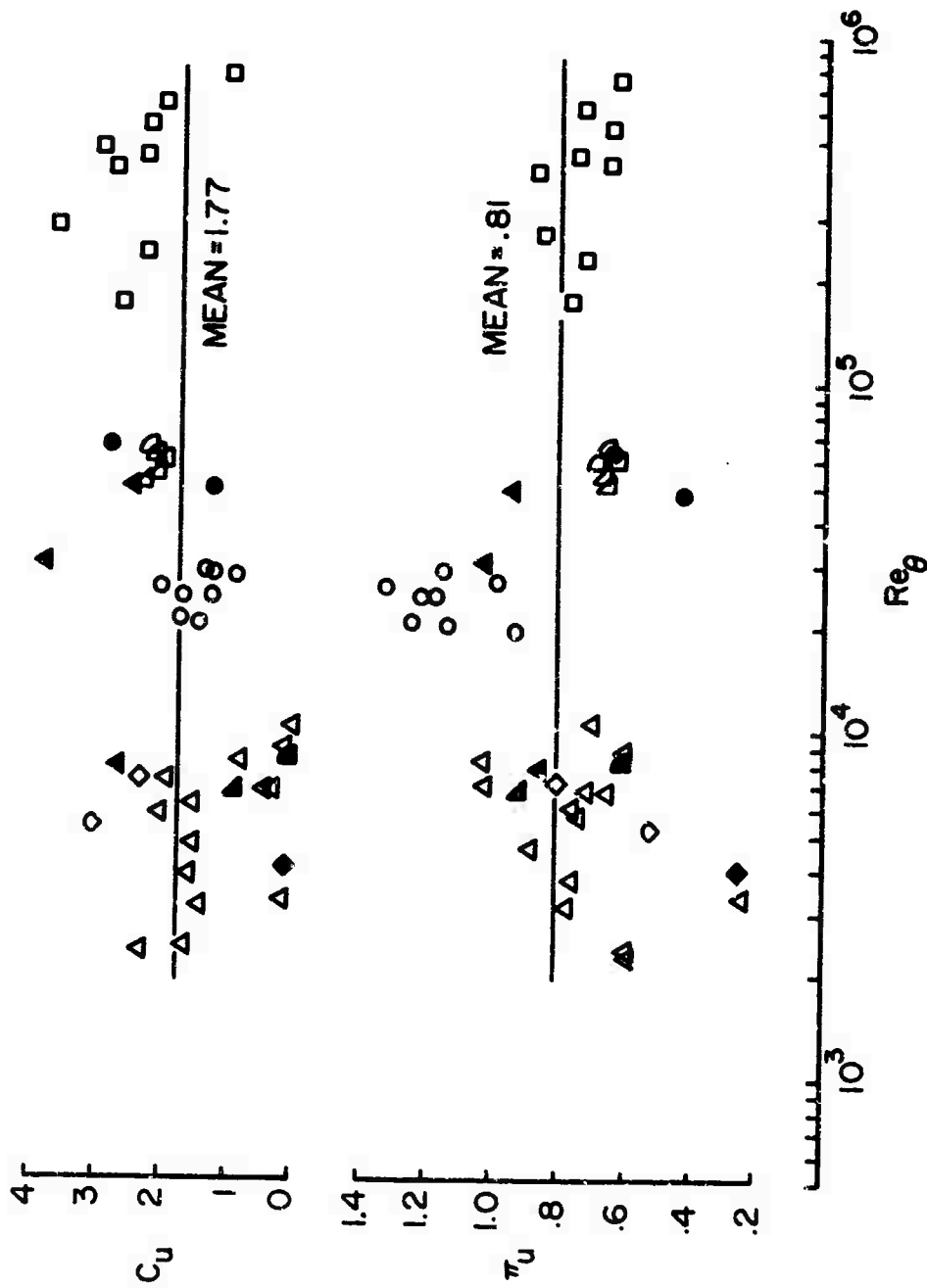
Figure 5. Profile Parameters C_u and Π_u versus Momentum Thickness Reynolds Number
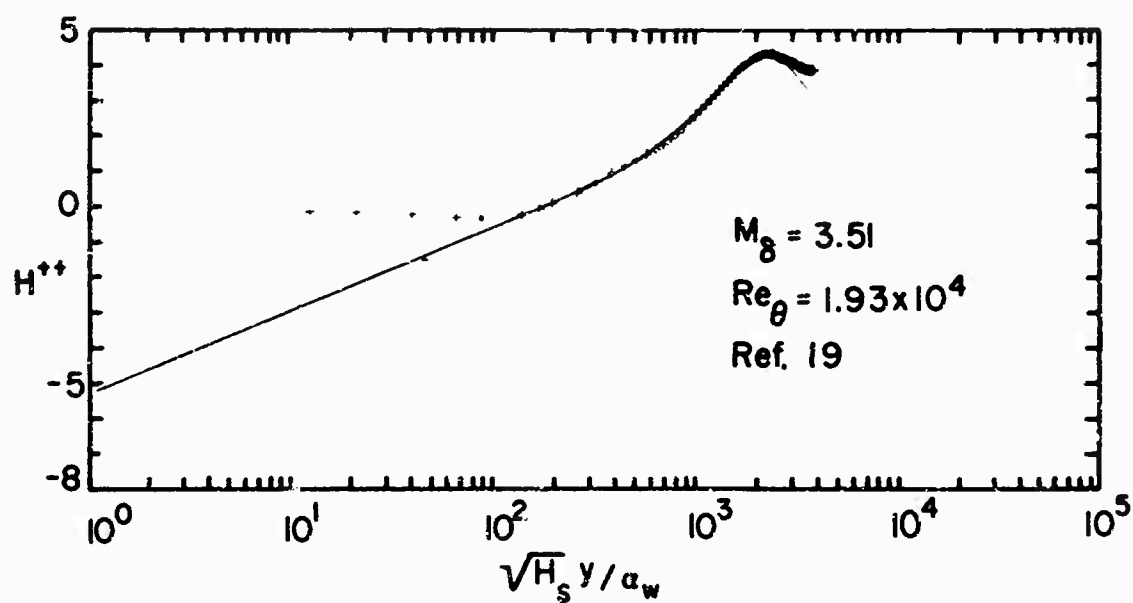
Figure 6. Non-dimensional Total Enthalpy Profile
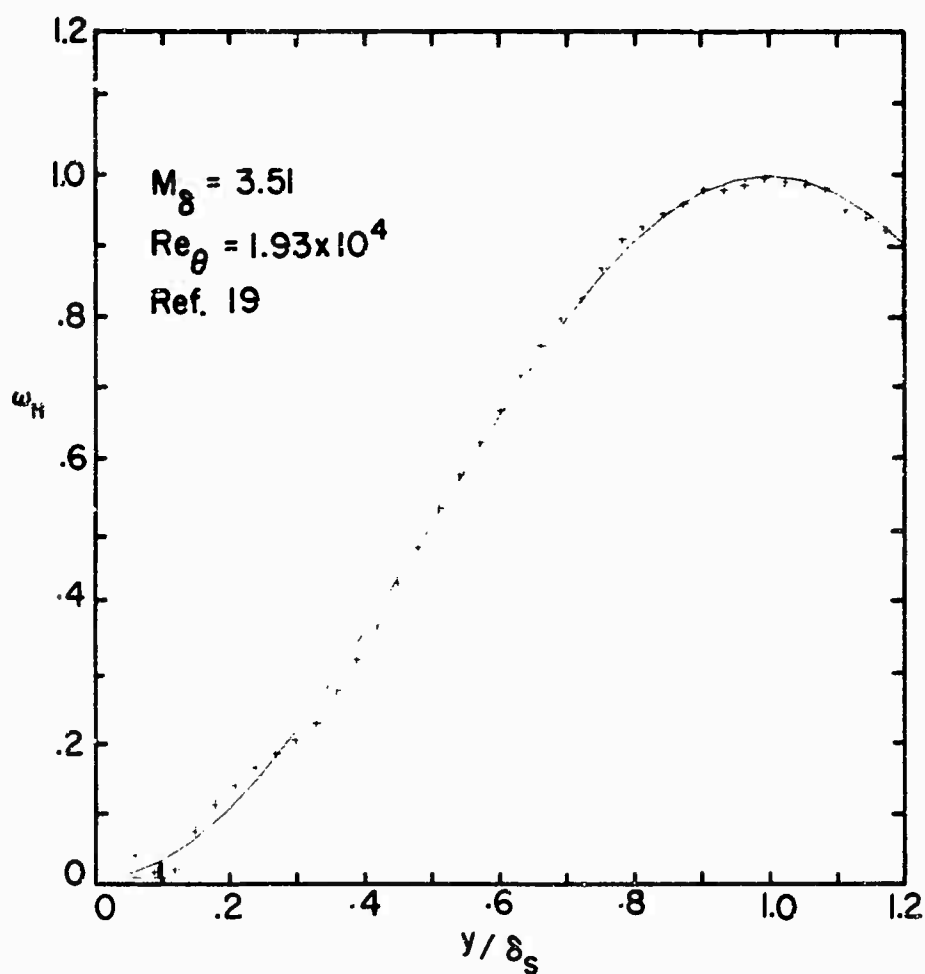
Figure 7. Wake Function for Total Enthalpy Profile

SOME BOUNDARY LAYER MEASUREMENTS ON A FLAT PLATE AT MACH NUMBERS FROM 2.5 TO 4.5

D G Fabey[1], H U Meier[2] and A G Sawyer[3]

SUMMARY

This paper reports an experimental investigation of the turbulent boundary layer on a large, thermally insulated flat plate, in which Mach number and total temperature profiles and shear stress at the wall were measured.

The measured velocity profiles are found to be in fairly good agreement with a number of theoretical treatments. Similarly, the measured skin-friction coefficients are fairly well predicted by flat-plate skin-friction laws

The form of the total temperature profile close to the wall suggests an increase in turbulent Prandtl number as the wall is approached. At all conditions, the wall temperature was found to be higher than would be expected in adiabatic flow conditions, whilst there was a substantial deficit of enthalpy flux within the boundary layer. No satisfactory explanation for these conflicting observations has yet been found.

NOTATION

B	additive constant in law of wall
C_f	local skin friction coefficient $= \tau_w / \frac{1}{2}\rho_e u_e^2$
d	probe diameter
F	temperature function $(T_t - T_w)/(T_{t_e} - T_w)$
M	Mach number
R	Reynolds number/m
T	static temperature
T_t	total temperature
u	velocity in x direction in boundary layer
Δu	deviation from logarithmic portion of velocity profile in the outer edge of the boundary layer
u_τ	friction velocity $= \sqrt{\tau_w/\rho_w}$
δ	boundary layer thickness at which $M/M_e = 0.99 \simeq u/u_e = 0.995$
δ_2	boundary layer momentum thickness
κ	von Karman constant in law of wall
τ_w	surface shear stress
ν	kinematic viscosity
Π	wake component

Suffices

e	edge of boundary layer
w	wall

1. INTRODUCTION

This paper briefly reports some measurements of the turbulent boundary layer on a large, thermally insulated flat plate, made in the 3ft x 4ft supersonic wind tunnel at RAE Bedford. These measurements are an extension of the experiments of Hastings and Sawyer (1), and were made as part of a joint research programme between RAE and DFVLR-AVA Göttingen. Complete results will be given in a later paper.

The tests covered a range of Mach numbers from 2.5 to 4.5, and a range of Reynolds numbers based on boundary-layer momentum thickness from about 5 x 10³ to 30 x 10³. Skin friction was measured using a floating-element balance, and velocity and temperature profiles across the boundary layer were measured using a

1 and 3 Royal Aircraft Establishment, Bedford, England

2 Deutsche Forschungs-und Versuchsanstalt für Luft und Raumfahrt, Aerodynamische Versuchsanstalt Göttingen, Germany

combined total-temperature and pitot-pressure probe developed at AVA Göttingen (3). The measurements are compared here with some current theories.

2. EXPERIMENTAL DETAILS

2.1 Flat Plate

The flat plate that was used for these tests has been described in detail by Hastings and Sawyer (1). It was about 0.9m (35in) wide and about 1.5m (65in) long, and was provided with 22 holes into which plain or instrumented plugs could be fitted, the latter carrying either the skin friction balances or the boundary-layer probe. The plate spanned the tunnel horizontally with a gap of 13mm between each side of the plate and the tunnel sidewall. For the present tests, an attempt was made to minimize heat transfer by providing layers of heat insulation on the back surface of the plate, and between the plate and the cantilevers which supported it. Another difference from the experiments of Hastings and Sawyer was the use of a roughness band to move transition forward towards the leading-edge of the plate. The band consisted of Ballotini (small glass spheres) 0.28mm (0.011in) in diameter, distributed sparsely from 2.54mm (0.1in) to 5.08mm (0.2in) downstream of the leading-edge.

2.2 Skin Friction Balances

For the present tests the skin-friction balance of Hastings and Sawyer was replaced by a commercially available balance, Kistler type 322c 102, having an element of diameter 9.75mm. Four specimens of this balance were tried, but results are presented only for those two which gave consistent and repeatable readings. The present measurements of skin friction are believed to be accurate to within 1% at the higher Reynolds numbers.

2.3 Combined Probe for Temperature and Pitot Pressures

Fig 1 shows the combined total temperature and pitot pressure probe used for the profile measurements; the development of this probe has been described in detail by Meier (3). For the measurements of total temperature, a small quantity of air was sucked past the chromel-alumel thermocouple junction situated just within the pitot entry. The pitot pressures were recorded by capsulo-weighbeam manometers.

2.4 Surface-Temperature Measurements

The surface temperatures were measured by chromel-alumel surface thermocouples, the second junctions of which were in a Zeira constant-temperature reference box. These temperatures were in good agreement with those derived from the cold resistance of platinum surface-hot-films installed to detect the beginning and end of the region of transition from laminar to turbulent flow (4).

2.5 Wind Tunnel and Test Conditions

At the time of the experiments of Hastings and Sawyer (1), the tunnel was equipped with a fixed wooden nozzle giving a Mach number of 4. This has now been replaced by a flexible nozzle, and there have also been modifications to the subsonic portion of the tunnel circuit to improve the steadiness of flow in the working section (5). These modifications include the installation of vortex generators, to make the final subsonic diffuser run full, and of a honeycomb and additional screens in the settling chamber.

In the present experiments, skin-friction and profile measurements were made at distances of 368, 623, 876, 1130 and 1394mm from the leading-edge. The nominal Mach numbers and unit Reynolds numbers of the tests are given in Table I.

TABLE I

M_e	...............R/m x 10^{-7}........................					
2.5	1.15	1.55	1.95	-	-	-
2.8	1.15	1.65	1.95	-	-	-
3.0	1.15	1.55	1.95	-	-	-
3.5	-	1.55	1.95	2.35	-	-
4.0	-	-	-	-	2.75	-
4.5	-	-	-	-	-	3.05

In the second phase of these experiments, to be reported separately, boundary-layer measurements were made in the range of unit Reynolds numbers down to 0.3 x 10^7/m.

3. RESULTS

3.1 Law of the Wall Representation of Velocity Profiles

Fig 2 shows some typical velocity profiles plotted semilogarithmically in 'law of the wall' coordinates which are based on the fluid properties (ρ, ν) obtaining at the wall. It may be seen that, at freestream Mach numbers of both 2.5 and 4.5, the profiles have a well-defined logarithmic region where we may write

$$\frac{u}{u_\tau} = \frac{1}{\kappa} \ln\left(\frac{u_\tau y}{\nu_w}\right) + B$$

Fig 3 shows values of the von Karman constant κ determined by the best straight-line fit to the inner region of the profiles ($y/\delta < 0.15$, $u_\tau y/\nu_w > 40$). The value of κ shows no appreciable dependence on Reynolds number, but increases significantly with Mach number, from about 0.48 at $M_e = 2.5$ to 0.60 at $M_e = 4.5$. The value suggested by Coles (6) for incompressible flow is 0.41.

Also shown in Fig 3 is the value of κ given by the correlation of Winter and Gaudet (7). Agreement with
the measurements is quite good at M_e = 2.5 and 3.5 but, at M_e = 4.5, the correlation noticeably underesti-
mates κ. The additive constant B in the law is found to vary only slightly with Mach number, and the
correlation of Winter and Gaudet is found to describe this variation fairly well.

Fig 4 shows the magnitude of Coles's (6) wake component Π defined, as illustrated in Fig 2, from the ratio
of the 'overshoot' of the velocity profile above the logarithmic line to the slope of this line:

$$\Pi = \frac{\kappa}{2} \frac{\Delta u}{u_\tau}$$

The values of Π obtained as shown in Fig 2 are somewhat sensitive to the line fitted to the logarithmic
part of the profile. They also depend on whether or not a probe displacement correction is made to the
profile. The points plotted in Figs 3 and 4 have been obtained from the best log-line fitted to uncorrec-
ted profiles. The vertical bars in these figures indicate the uncertainty in fitting this log-line, plus
the further uncertainty associated with a possible displacement correction of 0.15 times the probe diameter.

At the higher Reynolds numbers, Π is seen to have approximately the same value, 0.55, that Coles (6) found
in incompressible flow. The tendency for Π to decrease at lower Reynolds numbers, which is particularly
noticeable at M_e = 4.5, was also observed both by Coles, for incompressible flow, and by Hastings and
Sawyer at M_e = 4. This behaviour at low Reynolds number in compressible flow has been discussed tenta-
tively by Green (8) and will, it is hoped, be revealed more completely by the second phase of the present
experiments.

The anomalous values of Π in Fig 4, apparent at the highest Reynolds numbers at M_e = 2.5, are from the two
rearmost stations on the plate, in a region where the boundary layer was perturbed from its equilibrium,
flat-plate, condition by oblique shock waves running across the plate. These waves were generated by air
flowing through the gaps between the edges of the plate and the tunnel sidewalls in the proximity of the
plate leading-edge. (In later tests, these waves have been eliminated by fitting vertical fences along
the edges of the plate). Besides perturbing the velocity profiles, these waves also caused appreciable
flow convergence on the plate centre line, so that the twodimensional momentum-integral equation did not
apply. Outside this perturbed region, however, the twodimensional momentum balance on the plate centre-
line was satisfied to within 10 to 15 percent.

A final inference that has been made from the results shown in Fig 4 is that, in the present experiments,
the boundary-layer trip has not had a significant effect on the character of the velocity profiles.
Although Coles (7) showed that anomalous values of Π could be found close to tripping devices, the agree-
ment in the variation of Π with Reynolds number between the present measurements and those made by Hastings
and Sawyer, with transition free, suggests that even the profiles obtained closest to the roughness band
were with a boundary layer in a state of equilibrium. Further information on this point will be obtained
in the second phase of these experiments.

3.2 Rotta's Velocity Profile Family

Meier has described (9) a family of theoretical velocity profiles due to J C Rotta which are based on the
form of the law of the wall proposed by Rotta (10) for compressible flow, and on Coles's wake function.
In adiabatic flow at a given Mach number, the two free parameters of the family are the skin-friction
coefficient and the Reynolds number based on the boundary layer thickness. The values of these two para-
meters which give the minimum rms deviation between the theoretical and experimental velocity profiles may
be found using a computer.

A third parameter which may be varied during this iterative procedure is the probe displacement correction,
which is assumed constant across the boundary layer. Fig 5a shows how the fit between theory and experi-
ment is improved by making this displacement correction (for convenience, it is the theoretical profile,
rather than the experimental one which is displaced laterally in Fig 5a). For the example shown in Fig 5a,
the effect of this correction is to reduce the theoretical value of the skin friction coefficient by 5%,
although the corrected theoretical value remains appreciably higher than that measured by the skin-friction
meter.

Fig 5b shows how the displacement correction appears to be primarily a function of $u_\tau d/\nu_w$ (where d is the
probe diameter), with a small but significant variation with M_e. (The negative sign denotes the convention
of making the correction to the theoretical profile). By virtue of the way the correction is determined,
so as to minimize the rms deviation between theory and experiment, its value is dominated by the points
closest to the wall. Hence the correlation in "law-of-the-wall" variables shown in Fig 5b is to be expected.
Fig 5b shows only the probe corrections derived for x = 623mm, at which position there was very little
scatter. The other positions on the plate show clearly the variation with $u_\tau d/\nu_w$ but, because of increased
scatter, the variation with M_e is less well defined. Despite the scatter almost all the probe corrections
for 92 profiles fall within the broken curves on Fig 5b.

3.3 Mixing-length Analysis of Fenter and Stalmach

Allen suggested (11) a convenient and accurate method of predicting the local skin-friction coefficient
from a measured velocity profile. For adiabatic flow, he found, that the most accurate version of the law
of the wall in compressible flow was that derived by Fenter and Stalmach (12) on the basis of von Karman's
mixing-length hypothesis. This method has been applied to the present results in the manner suggested by
Allen; namely by using each point on the velocity profile in turn to deduce a value of C_f, and plotting
these values of C_f against the corresponding position y of the pitot probe. Fig 6a shows typical predic-
tions of C_f as a function of probe position at Mach numbers M_e = 2.5 and 4.5 and two values of R δ_2 at each
Mach number. A curve such as that for M_e = 4.5, R δ_2 = 4880 has two plateaux which apparently indicate two
different levels of skin-friction coefficient (inner and outer values). The inner value is a maximum and
gives good agreement with the C_f measured by the skin-friction balance. The outer value is a minimum and
its agreement with the measured C_f is, in general, less satisfactory and varies considerably with both

Mach number and Reynolds number. This variation in the predicted C_f between the inner and outer values across the logarithmic region of the boundary layer is most probably associated with a departure from the particular form of the law of the wall proposed by Fenter and Stalmach. The values of skin friction predicted from the inner plateau are compared with the directly measured values, on a percentage basis, in Fig 6b. These results confirm Allen's conclusions as to the usefulness of this method.

3.4 Comparison with Flat Plate Relations

In Fig 7, the predictions by the flat-plate skin-friction relations of Spalding and Chi (13) and Winter and Gaudet (7) are compared with the measurements. The comparisons are made on a percentage basis, with the theoretical value of C_f determined from the measured value of R δ_2. Fig 7a shows that, for the method of Spalding and Chi, the error at the higher Reynolds numbers is about +3% at M_e = 2.5, falling to -3% at M_e = 4.5. In addition, this figure shows that skin friction is appreciably underestimated at the lower Reynolds numbers and higher Mach numbers; the error is as much as 12% at the lowest Reynolds number at M_e = 4.5. Some of this underestimate is almost certainly due to the failure of the theory of Spalding and Chi to take account of the variation of the wake component at low Reynolds number, which was discussed in Section 3.1. The prediction method of Winter and Gaudet (7), illustrated in Fig 7b, appears slightly more accurate than that of Spalding and Chi. At high Reynolds numbers, the error given by this method is only about 1% at M_e = 2.5 falling to -2% at M_e = 4.5. However, like Spalding and Chi, Winter and Gaudet neglect the variation of wake component with Reynolds number and hence, at low Reynolds numbers, the underestimation of skin friction again increases to about 12% at M_e = 4.5. (The measurements by Winter and Gaudet, which were made on the sidewall of the RAE 8ft x 8ft tunnel, did not, of course, extend down to sufficiently low Reynolds numbers for the decay of the wake component to be observed).

3.5 Wall Temperatures

Despite the attempts made to insulate the flat plate described in Section 2.1 above, the wall temperatures were considerably higher than those based on a recovery factor $r = 0.89$ $(r = \sqrt[3]{Pr})$, the value commonly associated with a turbulent boundary layer (14). The total temperature selected for these tests would have given $T_w = 15^\circ C$ for $r = 0.89$ but, in fact, the wall temperatures were generally about $23^\circ C$ (Fig 8). The wall temperatures varied from day to day by about $\pm 2^\circ C$, but in no apparent systematic manner. The spanwise temperature variation across the plate was not measured but was believed to be small.

3.6 Total Temperature Profiles

Some typical measured total-temperature distributions across the boundary layer are shown in Fig 9 in terms of the function F where

$$F = (T_t - T_w)/(T_{t_e} - T_w)$$

and has values $F = 0$ at the wall and $F = 1$ in the freestream. The profiles measured at M_e = 2.5 and 4.5 at two Reynolds numbers are compared with the Crocco relationship (15)

$$F = (u/u_e)$$

and the Walz relationship (16)

$$F = (u/u_e)^2.$$

The Walz relationship is closer to the measured points than the Crocco relationship, at least near the outer edge of the boundary layer, but neither relationship is in good agreement with the data. Their failure is particularly marked close to the wall where, in some cases, total temperature increases as the wall is approached.

Fig 9 suggests that this increase in total temperature as the wall is approached is most in evidence at the higher Mach numbers. However, a survey of all the temperature profiles so far measured suggests that the region of increasing total temperature is not restricted to high Mach numbers alone, but occurs at all Mach numbers if the local value of

$$u_\tau y/\nu_w$$

becomes less than 50. Meier and Rotta have shown (17) how a total temperature variation of this type in the wall region can be predicted if an increase in turbulent Prandtl number occurs for values of $u_\tau y/\nu_w$ < 50. Fig 9 shows a typical prediction taken from reference 17 of the temperature distribution for M_e = 3.0 and $R\delta_2$ = 10100. An increase in turbulent Prandtl number near the wall would mean that in this region the turbulent heat exchange decreases more rapidly than the turbulent momentum exchange. A similar variation in turbulent Prandtl number is believed to occur at subsonic speeds (18) although other recent experiments have suggested that the Prandtl number first increases (for values of $u_\tau y/\nu_w$ < 200), reaches a peak at about $u_\tau y/\nu_w$ = 50 and then decreases as the wall is approached (19). Temperature measurement very close to the wall is, of course, exceedingly difficult and hence this particular aspect of the results should be regarded with some caution.

The absence of a significant overshoot in the temperature distribution in the outer part of the boundary layer means that the total enthalpy defect in the layer

$$\int_0^\delta (\rho/\rho_e) \, (u/u_e) \, (1 - T_t/T_{t_e}) \, dy$$

cannot be zero as it should be for a boundary layer on a thermally insulated surface. In fact, the nett enthalpy defect in the boundary layer is considerable, particularly at the higher Mach numbers.

Although the measured enthalpy-defect thicknesses show some scatter, it has been estimated, according to Reynolds analogy, that the wall would need to be maintained well below recovery temperature - of order 20°C at M_e = 2.5, but substantially more at M_e = 4.5 - to achieve the necessary heat transfer. In contrast, the measured wall temperatures are a few degrees above the normal adiabatic recovery temperature. Moreover, calculations of heat transfer through the thermal insulation on the plate indicate that the heat flux associated with the enthalpy defect could not be passed, either to the tunnel structure or to the flow over the back of the plate without appreciably higher driving temperature differences than are observed. It is not thought that the temperature probe is sufficiently inaccurate to be the cause of those discrepancies; hence, the loss from the thermal energy balance cannot at present be explained.

4. CONCLUSIONS

The main conclusions may be summarized under three headings.

(1) Velocity Profiles

The velocity profiles plotted in the law of the wall coordinates show a significant increase in the value of the von Karman constant κ as Mach number increases from M_e = 2.5 to 4.5. This agrees fairly well with the correlation of Winter and Gaudet, although the latter to some extent underestimates the increase in κ above M_e = 3.5 (Fig 3). At the higher Mach numbers, the decay of the wake component Π of the velocity profile at low Reynolds numbers is fairly well defined (Fig 4) and is consistent with the observations of Hastings and Sawyer and Green.

The measured velocity profiles can be fitted very closely to the family of theoretical velocity profiles proposed by J C Rotta. The agreement is particularly good if a probe displacement correction, dependent primarily upon $u_\tau d/\nu_w$ is made (Fig 5).

The technique proposed by Allen for estimating skin friction, using the mixing-length formulation of the law of the wall developed by Fenter and Stalmach, is found to be fairly accurate.

(2) Skin Friction Predictions

The flat-plate skin-friction laws of Spalding and Chi and Winter and Gaudet are in fairly good agreement with the measurements but, at high Mach numbers and low Reynolds numbers, significant deviations become apparent (Fig 7). Some of these deviations are attributable to the neglect by these prediction methods of the decay of the wake component of the velocity profile at low Reynolds number.

(3) Temperature Profiles

The wall temperatures are higher than expected on an adiabatic surface (Fig 8), suggesting heat transfer from the wall to the boundary layer. In contrast, the temperature profiles in the boundary layer show no significant overshoot and imply heat flow from the boundary layer to the plate (Figs 9 and 10). The observed defect in enthalpy flux does not seem attributable to errors in temperature measurement by the probe. No appreciable heat flow can pass through the insulation from the plate to the tunnel structure or to the stream past the back surface of the plate.

These temperature measurements present a paradox which will be the subject of further investigation.

REFERENCES

1. R C Hastings
   W G Sawyer
   Turbulent boundary layers on a large flat plate at M = 4.0. RAE TR 70040.

2. D G Mabey
   H U Meier
   W G Sawyer
   Experimental and theoretical studies of the boundary layer on a flat plate at Mach numbers from 2.5 to 4.5. (RAE TR in preparation).

3. H U Meier
   A combined probe for temperature and pressure measurements in boundary layers in compressible flow. AVA 68-A41 AIAA Journal Vol 7 No 3. March 1969.

4. D G Mabey
   Boundary layer transition measurements using a surface hot film downstream of distributed roughness at Mach numbers from 1.30 to 2.0. Journal Royal Aero Society Vol 9 No 650. February 1965.

5. D G Mabey
   W G Sawyer
   Reduction of flow unsteadiness in the maximum section of the 3ft x 4ft supersonic tunnel. (RAE TR in preparation).

6. D E Coles
   The turbulent boundary layer in a compressible fluid. Rand Report R403-PR. Sept 1962. ARC 24-497. February 1963.

7. K G Winter
   L Gaudet
   Turbulent boundary layer studies at high Reynolds number at Mach numbers between 0.2 and 2.8. RAE TR 70251. 1970.

8. J E Green
   A note on the turbulent boundary layer at low Reynolds number in compressible flow at constant pressure. RAE TR (to be issued).

9. H U Meier
   Experimentelle und theoretische Untersuchungen von turbulenten Grenzschichten bei Ueberschallströmung. Mitt Mpi Stroem. Forsch U AVA NR49 (1970) p1-116.

10. J C Rotta
    Über den Einfluss der Machschen Zahl und des Wärmeübergangs auf das Wandgesetz turbulenter Strömung. Z Flugwiss 7 (1959) Vol 9 p264-274.

11. J M Allen — Use of the Baronti-Libby transformation and Preston tube calibrations to determine skin friction from turbulent velocity profiles. NASA TND 4853. November 1968.

12. P J Fenter
    C J Stalmach — The measurement of local turbulent skin friction at supersonic speeds by means of surface impact pressure probes. DRL 392 CM 878. University of Texas. October 1957.

13. D B Spalding
    S W Chi — The drag of a compressible turbulent boundary layer on a smooth flat plate with and without heat transfer. Journal Fluid Mech Vol 18 Pt 1 pp117-143. January 1968.

14. H Schlichting — Boundary layer theory. 6th Edition McGrawHill. p668.

15. L Crocco — Transformation of the compressible turbulent boundary layer with heat exchange. AIAA Journal Vol 1 No 12 pp2723-2731. December 1962.

16. A Walz — Compressible turbulent boundary layers. Mechanics of turbulence, Gordon & Breach Science Publishers, New York. 1964. (Proceedings of colloquy on Mechanics of Turbulence, Marseilles 1961).

17. H U Meier
    J C Rotta — Experimental and theoretical investigation of temperature distributions in supersonic boundary layers. AIAA Paper 70-744. (to be published in AIAA Journal).

18. R Jenkins — Variation of the Eddy Conductivity with Prandtl modulus and its use in the prediction of heat transfer. Inst for Heat Transfer pp147-148. 1957.

19. L Blom — An experimental determination of turbulent Prandtl number in a developing temperature boundary layer. Holland - Eindhoven Technische Hogeschool Thesis - printed as US N70 - 32346.
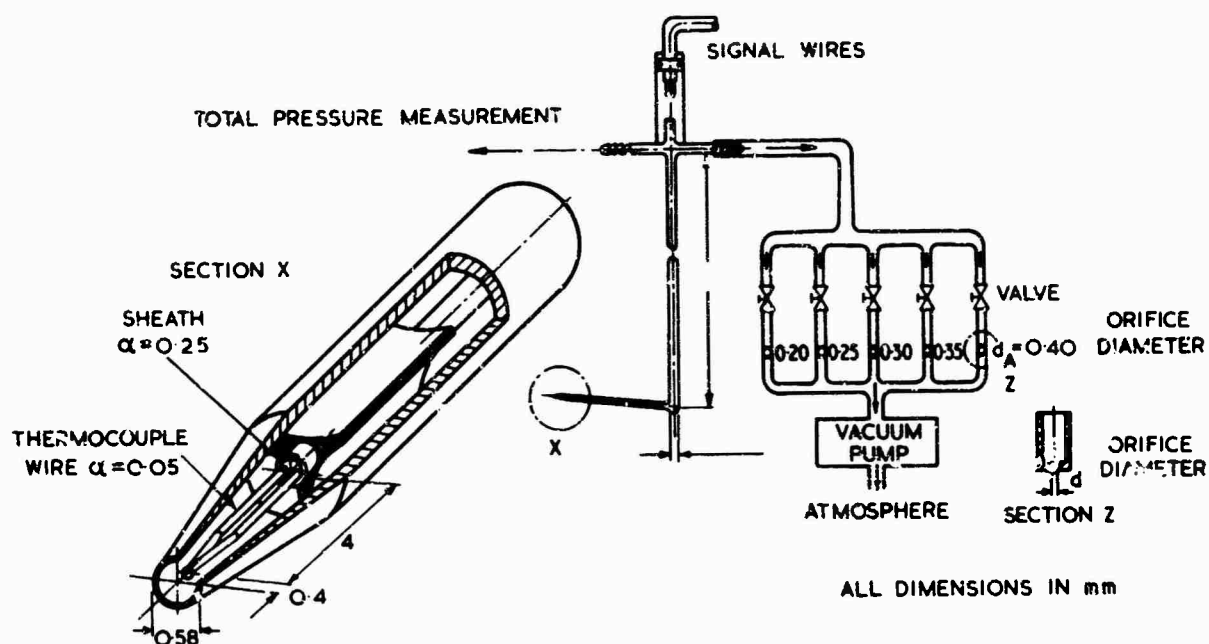
Fig.1 Combined total-temperature and pitot-pressure probe

Fig.2 Typical velocity profiles

$M_e = 2.5$

x (mm)
$\odot \begin{cases} 368 & 876 \\ 623 \end{cases}$
× 1130
+ 1384

$M_e = 3.5$

$M_e = 4.5$

$R\delta_2 \times 10^{-3}$

Fig.4   Variation of wake component

WINTER AND GAUDET

$M_e = 2.5$

$M_e = 3.5$

$M_e = 4.5$

$R\delta_2 \times 10^{-3}$
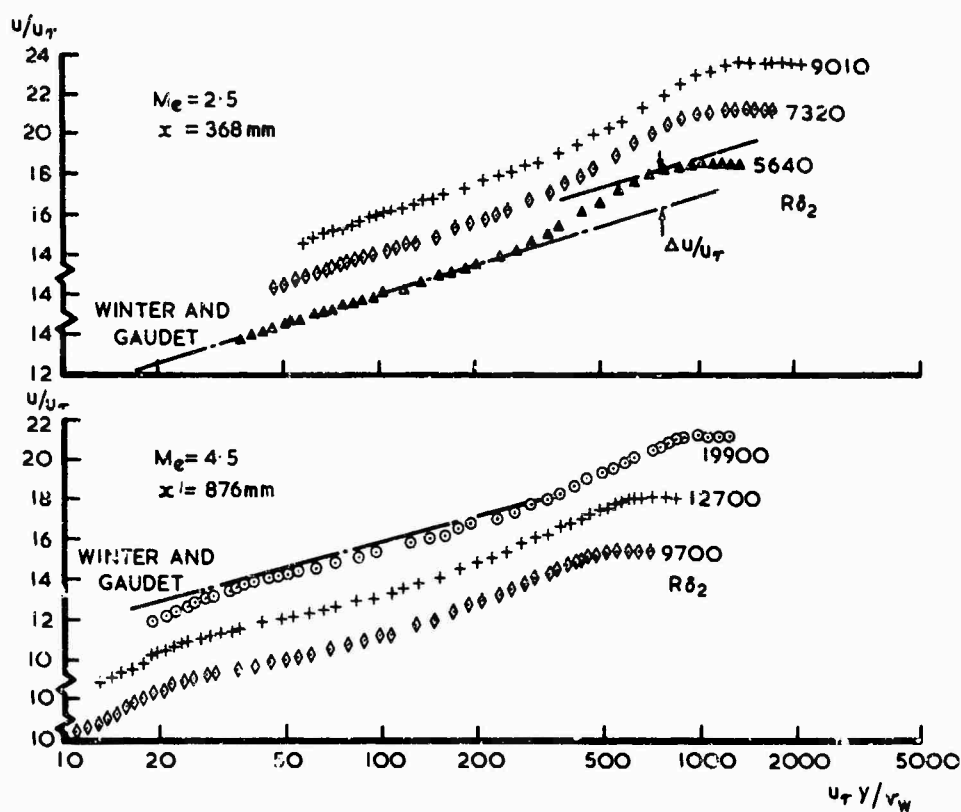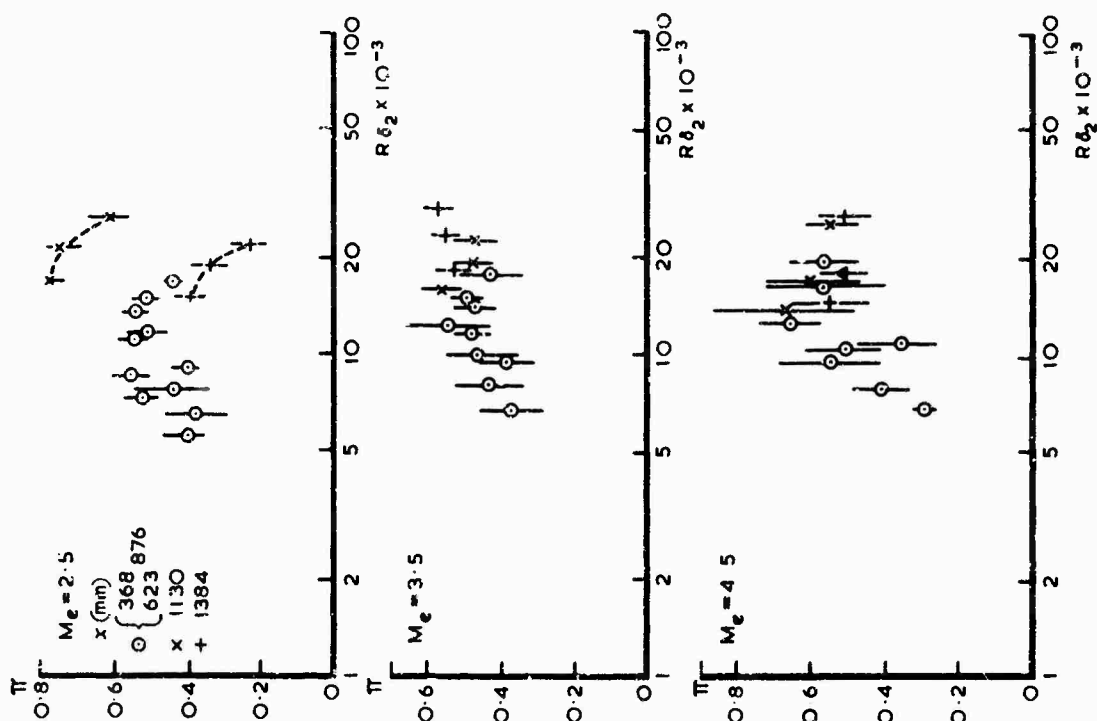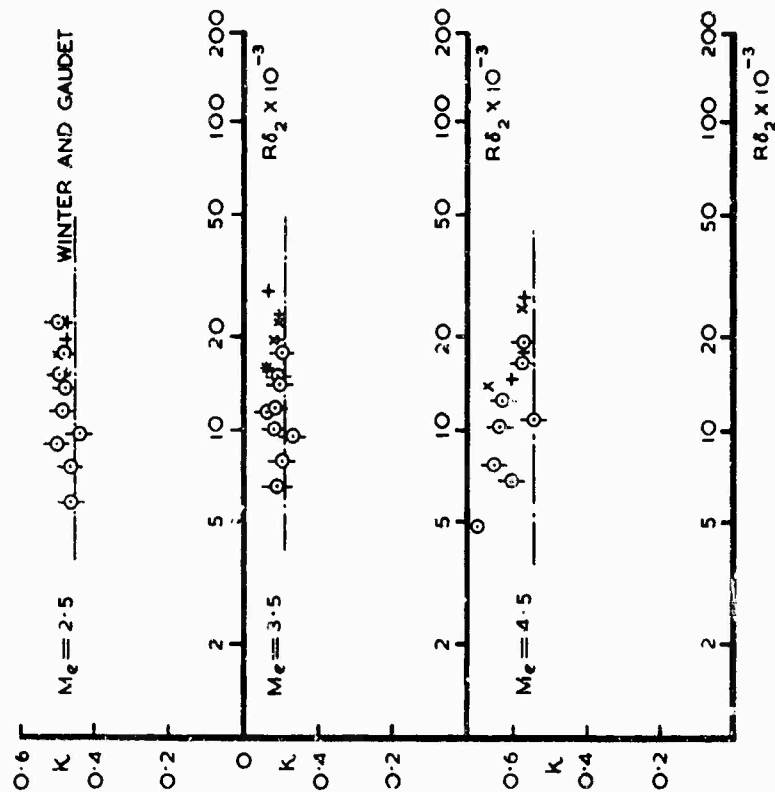
Fig.3   Von Kármán constant for logarithmic region of velocity profiles
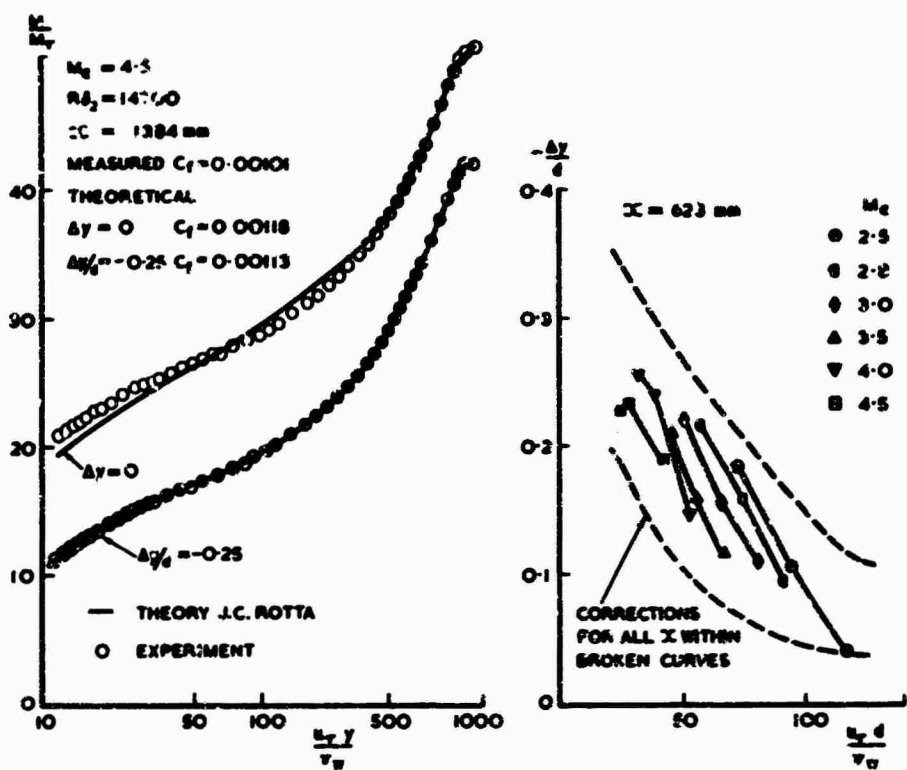
Fig.5   Pitot probe corrections
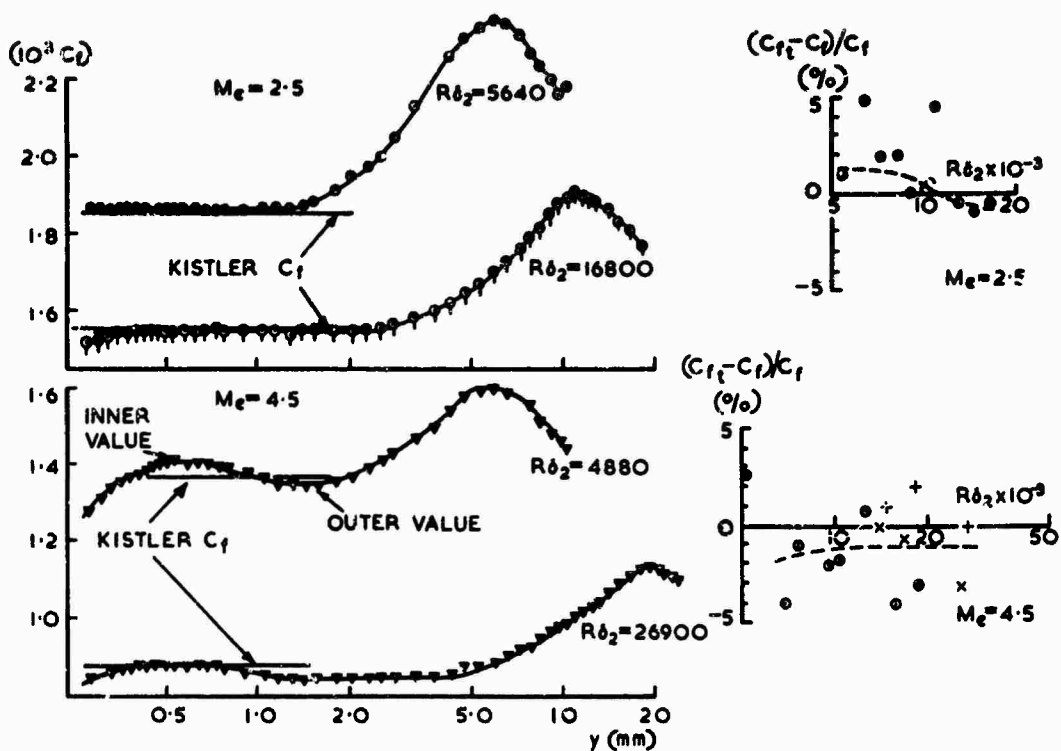
Fig.6   Skin-friction coefficients derived from Fenter and Stalmach law of wall

$(C_{f_t}-C_f)/C_f$

%

SPALDING
AND CHI

$M_e = 2.5$

$M_e = 4.5$

$R\delta_2 \times 10^{-3}$

$(C_{f_t}-C_f)/C_f$

%

WINTER

AND GAUDET

$M_e = 2.5$

$M_e = 4.5$

$R\delta_2 \times 10^{-3}$
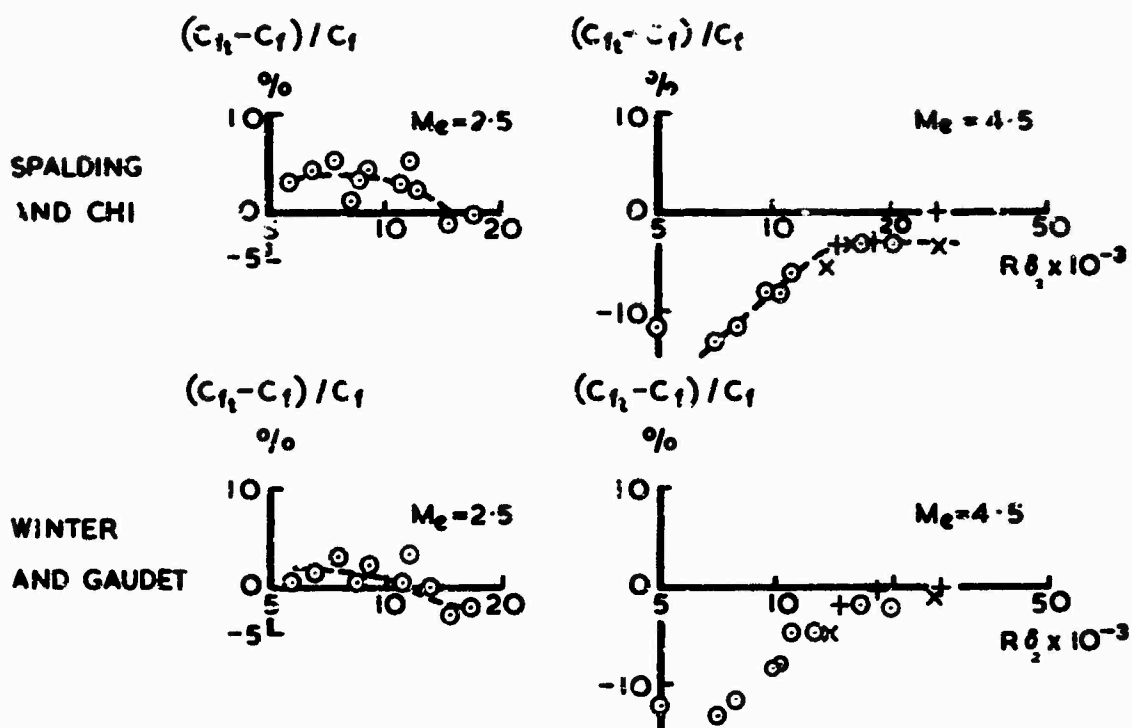
Fig.7   Comparison of estimated and measured skin-friction coefficients

$\dfrac{T_w}{T_{t_e}}$

$M_e = 2.5$

0.96

0.94

$T_w = T_r \ (r = 0.89)$

0.96

0.94

DIURNAL VARIATION OF
WALL TEMPERATURE

$M_e = 3.5$

$T_w = T_r$

0.94

0.92

$M_e = 4.5$

$T_w = T_r$

0   200   400   600   800   1000   1200   1400

x (mm)
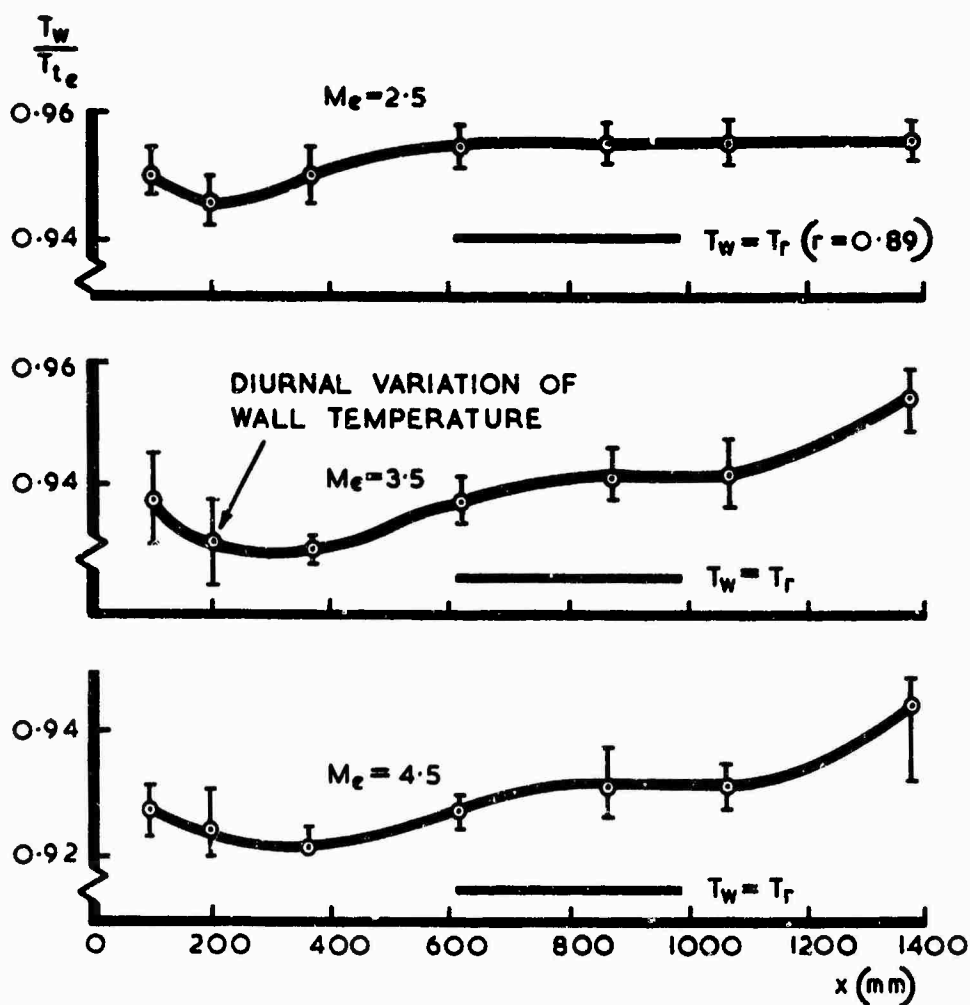
Fig.8   Variation of wall/total temperature ratio along plate

$\%_{\theta e}\ ^{u}/u_e\left(\dfrac{T_t}{T_e}-1\right)$

$M_e = 2\cdot5$

$\delta = 12\cdot3$ mm
$x = 876$ mm
$R\delta_2 = 16800$

$\delta = 6\cdot6$ mm
$x = 368$ mm
$R\delta_2 = 5640$

$M_e = 4\cdot5$

$\delta = 21\cdot5$ mm
$x = 1384$ mm
$R\delta_2 = 26900$

$\delta = 7\cdot3$ mm
$x = 368$ mm
$R\delta_2 = 4880$
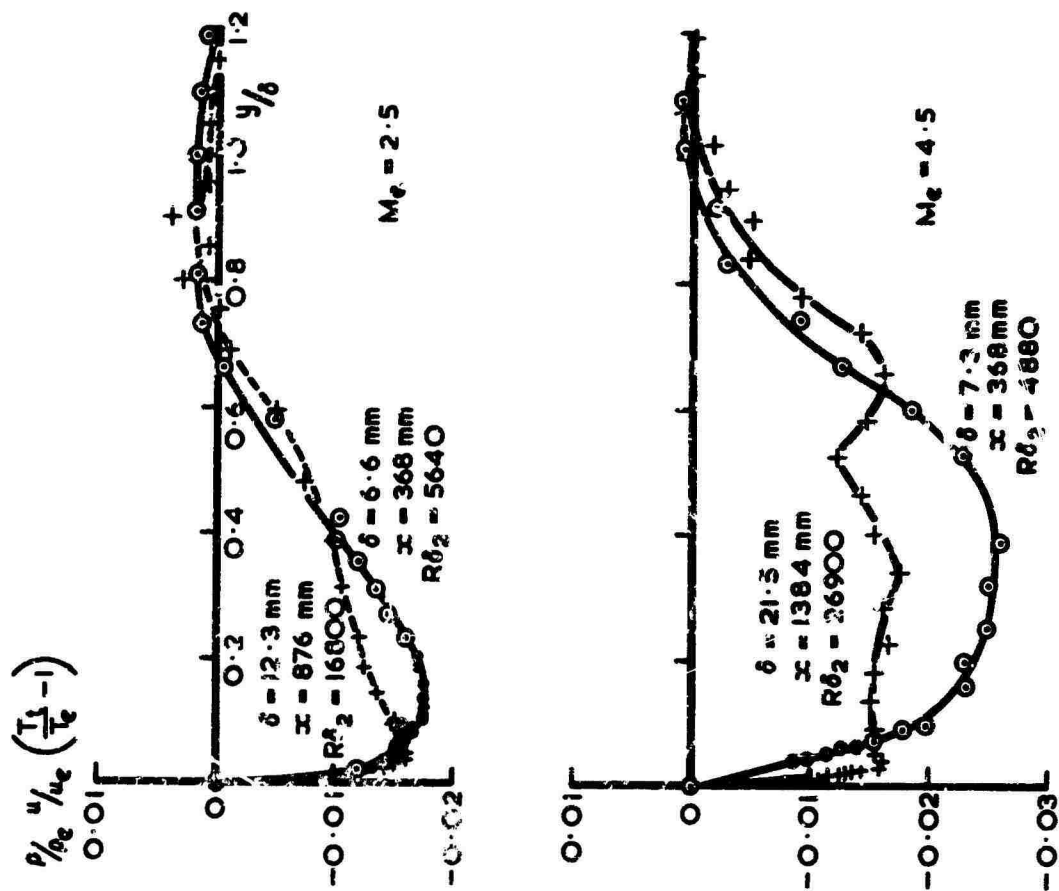
Fig.10   Energy flux across the boundary layer

$M_e = 3\cdot5$
$R\delta_2$
▲ 27700
⊙ 6530

$\dfrac{T_t}{T_w}$

$M_e = 3\cdot0$
$M_\tau = 0\cdot081$
$R\delta_2 = 10100$

$P_{T_t} = 0\cdot86$

$P_{T_t} = 1\cdot0$

P_{T_t} VARIES (AFTER MEIER AND ROTTA)

$\dfrac{M}{M_\tau} = \dfrac{u}{u_\tau}$

$\sqrt{\dfrac{T_w}{T_t}}$

$F = \dfrac{T_t - T_w}{T_{t_e} - T_w}$

$M_e = 2\cdot5$
$R\delta_2$
▲ 16800
⊙ 5640

CROCCO
WALZ

$M_e = 4\cdot5$
$R\delta_2$
▲ 26900
⊙ 4880
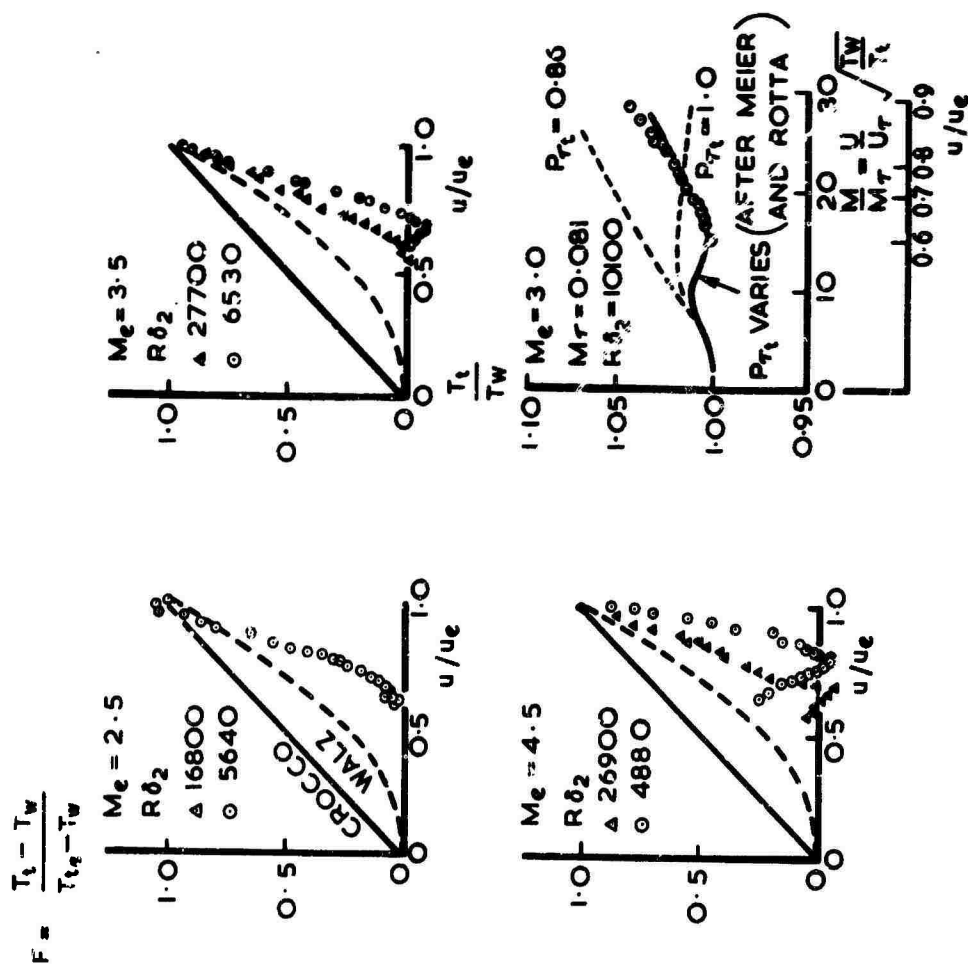
Fig.9   Variation of total temperature with velocity ratio

COMPARISONS BETWEEN SOME HIGH REYNOLDS NUMBER TURBULENT BOUNDARY LAYER
EXPERIMENTS AT MACH 4, AND VARIOUS RECENT CALCULATION PROCEDURES

by

D.J. Peake[*], G. Brakmann[†] and J.M. Romeskie[†]

SUMMARY

The objective of these studies was to assess the influence of streamwise pressure
gradients upon two-dimensional compressible turbulent boundary layers at high Reynolds
numbers, in the absence of 'end-wall effects' and effects of longitudinal curvature.
Boundary layers recovering to equilibrium conditions were of special interest.

Measurements were made at a Mach number of 4 of pressure distribution, local skin
friction and boundary-layer profiles along the internal surface of a parallel, circular
cross-section duct where an axisymmetric centre-body (that could be extended into the
duct) provided the means of imposing an adverse pressure gradient upon the test flow.
The Reynolds number based on the duct length of 33-inches was almost 50 million.

Results from three experiments are presented in this paper, namely a near zero pres-
sure gradient flow, an adverse pressure gradient case, and a flow relaxing downstream of
a step-induced separation. These results are compared against the seven recent and re-
spective calculation methods of Bradshaw/Ferriss, Nash, Chan, Zwarts, Cebeci/Smith,
Head/Green, and Stratford/Beavers, in terms of integral parameters, local skin friction
coefficients, and velocity profiles (where calculated).

In general, the boundary layer predictions of all the methods were in reasonable
agreement with experiment. The outstanding exception was the discrepancy observed between
the calculated and experimental skin friction results in the adverse pressure gradient
flow, which has been attributed tentatively to the static pressure gradient across the
boundary layer in the region of the streamwise pressure increase.

LIST OF SYMBOLS

APG	Adverse pressure gradient flow case
C_F	Local skin friction coefficient
C_p	Specific heat at constant pressure
C_{PP}	Preston tube pressure coefficient $= \dfrac{(P_P - P_E)}{q_E}$
d_C	Width of cobra probe head in direction of traverse normal to the wall
d_S	Diameter of static hole
D	Preston tube diameter
ε_t	Eddy viscosity
H	Shape factor in compressible flow $= \dfrac{\delta^*}{\theta}$; also enthalpy
H_1	Entrainment shape parameter $= \dfrac{\delta - \delta^*}{\theta} = \dfrac{1}{\theta}\int_0^\delta \dfrac{\rho u}{\rho_E u_E}\, dy$
H	Shape parameter $= \dfrac{1}{\theta}\int_0^\delta \dfrac{\rho}{\rho_E}\left(1 - \dfrac{u}{u_E}\right) dy$
H_{12}^i	Incompressible shape parameter, sometimes called velocity shape factor $= \dfrac{\int_0^\delta \left(1 - \dfrac{u}{u_E}\right) dy}{\int_0^\delta \dfrac{u}{u_E}\left(1 - \dfrac{u}{u_E}\right) dy}$
k_T	Thermal conductivity
ℓ	Mixing length
L_ε	Dissipation length
M	Mach number
P_C	Cobra probe pitot pressure
P	Local static pressure
P_0	Stagnation pressure
P_P	Preston tube pitot pressure
Pr_T	Turbulent Prandtl number
q	Dynamic pressure

[*] NAE, National Research Council of Canada, Ottawa, Ontario, Canada.

[†] Department of Mechanical Engineering, McGill University, Montreal, Quebec, Canada.

r	Temperature recovery factor = 0.89
R	Radius of duct
R_D	Reynolds number based on Preston tube diameter and local mainstream conditions
R_θ	Reynolds number based on boundary-layer momentum thickness and local mainstream conditions
RPG	Ring pressure gradient flow case
T	Static temperature
T_0	Stagnation temperature of mainstream
T_R	Recovery temperature at an adiabatic wall (r = 0.89)
u	Velocity
$u_{\tau W}$	Friction velocity = $\sqrt{\tau_W/\rho_W}$
X	Distance along duct wall, measured from cowl lip
y	Distance normal to duct wall
ZPG	Zero pressure gradient flow case

Greek

γ	Intermittency
δ	Boundary-layer thickness
δ^*	Displacement thickness = $\int_0^\delta \left(1 - \frac{\rho u}{\rho_E u_E}\right) dy$
Δ	Correction for cobra probe displacement effect
θ	Momentum thickness = $\int_0^\delta \frac{\rho u}{\rho_E u_E}\left(1 - \frac{u}{u_E}\right) dy$
μ	Absolute viscosity
ν	Kinematic viscosity = μ/ρ
ρ	Density
τ	Shear stress
ϕ	Angle subtended at duct centre by arc length of cowl
ψ	Yaw angle of cobra probe head

Subscripts

C	Compressible flow; cobra probe
D	Preston tube diameter
E	Local mainstream conditions at boundary-layer edge
i	Incompressible flow
0	Stagnation
P	Preston tube
R	Recovery
τ_W	Wall shear stress
W	Wall

Superscripts

'	Quantities evaluated at an intermediate temperature Fluctuating quantities in Section 2.

NOTE: (i) The factor $(1 - \frac{y}{R})$ was inserted into the integrands of the * terms when determining experimental values.

(ii) Additional symbols (not defined in the List), to be consistent with the seven calculation methods employed in this paper, are introduced and discussed in Section 2.

1.0 INTRODUCTION

The Proceedings[1,2] of the Conference held at Stanford University in 1968 indicated that many of the recent integral and differential calculation procedures for incompressible, two-dimensional, turbulent boundary layers can provide both rapid and reliable predictions of flows in arbitrary pressure gradients. This generality was restricted, nevertheless, to flows that did not interact significantly with the mainstream, or in other words, to those that were not close to separation. On the effects of compressibility, it was considered that additional data were required, especially for flows in adverse and relaxing pressure gradients, in preference to the expending of enormous effort on the proliferation of new theories — a state of saturation that has already occurred, of course, in the incompressible flow case.

Prior to the Stanford meeting, an experiment to include adverse and relaxing pressure gradients had already been devised by NAE and McGill University to obtain some definitive mean flow results at Mach 4, under conditions of high Reynolds number (R_θ of 30,000).

The comments at the Stanford meeting, therefore, provided substantial support for the present objectives. The experiment was then expanded in scope to provide a framework of results from three different boundary layer flows against which to test the compressible versions of some of the advocated methods at Stanford, as well as some other recent calculation techniques. The approaches chosen included the differential turbulent kinetic energy field methods of Bradshaw[3,4], Nash[5], and Chan[6,7], as well as the differential mean field method of Cebeci/Smith[8]. These were supplemented by the dissipation integral method of Zwarts[9], the entrainment integral method of Head/Green[10,11], and the momentum integral method of Stratford/Beavers[12]. From these attempts, it was anticipated that the most promising methods might be revealed for potential application to other important flow cases in aeronautical engineering.

Despite the fact that many sets of compressible turbulent boundary layer data are available, most have been measured in nominally zero pressure gradient, while those taken in flows with pressure gradient have often suffered from detrimental rig effects. The consequence is that few data-sets are of adequate quality to serve as a basis against which to compare the various calculation techniques. In particular, there is a scarcity of satisfactory measurements at high Reynolds numbers either in strong adverse (but without shock waves) or in relaxing pressure gradients, the latter flow type causing noteworthy embarrassment to most calculations.

Experiments conducted in nominally two-dimensional configurations, where adverse pressure gradients were applied remotely from the test surface, have been influenced to a greater or lesser degree by 'end-wall effects'. The boundary-layer growth on the end walls (unless this is controlled) induces a flow convergence both in the mainstream flow and in the test boundary layer (see Zwarts[9], for instance). The difficulties with end-wall effects are aggravated in supersonic flow, where shock-induced separations may also be involved. Longitudinal curvature of the test surface itself has provided an alternative means of generating an adverse pressure gradient[13,14,15,50], but there, the changes in static pressure along a normal to the surface may be substantial enough to invalidate the usual assumption of constant static pressure across the boundary layer*, even for moderate pressure gradients at low Mach numbers. In the Mach 6 case of Reference 15, for example, subsequent analysis[17] showed that, across the boundary layer thickness, the static pressure changed along a normal to the surface by as much as 80 percent of the wall pressure, and demonstrated that the isobars in the boundary layer were close to the linear extensions of the Mach lines in the mainstream. Amongst other factors that may adversely affect the quality of a 'standard boundary layer experiment' are difficulties with tripping devices, the unknown influence of local turbulence on pitot tube readings, the effects due to probe size, shape and displacement, the effects of outer intermittency and the sensitivity of integral thicknesses to the few data points near the wall.

To eliminate the undesirable secondary flow effects from end walls, a test surface comprising the inner wall of a circular cross-section, parallel duct is an obvious choice. A large constant radius test section should be provided so that there are no problems as a result of changing transverse curvature and rapidly thickening layers. A suitable ratio of test boundary-layer thickness to radius of curvature should be <0.1 for the effects of transverse curvature to be negligible. (In low speed flow[18], the effect of transverse curvature on the index of the power law of the turbulent boundary layer, was shown to be insignificant for ratios of boundary layer thickness to radius of curvature of up to 3.) A prescribed pressure field may then be generated conveniently by means of an axisymmetric centre-body located within the duct, the centre-body contour depending on the choice of supersonic or subsonic mainstream test conditions. Moreover, the pressure gradient conditions can be varied by altering the centre-body design without disturbing the instrumentation along the test surface, while the near zero pressure gradient case may be handled by retracting or removing the centre-body altogether.

As an additional variable, the duct length can be changed by building it in sections; there is then the provision to obtain an initial boundary-layer development under essentially zero pressure gradient conditions before commencing any pressure rise, a feature assisting the input of initialising boundary values in the calculation methods. A suitable length of wetted surface may also be added downstream of any applied pressure rise to investigate boundary layers recovering to equilibrium conditions.

With the centre-body removed, we may also study the difficult computational case of a boundary layer relaxing downstream of a local separation, induced, say, by a forward facing step (a shock/boundary-layer interaction flow configuration not unlike that investigated by Green[10,19]) or we may measure the three-dimensional boundary layer in the duct at angle of attack. The installing of instrumentation is facilitated by access to it from outside the rig; measurements of static and impact pressures at the wall, temperatures, and viscous flow profiles of both mean and fluctuating quantities being clear choices for any experiments of the kind outlined in the present paper.

The type of parallel duct discussed above forms the basis, in fact, of the test rig to be described in Section 3. The duct was placed in a Mach 4 mainstream in the NAE 5-ft × 5-ft wind tunnel to investigate three different boundary-layer flows under nominally two-dimensional conditions. The tests were performed at a Reynolds number of almost 50 million based on the 33-inch wetted length of test surface and undisturbed Mach 4 stream conditions, while heat transfer to or from the flow was assumed negligible. This assumption follows from the fact that with the tunnel open for rig servicing, the temperature of the test surface is that of the local ambient atmosphere. During the short duration

---

*longitudinal curvature also has a significant effect on the turbulence structure[16].

tunnel run, the stream stagnation temperature is also close to that of the local ambient atmosphere. Hence, because of the large heat capacity of the test surface, the resulting decrease in wall temperature is small, and the wall is close to an adiabatic temperature condition.

The first test was a near zero pressure gradient flow; the second was concerned with an adverse pressure gradient, the initial Mach 4 mainstream diffusing to Mach 2, downstream of which the boundary layer was permitted to relax at virtually constant pressure along a length of about 200 boundary-layer displacement thicknesses; while the third involved a boundary layer recovering downstream of a step-induced separation. The same physical length of nominally zero pressure gradient boundary layer was allowed to develop upstream of the pressure rise and upstream of the step.

This paper provides a description of the measurements made, and their comparisons with the aforementioned calculation methods; emphasis being placed on integral parameters, local skin friction coefficient and velocity profiles.

2.0 PREDICTION OF THE COMPRESSIBLE, TURBULENT BOUNDARY LAYER IN ARBITRARY PRESSURE GRADIENTS

An unsophisticated interpretation of a turbulent boundary layer is that it consists of a free shear layer constrained by a solid wall. The wake-like character is evidenced by the entrainment and intermittency phenomena, and by the sensitivity of the outer region of the boundary layer to pressure gradient and mainstream turbulence level. The wall constraint, on the other hand, reveals itself in the viscous, laminar sub-layer, and in the logarithmic part of the mean velocity profile.

Two similarity laws have been demonstrated to characterise the overall development of a turbulent boundary layer – at least, for flows in nominal equilibrium – called the 'law of the wall' and the 'law of the wake'. Given that the law of the wall applies (that is, there is a relationship between mean velocity and shearing stress velocity) then a convenient means of estimating the wall shearing stress is provided. The law of the wake, on the other hand, circumvents the necessity to stipulate the physics of the shear flow turbulence. References 1 and 2 hint that the inclusion of the law of the wall or other equivalent data appears to be a trait of the successful incompressible prediction methods, and it will be noted in the following discussion that the explicit or implicit inclusion of the wall law is a feature of all the compressible flow calculation methods used herein.

In the compressible, turbulent boundary layer, the fluctuating velocity field promotes transport of momentum and heat across the mean flow streamlines. It is the explicit or implicit description of this transport mechanism that constitutes the fundamental problem of calculating turbulent boundary layer development. For steady, two-dimensional turbulent boundary layer flow, the momentum and thermal energy equations contain essentially two unknowns: terms involving the time mean of the product of two fluctuating velocities, $\overline{-u'v'}$, known as the turbulent (or Reynolds) shear stress; and a term involving the time mean of the product of a fluctuating velocity and a fluctuating temperature, $\overline{-v'T'}$, (or sometimes expressed in terms of enthalpy $\overline{-v'H'}$). The relationships (if any) between these fluctuating quantities and the mean velocity and mean temperature distributions have never been strictly defined by experiments, reliance having been placed on empirical correlations. As McDonald points out in his concise assessment of certain compressible turbulent boundary layer methods in Reference 20, the success or failure of proposed methods of prediction will thus be associated directly with the way the mean flow variables are related to the temperature correlation, $\overline{v'T'}$, along with the procedure for representing possible temperature effects on the relationship between the mean velocity field and turbulent shear stress term, $\overline{-u'v'}$. We shall attempt to illustrate in this résumé of calculation methods used herein, how each of these correlations is described, and their possible advantages and shortcomings.

In the numerical solution of the boundary layer partial differential equations, the mean field is usually related to the turbulent stress and temperature correlations in an explicit form. Such relationships, for instance, those of 'eddy viscosity' or 'mixing length', are used in a large number of the incompressible calculation procedures; but their limitations in the compressible flow case are unclear. As Bradshaw points out in Reference 4, the assumption that the apparent eddy viscosity, ε_t, in the outer part of the boundary layer is a constant multiple of the integral of velocity defect across the boundary layer (ε_t being taken independent of the mean density profile and Mach number) may well be satisfactory for zero pressure gradient flow. Yet in view of the paucity of reliable experimental data, there is no reason to presume that such a state applies in compressible flows with pressure gradient. Bradshaw discusses further[4] that even in incompressible flow, large variations in dimensionless eddy viscosity (or mixing length) can occur in rapidly changing boundary layers; the latter are often encountered in compressible high speed flows and changes in density may affect the eddy viscosity or mixing length. We shall begin with commenting on those methods that do not utilise compressibility transformations, followed by those that do.

2.1 The Differential Turbulent Kinetic Energy Field Method of Bradshaw/Ferriss; and of Nash

Prior to the publication in 1966 (by Bradshaw et al[3]) of a method to calculate boundary layer development utilising the turbulent kinetic energy equation, most procedures, as we have inferred already, had relied upon the properties of the turbulence

(such as entrainment or local shear stress profile) to be related to the local mean flow conditions. For example, in the 'eddy viscosity' or 'mixing length' hypotheses, the assumption is made that the local shear stress in a boundary layer is governed by the local velocity gradient of the mean flow at that point.

Bradshaw et al[3] argued that there was a much closer relationship between the shear stress profile and the turbulence structure than between the shear stress and the mean velocity profile. Once the relations between the shear stress and the turbulence intensity, dissipation, and diffusion are known or are prescribed, the differential turbulent kinetic energy equation defining the rate of change of turbulent energy along a streamline, can be converted into an equation for the rate of change of turbulent shear stress (in a two-dimensional boundary layer). No assumption of the shear stress with respect to the mean velocity gradient is needed. The method of Bradshaw et al[3] relies exclusively on assumptions concerning the turbulence structure that were mainly deduced from detailed measurements in constant pressure low-speed, turbulent boundary layers. By invoking Morkovin's hypothesis[1] that the turbulence structure is unaffected by compressibility when Mach number (and hence density) fluctuations are small, the same empirical functions as used in incompressible flow[3] can be adopted for the compressible flow case[4]. Such a philosophy would appear more credible than the postulate that eddy viscosity relations between the shear stress and the mean flow are unaffected by compressibility. The mean flow is substantially altered by compressibility, especially in a longitudinal pressure gradient, but there is no justification for implying that the shear stress is altered correspondingly. Having adopted Morkovin's hypothesis, no supplementary physical input is required apart from the compressible version of the universal law of the wall for the inner boundary condition (and from which the wall shear stress is calculated). The temperature distribution across the boundary layer is prescribed by the Crocco relation (with a recovery factor, $r = 0.89$, consistent with an adiabatic wall):

$$C_p T + \tfrac{1}{2} r u^2 = C_p T_W$$

Entrainment (as a function of Mach number) is also required to scale the turbulent energy diffusion term, G. The mean continuity, momentum, and turbulent kinetic energy (shear stress) equations form a hyperbolic set whose solution is obtained by the method of characteristics. The distinctive feature of the method is that no compressibility transformations are needed. It is clear furthermore, that no simple transformation will reduce the compressible flow equations to a corresponding incompressible form.

Nash adopted the same physical reasoning as Bradshaw, to develop a three-dimensional method to calculate compressible turbulent layers[5]. With the third dimension removed, the method reduces essentially to Bradshaw's two-dimensional formulation, with but a few minor differences in the empirical input. Nash, however, elected to use a staggered-mesh, forward difference numerical scheme to solve the boundary layer equations, rather than the characteristics' routine used by Bradshaw.

2.2 Mixing-Length, Integral Turbulent Kinetic Energy Field Method of Chan

Following the pioneering work of Bradshaw et al, and Nash, an additional contribution to the technique of using the turbulent energy equation has been that of Chan, whose incompressible formulation[6] has recently been adapted to account for compressibility[7]. In this method, and what may at first sight appear to be the antithesis of Bradshaw's proposals, the phenomenological concept of mixing length is used. It is no longer correlated directly with the mean flow field of the turbulent boundary layer, however, but is scaled (in the outer layer) from an integral form of the turbulent kinetic energy equation. Hence the history of the turbulent state is considered explicitly and the mixing length correlation is permitted to vary as the boundary layer develops. Chan's method is thereby similar to the method of Bradshaw et al[4], except that in the use of an integral form of the turbulent kinetic energy equation, the pressure-velocity diffusion process is eliminated ($\int_0^\delta \frac{D}{\rho}\, dy \equiv 0$) and an assumption is made concerning the distribution of mixing length across the boundary layer.

Utilising the implication from Morkovin's hypothesis[21], and the research of Maise and McDonald[22], that compressibility will not significantly affect the character of the mixing length, the boundary layer is split into two regions: the laminar sub-layer and the exterior turbulent flow. In the former, van Driest's laminar damping is assumed, so that the mixing length is given by:

$$\ell = 0.41\, y\, [1 - \exp(-\tfrac{y}{A})]\ ,$$
$$\text{where} \qquad A = 26\, \frac{\mu}{\rho} \left(\frac{\rho}{\tau_{max}}\right)^{0.5}\ .$$

For flows in zero or favourable pressure gradients, τ_{max} identifies the surface shear stress, whereas in adverse pressure gradients, τ_{max} occurs in the sub-layer, away from the wall.

In the outer turbulent region, the turbulent shear stress term is related to the mixing length by:

$$\overline{-u'v'} = \frac{\varepsilon_{t_{outer}}}{\rho} \frac{\partial u}{\partial y} = \ell^2 \left(\frac{\partial u}{\partial y}\right)^2$$

while the turbulent kinetic energy and viscous dissipation are expressed in the form (see Reference 7):

$$\overline{-u'v'} = kq^2 = 0.15\ q^2 \ ; \ \epsilon_{t_{outer}} = \frac{(-u'v')^{1.5}}{L_\epsilon}$$

Inserting these quantities into the turbulent kinetic energy equation, and integrating across the boundary layer, a functional relation is obtained for the scaling of the mixing length, ℓ_3. The empirical inputs for k and the distribution of the dissipation length, L_ϵ, are taken from the incompressible flow formulation:

$$\frac{L_\epsilon}{\delta} = \frac{L_{\epsilon_E}}{\delta} \ \tanh\ \left[\frac{0.41}{L_{\epsilon_E}/\delta} \cdot \frac{y}{\delta} \right]$$

where $\qquad \dfrac{L_{\epsilon_E}}{\delta} = 0.09 \quad$ and $\quad \dfrac{\ell}{\ell_E} = \tanh\ \left[\dfrac{0.41}{\ell_E} \cdot y \right]$

When the scaling of the mixing length at the boundary layer outer edge is evaluated from the integral turbulent kinetic energy equation, the local state of turbulence is then known corresponding with the flow development upstream.

Once the turbulent state is provided, the two-dimensional boundary layer equations of motion (continuity, x-momentum and x-enthalpy) are transformed in terms of a stream function. In the enthalpy equation, the eddy conductivity:

$$-\rho\ \overline{v'H'} = \frac{k_T}{C_P} \ \frac{\partial H}{\partial y}$$

where the turbulent Prandtl number, $Pr_T = \dfrac{C_p \epsilon_t}{k_t} = 1$. The body surface is assumed to be thermally insulating.

The momentum equation is first of all linearised and both it and the thermal energy (enthalpy) equations are written into a finite difference form. The calculation is an iterative one: the momentum equation is integrated assuming a distribution of total enthalpy to produce a velocity field. This in turn is used to solve the enthalpy equation and the new total enthalpy distribution replaces the assumed one. The calculation is repeated until a criterion of convergence is satisfied. Details of the computation scheme are to be found in Reference 7.

2.3 Entrainment Integral Method of Head/Green

The next calculation procedure that we wish to include is a recent development by Green[11] of his earlier entrainment method[10], which used as its starting point Head's entrainment method for incompressible flow[23]. We remember that Head's physically realistic and simple formulation predicted the rate at which mainstream flow was entrained into the turbulent boundary layer. Green extended the basic assumptions of Head's method: namely, that in high Mach number flows, just as in those at low Mach number, the entrainment is related directly to the velocity defect in the outer region of the boundary layer, being adequately defined by a form parameter of the velocity profile:

$$H_1 = \frac{1}{\theta} \int_0^\delta \frac{\rho u}{\rho_E u_E} \ dy = \frac{\delta - \delta^*}{\theta}$$

It should be stressed that this integral method does not employ a transformation. Green indicates in Reference 10, in fact, that the compressibility transformations that he examined therein implied that the dimensionless entrainment rate, H_1, was invariant with Mach number in constant pressure boundary layers (which is not demonstrated in most experiments), and leads to the underestimating of boundary layer thickness at high Mach numbers.

The procedure for a solution is outlined in Reference 11. The boundary layer parameters are obtained by solving the momentum integral and entrainment equations simultaneously, with step-by-step progression downstream. Auxiliary relations for local skin friction coefficient, C_F, and a shape parameter, $\bar{H}$, are utilised, the latter being related to the usual shape factor H by:

$$H = (\bar{H} + 1)\ \frac{T_R}{T_E} - 1$$

$\bar{H}$, in turn, is explicitly related to H_1 (see Figure 25). The skin friction coefficient in an arbitrary pressure gradient is obtained from the incompressible skin friction law of Nash and Thompson coupled with the correlation[24] of Spalding/Chi for flat plate skin friction ($=C_{FO}$), to yield the following equation:

$$\left[\frac{C_F}{C_{FO}} + 0.5 \right] \left[\bar{H}\left(1 - 6.8\sqrt{\frac{C_{FO}}{2}} \right) - 0.4 \right] = 0.9\ .$$

C_F and C_{FO} occur at the same momentum thickness Reynolds number.

2.4 Momentum Integral Method of Stratford/Beavers

To retain a sense of perspective from the greater or lesser complexities of the aforementioned and subsequent methods (to be explained), the straightforward momentum integral correlation of Stratford and Beavers[12] first published in 1959, has also been included. These authors demonstrated that many of the momentum integral methods prior to

1960 could be expressed in the form:

$$\vartheta = f(M) \; \underline{X} \; R_{\underline{X}}^{-b} \; .$$

where $\underline{X}$ is an equivalent flat plate length defined by:

$$\underline{X} = P^{-1} \int_{0}^{X} P \, dX \; ,$$

and

$$P = [M/(1 + 0.2 \; M^2)]^4$$

The equivalent distance $\underline{X}$ is such that the actual boundary layer growth along the physical wetted length, X, upon attaining a final mainstream Mach number M. is the same as that which would occur over the distance $\underline{X}$ at a constant Mach number, M. If it is assumed that there is no variation of boundary layer thickness, δ, with Mach number, an accepted formula for incompressible flow may be used to derive momentum thickness, θ, and displacement thickness, δ^*, using algebraic expressions for the ratios θ/δ and δ^*/δ arranged to fit values given by a one-seventh power law, say. For mainstream Reynolds numbers of the order of 10^7, Stratford and Beavers proposed that:

$$\delta = 0.23 \; \underline{X} \; R_{\underline{X}}^{-0.1667}$$

$$\theta = 0.022 \; (1 + 0.1 \; M^2)^{-0.7} \; \underline{X} \; R_{\underline{X}}^{-0.1667}$$

$$\delta^* = 0.028 \; (1 + 0.8 \; M^2)^{0.44} \; \underline{X} \; R_{\underline{X}}^{-0.1667}$$

for a thermally insulated wall.

The ratio of compressible to incompressible skin friction coefficient at the same Reynolds number based on $\underline{X}$, for flow on a flat plate, is given by:

$$\frac{C_F}{C_{F_1}} = (1 + 0.1 \; M_E^2)^{-0.7}$$

and C_{F_1} has been taken herein from a correlation by Winter, Smith and Gaudet[25] for incompressible flat plate flow:

$$C_{F_1} = 0.0198 \; R_{\underline{X}}^{-0.1305}$$

Stratford and Beavers indicate that the equations above for δ and δ^* would be applicable only in mild or zero pressure gradients, while that for θ could be used generally. In this method, it is clear that no account is taken of the discrete turbulence structure of the boundary layer in a direct or an indirect way, and it might be expected that for non-equilibrium boundary layer flows, the method would yield poor results (see McDonald[20]).

2.5 Differential Mean Field Method of Cebeci/Smith

In the method of Cebeci and Smith[8], the algebraic details of which are somewhat complex, the continuity, momentum and thermal energy (enthalpy) equations are set down for two-dimensional flow, and the approach followed in which the turbulent boundary layer is regarded as a composite layer consisting of inner and outer regions. The two similarity laws, the law of the wall and velocity defect law of the wake, are assumed to be applicable. The Reynolds shear stress term is eliminated through the use of the eddy viscosity concept. An eddy viscosity is introduced in the inner region that is based on Prandtl's mixing length theory, with a modification to mixing length near the wall to account for the laminar sub-layer in the form suggested by van Driest (as in Chan's method). To account for compressibility, the density is again assumed variable, and a more sophisticated expression for the damping term in the van Driest law is used to account for the heat transfer in the sub-layer:

$$\epsilon_{inner} = \rho K_1^2 y^2 \left[1 - \exp\left\{ -\left(\frac{\nu_W}{\bar{\nu}}\right)^{\frac{1}{2}} \frac{y}{A} \right\} \right]^2 \left| \frac{\partial u}{\partial y} \right|$$

where $A = 26 \; \nu_W \left(\frac{\rho_W}{\tau_W}\right)^{\frac{1}{2}}$ and $\bar{\nu}$ is the mean value of ν obtained from averaging over an arbitrary distance, the sub-layer, for instance. The shear stress at the wall is thereby defined.

In the outer layer, the eddy viscosity is taken to depend upon the local density and intermittency, $\gamma(y/\delta)$, the latter function having been derived for incompressible flow as:

$$\gamma = \frac{1}{2} \left[1 - \text{erf} \; 5 \; \left(\frac{y}{\delta} - 0.78\right) \right]$$

The eddy-viscosity formula for the outer region is then:

$$\epsilon_{t_{outer}} = \rho K_2 u_E \delta^* \gamma \; , \qquad \text{where } K_2 = 0.0168 \; .$$

It is noteworthy that γ does depend upon the longitudinal pressure gradient in practical flows (see Fiedler and Head[26], for example), although such an effect is not included here. The inner and outer regions are matched at the y-station where $\epsilon_{t_{outer}} = \epsilon_{inner}$. As in Chan's method, the product $-\rho \overline{v'H'}$ in the enthalpy equation is again eliminated by utilising an eddy-conductivity concept and is introduced into the enthalpy equation by the definition of turbulent Prandtl number:

$$Pr_T = \frac{c_p \epsilon_t}{k_T}$$

It is taken as unity, although (as the authors state[8]) there is evidence to suggest that in the outer part of the boundary layer the turbulent Prandtl number approaches 2.

The boundary layer equations are then solved by first of all transforming (according to the Probstein/Elliot approach for laminar boundary layers) the physical co-ordinate system to remove the singularity at x = o and to stretch the co-ordinate normal to the flow. The laminar-type Levy-Lees transformation is then utilised to re-scale the boundary layer thickness to an order comparable to that of downstream distance. The fluid properties of specific heat at constant pressure, absolute viscosity, thermal conductivity of the fluid and enthalpy are, for convenience, expressed as power law functions of the local static temperature in the flow.

The method used to solve the boundary layer equations replaces the streamwise derivatives in both the momentum and thermal energy equations by finite differences. The momentum equation is solved in a linearised form, and the equations integrated normal to the wall utilising an implicit finite difference technique coupled with an increasing grid mesh.

2.6   The Dissipation Integral Method of Zwarts

Zwarts' approach[9,27] is based on a Crocco/Coles type transformation that reduces the compressible equations to a corresponding incompressible form. This enables the use of a reliable incompressible calculation procedure in solving the problem and Zwarts chose his own method for this purpose[27].

A two-layer model of the flow is adopted in the incompressible plane. The law of the wall is represented by the convenient expression given by Spalding in Reference 28 which includes both the laminar sub-layer, buffer layer, and the logarithmic region. The shear stress distribution in the inner layer is obtained by integrating the x-momentum equation employing the Spalding law of the wall and the continuity equation. The resulting specification of simultaneous velocity and shear stress profiles provides a solution of the inner layer.

In the outer region the velocity defect is expressed by a fourth order polynomial in (y/δ), and a constant eddy viscosity is assumed across the region:

$$\epsilon_{t_{outer}} = \frac{\tau}{\partial u/\partial y} = k\rho u_E \delta^* \; ,$$

an expression that was derived for boundary layers in nominal equilibrium. The constants in the polynomial are determined from the boundary conditions at both the mainstream and at the junction with the inner region. Across the junction, the continuity of shear stress, velocity and velocity gradient is necessary to prevent terms in the momentum equation from becoming too large in the blending region. (The remaining free parameter is determined from the integral kinetic energy equation.) The shear stress in the outer region follows from $\epsilon_{t_{outer}}$ and the defect equation. Having now specified simultaneous velocity and shear stress profiles, the outer region may be considered solved — but as Zwarts points out, with less conviction than the solution for the inner region, because of the controversy concerning the application of constant eddy viscosity when the flows are not in equilibrium. The constant, k, is normally assumed to be 0.018 (after Clauser[29]), but Zwarts has demonstrated that most velocity profiles measured in rigs immersed in supersonic wind tunnel flows experience the effects of high mainstream turbulence levels, which tend to fill out the velocity profiles.

Zwarts advocated an increase in k to compensate for high freestream turbulence levels at higher working section Mach numbers and k was set to 0.027 for the calculations presented herein. (The reader is referred to a further discussion on tunnel turbulence levels in Section 4.4, which implies that this value of k was perhaps too high.)

Coles has demonstrated that a correspondence between the incompressible and compressible continuity and x-momentum equations in two-dimensional flow can be established if the following transformation functions are introduced (where σ, η and ξ are as yet undetermined) to transform the stream function and to stretch the x and y variables:

$$\sigma(x) = \frac{\psi_1(x_1, y_1)}{\psi(x, y)}$$

$$\eta(x) = \frac{\rho_1}{\rho} \frac{\partial y_1}{\partial y}$$

$$\xi(x) = \frac{\delta x_1}{\partial x}$$

The transformation of the velocities then follows directly. These are substituted in the transport terms of the compressible momentum equation. Assuming the mainstream flow to be isentropic the momentum equation can be integrated. Its evaluation at the wall gives an expression for the transformed wall shear stress, which applies for rough or smooth walls and covers cases with mass transfer normal to the wall. The further assumption of a smooth wall in the integrated momentum equation yields one relation between the above three transformation functions. Following Crocco, the thermal energy equation is used to obtain

a second relation between the transformation functions, assuming a Prandtl number of unity and no heat transfer at the wall.

The third transformation, σ, was deduced by Zwarts via Coles "law of corresponding stations", once incompressible and compressible skin friction laws were supplied. For the incompressible flow, Spalding's wall law was assumed while the compressible skin friction coefficient form was assessed from compressible flat plate data. The equation derived for σ presupposes a constant pressure and adiabatic flow, and is only strictly true for this special case.

Zwarts' incompressible method is now combined with the transformation procedure to give a calculation method for two-dimensional compressible turbulent boundary layers in arbitrary pressure gradient, assuming the wall temperature to be equal to the mainstream stagnation temperature.

Numerically, once an external flow velocity distribution is prescribed the solution involves the simultaneous integration of four first order differential equations to determine the boundary layer parameters in the incompressible plane. The various compressible parameters of interest may subsequently be obtained using the appropriate transformations.

In closing this section, it is perhaps worth recapitulating that the methods of Zwarts and Cebeci/Smith presuppose near equilibrium conditions locally in the flow, relying upon explicit couplings between velocity gradient and shear stress. The methods of Bradshaw/Ferriss, Nash, and Chan, on the other hand, do not ignore the effects of turbulence history.

3.0 APPARATUS AND TEST

3.1 Wind Tunnel and Model Mounting

The tests were conducted in the NAE 5-ft × 5-ft blowdown wind tunnel at a nominal mainstream Mach number of 4, with the airstream stagnation pressure and temperature at 169 psia and 77°F. During a typical run of 12 seconds, the Reynolds number based on the test boundary-layer length of about 3 feet was close to 50 million in the Mach 4 flow.

The model was mounted on the strut pitching mechanism of the wind tunnel as shown on Figure 1. The roll gear was removed from the strut to shorten the moment-arm and thereby reduce the bending moment on the strut pitching linkage caused by the high loads during wind tunnel starting. The pitch system was locked so that the model was fixed at angles of incidence and yaw of 0° ± 10' with wind-off.

3.2 Model

The sectional drawing of the rig on Figure 2 illustrates its resemblance to an internal compression supersonic intake, whose internal geometry is composed of the long straight circular duct of 9-inch diameter and the translating, axisymmetric centre-body. In the cases of the zero pressure gradient and step-induced separated flows, the centre-body was held at its fully retracted position, and as such the weak shock wave disturbance from the 1° semi-cone angle spike tip just intersected the test boundary layer at the exit of the duct. The 'step' consisted of a ring of thickness 0.15 inch and width 0.5 inch, whose external diameter provided a close tolerance fit inside the duct. When used, the ring was locked to the duct wall such that the forward face of the ring was at X = 10 in. downstream of the sharp leading edge of the cowl. For the adverse pressure gradient flow, the centre-body was translated forward 21 inches (from the retracted position) in 0.5 sec., once the starting of the flow had been monitored and established by a pressure sensor in the duct. Activation of the centre-body was effected by a pressurised, hydraulic ram system (see Figure 1).

To yield the prescribed pressure distribution for the adverse pressure gradient flow, a method of characteristics was employed to design the centre-body contour, coupled with an assessment of the boundary-layer growth[9] on the internal duct surface and along the centre-body itself. At the extended (design) position of the centre-body, the mainstream flow along the test wall consisted of three regions of roughly equal length: those of the near zero, adverse (M = 4→2), and recovering pressure fields. An overall area compression ratio of about 5 was produced.

3.3 Measurements and Instrumentation

Measurements along the test wall were made of static pressure, Preston tube pitot pressure, and wall temperature. Pitot pressure profiles in the viscous flow and the mainstream pitot pressure and stagnation temperature were also recorded.

Static pressure orifices of 0.040-inch diameter were spaced at 0.5-inch intervals along the test surface at sixty-four streamwise stations. The static holes were grouped in sets of ten along diagonal rays (see Table 1) to avoid downstream disturbance of the boundary-layer flow at a nearby measuring station resulting from the local three-dimensional separations about the Preston tubes. In addition, at two axial stations, X = 11.75 inches and 21.75 inches, extra static holes were positioned around the duct circumference to check for two-dimensionality of the pressure field.

Preston tubes of 0.016-inch external diameter (see Figure 3) were adapted by means of brass collars to fit the static orifices, and were sealed at each static hole by a small

quantity of epoxy cement. Preston tube pressures were collected from all of the static orifice positions, ten at a time.

Harnesses of pneumatic tubing emanating from the seventy static orifice positions along the model test surface, conducted the surface pressures to a transducer/wafer switch assembly mounted on the outside of the cowl and protected from the tunnel mainstream by a cover. The transducer wafer unit consisted of seven 12-port wafer valves and seven minia- ture unbonded strain-gauge pressure transducers. Two equispaced ports on each wafer served as 'homes', such that three pneumatic zeroes could be obtained for each cycle of the wafer rotor. This is a necessary procedure to establish signal datum levels during a tunnel run in order to correct for transducer transient and case pressure effects.

Boundary-layer traverses for pitot pressure at six stations along the wall were ac- complished with a flattened, three-tube yawmeter or 'cobra' probe as shown on Figure 4. The two outer tubes are chamfered at 45° to form a yawmeter while the centre tube (0.028- inch wide by 0.012-inch high) measures pitot pressure. The probe is capable of translating at a preselected rate to a maximum extension of 0.8 inch in ten seconds. As it traverses through the flow, a yaw-servo system aligns the probe with the local mean flow direction, to determine any three-dimensionality of the boundary layer. A 0.5-inch diameter flat- ended steel cylinder into which the probe stem is effectively keyed provides the mechanism for yawing the probe. In so doing a small discontinuity is produced by the flat at the duct wall that might cause a tiny local flow disturbance.

An unshielded iron-constantan thermocouple, of lead diameter 0.002 inch, was mounted above the pitot orifice of the cobra probe head, to measure the variation of stagnation temperature through the boundary layer. The thermocouple was calibrated for recovery factor in an auxiliary experiment, but equipment problems unfortunately prevented the use of the thermocouple during the present tests.

The determination of wall temperature was achieved in the pressure gradient region in the upstream portion of the rig (see Table 1) and was found to be within ±5°F of the local adiabatic wall recovery temperature. The measurement was made by setting a very thin plate into the wall surface, to which the same size of unshielded thermocouple bead (as men- tioned above) was attached to the bottom surface of the plate. These thin wall plates attain equilibrium conditions quickly, but data were taken throughout the tunnel run to verify that a plateau in temperature was indeed achieved.

An additional thermocouple was mounted externally on the rig to measure the stagna- tion temperature of the mainstream. This was essentially similar in design to that used on the cobra probe and was intended to serve as a reference level against which to com- pare the output of the cobra probe thermocouple.

All of the electrical analogues of the pressure and temperature signals were relayed to the Honeywell-Brown chart recorders of the 5-ft × 5-ft tunnel data system and digitised for further processing. Analogue chart results were also gathered simultaneously during a tunnel run.

4.0 RESULTS

The essential results of the three experiments are shown on Figures 5 to 25 in terms of the distribution of Mach number, the velocity profiles and integral parameters, and the distributions of local skin friction coefficient along the duct. (Some of these results have been presented earlier[39] in a brief summary of the tests, but the comments and results herein supersede those of Reference 39.) To recapitulate, we remember that the three ex- periments were those in a near zero pressure gradient (ZPG), an adverse and recovering pressure field (APG), and the flow following a step-induced separation (RPG). The three abbreviations in brackets will be used as a shorthand notation in the following discussion.

4.1 Accuracy

The rms surface finish on the internal wall of the duct and the centre-body was close to 10 μinches with surface waviness better than 0.0002 inch per inch of surface. The maximum eccentricity between the centre-body centre-line and the duct was ±0.005 inch measured across a duct diameter.

The pitot pressures collected with the cobra probe were accurate to within ±0.04 psia. The positioning and backlash errors in the probe potentiometers and gearbox were measured on a comparator, resulting in translation and yaw accuracies within ±0.0005 inch and ±0.2° respectively.

The flattened three-tube geometry of the cobra head probe results in a displacement correction that is slightly larger than that normally taken for circular pitot tubes[30] in incompressible flow. Young and Maas[31], in some experiments with flattened tubes, made a tentative suggestion of an outward displacement correction of $0.24\ d_C$ towards the region of higher velocity, where d_C is the width of the probe face in the direction of traverse. This value has been accepted herein, for wall distances $y > 2d_C$, as Marson and Lilley[32] provide some evidence that displacement errors are not affected significantly by compres- sibility. For distances closer to the wall than $y = 2d_C$, the displacement error decreases continuously as the wall is approached, and may be expressed conveniently in terms of a function of d_C/y and $u_\tau d_C/\nu$, where the latter quantity when based on wall conditions varied between 100 and 500 in the present tests. An analogous representation of Macmil- lan's total displacement effect for $y/d_C \le 2$ was derived for the cobra probe, to include the above range of $u_\tau y/d_C$ as

$$\frac{\Delta}{d_C} = 0.24 - 0.04 \left(\frac{d_C}{y} - 0.5\right) \qquad\qquad 4.1.1$$

No corrections for the effect of turbulence on the pitot readings have been employed.

Errors due to large static pressure holes (i.e. relative to the boundary-layer displacement thickness, δ^*) can be important in the reduction of boundary-layer profile measurements and when using surface Preston tubes to determine surface shear stress. Rainbird[33] found that in subsonic and supersonic zero pressure gradient flows at high Reynolds numbers, large static orifices (where $d_S/\delta^* = 10$) gave pressure errors, ΔP, typically twenty times the value of the undisturbed surface shear stress. In the present experiments, the parameter d_S/δ^* was always ≤ 1 (except in the laminar boundary-layer region close to the duct leading edge), so that the influence of d_S/δ^* was not significant in the regions along the duct where there was turbulent flow. In fact the correlation of Franklin and Wallace[34] for deep holes has been adopted, but extended to compressible flow by inserting the local wall conditions of density and temperature. The following curve fit has been chosen to represent the correlation, namely:

$$\frac{\Delta P}{\tau_W} = 3.71 \left[1 - \exp\left\{-0.0021 \left(\frac{u_{\tau W} d_S}{\nu_W} - 95\right)\right\}\right] \qquad\qquad 4.1.2$$

except when $u_{\tau W} d_S/\nu_W < 200$, then,

$$\frac{\Delta P}{\tau_W} = \frac{1}{800} \left(\frac{u_{\tau W} d_S}{\nu_W}\right) + 0.5 \left(\frac{u_{\tau W} d_S}{\nu_W} \cdot \frac{1}{200}\right)^2 \qquad\qquad 4.1.3$$

The functional relationship in the above expression follows from the law of the wall and the assumption that the static pressure hole error will be a function of the velocity u at a distance y from the wall, which is dependent on d_S[33]. Hence, provided a law of the wall region exists in the adverse pressure gradient flow, we may argue that the hole error correction should be applicable there, as in the zero pressure gradient flow case, noting that local conditions at the wall should be used in the hole error formulae.

The inaccuracies in measurement and repeatability indicate that the maximum errors in local Mach number and skin friction determination are $\Delta M = \pm 0.02$ and $\Delta C_F = \pm 0.0001$.

The tunnel stagnation pressure is controlled typically to within $\pm 0.1\%$ of the mean stagnation pressure level during any given run, which is to within ± 0.2 psi in the present tests.

4.2 Mach Number Distributions Along the Duct

Figure 5 displays the Mach number distributions along the duct for the three test flows determined as a function of corrected wall static pressure (for hole error) to stream stagnation pressure. Isentropic flow through the duct was assumed in the zero pressure gradient (ZPG) and adverse pressure gradient (APG) cases, but a calculation was made for the loss in stagnation pressure through the oblique shock waves existing upstream and downstream of the ring, equal to about 30 percent of the Mach 4 mainstream stagnation pressure. The reflections of these shock waves are incident upon the test boundary layer in the RPG case near $X = 29$ inches where a noticeable sharp drop in Mach number occurs.

With the centre-body extended for the APG flow, the adverse pressure gradient commences virtually at its design position after 11.75 inches of near zero pressure gradient flow. The centre-body pressure field then compresses the mainstream from Mach 4 to Mach 2 along the following 10 inches of duct, according to an initial cosine and subsequent exponential function, that when plotted appears almost linear. A slightly favourable pressure gradient then materialises along the remainder of the duct.

4.3 Tests for Two-Dimensionality of the Boundary Layers

It was emphasised in Section 1 that one of the aims of the experiment was to produce a compressible turbulent boundary layer free from end-wall constraints.

Figures 6a and 6b show some sample circumferential variations in Mach number at $X = 11.75$ inches and 21.75 inches downstream of the leading edge. Reference to Figure 5 indicates that the former station is upstream of the applied pressure field in the APG case, whereas the latter is in the Mach 2 region. Examples from the three test flows are shown, plotted relative to the Mach number at the circumferential angle, $\phi = 50°$. For many of the runs, we note that the discrepancies around the periphery are contained within the maximum error band in Mach number measurement, $\Delta M = \pm 0.02$, although with the centre-body extended, there is a consistent trend in the sign of the variation at each station. We note further that with the centre-body retracted, the ZPG and RPG flows yield no real improvement in circumferential Mach number distribution, the implication being that the centre-body is situated concentrically within the duct.

The cobra head yawmeter probe provided a second means of determining whether any cross-flow was present in the test boundary layers. Figures 7a and 7b show some typical yaw angle outputs as a function of distance from the duct wall, at the traverse stations corresponding to $X = 16.62$ and 31.62 inches — refer to Figure 5 again for these positions relative to the pressure rise. The initial angular setting on the surface is denoted by $\psi = 0°$, but this does not necessarily represent an absolute zero angle of yaw. It is more revealing to compare the total yaw movement in the boundary layer relative to the mainstream setting at the extremities of the profiles. It will be seen that the skew angle

registered by the probe for the zero pressure gradient flow is within the 'deadband' error of ±0.2° for the instrument. Both the adverse pressure gradient and step-induced pressure gradient flows indicate a skewing in the inner layer of 1° to 1.5° relative to the mainstream direction. Such a small yaw is deemed acceptable, especially as it does not increase significantly between $X = 16.62$ and 31.62 inches.

A third method of checking for two-dimensionality is by means of oil dot flow visualisation, some examples of which are illustrated on Figure 8. The strips of thin paper adhesive tape were placed in the duct along the axial direction beginning at the cowl leading edge, and oil dots applied before a tunnel run. Because of the low energy flow at the base of the boundary layer, the limiting streamlines are very receptive to changing direction as a result of transverse pressure gradients. A plot of the shear stress trajectories, therefore, is a sensitive indicator of three-dimensionality in the inner regions of the viscous flow. The flow visualisation along more than half of the duct wall for the three test cases demonstrates no particular convergence or divergence; non-parallelism of the oil streaks with the tape edges is due to the tape being slightly offset from a longitudinal surface generator. Additional tapes, not shown, that adhered to the downstream region of the duct, demonstrated the same lack of skew.

From this examination, we feel that three-dimensionalities are small enough around the duct at a given axial station, to claim that nominal two-dimensional test conditions have been achieved.

4.4 Transition Location

As the Mach number of a supersonic mainstream increases, it becomes more and more difficult in wind tunnels to promote transition of a compressible laminar boundary layer by artificial means. This is due to an increasing stability of the laminar flow with increase of Mach number, that is accentuated with cooling of the wall. A three-dimensional roughness element, to cause transition at a length Reynolds number of about one million at Mach 4 (which would be close to the leading-edge of the cowl in the present experiment) would require a height about equal to the local boundary layer thickness. Now, the three-dimensional protuberance-type separations produced by each roughness element give rise to longitudinal vortices, whose effect would be unknown on enhancing the diffusion characteristics of the turbulent boundary layer. In addition, undesirable distortion of the mean boundary layer profiles would result. For these reasons, it was preferred to allow transition to develop naturally, when calculations through natural transition could then be attempted using the method of Cebeci and Smith[8].

The transition regions are indicated qualitatively by the reduction in oil streak lengths near the cowl leading-edge on Figure 8, and quantitatively on Figure 9, by the Preston tube measurements. The Preston tube correlations that determine skin friction coefficient (and which are listed in Section 4.5) cannot be accepted as accurate in laminar flow, of course, but the surface impact tube is, notwithstanding, a useful instrument to indicate the mean boundaries of the transition region. From these measurements, the transition region appears to commence at $X = 2$ inches at the trough of the C_F distributions (where R_X is 2.8 million); and to finish where the maximum in the C_F curve occurs, at $X = 6.5$ inches (where $R_X = 9$ million). The oil dot flow visualisation supports this diagnosis, although there is some evidence of a changing transition position around the duct.

At the high unit Reynolds number of the present tests of about 1.4 million per inch, an extrapolation of the results of Hastings and Sawyer[35] collected on a flat plate model at Mach 4, indicates consistency with the Preston tube results quoted above. Hastings and Sawyer also made visible the transition regions by sublimation of azobenzene coatings, and concluded that the surface pitots indicated a broader transition region than did the sublimation technique, although the sublimation patterns were certainly dependent on the time taken for their establishment.

The length of the transition region is surprising, perhaps, for it implies a relatively low mainstream turbulence level at the tunnel centre-line, in an intermittent blow-down facility not previously noted for its low turbulence content. The pressure fluctuations measured with flush-mounted microphones in the working-section wall at Mach 4[36] have been shown independent of those measured at the wall in the settling chamber. This result is attributable to the closure of the tunnel nozzle for Mach 4 operation, the small throat size restricting the propagation downstream of most of the control valve noise. The major source of the sound field at the tunnel centre-line must therefore be the turbulent boundary layers on the tunnel walls. However, since the fluctuating pressure field external to the boundary layer is swept downstream with a velocity of the same order as the mainstream[37] the pressure fluctuations would travel along the local directions of the Mach waves. The implication here is that the wall boundary layers not far downstream of the tunnel throat are the only parts of the tunnel viscous flow that can radiate acoustical disturbances to the tunnel centre-line in the vicinity of the rig (note that the duct itself provides an effective shield for the test flow). The fluctuating pressure level calculated using Reference 37 would imply a turbulence level (velocity fluctuations) of less than 0.1 percent at the high unit Reynolds numbers of the present experiments, all of which would appear to be consistent with the measurements of Pate and Schueler[38].

4.5 Local Skin Friction Measurements Compared with Calculations

The experimental skin friction data obtained from the correlations described in Appendix 1 are listed in Tables 2, 3, and 4, and shown on Figure 9a, for the respective flow cases of ZPG, APG and RPG. For these three flows, the Tables and the Figure indicate that the values of C_F given by the Preston tube Hopkins/Keener T'-method and the Sigalla

T'-method are nominally within ±5 percent of each other. For the most part, the Fenter/ Stalmach correlation yields consistently lower values, while the Hopkins/Keener T_W-method provides higher values. The Sommer/Short T'-R_θ correlation is close to the T' Preston tube correlations in the ZPG and RPG flows, and shows a general scattering of values about these Preston tube correlations in the APG case. By comparison, Wilson's R_θ method produces the largest C_F values of all the correlations considered herein.

From these cursory assessments, the bias has been to consider the Hopkins/Keener T'-method and the Sommer/Short T'-R_θ correlation as respective representatives of the Preston tube and velocity profile data. These are plotted on Figure 9b and compared against the various calculations described in Section 3.

We note first of all that most of the C_F calculations in the ZPG flow are virtually indistinguishable from the measurements. (A 10 percent spread does appear because the computations with the methods of Zwarts and Cebeci/Smith are somewhat above the other calculations due to higher C_F starting values.) The bottom graph on Figure 9b illustrates that the reattached boundary layer downstream of the ring generated separation exhibits a rapid recovery to a near zero pressure gradient development. All of the calculations except Bradshaw's and Nash's indicate C_F values that are higher than the measurements because of the difficulty in interpreting appropriate C_F starting conditions. In contradistinction, the calculations in the APG flow do not agree in trend with the experiment (the one exception being the Stratford/Beavers' method). In the upstream region of the pressure rise, the experiment indicates an increase in C_F whereas the calculations show a decrease. Further downstream, the experimental values of C_F overshoot the values that one would observe in a constant pressure flow (Zwarts found the same phenomenon[9]) while the calculated skin friction coefficients approach the constant pressure boundary layer values from below. In addition, the experiment shows an unexpected hump in the region of pressure rise preceding the entry to the flow relaxation at Mach 2. The hump, in fact, follows the trend of the Preston tube pressure coefficient, C_{PP}, rather than that of the Preston tube pressure itself (see Figure 10), as a result of a sudden local increase in the static pressure gradient. The bumpy character of the calculations employing the Zwarts and Cebeci/Smith methods is due to the utilisation of a different smoothing routine on the experimental static pressure data.

In view of the discrepancy between the calculations and the experimental APG results, which do we suspect as providing wrong information?

In the APG experiment, there is encouraging consistency between the values of C_F calculated from the Preston tubes and from the velocity profiles. To support the argument that the Preston tube correlation may be applied, we refer to the limitations on Preston tube calibrations given by Patel[44] and Brown and Joubert[48]. Patel showed that in incompressible flow, a pressure-gradient parameter that measured the strength of the streamwise pressure gradient as it affected the flow in the law of the wall region was $\alpha\nu/u_{\tau W}^3$, where $\alpha = \rho^{-1}(dp/dx)$. Through the pressure rise region of the present experiment, this parameter, using either wall (or intermediate temperature) values for determining ν, ρ and $u_{\tau W}$, is no larger than about 0.003, in the same region where $u_{\tau W}D/\nu$ increases to about 900. This value of $\alpha\nu/u_{\tau W}^3$ is clearly less than the value of 0.01 ascribed by Patel to yield a maximum error of 3 percent on Preston tube correlations in adverse pressure gradient. Correspondingly, Patel stipulated that $u_{\tau W}D/\nu$ should be $\leqslant 200$, however, and this value is exceeded. Nevertheless, Brown and Joubert[48], again in incompressible flow, considered that in severe adverse pressure gradients, the parameter $\alpha D/u_{\tau W}^2$ was a better criterion on which to base the failure of Preston tube correlations, than was $\alpha\nu/\rho u_{\tau W}^2$. For the APG case, $\alpha D/u_{\tau W}^2$ is no greater than 1.2, whereas Brown and Joubert stipulate the first signs of failure of the correlations will only occur when $\alpha D/u_{\tau W}^2 \geq 1.41$. The errors in measured C_F should be less than one percent, according to these criteria. For the existence of a logarithmic region in the boundary layer (which is seen on Figure 14), Brown and Joubert also suggested that $\alpha\nu/u_{\tau W}^3 < 0.05$, which it certainly is in the APG case, being around 0.003. Contrary to Patel's arbitrary limits on Reynolds number ($u_{\tau W}D/\nu$), the extrapolation of the area beneath the one percent error line on Brown and Joubert's plot of $\alpha\nu/u_{\tau W}^3$ versus $u_{\tau W}D/\nu$, would allow an almost infinite $u_{\tau W}D/\nu$ corresponding to $\alpha\nu/u_{\tau W}^3 = 0.003$. Finally, the specification of the 0.0167-inch diameter of the Preston tube was chosen to be within the permissible maximum and minimum limits suggested by Hopkins and Keener[40] (and consistent with an adequate response time when coupled to the pneumatic measuring system). McDonald's work[49] would additionally support the views expressed already that the pressure gradient is insufficiently adverse to affect seriously the character of the laminar sub-layer from its flat plate form, so that again, we would interpret that there is no violation of the universal law of the wall.

So far, then, the conclusion of these assessments is that the Preston tube correlations are valid in the APG flow case. Bradshaw[4] suggests that if the Preston tube correlations are believed, the large overshoot in skin friction witnessed in the relaxation from the adverse pressure gradient could occur "if the lifetime of the turbulent eddies were far longer in supersonic flow than in low-speed flow, but that none of our current physical ideas about turbulence support this". Having assessed the effects of streamwise pressure gradient thoroughly, the remaining test is to query the effect of pressure gradient normal to the streamwise flow direction.

McDonald[20] discussed that if the mainstream flow is of the simple-wave type, then to the usual boundary layer approximation

$$\left(\frac{\partial p}{\partial x}\right)_E = - \frac{1}{\sqrt{M_E^2 - 1}} \left(\frac{\partial p}{\partial y}\right)_E \qquad 4.5.1$$

That is, *in any supersonic flow with a large streamwise pressure gradient*, $(dp/dx)_E$, *the pressure gradient normal to the wall will also be large.* If a linear distribution of static pressure with distance from the wall is assumed to be given by equation 4.5.1 for the present APG flow, the static pressure at the boundary layer edge during the streamwise pressure rise becomes less than that at the wall. The recalculation of the skin friction coefficient of the Sommer/Short $R_\theta - T'$ method results in a reduction from 0.00128 to 0.00115 at the second profile station, and from 0.00149 to 0.00146 at the third station. Now the Preston tube correlations are based on mainstream values derived with reference to local wall static pressure that is assumed constant across the boundary layer. The effect of the normal pressure gradient then, is to increase the Mach number at the boundary layer edge; reference to equation A1.10 will indicate that C_F will be thereby reduced. *Thus we may contend that the Preston tube correlations are valid for adverse pressure gradient flows of the type discussed herein, provided the true mainstream values are used.* To accomplish this, the local boundary layer thickness must be known along the whole wetted length of the surface.

We now attempt to justify the trends of the calculation procedures as being correct. Why, if no normal pressure gradient is entered into the calculations do the computed C_F values compare (qualitatively, at least) with the measured C_F values that have taken account of an assumed normal pressure gradient? When reference is made to the logarithmic velocity profiles on Figure 14 for the APG flow (see traverse T2 at X = 16.62-inches), the profile determined when the normal pressure gradient is assumed, is little different from the profile plotted, which was derived assuming constant static pressure across the boundary layer. This result is not surprising because the only relevant Mach number in the inner layer law is that based on u_{TW} and speed of sound at the wall. The mainstream Mach number does not appear. Thus in the APG flow, the law of the wall region is not altered significantly in terms of mean velocity as a result of the normal pressure gradient and hence the skin friction calculated from assuming the properties of the inner region will furnish the correct trends in the C_F distributions. (The skin friction calculation in the Stratford/Beavers' method follows the trend of the Preston tube results on Figure 9 — with no normal pressure gradient — because the correlation contains a Mach number function based on M_E.)

4.6 Mach Number and Velocity Profiles

The Mach number profiles were calculated from the measured cobra probe pitot pressures and the wall static pressures (corrected for hole error as outlined in Section 4.1) using the Rayleigh pitot relationship. As well as assuming the constancy of static pressure across the boundary layer, the Mach number distributions in the APG flow case were also computed by utilising the linear reduction in static pressure across the boundary layer that was implied by equation 4.5.1. The profiles at stations T2 and T3 in the pressure rise are the most affected by normal pressure gradient.

References 35 and 50 provide evidence that a parabolic distribution of static temperature across the boundary layer:

$$\frac{T}{T_E} = \frac{T_R}{T_E} - \left(\frac{T_R}{T_E} - 1 \right) \left(\frac{u}{u_E} \right)^2 \qquad 4.6.1$$

agrees with the profiles for measured temperatures when the recovery factor is taken as 0.89 (that is, for zero heat flow). These quantities were used to reduce the present data into density and velocity profiles, assuming the same respective static pressure conditions listed above. The profile data for the three boundary layer test cases are listed in Tables 5 to 7.

Figures 11 and 12 present the experimental normalised Mach number and velocity profiles at each traverse station for all of the three boundary layer experiments. The 'roller-coaster' initial profiles measured in the ZPG and APG flows (both in nominal constant pressure regions) display some effects of the long transition length. The distortion of the initial profile in the RPG flow is a result of its proximity to the system of compression waves near the line of flow re-attachment, downstream of the ring. Severe static pressure gradients normal to the wall would be expected there, so that the RPG initial profile can only be considered qualitative at best. The distortions introduced into the boundary layer mean flow as it negotiates the abrupt changes caused by the ring shock/expansion wave system might be anticipated to decay slowly with distance downstream. Instead, the rapid destruction of the initial profile unevenness in the RPG (and ZPG) cases is attributable to the higher diffusion rate of the turbulent kinetic energy at Mach numbers near 4, than at the lower Mach numbers existing in the APG flow. In the latter case, the character of the initial profile is carried downstream in the flow, along the remainder of the boundary layer wetted length. Such a phenomenon is consistent with a falling non-dimensional entrainment rate as the Mach number reduces through the region of the pressure rise.

Semi-logarithmic plots of the velocity profiles are drawn on Figures 13, 14 and 15 and compared against Spalding's single formula for the law of the wall[28]. If the linear range is taken to be $100 < y u_{TW}/\nu_W < 300$, the profiles in the equilibrium ZPG and non-equilibrium RPG cases indicate reasonable agreement in slope with the wall law, their varying discrepancy in vertical displacement and slope from the wall law being caused perhaps by inaccuracies in the determination of u_{TW}. In the APG flow, the linearity boundaries on $y u_{TW}/\nu_W$ must be relaxed, for the pressure rise moves the profiles towards higher values of $y u_{TW}/\nu_W$. (In all of the above, the shearing stress velocity is based on the density at an adiabatic wall.) The third and fourth traverses of the APG flow demonstrate an irreclaimable lack of similarity in the inner regions, but the large changes in

the slopes of the linear regions cannot be attributed to the normal pressure gradient. It will be remembered that in Section 4.5, although the normal pressure gradient was seen to affect the skin friction coefficient, $u_{\tau W}$ itself was not changed, because M_E is not featured in the law of the wall. A further point to note is that the traverses at the entry to the relaxation region (T4 and T5) in the APG flow case, show that the flow in proceeding towards equilibrium overshoots the equilibrium gradient of the wall law to then recover subsequently by the time the fifth traverse station is reached.

Further insight into the experimental results of the three test cases is provided by the velocity defect profiles on Figure 16. For purposes of reference, the correlation of Winter and Gaudet[35] is plotted for constant pressure boundary layers at Mach 4. As before, $u_{\tau W}$ is based on the density at an adiabatic wall and (for the defect profiles) δ is taken at the distance from the wall where $u/u_E = 0.995$. An inspection of these profiles on Figure 16 suggests that wake similarity is not achieved in either the ZPG or APG flows until the boundary layer has travelled 20-inches or more downstream. The lack of simi- larity of the upstream profiles is credited to the history effects of the long transition length. What is further revealing is the large velocity defect of the RPG flow profiles, recovery towards a constant pressure condition occurring only at the fifth traverse station. (The sixth station has been affected by the ring shock wave system reflecting from the centre-line that causes a significant shock/boundary layer interaction.)

Figures 17 and 18 enable a comparison to be made between the experimental velocity profiles (plotted with respect to the physical coordinate, y, normal to the surface) and the turbulent energy calculation methods of Bradshaw/Ferriss, Nash, and Chan; as well as the methods of Zwarts and Cebeci/Smith. The turbulent energy methods were initialised just downstream of the leading-edge, with respectively Bradshaw's Mach 4 shear stress and velocity profiles (in the methods of Bradshaw/Ferriss and Nash), and in Chan's case, the shear stress profile was generated from Bradshaw's same velocity profile. The dummy start at the $X = 1.5$-inch station (which is located in the transition region of the physical flow field, of course) provided a long marching region of zero pressure gradient flow at Mach 4, before the pressure rise was applied in the APG case, to dampen any mismatching in input conditions. Bradshaw and Ferriss[51] indicate that 40 boundary-layer thicknesses downstream of the start should be more than adequate, for most purposes of calculation, to remove the effects of initial perturbations, and in the present comparisons, approximately 50 boundary-layer thicknesses were used.

The proximity of the first traverse station to the backward face of the ring in the RPG test case, resulted in the necessity of starting the calculation downstream of the step, at or near the first traverse station, T1. A number of plausible shear stress pro- files, that included a maximum value of τ away from the wall, was tried in the Bradshaw/ Ferriss calculation, but all except zero pressure gradient type profiles (when input with the first measured velocity profile downstream of the ring) produced instabilities in the downstream integrations. Hence the starting conditions for the ring case were not physi- cally realistic in the Bradshaw/Ferriss calculation; on the other hand, a realistic shear stress profile with $\tau_{max} \approx 1.5 \tau_W$ was found to work in Nash's method. The outcome of the two calculations, however, are little different.

The starting conditions for these and the remaining methods are listed on Table 8.

Figure 17 displays gratifying agreement between the calculated and experimental ZPG profiles, the turbulent energy and Cebeci/Smith methods indicating slightly fuller pro- files near the wall, while that of Zwarts is slightly less full than the experiment. The agreement between the Preston tube and corresponding cobra probe velocities is also satis- factory. The APG flow comparison is provided on Figure 18. Here we see that the inner regions of the experimental profiles are not predicted adequately by any of the methods, the profiles in the regions of pressure rise and recovery revealing a curious overshoot as though tending to behave in an accelerating flow. The differences between the APG vel- ocity profiles calculated by the turbulent kinetic energy methods of Bradshaw and Chan on the one hand, and Nash on the other, are also difficult to explain. In Nash's method, the dissipation length and the diffusion function differ by about 10 percent from the values given by Bradshaw and used by Chan. The other essential difference is in the mathematical treatments, and streamwise interpolation procedures, although Nash has done extensive tests (private communication) to prove his numerical accuracy. (Note that the relatively small effect of the normal pressure gradient on the velocity profile shape is not included on these experimental profiles plotted on Figure 18, but reference to Figure 12 will indi- cate that the remarks above will still apply.) Because of the difficulty in the RPG case of providing the correct shear stress input, the profiles are predicted in trend as shown on Figure 19, but do not demonstrate quantitative agreement.

4.7 Integral Parameters

For incompressible turbulent boundary layers in arbitrary pressure gradients, the Stanford Proceedings demonstrated that most calculation methods when compared with experi- ment will determine the momentum thickness adequately, the displacement thickness satis- factorily, and the skin friction coefficient to (very often) only fair or poor accuracy. Clearly, the crucial test for the success or failure of a computation method in compres- sible flow will still be the accurate prediction of the most sensitive and important parameter, C_F. As we have noted in Section 4.5, in the APG flow, the calculations all agree qualitatively with one another, but that their discrepancy with experiment was attributed to the effects of static pressure gradient normal to the wall.

Now although the velocity profiles in the disturbed boundary layer flows indicate

differences between experiment and calculation (especially in the APG and RPG cases) the integral parameters appear to yield closer agreement.

The integral properties were calculated from the velocity and density profiles (see Tables 5 to 7), accounting for the radius of the duct, a procedure contributing to the balancing of the momentum integral equation (of which more later). The equations defining displacement thickness, δ^*, momentum thickness, θ, and so on, are as for two-dimensional flow with the factor $(1 - y/R)$ inserted into the integrands. The effect of $(1 - y/R)$ upon the integral parameters is typically about 1 percent.

The integral parameters, δ^*, θ and shape factor, H, are plotted on Figures 20, 21 and 22 for the ZPG, APG and RPG test cases. With increasing X, typical flat plate variations of δ^* and θ increasing, and H slightly decreasing, are seen for the ZPG flow (Figure 20) and the same feature is discerned on Figure 22 for the RPG flow. In the ZPG flow, all calculation procedures provide good prediction, with the unsophisticated Stratford/Beavers' method yielding answers as valid as the more physically sound methods of Bradshaw/Ferriss and Green, for example. In the RPG case, the Stratford/Beavers' calculation again provides a good fit with the experimental results (Figure 22). The starting conditions for the RPG calculations are not all identical. It will be noted that re-adjustment of the initial point would collapse the curves onto a single line.

Figure 21 shows also that all calculation methods are useful in predicting δ^*, θ and H for the APG flow. No appreciable improvement with increase of method complexity appears obvious, so that one might conclude that the various models of the turbulence structure (where used) are all satisfactory — certainly, for the three test cases considered here. On the other hand, we still observe good results with methods which do not consider the turbulence structure. Furthermore, the experimental points when compared with Green's functional relationship[11] of the transformed shape parameter, $\bar{H}$, versus the entrainment shape parameter, H_1, (derived from flows relaxing downstream of shock/boundary layer interactions) are seen to indicate on Figure 25, a higher non-dimensional entrainment rate for a given H. Such discrepancies might be caused in part by the sensitivity of H_1 and $\bar{H}$ to the values of the experimental points near the wall. Inaccuracies in determining the cobra probe Mach number through the effect of the higher turbulence levels near the wall on the cobra pitot tube readings are unknown in compressible flow. In addition, the displacement effect induced by the relatively large lateral dimension of the cobra probe head with respect to its height, as a result of the local three-dimensional protuberance type separation at the wall — see References 52 and 53 — might perhaps not be well described by equations 4.1.2 and 4.1.3. Notwithstanding, if these discrepancies in H_1 and $\bar{H}$ between experiment and calculation were true, then it would not appear to hamper too seriously the prediction with Green's method.

As we have seen on Figure 21 for the APG case, there is a dominating influence of the pressure gradient on the compressible shape factor H, where the significant decrease through the pressure rise is well predicted by all of the seven calculation methods. The rapid return of H towards a flat plate constant pressure condition, in the Mach 2 relaxation region (the implication of which we note is also on the velocity defect profiles on Figure 16) is because the pressure gradient was apparently not steep enough for a significant loss of local equilibrium to occur. Although the Bradshaw/Ferriss calculation imposes a constraint on the development of the turbulence, concomitant with the assumptions in the method, if the calculated shear stress profiles are accepted as representative of the experimental flow, they disclose that a maximum is achieved in the profile equal to about $2.5 \tau_W$ at the traverse T3. This decays rapidly to almost zero pressure gradient form in the 6-inches between T3 and T5. Furthermore, the plotting of the incompressible velocity shape factor:

$$H_{12}^i = \int_0^\delta \left(1 - \frac{u}{u_E}\right)dy \bigg/ \int_0^\delta \frac{u}{u_E}\left(1 - \frac{u}{u_E}\right)dy \qquad 4.7.1$$

on Figure 24, confirms that the pressure gradient is relatively weak, for H_1^i in incompressible flow and in strong adverse pressure gradients reaches values of 2.4 or more. Consistent with this idea are the 'full' or convex rather than 'hollow' velocity profiles that are obtained throughout the test flow. Nevertheless, the APG case may be viewed as a good test for compressibility (the density increasing by a factor of 8 through the pressure rise) without the imposition of strong shock waves.

Winter[50] noted that the incompressible or velocity shape parameter, H_{12}^i, exerted a powerful influence on the skin friction coefficient in measurements on his waisted body model at Mach numbers up to 2.8. If this is so at Mach 4, a small change in H_{12}^i in going from the ZPG to the APG flow case produces a large and significant change in skin friction (Figure 9).

Finally, Figure 23 shows the experimental distribution of momentum thickness Reynolds number along the test surface, based on local external flow quantities. We should note the decrease in R_θ at the last traverse station of the APG flow. Here the boundary layers from the duct wall and the centre-body had coalesced, thereby restraining the growth of the test boundary layer. The corresponding decrease in δ^* and θ is indicated on Figure 21.

4.8 Closure of the Integrated Momentum Equation

McDonald noted that in some of the poorly predicted boundary layers examined in his paper in Reference 20, the two-dimensional von Karman momentum equation was sadly out-of-balance. He felt that the out-of-balance was much larger than that which could be blamed

on three-dimensional effects and pondered whether the usual neglect of the normal Reynolds stress terms in the von Karman equation was the contributing cause. The further possibility remained that normal pressure gradient effects were significant. We have noted already the large changes in skin friction coefficient resulting from the inclusion of a static pressure gradient across the boundary layer in the region of the pressure rise in the APG flow. We should like to consider this in further detail in relation to the closure of the momentum integral equation.

If only the normal Reynolds stress terms are neglected, the momentum equation can be written in the form (see Reference 20):

$$\frac{d\theta}{dX} + \frac{1}{u_E}\frac{du_E}{dX}(2\theta + \delta^*) + \frac{\theta}{\rho_E}\frac{d\rho_E}{dX} + \frac{1}{\rho_E u_E^2}\frac{d}{dX}\left[P_E\delta - \int_0^\delta \overline{P}dy\right] = \frac{C_F}{2} \qquad 4.8.1$$

When the static pressure is constant across the boundary layer, $P \neq P(y)$, and the equation reduces to its well known form. At the boundary layer edge,

$$\frac{dP_E}{dX} = \rho_E u_E \frac{du_E}{dX} \qquad 4.8.2$$

Utilising this in the momentum equation 4.8.1, we obtain

$$\frac{d}{dX}(\rho_E u_E^2\theta) - \delta^*\frac{dP_E}{dX} + \frac{d}{dX}\left[P_E\delta - \int_0^\delta \overline{P}dy\right] = \frac{C_F}{2} \qquad 4.8.3$$

If we now choose to integrate between the limits of $X = X_{START}$ and X, we obtain:

$$(\rho_E u_E^2\theta)_X - (\rho_E u_E^2\theta)_{X_{ST}} - \int_{X_{ST}}^X \delta^*dP + \left[P_E\delta - \int_0^\delta \overline{P}dy\right]_{X_{ST}}^X = \int_{X_{ST}}^X 0.5\ \rho_E u_E^2 C_F dX \qquad 4.8.4$$

In attempting to balance the momentum equation, the integral form is to be preferred over the differential form as the differentiation of experimental values leads to serious errors. We may set X_{ST} at the first traverse station, i.e. $X_{ST} = 11.62$-inches, and assess the balance with continuing progression downstream, from traverse station to traverse station. The calculated effects of the normal pressure gradient on θ and δ^* as well as on C_F were included in the APG case. The alternative is to calculate a momentum thickness by inserting the remaining terms from the experimental measurements and to compare this calculated result with the measured. This was not done because θ is generally insensitive to large changes in other parameters.

It was found that for the ZPG flow, the momentum integral equation indicated reasonable balance provided the skin friction coefficient of Wilson was utilised, although the right hand side of equation 4.8.4 was consistently low by about 5 percent.

In the APG flow, no agreeable balance was obtained until the normal pressure gradient terms were included. The balance was fair until the third profile at the entry of the recovery region was reached when the left hand side of equation 4.8.4 became 25 percent larger. In any event, the left hand side of the equation was again always higher than the right hand side, irrespective of the experimental C_F distribution assumed, and one must presumably attribute this to the omission of the longitudinal gradient of the Reynolds normal shear stress contribution.

5.0 CONCLUSIONS

Measurements have been made of three turbulent boundary-layer flows in a parallel duct, where the initial mainstream Mach number was 4 and the Reynolds number based on the 33-inch wetted surface was close to 50 million.

The outcome was that:

1. Nominal two-dimensional boundary layers were achieved.

2. The seven compressible turbulent boundary layer calculation methods used were all more-or-less successful in predicting the integral parameters of the zero pressure gradient, adverse pressure gradient, and recovering boundary-layer flows. Those methods that predicted mean velocity profiles did well in the zero pressure gradient flow, but not so well in the other two tests. No improvement in prediction was noted with increase of sophistication of the calculation method.

3. The skin friction distributions calculated by the seven boundary-layer methods were close to the Hopkins/Keener intermediate temperature correlation of the Preston tube results in the zero and recovering pressure fields. However, the calculated surface shear stress through the pressure rise in the adverse pressure gradient flow did not agree with the experiment, the discrepancy being assigned tentatively to the effects of normal static pressure gradients.

4. It is hoped that the reasonable comparison obtained between the calculations and the experimental results is sufficiently comprehensive and of practical use to encourage workers in the field of compressible turbulent boundary layers to engage in further and more refined experiments. Particular emphasis should still be placed on flows in adverse pressure gradients, and on flows recovering to equilibrium after experiencing

local gross disturbances. As well as the mean measurements accomplished, attention should be directed towards measuring the gradients of static pressure and stagnation temperature across the boundary layer, and where feasible, the measurement of turbulent shear stress. Such effort would seem more appropriate and useful than indulging in more and more variations on a theme of calculation.

6.0 ACKNOWLEDGEMENTS

The authors would like to acknowledge that the concept and design of the test originated with S. Molder and W.J. Rainbird. They would especially like to thank Y.Y. Chan, J.F. Nash and H.D. Harris, in addition, for their enthusiastic and constructive inputs throughout the course of the experiments and the analysis; and to W.J. Rainbird, P. Bradshaw, J.E. Green and M.R. Head, for their effective and critical discussion.

APPENDIX 1. LOCAL SKIN FRICTION CORRELATIONS

Several of the existing functional equations for calibrating Preston tubes in compressible flow were used, and compared with correlations based on the momentum thickness Reynolds number derived from velocity profile data.

In general, the compressible flow Preston tube data can be collapsed onto a relevant incompressible correlation:

$$R_{D_i}^2 \, C_{PP_i} = f \, [R_{D_i}^2 \, C_{F_i}] \tag{A1.1}$$

by writing:

$$R_{D_C}^2 \, C_{PP_C} = f \, [R_{D_C}^2 \, C_{FC}] \, , \tag{A1.2}$$

the subscripts i and C referring to incompressible and compressible flow, respectively, and where

$$R_{D_C}^2 \, C_{PP_C} = 8 \, [(P_P - P_E)D^2/4\rho_C v_C^2] \tag{A1.3}$$

and

$$R_{D_C}^2 \, C_{FC} = 8 \, [\tau_W D^2/4\rho_C v_C^2] \tag{A1.4}$$

R_D is the Reynolds number based on Preston tube diameter and local conditions at the edge of the boundary layer, C_{PP} is the Preston tube pressure coefficient, and C_F is the local skin friction coefficient. The remaining terms are defined in the List of Symbols.

The straightforward substitution of wall density and wall viscosity into the latter two equations did not satisfactorily collapse compressible flat plate Preston tube data onto the incompressible correlation of Preston. Hopkins and Keener[40],[41] demonstrated, however, that the effects of compressibility could be accounted for successfully by replacing the pressure difference $(P_P - P_E)$ by the dynamic pressure determined from this pressure difference, coupled with the adopting of an intermediate temperature hypothesis. This proposes that one relation for surface shear stress may be found for both incompressible and compressible flows if the density and kinematic viscosity are calculated at temperature, T', a value between the wall and external stream static temperature. The form of T' given in Reference 42 by Sommer and Short has been used herein:

$$T' = T_E \left[1 + 0.035 \, M_E^2 + 0.45 \left(\frac{T_W}{T_E} - 1\right)\right] \tag{A1.5}$$

where the wall temperature, T_W, is considered to be that of an adiabatic wall with recovery factor, $r = 0.89$:

$$T_W = T_R = T_E (1 + 0.178 \, M_E^2) \tag{A1.6}$$

The resulting functional equation for compressible flow, in the form of equation A1.2, becomes:

$$f_2(T')R_D^2(M_P/M_E)^2 = f[f_2(T')R_D^2 C_F] \tag{A1.7}$$

where

$$f_2(T') = \left(\frac{\mu_E}{\mu'}\right)^2 \frac{\rho'}{\rho_E} = \left(\frac{T' + 198.6}{T_E + 198.6}\right)^2 \left(\frac{T_E}{T'}\right)^4 \tag{A1.8}$$

with T in °R,

and

$$R_D = \frac{u_E D}{v_E} \tag{A1.9}$$

M_P is the Mach number calculated from the local static pressure (assumed constant across the boundary layer) and the Preston tube pressure, via the Rayleigh pitot equation. For consistency, the static hole error was still subtracted from the measured wall static pressure, although it is realised that none of the Preston tube correlations to date have involved this correction. It is noteworthy that Hopkins and Keener found[41] after their publication of Reference 40 that the equation for the law of the wall that is implied by the author's correlation factors did not agree adequately with measured velocity profiles. One reason for this discrepancy is probably due to the omission of the static hole error, or in other words, the inappropriate scaling of the local static pressure hole with respect to the size of the Preston tube. Secondly, we should note that Preston's original calibration in incompressible flow[43] has been shown to be somewhat in error, and revised calibration curves have since been evolved — see the work of Patel[44], for example.

Moreover, Patel determined that the values of the constants appearing in the logarithmic region of the law of the wall were in excellent agreement with measured velocity distributions in the wall region of both pipe and boundary layer flows. Hence the Hopkins/Keener correlations can be criticised on the basis of their determination with respect to Preston's incompressible flow calibration that was slightly in error.

The following table summarises the Preston tube correlations used herein:

METHOD	CALIBRATION FACTORS		EQUATION NUMBER
	$\log_{10}[R_{D_C}^2 c_{PP_C}]$ =	$m \log_{10}[R_{D_C}^2 c_{F_C}]$ + Constant	
HOPKINS/KEENER, T', (Ref.40,Eq.4)	$\log_{10}[f_2(T')R_D^2(M_P/M_E)^2]$	$1.132 \log_{10}[f_2(T')R_D^2 c_F]+1.517$	A1.10
HOPKINS/KEENER, T_W, (Ref.40,Eq.9)	$\log_{10}[f_2(T_W)R_D^2 c_{PP}]$	$1.162 \log_{10}[f_2(T_W)R_D^2 c_F]+1.552$	A1.11
SIGALLA, T', (Ref.45)	$\log_{10}[\nu_E/\nu')R_D(u_P/u_E)]^2$	$1.145 \log_{10}[f_2(T')R_D^2 c_F]+1.420$	A1.12
FENTER/STALMACH (Ref.46)	$\log_{10}\left[(\nu_E/\nu_W)R_D \sin^{-1}\left(\sqrt{\sigma_E}\frac{u_P}{u_E}\right)/\sqrt{\sigma_E}\right]^2$	$1.118 \log_{10}[f_2(T')R_D^2 c_F]+1.568$	A1.13

Hopkins and Keener[40] did simplify their intermediate temperature formulation to one that was based on wall results by replacing T' by T_W, see equation A1.11. Sigalla[45] also devised a reference temperature method where (P_P-P_E) in equation A1.3 was replaced by $0.5 \rho' u_P^2$, which thereby required the local static temperature to be determined as well as the Preston tube Mach number. Finally, Fenter and Stalmach[46], who utilised Wilson's theory[47] (see below) to develop a compressible law of the wall, applied this to obtain a Preston tube correlation in supersonic adiabatic flow, which resulted in equation A1.13.

Two methods, those of Wilson[47] and Sommer/Short[42] based on the momentum thickness Reynolds number of the boundary layer profiles were also used.

Wilson's correlation is:

$$\left(\frac{\sin^{-1}\sqrt{\sigma_E}}{\sqrt{\sigma_E}}\right)^{-2}\left(\frac{T_W}{T_E}\right)c_F = \frac{1}{[4.15 \log_{10}(R_\theta \frac{\mu_E}{\mu_W}) + 2.78]^2} \qquad \text{A1.14}$$

where

$$\sigma_E = \frac{0.2 M_E^2}{1 + 0.2 M_E^2} \qquad \text{A1.15}$$

In the Sommer/Short method[42], the properties of the flow such as density and viscosity are based on the reference temperature, T', see equation A1.5. The compressible equation for local skin friction in terms of Reynolds number based on momentum thickness and the von Karman/Schoenherr incompressible equation was derived as:

$$\left(\frac{T'}{T_E}\right)c_F = \frac{1}{17.076[\log_{10}(R_\theta \frac{\mu_E}{\mu'})]^2 + 25.112 \log_{10}(R_\theta \frac{\mu_E}{\mu'}) + 6.012} \qquad \text{A1.16}$$

In all of the methods where the wall temperature, T_W, is required, it is assumed to be given by equation A1.6. It should be emphasised that all of the above correlations were developed in nominally zero pressure gradient flows, with the postulate that they should still be adequate in mild, arbitrary pressure gradients. Patel in Reference 44 indicated the range of validity of Preston tube calibrations in incompressible flow (since updated by Brown and Joubert[48]) where Patel concluded that provided a logarithmic region existed, the calibrations could be used.

REFERENCES

1   Kline, S.J., Morkovin, M.V., Sovran, G., and Cockrell, D.J., eds.: "Computation of Turbulent Boundary Layers - 1968 AFOSR-IFP-Stanford Conference; Volume I - Methods, Predictions, Evaluation and Flow Structure". August 1968

2   Coles, D.E., Hirst, E.A., eds.: "Proceedings - Computation of Turbulent Boundary Layers - 1968 AFOSR-IFP-Stanford Conference; Volume II - Compiled Data". August 1968.

3   Bradshaw, P., Ferriss, D.H., Atwell, N.P., "Calculation of Boundary-Layer Development Using the Turbulent Energy Equation", NPL Aero. Rept. 1182, January 1966.

4   Bradshaw, P., Ferriss, D.H., "Calculation of Boundary-Layer Development Using the Turbulent Energy Equation. II - Compressible Flow on Adiabatic Walls". NPL Aero. Rept. 1217, November 1966; also Journal of Fluid Mechanics (1971), vol. 46, part 1, pp.83-110.

5   Nash, J.F., "An Explicit Scheme for the Calculation of Three-Dimensional Turbulent Boundary Layers", ASME Paper 71-FE-19, May 1971.

6   Chan, Y.Y., "Turbulent Boundary Layer Computations Based on an Extended Mixing Length Approach", AIAA Journal, vol. 8, no.10, October 1970, pp.1873-1875.

7   Chan, Y.Y., "Compressible Turbulent Boundary Layer Computations Based on an Extended Mixing Length Approach", Submitted to CASI Transactions, September 1971.

8   Smith, A.M.O., Cebeci, T., "Numerical Solutions of the Turbulent Boundary Layer Equations", Douglas Aircraft Company Report No. DAC 33735, May 1967.

9   Zwarts, F.J., "The Compressible Turbulent Boundary Layer in a Pressure Gradient", Ph.D. Thesis, McGill University, Department of Mechanical Engineering, July 1970.

10   Green, J.E., "The Prediction of Turbulent Boundary-Layer Development in Compressible Flow", Journal of Fluid Mechanics, vol. 31, part 4, 1968; pp.753-778.

11   Head, M.R., "Entrainment Approach, VKI Short Course on Turbulent Boundary Layers", VKI LS5, March 1968.

12   Stratford, B.S., Beavers, G.S., "The Calculation of the Compressible Turbulent Boundary Layer in an Arbitrary Pressure Gradient - A Correlation of Certain, Previous Methods", ARC R and M No. 3207, 1961.

13   Michel, R., "Résultats sur La Couche Limite Turbulence aux Grandes Vitesses", ONER Technical Memo. 22, July 1961.

14   McLafferty, G.H., Barber, R.E., "Turbulent Boundary Layer Characteristics in Supersonic Streams Having Adverse Pressure Gradients", United Aircraft Corporation Research Dept., R-1285-11, September 1957.

15   Kepler, C.E.D., O'Brien, R.L., "Supersonic Turbulent Boundary-Layer Growth Over Cooled Walls in Adverse Pressure Gradients", United Aircraft Corporation Research Department ASD-TDR 62-87, 1962.

16   Bradshaw, P., "The Analogy Between Streamline Curvature and Buoyancy in Turbulent Shear Flow", Journal of Fluid Mechanics, vol. 36, part 1, 1969, pp.177-191.

17   Myring, D.F., Young, A.D., "The Isobars in Boundary Layers at Supersonic Speeds", The Aeronautical Quarterly, vol. XIX, May 1968, pp.105-126.

18   Joseph, K.C., McCorquodale, J.A., Sridhar, K., "Power Law for Turbulent Cylindrical Boundary Layers", The Aeronautical Journal, vol. 75, January 1971, pp.46-48.

19   Green, J.E., "Reflection of an Oblique Shock Wave by a Turbulent Boundary Layer", RAE TR 68256, October 1968.

20   McDonald, H., "An Assessment of Certain Procedures for Computing the Compressible Turbulent Boundary Layer Development", Compressible Turbulent Boundary Layers, NASA SP-216, December 1968, pp.181-229.

21   Morkovin, M.V., "Mécanique de la Turbulence", Colloques Inter. du C.N.R.S., No. 108, 367, 1962. (Also available as "The Mechanics of Turbulence", New York; Gordon and Breach.)

22   Maise, G., McDonald, H., "Mixing Length and Kinematic Eddy Viscosity in a Compressible Boundary Layer", AIAA Journal, vol. 6, No. 1, January 1968, pp.73...

23   Head, M.R., "Entrainment in the Turbulent Boundary Layer", ARC R and M 3152, 1958.

24   Spalding, D.B., Chi, S.W., "The Drag of a Compressible Turbulent Boundary Layer on a Smooth Flat Plate with and without Heat Transfer", Journal of Fluid Mechanics, vol. 18, part 1, 1964, pp.117-143.

25   Winter, K.G., Smith, K.G., Gaudet, L., "Measurements of Turbulent Skin Friction at High Reynolds Numbers at Mach Numbers of 0.2 and 2.2", Recent Developments in Boundary Layer Research, AGARDograph 97, May 1965, pp.103-123.

26   Fiedler, H., Head, M.R., "Intermittency Measurements in the Turbulent Boundary Layer", Journal of Fluid Mechanics, vol. 25, 1966, pp.719...

27   Zwarts, F.J., "The Development of an Incompressible Turbulent Boundary Layer in an Arbitrary Pressure Gradient", McGill University, Department of Mechanical Engineering Report No. 65-7, October 1965.

28   Spalding, D.B., "A Single Formula for the Law of the Wall", Journal of Applied Mechanics, September 1961, pp.455-458.

29   Clauser, F.H., "Turbulent Boundary Layers in Adverse Pressure Gradients", Journal of the Aeronautical Sciences, vol. 21, No. 2, February 1954, pp.91-108.

30   MacMillan, F.A., "Experiment on Pitot Tubes in Shear Flow", ARC R and M 3128, 1957

31   Young, A.D., Maas, J.N., "The Behaviour of a Pitot Tube in a Transverse Total-Pressure Gradient", ARC R and M 1770, 1936.

32   Marson, G.B., Lilley, G.M., "The Displacement Effect of Pitot Tubes in Narrow Wakes", College of Aeronautics, Cranfield: COA Report No. 107, 1956.

33   Rainbird, W.J., "Errors in Measurement of Mean Static Pressure of a Moving Fluid due to Pressure Holes", DME/NAE Quarterly Bulletin, No. 1967(3), National Research Council of Canada, October 1967.

34   Franklin, R.E., Wallace, J.M., "Absolute Measurements of Static-Hole Error Using Flush Transducers", Journal of Fluid Mechanics, vol. 42, part 1, 1970, pp.33-48.

35   Hastings, R.C., Sawyer, W.G., "Turbulent Boundary Layers on a Large Flat Plate at M=4", RAE TR 70040, March 1970.

36 Westley, R., "Aerodynamic Sound and Pressure Fluctuations in a Supersonic Blowdown Wind Tunnel", National Research Council of Canada Aeronautical Report LR-272 January 1960.

37 Phillips, O.M., "On the Generation of Sound by Supersonic Turbulent Shear Layers", Journal of Fluid Mechanics, vol. 9, 1960, pp.1...

38 Pate, S.R., Schueler, C.J., "Radiated Aerodynamic Noise Effects on Boundary Layer Transition in Supersonic and Hypersonic Wind Tunnels", AIAA Journal, vol. 7, No. 3, March 1969, pp.450-457.

39 Peake, D.J., Romeskie, J.M., Brakmann, G., "Some Preliminary Assessments of Compressible Turbulent Boundary-Layer Studies at Mach 4 and at High Reynolds Numbers, Including Flows in Relaxing and Adverse Pressure Gradients", NRC DME/NAE Quarterly Bulletin 1971(1), April 1971, pp.27-76.

40 Hopkins, E.J., Keener, E.R., "Study of Surface Pitots for Measuring Turbulent Skin Friction at Supersonic Mach Numbers - Adiabatic Wall", NASA TN D-3478, 1956.

41 Keener, E.R., Hopkins, E.J., "Use of Preston Tubes for Measuring Hypersonic Turbulent Skin Friction", AIAA Paper No. 69-345, April 1969. (Also NASA TN D-5544, November 1969.)

42 Sommer, S.C., Short, B.J., "Free-Flight Measurements of Turbulent-Boundary-Layer Skin Friction in the Presence of Severe Aerodynamic Heating at Mach Numbers from 2.8 to 7.0. NACA TN 3391, 1955. (Also Journal of Aeronautical Sciences, vol. 23, No. 6, June 1956.)

43 Preston, J.H., "The Determination of Turbulent Skin Friction by Means of Pitot Tubes", ARC 15748, (FM 1883), 1953.

44 Patel, V.C., "Calibration of the Preston Tube and Limitations on its use in Pressure Gradients", Journal of Fluid Mechanics, vol. 23, part 1, 1965, pp.185-208.

45 Sigalla, A., "Calibration of Preston Tubes in Supersonic Flow", AIAA Journal, vol. 3, No. 8, August 1965, pp.1531...

46 Fenter, F.W., Stalmach, C.J., "The Measurement of Local Turbulent Skin Friction at Supersonic Speeds by Means of Surface Impact Pressure Probes", Report DRL 392, CM 878, University of Texas, 1957.

47 Wilson, R.E., "Turbulent Boundary-Layer Characteristics at Supersonic Speeds - Theory and Experiment", Journal of Aerospace Sciences, vol. 17, No. 9, September 1950, pp.585-594.

48 Brown, K.C., Joubert, P.N., "The Measurement of Skin Friction in Turbulent Boundary Layers with Adverse Pressure Gradients", Journal of Fluid Mechanics, vol. 35, part 4, 1969, pp.737-757.

49 McDonald, H., "The Effect of Pressure Gradient on the Law of the Wall in Turbulent Flow", Journal of Fluid Mechanics, vol. 35, part 2, 1969, pp.311-336.

50 Winter, K.G., Rotta, J.C., Smith, K.G., "Studies of the Turbulent Boundary Layer on a Waisted Body of Revolution in Supersonic Flow", ARC R and M No. 3633, 1970.

51 Bradshaw, P., Ferriss, D.H., "The Effect of Initial Conditions on the Development of Turbulent Boundary Layers", ARC CP 986, 1968.

52 Rainbird, W.J., Crabbe, R.S., Peake, D.J., Meyer, R.F., "Some Examples of Separation in Three-Dimensional Flows", CASI Journal, vol. 12, No. 6, December 1966, pp.409-423.

53 Peake, D.J., Rainbird, W.J., Atraghji, E.G., "Three-Dimensional Flow Separations on Aircraft and Missiles", To be published in AIAA Journal, 1971.

TABLE 1: LOCATIONS OF SURFACE STATIC PRESSURE ORIFICES AND 'COBRA' PROBE ORIFICE

COWL — COBRA PROBE UNIT — 0° φ (FRONT VIEW)
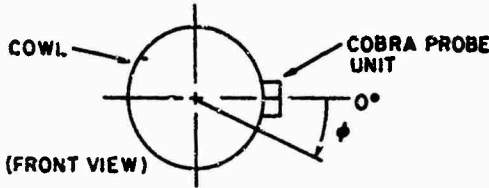
RAY ANGLE, φ (Degrees)	DISTANCE FROM LEADING EDGE, X (Inches)							
40	0.25		8.25	12.25	16.25	20.25	24.75	28.75
45	0.75	4.75	8.75	12.75	16.75	20.75	25.25	29.25
50	11.75	21.75	31.75					
55	1.25	5.25	9.25	13.25	17.25	21.25	25.75	29.75
60	1.75		9.75	13.75	17.75	22.25	26.25	30.25
65	2.25	5.75	10.25	14.25	18.25	22.75	26.75	30.75
70	2.75	6.75	10.75	14.75	18.75	23.25	27.25	31.25
75	3.25	7.25	11.25	15.25	19.25	23.75	27.75	32.25
80	3.75	7.75	15.75	19.75	24.25	28.25	32.75	
140	11.75	21.75						
230	11.75	21.75						
320	11.75	21.75						

Distance to:

							Distance to:
0	11.62	16.62	20.62	22.62	26.62	31.62	Cobra probe face
0		16.75					Adiabatic wall temperature probe

TABLE 2: SKIN FRICTION CORRELATIONS IN ZERO PRESSURE GRADIENT FLOW

C_F CALCULATED FROM CORRELATIONS BY FENTER & STALMACH, HOPKINS & KEENER, AND SIGALLA:
HOPKINS & KEENER CORRELATION WITH (1): ADIABATIC WALL RECOVERY TEMPERATURE,T_R, AND (2): INTERMEDIATE TEMPERATURE,T', AS INPUT;
STATIC PRESSURES CORRECTED FOR HOLE ERROR GIVEN BY FRANKLIN & WALLACE

P_0 = 168.9 PSIA; T_0 = 537.0 °R

X	P_W	ΔP F&W	M_E	u_E	T_E	ρ_E	T_R	T'	C_{PP}	R_D	$\frac{u_{\tau W} d_S}{\nu_W}$	C_F F&S	C_F HKTR	C_F HKT'	$u_{\tau W}$	C_F SIG
0.03	1.187	0.025	3.952	2210.5	130.2	0.00076	492.3	364.3	0.420	0.230E 05	0.247E 03	0.00143	0.00227	0.00187	131.2	0.00157
0.53	1.205	0.012	3.941	2208.9	130.8	0.00077	492.3	364.6	0.234	0.231E 05	0.199E 03	0.00103	0.00137	0.00118	104.1	0.00119
1.03	1.215	0.005	3.934	2208.0	131.1	0.00078	492.4	364.7	0.132	0.232E 05	0.162E 03	0.00073	0.00084	0.00078	84.2	0.00087
1.53	1.220	0.003	3.931	2207.7	131.3	0.00078	492.4	364.8	0.089	0.232E 05	0.144E 03	0.00059	0.00062	0.00060	74.4	0.00072
2.03	1.222	0.003	3.930	2207.4	131.3	0.00078	492.4	364.8	0.115	0.232E 05	0.141E 03	0.00057	0.00059	0.00059	73.1	0.00070
2.53	1.223	0.005	3.929	2207.4	131.3	0.00078	492.4	364.8	0.161	0.232E 05	0.155E 03	0.00067	0.00074	0.00070	79.9	0.00081
3.03	1.222	0.007	3.930	2207.6	131.3	0.00078	492.4	364.8	0.207	0.232E 05	0.175E 03	0.00082	0.00099	0.00089	90.2	0.00097
3.53	1.220	0.010	3.931	2207.6	131.3	0.00078	492.4	364.8	0.207	0.232E 05	0.191E 03	0.00095	0.00123	0.00107	99.1	0.00111
4.03	1.219	0.014	3.932	2207.7	131.2	0.00078	492.4	364.8	0.264	0.232E 05	0.209E 03	0.00095	0.00151	0.00129	108.6	0.00126
4.53	1.219	0.015	3.932	2207.8	131.2	0.00078	492.4	364.7	0.280	0.232E 05	0.214E 03	0.00114	0.00159	0.00135	111.2	0.00129
5.03	1.219	0.016	3.932	2207.7	131.2	0.00078	492.4	364.8	0.292	0.232E 05	0.218E 03	0.00117	0.00165	0.00139	112.9	0.00132
5.53	1.220	0.016	3.931	2207.6	131.3	0.00078	492.4	364.8	0.303	0.232E 05	0.221E 03	0.00119	0.00171	0.00144	114.6	0.00134
6.03	1.220	0.016	3.931	2207.6	131.3	0.00078	492.4	364.8	0.303	0.232E 05	0.221E 03	0.00119	0.00170	0.00143	114.2	0.00134
6.53	1.221	0.016	3.931	2207.6	131.3	0.00078	492.4	364.8	0.300	0.232E 05	0.221E 03	0.00117	0.00169	0.00140	113.2	0.00132
7.03	1.222	0.015	3.930	2207.5	131.3	0.00078	492.4	364.8	0.294	0.232E 05	0.219E 03	0.00115	0.00166	0.00137	111.8	0.00130
7.53	1.223	0.014	3.929	2207.4	131.4	0.00078	492.4	364.8	0.285	0.232E 05	0.216E 03	0.00112	0.00161	0.00132	109.8	0.00127
8.03	1.225	0.013	3.928	2207.3	131.4	0.00078	492.4	364.8	0.272	0.233E 05	0.212E 03	0.00109	0.00155	0.00127	107.7	0.00124
8.53	1.226	0.012	3.928	2207.1	131.4	0.00078	492.4	364.8	0.259	0.233E 05	0.209E 03	0.00106	0.00149	0.00122	105.4	0.00121
9.03	1.227	0.012	3.927	2207.1	131.5	0.00078	492.4	364.9	0.246	0.233E 05	0.205E 03	0.00104	0.00142	0.00119	104.2	0.00119
9.53	1.227	0.012	3.927	2207.0	131.5	0.00078	492.4	364.9	0.238	0.233E 05	0.202E 03	0.00102	0.00138	0.00117	103.2	0.00117
10.03	1.228	0.011	3.926	2207.0	131.5	0.00078	492.4	364.9	0.231	0.233E 05	0.200E 03	0.00101	0.00135	0.00115	102.2	0.00116
10.53	1.229	0.011	3.926	2206.9	131.5	0.00078	492.4	364.9	0.226	0.233E 05	0.199E 03	0.00100	0.00132	0.00114	101.8	0.00115
11.03	1.229	0.011	3.925	2206.8	131.6	0.00078	492.4	364.9	0.223	0.233E 05	0.198E 03	0.00099	0.00131	0.00113	101.3	0.00115
11.53	1.230	0.011	3.925	2206.7	131.6	0.00079	492.4	364.9	0.221	0.233E 05	0.197E 03	0.00099	0.00129	0.00112	101.0	0.00114
12.03	1.232	0.011	3.924	2206.4	131.7	0.00079	492.4	364.9	0.219	0.233E 05	0.197E 03	0.00099	0.00129	0.00112	100.9	0.00114
12.53	1.234	0.011	3.923	2206.2	131.7	0.00079	492.4	364.9	0.219	0.233E 05	0.196E 03	0.00098	0.00128	0.00111	100.6	0.00113
13.03	1.237	0.011	3.921	2205.9	131.8	0.00079	492.4	365.0	0.217	0.234E 05	0.196E 03	0.00098	0.00127	0.00110	100.2	0.00113
13.53	1.241	0.011	3.919	2205.5	131.9	0.00079	492.4	365.0	0.215	0.234E 05	0.196E 03	0.00097	0.00126	0.00109	99.8	0.00112
14.03	1.246	0.011	3.916	2205.0	132.1	0.00079	492.5	365.1	0.213	0.234E 05	0.196E 03	0.00097	0.00125	0.00109	99.6	0.00112
14.53	1.252	0.011	3.912	2204.6	132.2	0.00079	492.5	365.2	0.210	0.234E 05	0.196E 03	0.00096	0.00124	0.00108	99.0	0.00112
15.03	1.256	0.011	3.909	2204.2	132.4	0.00080	492.5	365.2	0.209	0.235E 05	0.196E 03	0.00096	0.00123	0.00107	98.8	0.00111
15.53	1.261	0.011	3.907	2203.9	132.5	0.00080	492.5	365.3	0.207	0.235E 05	0.196E 03	0.00095	0.00122	0.00107	98.3	0.00111
16.03	1.265	0.010	3.904	2203.7	132.6	0.00080	492.5	365.3	0.205	0.235E 05	0.196E 03	0.00095	0.00122	0.00106	98.1	0.00110
16.53	1.268	0.010	3.903	2203.6	132.7	0.00080	492.5	365.4	0.205	0.235E 05	0.196E 03	0.00095	0.00121	0.00106	97.8	0.00110
17.03	1.269	0.010	3.902	2203.5	132.8	0.00080	492.5	365.4	0.203	0.236E 05	0.196E 03	0.00094	0.00120	0.00105	97.7	0.00110
17.53	1.271	0.010	3.901	2203.4	132.8	0.00080	492.5	365.4	0.202	0.236E 05	0.195E 03	0.00094	0.00120	0.00105	97.4	0.00109
18.03	1.271	0.010	3.901	2203.4	132.8	0.00080	492.5	365.4	0.201	0.236E 05	0.195E 03	0.00093	0.00118	0.00104	97.1	0.00109
18.53	1.270	0.010	3.901	2203.5	132.8	0.00080	492.5	365.4	0.200	0.236E 05	0.194E 03	0.00093	0.00118	0.00104	96.8	0.00108
19.03	1.269	0.010	3.902	2203.6	132.7	0.00080	492.5	365.4	0.200	0.235E 05	0.194E 03	0.00093	0.00118	0.00104	96.8	0.00109
19.53	1.267	0.010	3.903	2203.7	132.7	0.00080	492.5	365.4	0.199	0.235E 05	0.184E 03	0.00093	0.00118	0.00104	96.7	0.00108

TABLE 2: (continued)

X	P_W	$\Delta P_{F\&W}$	M_E	u_E	T_E	ρ_E	T_R	T'	C_{PP}	R_D	$\dfrac{u_{TW}d_S}{\nu_W}$	C_P F&S	C_P HKTR	C_P HKT'	u_{TW}	C_P SIG
22.03	1.265	0.010	3.904	2203.9	132.6	0.00080	492.5	365.3	0.198	0.235E 05	0.193E 03	0.00093	0.00117	0.00103	96.6	0.00108
22.53	1.263	0.010	3.905	2204.1	132.6	0.00080	492.5	365.3	0.197	0.235E 05	0.193E 03	0.00093	0.00117	0.00103	96.4	0.00108
23.03	1.260	0.010	3.907	2204.3	132.5	0.00080	492.5	365.3	0.196	0.235E 05	0.192E 03	0.00092	0.00116	0.00103	96.4	0.00108
23.53	1.257	0.010	3.909	2204.6	132.4	0.00080	492.5	365.2	0.196	0.235E 05	0.191E 03	0.00092	0.00116	0.00103	96.3	0.00107
24.03	1.254	0.010	3.911	2204.9	132.3	0.00080	492.5	365.2	0.195	0.234E 05	0.191E 03	0.00092	0.00116	0.00102	96.2	0.00107
24.53	1.250	0.009	3.913	2205.2	132.2	0.00079	492.5	365.1	0.194	0.234E 05	0.190E 03	0.00092	0.00116	0.00102	96.1	0.00107
25.03	1.247	0.009	3.915	2205.4	132.1	0.00079	492.5	365.1	0.194	0.234E 05	0.190E 03	0.00091	0.00115	0.00102	96.1	0.00107
25.53	1.242	0.009	3.918	2205.8	131.9	0.00079	492.4	365.1	0.193	0.234E 05	0.189E 03	0.00091	0.00115	0.00102	96.1	0.00107
26.03	1.239	0.009	3.920	2206.1	131.8	0.00079	492.4	365.0	0.192	0.233E 05	0.188E 03	0.00091	0.00115	0.00102	96.2	0.00107
26.53	1.236	0.009	3.922	2206.3	131.8	0.00079	492.4	365.0	0.193	0.233E 05	0.188E 03	0.00092	0.00115	0.00102	96.3	0.00107
27.03	1.233	0.009	3.923	2206.6	131.7	0.00079	492.4	364.9	0.193	0.233E 05	0.188E 03	0.00092	0.00116	0.00102	96.5	0.00107
27.53	1.230	0.009	3.925	2206.8	131.6	0.00078	492.4	364.9	0.194	0.233E 05	0.188E 03	0.00092	0.00116	0.00102	96.7	0.00107
28.03	1.226	0.009	3.927	2207.1	131.5	0.00078	492.4	364.8	0.194	0.232E 05	0.187E 03	0.00092	0.00116	0.00103	96.8	0.00108
28.53	1.223	0.009	3.929	2207.4	131.4	0.00078	492.4	364.8	0.195	0.232E 05	0.187E 03	0.00092	0.00117	0.00103	97.0	0.00108
29.03	1.220	0.009	3.931	2207.6	131.3	0.00078	492.4	364.8	0.196	0.232E 05	0.187E 03	0.00092	0.00118	0.00103	97.2	0.00108
29.53	1.217	0.009	3.933	2207.9	131.2	0.00078	492.4	364.7	0.197	0.232E 05	0.187E 03	0.00093	0.00117	0.00103	97.3	0.00108
30.03	1.214	0.009	3.935	2208.2	131.1	0.00078	492.3	364.7	0.197	0.232E 05	0.187E 03	0.00093	0.00117	0.00103	97.2	0.00108
30.53	1.216	0.009	3.934	2208.0	131.1	0.00078	492.4	364.7	0.196	0.232E 05	0.187E 03	0.00093	0.00117	0.00103	97.2	0.00108
31.03	1.225	0.009	3.928	2207.2	131.4	0.00078	492.4	364.8	0.195	0.233E 05	0.188E 03	0.00092	0.00116	0.00103	96.8	0.00107
31.53	1.261	0.009	3.907	2204.2	132.5	0.00080	492.5	365.3	0.190	0.235E 05	0.190E 03	0.00091	0.00113	0.00100	95.2	0.00106
32.03	1.308	0.010	3.880	2200.4	133.9	0.00082	492.7	365.9	0.185	0.238E 05	0.193E 03	0.00089	0.00110	0.00098	93.3	0.00104
32.53	1.511	0.010	3.774	2185.0	139.5	0.00091	493.3	368.3	0.158	0.250E 05	0.203E 03	0.00080	0.00093	0.00086	85.1	0.00094
INS.	PSIA	PSIA		FT/SEC	°R	SLUGS/CU.FT.	°R	°R							FT/SEC	

TABLE 3: SKIN FRICTION CORRELATIONS IN ADVERSE PRESSURE GRADIENT FLOW

C_F CALCULATED FROM CORRELATIONS BY FENTER & STALMACH, HOPKINS & KEENER, AND SIGALLA;
HOPKINS & KEENER CORRELATION WITH (1): ADIABATIC WALL RECOVERY TEMPERATURE, T_R, AND (2): INTERMEDIATE TEMPERATURE, T', AS INPUT;
STATIC PRESSURES CORRECTED FOR HCLE ERROR GIVEN BY FRANKLIN & WALLACE

P_0 = 169.2 PSIA; T_0 = 537.0 °R

X	P_W	$\Delta P_{F\&W}$	M_E	U_E	T_E	ρ_E	T_R	T'	C_{PP}	R_D	$\frac{u_{\tau w} d_s}{\nu_w}$	C_F F&S	C_F HKTR	C_F HKT'	u_{TW}	C_F SIG
0.0	1.189	.025	3.952	2210.5	130.2	0.00077	492.3	364.3	0.420	0.230E 05	0.247E 03	0.00143	0.00227	0.00186	131.2	0.00157
0.5	1.207	.012	3.941	2208.9	130.8	0.00077	492.3	364.6	0.234	0.232E 05	0.199E 03	0.00103	0.00137	0.00118	104.1	0.00118
1.0	1.217	.005	3.934	2208.0	131.1	0.00078	492.4	364.7	0.132	0.232E 05	0.162E 03	0.00073	0.00084	0.00077	84.2	0.00067
1.5	1.222	.003	3.931	2207.7	131.3	0.00078	492.4	364.8	0.097	0.233E 05	0.144E 03	0.00059	0.00062	0.00060	74.3	0.00072
2.0	1.224	.005	3.930	2207.4	131.4	0.00078	492.4	364.8	0.089	0.233E 05	0.142E 03	0.00067	0.00059	0.00059	73.1	0.00070
2.5	1.225	.007	3.929	2207.4	131.3	0.00078	492.4	364.8	0.115	0.233E 05	0.155E 03	0.00067	0.00074	0.00070	79.9	0.00081
3.0	1.224	.010	3.930	2207.6	131.3	0.00078	492.4	364.8	0.161	0.233E 05	0.175E 03	0.00082	0.00099	0.00089	90.2	0.00097
3.5	1.222	.014	3.931	2207.7	131.2	0.00078	492.4	364.8	0.207	0.233E 05	0.192E 03	0.00099	0.00123	0.00107	99.1	0.00111
4.0	1.221	.015	3.932	2207.8	131.2	0.00078	492.4	364.3	0.264	0.233E 05	0.215E 03	0.00110	0.00151	0.00129	108.6	0.00125
4.5	1.220	.016	3.932	2207.7	131.2	0.00078	492.4	364.8	0.280	0.232E 05	0.216E 03	0.00114	0.00159	0.00135	111.2	0.00129
5.0	1.221	.016	3.932	2207.7	131.2	0.00078	492.4	364.8	0.292	0.233E 05	0.218E 03	0.00117	0.00165	0.00139	112.6	0.00132
5.5	1.221	.016	3.931	2207.6	131.3	0.00078	492.4	364.8	0.303	0.233E 05	0.221E 03	0.00119	0.00170	0.00144	114.6	0.00134
6.0	1.222	.016	3.931	2207.6	131.3	0.00078	492.4	364.8	0.303	0.233E 05	0.222E 03	0.00119	0.00170	0.00144	114.5	0.00134
6.5	1.222	.016	3.931	2207.5	131.3	0.00078	492.4	364.8	0.294	0.233E 05	0.221E 03	0.00117	0.00169	0.00143	114.1	0.00132
7.0	1.223	.015	3.930	2207.4	131.4	0.00078	492.4	364.8	0.285	0.233E 05	0.219E 03	0.00115	0.00166	0.00140	113.2	0.00132
7.5	1.224	.014	3.929	2207.3	131.3	0.00078	492.4	364.8	0.272	0.233E 05	0.216E 03	0.00112	0.00161	0.00137	111.8	0.00130
8.0	1.225	.013	3.928	2207.1	131.3	0.00078	492.4	364.8	0.256	0.233E 05	0.213E 03	0.00109	0.00155	0.00132	109.7	0.00127
8.5	1.226	.012	3.928	2207.0	131.5	0.00078	492.4	364.8	0.249	0.233E 05	0.209E 03	0.00106	0.00149	0.00127	107.6	0.00124
9.0	1.228	.012	3.927	2206.8	131.5	0.00078	492.4	364.8	0.246	0.233E 05	0.205E 03	0.00104	0.00142	0.00122	105.5	0.00121
9.5	1.229	.011	3.927	2206.9	131.6	0.00078	492.4	364.9	0.238	0.233E 05	0.203E 03	0.00101	0.00138	0.00119	104.2	0.00119
10.0	1.229	.010	3.927	2207.2	131.8	0.00079	492.4	364.9	0.226	0.233E 05	0.199E 03	0.00097	0.00132	0.00115	102.2	0.00116
10.5	1.231	.011	3.926	2206.8	131.5	0.00079	492.4	364.9	0.213	0.233E 05	0.195E 03	0.00097	0.00126	0.00110	100.0	0.00113
11.0	1.232	.013	3.925	2206.9	144.1	0.00084	492.8	364.9	0.213	0.240E 05	0.195E 03	0.00095	0.00126	0.00106	99.9	0.00113
11.5	1.342	.015	3.862	2135.2	154.2	0.00091	493.3	366.2	0.206	0.251E 05	0.205E 03	0.00090	0.00120	0.00099	96.6	0.00110
12.0	1.510	.020	3.775	2113.3	161.3	0.00099	493.8	368.2	0.192	0.262E 05	0.218E 03	0.00089	0.00110	0.00097	91.4	0.00105
12.5	1.711	.031	3.685	2093.3	170.4	0.00117	494.2	370.4	0.191	0.284E 05	0.239E 03	0.00087	0.00106	0.00092	88.6	0.00103
13.0	2.145	.044	3.524	2043.2	176.4	0.00132	494.9	374.5	0.184	0.301E 05	0.278E 03	0.00095	0.00098	0.00092	82.6	0.00099
13.5	2.541	.066	3.405	2007.9	185.6	0.00149	495.2	377.7	0.217	0.320E 05	0.334E 03	0.00102	0.00109	0.00111	84.0	0.00107
14.0	3.018	.086	3.286	2009.7	198.6	0.00170	496.7	381.2	0.250	0.341E 05	0.398E 03	0.00114	0.00118	0.00125	84.6	0.00114
14.5	3.623	.111	3.161	2043.5	206.3	0.00195	497.6	385.1	0.301	0.365E 05	0.487E 03	0.00118	0.00133	0.00129	86.5	0.00124
15.0	4.398	.137	3.031	2007.4	220.7	0.00219	498.7	389.4	0.323	0.386E 05	0.574E 03	0.00125	0.00136	0.00138	84.4	0.00127
15.5	5.168	.164	2.924	1932.5	231.1	0.00252	499.7	393.2	0.361	0.413E 05	0.671E 03	0.00128	0.00144	0.00138	84.2	0.00133
16.0	6.293	.188	2.794	1913.7	241.1	0.00284	501.2	398.3	0.378	0.437E 05	0.784E 03	0.00132	0.00147	0.00140	81.2	0.00135
16.5	7.451	.210	2.684	1934.7	251.0	0.00325	502.1	402.4	0.401	0.466E 05	0.902E 03	0.00133	0.00142	0.00143	79.2	0.00137
17.0	8.983	.235	2.563	1919.3	261.0	0.00361	503.5	407.6	0.405	0.489E 05	0.103E 04	0.00135	0.00141	0.00144	75.5	0.00138
17.5	10.416	.254	2.468	1832.0	270.0	0.00398	504.6	411.8	0.413	0.511E 05	0.115E 04	0.00138	0.00142	0.00147	72.9	0.00140
18.0	11.948	.273	2.380	1810.9	280.5	0.00442	505.6	415.9	0.430	0.535E 05	0.128E 04	0.00138	0.00147	0.00145	71.1	0.00136
18.5	13.841	.291	2.286	1815.4	287.5	0.00501	506.8	420.5	0.429	0.564E 05	0.141E 04	0.00137	0.00145	0.00142	67.9	0.00137
19.0	16.479	.317	2.174	1770.5	291.0	0.00555	508.3	426.2	0.421	0.589E 05	0.158E 04	0.00137	0.00142	0.00141	64.0	0.00136
19.5	18.999	.291	2.083	1731.2	293.0	0.00583	509.6	431.1	0.420	0.601E 05	0.173E 04	0.00144	0.00134	0.00149	61.2	0.00137
20.0	20.378	.317	2.038	1710.9	295.8	0.00595	510.2	433.6	0.453	0.606E 05	0.186E 04	0.00144	0.00134	0.00149	61.5	0.00143
21.5	20.981	.339	2.019	1702.3	296.8	0.00595	510.5	434.6	0.489	0.606E 05	0.195E 04	0.00151	0.00142	0.00157	62.6	0.00149

TABLE 3: (continued)

X	P_W	$\Delta P_{F\&W}$	M_E	u_E	T_E	ρ_E	T_R	T'	C_{PP}	R_D	$\dfrac{u_{TW}d_S}{V_W}$	C_F F&S	C_F HKTR	C_F HKT'	u_{TW}	C_F SIO
22.03	21.361	0.348	2.008	1696.9	297.3	0.00603	510.6	435.2	0.502	0.609E 05	0.199E 04	0.00154	0.00145	0.00160	62.9	0.00152
22.53	21.608	0.355	2.001	1693.4	298.3	0.00608	510.7	435.7	0.512	0.611E 05	0.202E 04	0.00156	0.00147	0.00162	63.1	0.00153
23.03	21.758	0.357	1.996	1691.3	298.9	0.00611	510.8	435.9	0.514	0.612E 05	0.203E 04	0.00156	0.00147	0.00163	63.0	0.00154
23.53	21.859	0.358	1.993	1689.9	299.3	0.00613	510.8	436.1	0.514	0.613E 05	0.204E 04	0.00156	0.00146	0.00163	62.9	0.00154
24.03	21.978	0.357	1.990	1688.3	299.7	0.00615	510.9	436.3	0.512	0.614E 05	0.204E 04	0.00156	0.00146	0.00161	62.7	0.00153
24.53	22.013	0.356	1.989	1687.8	299.9	0.00616	510.9	436.4	0.509	0.614E 05	0.204E 04	0.00155	0.00145	0.00160	62.6	0.00153
25.03	22.066	0.354	1.987	1687.1	300.1	0.00617	510.9	436.5	0.505	0.614E 05	0.204E 04	0.00154	0.00144	0.00160	62.4	0.00152
25.53	22.101	0.353	1.986	1686.6	300.2	0.00618	511.0	436.5	0.502	0.614E 05	0.204E 04	0.00154	0.00143	0.00159	62.2	0.00152
26.03	22.069	0.351	1.987	1687.0	300.1	0.00617	510.9	436.4	0.498	0.614E 05	0.203E 04	0.00153	0.00142	0.00158	62.0	0.00151
26.53	22.038	0.348	1.988	1687.4	299.9	0.00617	510.9	436.3	0.493	0.614E 05	0.202E 04	0.00153	0.00141	0.00157	61.9	0.00150
27.03	22.024	0.345	1.988	1687.6	299.9	0.00616	510.9	436.3	0.488	0.614E 05	0.201E 04	0.00152	0.00139	0.00155	61.6	0.00149
27.53	21.994	0.342	1.989	1688.1	299.8	0.00614	510.9	436.2	0.482	0.613E 05	0.200E 04	0.00150	0.00138	0.00154	61.4	0.00148
28.03	21.912	0.340	1.992	1689.2	299.5	0.00612	510.8	436.0	0.478	0.612E 05	0.198E 04	0.00149	0.00137	0.00153	61.3	0.00148
28.53	21.796	0.337	1.995	1690.8	299.0	0.00608	510.8	435.7	0.474	0.611E 05	0.196E 04	0.00148	0.00136	0.00152	61.2	0.00147
29.03	21.630	0.333	2.000	1693.1	298.3	0.00606	510.7	435.5	0.470	0.610E 05	0.195E 04	0.00147	0.00136	0.00152	61.2	0.00146
29.53	21.497	0.331	2.004	1695.0	297.8	0.00604	510.7	435.2	0.466	0.609E 05	0.193E 04	0.00146	0.00134	0.00150	61.1	0.00146
30.03	21.366	0.326	2.008	1696.8	297.3	0.00603	510.6	435.2	0.460	0.608E 05	0.192E 04	0.00144	0.00132	0.00150	60.9	0.00144
30.53	21.337	0.322	2.009	1697.2	297.2	0.00602	510.6	435.2	0.452	0.608E 05	0.190E 04	0.00143	0.00132	0.00148	60.6	0.00143
31.03	21.308	0.317	2.010	1697.6	297.1	0.00602	510.6	435.0	0.443	0.608E 05	0.189E 04	0.00141	0.00130	0.00146	60.2	0.00141
31.53	21.228	0.312	2.012	1698.8	296.8	0.00600	510.6	435.0	0.435	0.608E 05	0.187E 04	0.00139	0.00128	0.00144	59.9	0.00140
32.03	21.233	0.307	2.012	1698.7	296.8	0.00600	510.6	435.0	0.425	0.608E 05	0.185E 04	0.00137	0.00125	0.00142	59.4	0.00138
32.53	21.239	0.301	2.012	1698.6	296.8	0.00601	510.6	435.0	0.413	0.603E 05	0.185E 04	0.00137	0.00123	0.00139	58.8	0.00136
INS.	PSIA	PSIA		FT/SEC	°R	SLUGS/CU.FT.	°R	°H							FT/SEC	FT/SEC

TABLE 4: SKIN FRICTION CORRELATIONS IN RING PRESSURE GRADIENT FLOW

C_F CALCULATED FROM CORRELATIONS BY FENTER & STALMACH, HOPKINS & KEENER, AND SIGALLA;
HOPKINS & KEENER CORRELATION WITH (1): ADIABATIC WALL RECOVERY TEMPERATURE, T_R, AND (2): INTERMEDIATE TEMPERATURE, T', AS INPUT
STATIC PRESSURES CORRECTED FOR HOLE ERROR GIVEN BY FRANKLIN & WALLACE
P_0 = 120.7 PSIA; T_0 = 537.0 °R

X	P_W	ΔP F&W	M_E	u_E	T_E	ρ_E	T_R	T'	C_{PP}	R_D	$\dfrac{u_{\tau W} d_S}{\nu_W}$	C_F F&S	C_F HKTR	C_F HKT'	$u_{\tau W}$	C_F SIG
11.53	1.044	0.007	3.798	2188.6	138.2	0.00063	493.1	367.7	0.224	0.177E 05	0.167E 03	0.00106	0.00139	0.00121	101.5	0.00124
12.03	1.123	0.008	3.745	2180.6	141.1	0.00067	493.5	369.0	0.218	0.181E 05	0.175E 03	0.00104	0.00133	0.00117	98.7	0.00121
12.53	1.173	0.008	3.713	2175.7	142.9	0.00059	493.6	369.7	0.206	0.184E 05	0.177E 03	0.00101	0.00126	0.00112	95.6	0.00118
13.03	1.212	0.008	3.689	2172.2	144.3	0.00071	493.8	370.3	0.194	0.186E 05	0.177E 03	0.00097	0.00119	0.00107	92.8	0.00114
13.53	1.240	0.007	3.673	2169.5	145.2	0.00072	493.9	370.7	0.185	0.188E 05	0.177E 03	0.00094	0.00113	0.00103	90.7	0.00111
14.03	1.260	0.007	3.662	2167.6	145.9	0.00072	494.0	371.0	0.180	0.189E 05	0.177E 03	0.00093	0.00110	0.00103	90.4	0.00109
14.53	1.278	0.007	3.651	2165.9	146.5	0.00073	494.0	371.2	0.179	0.190E 05	0.179E 03	0.00092	0.00109	0.00100	89.4	0.00108
15.03	1.304	0.008	3.637	2163.6	147.3	0.00074	494.1	371.6	0.179	0.191E 05	0.181E 03	0.00092	0.00109	0.00099	88.8	0.00108
15.53	1.313	0.008	3.632	2162.8	147.6	0.00074	494.1	371.7	0.181	0.192E 05	0.183E 03	0.00093	0.00109	0.00100	88.4	0.00109
16.03	1.325	0.008	3.626	2161.7	148.0	0.00075	494.2	371.9	0.182	0.192E 05	0.185E 03	0.00093	0.00110	0.00100	88.7	0.00109
16.53	1.332	0.008	3.622	2161.1	148.2	0.00075	494.2	371.9	0.184	0.193E 05	0.186E 03	0.00093	0.00111	0.00101	88.6	0.00109
17.03	1.343	0.008	3.616	2160.1	148.6	0.00076	494.3	372.1	0.183	0.193E 05	0.187E 03	0.00093	0.00110	0.00101	88.8	0.00109
17.53	1.350	0.008	3.611	2159.2	148.9	0.00076	494.3	372.2	0.182	0.194E 05	0.188E 03	0.00093	0.00110	0.00101	88.5	0.00109
18.03	1.358	0.008	3.608	2158.8	149.0	0.00076	494.3	372.3	0.182	0.194E 05	0.188E 03	0.00093	0.00110	0.00100	88.3	0.00109
18.53	1.362	0.009	3.606	2158.5	148.5	0.00076	494.3	372.3	0.183	0.194E 05	0.189E 03	0.00093	0.00110	0.00101	88.1	0.00109
19.03	1.360	0.009	3.607	2158.4	149.1	0.00077	494.3	372.3	0.183	0.194E 05	0.189E 03	0.00093	0.00110	0.00101	88.2	0.00109
19.53	1.358	0.009	3.608	2158.8	149.0	0.00077	494.3	372.3	0.183	0.194E 05	0.189E 03	0.00093	0.00110	0.00101	88.3	0.00109
20.03	1.358	0.009	3.608	2158.8	149.0	0.00076	494.3	372.3	0.183	0.194E 05	0.189E 03	0.00093	0.00110	0.00101	88.3	0.00109
20.53	1.358	0.009	3.608	2158.8	149.0	0.00076	494.3	372.3	0.183	0.194E 05	0.189E 03	0.00093	0.00110	0.00101	88.3	0.00109
21.03	1.358	0.009	3.608	2158.8	149.0	0.00076	494.3	372.3	0.183	0.194E 05	0.189E 03	0.00093	0.00110	0.00101	88.3	0.00109
21.53	1.350	0.008	3.612	2159.5	148.8	0.00076	494.3	372.2	0.185	0.194E 05	0.188E 03	0.00093	0.00110	0.00102	88.7	0.00120
22.03	1.345	0.008	3.615	2160.0	148.6	0.00076	494.3	372.1	0.186	0.193E 05	0.188E 03	0.00094	0.00111	0.00102	88.9	0.00110
22.53	1.338	0.008	3.619	2160.6	148.6	0.00076	494.3	372.0	0.187	0.193E 05	0.188E 03	0.00094	0.00111	0.00102	89.2	0.00110
23.03	1.337	0.008	3.620	2160.7	148.3	0.00076	494.2	372.0	0.186	0.193E 05	0.187E 03	0.00094	0.00112	0.00102	89.1	0.00110
23.53	1.337	0.008	3.620	2160.7	148.3	0.00076	494.2	372.0	0.186	0.193E 05	0.187E 03	0.00094	0.00112	0.00102	89.1	0.00110
24.03	1.337	0.008	3.619	2160.7	148.3	0.00076	494.2	372.0	0.183	0.193E 05	0.186E 03	0.00093	0.00110	0.00101	88.6	0.00109
24.53	1.330	0.008	3.619	2160.7	148.3	0.00076	494.2	371.9	0.183	0.193E 05	0.185E 03	0.00093	0.00110	0.00101	88.6	0.00109
25.03	1.326	0.008	3.624	2151.4	148.1	0.00075	494.2	371.9	0.183	0.193E 05	0.185E 03	0.00093	0.00110	0.00101	88.7	0.00109
25.53	1.330	0.008	3.623	2161.3	148.1	0.00075	494.2	371.9	0.184	0.193E 05	0.186E 03	0.00093	0.00111	0.00101	88.9	0.00109
26.03	1.337	0.008	3.619	2160.7	148.3	0.00076	494.2	372.0	0.183	0.193E 05	0.186E 03	0.00093	0.00110	0.00101	88.6	0.00109
26.53	1.342	0.008	3.617	2160.3	148.5	0.00076	494.2	372.0	0.187	0.193E 05	0.187E 03	0.00093	0.00110	0.00101	89.1	0.00110
27.03	1.351	0.009	3.612	2159.4	148.8	0.00076	494.3	372.1	0.192	0.194E 05	0.189E 03	0.00094	0.00112	0.00101	89.8	0.00110
27.53	1.363	0.009	3.606	2158.4	149.2	0.00077	494.3	372.4	0.192	0.194E 05	0.192E 03	0.00096	0.00115	0.00103	89.1	0.00112
28.03	1.377	0.010	3.598	2157.1	149.6	0.00077	494.4	372.6	0.198	0.195E 05	0.196E 03	0.00077	0.00117	0.00104	90.5	0.00113
28.53	1.390	0.010	3.591	2156.0	150.0	0.00078	494.4	372.7	0.211	0.196E 05	0.202E 03	0.00101	0.00123	0.00107	92.4	0.00117
29.03	1.467	0.012	3.553	2149.5	152.3	0.00081	494.7	373.7	0.225	0.199E 05	0.215E 03	0.00105	0.00116	0.00111	93.4	0.00121
29.53	2.548	0.017	3.171	2075.0	178.4	0.00120	497.5	384.8	0.150	0.242E 05	0.278E 03	0.00080	0.00081	0.00082	76.4	0.00092
30.03	2.580	0.023	3.162	2073.7	179.0	0.00121	497.6	385.0	0.192	0.243E 05	0.306E 03	0.00093	0.00099	0.00098	78.3	0.00106
30.53	2.565	0.025	3.166	2074.7	178.7	0.00120	497.6	384.9	0.204	0.243E 05	0.312E 03	0.00097	0.00105	0.00102	79.7	0.00110
31.03	2.525	0.026	3.176	2079.8	178.6	0.00117	497.5	384.6	0.213	0.241E 05	0.313E 03	0.00099	0.00109	0.00105	80.8	0.00112
31.53	2.475	0.026	3.190	2089.1	176.9	0.00117	497.4	384.4	0.217	0.240E 05	0.311E 03	0.00101	0.00112	0.00107	80.8	0.00114
32.03	2.320	0.025	3.234	2089.1	173.7	0.00112	497.0	382.8	0.231	0.234E 05	0.303E 03	0.00104	0.00119	0.00113	83.9	0.00118
32.53	2.296	0.025	3.242	2090.7	173.1	0.00111	497.0	382.5	0.229	0.233E 05	0.300E 03	0.00104	0.00119	0.00112	83.9	0.00118
INS.	PSIA	PSIA		FT/SEC	°R	SLUGS/CU.FT.	°R	°R							FT/SEC	

TABLE 5.1

FLOW CASE: ZPG - ZERO PRESSURE GRADIENT

TRAVERSE T1 AT   X = 11.62 INS.; (RUN NO. 9527)

Stagnation Pressure, P_0 = 168.9 PSIA
Stagnation Temperature, T_0 = 537.0 °R

LOCAL MAINSTREAM CONDITIONS

M_E = 3.926   ; u_E = 2207.0 FT/SEC; ρ_E = 0.00078 SLUGS/CU.FT.

P_E (=P_W) = 1.228 PSIA; T_E = 131.5 °R

δ_{995} = 0.1566 IN.

INTEGRAL QUANTITIES

Displacement Thickness,	δ^*	= 0.0602 IN.
Momentum Thickness,	θ	= 0.0079 IN.
Momentum Thickness Reynolds Number	R_θ	= $0.1037 \cdot 10^5$
Compressible Shape Factor,	H	= 7.645
Incompressible Velocity Shape Factor	H^1_{12}	= 1.537
Shape Parameter,	$\bar{H}$	= 1.365
Entrainment Parameter,	H_1	= 23.78
C_F, WILSON		= 0.00134
C_F, SOMMER/SHORT		= 0.00116

PROFILE DATA

y-INS.	M/M_E	u/u_E	ρ/ρ_E	y-INS.	M/M_E	u/u_E	ρ/ρ_E
0.0090	0.3382	0.5664	0.3564	0.0916	0.8298	0.9433	0.7736
0.0120	0.4125	0.6546	0.3970	0.0948	0.8319	0.9442	0.7763
0.0149	0.4435	0.6873	0.4162	0.0980	0.8363	0.9459	0.7815
0.0178	0.4685	0.7121	0.4328	0.1008	0.8428	0.9485	0.7894
0.0211	0.4959	0.7375	0.4520	0.1040	0.8513	0.9518	0.7999
0.0243	0.5130	0.7526	0.4645	0.1063	0.8587	0.9546	0.8092
0.0276	0.5304	0.7673	0.4778	0.1095	0.8671	0.9577	0.8197
0.0304	0.5506	0.7836	0.4936	0.1155	0.8878	0.9651	0.8460
0.0331	0.5661	0.7956	0.5061	0.1211	0.9049	0.9710	0.8684
0.0363	0.5756	0.8027	0.5141	0.1270	0.9218	0.9766	0.8908
0.0386	0.5896	0.8130	0.5260	0.1330	0.9383	0.9819	0.9131
0.0423	0.5973	0.8184	0.5326	0.1385	0.9537	0.9866	0.9342
0.0455	0.6034	0.8226	0.5378	0.1441	0.9669	0.9906	0.9526
0.0483	0.6123	0.8288	0.5458	0.1505	0.9743	0.9927	0.9631
0.0511	0.6226	0.8357	0.5550	0.1565	0.9817	0.9949	0.9736
0.0538	0.6342	0.8432	0.5656	0.1620	0.9882	0.9967	0.9829
0.0566	0.6469	0.8513	0.5774	0.1680	0.9927	0.9980	0.9894
0.0598	0.6608	0.8598	0.5906	0.1740	0.9941	0.9983	0.9914
0.0626	0.6771	0.8694	0.6064	0.1791	0.9959	0.9988	0.9940
0.0658	0.6969	0.8806	0.6262	0.1851	0.9968	0.9991	0.9953
0.0686	0.7136	0.8896	0.6434	0.1906	0.9977	0.9993	0.9966
0.0713	0.7337	0.9000	0.6644	0.1961	0.9986	0.9996	0.9979
0.0741	0.7520	0.9090	0.6842	0.2025	0.9990	0.9997	0.9985
0.0778	0.7722	0.9185	0.7066	0.2081	0.9990	0.9997	0.9985
0.0796	0.7855	0.9246	0.7217	0.2145	0.9990	0.9997	0.9985
0.0833	0.8026	0.9321	0.7414	0.2200	0.9990	0.9997	0.9985
0.0861	0.8143	0.9370	0.7552	0.2260	0.9990	0.9997	0.9985
0.0888	0.8221	0.9402	0.7644	0.2316	0.9999	0.9999	0.9998

TABLE 5.2

FLOW CASE: ZPG - ZERO PRESSURE GRADIENT

TRAVERSE T2 AT   X = 16.62 INS.; (RUN NO. 9531)

Stagnation Pressure, P_0 = 168.9 PSIA
Stagnation Temperature, T_0 = 537.0 °R

LOCAL MAINSTREAM CONDITIONS

M_E = 3.909   ; u_E = 2200.6 FT/SEC; ρ_E = 0.00080 SLUGS/CU.FT.

P_E (=P_W) = 1.257 PSIA; T_E = 132.4 °R

δ_{995} = 0.2160 IN.

INTEGRAL QUANTITIES

Displacement Thickness,	δ^*	= 0.0853 IN.
Momentum Thickness,	θ	= 0.0116 IN.
Momentum Thickness Reynolds Number	R_θ	= 0.1496·10⁵
Compressible Shape Factor, H		= 7.332
Incompressible Velocity Shape Factor	H_{12}^1	= 1.454
Shape Parameter,	$\bar{H}$	= 1.328
Entrainment Parameter,	H_1	= 18.49

C_F, WILSON   = 0.00126

C_F, SOMMER/SHORT   = 0.00110

PROFILE DATA

y-INS	M/M_E	u/u_E	ρ/ρ_E	y-INS.	M/M_E	u/u_E	ρ/ρ_E
0.0090	0.3347	0.5577	0.3601	0.1059	0.7296	0.8960	0.6630
0.0125	0.3820	0.6159	0.3845	0.1086	0.7383	0.9005	0.6722
0.0159	0.4184	0.6570	0.4055	0.1118	0.7457	0.9042	0.6800
0.0183	0.4378	0.6775	0.4175	0.1141	0.7542	0.9083	0.6892
0.0215	0.4584	0.6983	0.4308	0.1174	0.7602	0.9113	0.6958
0.0239	0.4780	0.7172	0.4440	0.1201	0.7673	0.9147	0.7036
0.0267	0.4875	0.7261	0.4506	0.1257	0.7814	0.9212	0.7194
0.0294	0.4991	0.7367	0.4589	0.1316	0.7975	0.9285	0.7377
0.0322	0.5082	0.7448	0.4655	0.1367	0.8100	0.9339	0.7521
0.0350	0.5189	0.7541	0.4734	0.1418	0.8267	0.9409	0.7718
0.0373	0.5224	0.7571	0.4760	0.1468	0.8430	0.9475	0.7915
0.0405	0.5316	0.7648	0.4830	0.1533	0.8587	0.9536	0.8108
0.0432	0.5401	0.7718	0.4896	0.1593	0.8745	0.9596	0.8304
0.0455	0.5468	0.7773	0.4948	0.1648	0.8889	0.9648	0.8487
0.0488	0.5551	0.7839	0.5014	0.1703	0.8991	0.9684	0.8618
0.0511	0.5633	0.7902	0.5080	0.1758	0.9101	0.9722	0.8763
0.0538	0.5697	0.7952	0.5133	0.1818	0.9270	0.9778	0.8985
0.0566	0.5808	0.8035	0.5225	0.1864	0.9367	0.9810	0.9116
0.0589	0.5886	0.8092	0.5291	0.1915	0.9464	0.9841	0.9247
0.0621	0.5963	0.8147	0.5356	0.1970	0.9583	0.9879	0.9418
0.0644	0.6084	0.8232	0.5461	0.2016	0.9654	0.9899	0.9509
0.0676	0.6207	0.8316	0.5570	0.2076	0.9745	0.9926	0.9637
0.0699	0.6280	0.8365	0.5636	0.2131	0.9791	0.9940	0.9702
0.0727	0.6367	0.8421	0.5715	0.2187	0.9844	0.9955	0.9777
0.0750	0.6480	0.8494	0.5820	0.2237	0.9881	0.9966	0.9830
0.0782	0.6592	0.8563	0.5925	0.2293	0.9909	0.9974	0.9869
0.0805	0.6660	0.8605	0.5990	0.2352	0.9927	0.9979	0.9895
0.0833	0.6728	0.8645	0.6056	0.2408	0.9943	0.9984	0.9918
0.0856	0.6796	0.8685	0.6122	0.2463	0.9961	0.9989	0.9944
0.0888	0.6863	0.8724	0.6187	0.2518	0.9970	0.9991	0.9957
0.0911	0.6925	0.8759	0.6249	0.2569	0.9980	0.9994	0.9970
0.0944	0.7003	0.8803	0.6328	0.2629	0.9985	0.9996	0.9980
0.0967	0.7081	0.8846	0.6407	0.2684	0.9986	0.9996	0.9980
0.1003	0.7145	0.8880	0.6472	0.2734	0.9990	0.9997	0.9986
0.1031	0.7234	0.8927	0.6564	0.2790	0.9990	0.9997	0.9986

TABLE 5.3

FLOW CASE: ZPG - ZERO PRESSURE GRADIENT

TRAVERSE   T3   AT   X = 20.62 INS.; (RUN NO. 9537)

Stagnation Pressure, P_0 = 168.9 PSIA
Stagnation Temperature, T_0 = 537.0 °R

LOCAL MAINSTREAM CONDITIONS

M_E = 3.901   ; u_E = 2203.5 FT/SEC; ρ_E = 0.00080 SLUGS/CU.FT.
P_E ($=P_W$) = 1.270 PSIA; T_E = 132.8 °R
δ_{995} = 0.2615 IN.

INTEGRAL QUANTITIES

Displacement Thickness,	δ^*	= 0.1006 IN.
Momentum Thickness,	θ	= 0.0141 IN.
Momentum Thickness		
Reynolds Number	R_θ	= $0.1755 \cdot 10^5$
Compressible Shape Factor,	H	= 7.154
Incompressible Velocity		
Shape Factor	H_{12}^1	= 1.427
Shape Parameter,	$\overline{H}$	= 1.312
Entrainment Parameter,	H_1	= 13.92

C_F, WILSON   = 0.00113

C_F, SOMMER/SHORT   = 0.00107

PROFILE DATA

y-INS	M/M_E	u/u_E	ρ/ρ_E	y-INS	M/M_E	u/u_E	ρ/ρ_E
0.0090	0.3239	0.5407	0.3587	0.1220	0.7179	0.8885	0.6527
0.0135	0.3632	0.5906	0.3781	0.1275	0.7319	0.8959	0.6673
0.0164	0.3957	0.6289	0.3957	0.1330	0.7416	0.9009	0.6775
0.0187	0.4126	0.6479	0.4055	0.1376	0.7524	0.9063	0.6871
0.0215	0.4348	0.6716	0.4190	0.1422	0.7645	0.9122	0.7053
0.0239	0.4517	0.6889	0.4297	0.1468	0.7742	0.9168	0.7159
0.0267	0.4724	0.7093	0.4434	0.1514	0.7850	0.9223	0.7261
0.0299	0.4898	0.7257	0.4554	0.1574	0.7977	0.9276	0.7394
0.0322	0.5011	0.7360	0.4634	0.1630	0.8065	0.9315	0.7496
0.0345	0.5103	0.7442	0.4701	0.1680	0.8210	0.9377	0.7664
0.0368	0.5247	0.7566	0.4807	0.1731	0.8358	0.9439	0.7840
0.0396	0.5312	0.7621	0.4857	0.1781	0.8457	0.9478	0.7959
0.0414	0.5399	0.7693	0.4924	0.1827	0.8565	0.9521	0.8091
0.0442	0.5462	0.7745	0.4973	0.1878	0.8680	0.9565	0.8233
0.0465	0.5509	0.7782	0.5009	0.1929	0.8688	0.9568	0.8243
0.0497	0.5559	0.7822	0.5049	0.1984	0.8769	0.9599	0.8345
0.0525	0.5609	0.7861	0.5089	0.2030	0.8967	0.9671	0.8596
0.0548	0.5658	0.7900	0.5129	0.2095	0.9046	0.9699	0.8698
0.0580	0.5691	0.7925	0.5156	0.2145	0.9145	0.9733	0.8827
0.0607	0.5756	0.7974	0.5209	0.2196	0.9275	0.9777	0.8999
0.0635	0.5820	0.8022	0.5262	0.2246	0.9374	0.9809	0.9131
0.0663	0.5914	0.8092	0.5341	0.2297	0.9460	0.9837	0.9246
0.0681	0.6038	0.8180	0.5448	0.2352	0.9547	0.9865	0.9365
0.0713	0.6099	0.8223	0.5501	0.2403	0.9615	0.9886	0.9458
0.0732	0.6205	0.8295	0.5594	0.2454	0.9681	0.9906	0.9550
0.0759	0.6245	0.8323	0.5630	0.2504	0.9748	0.9926	0.9643
0.0792	0.6334	0.8381	0.5709	0.2550	0.9786	0.9937	0.9696
0.0815	0.6421	0.8438	0.5789	0.2615	0.9821	0.9948	0.9745
0.0838	0.6464	0.8466	0.5832	0.2665	0.9849	0.9956	0.9785
0.0865	0.6521	0.8502	0.5862	0.2716	0.9896	0.9970	0.9851
0.0893	0.6577	0.8537	0.5935	0.2771	0.9940	0.9982	0.9913
0.0916	0.6633	0.8572	0.5988	0.2822	0.9949	0.9985	0.9927
0.0944	0.6661	0.8588	0.6014	0.2873	0.9965	0.9990	0.9950
0.0971	0.6703	0.8614	0.6054	0.2923	0.9972	0.9992	0.9959
0.0994	0.6758	0.8646	0.6107	0.2969	0.9981	0.9994	0.9972
0.1054	0.6853	0.8702	0.6200	0.3025	0.9990	0.9997	0.9986
0.1114	0.6943	0.8754	0.6289	0.3066	0.9999	0.9999	0.9999
0.1169	0.7062	0.8821	0.6408				

TABLE 5.4

FLOW CASE: ZPG - ZERO PRESSURE GRADIENT

TRAVERSE T4 AT X = 22.62 INS.; (RUN NO. 9540)

Stagnation Pressure, P_0 = 168.9 PSIA
Stagnation Temperature, T_0 = 537.0 °R

LOCAL MAINSTREAM CONDITIONS

M_E = 3.905 ; u_E = 2204.1 FT/SEC; ρ_E = 0.00080 SLUGS/CU.FT.

P_E (=P_W) = 1.263 PSIA; T_E = 132.6 °R

δ_{995} = 0.2900 IN.

INTEGRAL QUANTITIES

Displacement Thickness,	δ^*	= 0.1129 IN.
Momentum Thickness,	θ	= 0.0156 IN.
Momentum Thickness Reynolds Number	R_θ	= 0.2017·10^5
Compressible Shape Factor,	H	= 7.226
Incompressible Velocity Shape Factor	H^1_{12}	= 1.396
Shape Parameter,	$\bar{H}$	= 1.298
Entrainment Parameter,	H_1	= 17.60
C_F, WILSON		= 0.00119
C_F, SOMMER/SHORT		= 0.00103

PROFILE DATA

y-INS.	M/M_E	u/u_E	ρ/ρ_E	y-INS.	M/M_E	u/u_E	ρ/ρ_E
0.0090	0.3522	0.5799	0.3687	0.1409	0.7223	0.8922	0.6553
0.0134	0.3877	0.6226	0.3877	0.1472	0.7344	0.8985	0.6680
0.0164	0.4147	0.6529	0.4033	0.1535	0.7455	0.9041	0.6798
0.0193	0.4260	0.6652	0.4101	0.1604	0.7563	0.9094	0.6915
0.0228	0.4450	0.6849	0.4220	0.1656	0.7706	0.9162	0.7072
0.0257	0.4586	0.6986	0.4309	0.1719	0.7834	0.9221	0.7216
0.0298	0.4719	0.7115	0.4398	0.1777	0.7971	0.9283	0.7372
0.0321	0.4790	0.7183	0.4447	0.1846	0.8115	0.9345	0.7539
0.0355	0.4861	0.7249	0.4496	0.1909	0.8258	0.9406	0.7708
0.0378	0.4967	0.7346	0.4572	0.1967	0.8346	0.9441	0.7813
0.0413	0.5053	0.7423	0.4634	0.2036	0.8496	0.9501	0.7995
0.0442	0.5138	0.7497	0.4696	0.2093	0.8613	0.9546	0.8139
0.0476	0.5191	0.7543	0.4735	0.2151	0.8738	0.9593	0.8295
0.0511	0.5261	0.7602	0.4788	0.2208	0.8859	0.9637	0.8448
0.0534	0.5347	0.7674	0.4853	0.2272	0.8978	0.9679	0.8602
0.0568	0.5397	0.7715	0.4893	0.2329	0.9105	0.9723	0.8768
0.0597	0.5481	0.7783	0.4958	0.2393	0.9214	0.9760	0.8911
0.0626	0.5563	0.7848	0.5024	0.2450	0.9321	0.9795	0.9055
0.0660	0.5628	0.7899	0.5076	0.2514	0.9418	0.9826	0.9185
0.0695	0.5693	0.7948	0.5129	0.2583	0.9514	0.9856	0.9316
0.0724	0.5788	0.8020	0.5207	0.2646	0.9596	0.9882	0.9429
0.0758	0.5897	0.8100	0.5299	0.2709	0.9681	0.9907	0.9547
0.0781	0.5973	0.8154	0.5364	0.2772	0.9746	0.9927	0.9638
0.0816	0.6079	0.8229	0.5456	0.2836	0.9799	0.9942	0.9713
0.0845	0.6168	0.8290	0.5535	0.2899	0.9827	0.9950	0.9752
0.0879	0.6284	0.8368	0.5639	0.2951	0.9873	0.9963	0.9817
0.0908	0.6342	0.8405	0.5692	0.3014	0.9900	0.9971	0.9856
0.0942	0.6413	0.8451	0.5757	0.3072	0.9928	0.9979	0.9895
0.0971	0.6483	0.8496	0.5822	0.3135	0.9937	0.9982	0.9909
0.1000	0.6525	0.8522	0.5862	0.3193	0.9952	0.9986	0.9931
0.1040	0.6563	0.8545	0.5897	0.3256	0.9961	0.9989	0.9944
0.1063	0.6597	0.8566	0.5929	0.3319	0.9971	0.9991	0.9957
0.1098	0.6652	0.8600	0.5982	0.3388	0.9977	0.9993	0.9967
0.1127	0.6689	0.8622	0.6017	0.3452	0.9986	0.9996	0.9980
0.1161	0.6743	0.8654	0.6070	0.3509	0.9990	0.9998	0.9993
0.1184	0.6823	0.8701	0.6148	0.3572	0.9996	0.9998	0.9993
0.1224	0.6850	0.8716	0.6174	0.3636	0.9995	0.9998	0.9993
0.1259	0.6915	0.8754	0.6240	0.3693	0.9995	0.9998	0.9993
0.1288	0.6968	0.8783	0.6292	0.3757	0.9999	0.9999	0.9999
0.1351	0.7084	0.8847	0.6410				

TABLE 5.5

FLOW CASE: ZPG - ZERO PRESSURE GRADIENT

TRAVERSE T5 AT   X = 26.62 INS.; (RUN NO. 9544)

Stagnation Pressure, P_0 = 168.9 PSIA
Stagnation Temperature, T_0 = 537.0 °R

LOCAL MAINSTREAM CONDITIONS

M_E = 3.922   ; u_E = 2206.3 FT/SEC; ρ_E = 0.00079 SLUGS/CU.FT.

$P_E (=P_W)$ = 1.236 PSIA; T_E = -131.8 °R

δ_{995} = 0.3283 IN.

INTEGRAL QUANTITIES

Displacement Thickness,	δ^*	= 0.1310 IN.
Momentum Thickness,	θ	= 0.0177 IN.
Momentum Thickness Reynolds Number	R_θ	= 0.2358·10^5
Compressible Shape Factor,	H	= 7.411
Incompressible Velocity Shape Factor	H_{12}^i	= 1.387
Shape Parameter,	$\bar{H}$	= 1.292
Entrainment Parameter,	H_1	= 16.10

C_F, WILSON   = 0.00114

C_F, SOMMER/SHORT   = 0.00099

PROFILE DATA

y-INS.	M/M_E	u/u_E	ρ/ρ_E	y-INS.	M/M_E	u/u_E	ρ/ρ_E
0.0090	0.3091	0.5284	0.3420	0.1667	0.7246	0.8956	0.6545
0.0109	0.3596	0.5938	0.3666	0.1731	0.7369	0.9019	0.6675
0.0146	0.3914	0.6316	0.3840	0.1794	0.7490	0.9078	0.6806
0.0181	0.4119	0.6545	0.3959	0.1863	0.7609	0.9135	0.6937
0.0211	0.4249	0.6686	0.4039	0.1926	0.7723	0.9188	0.7064
0.0246	0.4438	0.6881	0.4158	0.1990	0.7849	0.9245	0.7207
0.0281	0.4499	0.6943	0.4197	0.2070	0.7985	0.9305	0.7364
0.0309	0.4578	0.7022	0.4250	0.2139	0.8097	0.9352	0.7494
0.0350	0.4696	0.7136	0.4329	0.2197	0.8226	0.9406	0.7647
0.0373	0.4829	0.7261	0.4421	0.2260	0.8366	0.9462	0.7817
0.0413	0.4921	0.7346	0.4487	0.2318	0.8462	0.9499	0.7934
0.0442	0.5007	0.7423	0.4549	0.2381	0.8581	0.9545	0.8082
0.0476	0.5061	0.7471	0.4589	0.2450	0.8685	0.9583	0.8212
0.0511	0.5114	0.7517	0.4628	0.2525	0.8795	0.9623	0.8352
0.0539	0.5185	0.7577	0.4681	0.2588	0.8904	0.9661	0.8492
0.0580	0.5236	0.7621	0.4720	0.2657	0.9024	0.9703	0.8649
0.0609	0.5305	0.7678	0.4772	0.2778	0.9103	0.9729	0.8753
0.0643	0.5406	0.7761	0.4851	0.2790	0.9230	0.9771	0.8923
0.0678	0.5489	0.7827	0.4917	0.2853	0.9327	0.9802	0.9053
0.0712	0.5570	0.7891	0.4982	0.2922	0.9441	0.9838	0.9210
0.0752	0.5650	0.7952	0.5048	0.2991	0.9524	0.9863	0.9324
0.0781	0.5730	0.8012	0.5113	0.3054	0.9608	0.9888	0.9441
0.0816	0.5838	0.8092	0.5205	0.3124	0.9680	0.9909	0.9542
0.0845	0.5900	0.8136	0.5257	0.3187	0.9726	0.9923	0.9607
0.0885	0.5976	0.8190	0.5323	0.3256	0.9791	0.9941	0.9698
0.0914	0.6021	0.8221	0.5362	0.3331	0.9836	0.9954	0.9763
0.0942	0.6065	0.8252	0.5401	0.3394	0.9873	0.9964	0.9816
0.0983	0.6154	0.8312	0.5480	0.3463	0.9909	0.9975	0.9868
0.1011	0.6183	0.8331	0.5506	0.3532	0.9927	0.9980	0.9894
0.1052	0.6255	0.8379	0.5571	0.3595	0.9945	0.9985	0.9920
0.1127	0.6341	0.8435	0.5650	0.3659	0.9963	0.9989	0.9946
0.1190	0.6439	0.8497	0.5741	0.3722	0.9970	0.9991	0.9956
0.1259	0.6577	0.8582	0.5872	0.3791	0.9980	0.9994	0.9971
0.1328	0.6682	0.8645	0.5973	0.3860	0.9987	0.9996	0.9981
0.1397	0.6802	0.8715	0.6091	0.3924	0.9994	0.9998	0.9990
0.1460	0.6894	0.8767	0.6182	0.3987	0.9994	0.9998	0.9990
0.1529	0.7010	0.8831	0.6300	0.4050	0.9998	0.9999	0.9996
0.1593	0.7150	0.8906	0.6441				

TABLE 5.6

FLOW CASE: ZPG - ZERO PRESSURE GRADIENT

TRAVERSE T6 AT   X = 31.62 INS.; (RUN NO. 9548)

Stagnation Pressure, P_0 = 158.9 PSIA
Stagnation Temperature, T_0 = 537.0 °R

LOCAL MAINSTREAM CONDITIONS

M_E = 3.902   ; u_E = 2203.4 FT/SEC; ρ_E = 0.00080 SLUGS/CU.FT.

P_E (=P_W) = 1.270 PSIA; T_E = 132.8 °R

δ_{995} = 0.3653 IN.

INTEGRAL QUANTITIES

Displacement Thickness,	δ^*	= 0.1446 IN.
Momentum Thickness,	θ	= 0.0160 IN.
Momentum Thickness Reynolds Number	R_θ	= $0.2971 \cdot 10^5$
Compressible Shape Factor,	H	= 8.025
Incompressible Velocity Shape Factor	H_{12}^1	= 1.356
Shape Parameter,	$\overline{H}$	= 1.276
Entrainment Parameter,	H_1	= 17.17
C_F, WILSON		= 0.00104
C_F, SOMMER/SHORT		= 0.00090

PROFILE DATA

y-INS.	M/M_E	u/u_E	ρ/ρ_E	y-INS.	M/M_E	u/u_E	ρ/ρ_E
0.0090	0.3321	0.5741	0.3347	0.1541	0.6702	0.8739	0.5881
0.0103	0.3601	0.6093	0.3491	0.1598	0.6807	0.8797	0.5986
0.0140	0.3795	0.6325	0.3599	0.1667	0.6963	0.8880	0.6147
0.0170	0.3899	0.6445	0.3658	0.1725	0.7074	0.8938	0.6264
0.0205	0.4019	0.6580	0.3730	0.1794	0.7159	0.8980	0.6355
0.0240	0.4155	0.6728	0.3813	0.1857	0.7257	0.9028	0.6460
0.0275	0.4254	0.6833	0.3875	0.1926	0.7372	0.9083	0.6586
0.0304	0.4387	0.6970	0.3961	0.1996	0.7485	0.9136	0.6711
0.0344	0.4459	0.7042	0.4008	0.2059	0.7589	0.9183	0.6828
0.0367	0.4542	0.7123	0.4064	0.2128	0.7712	0.9237	0.6969
0.0401	0.4623	0.7202	0.4120	0.2191	0.7843	0.9293	0.7121
0.0436	0.4724	0.7297	0.4191	0.2255	0.7939	0.9333	0.7235
0.0470	0.4819	0.7384	0.4258	0.2318	0.8054	0.9379	0.7372
0.0505	0.4884	0.7442	0.4305	0.2381	0.8201	0.9437	0.7551
0.0534	0.4995	0.7541	0.4388	0.2444	0.8308	0.9477	0.7683
0.0563	0.5058	0.7594	0.4435	0.2519	0.8411	0.9516	0.7812
0.0597	0.5104	0.7634	0.4470	0.2588	0.8510	0.9551	0.7937
0.0637	0.5166	0.7685	0.4517	0.2652	0.8681	0.9611	0.8156
0.0660	0.5271	0.7772	0.4599	0.2721	0.8788	0.9647	0.8297
0.0706	0.5316	0.7807	0.4635	0.2784	0.8894	0.9682	0.8437
0.0735	0.5391	0.7851	0.4678	0.2847	0.9008	0.9719	0.8589
0.0770	0.5486	0.7941	0.4772	0.2922	0.9129	0.9756	0.8753
0.0804	0.5554	0.7992	0.4828	0.2980	0.9231	0.9788	0.8894
0.0833	0.5638	0.8054	0.4898	0.3049	0.9321	0.9815	0.9010
0.0868	0.5734	0.8125	0.4981	0.3112	0.9397	0.9837	0.9125
0.0902	0.5789	0.8163	0.5028	0.3170	0.9463	0.9856	0.9218
0.0937	0.5870	0.8220	0.5098	0.3233	0.9529	0.9874	0.9312
0.0965	0.5963	0.8284	0.5180	0.3360	0.9603	0.9895	0.9417
0.0994	0.6041	0.8336	0.5251	0.3371	0.9643	0.9906	0.9476
0.1029	0.6080	0.8362	0.5286	0.3440	0.9682	0.9916	0.9531
0.1063	0.6157	0.8412	0.5356	0.3503	0.9706	0.9923	0.9566
0.1092	0.6195	0.8436	0.5391	0.3567	0.9760	0.9937	0.9645
0.1127	0.6233	0.8460	0.5427	0.3630	0.9784	0.9944	0.9680
0.1161	0.6270	0.8484	0.5462	0.3688	0.9840	0.9958	0.9762
0.1196	0.6308	0.8507	0.5497	0.3757	0.9869	0.9966	0.9805
0.1270	0.6382	0.8552	0.5567	0.3808	0.9901	0.9974	0.9852
0.1339	0.6479	0.8611	0.5661	0.3872	0.9930	0.9982	0.9896
0.1403	0.6528	0.8639	0.5708	0.3941	0.9960	0.9989	0.9939
0.1460	0.6647	0.8708	0.5825	0.4004	0.9999	0.9999	0.9998

TABLE 6.1

FLOW CASE: APC - ADVERSE PRESSURE GRADIENT

TRAVERSE T1 AT   X = 13.62 INS.; (RUN NO.=9527)

Stagnation Pressure, P_0 = 69.2 PSIA
Stagnation Temperature, T_0 = 537.0 °R

LOCAL MAINSTREAM CONDITIONS

M_E = 3.926   ; u_E = 2206.9 FT/SEC; ρ_E = 0.00079 SLUGS/CU.FT.
$P_E (=F_W)$ = 1.231 PSIA; T_E = 131.5 °R
δ_{995} = 0.1522 IN.

INTEGRAL QUANTITIES

Displacement Thickness, $\delta^* = 0.0577$ IN.
Momentum Thickness, $\theta = 0.0075$ IN.
Momentum Thickness
Reynolds Number $R_\theta = 0.9820 \cdot 10^4$
Compressible Shape Factor, $H = 7.671$
Incompressible Velocity
Shape Factor $H_{12}^1 = 1.573$
Shape Parameter, $\bar{H} = 1.383$
Entrainment Parameter, $H_1 = 24.80$

C_p, WILSON   = 0.00136
C_p, SOMMER/SHORT   = 0.00118

PROFILE DATA

y-INS.	M/M_E	u/u_E	ρ/ρ_E	y-INS.	M/M_E	u/u_E	ρ/ρ_E
0.0090	0.3253	0.5486	0.3515	0.0897	0.8317	0.9438	0.7763
0.0135	0.3813	0.6185	0.3802	0.0920	0.8342	0.9448	0.7794
0.0168	0.4283	0.6707	0.4078	0.0985	0.8493	0.9508	0.7978
0.0187	0.4732	0.7157	0.4372	0.1036	0.8663	0.9572	0.8189
0.0220	0.4978	0.7384	0.4545	0.1091	0.8829	0.9632	0.8401
0.0253	0.5281	0.7646	0.4770	0.1141	0.8992	0.9689	0.8612
0.0276	0.5418	0.7758	0.4876	0.1197	0.9150	0.9743	0.8819
0.0308	0.5596	0.7899	0.5019	0.1243	0.9305	0.9793	0.9027
0.0331	0.5753	0.8018	0.5148	0.1298	0.9436	0.9835	0.9204
0.0363	0.5894	0.8121	0.5267	0.1353	0.9551	0.9870	0.9363
0.0391	0.6002	0.8197	0.5360	0.1399	0.9674	0.9907	0.9534
0.0423	0.6047	0.8229	0.5399	0.1450	0.9721	0.9920	0.9600
0.0446	0.6103	0.8267	0.5449	0.1510	0.9811	0.9947	0.9729
0.0474	0.6222	0.8347	0.5555	0.1565	0.9858	0.9960	0.9795
0.0506	0.6377	0.8448	0.5696	0.1620	0.9892	0.9970	0.9844
0.0534	0.6518	0.8537	0.5829	0.1676	0.9917	0.9977	0.9880
0.0552	0.6623	0.8601	0.5929	0.1726	0.9945	0.9984	0.9919
0.0584	0.6786	0.8697	0.6087	0.1781	0.9954	0.9987	0.9933
0.0607	0.6959	0.8795	0.6259	0.1832	0.9963	0.9989	0.9946
0.0640	0.7178	0.8913	0.6484	0.1887	0.9972	0.9992	0.9959
0.0667	0.7350	0.9002	0.6665	0.1938	0.9972	0.9992	0.9959
0.0690	0.7521	0.9087	0.6850	0.1998	0.9981	0.9994	0.9972
0.0718	0.7677	0.9161	0.7022	0.2048	0.9981	0.9994	0.9972
0.0741	0.7876	0.9252	0.7246	0.2108	0.9990	0.9997	0.9985
0.0773	0.7999	0.9306	0.7366	0.2159	0.9990	0.9997	0.9985
0.0801	0.8098	0.9348	0.7503	0.2210	0.9990	0.9997	0.9985
0.0819	0.8184	0.9384	0.7605	0.2256	0.9990	0.9997	0.9985
0.0851	0.8248	0.9410	0.7681	0.2306	0.9990	0.9997	0.9985
0.0874	0.8295	0.9429	0.7737	0.2357	0.9999	0.9999	0.9999

TABLE 6.2.1

FLOW CASE: APG - ADVERSE PRESSURE GRADIENT

TRAVERSE T2 AT   X = 16.62 INS ; (RUN NO.=9533)

Stagnation Pressure, P_0 = 169.2 PSIA
Stagnation Temperature, T_0 = 537.0 °R

LOCAL MAINSTREAM CONDITIONS

M_E = 2.901   ; u_E = 2011.2 FT/SEC; ρ_E = 0.00225 SLUGS/CU.FT.

P_E (=P_W) = 5.371 PSIA; T_E = 203.3 °R

δ_{995} = 0.1544 IN.

INTEGRAL QUANTITIES

Displacement Thickness,	δ^*	= 0.0495 IN.
Momentum Thickness,	θ	= 0.0096 IN
Momentum Thickness Reynolds Number	R_θ	= 0.2274·10⁵
Compressible Shape Factor,	H	= 5.137
Incompressible Velocity Shape Factor	H_{12}^1	= 1.579
Shape Parameter,	$\bar{H}$	= 1.443
Entrainment Parameter,	H_1	= 26.36

C_F, WILSON   = 0.00141

C_F, SOMMER/SHORT   = 0.00128

PROFILE DATA

y-INS.	M/M_E	u/u_E	ρ/ρ_E	y-INS.	M/M_E	u/u_E	ρ/ρ_E
0.0090	0.3695	0.5331	0.4801	0.1326	0.9756	0.9900	0.9709
0.0130	0.4563	0.6307	0.5233	0.1381	0.9815	0.9925	0.9779
0.0168	0.4945	0.6696	0.5451	0.1450	0.9845	0.9937	0.9814
0.0201	0.5255	0.6995	0.5642	0.1510	0.9866	0.9946	0.9839
0.0234	0.5491	0.7213	0.5795	0.1579	0.9888	0.9955	0.9866
0.0267	0.5690	0.7390	0.5929	0.1643	0.9896	0.9958	0.9876
0.0299	0.5857	0.7533	0.6045	0.1712	0.9910	0.9964	0.9892
0.0331	0.6020	0.7668	0.6161	0.1777	0.9919	0.9967	0.9902
0.0363	0.6165	0.7787	0.6268	0.1841	0.9926	0.9970	0.9911
0.0396	0.6272	0.7872	0.6348	0.1910	0.9926	0.9970	0.9911
0.0428	0.6399	0.7970	0.6445	0.1975	0.9926	0.9970	0.9911
0.0460	0.6525	0.8066	0.6542	0.2039	0.9932	0.9972	0.9918
0.0492	0.6661	0.8167	0.6650	0.2104	0.9932	0.9972	0.9918
0.0520	0.6749	0.8231	0.6721	0.2168	0.9940	0.9975	0.9927
0.0561	0.6878	0.8324	0.6828	0.2237	0.9940	0.9975	0.9927
0.0594	0.7100	0.8477	0.7014	0.2302	0.9947	0.9978	0.9936
0.0621	0.7274	0.8593	0.7165	0.2366	0.9947	0.9978	0.9936
0.0658	0.7452	0.8708	0.7323	0.2426	0.9954	0.9981	0.9944
0.0690	0.7636	0.8822	0.7489	0.2490	0.9954	0.9981	0.9944
0.0723	0.7824	0.8936	0.7665	0.2564	0.9961	0.9984	0.9953
0.0759	0.7999	0.9038	0.7831	0.2624	0.9961	0.9984	0.9953
0.0792	0.8223	0.9164	0.8050	0.2693	0.9961	0.9984	0.9953
0.0819	0.8398	0.9259	0.8225	0.2762	0.9969	0.9987	0.9962
0.0856	0.8553	0.9341	0.8383	0.2827	0.9976	0.9990	0.9971
0.0925	0.8847	0.9489	0.8691	0.2886	0.9980	0.9992	0.9976
0.0990	0.9091	0.9606	0.8955	0.2946	0.9980	0.9992	0.9976
0.1059	0.9289	0.9698	0.9174	0.3020	0.9987	0.9994	0.9984
0.1128	0.9468	0.9777	0.9376	0.3080	0.9994	0.9997	0.9992
0.1192	0.9598	0.9833	0.9525	0.3144	1.0001	1.0000	1.0001
0.1261	0.9651	0.9856	0.9586				

TABLE 6.2.2

FLOW CASE: APG - ADVERSE PRESSURE GRADIENT, ASSUMING
LINEAR STATIC PRESSURE GRADIENT NORMAL TO WALL

TRAVERSE T2 AT   X = 16.62 INS.

Stagnation Pressure, P_0 = 169.2 PSIA
Stagnation Temperature, T_0 = 537.0 °R

LOCAL MAINSTREAM CONDITIONS

M_E = 3.189   ; u_E = 2079.5 FT/SEC; ρ_E = 0.00213 SLUGS/CU.FT.
P_E ($\neq P_W$) = 4.492 PSIA; T_E = 177.0 °R

INTEGRAL QUANTITIES

Displacement Thickness,	δ^*	= 0.0485 IN.
Momentum Thickness,	θ	= 0.0173 IN.
Momentum Thickness Reynolds Number	R_θ	= 0.2763·10⁵
Compressible Shape Factor,	H	= 4.523
Incompressible Velocity Shape Factor	H_{12}^1	= 1.580
Shape Parameter,	$\bar{H}$	= 1.452
Entrainment Parameter,	H_1	= 23.76
C_F, WILSON		= 0.00128
C_F, SOMMER/SHORT		= 0.00115

PROFILE DATA

y-INS.	M/M_E	u/u_E	ρ/ρ_E	y-INS.	M/M_E	u/u_E	ρ/ρ_E
0.0090	0.3401	0.5184	0.5067	0.1326	0.9607	0.9854	0.9791
0.0130	0.4207	0.6136	0.5509	0.1381	0.9698	0.9889	0.9843
0.0168	0.4567	0.6523	0.5726	0.1450	0.9768	0.9915	0.9853
0.0201	0.4863	0.6821	0.5915	0.1510	0.9825	0.9936	0.9856
0.0234	0.5090	0.7039	0.6065	0.1579	0.9888	0.9959	0.9857
0.0267	0.5284	0.7219	0.6194	0.1643	0.9897	0.9962	0.9867
0.0299	0.5449	0.7366	0.6305	0.1712	0.9910	0.9967	0.9885
0.0331	0.5609	0.7505	0.6416	0.1777	0.9919	0.9970	0.9895
0.0363	0.5755	0.7628	0.6516	0.1841	0.9926	0.9973	0.9904
0.0396	0.5866	0.7718	0.6589	0.1910	0.9926	0.9973	0.9904
0.0428	0.5995	0.7822	0.6679	0.1975	0.9926	0.9973	0.9904
0.0460	0.6123	0.7922	0.6770	0.2039	0.9932	0.9975	0.9912
0.0492	0.6262	0.8027	0.6872	0.2104	0.9932	0.9975	0.9912
0.0520	0.6354	0.8096	0.6936	0.2168	0.9939	0.9978	0.9922
0.0561	0.6491	0.8195	0.7033	0.2237	0.9939	0.9978	0.9922
0.0594	0.6711	0.8350	0.7218	0.2302	0.9947	0.9980	0.9931
0.0621	0.6886	0.8467	0.7367	0.2366	0.9947	0.9980	0.9931
0.0658	0.7069	0.8586	0.7520	0.2426	0.9954	0.9983	0.9940
0.0690	0.7255	0.8703	0.7685	0.2490	0.9954	0.9983	0.9940
0.0723	0.7447	0.8818	0.7858	0.2564	0.9961	0.9986	0.9950
0.0759	0.7628	0.8924	0.8020	0.2624	0.9961	0.9986	0.9950
0.0792	0.7855	0.9050	0.8240	0.2693	0.9961	0.9986	0.9950
0.0819	0.8034	0.9146	0.8415	0.2762	0.9968	0.9988	0.9959
0.0856	0.8199	0.9231	0.8568	0.2827	0.9976	0.9991	0.9968
0.0925	0.8513	0.9385	0.8868	0.2886	0.9980	0.9992	0.9974
0.0990	0.8780	0.9509	0.9122	0.2946	0.9980	0.9992	0.9974
0.1059	0.9007	0.9610	0.9328	0.3020	0.9986	0.9995	0.9982
0.1128	0.9216	0.9698	0.9515	0.3080	0.9993	0.9997	0.9991
0.1192	0.9378	0.9764	0.9648	0.3144	1.0001	1.0000	1.0000
0.1261	0.9468	0.9800	0.9686				

TABLE 6.3.1

FLOW CASE: APG - ADVERSE PRESSURE GRADIENT

TRAVERSE T3 AT   X = 20.62 INS.; (RUN NO.=9535)

Stagnation Pressure, P_0 = 169.2 PSIA
Stagnation Temperature, T_0 = 537.0 °R

LOCAL MAINSTREAM CONDITIONS

M_E = 2.075   ; u_E = 1727.5 FT/SEC; ρ_E = 0.00560 SLUGS/CU.FT.
P_E (=P_W) = 19.247 PSIA; T_E = 288.5 °R
δ_{995} = 0.1501 IN.

INTEGRAL QUANTITIES

Displacement Thickness,	δ^*	= 0.0380 IN.
Momentum Thickness,	θ	= 0.0117 IN.
Momentum Thickness Reynolds Number	R_θ	= 0.3914·10^5
Compressible Shape Factor,	H	= 3.234
Incompressible Velocity Shape Factor	H_{12}^1	= 1.534
Shape Parameter,	$\bar{H}$	= 1.453
Entrainment Parameter,	H_1	= 15.76

C_F, WILSON   = 0.00158

C_F, SOMMER/SHORT   = 0.00149

PROFILE DATA

y-INS.	M/M_E	u/u_E	ρ/ρ_E	y-INS.	M/M_E	u/u_E	ρ/ρ_E
0.0090	0.4747	0.5781	0.6741	0.0792	0.8403	0.8976	0.8763
0.0125	0.5330	0.6375	0.6988	0.0828	0.8494	0.9040	0.8828
0.0164	0.5851	0.6879	0.7233	0.0861	0.8600	0.9113	0.8904
0.0197	0.6108	0.7118	0.7362	0.0893	0.8720	0.9195	0.8992
0.0225	0.6328	0.7318	0.7478	0.0925	0.8839	0.9276	0.9079
0.0262	0.6584	0.7543	0.7616	0.0967	0.8894	0.9312	0.9120
0.0290	0.6776	0.7709	0.7724	0.1036	0.9185	0.9503	0.9342
0.0327	0.6921	0.7832	0.7808	0.1100	0.9387	0.9630	0.9500
0.0363	0.7073	0.7958	0.7897	0.1174	0.9577	0.9748	0.9651
0.0396	0.7231	0.8087	0.7992	0.1234	0.9720	0.9835	0.9768
0.0432	0.7356	0.8188	0.8069	0.1303	0.9791	0.9877	0.9826
0.0460	0.7423	0.8241	0.8111	0.1367	0.9862	0.9919	0.9884
0.0492	0.7489	0.8294	0.8152	0.1432	0.9890	0.9935	0.9907
0.0529	0.7637	0.8409	0.8246	0.1501	0.9918	0.9952	0.9931
0.0561	0.7746	0.8493	0.8317	0.1560	0.9939	0.9964	0.9948
0.0594	0.7854	0.8575	0.8388	0.1625	0.9960	0.9976	0.9966
0.0630	0.7943	0.8641	0.8447	0.1694	0.9967	0.9980	0.9971
0.0667	0.8065	0.8732	0.8529	0.1763	0.9980	0.9988	0.9983
0.0695	0.8159	0.8801	0.8593	0.1827	0.9987	0.9992	0.9989
0.0727	0.8202	0.8832	0.8623	0.1887	0.9994	0.9996	0.9995
0.0764	0.8295	0.8899	0.8687	0.1961	1.0001	1.0000	1.0001

TABLE 6.3.2

FLOW CASE: APG - ADVERSE PRESSURE GRADIENT, ASSUMING
LINEAR STATIC PRESSURE GRADIENT NORMAL TO WALL

TRAVERSE T3 AT   X = 20.62 INS.

Stagnation Pressure, P_0 = 169.2 PSIA
Stagnation Temperature, T_0 = 537.0 °R

LOCAL MAINSTREAM CONDITIONS

M_E = 2.075   ; u_E = 1727.4 FT/SEC; ρ_E = 0.00535 SLUGS/CU.FT.

P_E ($\neq P_W$) = 18.414 PSIA; T_E = 288.6 °R

δ_{995} = 0.1485 IN.

INTEGRAL QUANTITIES

Displacement Thickness,	δ^*	= 0.0375 IN.
Momentum Thickness,	θ	= 0.0123 IN.
Momentum Thickness Reynolds Number	R_θ	= 0.4143·10^5
Compressible Shape Factor,	H	= 3.055
Incompressible Velocity Shape Factor	H^i_{12}	= 1.537
Shape Parameter,	$\overline{H}$	= 1.460
Entrainment Parameter,	H_1	= 15.11

C_F: WILSON   = 0.00154

C_F, SOMMER/SHORT   = 0.00146

PROFILE DATA

y-INS.	M/M_E	u/u_E	ρ/ρ_E	y-INS.	M/M_E	u/u_E	ρ/ρ_E
0.0090	0.4634	0.5707	0.6903	0.0792	0.8308	0.8929	0.8850
0.0125	0.5205	0.6295	0.7150	0.0828	0.8403	0.8995	0.8909
0.0164	0.5718	0.6795	0.7395	0.0861	0.8512	0.9071	0.8981
0.0197	0.5973	0.7034	0.7521	0.0893	0.8636	0.9155	0.9065
0.0225	0.6192	0.7234	0.7634	0.0925	0.8759	0.9237	0.9149
0.0262	0.6446	0.7460	0.7770	0.0967	0.8820	0.9278	0.9183
0.0290	0.6637	0.7626	0.7875	0.1036	0.9120	0.9472	0.9398
0.0327	0.6784	0.7751	0.7954	0.1100	0.9331	0.9604	0.9548
0.0363	0.6937	0.7880	0.8039	0.1174	0.9532	0.9726	0.9690
0.0396	0.7096	0.8011	0.8131	0.1234	0.9685	0.9818	0.9798
0.0432	0.7225	0.8114	0.8203	0.1303	0.9769	0.9867	0.9845
0.0460	0.7294	0.8170	0.8241	0.1367	0.9851	0.9914	0.9893
0.0492	0.7363	0.8225	0.8277	0.1432	0.9891	0.9937	0.9905
0.0529	0.7514	0.8343	0.8367	0.1501	0.9918	0.9953	0.9929
0.0561	0.7626	0.8429	0.8434	0.1560	0.9939	0.9965	0.9947
0.0594	0.7737	0.8513	0.8500	0.1625	0.9960	0.9977	0.9965
0.0630	0.7829	0.8582	0.8554	0.1694	0.9967	0.9981	0.9971
0.0667	0.7955	0.8675	0.8632	0.1763	0.9981	0.9989	0.9983
0.0695	0.8052	0.8746	0.8693	0.1827	0.9988	0.9993	0.9989
0.0727	0.8099	0.8780	0.8717	0.1887	0.9994	0.9996	0.9995
0.0764	0.8196	0.8850	0.8776	0.1961	1.0001	1.0000	1.0001

TABLE 6.4

FLOW CASE: APG - ADVERSE PRESSURE GRADIENT

TRAVERSE T4 AT   X = 22.62 INS.; (RUN NO.=9541)

Stagnation Pressure, P_0 = 169.2 PSIA
Stagnation Temperature, T_0 = 537.0 °R

LOCAL MAINSTREAM CONDITIONS

M_E = 2.000   ; u_E = 1693.0 FT/SEC; ρ_E = 0.00609 SLUGS/CU.FT.
P_E (=P_W) = 21.635 PSIA; T_E = 298.4 °R
δ_{995} = 0.2242 IN.

INTEGRAL QUANTITIES

Displacement Thickness,	δ^*	= 0.0444 IN.
Momentum Thickness,	θ	= 0.0146 IN.
Momentum Thickness		
Reynolds Number	R_θ	= 0.5351·10^5
Compressible Shape Factor,	H	= 3.030
Incompressible Velocity		
Shape Factor	H_{12}^i	= 1.423
Shape Parameter,	$\bar{H}$	= 1.353
Entrainment Parameter,	H_1	= 17.31

C_F, WILSON = 0.00150

C_F, SOMMER/SHORT = 0.00142

PROFILE DATA

y-INS.	M/M_E	u/u_E	ρ/ρ_E	y-INS.	M/M_E	u/u_E	ρ/ρ_E
0.0090	0.5051	0.6080	0.6899	0.1023	0.8633	0.9130	0.8939
0.0134	0.5885	0.6897	0.7279	0.1057	0.8720	0.9190	0.9003
0.0158	0.6298	0.7277	0.7489	0.1086	0.8821	0.9259	0.9076
0.0193	0.6602	0.7547	0.7652	0.1115	0.8949	0.9344	0.9171
0.0228	0.6946	0.7842	0.7846	0.1144	0.9006	0.9382	0.9213
0.0257	0.7165	0.8023	0.7975	0.1224	0.9159	0.9482	0.9329
0.0292	0.7219	0.8067	0.8007	0.1288	0.9255	0.9544	0.9402
0.0321	0.7307	0.8139	0.8060	0.1357	0.9323	0.9587	0.9455
0.0355	0.7395	0.8209	0.8113	0.1420	0.9377	0.9621	0.9497
0.0384	0.7446	0.8250	0.8145	0.1489	0.9404	0.9638	0.9518
0.0419	0.7498	0.8291	0.8177	0.1558	0.9444	0.9663	0.9549
0.0453	0.7566	0.8344	0.8220	0.1616	0.9470	0.9680	0.9570
0.0488	0.7616	0.8383	0.8252	0.1685	0.9550	0.9729	0.9633
0.0528	0.7650	0.8409	0.8273	0.1748	0.9616	0.9770	0.9686
0.0563	0.7683	0.8435	0.8294	0.1806	0.9668	0.9802	0.9728
0.0597	0.7732	0.8473	0.8326	0.1875	0.9694	0.9817	0.9749
0.0626	0.7798	0.8524	0.8369	0.1932	0.9759	0.9857	0.9801
0.0660	0.7863	0.8573	0.8411	0.2001	0.9797	0.9880	0.9833
0.0695	0.7928	0.8622	0.8453	0.2065	0.9823	0.9895	0.9854
0.0729	0.7960	0.8646	0.8475	0.2128	0.9836	0.9903	0.9864
0.0758	0.8023	0.8693	0.8517	0.2191	0.9874	0.9926	0.9896
0.0793	0.8087	0.8740	0.8559	0.2255	0.9925	0.9956	0.9938
0.0827	0.8134	0.8775	0.8591	0.2318	0.9938	0.9963	0.9948
0.0856	0.8196	0.8820	0.8633	0.2381	0.9951	0.9971	0.9959
0.0914	0.8258	0.8865	0.8676	0.2439	0.9951	0.9971	0.9959
0.0919	0.8380	0.8952	0.8760	0.2514	0.9963	0.9978	0.9969
0.0954	0.8455	0.9006	0.8813	0.2583	0.9976	0.9985	0.9979
0.0983	0.8544	0.9068	0.8876	0.2646	0.9976	0.9985	0.9979
				0.2703	0.9989	0.9993	0.9990
				0.2772	0.9989	0.9993	0.9990
				0.2836	1.0001	1.0000	1.0000

TABLE 6.5

FLOW CASE: APG - ADVERSE PRESSURE GRADIENT

TRAVERSE T5 AT   X = 26.62 INS.; (RUN NO.=9543)

Stagnation Pressure, P_0 = 169.2 PSIA
Stagnation Temperature, T_0 = 537.0 °R

LOCAL MAINSTREAM CONDITIONS

M_E = 1.988   ; u_E = 1687.4 FT/SEC.; ρ_E = 0.00617 SLUGS/CU.FT.

P_E (=P_W) = 22.035 PSIA; T_E = 299.9 °R

δ_{995} = 0.2437 IN.

INTEGRAL QUANTITIES

Displacement Thickness,	δ^*	= 0.0478 IN.
Momentum Thickness,	θ	= 0.0166 IN.
Momentum Thickness Reynolds Number	R_θ	= 0.5688·10^5
Compressible Shape Factor,	H	= 2.873
Incompressible Velocity Shape Factor	H_{12}^1	= 1.395
Shape Parameter,	$\overline{H}$	= 1.332
Entrainment Parameter,	H_1	= 13.98

C_F, WILSON   = 0.00151

C_F, SOMMER/SHORT   = 0.00144

PROFILE DATA

y-INS.	M/M_E	u/u_E	ρ/ρ_E	y-INS.	M/M_E	u/u_E	ρ/ρ_E
0.0090	0.4817	0.5780	0.6945	0.1109	0.8711	0.9161	0.9040
0.0128	0.6132	0.7072	0.7518	0.1144	0.8788	0.9215	0.9094
0.0158	0.6574	0.7471	0.7741	0.1178	0.8819	0.9236	0.9115
0.0199	0.6843	0.7706	0.7884	0.1207	0.8879	0.9278	0.9158
0.0234	0.7002	0.7842	0.7972	0.1247	0.8925	0.9309	0.9190
0.0269	0.7157	0.7972	0.8059	0.1276	0.8955	0.9329	0.9211
0.0309	0.7290	0.8081	0.8136	0.1345	0.8985	0.9350	0.9233
0.0338	0.7401	0.8172	0.8201	0.1420	0.9044	0.9390	0.9276
0.0373	0.7511	0.8261	0.8266	0.1478	0.9103	0.9430	0.9318
0.0407	0.7565	0.8304	0.8298	0.1547	0.9133	0.9450	0.9340
0.0442	0.7655	0.8375	0.8352	0.1616	0.9177	0.9479	0.9372
0.0470	0.7725	0.8430	0.8396	0.1679	0.9250	0.9527	0.9425
0.0499	0.7743	0.8444	0.8405	0.1737	0.9307	0.9565	0.9468
0.0534	0.7760	0.8458	0.8417	0.1806	0.9379	0.9612	0.9521
0.0563	0.7795	0.8485	0.8439	0.1869	0.9450	0.9657	0.9574
0.0603	0.7830	0.8512	0.8460	0.1926	0.9493	0.9685	0.9606
0.0643	0.7899	0.8565	0.8504	0.1996	0.9549	0.9721	0.9649
0.0672	0.7950	0.8604	0.8536	0.2070	0.9633	0.9773	0.9713
0.0706	0.8001	0.8643	0.8568	0.2139	0.9674	0.9800	0.9745
0.0747	0.8035	0.8669	0.8590	0.2203	0.9716	0.9825	0.9777
0.0775	0.8085	0.8707	0.8622	0.2266	0.9798	0.9876	0.9841
0.0810	0.8118	0.8732	0.8644	0.2329	0.9839	0.9902	0.9872
0.0845	0.8185	0.8781	0.8687	0.2393	0.9880	0.9927	0.9904
0.0879	0.8251	0.8830	0.8729	0.2456	0.9934	0.9959	0.9947
0.0914	0.8299	0.8866	0.8762	0.2514	0.9947	0.9968	0.9958
0.0948	0.8364	0.8913	0.8805	0.2588	0.9961	0.9976	0.9968
0.0983	0.8412	0.8948	0.8837	0.2652	0.9974	0.9984	0.9979
0.1011	0.8492	0.9006	0.8890	0.2715	0.9987	0.9992	0.9990
0.1046	0.8555	0.9051	0.8933	0.2772	1.0001	1.0000	1.0000
0.1075	0.8634	0.9107	0.8987				

TABLE 6.6

FLOW CASE: APG - ADVERSE PRESSURE GRADIENT

TRAVERSE T6 AT   X = 31.62 INS.; (RUN NO.=9549)

Stagnation Pressure, P_0 = 169.2 PSIA
Stagnation Temperature, T_0 = 537.0 °R

LOCAL MAINSTREAM CONDITIONS

M_E = 2.012   ; u_E = 1698.8 FT/SEC.; ρ_E = 0.00660 SLUGS/CU.FT.

P_E (=P_w) = 21.228 PSIA; T_E = 296.8 °R

δ_{995} = 0.2543 IN.

INTEGRAL QUANTITIES

Displacement Thickness, δ^* = 0.0448 IN.
Momentum Thickness, θ = 0.0161 IN.
Momentum Thickness
Reynolds Number R_θ = 0.4978·10^5
Compressible Shape Factor, H = 2.786
Incompressible Velocity H_{12}^1 = 1.393
Shape Factor
Shape Parameter, $\overline{H}$ = 1.331
Entrainment Parameter, H_1 = 15.64

C_F, WILSON   = 0.00156

C_F, SOMMER/SHORT   = 0.00149

PROFILE DATA

y-INS.	M/M_E	u/u_E	ρ/ρ_E	y-INS.	M/M_E	u/u_E	ρ/ρ_E
0.0090	0.5233	0.6162	0.7210	0.1092	0.8776	0.9191	0.9116
0.0128	0.5915	0.6829	0.7502	0.1155	0.8876	0.9261	0.9185
0.0158	0.6227	0.7120	0.7647	0.1213	0.9041	0.9376	0.9298
0.0193	0.6637	0.7490	0.7850	0.1270	0.9155	0.9453	0.9378
0.0222	0.6863	0.7688	0.7967	0.1345	0.9251	0.9518	0.9446
0.0252	0.7081	0.7875	0.8084	0.1403	0.9315	0.9560	0.9491
0.0281	0.7250	0.8017	0.8177	0.1466	0.9393	0.9613	0.9548
0.0309	0.7394	0.8136	0.8258	0.1524	0.9393	0.9613	0.9548
0.0350	0.7495	0.8218	0.8316	0.1581	0.9393	0.9613	0.9548
0.0378	0.7614	0.8315	0.8385	0.1644	0.9393	0.9613	0.9548
0.0407	0.7654	0.8346	0.8408	0.1708	0.9393	0.9613	0.9548
0.0436	0.7693	0.8377	0.8431	0.1760	0.9393	0.9613	0.9548
0.0465	0.7770	0.8438	0.8477	0.1823	0.9425	0.9633	0.9570
0.0493	0.7808	0.8469	0.8500	0.1880	0.9471	0.9664	0.9604
0.0528	0.7884	0.8528	0.8546	0.1938	0.9502	0.9684	0.9627
0.0557	0.7922	0.8558	0.8569	0.2007	0.9533	0.9704	0.9649
0.0591	0.8016	0.8630	0.8626	0.2065	0.9580	0.9734	0.9683
0.0620	0.8053	0.8658	0.8649	0.2128	0.9626	0.9764	0.9717
0.0655	0.8090	0.8686	0.8672	0.2185	0.9671	0.9793	0.9751
0.0689	0.8108	0.8700	0.8683	0.2243	0.9717	0.9822	0.9785
0.0724	0.8145	0.8728	0.8706	0.2312	0.9762	0.9851	0.9819
0.0752	0.8199	0.8769	0.8741	0.2358	0.9807	0.9880	0.9853
0.0781	0.8235	0.8797	0.8763	0.2416	0.9882	0.9926	0.9910
0.0816	0.8271	0.8824	0.8786	0.2479	0.9912	0.9945	0.9932
0.0845	0.8307	0.8850	0.8809	0.2542	0.9912	0.9945	0.9932
0.0879	0.8361	0.8890	0.8843	0.2606	0.9927	0.9954	0.9943
0.0902	0.8431	0.8942	0.8889	0.2663	0.9941	0.9963	0.9955
0.0942	0.8502	0.8994	0.8934	0.2726	0.9956	0.9973	0.9966
0.0971	0.8554	0.9031	0.8969	0.2784	0.9986	0.9991	0.9989
0.1034	0.8674	0.9118	0.9048	0.2842	1.0000	1.0000	1.0000

TABLE 7.1

FLOW CASE: RPG - RING PRESSURE GRADIENT

TRAVERSE T1 AT   X = 11.62 INS.; (RUN NO.=9528)

Stagnation Pressure, P_0 = 120.7 PSIA; (Downstream of Ring)
Stagnation Temperature, T_0 = 537.0 °R

LOCAL MAINSTREAM CONDITIONS

M_E = 3.788   ; u_E = 2187.2 FT/SEC.; ρ_E = 0.00064 SLUGS/CU.FT.

P_E (=P_W) = 1.058 PSIA; T_F = 138.7 °R

δ_{995} = 0.1936 IN.

INTEGRAL QUANTITIES

Displacement Thickness, δ^* = 0.0782 IN.
Momentum Thickness, θ = 0.0141 IN.
Momentum Thickness
Reynolds Number R_θ = 0.8644·10^4
Compressible Shape Factor, H = 5.551
Incompressible Velocity
Shape Factor H_{12}^1 = 1.431
Shape Parameter, $\bar{H}$ = 1.344
Entrainment Parameter, H_1 = 8.750

C_F, WILSON   = 0.00161

C_F, SOMMER/SHORT   = 0.00144

PROFILE DATA

y-INS.	M/M_E	u/u_E	ρ/ρ_E	y-INS.	M/M_E	u/u_E	ρ/ρ_E
0.0090	0.3951	0.5837	0.4579	0.0815	0.6543	0.8225	0.6327
0.0125	0.4694	0.6643	0.4992	0.0838	0.6618	0.8278	0.6390
0.0149	0.4985	0.6930	0.5173	0.0865	0.6704	0.8338	0.6463
0.0183	0.5177	0.7111	0.5298	0.0893	0.6772	0.8385	0.6523
0.0206	0.5303	0.7227	0.5383	0.0920	0.6846	0.8434	0.6587
0.0229	0.5419	0.7331	0.5463	0.0944	0.6935	0.8494	0.6666
0.0262	0.5560	0.7454	0.5563	0.0971	0.7067	0.8579	0.6785
0.0285	0.5643	0.7525	0.5622	0.0999	0.7132	0.8620	0.6844
0.0308	0.5703	0.7575	0.5666	0.1054	0.7224	0.8678	0.6928
0.0336	0.5742	0.7608	0.5695	0.1109	0.7356	0.8759	0.7052
0.0363	0.5849	0.7696	0.5774	0.1160	0.7480	0.8833	0.7171
0.0391	0.5875	0.7717	0.5794	0.1215	0.7617	0.8912	0.7303
0.0414	0.5901	0.7739	0.5814	0.1266	0.7751	0.8988	0.7436
0.0446	0.5927	0.7760	0.5833	0.1321	0.7869	0.9053	0.7554
0.0469	0.5927	0.7760	0.5833	0.1376	0.8024	0.9136	0.7712
0.0497	0.5960	0.7786	0.5859	0.1427	0.8170	0.9212	0.7864
0.0525	0.5960	0.7786	0.5859	0.1473	0.8338	0.9297	0.8042
0.0552	0.5979	0.7801	0.5873	0.1528	0.8484	0.9368	0.8199
0.0575	0.5979	0.7801	0.5873	0.1583	0.8658	0.9451	0.8391
0.0598	0.6005	0.7822	0.5893	0.1634	0.8811	0.9521	0.8563
0.0630	0.6030	0.7842	0.5913	0.1689	0.9000	0.9605	0.8780
0.0653	0.6081	0.7882	0.5952	0.1740	0.9169	0.9677	0.8977
0.0681	0.6132	0.7921	0.5992	0.1786	0.9335	0.9746	0.9174
0.0709	0.6232	0.7997	0.6071	0.1841	0.9546	0.9830	0.9430
0.0736	0.6330	0.8070	0.6150	0.1897	0.9705	0.9891	0.9627
0.0759	0.6396	0.8119	0.6204	0.1943	0.9893	0.9961	0.9863
0.0787	0.6461	0.8167	0.6258	0.1993	1.0001	1.0000	1.0000

TABLE 7.2

FLOW CASE: RPG - RING PRESSURE GRADIENT

TRAVERSE T2 AT   X = 16.62 INS.; (RUN NO.=9530)

Stagnation Pressure, P_0 = 120.7 PSIA; (Downstream of Ring)
Stagnation Temperature, T_0 = 537.0 °R

LOCAL MAINSTREAM CONDITIONS

M_E = 3.621   ; u_E = 2160.9 FT/SEC; ρ_E = 0.00075 SLUGS/CU.FT.

P_E (=P_W) = 1.334 PSIA; T_E = 148.3 °R

δ_{995} = 0.3168 IN.

INTEGRAL QUANTITIES

Displacement Thickness,	δ^*	= 0.1330 IN.
Momentum Thickness,	θ	= 0.0197 IN.
Momentum Thickness Reynolds Number	R_θ	= $0.2197 \cdot 10^5$
Compressible Shape Factor,	H	= 6.752
Incompressible Velocity Shape Factor	H^1_{12}	= 1.447
Shape Parameter,	$\bar{H}$	= 1.357
Entrainment Parameter,	H_1	= 10.93
C_F, WILSON		= 0.00122
C_F, SOMMER/SHORT		= 0.00108

PROFILE DATA

y-INS.	M/M_E	u/u_E	ρ/ρ_E	y-INS.	M/M_E	u/u_E	ρ/ρ_E
0.0090	0.2868	0.4771	0.3612	0.1422	0.6570	0.8451	0.6044
0.0111	0.3284	0.5333	0.3790	0.1482	0.6717	0.8544	0.6179
0.0135	0.3504	0.5614	0.3894	0.1542	0.6846	0.8623	0.6301
0.0173	0.3673	0.5823	0.3979	0.1597	0.6944	0.8682	0.6396
0.0211	0.3841	0.6022	0.4066	0.1653	0.7041	0.8739	0.6490
0.0229	0.3993	0.6199	0.4149	0.1712	0.7191	0.8825	0.6639
0.0257	0.4074	0.6289	0.4195	0.1772	0.7338	0.8906	0.6788
0.0285	0.4194	0.6422	0.4264	0.1827	0.7443	0.8963	0.6896
0.0317	0.4287	0.6523	0.4319	0.1887	0.7534	0.9010	0.6990
0.0345	0.4401	0.6643	0.4387	0.1952	0.7662	0.9076	0.7125
0.0377	0.4467	0.6712	0.4428	0.2007	0.7784	0.9137	0.7256
0.0405	0.4527	0.6773	0.4466	0.2058	0.7892	0.9189	0.7374
0.0437	0.4613	0.6860	0.4521	0.2118	0.8014	0.9247	0.7509
0.0460	0.4676	0.6923	0.4562	0.2173	0.8122	0.9297	0.7631
0.0492	0.4760	0.7004	0.4616	0.2242	0.8255	0.9357	0.7783
0.0525	0.4841	0.7083	0.4671	0.2293	0.8383	0.9413	0.7931
0.0552	0.4876	0.7116	0.4694	0.2352	0.8510	0.9466	0.8079
0.0575	0.4936	0.7172	0.4735	0.2412	0.8645	0.9522	0.8241
0.0607	0.4995	0.7227	0.4776	0.2472	0.8779	0.9576	0.8403
0.0640	0.5039	0.7268	0.4807	0.2527	0.8877	0.9614	0.8525
0.0667	0.5097	0.7320	0.4848	0.2578	0.8986	0.9656	0.8659
0.0695	0.5173	0.7388	0.4902	0.2647	0.9104	0.9700	0.8808
0.0727	0.5211	0.7421	0.4929	0.2707	0.9209	0.9738	0.8943
0.0759	0.5267	0.7470	0.4970	0.2762	0.9290	0.9767	0.9047
0.0787	0.5359	0.7549	0.5038	0.2822	0.9363	0.9792	0.9141
0.0815	0.5413	0.7595	0.5079	0.2886	0.9466	0.9828	0.9276
0.0842	0.5485	0.7654	0.5133	0.2937	0.9588	0.9869	0.9438
0.0874	0.5573	0.7726	0.5201	0.2997	0.9626	0.9881	0.9488
0.0902	0.5625	0.7769	0.5242	0.3052	0.9706	0.9907	0.9596
0.0930	0.5677	0.7810	0.5282	0.3103	0.9765	0.9926	0.9677
0.0957	0.5745	0.7863	0.5337	0.3167	0.9835	0.9948	0.9771
0.0990	0.5800	0.7906	0.5381	0.3227	0.9871	0.9960	0.9822
0.1017	0.5850	0.7944	0.5422	0.3278	0.9908	0.9971	0.9872
0.1049	0.5916	0.7995	0.5476	0.3347	0.9927	0.9977	0.9899
0.1072	0.5966	0.8031	0.5516	0.3397	0.9947	0.9983	0.9926
0.1132	0.6063	0.8102	0.5598	0.3457	0.9966	0.9989	0.9953
0.1192	0.6174	0.8182	0.5692	0.3513	0.9980	0.9994	0.9972
0.1252	0.6283	0.8259	0.5787	0.3572	0.9990	0.9997	0.9986
0.1307	0.6391	0.8332	0.5882	0.3628	1.0000	1.0000	0.9999
0.1367	0.6496	0.8402	0.5977				

TABLE 7.3

FLOW CASE: RPG - RING PRESSURE GRADIENT

TRAVERSE T3 AT   X = 20.62 INS.; (RUN NO.=9538)

Stagnation Pressure, P_0 = 120.7 PSIA; (Downstream of Ring)
Stagnation Temperature, T_0 = 537.0 °R

LOCAL MAINSTREAM CONDITIONS

M_E = 3.608   ; u_E = 2158.8 FT/SEC.; ρ_E = 0.00076 SLUGS/CU.FT.
P_E (=P_w) = 1.358 PSIA; T_E = 149.0 °R
δ_{995} = 0.3794 IN.

INTEGRAL QUANTITIES

Displacement Thickness,	δ^*	= 0.1466 IN.
Momentum Thickness,	θ	= 0.0227 IN.
Momentum Thickness Reynolds Number	R_θ	= 0.2472·10⁵
Compressible Shape Factor,	H	= 6.455
Incompressible Velocity Shape Factor	H^i_{12}	= 1.387
Shape Parameter,	$\bar{H}$	= 1.309
Entrainment Parameter,	H_1	= 10.65

C_F, WILSON   = 0.00121

C_F, SOMMER/SHORT   = 0.00107

PROFILE DATA

y-INS.	M/M_E	u/u_E	ρ/ρ_E	y-INS.	M/M_E	u/u_E	ρ/ρ_E
0.0090	0.3173	0.5153	0.3792	0.1606	0.6758	0.8548	0.6249
0.0130	0.3603	0.5701	0.3993	0.1671	0.6855	0.8608	0.6380
0.0164	0.3900	0.6056	0.4147	0.1740	0.6968	0.8677	0.6448
0.0192	0.4045	0.6222	0.4226	0.1800	0.7076	0.8740	0.6553
0.0225	0.4191	0.6384	0.4309	0.1869	0.7185	0.8803	0.6661
0.0257	0.4325	0.6528	0.4388	0.1929	0.7253	0.8842	0.6728
0.0285	0.4439	0.6648	0.4457	0.1993	0.7333	0.8887	0.6809
0.0317	0.4565	0.6778	0.4535	0.2058	0.7479	0.8965	0.6958
0.0350	0.4651	0.6864	0.4590	0.2122	0.7540	0.8998	0.7021
0.0382	0.4756	0.6968	0.4658	0.2187	0.7656	0.9058	0.7143
0.0419	0.4838	0.7047	0.4713	0.2246	0.7720	0.9090	0.7210
0.0446	0.4919	0.7124	0.4767	0.2316	0.7820	0.9141	0.7318
0.0478	0.4999	0.7198	0.4822	0.2380	0.7932	0.9195	0.7440
0.0511	0.5077	0.7270	0.4876	0.2431	0.8026	0.9240	0.7544
0.0543	0.5149	0.7335	0.4927	0.2500	0.8135	0.9291	0.7665
0.0575	0.5225	0.7402	0.4981	0.2569	0.8243	0.9340	0.7787
0.0612	0.5281	0.7452	0.5022	0.2629	0.8349	0.9387	0.7908
0.0640	0.5337	0.7500	0.5063	0.2693	0.8465	0.9438	0.8043
0.0672	0.5392	0.7547	0.5103	0.2758	0.8568	0.9482	0.8164
0.0704	0.5446	0.7593	0.5144	0.2822	0.8659	0.9519	0.8272
0.0732	0.5500	0.7638	0.5185	0.2882	0.8745	0.9555	0.8376
0.0764	0.5536	0.7667	0.5212	0.2942	0.8861	0.9601	0.8517
0.0801	0.5624	0.7739	0.5280	0.3002	0.8946	0.9634	0.8621
0.0833	0.5676	0.7781	0.5320	0.3057	0.9044	0.9672	0.8742
0.0865	0.5779	0.7862	0.5402	0.3130	0.9137	0.9707	0.8860
0.0902	0.5829	0.7901	0.5442	0.3195	0.9223	0.9738	0.8968
0.0934	0.5858	0.7923	0.5466	0.3259	0.9296	0.9765	0.9062
0.0957	0.5892	0.7949	0.5493	0.3324	0.9390	0.9798	0.9184
0.0994	0.5954	0.7996	0.5543	0.3388	0.9483	0.9831	0.9305
0.1026	0.5986	0.8020	0.5570	0.3453	0.9565	0.9859	0.9413
0.1059	0.6047	0.8065	0.5621	0.3513	0.9624	0.9878	0.9490
0.1095	0.6096	0.8100	0.5662	0.3582	0.9704	0.9905	0.9598
0.1123	0.6128	0.8124	0.5689	0.3642	0.9749	0.9920	0.9658
0.1165	0.6160	0.8147	0.5716	0.3701	0.9796	0.9935	0.9721
0.1229	0.6250	0.8211	0.5793	0.3770	0.9824	0.9944	0.9758
0.1293	0.6328	0.8265	0.5861	0.3835	0.9873	0.9960	0.9825
0.1353	0.6390	0.8307	0.5915	0.3899	0.9900	0.9968	0.9852
0.1418	0.6492	0.8376	0.6006	0.3964	0.9947	0.9983	0.9926
0.1473	0.6552	0.8416	0.6060	0.4028	0.9973	0.9991	0.9963
0.1547	0.6670	0.8493	0.6168	0.4065	1.0000	1.0000	0.9999

TABLE 7.4

FLOW CASE: RPG - RING PRESSURE GRADIENT

TRAVERSE T4 AT   X = 22.62 INS.; (RUN NO.=9539)

Stagnation Pressure, P_0 - 120.7 PSIA; (Downstream of Ring)
Stagnation Temperature, T_0 = 537.0 °R

LOCAL MAINSTREAM CONDITIONS

M_E = 3.619   ; u_E ≈ 2160.6 FT/SEC.; ρ_E = 0.00076 SLUGS/CU.FT.

P_E (=P_W) = 1.338 PSIA; T_E = 148.4 °R

δ_{995} = 0.4111 IN.

INTEGRAL QUANTITIES

Displacement Thickness,	δ^*	= 0.1616 IN.
Momentum Thickness,	θ	= 0.0237 IN.
Momentum Thickness Reynolds Number	R_θ	= 0.2847·10³
Compressible Shape Factor,	H	= 6.814
Incompressible Velocity Shape Factor	$\bar{H}^1_{12}$	= 1.370
Shape Parameter,	$\bar{H}$	= 1.293
Entrainment Parameter,	H_1	= 11.78
C_F, WILSON		= 0.00114
C_F, SOMMER/SHORT		= 0.00100

PROFILE DATA

y-INS.	M/M_E	u/u_E	ρ/ρ_E	y-INS.	M/M_E	u/u_E	ρ/ρ_E
0.0099	0.3184	0.5268	0.3650	0.1932	0.7031	0.8770	0.6427
0.0134	0.3615	0.5820	0.3858	0.2001	0.7120	0.8819	0.6515
0.0170	0.3847	0.6097	0.3980	0.2076	0.7198	0.8863	0.6594
0.0205	0.3993	0.6265	0.4061	0.2151	0.7300	0.8918	0.6700
0.0246	0.4156	0.6447	0.4155	0.2220	0.7398	0.8970	0.6801
0.0275	0.4269	0.6569	0.4222	0.2289	0.7473	0.9009	0.6880
0.0321	0.4384	0.6691	0.4292	0.2358	0.7560	0.9053	0.6972
0.0350	0.4511	0.6822	0.4372	0.2439	0.7658	0.9102	0.7077
0.0384	0.4635	0.6945	0.4452	0.2502	0.7778	0.9160	0.7209
0.0424	0.4715	0.7024	0.4505	0.2577	0.7917	0.9226	0.7363
0.0459	0.4794	0.7100	0.4556	0.2640	0.8004	0.9266	0.7461
0.0493	0.4886	0.7187	0.4621	0.2721	0.8108	0.9313	0.7579
0.0534	0.4957	0.7253	0.4670	0.2796	0.8200	0.9353	0.7684
0.0563	0.5032	0.7321	0.4723	0.2865	0.8315	0.9403	0.7819
0.0597	0.5124	0.7404	0.4789	0.2928	0.8426	0.9449	0.7951
0.0637	0.5215	0.7483	0.4856	0.3014	0.8514	0.9485	0.8056
0.0678	0.5286	0.7544	0.4908	0.3078	0.8631	0.9532	0.8197
0.0712	0.5326	0.7578	0.4939	0.3147	0.8695	0.9557	0.8276
0.0752	0.5391	0.7633	0.4988	0.3210	0.8801	0.9598	0.8407
0.0781	0.5443	0.7676	0.5027	0.3296	0.8882	0.9629	0.8509
0.0821	0.5545	0.7759	0.5107	0.3360	0.8994	0.9670	0.8649
0.0856	0.5612	0.7812	0.5160	0.3434	0.9084	0.9702	0.8764
0.0891	0.5678	0.7864	0.5212	0.3509	0.9165	0.9731	0.8869
0.0925	0.5728	0.7903	0.5252	0.3584	0.9226	0.9752	0.8948
0.0965	0.5808	0.7964	0.5318	0.3653	0.9326	0.9787	0.9079
0.1000	0.5888	0.8024	0.5384	0.3722	0.9435	0.9823	0.9224
0.1029	0.5951	0.8071	0.5437	0.3785	0.9523	0.9852	0.9342
0.1069	0.5983	0.8093	0.5463	0.3860	0.9591	0.9874	0.9434
0.1144	0.6102	0.8179	0.5565	0.3923	0.9654	0.9894	0.9519
0.1207	0.6155	0.8216	0.5610	0.4004	0.9826	0.9947	0.9755
0.1282	0.6200	0.8247	0.5650	0.4073	0.9826	0.9947	0.9755
0.1357	0.6290	0.8309	0.5729	0.4148	0.9858	0.9957	0.9801
0.1432	0.6407	0.8387	0.5834	0.4217	0.9904	0.9971	0.9865
0.1506	0.6479	0.8434	0.5900	0.4292	0.9937	0.9981	0.9911
0.1570	0.6551	0.8480	0.5966	0.4361	0.9960	0.9988	0.9943
0.1644	0.6622	0.8525	0.6030	0.4430	0.9973	0.9992	0.9962
0.1714	0.6733	0.8594	0.6137	0.4505	0.9984	0.9995	0.9977
0.1788	0.6829	0.8652	0.6230	0.4568	0.9998	0.9999	0.9997
0.1857	0.6924	0.8708	0.6322	0.4649	1.0000	0.9999	0.9999

TABLE 7.5

FLOW CASE: RPG - RING PRESSURE GRADIENT

TRAVERSE T5 AT X = 26.62 INS.; (RUN NO.=9545)

Stagnation Pressure, P_0 = 120.7 PSIA; (Downstream of Ring)
Stagnation Temperature, T_0 = 537.0 °R

LOCAL MAINSTREAM CONDITIONS

M_E = 3.616   ; u_E = 2160.1 FT/SEC.; ρ_E = 0.00076 SLUGS/CU.FT.

P_E ($=P_W$) = 1.344 PSIA; T_E = 148.6 °R

δ_{995} = 0.4163 IN.

INTEGRAL QUANTITIES

Displacement Thickness, δ^* = 0.1447 IN.
Momentum Thickness, θ = 0.0220 IN.
Momentum Thickness
Reynolds Number R_θ = 0.2620·10^5
Compressible Shape Factor, H = 6.579
Incompressible Velocity H_{12}^1 = 1.323
Shape Factor
Shape Parameter, $\overline{H}$ = 1.248
Entrainment Parameter, E_1 = 13.52

C_F, WILSON   = 0.00117

C_F, SOMMER/SHORT   = 0.00103

PROFILE DATA

y-INS.	M/M_E	u/u_E	ρ/ρ_E	y-INS.	M/M_E	u/u_E	ρ/ρ_E
0.0090	0.3722	0.5929	0.3940	0.1938	0.7480	0.9004	0.6901
0.0128	0.3946	0.6192	0.4061	0.2007	0.7555	0.9042	0.6980
0.0158	0.4209	0.6485	0.4211	0.2070	0.7588	0.9059	0.7015
0.0187	0.4406	0.6694	0.4331	0.2128	0.7658	0.9092	0.7090
0.0222	0.4559	0.6851	0.4427	0.2191	0.7766	0.9147	0.7208
0.0252	0.4741	0.7030	0.4546	0.2255	0.7861	0.9192	0.7312
0.0286	0.4910	0.7191	0.4661	0.2312	0.7932	0.9226	0.7391
0.0315	0.5005	0.7278	0.4727	0.2375	0.7990	0.9253	0.7456
0.0350	0.5111	0.7374	0.4802	0.2439	0.8060	0.9284	0.7534
0.0378	0.5219	0.7470	0.4881	0.2502	0.8140	0.9320	0.7626
0.0413	0.5308	0.7546	0.4947	0.2565	0.8208	0.9351	0.7704
0.0453	0.5391	0.7616	0.5009	0.2634	0.8298	0.9390	0.7809
0.0476	0.5450	0.7665	0.5055	0.2703	0.8384	0.9426	0.7910
0.0511	0.5518	0.7721	0.5107	0.2767	0.8461	0.9458	0.8001
0.0539	0.5602	0.7788	0.5173	0.2824	0.8527	0.9485	0.8080
0.0568	0.5668	0.7841	0.5225	0.2893	0.8613	0.9520	0.8184
0.0603	0.5701	0.7867	0.5252	0.2951	0.8699	0.9555	0.8288
0.0637	0.5766	0.7917	0.5304	0.3014	0.8731	0.9567	0.8328
0.0666	0.5815	0.7954	0.5344	0.3078	0.8805	0.9596	0.8419
0.0706	0.5883	0.8005	0.5400	0.3141	0.8868	0.9620	0.8497
0.0735	0.5961	0.8063	0.5465	0.3204	0.8938	0.9646	0.8585
0.0770	0.6043	0.8123	0.5534	0.3262	0.9011	0.9673	0.8677
0.0798	0.6105	0.8167	0.5587	0.3336	0.9062	0.9692	0.8742
0.0827	0.6180	0.8220	0.5652	0.3394	0.9141	0.9720	0.8843
0.0862	0.6240	0.8262	0.5705	0.3463	0.9236	0.9754	0.8966
0.0891	0.6285	0.8292	0.5744	0.3521	0.9287	0.9771	0.9032
0.0925	0.6344	0.8332	0.5796	0.3590	0.9336	0.9788	0.9097
0.0960	0.6388	0.8361	0.5836	0.3653	0.9416	0.9815	0.9201
0.0988	0.6446	0.8400	0.5888	0.3711	0.9484	0.9838	0.9293
0.1023	0.6485	0.8425	0.5924	0.3774	0.9543	0.9857	0.9371
0.1046	0.6510	0.8441	0.5946	0.3837	0.9620	0.9882	0.9476
0.1115	0.6553	0.8469	0.5986	0.3900	0.9659	0.9895	0.9528
0.1178	0.6599	0.8498	0.6028	0.3964	0.9707	0.9910	0.9593
0.1236	0.6669	0.8542	0.6094	0.4027	0.9752	0.9924	0.9655
0.1305	0.6739	0.8585	0.6159	0.4090	0.9790	0.9936	0.9707
0.1368	0.6807	0.8627	0.6225	0.4148	0.9823	0.9946	0.9752
0.1437	0.6898	0.8682	0.6313	0.4211	0.9874	0.9962	0.9823
0.1495	0.6966	0.8721	0.6378	0.4275	0.9897	0.9969	0.9855
0.1564	0.7032	0.8759	0.6444	0.4338	0.9923	0.9976	0.9891
0.1621	0.7111	0.8804	0.6522	0.4401	0.9939	0.9981	0.9914
0.1685	0.7163	0.8833	0.6574	0.4459	0.9973	0.9992	0.9962
0.1748	0.7253	0.8883	0.6666	0.4523	0.9989	0.9996	0.9985
0.1811	0.7330	0.8924	0.6744	0.4597	0.9991	0.9997	0.9987
0.1869	0.7418	0.8971	0.6836	0.4660	1.0000	0.9999	0.9999

TABLE 7.6

FLOW CASE: RPG - RING PRESSURE GRADIENT

TRAVERSE T6 AT   X = 31.62 INS.; (RUN NO.=9547)

Stagnation Pressure, P_0 = 120.7 PSIA; (Downstream of Ring)
Stagnation Temperature, T_0 = 537.0 °R

LOCAL MAINSTREAM CONDITIONS

M_E = 3.198   ; u_E = 2081.5 FT/SEC.; ρ_E = 0.00116 SLUGS/CU.FT.

P_E (=P_W) = 2.447 PSIA; T_E = 176.3 °R

δ_{995} = 0.3683 IN.

INTEGRAL QUANTITIES

Displacement Thickness,	δ^*	= 0.1269 IN.
Momentum Thickness,	θ	= 0.0227 IN.
Momentum Thickness Reynolds Number	R_θ	= 0.3319·10⁵
Compressible Shape Factor,	H	= 5.580
Incompressible Velocity Shape Factor	H^i_{12}	= 1.393
Shape Parameter,	$\bar{H}$	= 1.315
Entrainment Parameter,	H_1	= 14.84

C_F, WILSON   = 0.00123

C_F, SOMMER/SHORT   = 0.00110

PROFILE DATA

y-INS.	M/M_E	u/u_E	ρ/ρ_E	y-INS.	M/M_E	u/u_E	ρ/ρ_E
0.0090	0.3368	0.5164	0.4253	0.1644	0.7263	0.8719	0.6937
0.0134	0.3368	0.5164	0.4253	0.1708	0.7370	0.8784	0.7039
0.0175	0.4044	0.5977	0.4578	0.1771	0.7467	0.8841	0.7132
0.0211	0.4319	0.6282	0.4727	0.1834	0.7563	0.8897	0.7225
0.0240	0.4546	0.6522	0.4858	0.1903	0.7675	0.8960	0.7335
0.0281	0.4761	0.6741	0.4987	0.1978	0.7810	0.9035	0.7471
0.0304	0.4885	0.6864	0.5065	0.2042	0.7891	0.9078	0.7554
0.0338	0.5059	0.7031	0.5177	0.2111	0.8012	0.9142	0.7678
0.0373	0.5124	0.7092	0.5220	0.2185	0.8125	0.9201	0.7797
0.0401	0.5197	0.7160	0.5269	0.2255	0.8229	0.9254	0.7907
0.0436	0.5307	0.7260	0.5344	0.2318	0.8332	0.9304	0.8017
0.0465	0.5366	0.7312	0.5384	0.2387	0.8449	0.9361	0.8144
0.0505	0.5460	0.7395	0.5450	0.2450	0.8554	0.9411	0.8261
0.0545	0.5520	0.7447	0.5493	0.2514	0.8638	0.9450	0.8354
0.0580	0.5591	0.7508	0.5544	0.2594	0.8743	0.9498	0.8472
0.0614	0.5653	0.7561	0.5589	0.2657	0.8845	0.9543	0.8589
0.0649	0.5711	0.7609	0.5632	0.2726	0.8948	0.9588	0.8707
0.0689	0.5757	0.7647	0.5666	0.2796	0.9049	0.9632	0.8825
0.0724	0.5845	0.7719	0.5732	0.2870	0.9150	0.9674	0.8944
0.0758	0.5901	0.7764	0.5775	0.2939	0.9205	0.9697	0.9010
0.0793	0.5978	0.7826	0.5834	0.3003	0.9302	0.9736	0.9126
0.0827	0.6055	0.7886	0.5894	0.3072	0.9370	0.9764	0.9208
0.0856	0.6130	0.7944	0.5954	0.3135	0.9434	0.9789	0.9287
0.0891	0.6226	0.8017	0.6030	0.3204	0.9489	0.9811	0.9355
0.0925	0.6257	0.8040	0.6056	0.3279	0.9572	0.9842	0.9456
0.0960	0.6330	0.8094	0.6115	0.3342	0.9633	0.9866	0.9532
0.0994	0.6403	0.8147	0.6175	0.3417	0.9680	0.9883	0.9592
0.1023	0.6504	0.8220	0.6260	0.3486	0.9767	0.9916	0.9702
0.1057	0.6562	0.8261	0.6309	0.3555	0.9801	0.9928	0.9744
0.1098	0.6601	0.8288	0.6343	0.3630	0.9832	0.9940	0.9784
0.1127	0.6651	0.8323	0.6385	0.3693	0.9865	0.9952	0.9826
0.1155	0.6690	0.8350	0.6419	0.3757	0.9897	0.9963	0.9866
0.1190	0.6739	0.8383	0.6461	0.3814	0.9923	0.9972	0.9900
0.1230	0.6768	0.8403	0.6487	0.3877	0.9936	0.9977	0.9917
0.1270	0.6768	0.8403	0.6487	0.3952	0.9956	0.9984	0.9943
0.1299	0.6826	0.8441	0.6538	0.4021	0.9969	0.9989	0.9959
0.1334	0.6855	0.8460	0.6563	0.4079	0.9982	0.9993	0.9976
0.1374	0.6893	0.8485	0.6597	0.4154	0.9988	0.9995	0.9984
0.1403	0.6940	0.8516	0.6640	0.4223	0.9988	0.9995	0.9984
0.1443	0.7015	0.8565	0.6708	0.4292	0.9995	0.9998	0.9993
0.1472	0.7052	0.8589	0.6742	0.4361	0.9995	0.9998	0.9993
0.1512	0.7099	0.8618	0.6784	0.4430	0.9996	0.9998	0.9994
0.1581	0.7172	0.8664	0.6852	0.4493	1.0001	1.0000	1.0000

TABLE 8: INITIAL CONDITIONS FOR THE CALCULATION METHODS

METHOD	SPECIFIED INPUT	ZERO PRESSURE GRADIENT FLOW	ADVERSE PRESSURE GRADIENT FLOW	RING PRESSURE GRADIENT FLOW
1. BRADSHAW/ FERRISS	Streamwise Pressure Distribution	Experimental	Experimental	Experimental
	Calculation starts at X (INS.):	1.25	1.25	10.59
	Initial Velocity Profile:	Bradshaw's Mach 4 `	Bradshaw's Mach 4 `	Experimental and Modified
	Initial Shear Stress Profile:	Bradshaw's Mach 4 `	Bradshaw's Mach 4 `	Flat Plate; and with τ_{max} at $y>0$
	δ_{995} (IN.)	0.075	0.100	0.223
	$R_o = \frac{a_o}{\nu_o}$ (per IN.)	$7 \cdot 10^6$	$7 \cdot 10^5$	$7 \cdot 10^6$
	c_F	0.00120	0.00120	0.00120
2. NASH	Streamwise Mach Number Distribution	Experimental	Experimental	Experimental
	Calculation starts at X (INS.):	0.03	0.03	11.62
	Initial Velocity Profile:	Bradshaw's Mach 4 `	Bradshaw's Mach 4 `	Experimental
	Initial Shear Stress Profile:	Bradshaw's Mach 4 `	Bradshaw's Mach 4 `	τ_{max} at $y>0$
	δ_{995} (IN.)	0.055	0.055	0.20
	δ^* (IN.)	0.019	0.019	0.036
	θ (IN.)	0.0026	0.0026	0.0112
	$R_o \frac{a_o}{\nu_o}$ (per IN.)	$7 \cdot 10^6$	$7 \cdot 10^6$	$7 \cdot 10^6$
	c_F	0.00162	0.00162	0.00095
3. CHAN	Streamwise Mach Number Distribution	Experimental	Experimental	Experimental
	Calculation starts at X (INS.):	1.62	1.62	11.00
	Initial Velocity Profile:	Bradshaw's Mach 4 `	Bradshaw's Mach 4 `	Experimental
	$R_o = \frac{a_o}{\nu_o}$ (per IN.)	$7 \cdot 10^6$	$7 \cdot 10^6$	$7 \cdot 10^6$
4. HEAD/GREEN	Streamwise Mach Number Distribution	Experimental	Experimental	Experimental
	Calculation starts at X (INS.):	10.53	10.53	10.53
	Entrainment, $\Delta = \delta - \delta^*$	0.100	0.100	0.115
	θ (IN.)	0.009	0.009	0.014
	R_θ	10370	9820	8640
5. STRATFORD/ BEAVERS	Streamwise Mach Number Distribution	Experimental	Experimental	Experimental
	Calculation starts at X (INS.):	11.53	11.53	11.53
	δ^* (IN.)	0.0645	0.0645	0.118
	θ (IN.)	0.0084	0.0084	0.0162

TABLE 8: (continued)

METHOD	SPECIFIED INPUT	ZERO PRESSURE GRADIENT FLOW	ADVERSE PRESSURE GRADIENT FLOW	RING PRESSURE GRADIENT FLOW
6. CEBECI/SMITH	Streamwise Velocity Distribution	Experimental	Experimental	Experimental
	Calculation starts at X (INS.):	Leading-Edge	Leading-Edge	Velocity Profile Matched to Experimental at T1 by adding X = 650 INS.
	Transition Occurs at X (INS.):	3.07	3.07	3.07
	$R_E = \dfrac{u_E}{\nu_E}$ (per inch)	$0.138 \cdot 10^7$	$0.138 \cdot 10^7$	$0.101 \cdot 10^7$
	M_E	4.00	4.00	4.00
	T_E °R	128.2	128.2	128.2
7. ZWARTS	Streamwise Mach Number Distribution	Experimental	Experimental	Experimental
	Calculation starts at X (INS.):	4.9	4.9	27.0 (stretched due to ring perturbation)
	R_θ (Incompressible)	$0.154 \cdot 10^4$	$0.154 \cdot 10^4$	$0.121 \cdot 10^5$
	H^*, Energy Shape Factor	1.790	1.790	1.820
	$V^* = \sqrt{2/C_{F_1}}$	21.54	21.54	25.69
	Clauser Constant, k	0.027	0.027	0.027
	u/u_{TW} at Matching Point Between Inner and Outer Regions	18.17	18.17	22.43
	P_0	168.7	168.7	124.0
	T_0	298 °K	298 °K	298 °K
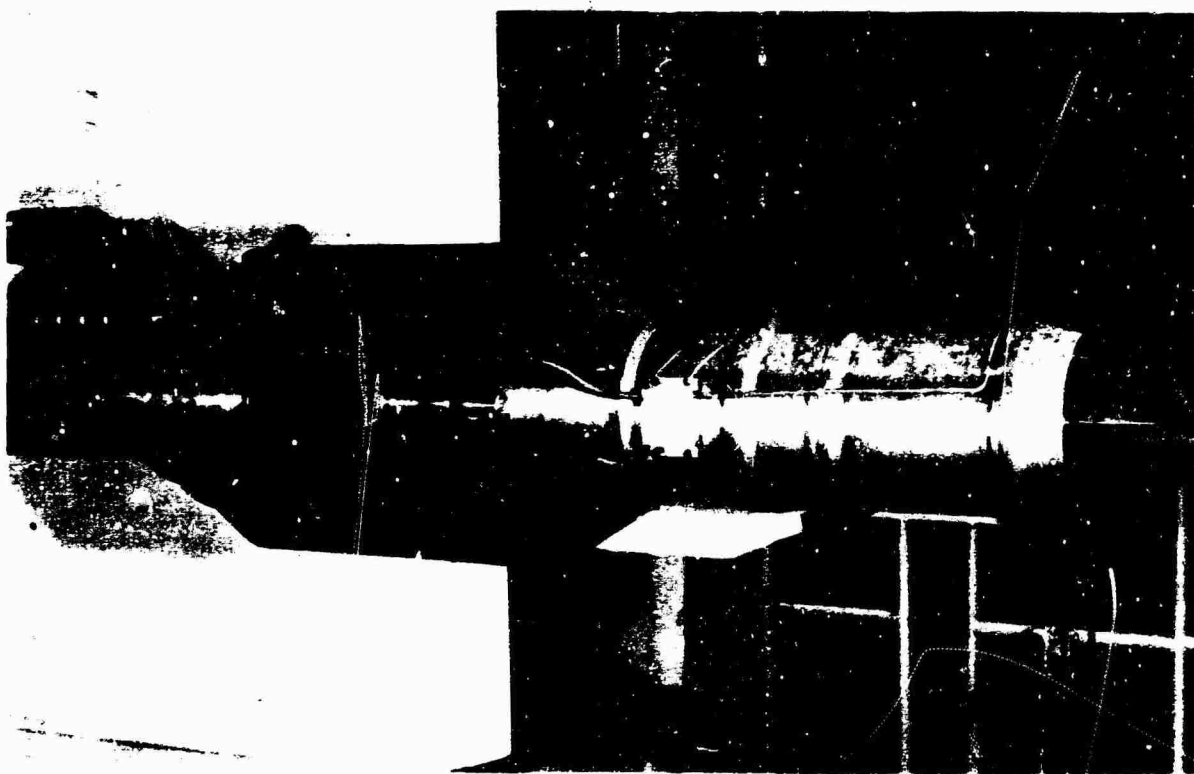
Fig.1   The parallel duct with centre-body extended, mounted in the NAE 5 x 5 ft wind tunnel

RING (USED WITH CENTRE-BOOY RETRACTEO)

⌐ THERMOCOUPLE

MACH 4 MAINSTREAM

RETRACTEO CENTRE-BOOY

TEST B/L SURFACE

T1   T2   T3 T4   T6   T6

X in

R_x BASED ON TEST LENGTH ~ 50 x 10^6

⊕ COBRA PROBE MOUNTING LOCATIONS

T I	11·62 INCHES FROM LEAOING EDGE
T 2	16·62
T 3	20·62
T 4	22·62
T 5	26·62
T 6	31·62

WETTEO TEST SURFACE LENGTH • 33·0 INCHES
INTERNAL DIAMETER OF COWL • 9·012 INCHES
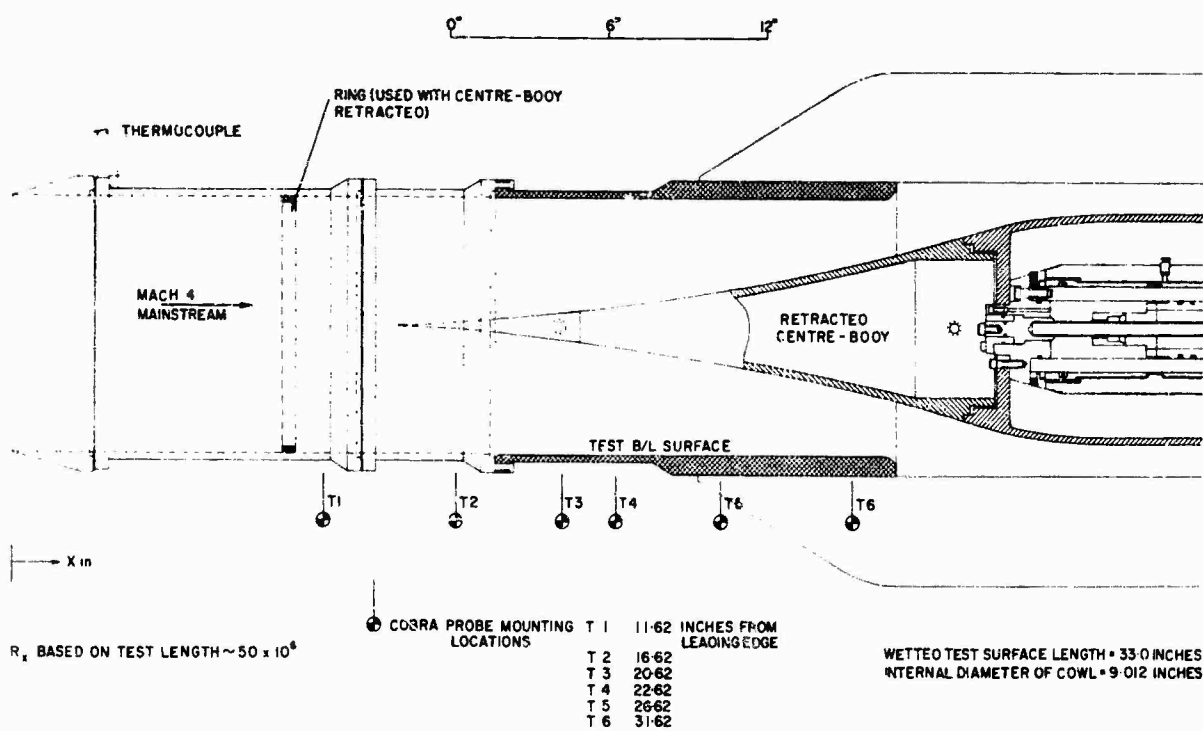
Fig 2   Section through parallel duct

O.D. = 0·016   'PRESTON' TUBE

r = 5 × O.D.

80°

r = 5 × O.D.

0·080

90°

0·008

EPOXY CEMENT

STATIC
PRESSURE
ORIFICE

BRASS
COLLAR

0·138   0·08

DUCT WALL

0·04

~0·1

0·025

0·008

0·038
0·040

0·0625

0·218
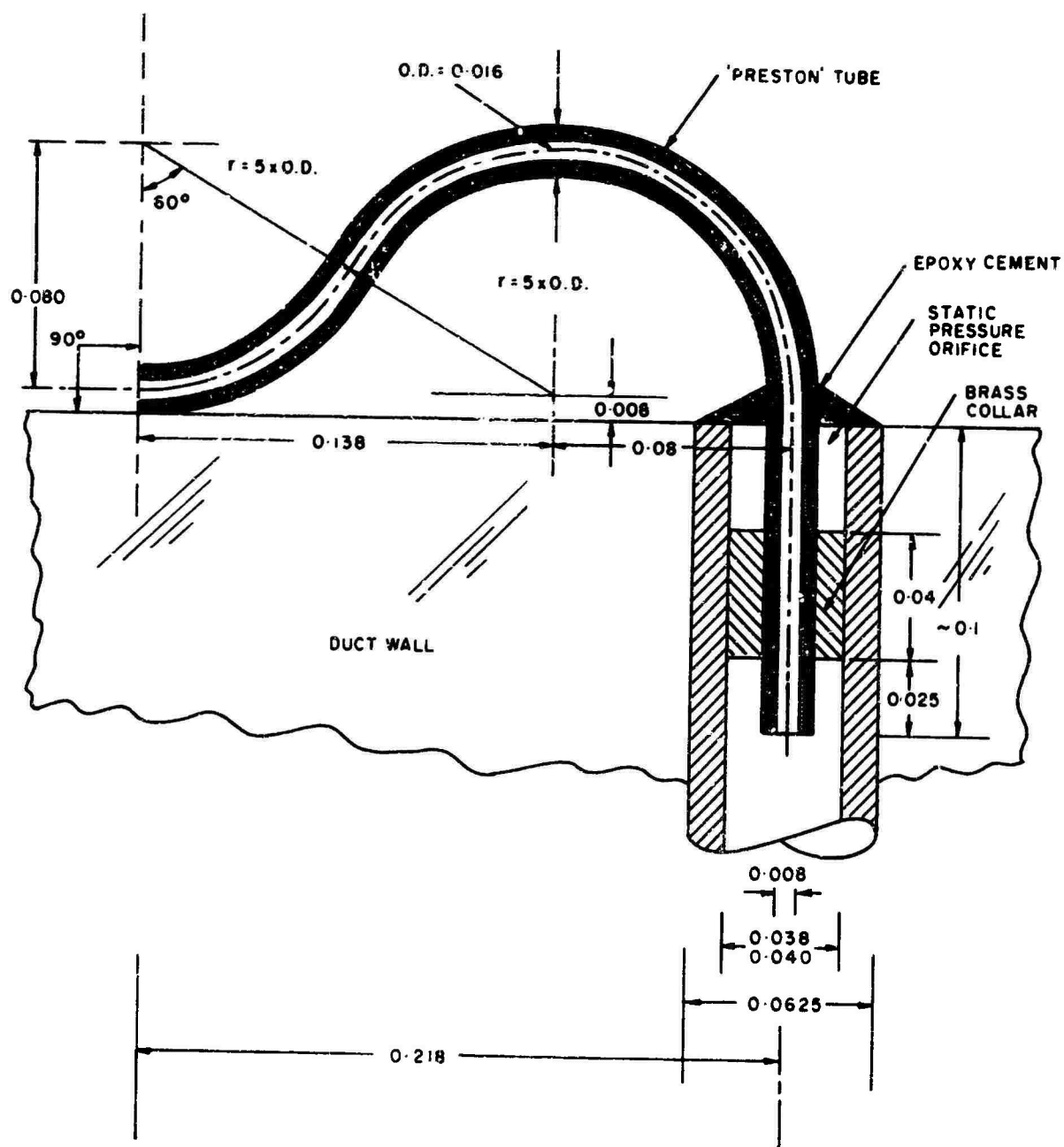
NOTE : ALL DIMENSIONS ARE IN INCHES

Fig. 3   Preston tube

SECTION IN PLAN VIEW

PLAN VIEW

SIDE ELEVATION
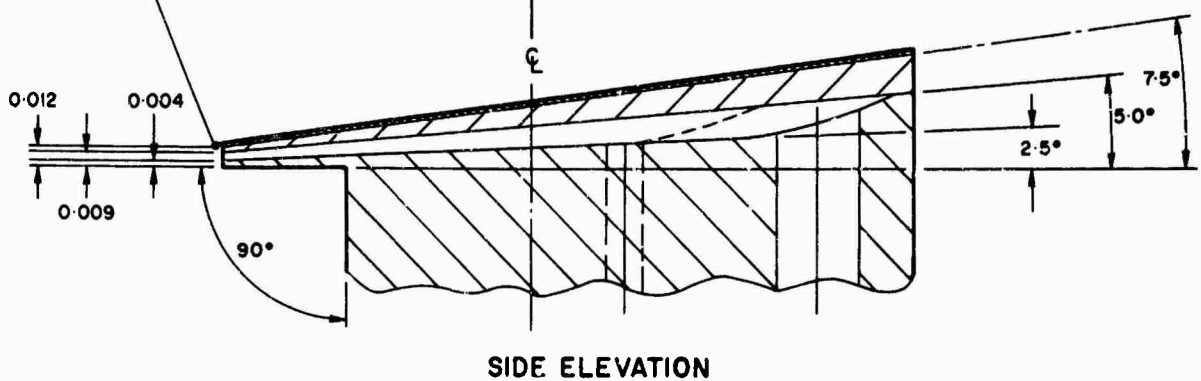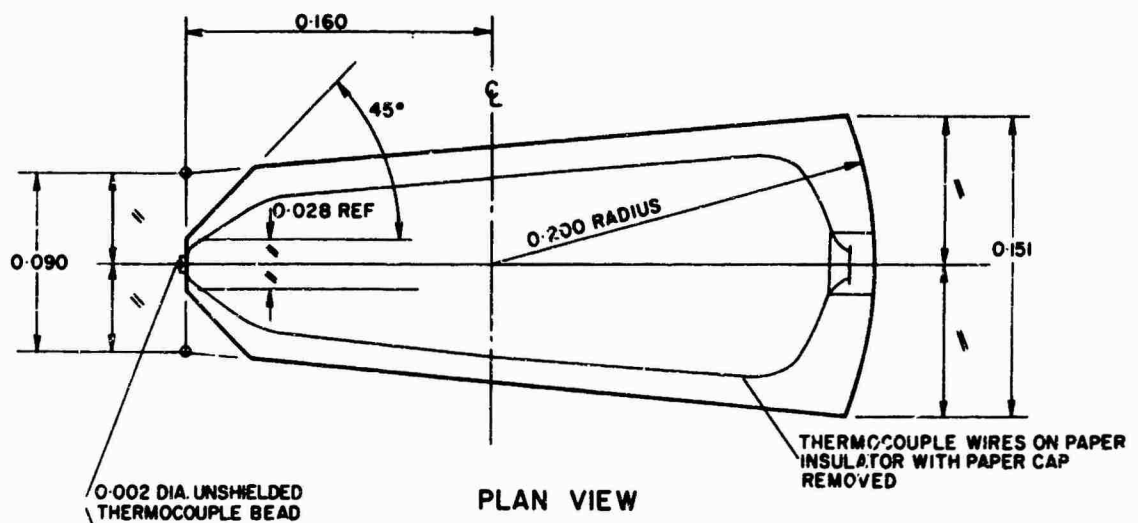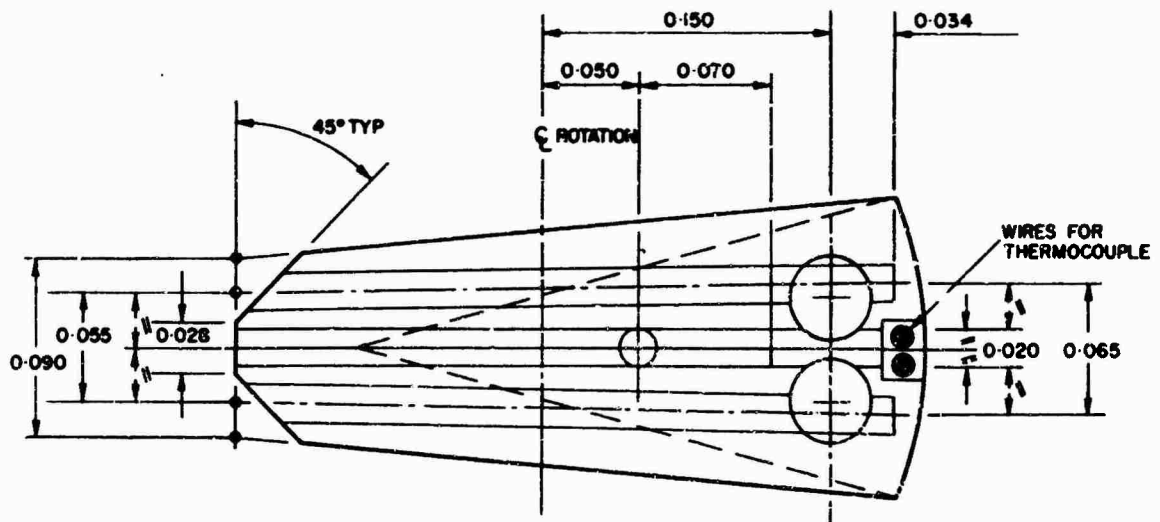
Fig.4   Cobra probe head
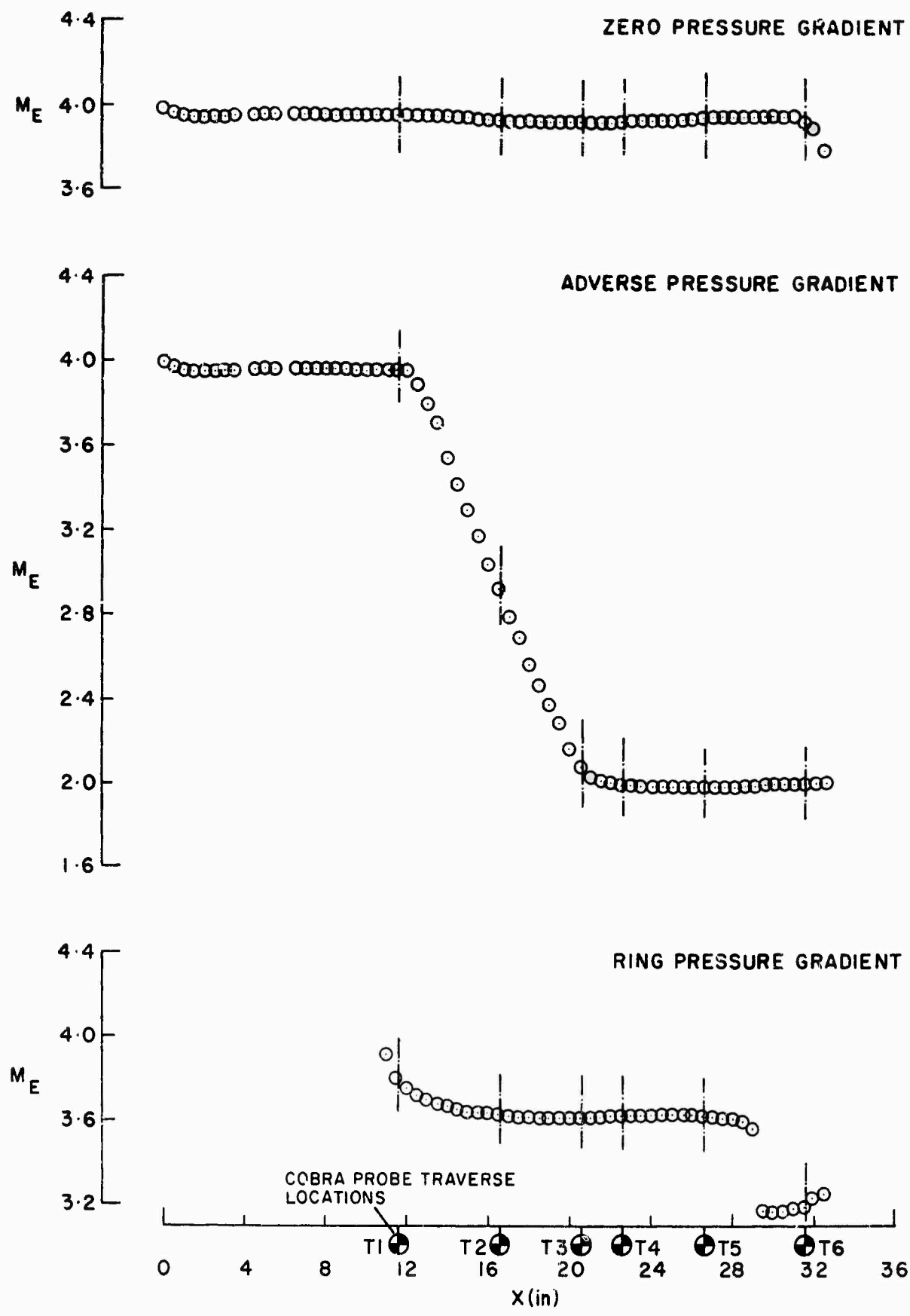
Fig.5 Mach number distributions along duct
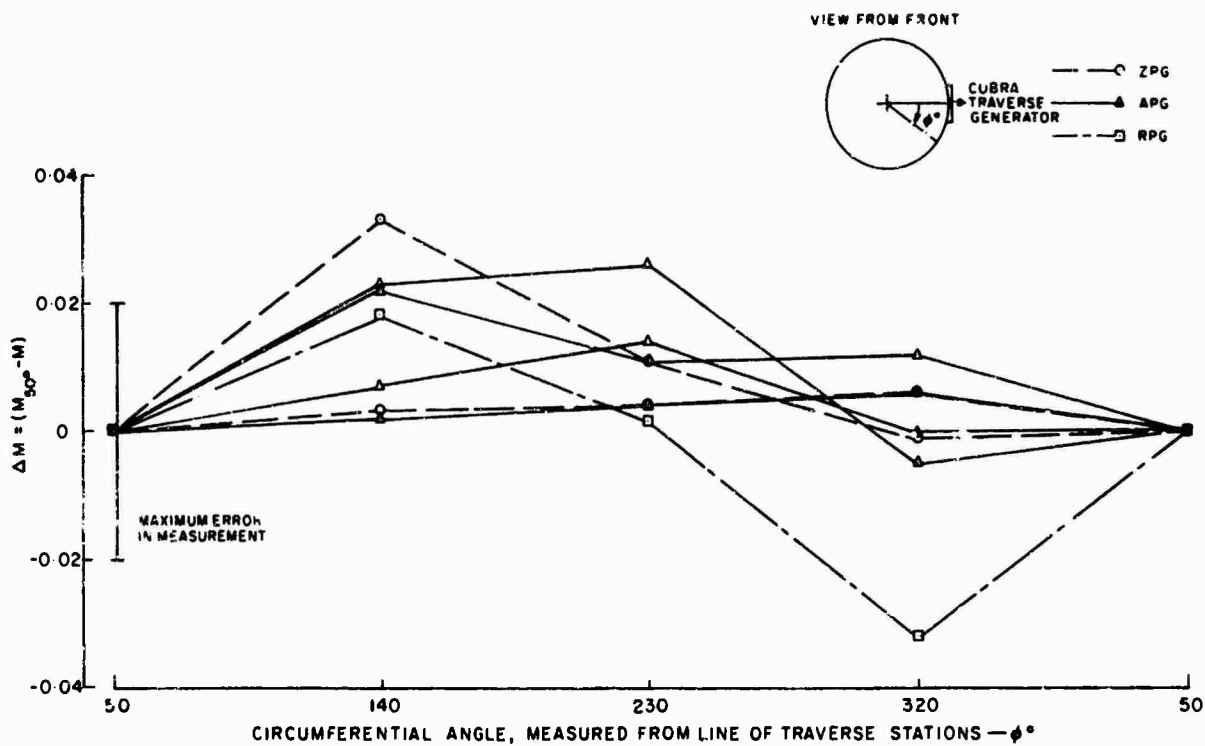
Fig.6a   Tests for flow two-dimensionality – Circumferential variation in Mach number at X=11.75 inches
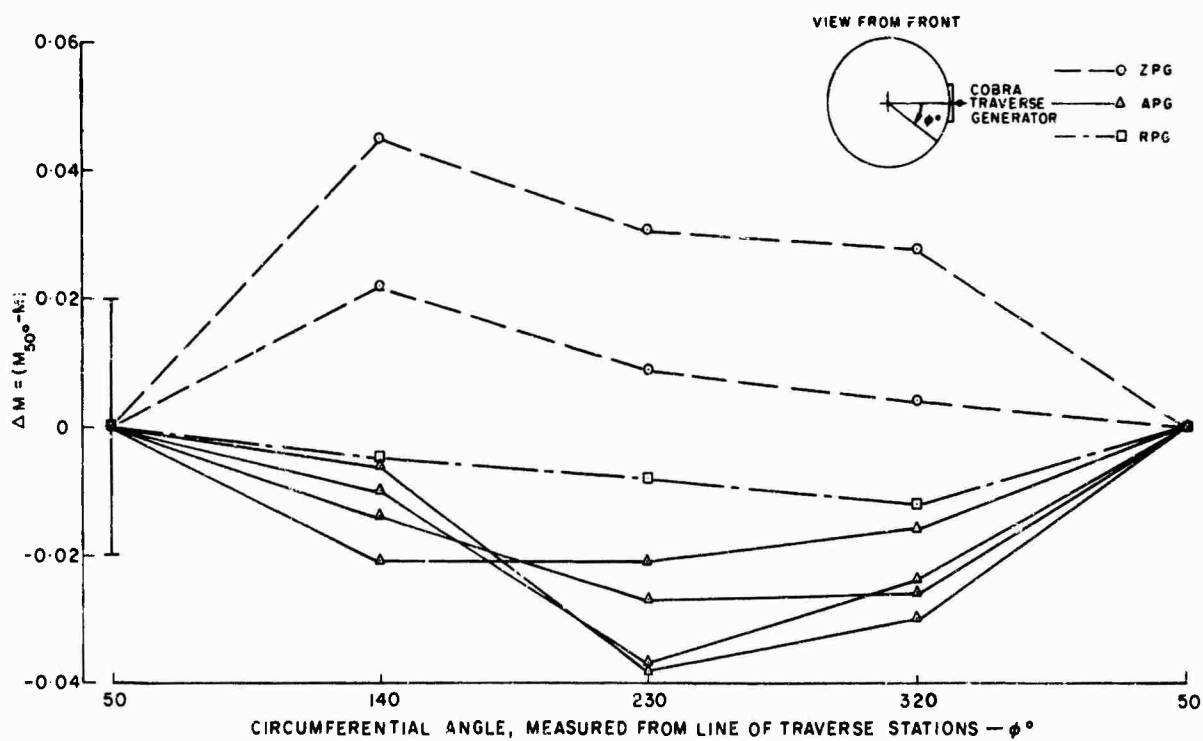
Fig.6b   Tests for flow two-dimensionality – Circumferential variation in Mach number at X=21.75 inches
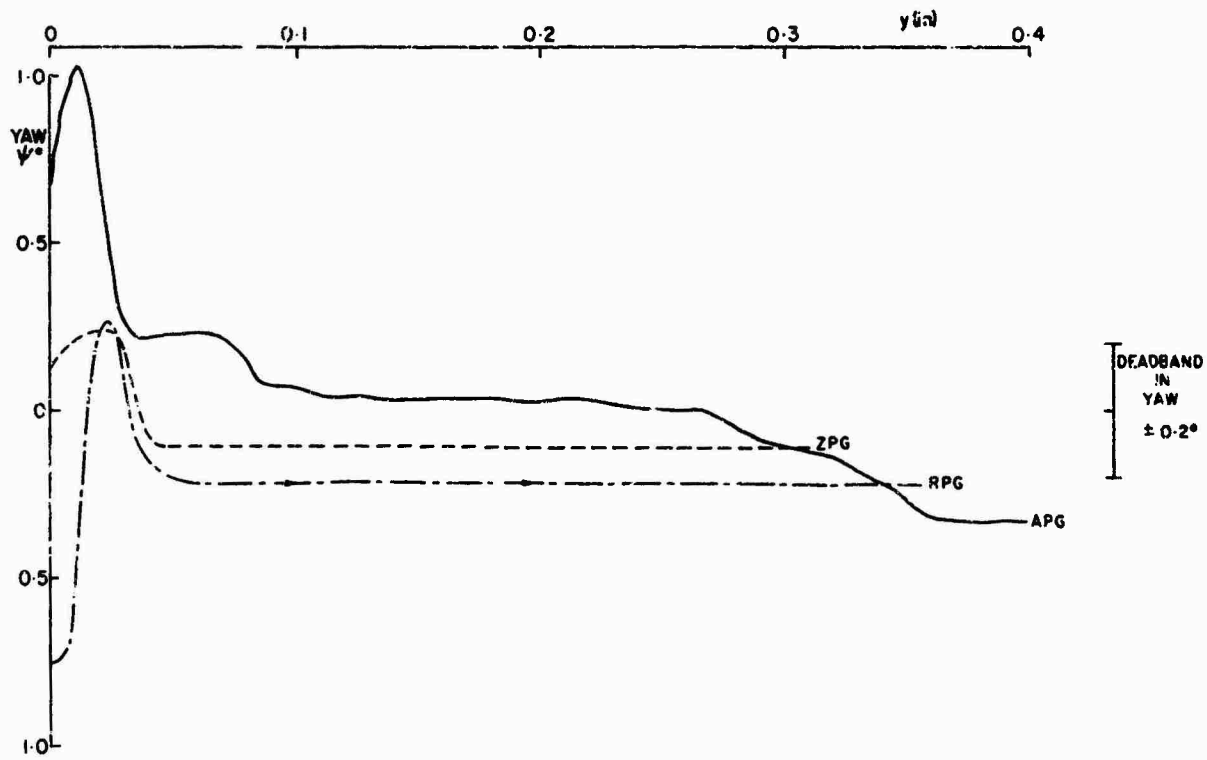
Fig.7a Tests for flow two-dimensionality – Skew in boundary layers at traverse station T2 (X=16.62 inches)
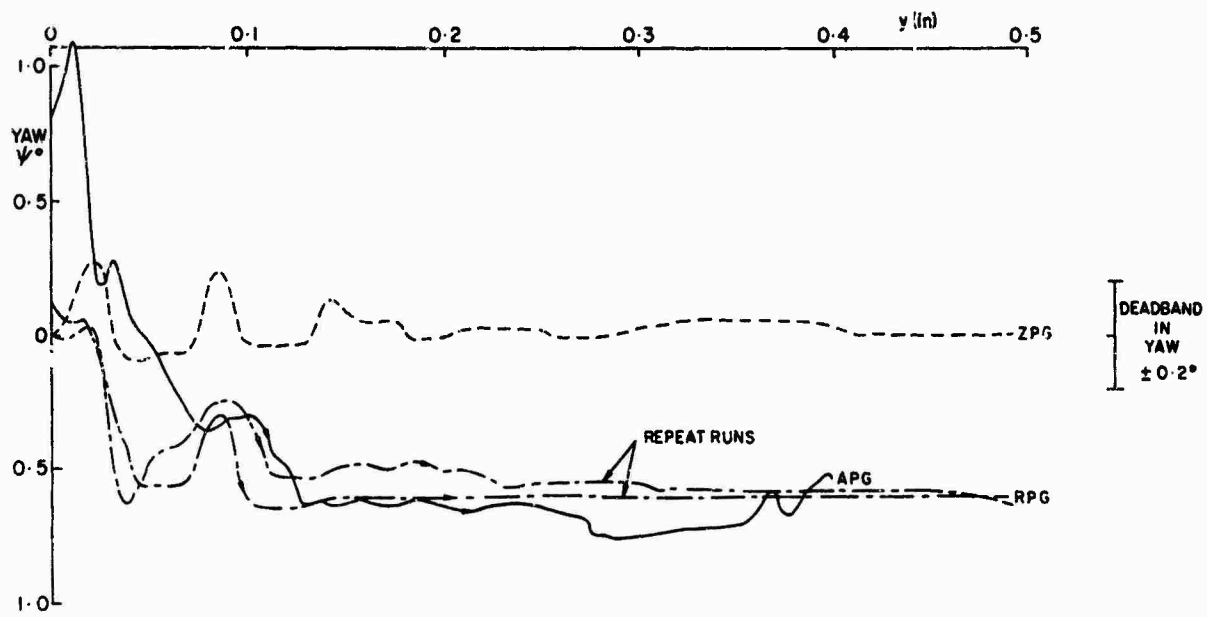
Fig.7b Tests for flow two-dimensionality – Skew in boundary layers at traverse station T6 (X=31.62 inches)
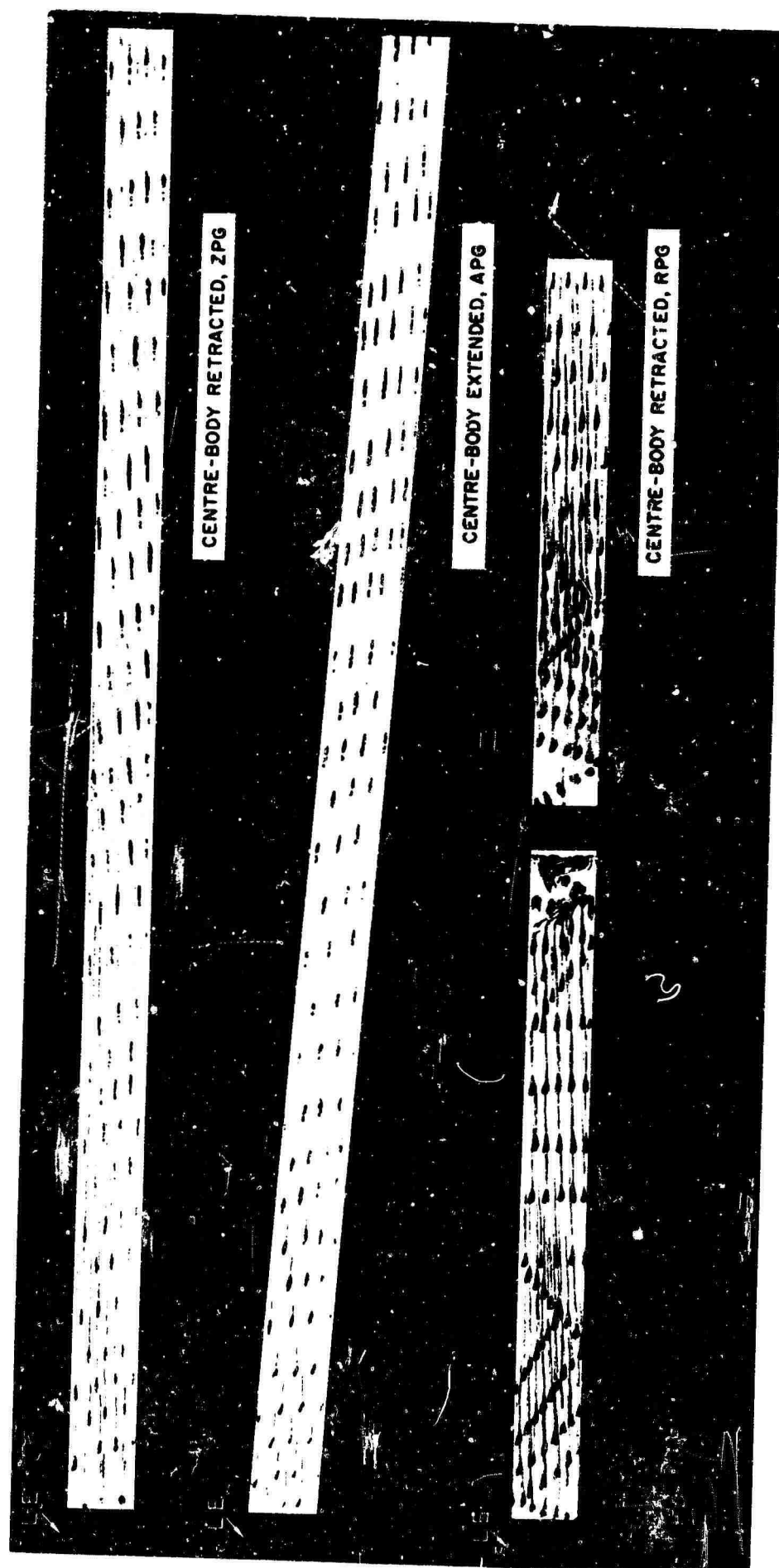
Fig. 8 Sample oil dot flow visualisation along the duct for the three-boundary-layer experiments
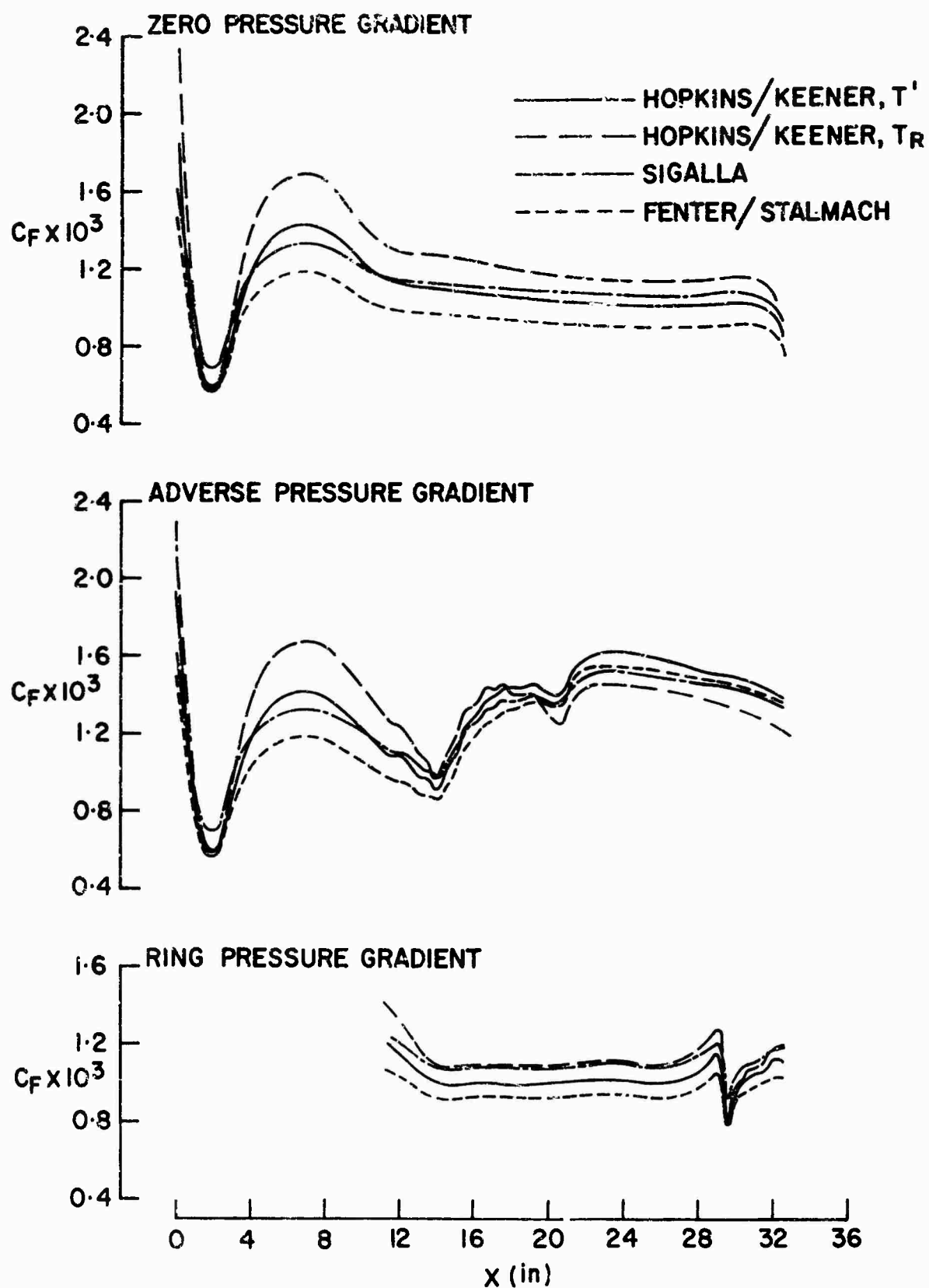
Fig.9a   Distributions of skin friction coefficient along the duct
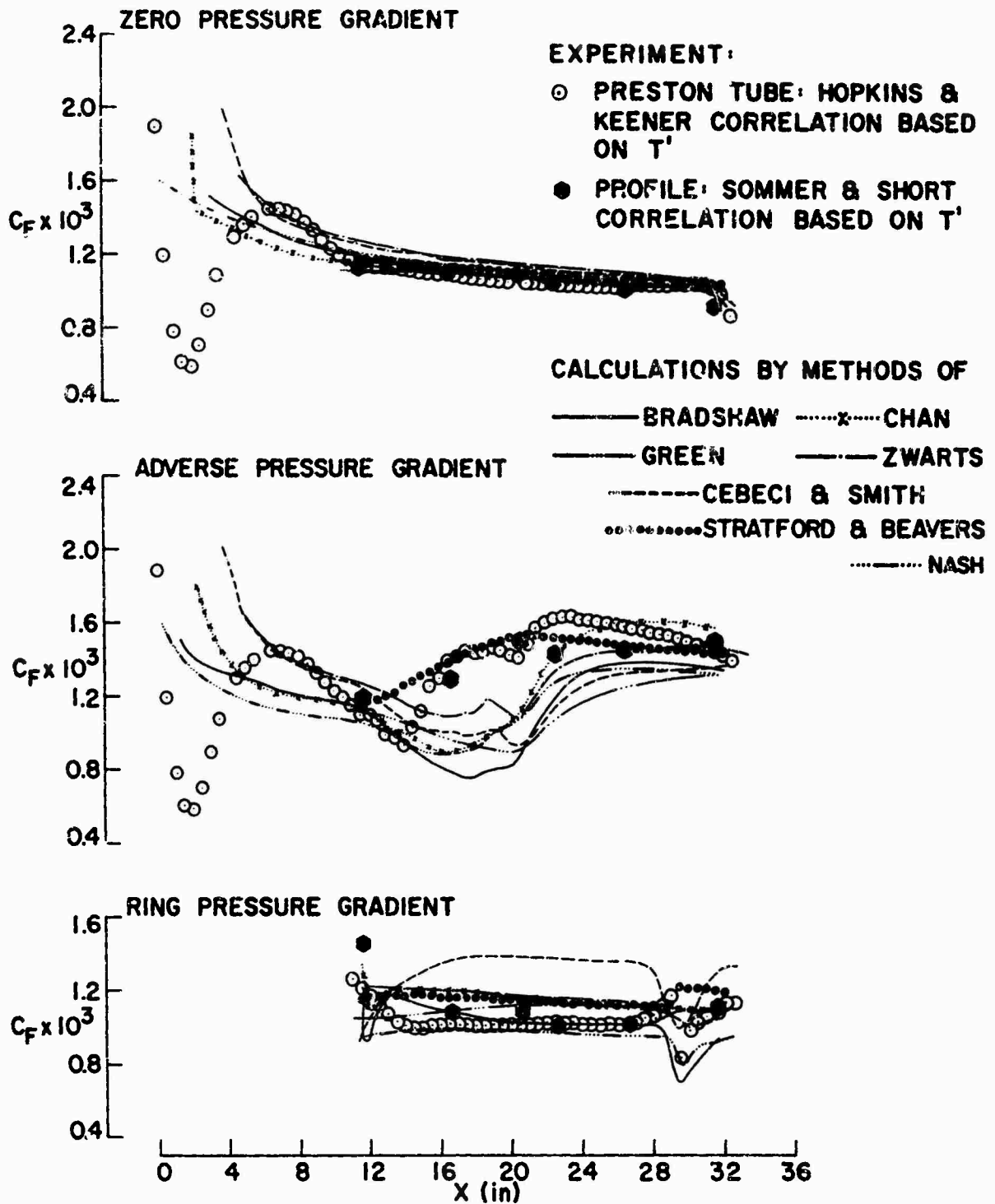
Fig.9b Distributions of skin friction coefficient along the duct
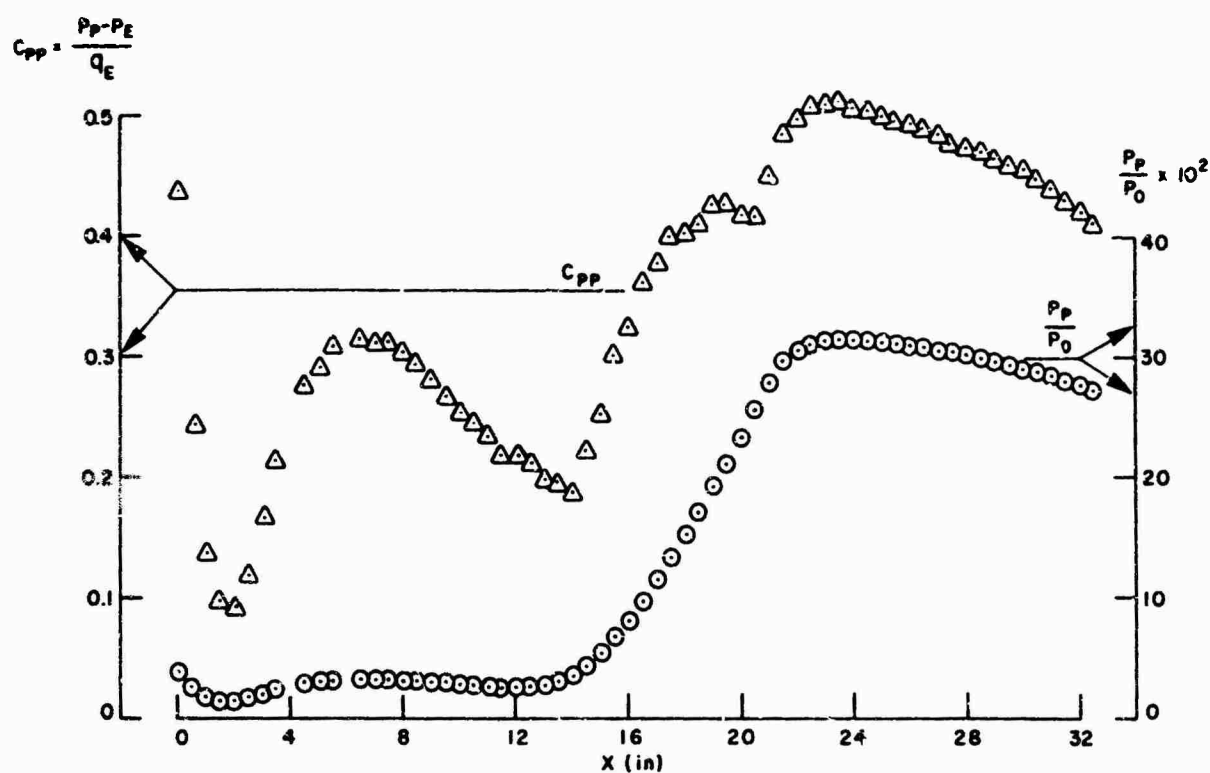
Fig.10 Preston tube pressures and pressure coefficients for adverse pressure gradient flow
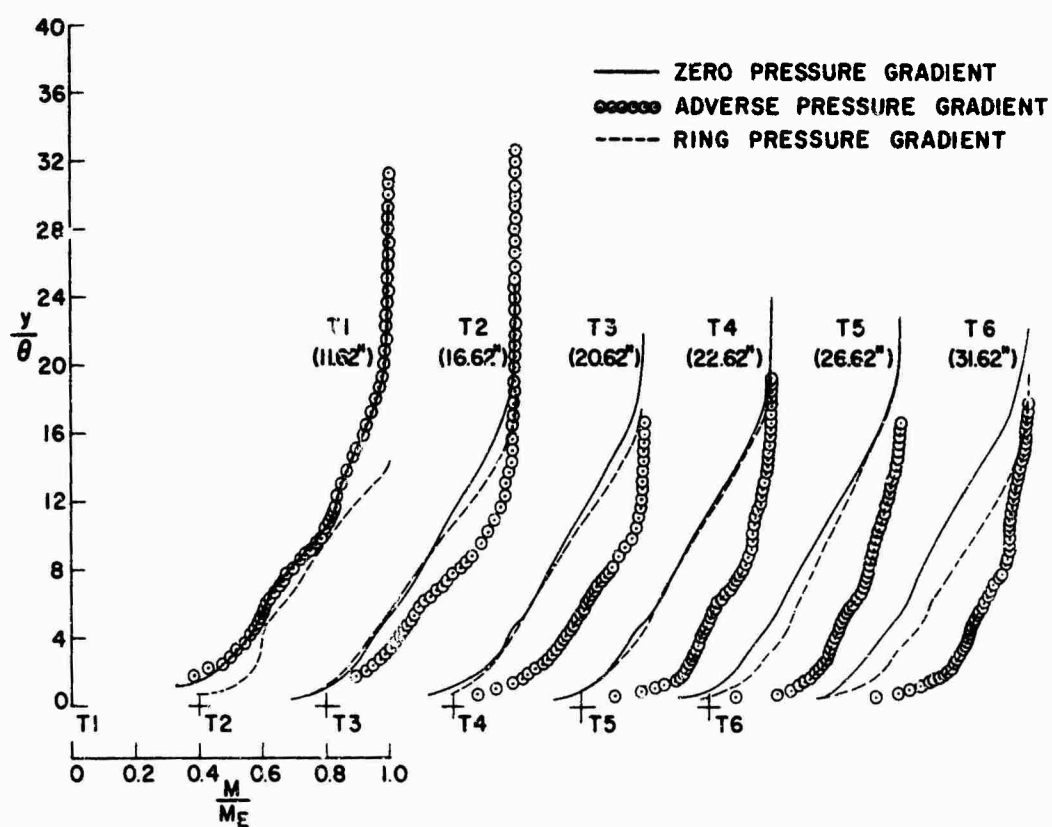
Fig.11 Normalised experimental Mach number profiles
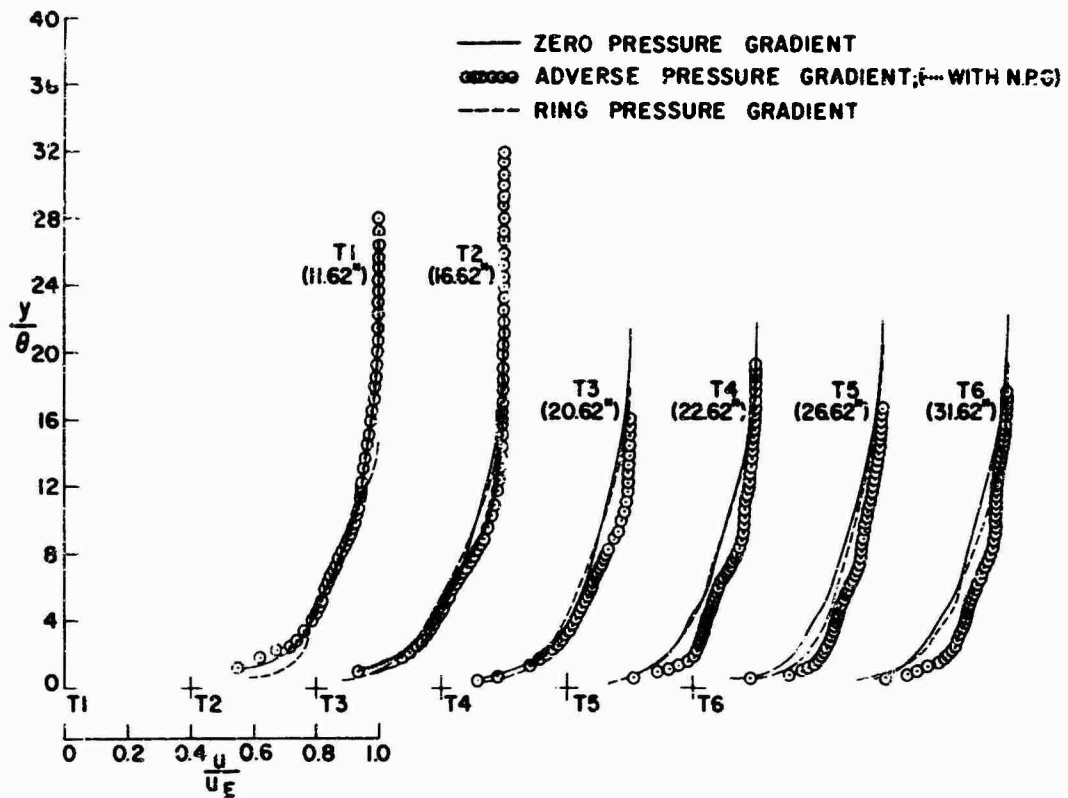
Fig.12   Normalised experimental velocity profiles
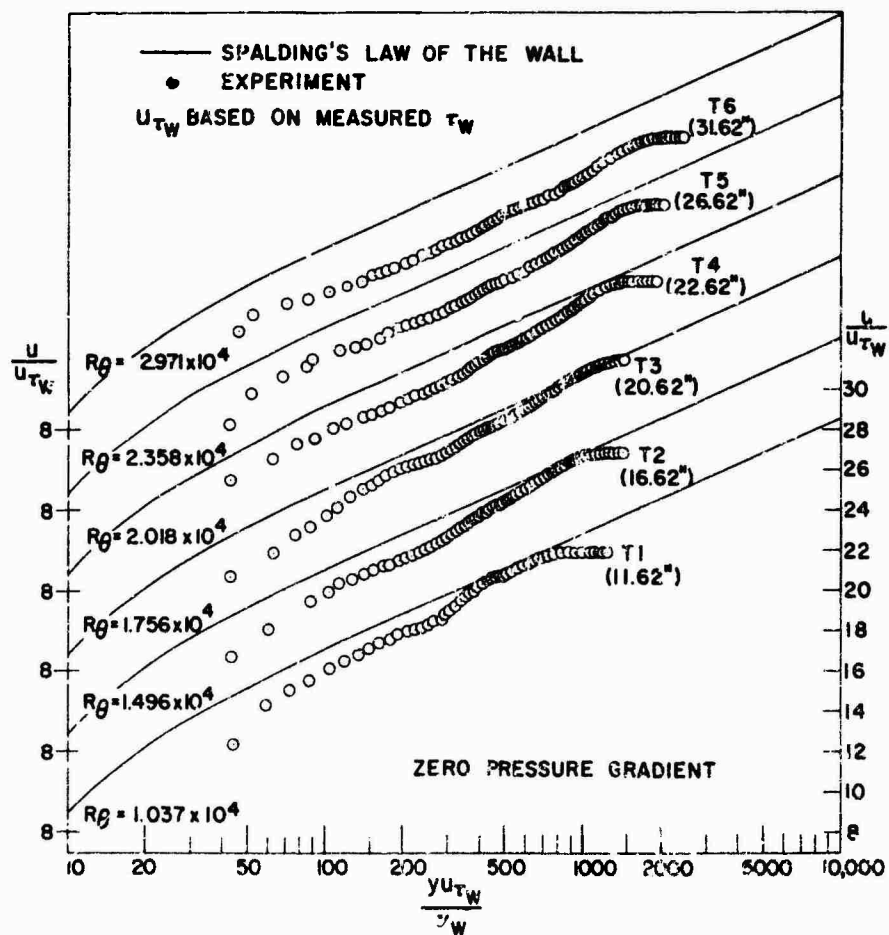
Fig.13   Experimental logarithmic velocity profiles: zero pressure gradient
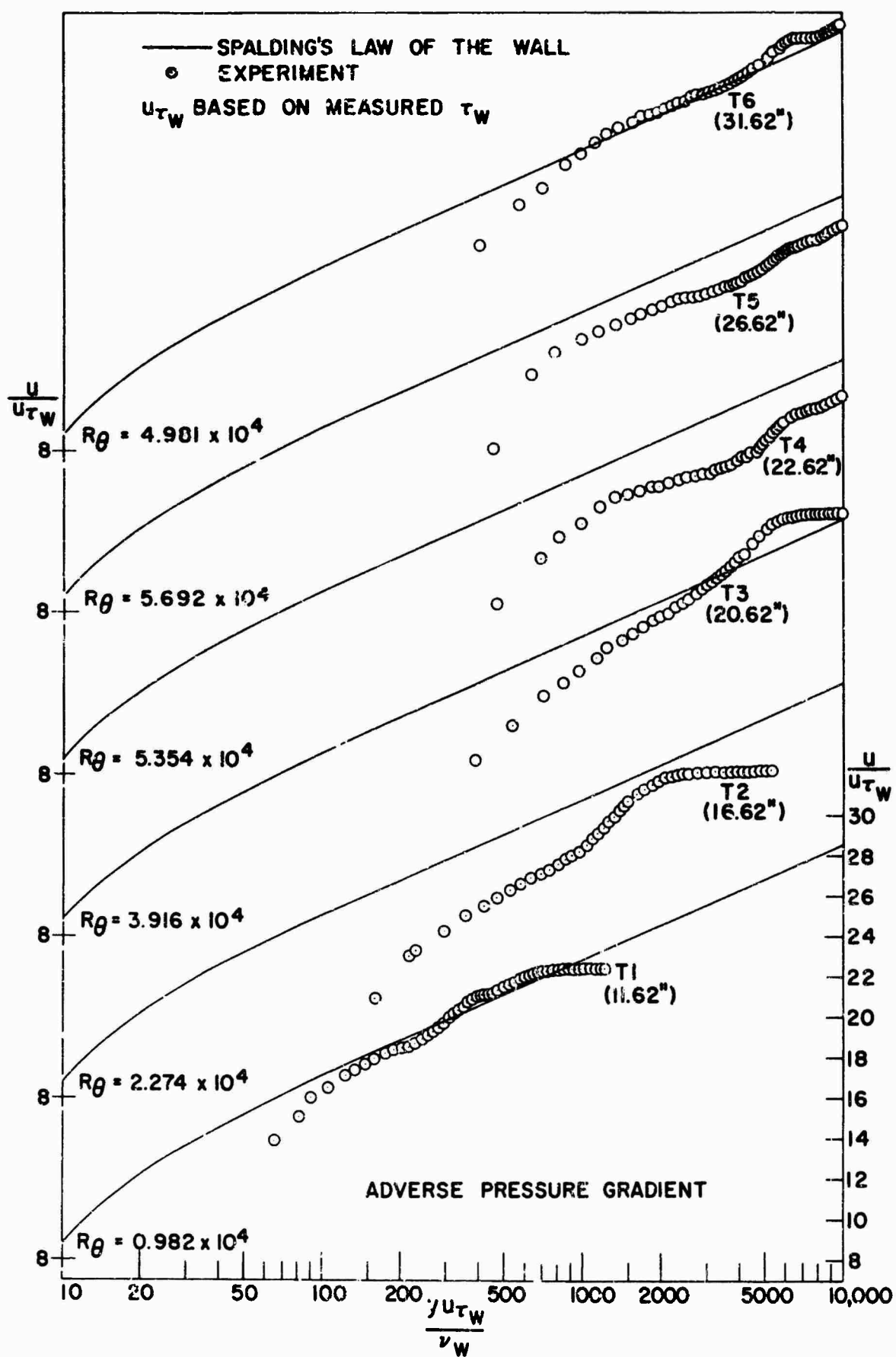
Fig.14 Experimental logarithmic velocity profiles: adverse pressure gradient
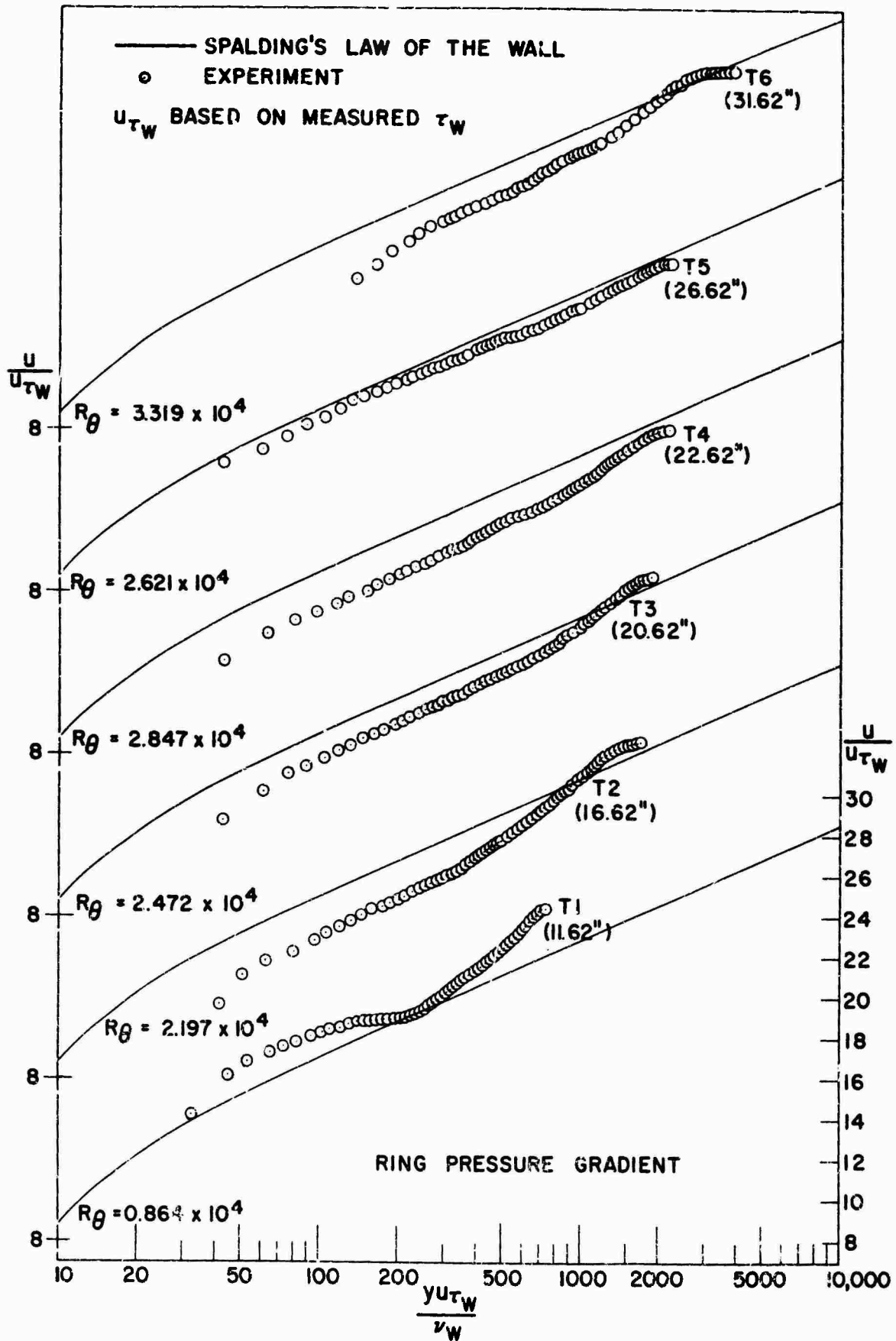
Fig.15 Experimental logarithmic velocity profiles: ring pressure gradient
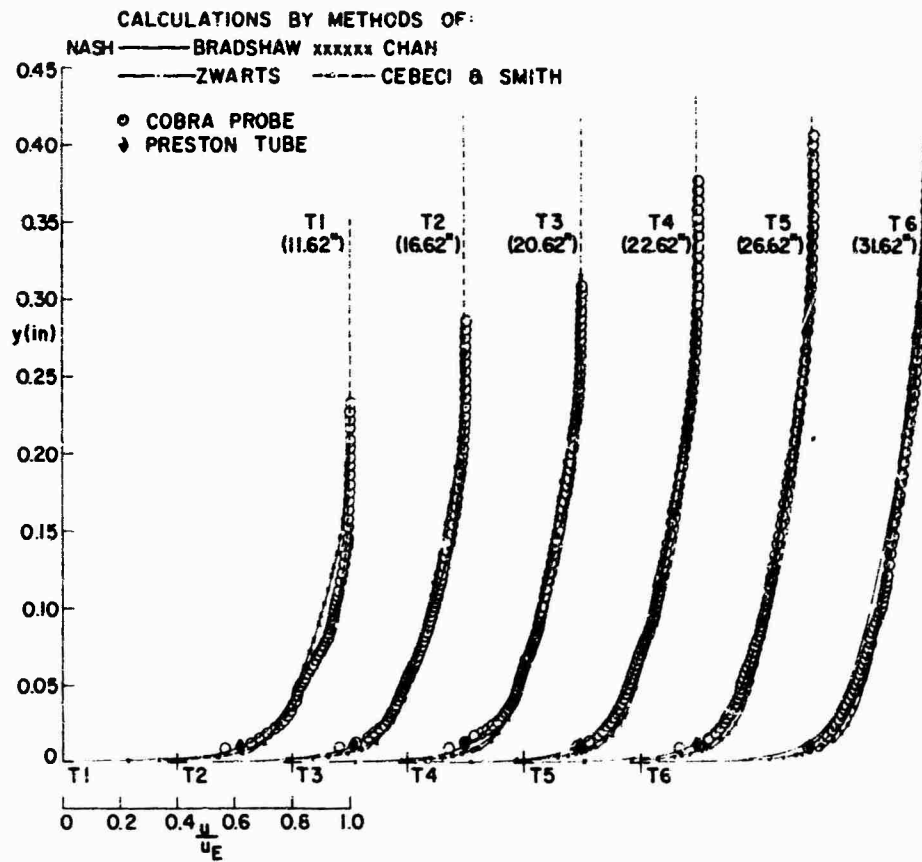
Fig.16   Experimental velocity defect profiles

CALCULATIONS BY METHODS OF:
NASH ———— BRADSHAW xxxxxx CHAN
————— ZWARTS ————— CEBECI & SMITH

o COBRA PROBE
⟩ PRESTON TUBE

Fig.17   Zero pressure gradient experimental velocity profiles compared with calculations

CALCULATIONS BY METHODS OF :
———— BRADSHAW xxxxxx CHAN ———NASH
————ZWARTS ————— CEBECI & SMITH

o COBRA PROBE
♦ PRESTON TUBE
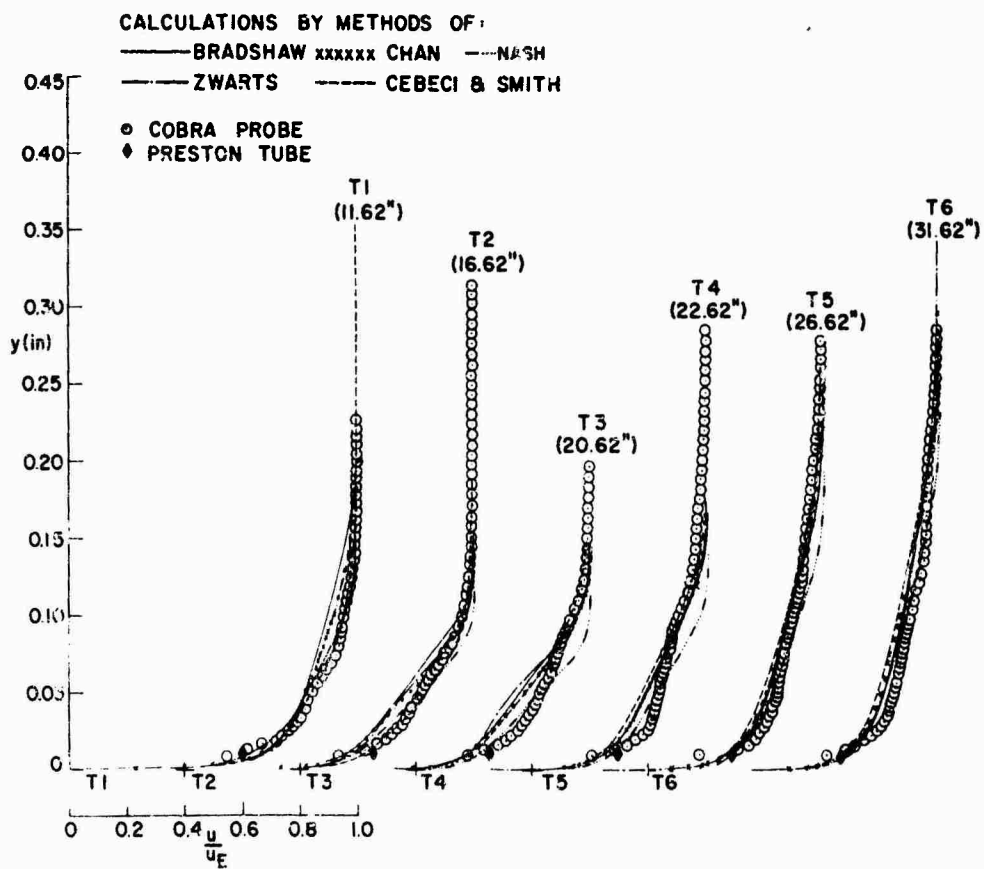
Fig.18   Adverse pressure gradient experimental velocity profiles compared with calculations
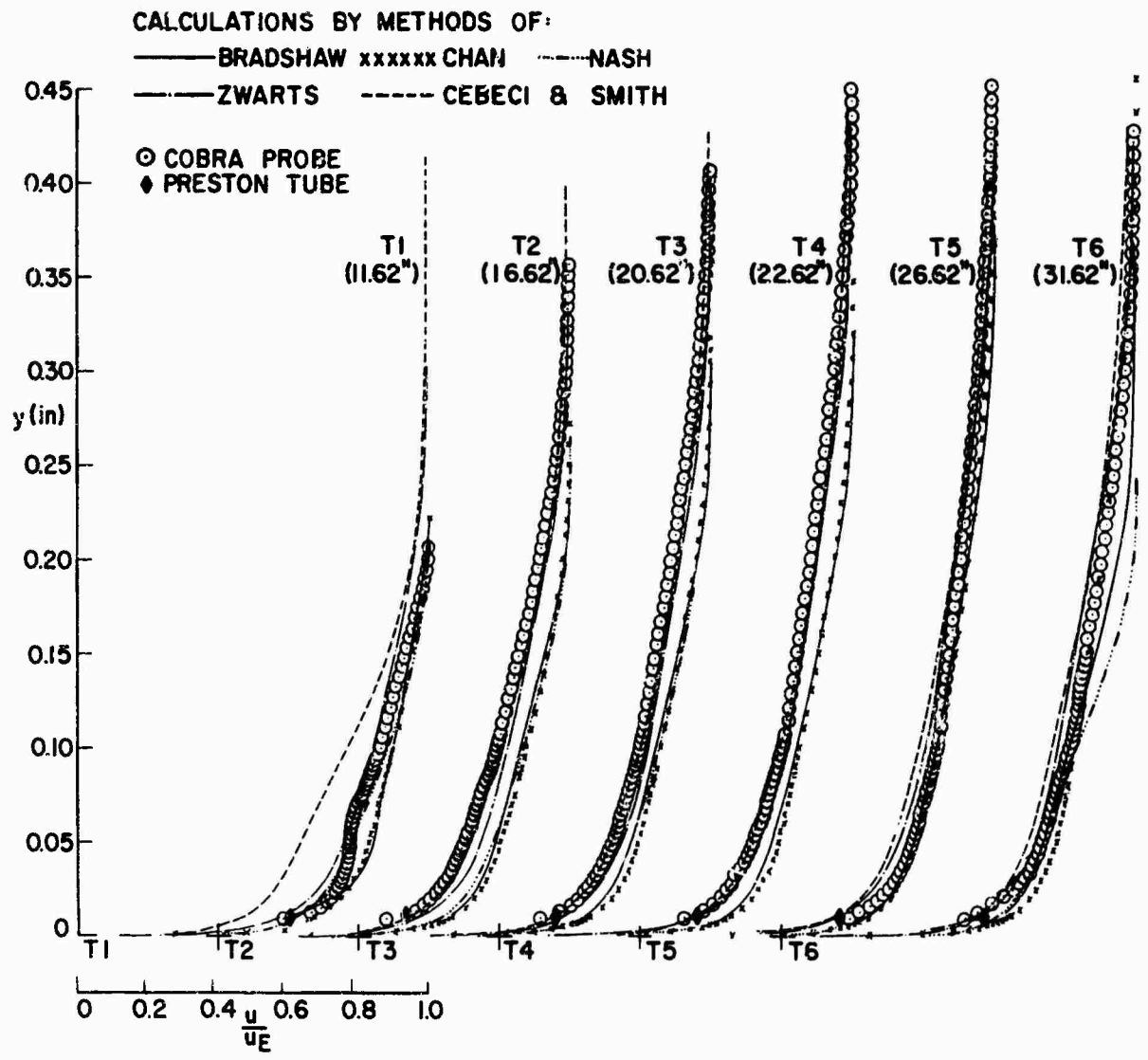
Fig.19 Ring pressure gradient experimental velocity profiles compared with calculations
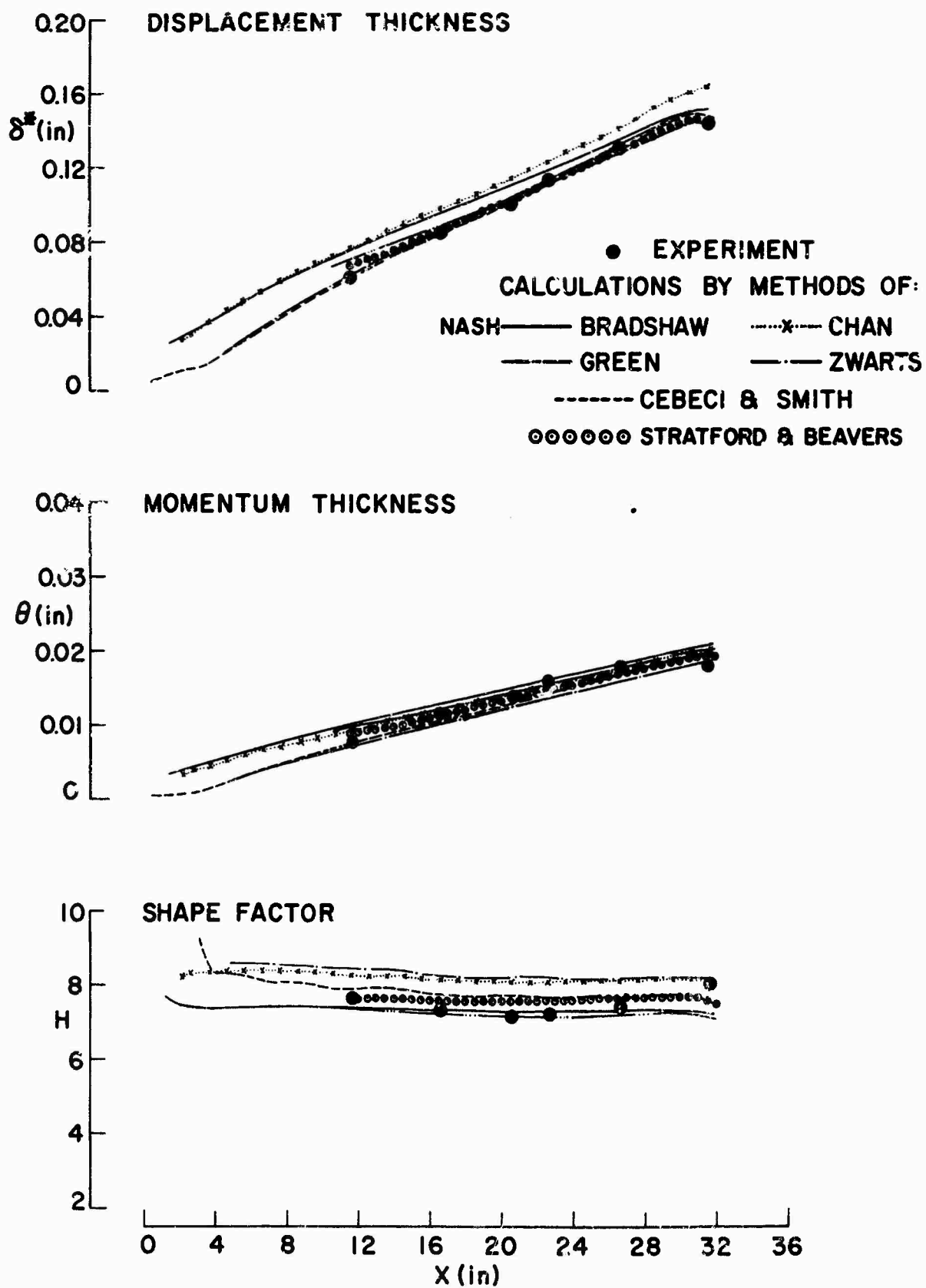
Fig.20   Integral parameters for zero pressure gradient flow
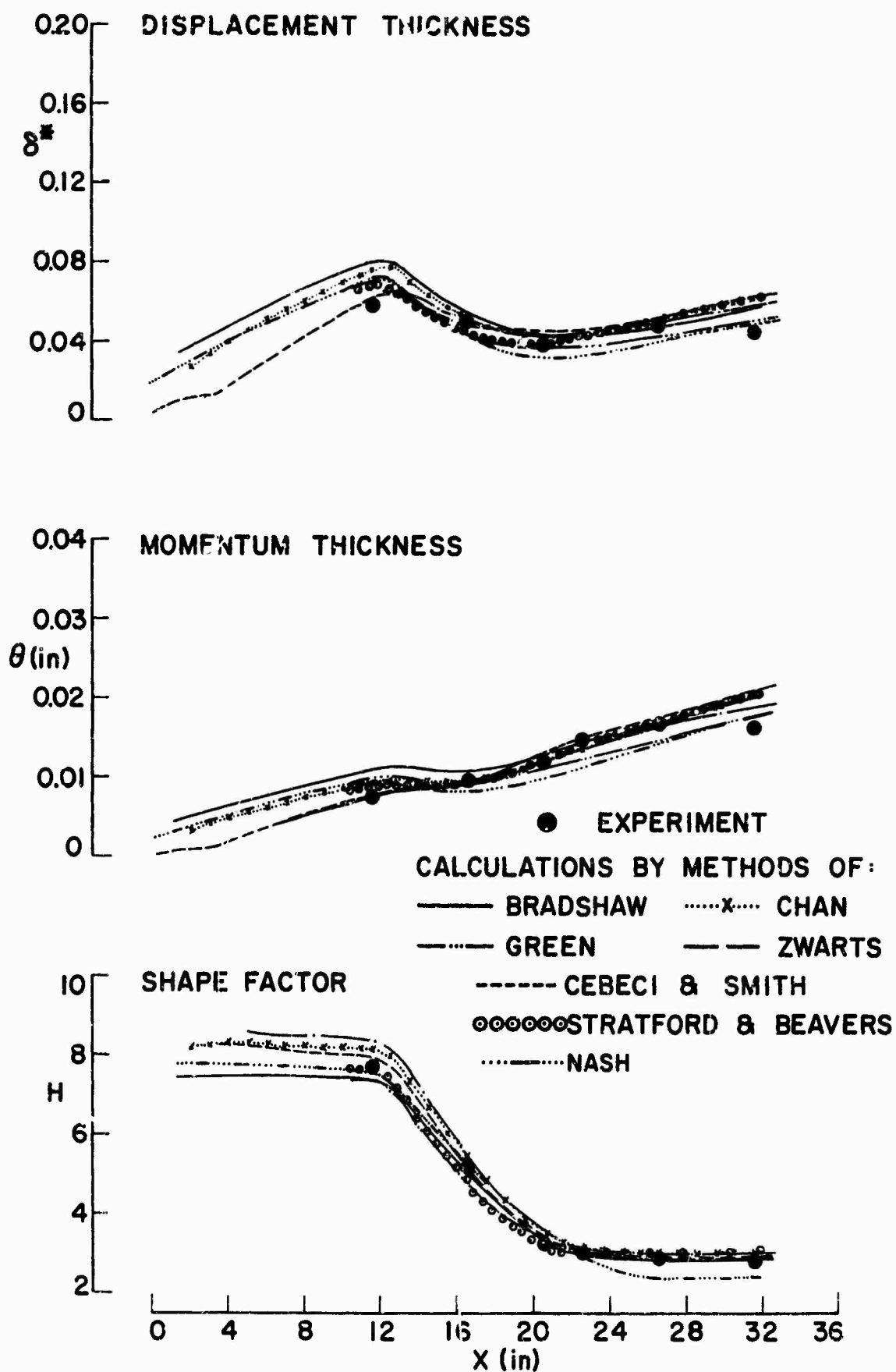
Fig.21   Integral parameters for adverse pressure gradient flow
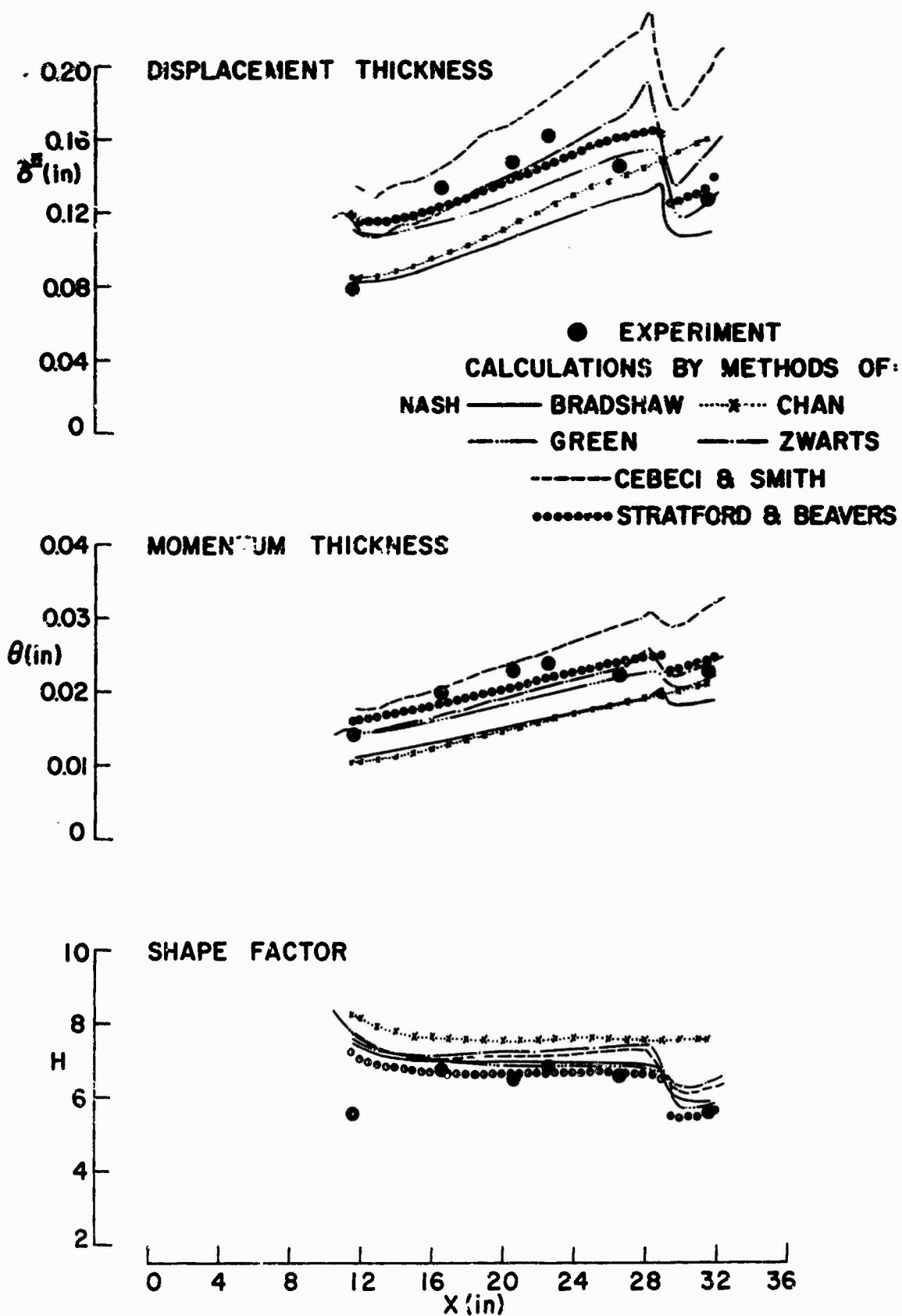
Fig.22 Integral parameters for ring pressure gradient flow
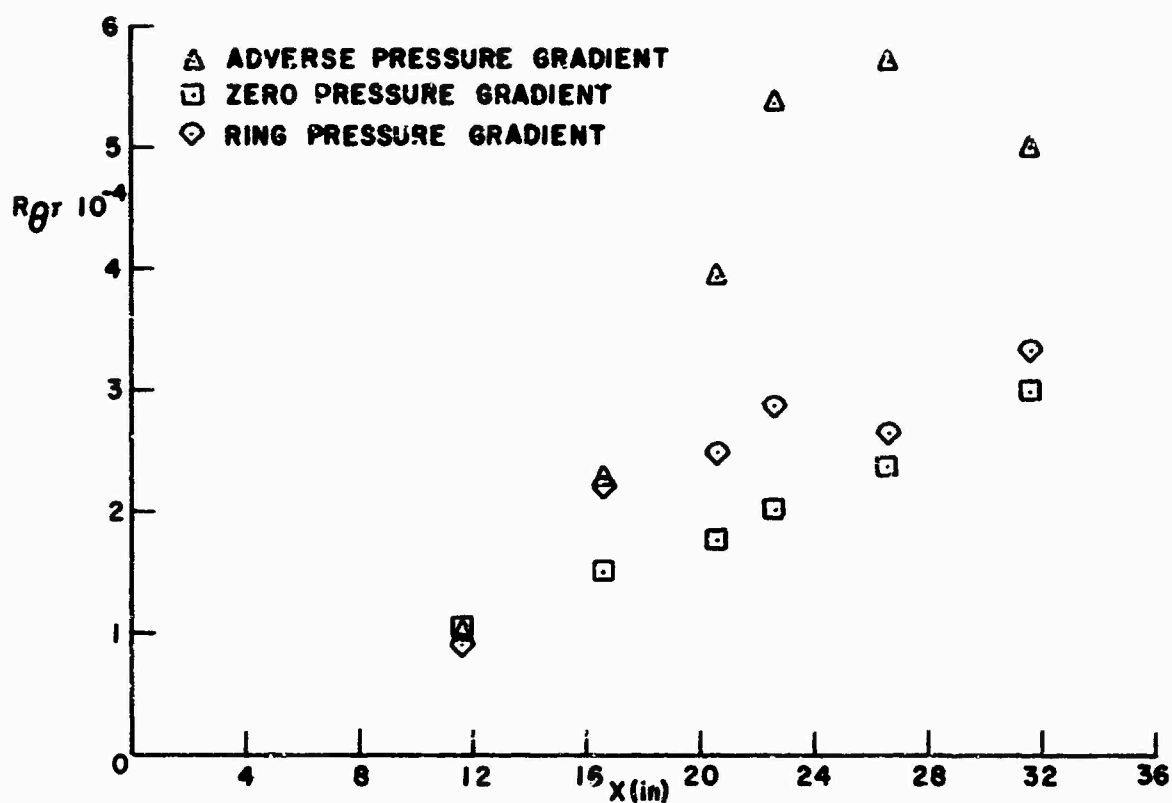
Fig.23 Experimental momentum thickness Reynolds number along the duct
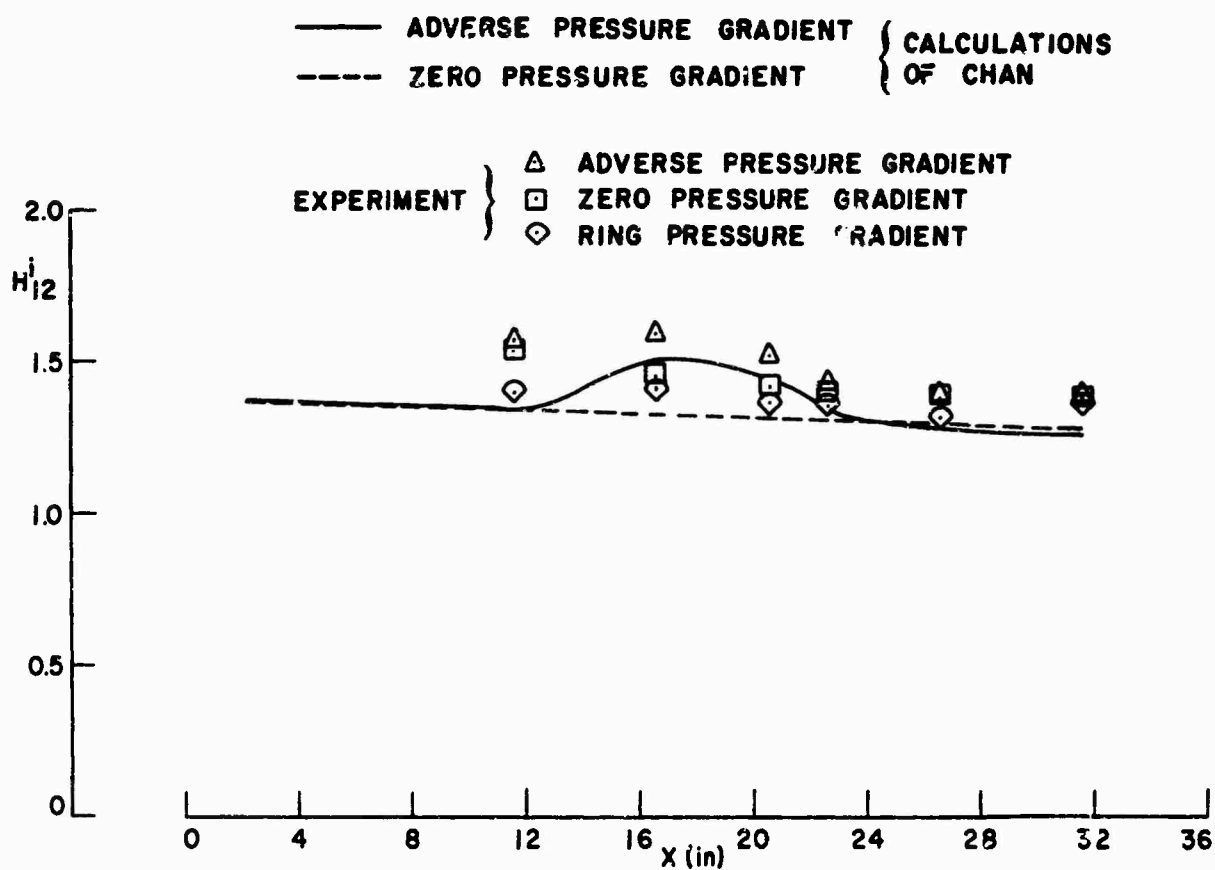
Fig.24 Influence of pressure gradient on incompressible velocity shape factor
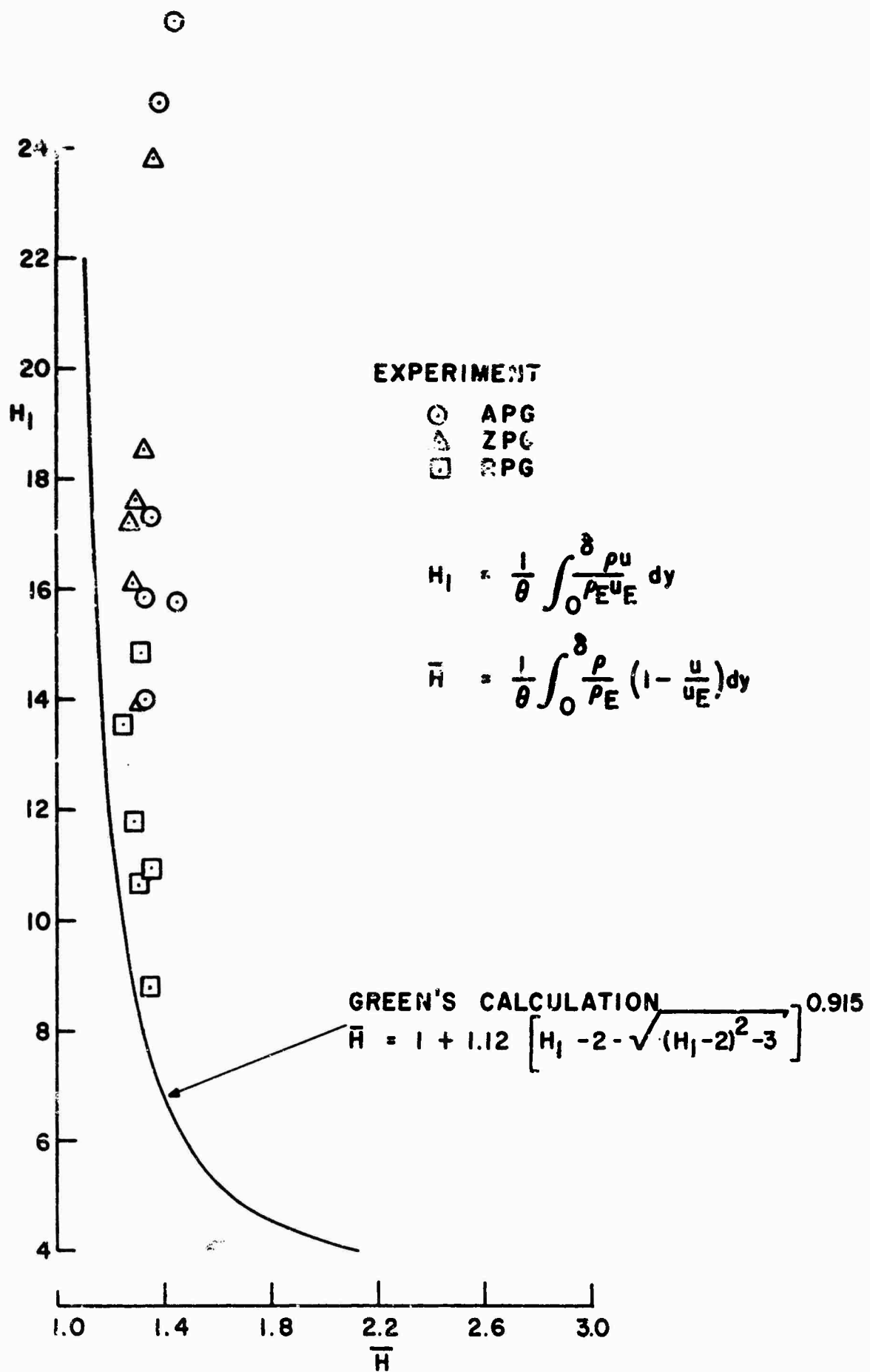
Fig.25 Green's shape parameters

THE STRUCTURE OF TURBULENCE IN SHEAR FLOWS

Leslie S. G. Kovasznay
The Johns Hopkins University
Baltimore, Maryland 21218

SUMMARY

In the first part experimental results concerning the structure of shear flows are reviewed. On one hand, results obtained by flow visualization techniques have given inspiration for devising plausible models rather than have provided numerical data to be compared with experiments. On the other hand, hot-wire anemometer records, especially by employing appropriate signal processing techniques have given quantitative data that can be used for direct comparison with theoretical predictions but not as much detail of the instantaneous flow field. In the second part theoretical possibilities are reviewed and arguments are presented for favoring a model consisting of random "sprinkled", but deterministic flow structures against models based on travelling waves. Finally there is an outline of a suggestion for a possible form of mean flow predictions schemes.

INTRODUCTION

Although turbulent shear flows are technologically more important forms of turbulence than homogeneous isotropic turbulence, progress was more modest due to their greater complexity. They were of course recognized rather early as being difficult, so basically two trends, or rather two attitudes were evident among the authors. Those who were concerned more with the intrinsic nature of the turbulent fluctuation field, than with making predictions of the shear stress and other transport properties, first attempted to extend to the shear flows the findings of the simpler homogeneous isotropic turbulence by relaxing only the condition of isotropy but not the homogeneity. This approach resulted first in the concept and later also in some experimental realization of the so called homogeneous turbulent shear flow. Conceptually this is the simplest possible shear flow since it has the same statistical properties everywhere in space. The experimental realization of such a flow is not easy, but success was reported in Refs. 1, 2 and 3. In a homogeneous shear flow experiment the scale of the turbulent fluctuating field is small compared to the overall dimensions of the mean flow, but on the other hand, in technological or geophysical situations such a flow would be comparatively rare. The alternate approach to shear flows is more pragmatic and one may group the "phenomenological" or "semi-empirical" theories, as those concerned with "medium like behavior". These efforts concentrate on predicting mean flow quantities such as the mean velocity distribution. and Reynolds stress distribution by "closing" the governing equations, with some ad-hoc, but (hopefully) physically plausible assumptions. This pragmatic approach has a long history going back to Boussinesq (Ref. 4) and the best known early contributions were made in the form of various mixing length theories. There is a current revival of this approach stimulated by the renewed demands of technology to supply reliable prediction methods for technologically interesting shear flows (Ref. 5). There are some conceptual difficulties in both approaches. In the case of homogeneous shear flows but also in considering the "medium-like behavior" of general shear flows, one implicitly regards the turbulent flow as another fluid with its own laws represented by some, yet unknown, constitutive equations. Such a picture of course would be more accurate in those regions of the fluid that are far away from the boundaries. One boundary is the solid wall, where the turbulent flow must accomodate itself to the wall through a viscous sublayer and the high velocity gradients associated with it. The other boundary is the turbulent-non-turbulent interface where the turbulent flow with high vorticity accomodates to an essentially irrotational outer flow through a relatively thin layer (Corrsin's superlayer). Most ideas about "medium-like behavior" imply that the postulated relationships are valid in the interior of turbulent flow away from these special regions. On the other hand, experiments reveal that the observed turbulent shear flows have turbulent structures with length scales as large or larger than the total thickness of the shear layer. Furthermore, experimental evidence accumulates indicating that intermittency, that is such a striking phenomenon at the turbulent-non-turbulent interface may be a more general phenomenon and it may be present everywhere in the turbulent flow, although obscured by the overlapping of different scales.

The usual theoretical treatment of turbulent shear flows consists of taking moments of the Navier-Stokes equations and writing up transport equations for the turbulent energy or for the Reynolds stress. The proper terms then can be identified as generation, convection, diffusion and dissipation. Usually at this point in the analysis it is recognized that there are far more dependent variables then there are governing equations that can be derived from the Navier-Stokes equations. Experiments, at least in principle, can supply the spatial distribution and temporal development of each one of the separate terms and overall qualitative conclusions can be drawn for the particular flow in question, but the actual solution of these equations is possible only after some very drastic assumptions are made to provide a "closure". The main difficulty seems to be the fact that the turbulent fluctuations in an inhomogeneous shear flow are of all spatial scales including very large ones that encompass the entire shear region. This is the principal reason why the flow cannot be treated as some special turbulent fluid, characterized by a single effective viscosity. Speculations concerning predictability of mean flow properties were developed quite independently from the information obtained from experiments aimed to measure the fluctuating fields, so the result is a

certain frustration on both sides. The "predictors" don't feel that turbulence measurements gave them important enough clues to improve their essentially pragmatic approach, while those concerned with the turbulent fluctuations themselves regard the prediction methods as still too crude and not entering into the heart of the matter. In Ref. 5 there is extensive discussion of this dilemma by authors representing all shades of opinion.

In such a state one must look to the new experimental data that became available only in recent years and then try to interpret it in such a manner that general conclusions about turbulent shears flows would be obtained. Special attention is given here to two major types of novel experimental data. One is the contribution of Kline, Reynolds and others at Stanford trying to understand the genesis of turbulence near the wall just outside of the viscous sublayer (Ref. 6). Their findings were based mainly on flow visualization techniques and the results were giving inspiration to many others working in the field. The other new experiments rely on using hot-wires but in a novel way, mainly by introducing new techniques in signal processing, such as conditional sampling and averaging and large scale space-time correlations or alternately short term averaging, short term correlations. These new efforts are carried out mainly in two groups, one at the Johns Hopkins University (Refs. 1, 15, 19) and the other one at the University of Southern California (Ref. 7). In these novel approaches one attempts to capture such salient features of the turbulent fluctuating field that would escape detection when using only spectral analysis of the signals.

REVIEW OF THE EXPERIMENTS

A few groups have made a serious effort to create a good approximation of a homogeneous shear flow in the laboratory (Refs. 1, 2, and 3). Essentially such a flow is created in a special wind tunnel in such a way that the mean velocity gradient

$$\frac{\partial U}{\partial y} = \text{constant}$$

over a large area. In addition turbulence is created so that its properties be constant across the entire flow. It was experimentally verified that the mean square fluctuations are essentially constant and the only important Reynolds stress was also constant across the entire flow. The main problem of creating such a flow is that somehow one must put different amounts of flow resistance along the different stream lines, since this drag producing structure is the one that also produces the turbulence, consequently the structure of turbulence may vary across the flow and this would destroy the originally sought homogenity. By ingeneous design and continuing painstaking effort such flows were actually obtained, and it was hoped that they represent a simple but still typical form of shear flow. In the actual measurements two important complicating properties have emerged, one is the encroachment on the flow by the wall boundary layers developing along on the tunnel walls, so that when traveling downstream the homogeneous "core" in the middle of the flow becomes narrower and narrower. Nevertheless this only is a minor point because the use of a large cross-section wind tunnel could over come this, at least in principle. The other and more fundamental difficulty is that in the central core of the homogeneous shear flow the characteristic length scale of the turbulence keeps increasing as the fluid moves down stream. This increase in length scale is not the result of the more rapid decay of small scale turbulence (as it is in a nearly isotropic flow behind grids where the small scale turbulence is dissipated faster than the large scale one) but is due to the actual generation of large scale motion. The length scale increase appears to be a phenomenon associated with a "reverse cascade" where turbulent energy is fed into the larger scale eddies if the large scale turbulence is deficient in energy level due to the peculiar form of creating the flow. As the length scale keeps increasing it is easy to see that finally it will reach the total width of the shear region. This behavior in a way reduces the importance of homogeneous turbulent shear flow as a possible simple model for actual shear flows.

Periodic excitation of a turbulent channel flow was reported in Ref. 8. The idea that turbulent shear flows may be decomposed into travelling wave modes came in the wake of the success of a similar approach in laminar instability theories. The work of Malkus (Ref. 9) has inspired mostly theoreticians but later the problem was restated and most extensively studied by Landahl (Ref. 10). According to his approach a turbulent flows may be, or should be, decomposed into travelling wave modes that are the eigenfunctions of the small perturbation equations using the actual turbulent mean velocity profiles. The experiments reported in Ref. 8 were carried out in a fully developed turbulent channel flow and the flow was excited by a given frequency sine wave introduced by vibrating ribbons, a technique similar to the one used extensively in laminar flow instability and transition experiments. Modern electronic techniques such as periodic sampling and averaging permitted the extraction of the coherent periodic component that in general is buried in the random noise type turbulent fluctuations. The conclusions of the experiments were rather simple. The excited modes propagate with a phase velocity that is lower than the maximum velocity in the channel. All experimentally observed modes decay rapidly and the rate of the decay is roughly proportional to the frequency, or in other words the decay per oscillation (per one wave length travelled) is about constant irrespective of frequency. The amplitude decreased to about 0.63 in one wave length travelled. Whether or not the experiments confirm the wave guide type of theories depends critically on the question what type of effective viscosity one assumes across the channel when calculating the eigenfunctions. By assuming only the molecular viscosity the solutions are far from the observed ones. On the other hand, the use of effective turbulent viscosity has an implied assumption and it is quite conceivable that only a frequency dependent and complex effective viscosity can do justice to this problem. But even in that case there would remain a great deal of arbitrariness as far as a complex, and frequency dependent turbulent viscosity is concerned and the dilemma is whether to introduce more and more arbitrary functions and arbitrary constants to fit the experiments or alternately accept a moderate discrepancy with experiments but use a more

simple and more plausible theory with very few arbitrary constants.

The group at Stanford University (Kline, Reynolds and others, see Ref. 6) was concentrating on the exploration and quantitive assessment of the rather dramatic phenomena observed at,or near the outer edge of the viscous sublayer. Unfortunately hot-wire anemometer records obtained in that region are confusing so the best data is from tracer techniques (dye or hydrogen bubbles). The typical event is a turbulent burst where a fluid filament lifts up, away from the wall and the new faster flow sweeps away the local event. When looking at the same phenomenon normal to the wall, one observes that in the wake of such a burst longitudinal vortices appear whose spacing is well discernible at least temporarily, but their actual location of course wanders from event to event. The whole concept of individual identifiable bursts introduces the idea of an intermittency in the generation of turbulence and the conjecture can be made that the generation of turbulent energy as well as the contribution to the Reynolds stress all occur in "chunks" that are essentially random in occurance, but have rather difinite forms. The bursting rates, though difficult to define quantitatively, appear to depend strongly on the local mean velocity profile that in turn depends on the mean pressure gradient, consequently "relaminarization" would occur whenever the bursting rate would drop to zero. Experimental evidence is abundant and the whole argument is qualitatively convincing (Ref. 6). The picture that was suggested in Ref. 11 consists of a random sequence of well defined bursts creating an intense activity carrying fluid outward, transporting a momentum defect (retarded fluid) from the proximity of the wall and thus creating the region of turbulence generation near the sublayer. Further support to this picture is the fact that when using suction over a porous wall it requires only very small rate to remove the active region in order to suppress turbulent fluctuations. The difficulty of designing a more quantitative experiments lies in the fact that even with a whole array of hot-wire anemometers it was not possible yet to construct the appropriate "detector function" that would identify a particular burst as it passes by the array of probes. Experiments by present author and an associate, (unpublished) were made in order to simulate such bursts by emitting small pulses from a small diameter hole in the wall (diameter smaller than the sublayer thickness). Interestingly enough the trajectory of these bursts coincided with the observed trajectories given in Ref. 6, but the bursts them-selves decayed in the turbulent flow and did not result in an avalanche of turbulent activity during their out-ward journey.

Quite independently Kaplan and Laufer (Ref. 7) have reported that a lateral spatial structure of the turbulent bursts can be observed by taking short-time correlations near the edge of the sublayer by using an array of transversely separated hot-wire probes. This experiment reveals a temporary periodic structure in the transverse direction that disappears when taking long-time correlations since then,by averaging over many bursts the striking features are "washed out" by the superpositions of many independ-ent events.

Intermittency appears to be a universal phenomenon in turbulence but it was only in 1961 that Kolomogorov (Ref. 12) st suggested that the small scale turbulence or in his wording the viscous dissi-pation is not a statistically homogeneous uniformly distributed scalar quantity even in locally isotropic turbulence, but must have a large scale "chunky" structure. His suggestion amounts to a picture consisting of fine scale turbulence imbedded in a larger scale turbulent flow in a random fashion. This new kind of internal intermittency may have a characteristic length scale of the "chunks" that is much larger than the fine scale turbulence itself. Experimental evidence to verify this suggestion is scarce, but most recently Kuo (Ref. 13) has made such measurements and indeed has found that this internal intermittency actually exists in homogeneous turbulence. If this phenomenon is universal a turbulent shear flow may be visualized as consisting both of regions that have originated in a relatively high shear region and of more inactive "milder" types of regions. One may visualize the actual state of affairs as a mixture of different scale turbulent flows that are coarsely mixed so different "chunks" of fluid have a different origin or alternately a different age. This may be especially true in very high Reynolds number turbulent boundary layers, most typically in atmospheric boundary layers, where different fluid masses may have left the high shear region near the ground at different locations upstream so their "age" is different. The actual intermittency at the free stream edge is already well documented and it may be just a more dramatic form of this basic and rath-er universal phenomenon but not an essentially different one (see Ref. 11).

The turbulent-non-turbulent interface was known for a rather long time but seldom was incorporated in the models that served to predict mean flow parameters in turbulent shear flows. For an excellent flow visualization technique see Ref. 14. The role of the interface is regarded sometime as an "active" surface through which the irrotational flow is ingested into the intensely rotational turbulent zone or alternately as a rather passive line of demarcation undulating fore and back around its mean position by responding to the large scale motion within the turbulent region. In order to clarify some of the ideas about the interface, detailed measurements were carried out by Kovasznay, Kibens and Blackwelder (Ref. 15) and a number of facts were conclusively established. The key to these experiments was the method of conditional sampling and averaging as well as the extensive application of long time-lapse space-time correlation measurements presented in the form of space-time correlations maps. A large portion of the findings is published in Ref. 15 so it is sufficient here just to reiterate some of the important conclusions. It should be mentioned here,that by adapting the same measuring techniques intermittency and conditional average velocities were obtained in a turbulent shear layer (Ref. 16).

The streamwise mean flow velocity at a given location (same distance y from the wall) is different in the turbulent and in the non-turbulent regions and this difference can amount to as much as 5% of the free stream velocity. This fact alone indicates that the turbulent portion of the fluid was slowed down relative
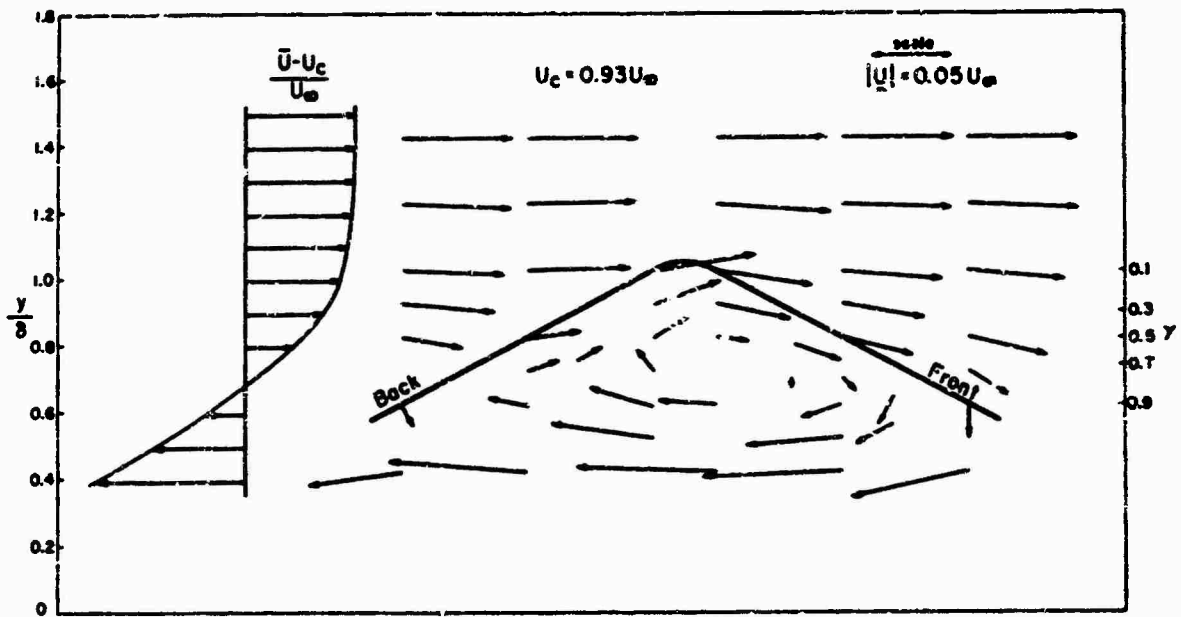
Figure 1. Composite velocity distribution in the outer region of the boundary layer. Coordinate system moves with average transport velocity U_c. Intermittency factor γ is shown on right.
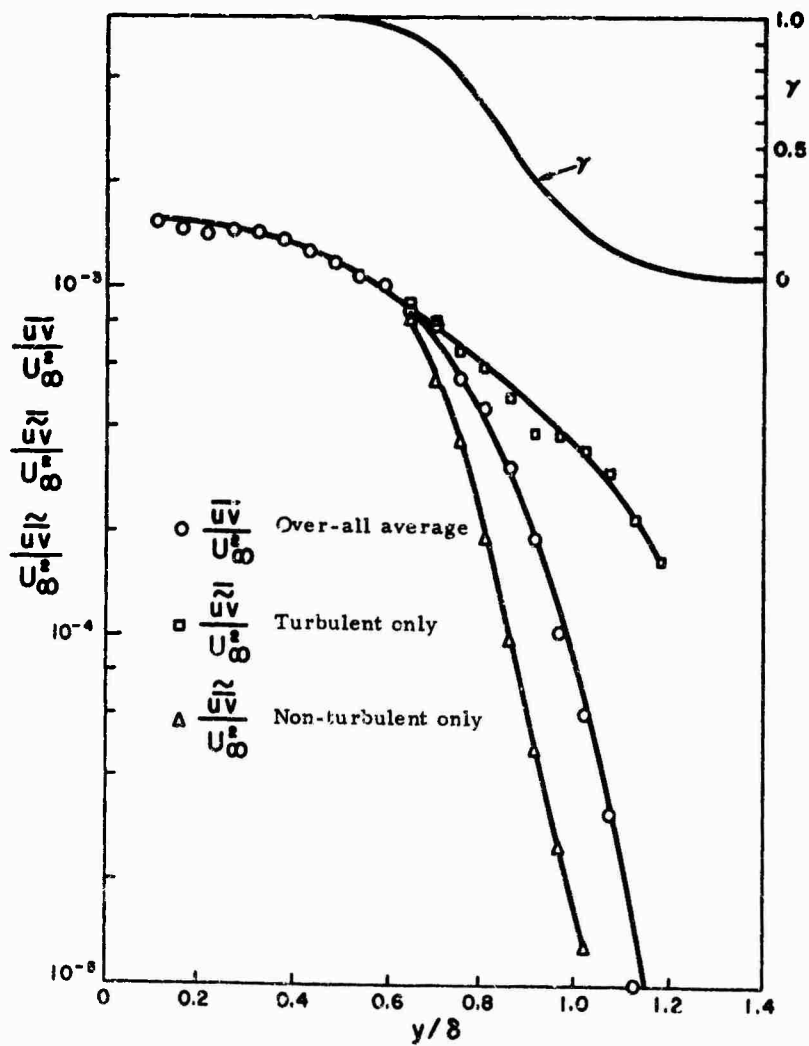
Figure 2. Zone averages of the tangential Reynolds Stress.
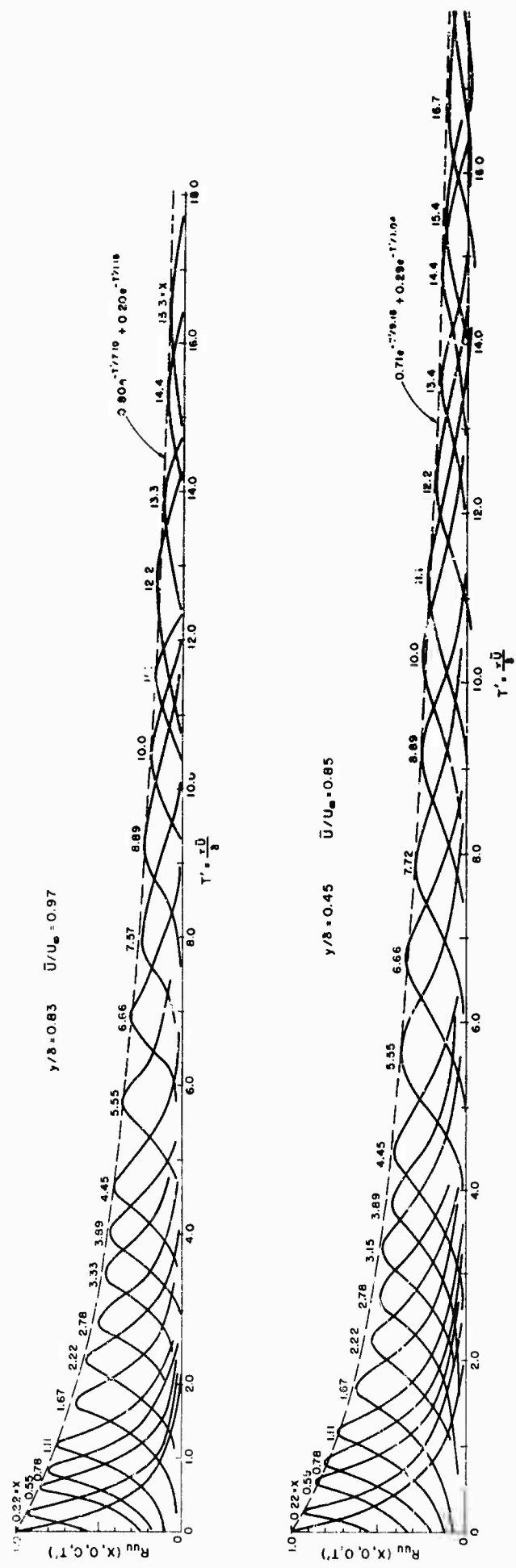
Figure 3. Space-time auto-correlations of u, $R_{uu}(X,0,0,T')$. The dashed lines represent the auto-correlations in a convected Eulerian frame. The spacial separation coordinate X is indicated at peaks.

to the outer non-turbulent fluid, therefore, the non-turbulent and essentially inviscid outer flow is "riding" over the wavy interface thus creating a fluctuating potential flow. Surprisingly the r.m.s. turbulent velocity fluctuation level shows no discontinuity across the interface. From the conditionally sampled and averaged velocity fluctuations it is possible to reconstruct the instantaneous velocity field of a "typical interface bulge" shown in Fig. 1. The presence of large potential fluctuations was first surprising but it is easy to see that the vorticity fluctuations must induce velocity fluctuations at a distance (Biot-Savart law) and the highly active turbulent motion must be accompanied by an irrotational induced motion that represents a potential flow in the incompressible case or alternately sound waves in the compressible case. The r.m.s. vorticity fluctuatous appear to be discontinuous at the interface although no direct measurements have been made on all three components of the instantaneous vorticity. Conditionally averaged Reynolds stress indicates an interesting behavior in the intermittent region shown in Fig. 2. It is clear that the Reynolds stress is carried essentially by the turbulent regime and the irrotational outer flow does not contribute to it.

The method of measuring space-time correlations of turbulent flows was pioneered by Favre (Refs. 17, and 18) and the results provided the first experimental indication as to what extent Taylor's hypothesis is valid. Using the concept of wave guide type travelling wave modes it also supplied the different phase velocities (celerité in French in the original work). For the present purpose it was adopted mainly to extract the large scale motion by using it in a novel manner (Ref. 15). First the space-time correlation measurements were carried out for very large separations in space and in time in order to determine the charactertic life-time of the large eddies. Surprisingly it was found that the large eddies have life-times so long that fluid particles would travel about ten boundary layers thicknesses with the free stream velocity while the large eddies decay only by a factor of $1/e$. If the large scale eddies have such a long life-time then it was found to be profitable to map out the detailed space-time correlations and plot them in three dimensions using the separation coordinates X, Y, Z, T and thus give a "signature" or rather a "portrait" of the large eddies. The method is given as follows: first place one hot-wire anemometer upstream at a fixed position in the flow then delay the signal obtained by a fixed time τ that is large compared to the (Eulerian) time scale of the turbulence. Then place a second hot-wire probe scanning in space around the down stream location where maximum correlation is expected, namely where a fluid lump leaving the upstream probe would arrive after travelling along the mean streamline for a time τ. The constant correlation contours will outline the "lasting" features of the large scale eddies. In actual experiment the role of the time delay τ is interchanged with the streamwise coordinate separation Δx for instrumental convenience, but the essential results are the same. Non dimensional separation coordinates were used throughout (see Ref. 15)

$$ X = \frac{\Delta x}{\delta} \; ; \qquad Y = \frac{\Delta y}{\delta} \; ; \qquad Z = \frac{\Delta z}{\delta} \; ; \qquad T = \frac{\tau U_0}{\delta} $$
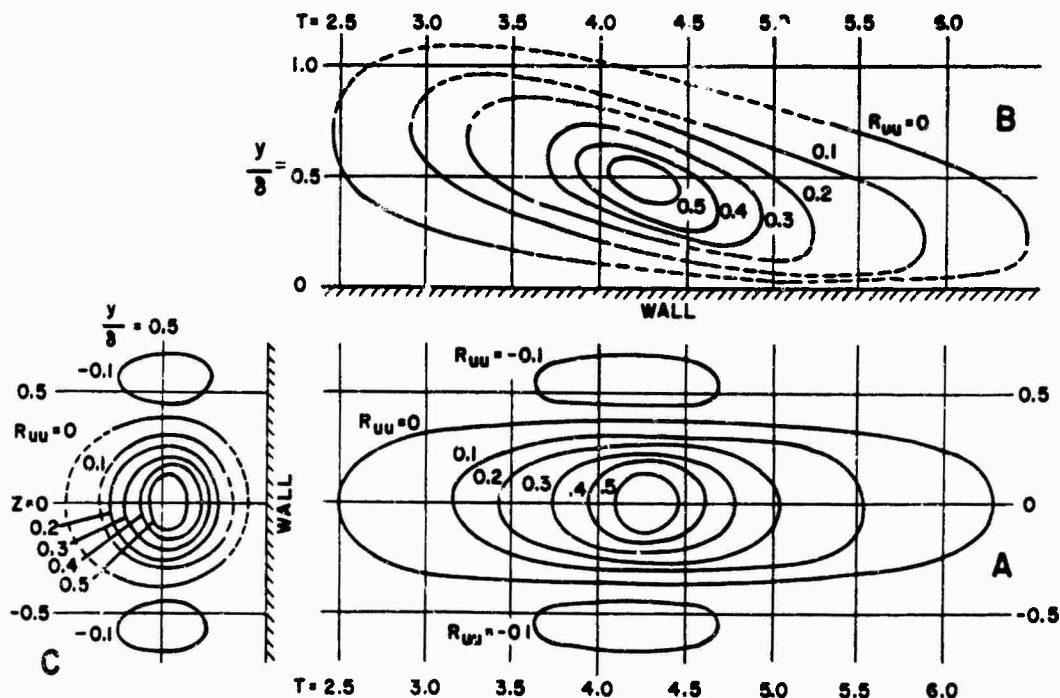
Figure 4. Three-dimensional representation of the space-time auto-correlation of u in the fully turbulent region, $R_{uu}(X_0, Y, Z, T)$ with $X_0 = 3.8$ at $y_0/\delta = 0.5$. Section A: Y = 0 plane. Section B: Z = 0 plane. Section C: T = 4.27 plane.
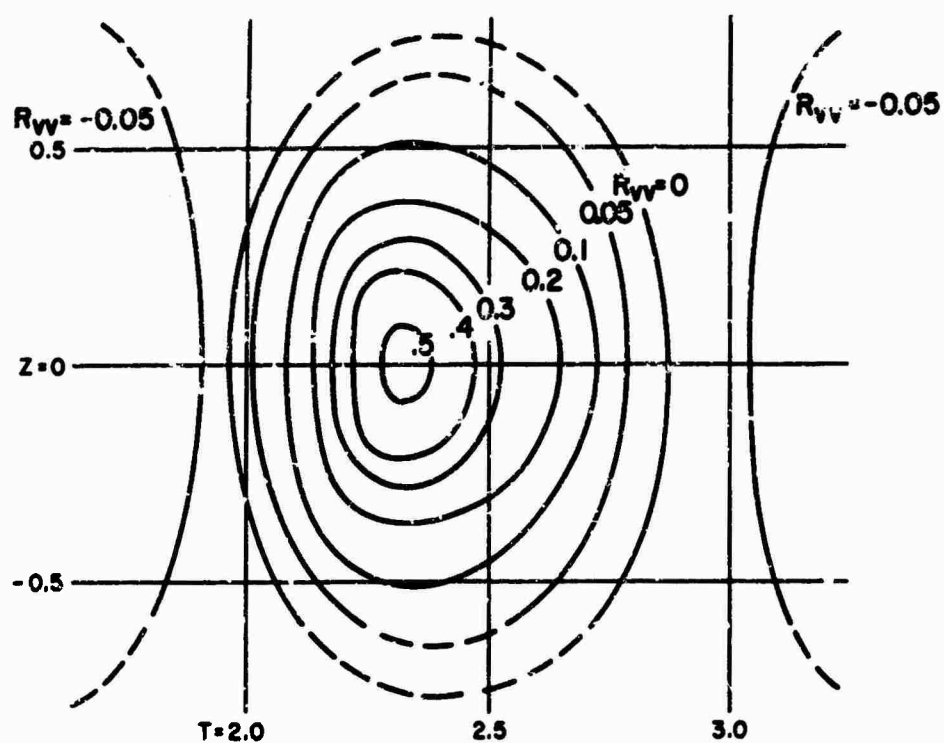
Figure 5. Space-time auto-correlation map of v at the half intermittency level, $R_{vv}(X_0 0, Z, T)$ with $X_0 = 2.25$ at $Y_0/\delta_0 = 0.8$.
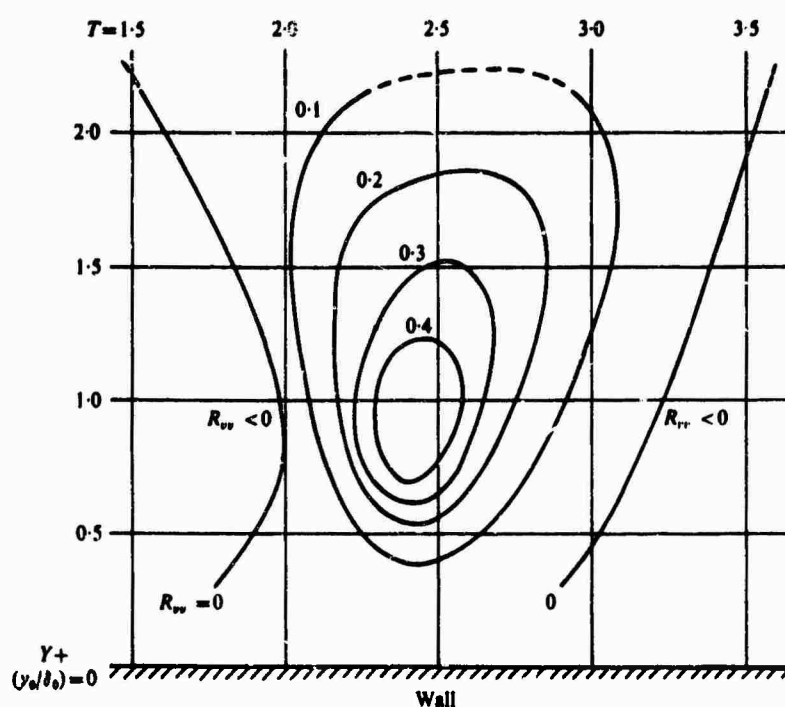
Figure 6. Space-time auto-correlation map of v in the normal Y-T plane, $R_{vv}(X_0, Y, 0, T)$ with $X_0 = 2.25$ at $Y_0/\delta_0 = 0.8$.
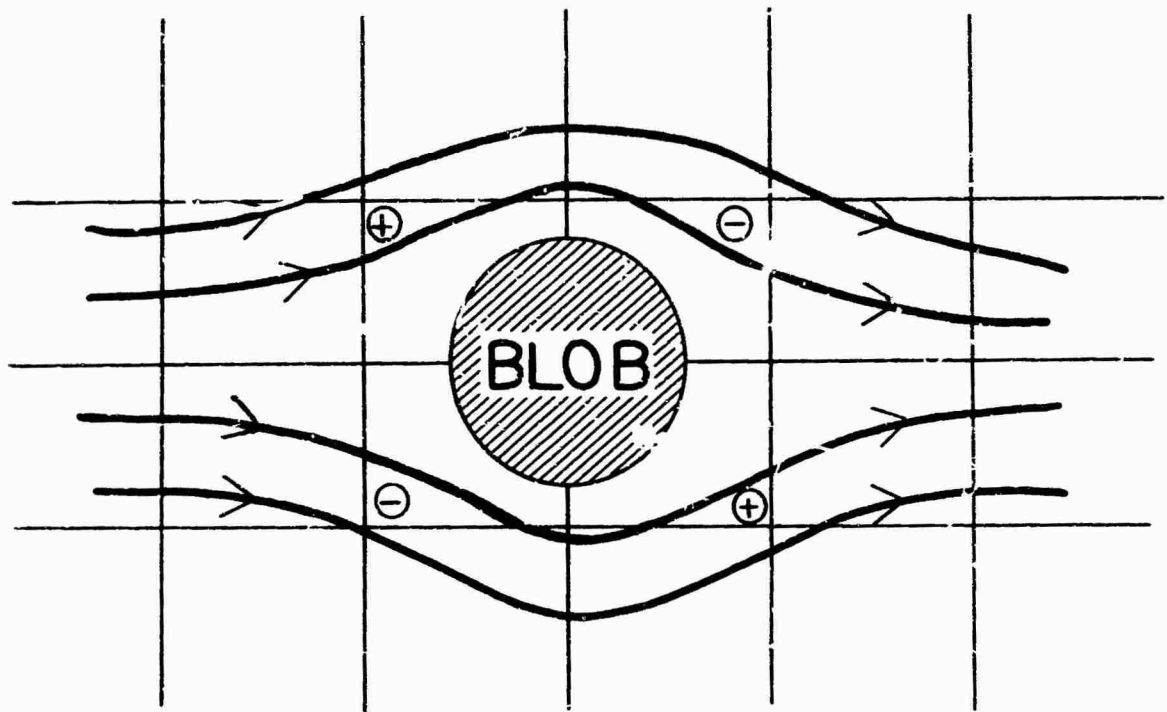
Figure 7. Streamlines around "Blob" must result in "four leaf clover" type I-w correlation pattern.
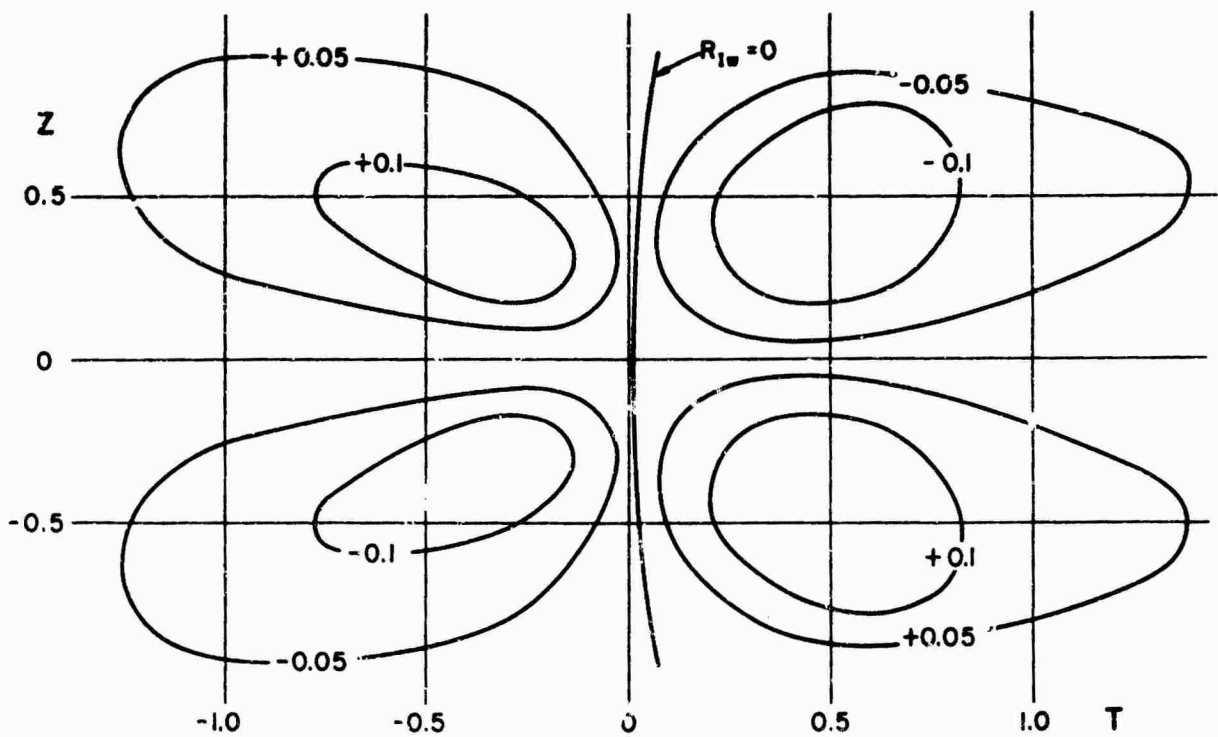
Figure 8. Space-time cross-correlation of I and w at the half intermittency level, $R_{Iw}(0, 0, Z, T)$ at $y_0/\delta_0 = 0.8$. Note "four leaf clover" pattern as predicted.

where δ is the boundary layer thickness and U_0 is the free stream velocity. The space-time correlation of the u and v velocity components are shown in Figs. 4, 5, and 6. Fig. 4 shows the R_{uu} correlation in three sections while figures 5 and 6 show the R_{vv} in two sections. It is interesting to see that the distances where significant correlation occurs extend to dimensions that are of the same order as the boundary layer thickness and it can amount to several times the boundary layers thickness in the streamwise direction in case of R_{uu} the correlation of the streamwise velocity component as shown in Fig. 4. The correlation pattern of the cross component (Figs. 5 and 6) is strikingly different and surprisingly enough the R_{vv} correlations extends well beyond the turbulent boundary layer into the outside irrotational flow. The explanation is simple, the outside flow responds to the "massage" of the turbulent motion by a corresponding inviscid potential flow that represents a far field of a turbulent agitation inside the boundary layer.

Correlations measurements were taken using the intermittency function I as one of the flow variables. The intermittency function I is defined as $I = 0$ for non-turbulent and $I = 1$ for turbulent state. Like any other fluctuating quantity it can be cross-correlated with any of the other fluctuating variables such as u, v, w (see Ref. 15). Cross-correlation between I and u is negative and it shows that the turbulent fluid also corresponds to the slower moving fluid. As the turbulent "bulges" or "blobs" move slower than the surrounding irrotational fluid the relative motion must be similar to that around a blunt body. Fig. 7 shows the probable model. The lateral component w must be alternately positive and negative as indicated on Fig. 7. The cross correlations between I and w then can be predicted as consisting of four lobes of alternating signs giving the "four leaf clover" pattern. Actual measurements are shown in Fig. 8 confirmed this prediction and gave increased confidence in the model proposed in Ref. 11.

The fact has been known for some time that rapidly accelerated boundary layers become similar to laminar ones and the conjecture was made that there is some kind of "reverse transition" or "relamin- arization". In the context of Ref. 5 this phenomenon occurs when the supply of turbulent bursts, there- fore the generation of turbulent energy, near the sublayer ceases and the turbulence in the outer part of the boundary layer decays according to its proper time scale. Experiments performed by Blackwelder and Kovasznay (Ref. 19) have shown that relaminarization is an unsuitable term because what really happens is a very slow decay of the existing turbulence and at the same time a rapid acceleration of the mean flow so that the remaining turbulent energy and Reynolds stress both becomes small compared to the kinetic energy of the mean flow. Nevertheless the fluctuations do not decay very much in abolute terms. Figures 9-12 show the typical results. Fig. 9 shows the shape of the duct used and the mean velocity and pressure distributions along the streamwise coordinate x. The boundary layer on the upper plane wall was under study. Due to the rapid change of cross section all data are displayed against the non-dimension- al stream function Ψ/ν instead of the coordinate y

$$\Psi \equiv \int_0^y U(\bar{y}) d\bar{y}$$

so that a constant value Ψ represents moving along the same mean streamline. Fig. 10 shows the intermittency factor during acceleration. Between stations $x = 1050$ cm. and $x = 1100$ cm. the intermittency γ is essentially negligible. The new increasing intermittency downstream is the result of the fact that the very high acceleration (high pressure gradient) can not be maintained indefinitely, so as the flow is becoming parrelled again, the gradient will drop below the critical level and new turbulent boundary layer is grown from near the wall and begins its new and independent existence. Both the total kinetic energy and the Reynolds stress, when measured along the same stream line, change only moderately in absolute terms if normalized with a fixed velocity U_0 (there may be some increase very near the wall) (Fig. 11) but they both rapidly decrease in terms of the local and therefore accelerated mean velocity U_{∞} (Fig. 12). What is being meant is that the concept of relaminarization is primarily due to "inflation" represented by the increase in the mean flow so that the essentially constant level of the kinetic energy and Reynolds stress represent smaller and smaller values in terms of the ever increasing mean velocity.

It must be mentioned here that the above argument was developed only for low Mach number flows where adequate measurements are available. At high supersonic Mach numbers the picture may be different because at high Mach numbers a rapid expansion does not result in a significant increase in the mean velocity, rather in a decrease in ambient pressure and temperature and the key to the phenomenon must be the cutting off the supply of turbulent bursts near the wall due to the very full, and very convex velocity profiles and to a lesser degree due to the lateral expansion of the stream tubes. More work is needed in this area because turbulent fluctuation measurements at high supersonic velocities are anything but easy and con- venient.

The counterpart of space-time correlations are the wave number and frequency spectra and such data was reported in Ref. 20. Although it is the exact counterpart of space-time correlation measurements it emphasizes spectral decomposition and brings out significantly the propagation properties of the wave-like Fourier components. On the other hand, the intermittent character of the flow is not brought out by Fourier analysis therefore, author does not find that particular representation very useful, except possibly for problems in sound generation by turbulence, where the coherent wave-like behavior is particularly important in assessing the far field of the generated sound.
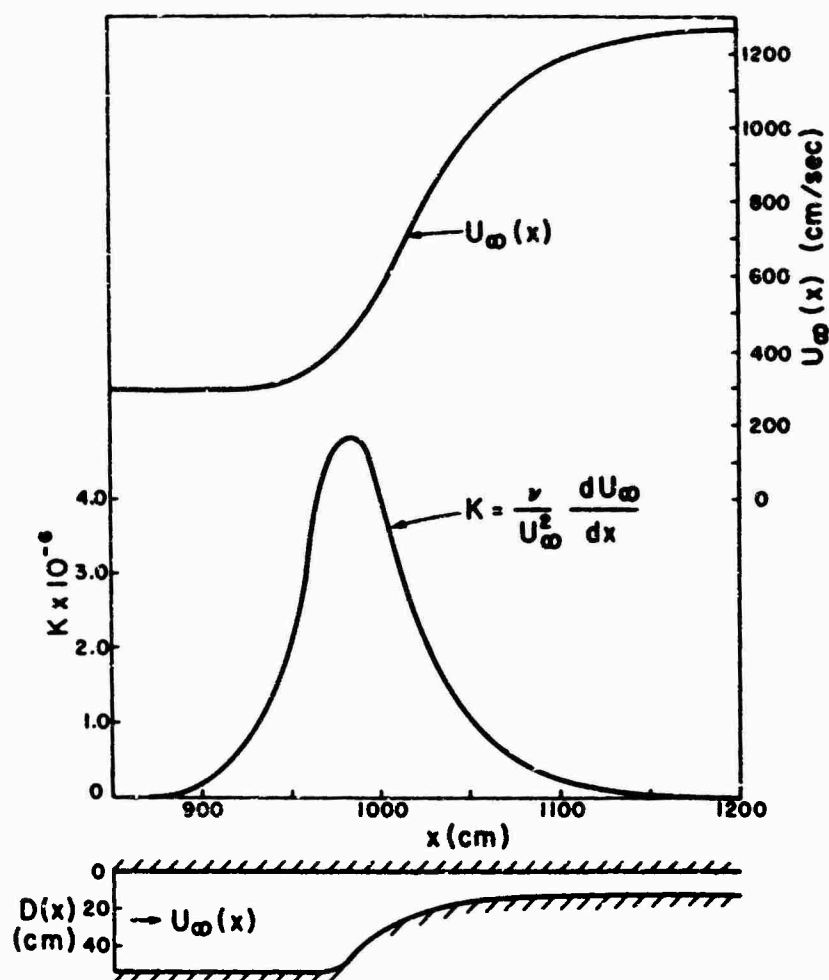
Figure 9. Shape of the contraction and the resulting velocity and pressure distributions.
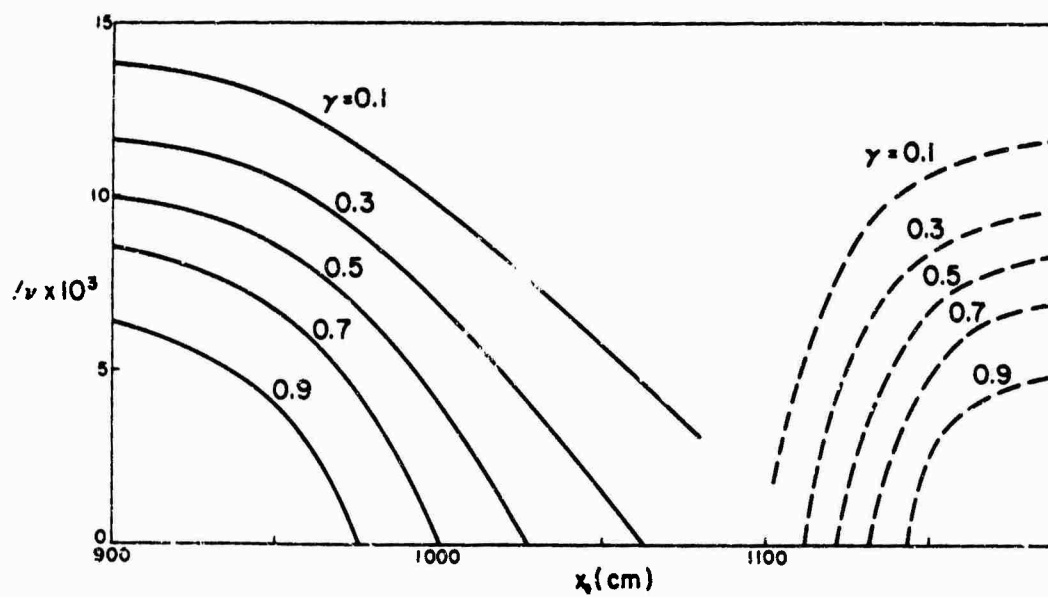
Figure 10. Variation of the intermittency factor in the accelerated boundary layer.
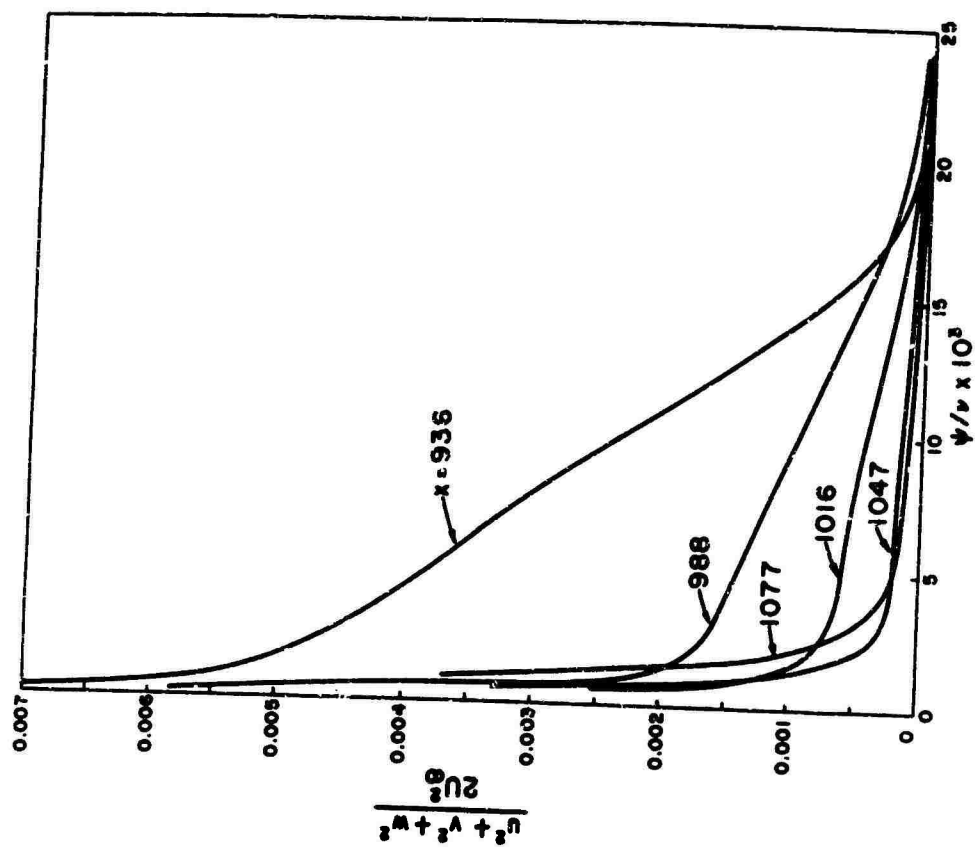
Figure 11. Distribution of the energy of the velocity fluctuations in the accelerated flow.
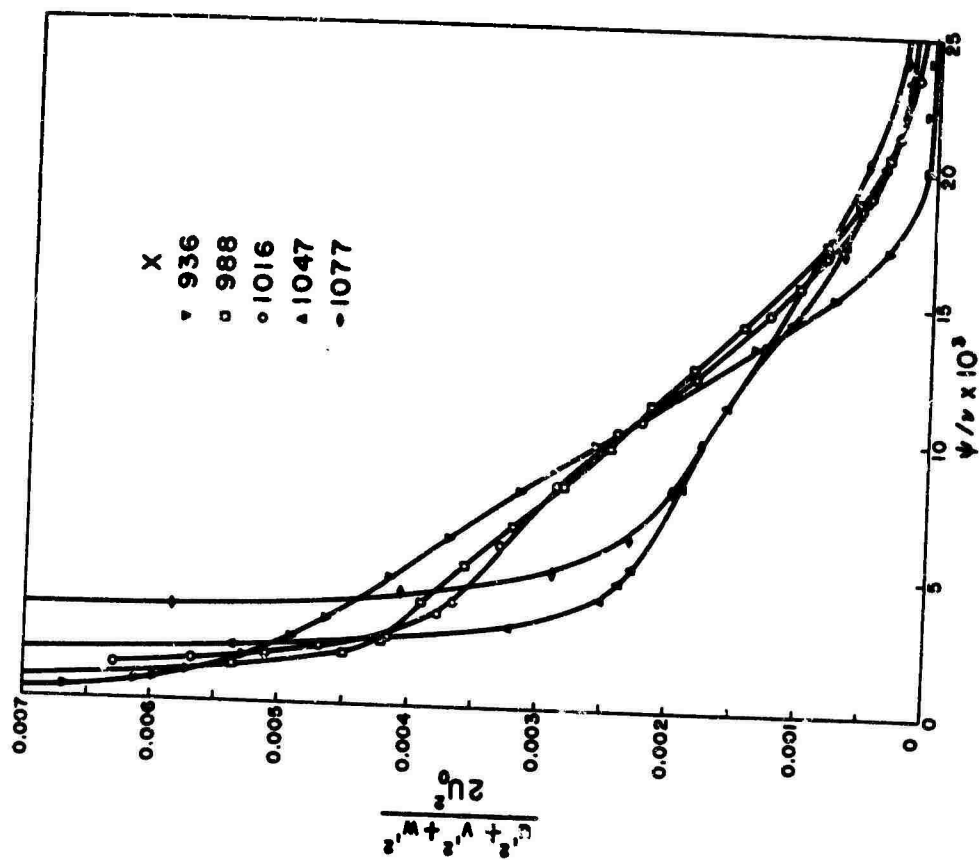
Figure 12. Distribution of the absolute energy of the velocity fluctuations in the accelerated flow.

DISCUSSION

The development of useful concepts toward an understanding of turbulent shear flow came from two directions. One was the demand for explanation of overall mean flow properties and the other was the availability of detailed measurements of the turbulent velocity fluctuations. The most simple and somewhat naive global idea is that the turbulent intensity $q^2 = \overline{u^2} + \overline{v^2} + \overline{w^2}$ while it indicates the level of activities so by extension also represents a quantity roughly proportional to the Reynolds stress $\overline{uv}$. The idea of the Reynolds stress being proportional to the total turbulent kinetic energy is especially appealing in "wall-turbulence" such as pipe or channel flow and in the turbulent boundary layer, where there is a constant replenishment of the turbulent energy from the wall area. It is less appealing in "free-turbulence" and in the central region near the axis of symmetry of wakes, jets, channel flows, etc. where the Reynolds stress must be zero, while the turbulent energy q^2 is not. If no other statistical quantity is specified the turbulent energy alone leaves no clues about the magnitude of the dissipation, which further implies that there are no clues about the scale of turbulence. At that level of complexity the only options open are either to assume that the scale is uniform or that it is small compared to the total width of the flow. Of course neither cannot be true in most turbulent shear flows, since the scale is both varying and also it can become quite large. At the next step one may define a single turbulent scale and at that point there is a dilemma because one of the important scales, the dissipation scale or Taylor's microscale is difficult to obtain experimentally especially at high Reynolds numbers and even more so in high Mach number flows, consequently the estimation of the total viscous dissipation is rather questionable. On the other hand, intergral scales appear to be large and proportional to the overall dimensions of the shear layer and relatively insensitive to the Reynolds number. So the integral scale reveals relatively little, it only gives a warning that transport of momentum, mass and heat all occur at scales up to and including the total width of the layer. The two types of scales are often related by a convenient argument, namely by invoking that at high Reynolds number there is an inertial range in the energy spectrum that is universal and that provides the transfer of energy from the large scale eddies to the dissipative small scale eodies.

A spectral approach has been favored by many experimentalists probably mostly for the simple convenience of using commercially available tunable filters, wave analysers, etc., to process the output of a single hot-wire rather then to use spatially separated probes or arrays. Conceptually, however, it is less than satisfactory in inhomogeneous flows where Taylor's hypothesis is no longer an accurate guide.

It is inevitable that on the next level of sophistication (or at least of complexity) some kind of two level model is necessary, mainly, to describe separately the large scale motion that is strongly non-isotropic and dominates the transport mechanism and a small scale motion that is responsible for viscous dissipation and hopefully it may be assumed as isotropic and homogeneous. This idea of course is not new, it was first suggested by Townsend in 1956 (Ref. 21). The real question is of course what kind of picture to assume for the large scale motion. And here several choices were explored. The first choice is a wave model and the most prominent exponent of this approach is Landahl (Ref. 10). It is evident from experiments that the general convection velocity of turbulent patterns is different from the local mean velocity or in other words Taylor's hypothesis is violated to some extent. The large scale entities called "waves" or "bursts" all travel along the flow at some intermediate velocity different from the local one (see, e.g. Ref. 18). The idea of solving a linarized Orr-Sommerfeld equation for a turbulent mean velocity distribution is very obvious and the largest scale modes can be calculated as eigenfunctions of such a problem. The difficulty with this approach however is the following: the observed space-time correlations do not extend laterally, neither do they show any oscillating or periodic behavior. As a result the actual experimentally observed phenomenon must be regarded as the superposition of a large number of such harmonic components with varying obliqueness or even as a continuous spectrum of them when calculating the dynamic behavior, the non-linear interaction of those components must dominate the phenomenon, therefore it appears desirable to choose an alternate model that can represent the actual flow field either with fewer components or with less non-linear interaction.

Another approach is the "proper eigenfunction" expansion of Lumley (Ref. 22). Here the flow is decomposed into eigenfunctions but these to be obtained from the orthonormal expansion of the correlation functions. The theory contains several alternate options and it includes further possibilities given in details below.

Randomly distributed but still deterministic structures appear to be an attractive representation of turbulent shear flows because they can incorporate most of the experimentally observed phenomena and they can still be tractable for prediction of mean flow properties. The idea was developed to a certain extent by Lumley himself (Ref. 24) and was further discussed by present author in Ref. 26. The approach rests on Rice's theorem (Ref. 23) broadly stating that a superposition of random distributed but identical shape model functions results in a new statistically stationary (homogeneous) function whose normalized double correlations and spectra are identical with those of the model function. The suggestion here is that the bursts observed near the sublayer generate typical "deterministic" entities, or elementary flow patterns, whose development, convection and decay through the shear layer would follow a single pattern but their occurence in space and in time is random and in the first approximation statistically independent (e.g. Poisson distribution). These structures however, decay while transfering energy into finer scale turbulence and the entire flow is permeated with fine scale turbulence that maybe regarded as a new viscous medium and possibly can be dealt with assuming a simple turbulent effective viscosity. Such a model can accomodate

the observed inhomogeneity of the shear flows. The experimentally identifiable events occuring at the intermittent outer edge as well as the internal intermittency of the dissipation can be all properly included. One must note however that decomposition into randomly occuring entities is not an orthonormal expansion, consequently the non-linear interactions must be dealt with in a different manner than customary in a spectral approach (See Ref. 26). In addition the question arises by what process can one obtain explicitly the model function themselves and here there is a definite dilemma. One approach would be, that by using Rice's theorem one could define model functions that yield the right space-time correlation and spectra leaving open the question of coarseness whether one has relatively rare events with high intensity or many small contributions of low intensity or small contributions of low intensity resulting in a nearly Gausian process. Another approach is to follow Lumley's procedure an example is given in Ref. 25.

From the point of view of predicting mean flow properties the most important consequence of the different time scales and the different life-time of the eddies is, that the past history of the flow very strongly determines the local response of the turbulent fluid to the rate of deformation at that point. In another word local properties may not fully determine local response except in the case of the quasi-homogeneous flow where conditions change so slowly in the flow direction that the evolution of the turbulence may be neglected. The other particular case is where similarity may be assumed, therefore all mechanisms are to remain similar and do not show explicity the transient nature. An important consequence of the above picture is that due to the role of large eddies a naive gradient diffusion model for momentum transport must be inadequate or in another word calculating the transport of momentum as the product of an effective turbulent viscosity and the rate of strain of the mean flow (or alternately similar quantities for other analogous transport quantities) must be naive since the large eddies will transport these quantities irrespective of the particular value of the mean flow gradients.

In view of all these it appears preferable to express the transport properties in a integral form rather than in a differential form. E.g. for a steady two-dimensional shear flow of finite width 2δ the streamwise component of the mean velocity $U(x,y)$ should be calculated as

$$U^2(x,y) = U_{inv}^2(x) + \frac{1}{N} \int_{-\infty}^{x+\delta} \int_{-\delta} K(x,y,x',y')\left[U^2(x',y') - U_{inv}^2(x') \right] dx'dy'$$

$$N(x,y) \equiv \int_{-\infty}^{x+\delta} \int_{-\delta} K(x,y,x',y') dx'dy'$$

where U_{inv} is the streamwise component of the mean velocity calculated from inviscid theory. If boundary layer assumption applies $U_{inv}(x)$ is a function of the streamwise coordinate x alone. The quantity K represents the transport activities of the turbulence and of course must be dependent in some way on the intergrated total turbulent energy. In order to effect a closure one must assume a mechanism of producing turbulent energy at the interfaces (at the wall and at the free stream) and conditioning its production according to the rate of bursts. This is of course only a sketch but the logical steps involved would be the following: turbulence exists upstream and is transported continuously downstream. There is a decay of the large scale eddies due to the activity of the finer scale turbulence that is responsible for its dissipation and this may be taken care by an effective turbulent viscosity. The large scale eddies in turn are generated by the turbulent bursts at the solid boundaries or alternately by the general Rayleigh type instability in case of "free-turbulence" (wakes, and jets with inflection profiles). The turbulent energy is responsible for the transport model and therefore for the form of the function of K which in turn redistributes the mean kinetic energy. Such a theory would be also far more practical for step-by-step calculation by a computer since it is stated in a integral form and not in a differential form. Naturally a suitable function for the bursting rates and a plausible expression for K must be obtained, so this is only a program not a full theory.

REFERENCES

(1) Champagne, F. H., Harris, V. G., Corrsin, S. J. Fluid Mech., 41, p. 81, 1970.

(2) Rose, W. G. J. Fluid Mech., 25, p. 97, 1966.

(3) Mulhearn, P. J., Luxton, R. E. Tech. Note F-17, Dept. Mech. Eng. University of Sidney, Nov. 1970.

(4) Boussinesq, T. Memoirs Présentés par Divers Savants, à L'Academie des Sciences, 1877.

(5) S. J. Kline et al (ed.) Proceedings Computation of Turbulent Boundary Layers, Thermosciences Div. Stanford Univ. 1969.

(6) Kline, S. J., Reynolds, W. C. J. Fluid Mech., 30, p. 741, 1967.
     Schraub, F. A.

(7) Kaplan, R. E., Laufer, J. Univ. of South. Cal., Aero. Dept. Rep. USCAE 110,
                                Nov. 1968.

(8) Hussain, A. K. M. F., Reynolds, W. C. Stanford Univ., Thermosciences Div. Report AFOSR
                                            70-1655 TR, May, 1970.

(9) Malkus, W. V. R. J. Fluid Mech. 1, p. 521, 1956.

(10) Landahl, M. T. J. Fluid Mech., 29, p. 441, 1967.

(11) Kovasznay, L. S. G. Annual Review of Fluid Mech., 2, p. 95, 1970.

(12) Kolmogorov, A. N. J. Fluid Mech., 13, p. 82, 1962.

(13) Kuo, Albert Yi-Shuong Experiments on the Internal Intermittency in Turbulent
                            Flow, Ph. D. Thesis, The Johns Hopkins Univ., 1970.

(14) Feidler, H., Head, M. R. J. Fluid Mech., 25, p. 719.

(15) Kovasznay, L. S. G., Kibens, V. J. Fluid Mech., 41, p. 283, 1970.
     Blackwelder, R. F.

(16) Wygnanski, I., Fiedler, H. E. J. Fluid Mech., 41, p. 327, 1970.

(17) Favre, A., Gaviglio, J., Dumas, R. J. Fluid Mech. 2, 313, 1957, ibid 3 p. 344, 1958.

(18) Favre A., Gaviglio, J., Dumas, R. Phys. Fluids 10, p. S138, 1967.

(19) Blackwelder, R., Kovasznay, L. S. G. The Johns Hopkins Univ., Dept. Mech., Interim Tech.
                                           Report No. 2, Contract DA-31-124-ARO-D-313, July,
                                           1970.

(20) Morrison, W. R. B. J. Fluid Mech., 39, p. 117, 1969.
     Kronauer, R. E.

(21) Townsend, A. A. The Structure of Turbulent Shear Flow, Cambridge Univ.
                      Press, 1956.

(22) Lumley, J. Proc. Int. Coll. Atmospheric Turbulence and Radio
                 Propagation, Nauka, Moscow. p. 166, 1967.

(23) Rice, O. Bell Syst. Tech. J., 23, p. 282, 1944, ibid 24, p. 46,
               1945.

(24) Lumley, J. L. Stochastic Tools in Turbulence, Academic Press, 1970.

(25) Payne, F. E., Lumley, J. L. Phys. Fluids Supplement, p. S194, 1967.

(26) Kovasznay, L. S. G. Turbulent Shear Flow, paper presented at the Convegno
                          Sulla Teoria Della Turbolenza, Roma, Italia, April 26-
                          29, 1971 (to be published in the proceedings).

ACKNOWLEDGEMENT

FREE TURBULENT MIXING: A CRITICAL EVALUATION
OF THEORY AND EXPERIMENT

by

Philip T. Harsha
Research Engineer
ARO, Inc.
Engine Test Facility
Arnold Air Force Station, Tennessee 37389, USA

SUMMARY

Because the problem of the analysis of free turbulent mixing is
complex, and some empiricism is always necessary to obtain a solution,
there has been a proliferation of models for the turbulent shear stress.
All of these models will correlate experimental data well in some
region of a particular flow, but not in others. None has been tested
over as broad a range of flow conditions as is possible. In this
study, a group of models for the turbulent shear stress, ranging from
the classical Prandtl mixing length theory to the newly-developed
kinetic energy models, are systematically confronted with a broad
range of experimental data. From this confrontation comes two sets
of conclusions--one detailing those models presently suitable for
engineering use, and the second establishing the models which show
promise of becoming more generally applicable with further development.

LIST OF SYMBOLS

a_1 - ratio of turbulent shear stress to turbulent kinetic energy, Eq (10)
a_2 - constant in expression for dissipation of turbulent kinetic energy, Eq (21)
b - width scale
c - constant
C - concentration of jet species
H - total (mean flow) energy
k - turbulent kinetic energy
K_A - constant in Alpinieri eddy viscosity expression, Eq (6)
K_F - constant in Ferri eddy viscosity expression, Eq (5)
K_P - constant in Prandtl eddy viscosity expression, Eq (4)
K_S - constant in Schetz eddy viscosity expression, Eq (8)
K_Z - constant in Zakkay eddy viscosity expression, Eq (7)
ℓ - mixing length
ℓ_k - mixing length for turbulent kinetic energy
L - function expressing radial variation of $\tau/\rho k$, Eq (14)
M - integral momentum increment, Eq (1)
Pr - turbulent Prandtl number
Pr_k - Prandtl number for turbulent kinetic energy
r_o - primary nozzle radius
$r_{1/2}$ - velocity half-width; r for which $U = 1/2 (U_c + U_o)$
$r_{1/2_m}$ - mass-flux half width; r for which $\rho U = 1/2 (\rho_c U_c + \rho_o U_o)$
Sc - turbulent Schmidt number
U,V - mean velocity components
u,v - fluctuating velocity components
x,y - coordinate directions
α - for plane flow = 0, for axisymmetric flow = 1
δ_r^* - axisymmetric flow displacement thickness
ϵ - kinematic eddy viscosity
ρ - density
τ - turbulent shear stress

Subscripts

o - outer-stream
c - centerline
j - primary jet

PREFACE

Free turbulent mixing can be defined as that class of turbulent flows in which there
is no direct effect of solid boundaries on the development of the flow. Plumes from
exhaust stacks and the wakes of aerodynamic bodies both involve free turbulent mixing, as
does the interaction of fuel and oxidizer in a combustor, or the interaction between the
exhaust of a rocket and the surrounding atmosphere. Clearly, the understanding of free
turbulent mixing flows is basic to the understanding of the fluid mechanics of many
different devices.

In all free mixing problems the analytical difficulty is the same: although the
equations of motion for a free mixing flow can be formulated, if the flow is turbulent,
these equations always contain more unknown terms than there are equations. In particular,

the momentum equation contains an unknown correlation of the fluctuating velocity components which behaves as a shear stress term--the Reynolds stress. In order to solve the turbulent momentum equation, a model for the Reynolds stress must be used. Evaluation of the model used requires experimental evidence.

To provide this evidence, a considerable number of experimental investigations of free turbulent mixing have been carried out. These have included investigations of both the mean flow structure of such flows and their fine scale turbulent structure. At the same time a number of models for the turbulent shear stress have been developed, some of which are modifications and generalizations of earlier models, and others which have attempted new approaches. Even to those working in the field, the number of experiments and models available presents a maze of often conflicting information.

In order to evaluate the state of the art in this important area, I have undertaken a critical review and evaluation of both the available experimental data and of the models that have been proposed for the turbulent shear stress in constant-pressure free mixing. The study has been carried out in two phases. In the first phase. I have critically examined all of the readily available free turbulent mixing data. From this review of the experimental data I have drawn a body of significant, accurate and completely reported experiments. The second phase then involves a review of the available analytical models for the turbulent shear stress. From this I have selected several models which seem to me to be significant. To evaluate the performance of these models, I have used each of them in a finite-difference scheme to calculate the particular flow condition represented by each of the experiments selected in the first phase. By using a numerical scheme common to all calculations, any program-dependence of the results is removed from the comparison. The overriding consideration in this evaluation is how well a given model stands up to the challenge of comparison of its predictions with experiment throughout the entire range of the free turbulent flows considered. Those models for the turbulent shear stress that best meet this challenge are those which have the widest range of applicability and thus the greatest engineering usefulness.

The material presented in this paper is a summary of a study carried out at the Arnold Engineering Development Center (AEDC). This study is reported in Reference 1 in far more detail than can be used here. In selecting the experiments and theoretical models to be considered, I have with some exceptions used only the most readily available papers and reports. With this limitation, the review of Ref. 1 is complete up through March 1970. Only limited reference is made to the Russian literature. This is because the requirements of this study eliminated all but the most detailed papers, and the Russian literature, at least as it is available in the United States, is seldom sufficiently detailed to survive the elimination process.

1. REVIEW OF EXPERIMENTAL DATA

The ultimate goal of this study was to provide a complete test of selected models for the turbulent shear stress over as broad a range of flow conditions as possible. Establishing the appropriate experimental data to use demands a certain sophistication, for not all experimental work is equally valuable, and unfortunately not all is equally correct. Thus the first part of the study involved a critical review and evaluation of the available experimental information. However, as the emphasis in this paper is on the confrontation of theoretical models for the turbulent shear stress with experimental data, the evaluation of the experimental data (which occupies more than 300 pages of Ref. 1) will not be considered in detail herein. Instead, the method of evaluation and the experimental data selected will be described.

Configurations ranging from the circular jet in still surroundings to supersonic wakes were considered in the evaluation of experimental data in Ref. 1. In judging the accuracy of a given experiment, I have taken the primary criterion to be how well the data satisfy the requirement, valid for a constant-pressure free mixing flow, that the integrated momentum increment at any axial station in a given flow be a constant, i.e., that

$$M \equiv \int_0^\infty \rho U (U - U_o) \, y^\sigma \, dy = \text{Constant} \tag{1}$$

where $\sigma = 0$ for a plane (symmetric) flow and $\sigma = 1$ for an axisymmetric flow. Since Eq (1) as written is valid only for symmetric flows, it was not used as a criterion for those few non-symmetric plane flows encountered. A second test, necessarily more subjective, is how well the results of a given experiment compare with those obtained in other experiments concerned with the same flow geometry.

Many experiments satisfy Eq (1) reasonably well (M varying ±10% from its average value) and if Eq (1) is satisfied two experiments concerned with the same flow geometry will generally agree well with one another. However, this does not mean that there is a great variety of experiments from which to choose for the purposes of a study such as this. The reason for this regrettable state of affairs is the wide variation in the detail with which an experiment is reported; particularly in the extent of the detail available about the experimental initial conditions. It is well known that many free mixing configurations eventually approach a "fully-developed" or "self-preserving" state; if "fully-developed" is defined as the state existing when nondimensional flow variables are functions of a local length scale and "self-preserving" as the state in which the local length scale is itself a function of axial distance, then "fully-developed" conditions occur in general before "self-preserving" ones. However, the spatial position at which such conditions occur depends entirely on the flow initial conditions. The length of the potential core region of jets is also entirely dependent on initial conditions such as mass- and momentum-flux ratio and

initial boundary layer thicknesses. If the adequacy of a theoretical prediction of a free mixing flow is to be properly assessed, the initial conditions of that flow must be well defined.

The experiments selected for use in this study are listed in Table 1. It will be noted that all but one of the selected experiments, which include a circular jet, coaxial jets with momentum, heat and mass transfer, a compressible circular jet, and a two-dimensional and an axisymmetric wake, include profiles of the turbulent shear stress, τ. This allows known initial conditions to be used in assessing the kinetic energy model. However, in some cases these profiles were not known at $x/D = 0$, and where this is the case the kinetic energy model calculations start at the axial location noted. Where necessary, the various transport coefficient ratios were taken from the experimental data. Thus, for Paulk[3], Pr = 0.60; for Chriss[5], Pr = 0.85, Sc = 0.85; and for Eggers[6], Pr = 0.60.

Table 1

Characteristics of the Selected Experiments

Investigator	Ref.	Type	U_j, m/sec	U_0/U_j	$\dfrac{\rho_0 U_0}{\rho_0 U_j}$	Re × 10^{-4}	Basis of Re	Initial Profiles U	H	C	τ	Location
Bradshaw, et al.	2	Circular Jet	(M = 0.03)	---	---	35.0	U_j, D_j	x			x	x/D = 2.0
Paulk	3	Coaxial Jet	125	0.371	0.417	10.9	U_j, D_j	x	x		x	x/D = 8.5
			123.5	0.125	0.138	10.75		x	x		x	x/D = 6.8
Forstall	4	Coaxial Jet	68.5	0.20	0.217	2.98	U_j, D_j	x				x/D = 0
			36.6	0.25	0.272	1.59						x/D = 0
Chriss	5	Coaxial Jet	1000	0.158	1.785	11.65	U_j, D_j	x	x	x	x	x/D = 5.4
			976	0.227	2.57	11.30		x	x	x	x	x/D = 4.6
			930	0.263	3.12	10.75		x	x	x	x	x/D = 4.6
			733	0.333	4.16	8.48		x	x	x	x	x/D = 4.0
			580	0.416	5.25	6.71		x	x	x	x	x/D = 4.8
			946	0.218	1.61	10.95		x	x	x	x	x/D = 5.9
			746	0.312	2.44	8.65		x	x	x	x	x/D = 5.3
			595	0.400	3.33	6.89		x	x	x	x	x/D = 4.8
Eggers	6	Circular Jet	539	---	---	265.0	U_j, D_j	x	x		x	x/D = 14.5
Chevray and Kovasznay	7	2D Wake	4[b]	---	---	0.16	U_j, θ_0[a]	x			x	x = 0
Chevray	8	Circular Wake	27.5[b]	---	---	275.0	U_0, D	x			x	x = 0

[a] θ_0 = momentum thickness at x = 0.
[b] U_0

2. THEORETICAL MODELS FOR THE TURBULENT SHEAR STRESS

2.1 Locally-dependent theoretical models in constant density flow

One of the best known formulations for the turbulent shear stress is the mixing length theory developed by Prandtl in 1925. The development of this theory is described in detail in many texts, for example, Schlichting[9]; basically it is founded on the idea that turbulent eddies can be thought of as transferring momentum laterally in the flow. With the condition that the eddies retain their identity as they travel a "mixing length" whereupon they mix instantaneously with other eddies, the mathematical statement of the mixing length theory becomes

$$\tau = \rho \, \ell^2 \left| \frac{\partial U}{\partial y} \right| \frac{\partial U}{\partial y} \tag{2}$$

In a free mixing flow the mixing length ℓ is ordinarily taken to be some fraction of the mixing region width b, i.e., $\ell = c \cdot b$.

Exchange coefficient models can all be traced back to the original Boussinesq concept[10], which is that the turbulent shear stress can be written in a manner analogous to the laminar shear stress, with the physical viscosity replaced by an effective exchange coefficient or eddy viscosity, ϵ. Thus for a turbulent flow

$$\tau = \rho \, \epsilon \, \frac{\partial U}{\partial y} \tag{3}$$

Of course, Eq (3) does no more than define ϵ, and some model for this parameter must still be developed. The most commonly used eddy viscosity formulation for incompressible flow is the model proposed by Prandtl[11] in 1942, which may be written

$$\epsilon = K_p \, b \, (U_{max} - U_{min}) \tag{4}$$

Here K_p is a constant, b a measure of the width of the mixing region, and U_{max} and U_{min} the maximum and minimum values, respectively, of the axial component of the mean velocity at a given cross section. Note that in this formulation ϵ is a function only of x.

2.2 Locally dependent models in variable density flow

There are four approaches that can be taken to the establishment of shear stress models in a variable density flow. The direct approach is to attempt to develop a model by correlating variable-density flow experimental data. Such an approach has been used by Ferri et al.[12], Alpinieri[13], and Zakkay et al.[14] Another approach is to attempt to derive a model in such a manner that the effects of density variation are included. The displacement thickness model developed by Schetz[15,16] falls into this class. The third approach is to use an empirical correction factor to adjust an incompressible-flow eddy viscosity model when used in a compressible flow. Examples of such correction factors and their use are given by Warren[17], Donaldson and Gray[18], and Peters[19]. Finally, the fourth approach is to attempt a transformation of the compressible-flow governing equations that will convert them to the appropriate constant-density form. The transformed equations can then, in principle at least, be solved using an incompressible formulation for the eddy viscosity. Solutions obtained using such techniques have been described by Libby[20] and Channapragada and Woolley[21].

The development of the eddy viscosity model proposed by Ferri and co-workers[12] proceeds from the observation that the Prandtl eddy viscosity model predicts that no mixing takes place when the streams involved are of equal velocity, even if substantial temperature or density differences exist between the streams. To resolve this difficulty they propose a simple adaptation of Eq (4), writing

$$\rho \epsilon = K_F \, r_{1/2_m} \left| \rho_o U_o - \rho_c U_c \right| \tag{5}$$

where $r_{1/2_m}$ is the radial location at which $\rho U = 1/2 \, (\rho_o U_o + \rho_c U_c)$. The recommended value of K_F is 0.025.

On the other hand, Alpinieri[13] experimentally established a flow for which $\rho_c U_c = \rho_o U_o$ and observed that mixing still occurred, although Eq (5) implies that no mixing will occur. Arguing that both the Prandtl (Eq 4) and Ferri models gave good results for some flows, Alpinieri reached the conclusion that the proper eddy viscosity formulation must contain a term which becomes important when $\rho_c U_c = \rho_o U_o$. This reasoning and a correlation of his experimental results led Alpinieri to an equation of the form

$$\rho \epsilon = K_A \, r_{1/2} \, \rho_o \, (U_c + U_o^2/U_j) \tag{6}$$

where U_j is the primary jet velocity and $r_{1/2}$ the radius at which $U = U_o + (U_c - U_o)/2$. Alpinieri recommended a value of $K_A = 0.025$.

Zakkay et al.[14] obtained an asymptotic form for the eddy viscosity through use of an asymptotic, linearized solution of the transformed governing equations. The transformation used was similar to that used by Libby[20], with turbulent Prandtl and Lewis numbers both taken to be unity. The resulting expression is

$$\epsilon = K_Z \, r_{1/2} \, U_c \tag{7}$$

with $K_Z = 0.011$.

The eddy viscosity model proposed for a free-mixing flow by Schetz[15,16] is considerably different from the preceding three models, in that it attempts to incorporate density variation in a somewhat more fundamental manner. Reasoning in analogy to the Clauser[22] model for a planar incompressible boundary layer, Schetz related the turbulent eddy viscosity to the displacement thickness of the turbulent mixing layer. Thus

$$\rho \epsilon = K_S \, (\rho_o U_o \, \pi \, \delta_r^{*2})/r_o \tag{8}$$

where

$$\pi \, \rho_o U_o \, \delta_r^{*2} = \int_o^\infty \left| \rho_o U_o - \rho U \right| 2\pi y \, dy \tag{9}$$

and $K_S \, \pi = 0.018$. Here, r_o is the radius of the inner jet nozzle.

2.3 History-dependent theoretical approaches

In recent years several methods for the calculation of turbulent flows which attempt to include the history of the flow have been reported[23-27], some of which have been applied to the computation of free turbulent flows. The turbulent shear stress is obtained in all of these methods as the result of the solution of an additional transport equation (or equations). Thus, in the method proposed by Nee and Kovasznay[23] an equation describing the transport of the total turbulent viscosity $n = \epsilon + \nu$ is devised and solved simultaneously with the momentum equation.

More direct models for the turbulent shear stress which relate it to the turbulent kinetic energy in the flow have been used for free mixing calculations by Lee and Harsha[24], Laster[25], and Rodi and Spalding[26]. Lee and Harsha and Laster both use the "linear" relation between shear and kinetic energy used also by Bradshaw et al.[27], which may be written

$$\tau = a_1 \, \rho \, k \tag{10}$$

where $k = 1/2 \, (u'^2 + v'^2 + w'^2)$, while Rodi and Spalding use the eddy viscosity model

$$\tau = c \, \rho \, k^{1/2} \, \ell_k \, \partial U/\partial y \tag{11}$$

in which c is a constant and ℓ_k is a kinetic-energy length scale which, in the method of Rodi and Spalding[26], is obtained from the solution of an additional transport equation for the quantity $(\ell_k k)$.

From the correlation of a large quantity of experimental data, Harsha and Lee[28] found that, in regions of strong shear,

$$a_1 = |\tau|/\rho\, k = 0.3 \qquad (12)$$

However, as the shear stress can take on negative values while the kinetic energy is always positive, and goes to zero on a centerline while the kinetic energy does not, Eq (10) cannot adequately represent all regions of a free mixing flow. Fortunately, an adequate representation is easily obtained.

If I write

$$\tau = a_1\, \rho\, k\, L(y) \qquad (13)$$

where $L(y)$ is a dimensionless number which ranges from 0 at $y = 0$ to unity at some point in the flow, say the point where $\partial U/\partial y = (\partial U/\partial y)_{max}$, call it y_{max}, and divide Eq (13) by its value at y_{max} (where $L = 1$), then

$$L(y) = \frac{\tau/\rho\, k}{(\tau/\rho\, k)_{y_{max}}} = \frac{\overline{uv}/k}{(\overline{uv}/k)_{y_{max}}} \qquad (14)$$

The function $L(y)$ can be obtained from experimental data, and Figure 1 shows the results. Also shown on Fig. 1 are curves representing the values of $(\partial U/\partial y)/(\partial U/\partial y)_{max}$ obtained from calculations for various flows. It can be seen that the agreement is relatively good. Note finally that if I write $L(y) \pm (\partial U/\partial y)/|\partial U/\partial y|_{max}$ then the appropriate sign for the shear stress is included.

Thus in this study I have used the "linear" kinetic energy model with

$$\tau = 0.3\, \rho\, k\, (\partial U/\partial y)/|\partial U/\partial y|_{max} \qquad 0 \le y \le y_{max} \qquad (15)$$

$$\tau = 0.3\, \rho\, k\, (\partial U/\partial y)/|\partial U/\partial y| \qquad y > y_{max} \qquad (16)$$

In regions of the flow in which the mixing layer does not have an axis of symmetry I have used Eq (16) throughout.

To obtain the turbulent kinetic energy I have used the parabolic form of the turbulent kinetic energy equation as written by Patankar and Spalding[29]. Bradshaw, et al.[27] have shown that if a convective form of the diffusion term in the kinetic energy equation is used, then it and the momentum equation form a hyperbolic system which can be solved by the method of characteristics. Such an approach has been followed for a compressible free mixing flow by Laster[25]. However, I have chosen the parabolic form (which implies gradient diffusion of turbulent kinetic energy) as gradient diffusion of mean flow energy, and mass seems to be reasonably well established for free mixing flows, and I can see no special reason, apart from mathematical elegance, for not assuming gradient diffusion of kinetic energy also. There is little experimental evidence

References for Data: Figure 1

Sym

○ Wygnanski, I., and Fiedler, H. E., J. Fluid Mech., 38, 3, 1969, pp. 577-612

□ Heskestad, G. J. Appl. Mech., 32, December 1965, pp. 721-724

◇ Bradbury, L. J. S., J. Fluid Mech., 23, 1, 1965, pp. 31-64

△ van der Hegge Zijnen, B. G., Appl. Sci. Research, A, 7. 4, 1958, pp. 250-276

◿ Bradshaw, P. et al., J. Fluid Mech., 19, 1964, pp. 591-624

● ∎ } Chevray, R. J. Basic Engineering, Trans. ASME, 90 D, 2, June 1968, pp. 275-284
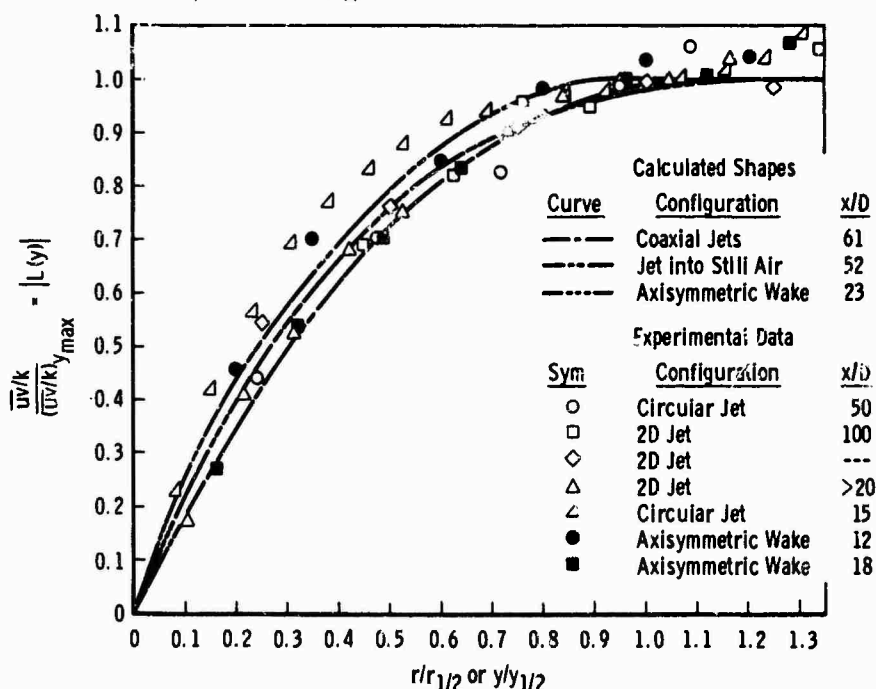
Fig. 1 Comparison of Calculated Length Scales with Those Inferred from Experiment

regarding the diffusion of turbulent kinetic energy; what little I have seen, e.g. Watt[30], seems to imply gradient diffusion but without much conviction.

The theoretical models I have selected to use for comparison with experiment are summarized in Table 2. For the most part, the values of the constants selected are those suggested in the papers describing the model.

3. THE NUMERICAL TREATMENT

The study described in this paper is concerned with a comparison of the predictions of various models for the turbulent shear stress; it is not concerned with the development of numerical techniques. Thus all calculations were made with the same computer program, which is a extension of the technique developed by Patankar[32] for the solution of an arbitrary number of simultaneous parabolic partial differential equations. With this program it was possible to make calculations using any of the eddy viscosity models listed in Table 2, as well as the kinetic energy model using the parabolic form of the turbulent kinetic energy equation. The system of equations used to describe every problem was formulated using the standard boundary layer assumptions; the equations themselves were

continuity

$$\frac{\partial}{\partial x}(\rho U) + \frac{1}{y^\alpha}\frac{\partial}{\partial y}(\rho V\, y^\alpha) = 0 \tag{17}$$

momentum

$$\rho U\frac{\partial U}{\partial x} + \rho V\frac{\partial U}{\partial y} = \frac{1}{y^\alpha}\frac{\partial}{\partial y}\left(\rho\epsilon\, y^\alpha\,\frac{\partial U}{\partial y}\right) \tag{18}$$

total (mean flow) energy

$$\rho U\frac{\partial H}{\partial x} + \rho V\frac{\partial H}{\partial y} = \frac{1}{y^\alpha}\frac{\partial}{\partial y}\left\{\frac{\rho\epsilon\, y^\alpha}{Pr}\left[\frac{\partial H}{\partial y} + \left(\frac{Pr}{Pr_k} - 1\right)\frac{\partial k}{\partial y} + (Pr - 1)\frac{\partial}{\partial y}\left(\frac{U}{2}\right)\right]\right\} \tag{19}$$

species (for a two-gas mixture with no chemical reaction)

$$\rho U\frac{\partial C}{\partial x} + \rho V\frac{\partial C}{\partial y} = \frac{1}{y^\alpha}\frac{\partial}{\partial y}\left(\frac{\rho\epsilon\, y^\alpha}{Sc}\frac{\partial C}{\partial y}\right) \tag{20}$$

and turbulent kinetic energy

$$\rho U\frac{\partial k}{\partial x} + \rho V\frac{\partial k}{\partial y} = \frac{1}{y^\alpha}\frac{\partial}{\partial y}\left[\frac{\rho\epsilon\, y^\alpha}{Pr_k}\frac{\partial k}{\partial y}\right] + \rho\epsilon\left(\frac{\partial U}{\partial y}\right)^2 - \frac{a_2\,\rho k^{3/2}}{\ell_k} \tag{21}$$

The "turbulent kinetic energy Prandtl number", Pr_k, was in all cases taken to be 0.70, while the dissipation constant a_2 was set equal to 1.5.

Table 2

Theoretical Models for the Turbulent Shear Stress

Model	Ref.	Expression for Eddy Viscosity	Expression for Turbulent Shear Stress	Width Parameter Core	Width Parameter Regime II	Value of Constant Core	Value of Constant Regime II	Ref. for Constant
Mixing Length	9	---	$\tau = \rho c^2 \ell^2 \frac{\partial u}{\partial y}\left|\frac{\partial u}{\partial y}\right|$	$1 = b$	$1 = 2r_{1/2}$	0.082	0.082	31
Prandtl Eddy Viscosity	11	$\epsilon = K_{p1}(U_{max} - U_{min})$	$\tau = \rho\epsilon\frac{\partial u}{\partial y}$	$1 = b$	$1 = 2r_{1/2}$	0.007	0.011	19
Schetz "Unified Theory" [a]	15	$\rho\epsilon = K_S\,\pi\psi_0 U_0\, \delta_r^{*2}/r_0$	$\tau = \rho\epsilon\frac{\partial u}{\partial y}$					15
Ferri	12	$\rho\epsilon = K_{F1}|\rho_0 U_0 - \rho_c U_c|$	$\tau = \rho\epsilon\frac{\partial u}{\partial y}$	$1 = b/2$	$1 = r_{1/2}\,\rho\, U^b$	0.025	0.025	12
Zakkay	14	$\epsilon = K_Z 1 U_c$	$\tau = \rho\epsilon\frac{\partial u}{\partial y}$	$1 = b/2$	$1 = r_{1/2}$	0.011	0.011	14
Alpinieri	13	$\rho\epsilon = K_A l\rho_0(U_c + U_0^2/U_j)$	$\tau = \rho\epsilon\frac{\partial u}{\partial y}$	$1 = b/2$	$1 = r_{1/2}$	0.025	0.025	13
Kinetic Energy	24	---	$\tau = a_1\rho\, kF\left(\frac{\partial u}{\partial y}\right)$					Present Study

[a] In this study, mixing length used for core.

[b] $r_{1/2}\rho U = r$ for which $\rho U = (\rho_c U_c + \rho_0 U_0)/2$.

4. RESULTS OF THE CONFRONTATION

All of the models listed in Table 2 were used to make detailed calculations of all of the experimental data listed in Table 1, for a total of 112 calculations. These are all described in Ref. 1, along with some additional calculations involving the use of the Donaldson and Gray[18] eddy viscosity correction and the Libby[20] compressibility transformation, which are not included in this paper. In order to conserve space and the patience of the reader, all of the calculations made are not reported here; instead, the techniques which performed best for each flow are described.

Comparisons of the various predictions made by the models tested were made using logarithmic plots of the centerline velocity decay. This method was chosen because such plots display clearly not only the local agreement (or lack of agreement) of a calculation with the data, but also the trend this agreement shows with axial distance. Lateral velocity profiles at various axial stations were not used because all calculations produce much the same shape if suitably normalized. Velocity data were chosen for the comparison because of their ready availability in the experimental literature.

As would perhaps be expected, there is no one locally-dependent theoretical model for the turbulent shear stress capable of producing satisfactory predictions for the entire range of free turbulent flows considered. However, certain of these models do perform fairly adequately over a limited range of experimental conditions. The history-dependent turbulent kinetic energy approach has shown that it can produce reasonably accurate predictions over the entire range of flows, given adequate knowledge of the initial shear stress.

For the incompressible jet into still air, the best results are obtained using the locally-dependent model developed by Ferri[12] (which is equivalent for this flow to the Prandtl eddy viscosity with a larger constant). The prediction of the kinetic energy theory is also reasonably good. These two models provide the best predictions for this flow, illustrated by Fig. 2. The experiment used to provide the initial conditions[27] does not provide data far downstream. A composite of the downstream data from all of the acceptable jet into still air experiments is represented by the data band. It can be seen that the Ferri model predicts a relatively gradual transition region, but beyond $x/D = 10$, the prediction follows the mean of the data. The kinetic energy theory, on the other hand, appears to overpredict both the velocity potential core length and the asymptotic rate of decay of centerline velocity. However, the kinetic energy theory provides the only reasonable prediction for the compressible jet into still air. Figure 3 shows this prediction as well as that for the Prandtl eddy viscosity model[11], which is one of the best eddy viscosity predictions. The kinetic energy calculation could not be started before $x/D = 14.45$, because of a lack of shear stress profiles before this point.

Fig. 2 Comparison of Best Predictions with Composite Data for Incompressible Jet-into-Still-Air

The best predictions for the coaxial air-air mixing data shown in Figs. 4 and 5 are made by the kinetic energy theory and, depending on the axial distance desired, the Prandtl eddy viscosity model or the Ferri model. Taking the latter two first, it will be noted that for incompressible flow the Ferri model is equivalent to the Prandtl model with a larger constant. Since both models predict the same rate of axial decay of centerline velocity, and this predicted rate is smaller than the observed rate, both models tend to intersect the data. Because of its higher
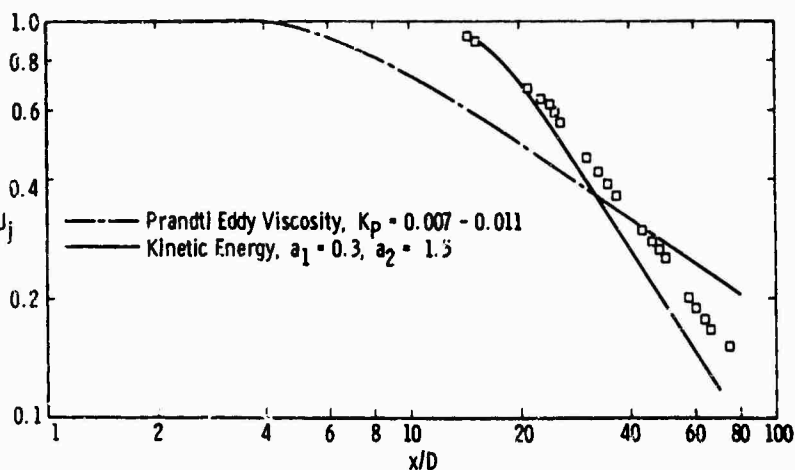
Fig. 3 Comparison of Best Predictions with Data for the Compressible Jet-into-Still-Air. Data from Eggers[6], $M_j = 2.22$

Curve	Model	Constants
——	Kinetic Energy	$a_1 = 0.3$, $a_2 = 1.5$
——	Prandtl Eddy Viscosity	$K_p = 0.07$ - 0.011
——	Schetz	$K_s \pi = 0.018$
——	Ferri	$K_f = 0.025$
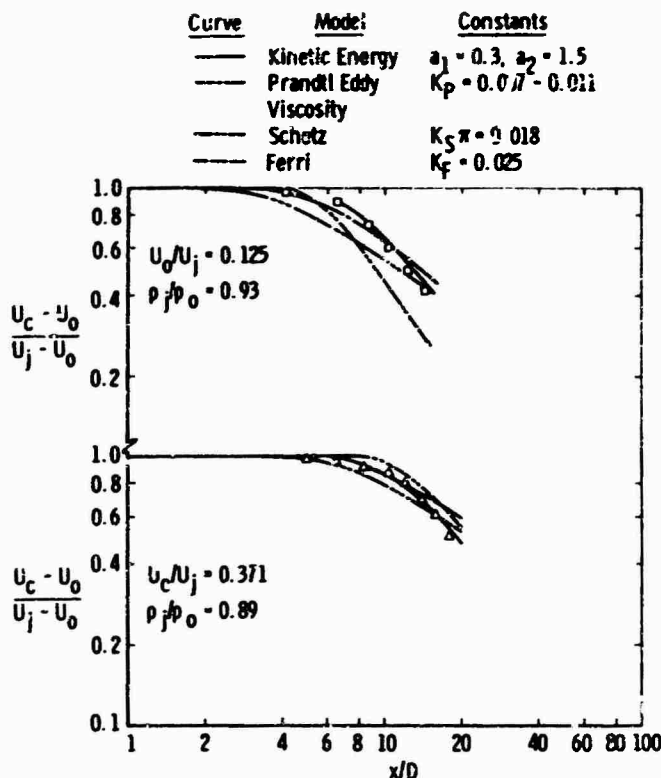
Fig. 4 Comparison of Best Predictions with Coaxial Air-Air Mixing Data of Paulk[3]

constant, the Ferri model predicts that the velocity decay will begin earlier, and thus the point of intersection will appear farther downstream. Hence, Figures 4 and 5 show that the Prandtl model provides the better prediction for $x/D < 20$.

The kinetic energy theory does quite well for these data. For the Paulk[3] data, the kinetic energy calculations were begun downstream of the potential core using measured shear stress profiles, while the calculations for the Forstall[4] data were begun at the nozzle exit using measured boundary layer thicknesses, 1/7 power law profiles, and the Prandtl eddy viscosity model to evaluate the turbulent shear stress. This approach is a simplified version of an approach to starting kinetic energy calculations using measured boundary layer velocity profiles and eddy viscosity profiles obtained by Maise and McDonald[33], which is now in use. The latter approach has proved quite successful for free-mixing flows which start from turbulent boundary layers.

For hydrogen-air mixing, only two of the models tested show the proper behavior: the kinetic energy theory and the Schetz displacement thickness model[15,16]. There are two features of the hydrogen-air data used here which most turbulent shear stress models could not predict: the decrease in velocity potential core length with increasing outer-stream-to-jet mass flux ratio, and the increase of slope of the decay curve also observed with increase of this ratio. Figures 6 and 7 illustrate the performance of the two recommended models. Both of these models exhibit an increase in velocity decay curve slope with increasing $\rho_o U_o / \rho_j U_j$, but it is not possible to determine whether these models will also predict a decrease in velocity potential core length as $\rho_o U_o / \rho_j U_j$ increases, as the Schetz model as used here incorporated the mixing length model for the core region, and it was not possible to start the kinetic energy calculations at $x/D = 0$. These figures do show that the level of agreement with the data is better for the kinetic energy theory than for the Schetz model. Some error is inherent in using the Schetz model (as compared to the kinetic energy theory in prediction of centerline decay), but the behavior of the Schetz model is such as to recommend it for further development.

Both the two-dimensional and the axisymmetric wake data used show an early rapid rise of centerline velocity followed by a region in which the center-line velocity increases more gradually, eventually approaching an asymptote. Thus there are two points for comparison between theory and experiment for these flows. The performance of the two best models for the axisymmetric wake is shown on Figure 8, while the comparison for the two-dimensional wake is shown on Fig. 9. It can be seen from these figures that the kinetic energy model again performs quite well for both the initial and asymptotic portions. For the axisymmetric wake, the Ferri version[12] of the Prandtl eddy viscosity model provides a good prediction, although it appears that the asymptotic trend of this model is to underpredict the centerline velocity, while the Zakkay model[14] provides a good prediction for the two-dimensional wake, including good agreement with the asymptotic trend of the data.

Curve	Model	Constants
——	Kinetic Energy	$a_1 = 0.3$, $a_2 = 1.5$
——	Prandtl Eddy Viscosity	$K_p = \begin{cases} 0.007 \\ 0.011 \end{cases}$
——	Schetz	$K_s \pi = 0.018$
——	Ferri	$K_f = 0.025$

Fig. 5 Comparison of Best Predictions with Coaxial Air-Air Mixing Data of Forstall[4]

Fig. 6 Comparison of Best Predictions with Coaxial Hydrogen-Air Mixing Data of Chriss[5]

Fig. 7 Comparison of Best Predictions with Coaxial Hydrogen-Air Mixing Data of Chriss[5]

Fig. 8 Comparison of Best Predictions with Axisymmetric Wake Data of Chevray[8]

Fig. 9 Comparison of Best Predictions with Two-Dimensional Wake Data of Chevray and Kovasznay[7]

5. CONCLUSIONS AND RECOMMENDATIONS

5.1 Recommendations for turbulent shear stress models-present use

There are two facets of a free mixing flow that a reliable model must be able to predict: the potential core length and the centerline velocity decay. If initial profiles of the turbulent shear stress are known or they can be reliably calculated, none of the locally-dependent methods considered in this study is nearly as powerful for the calculation of centerline velocity decay as the turbulent kinetic energy method. The capabilities of this method warrant its use wherever possible; however, because of a lack of available initial condition data, the performance of the kinetic energy method in predicting the potential core remains undemonstrated. There are many flow phenomena for which turbulent shear stress profiles and/or levels are unknown and it must be recognized that for engineering purposes such will always be the case. For these flows locally-dependent models must be used; the user must recognize that significant errors can result in some cases. Table 3 lists the locally-dependent kinematic eddy viscosity models that are recommended from the results of this study. The numbers in the column labeled "observed error" should

Table 3

Recommendations for the Use of Locally Dependent
Turbulent Shear Stress Models

Type of Flow	Recommended Model	Form of Expression	Constant	Recommended Range	Typical Observed Error This Study[a]
Jet-into-Still Surroundings	Ferri	$\epsilon = K_f r_{1/2}(U_{max} - U_{min})$	0.025	All	15% Low Transition Region)
Coaxial Air-Air	Prandtl	$\epsilon = K_p b(U_{max} - U_{min})$ $b = 2r_{1/2}$	0.007[b] 0.011[c]	$0 \le x/D \le 20$	26% High (x/D = 18)
	Ferri	$\epsilon = K_f r_{1/2}(U_{max} - U_{min})$	0.025	x/D > 20	40% High (x/D = 56)
Coaxial H_2-Air	Schetz	$\rho\epsilon = K_s \varphi_0 U_0 \delta_r^2 / r_0$	0.018	All	40% Low (x/D = 10.4)
Axisymmetric Wake	Ferri	$\epsilon = K_f r_{1/2}(U_{max} - U_{min})$	0.025	All	Small
2D Wake	Zakkay	$\epsilon = K_z r_{1/2} U_{CL}$	0.011	All	Small
Compressible Jet	Prandtl	$\epsilon = K_p b(U_{max} - U_{min})$ $b = 2r_{1/2}$	0.007[b] 0.011[c]	$20 \le x/D \le 60$	35% Low (x/D = 15) 30% High (x/D = 60)

[a]Error in prediction of centerline velocity.

[b]First regime.

[c]Second regime.

not be taken as the maximum error to be expected. Rather they represent typical maximum errors in centerline velocity predictions encountered in the course of this study; they should approximate the errors to be expected in general. The most widely applicable model is the Ferri eddy viscosity model[12] which formally reduces to the Prandtl[11] model for an incompressible flow. The Ferri model, however, does not work for the dissimilar gas case for which it was designed. Note, also, that the Prandtl model is listed in Table 3 for the compressible jet into still air, although the error involved in its use is very nearly prohibitive.

5.2 Recommendations for turbulent shear stress models-further development

Further attempts to modify the basic Prandtl eddy viscosity model or the mixing length theory to make them apply to more complex flows is a fruitless avenue of attack. The results of the review on which this paper is based have shown that none of the modifications of the Prandtl eddy viscosity model, including the Donaldson and Gray compressibility correction[18] are capable of greatly altering the basic shape of the axial centerline velocity decay curve, and the shape predicted by the Prandtl model and all of its derivatives is incorrect for complex (two-gas) flows. On the other hand, the displacement-thickness model proposed by Schetz is the only locally-dependent model to show the proper behavioral trends for hydrogen-air mixing. Because of this, its use should be investigated in other dissimilar-gas flows. Further work should be done in applying this model or a modification of it to coaxial single-gas flows, and further investigation of this model and its implications is recommended.

Given some knowledge of the initial turbulent shear stress, the turbulent kinetic energy method is capable of providing better and more uniform predictions over a wider range of flows than any other model investigated. Because of this, it clearly holds the greatest promise for future development. The most important area for future work is in establishing methods for the generation of the proper initial conditions. Another area for further work involves the establishment of better models for the terms in the kinetic energy equation. The models and constants used in this study have been developed rather crudely--they seem to work well, but that does not mean that there is no room for improvement.

It is somewhat disturbing that after all of the effort expended on research on free turbulent mixing, there is still no reliable way to make engineering calculations of any but the most basic free turbulent flows. In part this situation is a result of the diffuse nature of free turbulence research, with many workers in many laboratories investigating different facets of the problem. Seldom is their work widely reported, with the result that new workers in the field all too often have to repeat all of the previous mistakes in order to become aware of the deficiencies of the various models for the free turbulent shear stress. Too many attempts are made--perhaps due more to necessity than to desire--to analyze complicated flow systems while simple ones are not understood. Such analyses bury the turbulent shear stress models so deeply under assumptions for the other variables in the problem that when they fail, as they all too often do, their failure sheds no light on the turbulent shear stress model involved.

The study summarized here was undertaken to establish the state of the art in free turbulent mixing. This involved a critical analysis of the available free turbulent mixing experiments and of the available models for the free turbulent shear stress. One result of this study is the establishment of limits within which various shear stress models may be used, although possibly with considerable error. But a potentially far more important result is the demonstration of the accuracy of the history-dependent kinetic energy method. The methods of analysis which take into account the structure of the turbulent flow seem to offer the hope of escape from the blind alleys into which locally dependent models have led: methods which fail to take into account the fact that the flow is turbulent, and not laminar with some badly behaving viscosity, can never be made to agree with more than a small range of experiments. Clearly the time has come that methods of analysis of turbulent flow recognize that it is indeed turbulent.

Acknowledgement

References

1) Harsha, P. T., "Free Turbulent Mixing: A Critical Evaluation of Theory and Experiment". AEDC TR 71-36, Feb. 1971
2) Bradshaw, P., Ferriss, D. H., and Johnson, R. F. J. Fluid Mech. Vol. 19, 1964, pp. 591-624
3) Paulk, R. A., "Experimental Investigation of Free Turbulent Mixing of Nearly Constant Density Coaxial Streams," M.S. Thesis, The Univ. of Tennessee, Knoxville, Tenn., March 1969
4) Forstall, W. Jr., "Material and Momentum Transfer in Coaxial Gas Streams," Ph.D. Thesis, M.I.T., Cambridge, Mass. 1948
5) Chriss, D. E., "Experimental Study of the Turbulent Mixing of Subsonic Axisymmetric Gas Streams," AEDC TR 68-133, Aug. 1968
6) Eggers, J. M., "Velocity Profiles and Eddy Viscosity Distributions Downstream of a Mach 2.2 Nozzle Exhausting to Quiescent Air," NASA TN D-3601, Sept. 1966
7) Chevray, R. and Kovasznay, L.S.G., AIAA J., Vol. 7, No. 8, Aug. 1969, pp. 1641-1643
8) Chevray, R. J. Basic Eng., Trans. ASME Ser. D, Vol. 90, No. 2, June 1968, pp. 275-284
9) Schlichting, H., "Boundary Layer Theory," 4th Ed., New York, McGraw-Hill Book Co., 1960, pp. 477-480
10) ibid, p. 475
11) Prandtl, L., Z. Angew. Math Mech., Vol. 22, Oct. 1942, pp. 241-243
12) Ferri, A., Libby, P. A., and Zakkay, V. "Theoretical and Experimental Investigation of Supersonic Combustion", PIBAL-713, Polytechnic Institute of Brooklyn, Sept. 1962
13) Alpinieri, L. J., AIAA J., Vol. 2, No. 9, Sept. 1964, pp. 1560-1567
14) Zakkay, V., Krause, E., and Woo, S.D.L., AIAA J., Vol. 2, No. 11, Nov. 1964, pp. 1939-1947
15) Schetz, J. A., AIAA J., Vol. 6, No. 10, Oct. 1968, pp. 2008-2010
16) Schetz, J. A., "Unified Analysis of Turbulent Jet Mixing", NASA CR-1382, July 1969
17) Warren, W. R., "An Analytical and Experimental Study of Compressible Free Jets", Report 381, Aeronautical Engineering Lab., Princeton Univ. 1957
18) Donaldson, C. duP., and Gray, K. E. AIAA J., Vol. 4, No. 11, Nov. 1966, pp. 2017-2025
19) Peters, C. E., "Turbulent Mixing and Burning of Coaxial Streams Inside a Duct of Arbitrary Shape", AEDC TR 68-270, Jan. 1969
20) Libby, P. A., ARS J., Vol. 32, No. 3, Mar. 1962, pp. 388-396
21) Channapragada, R. S. and Woolley, J. P. "Turbulent Mixing of Parallel Compressible Free Jets", AIAA Paper 65-606, 1965
22) Clauser, F. H. "The Turbulent Boundary Layer". Advances in Applied Mechanics, Vol. 4, Oxford, Pergamon Press, 1956
23) Nee, V. W. and Kovasznay, L. S. G., Phys. Fluids, Vol. 12, No. 3, Mar. 1969, pp. 473-484
24) Lee, S. C. and Harsha, P. T., AIAA J., Vol. 8, No. 6, June 1970, pp. 1026-1032
25) Laster, M. L. "Inhomogeneous Two-Stream Turbulent Mixing Using the Turbulent Kinetic Energy Equation", AEDC TR 70-134, May 1970
26) Rodi, W. and Spalding, D. B., "A Two-Parameter Model of Turbulence and its Application to Free Jets" BL/TN/B/12, Dept. of Mech. Eng., Imperial College of Science and Technology, July 1969
27) Bradshaw, P., Ferriss, D. H., and Atwell, N. P., J. Fluid Mech., Vol. 28, Part 3, 1967, pp. 593-616
28) Harsha, P. T. and Lee, S. C., AIAA J., Vol. 8, No. 8, Aug. 1970, pp. 1508-1510
29) Patankar, S. V. and Spalding, D. B., Internat. J. Heat Mass Transfer, Vol. 10, 1967, pp. 1389-1411
30) Watt, W. E., "The Velocity-Temperature Mixing Layer". Ph.D. Thesis, Univ. of Toronto, 1967
31) Squire, H. B. and Trouncer, J. "Round Jets in a General Stream", A.R.C. R&M 1975, Jan. 1944
32) Patankar, S. V. "Heat and Mass Transfer in Turbulent Boundary Layers" Ph.D. Thesis, Imperial College of Science and Technology, 1967
33) Maise, G. and McDonald, H. AIAA J., Vol. 6, No. 1, Jan, 1968, pp. 73-80

JET TURBULENCE: DISSIPATION RATE MEASUREMENTS AND CORRELATIONS

by

Carl A. Friehe,[1] C. W. Van Atta[2] and Carl H. Gibson[3]
Department of Aerospace and Mechanical Engineering Sciences
University of California, San Diego
La Jolla, California 92037

SUMMARY

The rate of viscous dissipation in a turbulent jet is examined in some detail. A correlation of the mean rate of dissipation on the center-line in terms of the orifice Reynolds number and axial position is established. Measurements of the velocity and velocity derivative are described for a jet of orifice Reynolds number of 1.2×10^5. The spectrum of the square of the velocity derivative was found to be similar to those obtained for atmospheric boundary layer flows at very large Reynolds numbers when normalized with Kolmogoroff length and time scales. Spectra of higher order moments of the velocity derivative are also presented and compared to Novikov's predictions of the power law subranges.

1. INTRODUCTION

The mean rate of viscous dissipation of turbulent kinetic energy per unit mass of fluid, $\langle \epsilon \rangle$, is an important quantity in the energy budget for the turbulent jet. It is also of importance in determining the fine scale structure of the turbulence. In this paper the dissipation rate in a turbulent jet is examined in some detail. First, a correlation of $\langle \epsilon \rangle$ in terms of the independent variables of the flow is established. From this and other well-known results for the self-preserving jet, relations for the variations of the Taylor microscale and the Kolmogoroff length with Reynolds number and axial distance are derived. Secondly, experimental results of the fluctuations of the dissipation rate in a turbulent jet are presented and compared to similar measurements in atmospheric boundary layers.

2. CORRELATIONS

Landau and Lifshitz (1959) show by dimensional arguments that $\langle \epsilon \rangle$ is proportional to the cube of a characteristic velocity difference divided by a characteristic length, both representative of the mean flow. Gibson, Chen and Lin (1968) have used this method to correlate $\langle \epsilon \rangle$ for a sphere wake flow. For the jet, on the center-line, we take the mean center-line velocity U_m as the characteristic velocity and the mean width w as the characteristic length (see Fig. 1 for a sketch defining notation). For the self-preserving jet, it is well known that $U_m/U_o \sim (x/D - x_o/D)^{-1}$ (where x_o/D is the virtual origin) and $w \sim x$, which results in

$$\frac{\langle \epsilon \rangle D}{U_o^{3}} = c\left(\frac{x}{D}\right)^{-4} \tag{1}$$

where c = a constant to be determined, and the virtual origin has been neglected. Figure 2 shows a compilation of $\langle \epsilon \rangle$ data covering the range $20 \leq x/D \leq 70$ and $10^4 < Re_o < 5 \times 10^5$ ($Re_o = U_o D/\nu$) plotted according to the above formula. The data correlate fairly well, and a value of $c = 48$ is indicated. It should be noted that the measured values of $\langle \epsilon \rangle$ can be underestimated due to the finite hot-wire length effect (Wyngaard, 1969), but corrections for this effect have not been made to the data in Fig. 2.

With the equation (1) and results for the self-preserving jet (Wygnanski and Fiedler (1969)), the Taylor microscale $\lambda_f = [\langle u^2 \rangle / \langle (du/dx)^2 \rangle]^{1/2}$ may be calculated. (u and du/dx are the fluctuating streamwise velocity and its derivative, respectively.) Using $\langle u^2 \rangle^{1/2}/U_m = 0.29$, $U_m/U_o = 5.4 (x/D)^{-1}$ for $x/D > x_o/D$, and assuming local isotropy ($\langle (du/dx)^2 \rangle = \langle \epsilon \rangle / 15\nu$), the result is

$$\lambda_f = 0.88 \, (Re_o)^{-1/2} x \quad . \tag{2}$$

---

[1] Assistant Research Engineer

[2] Associate Professor

[3] Associate Professor

Wygnanski and Fiedler experimentally found $\lambda_f = 3.4 \times 10^{-3} x$ for a jet of $Re_o = 1 \times 10^5$, whereas the predicted value according to equation (2) is $\lambda_f = 2.8 \times 10^{-3} x$. Similarly, the Kolmogoroff length scale $\eta = [\nu^3/\langle\epsilon\rangle]^{1/4}$, is $\eta = (48 \, Re_o^3)^{-1/4} x$. Thus from the correlation of $\langle\epsilon\rangle$ and well-known results for the basic properties of the turbulent jet, certain features of the fine scale structure can be predicted.

3. EXPERIMENTAL ARRANGEMENT

The present measurements were made on the center-line of a jet at $x/D = 40$. The jet diameter D was 2.5 inches and the orifice Reynolds number $Re_o = 1.2 \times 10^5$. A linearized constant ane-mometer (Thermo-Systems, Inc.) was used with a 0.00015 diameter $\times$ 0.050 inches long platinum-plated tungsten hot-wire. The probe was aligned on the axis of the jet with a laser. The linearized signal proportional to the velocity was low-pass filtered and differentiated with a Tektronix 3A8 operational amplifier. The velocity and velocity derivative signals were recorded on an FM tape recorder. On playback, the signals were simultaneously digitized with a two channel 12 bit analog to digital converter with low-pass filtering used to reduce aliasing effects. Statistical and spectral analyses were performed on a CDC 3600 computer.

4. RESULTS

4.1 Statistics

A summary of the statistical results is presented in Table 1. The mean velocity ratio, U_o/U_m, and the streamwise intensity $\langle u^2 \rangle^{1/2}/U_m$ agree fairly well with the data of Wygnanski and Fiedler who

Table 1

$Re_o = 120,000$ Jet, $x/D = 40$, Centerline.

1. $U_o/U_m = 6.2$, $\langle u^2 \rangle^{1/2}/U_m = 0.25$

2. $S =$ Skewness, $K =$ Kurtosis, $\dot{u} = du/dx = -\dfrac{1}{U_m}\dfrac{du}{dt}$

   $S_u = 0.09$ $\qquad$ $K_u = 2.85$

   $S_{\dot{u}} = -0.46$ $\qquad$ $K_{\dot{u}} = 9.2$

   $S_{|\dot{u}|} \cong 2.7$ $\qquad$ $K_{|\dot{u}|} \cong 16.5$

   $S_{(\dot{u})^2} \cong 11$ $\qquad$ $K_{(\dot{u})^2} \cong 215$

   $S_{|\dot{u}|^3} \cong 40$ $\qquad$ $K_{|\dot{u}|^3} \cong 3660$

   $S_{(\dot{u})^4} \cong 70$ $\qquad$ $K_{(\dot{u})^4} \cong 7650$

reported 6.6 and 0.29, respectively. The velocity u was found to be very nearly Gaussian with skew-ness $S_u = 0.09$ and kurtosis $K_u = 2.85$. (For a random variable x ($\langle x \rangle = 0$), we use the definitions $S_x \equiv \langle x^3 \rangle / \langle x^2 \rangle^{3/2}$ and $K_x \equiv \langle x^4 \rangle / \langle x^2 \rangle^2$.) The present data on the statistics of the velocity deriva-tive lend support to the predictions of Wyngaard and Tennekes (1970) about the variations of $S_{\dot{u}}$ with $K_{\dot{u}}$, and $S_{\dot{u}}$ and $K_{\dot{u}}$ with $R_{\lambda f}$. ($R_{\lambda f}$ is the "turbulence Reynolds number" $= \langle u^2 \rangle^{1/2} \lambda_f/\nu$.) They presented data for $R_{\lambda f} = 200$ (a laboratory mixing layer) and $R_{\lambda f} > 2000$ (atmospheric boundary layer). The present data at $R_{\lambda f} = 540$, an intermediate value, agrees fairly well with their formu-las $-S_{\dot{u}} = 0.214 \, K_{\dot{u}}^{3/8}$, $-S_{\dot{u}} = 0.15 \, R_{\lambda f}^{3/16}$ and $K_{\dot{u}} = 0.44 \, R_{\lambda f}^{1/2}$. There have been other predictions about the statistics of the velocity derivative: Corrsin (1962) obtained $K_{\dot{u}} \sim R_{\lambda f}^{3/2}$, Tennekes (1968) obtained $K_{\dot{u}} \sim R_{\lambda f}$ and Saffman (1970) found $K_{\dot{u}} \sim R_{\lambda f}$ and $S_{\dot{u}} =$ constant. The present results, those of Kuo, and Wyngaard and Tennekes do not appear to confirm those predictions. It should be noted that the formula of Wyngaard and Tennekes relating $K_{\dot{u}}$ to $R_{\lambda f}$ does not describe results at low $R_{\lambda f}$ (< 200). Kuo (1970) measured $K_{\dot{u}}$ for $12 < R_{\lambda f} < 830$, and for $R_{\lambda f} < 200$, found $K_{\dot{u}} \sim R_{\lambda}^{0.2}$. Kuo (1970) obtained $K_{\dot{u}} = 10$ for a jet of $R_{\lambda f} = 830$, slightly less than predicted by Wyngaard and Tennekes. Kuo also investigated the effect of low pass filtering on $K_{\dot{u}}$: in the present experiments, the velocity derivative was low pass filtered at a cutoff frequency equal to 0.75 of the Kolmogoroff frequency. From Kuo's results, it can be estimated that $K_{\dot{u}}$ for the cutoff frequency equal to the

Kolmogoroff frequency would be 10 for our experiment.

4.2 Velocity Spectra

The cne-dimensional velocity and velocity derivative spectra, normalized with Kolmogoroff length and velocity scales, are presented in Fig. 3. In that notation $\check{\Phi}_u(k_{1K}) = \Phi_u(k)/((\epsilon)^{1/4}\nu^{5/4})$, $\check{\Phi}_{\dot{u}}(k_{1K}) = k^2\Phi_u(k)\nu^{1/4}/(\epsilon)^{3/4}$, and $k_{1K} = k(\nu^3/(\epsilon))^{1/4}$ where $\langle u^2\rangle = \int_0^\infty \Phi_u(k)dk$, $\langle(du/dx)^2\rangle = \int_0^\infty \Phi_{\dot{u}}(k)dk$ and use has been made of $k = 2\pi f/U_m$. The integral scale, $L_x = \pi\Phi_u(k\to0)/(2\langle u^2\rangle)$ was 10.5 cm and η was 0.016 cm. The spectra show the existence of an inertial subrange; using the derivative spectrum as a sensitive test of this, one decade of $k_{1K}^{1/3}$ is indicated. The one dimensional Kolmogoroff constant $\alpha_1 = \Phi_{\dot{u}}(f)/(2\pi U_m(\epsilon)^{2/3}k^{1/3})$ is 0.56, a value intermediate between 0.48 that has been reported from many measurements (Pond, et al. (1966))and 0.7 (Gibson, Stegen, Williams (1970)), for a high $R_{\lambda f}$ atmospheric boundary layer. The present value however, is subject to wire length corrections $(\ell_{wire}/\eta = 8.3)$ (Wyngaard 1969), and it is estimated that the correct value is 0.5.

4.3 Dissipation Rate Fluctuations

Recent evidence about the nature of the rate of dissipation in high Reynolds number atmospheric flows has shown that ϵ is intermittent in the turbulent field. (For a review, see Gibson, Stegen and McConnell (1970).) Kolmogoroff's original similarity theory did not take this into account; for example, the spectrum of ϵ in the inertial subrange is given by $\Phi_\epsilon \sim (\epsilon)^a k^b \sim (\epsilon)^2 k^{-1}$ from dimensional analysis. (Or, alternatively $k\Phi_\epsilon \sim (\epsilon)^2 =$ constant in the inertial subrange, according to the "cascade" model.) Kolmogoroff (1962) subsequently modified the original hypotheses, which Yaglom (1966) put in spectral form as $\Phi_\epsilon \sim k^{-1+\mu}$, where $\mu =$ a constant to be determined. The atmospheric measurements show $\mu = 0.33$ to 0.64 for the atmospheric boundary layer, and $\mu = 0.85$ for a low Reynolds number mixing layer (Wyngaard and Tennekes (1970)). It is desirable that similar measurements be made in large Reynolds number non-atmospheric flows, such as a jet, to determine the universal behavior, if any, of Kolmogoroff's modified theory (Stewart, Wilson and Burling (1970)). In addition to a determination of the constant μ at an "intermediate" Reynolds number, it is of interest to find out if the power spectra of Φ_ϵ, normalized with Kolmogoroff length and time scales, collapse onto a universal curve. Noting that $\int_0^\infty \Phi_x(k)\,dk = \langle(x - \langle x\rangle)^2\rangle$, we write

$$\check{\Phi}_\epsilon(k_{1K}) = \frac{\Phi_\epsilon(k)}{\left[\frac{\langle\epsilon^2\rangle}{\langle\epsilon\rangle^2} - 1\right]\eta\langle\epsilon\rangle^2} \qquad . \qquad \text{Taking} \quad \epsilon = 15\nu(\dot{u})^2 \quad ,$$

$$\check{\Phi}_\epsilon(k_{1K}) = \check{\Phi}_{\dot{u}}(k_{1K}) = \frac{\Phi_{\dot{u}}(k)}{\left[K_{\dot{u}} - 1\right]\eta\langle(\dot{u})^2\rangle} \qquad , \tag{3}$$

obtained by Wyngaard and Tennekes (1970). Hence we may define a subrange constant α_ϵ by $\check{\Phi}_\epsilon(k_{1K}) = \alpha_\epsilon k_{1K}^{-1+\mu}$. Figure 4 shows the present data, the data of Wyngaard and Tennekes for the $R_{\lambda f} = 200$ mixing layer, and the range of four spectra of Gibson, Stegen and McConnell (1970), plotted according to equation (3). They collapse onto a universal curve with a value of $\alpha_\epsilon = 0.5$. For the jet data, approximately one decade of a power law subrange is obtained with $\mu = 0.5$, in agreement with the atmospheric data of Gibson, Stegen and McConnell and Van Atta and Chen(1970). The low Reynolds number results of Wyngaard and Tennekes, while exhibiting about the same high wave number shape, do not show a $\mu = 0.5$ subrange, perhaps due to the absence of an inertial subrange. It should be noted that Stewart, Wilson and Burling (1970) obtained $\mu = 0.35$ in an atmospheric boundary layer; the reasons for the different values are not understood at the present time.

Novikov (1965) considered spectra of higher moments of $\dot{u}$ and predicted power law subranges given by

$$\Phi_{|\dot{u}|^n}(k) \sim k^{-1+(n-1)\mu} , \qquad n = 2, 3, 4 \ldots , \tag{4}$$

which for $n = 2$ reduces to Yaglom's result. By an analysis similar to that for $\Phi_{(\dot{u})^2}(k)$, we may

normalize the higher order spectra. The results for $n = 3$ and 4 are

$$\tilde{\Phi}_{|\dot{u}|^3}(k_{1K}) = \frac{\Phi_{|\dot{u}|^3}(k)}{\eta \left[\frac{S_{(\dot{u})^2} K_{\dot{u}}^{3/2}}{S_{|\dot{u}|}^2} - 1 \right] \langle |\dot{u}|^3 \rangle^2}$$

and

$$\tilde{\Phi}_{(\dot{u})^4}(k_{1K}) = \frac{\Phi_{(\dot{u})^4}(k)}{\left(K_{(\dot{u})^2} - 1 \right) n \langle (\dot{u})^4 \rangle^2}$$

The values for the skewness and kurtosis values of $|\dot{u}|$, $\dot{u}$ and $(\dot{u})^2$ are given in Table 1. Figure 5 shows the spectra of $\tilde{\Phi}_{|\dot{u}|^3}(k_{1K})$ and $\tilde{\Phi}_{(\dot{u})^4}(k_{1K})$. The results do not follow Novikov's prediction: power law subranges $|\dot{u}|^3$ do exist, $(\dot{u})^4$ but the slopes are not given by equation (4). If we take $\mu = 0.5$, the slope of the subrange for $\tilde{\Phi}_{|\dot{u}|^3}(k_{1K})$ would have been zero, and that for $\tilde{\Phi}_{(\dot{u})^4}(k_{1K})$ would be $+ 1/2$. Gurvich $|\dot{u}|^3$ and Zubkovskii (1965) did report agreement with $(\dot{u})^4$ Novikov's formula for a transverse velocity derivative measured in an atmospheric boundary layer with a sonic anemometer of limited spatial resolution. The present results do show a trend of the subrange slope approaching zero (white noise) as n increases. This result is not inconsistent with a model of the $|\dot{u}|^n$ time series approaching a time series of random delta function for large n. The large gradients in $\dot{u}$ are amplified as n increases, which results in the extremely large kurtosis values of $|\dot{u}|^n$ shown in Table 1 for $n = 2, 3, 4$. Portions of the actual time series of $\dot{u}$ and $(\dot{u})^4$ are shown in Fig. 6.

5. CONCLUSIONS

The mean rate of viscous dissipation $\langle \epsilon \rangle$ was found to be correlated by the method proposed by Landau and Lifshitz for a wide range of Reynolds numbers. With the correlation of $\langle \epsilon \rangle$ and well-known results for the self-preserving jet, quantitative formulas for the Taylor microscale and the Kolmogoroff length were developed. The above correlations may be useful in designing jet experiments and in modeling the rate of dissipation term in the full equations of motion.

The turbulence measurements indicated the existence of an inertial subrange of about one decade in wave number. The statistics of the velocity derivative were found to agree with the predictions of Wyngaard and Tennekes. The local rate of viscous dissipation was found to be intermittent, as has been previously observed in high Reynolds number atmospheric flows. The constant μ was found to be 0.5, and the normalized spectra of the dissipation rate for the jet, a mixing layer and the atmospheric boundary layer collapsed to a universal form at high wave numbers. Spectra of higher order moments of the velocity derivative did not agree with Novikov's prediction of the subrange slopes.

REFERENCES

Champagne, F. H. 1971 (Private communication).

Corrsin, S. 1962 Phys. Fl. 5, 1301.

Gibson, C. H., Chen, C. C., and Lin, S. C. 1968 A.I.A.A. J., 6, 642.

Gibson, C. H., Stegen, G. R., and Williams, R. B. 1970 J. Fluid Mech., 41, 153.

Gibson, C. H., Stegen, G. R., and McConnell, S. O. 1970 Phys. Fl. 13, 2448.

Gibson, M. M. 1963 J. Fluid Mech., 15, 161.

Gurvich, A. S. and Zubkouskii, S. L. 1965 Izv., Atmos. Ocean. Phys. Ser., 1, 797.

Kolmogoroff, A. N. 1962, J. Fluid Mech., 13, 82.

Kuo, A. 1970, Ph.D. Dissertation, Department of Mechanics, The Johns Hopkins University.

Landau, L. D. and Lifshitz, E. M. 1959 "Fluid Mechanics," Addison-Wesley, Reading, Mass., p. 119.

LaRue, J. and Friehe, C. A. 1971 (Unpublished).

Novikov, E. A. 1965 Izv., Atmos. Ocean. Phys. Ser., 1, 788.

Pond, S., Smith, S. D., Hamblin, P. F. and Burling, R. W. 1966, J. Atm. Sci., 23, 576.

Saffman, P. G. 1970 Phys. Fl., 13, 2193.

Stewart, R. W., Wilson, J. R. and Burling, R. W. 1970 J. Fluid Mech., 41, 141.

Tennekes, H. 1968, Phys. Fl., 11, 669.

Van Atta, C. W. and Chen, W. Y. 1970, J. Fluid Mech., 44, 145.

Wygnanski, I. and Fiedler, H. 1969, J. Fluid Mech., 38, 577.
Wyngaard, J. C. 1969, J. Sci. Inst. (J. Phys. E), 2, 983.
Wyngaard, J. C. and Tennekes, H. 1970, Phys. Fl., 13, 1962.
Yaglom, A. M. 1966, Sov. Phys. Dokl. 11, 26.

ACKNOWLEDGEMENTS
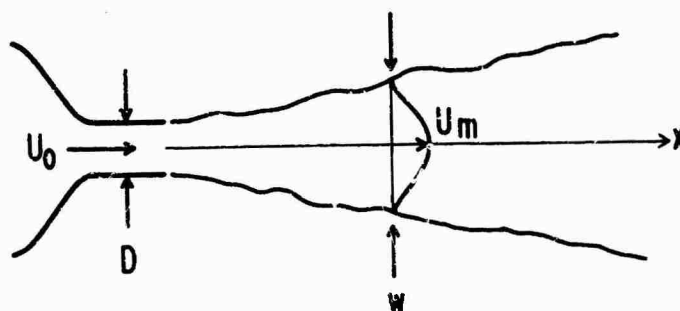
Figure 1.   Sketch of Axisymmetric Jet

LEGEND

□   LaRue and Friehe (1971),
    $Re_o = 2 \times 10^4$, D = 1 in.

○   Present Results,
    $Re_o = 1.2 \times 10^5$, D = 2.5 in.

◇   M. M. Gibson (1963),
    $Re_o = 5 \times 10^5$, D = 6 in.

◉   F. H. Champagne (1971),
    $Re_o = 5.8 \times 10^5$, D = 4 in.

○   F. H. Champagne (1971),
    $Re_o = 3.7 \times 10^5$, D = 4 in.
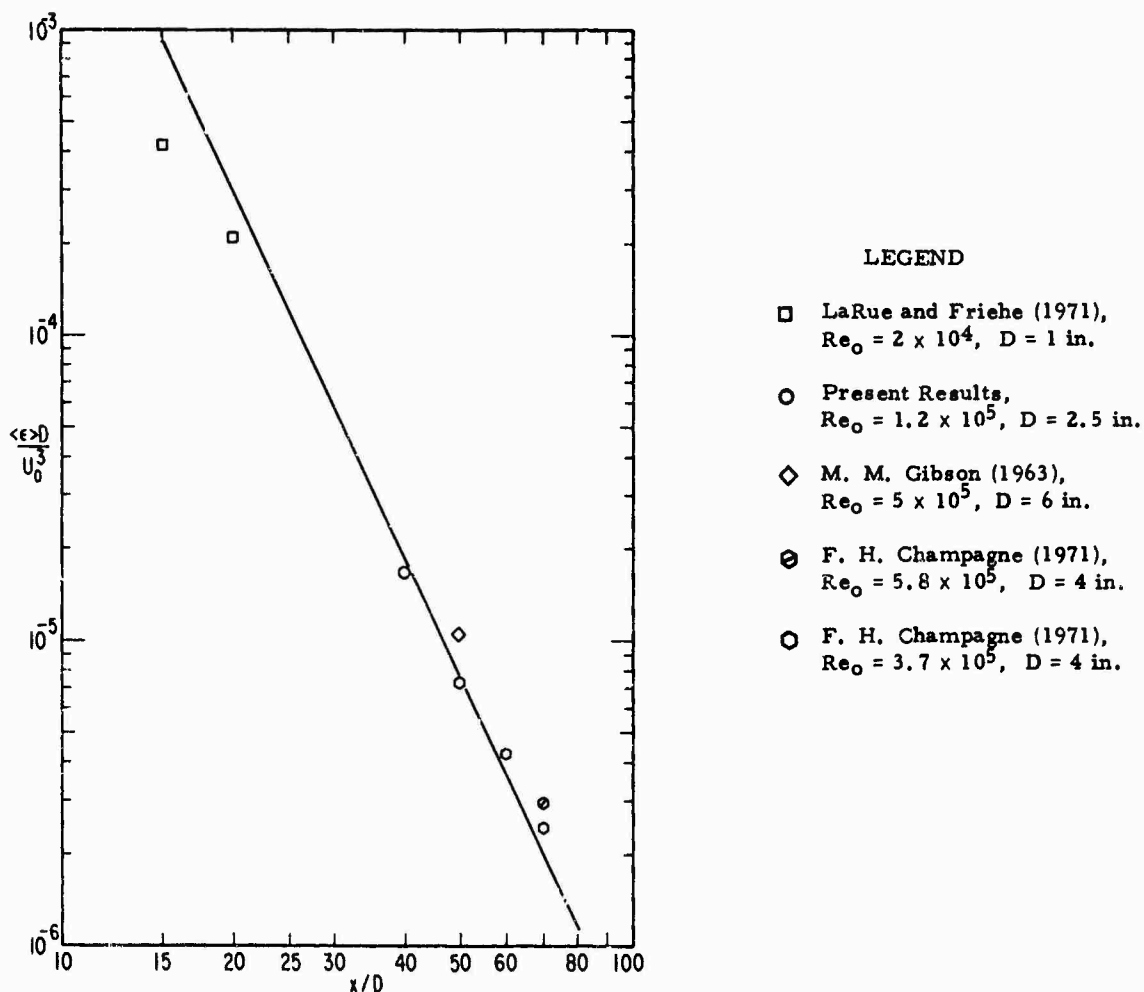
Figure 2.   Dissipation Rate Correlation
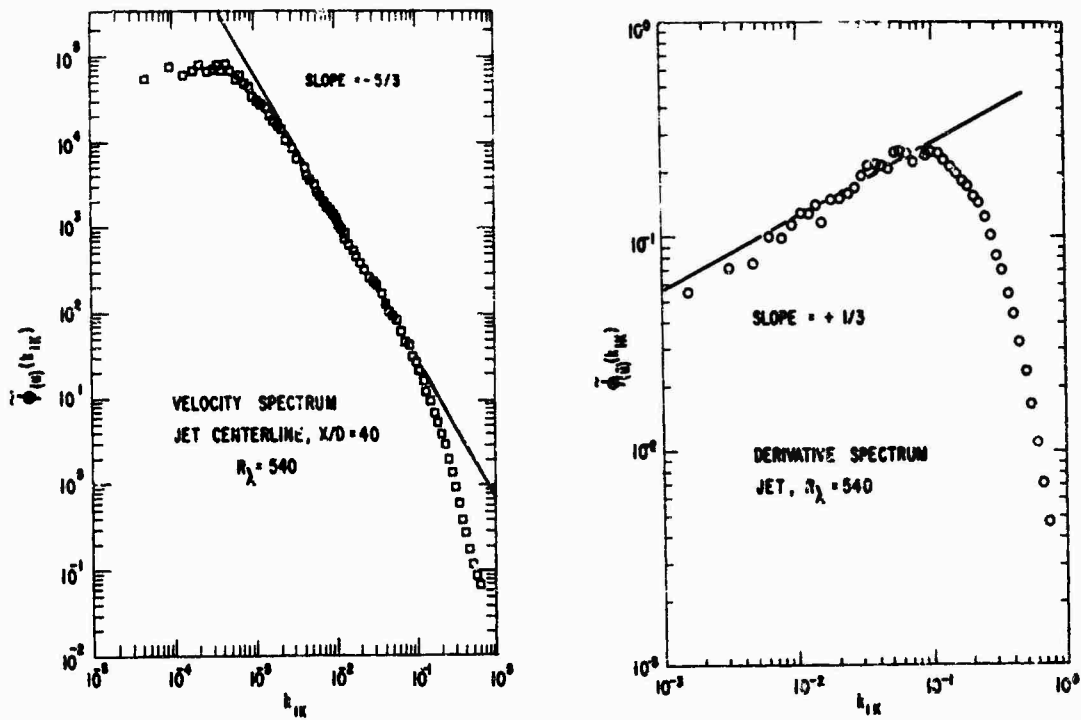
Figure 3. Velocity and Velocity Derivative Spectra
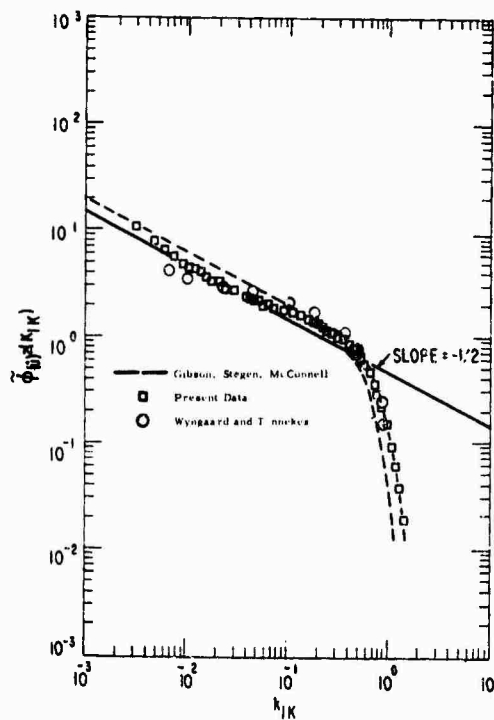
Figure 4. Dissipation Rate Spectra
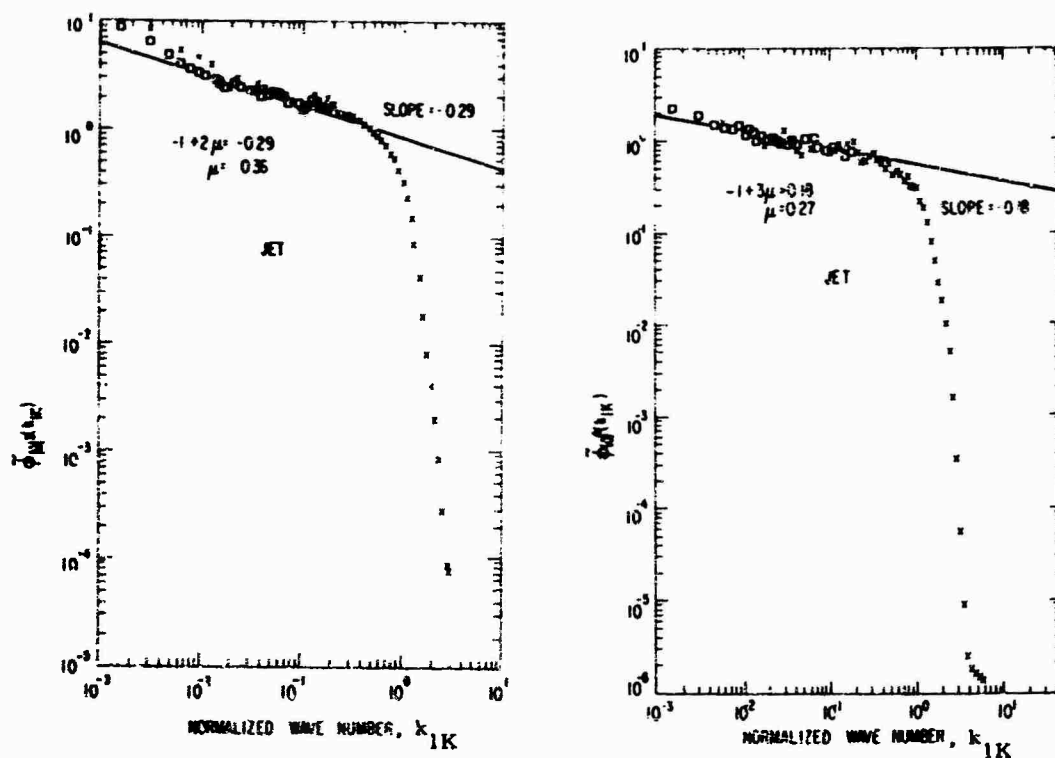
Figure 5. Third and Fourth Moment Derivative Spectra
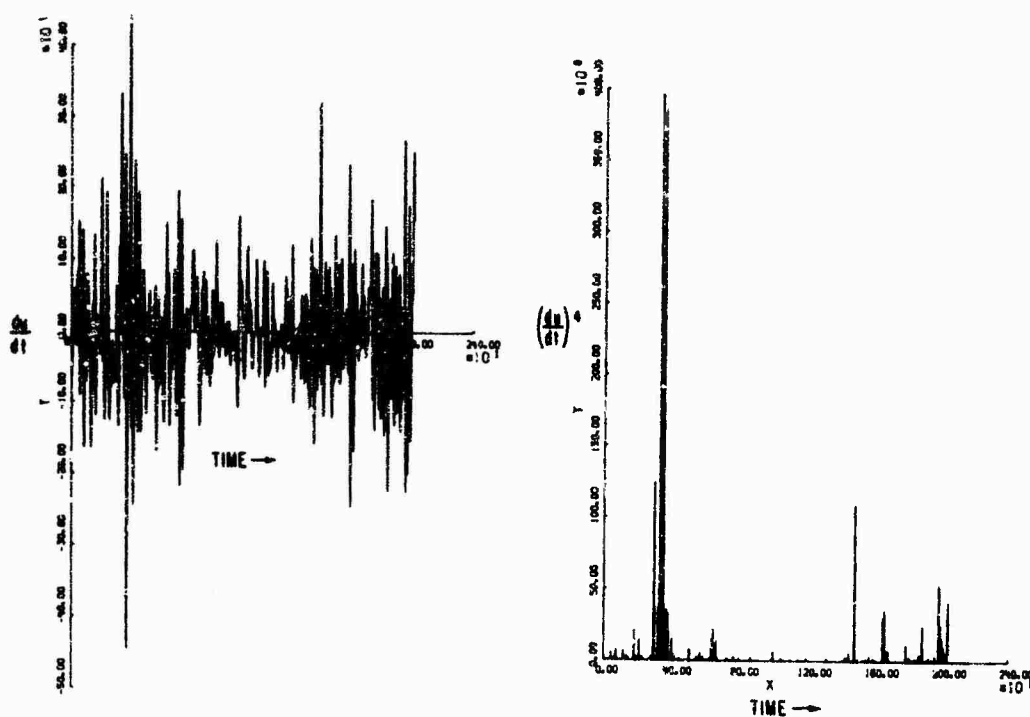
Figure 6. Time Series of $\frac{du}{dt}$ and $\left(\frac{du}{dt}\right)^4$

"VELOCITY AND DENSITY MEASUREMENTS IN A FREE JET"

by O.H. Wehrmann[*]

Vereinigte Flugtechnische Werke-Fokker GmbH., Bremen

The fluctuating properties in a turbulent flow are auc to convection, diffusion, production, dissipation and precuure transport. To perform an energy balance, not only velocity terms have to be measured but also the pressure or density components of the pressure transport term.

Velocity fluctuations can be measured by the well estarlished hot-wire technique; in contrast to this, the local measurement of the density fluctuations presents a certain problem, esspecially if the disturbance of the flow field by a density measuring would have to be kept as small as possible. To obtain a local measurement, a focussed laser beam Mach-Zehnder interferometer was used. The flow measurements were made for the flow field behind a 2,5 cm nozzle at a flow velocity of 43 m/sec. The flow in the center of the nozzle at the exit plane was laminar or made turbulent by the insertion of a screen. The measurements were made for three flow parameters:

(1) the velocity fluctuations u' in the flow direction U, (2) the density fluctuations ρ' and (3) the correlation $u'\rho'$. From these measurements, the pressure transport term in the x direction could be calculated.

NOTATION

A,B,C,D	Constants
E	Density fluctuations term (equ. 3)
I	Intensity
k	Wavenumber of light
l	Length
N	Number of shifted fringes
p	Pressure
R	Correlation coefficient
r	Radius
r_o	Nozzle Radius
U,V,W	Velocity components
u',v',w'	Fluctuating velocity components
X,Y,Z	Coordinates
λ	Wavelength of light
β	Gladstone constant
ρ	Density
ρ'	Fluctuating density
ρ_{st}	Density of standard atmosphere
Γ	Vortex strength

[*] Dr.-Ing., Head of Theoretical Aerodynamics Department

1. INTRODUCTION

If one assumes the validity of the Navier Stokes eccuation to describe the fluctuating properties in a turbulent flow, than complete experimental proof of such an assumption is still missing because certain terms have not been measured. For the case of a turbulent, unheated jet at subsonic velocities, the simplified equation would read as follows:

$$\frac{\partial}{\partial x}\left[\bar{U}(\overline{u'^2}+\overline{v'^2}+\overline{w'^2})\right] \;+\; \frac{1}{y}\frac{\partial}{\partial y}\left[\bar{V}(\overline{u'^2}+\overline{v'^2}+\overline{w'^2})\right]$$

Convection

$$+\frac{\partial}{\partial x}\left[\bar{U}\,(\overline{u'^2+v'^2+w'^2})\right] \;+\; \frac{1}{y}\frac{\partial}{\partial y}y\left[\overline{v'(u'^2+v'^2+w'^2)}\right]$$

Diffusion

$$+\,2\left[\overline{u'^2}\frac{\partial\bar{U}}{\partial x}+\overline{v'^2}\frac{\partial\bar{V}}{\partial y}+\overline{u'v'}\,\frac{\partial\bar{U}}{\partial y}\right]+\frac{2}{\varsigma}\left[\frac{\partial\overline{u'p}}{\partial x}+\frac{1}{y}\frac{\partial}{\partial y}(y\overline{v'p})\right]$$

Production   **Pressure transport**

$$+2\nu\left[\overline{(\tfrac{\partial u_j'}{\partial x})^2}+\overline{(\tfrac{\partial u_j'}{\partial y})^2}+\overline{(\tfrac{\partial u'}{\partial z})^2}+\overline{(\tfrac{\partial v'}{\partial x})^2}+\overline{(\tfrac{\partial v'}{\partial y})^2}+\overline{(\tfrac{\partial v'}{\partial z})^2}+\overline{(\tfrac{\partial w'}{\partial x})^2}+\overline{(\tfrac{\partial w'}{\partial y})^2}+\overline{(\tfrac{\partial w'}{\partial z})^2}\right] = 0$$

Dissipation

In the past, the terms containing velocity components were measured by the well established hot-wire technique. But the terms related to the pressure transport can only be estimated under the assumption, that the equation itself is correct and that by performing an energy balance the numerical value can be determined. Strictly speaking, such a method is no proof of the theory whatsoever, because the "proof" is a priori given by the applied method. [1]

Therefore, the need exists for a device to measure the density or pressure fluctuation in a local area of a turbulent flow to perform a real energy balance. Such a device was used in form of a focussed Mach-Zehnder interferometer, where the light source consists of a Helium Neon Laser. The characteristics of the equipment will be described later; by combining the hot-wire method with the interferometer method, velocity and density fluctuations could be measured and the correlation between the two flow parameters determined.

Generally , two types of flow behind a nozzle exist, depending of the conditions of the experimental arrangement. These might be called the boundary conditions at the exit plane of the nozzle. - In the first case, the air approaching the nozzle flows out of a large reservoir and can be considered laminar, in the second case, the air flow at the exit of the nozzle is already turbulent.

Close to the nozzle, at distances of the order x/r_0: 0...10, the two flow fields will be completely different, but at large enough distances, the flow fields will become similar (similarity hypothesis). The present study was confined to measurements at short distances to study the two different types of flow; also the only fluctuating velocity to be measured was the u' component.

2. EXPERIMENTAL ARRANGEMENT

The measurements were made under well controlled conditions. To ensure reliability of the hot-wire and interferometer measurements, the air in the area of the experimental setup was kept under the following conditions:
dust and particle free by an electrostatic filter, temperature constant to $\pm$ 0.5 F, and humidity at 70 % $\pm$ 1 %. The speed of the airflow was kept constant to $\pm$ 0.5 % by an electronic device; all line voltages were regulated to $\pm$ 0.1 %. The Constant Temperature hot-wire set was a DISA 55 DO 1 type with linearizer 55D10 and Correlator. RMS measurements were made by two DISA 55 D 35 RMS meters. The electronical components of the interferometer were of own design. (Figure 1).
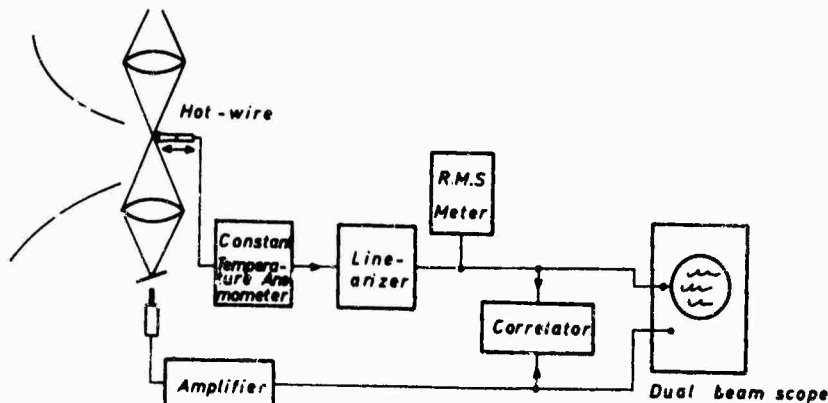
Fig. 1 Experimental arrangement

A 1'' nozzle was connected to a settling chamber; by insertion of screens with different mesh sizes inside the nozzle the flow at the exit could be made turbulent. The interferometer with the hot-wire probe together were fastened to a movable platform, which could be positioned in two coordinates (X and Y direction). In addition, the hot-wire could be moved against the platform itself to change the spacing between the focal point of the interferometer and the wire itself. This was necessary for calibration purposes and for correlation measurements.

2.1. FOCUSSED LASER INTERFEROMETER

Density measurementes in general can be made by the well-known Mach-Zehnder interferometer, where the influence on the speed of light by the changes in density can measured. To ensure a reliable measurement, the other parameters such as humidity and temperature have to be kept constant if one desires an uncomplicated method. The advantage of such an instrument is the fact, that no probe has to be inserted in the flow, the disadvantage can be seen in the fact, that the received signal is the integrated signal along the path of light. A local information can not be retrieved from the measured signal. To overcome this difficulty, a focussed laser beam interferometer was built. Generally every Mach-Zehnder interferometer uses two light beams (or light rays) which interfere with each other. One of the beams (measuring beam) passes through the medium to be measured, whereas the other beam (reference beam) is shielded. In the area of intersection of the two beams, changes in the measuring beam influence the location of the fringes. For a fixed point in the plane of intersection, an amplitude modulation occurs as a consequence of the fringe movement. The transfer functions are:

a) the output of the Mach-Zehnder interferometer

$$\Delta\varsigma/\varsigma_{st} = \Delta N \cdot \lambda / \beta \Delta L \qquad (1)$$

if ΔL is known, it follows:

$$\Delta\varsigma/\varsigma_{st} = \Delta N \cdot \lambda / \beta \cdot L \qquad (1a)$$

The change in density is therefore proportional to the change in the fringe position.
b.) The intensity between two adjacent fringes:

$$I(L) = A(1 - \cos 2\pi K \Delta L) = \beta \cdot \sin^2 \pi K \cdot \Delta L \qquad (2)$$

The change in intensity is therefore nonlinear for a linear phase or length change. These equations are valid for each light ray of the light beam. For a given system it follows from (1)

$$\Delta\varsigma \cdot \Delta L = C \cdot \Delta N$$

For the case of the focussed beam, the beam entering the test area is expanded by a lens system 1 (in the present case to 2" as compared to 1/25" originally) and is focussed at the focal point, which is considered to be the measuring point. The beam, after passing the focal point, expands again, and is refocussed by a second lens system 2 to interfere with the reference beam.(Figure 2).
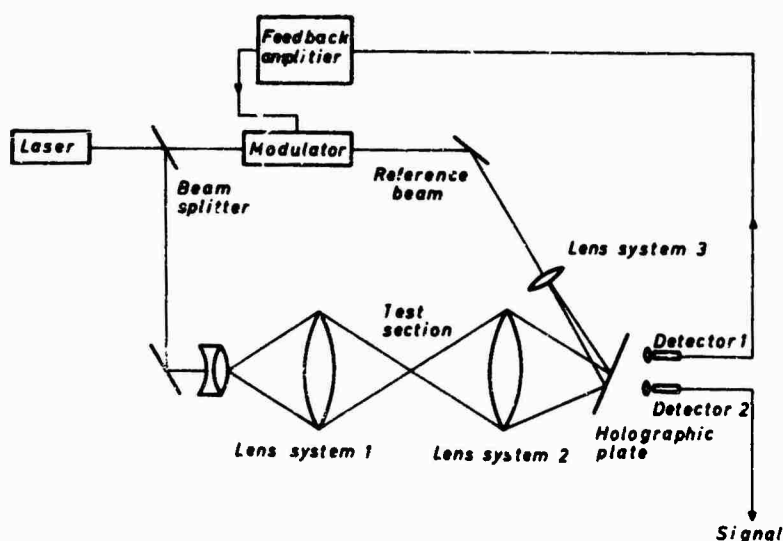
Fig. 2 Focussed laser interferometer

A simplified explanation of the working principle is as follows:

Each light ray travelling through the test section is influenced by the different density changes along his path. At the focal point, the density changes influence each ray by the same amount, so that each light ray contains a certain percentage of information about the focal point.

Dividing each ray in small elements of constant length ΔL on might write (1b):

$$\Delta \varsigma = D \cdot \Delta N \qquad (3)$$

For a given ray it follows:

$$\varsigma_1 = \sum_1^{n-1} \varsigma_{1,i} + \varsigma_{jj}$$

$$\varsigma_2 = \sum_1^{n-1} \varsigma_{2,i} + \varsigma_{jj}$$

where ς_{jj} is the density change at the focal point

Adding the signals of m rays together

$$\varsigma_m = \sum_1^m \sum_1^{n-1} \varsigma_{j,i} + m \cdot \varsigma_{jj} \qquad\qquad E = \sum_1^m \sum_1^{n-1} \varsigma_{j,i} \qquad (4)$$

ς_{jj} is the density fluctuation to be measured, which differs from the received signal ς_m by the term. This term E depends of the correlation factor of the fluctuation elements and depends therefore of the existing flow field; ist can be assumed, that certain amplitudes and frequencies are cancelling each other because of phase differences. The amplitude of the fluctuations at the focal point is amplified by the factor m and enhances the signal against the background of the signal E; with other words the ratio ς_{jj} / E is the signal to noise ratio.

The signal beam and the reference beam interfere on a plane, which is a glass plate containing the holographic picture of the test section without flow. (Stored beam technique). The changes of the holographic picture by the signal beam are measured by a photocell. A second photocell delivers a signal for the feedback system of the fringe stabilizer.

Normally, the stability of the fringe pattern of the holographic picture is influenced by changes in the interferometer, partially because of length changes in the interferometer due to temperature changes or very small changes in the frequency of the laser light. The automatic fringe adjusting system operates in the frequendy range from 0 to 10 Hz and intensities of $\Delta\varsigma'/\varsigma = 10^{-5}$ could be measured. The adjustment also defines the operating point of the system at a location of 1/4 between two adjacent fringes. Here, the modulation characteristics according to (2) can be considered linear for small modulation amplitudes. The stabilization is accomplished by the modulator in the reference beam. The error signal of the second photocell is amplified and the modulator influences, the phase of the beam to reestablish the wave front pattern.

To calibrate the instrument, an error signal was fed in the open loop of the feedback system and the generated output voltage was measured. The operating point was checked on the scope.

Since the connection between density ς and the pressure p in the adiabatic state is given by the law for a perfect gas, a calibration for the pressure fluctuation is easily accomplished.

A more detailed description is given under [2]

3. MEASUREMENTS

The flow measurements were made behind a 1" nozzle at a flow velocity of 43 m/sec. The flow in the center of the nozzle at the exit plane was laminar or made turbulent by the insertion of a screen. Three flow parameters: the velocity fluctuations u' in the flow direction U, the density fluctuations ϱ' and the correlation $u'\varrho'$ were measured. The pressure transport term in the X direction was calculated by the use of the correlation measurements.

To display the results of the measurements in a more visible and understandable way, the results were plotted in the form of maps of the flow field for one of the three parameters.

The lines in such a map represent the isofluctuations of the velocity, or the density, the isocorrelation and the isopressure transport measurements. Before an analysis is made, a few remarks about the two different types of flow are necessary. The present investigation deals with the flow field close to the nozzle, where the characteristics of the two flow types differ remarkably; both types have in common, that the flow close to the nozzle is in some kind of a transition stage and that the final stage of self preservation will be reached at a much larger distance. Therefore, the amplitude of the turbulent fluctuations, their growth or decay and the spectral distribution will undergo changes as the fluid is moving downstream.

The laminar jet becomes turbulent mainly by the instability of the free shear layer. Here, wave like disturbances in a certain frequency range grow in amplitude to form a vortexlike flow movement. After further amplification, the vortices diffuse in smaller elements, whose fluctuating components are feeding the laminar core region of the jet. According to the general experience, the laminar core ceases to exist after a distance of $X/r_0 > ?$ and the process of equalization continues until some kind of self preservation for the whole jet area occurs. Details of this type of flow were already reported. [3,4,5]

The turbulent jet in some way represents the opposite type of flow. At the exit of the nozzle the turbulent fluctuations of the jet core interact with the free shear layer. Depending of the flow conditions, especially the contour of the nozzle, the free shear layer at the rim of the nozzle might still be laminar. Whereas in the laminar case the free shear layer will become unstable by disturbances from the outside area, the free shear layer of the turbulent jet will be influenced by the turbulent fluctuations of the core and by disturbances from the outside area. Hence, at the exit of the nozzle the turbulent fluctuations inside the jet interfere with the free shear layer. This way, two turbulent areas, jet core and free shear layer, with different amplification and distribution mechanism are interacting with each other. Because of the spread of the total jet, both areas are growing in size with increasing downsteam distance. At the interaction, flow adjustments in form of energy transfer are necessary to accomplish the unification of the two different turbulent regimes. Still, at a sufficiently large distance, the distribution of the fluctuating quantities of the two jet types are similar.

3.1. GRAPHICAL REPRESENTATION AND ANALYSIS

The contourmaps represent nondimensionalized quantities $e \cdot \mu \cdot u'/U$, $\varsigma'/\varsigma_{\mu}$ and R. The rim of the nozzle is located at $x/r_0 = 0$ and $y/r_0 = 1$. Measurements at distances x/r_0 smaller 2 could not be obtained because of the mechanical interference of the interferometer with the windtunnel system.

Laminar case
Figure 3 shows the results of the u' measurements.
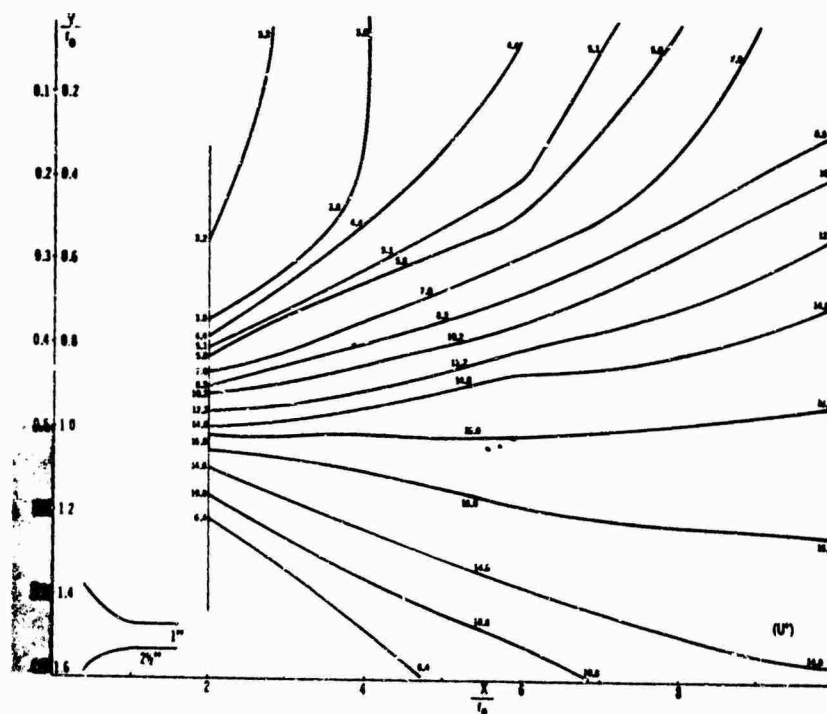
Fig. 3 Isovelocity fluctuations of the laminar jet

The fluctuations in the free shear layer occur at a distance Y/r_0 of 1.05. At the starting point of the measurements $X/r_0 = 2$, the fluctuations in the free shear layer are already amplified to the saturation level, so that no further increase in amplitude is possible. The fluctuations therefore spread in a jet like manner into the core region and into the outside area of the free shear layer.

Figure 4 shows the corresponding density measurements
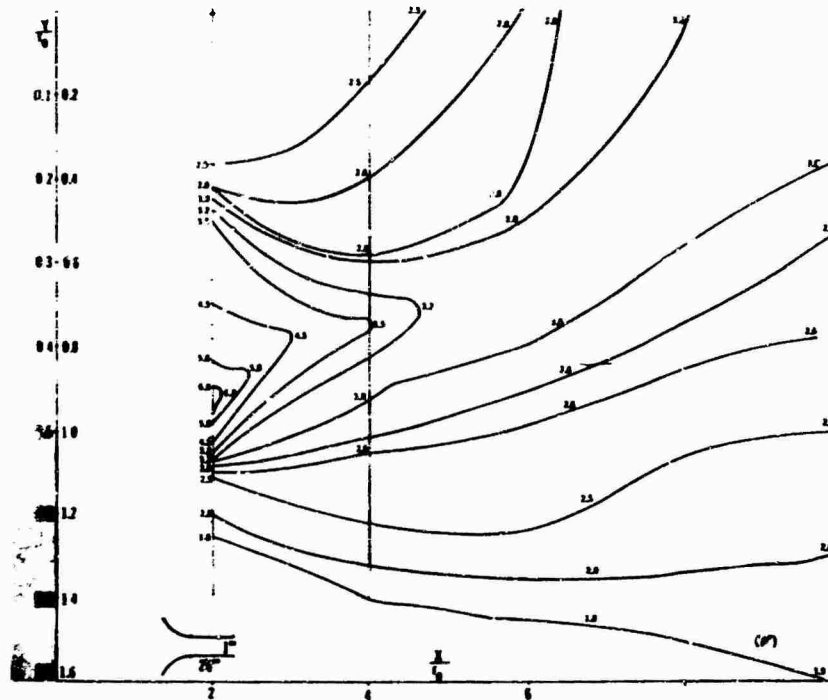
Fig. 4 Isodensity fluctuations of the laminar jet

The maximum of the fluctuations is located at $X/r_0 = 2$ and $Y/r_0 = 0.9$. In contrast to the velocity fluctuations, the map shows closed curves in the core region. Their intensity decreases with increasing distance, whereas the lines in the free shear layer region $Y/r_0 = 0.8$ to 1.2 remain constant in amplitude. The gradient $d\rho/dr$ derived at the location where the lines close, has an inclination against the centerline of the flow field and points towards the rim of the nozzle. The maximum of the density fluctuations does not coincide with the path lines of the vortices. Therefore the increase of the vortex strength with increasing downstream distance is due to an increase in vortex diameter and not to a local increase in density.
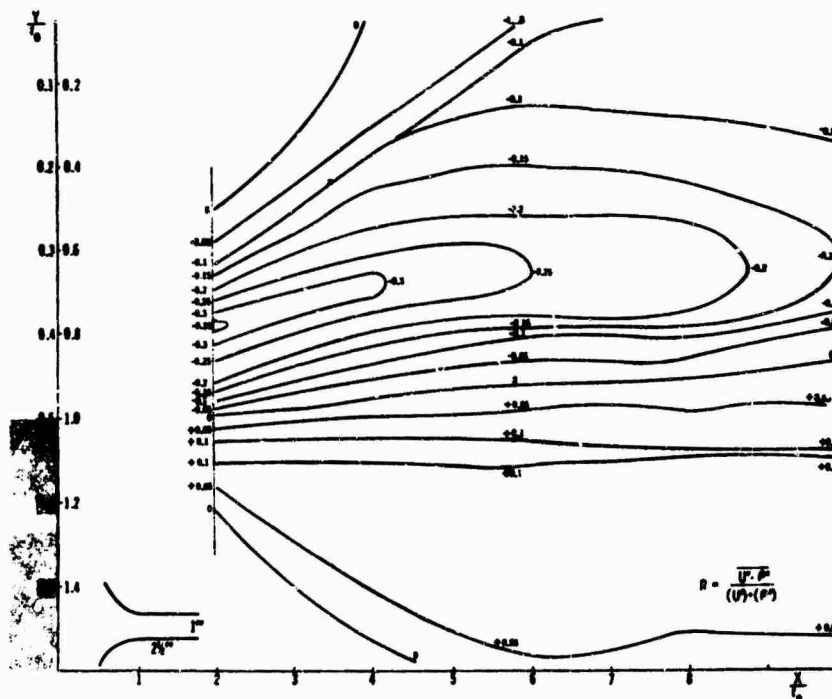
Fig. 5 Isocorrelation of the laminar jet

The value 0 of the correlation (Figure 5) is a nearly straight line at $Y/r_0 = 1$. Above that line, towards the center of the jet, the correlation is negative indicating the extraction of momentum from the center to supply the fluctuations in the free shear layer. The largest value of the correlation occurs at the location $y/r = 0.8$ and $X/r = 2$.
The transport term is plotted in Figure 6.
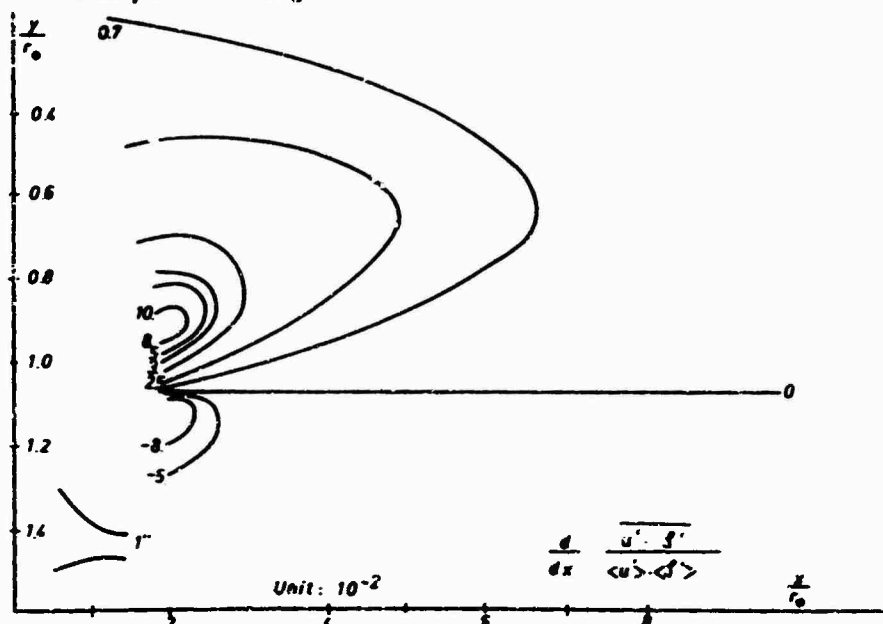
Fig. 6 Isopressure transport of the laminar jet

The maximum lies again to the nozzle at $X/r_0 = 2$, $Y/r_0 = 0.9$. The lines indicate that the direction of transport is from the inside region of the jet towards the region, where the free shear layer is developing.

B. Turbulent case
As mentioned before, the turbulent case can not be explained by a simple model. A vortex-like phenomena does not exist, because of the turbulent character of the core region. Still, the boundary layer has a turbulence enhancing character, but at a lower spatial amplification (Figure 7).
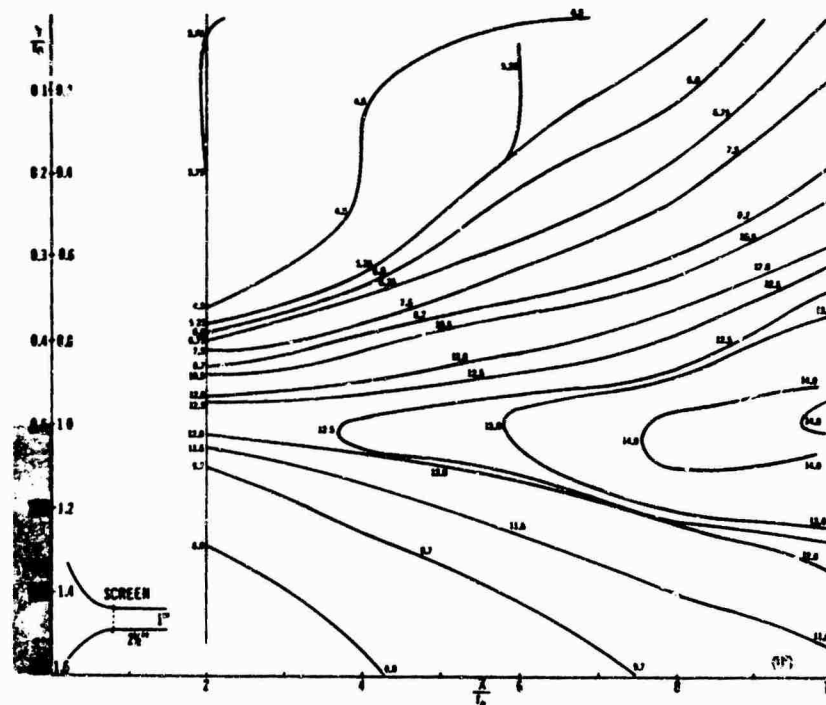
Fig. 7 Isovelocity fluctuation of the turbulent jet

The relative maximum of the fluctuations again lies on the line $Y/r_0 = 1$, but the intensity still increases with increasing downstream distance. Outside this area, the lines show a similarity with the laminar case and show a spread towards the center and the outside. For a given X/r_0 close to the nozzle, the intensity of the fluctuations in the core region is much larger, because the jet is already turbulent.

At a certain distance behind the nozzle, approximately $X/r_0 = 3$, the free shear layer turbulence starts to interact with the turbulence of the core region. In the free shear layer, the growth

per unit length is larger because of the velocity gradient in the shear layer. In the centerline of the flow, where the flow is already turbulent, the gain rate is much smaller. At a certain distance, the turbulent characteristics of the two areas will equalize. Such an area is located at $Y/r_0 = 0.2$ to 0.6 and $X/r_0 = 6$ to 10.

Therefore the distribution of the density fluctuations shows a quite different display (Figure 8).
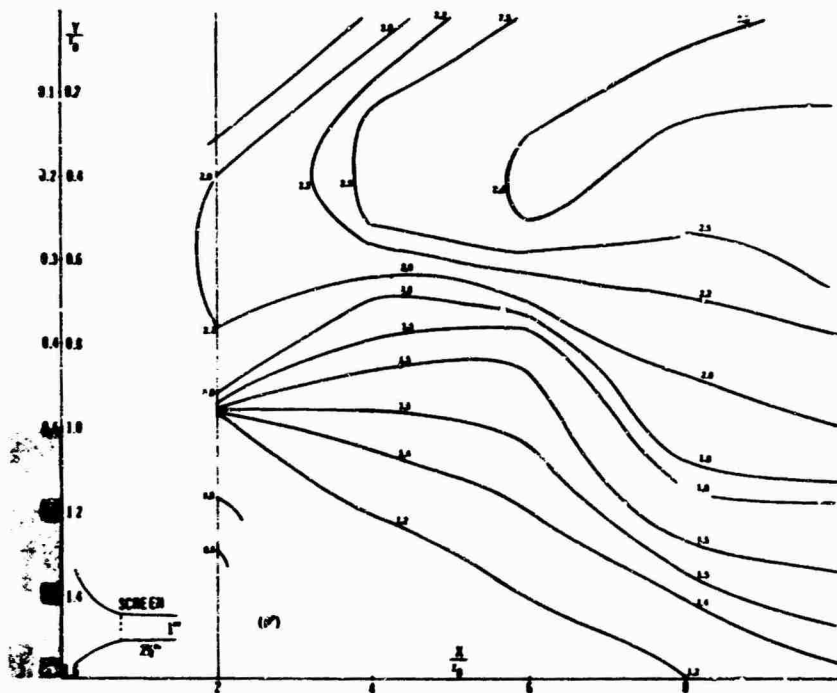
Fig. 8 Isodensity fluctuations of the turbulent jet

The maximum of the fluctuations is removed from the neighbourhood of the nozzle to the inside area of the jet, where the flow adjustment occurs. The location is at $X/r_0 = 6$ to 10 and $Y/r_0=0.5$ to 0.1.

The intensity of the fluctuations in the free shear layer is smaller, indicating the smaller growth rate.
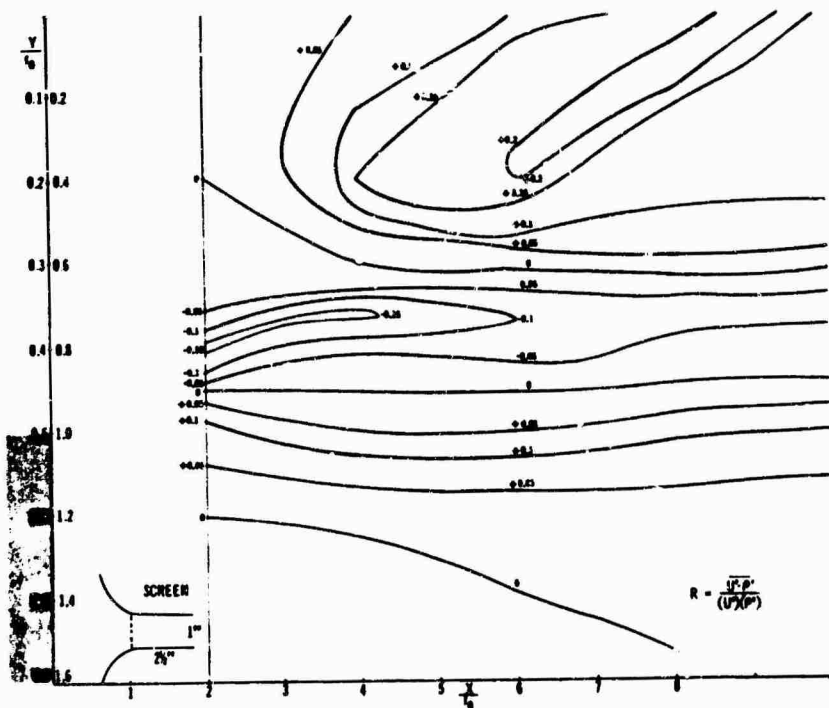
Fig. 9 Isocorrelation of the turbulent jet

Twice, the correlation reaches the value zero at $Y/r_0 \cdot 0.9$ and $Y/r_0 = 0.6$. Between these lines, the correlation changes the sign.

The effect of the two flow regimes is also represented in Figure 10.
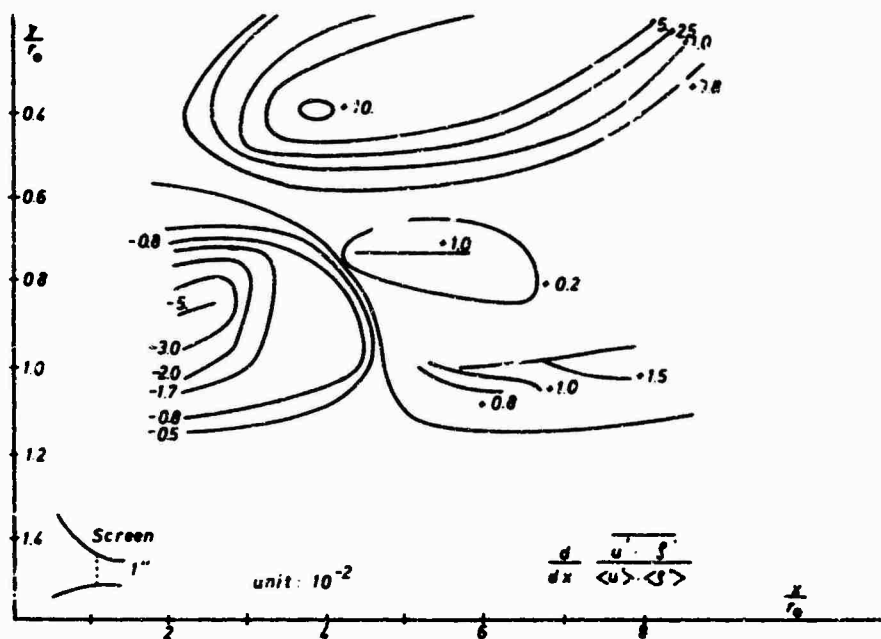
Fig. 10 Isopressure transport of the turbulent jet

4. LITERATURE

1. I. Wygnanski, H.E. Fiedler: Some Measurements in the Solf Preserving Jet
   Boeing Scientific Research Laboratories Document D1-82-0712 April 1968

2. O.H. Wehrmann: Focussed Laser Interferometer (to be published)

3. O.H. Wehrmann, R. Wille: Beitrag zur Phänomenologie des laminar-turbulenten
   Überganges im Freistrahl bei kleinen Reynoldszahlen   Boundary Layer Researoh,
   Springer Verlag 1958 pp. 387 - 403

4. P. Freymuth: On transition in a separated boundary layer
   Journal of Fluid Mechanics 1966 vol. 25, part 4 pp. 683 - 704

5. A. Michalke: Vortex formation in a free boundary layer according to stability theory
   Journal Fluid of Mechanics 1965 vol. 22, part 2 pp. 371 - 383

AN EXPERIMENTAL INVESTIGATION OF CURVED TWO-DIMENSIONAL TURBULENT JETS

by

C. Schwartzbach
Technical University of Denmark
Department of Fluid Mechanics
2800 Lyngby, Denmark

SUMMARY

Hot-wire measurements of mean velocity and normal turbulent stress in the direction of flow are presented for the flow field generated by a plane jet reattaching to a flat plate adjacent to the jet nozzle. Measurements were made in longitudinal and lateral traverses of the curved jet flow and in the two wall jet flows, that emerge from the reattachment region, one in the downstream direction carrying all the mass flow issued from the nozzle as well as the mass flow, that has been entrained along the outer boundary of the curved jet, and another backward flowing wall jet, that returns the mass flow entrained along the inner boundary of the curved jet to the separation bubble.

Measurements were made in two series for thirteen different positions of the adjacent plate thereby providing data for differing values of jet curvature and jet pathlengths.

Integral methods were used on the experimental data in an attempt to evaluate the effect of jet curvature on the entrainment along the external and internal boundaries of the curved jet.

NOTATION

a	nozzle width	U_o	jet velocity in nozzle
C	empirical constant in Sawyer's expression for entrainment	U_m	maximum velocity in jet profile
E	entrainment parameter	$\overline{u^2}$	tangential component of normal turbulent stress
h	wall offset	x,y	coordinates
H	$\frac{h}{a}$	x_o, s_o	virtual origins of jet flows
I_1, I_2	velocity profile integral parameters	α	wall angle of inclination
J	momentum flux in jet flow	η	$\frac{y}{L_o}$ or $\frac{n}{L_o}$
L_o	characteristic width of jet flow		
n	coordinate in direction normal to s	λ	$\dfrac{\dot{Q}_E}{\dot{Q}_I}$
$\dot{Q}$	volume flow rate integral		
$\dot{Q}_o$	volume flow rate issuing from nozzle	ρ	fluid density
$\dot{q}$	$\dfrac{\dot{Q}}{\dot{Q}_o}$	σ	Görtler jet spread parameter

Subscripts

R	radius of curvature of jet flow	E,I	denotes external and internal boundaries of curved jet flow
s	coordinate in direction along maximum velocity points of curved jet profiles	R	denotes reattachment point or region
U	velocity in direction x or s in jet flow	w	denotes wall jet

1. INTRODUCTION

The experimental investigation reported here is part of a larger investigation of the plane jet reattachment phenomenon, which previously has been analysed and investigated by Bourque & Newman (1960), Sawyer (1960) and (1963), Bourque (1967), Perry (1967) and Boucher (1968). The flow field is shown in Figure 1. A plane jet of air, issuing from a slot nozzle, reattaches to an adjacent, flat plate, thereby creating a region of recirculating flow between the jet and the adjacent plate. In this separation bubble the static pressure is reduced compared to the ambient pressure. The reduced pressure causes the deflection of the jet towards the wall. The main aspect of this flow field is the curved jet, which is subject to a lateral pressure gradient, and, since the subpressure is not uniform, a longitudinal pressure gradient as well.
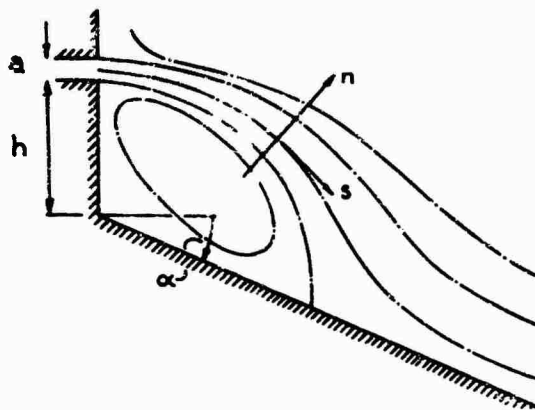
Figure 1. Scematic of nozzle and adjacent
plate geometry, and approximate
streamline pattern.

The most obvious example of an application of such a flow field is in fluid amplifica-
tion devices. The purpose of the abovementioned analyses has been the prediction of the
subpressure in the recirculating region and the length of this region, data nescessary
for the design of fluid amplifiers.

The controversial point in the analyses of the jet reattachment phenomenon has been the
inability of a simple integral analysis to predict the behaviour of the jet flow at lar-
ge angles of inclination of the adjacent flat plate. Sawyer (1963) assumes an effect of
curvature on the rates of entrainment of the two edges of the jet and obtains improved
correlation between theory and experiment. Bourque (1967) obtains very accurate predic-
tions by using a hypothesis on the path of the dividing streamline, that diverts from
the simple circular path assumption, and Perry (1967) obtains equally good predictions
by assuming a base pressure different from the average separation bubble pressure. None
of the authors presents experimental results, that make it possible to evaluate the dif-
ferent and somewhat contradictory assumptions.

Part of such experimental results are presented here.

2. INTEGRAL EQUATIONS

2.1 Basic analysis

The results of classical analysis of plane, turbulent jet flows are used as basis for eva-
luation of experimental results. Following Townsend (1956) the state of self-preservation
is consistent with the conditions:

(2.1.1) $$L_o = \text{constant} \times (x-x_o)$$

and

(2.1.2) $$U_m = \text{constant} \times (x-x_o)^{-0.5}$$

It is well known, that a plane, turbulent jet closely follows these conditions a short di-
stance downstream from the nozzle, although the state of self-preservation is not reached
until about 50 nozzle widths downstream from the nozzle. This is connected with the fact,
that the mean velocity profile approaches its similarity form much faster than the profi-
les of turbulent stresses.
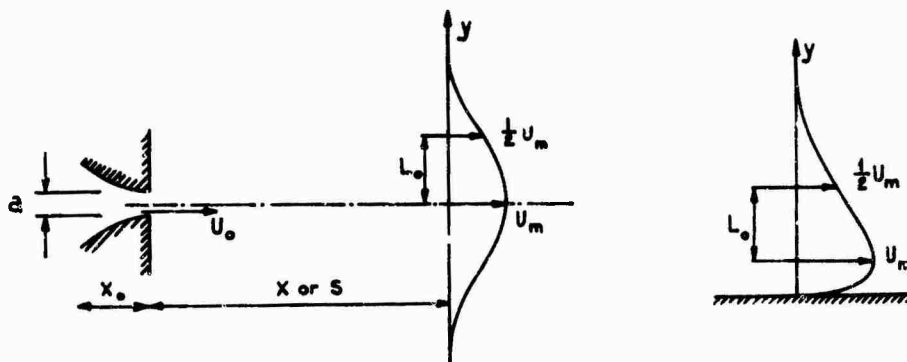
Figure 2. Coordinate system and typical velocity profiles for plane
free jet and wall jet in still surroundings.

When a suitable mean velocity profile has been assumed the volume flow rate integral and momentum flux integral can be expressed:

(2.1.3)
$$\dot{Q} = \int_{-\infty}^{+\infty} U \, dy = U_m L_o \int_{-\infty}^{+\infty} f(\eta) \, d\eta = U_m L_o I_1$$

and

(2.1.4)
$$J = \int_{-\infty}^{+\infty} \rho U^2 dy = \rho U_m^2 L_o \int_{-\infty}^{+\infty} f^2(\eta) \, d\eta = \rho U_m^2 L_o I_2$$

where $f(\eta) = \dfrac{U}{U_m}$ represents the mean velocity profile.

The constants:
$$I_1 = \int_{-\infty}^{+\infty} f(\eta) \, d\eta \quad \text{and} \quad I_2 = \int_{-\infty}^{+\infty} f^2(\eta) \, d\eta$$

are velocity profile integral parameters.

For the free, plane turbulent jet the total momentum flux per unit length is constant and equal to the momentum flux per unit length issuing from the nozzle, while the volume flow rate integral increases with the distance from the nozzle due to entrainment. Using equations (2.1.1), (2.1.2) and (2.1.3) the total volume flow rate per unit length can be expressed as:

(2.1.5)
$$\dot{Q} = \text{constant} \times (x-x_o)^{0.5}$$

The volume flow rate per unit length, that emerges from the nozzle, can be expressed as:

(2.1.6)
$$\dot{Q}_o = U_o \, a \, I_{Q_o}$$

where I_{Q_o} is a nozzle volume flow rate coefficient.

The total volume flow rate, equation (2.1.5), may be regarded as composed of three components:

(2.1.7)
$$\dot{Q} = \dot{Q}_o + \dot{Q}_{entrained,1} + \dot{Q}_{entrained,2}$$

The volume flow rates due to entrainment along the two edges of the jet along its path from the nozzle to the station in question grow with the distance from the nozzle and are, for a straight jet, equally large.

2.2 Curved jet volume flow rate

For a curved jet the total volume flow rate can not be expected to vary according to equation (2.1.5) since equation (2.1.4), which is inherent in equation (2.1.5), must be modified to include pressure forces. The lateral pressure gradient associated with the curvature of the jet introduces a pressure term in the momentum equation, and the condition, which for a straight jet says, that the momentum flux integral is constant along the path of the jet, must be modified to say, that the integral of momentum flux and pressure forces across the jet profile is constant along the path of the jet.

What is emphasized in this paper, however, is the volume flow rate integral, and here equation (2.1.3) is valid, if experimental data for U_m and L_o are used, and if an appropriate velocity profile is assumed.

The equations of importance for the evaluation of the volume flow rate in the curved jet flows are thus:

(2.2.1)
$$\dot{Q} = U_m L_o I_1$$

and

(2.2.2)
$$\dot{Q} = \dot{Q}_o + \dot{Q}_E + \dot{Q}_I$$

which using equation (2.1.6) can be written in non-dimensional form:

(2.2.3)
$$\dot{q} = 1 + \dot{q}_E + \dot{q}_I$$

where now $\dot{q}_E$ and $\dot{q}_I$ may be different.

As a measure of an eventual asymmetry in the entrainment rates on the external and internal boundaries of the curved jet serves the parameter:

(2.2.4)
$$\lambda = \frac{\dot{q}_E}{\dot{q}_I}$$

2.3 Wall jet volume flow rate

The analytical treatment of wall jet flows is very similar to that given to free jet flows. The total volume flow rate in a wall jet can be expressed:

(2.3.1)
$$\dot{Q}_w = \int_0^\infty U \, dy = U_m L_o \int_{\eta_o}^\infty f(\eta) \, d\eta = U_m L_o I_{1,w}$$

16-4

where $f(\eta)$ is an appropriate function.

2.4 Volume flow rate division

At the boundary of the reattachment region the curved jet represents a total volume flow rate, that using equation (2.2.3) can be expressed:

$$(2.4.1) \qquad \dot{q}_R = 1 + \dot{q}_{E,R} + \dot{q}_{I,R}$$

The volume flow rates due to entrainment are unknown, while $\dot{q}_R$ can be found using equations (2.1.3) and (2.1.6) and experimental data for U_a and L_o.
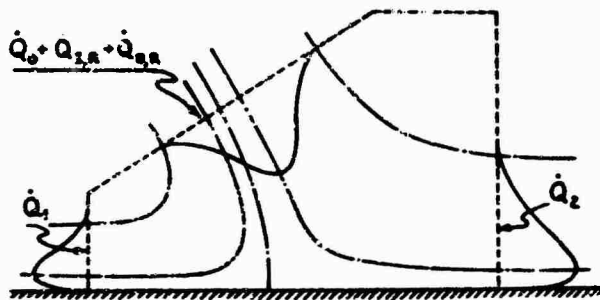
Figure 3. Reattachment region.

In an incompressible flow field the volume flow rates into and out of the reattachment region must be in balance. The same condition must be valid for the recirculating region. Therefore the following non-dimensional equations can be established for the volume flow in the reattachment region shown on Figure 3:

$$(2.4.2) \qquad \dot{q}_R = \dot{q}_1 + \dot{q}_2$$

$$(2.4.3) \qquad \dot{q}_1 = \dot{q}_{I,R}$$

$$(2.4.4) \qquad \dot{q}_2 = 1 + \dot{q}_{E,R}$$

$$(2.4.5) \qquad \lambda = \frac{\dot{q}_{E,R}}{\dot{q}_{I,R}} = \frac{\dot{q}_2 - 1}{\dot{q}_1}$$

In establishing these equations a couple of simplifications have been used:

a) That the curved jet has maintained its character as a free jet right to the boundary of the reattachment region.

b) That no entrainment takes place on the external boundary of the reattachment region.

The equations (2.4.2) to (2.4.5) should with appropriate experimental data be able to provide some information about the entrainment rates and the influence of jet curvature upon these. But with the underlying simplifications the equations can not be expected to be more than crude approximations.

3. PRESENTATION OF EXPERIMENTAL DATA

3.1 Review of experiments

With reference to Figure 1 measurements were made in two series:

    Series 1: $\alpha = 0$
                $H = 6, 10, 13.6, 18$ and 22

    Series 2: $H = 10$
                $\alpha = -30.95, -21.80, -11.31, 0, 11.31, 21.80, 30.95, 38.65$ and 45.00 deg.

Measurements were made with DISA hot-wire equipment. All measurements were made with nozzle width $a = 3.0$ mm. The nozzle velocity U_o was adjusted at about 52 m/sec to give a nozzle Reynolds' Number of 10^4. Thus the nozzle velocity is low enough to ensure incompressibility and high enough to ensure a fully turbulent jet.

To keep space requirements down only measurements of series 1 are presented in the graphs. Results of series 2 measurements have been included in Table 1 and in Figure 15, and are referred to in the text.

The following groups of measurements were made:

a) Determination of the locus of maximum velocity of the curved jet from the nozzle to the reattachment region. Hereby a measure of the jet curvature was achieved.

b) Longitudinal traverses of the curved jet along the locus of maximum velocity. For series 1 Figures 4 and 5 show the results in terms of maximum velocity decay and normal turbulent stress in the direction of flow as function of distance from the nozzle along the path. Straight jet data are included for comparison.
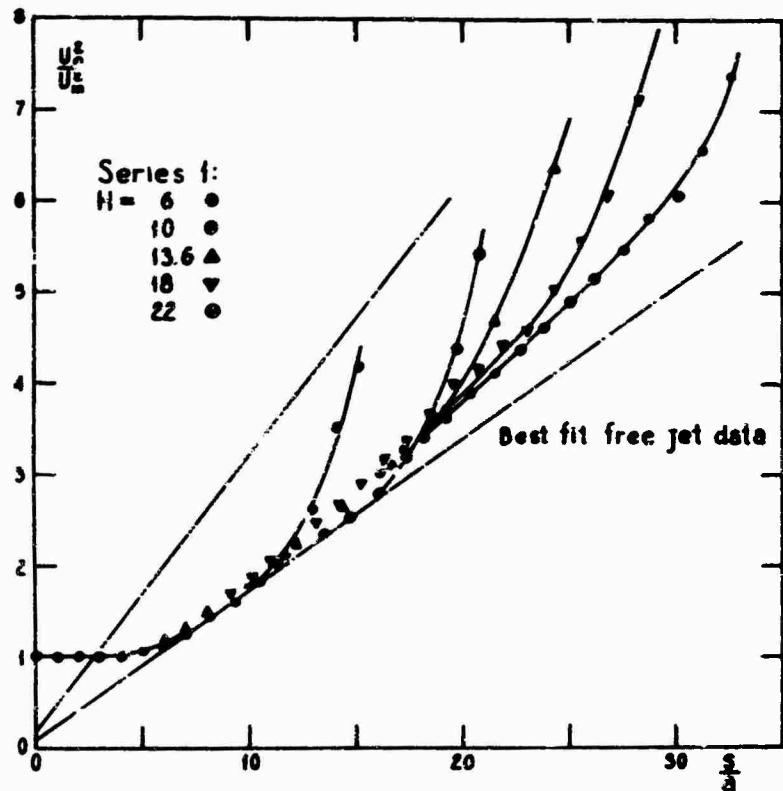
Figure 4.   Variation of maximum velocity with jet path-
length for curved jets.
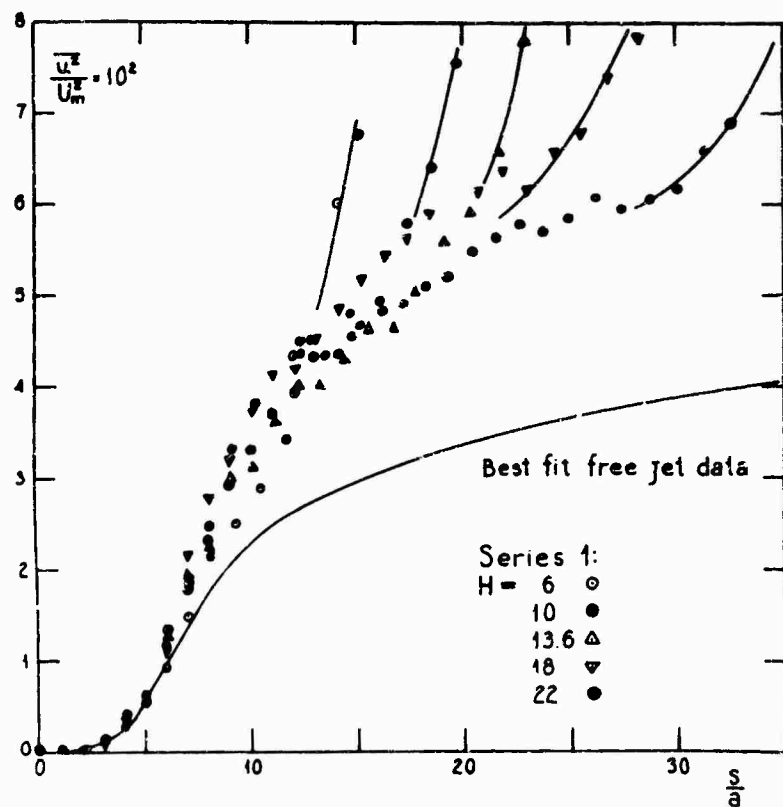
Figure 5.   Variation of normal turbulent stress in the
direction of flow at the point of maximum
velocity with jet pathlength for curved jets.

c) Lateral traverses of the curved jet at several stations of and normal to the lo-
cus of maximum velocity. Figure 6 shows typical lateral distributions of mean ve-
locity and normal turbulent stress for series 1, H = 18, 12 nozzle widths down-
stream from the nozzle. From these measurements Figure 7 was deduced, showing the
variation of jet width L_0 as function of s/a for all series 1 measurements.

d) Longitudinal traverse of the two wall jets flowing in opposite directions from
the reattachment region. Figures 8 and 9 show the maximum velocity variations a-
long the plate for series 1 measurements.

e) Lateral traverses of the two wall jets. Figure 10 shows typical mean velocity and
normal turbulent stress distributions for series 1, H = 18, in the backward flow-
ing (left) and downstream flowing (right) wall jets. From these measurements Fi-
gures 11 and 12 were deduced, showing the variation of wall jet width L_0 as func-
tion of distance along the plate measured from the reattachment point.
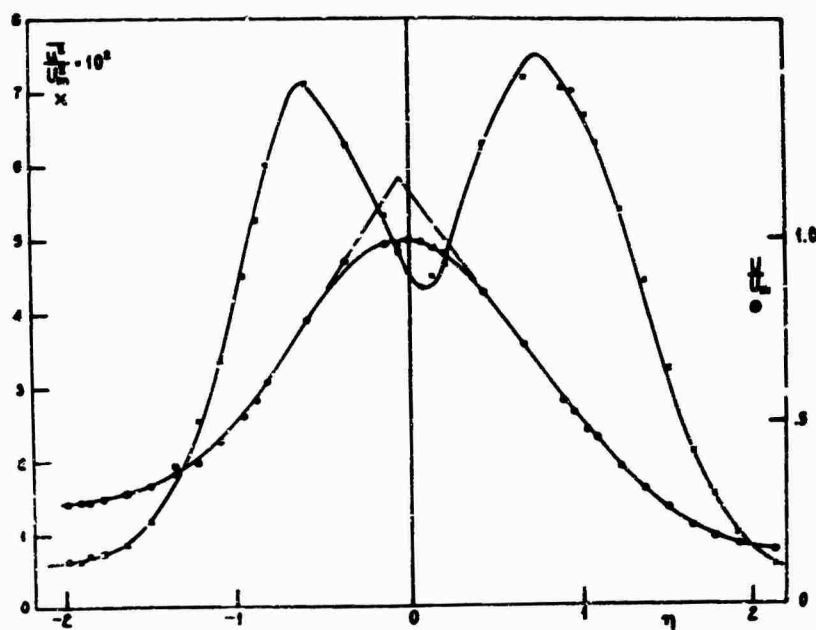
Figure 6.   Examples of mean velocity and normal turbulent
            stress profiles for curved jets.
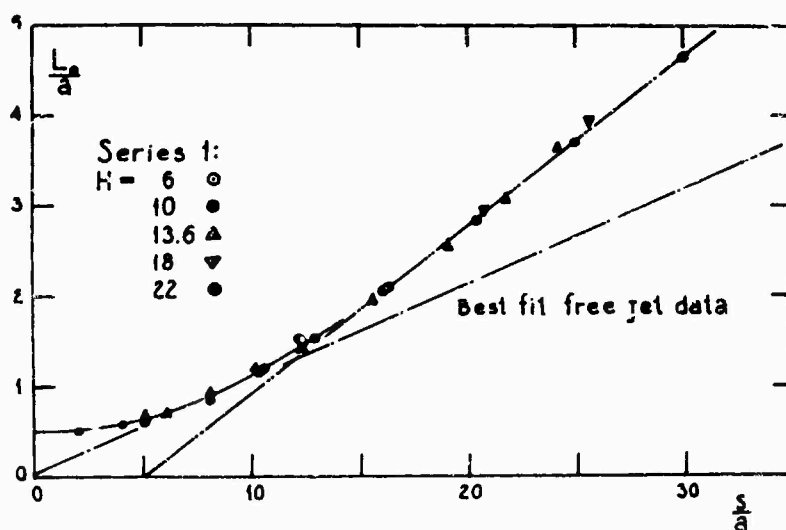
Figure 7.   Variation of characteristic jet width with jet
            pathlength for curved jets.
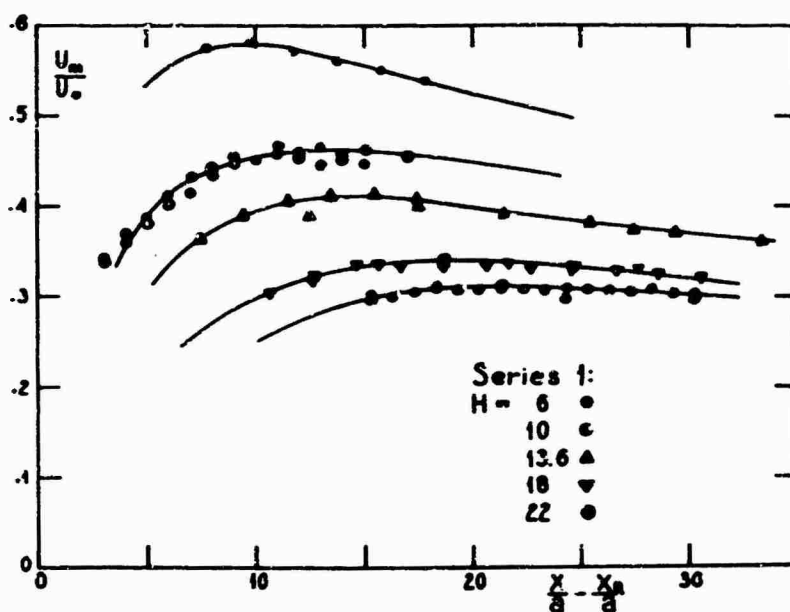
Figure 8. Variation of maximum velocity with distance from re-attachment point for downstream flowing wall jets.
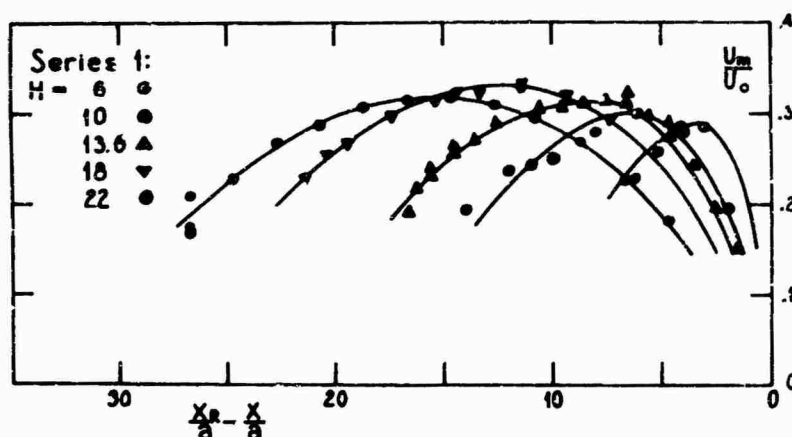
Figure 9. Variation of maximum velocity with distance from re-attachment point for backward flowing wall jets.
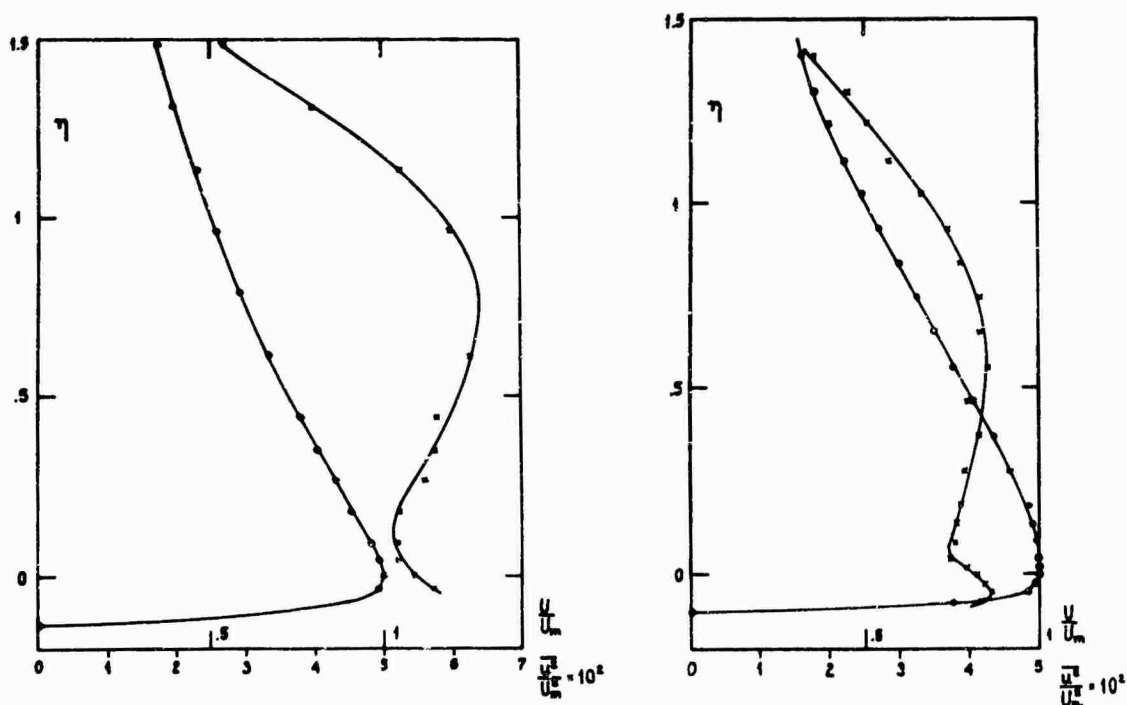
Figure 10. Examples of mean velocity and normal turbulent stress profiles for backward flowing (left) and downstream flowing (right) wall jets.
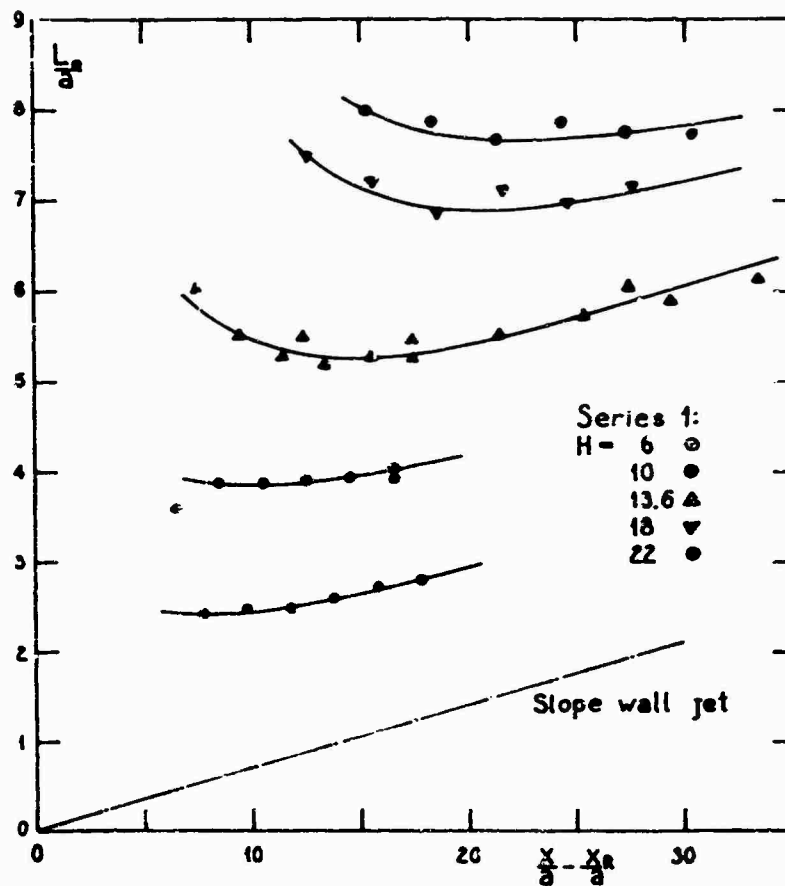
Figure 11. Variation of characteristic jet width with distance from reattachment point for downstream flowing wall jets.
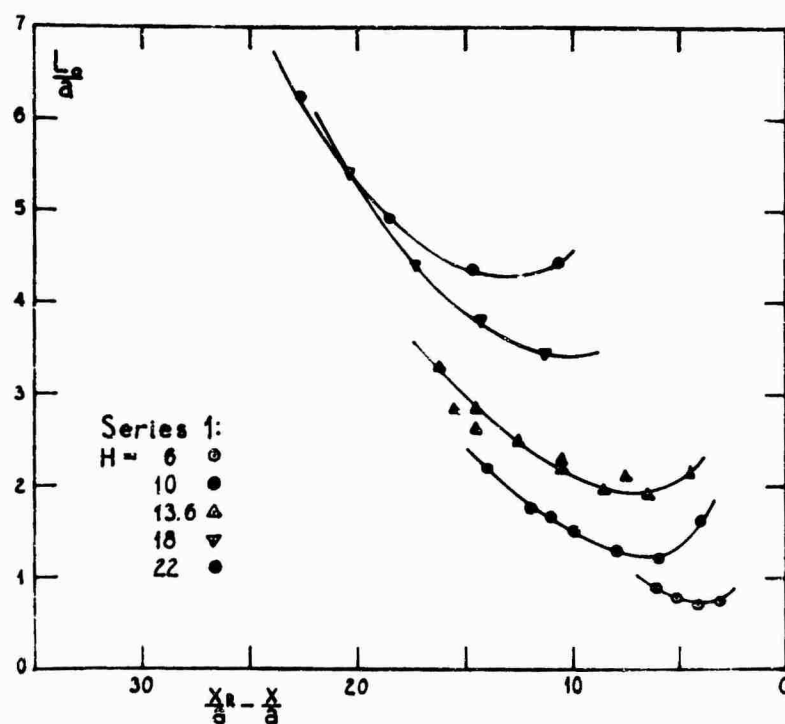
Figure 12. Variation of characteristic jet width with distance from reattachment point for backward flowing wall jets.

3.2 Mean velocity and turbulent stress profiles

The mean velocity profile of the curved jet shown on Figure 6 is quite similar to the profile found in a straight jet. There are slight differences, that should be noted, however:

a) The mean velocity profile is slightly asymmetric, the maximum velocity point is displaced from the mid-point of the line between the two half-maximum velocity points towards the internal boundary of the jet. Also, associated herewith, the mean velocity gradient is higher on the internal side than on the external side.

b) The mean velocity does not approach zero on the internal side of the jet. This is due to the fact, that in this region there is a high level of turbulence even where the mean velocity is vanishing. Hot-wire measurements are not reliable under such conditions, and the mean velocity profile can be regarded as being in error in this region.

The turbulent stress profile shown on Figure 6 is typical for the many profiles, that were measured. These profiles are asymmetric to a higher degree than the mean velocity profiles and the following traits should be noted:

c) The minimum near the point of maximum velocity is displaced towards the external side of the jet.

d) The two peaks in the regions of maximum shear are not equally wide, the peak on the external side of the jet being wider. This is a general trait found in all measured turbulent stress profiles.

e) The peak values of the turbulent stress profile are slightly different. In this particular profile the highest value is found on the external side of the jet, and this was the case for a majority of the profiles. In some profiles, however, the highest peak value was found on the internal side, but it was not possible to find a correlation between this variation and any relevant parameter.

The mean velocity profiles of the wall jets shown on Figure 10 are very similar to that found in an ordinary wall jet. The only aspect of the profile in the downstream flowing wall jet, that must be noted, is that the layer between the wall and the maximum velocity point is thinner than found in an ordinary wall jet. This is due to the proximity of the reattachment region.

The mean velocity profile of the backward flowing wall jet also has a relatively thin wall layer and the profile is slightly distorted, but the characteristic wall jet profile shape is very clear.

The slight asymmetry of the curved jet mean velocity profile does not have a marked influence on the constant I_1 in the volume flow rate integral, equation (2.1.3), but indicates different entrainment rates on the two sides of the jet. In the calculation of the curved jet volume flow rate development a value of $I_1 = 2.10$ has been used. For comparison an exponential profile gives a value of 2.13 and the Görtler profile a value of 2.27. For the ordinary wall jet profile a value $I_{1,w} = 1.31$ seems appropriate, but in this work the deviations in the wall jet profiles and the unusual thinness of the wall layers have been accounted for.

3.3 Spread rates

The development of the curved jet characteristic width is shown on Figure 7, where all points tend to fall on a single curve. Most noteworthy results are, that the curved jets spread linearly and at an increased rate compared to the straight jet measurements. The curved jets in series 1 have a spread rate, that average at:

$$(3.3.1) \qquad \frac{L_o}{a} = 0.186\left\{\frac{s}{a} - 5.0\right\}$$

compared to the average for straight jets:

$$(3.3.2) \qquad \frac{L_o}{a} = 0.1o5\left\{\frac{x}{a} + 1.5\right\}$$

For the curved jets the characteristic width L_o has been found as half the distance between the two half-maximum velocity points.

The curved jets in series 2 measurements also averaged at about the same spread rate as given in equation (3.3.1), but the virtual origins tended for large plate inclinations towards a point 6.5 nozzle widths downstream from the nozzle.

In terms of the well known Görtler jet theory, where the spread rate is characterized by the spread parameter σ, the curved jets average at $\sigma = 4.7$, while the value for straight jets is $\sigma = 7.7$.

Figure 11 shows, that for the downstream flowing wall jets the spread rates approach the value found in an ordinary, established wall jet. Figure 12 indicates a rather strong, but systematic variation of the wall jet characteristic width in the backward flowing wall jets.

3.4 Volume flow rate developments

Based on the experimental data presented above the volume flow rate developments of the curved jet as well as the two wall jets were calculated using equations (2.2.1) and (2.3.1). The results of these calculations are presented in Figures 13 and 14 for series 1 measurements.
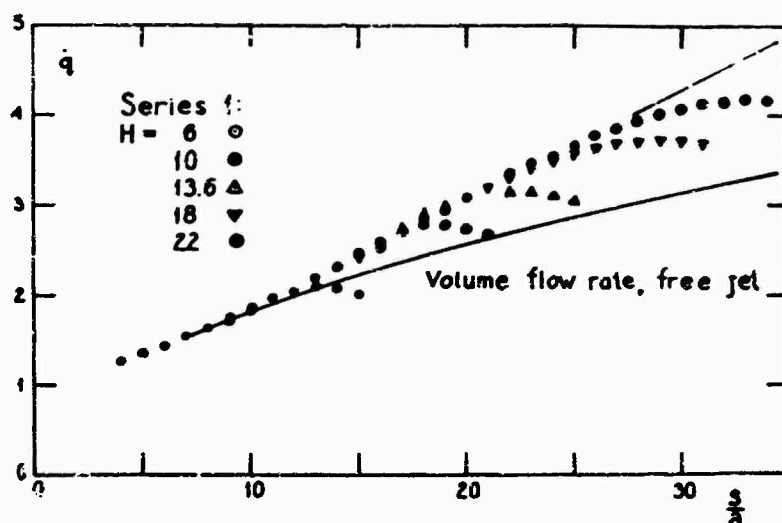
Figure 13. Variation of total volume flow rate with jet pathlength for curved jets.
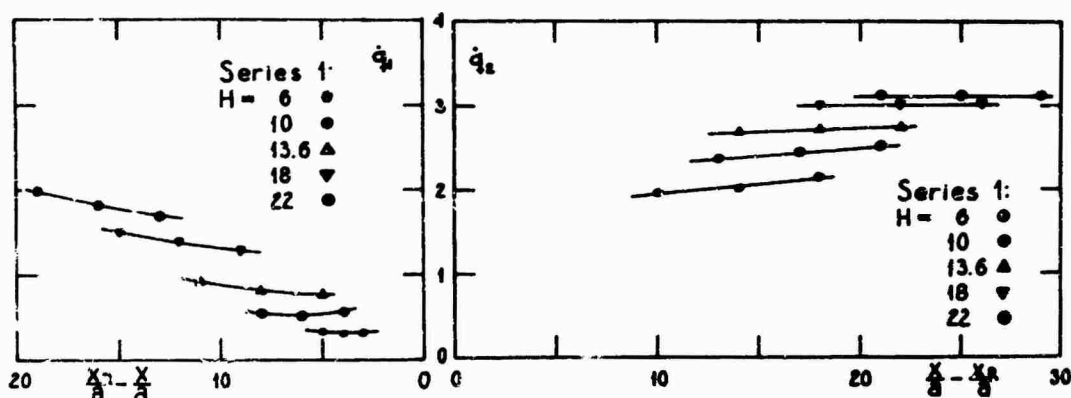
Figure 14. Variation of volume flow rate with distance from reattachment point for backward flowing (left) and downstream flowing (right) wall jets.

The volume flow rates of the three jet flows at the stations, where they enter respectively leave the reattachment region, are estimated from Figures 13 and 14 and used in Table 1. Also included in Table 1 are similar results from series 2 measurements. Numbers in round brackets are not results based on measurements, but have been found using interpolation in the plots of series 2 measurements. Equations (2.4.2) to (2.4.5) are then used in Table 1 to provide data for Figure 15, which show entrainment asymmetry parameter λ as function of the average value of L/R for each curved jet. In Figure 15 are included for comparison a set of curves suggested by Sawyer (1963). The two values of Sawyer's parameter C are those, which Sawyer found to give best correlation between prediction and experiment for the position of the reattachment point on a parallel, offset plate, C = 5.29 (series 1), and an inclined plate, C = 7.87 (series 2).

Column 5 in Table 1 shows, that there is an excess volume flow rate in the two wall jet flows combined. The reason for this discrepancy probably is, that the curved jet does not cease to entrain fluid at the station, where the pressure rises at the boundary of the reattachment region. A study of the development of the volume flow rate in the curved jets has shown, that at the rate of increase of volume flow rate found in Figure 13, the curved jets will reach the combined volume flow rate of the two wall jets long before the station, where they hit the plate. The excess volume flow rate in column 5 is therefore being regarded as due to difficulties in measuring the velocity profiles in a distorted curved jet at the boundary of the reattachment region.

Table 1

1	2	3	4	5	6	7	8
H or α	$\dot{q}_R$	$\dot{q}_1$	$\dot{q}_2$	$\dot{q}_1+\dot{q}_2-\dot{q}_R$	$\dot{q}_2-1$	λ	$\frac{L_c}{R}$
Series 1							
6	2.10	0.31	1.95	0.16	0.95	3.06	0.057
10	2.79	0.51	2.38	0.10	1.38	2.70	0.074
13.6	3.18	0.79	2.70	0.31	1.70	2.15	0.082
18	3.74	1.28	3.02	0.56	2.02	1.57	0.091
22	4.18	1.73	3.12	0.67	2.12	1.22	0.096
Series 2							
-30.95	(2.24)	0.48	1.80	(0.04)	0.80	1.66	0.023
-21.80	(2.34)	0.48	1.95	(0.09)	0.95	1.98	0.042
-11.31	(2.51)	0.48	2.10	(0.07)	1.10	2.29	0.061
0	2.79	0.51	2.38	0.10	1.38	2.70	0.074
11.31	(3.21)	0.65	2.69	(0.13)	1.69	2.60	0.086
21.80	(3.70)	0.97	3.00	(0.27)	2.00	2.06	0.097
30.95	4.18	1.47	3.38	0.67	2.38	1.61	0.109
38.65	4.70	2.06	4.02	1.38	3.02	1.47	0.112
45.00	5.20	2.60	4.65	2.05	3.65	1.40	0.118
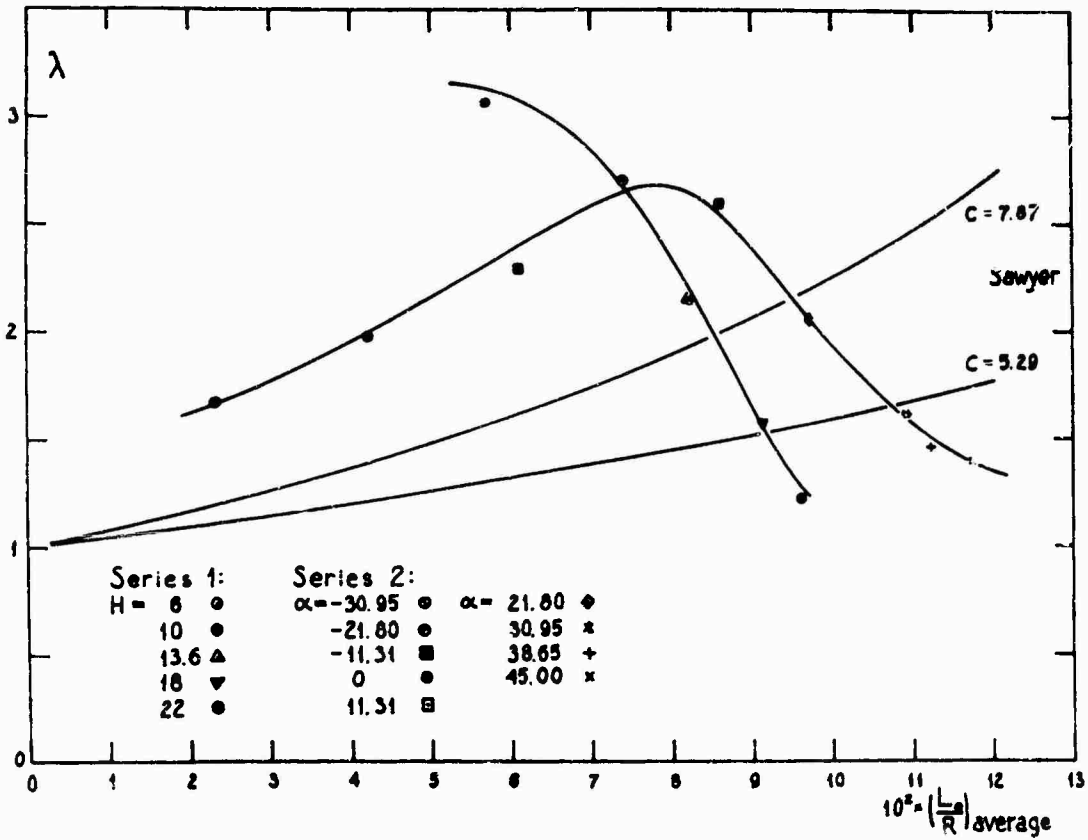
Figure 15. Entrainment asymmetry parameter λ versus average relative curvature for curved jets. Two curves representing theory of Sawyer (1963) are included for comparison.

4. DISCUSSION

The measurements presented in Figures 4, 5, 6 and 7 show, that the curved reattaching jet behaves in a way very similar to the ordinary straight jet, but that the spread rate and turbulence intensity are strongly increased. For the five sets of measurements belonging to series 1 there is no clear variation, that must be attributed to the curvature of the jet. The spread rate in particular shows little variation from the average. The results of series 2 measurements lead to similar observations.

The calculation of the entrainment asymmetry parameter λ is presented in Table 1 and the results are shown on Figure 15. In view of the very little variation in the overall behaviour of the curved jets it is noteworthy, that λ vary very strongly with the jet curvature. The variation does not follow the prediction by Sawyer (1963). The decrease of λ with increasing curvature indicates, that the curvature is not the dominant factor in the interaction between the curved jet and its surroundings. The still, ambient fluid on the external side of the jet can hardly play an active part in the reattachment phenomenon, rather the characteristics of the flow field are determined by the interaction between the curved jet and the flow in the recirculating region.

5. CONCLUSION

Measurements in curved, reattaching jets show, that the spread rate and turbulence intensity are increased about 75 % compared to straight jet data.

A volume flow rate balance in the reattachment region show, that there is a marked difference in the entrainment rates on the two sides of the jet. The entrainment asymmetry does not vary systematically with the jet curvature and vanish for large curvatures in contrast to what has been expected from theory. Although curvature may have some influence on the entrainment of a curved, reattaching jet, this influence is not as simple as suggested by Sawyer (1963).

6. REFERENCES

Townsend, A. A. (1956): The Structure of Turbulent Shear Flow.

Cambridge University Press, 1956.

Bourque, C. & Newman, B. G. (1960): Reattachment of a Two-Dimensional, Incompressible Jet to an Adjacent Flat Plate.

Aero. Quart. 11, 201.

Sawyer, R. A. (1960): The flow due to a two-dimensional jet issuing parallel to a flat plate.

JFM, 9, 543.

Sawyer, R. A. (1963): Two-dimensional reattaching jet flows including the effects of curvature on entrainment.

JFM, 17, 481.

Bourque, C. (1967): Reattachment of a Two-Dimensional Jet to an Adjacent Flat Plate.

Advances in Fluidics, The 1967 Fluidics Symposium, ASME.

Perry, C. C. (1967): Two-Dimensional Jet Attachment.

Ph.D. Dissertation, University of Michigan, 1967.

Boucher, R. F. (1968): Incompressible Jet Reattachment Analysis using a Good Free Jet Model.

Third Cranfield Fluidics Conference, 1968.

THE EFFECT OF DENSITY DIFFERENCE ON THE TURBULENT MIXING LAYER*

by

Garry Brown and Anatol Roshko
California Institute of Technology
Pasadena, California 91109

SUMMARY

An experimental study has been made of the turbulent mixing layer between two streams of different gases, especially nitrogen and helium. This was made in a new flow apparatus, designed to produce good quality flow at pressures up to 10 atmospheres with run times as low as 1 or 2 seconds. High-speed measurement techniques, including a novel density probe, were used.

Shadowgraphs of the turbulent mixing layer reveal a large-scale structure rather similar to that in the late stages of instability development in a laminar free shear layer. This structure is s   even in cases of uniform density.

The similarity proper. =s of the mixing layers are established from profiles of mean velocity and density, and from these the basic flow parameters are computed; spreading rate, dissipation rate, shear stress distribution. It is found that a large density ratio (e.g., 7:1) in the two streams does not have a great effect on the spreading rate: this contrasts with the large effect of Mach number on the turbulent spreading of a free shear layer at the edge of a supersonic flow. A brief analysis compares the effects of density nonuniformities in low speed flow and those due to compressibility at high Mach number.

1. INTRODUCTION

The present work had its motivation from several problems in free turbulent mixing, in particular, problems connected with density nonuniformities. There has been remarkably little recent progress with this problem. One aspect is the question of the effect of Mach number on the spreading parameter σ; probably the earliest attempt to find such a correlation was that by Korst and Tripp[1] in 1957. It has been generally agreed by most authors since then that the spreading rate decreases (σ increases) with increasing Mach number, but quantitative agreement has been woefully lacking. There is even some qualitative disagreement. Regarding a blown-off boundary layer as a free shear layer, Fernandez and Zukoski[2] found that the spreading rate at M = 2.6 in adiabatic flow is greater than at M = 0; they do not actually state that conclusion, but it follows from their suggestion that entrainment rate is independent of Mach number. On the other hand, Alber and Lees[3] suggest, on the basis of several experimental results in the literature, that the entrainment rate of free turbulent shear layers decreases rapidly with increasing Mach number, varying in adiabatic flow as the square of the density ratio across the layer, consistent with decreasing spreading rate. (The blown-off turbulent boundary layer should probably not be regarded as a free mixing layer.)

The attempt to connect the shear layer parameters with density ratio has been central or implicit in practically every theoretical and experimental approach to the problem. The enthusiasm for this approach probably derives from the success that density transformations of the Howarth-Dorodnitsyn type have had in the case of attached boundary layers. Implicit in the transformation methods, is that the effect of density nonuniformity is universal, whether it be due to compressibility, i.e., Mach-number dependence; or due to temperature variation, say at low Mach number; or due to variation in composition, as in the mixing between different gases. However, there have been no serious attempts made to determine whether in fact the different cases of density nonuniformity are similar. The many experiments on coaxial, axisymmetric jets, which include examples with various combinations of different gas compositions or temperatures at low speeds, have not clarified these problems. One reason, we believe, is that it is difficult to pose a scientifically simple problem in the case of axisymmetric flows with density nonuniformities. In the regions of important nonuniformity, such flows generally do not have similarity properties.

On the other hand, similarity arguments show that a turbulent mixing layer between two uniform flows having velocities U_1, U_2 and densities ρ_1, ρ_2, respectively, will grow linearly in the x direction; the velocity profile U/U_1 and density profile ρ/ρ_1, as well as the shear stress profile $\tau/\rho_1 U_1^2$, will be functions of the similarity variable y/x and the parameters U_2/U_1 and ρ_2/ρ_1. It was for these reasons that we thought it important to study the plane mixing layer between two gases of different densities at low Mach number, and undertook to overcome the difficult experimental problems associated with this configuration.

---

2. APPARATUS

The requirements which we felt were important were as follows: (i) High Reynolds number, comparable to that in the Liepmann-Laufer experiment; (ii) High density ratio, at least a value of 2, and preferably more, so that the dynamic effect of density nonuniformity could be exhibited, and values would be comparable to those in the supersonic case at high M.

To achieve a density change in air by heating one stream is for many reasons rather impractical. We therefore decided to achieve density differences by using different gases, in particular the combination of nitrogen and helium which gives a density ratio of 7. We use bottled gases and do not recover them. To achieve high Reynolds number yet keep mass flow rates down to economical values, we decided to design the apparatus for operation at high pressures. (For a given Reynolds number, mass flow rate is inversely proportional to pressure.) This reasoning led to the design of a new kind of short-running-time, high-pressure wind tunnel in which the test section can be pressurized to 10 atmospheres. Two gas streams each supplied from eight 2000 p.s.i. bottles are brought together at the exit of two 4 in. x 1 in. nozzles in the test section, shown in figure 1. This section is enclosed by a cylinder which slides over and seals against the circular plates at both ends of the section and the whole tank can then be pressurized. The upstream and downstream valves which control the flow rates and pressure in the tank were chosen partly on the basis of their time response. The resulting facility establishes steady flow in the test section in less than 300 milli-seconds with velocities up to 50 ft/sec. This means that experiments with flow durations of only 1 or 2 seconds are possible. The free stream turbulence level is between 0.1 and 0.5%.

Operating at a pressure of 10 atmospheres, the Reynolds number is the same as in a facility with 40 in. x 10 in. nozzles operating at 1 atmosphere and the same velocity.
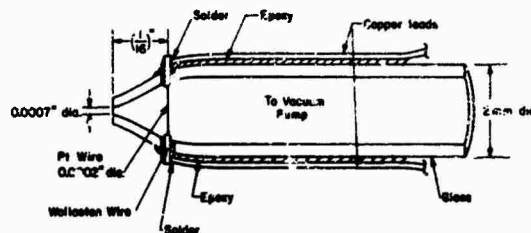
Fig. 2. Density Probe

Fig. 1. Test section showing the two nozzles, adjustable side walls and traversing probe. Glass end walls enclose the nozzles and test section. Pressure cylinder in raised position visible in upper portion of picture.

Besides being more economical of mass flow, the higher pressure is helpful for optical visualization and in general increases measurement sensitivity. Disadvantages are the smaller dimensions and higher frequencies of turbulent variations.

Adjustable side walls which span the test section are used to adjust or remove pressure gradients in the flow. Preliminary adjustments for minimum pressure gradient are made using two solid walls and then one wall is replaced by a 10% open slotted wall. This has proved very satisfactory.

Measurements of the mixing region have been made within the first six inches downstream of the splitter plate. For a flow of 50 ft/sec at 10 atmospheres the momentum thickness of the boundary layer leaving the splitter plate, estimated using Thwaites' method, is .001". (The thickness of the splitter plate at the end is approximately .002".) For a typical free shear layer entrainment rate of .035 the momentum thickness has become 10 times this initial value ¼" downstream, a criterion sometimes quoted for similarity. The criterion quoted by Alber and Lees $(x/\sigma\theta_i > 10)$ requires a distance of 120 times the initial momentum thickness for the attainment of a similarity profile (.12" in our case), while the criterion given by Bradshaw[4] recommends 1000 times the initial momentum thickness or 1" in our case.

3. MEASUREMENT TECHNIQUE

To make measurements in a turbulent flow of unknown composition with high turbulent levels and frequencies and a flow duration time of only a few seconds is a rather difficult requirement. As a minimum, mean density and velocity profiles must be obtained to establish the essential features of the mixing region. The instruments used to obtain these were a fast electronic (Barocel) manometer and pitot tube and a density probe developed especially for this study, described in detail in reference 5.

The density probe is sketched in figure 2. In operation the probe is attached to a vacuum pump and the wire maintained at some fixed temperature above its surroundings with the usual feedback bridge. With a vacuum pump of sufficient capacity (not very large) the power required to keep the wire at this temperature depends only on the stagnation properties of the gas being sampled. If the sampled gas moves relative to the probe then to order M^2 these properties have the same value if evaluated at static conditions as they do at stagnation conditions. That is, for small Mach number the output of the probe depends on the gas being sampled and not its velocity. The accuracy with which this is true depends on the Mach number and essentially on the range of variations in molecular weight of the gas being sampled. In our case the difference in output between all nitrogen and all helium at 90 p.s.i. was 1.5 volts and sensitivity to velocity was less than 1% of this for velocities up to 60 ft/sec.

In order to obtain a complete density and velocity profile in one run a traversing gear was designed to move the probes in steps of .001 inch at the command of an input voltage pulse train. The device, which incorporates a stepping motor, low friction ball screw and special electronic pulsing circuit, will traverse the probes at any rate up to 1 inch/second (1000 pulses/second) and so, by counting pulses, will give the position to within .001" at any instant of time. An electronic coupler synchronizes this traversing mechanism with a fast analog channel selector, an A/D converter and a digital incremental tape recorder. The resulting system will step the probe .001", sample the voltage output of the density probe, convert it to a digital number and write it on magnetic tape, switch to the pitot tube output, form the conversion, write this number on the tape, step the probe another .001", etc. A computer then processes the tape. A complete traverse of 1½" with a measurement every .001" of density and pitot pressure is made in a typical run time of 3 seconds.

4. FLOW STRUCTURE

The most surprising result of this study was the very pronounced large structure which photographs of the shear layer revealed (Figs. 3 and 4). To the authors' knowledge
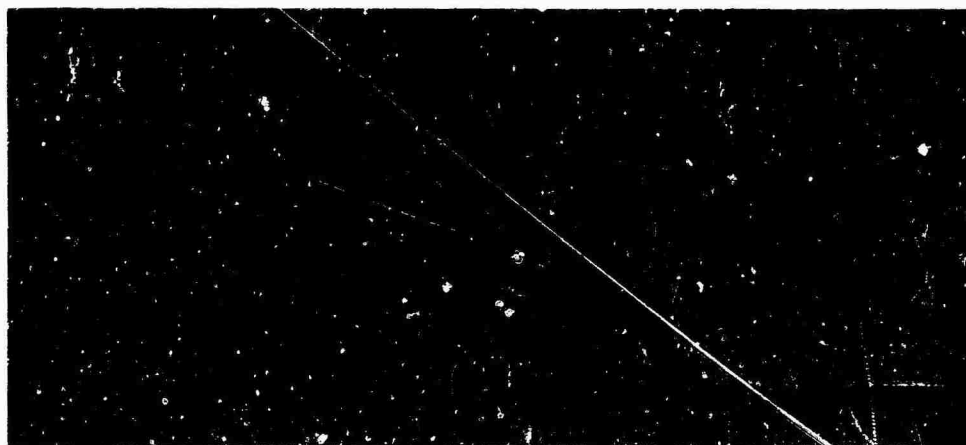
Fig. 3. Shadowgraph of mixing layer. $U_2/U_1 = 1/7$, $\rho \neq$ const.
Lower (high speed) stream is N_2; upper (low speed) stream is air.

these "two-dimensional" "big eddies" have not previously been observed, nor expected from the various correlation measurements that have been made in turbulent shear layers. These shadowgraphs were obtained using parallel light from a spark source with the photographic plate placed inside the pressure vessel, against the glass end-wall of the test section. That this structure is an essential feature of the plane shear layer, and not forced by an oscillation of the central splitter plate, not produced by an upstream or downstream flow resonance, not changed by a trip-wire on the splitter plate (at some distance from the trip), not a three-dimensional spiral vortex, has been confirmed by many experiments.

Figure 3 is the shear layer between two streams having essentially the same density (one is air, the other nitrogen) and having a velocity ratio of 7:1 (figure 5, discussed in section 5 shows the extent to which this uniform density shear layer grows linearly, in the mean). Figure 4 is the shear layer between nitrogen and helium, again with a velocity ratio of 7:1 and with the helium on the low speed side. It may be of interest to note here that for an "analogous" supersonic mixing layer with the same density ratio, one stream would be at $M_1 = 5.5$ and the other at $M_2 = 0.3$ (assuming adiabatic conditions).

Fig. 4. Shadowgraph of mixing layer. $U_2/U_1 = 1/7$; $\rho_2/\rho_1 = 1/7$.
Lower (high speed) stream is N_2; upper (low speed) stream
is He. Upper wall is deflected to maintain uniform
pressure.

The photographs pose many questions and suggest some interesting possibilities.
The wavy structure is reminiscent of the late stages of instability waves in laminar free
shear layers (Michalke & Freymuth[6]), but here, the "instability" repeats itself continu-
ously with increasing distance downstream. The idea of "laminar-like" instability behavior
in turbulent flow is not new. For example, vortex shedding in turbulent flow persists to
very high Reynolds number[7]; an analogous phenomena is observed near the end of the potential
core in jets[8]. Liepmann[9] at one time suggested the name "turbular fluid" for the fine scale
turbulent motion in which the large scale instability develops. Of course, many of the con-
temporary ideas about development of large scale structure from instabilities in turbulent
shear flow originate with Townsend[10]. But his picture of the large structures is somewhat
different, emphasizing three-dimensional eddies (with vorticity axes parallel to the x-y
plane), rather than what appears to be a nearly two-dimensional large structure in the
photographs we have obtained.

It is clear from the photographs that the scale of the instability structure in-
creases downstream, probably linearly like the thickness of the layer. How the earlier,
smaller structures are used up and replaced by larger ones is still to be studied, using
high speed motion pictures, intermittency probes, etc.

5. RESULTS

5.1 Uniform density

For comparison with the results of other investigators and to provide a reference
experiment for the experiment with two gases, measurements were made in the shear layer
between streams of nitrogen at two values of the velocity ratio, 1:7 and 1:$\sqrt{7}$ respectively.
The maximum velocity in each case was 35 ft/sec and the pressure was 7 atm. The multi-
plexing and digital recording techniques described in section 3 made it possible to traverse
a pitot tube and a hot wire side by side ($\frac{1}{2}$" apart) so that any effect of the pitot tube's
slower response time or of the fact that the two probes average differently would be appar-
ent. In each case approximately eight traverses at distances from $\frac{1}{2}$" to 4" downstream of
the splitter plate were made. For each run a traverse of $1\frac{1}{2}$" (or less) produced some 1500
measurements for each probe and a mean profile was found by fitting, in a least square
sense, a high order polynomial (16 to 20) to all 1500 points. Increasing the order beyond
this produced no significant change in the resulting profiles. Figure 5a is a similarity
plot from the smoothed pitot tube profiles for all 10 runs at the velocity ratio 1:7. The
origin of x for this plot was found by extrapolating a straight line through the energy
thicknesses determined at each traverse. This origin was .25" upstream of the splitter
plate edge. Deviations on the low speed side are larger than on the high speed side, partly
because the relative fluctuation level is much larger on the low speed side, partly because
the pitot pressure is only 1% of its free stream value which makes for larger relative
errors in measurement, and partly because the side-wall begins to introduce a pressure gra-
dient as the shear layer encroaches. A similar plot for the same runs from the smoothed hot
wire profile is virtually indistinguishable from this one. Even less scatter was obtained
for the velocity ratio of 1:$\sqrt{7}$ (Fig. 5b).

VELOCITY
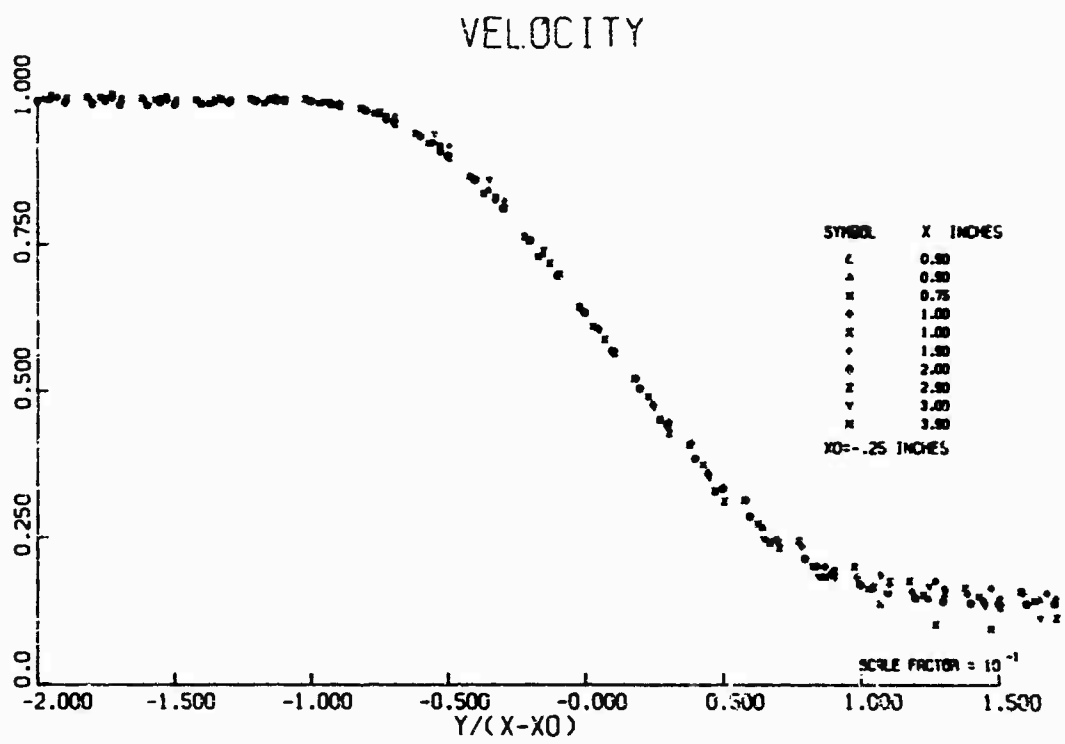
Fig. 5a. Similarity plot (ρ = const, U_2/U_1 = 1/7).

VELOCITY
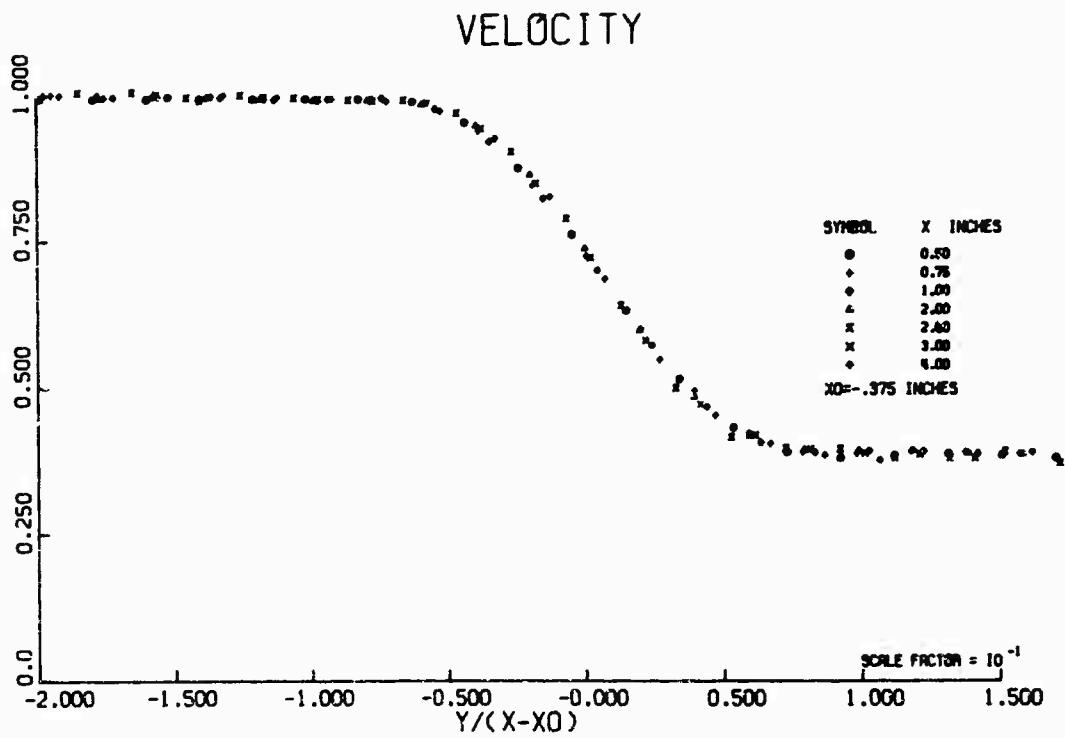
Fig. 5b. Similarity plot (ρ = const, U_2/U_1 = 1//7).

A summary of the essential parameters, σ, maximum shear stress, τ_m, and energy dissipation rate, $\dot{E}$, is presented in Table I (where $\Delta U = U_2 - U_1$). The maximum shear stress has been calculated using the relation

$$\tau_m = \int_{-\infty}^{\eta_o} \rho U (U - U_2) d\eta = \int_{\eta_o}^{\infty} \rho U (U_1 - U) d\eta$$

(which defines the dividing stream line η_o) and the energy dissipation rate from

$$\dot{E} = \int_{-\infty}^{\infty} \frac{1}{2} \rho U (U_1 - U)(U - U_2) d\eta$$

where $\eta = y/x$.

Table I. Shear layer parameters for uniform density.

U_2/U_1	σ	$\tau_m/\rho (\Delta U)^2$	$\dot{E}/\rho (\Delta U)^3$
* 0	11.3	.0115	.0078
1:7	12.8	.0136	.0085
1:$\sqrt{7}$	18.7	.0168	.0105

*From data of Liepmann & Laufer[11]

The parameter σ, which is inversely proportional to the spreading angle, has been determined by generalizing the definition which Reichardt used at $U_2 = 0$. By definition $\sigma = 1.32/\Delta\eta$ where $\Delta\eta$ is the angular distance between two rays η_1 and η_2 defined by

$$u(\eta_1) - U_2 = \sqrt{0.9}(U_1 - U_2) \quad \text{and} \quad u(\eta_2) - U_2 = \sqrt{0.1}(U_1 - U_2)$$

These rays can be experimentally determined accurately; in the case $U_2 = 0$ and uniform density they are the points at which the dynamic pressure is 10% and 90% respectively of its free stream value. The values of σ obtained from the above definition are very close to those obtained from the more elaborate least-square fitting of Görtler's solution to the experimental profiles.

In addition to the comparison with Liepmann and Laufer's data at $U_2 = 0$ we were able to compare our results with the measurements at various values of U_2/U_1 by Miles and Shih[12], who kindly made available to us their original data from which we determined σ using the formula above. These results are shown in figure 6. Also included are two
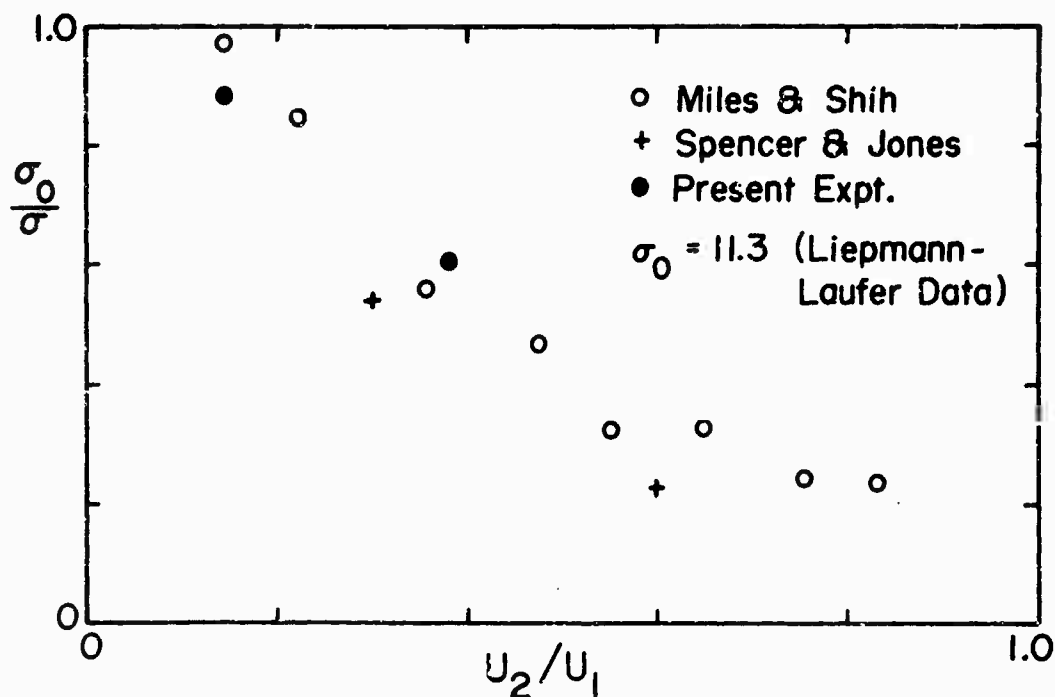
Fig. 6. Effect of velocity ratio on spreading rate (ρ = const).

points determined from data in reference 13. There is a systematic difference between the results of references 12 and 13. The differences may possibly be related to the free stream turbulent intensities (about 3% and 0.1% respectively, cf. 0.1 - 0.5% in our case) or the shear layer width-to-length ratios (about 0.8 and 0.3 resp., cf. about 1.0 in our case).

5.2 Variable density

Three particular cases have been studied in which the density ratio was seven (helium on one side and nitrogen on the other). In the first two cases the velocity ratio was $1:\sqrt{7}$, with helium on the high speed side in one case (ρU^2 the same in both streams) and nitrogen on the high speed side in the other. (The latter would correspond to an "analogous" supersonic mixing layer with one stream at $M_1 = 5.9$ and the other at $M_2 = .84$.) In the third case the velocity ratio was 1:7 with helium on the high speed side, that is ρU the same in both streams. This is a particularly interesting situation since it allows a sensitive comparison between simple eddy-viscosity theory and experiment. For example, if the ratio of the eddy viscosity to eddy diffusivity (the Schmidt number) is 1 the theory predicts ρU constant everywhere across the layer, a result which from experiment is far from true.

In all cases the maximum velocity was 35 ft/sec and the ambient pressure seven atmospheres. The density probe and the pitot tube were mounted side by side ($\frac{1}{2}$" apart) and, as in the uniform density case, the probes were traversed approximately $1\frac{1}{2}$" across the shear layer in 3 seconds and a measurement of the density and pitot pressure made every .001". An example of a density traverse is shown in figure 7 in which all 1500 measurements have been plotted. It is immediately apparent firstly that the density is nowhere greater than
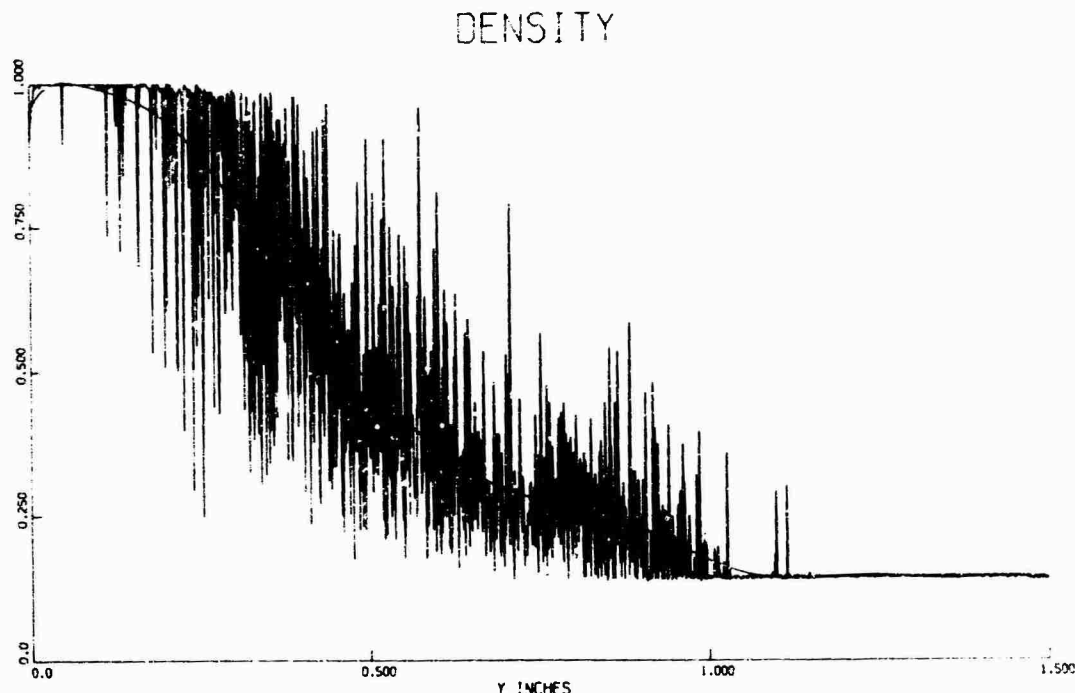
Fig. 7. Single traverse with density probe ($U_2/U_1 = 1/7$, $\rho_2/\rho_1 = 7$).

nitrogen or less than helium, and secondly that the variation in density at any point is of the same order as the density difference between the two streams. This is consistent with the large structure, evident in the shadowgraph, which one imagines can convect gas from one side of the layer to the other.

From the measurement of density and pitot pressure at each step in the traverse the velocity at each step is obtained using the Bernoulli equation. No attempt has been made to try and take account of the different response times of the density and pitot probes, nor of the fact that the probes are not at exactly the same point. The excellent agreement between the hot-wire and pitot tube results for mean velocity in the uniform density case and the fact that the resulting velocity profiles for variable density are smooth and monotonically increasing (which intuitively one expects) lead us to believe that these different response times do not introduce serious errors.

The resulting similarity profiles for density and velocity for the two cases in which the velocity ratio is $1:\sqrt{7}$ are shown in figure 8, and a summary of the essential

DENSITY AND VELOCITY

DEN2 : DEN1 = 7:1

VEL2 : VEL1 = .38:1

SCALE FACTOR = 10^{-1}

Y/(X-X0)

Fig. 8a. Similarity profiles for density and velocity ($U_2/U_1 = 1/\sqrt{7}$; $\rho_2/\rho_1 = 7$).

DENSITY AND VELOCITY

DEN2 : DEN1 = 1:7

VEL2 : VEL1 = .36:1

SCALE FACTOR = 10^{-1}

Y/(X-X0)
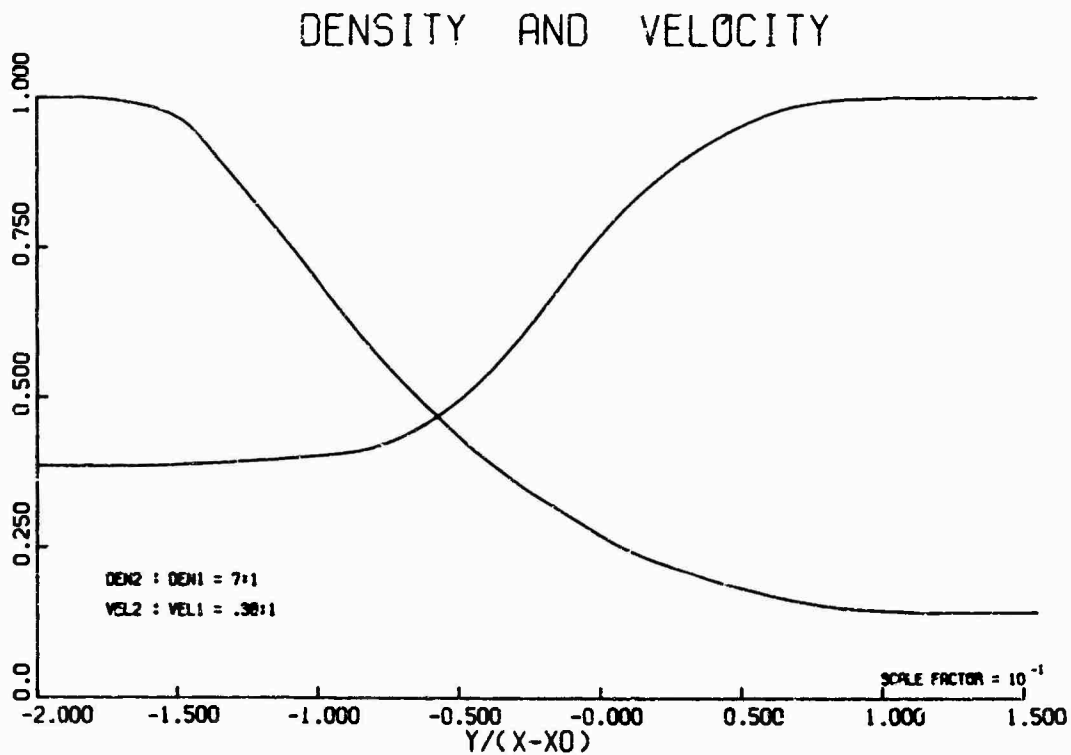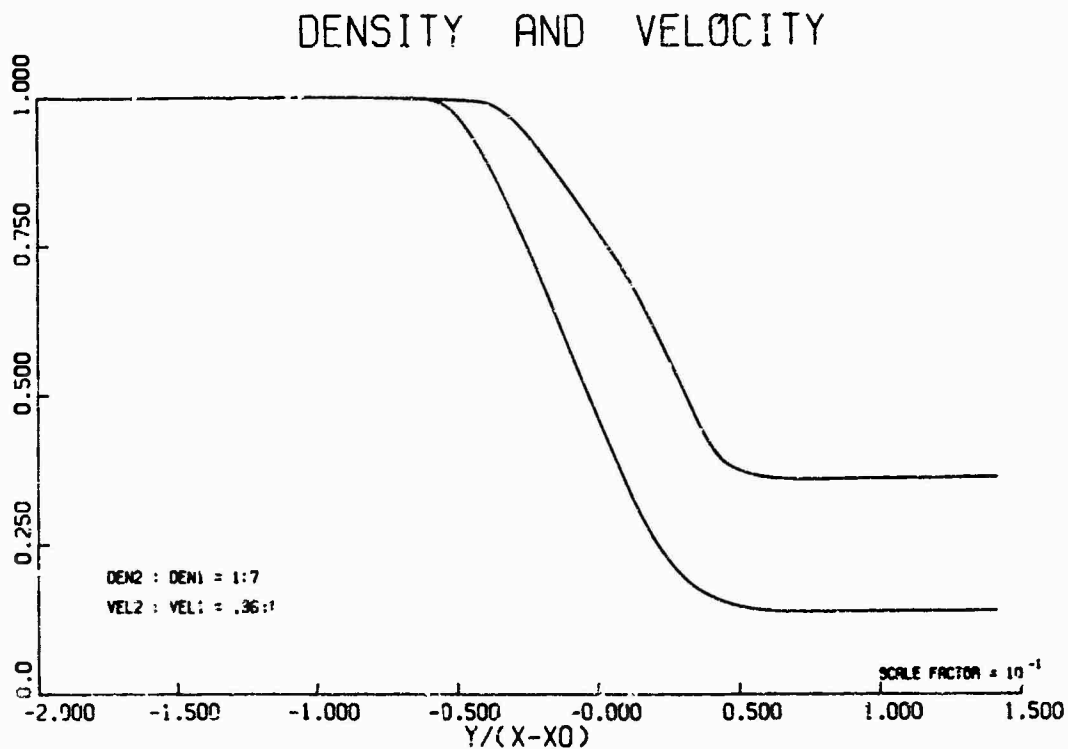
Fig. 8b. Similarity profiles for density and velocity ($U_2/U_1 = 1/\sqrt{7}$; $\rho_2/\rho_1 = 1/7$).

parameters, including those for the comparable uniform density cases is presented in Table II (where $\bar{\rho} = \frac{1}{2}(\rho_1 + \rho_2)$). At the time of writing only a few runs in each case had been processed so that the accuracy of these results is not quite as good as in the uniform density case.

Table II. Effect of density ratio on shear layer parameters.

ρ_2/ρ_1	U_2/U_1	σ	$\tau_m/\bar{\rho}\Delta U^2$	$\dot{E}/\bar{\rho}\Delta U^3$
1	1:7	12.8	.0136	.0085
7:1	1:7	9	.0097	.0066
1	1:$\sqrt{7}$	18.7	.0168	.0105
7:1	1:$\sqrt{7}$	15	.0093	.0072
1:7	1:$\sqrt{7}$	23	.0106	.0064

The effect of density ratio on the turbulent spreading of a shear layer does not appear to be as great as had been believed. Comparing the last two cases, for which the density ratio varies by a factor of 49, the variation in spreading angle is only 1.5.

On the other hand, in the turbulent shear layer at the edge of an adiabatic supersonic flow, the spreading angle is observed to decrease (σ increases) considerably with increasing Mach number. This change is often attributed to the effect of the corresponding increase of the density ratio $\rho_1/\rho_2 = T_2/T_1$. In most experiments T_2 is equal to the stagnation temperature of the supersonic flow. In figure 9 the spreading
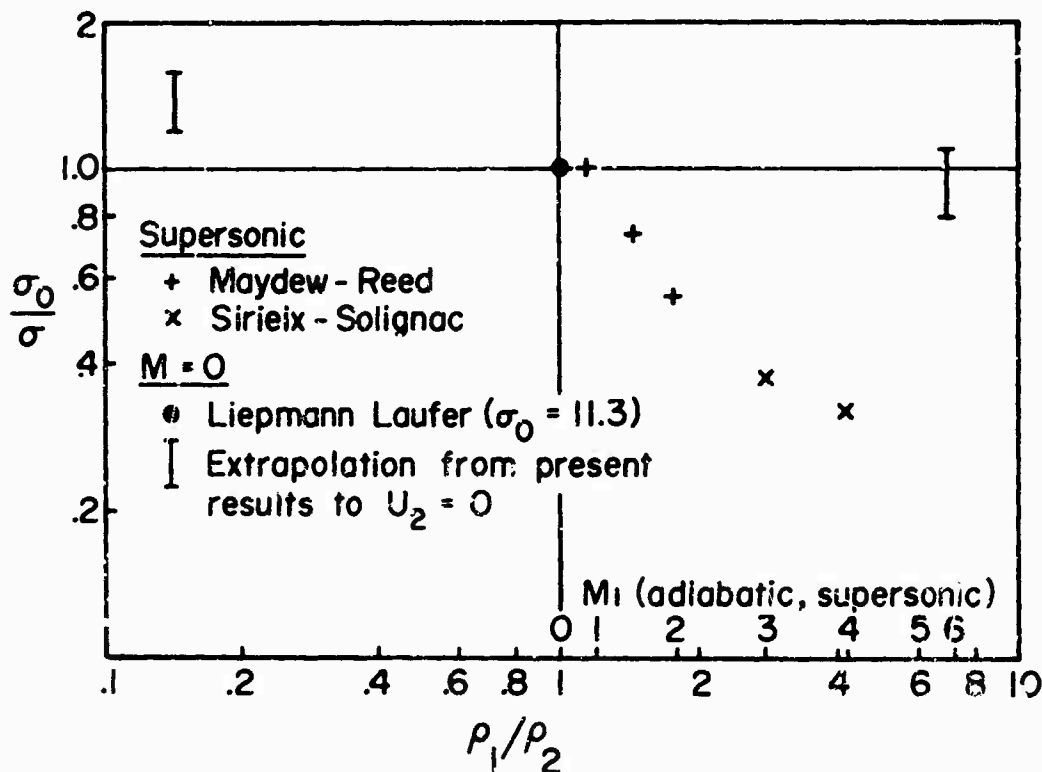
Fig. 9. Effect of density ratio on spreading parameter. Comparison of supersonic and incompressible cases.

parameter in supersonic flow, normalized with the Liepmann-Laufer value, from the experiments of Maydew and Reed[14] and Sirieix and Solignac[15] has been plotted against the density ratio. Also shown are normalized values of the spreading angle from our experiments on mixing between He and N_2 at values of $\rho_1/\rho_2 = 7$ and $1/7$, respectively. The values shown are estimates obtained by extrapolating from our finite values of U_2/U_1 to $U_2/U_1 = 0$ ($U_2 = 0$ in the supersonic experiments). From this figure it is clear that density ratio alone does not explain the changes in spreading angle of a turbulent mixing layer at the edge or a supersonic flow.

6. THEORY

6.1 Equations

An explanation for the essential difference between shear layers having the same velocity and density ratio but one supersonic and the other incompressible can be found in the equations which describe them. With the usual approximation that gradients in x are small compared with gradients in y and that values of $\sqrt{u'^2}$ and $\sqrt{v'^2}$ are comparable, the continuity and momentum equations

$$\frac{\partial}{\partial x} (\rho U) + \frac{\partial}{\partial y} (\rho V + \overline{\rho' v'}) = 0 \tag{1}$$

$$\frac{\partial}{\partial x} (\rho U^2) + \frac{\partial}{\partial y} (\rho UV + U \overline{\rho' v'}) = - \frac{\partial}{\partial y} (\rho \overline{u'v'}) \tag{2}$$

$$\frac{\partial}{\partial y} (\overline{\rho v'^2}) = - \frac{\partial p}{\partial y} \tag{3}$$

are the same for both flows. The essential difference arises from differences in the other equation to be satisfied, namely the energy equation in supersonic flows and the diffusion equation in incompressible flow. The diffusion equation for the ith component having n_i molecules/unit volume is

$$\frac{\partial n_i}{\partial t} + \text{div}(n_i \underaccent{\tilde}{V}) = \text{div} (\rho \mathcal{D} \text{ grad } \frac{n_i}{\rho})$$

Summed over all i and noting that n is constant (to order M^2) gives for a two-dimensional boundary layer flow

$$\frac{\partial U}{\partial x} + \frac{\partial V}{\partial y} = - \frac{\partial}{\partial y}\left(\frac{\mathcal{D}}{\rho} \frac{\partial \rho}{\partial y}\right) \tag{4}$$

For a turbulent shear layer the same reasons that lead one to postulate a large Reynolds stress relative to the viscous stress also lead to the omission of the molecular diffusivity, and the diffusion Eq (4) becomes

$$\frac{\partial U}{\partial x} + \frac{\partial V}{\partial y} = 0 \tag{5}$$

where U and V are now the time averaged velocities. (In passing one may note that the substitution of ρV for $\rho V + \overline{\rho' v'}$ in Eq (1), (2) and (5) leads to three equations whose form is identical with the corresponding laminar equations except that an eddy diffusivity and viscosity defined by

$$\overline{\rho' v'} = - \mathcal{D}_T \frac{\partial \rho}{\partial y}$$

$$\overline{u'v'} = - \nu_T \frac{\partial u}{\partial y}$$

replace the molecular diffusivity and viscosity.)

For a supersonic boundary layer the energy equation

$$\rho \frac{Dh}{Dt} - \frac{Dp}{Dt} = \mu \left(\frac{\partial U}{\partial y}\right)^2 + \frac{\partial}{\partial y} \left(k \frac{\partial T}{\partial y}\right)$$

becomes, with the assumption of a perfect gas and the substitution of continuity and the equation of state,

$$\frac{1}{\gamma-1} \frac{\partial p}{\partial t} + \frac{\gamma}{\gamma-1}\left[\frac{\partial}{\partial x} (pU) + \frac{\partial}{\partial y} (pV)\right] - U \frac{\partial p}{\partial x} - V \frac{\partial p}{\partial y} = \mu\left(\frac{\partial U}{\partial y}\right)^2 + \frac{\partial}{\partial y} \left(k \frac{\partial T}{\partial y}\right)$$

Substitution of $p = \bar{p} + p'$ etc. and again supposing a sufficiently large Reynolds number for molecular viscosity and conductivity to be negligible compared with their turbulent counterpart, leads to

$$\frac{\partial U}{\partial x} + \frac{\partial V}{\partial y} + \frac{1}{p}\left(\frac{\partial}{\partial y} \overline{p'v'} + \frac{1}{\gamma} v \frac{\partial p}{\partial y}\right) = 0 \tag{6}$$

for steady flow. (Gradients in y have been assumed large compared with gradients in x; $\overline{p'u'}$ of the same order as $\overline{p'v'}$; $\frac{\partial p}{\partial x} = 0$; $\frac{\gamma-1}{\gamma} v' \frac{\partial p'}{\partial y}$ of the same form but smaller than $\frac{\partial}{\partial y} \overline{p'v'}$.)

If the last two terms in Eq (6) are negligible, this equation becomes identical with the turbulent diffusion Eq (5). Then, and only then, would there be no distinction between the various cases in which there is a density difference, due either to a difference in molecular weights, heating effects, or high speed compressibility effects.

To assess the role of the last two terms in Eq (6) the following estimates can be made.

6.2 Orders of magnitude estimates

The orders of magnitude of the terms in the x momentum equation require that

$$\overline{u'v'} \sim \alpha U \Delta U$$

where α is a measure of the spreading angle $(\Delta y/\Delta x)$ for the layer. It is reasonable to suppose that $\overline{u'v'} \sim u'v'$ (where by u' is meant the rms fluctuation level) and that $u' \sim \Delta U$ even in the case of compressible flow. It follows that

$$v' \sim \alpha U$$

(if it is assumed that $v' \sim u'$ $(\sim \Delta U)$ then $\alpha \sim \Delta U/U$, which is the usual incompressible result).

An estimate for $V \partial p/\partial y$ can now be made since the y momentum Eq (3) relates $\partial p/\partial y$ to v'. Likewise, if it is supposed that p' is at least of the same order as the mean variation in static pressure then $\overline{p'v'} \sim \rho v'^3$ and the energy Eq (6) written as an order of magnitude equation is

$$\alpha \Delta U \; ; \; V + \alpha^3 U M^2 + V \alpha^2 M^2 = 0$$

Clearly, for small Mach number the last two terms are negligible and the energy Eq (6) reduces to the diffusion Eq (5). That is, the shear layer between gases having different molecular weights will be the same as that between a hot and cold gas with the same density and velocity ratio.

However, it is clear that for Mach number sufficiently large, α must depend on M for the last two terms to remain of the same order as the first two. This dependence is evidently

$$\alpha \sim \frac{1}{M} \left(\frac{\Delta U}{U} \right)^{\frac{1}{2}}$$

This result does qualitatively describe the experimental results which are available (Fig. 9). The velocity v' now decreases with Mach number but so too does α so that the turbulent terms which have been neglected in deriving the equations are still negligible. (The basic assumption used, that $u' \sim \Delta U$, implies an oscillation of the shear layer with an amplitude equal to some fraction of its thickness. If the effect of high Mach number is to reduce this amplitude, then the dependence of α on M is even stronger.)

7. CONCLUDING REMARKS

We wish to draw attention particularly to two findings from these experiments on a plane turbulent mixing layer:

(1) A large, wave-like, structure, which increases in scale with distance from the origin of the shear layer is an essential feature of the uniform or variable density free shear layer at low Mach numbers.

(2) We conclude that in subsonic flow a large density difference, whether arising from differences in molecular weight or temperature, has relatively small effect on the spreading of a turbulent mixing layer. The large effect that has been observed when one stream is supersonic must be related more to Mach number than to density difference. Order of magnitude arguments about the turbulent terms in the equations of motion show that the pressure velocity correlations and the variation in mean static pressure are not negligible at high Mach number as transformation theories (e.g., of the Howarth-Dorodnitsyn type) usually suppose.

8. REFERENCES

1. Korst, H. H., and Tripp,W., "The Pressure on a Blunt Trailing Edge Separating Two Supersonic Two-Dimensional Air Streams of Different Mach Number and Stagnation Pressure but Identical Stagnation Temperature," Proceedings of the Fifth Midwestern Conference on Fluid Mechanics, University of Michigan, Ann Arbor, Michigan,pp. 187-199, April 1957.

2. Fernandez, F. L. and Zukoski, E. E., "Experiments in Supersonic Turbulent Flow with Large Distributed Surface Injection," AIAA J. 7 (1969) 1759-1769.

3. Alber, I. E., and Lees, L., "Integral Theory for Supersonic Turbulent Base Flows," AIAA J. 6 (1968) 1343-1351.

4. Bradshaw, P., "The Effects of Initial Conditions on the Development of a Free Shear Layer," J. Fluid Mech. 26 (1966) 225-236.

5. Brown, G. L., and Rebollo, M. R., "A Small, Fast-Response Probe to Measure Density," submitted to AIAA Journal.

6. Michalke, A., and Freymuth, P., "The Instability and the Formation of Vortices in a Free Boundary Layer," Symposium on Separated Flow, AGARD Conf. Proc. No. 4, 1966.

7. Roshko, A., "Experiments on the Flow Past a Circular Cylinder at Very High Reynolds Number," J. Fluid Mech. 10 (1961) 345-356.

8. Crow, S. C., "Orderly Structure in Jet Turbulence," Boeing Sci. Res. Labs., Document D1-82-0991, 1970.

9. Liepmann, H. W., "Free Turbulent Flow," in Mécanique de la Turbulence (Centre National de la Recherche Scientifique, Paris, 1962), pp. 211-227.

10. Townsend, A. A., "The Structure of Turbulent Shear Flow," Cambridge Univ. Press, 1956, Chap. 6.

11. Liepmann, H. W., and Laufer, J., "Investigation of Free Turbulent Mixing," Technical Note 1257, August 1949, NACA.

12. Miles, J. B., and Shih, J., "Similarity Parameter for Two-Stream Turbulent Jet-Mixing Region," AIAA J. 6 (1968) 1429-1430.

13. Spencer, B. W., and Jones, B. G., "Statistical Investigation of Pressure and Velocity Fields in the Turbulent Two-Stream Mixing Layer," AIAA Paper No. 71-613.

14. Maydew, R. C., and Reed, J. F., "Turbulent Mixing of Compressible Free Jets," AIAA J. 1, (1963) pp. 1443-1444.

15. Sirieix, M., et Solignac, J-L., "Contributions a l'Étude Expérimentale de la Couche de Mélange Turbulent Isobare d'un Écoulement Supersonique," Symposium on Separated Flow, AGARD Conf. Proc. No. 4, 1966.

FLUID DYNAMIC PROPERTIES OF TURBULENT WAKES OF HYPERSONIC SPHERES

by

J.G.G. Dionne, D. Heckman, C. Lahaye, L. Sévigny & L. Tardif
Defence Scientific Service Officers
Defence Research Establishment Valcartier, DRB, DND, Canada
P.O. Box 880, Courcelette, P.Q. Canada

SUMMARY

The availability of reliable spatially-resolved measurements of the behavior of such wake variables as velocity, mass density, temperature, and charge density is of particular importance to the understanding and modeling of turbulent hypersonic wakes. An experimental program to obtain such data has been carried out at the Defence Research Establishment Valcartier. The present paper presents representative data concerning the mean behavior of velocity and density in the wakes of hypersonic spheres launched at Mach 13 and a $P_\infty D$ of 20 torr-inches. The variation with axial distance of the velocity, density, and temperature defects and of the velocity and density wake radii are given and are compared with other similar data and with schlieren data obtained under the same conditions. Data on turbulent characteristics such as velocity fluctuations, ionization scale lengths and wake intermittency are also given. Finally, the total momentum in the wake is estimated from the measured velocity and mass density distributions.

1. INTRODUCTION

In recent years, a very considerable effort has been devoted to the study of the turbulent wakes generated by hypersonic projectiles. Of particular importance to the understanding and modeling of such wakes is the availability of reliable spatially-resolved measurements of the behavior of such wake variables as velocity, mass density, temperature and electron density. The ballistic range facility permits such measurements to be made on the free wakes behind various models over a range of axial distance extending from a few body diameters to several thousands of body diameters.

A program of experimental investigation of the mean and fluctuating properties in turbulent wakes behind 1.0 inch and 2.7 inch diameter spheres mainly flown at about Mach 13.5 is now being completed in the ballistic range facilities of the Defence Research Establishment Valcartier (DREV). The program includes the means to determine the spatially-resolved distributions of such wake variables as velocity, mass density, charge density, and temperature. The sequential spark experiment makes use of a series of electrical discharges to measure the velocity distribution of the wake. The ionized path left by the discharge acts as a tracer which is carried by the velocity of the wake. Transverse arrays of axial pairs of continuum ion probes are utilized to study the distribution of ionization. Correlation of the signals from individual axial pairs can be used to determine a convection velocity. The array technique also provides data on the distribution of scales across the wake and on wake intermittency. An electron beam fluorescence probe is used to determine the distribution of mass density. The fluorescence induced at any point along the path of the electron beam is proportional to the gas density at the point. Under the assumption of an isobaric wake, the temperature can be inferred from the density. New and unique data on the wakes of supersonic and hypersonic spheres have been generated with these techniques (1 to 5).

The present paper concerns itself with the presentation of the results of a program of measurements on sphere wakes using the above-mentioned techniques under identical conditions of Mach number (M≈13) and corresponding values of pressure times sphere diameter ($P_\infty D \approx 20$ torr-inches). Measurements with the probe array and the electron beam techniques have been made on 2.7 inch diameter spheres at a pressure of 7.6 torr, the maximum practical operating pressure of the electron beam. Measurements with the sequential spark technique have been made on a smaller range facility using 0.59 inch diameter spheres at a pressure of 35 torr. A brief description is given of the experimental techniques and of the methods of recording and data reduction. Mean radial and axial characteristics of the velocity, mass density and temperature of the wake are presented and compared with other data. The velocity and density data also provide a measure of the dependence of wake growth on axial distance. These growth data are compared with those measured with the schlieren technique under comparable conditions. Additional information is provided on the turbulent characteristics of the wake. The standard deviation of the data about the mean distribution is used as an estimate of the intensity of the turbulent fluctuations of the velocity and the mass density. The distribution of space scales in the wake is inferred from the probe array signals. Probe data on wake transition and intermittency are also presented. Finally, the mean distributions of velocity and mass density are used to calculate the total momentum in the wake.

2. THE EXPERIMENTAL TECHNIQUES

2.1 Electrostatic Probe Array Technique

Attempts to measure the turbulent properties of hypersonic wakes using pairs of electrostatic probes have become widespread during the last few years (6,7,8,9), despite the well-known difficulties encountered in interpreting the probe current. Some of the less controversial aspects of this work have involved the measurement of velocities in the wake, using the well-known technique of a pair of probes, separated by a known distance, and inserted in the wake so that a line through their collecting elements would be parallel to the direction of the mean flow (4). Essentially, the upstream probe detects a signal representative of local fluctuations in the ionization pattern of a turbulent hypersonic wake; the downstream probe detects essentially the same signal but lagged in time according to the distance of separation of the probes. The time lag can be determined by cross-correlation of the probe signals, and together with the known probe separation, used to determine the wake velocity. The velocity determined by such a pair of probes should be labeled a convection velocity in order to possibly distinguish it from the mean local wake velocity at the same point in the wake(10).

The most recent application of paired electrostatic probes at DREV has involved the use of transverse arrays of eight probe pairs to survey the wake of hypersonic spheres (11). A typical survey array is shown in Figure 1. The individual probe pairs are separated by multiples of 1.25 inch or somewhat less than a body radius for a 2.7 inch diameter sphere. The individual electrostatic probes are constructed by stripping the outer conductor and insulator from micro-coax to leave the central conductor exposed. Bias is supplied by a current-to-voltage preamplifier which drives the length of cable required to lead the signals to the exterior of the range. The preamplifiers are all housed in the wedge-shaped box above the array as shown in Figure 1. The survey array station is located in a section of the range which has been lined with a smoothly profiled fiberglas wedge treatment in order to minimize the effects of shock reflections. Further details of the experimental equipment are given in a recent paper (11).

From the exterior of the range, the signals are led to a central recording station where the signals from pairs of probes are recorded on 35 millimeter film via the use of double beam oscilloscopes and Fastax cameras. Timing marks from a central timer are imposed every millisecond on all film traces by means of z-modulation of the oscilloscope beams, and serve to synchronize all signals in time with respect to all other signals and with respect to the position of the projectile. The pairs of signals from various pairs of probes are digitalized by a computer-driven film reader at a frequency of about 400 kiloHertz. Each signal is divided into 0.5 millisecond segments, and each such segment is cross-correlated with the corresponding signal segment from the other probe of a given pair. Figure 2 illustrates a typical cross-correlation curve obtained from a pair of such signal segments. The point of tangency between this curve and the envelope of the family of cross-correlation curves for all possible separation distances between a pair of probes determines the appropriate time lag for travel of a given fluctuation in ionization level from one probe to the other of the probe pair. Of course, the intercept of the cross-correlation curve on the zero lag axis represents the value of the space correlation for the probe separation employed (generally 0.14 diameter for a 2.7 inch sphere model). The time lags are used to infer velocity history as a function of axial distance using the known separation distance; the radial position of the probe pair is determined by projectile trajectory data. Scale history data is similarly inferred, as well as intermittency data.

2.2 The Sequential Spark Technique

The use of sparks for the measurement of the velocity distribution in flowfields is founded on the following three properties of the spark: the ionization of a narrow filament of gas, the strong emission of light from that filament and the persistence of appreciable ionization for some time after the spark. When a spark is made across a flowfield (for example, the wake of projectile) the ionized filament formed by this spark is displaced at the velocity of the neutrals. Successive sparks made at selected intervals retrace the displaced path of the first spark due to the persistence of the ionization. The light emitted by the sparks can be used to make a photographic record of the successive positions of the ionized path. This record of the displacement can be used in conjunction with the time interval between the sparks to calculate the velocity distribution of the flowfield. Figure 3 shows the stereo photographs of four sequences of sparks made in the wake of a one inch diameter aluminum sphere travelling at 14,500 ft/s at an ambient pressure of 100 torr. These four sequences (from left to right in each of the stereo photographs) were made at axial distances of 500, 900, 1,500 and 2,750 body diameters with spark intervals of 35, 75, 120 and 175 microseconds respectively.

The application of the sequential spark technique to the measurement of the velocity in the wake of free flight projectiles in a ballistic range necessitated the use of relatively large electrode gaps (5 to 7 inches) to allow for the dispersion of the projectiles and to provide a reasonable coverage of the wake of one inch diameter spheres. These large gaps, in turn necessitated the use of very high voltage, short duration pulses in order to achieve rapid breakdown of the gap. Current-wise, the intensity of the spark had to be sufficient for photography. Time-wise, the possibility of repeating the pulses at a minimum interval of a few microseconds was required. The equipment which was designed produces 90 kv pulses having durations of 0.8 microsecond with a maximum current of 20 amperes available for the discharge. Pulses can be repeated at intervals from 3 to 200 microseconds, the limitation at higher time intervals coming from the persistence of the ionization produced by the sparks. The development of a technique for selecting the spark position in an array of electrode pairs has permitted the production of multiple spark sequences on the same sphere firing as can be seen in Figure 3. This feature of the spark technique facilitated considerably the collection of statistically meaningful amounts of data required for the determination of the mean characteristics of the turbulent wake of hypersonic spheres.

Experimentation with the spark technique showed that the sparks did not generally pass through the center of the wake along straight lines and that precise stereo recording and analysis of the sparks traces was necessary if spatially resolved measurements of the wake velocity were to be obtained. The stereo system which has been used to photograph the sparks consists of two cameras whose optical axes lie in the horizontal plane and intersect in the center of the range at the spark station. One camera looks downrange at 60 degrees from the flight axis, while the other looks in an uprange direction, also at 60 degrees from the flight axis. Four plumb lines spaced at 8.5 inches and two catenary lines at 12 inch spacing are used as references for the precision stereo system. The catenary lines are also used as references for the flash X-ray photoattitude system of the range. The use of the same reference lines for the photoattitude and the spark station stereo systems permits the accurate positioning of the projectile with respect to the spark traces. Shadows of the horizontal and vertical reference lines can be clearly seen in the stereo photographs of Figure 3.

The data reduction of the stereo photographs is made on a stereo projector assembly which reproduces the geometry of the range stereo system. Alignment of the system is made from the shadows of the reference lines on the stereo photographs. Coordinates of numerous points of each spark traces are determined using standard photogrammetric techniques. The position of the projectile with respect to the spark traces is determined from the flash X-ray photoattitude system of the range with an accuracy better than 0.05 inch. Before a velocity of the wake can be calculated from the successive positions of the spark, it is necessary to make the assumption that the velocity in the z direction is equal to zero. Once this assumption is made, the velocity components can be computed from the horizontal distance between

consecutive spark traces and from the time intervals between the sparks.

Figure 4 shows the radial profiles of axial and lateral velocities obtained from the spark sequence seen on the left of the stereo photographs of Figure 3. The notation V12 indicates the velocity profile computed from the first and second sparks and V23 from the second and third sparks. The wake velocity is normalized with respect to the projectile velocity V_∞ and the radial distance R is normalized to the sphere diameter. The graph on the left shows the axial wake velocity calculated from the spark traces in the x y plane while the graph on the right gives the lateral velocity calculated from the spark traces in the y z plane, where x is the direction of flight, y is the transverse horizontal axis of the range and z the vertical one. A detailed description of the sequential spark technique and of its application to ballistic range measurements is given in a recent paper (12).

2.3 Electron Beam Fluorescence Probe

The electron beam fluorescence probe has been used extensively in low-density wind tunnels and shock tubes to measure local gas density and temperature (13) and has been extended in the past few years to the study of wakes generated in free-flight ballistic ranges (5,14,15,16). The fluorescence probe relies on the fact that if a collimated beam of energetic electrons is directed into an air or a nitrogen gas flow, a small fraction of the electrons collides with the gas molecules and excites them to a radiative state. The spontaneous emission appears as an intense fluorescence where the predominent radiation is emitted by the second positive system of the neutral nitrogen molecule, N_2 (2+), and by the first negative system of the singly ionized nitrogen molecule, N_2^+ (1-). As the fluorescence is confined within the electron beam diameter (a few millimeters), the intensity of the fluorescence at any position along the electron beam will be dependent upon the number of gas molecules, i.e. the gas density. Thus measurement of the fluorescence intensity emitted by a small segment of the electron beam will provide an evaluation of the gas density in the small volume defined by the length of the segment and the diameter of the beam. At pressures below 1 torr, the (0.0) band of the N_2^+ (1-) system gives the strongest emission of the N_2 spectrum and its intensity is proportional to pressure. At higher pressures, the radiation from this band starts to be quenched and the intensity-pressure curve reaches a plateau in the 5 torr region. The emission from the (0.0) band of the N_2 (2+) system increases in relative intensity with pressure and quenching effects occur only at higher pressures. Detailed studies of the excitation and emission processes have been performed by Muntz (13) and Camac (17).

In aeroballistic range applications, where operation of the technique at pressures as high as 10 torr is necessary to achieve free stream Reynolds numbers high enough to produce turbulent wakes, the N_2 (2+) (0.0) band is used because of its high intensity, its reduced sensitivity to quenching and its quasi-linear variation with gas density.   In this application, the fluorescence probe has two interesting features, namely an adequate space resolution and no mechanical interference. Thus discrete point measurements of density can be performed at any point in the flowfield, even on the projectile flight path.

The fluorescence probe instrumentation consists of an electron beam generator and a twelve-channel fluorescence detector system. A schematic layout of the apparatus is shown in Figure 5. The electron beam is produced outside the ballistic range tank and   is introduced inside through a water-cooled triple nozzle-skimmer arrangement installed at the end of a long drift tube evacuated by a three-stage differential-pumping system. The instrument is capable of producing a 100 Kv beam of 1 to 2 mA current with a diameter of 2 mm when it enters a test section at pressures as high as 10 torr. The detector set-up is made of three separate optical systems (Figure 5); each consisting of a single quartz lens and four slits defining four fields of view on the electron beam. A 12 stage photomultiplier measures the intensity of the light collected from each field of view within a spectral window determined by an interference filter centered at 3375Å with a 55Å bandwidth. The twelve fields of view measuring the fluorescence intensity at twelve positions along the electron beam are each 1.2 mm wide and 12 mm high. Figure 6 is a photograph of the inside installation of the test section showing on the right the 30 inch-long electron-beam drift tube with water-cooled exit -nozzles entering the ballistic range. Facing the drift tube, there is a collector cup. The three optical systems are shown at the top and bottom. The photomultiplier outputs are displayed on oscilloscope screens and photographed by high speed 35 mm cameras giving a time resolution of 4 microseconds throughout a record length of 0.3 second.

The recorded signals are digitized and analysed using a high speed digital computer. The analytical scheme takes into account the departure from linearity of the fluorescence intensity versus density curve and it corrects for the attenuation the electron beam experiences as it traverses regions of nonuniform gas density. To achieve this attenuation correction, an iterative technique makes use simultaneously of the information content of the twelve data channels recorded on each firing. A more detailed description of the calibration and of the signal analysis is given in reference 16.

3.0 MEAN CHARACTERISTICS OF THE WAKE

The data presented in this paper are the results of a total of 34 firings of spheres made at Mach 13 and at a $P_\infty D$ of 20 torr-inches. Fifteen 2.7 inch diameter spheres were launched for the electrostatic probe array technique. As mentioned earlier, the array consisted of eight axial pairs of probes located close to the flight axis in a transverse configuration. For one third of the firings, the transverse array was located symmetrically with respect to the flight axis. For the other firings, it was located to one side of the flight axis permitting a better coverage of the radial distribution. Eleven 0.59 inch diameter spheres were observed with the spark technique and radial profiles of velocity were measured at axial distances of 305, 715 and 1200 diameters behind the spheres. Finally eight 2.7 inch diameter spheres were observed by the electron beam experiment with ten detectors located asymmetrically with respect to the flight axis along the electron beam.

3.1 Velocity

The wake velocity is obtained from the probe array technique by cross-correlating 0.5 millisecond

segments of signals from axial pairs of probes (Figure 2). The time lag determined by the points of tangency of the straight line with the correlation curves is used in conjunction with the probe spacing (0.14D) to calculate a convection velocity. The coordinates of this velocity measurement are R/D, the radial distance between the probe tip and the flight axis and X/D, the axial distance in sphere diameters corresponding to the position of the projectile at the center of the 0.5 millisecond segment of signals. The value of R/D is exact for all practical purposes and X/D is known within 15 diameters because of the use of 0.5 millisecond segments. For each pair of probes, an axial characteristic of wake velocity is determined at a fixed radial distance. To obtain a radial profile of velocity with a reasonable number of data points, it is necessary to group the data covering a band of axial distance. Bands of 30, 60 and 100 diameters have been used and have shown consistent results. The logical approach is probably to use a narrow band at small axial distances and a larger band at large axial distances. Figure 7 shows a typical radial profile of velocity measured at an axial distance of 420 diameters. A band of axial distance of 60 diameters has been used in this case. The wake velocity (V_w) is normalized to the projectile velocity and the radial distance R to the sphere diameter. Study of a number of these radial profiles collected with the sequential spark and the probe array technique has revealed that the shape of the profile is well approximated by gaussian curves. The full curve in Figure 7 represents the least mean square fit of a gaussian expression of the form:

$$V_w/V_\infty = (V_0/V_\infty) \exp (-(R/r)^2)$$

where V_0/V_∞ and r/D are the parameters of the fit. V_0/V_∞ represents the wake axis velocity and r/D is a parameter related to the velocity radius. The standard deviation of the data with respect to the fitted curve (σ_X) is 0.015 or 0.236 when normalized to the wake axis velocity.

Velocity data from the sequential spark experiment comes out directly in the form of a radial profile measured at a predetermined axial distance in the wake (Figure 4). By using the same settings on each firing, a sample of radial profiles can be collected at the same axial distance. Figure 8 shows a typical sample of radial profiles measured at 305 diameters behind 0.59 inch diameter spheres. The full curve represents the gaussian curve fitted through the data. The open circles give the mean curve obtained from the data. It can be seen that the gaussian curve fits reasonably well. The standard deviation of the data with respect to the fitted curve is 0.137 when normalized to the axis velocity.

The least mean square fits of gaussian curves on the radial profiles of wake velocity yield two quantities, the axis velocity (V_0/V_∞) and the velocity profile radius (r/D), which are sufficient to fully characterize the mean velocity distribution in the turbulent core. Figure 9 shows the characteristics of axis velocity versus axial distance. Open circles represent the data collected with the electrostatic probe technique at a projectile velocity of 14,500 fps and at a $P_\infty D$ of 20 torr-inches. Open triangles represent the data collected with the spark technique under the same conditions. Good agreement is observed between these two sets of data. Also given (full triangles) are data obtained with the spark technique at a $P_\infty D$ of 40 torr-inches; a slight dependence of wake velocity on $P_\infty D$ is apparent at small axial distance (X/D < 1000). The velocity decay follows a power law of minus unity in the region from 300 to 1000 diameters. The 90% confidence interval on the axis velocity is indicated. A restriction is placed on the level of confidence as the theory used to calculate it (18) is exact for linear regressions only, which is not the case for the gaussian curve. Open squares refer to mean wake velocities measured by Fox and Rungaldier (19) using hot wire and cooled film anemometers under conditions widely different from those used with the probe array and the spark techniques ($V_\infty = 6,000$ fps and $P_\infty D = 380$ torr-inches). These data extend into the far wake where the asymptotic -2/3 power law decay is observed. Agreement of the anemometer data with the probe array and the spark data in the intermediate wake (X/D < 1000) is considered a pure coincidence due to the opposing action of three different factors: the strong dependence on Mach number (3) tends to decrease the velocity ratio (V_0/V_∞) measured by the anemometer technique; the relatively weaker dependence on $P_\infty D$ tends to increase it, while the off-axis effect tends to decrease it.

Figure 10 shows the velocity radius data derived from the least mean square fits of gaussian curves for the same sets of probe array and spark data presented in Figure 9. Again probe array and spark data show good agreement. The width of the velocity profiles seems to be independent of $P_\infty D$ and this observation is corroborated by measurements made at the same Mach number and at a $P_\infty D$ of 100 torr-inches with the spark technique (20). The data follow a 1/3 power law growth past 300 sphere diameters. Below 300 diameters, the velocity radius seems to be constant. A similar behavior is observed on measurements made at 9000 fps and 100 torr-inches with the spark technique (20). The velocity radius data in Figure 10 are compared with data measured from schlieren photographs of the turbulent wake. Despite the fact that the schlieren data cover almost an order of magnitude of variation in $P_\infty D$, no $P_\infty D$ dependence can be detected. The 90% confidence level in the case of the schlieren data is an exact level which has been calculated with the "t" distribution to correct for sample size. The full line represents the 1/3 power law which has been fitted to the schlieren data. The schlieren radius is appreciably larger than the velocity radius at large axial distances. The two radii coincide at about 300 sphere diameters and below this point, the schlieren radius is smaller than the velocity radius.

Comparisons of the wake axis velocity and of the velocity radius of Figures 9 and 10 measured at Mach 13 and at a $P_\infty D$ of 20 torr-inches shows good agreement between the probe array and the sequential spark techniques. However a better indication of this agreement is obtained from the comparison of the original velocity data. Figures 11 and 12 show comparisons of the raw velocity data collected with both techniques under the above mentioned conditions. Figure 11 shows the data measured at radial distances from 0.8 to 0.9 diameters and Figure 12. the data measured at radial distances from 1.6 to 1.7 diameters. In Figure 11, the spark data (full circles) shows slightly higher velocity than the probe array data (open circles) at small axial distances. The two techniques observe roughly the same scatter in the velocity. These two graphs illustrate the remarkable agreement of the two techniques.

3.2 Density and Temperature

The density distribution in the wakes of hypersonic spheres is measured with the electron beam fluorescence probe technique as described earlier. The data were collected on eight firings of 2.7 inch

spheres launched at a velocity of 14,500 ft/s in a nitrogen atmosphere at 7.6 torr ($P_\infty D$ - 20 torr-inches) The data extends up to 3000 body diameters in the axial direction and covers from -1.0 to 3.5 body diameters in the radial direction.

At each radial position, the density measured is averaged over an axial length travelled by the projectile corresponding to a length of wake of approximately 1 body diameter convected by the measuring station. The appropriate axial length is calculated from the center-line velocity ratio determined by the sequential sparks and by the electrostatic probes. The mean density estimate thus obtained is plotted for each radial position at a given axial position as shown in Figure 13. On this radial distribution, an analytical expression of the form

$$\frac{\rho}{\rho_\infty} = \frac{A}{(1-A)\ \exp\ (-(R/D)^2/B)\ +\ A}$$

where A and B are parameters, is fitted by the least mean square method. The parameter A corresponds to the center-line density ratio ρ_0/ρ_∞, while the overall expression is used to evaluate the radius of the wake by calculating the half-width of the distribution at the 1/e height. To compare with the L.M.S. fit, the density ratio averaged every ten points has been computed. The error bars correspond to the scatter of the data about the average value. This data reduction procedure has been applied at every axial position from 30 to 3000 body diameters. The center-line density defect as obtained from the radial profiles is presented in Figure 14. The density defect decreases very slowly and does not achieve a constant decay rate before approximately 800-900 diameters where a -2/3 power law is a good representation. The 90% confidence level noted on each point is computed from the L.M.S. fit on each radial profile.

The wake radius variations with axial distance behind the hypersonic sphere have been evaluated making use of the analytical expression for the radial profile for each axial position and are shown in Figure 15. The wake density radius is compared with the fitted schlieren radius curve already presented in Figure 10. Up to 200 diameters, the density radius is larger than the schlieren radius. This observation suggests that the density profiles measure the inviscid wake radius until the viscous core has grown into the inviscid layer. Further than 200 diameters, the wake radius defined by the density profiles stays smaller than the radius measured from the schlieren photographs. Comparison of these data with the wake radius data obtained from the velocity profiles measured with the electrostatic probes and with the sequential sparks (Figure 10),shows a very similar behavior. One should also keep in mind that, when the wake radius exceeds 3.0 diameters, the radial density profiles are not well defined as there are no data further than 3.5 diameters from the wake axis.

If one assumes that the gases in the wake follow the perfect gas law and that the pressure behind the model rapidly reaches an equilibrium with the ambient pressure (21), then the density measurements may be used to infer the temperature distribution. Under these assumptions and ignoring compressibility, the center-line temperature defect has been inferred from the center-line density ratio and is shown in Figure 16. The temperature begins its decay earlier behind the model than does the density defect and it is best represented by a -1 power law. A similar behavior has been observed for the variation of the velocity defect, as shown in Figure 9.

4.0 TURBULENT CHARACTERISTICS OF THE WAKE

The knowledge of the turbulent characteristics constitutes an important requisite if good modeling of the wake is to be achieved. The ability of some of the experimental techniques to measure the turbulent characteristics may be questioned because of inherent averaging in the measuring processes. However, it is possible to obtain some useful indications from all experiments. Short-comings of the techniques will be discussed as the data are presented. Some discussion is given concerning the question as to whether the wake measured under the present ambient conditions is, in fact, fully turbulent. With a free-stream Reynolds number of 2×10^5 based on body size, the transition of the wake from laminar to turbulent can be expected to occur at some axial distance behind the sphere. Information bearing on the transition and intermittency aspects of the wake flow is available from the measurements however, and provides a considerable amount of insight into these topics.

4.1 Velocity and Density Fluctuations

Measurements of velocity with the probe array and the spark technique,and of mass density with the electron beam technique all exhibit some scatter of the data as illustrated by the radial profiles of Figures 7, 8 and 13. Under the assumptions of normality and of uniform standard deviation across the radial profile, the standard deviation of the data with respect to the fitted radial profile can be used as an indication of the scatter provided the fitted curve follows the data reasonably well. Comparison of the standard deviation about the fitted curve with the so-called pure standard deviation measured about the mean profile for a large number of radial profiles shows consistent results and indicates that the lack of fit is not too important. Figure 17 shows the standard deviation of the data about the fitted radial profiles for the velocity and density data presented earlier. To facilitate comparison between the velocity and density data, the standard deviation has been normalized to the axis velocity and to the axis density defect respectively. The 95% confidence levels calculated from the χ^2 distribution are also given. All four sets of data show a weak trend of an increasing ratio of rms fluctuation level to mean level with increasing axial distance. Data measured by the spark technique at $P_\infty D$ of 20 and 40 torr-inches show identical levels of scatter.

A marked difference in the absolute level of scatter is observed between the three experimental techniques. This difference is not unexpected in view of the different averaging in the measuring and the data reduction processes. Examination of these processes furnishes some explanation of the observed difference in the level of fluctuations. The correlation over a segment of signal of 0.5 millisecond duration from axial pairs of electrostatic probes can be expected to give an average velocity representative of the length of wake convected by the probes during the time of measurement. This measurement must

not be confused however, with the well-averaged convection velocity measurements that can be made in a low speed jet, for example. Wake measurements are transient measurements. In most cases, the probe signal correlation is dominated by the most strongly ionized blob in the segment of signal and for this reason, the probe velocity estimates are less averaged and more instantaneous than might be expected. A more basic way of looking at the averaging is to examine the quantities required for the determination of velocity: distance and time. The time lag determined by the correlation is dependent on the wake velocity and consequently increases with axial distance. The distance over which the velocity is estimated is equal to the separation of the axial pairs of probes. This distance is 0.14 sphere diameter. The velocity measured is an average velocity along that distance. The measurements of velocity with the spark technique presents a good analogy to the measurements with the probe array technique. The interval between consecutive sparks is adjusted at each axial distance to obtain a displacement of about half a body diameter on the axis of the wake and a smaller displacement at the edge. For purposes of comparison with the probe array, a value of one quarter of a body diameter can be used. The volume of gas seen by the detectors in the electron beam experiment is determined by the diameter of the beam which varies from 2 to 8 mm along its useful length because of Coulomb spreading. Perpendicular to the beam, the field of view is limited by a slit to 1.2 mm. These dimensions are very small compared with the projectile diameter (2.7 inches) and consequently the averaging should not be important. Averaging in this case comes from the data reduction process. As explained earlier, estimates of density comes from axial segments of wake varying in length between 1.0 and 2.4 sphere diameters. As a conclusion, it can be said that some of the difference in the level of fluctuations observed with the three techniques can be explained in terms of the averaging produced by each experiment; the absolute level of fluctuations are higher than those measured here because of the averaging and the trend towards an increasing level of fluctuations with increasing axial distance is probably real.

4.2 Transition

For the launched conditions of most of the 2.7 inch diameter spheres fired to obtain the present data (Mach 13 and 7.6 torr), the freestream Reynolds number (per foot) is almost 10^6. The Reynolds number based on sphere diameter is consequently about 2×10^5, and from the data of Wilson (22), the normalized transition distance is about 7 diameters behind the projectile. The program from which the present results were derived was undertaken to provide the data on turbulent wakes which could be used for theoretical modeling. The state of the turbulence in the wake is thus of considerable importance. It is asserted in the literature on the basis of schlieren studies (22) that in general behind blunt bodies, transition occurs abruptly from straight laminar flow to what appears to be well-developed turbulence within a few body diameters. However some observations made on our 7.6 torr, 2.7 inch diameter sphere data lead us to express some reservations regarding the character of the turbulence in the first two or three hundred body diameters of wake behind such spheres. In the near wake (X/D less than 100 D), signal detected by arrays of electrostatic probes seems deficient in higher frequency components; higher frequency components make their appearance in the axial distance region extending from about 100 to 300 diameters (Figure 18). Examination of the statistics of the turbulent interface or intermittency indicates that in the near wake the standard deviation of the front radius with respect to the mean radius is in fact larger at 7.6 torr than it is at higher pressures. The same remark can be made regarding the size of scales at 7.6 torr and higher pressures. There is some reason to believe that at $P_\infty D = 20$ torr-inches, the turbulent fluctuations in the near wake of a 2.7 inch diameter sphere as seen by ion probes resemble something that one might expect to detect in a quasi-laminar unstable flow.

4.3 Intermittency

If a probe, such as a hot wire, were immersed in a turbulent fluid, and the electrical signal from the probe were found to contain bursts of random signal variation separated by periods of zero-fluctuation quiescent signal, then, provided the probe apparatus was not defective, the turbulent fluid would be said to be intermittent. Intermittency at a point in a turbulent fluid can be estimated by comparing the average ratio of the time duration of turbulent signal to the total time. In a turbulent wake as in a turbulent jet, intermittency generally tends to unity on the axis of the flow and falls toward zero as one moves away from the axis towards the boundaries.

The intermittency of the wake of 2.7 diameter hypersonic spheres launched at 7.6 torr has been estimated from the raw signal data of the survey array of electrostatic probes. Very simply, the signal of each probe in an array data round, which corresponds to one value of R/D (normalized radial distance) has been divided up into consecutive 0.5 millisecond segments, and the intermittency calculated for each segment. There is always a continuous overall decay in the charge density levels with increasing axial distance in the wake behind a hypersonic sphere; nevertheless, intermittency was estimated by designating relatively featureless segments of signal as being laminar, the other portions as turbulent, and subsequently calculating the percentage of turbulent fluid. The value of intermittency was attributed to the axial distance X/D pertaining to the middle of 0.5 millisecond segment being measured. Calculations of intermittency as a function of radial distance were thus prepared for each data round as a function of R/D and X/D.

Mathematically, the intermittency factor Γ can be written as

$$\Gamma (y) = \text{prob} \left[y \leqslant Y(t) \leqslant \infty \right]$$

where y is a variable representing radial position with respect to the wake and Y (t) the instantaneous location of the front between turbulent and non-turbulent fluid. If one assumes a gaussian distribution function for Y (t), the intermittency factor may be written as

$$\Gamma (y) = \frac{1}{2} \left[1 - \text{erf} \frac{(R/D - \delta/D)}{\sqrt{2} \ \sigma/D} \right]$$

where

$$\text{erf } x \cdot \frac{1}{\sqrt{\pi}} \int_0^x \exp\ (-\xi^2)\ d\xi$$

and the two fittable parameters in this expression are δ/D, the normalized average position of the turbulent interface and σ/D, the standard deviation of the gaussian distribution.

The above expression has been used to fit the intermittency data. The mean intermittency radius (normalized to the projectile diameter) δ/D derived from these fits is shown in Figure 19 by the open circles. The solid line is the schlieren wake radius represented by $0.4(X/D)^{1/3}$ appropriate to Mach 13, the intermittency wake radius is apparently seen to also follow the $(X/D)^{1/3}$ law in the near wake, although the mean intermittency radius is only about 2/3 of the schlieren wake radius.

The standard deviation describing the distribution of the interface about the mean position estimated by the fits is given in Figure 20, again by the open circles. Comparison with DREV data at higher pressure shows similar behavior, although σ/D is larger at low pressure. Also shown are data at approximately Mach 14 obtained by Schapker (23) and by Levensteins and Krumins (24) from measurements of wake edge statistics on schlieren photographs. The Reynolds number range is also very similar to that employed at DREV. It is apparent that the DREV survey array probe data is consistently higher than the other data, by at least a factor of 2. Nevertheless the trend of the data is reasonably similar. Since the ion probe makes a point measurement while some degree of integration must be assigned to the schlieren wake radius measurements, the gap in the data comparison is at least in the right direction.

4.4 Space Scales

Scale data have been estimated from the pairs of ion probes constituting the individual axial pair elements in the survey array. The distribution of scale data was found to be independent of radius at any given axial distance behind the projectile. Accordingly the data is plotted as a function of axial distance in Figure 21, showing the position of the quartile points, i.e. 50% of the scale data falls between the lower and upper quartile points. In the 7.6 torr scale data a number of points have been removed at X/D values near 100 because they indicated scales greater than one sphere diameter, and were considered to be representative of laminar instabilities rather than turbulence.

Independent effort at DREV has indicated that the ion probe current data at 7.6 torr is dominated by scalar quantities. Nevertheless the scale data estimated from the probe results falls below data measured at other laboratories. Figure 21 also shows contrast fluctuation scale data from schlieren measurements at MIT (25) and $P_\infty D$ of 16 torr-inches and scale data from anemometer measurements on spheres at Mach 5 by Fox and Rungaldier at TRW (19). The scale data from the anemometer indicated by the small open squares lying closest to the DREV data is actually sensitive to velocity fluctuations, the other data representing scalar temperature fluctuations lies further from the curves. Generally it appears that DREV ion probe scale data lies below similar data obtained at other laboratories.

5.0 MOMENTUM DEFECT

The momentum defect or drag can be calculated at each axial station in the wake, using the radial distributions of velocity and density, from the following expression:

$$\frac{C_D A}{D^2} \cdot 4\pi \int_0^\infty \frac{V}{V_\infty}\ \frac{\rho}{\rho_\infty}\ (1-\frac{V}{V_\infty})\ \frac{R}{D}\ d(\frac{R}{D})$$

where C_D is the drag coefficient which is assumed to be equal to 0.9 for hypersonic spheres. This expression has been evaluated using the fitted gaussian curve on the radial profile of velocity and the fitted expression on the density profile at an axial distance of 320 diameters. Figure 22 shows curves of the velocity and the density profiles together with a curve of the integrand of the expression given above. The vertical dotted line indicates the position of the turbulent front determined from schlieren measurements (Figure 10). A value of 1.5 is obtained from $C_D A/D^2$. This value is more than twice as large as the expected value of 0.7 for the total momentum defect. This large discrepancy can be attributed, in large part, to the long tail of the fitted gaussian function representing the radial profile of velocity. The velocity data used to fit the gaussian expression cover a radial distance from 0 to about 2.5 diameters (Figure 8). Indications have been obtained on measurements at 9000 ft/s. with the spark technique (20) that the gaussian curve does not fit at the edge of the turbulent wake because of the abrupt fall off of the velocity in the inviscid region. Furthermore, the velocity data shown in Figure 8 are biased toward high velocity at large R/D because low velocity data have been neglected due to the lack of resolution of the technique. For these reasons, the integrand curve in Figure 22 is not realistic beyond R/D = 2.5 or 3.0 diameters and this curve should decay much more abruptly to zero past that point.

An attempt has been made to use the intermittency data of Figures 19 and 20 measured with the probe array technique to obtain a more rapid fall-off of the gaussian curve at the edge of the wake. A least mean square fit of a modified gaussian:

$$V/V_\infty = (V_0/V_\infty)\ \exp\ (-(R/r)^2) \cdot \ \Gamma\ (R/D,\ \delta/D,\ \sigma/D)$$

has been made on the velocity data of Figure 8 where $\Gamma\ (R/D,\ \delta/D,\ \sigma/D)$ is the intermittency factor. Values of 2.1 for δ/D and of 0.84 for σ/D have been used in the calculation. The result is shown in Figure 23. The fitted axis velocity remained about the same as in the previous fit and the profile radius (defined by $(V_0/V_\infty)/e$) decreased from 2.5 to 2.2D. Using this new expression for the velocity, a value of 0.9 has been obtained for $C_D A/D^2$. This value is considerably smaller than in Figure 22 but still higher than the expected value of 0.7. No attempt has been made to correct the density using the intermittency data. Such a correction would tend to increase the value of the integral. The value obtained for $C_D A/D^2$ is reasonable in view of the poor knowledge of the velocity distribution at the edge of the wake.

6.0 CONCLUSIONS

Spatially-resolved velocity distributions measured by the sequential spark technique and by survey arrays of ion probe axial pairs are in excellent agreement under conditions of similar Mach number and equal $P_\infty D$ values.

The velocity distribution is well fitted by gaussian expressions of the form $(V_0/V_\infty)\exp\left(-(R/r)^2\right)$, except perhaps at the edges of the turbulent core. The axial parameter V_0/V_∞ decays slowly until about 300 diameters behind the projectile; between 300 and 1000 diameters it appears to decay as the minus unity power of normalized axial distance (X/D). The velocity radius remains relatively constant until 300-400 diameters where it equals the schlieren radius. Thereafter it appears to be increasing as the 1/3 power of normalized axial distance (X/D).

The density profile data has been fitted reasonably well by an analytical expression containing amplitude and width parameters. The axial density defect $(\rho_\infty - \rho_c)/\rho_\infty$ decays slowly until about 800-900 diameters, thereafter it decays with an apparent minus 2/3 power law. The wake density radius is greater than the schlieren radius until about 200 diameters behind the projectile, thereafter the density radius remains smaller than the schlieren radius. Temperature defect data on the wake axis derived from density data by ignoring compressibility appear to decay with a minus unity power law, apparently from the region of X/D of about 300, similar to the behavior of axial velocity.

Velocity and mass density fluctuation data have been estimated assuming uniformity of the standard deviation across the wake with respect to the fitted mean profiles, and normalizing by the appropriate velocity or density defect. Because of the inherent averaging in the methods of analysis employed by the various experimental techniques, these results, which run between 10 and 20 percent for density and 20 and 30 percent for velocity, probably underestimate the true rms fluctuation levels. There is an apparent trend towards increasing fluctuation levels between 100 and 1000 diameters of axial distance X/D.

While transition should occur within about seven diameters from the neck for a 2.7 inch sphere wake at 7.6 torr, observations on ion probe signals indicate that the wake may be less than fully turbulent out to somewhere between 100 and 300 diameters. Intermittency and scale data at 7.6 torr with these spheres apparently indicate higher standard deviation of the turbulence interface and larger scale sizes in the near wake than at higher ambient pressures.

Intermittency data estimated from the signals from individual probes in the survey array of ion probes have been fitted with gaussian distribution functions. The resulting intermittency radius data appear to lie on a power law curve of about 2/3 of the schlieren wake radius. The standard deviation, normalized to the sphere diameter, describing the position of the interface is about twice as large as comparable data from schlieren wake radius measurements.

Space scale data from pairs of ion probes decrease with axial distance X/D in the region between 100 and 1000 diameters behind the projectile, becoming quite small compared to the schlieren radius. These data appear to lie well below Mach 16 contrast fluctuation scale data and Mach 5 anemometer data.

An attempt has been made to use the measured velocity and density profile data to calculate momentum in the wake. If the fitted distributions to the data are employed in the calculation, a value of $C_D A/D^2$ equal to 1.5, or more than twice the expected value of 0.7, is obtained. The reasons for the discrepancy are related to the fact that the major contribution to the integrand in the integral expression for C_D comes from the regions of the wake edge where the distributions are ill-defined and where the gaussian distribution is a poor fit to the data. When the velocity distribution was refitted with a gaussian distribution modified by the intermittency function, an improved fit to the velocity data was obtained and the value of $C_D A/D^2$ was estimated at 0.9.

7.0 ACKNOWLEDGEMENTS

(1)   D. Heckman, L. Tardif, and C. Lahaye, "Experimental Study of Turbulent Wakes in the CARDE Free-Flight Range", Proceedings of the Symposium on Turbulence of Fluids and Plasmas, Vol. XVIII, Polytechnic Press of the Polytechnic Institute of Brooklyn, N.Y. 1968.

(2)   C. Lahaye, E.G. Léger, and A. Lemay, "Wake Velocity Measurements Using a Sequence of Sparks", AIAA Journal, Vol. 5, No. 12, pp. 2274-2276, December 1967.

(3)   C. Lahaye, L. Jean, and H. Doyle, "Velocity Distributions in the Wake of Spheres", AIAA Journal, Vol. 8, No. 8, pp. 1521-1523, August 1970.

(4)   D. Heckman, A. Cantin, A. Emond, and A. Kirkpatrick, "Convection Velocity Measurements in Hypersonic Wakes", AIAA Journal, Vol. 6, No. 4, pp. 750-752, April 1968.

(5)   L. Tardif, and J.G.G. Dionne, "Density Distribution in Turbulent and Laminar Wakes", AIAA Journal, Vol. 6, No. 10, pp. 2027-2029, October 1968.

(6)   A. Tate, P.W.W. Fuller, C.R. Wall, "Double Langmuir Probes for Hypervelocity Wakes", IEEE Trans-

actions on Aerospace and Electronic Systems, Vol. AES-3, No. 2, pp. 309-320, March 1967.

(7)   R.E. Slattery, W.G. Clay, and J. Herrmann, "Gas and Electron Density Fluctuations in a Weakly Ionized Hypersonic Wake", Proceedings of the Symposium on Turbulence of Fluids and Plasmas, MRI Symposia Series, Vol. XVIII, Polytechnic Press, 1970.

(8)   I.P. French, T.E. Arnold, and R.A. Hayami, "Ion Distributions in Nitrogen and Air Wakes Behind Hypersonic Spheres", AIAA Paper No. 70-87, presented at the AIAA 8th Aerospace Sciences Meeting, January 10-21, 1970.

(9)   A. Cantin, A. Emond, and D. Heckman, "Observations on Electrostatic Probe Behavior in Collision-Dominated Ionized Turbulent Gas Flows in Ballistic Ranges", ICIASF '69 Record of the 3rd International Congress on Instrumentation in Aerospace Simulation Facilities, pp. 20-33, May 1969.

(10)   M.J. Fisher, and P.O.A.L. Davies, "Correlation Measurements in a Non-Frozen Pattern of Turbulence", Fluid Mechanics, Vol. 18, No. 1, pp. 97-116, January 1963.

(11)   D. Heckman, A. Emond, A. Fitchett, and L. Sérigny, "Mean and Fluctuating Charge Density Measurements in Turbulent Hypersonic Sphere Wakes", ICIASF '71 Record, presented to the 4th ICIASF Congress, Von Karman Institute, Rhode-Saint-Genèse, June 21-23, 1971.

(12)   C. Lahaye, E. Léger, M. Dufresne, H. Doyle, and P. Soucher, "The Sequential Spark as a Tool for Wake Velocity Studies in Ballistic Ranges", ICIASF '71 Record, presented to the 4th ICIASF Congress, Von Karman Institute, Rhode-Saint-Genèse, June 21-23, 1971.

(13)   E.P. Muntz, "The Electron Beam Fluorescence Technique", AGARDograph 132, December 1968.

(14)   J.G.G. Dionne, et al., "Mass Density Measurements in Hypersonic Wakes", AGARD Conference Proceedings No. 19, Fluid Physics of Hypersonic Wakes, Colorado State University, May 1967.

(15)   J.G.G. Dionne, and L. Tardif, "Mean Density and Temperature Data in Wakes of Hypersonic Spheres", AIAA Journal, Vol. 8, No. 9, pp. 1707-1709, September 1970.

(16)   J.G.G. Dionne, and L. Tardif, "An Application of the Electron Beam Fluorescence Probe in Hyper-ballistic Range Wake Studies", ICIASF '71 Record, presented to the 4th International Congress on Instrumentation in Aerospace Simulation Facilities, Von Karman Institute for Fluid Dynamics, Rhode-Saint-Genèse, Belgium, June 21-23, 1971.

(17)   M. Camac, "Flow Field Measurements with an Electron Beam", AIAA Paper 68-722, 1968.

(18)   N.R. Draper, and H. Smith, "Applied Regression Analysis", Chapter X, John Wiley & Sons, Inc., 1966.

(19)   J. Fox, and H. Rungaldier, "Anemometer Measurements of Velocity and Density in Projectile Wakes", AIAA Journal, Vol. 9, No. 2, pp. 270-276, February 1971.

(20)   C. Lahaye, "Velocity Distributions in Sphere Wakes", to be published.

(21)   P.S. Lykoudis, "A Review of Hypersonic Wake Studies", AIAA Journal, Vol. 4, No. 4, pp. 577-590, April 1966.

(22)   L.N. Wilson, "Body-Shape Effects on Axisymmetric Wakes: Transition", AIAA Journal, Vol.4, No. 10, pp. 1741-1747, October 1966.

(23)   R.L. Schapker, "Turbulence Front Statistics of Wakes from Bodies in High-Speed Flight", ISD-TR-65-158, Research Report 217, AVCO Corporation, June 1965.

(24)   Z.J. Levensteins, and M.V. Krumins, "Aerodynamics Characteristics of Hypersonic Wakes", AIAA Journal, Vol. 5, No. 9, pp. 1596-1602, September 1967.

(25)   J. Herrmann, R.E. Slattery, and W.G. Clay, "Measured Properties of the Wakes of Hypersonic Cones", AIAA Paper 68-687, Los Angeles, California, 1968.

Fig 1. Survey array of ion probes
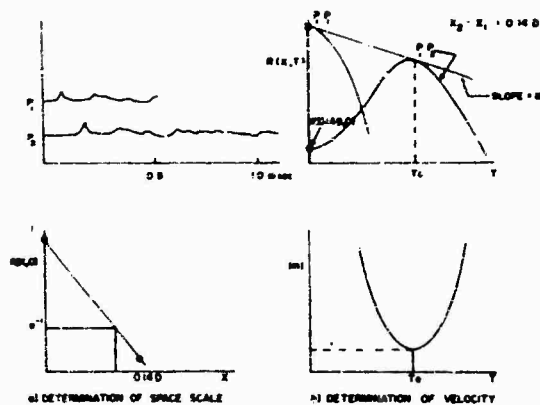
Fig 2. Scales and velocity determination
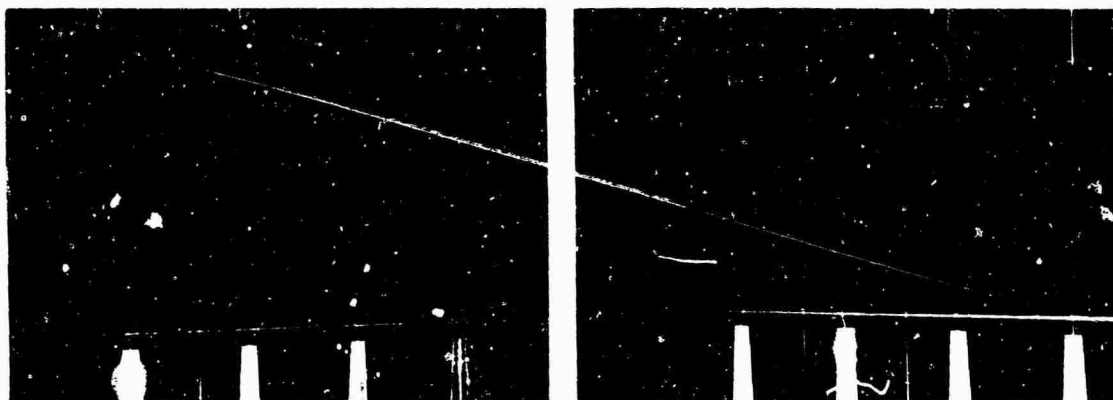
Fig 3. Stereo photographs of 4 spark sequences. Sequence 1 produced the result in Fig 4
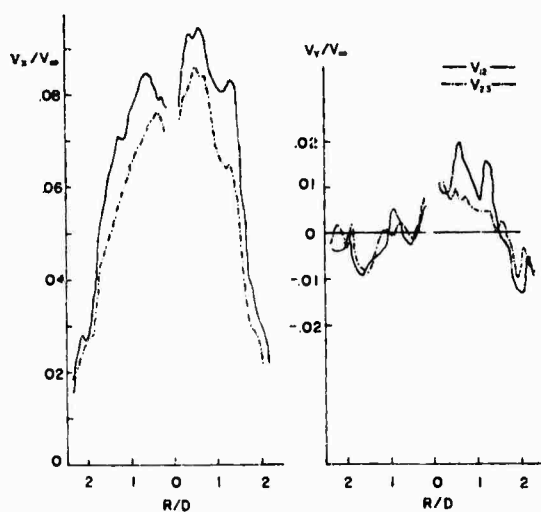
Fig 4. Typical velocity profile from sparks
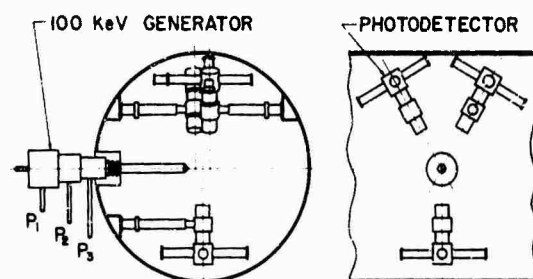
Fig 5. Electron beam experiment schematic

Fig 6. Electron beam apparatus

Fig 7. Radial profile of wake velocity from the ion probe array

Fig 8. Radial profile from sparks
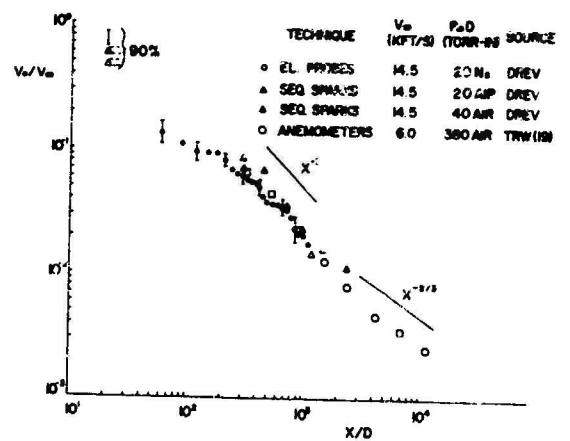
Fig 9. Axis velocity in sphere wakes

Fig 10. Velocity profile radius in wake sphere
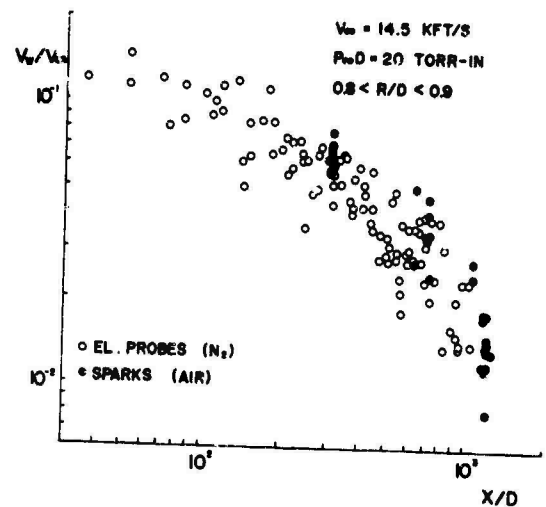
Fig 11. Comparison of velocities measured in sphere wakes with the probe array and the spark techniques at radial distances from 0.8 to 0.9 diameter
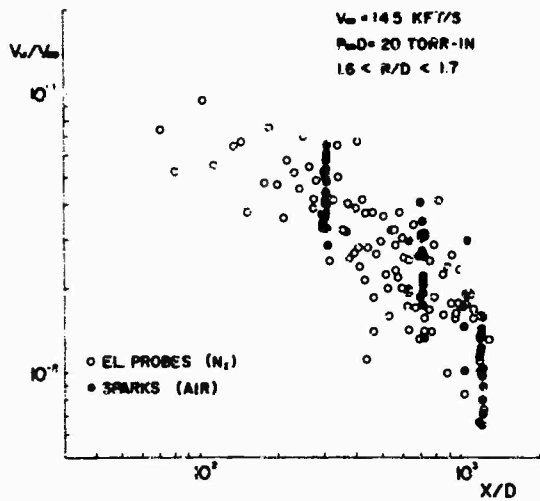
Fig 12. Comparison of velocities measured in
sphere wakes with the probe array
and the spark techniques at radial
distances from 1.6 to 1.7 diameters

Fig 13. Radial profile of density in the wake

Fig 14. Density defect on axis of wake
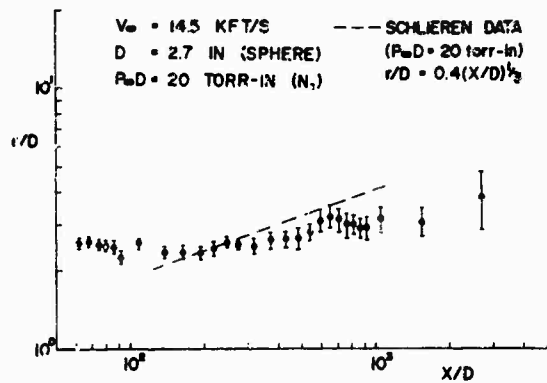
Fig 15. Radius of wake density profile

Fig 16. Temperature defect on axis of wake
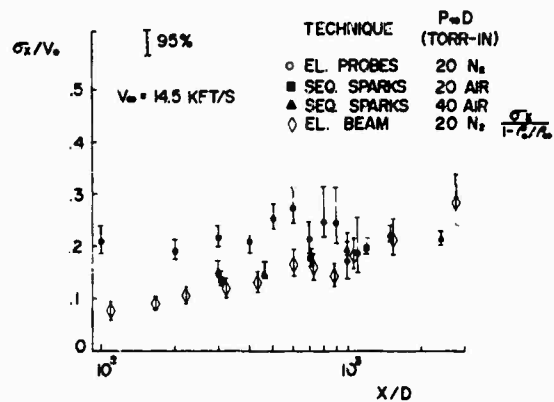
Fig 17. Apparent "intensity" of velocity
and density fluctuations in wake
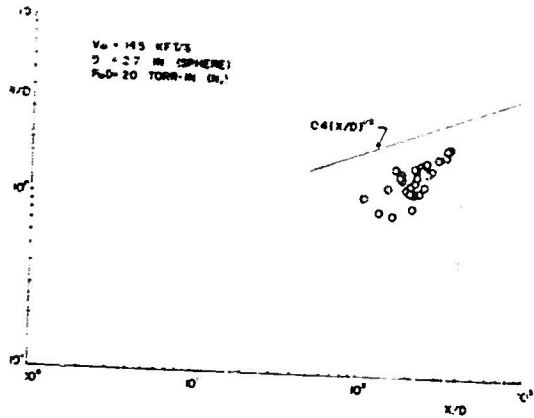
Fig 18. Position of wake transition
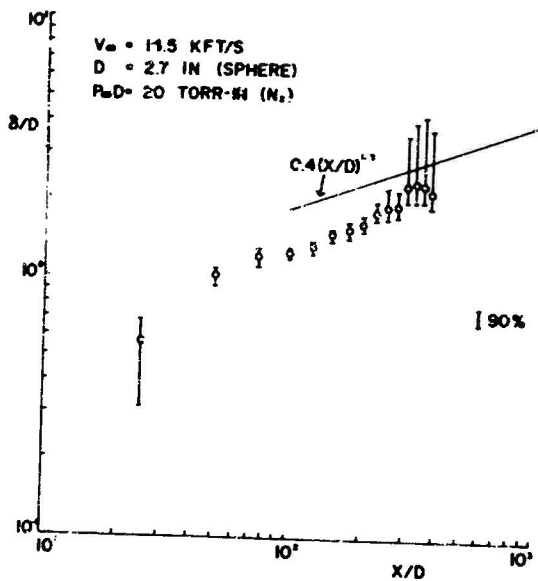
Fig 19. Mean position of turbulence interface or the intermittency radius
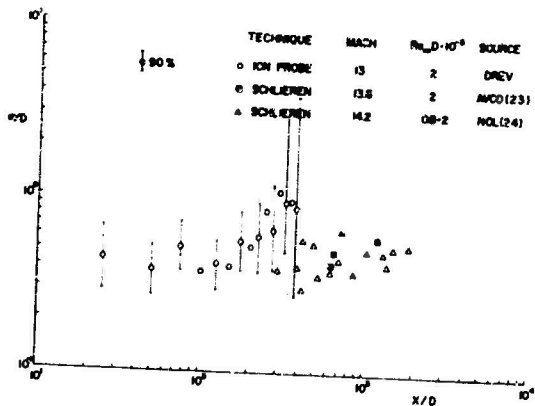
Fig 20. Standard deviation of the position of the turbulence interface
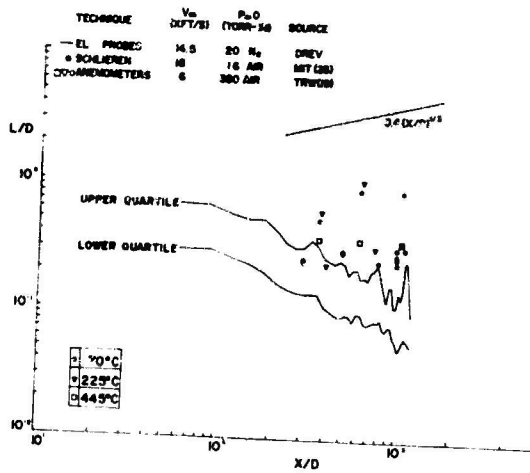
Fig 21. Comparison of space scales measured in sphere wakes
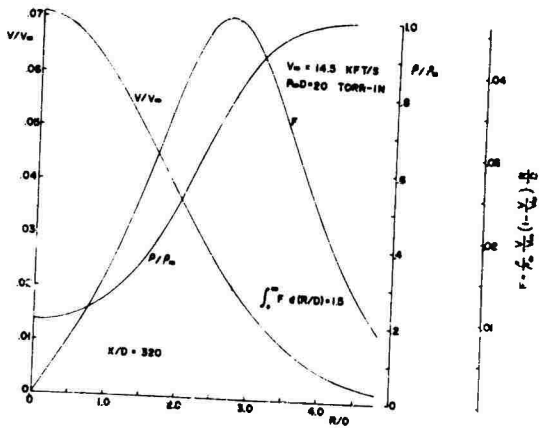
Fig 22. Calculation of the momentum defect from the radial profiles of velocity and density determined by fitting the data obtained by experimental measurements
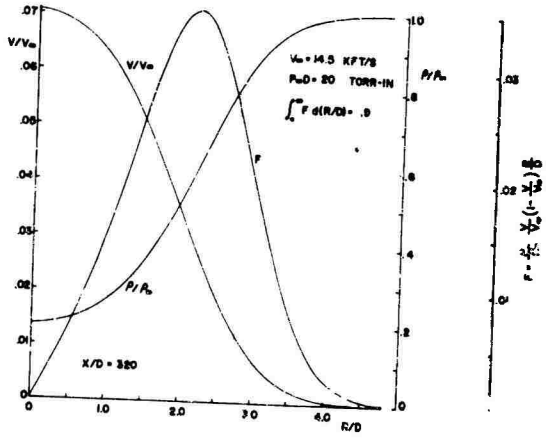
Fig 23. Calculation of the momentum defect. In this case the fit to the velocity curve is modified from that in Fig 22 by the introduction of the intermittency function

MEASUREMENTS OF THE INSTANTANEOUS SPATIAL DISTRIBUTION OF A PASSIVE SCALAR IN AN AXISYMMETRIC TURBULENT WAKE

by

Arthur M. Schneiderman[*]

Avco Everett Research Laboratory, Everett, Mass. U.S.A. 02149

SUMMARY

The spatial mixing field in the turbulent wake of a longitudinally aligned truncated cylinder at a Mach number of 2.5 and a Reynolds number of 10^6 (based on diameter) is observed experimentally using the laser planogram technique. The instantaneous spatial distribution of a tracer material introduced at the model is characterized statistically by estimates of the probability density function, energy spectrum and autocovariance coefficient of the measured fluctuations. Wake axis measurements over the region from 138 to 182 body diameters yield turbulent concentration fluctuations of 25% and skewness and kurtosis of +0.18 and +0.16, respectively. A centerline intermittency of approximately 82% is observed. A classical turbulence spectrum with a well defined break from a flat to a $k^{-5/3}$ inertial subrange is found. The autocovariance coefficient yields a macroscale which is approximately half the transverse scale length. The wake boundary is observed to be substantially more contorted than had previously been suspected.

NOTATION

α	characteristic response frequency	M_K	central moments of the probability density function
β	Kolmogoroff constant		
ϵ	turbulent eddy viscosity	$\dot{m}_c$	mass flow rate of carrier gas
θ	scattering angle	$\dot{m}_p$	mass flow of particulates
κ	numerical factor for drag coefficient	m	magnification: image size/object size
λ	wavelength of the light source	n	local number density of scattering centers
λ_g	Taylor microscale	n_o	number density of scattering centers in the aerosol generator
Λ	integral scale		
μ	viscosity	PSD	power spectral density
ν	kinematic viscosity	R	distance of the lens from the light sheet
ξ	lag of the autocovariance coefficient	r	power law exponent for σ^2 vs Z
ρ_∞	free stream gas density	Re_λ	turbulence Reynolds number based on u', λ_g, and ν
$\rho_{A\ell}$	mass density of solid aluminum		
ρ_c	density of carrier gas in aerosol generator	R_T	turbulence Reynolds number based on u', L, and the turbulent eddy viscosity
ρ_p	mass density of particulate matter	S	skewness
σ	standard deviation of the concentration fluctuations	s	distance of the film from the lens
		S_o	light scattered by an individual particle
σ'	standard deviation of the wake boundary	t	light sheet thickness
		u'	rms velocity fluctuation
ϕ	phase angle between particle and fluid velocities	u_f'	fluctuating fluid velocity
		u_p'	particle velocity
χ	turbulent dissipation rate of a passive scalar	u_f^p	amplitude of fluid velocity
		u_p^p	amplitude of particle velocity
ω	angular frequency	V_∞	free stream velocity
		V_w	local mean wake velocity
		Z	axial coordinate measured from the end of the cylinder
A	cross sectional area of the cylinder		
A_w	local mean wake cross sectional area	Z_o	virtual wake origin
$\bar{c}$	mean tracer concentration		
C_D	drag coefficient		
$C(k_e\xi)$	autocovariance coefficient		
d	particle diameter		
D	diameter of the cylinder		
$\mathcal{D}$	dilution factor		
D_ℓ	lens diameter		
e	laser planogram film exposure		
E	energy of the light sheet		
F	lens focal length/diameter		
f	temporal frequency		
f	lens focal length		
h	height of the light sheet		
i_1, i_2	Mie scattering parameters		
I	turbulent intensity $= \sigma/\bar{c}$		
K	kurtosis		
k	wave number		
k_e	energy containing wave number		
k_K	Kolmogoroff wave number		
k_n^K	Nyquist wave number		
L	transverse scale length (Eq. 5)		
ℓ	mean free path		
M	Mach number		

---

[*]Principal Research Scientist

1. INTRODUCTION

The concentration field of a passive scalar material in a turbulent flow depends on both spatial and temporal coordinates. In order to more fully understand scalar mixing mechanisms, it is necessary to measure this dependence. However, such a full specification of the flow field would clearly represent a monumental experimental task. The majority of past turbulence measurements have involved a determination of the temporal history at one or perhaps two discrete points in space. From these temporal statistics, the characteristics of the spatial field are deduced using Taylor's hypothesis, either directly or with modification in the form of space-time correlations. The use of these methods can be questioned in shear flows, especially when large scale turbulent structure is considered, since such flows are in general both inhomogeneous and anisotropic.

To obtain further insight into turbulent mixing, an instantaneous spatial mapping of a turbulent shear flow has been undertaken. Previous techniques, such as schlieren, shadowgraph, or interferometric studies integrated across the wake with a subsequent loss of spatial detail. It is difficult, if not impossible, to extract convincing quantitative data from such measurements[1] and it will be shown that even qualitative conclusions about the nature of the wake boundary may be suspect.

The present data are unique in that they are the result of direct measurement of the spatial mixing field and are not dominated by integration problems. These data were obtained using the laser planogram technique which has been described elsewhere.[2] This technique, as applied to the wake of a longitudinally aligned cylinder, is shown schematically in Fig. 1. A passive scalar particulate tracer is introduced into the model boundary layer where it essentially becomes uniformly mixed, thus tagging each fluid element. The concentration of the tracer at some downstream position is, therefore, a measure of the turbulent mixing field of the wake. To detect the tracer distribution, a pulsed planar laser sheet is passed along the axis of the wake in the meridian plane, and the light scattered at $90°$ by the tracer particles is recorded photographically. The resulting wake laser planogram is scanned to yield digitized film density as a function of position in the wake. A preprocessing program applies various calibrations which convert these raw data to concentrations. Standard digital techniques are then applied to determine several statistical properties of the turbulent concentration fluctuations.

2. TURBULENT WAKE MIXING EXPERIMENT

Figure 2 is a schematic drawing of the experimental configuration used in this study. The essential components are a short duration wind tunnel, an aerosol generator to produce the tracer material, a pulsed light source, and a precision camera. The experiment is instrumented to document various operating conditions.

2.1 The Short Duration Wind Tunnel

The short duration wind tunnel is a modified Ludwieg tube[3] which produces 30×10^{-3} seconds of steady flow through the test section at a Mach number of 2.5 and a Reynolds number of $1.5 \times 10^{6}/cm$ using $300°K$ stagnation temperature clean air. The model, in this case a 6.3 mm diameter truncated cylinder, extends 45 cm upstream through the nozzle throat and is supported by streamlined supports in the subsonic portion of the nozzle. In this way the effect of the turbulent wakes of the supports is minimized by the inviscid turbulent decay which occurs in the nozzle expansion. In addition, the data are obtained in a plane normal to the plane of the supports.

Photographic measurements of the model location indicate negligible model motion during the run if proper initial alignment is maintained.

The model extends into the 12.7 cm square test section. This test section contains 1.3 m of continuous windows on all four sides. The windows are schlieren quality fused silica of excellent optical finish. The test section is designed to hold the windows in such a way as to minimize distortion and window motion.

The end of the cylinder produces a weak wave pattern which upon reflection from the square test section is further weakened by this defocusing effect. The resulting density fluctuations are estimated to be very small compared to the measured concentration fluctuations and so the effect of wall reflections is most likely negligible. This has been confirmed by shadow photographs which indicate that only waves at the Mach angle are present in the test section flow.

The dump system is used to ensure that the final system pressure is below the test section design limit and also prevents reflected waves from reaching the test section during the test time. The initial pressure in the dump system is chosen to minimize nozzle start up time and eliminate transients by matching the acoustic impedance of the nozzle to that of the dump system.

2.2 The aerosol generator

The overall requirements for a suitable tracer material have been described in reference 2. In practice, the most stringent requirement is that of film exposure. It can be shown (see Appendix 1) that the mean exposure (energy/area) obtained in a laser planogram is given by

$$e = \frac{1}{16n} \left[n \; \frac{1}{2} \; (i_1 + i_2) \right] \left[\frac{\lambda^2 E}{h} \right] \left[\frac{1}{(1+m)^2} \; \frac{1}{F^2} \right] \tag{1}$$

The first bracketed term represents the light scattering characteristics of the aerosol with n the mean number density of scattering centers. The polarization components of the Mie scattered light, i_1 and i_2 (see, for example, reference 4), depend on the particle diameter, wavelength of the light source, index of refraction of the scattering material and the scattering angle. The second term characterizes the light source of wavelength λ and pulse energy E which is assumed unpolarized. The height of the light

sheet, h, also appears in this term. The final term in Eq. (1) characterizes the collection optics where F is the numerical F-number (focal length/lens diameter) and m is the system magnification (image size/object size).

For a given light source, camera and film, the aerosol requirements can be determined from the first term.

The tracer material used in the present study is generated by an exploding wire aerosol generator similar to that described by Karioris and Fish.[5] Approximately 7500 joules are dumped into an 0.1 gm strip of aluminum in a 10 liter chamber containing argon at STP. This yields an aluminum aerosol at a mass density of particulate material, $\rho_p = 8 \mu$ gms/cm^3 (based on a measured 80% generation efficiency). Since $n \frac{\pi d^3}{6} \rho_{A\ell} = \rho_p$, where $\rho_{A\ell}$ is the density of a solid aluminum particle of diameter d,

$$n \frac{1}{2} (i_1 + i_2) = \frac{3}{\pi} \frac{\rho_p}{\rho_{A\ell}} \frac{i_1 + i_2}{d^3} \qquad (2)$$

The number density of particles in the wake can be related to the number density in the generator, n_o, by defining a dilution factor, α, such that $n = \alpha n_o$. The dilution is caused by the entrainment of free stream fluid and can be estimated by noting that the mass flow of particulates, $\dot{m}_p$, is conserved so that

$$\dot{m}_p = (\alpha n_o) \rho_{A\ell} \frac{\pi d^3}{6} V_w A_w = n_o \frac{\pi d^3}{6} \rho_{A\ell} \frac{\dot{m}_c}{\rho_c}$$

where $\frac{\dot{m}_c}{\rho_c}$ is the volumetric flow rate of carrier gas in the aerosol generator (where $\alpha = 1$) and V_w and A_w are the local mean wake velocity and cross sectional area. Thus,

$$\alpha = \frac{1}{V_w A_w} \frac{\dot{m}_c}{\rho_c} \qquad (3)$$

It is important to evaluate $\frac{\dot{m}_c}{\rho_c}$ at the aerosol generator conditions to eliminate the density reduction which occurs due to the expansion process between the generator and the injection holes.

The results of combining Eqs. (1), (2) and (3) for the conditions of the present experiment are shown in Fig. 3. Based on the film density of the laser planograms described below, it is estimated that the actual exposure was ~ 1.5 x 10^{-3} ergs/cm^2 which yields a particle diameter of 0.02μ. This diameter is identical to the value determined by Karioris and Fish[5] from electron micrographs of collected particles.

The frequency response, defined by the ratio of the amplitudes of the particle velocity, u_p, to fluctuating fluid velocity, u_f, of such particles is given by (Appendix 2)

$$\frac{u_p}{u_f} = \frac{1}{[1 + (f/\alpha)^2]^{\frac{1}{2}}} \qquad (4)$$

where α is the characteristic response frequency and f is the fluctuating frequency. Using drag results by Millikan[6] one finds that the tracer particles will follow 10 MHz velocity fluctuations to within 90%. If one estimates the maximum possible Lagrangian temporal fluctuation frequency by using the Eulerian temporal frequency based on the RMS velocity fluctuation level and the Kolmogoroff wave number, the resulting frequency is 2 MHz. Thus, even with this gross overestimate of the frequency, the particles easily track the turbulent fluctuations throughout the entire turbulent spectrum. Note that the Lagrangian fluctuations are much weaker than the Eulerian fluctuations since their strength is related to the degree to which Taylor's Hypothesis fails.

Estimates of agglomeration rates due to Brownian motion and enhancement effects from gradient induced diffusion indicate that the present aerosol is stable throughout its lifetime. In addition, the laser energy density is low (10^5 watts/cm^2) so that it does not actively affect the aerosol. Estimates of particle induced dissipation show it to be negligible. The total particle-carrier mass flow is less than 1% of the boundary layer flow rate and therefore has a negligible effect on the integral wake properties. The molecular Schmidt number of 2000 (based on a diffusivity given by the Einstein equation) ensures that diffusion errors in particle tagging will be minimal.

The aluminum aerosol is prepared several minutes before use to allow it to reach a uniform state. Flow is then established into the model a few seconds before the run. The aerosol is bled into the model boundary layer through a series of 100, 1/32" diameter holes distributed over a region of the model extending 22 to 44 diameters upstream of the end of the cylinder. The existence of symmetric injection has been verified from base region wake laser planograms.

It is therefore concluded that the aerosol generator produces a detectable, passive scalar tracer of .02μ diam. at typically 2 x 10^{10}/cm^3 (based on ρ_p) in the wake and that these particles accurately follow the fluctuating flow.

2.3 Pulsed light source

The light source used for obtaining laser planograms is an AERL Model C100 pulsed nitrogen laser.

This laser operates at 3371 $\mathring{A}$ with a power of 150 kw and a pulse time of 10^{-8} sec (which provides photographic shuttering for the system). Its output is a 3 mm x 50 mm sheet which is directed along the wake axis by several mirrors and lenses. The last mirror is placed within the test section. The density field about this mirror produces negligible laser beam degradation. The optical system reimages the laser input aperture at the observation station. Beam divergence accounts for a 15% variation in exposure over the field of view of the laser planogram and is corrected for in the data processing. The mean concentration is obtained by replacing the laser source with a flashlamp system which produces a pulse of 2×10^{-3} sec. This represents approximately 100 Eulerian integral times so that it adequately yields the temporal mean.

2.4 The precision camera

An F/3, 150 mm focal length quartz lens is used for photographing the 90° scattered light. This lens has a measured resolution of better than 0.5 mm at the magnification of 0.12 used in obtaining the data. The lens is held in a rugged 4 x 5 format camera. Kodak 2485 High Speed Recording Film is used and gives an estimated sensitivity of 1.5×10^{-3} ergs/cm^3 at 1D above gross fog (film background).

2.5 Instrumentation

For each run, the initial aerosol size and number density, test section static pressure, laser output energy and reference mean wake concentration were monitored and used to standardize the data.

Tunnel operation was reproducible to better than $\pm$ 10% based on test section static pressure measurements. These variations are attributable to variation in diaphragm burst pressure. The measured test section static pressure was in agreement with calculated values at $M = 2.5$. Based on this agreement, the remaining free stream properties were taken as their theoretical values.

3. DATA PROCESSING

The digitized data obtained from microdensitometer scans of the wake laser planogram are analyzed statistically by standard digital techniques. [7,8] This section contains a brief summary of the procedures used. The data are analyzed in two parts. First a preprocessing program converts the film density to exposure and adjusts the data for experimental variations. These data are then supplied to a statistics program which computes the parameters of interest.

The preprocessing program uses a film sensitivity calibration curve which is generated for each individual laser planogram. This calibration is accomplished by exposing an unused portion of the film at various known intensities using the pulsed nitrogen laser. This avoids color or exposure time effects on film calibration. A scan of this calibration region then permits generation of a conversion curve from film density to exposure. A similar preprocessing procedure is used in obtaining the mean concentration data from the flashlamp photographs.

After this calibration, the data are adjusted for the spatial variation in exposure due to measured laser sheet divergence and for run to run variations in laser energy and mean tracer concentration. At this point, any prescribed deterministic trend is removed from the data. For example, nonstationary variations in mean concentration (in the case of similar flow $\sim z^{-2/3}$ where z is the axial distance from the virtual wake origin) or systematic experimental errors involving off-axis lens distortion.

It should be noted that standard techniques provide results which are directly interpretable only when the variable is statistically stationary. To the order of the presently employed stochastic functions, this requires that the mean, variance and autocovariance coefficient be constant over the data length. In general, it is to be expected that if any or all of these quantities vary they will affect the results. For example, slow variations can lead to distortion of the low frequency spectrum and inaccurate correlations at large lags. These can lead to substantial errors in the turbulent intensity, Kolmogoroff constant, and integral scale for example. Estimates of such errors based on the measured mean concentration indicate that they are negligible in the present case.

The statistics program first uses the preprocessed data to determine the probability density function. The sample is standardized to have zero mean and unit variance and the histogram computed along with the various relevant moments.

The energy spectrum is estimated from the Fourier transform of the preprocessed data after removal of the numerical mean. This transform is accomplished using the Cooley-Tukey Fast Fourier Transform Algorithm[9] in conjunction with a remote disc storage scheme. [10] The spectrum is then normalized by the measured variance. This process is repeated for the individual realizations and the results are ensemble averaged. The autocovariance coefficient is computed from the inverse transform of the ensemble averaged spectrum. The resulting data are computer plotted.

4. EXPERIMENTAL RESULTS

Figure 4 contains an ensemble of ten wake laser planograms obtained under the conditions described in Section 2.

The qualitative behavior of the wake boundary is substantially more rugged than would be expected from schlieren or shadowgraph pictures of similar flows. It is easy to see, however, how such detail could be lost when one views a two-dimensional projection of such a flow. Previous laser planogram measurements[2] obtained with larger tracer particles showed similar structure. The mapping of the mean concentration field indicates that the radial concentration profile centerline concentration and wake size are self preserving over the region covered by the present data. For such a wake, the mean radial profile is a Gaussian with standard deviation or "transverse scale length", L given by

$$\left(\frac{\cdots}{\sqrt{C_D A}} \right)^3 = \frac{3}{4\pi} \frac{1}{R_T} \frac{Z-Z_0}{\sqrt{C_D A}} \tag{5}$$

where $\sqrt{C_D A}$ is the model drag diameter, $Z-Z_0$ is the axial distance from the virtual wake origin, and R_T, a turbulence Reynolds number, is a constant. The value of $Z_0/D \cong 0$ was determined from a plot of L^3 vs Z by finding the Z axis intercept of the best fit straight line through the data at large Z. The value of R_T based on an estimate of C_D is consistent with other reported values of 12.8[11], 12.5[12] and 14.1[13]. It is therefore concluded that this coarse boundary behavior is consistent with typical turbulent wake flow.

On axis scans were obtained for the ten wake laser planograms of Fig. 4. A $50\mu \times 50\mu$ scanning slit was used with a sampling interval of 16μ. This interval produced 2048 samples in the available data length. High frequency filtering was accomplished by averaging readings at 2μ steps in the 16μ sampling interval, thus preventing aliasing errors. A set of typical film density scans is shown in Fig. 5.

Figures 6-9 are ensemble averaged estimates of the probability density function, energy spectrum and autocovariance coefficient obtained from the axis scans. The data processing procedures were described in Section 3.

4.1 The probability density function (pdf)

The histogram shown in Fig. 6 yields an estimate for the pdf of the turbulent concentration fluctuations after extraction of the mean value, $\bar{c}$. The concentration is measured in units of its standard deviation, σ. The resulting turbulent intensity, $1 = \frac{\sigma}{c}$, was 0.25.

Other properties of the pdf can be expressed as functions of its central moments, M_k. Thus, the skewness $S \equiv M_3/2_\sigma{}^3$ and the kurtosis, $K \equiv \frac{1}{2} (M_4/\sigma^4 - 3)$. Note that $M_0 = 1$, $M_1 = 0$, and $M_2 = \sigma^2$. For comparison purposes, $S = K = 0$ for a Gaussian pdf. The measured values of skewness and kurtosis were +0.18 and +0.16, respectively.

The intermittency factor was estimated directly from high contrast prints of the laser planograms by finding the fraction of a line drawn through the axis which lies within the wake boundary. This leads to a value of 82% on the wake axis.

Qualitative conclusions regarding the implications of these results can be drawn by comparison of data for other turbulent flows. For example, Gibson[14] has studied the near (non-similar) sphere wake. For his premixed wake (measuring a passive scalar), he obtains skewness and kurtosis values of +0.30 and +.975 at $Z/D = 2.17$ and +0.885 and +10.2 at $Z/D = 7.5$. He attributes the high kurtosis values at $Z/D = 7.5$ to unmixed tracer material that has left the wake, probably upon injection. The lack of high kurtosis values in the present case along with the lack of appearance of such regions in the laser planograms is consistent with this view.

Demetriades[15] has observed a bimodal behavior to the pdf of electron density fluctuations in a turbulent jet. His double-peaked histograms have skewness and kurtosis values as high as 7 and 25, respectively, at short distances from the jet exit. He attributes this phenomenon to remnants of the jet transition. No such indications of transition remnants appear in the present data. Demetriades' data at large distances appear more consistent with the present results.

The present intermittency result, and the general qualitative behavior of the wake boundary, appear to be in substantial disagreement with turbulent front structure deduced by Demetriades[16]. In a very similar flow field he observed no vorticity free regions on the wake axis and concluded that his wake boundary "resembles a straight cylinder with (a) rough surface". He compared his results to those of Gibson et al.[17] and Hwang and Baldwin[18] who both observed substantial centerline intermittency. Demetriades presented arguments based on model shape to rationalize this discrepancy. He pointed out a study by Gartshore[19] which concluded that the standard deviation of the wake boundary, σ', is related to R_T by $\sigma'/L = 2.97/\sqrt{R_T}$. Also, Behrens[20] has suggested that R_T is related to body bluntness, varying from ~ 1 for very blunt bodies to ~ 10 for very slender shapes. Thus Demetriades concludes that σ'/L is large for blunt bodies and small for slender ones and hence the wake boundary is rough for blunt bodies and smooth for slender bodies. The similarity in the flow conditions suggests that the present data should be directly comparable to Demetriades results. However, the present results show a centerline intermittency and a strongly contorted boundary and are much more suggestive of the results of Gibson et al. and Hwang and Baldwin than those of Demetriades. Of course, one must recognize the possibility that this discrepancy results from a fluid mechanical difference between vorticity and a passive wake scalar. This question requires further study.

4.2 The energy spectrum (PSD)

The periodogram shown in Fig. 7 is an ensemble averaged estimate of the energy spectrum of concentration fluctuations. The spectrum is characterized by a flat low frequency region which breaks at a wave number of 0.12 mm^{-1} into a well defined $k^{-5/3}$ inertial subrange. This measured energy containing wave number, k_e, along with the variance obtained from the pdf, σ^2, were used to normalize the data of Fig. 7. Experimental errors begin to affect the measured spectrum at $k/k_e = 10$. At higher wave numbers the data are untrustworthy. The Nyquist frequency[7] corresponds to $k_n/k_e = 180$ so that only points below $k/k_e = 90$ are shown.

The Kolmogoroff wave number, $k_K \equiv (\epsilon/\nu^3)^{1/4}$ was estimated by use of the dissipation rate $\epsilon \cong k_e u'^3$.[21] The kinematic viscosity was determined at the free stream temperature and pressure; the

RMS velocity fluctuation level was based on intensity measurements by Demetriades[11] under similar flow conditions. Using the measured value of k_e, a value of $k_K \cong 100$ mm^{-1} was obtained. This represents a ratio $\dfrac{k_K}{k_e} = 850$ and corresponds to a turbulence Reynolds number.[21]

$$Re_\lambda \equiv \frac{u'\lambda_g}{\nu} \cong \sqrt{15} \left(\frac{k_K}{k_e} \right)^{2/3} = 360.$$

Uberoi and Freymuth[22] have shown that a turbulence Reynolds number of at least 100 is required for the existence of a well defined inertial subrange while a value of 360 should produce a $k^{-5/3}$ spectrum past $k/k_e = 100$. Thus, a well developed inertial subrange is expected.

Shown also in Fig. 7 is the von Karman interpolation formula[23] which has successfully characterized energy spectra of most low speed incompressible turbulent flows (see, for example, Ref. 22). The present data are in reasonable agreement with this correlation. The lowest wave number point, however, is a factor of two above the expected value. In order to determine whether this point represents a turbulent contribution to the spectrum, an estimate was made of any additive deterministic signal content. The local mean of the ten realizations was determined and smoothed using a smoothing function of 1% of the data length. The resulting mean field estimate was subtracted from each realization and the spectrum was computed. This dropped the lowest frequency point by a factor of two and brought it in line with the remaining points. No other qualitative effect on the spectrum was observed. The low frequency adjusted data is also shown in Fig. 7. Because the unadjusted data may represent a real aerodynamic (albeit deterministic) feature of the wake, it is shown as the primary data of this figure. Similar improvement was noted in the autocovariance coefficient (see below). This deterministic contribution to the signal may be due to either an aerodynamic artifact such as shock reflection, or vortex shedding (its frequency corresponds to a Strouhal number[24] of ~ 0.1 compared to an expected value[22] of ~ 0.2) or a systematic experimental error such as lens distortion. It is not due to nonstationarity in the mean of the concentration, since adjusting the data for a $Z^{-2/3}$ mean concentration had negligible effect. This is to be expected at this wake location since the mean varies less than 15% over the data length.

Several previous investigations (e.g., Refs. 25 and 26) have yielded energy spectra possessing low wave number peaks. Demetriades[25] has attributed such peaks in his data to remnants of the transition from a laminar to turbulent wake. The peaks become less pronounced with increasing axial distance. Lewis and Behrens[26] report similar low wave number peaks even at high Reynolds numbers with turbulent model boundary layers. Their detailed base region flow field measurements lead them to conclude that an inner laminar shear layer exists which forms an initial laminar core within the wake. When this core undergoes transition a large scale (low wave number) structure is produced.

As can be seen from Fig. 7, no peak exists in the low wave number spectrum indicating the absence of excess energetic large scale structures for wave numbers greater than 0.1 k_e. This result may be reconciled to Demetriades' result by noting that the present model Reynolds number is two orders of magnitude larger. The model boundary layer and near wake are both fully turbulent and no relaminarization is expected or observed.

In comparing the present results to those of Lewis and Behrens, it should be noted that the present model Reynolds number is one order of magnitude larger than theirs and the data were obtained at a further downstream wake location.

The Kolmogoroff constant, β, for the inertial subrange of the one dimensional spectra of a passive scalar is defined by

$$(\text{PSD}) \ (k_K{}^3) \ \left(\frac{\nu}{\chi} \right) \equiv \beta \ \left(\frac{k}{k_K} \right)^{-5/3} \tag{6}$$

The dissipation rate, χ, can be approximated by

$$\chi = - \frac{d}{dt} \ (\sigma^2) \cong r \ \frac{V_\infty}{Z} \ \sigma^2 \tag{7}$$

where Taylor's hypothesis has been used in the form $\dfrac{d}{dt} = V_\infty \dfrac{d}{dZ}$ and $\sigma^2 \sim Z^{-r}$ is assumed. Taking $r = 2/3$, the value for a passive scalar in a self similar wake, one finds $\beta = 0.7$ using Eqs. (6) and (7).

Gibson and Schwartz[26] have reported values of $\beta = 0.33$ to 0.44 and Grant[27] et al. find $\beta = 0.31$. More recently, Gibson[28] et al. have reported measurements of β in the atmospheric boundary layer of 1.17 which compares more closely to the present data. Gibson et al. attribute the higher values of β to anisotropy and intermittency in their flow. Their arguments can be used to infer that the large value of β obtained in the present case is indicative of wake anisotropy in addition to the observed intermittency.

4.3 The autocovariance coefficient

The autocovariance coefficient is obtained from the autocorrelation function by adjusting for the numerical mean and normalizing by the variance, σ^2.

Figure 8 is an estimate of the autocovariance coefficient obtained from the energy spectrum. The effect of the low wave number deterministic structure noted previously manifests itself in the failure of the autocovariance to approach zero at large lags. Using the previously described correction, the resulting autocovariance oscillated randomly about zero (dashed curve in Fig. 8). These remaining oscillations

were the result of the finite number of samples used and truncation of the energy spectrum.

These meanderings of the autocovariance at large lags lead to large variations in the computed integral scales. This effect is shown in Fig. 8 where the partial integral scale obtained by integration up to a given lag is shown as a function of that lag. A unique value of the integral scale does not occur.

Comparison of the measured spectrum of Fig. 7 with the von Karman interpolation formula suggests that it may provide a useful means of estimating the integral scale. For such a spectrum $k_e \Lambda \cong .75$.[29] The assumption of a von Karman interpolation formula leads to an autocovariance coefficient given by

$$C(k_e \xi) = \frac{2^{2/3}}{\Gamma(1/3)} \; (k_e \xi)^{1/3} \; K_{1/3} \; (k_e \xi)$$

where $K_{1/3}$ is a modified Bessel function of order $1/3$ (Macdonald function). In Fig. 9, this autocovariance coefficient is compared to an expanded plot of the data of Fig. 8. Also shown in Fig. 9 is an exponential autocovariance coefficient adjusted for best fit through the short lag data. This exponential form yields a value of $k_e \Lambda = 1.1$. After adjusting the data for deterministic trends, the exponential fit yields $k_e \Lambda = 0.9$.

The poor fit of the von Karman autocovariance is probably due to deviations of the spectrum data from the interpolation formula in the vicinity of $k/k_e = 1$. It is felt that the exponential form, even though it yields a physically unreasonable spectrum (i.e., k^{-1} inertial subrange), is an alternate means of estimating the macroscale in the present case. Precedent for the use of exponential forms for the autocovariance have been described by Hinze.[30] The three values of Λ which follow from the different values of $k_e \Lambda$ are $\Lambda = 6.2$, 7.5 and 9.2 mm. The measured transverse scale length (Eq. 5) had an average value of $L = 11.2$ mm and varied by $\pm 5\%$ over the data length. Hence the present experiment yields $\Lambda = (1/2 \text{ to } 3/4) L$ within the experimental error.

Demetriades[16,31] has shown that for a large variety of low speed flows, the velocity macroscale is equal to the transverse scale length while the temperature and density scales vary from $0.5 L$ on axis to $1.0 L$ near the wake edge. The present data indicate that the spatially deduced macroscale of a passive scalar species behaves in a similar fashion to those of temperature and density.

The turbulent microscale, λ_g, can be determined from the "osculating parabola" of the autocovariance coefficient. It can easily be shown that for a von Karman interpolation formula spectrum,

$$k_e \lambda_g \cong 1.7 \left(\frac{k_e}{k_K}\right)^{2/3} = 10^2 \text{ in the present experiment. The measured value shown in Fig. 9 is}$$

$k_e \lambda_g = 0.13$, which is an order of magnitude larger than expected. Also note that $\lambda_g \cong 1$ mm which is a dimension of order of system resolution. It is therefore likely that this measurement is dominated by experimental limitations and is not characteristic of the microscale.

5. SUMMARY AND CONCLUSIONS

The instantaneous mixing field of an axisymmetric wake has been studied to yield its statistical properties. Laser planograms indicate that the wake boundary is much coarser and more contorted than was previously expected.

Ensemble averaged statistical properties of concentration fluctuations have been estimated from centerline scans. The probability density function is nearly Gaussian with a skewness of $+0.13$ and a kurtosis of $+0.16$. The intensity of the concentration fluctuations is 25%. A non-unity (82%) centerline intermittency was observed. The small kurtosis values indicate the absence of transition remnants or islands of unmixed fluid as have been observed by others.

The measured energy spectrum is in qualitative agreement with the von Karman interpolation formula although the break point in the data appears more distinct. There appears to be no excess large scale, energetic structure present in the low wave number spectrum for wave numbers greater than $0.1 k_e$. The spectrum yields a value of $\sim .7$ for the Kolmogoroff constant, β, which suggests possible anisotropy and/or intermittency effects.

The autocovariance coefficient yields an integral scale equal to $1/2$ to $3/4$ of the transverse scale length. The present results are shown to be in general agreement with several previous studies by other investigators. In these other studies, the spatial properties are deduced from temporal measurements by invoking Taylor's hypothesis. Since the present data are direct spatial measurements, the agreement suggests that the use of Taylor's hypothesis in this case leads to consistent results.

ACKNOWLEDGMENTS

REFERENCES

1.   M. S. Uberoi and L. S. G. Kovasznay, J. of Appl. Phys. 26, 19 (1955).

2.   A. M. Schneiderman and G. W. Sutton, Phys. Fluids 13, 1679 (1970).

3.   A. J. Cable and R. N. Cox, The Aeronautical Quarterly, May 1963, pg. 143.

4.   H. C. Vander Hulst, Light Scattering by Small Particles, John Wiley and Sons, Inc., New York, N. Y. 1957.

5.   Frank G. Karioris and Birney R. Fish, Journal of Colloid. Science, 17, 155 (1962).

6.   R. A. Millikan, Phys. Rev. 22, 1 (1923).

7.   Julius S. Bendat and Allan G. Piersal, Measurement and Analysis of Random Data, John Wiley & Sons, Inc., N. Y. 1966.

8.   R. B. Blackman and J. W. Tukey, The Measurement of Power Spectra, Dover Publications, Inc., N. Y. 1958.

9.   James Cooley and John W. Tukey, Math. Comp. 19, 297 (1965).

10.   Norman M. Brenner, IEEE Transactions on Audio and Electronics, AU-17, 128 (1969).

11.   Anthony Demetriades, AIAA Journal 6, 432 (1968).

12.   Townsend, A. A., The Structure of Turbulent Shear Flows, Cambridge University Press, Cambridge 1956.

13.   A. A. Hall and G. S. Hislop, Proc. Cambridge Phil. Soc. 34, 345 (1938).

14.   Carl H. Gibson, Russel R. Lyon and Ian Hirschsohn, AIAA Journal 8, 1859 (1970).

15.   Anthony Demetriades and Ernest L. Doughman, "Bimodal Electron Behavior in a Turbulent Reacting Jet", AIAA paper No. 70-731.

16.   Anthony Demetriades, J. Fluid Mech. 34, 465 (1968).

17.   C. H. Gibson, C. C. Chen and S. C. Lin, AIAA Journal 6, 642 (1968).

18.   N. H. C. Hwang and L. V. Baldwin, 1966 Trans. Am. Soc. Mech. Engr. Ser. D., J. Basic Engr. 88, 261 (1966).

19.   Ian S. Gartshore, J. Fluid Mech. 24 89 (1966).

20.   W. Behrens, GALCIT Hypersonic Project IM-15, California Institute of Technology, Pasadena, Calif. 1963.

21.   J. O. Hinze, Turbulence, McGraw-Hill Book Company, Inc., N. Y. (1959) pg. 185.

22.   Mahinder S. Uberoi and Peter Freymuth, Phys. Fluids 12, 1359 (1969).

23.   Hinze, ibid pg. 199.

24.   S. Goldstein, Modern Developments in Fluid Dynamics, Dover Publications, Inc., New York, N. Y. 1965, pg. 571.

25.   A. Demetriades, Final Report, Wake Structure Measurements Advanced Penetration Problems, SAMSO TR 70-58.

26.   J. E. Lewis and W. Behrens, AIAA Journal 7, 664 (1969).

27.   C. H. Gibson and W. H. Schwartz, J. Fluid Mech. 16, 365 (1963).

28.   H. L. Grant, B. A. Hughes, W. M. Vogel and A. Moilliet, J. Fluid Mech. 34, 423 (1968).

29.   Carl H. Gibson, Gilbert R. Stegen and Robert Bruce Williams, J. Fluid Mech. 41, 153 (1970).

30.   Hinze, ibid pg. 200

31.   Hinze, ibid pg. 52

32.   Anthony Demetriades, Phys. Fluids 11, 1841 (1968).

APPENDIX 1 - Laser Planogram Exposure

Consider a planar light sheet of thickness t (in the x direction) which propagates in the z direction and lies in the yz plane. A lens located on the x axis a distance R from the sheet images the yz plane at distance s from the lens. Let S_0 be the light energy scattered from an individual particle within the sheet which is collected by the lens. If n is the number density of scatterers then the lens collects from an elemental volume tdy dz an energy of nt dx dy S_0. This energy is imaged on an area dx' dy' of the film so that the film exposure, e, (energy/area) is

$$e = \frac{nt\ dx\ dy\ S_0}{dx'\ dy'} \tag{8}$$

Defining the magnitification, m, by dx' = mdx, dy' = mdy,

$$e = \frac{1}{m^2}\ n\ S_0\ t \tag{9}$$

Now, it can be shown[4] that

$$S_0 = \frac{E}{th}\ \frac{\frac{1}{2}(i_1 + i_2)}{(\frac{2\pi}{\lambda})^2\ R^2}\ \frac{\pi D_\ell^2}{4} \tag{10}$$

where E is the energy of the light sheet of thickness t and height h, i_1 and i_2 are the polarization components of the scattered light[4] and depend on the particle size index of refraction, the light wavelength, λ, and the scattering angle, Θ, and D_ℓ is the lens diameter. It is assumed that i_1 and i_2 is approximately constant for $\Theta = 0$ to D_ℓ/R, i.e. that $D_\ell/R \ll 1$.

Combining (10) and (9),

$$e = \frac{1}{16\pi}\left[n\ \frac{1}{2}(i_1 + i_2)\right]\left[\frac{\lambda^2 E}{h}\right]\left[\frac{1}{m^2}\ \frac{D_\ell}{R}\right]^2 \tag{11}$$

Further simplification occurs by noting that m = s/R and $\frac{1}{f} = \frac{1}{R} + \frac{1}{s}$ where f is the lens focal length. Thus $D_\ell/R = \frac{m}{1+m}\ \frac{1}{F}$ where $F \equiv f/D_\ell$ is the numerical F-number of the lens. Finally

$$e = \frac{1}{16\pi}\left[n\ \frac{1}{2}(i_1 + i_2)\right]\left[\frac{\lambda^2 E}{h}\right]\left[\frac{1}{(1+m)^2}\ \frac{1}{F^2}\right] \tag{12}$$

The groupings of terms on the right indicates the contributions to the film exposure of the scattering properties of the particles, the light source, and the collection optics respectively. For a given light source, the optimum aerosol properties (see for example Fig. 3) and collection optics can easily be determined. For example a faster lens (lower F) improves exposure substantially while demagnification below m ~ .5 produces small effect.

APPENDIX 2 - Particle Frequency Response

The tracking fidelity of the tracer particles can be estimated by considering the motion of a single particle in a periodic flow field of angular frequency ω. Assume a flow velocity $u_f' = u_f e^{j\omega t}$ and a particle velocity $u_p' = u_p e^{j\omega t}$. For particle Reynolds numbers less than unity, the drag on a particle is given by the Stokes equation with the Cunningham correction for slip effects so that

$$Drag = \frac{3\pi\ \mu\ d\ (u_f' - u_p')}{1 + \frac{\kappa \ell}{d}} \tag{13}$$

where μ is the viscosity, d is the particle diameter, ℓ is the mean free path and κ is a numerical factor of order unity (but dependent on ℓ and d). If the particles density, ρ_{AL}, is large compared to the gas density, then the drag force can be equated to the particle mass times its acceleration, du_p'/dt, with the result,

$$\frac{3\pi\ \mu\ d\ (u_f - u_p)\ e^{j\omega t}}{1 + \frac{\kappa \ell}{d}} = \rho_{AL}\ \frac{\pi d^3}{6}\ j\omega u_p'\ e^{j\omega t} \tag{14}$$

Thus,

$$\frac{u_p'}{u_f} = \frac{1}{\left[1 + (\frac{f}{\alpha})^2\right]^{1/2}} \tag{15}$$

where

$$a = \frac{9\mu}{\rho_{AL} \pi d^2 \left[1 + \frac{K\ell}{d} \right]}$$

Note that the phase angle between the flow and particle velocity is $\phi = \tan^{-1} \frac{f}{a}$.
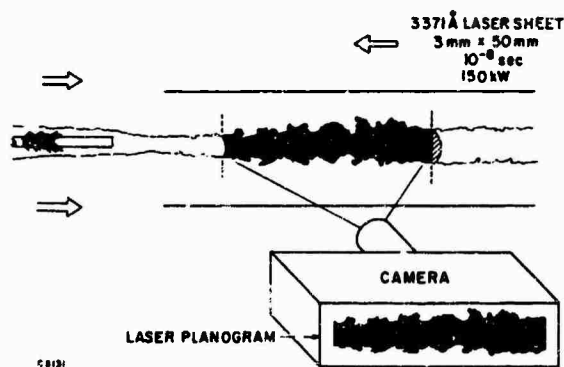
Fig. 1   The laser planogram technique.
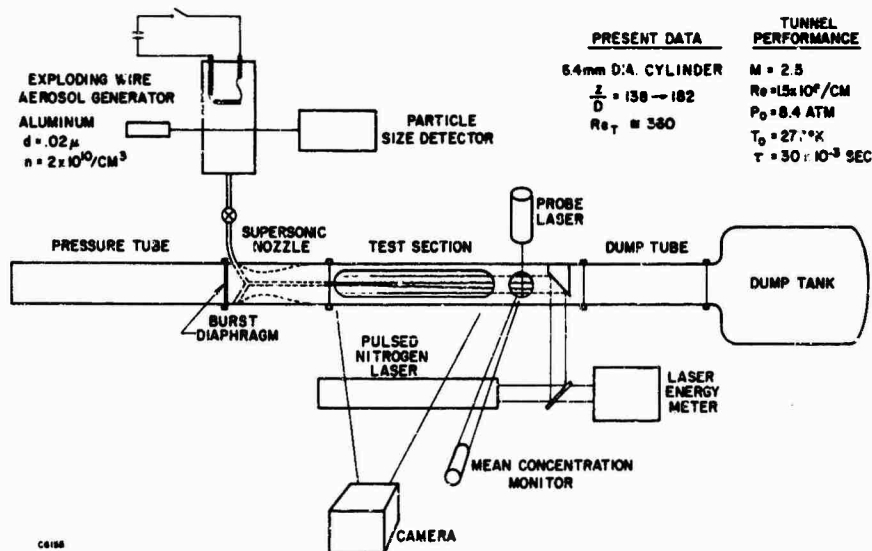
Fig. 2   Schematic of the experimental arrangement.
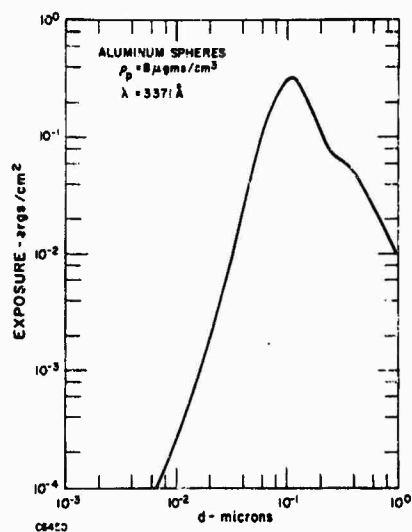
Fig. 3   Computed film exposure as a function of aerosol particle size.

WAKE LASER PLANOGRAMS   TRUNCATED CYLINDER

$M = 2.5$ $Re_D = 10^6$ $\frac{Z}{D} = 138$ TO 182

⟵ FLOW DIRECTION   ⟵ FLOW DIRECTION
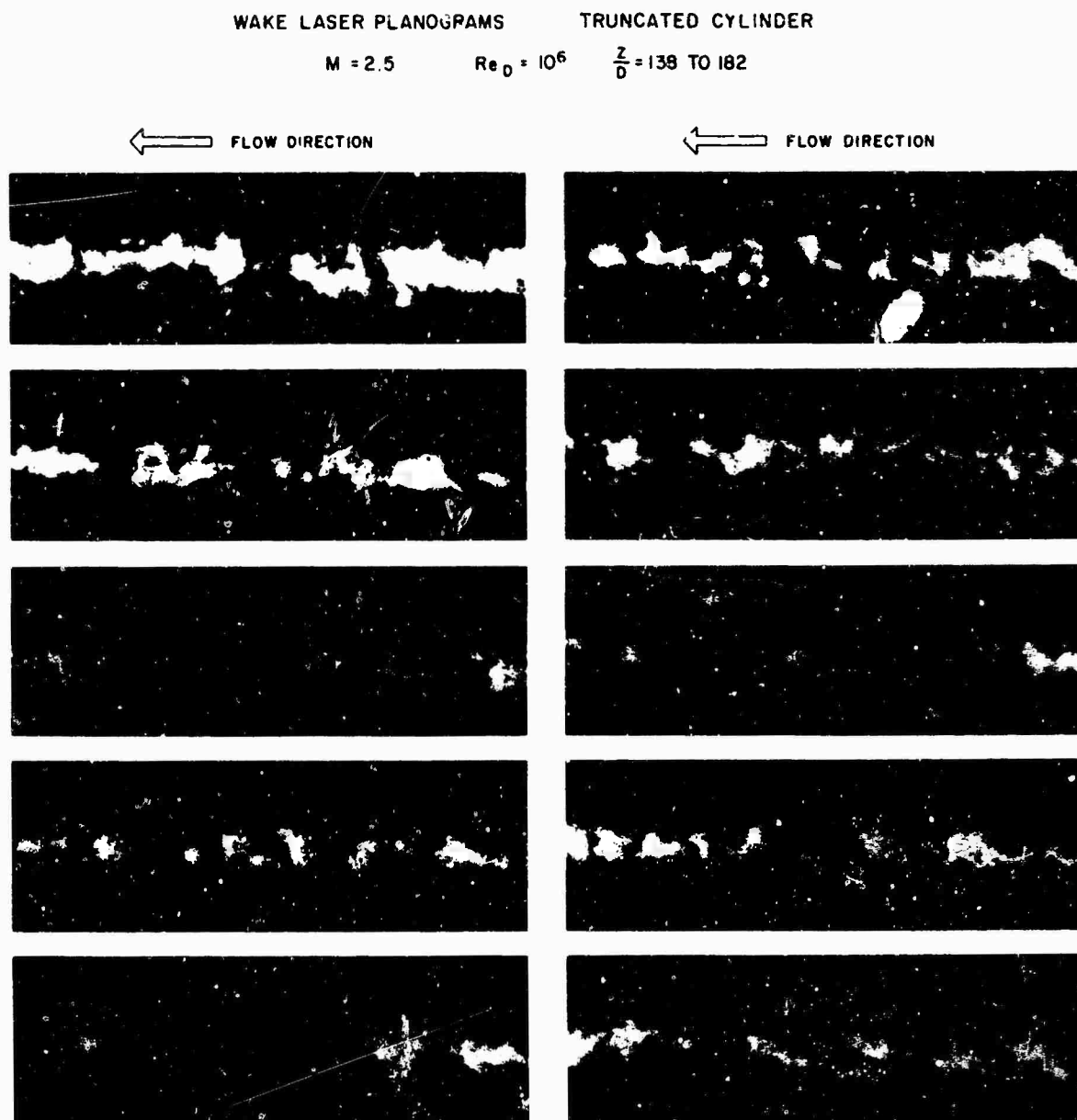
Fig. 4   An ensemble of wake laser planogram realizations.
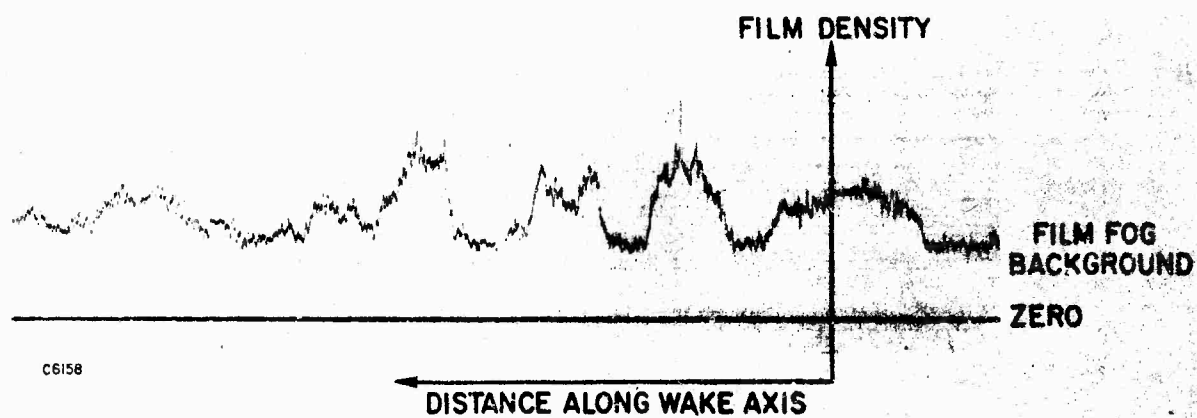
Fig. 5   Typical centerline scans of wake laser planograms.
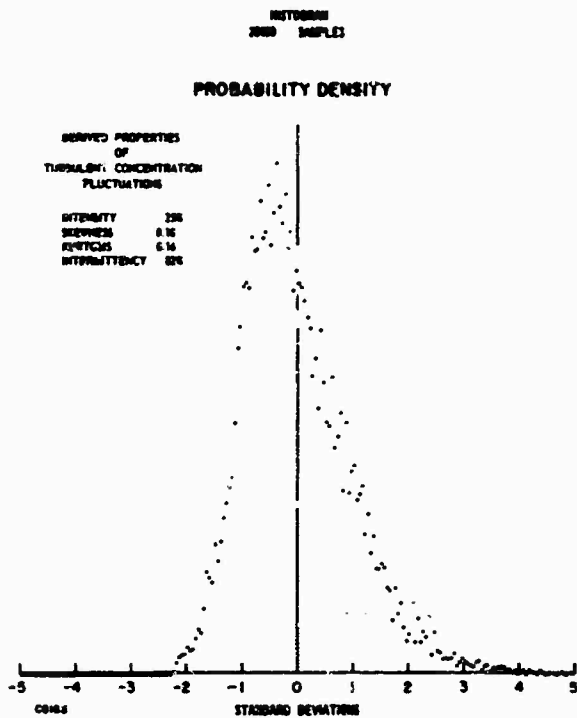
Fig. 6   Ensemble average histogram of the con-
centration fluctuations.
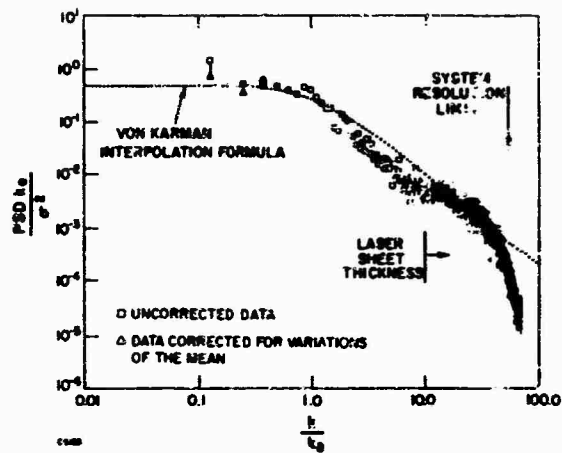
Fig. 7   Ensemble averaged estimate of the
energy spectrum. The adjusted points
have been corrected for deterministic
components.
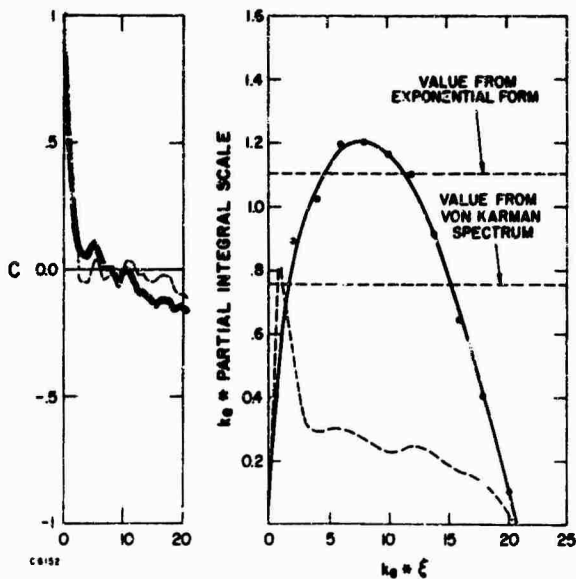
Fig. 8   Autocovariance coefficient determined
from the spectrum of Fig. 7. Also
shown is the partial integral scale. The
dashed curves result from correcting
the data for low frequency deterministic
effects.
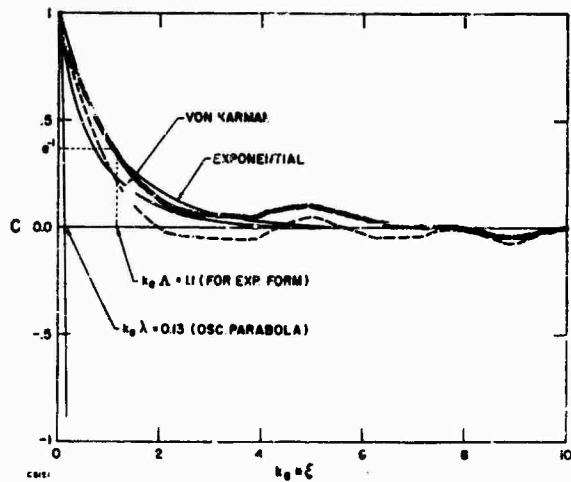
Fig. 9   Expanded plot of the autocovariance
coefficients of Fig. 8 showing a com-
parison of the data with two analytic
forms.

RECENT ATTEMPTS TO DEVELOP A GENERALLY APPLICABLE
CALCULATION METHOD FOR TURBULENT SHEAR FLOW LAYERS

J. C. Rotta[*)]

Deutsche Forschungs- und Versuchsanstalt
für Luft- und Raumfahrt E. V.
Aerodynamische Versuchsanstalt Göttingen

Bunsenstr. 10
34   Göttingen
Germany

SUMMARY

Calculation methods are discussed, which are based on the differential equations for the Reynolds stresses.
The considerations restrict themselves to two-dimensional flow fields, for which the usual boundary layer
approximations apply. In many of the proposed methods of this kind, the equation for the kinetic fluctuation
energy plays a central role. The transport equation for the Reynolds shear stress includes as special cases
Prandtl's eddy viscosity relation and Bradshaw's assumption of a constant ratio of shear stress to kinetic
fluctuation energy. A differential equation for the integral length scale is derived from Navier Stokes equa-
tions, and the closure assumptions are given. It turns out that the simplified version of the length scale
equation, used by some authors, is not capable of reproducing the characteristics of different kinds of
flows. The main reason for this shortcoming is found in an oversimplification of the turbulence production
term of the length scale equation. The arguments are illustrated by calculated results.

NOTATION

a_1	ratio $-\overline{uv}/\overline{q^2}$	u_1	reference velocity, $u_1 = U_\infty - U_c$
b	width of wake	u_τ	wall shear stress velocity, $u_\tau = \sqrt{\tau_w/\rho}$
c_d	drag coefficient	x, y, z	cartesian coordinates and cylindrical
d	diameter of cylinder		coordinates (y = radius)
L	integral length scale, defined by Eq. (21)	ϵ	dissipation, Eq. (2)
		$\varkappa$	v. Kármán constant, $\varkappa = 0.4$
L_{12}, $L_{12,n}$	integral length scales, Eqs. (26) and (27)	ν	kinematic viscosity
P	mean static pressure	ρ	density, assumed is $\rho = 1$
p	pressure fluctuation		
q^2	$= u^2 + v^2 + w^2 = u_i u_i$	**Subscripts**	
		∞	free stream conditions
R_{ij}	two-point correlation function	c	centre of symmetrical flows
$R_{(ik)j}$, $R_{i(kj)}$	two-point triple correla- tion functions, Eq. (25)	i, j, k...	notation of cartesian coordinates (i = 1, 2, 3 etc.)
r	vectorial distance of the points in space	T	turbulent interaction
r_y	distance of the points in y-direction	M	mean flow interaction
		Overbars denote ensemble averages.	
U, V	mean velocity components		
u, v, w	fluctuations of velocity components		

1. INTRODUCTION

Despite the enormous progress in computer sciences and numerical mathematics, it is impracticable to
produce general solutions of the Navier Stokes equations, which are needed to attack the problem of turbu-
lent fluid flow in a rigorous manner. Even if the mean motion is steady and plane or axisymmetric, the
associated turbulent motion is three-dimensional and unsteady. A numerical approach to such flows of high
Reynolds numbers is clearly out of the question at the present time. Therefore, the semi-empirical me-
thods are the only resources available, to treat problems of technical importance with some degree of suc-
cess. These semi-empirical methods are characterized by the fact that the random, unsteady, three-dimen-

---

[*)]   Dr. -Ing. E. h. , Aerodynamics Department

sional motion of turbulence is described by statistical mean quantities. The statistical quantities are related to each other by a set of differential equations. Empirical assumptions have to be introduced to establish such a set of differential equations.

The shortcomings of simple relations, like the eddy viscosity formula and the mixing length formula, are well known. Nevertheless, quite good results have been achieved in recent years. The decisive disadvantage of these relations is that their application to a particular flow problem requires ad hoc assumptions with regard to magnitude and distribution of eddy viscosity or mixing length. This circumstance prevents the formulation of a unified approach to turbulent flows. However, engineers need methods which are able to predict the main characteristics of a wide class of flows.

Many attempts to develop a generally applicable method have been made, beginning with the works of A. N. Kolmogorov [1] and L. Prandtl [2], which are based on the equation for the kinetic fluctuation energy. These methods have been formed in a heuristic manner. Subsequently, P. Y. Chou [3] and the present writer [4] started directly from differential equations for the Reynolds stress tensor, which are derived from Navier Stokes equations, and introduced certain closure assumptions to make these equations tractable. This early work could not aquire any practical importance, since the numerical treatment of such complicated systems of differential equations was not feasible at that time. The interest in such methods has been revived, since modern high speed computers offer the possibility to numerically solve complicated systems of partial differential equations. Reference is made to the work of B. J. Daly and F. H. Harlow [5], T. H. Gawain and J. W. Pritchett [6], T. S. Lundgren [7], V. W. Nee and L. S. G. Kovasznay [8], and P. G. Saffman [9].

There is not yet evidence that any of the existing methods can successfully be applied to nearly all cases of turbulent flow. Such a method can be developed only step by step. Therefore, it appears to be worthwhile to restrict the consideration to two-dimensional incompressible flow fields, for which the usual boundary layer simplifications apply. Only one of the coordinates of the Reynolds stress tensor is important in such flows. This paper reports on calculations, which are based on the transport equations for shear stress, fluctuation energy and length scale. Although these calculations are not yet completed, some important conclusions can already be drawn.

2. TRANSPORT EQUATIONS FOR SHEAR STRESS AND KINETIC FLUCTUATION ENERGY

If the unsteady velocity components and the pressure are separated into mean and fluctuating parts, and then are inserted into the equations of motion, the equations for the mean velocities are obtained, in which the Reynolds stresses $-\rho \overline{u_i u_j}$ appear as unknown quantities, where cartesian tensor notation is used, and the overbar denotes ensemble averages. Additional equations for $\overline{u_i u_j}$ are derived from the Navier Stokes equations. These are given in the literature on turbulent flows [10, 11, 12] and need not be repeated here in their full form. A substantial simplification is achieved, if the considerations are restricted to high Reynolds number flows. In this case, not only the mean Stokes stresses are negligible, but also most of the viscous terms in the equations for $\overline{u_i u_j}$. The remaining viscous terms are of the type $\nu \overline{(\partial u_i/\partial x_k)(\partial u_j/\partial x_k)}$. They can be expressed by a single scalar quantity, ϵ , if the concept of local isotropy is applied. The idea behind this assumption is that, for high Reynolds numbers, the turbulent spectra extend over a very large range of wave numbers, and that the contribution to $\overline{(\partial u_i/\partial x_k)(\partial u_j/\partial x_k)}$ come mainly from the large wave number part of the spectra. Kolmogorov, Heisenberg, and v. Weizsäcker have pointed out that the motion of the large wave components is statistically independent of the energy containing part of the spectra and assumes a universal, isotropic form. The isotropic tensor has the form

$$\nu \overline{\left(\frac{\partial u_i}{\partial x_k} \frac{\partial u_j}{\partial x_k}\right)^2} = \frac{1}{3}\delta_{ij}\epsilon \quad , \tag{1}$$

where δ_{ij} is the unit tensor, and the summation convention for repeated indices is used. ϵ equals the rate of dissipation per unit mass and time

$$\epsilon = \nu \overline{\frac{\partial u_i}{\partial x_k}\left(\frac{\partial u_i}{\partial x_k} + \frac{\partial u_j}{\partial x_k}\right)} \quad . \tag{2}$$

With the high Reynolds number assumptions and the familar boundary layer simplifications, the equations for the Reynolds shear stress, $-\rho \overline{uv}$, and the kinetic fluctuation energy, $q^2/2$, of plane and axisymmetric flows read as follows, if the density is put $\rho = 1$:

Reynolds shear stress

$$U\frac{\partial \overline{uv}}{\partial x} + V\frac{\partial \overline{uv}}{\partial y} + \overline{v^2}\frac{\partial U}{\partial y} - \overline{p\left(\frac{\partial u}{\partial y} + \frac{\partial v}{\partial x}\right)} + \frac{\partial}{\partial y}\overline{(v^2 + p)u} = 0 \quad , \tag{3}$$

Kinetic fluctuation energy

$$U \frac{1}{2} \frac{\partial \overline{q^2}}{\partial x} + V \frac{1}{2} \frac{\partial \overline{q^2}}{\partial y} + \overline{uv} \frac{\partial U}{\partial y} + \epsilon + \frac{1}{y^j} \frac{\partial}{\partial y}\left[y^j \overline{\left(\frac{q^2}{2} + p\right)v} \right] = 0 \quad , \tag{4}$$

j = 1   axisymmetric mean flow   ,

j = 0   plane mean flow   .

The equations for the mean motions are

Continuity

$$\frac{\partial U}{\partial x} + \frac{1}{y^j} \frac{\partial(y^j V)}{\partial y} = 0 \quad , \tag{5}$$

Momentum in x-direction

$$U \frac{\partial U}{\partial x} + V \frac{\partial U}{\partial y} = -\frac{dP_\infty}{dx} - \frac{1}{y^j} \frac{\partial(y^j \overline{uv})}{\partial y} \quad . \tag{6}$$

Eqs. (3) to (6) are first order approximations. It may be noticed that Eq. (3) has the same form for plane and axisymmetric flows.

The restriction to high Reynolds number flows seems to cause a severe limitation of the applicability at first sight. The high Reynolds number approach does not apply to regions close to solid surfaces. This disadvantage appears to be not too serious, since here the flow can be described by a few local parameters. Effects of pressure gradient, addition or removal of fluid through the porous surface and other effects can be estimated with the aid of the mixing length relation. Nevertheless, it is desirable to have a better formalism, which holds also near solid surfaces. Moreover, one wishes to be able to predict the development of turbulent flow from the preceding laminar regime. Calculations performed by G.S. Glushko [13] and I.E. Beckwith and D.M. Bushnell [14] indicate, that this might be achieved with semiempirical methods. Thus, in the future, an extension of the validity over the whole range of Reynolds numbers is required. However, there are a number of important problems, which must be solved first. This fact justifies the restriction to high Reynolds number flows at this moment.

3. CLOSURE ASSUMPTIONS

In order to make Eqs. (3) to (6) determinate, closure assumptions have to be introduced for the dissipation, ϵ, the pressure-shear velocity correlation term $\overline{p(\partial u/\partial y + \partial v/\partial x)}$, the kinetic energy diffusion $\overline{(q^2/2 + p)v}$, and the shear diffusion $\overline{(v^2 + p)u}$.

At high Reynolds numbers, the process of viscous dissipation is governed by a continued energy transfer from big to small eddies, such that the rate of dissipated energy is independent of viscosity. For this reason, ϵ is expressed by the relation

$$\epsilon = c\left(\overline{q^2}/2\right)^{3/2}\Big/ L \quad , \tag{7}$$

where L is a length scale of the big eddies and c is a dimensionless coefficient. This formula has been used by many authors.

The pressure fluctuations can be expressed as a space integral of the velocity field. They are separated into two parts,

$$p = p_T + p_M \quad , \tag{8}$$

the one, p_T, being caused by interactions of velocity fluctuations. The other part, p_M, is produced by interaction of the mean velocity gradients with velocity fluctuations. The first part of the pressure-shear velocity correlation term may be determined from the previously [4] suggested relation,

$$\overline{p_T\left(\frac{\partial u_i}{\partial x_j} + \frac{\partial u_j}{\partial x_i}\right)} = -2k_p \epsilon \frac{\overline{u_i u_j} - \overline{q^2}\delta_{ij}/3}{\overline{q^2}} \quad , \tag{9}$$

which gives, if Eq. (7) is inserted,

$$\overline{p_T\left(\frac{\partial u}{\partial y} + \frac{\partial v}{\partial x}\right)} = -k_p c \sqrt{\overline{q^2}/2} \frac{\overline{uv}}{L} \quad . \tag{10}$$

For the second part, an integral expression can be derived from the Navier Stokes equations, which sug-

gests as the simplest relation

$$\overline{P_M(\frac{\partial u}{\partial y} + \frac{\partial v}{\partial x})} \sim \overline{q}^2 \frac{\partial U}{\partial y} \quad . \tag{11}$$

Since only the kinetic fluctuation energy equation is used instead of equations for each of the velocity fluctuation components, u, v, w, the value of $\overline{v^2}$ in Eq. (3) is to be expressed as a fraction of $\overline{q^2}$. Therefore, the production term of Eq. (3) and the term of Eq. (11) are condensed into one expression,

$$\overline{v^2} \frac{\partial U}{\partial y} - \overline{P_M(\frac{\partial u}{\partial y} + \frac{\partial v}{\partial y})} = a_p \frac{\overline{q^2}}{2} \frac{\partial U}{\partial y} \quad . \tag{12}$$

The turbulent energy diffusion is approximated by

$$\overline{(q^2/2 + p)v} = - k_q \sqrt{\overline{q^2}/2} \, L \frac{\partial(\overline{q^2}/2)}{\partial y} \quad , \tag{13}$$

and a similar relation is used for the diffusion term of Eq. (3),

$$\overline{(v^2 + p)u} = - k_{qr} \sqrt{\overline{q^2}/2} \, L \frac{\partial \overline{uv}}{\partial y} \quad . \tag{14}$$

These gradient diffusion models are used by many authors, but there is little justification from physical arguments. They are used for the lack of anything better.

There are five coefficients, namely c_p, k_p, a_p, k_q, and k_{qr}. In addition, the determination of the length scale, L, which makes allowance for the space structure of turbulence, requires a fifth equation. The closure assumptions for this equation will bring in some more coefficients. The idea is to consider all these coefficients as universal constants, although they are not strictly universal in real turbulent flow fields. Only numerical calculations of flow cases will show, firstly, whether the system of equations is able to predict qualitatively the actual behavior of several shear flows, and secondly, how well the calculated results agree quantitatively with available data. It may be admitted, the indispensable requirement that Eqs. (3) and (4) conform to the logarithmic velocity law in the layer of constant shear stress near a solid wall, imposes conditions on the choice of the coefficients and consequently reduces the number of the free coefficients. We will discuss the given equations a little further before we proceed with the treatment of the length scale equation.

Two different assumptions for the shear stress have previously been used in connection with the kinetic fluctuation energy equation. The first was suggested by L. Prandtl [2], where the shear stress is determined from the eddy viscosity concept,

$$- \overline{uv} = k \sqrt{\overline{q^2}/2} \, L \frac{\partial U}{\partial y} \quad . \tag{15}$$

A number of authors have applied this relation with their methods. The second assumption, which was applied by P. Bradshaw [15] to boundary layer calculations, postulates a constant ratio of shear stress to kinetic fluctuation energy,

$$- \overline{uv} = a_1 \overline{q^2} \quad . \tag{16}$$

These assumptions are replaced by the transport equation for shear stress, Eq. (3), for several reasons. Eq. (16) fails, when the shear stress changes its sign. The assumption made in Eq. (15) is not compatible with Eq. (3) in general cases. For example, in asymmetric shear flows, the shear stress, $- \overline{uv}$, and the velocity gradient, $\partial U/\partial y$, change their signs at different positions. It is interesting to note that both Prandtl's eddy viscosity relation, Eq. (15), as well as Bradshaw's assumption of a constant ratio of shear stress to kinetic energy, Eq. (16), are included in Eq. (3) as special cases. This is shown as follows:

1. Neglect the terms of convective and diffusive transport (nearly homogeneous turbulent field). Then Eq. (3) reduces to

$$- \overline{uv} = \frac{a_p}{k_p c_p} \sqrt{\overline{q^2}/2} \, L \frac{\partial U}{\partial y} \quad . \tag{17}$$

This relation is identical with Eq. (15), if

$$k = \frac{a_p}{k_p c_p} \quad . \tag{18}$$

2. Insert Eq. (16) in Eqs. (3) and (4). Then Eqs. (3) and (4) are identical, if the following conditions are met

$$a_p = 4a_1^2 \; (=0.09) \quad , \quad k_p = 1 \quad , \quad k_{qT} = k_q \quad . \tag{19}$$

Under these conditions, Eq. (3) and Eq. (4) yield a constant ratio of $-\overline{uv}/q^2$, if the initial and boundary conditions permit this, as is the case for boundary layers. In other cases, e.g. wake flow, the two equations have different solutions.

The conditions, given by Eq. (19) can serve as a guide for selecting suitable values of the coefficients. In addition, it is mentioned that the isotropic turbulence relations give $a_p = 4/15 \approx 0.267$. This value is nearly three times the value of Eq. (19).

4. NUMERICAL SOLUTIONS FOR ASYMPTOTIC PLANE WAKE FLOW

The equations were applied to the case of asymptotic plane wake flow at large distances, x, downstream of a cylinder in a uniform stream of velocity, U_∞. The axis of the cylinder is parallel to the z-coordinate. An implicit iterative finite difference scheme has been used to calculate the development of the flow, starting with given distributions of U, q^2, and $\overline{uv}$ at a certain plane $x = $ const. The length scale, L, was assumed independent of y:

$$\frac{L}{b} = \text{const} \quad , \tag{20}$$

where b is the half width of the mean velocity defect distribution, at a point half way between the central velocity and free stream velocity.

With increasing x, the calculated distributions asymptotically approach the familar self-similar distributions, where the width of the wake spreads as $b \sim x^{1/2}$. The calculation was continued until self-similarity was established. Naturally, the rate of spread depends on the assumed value of L/b. Fig. 1 shows the parameter $b/(xc_d d)^{1/2}$ as a function of L/b, where c_d is the drag coefficient and d the diameter of the cylinder. These calculations are based on values of the coefficients in accordance with Eq. (19). The main outcome of these calculations is the strong influence of the coefficients of diffusion terms, $k_q = k_{qT}$. The curve for $k_q = 0.6$ has a maximum value $b/(xc_d d)^{1/2} = 0.208$. Thus the experimental value of $b/(xc_d d)^{1/2} = 0.25$ [16] is not met with $k_q = 0.6$, regardless of the value chosen for L/b. In addition, the line of mixing length theory is also indicated in Fig. 1.

The choice of k_q and L/b also influences strongly the distributions of mean defect velocity, fluctuation energy and shear stress. This follows from Fig. 2, where the distributions are plotted in non-dimensional form as functions of y/b. Calculations with three different values of k_q are shown, where L/b is selected from Fig. 1 so as
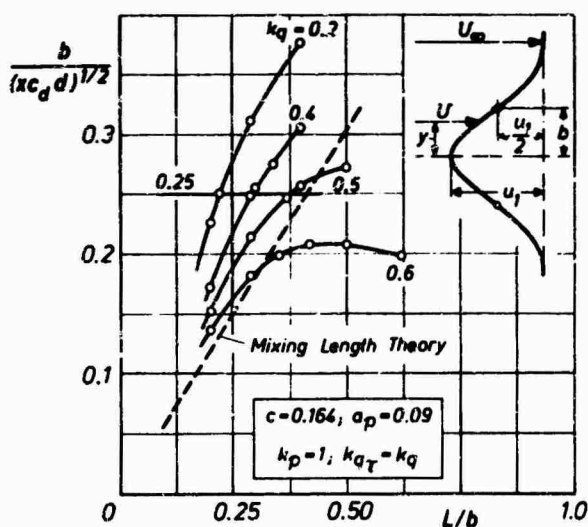
Fig. 1. Asymptotic width of plane wake flow vers. L/b. Eqs. (3) to (6)
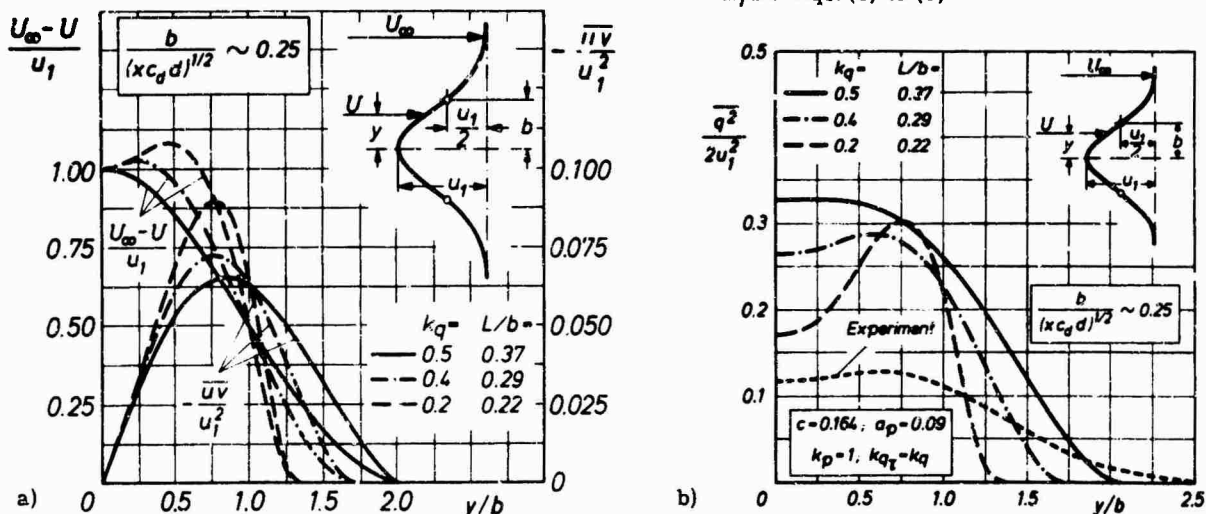
Fig. 2. Asymptotic distributions of plane wake flow. Eqs. (3) to (6)
  a) Mean velocity defect and Reynolds shear stress
  b) Kinetic fluctuation energy

to reproduce a value of $b/(x c_d)^{1/2} = 0.25$. For $k_q = 0.2$ and 0.4 , saddle shaped profiles of mean velocity are obtained. The velocity profile for $k_q = 0.5$ agrees perfectly with the relation, which was given by T o w n s e n d [12] as an approximation to the experimental distribution. As seen from Fig. 2b, the calculated distributions of $\overline{q^2}/(2 u_1^2)$ are all substantially higher than the experimental results by T o w n s e n d. If Prandtl's eddy viscosity relation is used instead of Eq. (3), no saddle shaped mean velocity distributions occur, and the magnitude of k_q has a minor effect.

5. LENGTH SCALE EQUATION

The given system of equations cannot be applied to general flow cases, unless a general relation for the length scale, L , is available. Before a length scale equation can be derived from the Navier Stokes equation, the length scale has to be defined. The magnitude of L , as used in the preceding equations, has the meaning of a length characteristic for the energy carrying eddies. Thus, in shear flows, for which the boundary layer simplifications apply, an integral scale, defined by

$$\overline{q^2} L = \frac{3}{8} \int_{-\infty}^{\infty} R_{ii}(r_y) \, dr_y \qquad , \qquad (21)$$

appears to be an appropriate quantity, where

$$R_{ii}(r_y) = \overline{u_i(x, y, z) \, u_i(x, y + r_y, z)} \qquad (22)$$

is the two point correlation function, Fig. 3, and

$$\overline{q^2} = \overline{u_i(x, y, z) \, u_i(x, y, z)} = R_{ii}(0) \qquad . \qquad (23)$$
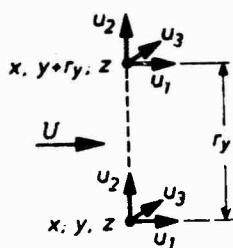
Fig. 3. Definition of two-point correlation function and integral length scale

The factor 3/8 in Eq. (21) causes L to be identical with the well known lateral integral length scale in an isotropic turbulence field. If solid walls are present, the range of integration is limitted by the solid wall.

The following operations have to be made in order to derive the integral length scale equation:

1. Multiply the Navier Stokes equation of velocity component $U_i + u_i$ at location x, y, z with the fluctuation component, u_i , at point x, $y + r_y$, z and take the average.

2. Multiply the Navier Stokes equation of velocity component $U_i + u_i$ at location $x, y + r_y, z$ with the fluctuation component, u_i , at point x, y, z and take the average.

3. Add the equations of all three components and integrate along r_y . Again the high Reynolds number approach is used (local isotropy), boundary layer simplifications are introduced and only first order terms are retained.

With repeated application of the continuity equation, the operations result in the following equation for the product, $\overline{q^2}/2 \, L$:

$$\frac{1}{2} \frac{\partial}{\partial x} (U \overline{q^2} L) + \frac{1}{2} V \frac{\partial(\overline{q^2} L)}{\partial y} + \frac{3}{16} \left[(\frac{\partial U}{\partial y})_y \int_{-\infty}^{\infty} R_{21} dr_y + \frac{1}{y^i} \int_{-\infty}^{\infty} (y + r_y)^j \left(\frac{\partial U}{\partial y}\right)_{y + r_y} R_{12} dr_y \right] -$$

$$- \frac{3}{16} \int_{-\infty}^{\infty} \frac{\partial}{\partial r_k} (R_{(ik)i} - R_{i(ik)}) dr_y + \frac{3}{16} \frac{1}{y^j} \frac{\partial}{\partial y} \left\{ y^j \int_{-\infty}^{\infty} (R_{(12)i} + \overline{pv} + \overline{vp}) dr_y \right\} = 0 \qquad , \qquad (24)$$

where

$$R_{12} = \overline{u(y) v(y + r_y)} \qquad ,$$

$$R_{21} = \overline{u(y + r_y) v(y)} \qquad ,$$

$$R_{(ik)j} = \overline{u_i(y) u_k(y) u_j(y + r)} \qquad , \qquad \Bigg\} \qquad (25)$$

$$\overline{pv} = \overline{p(y) v(y + r_y)} \qquad ,$$

$$\overline{vp} = \overline{p(y + r_y) v(y)} \qquad .$$

Equation (24) will be referred to as the length scale equation. The first two terms of Eq. (24) are the convection terms. The third term represents turbulent production, the fourth term[1] acts as dissipation, and the last term stands for turbulent diffusion transport.

6. CLOSURE ASSUMPTIONS FOR THE LENGTH SCALE EQUATION

Closure assumptions are required for the last three terms of Eq. (24). Most striking is the complicated form of the production term in contrast to the simple expression of the production term in the equation of kinetic fluctuation energy, Eq. (4). In particular, the value of $\partial U/\partial y$ at position $y + r_y$ and thus the mean velocity distribution of the whole plane, $x = $ const, enters the equation. It will be shown later that this fact needs further attention.

One way to treat the second integral is to expand $\partial U/\partial y$ in a Taylor series with respect to y and define the following length scales:

$$L_{12} = \frac{3}{16\,\overline{uv}} \int_{-\infty}^{\infty} (R_{12} + R_{21})\,dr_y \quad , \tag{26}$$

$$L_{12,n} = \left[\frac{3}{16(n-1)!\,\overline{uv}} \int_{-\infty}^{\infty} R_{12}\,r_y^{n-1}\,dr_y \right]^{1/n} \quad . \tag{27}$$

Then, the production term of Eq. (24) is represented by the series

$$\frac{3}{16} \left[\left(\frac{\partial U}{\partial y}\right)_y \int_{-\infty}^{\infty} R_{21}\,dr_y + \frac{1}{y^j} \int_{-\infty}^{\infty} (y + r_y)^j \left(\frac{\partial U}{\partial y}\right)_{y+r_y} R_{12}\,dr_y \right]$$

$$= \overline{uv}\left[L_{12}\frac{\partial U}{\partial y} + \frac{1}{y^j}\sum_{n=2}^{\infty} L_{12,n}^n \frac{\partial}{\partial y}\left(y^j \frac{\partial^{n-1}U}{\partial y^{n-1}}\right) \right] \quad . \tag{28}$$

This relation can be used in combination with the assumption that all the length scales are in constant ratio to L. In case that a symmetric shape of R_{12} is assumed, the terms of even values of n vanish. For numerical calculations, only one or two terms of the series can be retained. According to measurements made by W. G. Rose [17] in a homogeneous shear flow, the ratio of the length scales is

$$\zeta = \frac{L_{12}}{L} \approx 1.2 \quad . \tag{29}$$

The fourth term of Eq. (24) represents the transport of mechanical energy in wave number space. In analogy to Eq. (7) we put

$$-\frac{3}{16} \int_{-\infty}^{\infty} \frac{\partial}{\partial r_k} (R_{(ik)i} - R_{i(ki)})\,dr_y = c_L\,c\left(\frac{\overline{q^2}}{2}\right)^{3/2} \quad . \tag{30}$$

An estimation of the coefficient, c_L, is gained from a comparison with the decay law of kinetic fluctuation energy in a uniform stream behind a grid. Theoretical predictions, based on Birkhoff's and Loitsianski's invariant theory as well as on experimental data of recent experiments [18] correspond to a value of c_L between 0.667 and 0.8.

With respect to the flux of diffusion, the expression

$$\int_{-\infty}^{\infty} (R_{(i2)i} + \overline{pv} + \overline{vp})\,dr_y = -k_{qL}\sqrt{\overline{q^2}/2}\,L\left\{L\,\frac{\partial(\overline{q^2}/2)}{\partial y} + \alpha_L\,\frac{\overline{q^2}}{2}\,\frac{\partial L}{\partial y}\right\} \tag{31}$$

appears reasonable, where k_{qL} and α_L are two additional coefficients. With this assumption we have a flux of diffusion at constant L and one at constant $\overline{q^2}/2$. At the free boundaries (jet and wake flow, outer edge of boundary layers) the field quantities $\partial U/\partial y$, $\overline{uv}$, and q^2 tend to zero, but L may be finite. Energy production and dissipation become small when compared with the convection and diffusion. These conditions cannot be satisfied simultaneously, unless

---

[1] This term is expressed in cartesian coordinates.

$$k_q = k_{qL} \quad .$$

(32)

If Eq.(24) is applied to the fully turbulent part of the law of the wall, the convection terms vanish, but diffusive transport does not. The requirement that the length scale equation is compatible with the law of the wall provides an important relation between the coefficients of the length scale equation and the v. Kármán constant, $\varkappa$. That is, the value of $\varkappa$ is determined, if a set of coefficients is assumed or, vice versa, a constraint is imposed on the choice of one of the coefficients, if a value of $\varkappa$ (e.g. $= 0.4$) is prescribed.

7. APPLICATION OF THE LENGTH SCALE EQUATION WITH SIMPLIFIED PRODUCTION TERM

The simplest assumption is to retain only the first term of the series of the production term of Eq.(28). The length scale equation in this version has been used by several authors [19, 20]. In particular Rodi and Spalding [19] have achieved interesting results for jet flow. We have applied the length scale equation, in conjunction with Eqs.(3) to (6), to the plane wake flow.
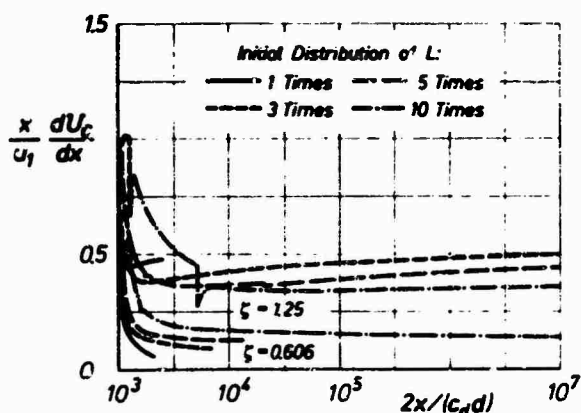
Fig. 4. Development of mean center velocity gradient of plane wake flow Eqs.(3) to (6). Eq. (24) with production term, Eq. (28)

$c = 0.164;\ a_p = 0.09;\ k_p = 1;$
$k_q = k_{qT} = 0.4;\ c_L = 0.8;\ \alpha_L = 0.5$

The main results of these calculations are shown in Fig. 4, where the mean center velocity gradient, $(x/u_1)dU_c/dx$, is plotted versus the dimensionless distance in mean flow direction, $2x/(c_d d)$. Two groups of runs are shown. With the first group we adopted the law of the wall constraint $(\varkappa = 0.4)$. With the chosen coefficients, a value of $\zeta = 0.606$ was obtained. With the second group of runs the constraint of the law of the wall was dropped and $\zeta = 1.25$ was assumed. The individual curves of each group differ in that the initial distribution of L was multiplied by 3, 5, and 10, respectively. Jumps in the curves occur every time, when the number of mesh points is reduced by a factor $1/2$.

It is seen that the curves of the first group decrease continuously for larger downstream distances. None of the curves approaches the state of self-similarity, characterized by $(x/u_1)dU_c/dx = 0.5$. At the same time, the ratios $\overline{q^2}/(2u_1^2)$ and $-\overline{uv}/u_1^2$ decrease continuously. The curves of the second group, however, approach well the value of $(x/u_1)dU_c/dx = 0.5$. Thus self-similar distribu-

tions of $(U_\infty - U)/u_1$, $-\overline{uv}/u_1^2$, and $\overline{q^2}/(2u_1^2)$ are established, if the calculations are continued over a sufficiently long time.

Several variations have been tried, but it became evident that the actual behavior of wake flow is not reproduced by the calculations if the simple form of the length scale equation is used in conjunction with the wall flow constraint. This is a very important finding which, in effect, disqualifies the simple form of the length scale equation as a generally applicable equation.

8. SOLUTIONS WITH TRANSPORT TERMS OMITTED

The conclusion from the foregoing investigations is that the production term is over-simplified, if only the first term of the series, Eq.(28), is retained. This becomes clear also from the unsatisfactory fact that the solution of the law of the wall is dominated by the diffusion term. There is effectively no solution, if the diffusion term is neglected. This situation changes if two terms of the production are retained.

In this context, it is informative to study solutions of the equations if the diffusion terms are neglected altogether. The relations become particularly simple for such flow cases, in which the convective transport terms are absent. From Eq.(3) and (4) the following relations are obtained

$$\left. \begin{aligned} -\frac{\overline{uv}}{\overline{q^2}} &= \frac{1}{2}\sqrt{a_p/k_p} \quad , \\[2ex] L\frac{dU}{dy} &= |\overline{uv}|^{1/2} c\left(\frac{k_p}{a_p}\right)^{3/4} \quad . \end{aligned} \right\}$$

(33)

The first relation states that the ratio of $-\overline{uv}/q^2$ is constant everywhere. The second relation is the mixing length formula, if $c(k_p/a)^{3/4} = 1$.

Combination of Eq. (4) and (24) yields

$$L^2 = \frac{c_L - \zeta}{\zeta_3} \frac{y^j \, \partial U/\partial y}{\partial(y^j \partial^2 U/\partial y^2)/\partial y} \qquad , \qquad (34)$$

where $\zeta_3 = (L_{12,3}/L)^3$. This relation shows some resemblance to v. Kármán's similarity theory. From the law of the wall constraint we have

$$\frac{c_L - \zeta}{\zeta_3} = 2\varkappa^2 \qquad . \qquad (35)$$

Finally, Eqs. (33) and (34) can be combined to give

$$\frac{1}{y^j} \frac{\partial}{\partial y} \left(y^j \frac{\partial^2 U}{\partial y^2} \right) = 2\varkappa^2 \frac{(\partial U/\partial y)^3}{\overline{uv}} \qquad , \qquad (36)$$

where $\varkappa$ is the only empirical constant. The main difference of this relation from v. Kármán's relation is that it is a differential equation of third order, whereas v. Kármán's equation is of second order. Thus an additional boundary condition can be satisfied with Eq. (36).

Eq. (36) has been applied to three cases:

1. Straight Couette flow,

2. Flow strough a cylindrical pipe,

3. Pressure flow through a channel of infinite width.

In the case of straight Couette flow, an analytical solution can be given, which includes an elliptical integral of the first kind, whereas in the cases of pipe and channel flow, Eq. (36) was numerically solved using a Runge-Kutta method. The velocity distributions ·ressed as the velocity defect, and the length scales are shown in Fig. 5. The length scale has a singularity at the center of pipe and channel, respectively. The differences between the axisymmetric and plane case are noteworthly. In Fig. 5a the experimental velocity distribution after Nikuradse [21] is also given. The velocity distributions are qualitatively correct in all three cases, although the quantitative agreement with experiment is not as good as desired.
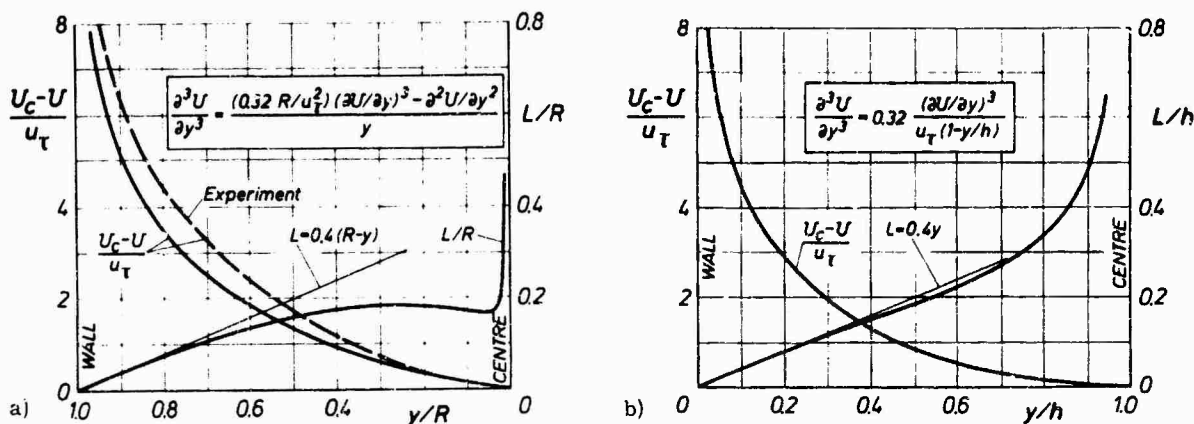
Fig. 5. Distributions of mean velocity (velocity defect law) and length scale of pipe and plane channel flow. Diffusion terms omitted.
a) Pipe flow ; R = radius of pipe
b) Channel flow; h = half height of channel

The purpose of this investigation is to show that the equations, with diffusion terms omitted, give correct results, if proper assumptions for the production term of the length scale equation are used. The diffusion terms are important to achieve better agreement with the actual flow, but their effect is not dominating.

9. REFINED ASSUMPTIONS FOR THE LENGTH SCALE EQUATION

As the next step, we tried to include the two term expression of the length scale production term in wake flow calculations. However, numerical instability occurred with the finite difference method because of the third order derivative. Perhaps this instability can be overcome with a more refined method. This question is left to be investigated. For the present we escaped from the dilemma by using the following approach. The correlation functions are approximated by

$$R_{12} = R_{21} = \overline{uv} \left\{ 1 - \frac{1}{64} (r_y/L)^6 + \frac{a}{4} [1 - \frac{1}{16} (r_y/L)^4](r_y/L)^2 - \frac{b}{16} [1 - \frac{1}{4} (r_y/L)^2](r_y/L)^4 \right\} \qquad (37)$$

A. '

for $-2L \leq r_y \leq 2L$ and

$$R_{12} = R_{21} = 0 \quad \text{for} \quad |r_y| \geq 2L \quad , \tag{38}$$

where a and b are two dimensionless quantities. By definition of Eq. (26) it follows that

$$\zeta = \frac{L_{12}}{L} = \frac{9}{7} - \frac{2}{7} a + \frac{3}{35} b \quad . \tag{39}$$

The quantities a and b are determined from Eq. (39) and the constraint of the law of the wall, if ζ, $\varkappa$ and the other coefficients are given.

With these relations included in the length scale equation, Eq. (24), asymptotic self-similar distributions are produced. Results are shown in Fig. 6 and are compared with the results, based on a constant value
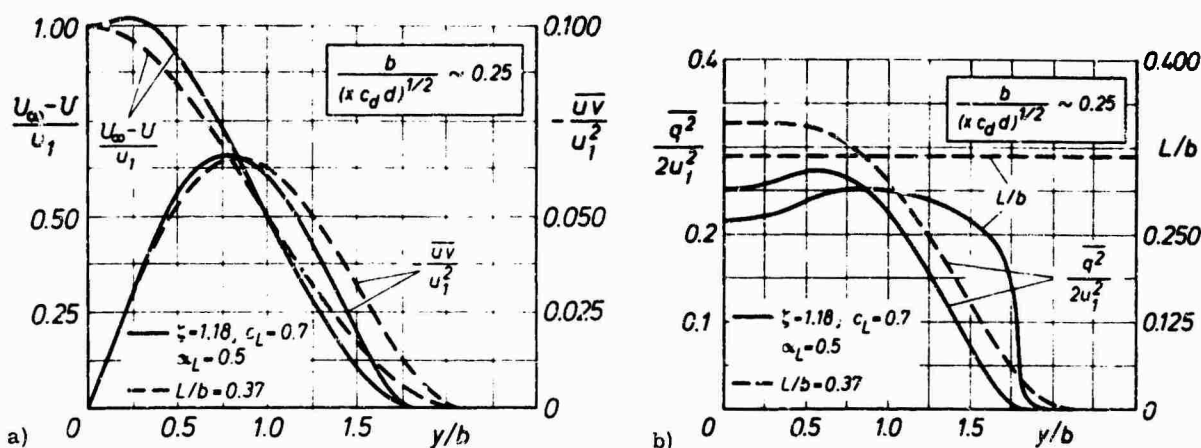
Fig. 6. Asymptotic distributions of plane wake flow. Eqs. (3) to (6)

$$c = 0.164, \quad a_p = 0.09, \quad k_p = 1, \quad k_q = k_{q\tau} = 0.5$$

—·— L from Eqs. (24) and (37)
——— L/b = assumed
a) Mean velocity defect and Reynolds shear stress
b) Kinetic fluctuation energy and length scale

of L/b . The value of $\zeta = 1.18$ was chosen to give a dimensionless width of $b/(\varkappa c_d d)^{1/2} = 0.25$. With regard to the equations for shear stress and kinetic fluctuation energy, the same coefficients are used as for the calculations shown in Fig. 2. The mean velocity distributions are slightly saddle shaped. Of course, the agreement with experimental data can easily be improved by modification of the coefficients. The main point was to show that, in this way, different types of turbulent flow can be reproduced, at least qualitatively, with the same set of coefficients. Fig. 6b shows that the kinetic fluctuation energy is lower as calculated with constant L/b . The calculated length scale varies only little over most part of the turbulent flow regime.

10. CONCLUDING REMARKS

Striving for a unified approach to turbulent shear flow calculation, it appears reasonable to concentrate oneself first to two-dimensional layer flows. A formalism has been discussed, in which the Reynolds shear stress is determined from the transport equations for fluctuation energy, shear stress, and length scale. The transport equation for the shear stress includes Prandtl's eddy viscosity relation and Bradshaw's concept of constant ratio of shear stress to fluctuation energy as special cases, depending on the choice of the empirical coefficients.

No perceptibly better results could be achieved with the shear stress transport equation than with the Prandtl eddy viscosity relation. It is believed, however, that the advantages of the shear stress transport equation will come to light, when it is applied to other flow cases.

The most important conclusion to be drawn from the present calculations is that the production term of the length scale equation deserves special attention. Realistic results for flows with free and solid boundaries cannot be obtained, if this term is oversimplified.

Furthermore, it was found that the turbulent diffusion terms strongly influence the rate of spread and the shape of mean velocity distribution of wake flow, whereas for Couette, pipe, and channel flow, the influence of diffusion is obviously weaker. Actually, the gradient diffusion formulae give only a poor description of the real processes. It is a disappointing fact that no use has been made, so far, of the available knowledge on the intermittent structure of turbulent flow near free boundaries.

Much further work is left to be done. Calculations for many flows, such as free jets, boundary layers etc., have to be performed and compared with experimental data. Numerous combinations of the coefficients and

modifications of the closure assumptions have to be tested. Not until then a final set of coefficients can be fixed. The numerical procedures have to be improved. There is some hope that finally a method will be accomplished, which is capable of reproducing a rather wide class of turbulent flows.

11. REFERENCES

[1]   Kolmogorov, A. N.   Equations of Turbulent Motion of an Incompressible Fluid
                         Izv. Akad. Nauk. SSSR Ser. fiz. VI No. 1-2, (1942), pp. 56-58

[2]   Prandtl, L.   Ueber ein neues Formelsystem für die ausgebildete Turbulenz
      Wieghardt, K.   Nachr. Akad. Wiss. Göttingen, Math.-Phys. K'. (1945), S. 6-19

[3]   Chou, P. Y.   On Velocity Correlations and the Solutions of the Equations of Turbulent
                         Fluctuation
                         Quart. Appl. Math., Vol. 3 (1945), pp. 38-54

[4]   Rotta, J. C.   Statistische Theorie nichthomogener Turbulenz
                         1. Mitt.: Z. Phys. 129 (1951), S. 547-572
                         2. Mitt.: Z. Phys. 131 (1951), S. 51-77

[5]   Daly, B. J.   Transport Equations in Turbulence
      Harlow, F. H.   Phys. Fluids, Vol. 13 (1970), pp. 2634-2649

[6]   Gawain, T. H.   A Unified Heuristic Model of Fluid Turbulence
      Pritchett, J. W.   J. Comp. Phys. 5 (1970), pp. 383-405

[7]   Lundgren, T. S.   Turbulent Pipe and Channel Flow
                         Phys. Fluids, Vol. 14 (1971), pp. 225-230

[8]   Nee, V. W.   Simple Phenomenological Theory of Turbulent Shear Flows
      Kovasznay, L. S. G. Phys. Fluids, Vol. 12 (1969), pp. 473-484

[9]   Saffman, P. G.   A model for inhomogeneous turbulent flow
                         Proc. Roy. Soc. London A. 317 (1970), pp. 417-433

[10] Rotta, J. C.   Turbulente Strömungen
                         Verlag B. G. Teubner, Stuttgart 1971

[11] Rotta, J. C.   Turbulent Boundary Layers in Incompressible Flow
                         Progr. Aero. Sci. 2 (1962), pp. 1-219
                         Ed.: A. Ferri, D. Küchemann, L. H. G. Sterne, Pergamon Press, Oxford

[12] Townsend, A. A.   The Structure of Turbulent Shear Flow
                         Cambridge, University Press 1956

[13] Glushko, G. S.   Turbulent boundary layer on a flat plate in an incompressible fluid
                         Izv. Akad. Nauk. SSSR Ser. Mek. No. 4 (1965), pp. 13-23.
                         Translation NASA TT F. 10, 080

[14] Beckwith, I. E.   Detailed description and results of a method for computing mean and
      Bushnell, D. M.   fluctuating quantities in turbulent boundary layers
                         NASA TN D-4815, 1968

[15] Bradshaw, P.   Calculation of boundary-layer development using the turbulent energy
      Ferriss, D. H.   equation
      Atwell, N. P.   J. Fluid Mech., Vol. 28 (1967), pp. 593-616

[16] Schlichting, H.   Boundary Layer Theory
                         6. Ed. 1968, McGraw-Hill Book Comp., New York

[17] Rose, W. G.   Results of an attempt to generate a homogeneous turbulent shear flow
                         J. Fluid Mech., Vol. 25 (1966), pp. 97-120

[18] Comte-Bellot, G.   The use of a contraction to improve the isotropy of grid-generated
      Corrsin, S.   turbulence
                         J. Fluid Mech., Vol. 25 (1966), pp. 657-682

[19] Rodi, W.   A Two-Parameter Model of Turbulence, and its Application to Free Jets
      Spalding, D. B.   Wärme- und Stoffübertragung 3 (1970), S. 85-95

[20] Wolfshtein, M.   On the Length-Scale-of-Turbulence Equation
                         Proc. XII Israel Ann. Conf. AVIATION and ASTRONAUTICS, March 1970.
                         Israel Journal of Technology, Vol. 8, No. 1-2 (1970), pp. 87-99

[21] Nikuradse, J.   Gesetzmäßigkeiten der turbulenten Strömung in glatten Rohren
                         VDI-Forschungsheft 356 (1932), S. 1-36

AN EXPERIMENTAL STUDY OF THE
COMPRESSIBLE TURBULENT BOUNDARY LAYER
WITH AN ADVERSE PRESSURE GRADIENT

Robert L.P. Voisinet*
Roland E. Lee**
William J. Yanta*
Naval Ordnance Laboratory
White Oak, Silver Spring, Maryland 20910 USA

SUMMARY

The results of a detailed experimental investigation of the compressible turbulent boundary layer in an adverse-pressure-gradient regime are presented. The studies were conducted on a flat nozzle wall for Mach numbers between 4.1 and 4.9, at momentum thickness Reynolds numbers from 5800 to 69,000 and at wall-to-adiabatic-wall temperature ratios of 1.0 and 0.8. Complete and often redundant profile measurements were taken with Pitot and static-pressure probes and conical equilibrium and fine-wire temperature probes. The wall shear and surface heat transfer were measured directly with a skin-friction balance and a heat-transfer gage. The effect of the adverse-pressure-gradient flow on the boundary-layer flow structure, friction drag, and heat transfer, as compared with zero- and favorable-pressure-gradient flow, is discussed. A test showing the effect of nozzle throat cooling on the downstream boundary layer is also reported. This throat cooling caused significant changes in the downstream temperature profiles and recovery factor with no effect on the local wall shear.

NOTATION

B	–	constant in equation 8	β_{δ}	–	pressure gradient parameter = $(\delta/\tau_w)dP/dx$
c_f	–	skin-friction coefficient			
H	–	compressible shape factor δ^*/θ	γ	–	ratio of specific heats
K	–	Karman's constant	δ	–	boundary-layer thickness
M	–	Mach number	δ^*	–	displacement thickness
P	–	pressure	θ	–	momentum thickness
P_s	–	static pressure	θ_E	–	energy thickness
P_{t2}	–	Pitot pressure	θ_h	–	total enthalpy thickness
Pr	–	Prandtl number	μ	–	viscosity
r	–	recovery factor	ν	–	kinematic viscosity
Re_θ	–	momentum thickness Reynolds number	Π	–	Coles' profile parameter
St	–	Stanton number	ρ	–	density
T	–	temperature	τ	–	shear stress
u	–	velocity	ω	–	Coles' wake function
u_τ	–	shear velocity = $\sqrt{\tau_w/\rho_w}$	Subscripts		
			aw	–	adiabatic wall conditions
u^+	–	u/u_τ	e	–	freestream conditions
			o	–	tunnel supply conditions
x	–	distance along plate from nozzle throat	w	–	wall conditions
y	–	distance normal to plate	t	–	stagnation conditions
			Superscripts		
y^+	–	$u_\tau y/\nu_w$	'	–	ideal properties calculated from P_s, P_o, and T_o

1. INTRODUCTION

The prediction of compressible turbulent boundary-layer flows, being of an empirical nature, relies heavily on experimental data. Therefore, it is understandable that there is a definite need for complete and/or redundant boundary-layer experimentation. The objective of the experimental boundary-layer investigation at the Naval Ordnance Laboratory (NOL) is to study the two-dimensional compressible turbulent boundary-layer flow in a thorough, detailed, and systematic manner. Since the boundary-layer behavior is influenced by many factors, the experimental approach is to carefully define and isolate each factor, measure its effect, and correlate the results. The effects of moderate heat transfer and

---

*Aerospace Engineer, Aerophysics Division
**Chief, Boundary Layer Group, Aerophysics Division

favorable pressure gradient on the turbulent boundary layer have been reported earlier[1,2]. This paper describes a subsequent investigation into the effects of adverse pressure gradient on the compressible turbulent boundary-layer flow.

2. EXPERIMENTAL SETUP AND TEST CONDITIONS

The experiment was performed in the NOL Boundary Layer Channel[3] shown in Figure 1. The two-dimensional supersonic half-nozzle, the main component of the facility, has for one wall a flat plate, eight feet long and 12 inches wide, along which the boundary-layer measurements were made. The opposite wall, a flexible contoured plate, was adjusted to produce a pressure gradient flow over the flat test plate. This adjustment provided for an expansion of the flow to Mach 4.9 as in conventional nozzle designs followed by a deceleration in the form of a linear change with streamwise distance in the degree of pressure gradient. This approach allowed for a smooth transition from the favorable to adverse-pressure-gradient regimes with no shock wave interference. Furthermore, since the pressure gradient was generated on a flat test plate, effects due to longitudinal curvature were eliminated. The nozzle contour was computed by using the desired test plate pressure distribution in a method-of-characteristics computer program and correcting for the boundary-layer displacement thickness. A comparison of the prescribed and measured streamwise pressure distribution is shown in Figure 2.

Complete boundary-layer data were obtained at six locations along the flat test plate, at 37, 60, 70, 78, 84, and 90 inches from the nozzle throat. The 37-inch station was located in a favorable-pressure-gradient region while the remaining stations were located in varying degrees of adverse pressure gradient. Tests were conducted at tunnel supply pressures between 1 and 10 atmospheres and supply temperatures of 605°R and 762°R. The wall temperature was maintained constant by cooling the test plate with water. These conditions provided a range of Reynolds number per foot from 6×10^5 to 7.5×10^6 at wall-to-adiabatic-wall temperature ratios of 1.0 and 0.8. Typical boundary-layer thicknesses ranged from 1.5 to 3.5 inches which allowed for detailed probing of the boundary layer, including the sublayer.

3. INSTRUMENTATION AND PROBES

Since the region near the wall of a supersonic turbulent boundary layer is of such importance to the analysis of flow structure, friction drag and heat transfer, the design of probes to accurately measure the flow parameters in this region is necessary. For this reason, probe development became an integral part of the testing program.

Boundary-layer Pitot-pressure profiles were obtained using a flattened Pitot probe with a rectangular 0.003 x 0.100-inch inlet. Due to the small size of the probe and its use near the wall, two phenomena, viscous flow interaction and probe-wall interference, were encountered. The small opening of the
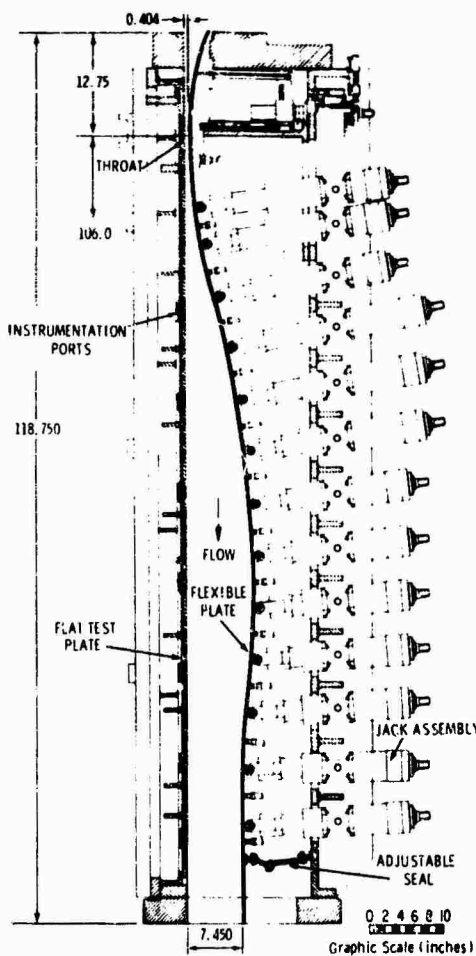
FIGURE 1 NOL BOUNDARY LAYER CHANNEL
ADVERSE-PRESSURE-GRADIENT CONFIGURATION
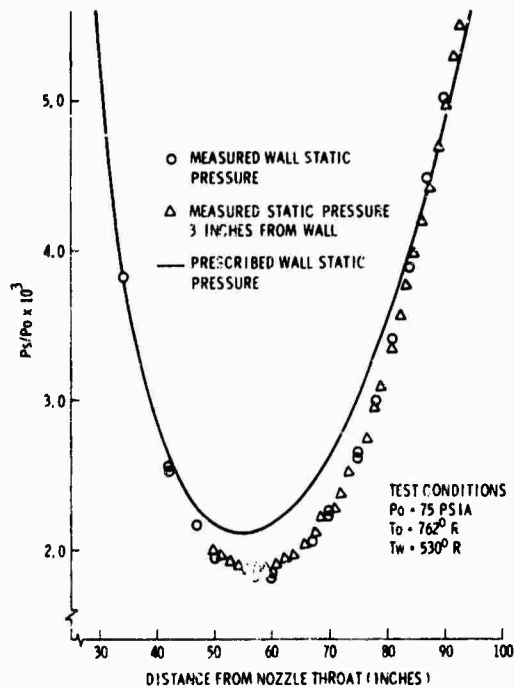
FIGURE 2 STREAMWISE STATIC-PRESSURE DISTRIBUTION

probe combined with the low density in the inner region of the boundary layer resulted in an induced pressure measurement caused by a Knudsen number effect. Since there were no data available in the slip flow regime for the probe geometry used, the viscous flow interaction correction to the Pitot pressure was determined by calibrating the probe in a low density wind tunnel. This viscous correction is shown in Figure 3 for Mach numbers between 0.1 and 0.4 and Reynolds numbers, based on probe inlet height, between 0.5 and 50.0

The second correction to the Pitot-pressure data, probe-wall interference, was determined for the probe geometry used by relying on the shear balance data to provide the velocity gradient at the wall. This correction (shown in Figure 4) was compiled from adiabatic profile data measured in zero, favorable, and adverse-pressure-gradient flows. The effects of both the viscous flow interaction and probe-wall interference corrections on a Mach number profile near the wall are shown in Figure 5.

The stagnation temperature through the boundary layer was measured simultaneously with the Pitot pressure by using a double-probe traverse. Redundant measurements were taken using two temperature probe configurations -- a conical equilibrium temperature probe[4] and a fine-wire stagnation temperature probe[5]. The conical equilibrium temperature probe, a 10-degree platinum cone with a 0.050-inch-diameter base, provided excellent data through the outer part of the boundary layer, however, its size limited its usefulness in probing the inner region. For this inner region, the cone temperature was linearly extrapolated to the measured wall temperature. With the development of the fine-wire stagnation temperature probe, temperature profile measurements were extended into this region near the wall. The fine wire probe consists of a fine wire (0.001-inch diameter, 0.140-inch long) placed normal to the flow with a chromel-alumel thermocouple junction at its center. The local stagnation temperature was computed from the measured wire center and support temperatures and the corresponding measured Pitot pressure with application of conventional empirical equations for predicting the heat exchange to and from the wire. Using the local Mach number distribution, the local static temperature was evaluated. Figure 6 is an example of such a fine-wire temperature probe profile near the wall. Shown for comparison is the temperature derivative at the wall computed from heat-transfer measurements.

Skin friction and heat transfer, two parameters often deduced from profile measurements, were measured directly in these tests with a floating element skin-friction balance manufactured by Kistler Instrument Corporation and a micro-foil heat-transfer gage purchased from the Rdf Corporation.

An additional measurement needed for compressible adverse-pressure-gradient profile evaluations is the local static-pressure variation normal to the wall. This pressure variation is the result of the superposition of the non-uniform isentropic flow of the freestream onto the boundary layer. Three techniques were used in evaluating this static pressure variation through the boundary layer. First, the static pressure was calculated from a strictly isentropic method-of-characteristics nozzle flow computation. Input to this calculation included the experimental streamwise wall pressure distribution and the measured displacement thickness along the test plate. The second method was to measure the static pressure through the boundary layer directly using a 0.040-inch OD static pressure probe. The tip of the probe was a 10-degree cone and four static pressure orifices were located on the cylindrical tubing 20 probe diameters from the tip. The probe data were corrected for flow angularity effects where the direction of the local streamlines was determined from the previously mentioned isentropic flow calculations. In the third approach the static pressure external to the boundary layer was calculated from isentropic flow equations using the ratio of local Pitot to tunnel supply pressure. A comparison of the data from these three methods is shown in Figure 7. Since the flat test plate is essentially a wall of symmetry to a conventional nozzle, the isobars are normal to the test plate at the wall and the static pressure variation becomes apparent only in the outer region of the boundary layer. For this reason, the static pressure profiles used for final analysis were determined by extrapolating the external static pressure from method three to the measured wall pressure while keeping in mind the shape of the profile as computed from methods one and two.
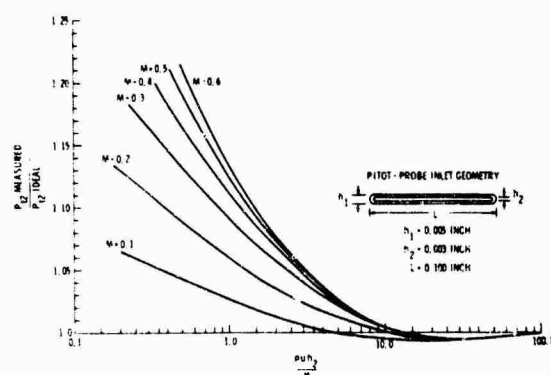
FIGURE 3 PITOT PROBE VISCOUS FLOW INTERACTION CORRECTION
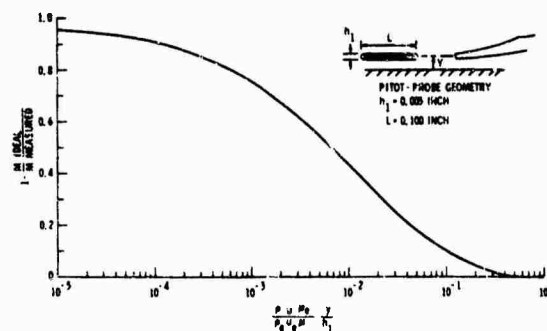
FIGURE 4 PITOT PROBE-WALL INTERFERENCE CORRELATION
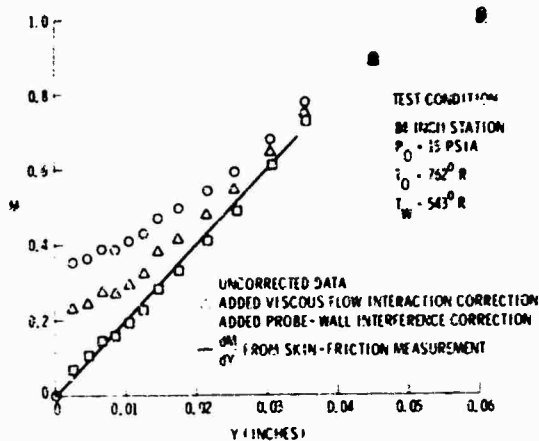
FIGURE 5 TYPICAL MACH NUMBER PROFILE NEAR WALL
WITH PITOT PROBE CORRECTIONS
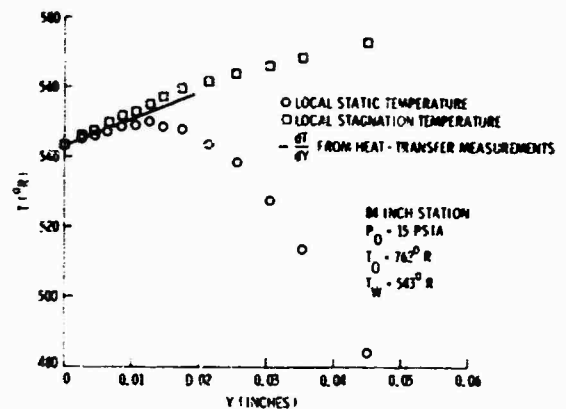
FIGURE 6 TYPICAL FINE-WIRE TEMPERATURE PROFILE NEAR WALL
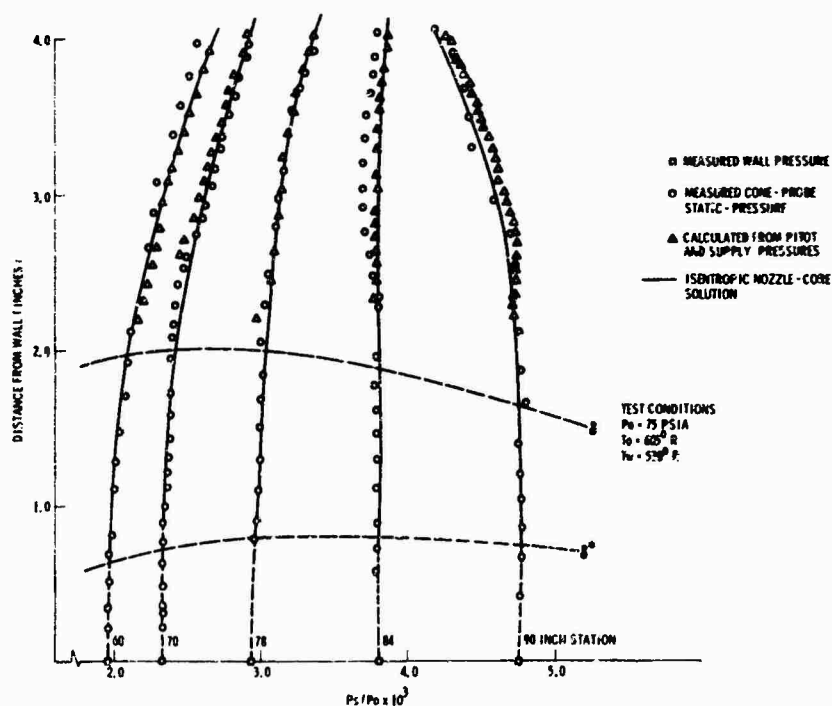
FIGURE 7 NORMAL STATIC PRESSURE DISTRIBUTION

4. DATA REDUCTION

The incorporation of the static-pressure variation into profile and integral parameter definitions is of importance since the determination of the boundary-layer thickness and boundary-layer flux deficits must be referenced to the so-called "ideal" flow properties[6,7]. These ideal properties, calculated from the local static pressure and the tunnel supply pressure and temperature, represent the inviscid flow if the boundary layer were not present. The modified integral parameter definitions used in this report are

displacement thickness

$$\delta_*' = \frac{1}{\rho_w u_w} \int_0^\delta (\rho'u' - \rho u)\, dy \tag{1}$$

momentum thickness

$$\theta' = \frac{1}{\rho'_w u'_w{}^2} \int_0^\delta \rho u(u'-u) \ dy \qquad (2)$$

energy thickness

$$\theta_E' = \frac{1}{\rho'_w u'_w{}^3} \int_0^\delta \rho u(u'^2-u^2) \ dy \qquad (3)$$

total enthalpy thickness

$$\theta_H' = \frac{1}{\rho'_w u'_w} \int_0^\delta \rho u(\frac{h_t}{h_{te}} - 1) \ dy \qquad (4)$$

where the primed quantities refer to the ideal flow quantities and δ is defined as the distance from the wall where $u/u' = 0.995$. The modified integral thicknesses are referenced to the ideal properties at the wall because properties at the edge of the boundary layer are not constant. The modified definitions simplify to the classical definitions when the static pressure is constant through the boundary layer.

5.   TWO-DIMENSIONALITY

Analyses of boundary layer flows in a two-dimensional facility of this type are usually questioned as to the two-dimensionality of flow. This question is intensified when an adverse pressure gradient is imposed. For this reason, two investigations into two-dimensionality were made. First, an oil smear technique was used to obtain surface streamline traces on the flat test plate. A photograph of the results (shown in Figure 8) indicates that although the surface streamlines converge at the sides of the plate, there is a central region, approximately six inches wide, where the surface streamlines are parallel. This is consistent with earlier investigations for a zero-pressure-gradient nozzle configuration where profiles taken three inches off centerline showed no influence of cross flow.

The second evaluation of two-dimensionality was made using a streamwise momentum balance. The classical von Karman momentum integral equation was considered first in the form
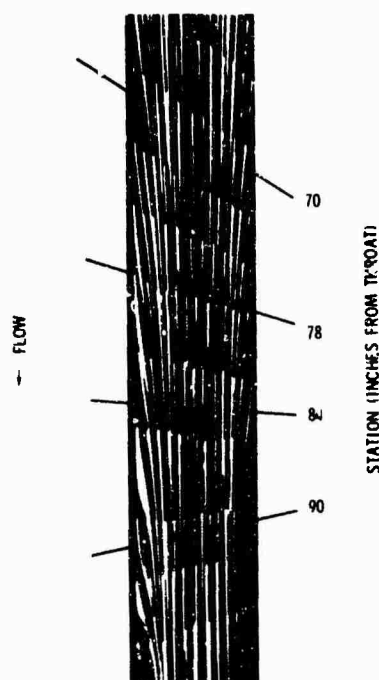
FIGURE 8 OIL SMEAR TEST ON FLAT TEST PLATE
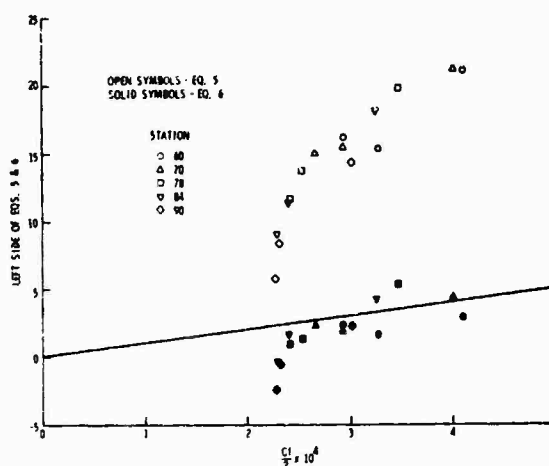
FIGURE 9 STREAMWISE MOMENTUM BALANCE

$$\frac{d\theta}{dx} + \frac{\theta}{u_e} \frac{du_e}{dx} \left[H + 2 - M_e^2 \right] = \frac{C_f}{2}$$ (5)

An evaluation of the terms in the equation points out a momentum deficit of magnitude greater than any expected experimental error. However, by modifying the equation to include the effect of normal static-pressure variation in the form[8]

$$\frac{d\theta}{dx} + \frac{\theta}{u_e} \frac{du_e}{dx} \left[H + 2 - M_e^2 \right] + \frac{P_o}{\rho_e u_e^2} \frac{d}{dx} \int_0^\delta \frac{(P_{se} - P_s)}{P_o} \, dy = \frac{C_f}{2}$$ (6)

we find that the added term in the equation is indeed of the magnitude necessary to compensate for the momentum deficit. Figure 9 shows the relative agreement between the right and left hand sides of equations 5 and 6. Good agreement is achieved when one considers the inaccuracies encountered in differentiating experimental data. Thus, both evaluations indicate the flow to be two dimensional at least within the center six inches of the flow.

6. VELOCITY PROFILES

Velocity profiles along the test plate changed considerably as the magnitude of the pressure gradient was varied. Typical velocity profiles (shown in Figure 10) depict these changes and point out the difficulty in assigning simple power-profile shapes to the adverse-pressure-gradient profiles.

Correlations of the profile results in terms of the Law of the Wall and Law of the Wake are shown in Figure 11. For the cases presented, the shear velocity was computed from the shear balance data and the density at the wall. Due to the complexity of the flow with static pressure variations, no attempt has been made to obtain a compressible transformation of the data. The profile data were compared to the formulation of Coles[9] in the form

$$u^+ = y^+ \qquad\qquad \text{for } y^+ < 11$$ (7)

$$u^+ = \frac{1}{K} \ln y^+ + B + \frac{\Pi}{K} \omega \left(\frac{y}{\delta_c}\right) \qquad \text{for } y^+ > 11$$ (8)

where

$$u^+ = \frac{u}{u_\tau} \qquad\qquad y^+ = \frac{y u_\tau}{\nu_w} \qquad\qquad u_\tau = \frac{\tau_w}{\rho_w}$$

Karman's constant K was assigned the value 0.40 and the value of B was determined from a best fit of the data in the logarithmic region. The definition of δ_c was the value of y at which the slope of the velocity profile $\partial(u^+)/\partial(\ln y^+)$ near the edge of the boundary layer was equal to $1/K$. By defining Coles' wake function, as suggested by Hinze[10],

$$\omega \left(\frac{y}{\delta_c}\right) = 1 - \cos \left(\pi \frac{y}{\delta_c}\right)$$ (9)

the Π parameter was determined from the boundary condition at δ_c, namely $\omega(1) = 2$.

Experimentally determined values of B and Π from adiabatic profiles are plotted versus momentum thickness Reynolds number in Figures 12 and 13. Values of B ranged from 4.7 to 6.2; however, this variation was difficult to interpret due to the combined effects of Mach number, pressure gradient, Reynolds number, and accuracy of τ_w. The dependence of Π on Re_θ' showed a slight tendency for Π to increase with increasing Re_θ'. Values of Π showed a definite increase with increasing adverse pressure gradient. It is anticipated that further evaluation of the data in terms of a compressible transformation will result in a more complete correlation.

7. TEMPERATURE PROFILES AND UPSTREAM HISTORY EFFECTS

Typical temperature-velocity correlations of the adiabatic-wall and moderate heat-transfer tests are shown in Figures 14 and 15 for the stations under investigation. Both fine-wire and conical-equilibrium temperature profiles are plotted for selected cases. Also shown for comparison with the data are the correlations of Crocco and Walz in the form

Crocco relation

$$\frac{T_t - T_w}{T_{te} - T_w} = \frac{u}{u_e}$$ (10)

Walz' relation

$$\frac{T_t - T_w}{T_{te} - T_w} = \frac{T_e[\frac{T}{T_e} + \frac{\gamma-1}{2} M_e^2 (\frac{u}{u_e})^2] - T_w}{T_{te} - T_w}$$

(11)

where

$$\frac{T}{T_e} = \frac{T_w}{T_e} + \left(\frac{T_{aw} - T_w}{T_e}\right) \frac{u}{u_e} + \left(1 - \frac{T_w}{T_e}\right)\left(\frac{u}{u_e}\right)^2$$

Several trends in the adverse-pressure-gradient data can be observed. Generally, the data showed better agreement with the formulation of Walz than Crocco, a trend generally considered characteristic of nozzle-wall boundary-layer flows. Furthermore, the agreement with Walz's formulation was better in the inner region of the boundary layer than the outer with an inflection in the profile occurring at approximately the edge of the sublayer. None of the profiles exhibited a total temperature overshoot in the outer part of the boundary layer but rather a temperature deficit seemed to be indicated. This trend, consistent with previously reported zero and favorable-pressure-gradient results will be considered later. The effect of the adverse pressure gradient on the stagnation temperature-velocity correlation was to shift the profile towards the Crocco relation. Although a part of this trend
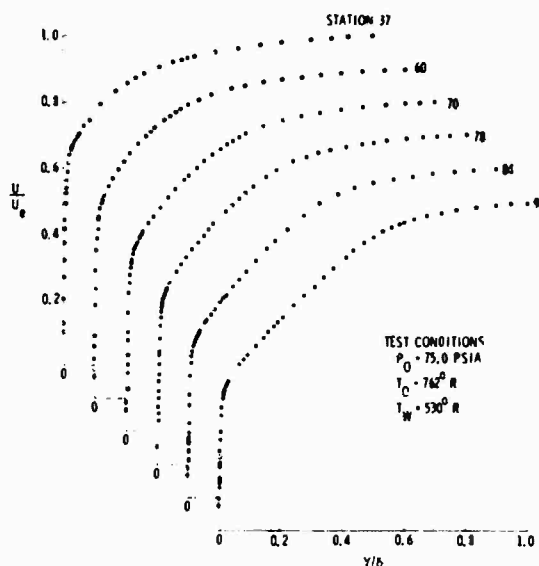
FIGURE 10 TYPICAL VELOCITY PROFILES ALONG TEST PLATE
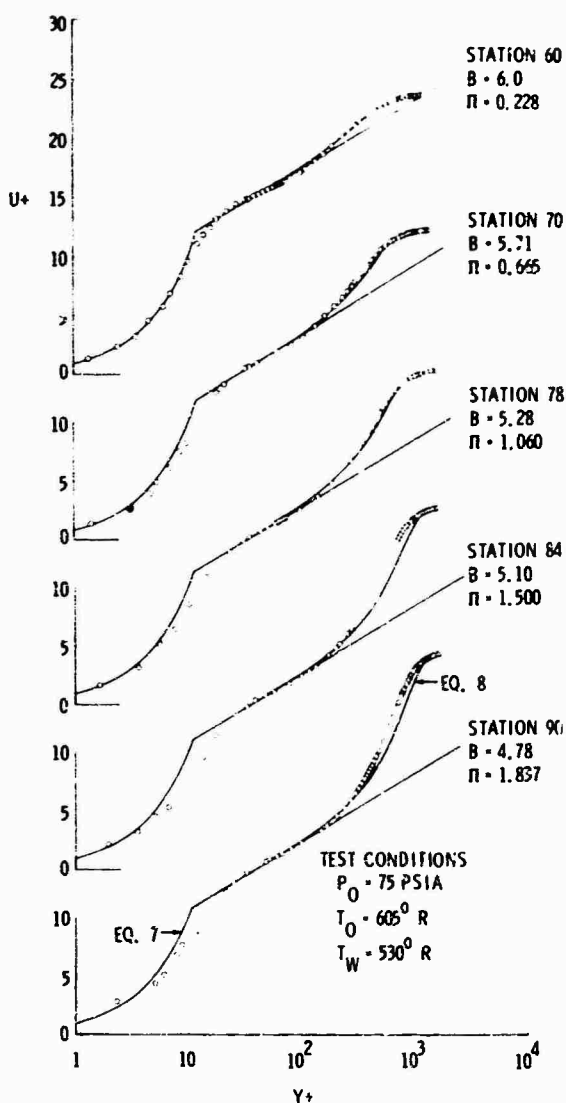
FIGURE 11 TYPICAL LAW OF THE WALL AND WAKE CORRELATIONS
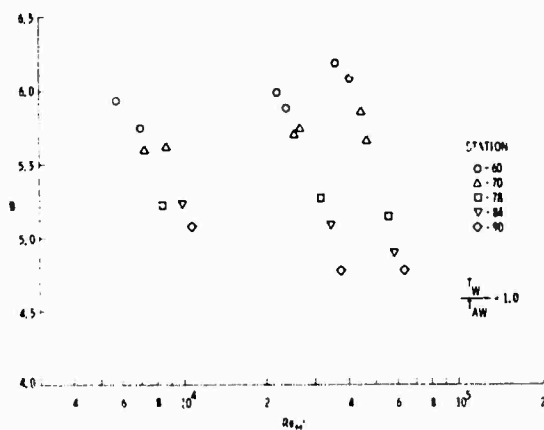
FIGURE 12 VARIATION OF B WITH Re_{θ}'
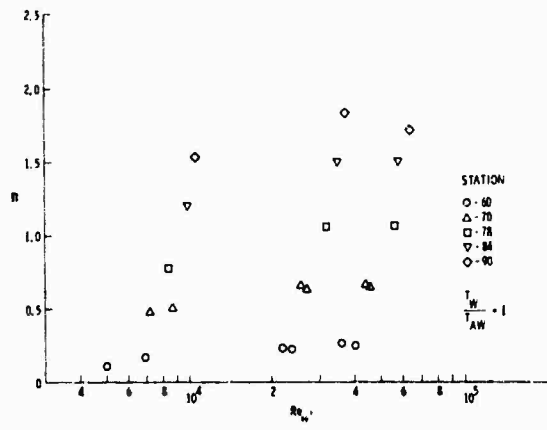
FIGURE 13 VARIATION OF Π WITH Re_{θ}'

may be attributed to temperature relaxation within the boundary layer, it is felt that the relative magnitude of this effect is small compared to the influence of the pressure gradient.

As noted by Bushnell[11] et al, the temperature-velocity correlation applicable to nozzle-wall boundary layers differs considerably from flat plate boundary layers. This difference appears to be due to upstream history effects on the boundary layer; however, the relative contributions from pressure and temperature history are still under investigation. For the tests reported here, a temperature deficit in the outer part of the boundary layer is seen especially for the case of moderate heat transfer. For this condition, a wall-to-adiabatic-wall temperature ratio of 0.8 was maintained constant along the entire nozzle wall including the nozzle throat area. This cooling of the plate at the throat appears to be the cause of the temperature deficit in the downstream boundary-layer profiles. As an illustration of this effect, Figure 16 shows two locally adiabatic total-temperature profiles taken under different nozzle throat cooling conditions. It can be seen that although both profiles were locally adiabatic, cooling the nozzle throat region did indeed cause a temperature deficit in the outer part of the boundary layer. For a truly adiabatic condition at the throat, it is expected that the profile would shift further, to the point of developing the expected overshoot in the outer portion of the boundary layer. The effect of this temperature discrepancy on certain temperature-dependent integral parameters was significant as shown in Table 1. A local recovery factor dependence on the throat cooling was discovered and will be discussed in the next section; however, no effect was noticed on the wall shear measured with a skin-friction balance.

Parameter	Mild Throat Cooling	Severe Throat Cooling
(T_w/T_{aw}) Throat	0.94	0.82
δ	2.43	2.72
$\delta^{*\prime}$	1.019	1.019
$\theta^{\prime}$	0.0991	0.124
θ_L	0.179	0.2245
$\theta_H^{\prime}$	-0.0212	- .0635
$H^{\prime}$	10.27	8 .1

Table 1. Effect of nozzle throat cooling on boundary-layer profile parameters

8. HEAT TRANSFER AND SKIN FRICTION

The adiabatic-wall condition for this series of tests was prescribed as the condition at which the local heat transfer is zero as measured with a heat transfer gage. At this condition the recovery factor was determined from the local Mach number and the wall and tunnel supply temperatures. As mentioned previously, an effect on the recovery factor was noticed for the case of nozzle throat cooling. Varying the amount of cooling in the nozzle throat region resulted in a significant change in the downstream recovery factor
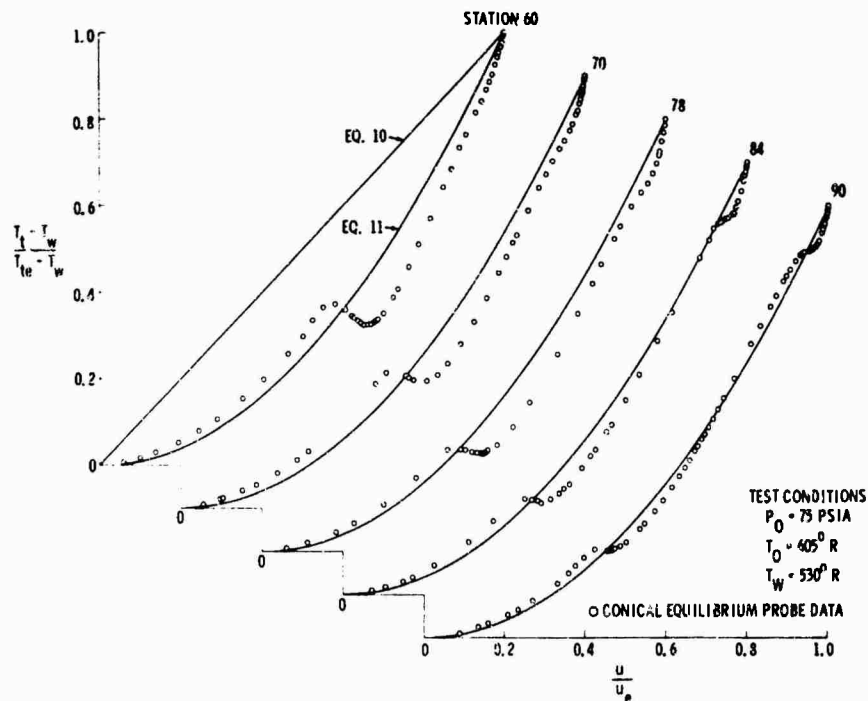
FIGURE 14 ADIABATIC-WALL TEMPERAURE-VELOCITY CORRELATION
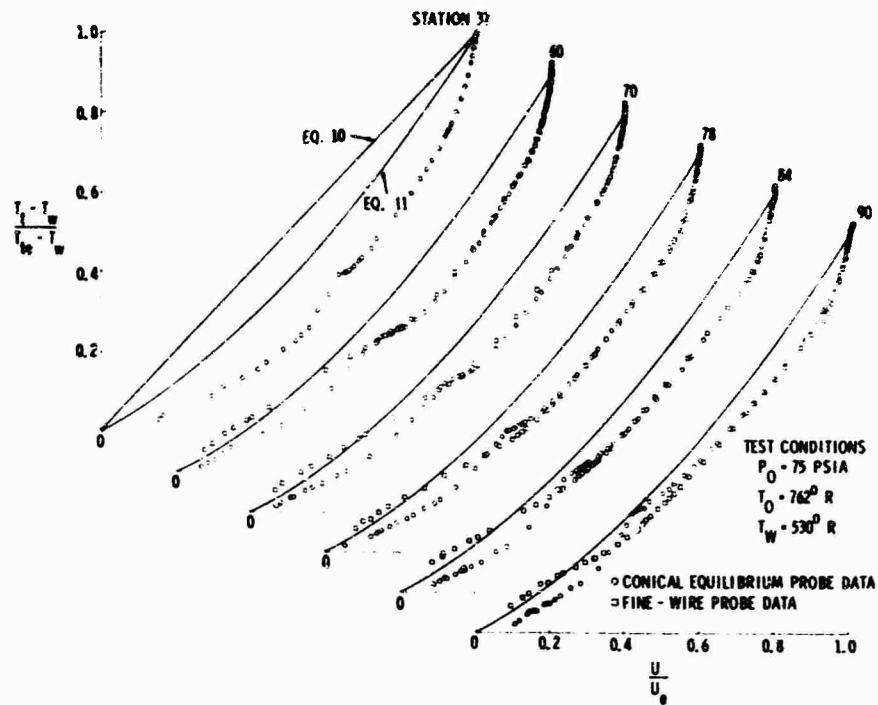
FIGURE 15 MODERATE-HEAT-TRANSFER TEMPERATURE-VELOCITY CORRELATION
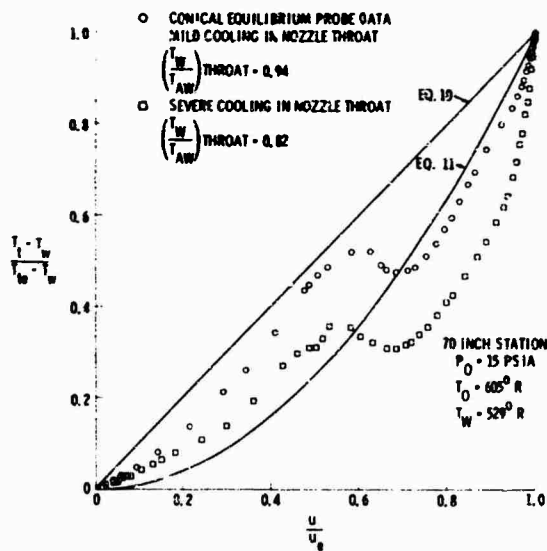
FIGURE 16 EFFECT OF NOZZLE THROAT COOLING ON DOWNSTREAM TEMPERATURE-VELOCITY CORRELATION
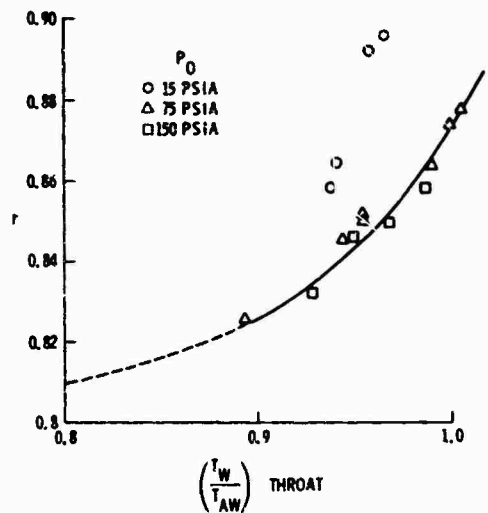
FIGURE 17 DOWNSTREAM RECOVERY FACTOR VARIATION WITH THROAT COOLING
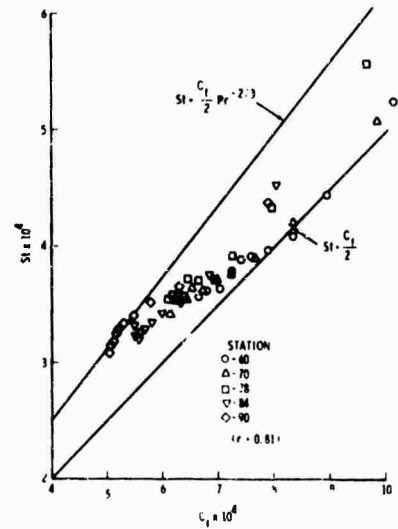
FIGURE 18 REYNOLDS ANALOGY CORRELATION
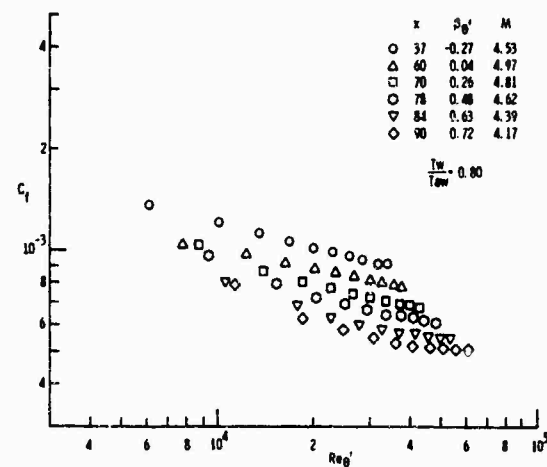
FIGURE 19 MODERATE-HEAT-TRANSFER SKIN-FRICTION DATA

as shown in Figure 17. Although a Reynolds number dependency is also indicated for this correlation, no attempt was made at this correction due to the limited amount of data available. The change in recovery factor is especially important to the determination of Stanton number for the case of moderate heat transfer since T_w/T_{aw} at the throat equals 0.8 and the value of the downstream recovery factor becomes 0.81 rather than the conventional 0.89. A correlation of the moderate-heat-transfer data in terms of Reynolds analogy for a constant recovery factor equal to 0.81 is shown in Figure 18. The data indicate a Reynolds number effect which is most likely due to the previously mentioned recovery factor dependence. Adverse pressure gradient effects are difficult to interpret due to this Reynolds number dependency.

The skin-friction coefficients obtained for the six stations under moderate heat-transfer conditions are shown plotted against momentum thickness Reynolds number in Figure 19. The data show the expected trend of decreasing skin-friction coefficient with adverse pressure gradient for a constant value of momentum thickness Reynolds number. Furthermore, the data could be correlated in terms of the pressure gradient parameter $\beta_\theta = \theta'/\tau_w\ dp/dx$, the same parameter reported earlier for favorable-pressure-gradient flows.

9. CONCLUSION

A detailed experimental investigation of the compressible turbulent boundary layer in an adverse-pressure-gradient regime was conducted in the NOL Boundary Layer Channel. The nozzle-wall boundary-layer flow was exposed to a range of pressure gradients at Mach numbers between 4.1 and 4.9 for both adiabatic-wall and moderate-heat-transfer conditions. Complete and often redundant measurements of the boundary layers were made with Pitot and static-pressure probes, conical equilibrium and fine-wire stagnation temperature probes, a shear balance and a heat-transfer gage. Analysis of the experiment has led to the following conclusions.

a. A variable contour two-dimensional supersonic nozzle is well suited to adverse-pressure-gradient investigations since the flow remains shock-free and effects due to longitudinal curvature are eliminated.
b. Two corrections to the Pitot-pressure data must be considered in the region near the wall of a compressible turbulent boundary layer due to the effects of viscous flow interaction and probe-wall interference. These corrections are presented for a rectangular-inlet Pitot-probe configuration.
c. Experimental normal static-pressure profiles agree well with a strictly isentropic method-of-characteristics computation.
d. The flow in the Boundary Layer Channel was shown to be two-dimensional at least within the center six inches of the test plate by surface streamline traces and a modified streamwise momentum balance which incorporated the static-pressure variation normal to the plate.
e. Adverse-pressure-gradient velocity profiles correlate well with the Law of the Wall and Law of the Wake.
f. Upstream temperature history causes a temperature deficit in the outer part of the downstream temperature profiles, a change in value of certain temperature-dependent integral parameters, and a change in the local recovery factor.
g. The effect of the adverse pressure gradient on the temperature-velocity correlation is to accelerate the shift of the profile from the quadratic towards the linear relation.
h. The effect of the adverse pressure gradient on skin friction is to lower the value of C_f for a constant value of momentum thickness Reynolds number.
i. The skin friction coefficient and Stanton number correlate well with Reynolds Analogy when the appropriate recovery factor is used to compensate for the upstream temperature history.

REFERENCES

1. Lee, R.E., Yanta, W.J., and Leonas, A.C., "Velocity Profile, Skin-Friction Balance, and Heat-Transfer Measurements of the Turbulent Boundary Layer at Mach 5 and Zero Pressure Gradient," NOLTR 69-106, June 1969
2. Brott, D.L., Yanta, W.J., Voisinet, R.L., and Lee, R.E., "An Experimental Investigation of the Compressible Turbulent Boundary Layer with a Favorable Pressure Gradient," NOLTR 69-143, August 1969
3. Lee, R.E., Yanta, W.J., Leonas, A.C., and Carner, J., "The NOL Boundary Layer Channel," NOLTR 66-185, November 1966
4. Danberg, J.E., "The Equilibrium Temperature Probe, a Device for Measuring Temperatures in a Hypersonic Boundary Layer," NOLTR 61-2, December 1961
5. Yanta, W.J., "A Fine-wire Stagnation Temperature Probe," NOLTR 70-81, June 1970
6. Kepler, C.E. and O'Brien, R., "Supersonic Turbulent Boundary Layer Growth Over Cooled Walls in Adverse Pressure Gradients," ASD-TDR-62-87, Wright-Patterson Air Force Base, October 1962.
7. Rogdyah, W.G. and Sakhay, V., "An Experimental Investigation of Hypersonic Turbulent Boundary Layers in Adverse Pressure Gradient," AIAA paper No. 68-44, January 1968
8. McDonald, H., "An Assessment of Certain Procedures for Computing the Compressible Turbulent Boundary Layer Development," paper No. 6, "Compressible Turbulent Boundary Layers, NASA SP-216, December 1968
9. Coles, D., "The Law of the Wake in the Turbulent Boundary Layer," J. Fluid Mech., Vol. 1, p 191, 1956
10. Hinze, J.O., Turbulence, McGraw-Hill Book Co., Inc., 1959, p 507
11. Bushnell, D.M., Johnson, C.B., Harvey, W.D., and Feller, W. V., "Comparison of Prediction Methods and Studies of Relaxation in Hypersonic Turbulent Nozzle-Wall Boundary Layers," NASA TN-D-5433, 1969

THE SUPERSONIC TURBULENT BOUNDARY LAYER IN AN ADVERSE PRESSURE GRADIENT--EXPERIMENT AND DATA ANALYSIS

Walter B. Sturek*

U. S. Army Ballistic Research Laboratories, Aberdeen Proving Ground, Maryland 21005

and

James E. Danberg**

University of Delaware, Newark, Delaware 19711

SUMMARY

Experimental measurements of the profile characteristics of the supersonic turbulent boundary layer in a region of moderate adverse pressure gradient along a two-dimensional isentropic ramp model are reported. The data are for a closely adiabatic wall, $Re_\theta = 1.9$ to 4.2×10^4 at a tunnel nozzle setting of $M = 3.54$. Detailed surveys of impact pressure, static pressure and total temperature were made, and wall shear stress was measured using the Preston tube technique. In addition to the mean profile data, fluctuation data were obtained using constant temperature hot-wire anemometry in the zero pressure gradient flow upstream of the ramp model and in the adverse pressure gradient flow along the ramp model.

Turbulent boundary layer equations applicable to compressible flow over a surface with longitudinal curvature are analyzed. Corrections for longitudinal curvature to the equation for conservation of streamwise momentum are shown to be small and of the same order of magnitude as the contribution of the wall shear stress. The data are shown to correlate in law of the wall and velocity defect dimensionless coordinates using an integral compressibility transformation that follows directly from Prandtl's mixing length approximation of the Reynolds' stress. Eddy viscosity and mixing length distributions for the zero pressure gradient boundary layer were determined directly from the experimental data and agree qualitatively with previously published findings. The measured value of skin friction coefficient is 20 percent less for the flow over the ramp model than for the zero pressure gradient flow upstream.

NOTATION

c_f	skin friction coefficient	δ_u	boundary layer velocity thickness
e	voltage across the hot wire probe	θ	boundary layer momentum thickness
p	pressure	θ_E	boundary layer energy thickness
u_τ	friction velocity, $(\tau_w/\rho_w)^{1/2}$	θ_H	boundary layer enthalpy thickness
u^{++}	transformed dimensionless velocity, defined by Eq (10)	κ	inverse longitudinal curvature
		ρ	density
x	streamwise distance	τ	shear stress
y	distance normal to the local surface	Π	Coles' wake parameter
y^+	dimensionless distance normal to the local surface, $u_\tau y/\nu_w$	ϵ	kinematic eddy viscosity

Subscripts

C	law of the wall constant		
		aw	adiabatic wall
K	constant in Prandtl's mixing length relation $\ell = K y$	o	supply header condition
M	Mach number	t	local stagnation condition
R	local radius of longitudinal curvature	w	property evaluated at the wall
Re_θ	momentum thickness Reynolds' number	δ	property evaluated at $y = \delta$
T	temperature	∞	reference condition, property evaluated external to the boundary layer
$U = u + u'$	velocity in the streamwise direction		

Superscripts

$V = v + v'$	velocity normal to the local surface	(')	indicates "ideal" property, calculated using measured p, constant $p_t = p_o$ and $T_t = T_{t_\infty}$; also indicates fluctuation component
β	curvature correction factor, $1/(1 + \kappa y)$		
δ	boundary layer thickness	(¯)	time averaged quantity
δ^*	boundary layer displacement thickness		

---

* Aerospace Engineer
** Associate Professor, Department of Mechanical and Aerospace Engineering

1. INTRODUCTION

Recent application of numerical techniques to obtain solutions to the boundary layer equations has focused attention on the need for accurate, detailed measurements of boundary layer characteristics. The proposed numerical procedures for the compressible turbulent boundary layer cannot be properly evaluated because data available are not sufficiently accurate, detailed or comprehensive.

Data existing in the literature for the supersonic turbulent boundary layer in an adverse pressure gradient are particularly poor. This is due to difficulty experienced in obtaining reliable test conditions and due to the fact that the measurements reported have been incomplete. Measurements of wall shear stress have not been reported for the configuration of this experiment and measurements of the static pressure profile through the boundary layer have been either omitted or of insufficient detail and accuracy. References 1 and 2 report measurements of the supersonic turbulent boundary layer characteristics along a surface with longitudinal concave curvature.

This experiment has been conducted with the objective of obtaining a good quality flow that could be measured accurately and would enable a complete set of measurements to be taken in sufficient detail to reveal the physics of the mean flow. Beyond the experimental objective, the intent is to use the data to further basic understanding of the supersonic turbulent boundary layer.

2. THE EXPERIMENT

2.1 Test Facility

The experiment was performed in Supersonic Wind Tunnel No. 2 of the Ballistic Research Laboratories, Aberdeen Proving Ground, Maryland. This is a continuous operating, asymmetric, flexible nozzle research tunnel. The test section size is 6 x 6 inches and extends for 22 inches beyond the nozzle exit. The test section boundary layer is a fully developed turbulent boundary layer approximately one inch thick that has developed naturally along a smooth flat surface.

2.2 Model

An isentropic ramp model was used to create the region of adverse pressure gradient. The model was designed to create a streamwise pressure gradient severe enough to measure accurately but not severe enough to cause the formation of a shock wave in the vicinity of the measuring stations. The contour was calculated using Prandtl-Meyer turning angles. No attempt was made to adjust the model contour for boundary layer growth.

The front edge of the model had a thickness of 0.010-inch. When mounted in the test section, the front edge was glued to the floor of the tunnel and lacquer putty used to form a smooth transition from the tunnel floor to the surface of the model. The model was instrumented with six 0.040-inch diameter static pressure holes drilled normal to the local surface at one inch intervals along the centerline. In addition, eleven 0.025-inch diameter static pressure taps were located off centerline at the last three stations on the model. The model and its' position relative to the nozzle exit is shown in Figure 1. Also shown is the location and designation of the test stations and the wall thermocouple which is positioned 0.050-inch below the test surface of the tunnel.
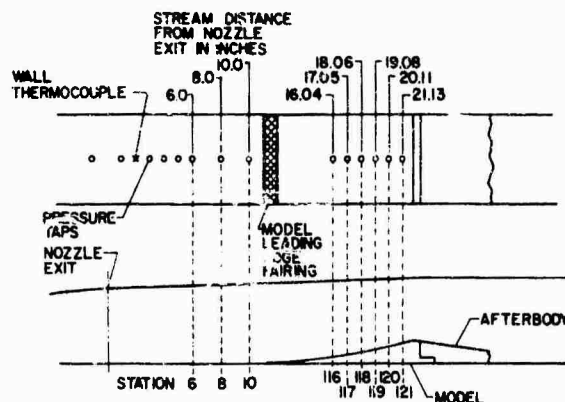
Figure 1. Location of Model and Test Station Identification

2.3 Procedure

The profile surveys of impact pressure, static pressure and recovery temperature were made during separate test runs since the survey mechanism could accommodate only one probe at a time. The survey mechanism was designed to traverse the boundary layer at an angle perpendicular to the local surface. The tunnel was allowed to come to equilibrium with the surrounding room conditions as indicated by the wall temperature thermocouple before any data were taken. The probes were positioned and data recorded manually. Data was obtained for three values of tunnel total pressure at a tunnel total temperature of 560 R. Tunnel total pressure variation was less than $\pm$ .25% and the tunnel total temperature was controlled within $\pm$ 1°F or $\pm$ .18%. Assuming a wall recovery factor of 0.88, the ratio $(T_w - T_{aw})/T_{aw} \approx$ 0.021 shows that the wall was closely adiabatic.

2.4 Instrumentation

The impact probe used had a tip opening that was 0.060 x 0.005-inch with a lip thickness approximately 0.001-inch. The tube was flattened in a manner that enabled measurements to be made within 0.005-inch of the wall.

Static pressure probes were constructed in two configurations, flat plate and cone-cylinder. These probes are shown in Figure 2. The flat plate probe was a 0.125-inch thick steel plate with a 20 degree razor sharp leading edge. Ten 0.040-inch diameter holes were located 1.125-inches from the leading edge and spaced 0.125-inch apart. The bottom edge of the probe was curved to enable it to seat flush with the model surface. This configuration was considered desirable due to the angularity of the flow over the curved surface of the model. The cone-cylinder probe was constructed with a 0.050-inch diameter cylindrical body. The half-angle of the cone portion was 10 degrees. Two static holes of 0.0135-inch diameter were located 10 diameters downstream of the start of the cylindrical portion and 5 diameters upstream of the bend where the tube connects to the probe support.

Figure 2. Static Pressure Probes

The probe used to measure the total temperature through the boundary layer was of a wedge configuration. It was constructed of lexan plastic and had a 0.005-inch diameter iron-constantan thermocouple located at the center of the wedge tip. The lead wires were placed in a groove machined along the front edge and sides of the plastic wedge and covered with epoxy cement. Only the spot welded junction of the thermocouple was exposed to the flow. The recovery factor as a function of Mach number for this probe was established by a separate test.

The side walls of the test facility are glass permitting observation of the flow from the nozzle throat to the end of the test section. Flow visualization has been obtained using single plate laser interferometry and schlieren photography. Figure 3 shows a schlieren picture of the flow over the ramp model. The weak shock formed at the leading edge of the ramp model is visible as is the turbid structure within the boundary layer and the irregular outer edge. Also apparent is the decreasing boundary layer thickness as the flow is compressed by the increasing static pressure.

Figure 3. Schlieren of Flow Over the Ramp Model

2.5 Two Dimensionality

The two dimensionality of the flow is of great concern in a facility of the type used for these tests. This concern is intensified when a pressure gradient is imposed on the flow. Two tests were conducted in an effort to evaluate the departure from two dimensionality for the conditions of this test: (1) oil flow visualization and (2) wall pressure measurements off centerline at the last three stations on the ramp model.

A picture showing the result of oil flow development over the ramp model is shown in Figure 4. Streamlines along the surface of the model near the centerline do not diverge appreciably; however, considerable divergence of streamlines near the side walls does take place. Wall pressure measurements on a line normal to the centerline at the last three stations on the ramp model established that a region exists in the flow over the ramp model, approximately one inch to either side of the centerline, in which the lateral pressure gradient is very close to zero.
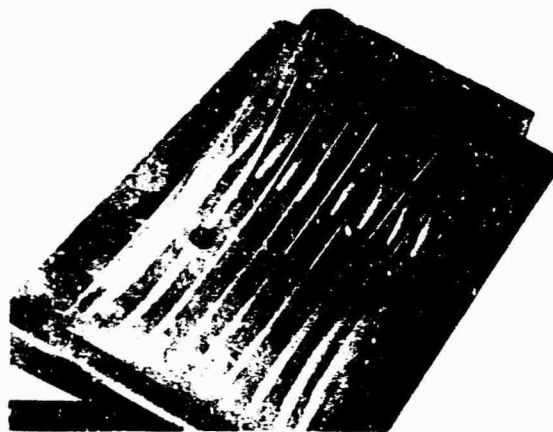
Figure 4.   Oil Flow Development

2.6   Boundary Layer Profiles

Preliminary profile calculations using uncorrected cone-cylinder static pressure data revealed a Mach number greater than the tunnel nozzle setting beyond the region of the boundary layer for the first station on the ramp model. This led to calculating the static pressure from impact pressure measurements assuming a constant total pressure equal to the tunnel total pressure. The profile resulting from this calculation is shown in Figure 5 along with corrected cone-cylinder and flat plate static pressure probe data. The solid line represents a fairing of what is felt to be the best data.
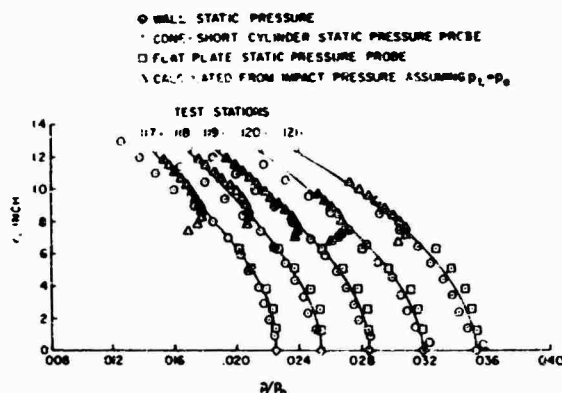
Figure 5.   Static Pressure Profiles

The profile calculations were performed on the BRL digital computer. Tables of experimental measurements of impact pressure, static pressure and recovery temperature versus distance normal to the surface and recovery factor versus Mach number were introduced into the computation routine. Calculations were performed at the value of y corresponding to each measurement of impact pressure. A three point interpolation was performed to determine the value of static pressure and recovery temperature at the specified value of y. The appropriate recovery factor was determined by interpolation after the Mach number was calculated from the Rayleigh pitot formula. Knowing Mach number, static pressure and total temperature; values of velocity, static temperature and density were calculated using perfect gas relations. Integral properties of the boundary layer were calculated using a trapezoidal numerical integration routine. Examples of the profile data are shown in Figure 6 plotted versus the distance normal to the local surface.
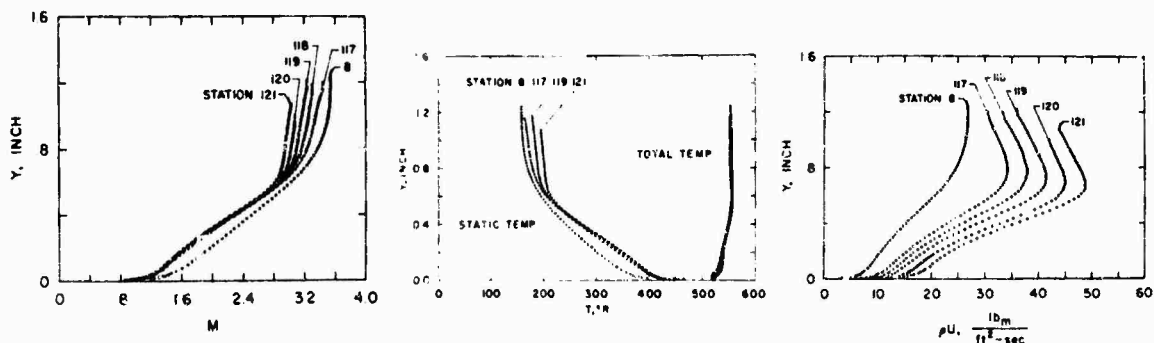
Figure 6.   Examples of Mach Number, Temperature and Mass Flux Profiles

2.7 Hot Wire Measurements

Measurements were made using constant temperature hot wire anemometry at Station 8 in the zero pressure gradient flow and at Stations 117, 118 and 119 in the flow over the ramp model. A tungsten wire coated with platinum of 0.00025-inch diameter and 0.010-inch length was used. Figure 7 shows an example of the fluctuation data plotted as the ratio of the local value of the measurement to an arbitrary reference value. Sufficient data have not been accumulated to properly obtain turbulence intensities. This data is considered to be preliminary; however, a very interesting trend is apparent. As the flow is compressed by the increasing static pressure and the boundary layer thickness decreases, a pronounced peak appears in the profile of the turbulent fluctuations. A uniform region of low fluctuating signal is indicated beyond the edge of the boundary layer both for the zero pressure gradient and the adverse pressure gradient flows.
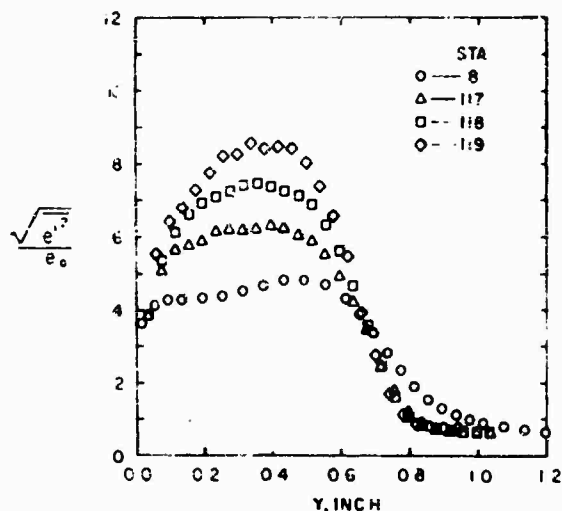
Figure 7. Turbulent Fluctuation Data

2.8 Skin Friction Measurements

Wall shear stress has been measured using the Preston tube technique. The tube used here was 0.125-inch in diameter. Tests have been conducted by various researchers for the purpose of evaluating the Preston tube as a means of measuring local skin friction. These tests indicate that the Preston tube can be expected to yield measurements of wall shear stress within an accuracy of ± 15% for the conditions of this experiment. The value of wall shear stress was calculated using Equation (2b) of reference 3 since it was established from data obtained in a test facility similar to the one used for this experiment. Also, τ_w is calculated from measurements of wall properties so no uncertainty is introduced into the wall shear stress due to the determination of the free stream conditions. This is particularly desirable due to the uncertainty in defining the free stream conditions for the flow over the ramp model.

The skin friction data of this report are compared to the empirical correlation of Spalding and Chi[4] and to other experimental measurements in Figure 8. The skin friction data of this report are approximately 8% and 35% low for the zero pressure gradient and adverse pressure gradient flow respectively compared to the correlation of Spalding and Chi. The correlation of Spalding and Chi predicts a greater value of c_f in the region of adverse pressure gradient than in the region of zero pressure gradient. This is opposite to that indicated by the experimental data.
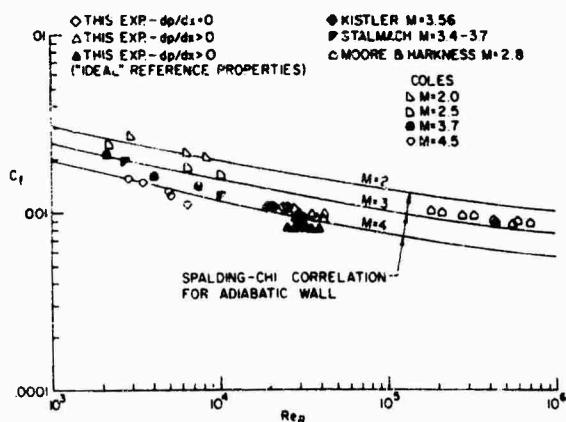
Figure 8. Skin Friction Data Comparison

3. ANALYSIS OF THE EXPERIMENTAL DATA

3.1 Equations of Conservation of Mass and Momentum

Considerable experimental evidence has been given in the form of profiles of the mean properties (Mach number, mass flux, temperature) showing distinct differences in the profile shapes between the zero pressure gradient and the adverse pressure gradient flows. It is obvious that the boundary layer equations as applicable to the flow over the ramp model must contain terms that include the effects of the pressure gradient normal to the model surface, pressure gradient in the streamwise direction and the curvature of the surface.

Tetervin[5] has derived the conservation equations in a form applicable to the compressible turbulent boundary layer over a surface with both longitudinal and transverse curvature. The equations were derived by considering the continuity equation and the Navier-Stokes equations in their most general form. By considering a two-dimensional steady mean flow over a surface with longitudinal curvature and restricting κ to be $O(1)$, the conservation equations can be written as:

Conservation of Mass

$$\frac{\partial}{\partial x} \ (\rho u) + \frac{\partial}{\partial y} \ [(1 + \kappa y) \ (\rho v + \overline{\rho' v'})] = 0 \tag{1}$$

Conservation of Momentum

$$\left(\frac{1}{1+\kappa y}\right) \rho u \ \frac{\partial u}{\partial x} + (\rho v + \overline{\rho' v'}) \ \frac{\partial u}{\partial y} = -\frac{1}{1+\kappa y} \ \frac{\partial p}{\partial x} + \frac{\partial}{\partial y} \ (\mu \ \frac{\partial u}{\partial y} - \overline{\rho u' v'}) \tag{2}$$

$$\frac{\rho}{2} \ \frac{\partial}{\partial y} \ (\overline{v'^2} + \overline{w'^2}) - \frac{\kappa}{1+\kappa y} \ \rho u^2 = -\frac{\partial p}{\partial y} \tag{3}$$

The actual physical scaling, δ/R, is approximately 0.02 for the flow over the ramp model. The importance of including terms arising from the longitudinal curvature in Equations (1), (2) and (3) will now be examined by numerical integration using the tabulated profile data.

3.2 Conservation of Mass

Integrating Equation (1) in the y direction yields

$$(1 + \kappa y) \ (\rho v + \overline{\rho' v'}) = -\int_0^y \ \frac{\partial}{\partial x} \ (\rho u) \ dy \tag{4}$$

Longitudinal curvature enters this calculation only as the factor $(1+\kappa y)$ which is approximately 0.98 at $y = \delta$ for this experiment. Hence, the mass flux in the y direction at $y = \delta$ is increased approximately 2% by longitudinal curvature over the integral of the partial derivative of the streamwise mass flux.

3.3 Conservation of Momentum Normal to the Surface

Since the fluctuation terms in Equation (3) were not evaluated in this experiment, the equation for conservation of momentum in the y direction will be considered in the following form.

$$\frac{\kappa}{1+\kappa y} \ \rho u^2 = \frac{\partial p}{\partial y} \tag{5}$$

This equation can be written in integrated form as

$$p(y) = p_w + \int_0^y \ \frac{\kappa}{1+\kappa y} \ \rho u^2 dy \tag{6}$$

A typical static pressure profile obtained by numerical integration of Equation (5) is shown in Figure 9 compared to the measured profile. The bars indicate an uncertainty of $\pm$ 2% about the measured value. The trend indicated by both profiles is in agreement throughout the boundary layer. The profiles agree within +0 and -2 percent within the boundary layer, but greater divergence is indicated beyond the edge of the boundary layer.

3.4 Conservation of Streamwise Momentum

Combining Equation (1) with Equation (2) and integrating across the boundary layer yields the following relation.

$$\frac{d}{dx}\int_0^\delta \ \beta \rho u^2 dy - u_\delta \beta_\delta \ \frac{d}{dx}\int_0^\delta \ \rho u dy - \int_0^\delta u \left[\int_0^y \ \frac{\partial}{\partial x} \ (\rho u) \ dy \right] \beta^2 \kappa dy$$

$$+ \ \frac{d}{dx}\int_0^\delta \ \beta p dy - \beta_\delta p_\delta \ \frac{d\delta}{dx} = \int_0^\delta \ \frac{\partial \tau}{\partial y} \ dy = -\tau_w \tag{7}$$

where $\qquad$ $\beta = 1/(1 + \kappa y)$ $\qquad$ and $\qquad$ $\tau = \mu \, (\partial u/\partial y) - \overline{\rho u' v'}$.

• MEASURED

$$- \quad p_w + \int_0^y \frac{\kappa}{1+\kappa y} \rho u^2 dy$$

$\vdash\!\dashv \pm 2\%$
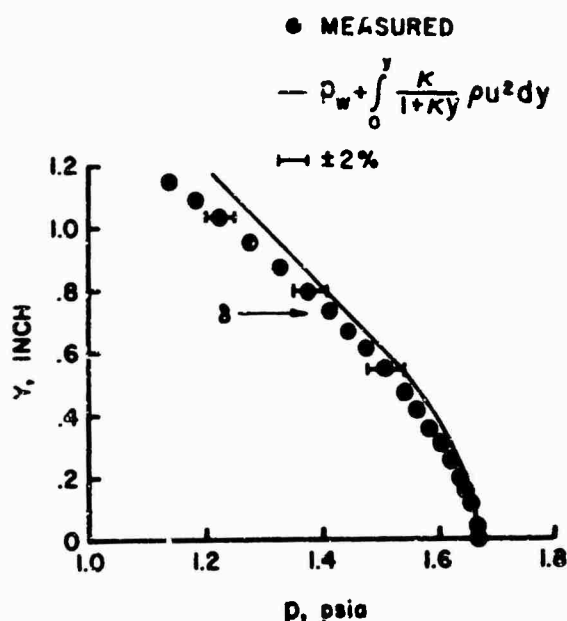
Figure 9. Static Pressure Profile Calculated from Mean Profile Data

The numerical integration of the first, second and fourth terms on the LHS is easily accomplished. The third term, however, requires knowledge of the quantity $\partial/\partial x \, (\rho v)$ as a function of position through the boundary layer. This quantity has been evaluated along lines of constant mass flux using a least squares technique. An example showing the trend of the lines of constant mass flux is shown in Figure 10 compared with the trend of the boundary layer thickness. It is obvious that even though the boundary layer is becoming less thick, mass is being entrained within the boundary layer. An example of the distribution of $\partial/\partial x \, (\rho u)$ is shown in Figure 11.
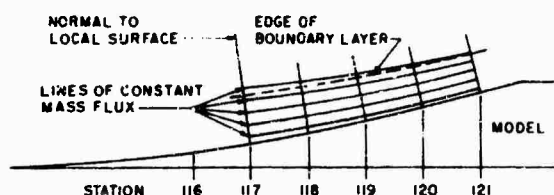
Figure 10. Lines of Constant Mass Flux

A discriminating appraisal of the effect of including corrections for longitudinal curvature can be made by considering the balance of streamwise integrated momentum. By making the substitutions

$$I_1 = \int_0^\delta \beta \rho u^2 dy \quad , \quad I_2 = \int_0^\delta \rho u dy \quad , \quad I_3 = \int_0^\delta u \left[\int_0^y \frac{\partial}{\partial x} \, (\rho u) \, dy \right] \beta^2 \kappa dy \quad , \quad I_4 = \int_0^\delta \beta p dy$$

into Equation (7) and integrating the resulting expression in the streamwise direction, the following relation for the streamwise integrated balance of momentum is obtained.

$$\int_a^b dI_1 - \int_a^b u_\delta \beta_\delta dI_2 - \int_a^b I_3 dx + \int_a^b dI_4 - \int_a^b \beta_\delta p_\delta d\delta = - \int_a^b \tau_w dx \tag{8}$$

Equation (8) has been evaluated numerically from station to station. An example of this calculation is tabulated in Table 1, where the individual terms in Equation (8) are numbered consecutively starting from the left.

Table 1. Streamwise Integrated Momentum $(lb_f\text{-}in/ft^2)$, Equation (8)

Sta	T_1	$-T_2$	T_3	T_4	T_5	LHS	RHS
117	0	0	0	0	0	0	0
118	46.34	68.18	0.728	13.32	4.93	2.66	1.08
119	71.21	115.16	1.453	25.83	11.57	5.10	2.26
120	101.46	165.48	2.151	37.90	20.46	3.51	3.55
121	144.43	232.45	2.812	53.07	24.99	7.15	4.99

The result of these calculations is best evaluated by plotting the LHS of Equation (8) versus streamwise position. This plot is shown in Figure 12 compared to the RHS. Also shown for comparison is the result obtained upon setting $\kappa = 0$. The data appear to be consistent through Station 119; however, an inconsistency is indicated at Station 120. No reason for this discrepancy has been identified in the profile data.

STATION 118

$$\frac{dp}{dx} \approx .180 \text{ psi/inch}$$

$$\delta = .764 \qquad M_\delta = 3.14$$
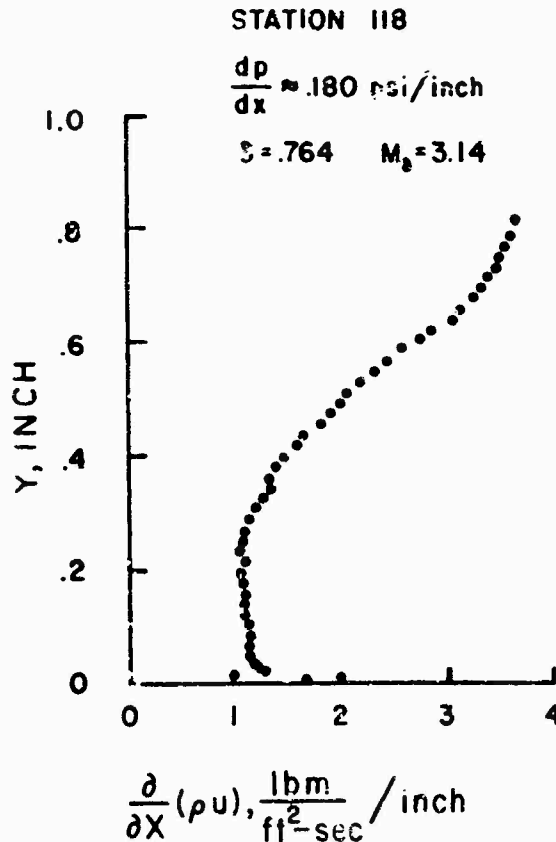
Figure 11. The Distribution of $\partial(\rho u)/\partial x$

STREAMWISE POSITION, INCHES FROM NOZZLE EXIT
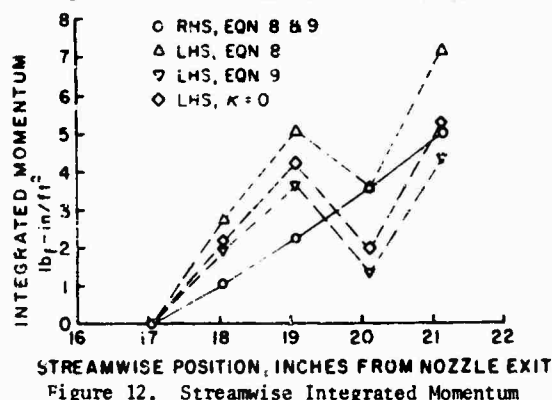
Figure 12. Streamwise Integrated Momentum

The agreement shown between the LHS and RHS of Equation (8) is not impressive and, surprisingly enough, better agreement is achieved by disregarding the curvature correction entirely. The lack of agreement between the LHS and RHS of Equation (8) can be considered to be the effect of neglecting terms deemed negligible in the order of magnitude analysis. Values of these neglected terms were also determined by numerical integration. One term was found to provide a significant contribution. Rewriting Equation (8) including this term yields

$$\int_a^b dI_1 - \int_a^b u_\delta \beta_\delta dI_2 - 2\int_a^b I_3 dx + \int_a^b dI_4 - \int_a^b \beta_\delta p_\delta d\delta = -\int_a^b \tau_w dx \qquad (9)$$

The agreement by the LHS of Equation (9) with the integrated wall shear stress is also shown in Figure 12. It is seen that the agreement has been improved and that the LHS of Equation (9) provides better agreement with the RHS than that obtained neglecting the curvature correction. It should be emphasized that in evaluating the LHS of Equations (8) and (9), the difference is taken between very large numbers to yield an answer that is approximately .3% of the largest term. This implies that the experimental profiles must be extremely accurate to achieve good agreement. Evaluation of the streamwise integrated momentum provides a very discriminating check on the experimental data and is a means for investigating the importance of individual terms in the equations of motion in addition to an order of magnitude analysis. This procedure also provides a means for quality comparison with other experimental data.

3.5 Law of the Wall Analysis

The following integral relation for a compressible law of the wall is obtained by applying Prandtl's mixing length approximation to the Reynold's stress and assuming that the mixing length, $\ell = K\,y$.

$$\frac{u_\delta}{u_\tau} \int_0^{u/u_\delta} \left(\frac{\rho}{\rho_w}\right)^{1/2} d\left(\frac{u}{u_\delta}\right) = u^{++} = \frac{1}{K} \log_e (y^+) + C \tag{10}$$

A compressible "law of the wall" and "law of the wake" can be formed using Equation (10) by substituting values for K and C that have yielded good correlation of incompressible turbulent boundary layer data. An expression linking the "wall law" and the "wake law" in the logarithmic region of overlap can be written as

$$u^{++} = 2.5 \log_e (y^+) + 5.1 + 2^- \Pi \omega (y/\delta) \tag{11}$$

where ω is Coles' wake function which can be approximated by $\omega = 2 \sin^2 (\pi y/2\delta)$ and Π, Coles' wake parameter, is to be determined. Values of Π have been determined from the experimental data by evaluating Equation (11) at $y = \delta$. The values obtained are shown plotted versus Mach number and momentum thickness Reynolds number in Figure 13.
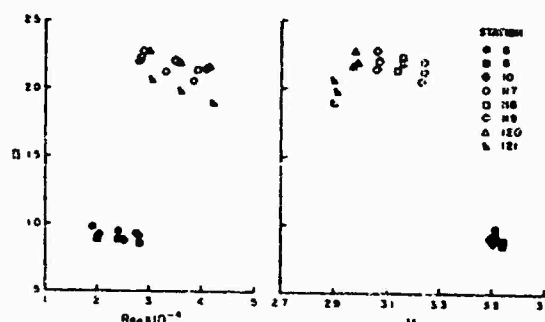
Figure 13. Values of Π, Coles' Wake Parameter

The zero pressure gradient data show a slight tendency for Π to decrease with increasing Re_θ. The data for $dp/dx > 0$ exhibit the trends of Π decreasing with increasing M and decreasing with increasing Re_θ. The trend of Π decreasing with increasing M agrees with the trend indicated for the transformed variables of Baronti and Libby[6] who considered data for $dp/dx = 0$. However, the trend noted by Baronti and Libby of Π increasing with increasing Re_θ is opposite to that indicated by the adverse pressure gradient data of this report. The change in value of Π with M and Re_θ is insignificant compared to the change in value with the change in flow configuration. Since Π is considered to be constant for an "equilibrium" turbulent boundary layer, the change in Π along the ramp model (which is the same as the variation with M) can be considered to be a "relaxing" effect. Representative values of Π for $dp/dx = 0$ and $dp/dx > 0$ are 0.90 and 2.10 respectively. These values are both high compared to the value of 0.55 which has been found to yield good correlation of incompressible zero pressure gradient data for sufficiently high values of Re_θ.

Examples of the correlation achieved using Equation (11) are shown in Figure 14. The slope of the logarithmic line agrees well with the experimental data; however, the value of 5.1 is too high for $dp/dx = 0$ and too low for $dp/dx > 0$. Values for this constant have been calculated by evaluating Equation (10) at $y/\delta \approx 0.1$. The values obtained for C are shown in Figure 15 plotted versus M and Re_θ. The data for $dp/dx = 0$ show no dependence on Re_θ. The data for $dp/dx > 0$ tend to increase with increasing Re_θ and decreasing M. Representative values of C for $dp/dx = 0$ and $dp/dx > 0$ are 4.7 and 6.1 respectively. This represents a small correction to the value of u^{++}. The uncertainty in C can be accounted for by an uncertainty in the wall shear stress. As an example, it was found that increasing the wall shear stress by 10% resulted in agreement with Equation (10) at $y/\delta \approx 0.1$ for a typical profile on the ramp model. This is comparable to the accuracy of the experimental determination of wall shear stress using the Preston tube technique.

A "wake law" can be formed using Equation (11) as

$$u_\delta^{++} - u^{++} = -2.5 \log_e (y/\delta) + 2.5 \Pi (2 - \omega) \tag{12}$$
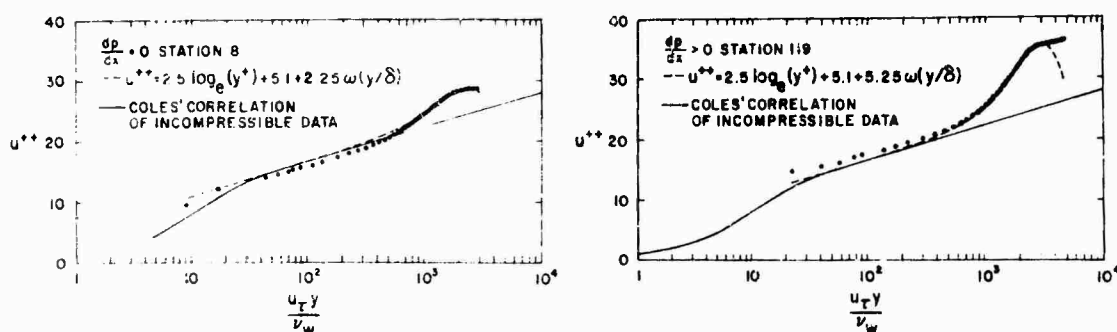
Figure 14. Compressible Law of the Wall Velocity Profiles

Figure 15. Values of C, Law of the Wall Constant

Figure 16. Velocity Defect Data Correlation
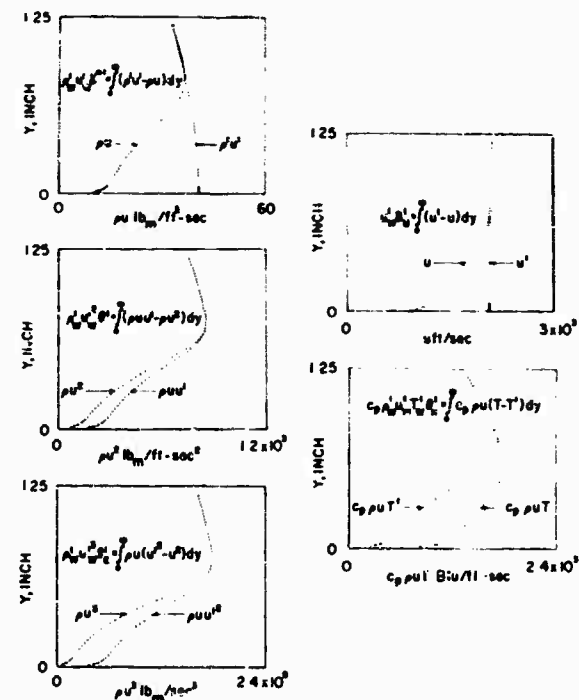
Figure 17. Integral Properties of the Boundary Layer
for the Flow Over the Ramp Model

Figure 16 shows an example of the correlation achieved using Equation (12). The agreement is considered to be very satisfactory.

3.6 Integral Properties for Flow With Significant Static Pressure Variation Normal to the Surface

Conventional definitions of the integral properties of the boundary layer must be modified when considering flows with significant static pressure variation through the boundary layer due to the lack of a free stream region with constant properties. The need to modify conventional definitions of the integral properties has been recognized by other researchers[1,2], but no agreement as to the best interpretation has been reached.

The integral properties are defined here by considering the flux deficit appearing within the boundary layer referenced to "ideal" properties calculated using the experimentally determined static pressure profile. The integral thicknesses are referenced to the ideal properties at the wall. These definitions reduce to the classical definitions of the integral properties for the case of constant static pressure through the boundary layer. The integral properties according to this interpretation are

displacement thickness

$$\rho'_w u'_w \delta^{*'} = \int_0^\infty (\rho' u' - \rho u)\, dy \qquad (13)$$

momentum thickness

$$\rho'_w u_w'^2 \theta' = \int_0^\infty \rho u\, (u' - u)\, dy \qquad (14)$$

energy thickness

$$\rho'_w u_w'^3 \theta'_E = \int_0^\infty \rho u\, (u'^2 - u^2)\, dy \qquad (15)$$

velocity thickness
$$u'_w \delta'_u = \int_0^{\infty} (u' - u)\, dy \tag{16}$$

enthalpy thickness
$$c_p \rho'_w u'_w T'_w \theta'_H = \int_0^{\infty} c_p \rho u\, (T - T')\, dy \tag{17}$$

where the ideal properties ρ', u', T', are calculated from the measured static pressure profile assuming constant total temperature equal to the value in the free stream and constant total pressure equal to the tunnel total pressure. The integral properties according to this interpretation are illustrated in Figure 17. The profiles in Figure 17 were formed using the experimental data and accurately represent the measured flux of the quantity indicated. The definitions given above for $\delta^{*'}$ and θ' are identical to those of McLafferty and Barber[1]. The only difference is that McLafferty and Barber inferred a static pressure profile from measurements of tunnel total pressure, impact pressure and wall pressure while measured values of static pressure are used here. An important feature of this definition is that the integral thickness does not depend upon the value chosen for the boundary layer thickness since the ideal properties become identical to the actual properties near the edge of the boundary layer.

The integral thicknesses were calculated in two ways for the adverse pressure gradient data: (1) using the calculated "ideal" properties for reference as discussed above, and (2) using measured values of density and velocity at the position of maximum mass flux for the reference values. The integral thicknesses are compared in Figure 18. The boundary layer thickness, δ, is the position of maximum mass flux for the adverse pressure gradient profiles and the position for $u = .995\, u_{max}$ for the zero pressure gradient profiles.

It is seen that $d\delta^{*'}/dx$ has a steeper slope than $d\delta^*/dx$. In contrast, the slope of $d\theta/dx$ is steeper than $d\theta'/dx$. The shape factor, H', changes considerably along the ramp model while H changes but slightly. The velocity thickness is the only integral property that does not exhibit significantly different behavior for the two methods of calculation. These results indicate that calculation procedures employing integral relations can yield questionable results when regions of significant static pressure variation normal to the surface are encountered.
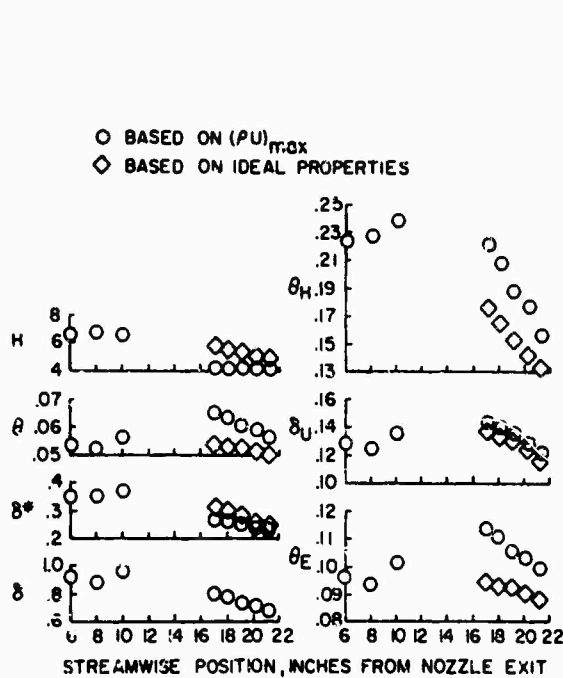
Figure 18. Integral Thicknesses Versus Streamwise Position
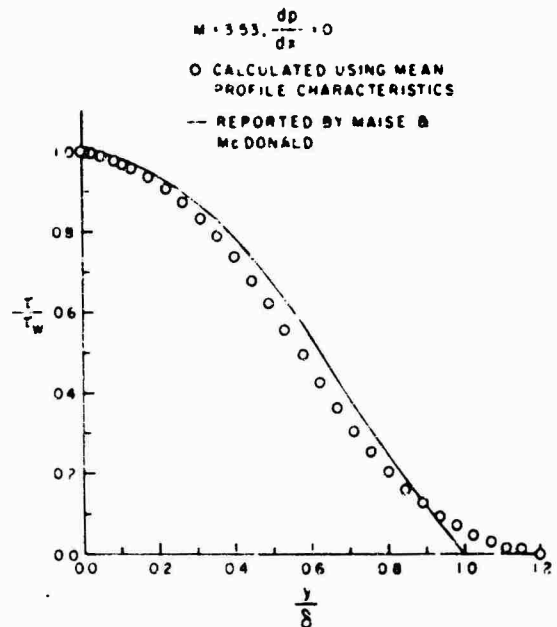
Figure 19. Shear Stress Profile

3.7 Eddy Viscosity and Mixing Length Distributions

The distribution of eddy viscosity or mixing length is used as an input to computation schemes for predicting turbulent boundary layer development. In the absence of direct measurements of the shear stress distribution for the compressible turbulent boundary layer with which to determine the eddy viscosity or mixing length distributions directly, Maise and McDonald[7] reported a series of computations that involved a law of the wall velocity correlation and numerical integration of the boundary layer equations. The results obtained by Maise and McDonald have been widely used and seemingly confirmed by the success of boundary layer computation procedures using these results.

In order to calculate the eddy viscosity and mixing length distributions directly from mean profile data, it is necessary to calculate the distribution of the shear stress and the derivative du/dy. The shear stress distribution has been calculated using the relation

$$\tau(y) = \tau_w + \frac{c_f}{2\theta}\left[\int_0^y \rho u^2 dy - u\int_0^y \rho u dy\right] \tag{18}$$

where the substitution

$$\frac{c_f}{2\theta} = \frac{1}{\delta}\frac{d\delta}{dx}$$

has been invoked. The derivation of Equation (18) involves the assumption of similarity (which is not satisfied in a turbulent boundary layer). Meier and Rotta[8] used a similar relation and give a discussion of the inaccuracies involved. The result achieved using the profile data of this experiment is shown in Figure 19 compared to the profile of reference 7. The profiles are essentially identical out to $y/\delta \approx 0.6$ where an inflexion point occurs for the data of this experiment. Also, the shear stress approaches zero asymptotically beyond $y/\delta = 1$ in contrast to the profile reported in reference 7.

The velocity derivative, du/dy, has been determined directly from the mean profile data using a central difference technique. Figure 20 shows examples of the result obtained for both dp/dx = 0 and for the flow over the ramp model. These profiles reveal significant differences between the two flow situations. One indication is that the production of turbulence energy, which is proportional to du/dy, is greater in the wake portion of the boundary layer for the flow over the ramp model than for the zero pressure gradient flow. This agrees with the trend of the fluctuation data obtained.
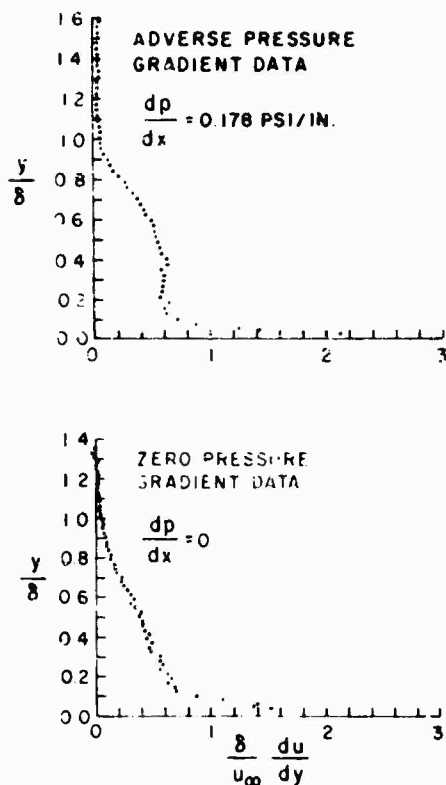
Figure 20. Distribution of the Velocity Derivative, du/dy
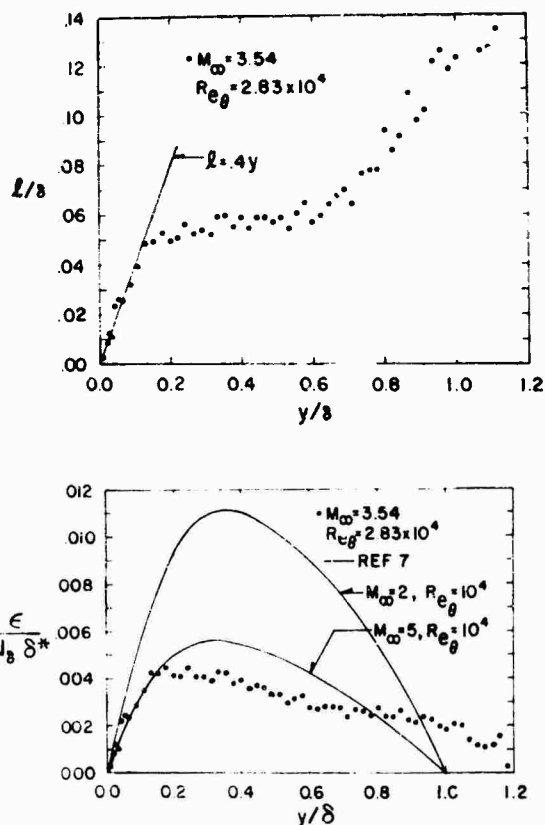
Figure 21. Mixing Length and Eddy Viscosity Distributions

The shear stress and velocity derivative distributions have been combined to calculate the eddy viscosity and mixing length distributions according to the following relations.

$$\ell = \left[\frac{\tau}{\rho}\frac{1}{(du/dy)^2}\right]^{1/2} \tag{19}$$

$$\epsilon = \frac{\tau}{\rho\ du/dy} \tag{20}$$

These distributions are shown in Figure 21. The mixing length distribution shows excellent agreement with the well accepted relation $\ell = 0.4\,y$ near the wall; but the level of the plateau is significantly less than the value reported in reference 7 of 0.09. The behavior beyond $y/\delta = 0.6$ is questionable due to the decreased accuracy for determining du/dy and the point of inflexion in the shear stress profile. The distribution of eddy viscosity shows qualitative agreement with that of reference 7 although, like the mixing length, the magnitude of the peak value and the behavior in the outer wake are different. Although not shown here, a Reynolds number dependence for the mixing length and eddy viscosity distributions greater than that reported in reference 7 were obtained in these calculations.

4. CONCLUSIONS

An experimental investigation of the supersonic turbulent boundary layer in a region of moderate adverse pressure gradient created by a two-dimensional isentropic ramp model has been conducted at a Mach number of 3.5 for a closely adiabatic wall. Values of momentum thickness Reynolds number ranged from

1.9 to 4.2 x 10^4. All the parameters needed to enable calculation of a complete set of mean profile characteristics have been measured. Analysis of the experimental data has led to the following conclusions.

(1) Corrections for longitudinal curvature to the equation for conservation of streamwise momentum represent small corrections to the individual terms involved; but the corrections are of the same order of magnitude as the contribution of the wall shear stress.

(2) The conservation of momentum normal to the surface is adequately represented by the balance of centrifugal force by the normal pressure gradient.

(3) The integral compressibility transformation defined by Equation (10) yields good correlation of the experimental data with the "law of the wall" and "law of the wake" written using values of "universal" constants that have given good correlation of incompressible turbulent boundary layer data.

(4) The value of the skin friction coefficient for the flow over tne ramp model is 20 percent less than that for the zero pressure gradient flow immediately upstream of the ramp model.

(5) The distribution of the velocity derivative, du/dy, through the supersonic turbulent boundary layer for flow over the ramp model is significantly unlike that for the zero pressure gradient flow.

(6) The distributions of mixing length and eddy viscosity calculated from the experimental data are similar in trend to that reported by Maise and McDonald; however, the peak values reported here are significantly less.

(7) The profile of turbulent fluctuations exhibits the trend of becoming more peaked near the edge of boundary layer as the flow develops over the ramp model. This is in sharp contrast to the nearly constant profile observed in the zero pressure gradient flow.

More details concerning the experiment are available in references 12 and 13.

REFERENCES

1. George H. McLafferty and Robert E. Barber, "Turbulent Boundary Layer Characteristics in Supersonic Streams Having Adverse Pressure Gradients," United Aircraft Corporation Research Report No. R-1285-11, September 1959.

2. W. G. Hoydysh and V. Zakkay, "An Experimental Investigation of Hypersonic Turbulent Boundary Layers in Adverse Pressure Gradient," AIAA Journal, Vol. 7, No. 1, January 1969, pp. 105-116.

3. William J. Yanta, David L. Brott and Roland E. Lee, "An Experimental Investigation of the Preston Probe Including Effects of Heat Transfer, Compressibility and Favorable Pressure Gradient," AIAA Paper No. 69-648, presented at the AIAA 2nd Fluid and Plasma Dynamics Conference, June 1969.

4. D. B. Spalding and S. W. Chi, "The Drag of a Compressible Turbulent Boundary Layer on a Smooth Flat Plate With and Without Heat Transfer," Journal of Fluid Mechanics, Vol. 18, Part I, January 1964, pp. 117-143.

5. Neal Tetervin, "An Exploratory Theoretical Investigation of the Effect of Longitudinal Surface Curvature on the Turbulent Boundary Layer," NOL TR 69-22, February 1969.

6. Paolo O. Baronti and Paul A. Libby, "Velocity Profiles in Turbulent Compressible Boundary Layers," AIAA Journal, Vol. 4, No. 2, February 1966, pp. 193-202.

7. George Maise and Henry McDonald, "Mixing Length and Kinematic Eddy Viscosity in a Compressible Boundary Layer," AIAA Paper No. 67-199, presented at the AIAA 5th Aerospace Sciences Meeting, January 1967.

8. H. U. Meier and J. C. Rotta, "Experimental and Theoretical Investigations of Temperature Distributions in Supersonic Boundary Layers," AIAA Paper No. 70-744, presented at the AIAA 3rd Fluid and Plasma Dynamics Conference, June 1970.

9. Donald E. Coles, "Measurements in the Boundary Layer on a Smooth Flat Plate in Supersonic Flow. III. Measurements in a Flat-Plate Boundary Layer at the Jet Propulsion Laboratory," Jet Propulsion Laboratory Report No. 20-71, June 1953.

10. C. J. Stalmach, Jr., "Experimental Investigations of the Surface Impact Probe Method of Measuring Local Skin Friction at Supersonic Speeds," University of Texas Defense Research Laboratory Report No. DRL-410, January 1958.

11. D. R. Moore and J. Harkness, "Experimental Investigations of the Compressible Turbulent Boundary Layer at Very High Reynolds Numbers," AIAA Journal, Vol. 3, No. 4, April 1965, pp. 631-638.

12. W. B. Sturek, "An Experimental Investigation of the Supersonic Turbulent Boundary Layer in a Moderate Adverse Pressure Gradient. Part I. A Detailed Description of the Experiment and Data Tabulation," Ballistic Research Laboratories Report No. 1506, September 1970.

13. W. B. Sturek and J. E. Danberg, "Experimental Measurements of the Supersonic Turbulent Boundary Layer in a Region of Moderate Adverse Pressure Gradient," AIAA Paper No. 71-162, presented at the AIAA 9th Aerospace Sciences Meeting, January 1971.

TURBULENT BOUNDARY LAYERS AT SUPERSONIC AND HYPERSONIC SPEEDS*

G.T. Coleman, G.M. Elfstrom and J.L. Stollery
Aeronautics Department
Imperial College
Prince Consort Road
LONDON S.W.7.

SUMMARY

The growth of a compressible turbulent boundary layer over flat plate and compression corner models has been studied at a Mach number of 9 in the Imperial College No.2 Gun Tunnel. Local Mach numbers between 3 and 9 were achieved on a flat plate by varying the incidence from 0 to 26.5°. The local unit Reynolds numbers used were between 1.5×10^5 and 7×10^5/cm. The measurements, which include pressure and heat transfer rate distributions and pitot pressure profiles across the boundary layer, extend the range of existing data and are used to test some current prediction methods and to emphasise some features of lower Mach number flows. Heat transfer rate distributions at Mach numbers of 3, 5 and 9 show an increasing discrepancy between experiment and theory as the Mach number rises, the data being higher than the predicted value but approaching it asymptotically with increasing momentum thickness Reynolds number (Re_θ). The boundary layer profiles taken at Mach 9 grew fuller as Re_θ decreased; both of these results are associated with the slow development of the wake component of the turbulent boundary layer profile at high Mach numbers.

The effect of an adverse pressure gradient has been studied using a compression corner and it has been shown that large deflections are needed to separate the turbulent boundary layer and that the upstream influence of the corner and the effect of wall temperature are small.

LIST OF SYMBOLS

C_f	skin friction coefficient	u	velocity
C_{f_∞}	C_f at start of interaction region (Eq 4)	x	distance from the leading edge along the plate
C_p	pressure coefficient		
F_c, F_{R_θ}	Spalding-Chi empirical functions (Ref.2)	x_t	x to the transition point
H	total enthalpy	y	distance normal to the surface
L	length of flat plate to the hinge line	α	flap angle
M	Mach Number	Γ	energy thickness
p	pressure	δ	boundary layer thickness, y at $M \approx 0.99 M_e$
$\dot{q}$	heat transfer rate to the surface	δ_L	δ evaluated at hinge line
Re	Reynolds Number	θ	momentum thickness
St	Stanton Number, $\dot{q}/\rho_\infty u_\infty (H_r - H_w)$	ρ	density

SUBSCRIPTS

o	reservoir	i, INC	incipient
∞	freestream	r	adiabatic
$\star$	Eckert reference value	w	wall
e	edge of boundary layer		

1. INTRODUCTION

Most compressible turbulent boundary layer studies have been conducted at supersonic Mach Numbers so that beyond M=5 there is little data. This is in part due to the rapid increase in transition Reynolds Number with Mach Number which makes 'long runs' of turbulent flow difficult to achieve in hypersonic wind tunnels. However, the Imperial College No.2 Gun Tunnel, the design and performance of which are described in ref.1, was specifically built to generate hypersonic, high Reynolds Number flows. The present investigations were undertaken to extend the range of existing data, to test some current theoretical predictions over a wide range of Mach Numbers and wall conditions.

2. FLAT PLATE BOUNDARY LAYER STUDIES

Heat transfer rate distributions at Mach Numbers of 3, 5 and 9 were obtained over flat plates, with sharp leading edges, instrumented along the centre line with thin film platinum-on-glass resistance thermometers. Two models were used, one 12.7 cm wide and 30 cm long, and a larger one 17.7 cm wide and 76 cm long. Local Mach Numbers of 3 and 5 were obtained in the same facility by inclining the shorter flat plate at 26.5° and 15° respectively to the Mach 9 test flow. Turbulent compressible boundary layer behaviour at low Mach numbers is adequately predicted by theory so that the Mach 3 data

could be used as a standard for comparison with theory. At Mach 7 transition occurred very close to the leading edge and the raw data (fig.1) compare well with the predictions of Spalding and Chi (ref.2). At Mach 5 transition moved downstream, being closer to the leading edge at the higher unit Reynolds Number test condition (fig.2).

Mach 9 data were obtained from the larger flat plate; results for three unit Reynolds Numbers under natural transition conditions are shown in fig.3. To extend the turbulent Reynolds Number range covered in the tests further Mach 9 data were obtained by tripping the flow using a row of delta-shaped vortex generators 1 mm high and 3 mm apart placed 1 cm from the leading edge at 30° to the flow direction. For both the highest and lowest unit Reynolds Number tests the effect of the trip was to move transition upstream, almost to the trip position; this is clearly seen in fig.4. To analyse the tripped data, the results had to be matched with the untripped data. This was done by fitting the heat transfer distributions as far downstream as possible, as indicated in figs. 3 and 4, thereby effectively 'lengthening' the flat plate.

The difficulty and inaccuracy of defining a virtual origin for a turbulent boundary layer was avoided by calculating the energy thickness Γ by numerical integration of the heat transfer rate distributions.
Thus

$$\Gamma(x_1) = \frac{\int_0^{x_1} \dot{q}(x)dx}{c_e \, u_e (H_e - H_w)} \tag{1}$$

For the tripped flow Γ was assumed to be the same as for the untripped data at the matching point and then Γ determined by working upstream and downstream of this point using Eq (1). The momentum thickness was calculated from the relation

$$Re_\theta = \frac{Re_\Gamma}{\left[\dfrac{2St}{C_f}\right]\left[\dfrac{H_r - H_w}{H_e - H_w}\right]} \tag{2}$$

where the Reynolds analogy factor $(2St/C_f)$ was taken as $1 \cdot 16$ and the recovery factor r as $0 \cdot 9$ throughout.

All the heat transfer data are plotted against Re_θ in fig.5. A comparison with data from other sources is made in ref.3. In fig.6 all our turbulent data have been converted to equivalent incompressible values using the empirical Mach number dependence given by the theory of Spalding and Chi. It is clear that the good agreement between this theory and the experimental data at supersonic Mach Numbers is not maintained under hypersonic conditions. The high Mach Number data lie above the predicted values, the discrepancy being greatest at low values of Re_θ. This is probably related to the slow development of the wake component π in the turbulent boundary layer velocity profile. A more detailed discussion of this point is given in ref.4 where it is suggested that at hypersonic speeds the fully developed or asymptotic profile will only be reached at large values of Re_θ; for example at a Mach Number of 6, Re_θ must be in excess of 20,000 for adiabatic wall conditions. The report indicates that for lower values of Re_θ the skin friction and heat transfer coefficients could exceed the Spalding-Chi values by as much as 15%. It is of interest to note that with reference to fig. 6 our Mach 9 heat transfer data are 13% high just downstream of transition. However, at Mach 3 there is good agreement with theory and only slightly poorer agreement at Mach 5.

Boundary layer pitot pressure profiles were measured at a Mach Number of 9 using a rake assembly $74 \cdot 2$ cm from the leading edge of the large flat plate; the accuracy of data close to the wall was limited by probe size. The resultant Mach Number profiles for three values of Re_θ (fig.7) are typically turbulent in shape and become fuller with decreasing Re_θ; this effect is again attributed to the increasing strength of the wake component as Re_θ increases. The differing shapes of the outer part of the boundary layer are clearly seen in the velocity profile plots of fig.8, obtained by assuming the Crocco linear temperature relation with a recovery factor of $0 \cdot 9$. The magnitude of the wake component can be estimated from this figure by considering the ratio of the overshoot from the log line to the slope of the log line. Difficulty arises because of uncertainty in determining these quantities; however, for our data the estimated value of π increases from zero at $Re_\theta = 4000$ to $0 \cdot 05$ at $Re_\theta = 16000$; the latter result suggests that at Mach 9 under cold wall conditions Re_θ must be considerably in excess of 16000 for a turbulent boundary layer to be fully developed. This is consistent with the suggestions made in ref.4.

3. COMPRESSIBLE TURBULENT BOUNDARY LAYERS IN A STRONG ADVERSE PRESSURE GRADIENT

The effect of a strong adverse pressure gradient was studied at Mach 9 using a sharp flat plate plus trailing edge flap instrumented for surface pressure measurements along the centre line. The wall temperature could be varied within the range $295°K \leqslant T_w \leqslant 770°K$ and held to $\pm 10°K$ over the model by means of an embedded electric heating element.

The effect of increasing flap angle on the surface distribution is shown in fig.9, from which it is seen that large deflections are needed to separate the turbulent boundary layer. Separation has been detected by looking for a 'knee' in the pressure distribution. Judged in this way the flow at $\alpha = 30°$ is attached and there is an upstream influence of less than a single boundary layer thickness. At higher angles a pressure plateau of increasing length rapidly develops, followed by a pressure overshoot which increases as the flap angle is enlarged. An incipient separation angle of 30° was obtained from a plot of separation length ahead of the hinge line against α.

The influence of wall temperature on incipient separation appears small but adverse, i.e. heating the wall promotes slightly earlier separation (fig.10). In a well separated flow there is a similar effect - raising the wall temperature slightly increases the extent of the separated region. Fig.11 shows that the Reynolds number effect on attached flow is negligible, however raising the unit Reynolds number markedly increases the separated length of a well-separated flow.

Fig.12 shows our results added to a recent collection of incipient separation data by Roshko and Thomke (ref.5). The Reynolds number is based on δ at the hinge line either as measured or as calculated from the formula

$$\delta_L = \frac{0 \cdot 154(L - x_t)}{\left[Re_{L-x_t} \left(\frac{T_\infty}{T_4}\right)^{1 \cdot 67}\right]^{1/7}} \quad , \tag{3}$$

taken from ref.9. Our data show a much weaker dependence on Reynolds number than that shown by Kuehn's results, though both show α_i decreasing with Re_4. Roshko and Thomke's results at a much higher Re_δ show the opposite trend; these differences may be associated with the slow development of the wake component of the turbulent boundary layer velocity profile.

A successful empirical correlation of the pressure rise to incipient separation is shown in fig.13; this is discussed further in ref.3. In all cases the value of C_{f_∞}, the skin friction coefficient at the beginning of interaction has either been measured or calculated from ref.9, using the relation

$$C_{f_\infty} = \frac{0 \cdot 058}{\left[Re_{L-x_t}\right]^{1/5}\left[0 \cdot 5\left(\frac{T_w}{T_\infty} + 1\right) + 0 \cdot 04M_\infty^2\right]^{0 \cdot 65}} \quad . \tag{4}$$

The correlation of fig.13 is redrawn in fig.14 to show the behaviour of α_i with M under adiabatic wall conditions at an effective Reynolds number of 4×10^6. The pattern of the raw data scaled to these conditions is in sharp contrast to the prediction of Todisco and Reeves' momentum integral theory (ref.10).

Incipient separation must basically depend on Mach Number, Reynolds Number and wall temperature ratio. The correlation of fig.13 adequately accounts for the effects of M and T_w/T_0, but not for the diverse Reynolds Number trends of fig.12. A recent analysis of incipient separation conditions for the hypersonic case (ref.11) using theoretical boundary layer profiles given by Green (ref.12) suggests how the Reynolds Number reversal trend may be associated with the development of the wake component.

4. CONCLUSION

A Gun Tunnel has been used for turbulent boundary layer studies in the Mach Number range 3 to 9. There is an increasing discrepancy between measurements of heat transfer and the predictions of Spalding-Chi theory as the Mach Number is increased. This is connected with the slow development of the wake component of the turbulent boundary layer velocity profile as the Mach Number is increased. At very high Mach Numbers it will be extremely difficult to achieve turbulent boundary layers which have reached their asymptotic behaviour. The effect of a strong adverse pressure gradient at a compression corner has demonstrated the extreme resistance to separation of the turbulent boundary layer.

5. REFERENCES

1. Needham, D.A., Elfstrom, G.M., Stollery, J.L., "Design and Operation of the Imperial College No.2 Hypersonic Gun Tunnel", 1.C. Aero Report 70-04, Imperial College, London, 1970.

2. Spalding, D.B., Chi, S.W., "The Drag of a Compressible Turbulent Boundary Layer on a Smooth Flat Plate With and Without Heat Transfer", JFM, vol.18, part 1, pp. 117-143.

3. Elfstrom, G.M., Coleman, G.T., Stollery, J.L., "Turbulent Boundary Layer Studies in a Hypersonic Gun Tunnel", Paper 11, 8th International Shock Tube Symposium, London, July 1971; also available as I.C. Aero Report 71-11, Imperial College, London, 1971.

4. Hastings, R.C., Sawyer, W.G., "Turbulent Boundary Layers on a Large Flat Plate at M=4", RAE TR 70040, March 1970.

5. Roshko, A., Thomke, G.J., "Supersonic, Turbulent Boundary-Layer Interaction With a Compression Corner at Very High Reynolds Number", Presented at the Symposium on "Viscous Interaction Phenomena in Supersonic and Hypersonic Flow", USAF ARL, Ohio 1969.

6. Sterrett, J.R., Emery, J.C., "Experimental Separation Studies For Two-Dimensional Wedges and Curved Surfaces at Mach Numbers of 4.8 to 6.2", NASA TN D-1014, 1962.

7. Drougge, G., "An Experimental Investigation of the Influence of Strong Adverse Pressure Gradients on Turbulent Boundary Layers at Supersonic Speeds", Presented at 8th International Congress on Theoretical and Applied Mechanics, Istanbul, 1952. Also FFA Report 46, Sweden, 1953.

8. Kuehn, D.M., "Experimental Investigation of the Pressure Rise Required for the Incipient Separation of Turbulent Boundary Layers in Two-Dimensional Supersonic Flow", NASA Memo 1-21-59A, 1959.

9. Popinsky, Z., Ehrlich, C.F., "Development Design Methods for Predicting Hypersonic Aerodynamic Control Characteristics", USAF Technical Report AFFDL-TR-66-85, 1966.

10. Todisco, A., Reeves, B.L., "Turbulent Boundary Layer Separation and Reattachment at Supersonic and Hypersonic Speeds", Presented at the Symposium on "Viscous Interaction Phenomena in Supersonic and Hypersonic Flow", USAF ARL, Ohio, 1969.

11. Elfstrom, G.M., "Turbulent Separation in Hypersonic Flow", Ph.D. Thesis, University of London, 1971.

12. Green, J.E., "A Note on the Turbulent Boundary Layer at Low Reynolds Number in Compressible Flow at Constant Pressure", R.A.E. report to be published.
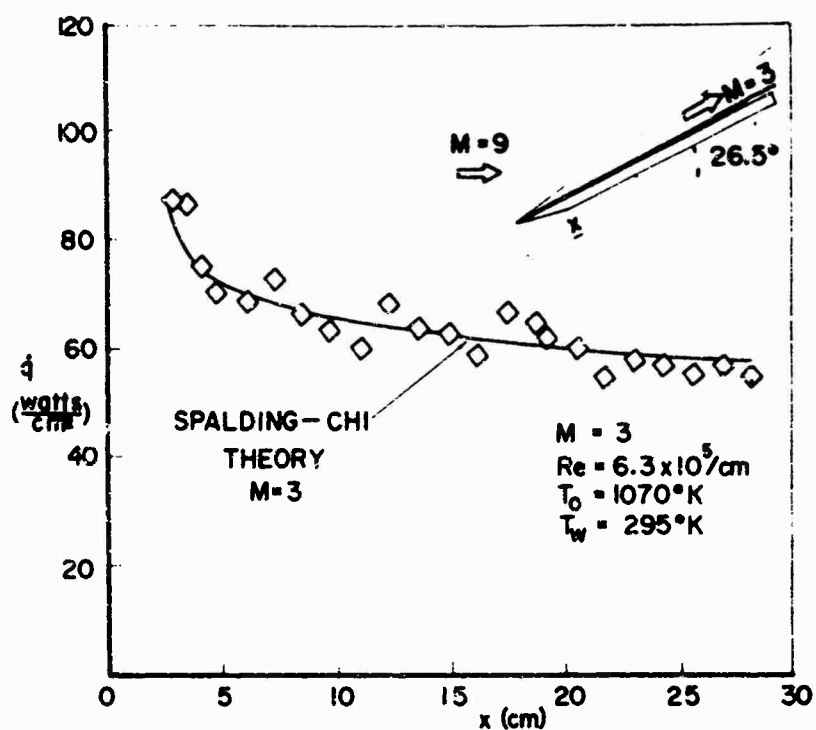
Fig. 1   Flat plate heat transfer rate measurements at M=3
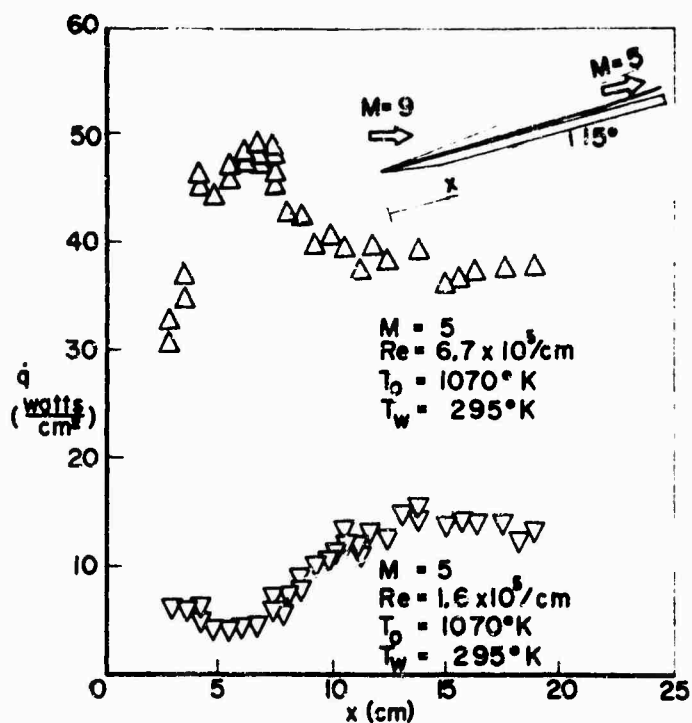
Fig. 2   Flat plate heat transfer rate measurements at M=5
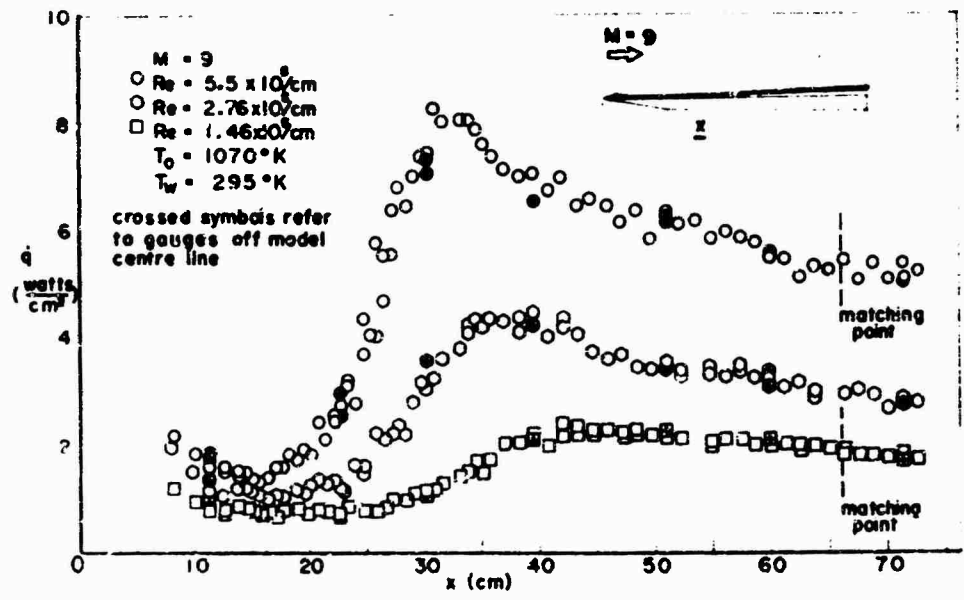
Fig. 3   Flat plate heat transfer rate measurements at M=9
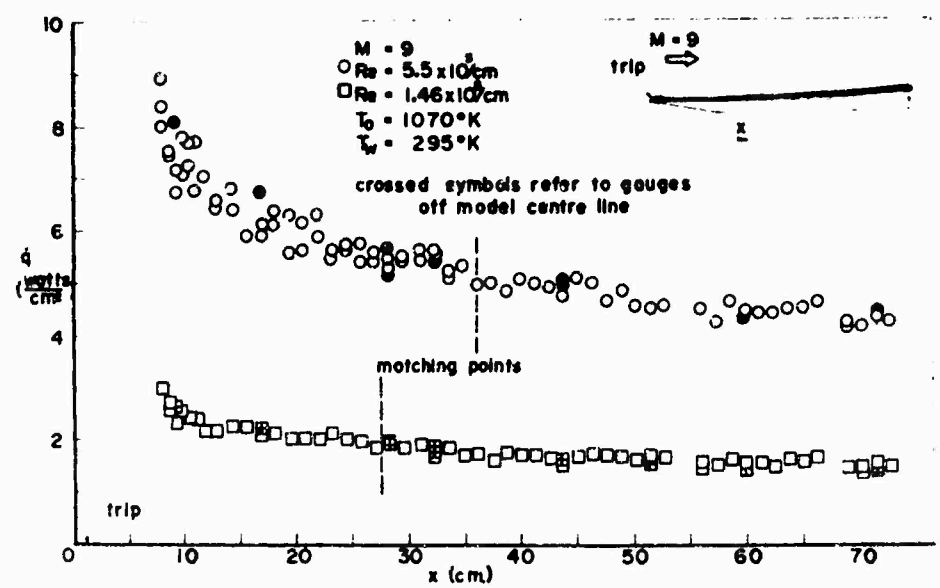
Fig. 4   The effect of a trip on flat plate heat transfer rate measurements at M=9
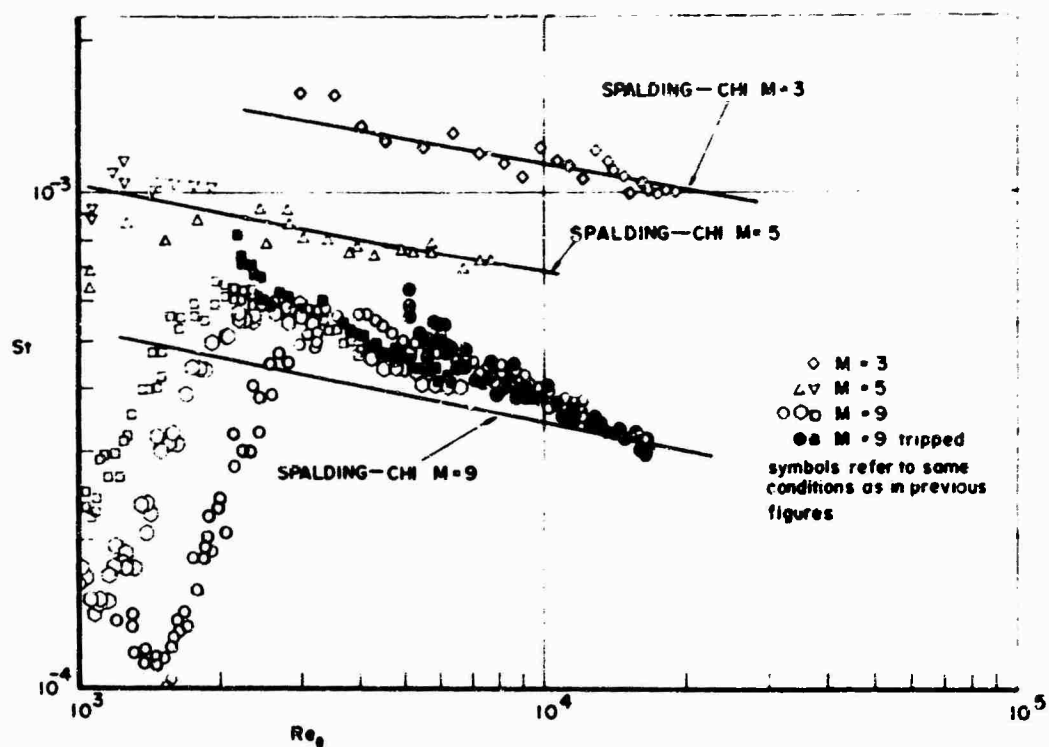
Fig. 5   Stanton Number comparisons
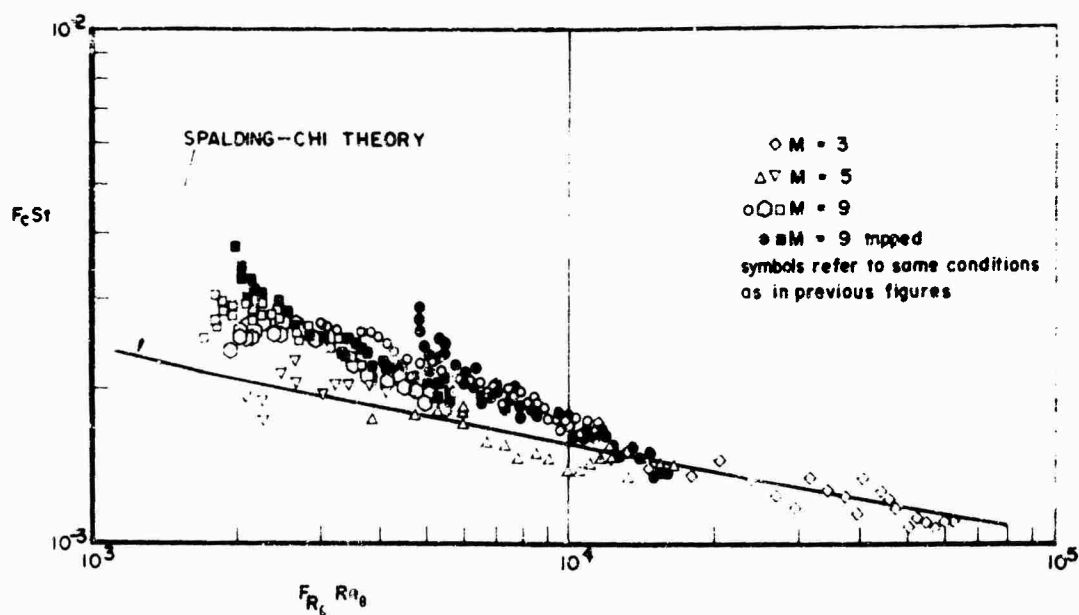
Fig. 6   Stanton Number converted to equivalent incompressible values
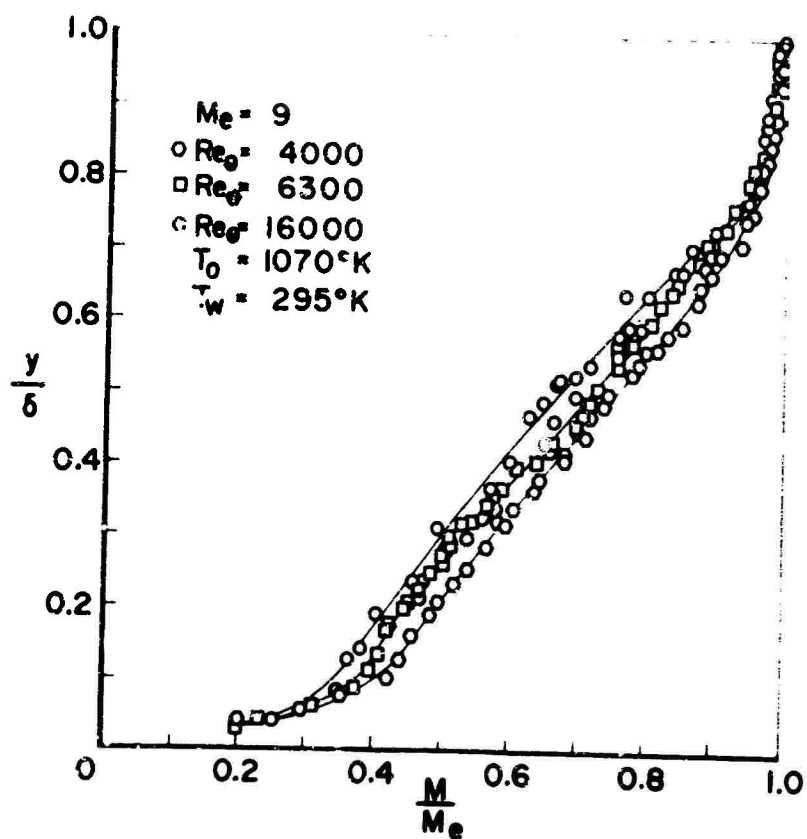
Fig. 7   Mach Number profiles on a flat plate at   M = 9
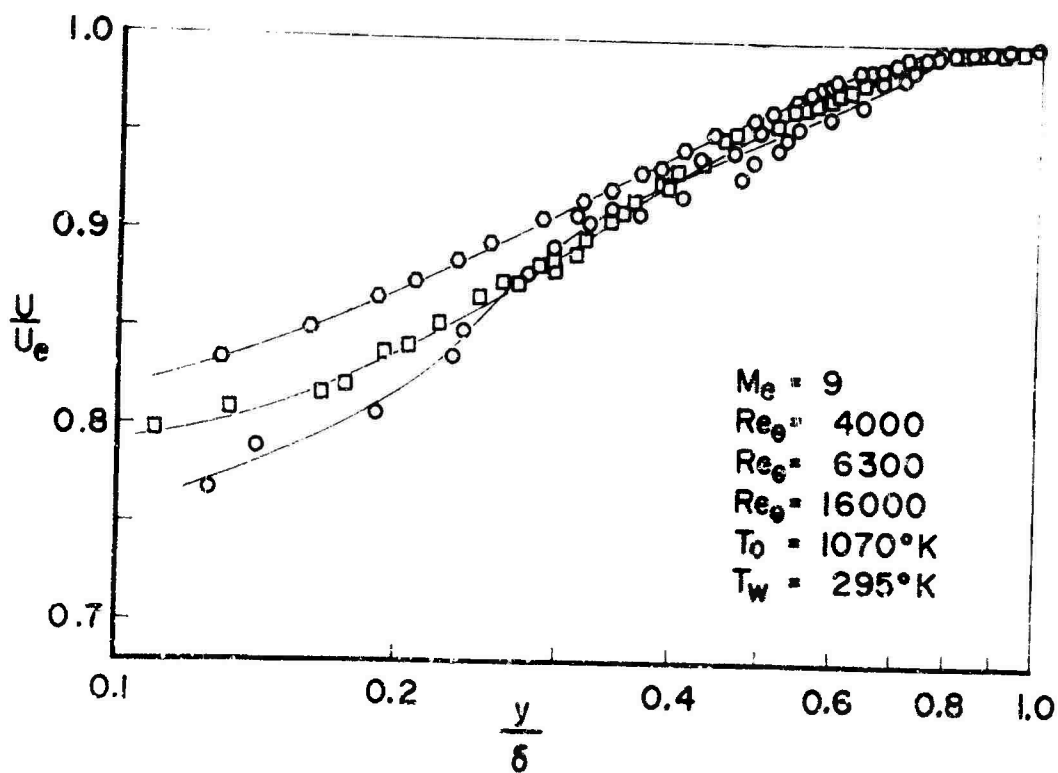
Fig. 8   Velocity profiles on a flat plate at   M = 9
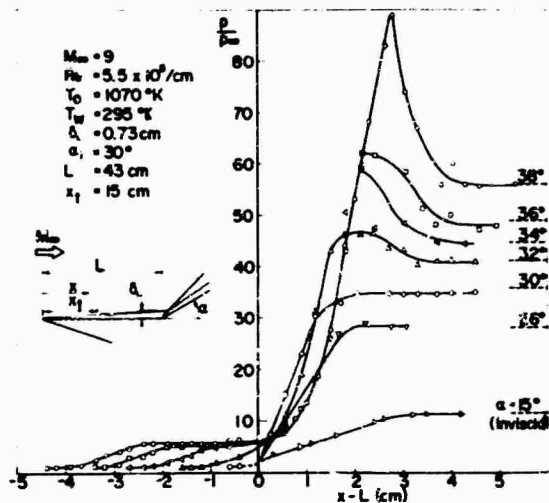
Fig. 9   Static pressure distributions on a
          wedge compression corner at M=9
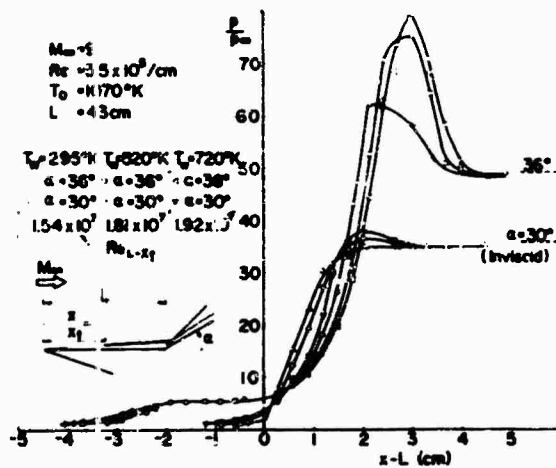
Fig. 10   Effect of wall temperature on static
          pressure distributions on a wedge
          compression corner at M=9
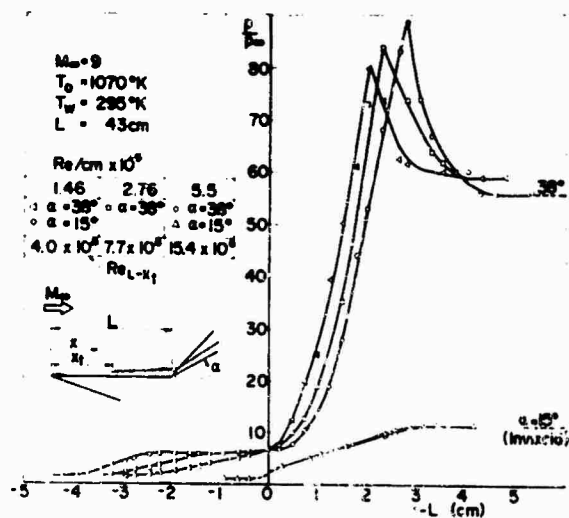
Fig. 11   Effect of unit Reynolds Number on static
          pressure distributions on a wedge
          compression corner at M=9
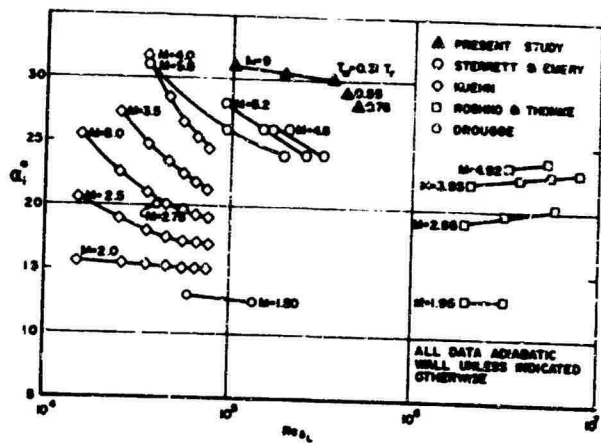
Fig 12   Incipient separation angle for turbulent flow
over a wedge compression corner
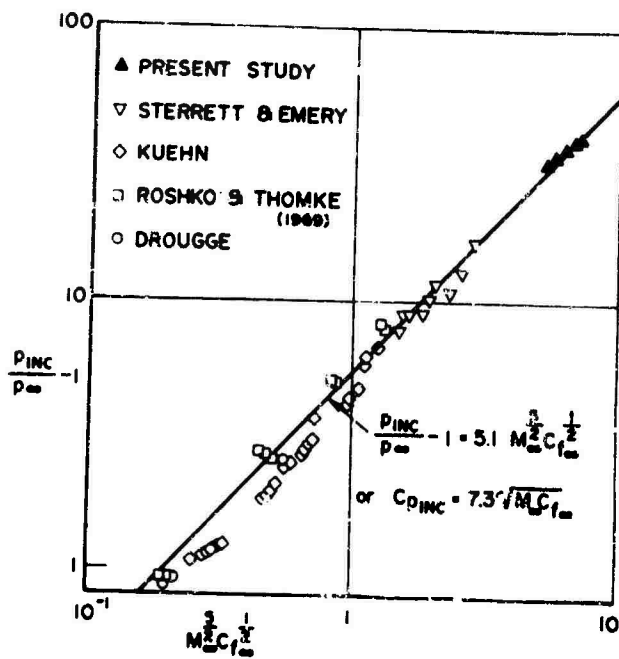
Fig. 13   Correlation of pressure rise to
incipient separation
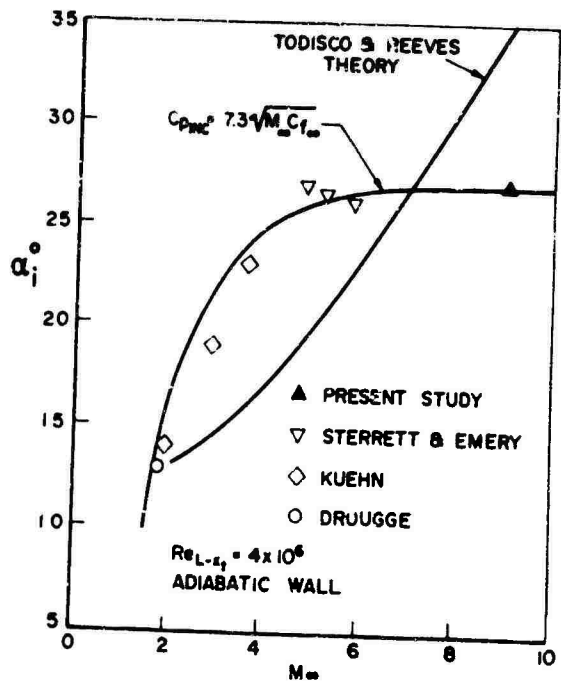
Fig. 14   Variation of incipient separation
angle with Mach Number

AN EXPERIMENTAL INVESTIGATION OF THE TURBULENT BOUNDARY LAYER ALONG A STREAMWISE CORNER

by O. O. Mojola[*] and A. D. Young[**]
Queen Mary College, University of London,
Mile End Road, London E.1.

SUMMARY

A selection of the results are presented of an extensive experimental investigation of steady incompressible turbulent boundary layer along a smooth 90-degree streamwise corner, formed by a pair of identical intersecting flat plates, with the freestream velocity directed parallel to the cornerline.

Detailed explorations of the flow, with and without external pressure gradients, included the determination of static pressure fields, the mean velocities, wall shear stresses, and the components of the Reynolds (turbulent) stress tensor.

A secondary flow towards the corner along the plane of symmetry and outwards from it close to the walls forming the corner is a vital and characteristic feature and is clearly reflected in the mean and turbulence flow measurements. In particular it modifies the relations between the shear stress components and turbulence energy and mean velocity distribution so as to make any simple extension of current methods of turbulent boundary layer prediction unlikely to be applicable in such a flow.

NOTATION

ρ, ν	density and kinematic viscosity of the fluid
x, y, z	a right-handed rectangular system of coordinates with origin at the corner leading edge, x along the cornerline and y, z parallel to the walls
U, V, W	mean velocity components in the x, y, z directions respectively
u, v, w	the corresponding velocity fluctuations
p, p'	mean and fluctuating static pressure
C_p	pressure coefficient, $(p - p_{ref.})/\tfrac{1}{2}\rho U^2_{ref.}$
$\rho \overline{u_i u_j}$	Reynolds stress components
τ_w	local wall shear stress $\mu(\partial U/\partial y)_{y.0}$ or $\mu(\partial U/\partial z)_{z.0}$
τ_{w2D}	asymptotic value of τ_w in an effectively two-dimensional bordering region far from the corner
δ_s	boundary layer thickness in the plane of symmetry measured along the corner bisector
δ_{2D}	boundary layer thickness in the 'two-dimensional' region well away from the corner
U_∞	local freestream velocity just outside the boundary layer
$P_{ref.}$, $U_{ref.}$	reference pressure and velocity, respectively

1. INTRODUCTION

A programme of work is currently in progress at Queen Mary College, London, directed at investigating boundary layer flows inside streamwise corners as part of the more general problem of the flow in wing-body junctions. Part of this programme on laminar and transitional boundary layer flow in a streamwise corner has already been reported by Zamir and Young [24]. They found that even in zero pressure gradient there were marked changes of velocity profile in the laminar boundary layer with distance downstream associated with the development of a secondary flow. This secondary flow was towards the corner close to the plane surfaces forming the corner and outwards from the corner in the plane of symmetry. This is in fact oppesite in sense to that demonstrated by various workers who have investigated turbulent flow in a streamwise corner, including the results reported here, and Zamir and Young showed by a flow visualisation technique the reversal in the direction of the secondary flow as the boundary layers passed through transition from laminar to turbulent. This transition process occurred in the corner at a local Reynolds number (in terms of the distance from the leading edge) of about 2×10^5. Zamir and Young noted that the extent of the corner influence with the flow laminar was confined to about two boundary layer thicknesses from the corner, and that an adverse pressure gradient readily induced separation, whilst a favourable one tended to delay the process of transition but did not alter its character.

The present paper reports briefly some results obtained with the boundary layer flow turbulent. Most of the investigations of turbulent corner flows to date [1-22] have been concerned with fully

developed or developing flows in closed or open conduits of non-circular section; here we are concerned with the basic case of a streamwise corner formed by two plates at right angles to each other and of span limited only by the geometry of the wind tunnel in which the tests were made. This investigation included measurements of the mean flow as well as of the turbulent velocity components and Reynolds stresses for zero pressure gradient and with an adverse streamwise pressure gradient.

2. EXPERIMENTAL FACILITIES AND TECHNIQUES

The programme has been carried out in a low speed closed-circuit wind tunnel with a freestream turbulence level of about 0.03 per cent. The corner model and traversing gear used were the same as those used by Zamir and Young and described in Ref.24.

Briefly, the corner model consisted of two identical smooth flat plates made of mild steel, fitted with 127 mm chord aerofoil-shaped leading edge units and wooden spanwise extensions, and joined to form a sharp 90-degree streamwise corner. Each intersecting surface had a total chord of 1.32 m and a span of 0.61 m. To obtain very good symmetry of flow variables about the bisecting plane, the model was symmetrically mounted in the tunnel working section, as indicated in Fig.1.
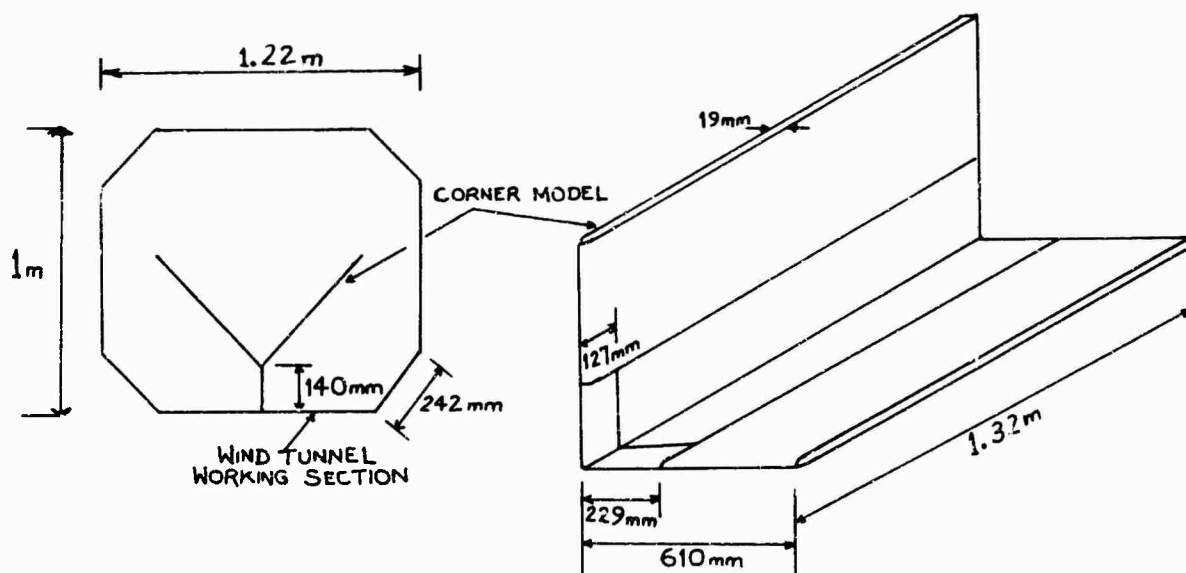
Figure 1. The Experimental Set-up (not to scale).

The traversing gear had 2 micrometers for fine lateral adjustments (to within 0.025 mm) and rotary handles for coarse movement in the streamwise direction and slow yawing of the probe's vertical support about its axis.

Two streamwise rows (at 0.089 m and 0.203 m from the corner) of 0.81 mm diameter static pressure holes set in the surface of each steel place and additional static holes on a third corner plate (made out of perspex otherwise identical to the steel plates) allowed very detailed measurements of the wall static pressure field to be made, as close as 2.5 mm from the corner. A 0.71 mm diameter static pressure tube of conventional design was used to measure the static pressure variation across the corner boundary layer.

Streamwise mean velocities were determined using both total head tubes and single normal hot wire probes; the results obtained with the two instruments generally differed little.

The Preston-tube technique was adopted in the form suggested by Patel [23] for the measurement of wall shear stresses. A total head tube with outside and inside diameters of 1.19 mm and 0.84 mm was generally used, but in a number of cases another tube with outside and inside diameters of 0.41 mm and 0.18 mm respectively was also used to check for consistency of results obtained with tubes of different diameters and diameter ratios.

Measurements of V, W, and $\overline{u_i u_j}$ were made using nonlinearised constant temperature anemometers Type 55A01 and Analog Correlator Type 55D70, manufactured by DISA Electronics (Denmark). The DISA line of probes was also used; this included the miniature single and X-wire probes for the determination of U and u^2, and the miniature X-probes for determining V, W, v^2, w^2, $\overline{uv}$, $\overline{uw}$ and $\overline{vw}$.

3. A PRELIMINARY PROGRAMME

In a preliminary experimental programme, exploratory measurements of a turbulent corner layer developing naturally from an initial laminar flow in a nearly zero pressure gradient were made. With a free stream velocity of about 30 m/s and a turbulence level of 0.03 per cent, turbulent bursts appeared first at the corner at about 0.15 m from the leading edge, corresponding to $U_\infty x / \nu \simeq 3 \times 10^5$, which is a little higher than the value of 2×10^5, reported by Zamir and Young [24] based on their rather more detailed measurements of the transition process in a comparable pressure field and free stream turbulence.

Although the flow in transverse planes (Y-Z planes) was partly laminar and partly turbulent over most of the chord, detailed measurements within the turbulent 'tongue' well downstream of the corner transition point were found to be very similar to the subsequent results obtained for the artificially induced turbulent layers, which form the subject of the main programme.

4. THE MAIN PROGRAMME

4.1 Scope and design of the experiments.

Transition was artificially provoked by means of a 25.4 mm wide sandpaper strip spanning the entire corner model. The roughness height, including the strip thickness, was about 0.75mm; with its up-stream edge 25.4 mm downstream of the corner leading edge, it was possible to realise away from the corner, in constant pressure, an asymptotic two-dimensional layer growing as $x^{0.80}$ approximately.

Very detailed studies of the corner region were conducted in two pressure fields (Fig. 2, a, b, c): one case of practically constant pressure obtained by simply setting the cornerline parallel to the free-stream, and one case of an adverse pressure gradient induced by means of a vertical V-shaped trailing-edge flap. It should be observed that in the former case the wall static pressure is indeed practically constant over much of the working surface; in the latter case there are spanwise variations in pressure reaching a maximum of about 6.2 per cent of $\frac{1}{2}\rho U^2_{Ref.}$ at x = 1.165 m.

4.2 Static pressure within the boundary layer.

In the case of practically uniform free stream pressure, the static pressure variation within the boundary layer in the corner was measured at a number of x-stations; a typical pattern of isobars is indicated in Fig. 2d. It can be seen that the general tendency is for the pressure to increase towards the outer edge of the boundary layer, the maximum value of $\Delta p / \frac{1}{2}\rho U^2$ being about 0.01~0.03, which agrees well with the findings of Leutheusser [16] for rectangular ducts and of Bragg [11] for the semi-infinite corner boundary layer. No corrections have been applied to the present data for any possible effects of transverse mean and fluctuating velocities on the static tube readings.

4.3 Mean velocities and the boundary layer growth.

In the present work a major effort has been directed at establishing the full streamwise development of the U-field, thus providing a more comprehensible picture of the corner layer growth (longitudinal and transverse) than hitherto reported. The corner region was mapped at x = 0.152, 0.228, 0.305, 0.381, 0.458, 0.559, 0.660, 0.787, 0.940 and 1.091 m in the case of zero pressure gradient, and additionally at x = 1.192 and 1.245 m in the adverse pressure field. In the latter case, flow separation was found to occur first at the corner at x = 1.2. ± 0.02 m; it then receded downstream with increasing spanwise distance from the cornerline.

Typical iso-velocity contours are shown in Fig. 3a. A noteworthy feature of these results is the distortion of the contours near the corner as the result of a transverse circulatory motion now generally recognised as the 'secondary flow' of Prandtl's second kind [27]. The measured magnitude and the direction of the secondary flow velocity vectors in zero pressure gradient are indicated in Fig. 3a by arrows drawn against a background of the U-contours. As Prandtl had predicted nearly half a century ago, the secondary motion is such that there is a flow into the corner roughly along the corner bisector, accompanied by an outflow from the corner along either wall. It is to be noted that although the secondary flow vectors attain their maximum values ($\simeq 3\%$ of U_∞ for the case shown) near the corner bisector, they are not entirely confined to the corner vicinity but are still evident away from the corner, albeit in diminished strength. The secondary flow field measured in these tests is generally similar, but not identical, to those reported for fully-developed and developing flows in square ducts; this is not surprising although there are important differences between the flows. In the adverse pressure field, the secondary flow magnitude shows a general increase, reaching a maximum of about 0.07 U_∞ just upstream of the corner separation point.

The boundary layer growth in the plane of symmetry in the corner (δ_s) is compared with the two-dimensional growth far from the corner (δ_{2D}), with and without pressure gradients, in Fig. 3b. With zero pressure gradient, it is found that δ_s/δ_{2D} decreases with x; an empirical correlation of the present data suggests

$$\delta_s / \delta_{2D} \simeq 5.81 \left(U_\infty \delta_s / \nu\right)^{-0.115}$$

so that if, as usual, $\delta_{2D} \propto x^{0.80}$, then $\delta_s \propto x^{0.718}$, indicating approximately a 10 per cent reduction in growth rate as compared with two-dimensional flow. This can be readily attributed to a thinning action due to the secondary flow into the corner. Because of its premature separation in the adverse pressure field, the boundary layer near the corner thickens more rapidly than that far from the corner.

4.4 Wall shear stresses.

Preston-tube measurements of the wall shear stresses (τ_w) with and without pressure gradients are presented in Fig. 3, c and d. From a theoretical value of zero at the corner, the wall shear stress rises

sharply in zero pressure gradient to a local maximum near the corner; it then drops slightly and subsequently rises again slowly approaching its asymptotic two-dimensional value at a distance of about $2 \delta_{2D}$ from the corner. The peculiar 'kink' in an otherwise smooth distribution of τ_w reflects a scouring action of the secondary flow on the wall region.

In the adverse pressure gradient the wall stress field presents a similar picture, but with the added feature of rapidly diminishing stress and stress gradient near the corner. At the corner itself the stress remains zero but the stress gradient is progressively reduced from a positive value to what can be inferred as zero at the corner separation point, and a negative value further downstream. Hence it can be inferred that

$$\left(\frac{\partial^2 U}{\partial y \, \partial z} \right)_{y=z=0} = 0$$

is the criterion for the beginning of flow separation on the corner line.

4.5 Turbulence measurements.

A typical survey of the components of the Reynolds stress tensor in zero pressure gradient is presented in Figs. 4 a - f in the form of contours.

It is interesting to note that the turbulence field is far more distorted by the secondary flow than is the U-field. This, however, is not unexpected since whilst V and W are comparable to u, v, w they are at least one order of magnitude smaller than U.

As in two-dimensional boundary layers, we find that $\overline{u^2}$ is greater than both $\overline{v^2}$ and $\overline{w^2}$. Not unexpectedly near the y = 0 wall $\overline{v^2} < \overline{w^2}$ while near the z = 0 wall the opposite is true.

It is also to be noted that of the shear stresses (per unit density) $\overline{v \, w}$ is generally the greatest in or near the plane of symmetry, and that in the half corner region bounded by the corner bi-sector and the y = 0 wall $\overline{u \, v}$ generally exceeds $\overline{u \, w}$, the converse being the case in the other half.

The $\overline{u^2}$ stress has been measured very extensively; the measurements of the other stresses have been largely confined to the plane of symmetry. Typical surveys in the plane of symmetry with and without pressure gradients are given in Fig. 5. The stresses are not dissimilar in magnitude from those found in a two-dimensional boundary layer of similar history, but several distinctions can be made. In the zero pressure gradient case, for example, we notice that because of the constraining influence of the corner geometry the point of maximum $\overline{v^2}$ or $\overline{w^2}$ is shifted well away from the corner while $\overline{u^2}$ apparently attains its peak value deep inside the corner. We also notice that in the outer layers the shear stresses are particularly influenced by the secondary flow, and hence may neither be simply related to the mean velocity gradient via a constant eddy viscosity nor to $\overline{q^2}$ by a constant factor, where $\overline{q^2} = \overline{u^2} + \overline{v^2} + \overline{w^2}$. Since such relations provide the basis of current methods of turbulent boundary layer prediction methods, the corner flow is unlikely to be successfully predicted by them and calls for a new approach.

Except for the phenomenal rise in the value of $\overline{v \, w}$ as the corner separation point is approached, the effects of an adverse pressure field on the turbulent field are found to be generally similar to those observed in two-dimensional retarded layers.

5. CONCLUSIONS AND CONCLUDING REMARKS

We conclude that

(i) Secondary flows arise spontaneously in a semi-infinite turbulent corner layer; they are directed such that the layers with vanishing skin friction near the corner are re-energised through a continuous supply of higher energy fluid from the outer portion of the boundary layer moving towards the corner along the plane of symmetry and outwards from the corner close to the walls.

(ii) The streamwise growth of the boundary layer near the corner is somewhat reduced by the secondary motions; in the plane of symmetry in zero pressure gradient, for example, the boundary layer grows about 10% slower than its two-dimensional counterpart.

(iii) Unlike the laminar boundary layer in a corner [24] the turbulent corner layer is relatively stable in zero or mild pressure gradients in spite of the zero shear stress along the corner itself. Flow separation, when it does occur, under the influence of a strong adverse pressure gradient, is associated in the corner with the vanishing of the shear stress gradient.

(iv) The turbulence field strongly reflects the secondary flow, and a simple extension of current prediction methods to the corner flow seems unlikely to be fruitful.

(v) As evident in the wall shear stress distributions, the wall region of the corner layer settles down to its two-dimensional form more rapidly than the outer region, but on the whole the effects of the corner are largely confined within approximately 3 ~ 4 boundary layer thicknesses from the corner.

REFERENCES

1. Nikuradse, J.: Untersuchungen uber die Geschwindigteitsvertelung in turbulenten stromungen. Thesis Gottingen V.D.I. - Forsch.281, 1926.

2. Brundrett, E.; and Baines, W.D : The production and diffusion of vorticity in duct flow. J. Fluid Mechanics, Vol.19, 1964, p.375-392.

3. Delleur, J.W.; and McManus, D.S.: Secondary flow in straight open channels. Proc. 6th Midwest Conf. on Fluid Mechanics, Austin, Texas, 1959, p.81-97.

4. Hoagland, L.C.; Fully developed turbulent flow in straight rectangular ducts - Secondary flow, its cause and effect on the primary flow. Sc.D. Thesis, M.I.T., 1960.

5. Tracy, H.J.: Turbulent flow in a three-dimensional channel. A.S.C.E. Jour. Hydraulics Div., Vol.91, 1965, p.9-35.

6. Hinze, J.O.: Secondary currents in wall turbulence. Physics of Fluids, Vol.10, 1967, p.S122-S125.

7. Liggett, J.A.; Chiu, C.L.; and Mizo, L.S.: Secondary currents in a corner. A.S.C.E. Jour. Hydraulics Div., Vol.91, 1965, p.99-117.

8. Paradis, M.S.: Couche limite turbulente à l'interieur d'un dièdre. M.A.Sc. Thesis, Université Laval, Canada, 1963.

9. Eichelbrenner, E.A.: Remarques sur la determination de l'écoulement secondaire dans la couche limite turbulente à l'interieur d'un dièdre. La Recherche Aerospatiale, Vol.104, 1965.

10. Toan, N.K.: Couche limite turbulente à l'interieur d'un dièdre avec gradient de pression. M.A.Sc. Thesis, Université Lavel, Canada, 1968.

11. Bragg, G.M.: The turbulent boundary layer in a corner. Ph.D. Thesis, University of Cambridge, 1965. See also J. Fluid Mechanics, Vol.36, 1969, p.485-503.

12. Gersten, K.: Corner interference effects. AGARD Rep.299, 1959.

13. Rodet, E.: Etude de l'écoulement d'un fluide dans un tunnel prismatique de section trapezoidele. Publications Scientifiques et Techniques du Ministère de l'Air, No.369, 1960.

14. Gessner, F.B.; and Jones, J.B.: A preliminary study of turbulence characteristics of flow along a corner. A.S.M.E., J.Basic Engineering, Vol.83, 1961, p.657-662.

15. Gessner, F.B.; and Jones, J.: On some aspects of fully developed turbulent flow in rectangular channels. J.Fluid Mechanics, Vol.23, 1965, p.685-713.

16. Leutheusser, H.J.: Turbulent flow in rectangular ducts. A.S.C.E. Jour. Hydraulics Div., Vol.89, 1963, p.1-19.

17. Eckert, E.R.G.; and Irvine, T.F.: Flow in corners of passages with non-circular cross-sections. A.S.M.E., Vol.78, 1956, p.709.

18. Cremers, C.J.; and Eckert, E.R.G.: Hotwire measurements of turbulence correlations in a triangular duct. A.S.M.E. J. Applied Mechanics, Vol.29, 1962, p.609-614.

19. Veenhuizen, S.D.; and Meroney, R.N.: Secondary flow in a bounday layer, Colorado State University Report CER 68-695 DV-RNM28, 1969.

20. Perkins, H.J.: The turbulent corner boundary layer. Ph.D. Thesis, University of Cambridge, 1970.

21. Ahmed, S.; and Brundrett, E.: Turbulent flow in non-circular ducts. Int. Jour. Heat & Mass Transfer, Vol.14, 1971, p.365-375.

22. Prandtl, L.: Uber den Reibungwiderstand stromerder Luft. Ergeb. Aerodyn. Versuch, Göttingen, III series, 1927.

23. Patel, V.C.: Calibration of the Preston tube and limitations on its use in pressure gradients. J. Fluid Mechanics, Vol.23, 1965, p.185-209.

24. Zamir, M.; and Young, A.D.: Experimental investigation of the boundary layer in a streamwise corner. The Aeronautical Quarterly, Vol.XXI, Nov.1970, p.313-339.

25. Mojola, O.O.: Turbulent boundary layer along a streamwise corner. Ph.D. Thesis, University of London (in preparation).

(a) Streamwise pressure distributions along surface 0.089 m from corner.

● Zero pressure gradient
× Adverse pressure gradient

(b) Spanwise pressure distributions, zero pressure gradient.

(d) Isobars, $x = 0.940$ m, zero pressure gradient.

$$\frac{p - p_{ref}}{\frac{1}{2}\rho U_{\infty}^2} \times 10^2$$

(c) Spanwise pressure distributions, adverse pressure gradient.

Fig. 2. Static Pressure Distributions
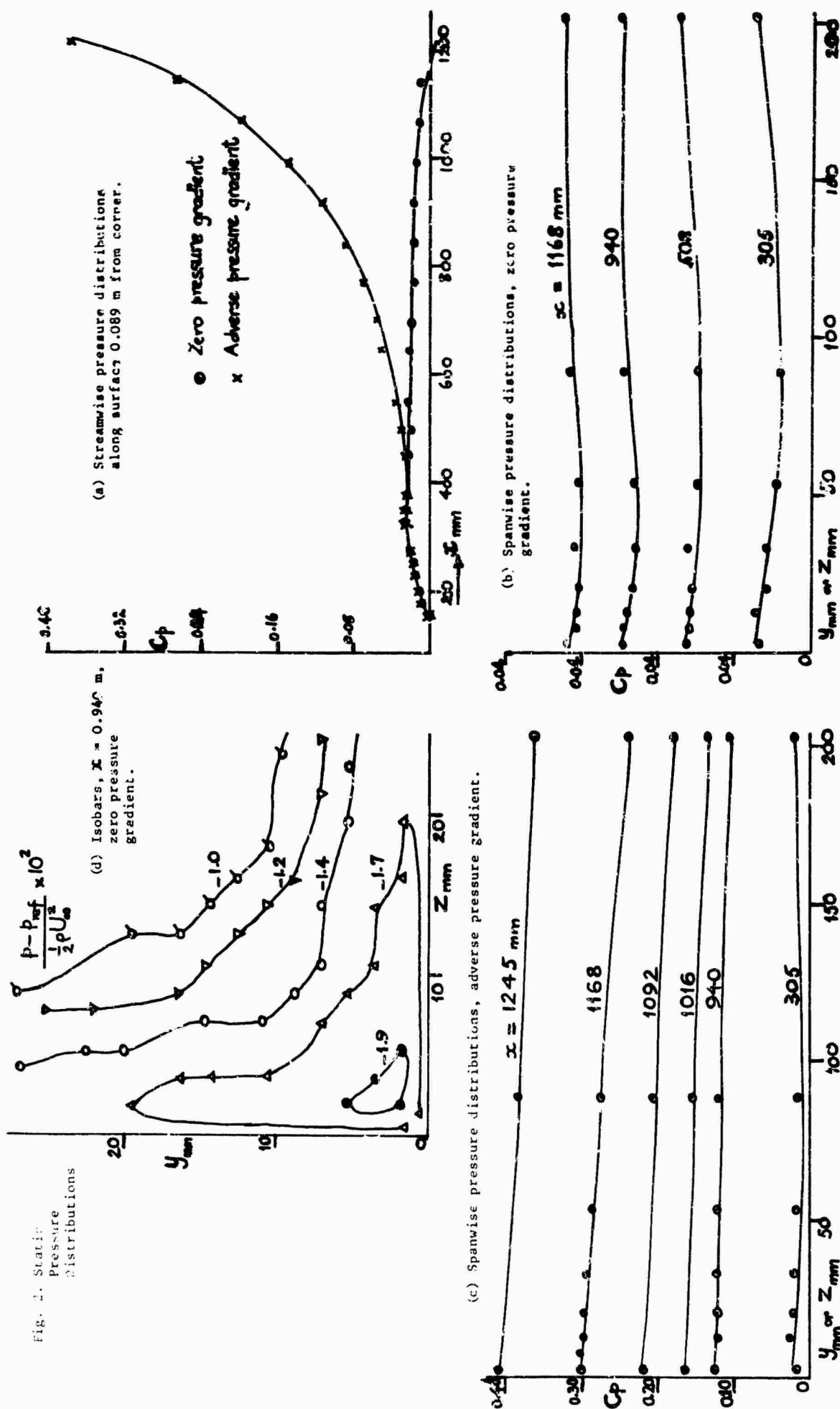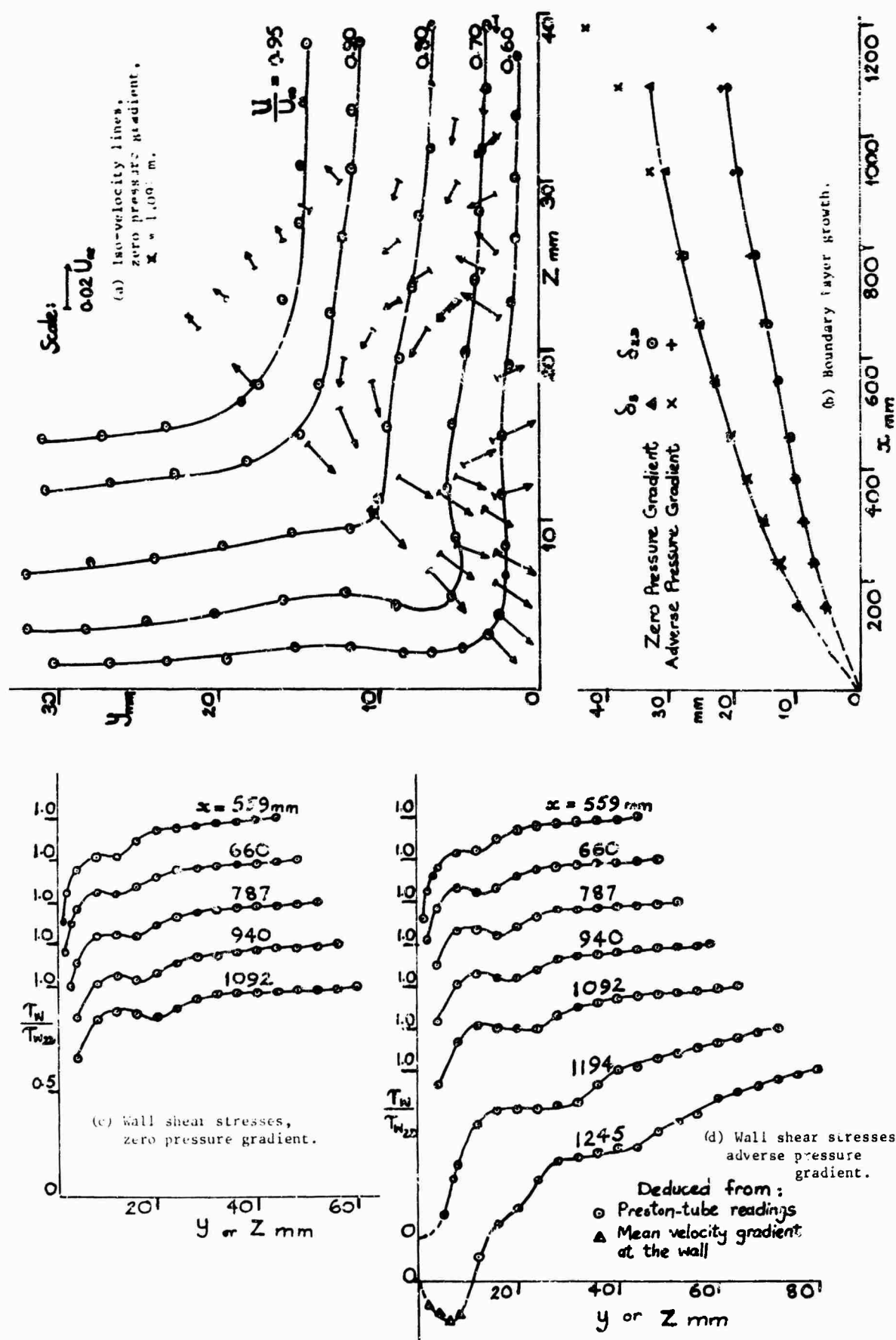
Fig. 3. Mean Flow Measurements.
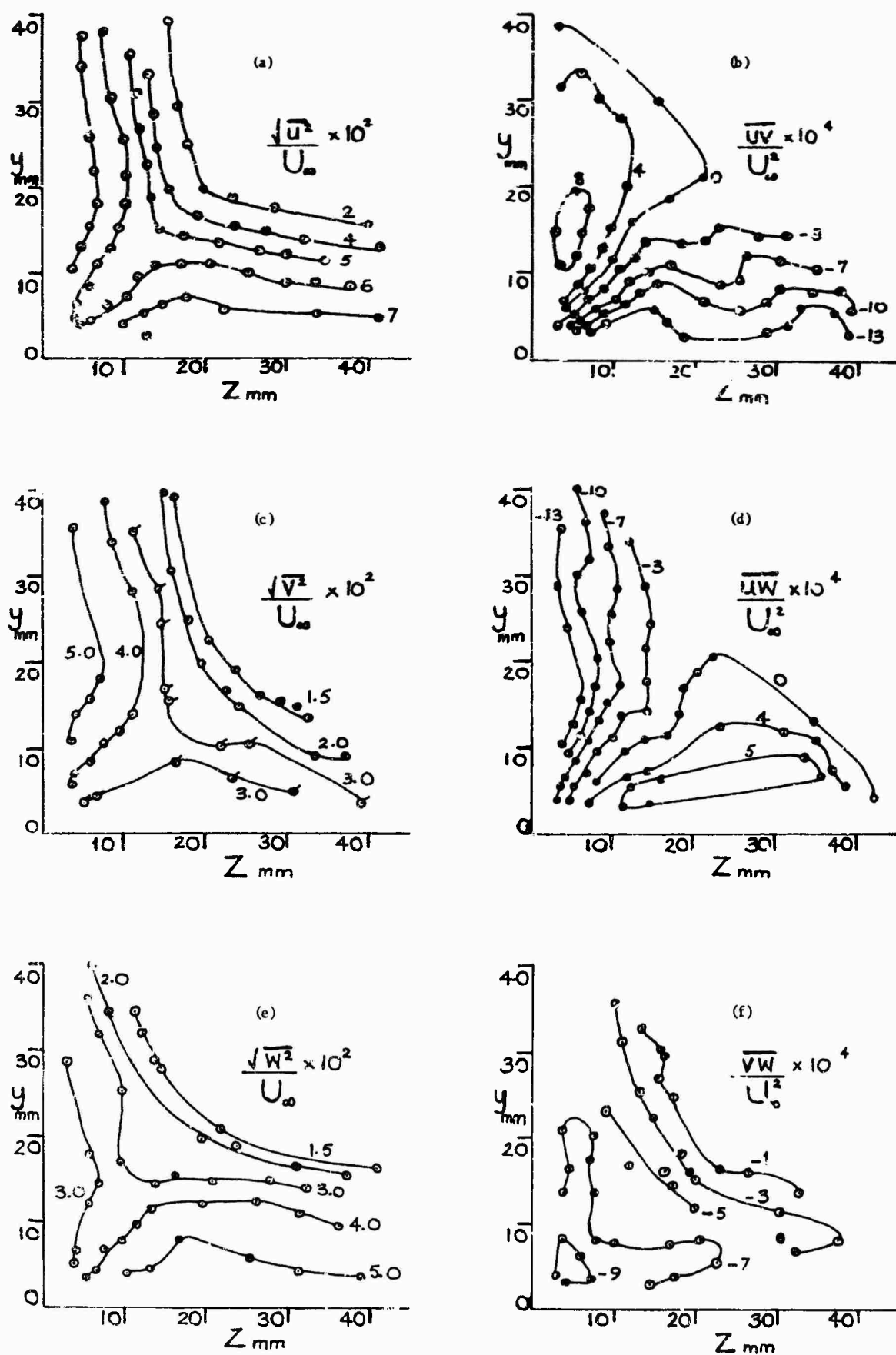
Fig. 4.   Typical Reynolds Stress Contours, $X \leftarrow 1.091$ m, zero pressure gradient.
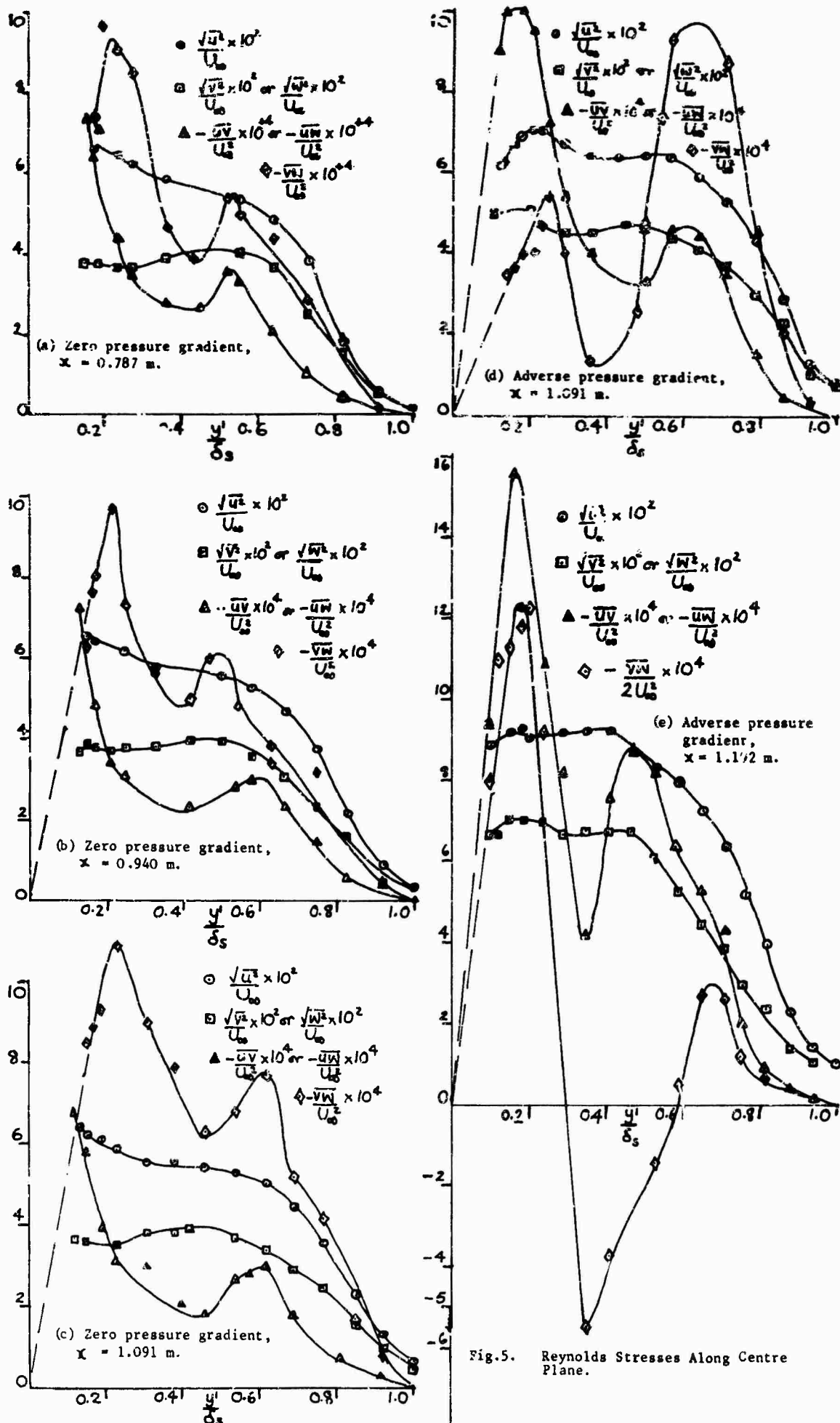
Fig.5. Reynolds Stresses Along Centre Plane.

COUCHE LIMITE TURBULENTE AVEC INJECTION A LA PAROI D'UN MÊME GAZ OU D'UN GAZ ETRANGER.

par T. LILI (*) et R. MICHEL (**)
OFFICE NATIONAL D'ETUDES ET DE RECHERCHES AEROSPATIALES (ONERA)
92 - CHATILLON (France)

SUMMARY

An improved mixing-length model is applied to the theorical determination of turbulent boundary layer, with transfer of fluid at the wall, and the results are compared point by point with available experimental evidence.

In the incompressible field, there are first provided some solutions to the local equations of an equilibrium boundary layer, to define the requisite set of velocity profiles and skin friction law for an air injection with pressure gradient. Next, the velocity and concentration profiles are worked out for foreign gas injected. Lastly, the solution is extended to cover the general case of a compressible fluid, leading to a systematic set of results for the effect of injection upon skin-friction and heat transfer shown as a function of Mach number and wall temperature.

NOTATIONS -

x,y	Coordonnées longitudinale et normale $\left(\eta = \dfrac{y}{\delta}\right)$		C_f	Coefficient de frottement $2\tau_p/\rho_e u_e^2$
ℓ	Longueur de mélange $(L = \ell/\delta)$		C_h	Coefficient de flux de chaleur $\phi_p/\rho_e u_e(H_p-H_w)$
u,v	Composantes de la vitesse		C_m	Coefficient de transfert de masse par diffusion

ϕ,s Nombres de PRANDTL et de SCHMIDT $\dfrac{\mu C_p}{\lambda}$ et $\dfrac{\mu}{\rho D}$

M Nombre de Mach

p,ρ Pression et masse volumique

h,H Enthalpie et Enthalpie totale

T Température (h/C_p)

C_i Concentration massique ρ_i/ρ

C_p Chaleur spécifique $\sum_i C_i C_{pi}$

μ,λ,D Viscosité, conductibilité, diffusion

C_m Coefficient de transfert de masse par diffusion $Q_{2p}/\rho_e u_e(C_{2p}-1)$

R_ℓ Nombre de Reynolds $\dfrac{\rho_e u_e L}{\mu_e}$

δ Epaisseur de la couche limite

θ,θ_c Epaisseurs intégrales

$$\theta = \int_0^\delta \frac{\rho u}{\rho_e u_e}\left(1 - \frac{u}{u_e}\right)dy \quad ; \quad \theta_c = \int_0^\delta \frac{\rho u}{\rho_e u_e}\frac{C_1}{C_{1p}}dy$$

P Paramètre d'injection $\rho_p v_p/\rho_e u_e$

r Facteur de récupération $(H_{ad}-h_e)/(H_e-h_e)$

τ,ϕ,Q Frottement, flux de chaleur, flux de diffusion, totaux.

INDICES -

e	écoulement extérieur
p	paroi
1	gaz injecté
2	gaz principal
ℓ	laminaire
t	turbulent
ad.	paroi adiabatique. $\phi_p = 0$

1 - INTRODUCTION

Le présent travail est consacré à la détermination théorique et à la comparaison à l'expérience de solutions relatives à l'influence d'un transfert de fluides à la paroi, sur le développement d'une couche limite turbulente. On y considère le cas de l'injection répartie d'un gaz qui peut être le même que celui de l'écoulement principal, ou un gaz étranger, en absence toutefois de réaction chimique.

Le traitement est basé sur un schéma amélioré de longueur de mélange grâce auquel une expression du frottement, du flux de chaleur et du flux de diffusion sont disponibles pour toute la couche limite. Une résolution numérique des équations locales de couche limite est ainsi possible pour le cas général de conditions aux limites quelconques ; on présentera effectivement l'application à quelques cas expérimentaux d'une technique de calcul par différences finies.

Au préalable, il a semblé utile de rechercher des solutions particulières, en se plaçant dans des cas pour lesquels les dérivées longitudinales des profils de couche limite peuvent être négligées. Ces solutions de similitude auront l'intérêt de fournir un ensemble de résultats grâce auxquels l'influence des différents paramètres intervenant dans le développement d'une couche limite turbulente avec injection de fluide pourra être déterminée systématiquement.

2 - EQUATIONS GENERALES - HYPOTHESES DE BASE

2.1 Equations générales

Considérant le cas général de l'écoulement plan d'un fluide compressible, avec injection répartie d'un gaz qui peut être le même que celui de l'écoulement principal, ou un gaz étranger mais sans réaction chimique,(mélange binaire), les équations locales de la couche limite sont les suivantes :

équation de continuité :
$$\frac{\partial \rho u}{\partial x} + \frac{\partial \rho v}{\partial y} = 0 \qquad (1)$$

équation de quantité de mouvement :
$$\rho u \frac{\partial u}{\partial x} + \rho v \frac{\partial u}{\partial y} = \frac{\partial \tau}{\partial y} + \rho_e u_e \frac{du_e}{dx} \qquad (2)$$

équation de l'énergie :
$$\rho u \frac{\partial H}{\partial x} + \rho v \frac{\partial H}{\partial y} = \frac{\partial}{\partial y}(u\tau - \phi) \qquad (3)$$

Ces trois premières équations s'appliquent aux caractéristiques moyennes du mélange. Le frottement et le flux de chaleur $\tau = \tau_\ell + \tau_t$ et $\phi = \phi_\ell + \phi_t$ seront discutés plus loin.

(*) Ingénieur Stagiaire, Direction d'Aérodynamique.

(**) Chef de Division de Recherches, Direction d'Aérodynamique.

Il faut leur joindre l'équation de conservation pour l'une des deux espèces en présence ; elle s'écrit :

$$\rho u \frac{\partial C_i}{\partial x} + \rho v \frac{\partial C_i}{\partial Y} = - \frac{\partial Q_i}{\partial Y} \qquad (4)$$

l'indice i représentant soit le gaz injecté (i = 1) soit le gaz principal (i = 2). Q_i est le flux de diffusion de l'espèce considérée, $Q_i = Q_{il} + Q_{it}$

2.2 Hypothèses de base :

On utilisera un schéma amélioré déjà présenté et appliqué (réf. 1), plus spécialement dans le cas du fluide incompressible.

Le terme de frottement turbulent est exprimé par la formule classique de longueur de mélange dans la partie extérieure de la couche limite. On a retenu la formule universelle :

$$\frac{l}{\delta} = 0{,}085 \; \text{th} \left(\frac{k}{0{,}085} \; \frac{y}{\delta} \right) \qquad (5)$$

Dans la sous-couche visqueuse, l'expression est corrigée pour tenir compte des effets de la viscosité sur la turbulence. L'expression générale du frottement total est mise ainsi sous la forme

$$\tau = \mu \frac{\partial u}{\partial y} + \rho F^2 l^2 \left| \frac{\partial u}{\partial y} \right| \frac{\partial u}{\partial y} \qquad (6)$$

Faisant appel aux données de VAN DRIEST, relatives à la sous-couche visqueuse de plaque plane en incompressible, on a généralisé la relation proposée par cet auteur, en supposant que pour le cas général, F était fonction du rapport du frottement turbulent au frottement laminaire. On a montré qu'en fait, la fonction pouvait être explicitée également par rapport au frottement total par la relation :

$$F = 1 - \exp \left[\frac{-l}{26 k \mu} (\tau \rho)^{1/2} \right] \qquad (7)$$

La fonction correctrice est nulle à la paroi ; elle tend vers 1 quand l'écoulement devient pleinement turbulent.

On introduira pour clarifier l'écriture une viscosité turbulente ε, définie, pour être en accord avec l'expression précédente du frottement turbulent, par $\varepsilon = \rho F^2 l^2 \left| \frac{\partial u}{\partial y} \right|$. Le frottement, le flux de chaleur et le flux de diffusion s'écrivent alors :

$$\tau = (\mu + \varepsilon) \frac{\partial u}{\partial y} \; ; \; \phi = - \left(\frac{\mu}{\mathcal{P}} + \frac{\varepsilon}{\mathcal{P}_t} \right) \frac{\partial h}{\partial y} + Q_2 (h_2 - h_1) \; ; \; Q_i = - \left(\frac{\mu}{S} + \frac{\varepsilon}{S_t} \right) \frac{\partial C_i}{\partial y} \qquad (8)$$

$\mathcal{P}$ et $\mathcal{P}_t$ sont les nombres de PRANDTL, laminaire et turbulent ; on a utilisé dans les applications présentes $\mathcal{P} = 0{,}725$ et $\mathcal{P}_t = 0{,}89$

S et S_t sont les nombres de SCHMIDT, laminaire et turbulent ; leurs valeurs seront discutées lors de l'application au cas de l'injection d'un gaz étranger.

3 - SOLUTION D'EQUILIBRE - INJECTION D'AIR EN INCOMPRESSIBLE

3.1 Principe général.

On a montré (réf. 1) qu'il est possible en fluide incompressible, et dans le cas de l'injection du même gaz que celui de l'écoulement principal (injection d'air), de déterminer des solutions asymptotiques (nombre de Reynolds tendant vers l'infini) dans le cas de couches limites d'équilibre.

Le principe de ce traitement dont on va rappeler les principaux résultats est essentiellement le suivant :

A grand nombre de Reynolds on peut distinguer dans la couche limite, une "région intérieure" dans laquelle se manifestent les effets de la viscosité mais où les forces d'inertie sont faibles devant les forces de frottement, d'une "région extérieure" dans laquelle les forces de frottement et d'inertie sont du même ordre mais où l'écoulement est essentiellement turbulent.

On peut traiter séparément ces deux régions et obtenir, moyennant l'utilisation de variables appropriées, des résultats indépendants du nombre de Reynolds.

Une propriété importante est qu'il doit exister un recouvrement des lois relatives aux deux régions. On a montré (réf. 1) que cette condition dictait d'une part le choix des variables à utiliser et permettait d'autre part d'établir la loi pour le frottement de paroi.

3.2 Région intérieure - loi de paroi.

On considère la région suffisamment proche de la paroi pour que les forces d'inertie soient faibles devant les forces de frottement visqueux et turbulent ; il en est de même, si le nombre de Reynolds est assez grand, de la force de pression.

L'équation de quantité de mouvement prend ainsi la forme très simplifiée :

$$\left(\frac{\partial \tau}{\partial Y} \right)_p = \rho v_p \frac{\partial u}{\partial y} \quad \text{soit} \quad \tau = \tau_p + \rho v_p u$$

Joignant l'expression (6) du frottement total, en tenant compte du fait que la longueur de mélange demeure sensiblement $l = ky$, on a simplement à résoudre l'équation :

$$\frac{\tau}{\tau_p} = 1 + v_p^+ u^+ = \frac{\partial u^+}{\partial y^+} + F^2 K^2 y^{+2} \left| \frac{\partial u^+}{\partial y^+} \right| \frac{\partial u^+}{\partial y^+} \qquad (9)$$

La fonction correctrice étant alors : $F = 1 - \exp \left[- \frac{y^+}{26} \left(1 + v_p^+ u^+ \right)^{1/2} \right]$

(on a utilisé les notations classiques : $u^+ = \dfrac{u}{u_\tau} \; ; \; v_p^+ = \dfrac{v_p}{u_\tau} \; ; \; y^+ = \dfrac{u_\tau y}{v} \; ; \; u_\tau^2 = \dfrac{\tau_p}{\rho}$)

Un programme de résolution des équations précédentes a été établi et appliqué pour différentes valeurs du paramètre de transfert de fluide v_p^*. Il a permis de déterminer l'influence de l'injection (et de l'aspiration) sur la distribution des vitesses dans la sous-couche visqueuse et dans la région turbulente de paroi.

Pour analyser plus aisément les résultats et pour préparer la définition de la variable déficitaire qu'on devra choisir pour la région extérieure, il convient de rechercher la variable transformée qui donne à la loi de paroi une forme logarithmique lorsque l'écoulement devient pleinement turbulent ($\tau_{\ell} \neq 0$, $F = 1$) On trouve immédiatement qu'il faut faire intervenir :

$$V^* = \frac{2}{v_p^*}\left[\left(1 + v_p^* u^*\right)^{1/2} - 1\right] \qquad (10)$$

variable déjà utilisée en fait par différents auteurs et notamment par STEVENSON (réf. 2) dans l'analyse des expériences.

Les résultats établis par la résolution de l'équation 9 sont donnés figure 1 sous la forme $V^*(y^*)$. On observe que les courbes obtenues aux différents v_p^* tendent vers une partie logarithmique qui dépend relativement peu de v_p^*, spécialement dans le cas de l'injection. On pourra souvent à titre d'approximation, retenir avec injection la loi turbulente de paroi imperméable :

$$V^* = \frac{1}{k}\log y^* + 5,25 \quad (k \approx 0,41) \qquad (11)$$

3.3 Région extérieure - Loi de vitesse déficitaire.

Renvoyant à la référence 1 pour les détails du développement, on rappellera ici les aspects principaux du traitement effectué pour la région extérieure.

La variable donnant à la loi de paroi une forme logarithmique étant V^*, la variable à utiliser pour la région extérieure est :

$$V_e^* - V^* = \frac{2u_\tau}{v_p}\left[\left(1 + \frac{v_p u_e}{u_\tau^2}\right)^{1/2} - \left(1 + \frac{v_p u}{u_\tau^2}\right)^{1/2}\right] \qquad (12)$$

Le traitement concerne une couche limite d'équilibre, pour laquelle, par définition, $V_e^* - V^*$ est une fonction de η indépendante de l'abscisse ; on pose par conséquent :

$$V_e^* - V^* = F'(\eta) \quad \text{avec} \quad \eta = \frac{y}{\delta}$$

La région étudiée est celle d'un écoulement turbulent établi pour lequel :

$$\tau = \tau_t = \rho\ell^2\left|\frac{\partial u}{\partial y}\right|\frac{\partial u}{\partial y} \quad \text{avec} \quad L = \frac{\ell}{\delta} = 0{,}085\,\text{th}\left(\frac{k\eta}{0{,}085}\right)$$

Introduisant ces hypothèses dans l'équation de quantité de mouvement, celle-ci devient une équation différentielle ordinaire, dont la résolution va fournir le profil des vitesses déficitaires recherché. On obtient ainsi, pour un nombre de Reynolds tendant vers l'infini :

$$\left(L^2 F''^2\right)' = 2\bar{\beta}F' + \left(\frac{1}{F_1} + 2\bar{\beta}\right)\eta F'' \qquad (13)$$

$$\text{avec}\quad \bar{\beta} = \frac{1}{\left(\frac{C_f}{2} + \frac{v_p}{u_e}\right)^{1/2}}\,\frac{\delta}{u_e}\,\frac{du_e}{dx}$$

Elle fait intervenir comme seul paramètre, le paramètre de gradient de pression $\bar{\beta}$.

Profils de vitesse déficitaire.

Grâce à l'utilisation de la variable $V_e^* - V^*$ et du paramètre $\bar{\beta}$ transformés, l'équation (13) est strictement identique à celle qu'on avait pu établir en (réf. 1) pour une paroi imperméable. Les profils de vitesse déficitaire établis dans ce cas, sont donc directement utilisables avec injection pour la variable transformée. Reproduits figure 2, ils permettront, après retour à la vitesse physique u, de déterminer l'influence combinée de l'injection et du gradient de pression sur le profil des vitesses dans une région extérieure qui couvre, en fait, la plus grande partie de la couche limite.

C'est également pour la variable transformée qu'est présentée, figure 3, une comparaison à l'expérience, destinée à contrôler que les profils expérimentaux peuvent être effectivement représentés par la famille des profils théoriques et dans laquelle on s'est placé à même valeur du facteur de forme du profil déficitaire. Les résultats de MICKLEY et DAVIS (réf. 3) sont relatifs à une plaque plane ; ceux de MAC-QUAID (réf. 4) portent sur des écoulements avec gradient de pression, positif et négatif. L'accord avec la solution proposée est satisfaisant dans les trois cas.

Frottement de paroi.

La relation pour le coefficient de frottement s'obtient en utilisant le recouvrement de la loi de paroi et de la loi déficitaire, toutes deux de forme logarithmique dans la région en question. Pour la paroi imperméable on détermine ainsi la formule exprimant le coefficient de frottement, en fonction du nombre de Reynolds de l'épaisseur de déplacement :

$$\left(\frac{2}{C_f}\right)^{1/2} = \frac{1}{k}\log R_\delta^* + D^*$$

où D^* est une fonction du paramètre de gradient de pression β (ou de G) dont on a donné les valeurs réf. 1.

On a montré réf. 1 que la même formule s'applique avec injection, lorsqu'on utilise des grandeurs transformées $\overline{C_f}$, V_e, $\overline{\delta}^*$:

$$\frac{V}{u_e} = \left(\frac{C_f}{\overline{C_f}}\right)^{1/2} = \frac{C_f u_e}{v_p}\left[\left(1 + \frac{2v_p}{u_e C_f}\right)^{1/2} - 1\right] \quad ; \quad \overline{\delta}^* = \int_0^\delta\left(1 - \frac{V^*}{V_e^*}\right)dy$$

Cette représentation a permis effectivement, réf. 1, de regrouper les résultats expérimentaux de frottement de paroi avec injection sur la courbe $C_f(R_f)$ de la plaque plane imperméable.

Sur un plan pratique, on cherche souvent à analyser les résultats expérimentaux en examinant le rapport cf/cf_0, cf_0 étant le frottement sans injection, au même nombre de Reynolds R_θ. On a trouvé que ce rapport était dans la solution, peu sensible à la valeur du nombre de Reynolds. La figure 4 montre que la solution représente dans l'ensemble assez correctement les valeurs cf/cf_0 de l'expérience (réf. 5. 6 et 7).

4 - SOLUTIONS DE SIMILITUDE LOCALE.

4.1 Principe et équations dans le cas général.

Considérant maintenant le cas général d'un fluide compressible, pouvant comporter l'injection d'un gaz étranger, l'hypothèse faite précédemment d'une couche limite d'équilibre est beaucoup plus discutable. A grand nombre de Reynolds, elle revient de toutes façons à une similitude faite directement sur u/u_e. C'est plus simplement dans cette hypothèse de similitude directe qu'on va se placer pour le cas général. On l'appliquera également à l'enthalpie d'arrêt et à la concentration et l'on posera par conséquent :

$$\frac{u}{u_e} = f'(\eta) \quad ; \quad \frac{H}{H_e} = g'(\eta) \quad ; \quad C_2 = j'(\eta) \quad ; \quad \eta = y/\delta$$

Ne cherchant plus à distinguer des régions intérieure et extérieure, τ, ϕ et Q sont donnés par leurs expressions complètes (8), ou avec les notations précédentes :

$$\frac{\tau}{\rho_e u_e^2} = \frac{\mu/\mu_e}{R_\delta} f'' + F^2 L^2 \frac{\rho}{\rho_e} f''^2 \quad ; \qquad \frac{-Q_2}{\rho_e u_e} = \left(\frac{\mu/\mu_e}{S R_\delta} + \frac{F^2}{S_t} L^2 \frac{\rho}{\rho_e} f''\right) j''$$

$$-\frac{\phi}{\rho_e u_e H_e} = \left(\frac{\mu/\mu_e}{9 R_\delta} + \frac{F^2}{S_t} L^2 \frac{\rho}{\rho_e} f''\right)\left(g'' - f'f'' \frac{u_e^2}{H_e}\right) + \frac{Q_2}{\rho_e u_e} \frac{C_{p1} - C_{p2}}{C_p}\left(\varsigma' - f'^2 \frac{u_e^2}{2 H_e}\right)$$

L'hypothèse de similitude appliquée à l'équation de quantité de mouvement, à l'équation d'énergie et à l'équation de conservation du gaz principal conduit aux trois équations différentielles ordinaires

$$\left(\frac{\tau}{\rho_e u_e^2}\right)' = f''\left(\frac{\rho v}{\rho_e u_e} - \eta f' \frac{\rho}{\rho_e} \frac{d\delta}{dx}\right) + \frac{\delta}{u_e} \frac{du_e}{dx}\left(\frac{\rho}{\rho_e} f'^2 - 1\right) \tag{14}$$

$$\left(\frac{u\tau - \phi}{\rho_2 u_e H_e}\right)' = g''\left(\frac{\rho v}{\rho_e u_e} - \eta f' \frac{\rho}{\rho_e} \frac{d\delta}{dx}\right) \tag{15}$$

$$\left(-\frac{Q_2}{\rho_e u_e}\right)' = j''\left(\frac{\rho v}{\rho_e u_e} - \eta f' \frac{\rho}{\rho_e} \frac{d\delta}{dx}\right) \tag{16}$$

La dérivation est effectuée par rapport à η. La masse volumique est exprimée au moyen de l'équation d'état du mélange, qui donne en supposant que les deux composants sont des gaz parfaits :

$$\frac{\rho_g}{\rho} = \frac{h}{h_e}\left[\frac{M_2}{M_1} + C_2\left(1 - \frac{M_2}{M_1}\right)\right] \quad (M_1 \text{ et } M_2 \text{ masses molaires} \; ; \; C_2 = j')$$

La vitesse verticale et $\frac{\rho v}{\rho_e u_e}$ s'expriment par l'équation de continuité.

Les conditions aux limites utilisées pour résoudre le système sont d'abord les conditions classiques d'adhérence à la paroi et d'écoulement extérieur sans frottement dont les caractéristiques sont données :

en $\eta = 0 : f' = 0$ et $\begin{cases} g' = h_p/H_e & \text{(température imposée)} \\ \text{ou } \frac{g''}{9} + \frac{C_{p2} - C_{p1}}{S C_p} j'' g' = \frac{-\phi_p}{\rho_e u_e H_e} \frac{\mu_e}{\mu_p} R_\delta & \text{(flux de chaleur imposé)} \end{cases}$

en $\eta = 1 : f' = 1 \; (u = u_e) \; ; \; g' = 1 \; (H = H_e) \; ; \; j' = 1 \; (C_2 = 1) \; ; \; f'' = 0 \; (\tau = 0)$

La condition relative à la concentration à la paroi s'établit moins simplement. On schématise la paroi poreuse par une ligne séparant un côté réservoir d'injection d'un côté écoulement. On doit concevoir dans le cas général, qu'une discontinuité a lieu au niveau de cette ligne pour la concentration d'une espèce i. Ecrivant la conservation de la masse de cette espèce au niveau de la paroi, on obtient (en négligeant le flux de diffusion du côté réservoir):

$$Q_{ip} = \rho_p v_p \left(C_{ip-} - C_{ip+}\right)$$

l'indice (+) étant relatif au côté écoulement, l'indice (-) au côté réservoir.

Appliquant ceci au gaz principal, on obtient avec les notations adoptées, la condition pour la concentration à la paroi :

$$\frac{\mu_p}{\mu_p S_p} \frac{j''_p}{R_\delta} = \frac{\rho_p v_p}{\rho_e u_e}\left(j'_p - C_{2p}\right)$$

Dans le cas d'injection d'un gaz étranger simple, on admet très généralement que le gaz principal ne traverse pas la paroi, soit $C_{2p} = 0$.

Six paramètres indépendants déterminant la famille des solutions du système sont les suivants :

Nombre de Reynolds $R_\delta = \rho_e u_e \delta/\mu_e$; Nombre de Mach Me; paramètre de gradient de pression $\frac{\delta}{u_e} \frac{du_e}{dx}$; Enthalpie ou flux de chaleur h_p ou ϕ_p; taux d'injection $\rho_p v_p/\rho_e u_e$; concentration initiale C_{2p}.

Apparaissent également à priori $d\delta/dx$, ainsi que les valeurs initiales f''_p, g''_p, j''_p ; ces quatre quantités sont en fait des paramètres propres de la solution et se déterminent, après itération, pour que les conditions aux limites soient satisfaites.

4.2 Application à l'injection d'air en compressible (plaque plane).

La technique précédente a été appliquée dans le cas d'injection d'air dans l'air, pour étendre au cas général du fluide compressible à nombre de Mach extérieur et température de paroi quelconques, les résultats acquis en incompressible.

Le système des équations à résoudre est celui des équations de quantité de mouvement et d'énergie (14) et (15) ;

la diffusion n'intervient évidemment pas.

On s'est limité jusqu'ici au cas de la plaque plane, le terme en $\frac{f}{u_e}\frac{du_e}{dx}$ disparaissant alors de l'équation (14). Les paramètres indépendants se réduisent au nombre de Reynolds R_{δ}, au nombre de Mach M_e, à l'enthalpie ou au flux de chaleur h_p ou ϕ_p, et au taux d'injection $\rho_p v_p / \rho_e u_e$.

Un programme de résolution des équations (14) et (15) a été établi et appliqué systématiquement pour déterminer les profils de vitesse et d'enthalpie ainsi que le frottement et le flux de chaleur de paroi, à différentes valeurs de M_e et de h_p et pour différents taux d'injection. On a pris pour les nombres de PRANDTL laminaire et turbulent $P = 0,725$ et $P_t = 0,89$. On s'est placé à un nombre de Reynolds suffisamment élevé pour que la solution corresponde à un écoulement turbulent établi.

Des exemples des résultats obtenus sont donnés figure 5 :

On y présente d'abord les profils de vitesse à $M = 7$ et $T_p/T_{ad} = 0,5$ pour différents taux d'injection ; on trouve que l'effet de l'injection est comparable à celui d'un gradient de pression positif ; il donne lieu à une déformation du profil dans le sens d'une augmentation sensible de son paramètre de forme.

On donne également les profils température-vitesse : l'observation à faire est qu'ils sont très peu sensibles à l'effet d'injection.

On a considéré le cas de la paroi adiabatique, $\phi_p = 0$, l'enthalpie de paroi H_{ad} ou le facteur de récupération devenant alors un paramètre propre déterminé par la solution. On observe que le facteur de récupération décroît quand le taux d'injection augmente, décroissance plus prononcée lorsque le nombre de Mach est plus grand.

On a porté enfin à $M = 2$ et $M = 7$ et pour plusieurs valeurs de T_p/T_{ad}, les rapports C_f/C_{f_o} et C_h/C_{h_o} du coefficient de flux de chaleur à ceux qu'on obtient au même R_{δ} pour la paroi imperméable. L'injection donne lieu à une diminution très évidente du frottement et du flux de chaleur, l'effet augmentant nettement avec le nombre de Mach.

4.3 Application à l'injection d'un gaz étranger (plaque plane)

La technique a été appliquée dans le cas de l'injection d'un gaz étranger, en se limitant encore, compte tenu du nombre de paramètres, au cas de la plaque plane. Un programme numérique de résolution des équations (14) (15) et (16) a été mis au point, grâce auquel a été entreprise la détermination de résultats systématiques sur les profils de vitesse et de concentration et sur le frottement et le flux de chaleur.

Au stade actuel, les résultats sont acquis pour une injection d'hélium et de gaz carbonique en fluide incompressible. Pour un gaz donné, les paramètres sont alors simplement le nombre de Reynolds et le taux d'injection.

Pour la viscosité μ, le coefficient de diffusion et le nombre de SCHMIDT $S = \mu/\rho D$, on a utilisé les résultats établis en application de la théorie moléculaire des gaz par HIRSCHFELDER, CURTISS et BIRD (réf. 8) pour les coefficients de transport des gaz simples et des mélanges. La viscosité et le nombre de SCHMIDT, fonction de la concentration et du rapport des masses molaires du gaz injecté et du gaz principal, varient dans la couche limite.

Le nombre de SCHMIDT turbulent a été supposé constant, sa valeur étant choisie en fonction des résultats expérimentaux obtenus pour les profils de concentration. Pour l'hélium, les expériences de KENDALL nous ont conduit à retenir comme valeur plausible $S_t = 0,9$. Pour le gaz carbonique on a utilisé la valeur provisoire $S_t = 1$.

Quelques exemples des résultats obtenus pour une injection d'hélium sont donnés figure 6.

On y montre d'abord des profils typiques de concentration déterminés à différents taux d'injection, C_1 étant porté en fonction de u/u_e ; on observera l'allure sensiblement linéaire des profils concentration-vitesse. En ce qui concerne les profils u/u_e on dira seulement que l'injection d'hélium donne lieu à une déformation du profil des vitesses plus sensible mais qualitativement comparable à la déformation apportée par l'injection d'air.

Le coefficient de frottement C_f et le coefficient de transfert de masse par diffusion à la paroi C_m, sont portés respectivement, selon une représentation coutumière, en fonction du nombre de Reynolds R_e et du nombre de Reynolds de l'épaisseur caractéristique des concentrations θ_c (rappelons que $C_m = q_{1p}/\rho_e u_e C_{1p}$ et $\theta_c = \int_0^{\delta} \frac{\rho u}{\rho_e u_e} C_1 \, dy$). Il est évident que l'injection donne lieu à une diminution importante et comparable des deux coefficients. Pour juger de l'influence de la valeur choisie pour le nombre de SCHMIDT turbulent, les calculs ont été effectués également avec $S_t = 0,75$; l'effet est relativement sensible.

Une comparaison avec les résultats expérimentaux de KENDALL (réf. 7) obtenus dans le cas de l'injection d'un mélange Hélium-Air a été effectuée. La concentration en hélium était très faible et les résultats concernant le coefficient de frottement ont pu être assimilés à ceux d'une injection d'air figure 4.

Une discussion de la valeur du nombre de SCHMIDT turbulent a été faite par KENDALL qui en a proposé lui-même une détermination tout à fait plausible, basée sur l'existence d'une loi de paroi pour les concentrations. On a pris les nombres de SCHMIDT turbulents ainsi proposés pour chaque expérience dans l'application de la solution aux conditions des dites expériences.

La figure 6 donne la comparaison de trois des profils expérimentaux de concentration d'hélium, aux profils théoriques déterminés dans la même plage de nombres de Reynolds $R_{\theta c}$; l'accord est effectivement tout à fait satisfaisant. Les courbes du coefficient de diffusion en fonction du nombre de Reynolds $R_{\theta c}$ ne font également apparaître que des différences assez faibles entre le calcul et l'expérience.

La solution a également été appliquée de façon systématique dans le cas d'une injection de gaz carbonique, dans l'hypothèse provisoire d'un nombre de SCHMIDT turbulent égal à l'unité. Joints à ceux qui avaient déjà été déterminés pour l'injection d'air et d'hélium, les résultats ont permis de mettre en évidence l'influence essentielle de la masse molaire du gaz injecté. La figure 8 représente dans les trois cas, le rapport du C_f au C_{f_o} obtenu sans injection à même valeur du nombre de Reynolds de l'épaisseur de quantité de mouvement ; elle montre clairement que la diminution du coefficient de frottement est d'autant plus importante que la masse molaire du gaz injecté est plus faible.

5 - CALCUL PAR DIFFERENCES FINIES

Les solutions semblables ont pour intérêt de fournir aisément des familles de résultats et de mettre ainsi en évidence l'influence des principaux facteurs agissant sur la couche limite dans le cas de l'injection : elles ont l'inconvénient de supposer des conditions aux limites qui ne sont évidemment pas toujours satisfaites et dont peuvent s'écarter notablement les conditions de certaines expériences. Dans le cas d'existence de gradients de pression par exemple, ceux-ci donneront rarement lieu à une couche limite d'équilibre ; de plus on observera souvent une variation longitudinale appréciable du taux d'injection.

Le schéma de longueur de mélange fournissant une expression du frottement total pour toute la couche limite, il est possible de traiter numériquement le problème général de conditions aux limites quelconques, en entreprenant une résolution des équations locales complètes de la couche limite au moyen, par exemple, d'une technique de différences finies. Une telle méthode a été mise au point et appliquée jusqu'ici pour une injection d'air dans le cas du

fluide incompressible.

Ne pouvant entrer ici dans les détails de la technique numérique, on dira seulement qu'un echéma implicite a été utilisé pour écrire l'équation de quantité de mouvement sous la forme d'une équation aux différences. On a choisi les variables x et $\eta = y/\delta$, la grille suivant η étant déterminée pour donner lieu à des valeurs imposées de u/u_e ; un nombre de points suffisant est ainsi toujours obtenu pour la sous-couche visqueuse. Les calculs ont été effectuée à partir d'une station initiale x_0 en laquelle on e'est fixé le profil de vitesses, en l'occurance le profil expérimental.

La figure 9 montre les résultats d'un tel calcul effectué dans les conditions des expériences de MAC QUAID (réf.4 et 9). Il s'agissait d'une étude de l'injection d'air dans un écoulement comportant une variation de la vitesse extérieure, à laquelle est liée une variation du taux d'injection v_p/u_e. Les cas I et II présentés ici correspondent respectivement à des gradients de pression positif et négatif ; le cas d'une discontinuité de $\frac{v_p}{u_e}$ a également été étudié (paroi poreuse suivie d'une paroi sans injection, avec u_e constant).

On donne, figure 9, les profils de vitesse calculée aux différentes etations par la méthode de différences finies ; leur accord avec les profils expérimentaux est tout à fait satisfaisant. L'évolution du coefficient de frottement est aussi représentée très correctement par le calcul.

6 -- CONCLUSION.

L'utilisation d'un schéma amélioré de longueur de mélange a permis d'obtenir des résultats théoriques cohérents sur les couches limites turbulentes avec injection de fluide.

En fluide incompressible, la correction de sous-couche visqueuse que comporte le echéma semble rendre compte raisonnablement du comportement au voisinage de la paroi. La détermination de solutions d'équilibre pour la couche limite extérieure a permis d'aboutir à des résultats systématiquee jusque là inexistante, sur l'influence combinée de l'injection et du gradient de pression.

En fluide compressible, la détermination de solutions de similitude locale, paraît susceptible de fournir les résultats systématiques dont on souhaite disposer quant à l'effet d'injection aux différents nombres de Mach et aux différentes températures de paroi.

Dans le cas de l'injection d'un gaz étranger, la solution de similitude permet encore de déterminer des profils de vitesse et de concentration qui semblent en accord avec les expériences disponiblee. Elle confirme l'effet essentiel de la masse molaire du gaz injecté sur le coefficient de frottement de paroi dont elle semble fournir une estimation raisonnable. Les mêmes résultats sont attendus pour le coefficient de transfert de chaleur, d'une application actuellement en cours de la technique de calcul au cas du fluide compressible.

La mise en oeuvre d'une technique de différences finies et son application en incompressible à des cas de non-similitude, conduit également à un accord avec l'expérience qui semble justifier les hypothèses du schéma utilisé.

REFERENCES -

1 - MICHEL R.   Application d'un echéma de longueur de mélange à l'étude des couches limitee d'équilibre.-
    QUEGARD C.   ONERA, N.T. 154 (1969).
    DURANT R.

2 - STEVENTSON T.N.   Experiments on injection into an incompressible turbulent boundary layer - College of Aero-
                      nautics, Cranfield, Rep. Aero, 177 (1964).

3 - MICKLEY H.S.   Momentum transfer for flow over a flat plate with blowing - NACA, T.N. 4017 (1957).
    DAVIS R.S.

4 - MC QUAID J.   Experiments on incompressible turbulent boundary layers with distributed injection -
                  A.R.C., R & M 3549 (1968).

5 - SIMPSON R.L.   The turbulent boundary layer on a porous plate : experimental skin friction with variable
    MOFFAT R.J.   injection and euction - Int. J. Heat Mass Transfer, Vol. 12, pp. 771-789 (1969).
    KAYS V.M.

6 - TENNEKES   Similarity laws for turbulent boundary layers with suction or injection - Report V.T.H, 199,
               Dept. of Aeronautical Engr., Technological Univ. Delft (1964).

7 - KENDALL R.M.   Interaction of mass and momentum transfer in the turbulent boundary layer - Sc. D. Thesis,
                   M.I.T. (1959).

8 - HIRSCHFELDER J.O   Molecular theory of gases and liquids - John Wiley and Sons, New York (1954).
    CURTISS C.F.
    BIRD R.B.

9 - MC QUAID J.   The calculation of turbulent boundary layers with injection -- A.R.C., R & M 3542 (1968).
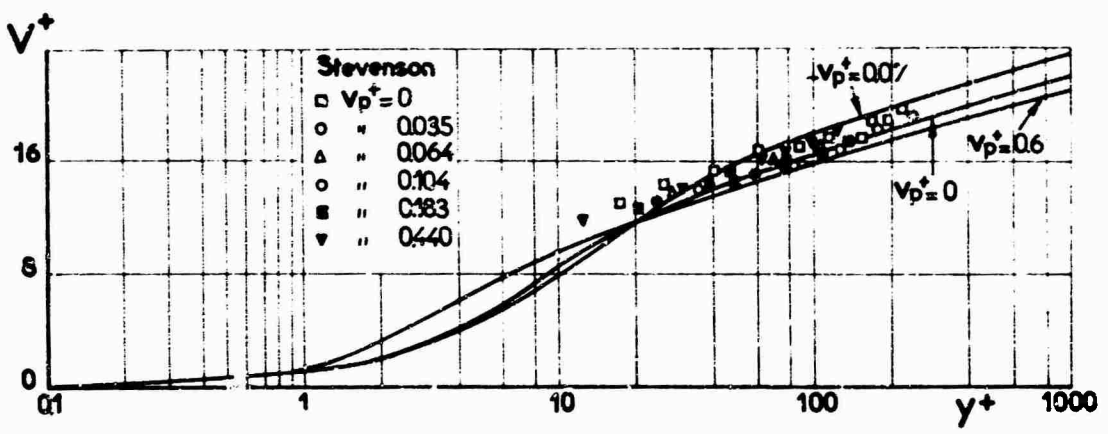
Fig. 1 – Loi de paroi avec injection d'air en incompressible.
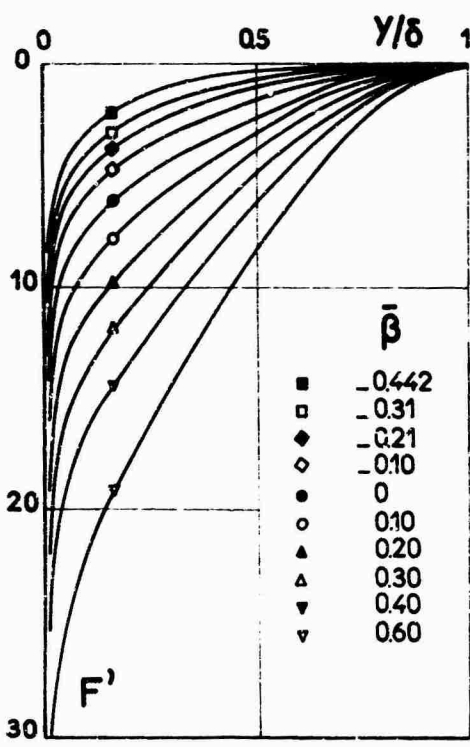
Fig. 2 – Famille des profils déficitaires de la solution
(incompressible).
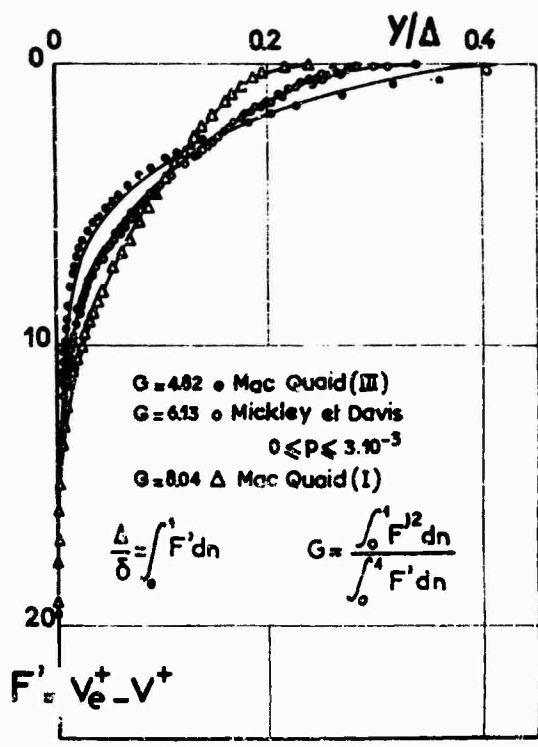
Fig. 3 – Comparaison à l'expérience (incompressible).
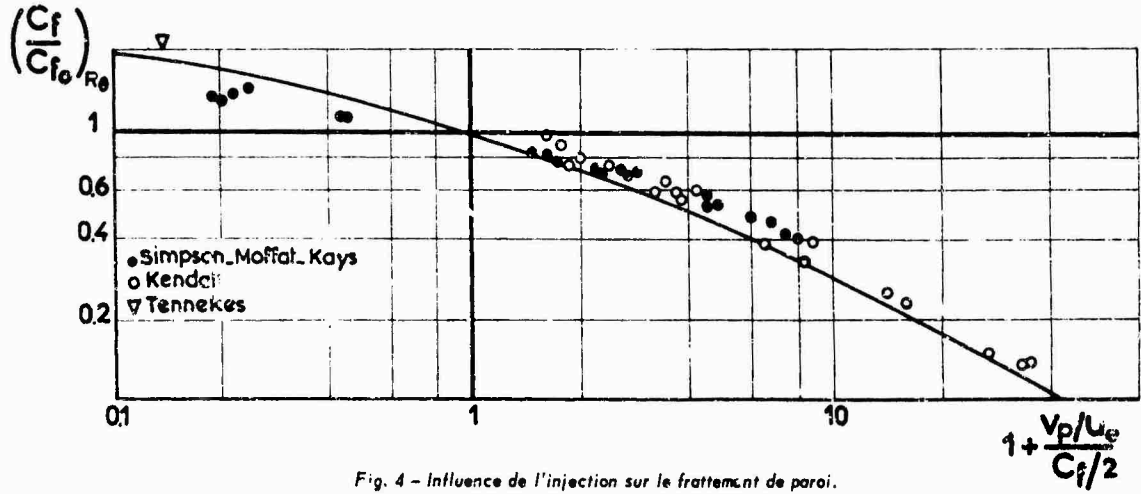
Fig. 4 – Influence de l'injection sur le frottement de paroi.
Plaque plane incompressible.
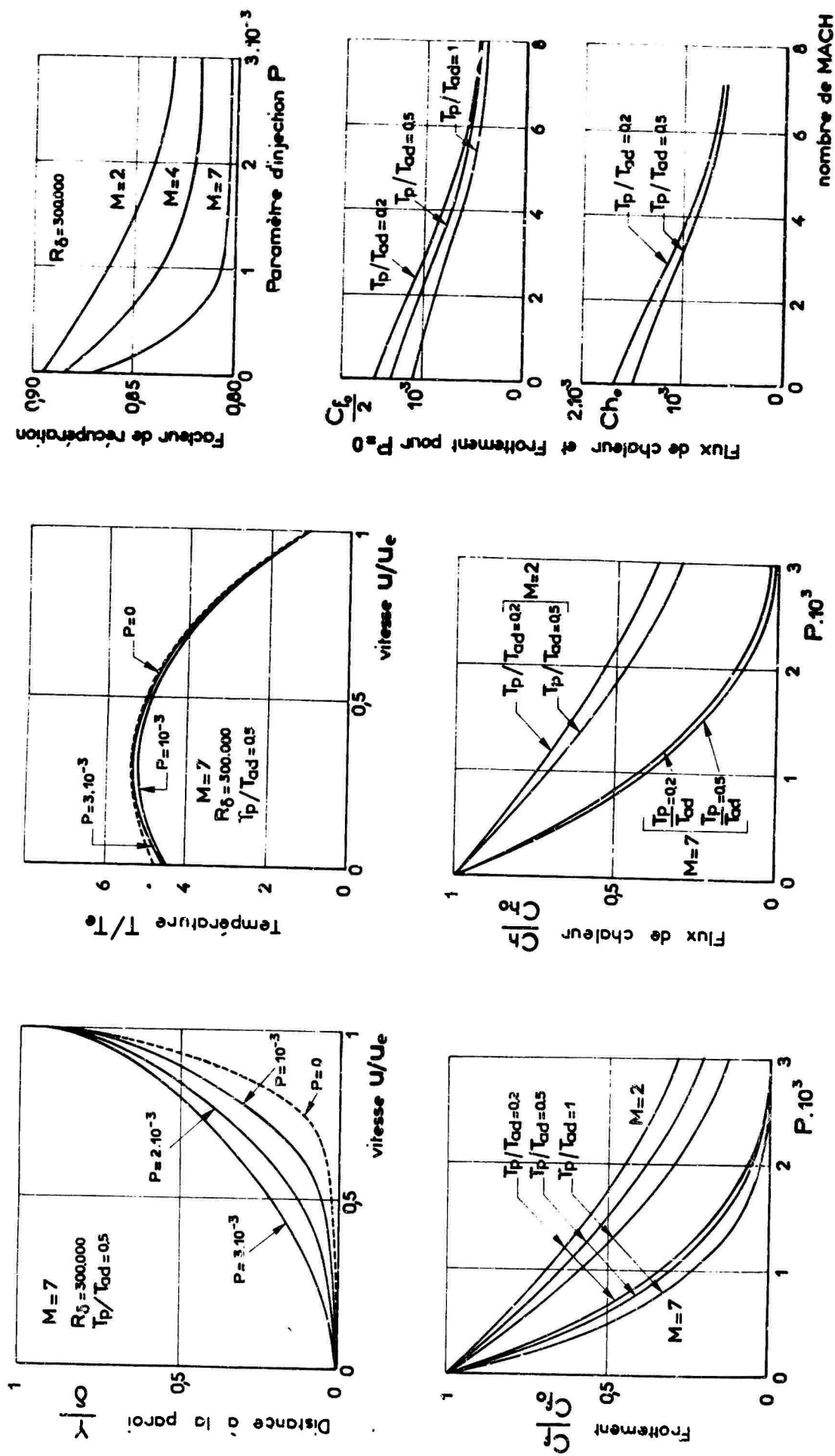
Fig. 5 – Résultats de la solution de similitude locale pour l'injection d'air en compressible (Plaque plane $R_\delta \sim 3.10^5$).
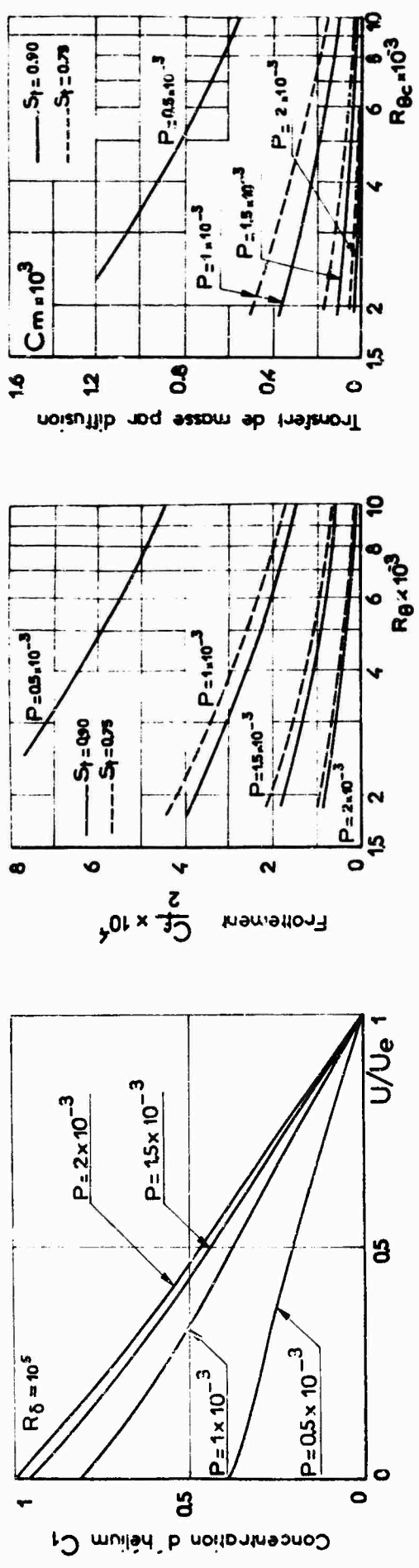
Fig. 6 — Résultats de la solution de similitude locale pour l'injection d'Hélium en incompressible.
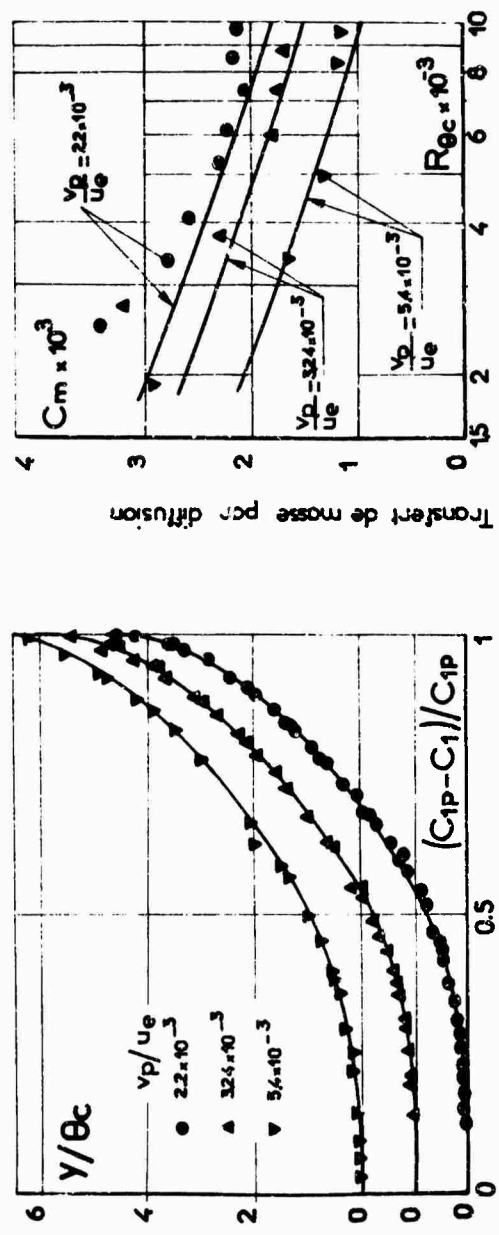
Fig. 7 — Comparaison aux expériences de Kendall (Injection d'un mélange Air-Hélium).
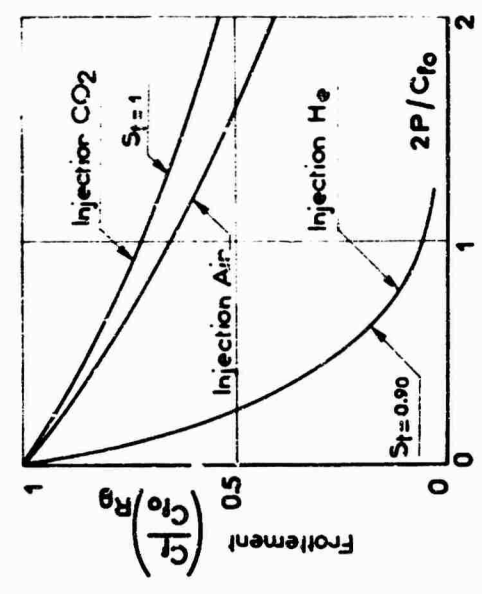
Fig. 8 — Influence de la masse molaire du gaz injecté.

24-9
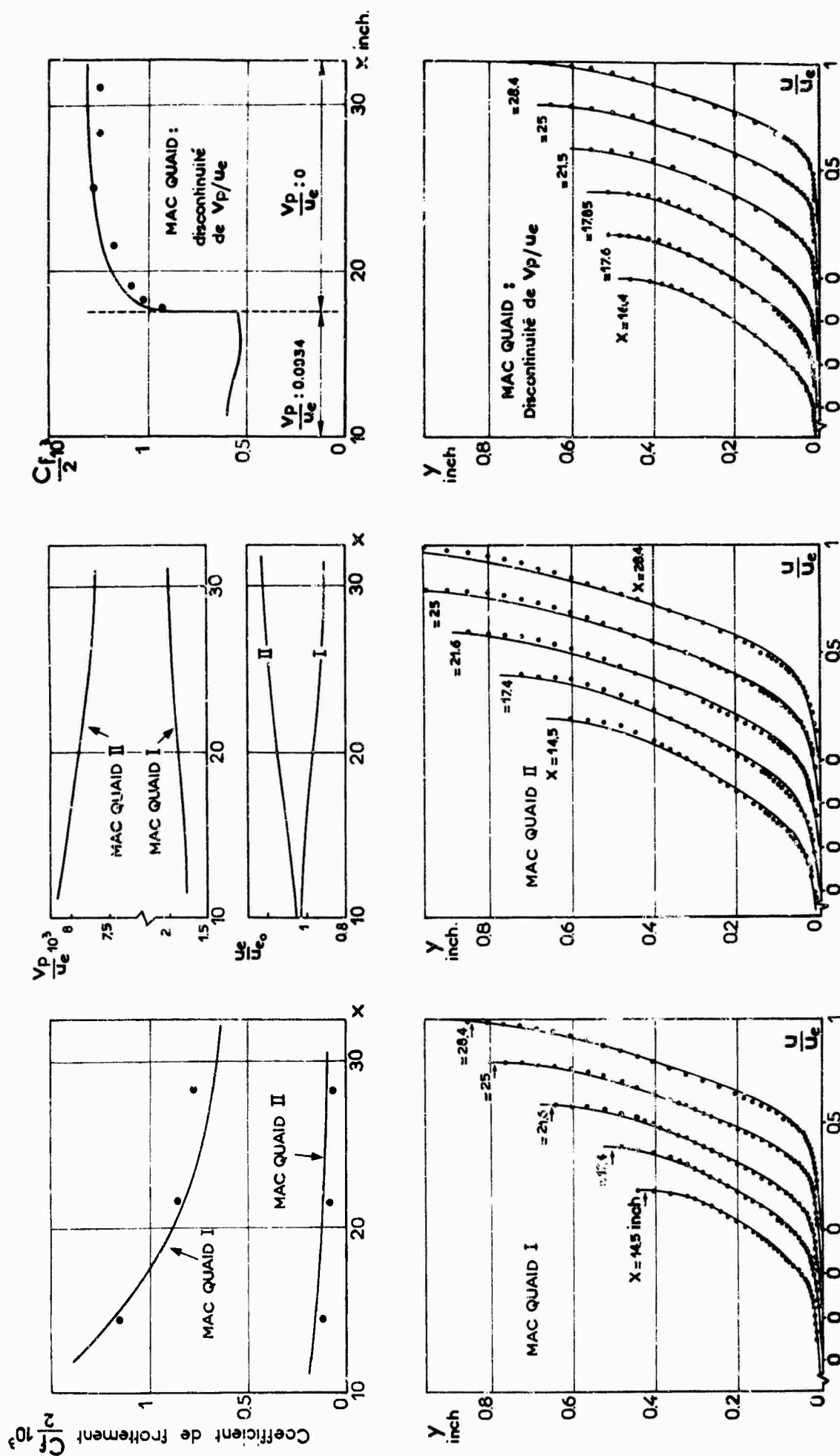
Fig. 9 – Calcul par différences finies. Comparaison aux expériences de Mac Quaid.

A SURVEY OF DATA FOR TURBULENT BOUNDARY LAYERS WITH MASS TRANSFER

by

Donald Coles
Professor of Aeronautics, California Institute of Technology
Consultant, The RAND Corporation

SUMMARY

A critical survey is made of available experimental data on turbulent boundary layers with mass transfer in the absence of complicating factors such as compressibility and pressure gradient. The attitudes and methods are similar to those in the survey paper, "The Young Person's Guide to the Data", which was prepared for the 1968 Stanford conference on computation methods.

Two approaches to the data show particular promise. The first is the mixing-length approach, which leads (as is well known) to a set of modified coordinates such that the classical similarity laws outside the sublayer seem to remain valid down to the last detail, at least for moderate values of suction or blowing. The second approach is more original; it is an attempt to generalize the kind of analysis often used to develop similarity laws for free shear flows such as wakes or jets, while preserving intact an argument, originally due to Millikan, which extends these ideas to the case of boundary-layer flow. The essential step is definition of a characteristic velocity (qua friction velocity) in terms of a characteristic stress (qua wall stress) which occurs somewhere in the layer. A strong precedent for such a step can be found in the usual treatment of surface roughness. So far, the best choice for the characteristic stress seems to be some kind of average value for the sublayer.

I. THE METHOD OF THE MIXING LENGTH

A. RATIONALE

Elements of the method. It is not easy to describe precisely what is meant by the term mixing-length theory, since the theory has almost as many variations as it has adherents. In its simplest form, however, the theory has three main elements. The first, a definition of mixing length, usually involves some analogy with the mean free path of the kinetic theory of gases. A leading variant is Prandtl's definition of 1925,

$$\tau = \rho \ell^2 \left(\frac{du}{dy}\right)^2 \tag{1}$$

The second element is a statement about the relationship of ℓ to some more accessible variable of the problem. Here a leading variant is Prandtl's proposal of 1933, originally inspired by an examination of Nikuradse's measurements in pipe flow;

$$\ell = \kappa y \tag{2}$$

in which the constant κ is usually alleged to be universal.

The third element is an expression for τ. For example, the crudest useful approximation for flow near a wall is

$$\tau = \tau_w \tag{3}$$

Note that the three equations (1) – (3) have been deliberately chosen to manufacture a logarithmic dependence of u on y,

$$\frac{u}{(\tau_w/\rho)^{\frac{1}{2}}} = \frac{1}{\kappa} \ell n \, y + \text{constant} \tag{4}$$

Note also that the result (4) is typical of a pure mixing-length theory, in that it provides a description of one fragment of the mean flow, unconnected with any description of adjacent fragments. As long as the ordinary fluid viscosity is ignored, no proper boundary conditions are available for evaluating the constant of integration in equation (4). The theory therefore has to be supplemented by dimensional arguments or by experimental evidence or both. For the case of a smooth wall, it is generally agreed that the variable y should be scaled on the viscous length $\nu/(\tau_w/\rho)^{\frac{1}{2}}$, not only in the viscous sublayer but in the wall-dominated part of the fully turbulent region as well. This being so, equation (4) can be transcribed as

$$\frac{u}{(\tau_w/\rho)^{\frac{1}{2}}} = \frac{1}{\kappa} \ell n \, \frac{y(\tau_w/\rho)^{\frac{1}{2}}}{\nu} + c_o \tag{5}$$

where c_o is now dimensionless.

A private view. The mixing-length theory has an excellent track record in dealing with effects of roughness and compressibility. These successes of the theory have not been achieved without pain, however. One major difficulty is the ambiguity already mentioned. For example, Prandtl in 1945 proposed replacing equation (1) by an equation $\tau = \rho \ell E^{\frac{1}{2}}(\partial u/\partial y)$, where E is turbulent energy per unit mass. A laminar term might also be included either in (1) or in (2), perhaps in the manner of the well-known damping hypothesis suggested by Van Driest in 1956. An alternative form of (2), $\ell = \kappa(\partial u/\partial y)/(\partial^2 u/\partial y^2)$, was used by Karman as early as 1930. An additional degree of freedom appears in the analysis if the density ρ is not constant. Finally, the approximation $\tau = \tau_w$ in (3) is clearly inaccurate in many situations and deserves on the face of it to be replaced by some better approximation, such as $\tau = \tau_w + y(dp/dx)$ for flow with pressure gradient or $\tau = \tau_w + \rho v_w u$ for flow with mass transfer. In fact, the advent of large computers has allowed τ to be specified via an equation for conservation of mean momentum in differential form. Unfortunately, as these variations and others have been explored, experience has shown that a more elaborate formulation does not automatically lead to a better result.

My own attitude toward the mixing-length theory is that I view the basic hypotheses of the theory as essentially unprovable. I am therefore not surprised that the arguments used in the literature sometimes have an almost theological flavor. The mixing length, like the eddy viscosity, is simply not a real physical quantity, by which I mean a quantity capable of being evaluated experimentally by more than one method. The mean velocity u qualifies as a real quantity by this criterion, at least to the extent that any mean value in a turbulent flow can do so. So does the turbulent shearing stress τ, since it can be evaluated either (a) from its definition as a covariance - $\overline{\rho u'v'}$ or (b) from the mean momentum equation as an apparent force which is required to account for the observed accelerations. The mixing length ℓ, on the other hand, can be evaluated in only one way, by using known functions u and τ in the definition (1) or in some equivalent expression.

B. FLOW WITH MASS TRANSFER

The law of the wall. The analytical literature of turbulent mass transfer includes by now numerous variations on the mixing-length theme.* However, my purpose in this paper is to examine experimental contributions to the subject, not analytical ones. I will therefore consider only the most popular formulation, which replaces (3) by

$$\tau = \tau_w + \rho v_w u \tag{6}$$

It follows that (4) is replaced by

$$\frac{2}{v_w}\left(\frac{\tau_w}{\rho} + v_w u\right)^{\frac{1}{2}} = \frac{1}{\kappa} \ln y + \text{constant} \tag{7}$$

where the constant may now depend on v_w as well as τ_w. One form of equation (7), the bilogarithmic law of Black and Sarnecki, puts "constant" $= -(1/\kappa)\ln(d)$ and retains u as dependent variable. The result can be written

$$\frac{u}{(\tau_w/\rho)^{\frac{1}{2}}} = \frac{v_w}{(\tau_w/\rho)^{\frac{1}{2}}}\left[\frac{1}{2}\frac{1}{\kappa}\ln\left(\frac{y}{d}\right)\right]^2 - \frac{(\tau_w/\rho)^{\frac{1}{2}}}{v_w} \tag{8}$$

Another form, the square-root law of Stevenson and others, retains log(y) as independent variable, introduces (arbitrarily) the viscous length scale $\nu/(\tau_w/\rho)^{\frac{1}{2}}$, and invokes the limit $v_w = 0$ at the outset to obtain an equation for what I will call the pseudo-velocity profile,

$$\frac{2(\tau_w/\rho)^{\frac{1}{2}}}{v_w}\left[\left(1+\frac{\rho v_w u}{\tau_w}\right)^{\frac{1}{2}} - 1\right] = \frac{1}{\kappa}\ln\frac{y(\tau_w/\rho)^{\frac{1}{2}}}{\nu} + c \tag{9}$$

In the discussion which follows, I want to test the suitability of equation (9) for describing effects of mass transfer in turbulent flow. First, however, I want to point out some conceptual difficulties with this equation in two limiting cases.

The asymptotic suction layer. Let the asymptotic suction layer be defined in general by the condition $\partial/\partial x = 0$ and in particular by the condition $d\theta/dx = 0$. The momentum-integral equation for constant pressure,

$$-\frac{\rho v_w u_\infty}{\tau_w} = 1 - \frac{\rho u_\infty^2}{\tau_w}\frac{d\theta}{dx} \tag{10}$$

then yields an equivalent condition, $-\rho v_w u_\infty = \tau_w$, having an obvious physical interpretation.

---

* This literature can be retraced with the aid of the recent survey article by Jeromin in Volume 10 of "Progress in Aeronautical Sciences", Pergamon, 1970. The 1958 paper by Black and Sarnecki and the first 1963 paper by Stevenson are especially informative.

The flow in question is extremely difficult to realize experimentally, and may have to be approximated in practice by a turbulent boundary layer which is first allowed to grow and then is subjected to sufficiently strong suction so that $d\theta/dx$ is locally negative; see especially Dutton (1955). But $1 + \rho v_w u_\infty/\tau_w$ has the same sign as $d\theta/dx$. The combination $1 + \rho v_w u/\tau_w$, which is really τ/τ_w in disguise, according to equation (6) may therefore be negative in some region near the edge of the boundary layer, and the left side of the profile equation (9) will be imaginary. I doubt that there is any attractive exit from this well-known dilemma within the limitations of mixing-length theory. In any event, difficulties are almost inevitable in any application of formulas derived from equation (7) to flows with strong suction.

The blowoff condition. The blowoff limit is defined by the boundary condition $\tau_w = 0$. The difficulty here arises during an empirical passage from a wall law to a defect law. Given that the presence in the profile equation of a term representing the wake-like character of the outer flow is appropriate when $v_w = 0$ (Coles 1968), a tentative but plausible (and partially successful; see below) generalization of equation '9) is

$$\frac{2(\tau_w/\rho)^{\frac{1}{2}}}{v_w}\left[(1 + \frac{\rho v_w u}{\tau_w})^{\frac{1}{2}} - 1\right] = \frac{1}{\varkappa}\ln\frac{y(\tau_w/\rho)^{\frac{1}{2}}}{\nu} + c + \frac{2\Pi}{\varkappa}\sin^2(\frac{\pi}{2}\frac{y}{\delta}) \qquad (11)$$

where in principle the parameter Π may depend on both v_w/u_∞ and $v_w/(\tau_w/\rho)^{\frac{1}{2}}$. Now consider the limit $\tau_w = 0$ in equation (11), assuming that the $\sin^2$ form of the wake term is preserved in the limit. Discard the log term (including the constant c) on the ground that it must be replaced in any event by a suitable sublayer approximation which will vanish for vanishing argument. Alternatively, note that the viscosity ν should not enter into any description of the flow when $\tau_w = 0$. It then follows that the limiting flow has no intrinsic scale and is necessarily conical (wedgical), with u/u_∞ a function of y/δ only. Finally, apply an obvious boundary condition in the free stream to obtain $\Pi/\varkappa = (u_\infty/v_w)^{\frac{1}{2}}$. The desired limit is seen to be

$$(\frac{u}{u_\infty})^{\frac{1}{2}} = \sin^2(\frac{\pi}{2}\frac{y}{\delta}) \qquad (12)$$

Now the momentum-integral equation for the blowoff condition is evidently

$$\frac{v_w}{u_\infty} = \frac{d\theta}{dx} \qquad (13)$$

with both sides independent of x. I submit that the hypothetical flow described by the blowoff limit, equation (12), cannot differ very much from the flow in a plane mixing layer between a uniform stream and a fluid at rest. The numerical value of v_w/u_∞ (or $d\theta/dx$) can therefore be estimated a priori to be approximately 0.035 (Liepmann and Laufer 1947). I know of one experimental study, by Mugalev (1959), which includes data for a blowing rate of almost this magnitude for boundary-layer flow past a flat plate. Although the data are not completely reported, the one published mean-velocity profile with $v_w/u_\infty = 0.0293$ shows the expected S-shape, close enough to a $\sin^2$ function, and the experimental value for the shape factor (displacement thickness/momentum thickness) is close to four, again the expected value. The formula (12), on the other hand, requires a $\sin^4$ variation for the mean velocity u, and a shape factor exceeding six. Consequently, I expect equation (11), and by implication equation (9), to fail for flows with sufficiently strong blowing as well. I have not tested the possibility that a different point of departure for construction of a defect law, such as the formula (8) proposed by Black and Sarnecki, might eliminate this particular difficulty without introducing new and unwelcome difficulties for other values of v_w.

The intercept, c. The most important issue in connection with equation (9) is to establish the dependence of the dimensionless constant of integration c on the dimensionless ratio $v_w/(\tau_w/\rho)^{\frac{1}{2}}$. Mickley and Davis (1957) and Black and Sarnecki (1958) reached quite opposite conclusions about c using the same Mickley-Davis blowing data, data which are now known to involve highly erroneous estimates of surface friction. Stevenson (1963a), relying on his own blowing experiments on a body of revolution, concluded that the parameter c in equation (9), like the parameter $\varkappa$, is essentially unaffected by mass transfer. His figure 2 reinforces this conclusion for the suction data considered by Black and Sarnecki as well. Simpson (1967) carried out extensive new measurements in flat-plate flows with both blowing and suction, and proposed a different condition; namely, that equation (9) always passes through the point $u/(\tau_w/\rho)^{\frac{1}{2}} = y(\tau_w/\rho)^{\frac{1}{2}}/\nu = K = 11$, regardless of the value of v_w. Here the parameter K represents the intersection of the log profile with a linear sublayer when $v_w = 0$; that is

$$\frac{u}{(\tau_w/\rho)^{\frac{1}{2}}} = \frac{y(\tau_w/\rho)^{\frac{1}{2}}}{\nu} = \frac{1}{\varkappa}\ln\frac{y(\tau_w/\rho)^{\frac{1}{2}}}{\nu} + c_0 \qquad (14)$$

or

$$K = \frac{1}{\varkappa}\ln K + c_0 \qquad (15)$$

My favorite values $\varkappa = 0.41$ and $c_0 = 5.0$ then require K = 10.805.

Simpson's condition implies for c

$$c = c_0 + 2 \frac{(\tau_w/\rho)^{\frac{1}{2}}}{v_w} [(1 + K \frac{v_w}{(\tau_w/\rho)^{\frac{1}{2}}})^{\frac{1}{2}} - 1] - K \qquad (16)$$

As the blowing limit $\tau_w = 0$ is approached, this becomes

$$c \approx c_0 - K \qquad (17)$$

and as the asymptotic suction limit is approached,

$$c = c_0 - 2 (\frac{2}{C_f})^{\frac{1}{2}} [(1 - K(\frac{C_f}{2})^{\frac{1}{2}})^{\frac{1}{2}} - 1] - K \qquad (18)$$

where $C_f = 2\tau_w/\rho u_\infty^2$ is the local friction coefficient. Evidently C_f cannot exceed the value $2/K^2$. For this value of C_f, the ratio $v_w/(\tau_w/\rho)^{\frac{1}{2}}$ takes its most negative value, $-1/K$, and c from equation (16) becomes

$$c = c_0 + K \qquad (19)$$

Simpson's condition seems to me to be highly contrived. His reference point is not a fixed point in any attractive set of coordinates, and for $v_w \neq 0$ is unrelated to any intersection of the logarithmic profile formula (9) with a laminar sublayer formula modified to take mass transfer into account. It is a particularly awkward fact that no intersection exists outside the limited range $- 0.087 < v_w/(\tau_w/\rho)^{\frac{1}{2}} < 0.400$, although some of the data to be considered shortly do in fact fall outside this range.

Nevertheless, Simpson's version of the mixing-length formulation works like black magic, and <u>Simpson's condition on c leads to a highly successful consolidation of blowing and suction data for small to moderate values of v_w</u>.

<u>Experimental data</u>. The conclusion just stated is based on a fit of various data to the full profile equation (11), using equation (16) to compute the intercept c. The methods and even several of the programs are essentially the same as in my 1968 Stanford paper, except that the parameter $v_w/(\tau_w/\rho)^{\frac{1}{2}}$ and the intercept c are now updated in each step of the iteration procedure.

For Simpson's flows of conventional type; i.e., flows with constant or continuously varying v_w, local values of C_f inferred from this fitting operation are compared in figure 1 with Simpson's "best estimate". A discrepancy of about ten percent seems to be characteristic, even for $v_w = 0$. The quality of the profile fit is illustrated for several pseudo-velocity profiles in figure 2, which confirms that the effect of increasing v_w on the parameter c is qualitatively the same as the effect of increasing surface roughness. Figure 2 also makes another point: <u>the parameter Π, which measures the maximum departure of the profile from the log function near the free stream, is very nearly independent of v_w</u>. This observation is not entirely new. Several authors, particularly Stevenson (1963b), have previously converted equation (11) to a defect law for the pseudo-velocity $2(\tau_w/\rho)^{\frac{1}{2}}[(1 + \rho v_w u/\tau_w)^{\frac{1}{2}} - 1]/v_w$ and have noted the insensitivity of the result to variations in v_w. In view of the fact that the controversial intercept parameter c drops out during conversion to defect-law form, agreement on this point is hardly surprising.

However, I can go a little further. Figure 3a shows the parameter Π plotted against R_θ for Simpson's flows of conventional type. Also shown for reference is the trace of Wieghardt's measurements on a solid surface. <u>Note that Simpson's data faithfully reproduce the well-established decrease of Π at low Reynolds numbers (cf. Coles 1962, appendix A; Simpson 1970), including the indication of a lower limit for turbulent flow at a Reynolds number R_θ of about 600. For practical purposes, the profile formula (11) in defect form therefore provides a representation in which effects of mass transfer are as difficult to detect as are effects of surface roughness.</u> Even the slightly diminished values of Π for moderate Reynolds numbers in figure 3a can reasonably be interpreted as an effect of the relatively high free-stream turbulence level in Simpson's experiments.

This picture is confirmed by data from other sources. Figure 4 shows pseudo-velocity profiles, and figure 3b shows Π against R_θ, for the measurements with blowing by McQuaid (1966). The last three profiles in figure 4, with v_w/u_∞ in the range 0.008 to 0.014, are from the series with v_w increasing at fixed x; they show an appreciable rise in Π. Consequently, I suggest that the maximum blowing rate for which the defect law is invariant in Simpson's formulation is roughly 0.010.

Figures 5 and 3c show the same quantities for the measurements with blowing by Mickley and Davis (1957). Here the observed decrease in Π as v_w increases would ordinarily be interpreted as an effect of a negative pressure gradient which was unfortunately present in these experiments.

Finally, figure 6 shows several pseudo-velocity profiles from the measurements with small rates of suction by Favre et al. (1966) and one typical profile from the series of suction experiments by Tennekes (1964). The strength of the wake component seems to be uniformly and abnormally small for Favre's flows, including the flow with $v_w = 0$, but abnormally large for Tennekes' flow. In both cases the reason is unknown.

Epilogue. On the experimental side, my opinion is that neither the blowoff condition nor the asymptotic suction layer is adequately documented. The latter flow is especially difficult. If a long run of solid surface is provided, to obtain a relatively thick boundary layer, the relaxation to the asymptotic suction state may be very slow (because there is an initial excess of turbulent energy at low wave numbers which may take a long time to disappear). On the other hand, if suction is applied very early, the Reynolds number will remain small and relaminarization may occur. This problem was recognized by Dutton, Tennekes, and other investigators, but definitive experiments are still needed.

On the analytical side, there is strong evidence that the defect law associated with the pseudo-velocity profile (11) is insensitive to moderate values of suction and blowing, and that Simpson's condition on the intercept parameter c is realistic. It follows that the effect of mass transfer on the local friction law, on the shape factor, on the local shearing-stress profile, and so on, are all under excellent engineering control. Because this conclusion is an empirical one, it is limited in several directions. It should be accepted with caution outside the range (say) $-0.004 < v_w/u_\infty < 0.010$ or for Reynolds numbers beyond the very limited range of the available data. With these reservations, I view the results described so far as an unequivocal success for the mixing-length theory as an engineering tool.

II. THE METHOD OF CHARACTERISTIC SCALES

A. RATIONALE

Free shear flows. Similarity arguments are the traditional means of approach to the classical turbulent free shear flows, such as the symmetrical jet or wake, which incorporate single local scales for velocity and length. Moreover, this approach is invariably supported by experiment when the experimental conditions are carefully enough arranged, which is to say when scales associated with the environment or with initial conditions have dropped out of the picture. The key point is that a Galilean-invariant velocity scale, say u_0, always defines itself operationally during normalization of the profile of mean velocity or of mean-velocity defect. Given that this is the only local velocity scale in a free shear flow, it must also be the proper one for making the Reynolds stresses non-dimensional. Typical similarity assumptions are then of the form $u/u_0 = f(y/\delta)$ and $\tau/\rho u_0^2 = h(y/\delta)$, with one relationship between f and h provided by the momentum equation. The problem then reduces itself to (a) specifying one or the other of these functions or (b) determining - usually by some quite explicit statement about the turbulent mixing mechanism - a second relationship between f and h. Confidence in the similarity principles just described is strong enough so that there is usually no hesitation in extending them to less classical free shear flows such as the wake in a pressure gradient or the radial jet.

Millikan's argument. From the point of view of dimensional analysis and similarity, the essential feature of a free shear flow is that the fluid viscosity is not material. This is no longer the case if a wall is present, and the extension of similarity principles to boundary layers and other such flows has had a long and difficult history. Unless the circumstances are quite exceptional, turbulent boundary layers are known to involve two length scales. One is an overall scale, say δ; the other is a sublayer scale, say y_0, which ordinarily represents the influence of viscous damping near the wall or the influence of surface roughness. The name of the similarity game, however, is still the same; it is to determine the nature of these scales, in as much detail as possible, by applying conservation laws and by invoking or inventing appropriate boundary conditions at the wall or elsewhere. In this process it is usually assumed that the influence of external factors such as pressure gradient or mass transfer is to modify the relationships among existing scales without introducing new ones.

The role of the two length scales in a normal boundary layer is epitomized by an argument due originally to Millikan (1938). Suppose that for a given flow the mean-velocity profile near the wall has the form of the law of the wall,

$$\frac{u}{u_0} = f\left(\frac{y}{y_0}\right) \tag{20}$$

and that the profile outside the sublayer has the form of the defect law,

$$\frac{u_\infty - u}{u_0} = g\left(\frac{y}{\delta}\right) \tag{21}$$

Either or both of these formulas may involve hidden parameters which depend on pressure gradient, mass-transfer rate, and so on. Any such parameter must clearly be (a) dimensionless and (b) constant throughout the flow, since the implicit dependence of u on x is supposed to be completely contained in the x-dependence of u_∞, δ, u_0 and y_0. The hidden parameters can be and often are interpreted as criteria for equilibrium.

Now suppose that these two representations have a common region of validity (with respect to the coordinate y). In the common region,

$$\frac{y}{u_o} \frac{\partial u}{\partial y} = \frac{y}{y_o} f'(\frac{y}{y_o}) = F(\frac{y}{y_o}) \tag{22}$$

while at the same time

$$\frac{y}{u_o} \frac{\partial u}{\partial y} = - \frac{y}{\delta} g'(\frac{y}{\delta}) = G(\frac{y}{\delta}) = G(\frac{y}{y_o} \frac{y_o}{\delta}) \tag{23}$$

Provided that the ratio y_o/δ is not an invariant of the flow, it follows that $F = G = $ constant in the common region. Call this constant $1/\varkappa$. Then

$$\frac{u}{u_o} = f(\frac{y}{y_o}) = \frac{1}{\varkappa} \log \frac{y}{y_o} + c \tag{24}$$

where c is a second constant. It is an important property of this argument that the fluid viscosity does not appear explicitly.

In principle, the two dimensionless constants $\varkappa$ and c in equation (24) may depend on the hidden parameters in the original similarity laws; and this dependence, if it is sufficiently strong, can presumably be detected experimentally. To do so, however, requires the coordinates u/u_o and y/y_o (i.e., the scales u_o and y_o) to be defined in advance. Discussions of this point therefore tend to be somewhat circular.

The characteristic stress. I believe that Millikan's reasoning is so simple and so elegant that it must also be in some sense correct. I will therefore attempt in this section to adapt the essential ingredients of Millikan's demonstration to other specific cases, preserving as far as possible the traditional simplicity of the similarity approach to free shear flows. However, it is important to keep in mind the empirical and accidental aspects of the situation in the case of boundary-layer flow. For example, if it were easy to measure τ and difficult to measure u, instead of the other way around, the concept of similarity would undoubtedly have evolved first for the quantities τ/τ_w or τ/τ_{max}. In any event, the preponderance of the evidence is that a similarity law like

$$\tau/\rho u_o^2 = h(y/\delta) \tag{25}$$

is an adequate approximation for an equilibrium flow past a solid wall; i.e., a flow for which the defect law applies. A non-trivial case in point is uniform pipe or channel flow, for which τ is known to be precisely linear in y/δ regardless of the viscosity. Another case in point is the continuously separating boundary layer, for which the concept of a sublayer is very nearly moot. For a general boundary-layer flow the term "approximation" recognizes the fact that equation (25) for τ and equation (21) for u are unlikely both to be rigorously correct, even outside the sublayer, because of their rather intricate connection through the non-linear equation of mean momentum. This point has been made before by Clauser and others, but in my opinion it is not central to what follows.

Consider therefore the special case of flow in a pipe or channel or in a boundary layer at constant pressure. For these flows there is particularly convincing evidence that the scale u_o which is appropriate for scaling the velocity defect $u_\infty - u$ is also appropriate for scaling the stress τ, just as in free shear flow. More precisely, the definition

$$\rho u_o^2 = \tau_w \tag{26}$$

seems to be a proper generalization of experience with free shear flows, with τ_w substituting for τ_{max} as the characteristic stress which is formally identified with ρu_o^2. What is remarkable is that this conclusion holds for both smooth and rough walls if τ_w is interpreted simply as force per unit area. Viewed from the free stream, the similarity laws do not depend on the nature of the surface constraint; they depend only on the velocity scale u_o associated with the characteristic stress level close to the wall, no matter how this stress is actually applied. Given an experimental mean-velocity profile outside the sublayer in the viscosity-independent defect form (21), and given also a stress distribution in the form (25), it might be virtually impossible to decide whether the surface in question is rough or smooth. This observation is central to what follows.

Example and synthesis. To fix the ideas, let us develop the method of characteristic scales for the case of a turbulent boundary layer on a smooth wall at constant pressure. The stress near the wall is then constant to a first approximation. Since the no-slip condition requires $\tau = \mu \, \partial u/\partial y + O(y^3)$, the mean-velocity profile behaves like

$$u = \frac{\tau_w}{\mu} y + \ldots \tag{27}$$

for small enough y. This expression will have the form (20), and hence will be a suitable ingredient for Millikan's argument, only if $\tau_w y_o/\mu u_o = $ constant. There is no loss of generality in putting the constant in question equal to one, whereupon

$$\mu \frac{u_o}{y_o} = \tau_w \tag{28}$$

This condition, according to the terms of its derivation, has a broad charter; the only important stipulation is that the mean flow close enough to the wall be controlled by viscosity. Furthermore, the fluid viscosity has now been introduced in a natural way, through the boundary condition at the wall. But the plausible definition (26) and the similarity constraint (28) have completely determined the scales u_o and y_o:

$$u_o = (\tau_w/\rho)^{\frac{1}{2}} \tag{29}$$

$$y_o = \nu/(\tau_w/\rho)^{\frac{1}{2}} \tag{30}$$

To sum up: the key elements of the method of characteristic scales can be stated heuristically in the form
(a) the combination ρu_o^2, where u_o is the natural scale for the mean-velocity defect, is identified with some characteristic stress level near the wall (cf. the indifference of the defect law in the case of smooth and rough walls), and
(b) the laminar edition of the mean-velocity profile near the wall is expressed in the form of a generalized law of the wall, $u/u_o = f(y/y_o)$ (cf. the need to preserve the essential features of Millikan's argument).

B. FLOW WITH MASS TRANSFER

The law of the wall. The method of characteristic scales requires the velocity scale u_o which appears in the defect law to be tied to some characteristic stress τ_o through the definition $\rho u_o^2 = \tau_o$. It also requires the elements of Millikan's argument, as outlined in equations (20) - (24), to be preserved throughout. Suppose therefore that equilibrium flows with mass transfer are characterized by a law of the wall,

$$\frac{u}{u_o} = f(\frac{y}{y_o}) \tag{31}$$

and by a defect law

$$\frac{u_\bullet - u}{u_o} = g(\frac{y}{\delta}) \tag{32}$$

which have some common region of validity. In this region the profile must be logarithmic:

$$\frac{u}{u_o} = \frac{1}{\kappa} \ln \frac{y}{y_o} + c_o \tag{33}$$

When the scale y_o is eventually defined, the definition can presumably incorporate any constant factor which is required to adjust the parameter c_o to some standard value. Moreover, experience with roughness provides a persuasive precedent for taking the constant κ as invariant. I will therefore assume that both κ and c_o are universal constants, independent of mass transfer, when y_o is properly defined.

The sublayer. Now suppose that the mean velocity is represented well enough in the sublayer by a straightforward generalization of the linear profile equation (27),

$$u = \frac{\tau_w}{\rho v_w} (e^{\frac{y v_w}{\nu}} - 1) \tag{34}$$

or

$$\frac{u}{u_o} = \frac{\tau_w}{\rho v_w u_o} (e^{\frac{y}{y_o} \frac{\rho v_w u_o}{\tau_w} \frac{\tau_w y_o}{\mu u_o}} - 1) \tag{35}$$

This representation of the profile will be consistent with the form (31) if $\tau_w y_o/\mu u_o$ is a constant,

$$\frac{\tau_w y_o}{\mu u_o} = 1 \text{ , say} \tag{36}$$

and if in addition

$$\frac{\rho v_w u_o}{\tau_w} = \text{constant} = M \text{ , say} \tag{37}$$

The second condition (37) is apparently a requirement for equilibrium.

The stress at the intersection, T, and the intercept, c. The problem is to specify some characteristic stress τ_o which then defines the velocity scale u_o;

$$\rho u_o^2 = \tau_o \tag{38}$$

Unless $\tau_o = \tau_w$, of course, information will be required about the stress away from the wall. To the same approximation as in (34), the local stress is given by

$$\tau = \tau_w + \rho v_w u \quad (\text{exact if } \partial/\partial x = 0) \tag{39}$$

The only distinguished point in the boundary layer, besides the wall and the free stream, is the intersection of the laminar and logarithmic curves. This intersection will play a prominent part in what follows. Let $u = U$, $y = Y$, $\tau = T$ denote conditions at the intersection. Then equations (35), (33), and (39) imply

$$M\frac{U}{u_o} = e^{M\frac{Y}{y_o}} - 1 \tag{40}$$

$$\frac{U}{u_o} = \frac{1}{\kappa} \ln \frac{Y}{y_o} + c_o \tag{41}$$

$$\frac{T}{\tau_w} = 1 + M\frac{U}{u_o} \tag{42}$$

where M is defined by equation (37).

The two transcendental equations (40) and (41) can obviously be solved once and for all for U/u_o and Y/y_o as functions of the mass-transfer parameter $M = \rho v_w u_o/\tau_w$. The quantity T/τ_w is also known from equation (42). With $\kappa = 0.41$ and $c_o = 5.0$, it is found that there is no solution for negative M(suction) if $M < -.0665$; similarly, there is no solution for positive M (blowing) if $M > 14.03$. For values of M between the two limits, the curves (40) and (41) have either two or three intersections, as indicated in figure 7. To avoid confusion about which intersection is wanted, M can be replaced as independent variable by the combination $M/(T/\tau_w) = \rho v_w u_o/T$. This last parameter is of order unity for both special values of M; specifically, it is - 1.178 for suction and 1.059 for blowing.

The equilibrium parameter $M = \rho v_w u_o/\tau_w$ and the intersection parameters U/u_o, Y/y_o and T/τ_w are plotted in figure 8 against the independent variable $\rho v_w u_o/T$. When the abscissa is less than - 1.178, the intersection cited in the figure is not the one which is usually taken to define the edge of the sublayer; instead, it is the intersection of a suction plateau with the log profile.* When the abscissa is greater than 1.059, on the other hand, the intersection cited in the figure approaches the fixed point $Y/y_o=U/u_o=0.136$.

One further preliminary observation belongs here. Elimination of y_o from the logarithmic profile equation (33), using the normalization condition $\mu u_o/y_o = \tau_w$, gives

$$\frac{u}{u_o} = \frac{1}{\kappa} \ln \frac{yu_o}{\nu} + c \tag{43}$$

where

$$c = c_o - \frac{1}{\kappa} \ln \frac{\rho u_o^2}{\tau_w} \tag{44}$$

The method of characteristic scales, like the method of the mixing length, will therefore also involve a displacement of the log profile in coordinates u/u_o, $\ln(yu_o/\nu)$, very like the displacement associated with surface roughness.

The velocity scale, u_o. It remains to choose the characteristic stress $\tau_o = \rho u_o^2$ and thus to determine the local velocity scale u_o (and incidentally the local length scale $y_o = \mu u_o/\tau_w$). As usual, my technique will be to fit measured mean-velocity profiles to a complete profile formula, including a wake component;

$$\frac{u}{u_o} = \frac{1}{\kappa} \ln \frac{yu_o}{\nu} + c + \frac{2\Pi}{\kappa} \sin^2 (\frac{\pi}{2} \frac{Y}{\delta}) \tag{45}$$

where c depends on u_o and τ_w through equation (44). The parameter Π in equation (45) is

---

* This point is illustrated in figure 7 for the particular case $M = -0.05$. The normal intersection is at $Y/y_o \sim 19$, $U/u_o \sim 12$, whereas the plateau intersection is at $Y/y_o \sim 470$, $U/u_o \sim 20$. The implied generalization of the profile shape may not be entirely academic for flows undergoing relaminarization; cf. figure 8 (run 1-580) in the thesis by Tennekes (1964).

readily eliminated in favor of u_0, δ, τ_w, and u_∞. Hence if τ_w were accurately known, the parameters u_0 and δ could be determined by forcing an optimum fit for the central part of the profile. However, I prefer to treat τ_w as uncertain, especially for large blowing rates, and to test various hypotheses for $\tau_0 = \rho u_0^2$ to see whether or not plausible values are obtained for $c_f = 2 \tau_w/\rho u_\infty^2$.

First, suppose that $\tau_0 = \tau_w$, the stress at the wall. Then $c = c_0$, from equation (44), and the fitting operation is indifferent to the value of v_w for the profile.*

Second, suppose that $\tau_0 = T$, the (laminar) stress at the intersection of the sublayer profile and the logarithmic profile. Then the definitions (37) for M and (42) for T, together with the normalizing condition (36), imply

$$\frac{\rho u_0^2}{\tau_w} = \frac{u_0 y_0}{\nu} = 1 + M\frac{U}{u_0} = (1 - \frac{v_w}{u_0}\frac{U}{u_0})^{-1} \qquad (46)$$

Since U/u_0 is known as a function of M (cf. figure 8, where the abscissa $\rho v_w u_0/T$ should be interpreted temporarily as v_w/u_0), so are $u_0 y_0/\nu$, v_w/u_0, and c. In fact, $1 + MU/u_0$ is temporarily equal to $\exp(MY/y_0)$, according to equation (40), and therefore $c = c_0 - (M/k)(Y/y_0)$.

All of Simpson's data which are acceptably close to turbulent equilibrium have been processed by the two alternative schemes just described. Values inferred for the local friction coefficient c_f are compared to Simpson's "best estimate" in figure 9. Except for the highest blowing rates, for which Simpson's estimate of c_f is quite uncertain, the discrepancies are clearly in opposite directions and of comparable magnitude. An intermediate assumption, that τ_0 should be taken as the arithmetic mean of τ_w and T, was therefore tested also, with the improved outcome shown in the figure.

According to figure 9, the characteristic-scale method is able to generate acceptable values for c_f when the characteristic stress $\tau_0 = \rho u_0^2$ has some value intermediate between τ_w and T, perhaps a little closer to τ_w. To investigate this point, a few profiles from the work of Simpson and of Davis were processed further. In each case, the value of c_f obtained via Simpson's version of the mixing-length analysis (see Section I) was accepted as a correct value; i.e., a satisfactory substitute for a direct measurement of c_f. The parameter ρu_0^2 was then varied between τ_w and T to establish the particular value for ρu_0^2 which would reproduce exactly this mixing-length c_f. The results, in terms of a combination $(\rho u_0^2 - \tau_w)/(T - \tau_w)$ which varies from zero when $\rho u_0^2 = \tau_w$ to unity when $\rho u_0^2 = T$, are plotted against v_w/u_0 in figure 10, together with a scatter band corresponding to an uncertainty of $+ 0.0002$ in c_f (roughly $\pm$ 5 percent in c_f when $v_w/u_0 = 0$; $\pm$ 50 percent in c_f when $v_w/u_0 = 0.3$).

A new hypothesis. For a variety of reasons, I now want to propose an alternative hypothesis for the characteristic stress. Let τ_0 be tentatively defined as an integral mean in the sublayer; i.e.,

$$\tau_0 = \rho u_0^2 = \frac{1}{Y}\int_0^Y \tau \, dy \qquad (47)$$

I view this equation (47) as the central relationship in this paper. The practice of evaluating τ as the laminar stress $\mu \partial u/\partial y$ yields immediately

$$\rho u_0^2 = \mu \frac{U}{Y} \qquad (48)$$

or, after slight rearrangement.

$$\frac{U}{u_0} = \frac{Y u_0}{\nu} \qquad (49)$$

The usual normalizing condition $\tau_w = \mu u_0/y_0$ then gives

$$\frac{\rho u_0^2}{\tau_w} = \frac{U/u_0}{Y/y_0} = \frac{y_0 u_0}{\nu} \qquad (50)$$

where the right-hand side is a known function of the equilibrium mass-transfer parameter M. So is

$$\frac{v_w}{u_0} = \frac{\rho v_w u_0}{\rho u_0^2} = M \frac{\tau_w}{\rho u_0^2} \qquad (51)$$

A curve can therefore be plotted in figure 10 to show the quantitative consequences of the integral-scale hypothesis (47). Among these consequences is a shift of ρu_0^2 toward τ_w for the case of blowing, as desired. The course of the curve is also consistent with the course of the data.

---

* The sublayer profile given by equation (35) will obviously change position according to the value of the parameter $M = \rho v_w u_0/\tau_w$, but this portion of the profile is not normally involved in the fitting operation.

Experimental data. Typical profiles from the work of several authors (the same profiles presented earlier in figure 2 and figures 4-6 in terms of the mixing-length theory) are shown again in figures 11-14 after processing via the integral-scale hypothesis, equation (47). The quality of the fit is definitely inferior to that in the earlier figures. In particular, there is a tendency for the data in the inner 10 to 15 percent of the profile to fall above the analytical curves for the case of suction, and below the curves for the case of moderate blowing. That the discrepanies may be partly of experimental origin is suggested by the fact that they are present in some of the data even for the case $v_w = 0$. However, if the measurements are accurate, it may be necessary to reconsider the assumption that Karman's constant κ is unaffected by mass transfer. Tennekes (1964) chose to go in this direction in analyzing his own suction data.

To test the suitability of the equilibrium parameter $M = \rho v_w u_0 / \tau_w$ as a measure of externally imposed mass-transfer conditions, the profile parameter Π is plotted against M in figure 15. Because the test is a sensitive one, I have used only what I consider to be the best available data and have omitted profiles for which R_θ is less than 3000, in order to reduce the scatter (cf. figure 3). The result is encouraging; moreover, the figure demonstrates the advantages of working with finite v_w (which is easily measured) rather than with finite dp/dx (which is not) in any attempt to generalize the concept of similarity.

Finally, values of the local friction coefficient C_f inferred using the integral-scale hypothesis are compared in figures 16-18 with values of C_f inferred using Simpson's version of the mixing-length method. Either method seems to be satisfactory for estimating surface friction, even for quite large blowing rates. However, one method or the other (or perhaps both) may not account properly for effects of Reynolds number; observe the dashed line in each of figures 16-18, which is a worst-case data trajectory for a flow with fairly strong constant blowing. There is also a suggestion that C_f does not continue to decrease along the plate, but actually increases in the region of the trailing edge. This effect may be an upstream influence of the rather traumatic change in surface boundary conditions which occurs at the end of the test surface.

Epilogue. I have several comments about experimental technique in future mass-transfer research of the kind considered here. Experience has shown that a thick porous surface is much to be preferred, because it minimizes effects of local static pressure variations on the local transfer rate. Measurements for the case $v_w = 0$ should be part of any test program. I am obliged to complain again that hot-wire anemometers are not used as often as they should be for mean-flow measurements. Finally, I hope that blowing rates as large as $v_w/u_\infty = 0.05$ will eventually be investigated, to clarify the nature of the hypothetical blowoff condition at constant pressure.

I do not want to leave an impression that the idea of using a characteristic stress evaluated away from the wall to define a characteristic velocity scale in flows with mass transfer is entirely original. For the case of moderate blowing, for example, Mickley and Smith (1963) have proposed the use of the maximum shearing stress, which occurs relatively near the wall. However, their proposal breaks down for flows with suction, whereas the present proposal does not. In fact, the most attractive feature of the integral-scale hypothesis as formulated here is its generality. As long as $\tau = \mu \partial u/\partial y$ is taken as a valid approximation in the sublayer, equations (48), (49), and (50) will hold independently of the particular conditions which determine the actual intersection of the sublayer and logarithmic profile curves. There is therefore a clear prospect that the method of characteristic scales can be developed into a vehicle for studying combined effects of mass transfer, pressure gradient, and even lateral curvature.

REFERENCES

Black, T. J. and Sarnecki, A. J.   1958   ARC, R & M 3387

Coles, D.   1962   Rand Corp., Rep. R-403-PR

Coles, D.   1968   Proc. AFOSR-IFP-Stanford Conf., Computation of Turbulent Boundary Layers, Vol. II, pp. 1-45

Dutton, R. A.   1955   Ph.D. Thesis, Univ. Cambridge

Favre, A., Dumas, R., Verollet, E., and Coantic, M.   1966   J. de Mécanique 5, pp. 3-23

Liepmann, H. W. and Laufer, J.   1947   NACA, TN 1257

McQuaid, J.   1966   Ph.D. Thesis, Univ. Cambridge

Mickley, H. S. and Davis, R. S.   1957   NACA, TN 4017

Mickley, H. S. and Smith, K. A.   1963   AIAA J. 1, p. 1685

Millikan C. B.   1938   Proc. 5th Int'l. Congr. Appl. Mech., Cambridge, pp. 386-392

Mugalev, V. P.   1959   Izv. VUZ, Aviatsionnaia Tekhnika, No. 3, pp. 72-79

Simpson, R. L.   1967   Ph.D. Thesis, Stanford Univ.

Simpson, R. L.   1970   J. Fluid Mech. 42, pp. 769-802

Stevenson, T. N.   1963a   Coll. Aeron., Cranfield, Rep. Aero No. 166

Stevenson, T. N.   1963b   Coll. Aeron., Cranfield, Rep. Aero No. 170

Tennexes, H.   1964   Thesis, Delft
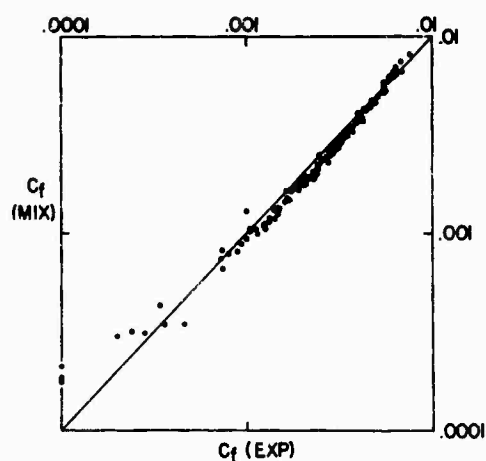
Figure 1. Data of Simpson (1967). Abscissa, C_f(EXP), is Simpson's "best estimate"of local friction coefficient. Ordinate, C_f(MIX), is obtained by fit of each profile to equations (11) and (16).
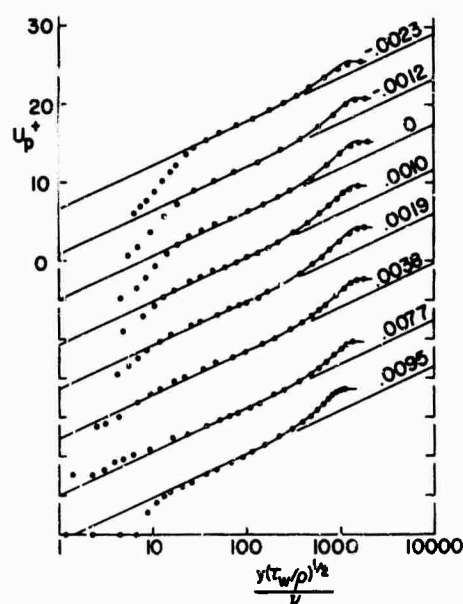
Figure 2. Data of Simpson (1967). Typical profiles fitted to equations (11) and (16). Ordinate, U_p^+, is pseudo-velocity given by left side of equation (11). Numbers are values of v_w/u_∞ for each profile.
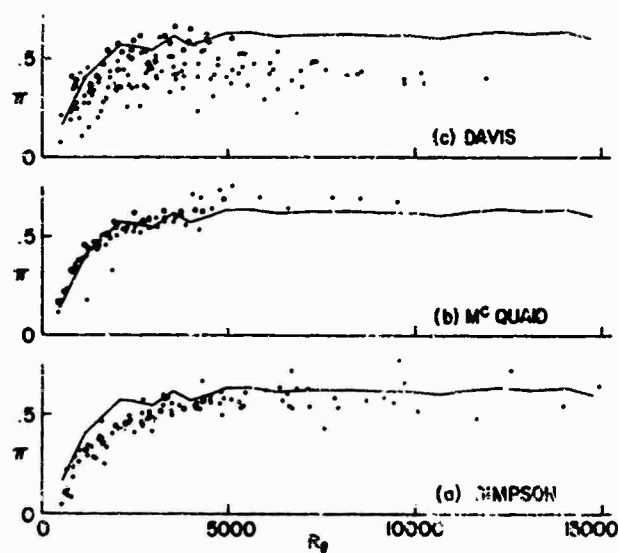
Figure 3. (a) Data of Simpson (1967). (b) data
of McQuaid (1966). (c) Data of Mickley and Davis
(1957). The strength of the wake component as a
function of local Reynolds number. Jagged line
is trace of Wieghardt's data at 33.0 m/sec with
$v_w/u_\infty = 0$.
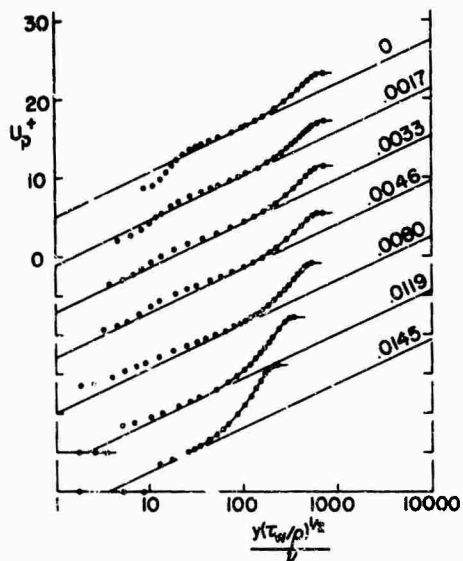
Figure 4. Data of McQuaid (1966).
Notation as in figure 2.
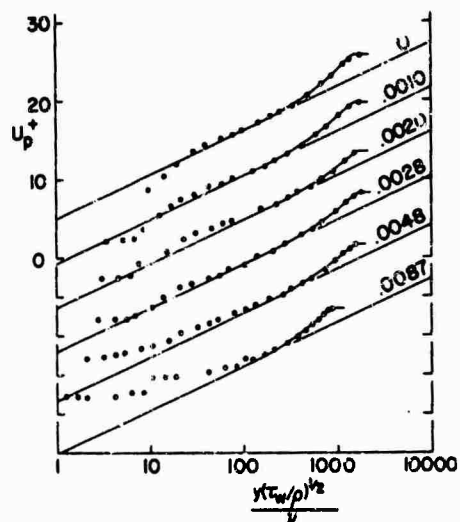
Figure 5. Data of Mickley and
Davis (1957). Notation as in
figure 2.
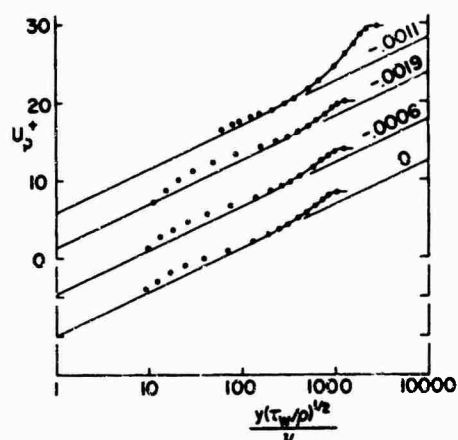
Figure 6. Data of Tennekes (1964, top profile) and of Favre et al. (1966). Notation as in figure 2.
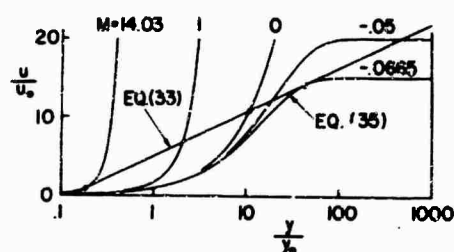
Figure 7. Intersections of the logarithmic curve, equation (33), with the laminar sublayer curve, equation (35).
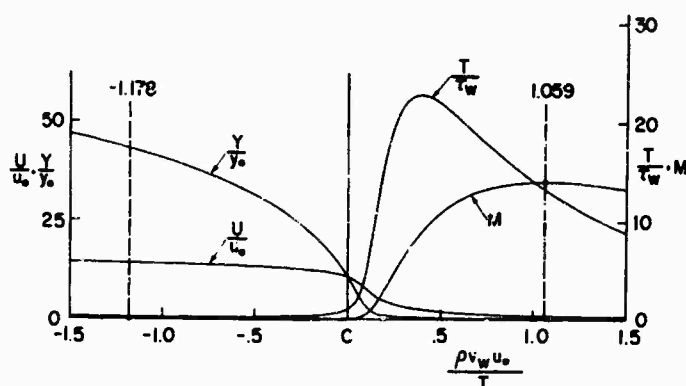
Figure 8. Conditions at the edge of the sublayer (solution of equations (40) and (41)), interpreted using equations (42) and (37).
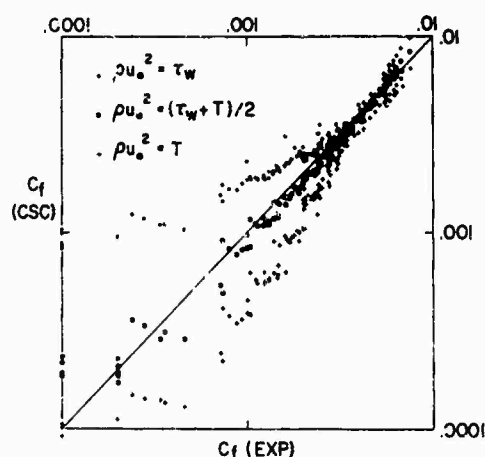
Figure 9. Data of Simpson (1967). Abscissa, C_f(EXP), is Simpson's "best estimate" of local friction coefficient. Ordinate, C_f(CSC), is obtained by fit of each profile to equation (45), using three definitions for characteristic stress ρu_o^2 as noted.
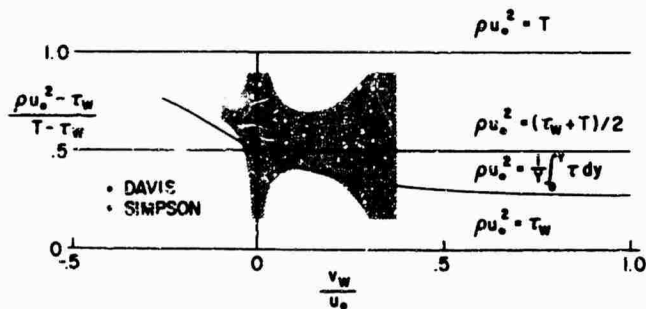
Figure 10. Test of best assumption for characteristic stress ρu_o^2. Data points show values of ρu_o^2 which reproduce C_f obtained by mixing-length method (i.e., C_f(MIX) in figure 1).
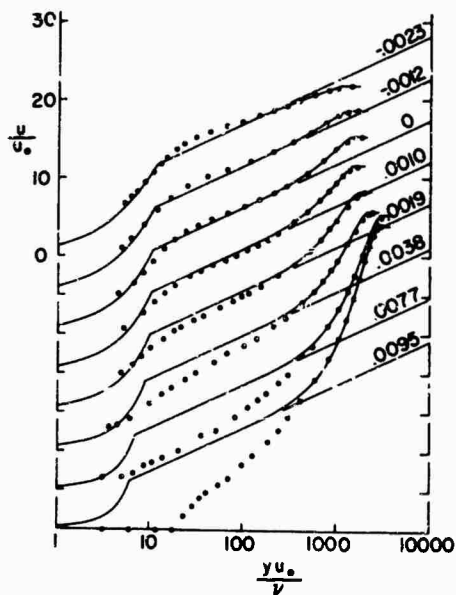
Figure 11. Data of Simpson (1967). Typical profiles fitted to equation (45), using equations (50) and (44). Numbers are values of v_w/u_∞ for each profile.
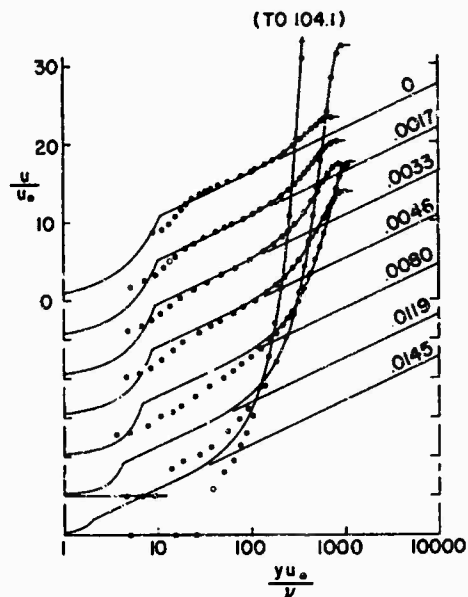
Figure 12. Data of McQuaid (1966). Notation as in figure 11.
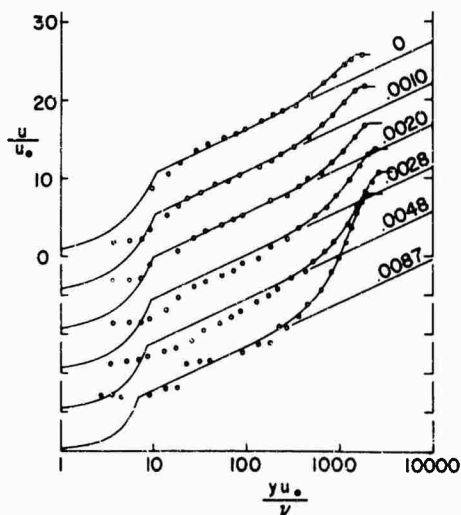
Figure 13. Data of Mickley and Davis (1957). Notation as in figure 11.
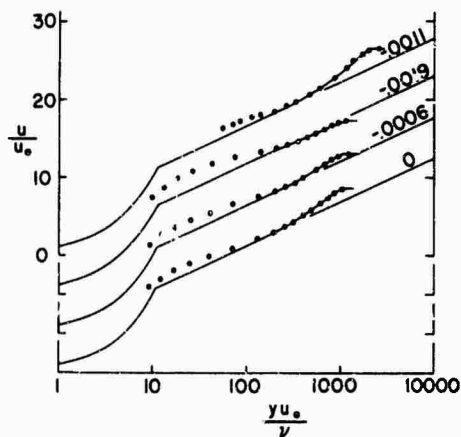
Figure 14. Data of Tennekes (1964; top profile) and of Favre et al. (1966). Notation as in figure 11.
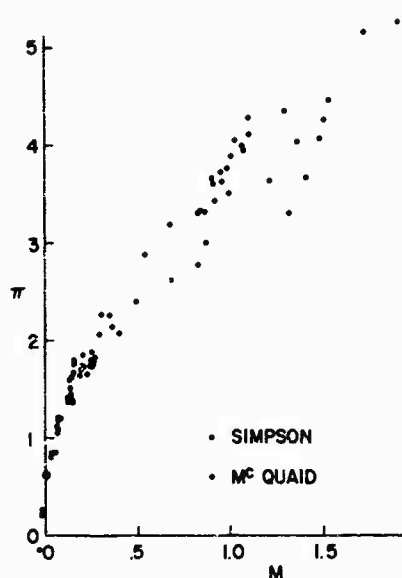
Figure 15. Test of relationship between profile shape parameter Π and external parameter M.
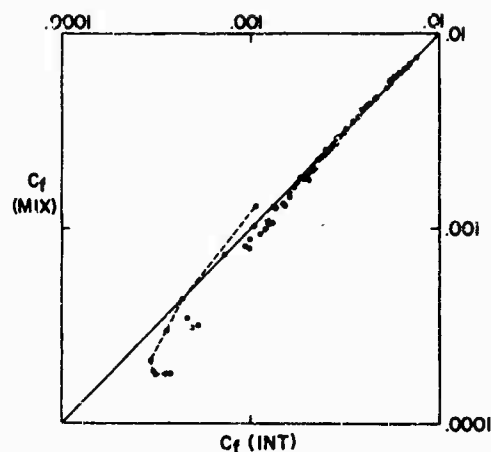
Figure 16. Data of Simpson (1967). Abscissa, $C_f(INT)$, is obtained by fit of each profile to equations (41), (50) and (44), with integral definition for ρu_o^2. Ordinate, $C_f(MIX)$, is same as in figure 1. Dashed line is trace of data for flow 121266 ($v_w/u_\infty = 0.0094$).
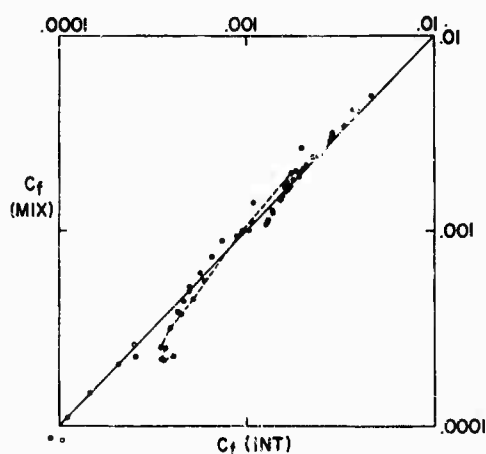
Figure 17. Data of McQuaid (1966). Notation as in figure 16. Dashed line is trace of data for flow with $u_\infty = 150$ fps ($v_w/u_\infty = 0.0079$).
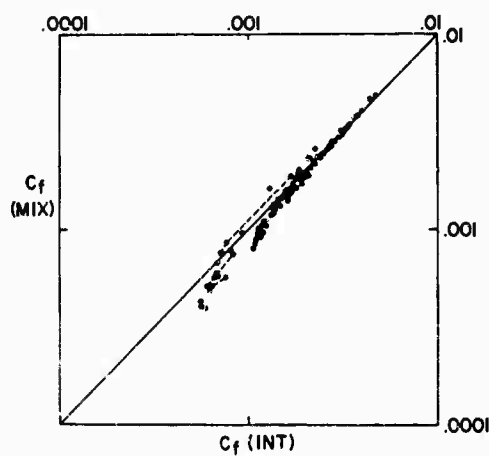
Figure 18. Data of Mickley and Davis (1957). Notation as in figure 16. Dashed line is trace of data for flow C-10-20 ($v_w/u_\infty = 0.0095$).

THE SUPPRESSION OF SHEAR LAYER TURBULENCE IN ROTATING SYSTEMS

James P. Johnston
Associate Professor
Mechanical Engineering Department
Stanford University
Stanford, California 94305
U.S.A.

SUMMARY

Stabilization of turbulent boundary layer type flows by the action of Coriolis forces engendered by system rotation is studied. Experiments on fully-developed, two-dimensional flow in a long, straight channel that was rotated about an axis perpendicular to the plane of mean shear are reviewed to demonstrate the principle effects of stabilization. In particular, the delay of transition to turbulence on the stabilized side of the channel to high Reynolds number ($\overline{u}_m h/\nu$) as the rotation number ($|\Omega|h/\overline{u}_m$) is increased is demonstrated. A simple method, that utilizes the eddy Reynolds number criterion of Bradshaw, is employed to show that rotation induced suppression of transition may be predicted for the channel flow case. The applicability of the predictive method to boundary layer type flows is indicated.

NOTATION

c_f	- wall shear stress coefficient in channel flow, $2\tau_w/\rho\overline{u}_m^2$
$c_{f\delta}$	- wall shear stress coefficient in boundary layer flow, $2\tau_w/\rho\overline{U}^2$
D	- channel half width, h/2
h	- channel width
L	- dissipation length scale, see Eq (7)
ℓ	- mixing length, see Eq (4)
m	- a parameter, see Eq (15b)
R	- eddy Reynolds number, see Eq (7)
Re	- channel Reynolds number, $\overline{u}_m h/\nu$
Re_δ	- boundary layer Reynolds number, $\overline{U}\delta/\nu$
Ri	- gradient Richardson number, see Eq (1)
Ro	- channel rotation number, $|\Omega|h/\overline{u}_m$
Ro_δ	- boundary layer rotation number, $2|\Omega|\delta/\overline{U}$
S	- "low speed" limit of Richardson number, $-2\Omega/(\partial\overline{u}/\partial y)$
So	- reference value of S, the ratio $S/So = \ell/\ell_o$
u,v,w	- components of velocity along x,y,z; $(\overline{})$ is time mean value; $()'$ fluctuating part
$\overline{u}_m$	- area averaged, time mean velocity for two-dimensional channel flow
u_τ	- wall shear velocity, $\sqrt{\tau_w/\rho}$
$\overline{U}$	- boundary layer free-stream velocity
x,y,z	- cartesian coordinates fixed in rotating system
β	- a parameter, see Eqns (5) and (6)
δ	- boundary layer thickness
η	- dimensionless y coordinate, y/D
ℓ	- Karman's "constant", ≈ 0.4
τ	- total fluid shear stress, $[\mu(\partial\overline{u}/\partial y) - \rho(\overline{u'v'})]$, viscous plus Reynolds stress
τ_w	- wall shear stress
Ω	- angular velocity of system relative to inertial space, oriented along z axis in this paper
$()_o$	- subscript to denote conditions evaluated at zero-rotation ($\Omega = 0$) with all other parameters fixed

1. INTRODUCTION

There are many free and bound shear flows where non-conservative centrifugal or buoyancy forces act in the mean flow plane and are also perpendicular to the mean velocity (or streamlines). A boundary layer on a curved wall is simple example of such a flow. The non-conservative, normal body forces may cause significant changes in the occurrence, structure and production of turbulence. If these non-conservative body forces are of sufficient magnitude and "stabilizing", i.e. characterized by positive Richardson numbers, turbulence may be completely suppressed at relatively high Reynolds number. Shear layers with stable density stratification in a gravity field are commonly cited illustrations of this effect.

The boundary layers on the blades of radial flow, centrifugal compressor and pump impellers have Coriolis forces that act perpendicular to the mean velocity. These shear flows are closely related to flows with centrifugal body forces [7]. There have been enough observations [Ref's. 1 to 6] on boundary layers in steadily rotating systems to strongly suggest that the Coriolis forces that arise here contribute to stabilization of suction surface boundary layers and destabilization of pressure surface layers. For example, if a centrifugal impeller blade boundary layer is turbulent, the principal effects of stabilization on the suction surface are reduced Reynolds stress, wall shear stress, eddy viscosity and mixing length. For high rotational speeds the Coriolis forces can become large enough to totally suppress transition from laminar to turbulent flow. These effects are important to centrifugal impeller design as they may, among other things, severely limit

the pressure recovery (diffusion) that can be applied to suction surface boundary layers without causing flow separation.

Figures 1 and 2 illustrate and define the particular type of problem under investigation; (i) the two-dimensional turbulent boundary layer in time-mean-steady flow relative to a steadily rotating surface, and (ii) fully-developed, two-dimensional turbulent flow between steadily rotating, parallel channel walls. The axis of system rotation is perpendicular to the plane of the mean flow as illustrated. Positive rotational velocity, $\Omega > 0$, is defined to be counterclockwise with respect to the streamwise, x , coordinate and the normal, y , coordinate. With positive rotation a fluid particle is subject to a negative streamwise component of Coriolis acceleration. $-2\Omega v$, and a positive normal component, $+2\Omega u$.
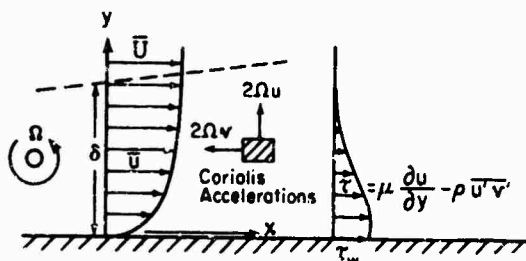
Fig. 1   Two-dimensional boundary layer on rotating surface. Layer unstable with $\Omega > 0$, as shown.
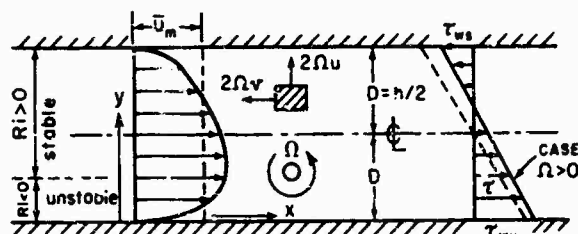
Fig. 2   Fully-developed, two-dimensional, rotating channel flow.

An appropriate measure of the relative local stability of a shear layer flow subject to a non-conservative body force is the gradient Richardson number [7] which for the case of rotating, straight shear layers is defined by

$$\text{Ri} \triangleq - 2\Omega \left(\frac{\partial \overline{u}}{\partial y} - 2\Omega \right) \Big/ \left(\frac{\partial \overline{u}}{\partial y} \right)^2 = S(1 + S) \tag{1}$$

The parameter S , the limiting value of Ri that results when rotation effects become very small, may be loosely interpreted as the ratio of the mean, local Coriolis body force, $-2\Omega\overline{u}$, to a quantity, $\overline{u}(\partial\overline{u}/\partial y)$, proportional to the inertia forces in the flow relative to the rotating system. The flow tends to be "stabilized" by rotation in regions where Ri is positive and "destabilized" where Ri is negative. Namely, fluid particles perturbed in a direction perpendicular to the mean flow feel a net restoring force if Ri > 0, but if Ri < 0 the unbalanced part of the Coriolis force will tend to accelerate the disturbed particle away from its initial position. One sees from Eq (1) that neutrally stable layers (Ri = 0) exist when (a) $\Omega = 0$, the zero-rotation condition, or (b) $(\partial\overline{u}/\partial y)-2\Omega = 0$, the absolute mean vorticity is zero. For example, neutrally stable layers commonly occur in the free-stream (or inviscid) flow regions in centrifugal compressor impellers that draw fluid from an atmosphere at rest even though the blade surface boundary layers, where the absolute vorticity cannot be zero, are not neutrally stable.

In Fig 2 the stable and unstable regions (or sides) of the channel flow case are shown in conjunction with the mean velocity and shear stress profiles. Although the shear stress profile is necessarily linear for fully-developed flow [2], neither it nor the mean velocity profile are symmetric about the channel centerline, y=D=h/2 , unless the flow is totally laminar, or Ω=0 . In the case of clockwise rotation, $\Omega < 0$, the stable and unstable regions would be interchanged in Fig 2, and the velocity and stress profiles would be reversed with respect to the centerline.

For boundary layers, Fig 1, the global effects of rotation may be expressed through a parameter, the rotation number, $\text{Ro}_\delta = 2\Omega |\delta/\overline{U}$. The rotation number for channel flow is Ro = $|\Omega| h/\overline{U}_m$. In either case the rotation number represents the ratio of Coriolis forces to inertial forces, and it is the inverse of a Rossby number whose value (1/Ro > 5) is large for the work described here.

In Section 2 some experiments on the channel flow case will be discussed to illustrate the effects of rotation on turbulent flow structure and transition to turbulence. Following this, in Section 3, a simple transition theory will be presented that makes use of the idea that the local eddy Reynolds number introduced by Bradshaw [8] must, at some point of the mean velocity profile, equal or exceed a critical value of 30^4 ($k \approx 0.4$ is the Karman constant) in order that turbulent flow be self-maintaining.

2. THE ROTATING CHANNEL EXPERIMENTS

In this section I shall be discussing some aspects of the experiments carried out by Halleen and Johnston [1] together with some more recent results obtained in the same rotating channel apparatus.

The channel itself is 59 inches long, 11 inches in span along the direction of the axis of rotation, and has a nominal width of h $\approx$ 1.54 inches. Water can be pumped through the channel at measured rates of flow, and it can be driven about its spanwise axis at any rotational speed from 1/4 rpm up to nearly 20 rpm. The experiments were conducted in the region of the channel located at x = 45 to 52 inches from inlet and at the

central plane, 5 1/2 ± 2 inches up from an end wall. In this region the mean flow was found to be very close to fully-developed and two-dimensional, i.e. nearly free of secondary flow effects generated on the end walls. The distance from inlet to test region, $x/h \approx 30$, is rather short for the development of a complete state of fully-developed flow. However, the inlet design (abrupt contraction) assured rapid streamwise development of the side wall boundary layers and provided a strong level of disturbance that promoted transition at minimum Reynolds number.

Flow visualization studies, mean velocity profile measurements, and wall shear stress determinations by Preston tubes, log-law cross plot and direct profile slope at the wall were carried out for a variety of conditions that covered a range of $3.6 \times 10^3 < \text{Re} < 5.7 \times 10^4$ and $0 \leq \text{Ro} < 0.21$. Only a few of the most pertinent results will be discussed here and primary emphasis will be placed on the conditions that existed at, or near, the stabilized side of the flow where gradient Richardson numbers were positive.

Visualization of the wall layers was accomplished by two techniques. The first utilized the very slow injection of dye-colored water through very narrow (0.005 inch wide) slots cut spanwise across the 11 inch high channel walls. The second, and more recently developed, method is the hydrogen-bubble technique [9]. In the application of the latter method the bubble generating wire (~.001 inch diam. platinum) was placed along the spanwise direction, normal to $\overline{u}$ and parallel to the axis of rotation. The wire could be traversed out to any distance y from the wall. With the development of good lighting techniques and extreme water clarity, good 16 mm motion picture films were recently produced of the wall-layer flow structures by D. K. Lezius (PhD candidate).

The principle visual results were quite revealing. First, with no system rotation and for $\text{Re} > 3600$ the wall-layers* exhibited the now well known structural characteristics of turbulent boundary layers, the spanwise streaky structure and the streak lifting and break up phenomena discussed by Kline, et. al. [10]. With channel rotation, the structures observed in the stabilized side of the flow differed from the case of zero-rotation and from the structures seen on the destabilized side. On the stable side (Ri > 0) the flow progressed from a fully turbulent state to totally laminar flow when Ro was increased at fixed Reynolds number. However, on the unstable side (Ri < 0) the flow always remained fully turbulent, and, superimposed on this turbulent flow, a pattern of large scale, longitudinal, contra-rotating vortices began to appear at higher Ro values. The latter phenomena is discussed briefly by Halleen and Johnston [1] and Johnston [2] and is the subject of current work by Lezius. These large scale vortex effects seen on the unstable side of the channel will not be pursued here since our main concern is with the stable side flow conditions.

Figure 3 is a series of photographs of hydrogen-bubble time lines generated with the wire held deep in the wall-layer on the stable side. Each picture illustrates the structure in the plane of the wall for progressively higher values of Ro at a fixed value of $\text{Re} \approx 1.38 \times 10^4$. At Ro = 0, and in the other pictures, the irregular spanwise array of low speed streaks is evident (see Fig 10a of Kline, et. al. [10] for comparison). As Ro increases the streak structure persists over the whole spanwise field until, at a critical value of Ro, patches of plane laminar flow start to occur between turbulent regions. Laminar flow is indicated in those areas of the picture (Ro = 0.126) where time lines proceed downstream in parallel arrays. At high rotational speeds, the stable wall flow appeared to be laminar with the intermittent appearance of highly damped patches, or spots, of turbulence. Finally, at Ro roughly 1.5 times its critical value when laminar regions were first observed, the stable side wall-layers became completely steady and laminar. The turbulent spots observed in the final phases of the transition process are reminiscent of the "Emmons spot" structure observed in natural boundary layer transition. However, one cannot draw this analogy too closely since the spots observed here decay in size as they move downstream rather than grow as do the "Emmons" spots.

The first definite appearance of laminar regions as Ro is increased was found to be Reynolds number dependent. Two types of points representing the results by the two visual techniques are shown in Fig 4. The crosses connected by the dashed lines denote two scenes in our films between which transition has occurred. The round points on Fig 4 indicate the condition when laminar areas were first detected visually in the dye studies [1] of the stable side sublayers. A transition line might be drawn through these points to indicate that only for Ro values below the line can a fully turbulent state be maintained. An attempt to predict this transition line, the lines in Fig 4, is outlined in the following section. Before proceeding to that analysis it is useful to present a few more experimental results that (i) confirm the visual evidence and (ii) are useful in the analysis to follow.

Mean velocity profiles in law of the wall coordinates on the stable side of the channel are presented in Fig 5 and 6 for two Reynolds numbers. At $\text{Re} = 3.5 \times 10^4$, Fig 6, all profiles were obtained in the turbulent flow regime at Ro values below the transition value estimated from Fig 4 to be ~0.20 at this Reynolds number. However, in Fig 5, where Re is lower, the flow should be transitional or laminar for $\text{Ro} \gtrsim 0.10$. Therefore it is not surprising that the profiles in Fig 5 at Ro = 0.117, 0.166 and 0.210 have a laminar shape compared to the other profiles in Fig 5 and the profiles in Fig 6 which approach

─────────

*Here the term wall-layers refers to those regions commonly referred to as laminar sublayers, buffer layers and inner parts of the fully-turbulent layers, see [10].

(a) $k = 0.4$, $m = 1.0$

(b) $\beta = 6.0$, $m = 1.0$

(c) $\beta = 6.0$, $k = 0.4$

Fig. 4   Transition in rotating channel flow.
Circles - dye injection observations
[1]: ● observer stationary, ○ observer
rotating. Crosses - film scenes using
bubbles; upper cross definitely laminar
or transitional, lower cross flow defi-
nitely turbulent. Solid lines theory.
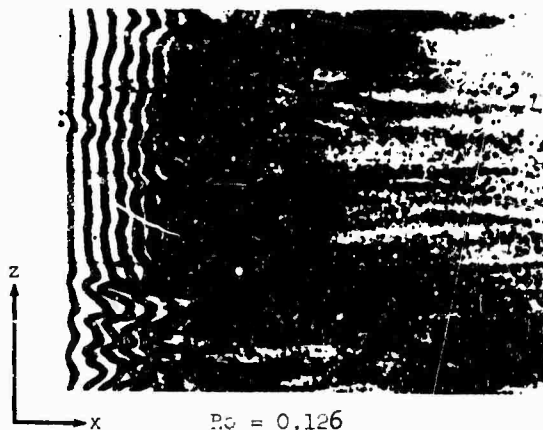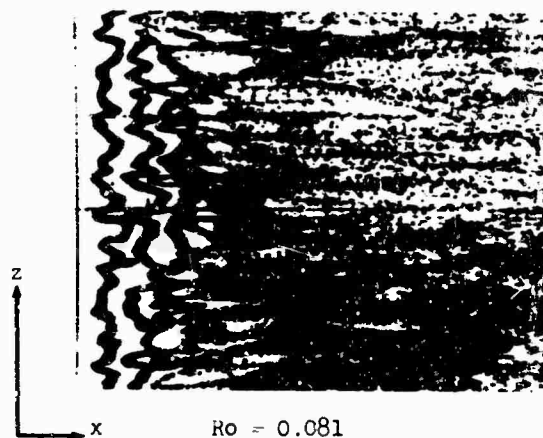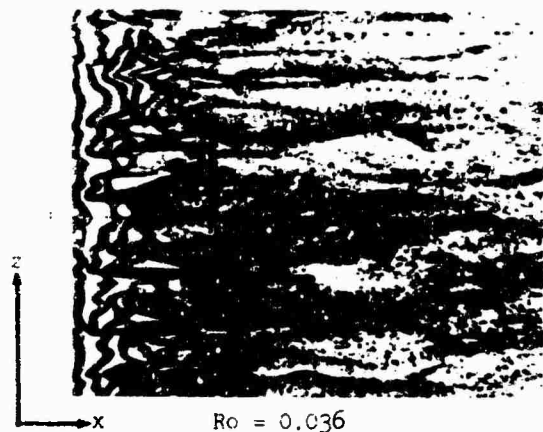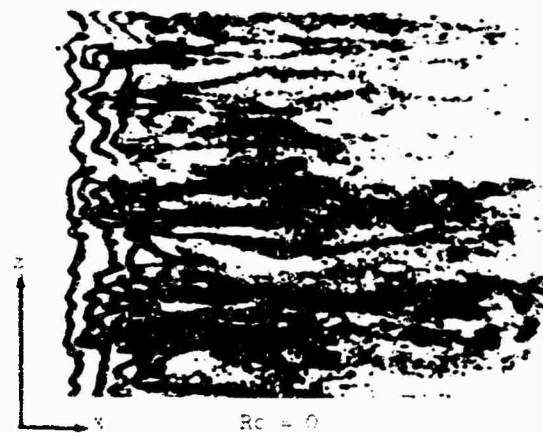
Fig. 3   Wall layer flow structure by pulsed bubble wire at $yu_\tau/\nu = 2$ set parallel to
z (axis of rotation). Wire located along left hand edge of photos. Flow
$Re = 1.38 \times 10^4$. From films by D. K. Lezius.

a characteristic turbulent shape such as the rotating turbulent law of the wall $(\overline{u}/u_\tau) = (1/4)\ell n(yu_\tau/\nu) + B - \beta(2\Omega y/u_\tau)$ suggested by Bradshaw [7].
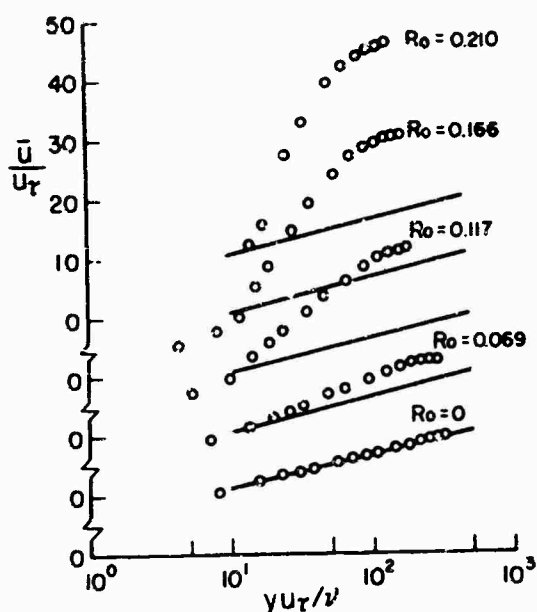
Fig. 5   Mean velocity profiles on stable side of channel, Re = 1.15 x 10⁴, lines are $5.8 \log_{10} (yu_\tau/\nu) + 5.0$.
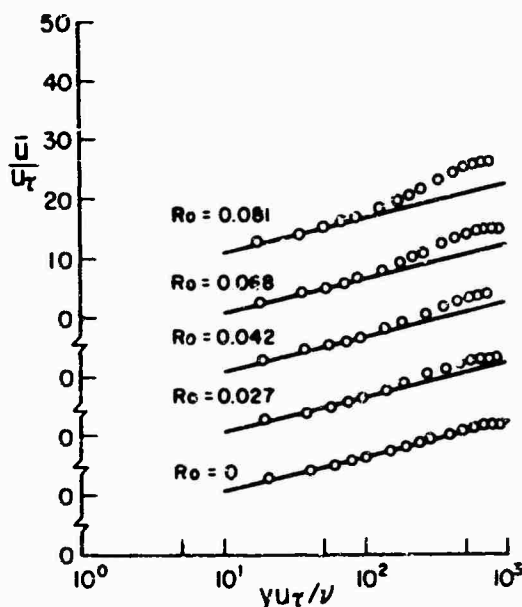
Fig. 6   Mean velocity profiles on stable side of channel, Re = 3.5 x 10⁴, lines are $5.8 \log_{10} (yu_\tau/\nu) + 5.0$.

At zero-rotation, the wall shear stress coefficient in the two-dimensional flow (central) region of our channel was found [1] to fit the simple relationship

$$c_{fo} = 2\tau_{wo}/\rho\overline{u}_m^2 = 0.0706 \ Re^{-1/4} \tag{2}$$

to better than $\pm 7\%$ over the range $1.15 \times 10^4 \leq Re \leq 3.52 \times 10^4$. The air flow data of McMillan and Johnston [11] in a channel of 10:1 aspect ratio and the data of Hussain and Reynolds [12] in a 48:1 channel, as well as older data covering the same range of Reynolds numbers, fit Eq (2) to the same limits of uncertainty. The low Reynolds number data of Patel and Head [13] agree with Eq (2) from the lower limit of turbulent flow, $Re \approx 2 \times 10^3$, up to 4×10^3.

When the channel [1] was in rotation, the measured wall shear stress on the stable side was lower, and the stress on the unstable side higher, than the zero-rotation stress at the same Re. At low Ro values, the ratio of wall-shear velocity, u_τ, to its zero-rotation value, $u_{\tau o}$, at the same Reynolds number may be estimated by the data fit

$$\sqrt{(\tau_w/\tau_{wo})} = u_\tau/u_{\tau o} = 1 \pm 1.75 \ Ro \tag{3}$$

The negative sign refers to the stable-side wall-stress, and the result applies only when the flow is fully turbulent. Once transition occurs, $u_\tau/u_{\tau o}$ drops well below the value predicted by Eq (3). On the unstable side, where the positive sign applies, it appeared that the wall shear ratio was independent of Reynolds number as implied by Eq (3) only up to a critical Ro; above the critical Ro $u_\tau/u_{\tau o}$ tended to approach a constant value as Ro increased. The reasons for this behavior are not yet understood, but leveling of $u_\tau/u_{\tau o}$ may be associated with the onset of the large-scale, longitudinal vortex structure mentioned in the discussion of the visual results.

The final experimental results to be presented are the profiles of mixing length, defined by

$$\ell \triangleq (\tau/\rho)^{1/2}\Big/\left|\partial\overline{u}/\partial y\right| \tag{4}$$

ℓ was deduced from the measured velocity profile slopes and measured wall shear stresses. The profile of τ was assumed to be linear, Fig 2, because fully-developed flow was assumed.

Figure 7a displays ℓ_o versus y for zero-rotation. The flow was not quite fully-developed, as assumed, because near the center of the channel (y > 0.04 ft) ℓ_o is seen to depend on distance, x/h, from the channel inlet. The ratio of ℓ to ℓ_o, its zero-rotation value at the same y, is plotted versus gradient Richardson number in Figs 7b and 7c. These data, when compared to the solid lines, appear to follow the trends of the simple "Monin-Oboukhov" formulas suggested by Bradshaw [7]. For the stable side, Fig 7b, the "Monin-Oboukhov" formula is

$$\ell/\ell_c = (1 + \beta\ Ri)^{-1} \qquad (5)$$

and for the unstable side, Fig 7c, where the minimum possible value of Ri is -0.25,

$$\ell/\ell_c = 1 + \beta\ Ri \qquad (6)$$

Because of the high degree of uncertainty in the ℓ/ℓ_c data it would be difficult to choose a unique value for β, the empirical constant, on either side of the channel. In fact it appears that β itself is probably not a constant but may depend on Re and Ro. At best, $\beta \approx 6$ appears to be a good median value on the stable side, and on the unstable side of the channel.

Fig. 7a Profiles of mixing length at zero-rotation. Data of this Figure, Fig (7b) and (7c) from [1].

Fig. 7b Mixing length ratio versus Richardson number on stable side. Lines represent Eq (5).
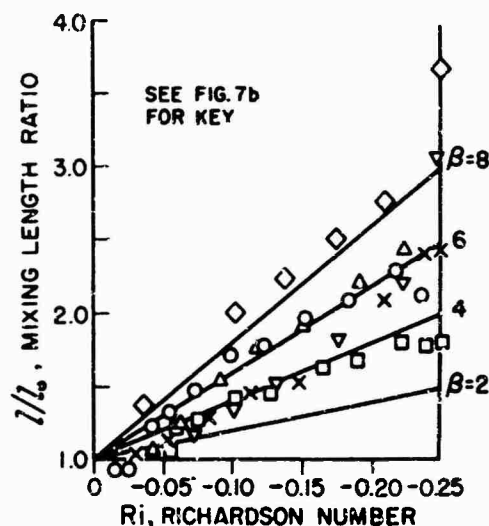
Fig. 7c Mixing length ratio versus Richardson number on unstable side. Lines represent Eq (6).

3. A CRITERION FOR THE MAINTENANCE OF BOUND TURBULENT SHEAR FLOW

The desirability of a predictive theory that permits the calculation of the effects of Coriolis, or other body forces, on the final transition to, and reverse transition from, a fully turbulent state is obvious. The problem may be approached from the laminar side by methods of linear stability theory (see [2] and [14]) but this approach has not been too successful thus far because of the complex non-linear effects that are essential to the actual transition process. It is probably better, to work backwards, e.g. by systematic increase of Ro from a turbulent state, and ask the question: how high, at a given Reynolds number, may Ro become before a stabilized layer is no longer able to produce new turbulence energy and stress as fast as these quantities are destroyed by viscosity? That is, what are the conditions for self-maintenance of the fully turbulent state? The data presented in Fig 4 answer this question for rotating channel flow over a limited range of Reynolds number. This section advances a procedure for prediction, and hence extrapolation, of these results.

An elementary criterion for the necessary conditions for maintenance of a bound turbulent shear flow where Reynolds stress production is mostly in the wall-layers was given recently by Bradshaw [8] in connection with his attempt to generalize various previous proposals concerning criteria for reverse transition (also called relaminarization or laminarization) in turbulent boundary layers. Very simply stated the criterion says that fully turbulent flow <u>cannot</u> be maintained once there exists <u>no</u> region, or point, in the layer where the dynamics of the energy carrying fraction of turbulence is independent of laminar viscosity. In quantitative terms he reduced this idea to the statement that when the maximum value of the eddy Reynolds number is less than 30 k, where $k \approx 0.4$ is Karman's constant, turbulent shear flow cannot maintain itself and tends toward a laminar

state. Eddy Reynolds number R is defined in terms of the local total shear stress τ and L, the local dissipation length scale, i.e.

$$R \triangleq (\tau/\rho)^{1/2} L/\nu \tag{7}$$

where $L \triangleq (\tau/\rho)^{3/2}/(\text{the rate of dissipation of turbulence energy})$.

3.1 Application to Rotating Boundary Layers

This criterion is applicable to turbulent boundary layers since R attains its maximum value in the wall-layer regions where local rates of turbulence production are high and nearly equal to local dissipation rates. Production and dissipation are large compared to rates of diffusion and convection of turbulence energy and stress in the wall layers. For these conditions, the single length scale L is an appropriate scale factor for the energy containing eddies. Hence a critical magnitude of a single Reynolds number, R, that represents the ratio of turbulence scale inertia forces to the viscous forces tending to dissipate turbulence should be appropriate to denote the condition of self maintaining turbulence.

Near the wall in a boundary layer L equals the mixing length. Up to $y/\delta = 0.2$, $L = \ell = \Lambda y (\ell/\ell_o)$ where $\ell_o = \Lambda y$ is the approximate zero-rotation variation of mixing length with distance from the wall, and δ is the boundary layer thickness. In the outer parts of the layer $(y/\delta > 0.2)$ L becomes close to constant, and then decreases to zero near $y/\delta = 1$ (Bradshaw, Ferris and Atwell [15]). For zero and moderate streamwise pressure gradient $\tau \approx \tau_w$ out to $y/\delta = 0.2$, and τ decreases to zero at $y/\delta = 1$. Thus the maximum value of eddy Reynolds number occurs close to $y/\delta = 0.2$ and it is approximated by

$$R_{max} = 0.2\Lambda \sqrt{c_{f\delta}/2} \, Re_\delta (\ell/\ell_o)_{y/\delta} = 0.2 \tag{8}$$

where $c_{f\delta}$ is the wall shear stress coefficient and Re_δ is the Reynolds number based on δ and free stream velocity, U.

For zero-rotation $\ell/\ell_o = 1$. For steady state rotation where $Ri > 0$ (stabilized flow), Eq (5) provides a rough approximation for ℓ. If we consider only the case of small rotation effects, $Ri \approx S$, Eq (5) simplifies to

$$\ell/\ell_o \approx 1 - \beta S = 1 - \beta So(\ell/\ell_o) \approx 1 - \beta So \tag{9}$$

$So = -2\Omega \, \ell_o/u_\tau$ where the definitions of S and ℓ are combined and the assumption $\tau = \tau_w$ is employed. ℓ/ℓ_o is now evaluated from Eq (9) at $y/\delta = 0.2$ using the assumption $\ell_o = \Lambda y$.

$$(\ell/\ell_o)_{y/\delta} = 0.2 = 1 - 0.2\Lambda \beta \, Ro_\delta \sqrt{2/c_{f\delta}} \tag{10}$$

When Eq (10) is substituted into (8) and R_{max} set equal to 30Λ, the result below is obtained:

$$Re_\delta \left[\sqrt{c_{f\delta}/2} - 0.2 \, \beta \, \Lambda \, Ro_\delta \right] \geq 150 \tag{11}$$

Eq (11) expresses the overall conditions required to maintain a fully turbulent boundary layer with zero, or small, free stream pressure gradient on a slowly rotating surface where rotation is stabilizing, i.e. $Ri > 0$. There are no data that permit one to verify this result directly. However we see that it yields the qualitatively expected results. That is, for a given Reynolds number the effect of increased boundary layer rotation number, Ro_δ, is to drive a turbulent layer toward a laminar state if $c_{f\delta}$ decreases or stays constant at fixed Re_δ. The increase of $c_{f\delta}$ with increase of Ro_δ on a stable side layer is not expected.

All current data sources on rotating turbulent boundary layers [4,5,6] violate at least one of the assumptions of the theory. More important however, none of the investigators made any systematic attempt to observe the conditions of Coriolis force induced reverse transition. Thus, even if improvements were made in the simple result above, Eq (11), it could not be checked directly. However, Halleen and Johnston [1] carried out the necessary observations, Fig 4, for fully-developed channel flow, and therefore these data are used to check the utility of the reverse transition criterion.

3.2 Application to Rotating Channel Flow

For channel flow, as in the previous analysis, we must provide estimates for τ and L in order to compute the eddy Reynolds number which is now written as

$$R = \frac{Re}{2} \sqrt{\frac{c_{fo}}{2}\left(\frac{\tau}{\tau_{wo}}\right)} \left(\frac{L_o}{D}\right)\left(\frac{L}{L_o}\right) \tag{12}$$

where Re is the channel width Reynolds number and c_{fo} is the zero-rotation wall shear stress coefficient for channel flow that is to be calculated using Eq (2).

The linear shear stress profile for fully-developed channel flow is

$$\frac{\tau}{\tau_{wo}} = \frac{\tau_{ws}}{\tau_{wo}} - \frac{\eta}{2}\left(\frac{\tau_{ws}}{\tau_{wo}} - \frac{\tau_{wu}}{\tau_{wo}}\right) \tag{13}$$

The dimensionless distance $\eta \doteq y/D$ is measured from the stable side ($\Omega < 0$ in this case using the notation of Fig 2) where the stable side wall stress, τ_{ws}, is taken to be positive in comparison to the unstable side wall stress, τ_{wu}, which is a negative number. The values of τ_{ws} and τ_{wu} in this analysis are obtained from the empirical results given in Eq (3) which is rewritten for our purposes in the forms

$$\tau_{ws}/\tau_{wo} = (1 - 1.75 \ Ro)^2 \tag{14a}$$

and

$$\tau_{wu}/\tau_{wo} = -(1 + 1.75 \ Ro)^2 \tag{14b}$$

Again the dissipation length is set equal to the mixing length in the turbulent wall-layer regions, and it is assumed that

$$L_c/D = \ell_c/D = \star\eta \quad (\text{for } 0 < \eta \leq m) \tag{15a}$$

$$L_c/D = \star m \quad (\text{for } \eta > m) \tag{15b}$$

The peak values of R will, because τ decreases as η increases, occur at $\eta \leq m$. The cut-off parameter m at which L_o levels out is, for the time being, not specified, but values of $m < 0.2$, the value used for boundary layers are not to be expected. The maximum possible value of m is 1.0 which fixes the maximum value of L_o at the channel centerline, $\eta = 1$: this is a physically unrealistic case, but as will be shown the one which tends to give the best results.

The effect of rotation on L is again calculated for the stable side by use of Eq (5) and the assumption $(L/L_o) = (\ell/\ell_o)$. The Richardson number, Ri, is computed from Eq (1) where the value of the parameter S is obtained by use of definitions for S and ℓ, see Notation and Eq (4), and by defining a parameter So $\doteq S(\ell_o/\ell)$, so

$$So = -\frac{2\Omega\ell_o}{\sqrt{\frac{\tau}{\rho}}} = \frac{Ro\,(\ell_o/D)}{\sqrt{\frac{c_{fo}}{2}\left(\frac{\tau}{\tau_{wo}}\right)}} \tag{16}$$

The parameter So, which may be computed directly once Re, Ro, β, $\star$ and m are specified, permits S to be obtained from Eq (5) put in the form

$$S(1 + \beta \ S(S + 1)) = So \tag{17}$$

This cubic equation is solved for S to obtain Ri and $L/L_o = S/So$.

The method and equations given above were used to calculate profiles of R versus η for given values of Re and Ro and various assumed values of β, $\star$ and m. Then the maximum, or peak, values of eddy Reynolds number were compared to the critical value $30\star$. If R_{max} fell below this limit the flow was judged to be transitional or laminar and incapable of maintaining a fully-turbulent state.

The calculated transition lines are compared to the full range of channel flow experiments in Fig 4a for $\beta = 0^*$, 2, 4, 6 and 8 with $\star = 0.4$ and m = 1.0. The regions below the lines are supposed to be turbulent and regions above are laminar or transitional. The most likely value of $\beta = 6$, see Fig 7b, permits good agreement with the data, but it could be argued that any β in the range 4 to 8 is equally valid. With $\beta = 6$ and m = 1, $\star$ was varied by ~ ± 10% to give the curves shown on Fig 4b. The exact value of the Karman constant does not appear to be vital to the analysis. Finally, the effects of m, the cut-off ratio for the mixing length distribution is examined in Fig 4c. Here the transition line is most sensitive to m at low- and zero-rotation and then only when m drops below 0.3. Hence use of $\beta = 6$, $\star = 0.4$ and m = 1 in this simple theory produces very reasonable results for existing rotating channel flow data on final transition to turbulence.

---

*The effect noted at $\beta = 0$ is entirely due to the shear stress assumptions, Eq (14). If $\tau_{ws} = \tau_{wu} = \tau_{wo}$ and $\beta \approx 6$ a curve very close to $\beta = 0$ in Fig 4a is generated. This indicates the importance of proper calculation of effects of Ro on both τ and ℓ.

-. CONCLUSIONS

The principal purpose of this paper has been to demonstrate the existence of a little known phenomenon - the stabilization of fully-turbulent shear-layer flow by Coriolis body forces caused by system rotation.

Channel flow experiments have shown that Coriolis forces on the stabilized side of the channel, where the gradient Richardson number is positive, cause a reduction in Reynolds shear stress and mixing length. Visual examination of the wall layer flow structure revealed that fully-turbulent flow cannot be sustained at high values of the rotation number, Rc, even when Reynolds numbers are as much as an order of magnitude higher than transition values at zero-rotation.

We hoped that the eddy Reynolds number criterion, which gives a condition required for a self-maintaining turbulent shear layer, could be applied to rotating flow with Coriolis stabilization. The criterion was applied to the turbulent boundary layer case, but lack of sufficient data precluded a direct check of the results. Application of the criterion to the prediction of the experimental transition limits in the case of channel flow was quite successful when carried out at fixed values of the constants (β, Λ and m) used in the calculation.

5. REFERENCES

1. Halleen, R. M. and Johnston, J. P. [1967], "The Influence of Rotation on Flow In A Long Rectangular Channel-An Experimental Study", Report MD-18, Mech. Engrg. Dept., Stanford University.

2. Johnston, J. P. [1970], "The Effects of Rotation on Boundary Layers In Turbomachine Rotors", Report MD-24, Mech. Engrg. Dept., Stanford University.

3. Moore, J. [1967], "Effects of Coriolis On Turbulent Flow In Rotating Channels", Report No. 89, M.I.T. Gas Turbine Laboratory.

4. Moore, J. [1969], "The Development of Turbulent Layers In Centrifugal Machines", Report No. 99, M.I.T. Gas Turbine Laboratory.

5. Litvai, E. and Preszler, L. [1969], "On The Velocity Profile Of The Turbulent Boundary Layer On Rotating Impeller Blading", Periodica Polytechnia, Mech. Engrg., Budapest, 13, pp. 215-228.

6. Gruber, J. and Litvai, E. [1969], "An Investigation of The Effects Caused By Fluid Friction In Radial Impellers", Proceedings of the 3rd Conference on Fluid Mechanics and Fluid Machinery, Akademiai Kindo Budapest, 1969, pp. 241-247.

7. Bradshaw, P. [1969a], "The Analogy Between Streamline Curvature and Buoyancy In Turbulent Shear Flow", J. Fluid Mech., Vol. 36, Part 1, pp. 177-191.

8. Bradshaw, P. [1969b], "A Note on Reverse Transition", Jour. of Fluid Mech., Vol. 35, Part 2, pp. 387-390.

9. Schraub, F. A., Kline, S. J., Henry, J., Runstadler, P. W. and Littell, A., [1965], "Use of Hydrogen Bubbles For Quantitative Determination of Time-Dependent Velocity Field In Low-Speed Water Flows", Trans. ASME (Ser. D), Vol. 87, pp. 429-444.

10. Kline, S. J., Reynolds, W. C., Schraub, F. A. and Runstadler, P. W., [1967], "The Structure of Turbulent Boundary Layers", J. Fluid Mech. Vol. 30, Part 4, pp. 741-773.

11. McMillan, O. J. and Johnston, J. P. [1970], "Performance Of Low-Aspect-Ratio Diffusers With Fully Developed Turbulent Inlet Flows", Report PD-14, Mech. Engrg. Dept., Stanford University.

12. Hussain, A.K.M.F. and Reynolds, W. C. [1970], "The Mechanics Of A Perturbation Wave In Turbulent Shear Flow", Report No. FM-6, Mech. Engrg. Dept., Stanford University.

13. Patel, V. C. and Head, M. R. [1969], "Some Observations On Skin Friction and Velocity Profiles In Fully Developed Pipe And Channel Flows", J. Fluid Mech., Vol. 38, Part 1, pp. 181-201.

14. Potter, M. C. and Chawla, M. D. [1970], "The Stability of Boundary Layer Flow Subject to Rotation" (Private communication) also: Ph.D. Thesis by M. D. Chawla, Michigan State University, 1969.

15. Bradshaw, P., Ferriss, D. H. and Atwell, N. P., [1967], "Calculations of Boundary Layer Development Using The Turbulent Energy Equation", J. Fluid Mech., Vol. 28, p. 593.

6. ACKNOWLEDGEMENTS

DEVELOPMENT OF A TURBULENT BOUNDARY LAYER
ON A FLAT PLATE IN AN EXTERNAL TURBULENT FLOW

G. CHARNAY*, G. COMTE-BELLOT**, J. MATHIEU***
LABORATOIRE DE MECANIQUE DES FLUIDES DE L'ECOLE CENTRALE DE LYON

SUMMARY

The development of a turbulent boundary layer on a flat plate has been experimentally investigated in the presence of an external turbulent flow generated by grids.

With reference to a turbulent boundary layer evolving in an undisturbed flow the following results have been observed when the external turbulence level is increasing :

- the boundary layer grows more rapidly ;
- the wall shear stress is higher ;
- in the outer region of the layer the mean velocity profile becomes flatter and the law of the wake is modified. In the same region the turbulent levels are increased ;
- the turbulent shear stress and the turbulent kinetic energy production become larger.

Various integral length scales of the external turbulent flow have also been used. A discernable effect has been observed on the integral scales of the boundary layer only.

A rearrangement of the external isotropic turbulence, due to the straining process of the mean existing velocity/gradient in the boundary layer is tentatively proposed.

RESUME

Le développement d'une couche limite turbulente sur plaque plane, sans gradient de pression, en présence d'un écoulement extérieur turbulent est étudié.

Par rapport à une couche limite turbulente non perturbée, lorsque l'intensité de la turbulence extérieure augmente on observe :

- l'épaississement plus rapide de la couche,
- l'augmentation du coefficient de frottement à la paroi,
- l'aplatissement des profils de vitesses moyennes dans la zone de sillage et la modification de la loi de sillage qui s'infléchit. Dans la même zone les valeurs efficaces des fluctuations de vitesses sont accrues,
- l'augmentation dans la partie externe de la couche des tensions turbulentes et de la production d'énergie turbulente,
- l'accroissement des échelles intégrales de turbulence.

Différentes échelles intégrales ont été aussi utilisées pour l'écoulement extérieur. Il a été seulement observé un effet perceptible sur les échelles intégrales de la couche limite.

Une restructuration de la turbulence extérieure isotrope par le gradient de vitesse moyenne de la couche limite, conduisant à l'apparition de tensions turbulentes supplémentaires, semble pouvoir expliquer les résultats expérimenteux obtenus.

MAIN NOTATIONS USED

OX_i : axes (X_1 in the flow direction, X_2 normal to the plate)

X_1 : distance from the leading edge of the plate.

δ : thickness of the boundary layer $U_1(\delta) = 0.99 U_1^o$

U_i : mean velocity components in the X_i directions.

u_i : fluctuating velocity components.

$\widetilde{u_i}$: $\left[\overline{u_i^2} \right]^{1/2}$

$\overline{u_1 u_2}$: velocity correlation at a point.

U_1^o : mean velocity in external flow.

u_i^o : fluctuating velocity components in external flow.

U_f : friction velocity.

R_δ : Reynolds number based on δ $\left(\frac{U_1^o \delta}{\nu} \right)$

C_f : skin friction coefficient.

ν : coefficient of kinematic viscosity.

$L_{11,2}$: transverse integral length scale (u_1 fluctuation).

$L_{11,2}^o$: transverse integral length scale in external flow (u_1 fluctuation).

(For other notations refer to Fig. 1)

1. INTRODUCTION

In a number of practical situations, boundary layers evolve in presence of an external stream exhibiting large unsteady velocity variations. This manifests itself either as pulsations at fixed frequencies, or as random disturbances. The former occurs in case of airfoils belonging to the downstream stages of a multistage turbomachinery, the later to planes having to cope with turbulent atmospheres.

The present investigation is focused on the basic problem of a boundary layer on a smooth plane wall, without mean pressure gradient, but with turbulence in the external stream. SUGAWARA, SATO, KOMATSU and OSAKA (1953), then KLINE, LISIN and WAITMAN (1960) have already observed that high levels of free stream turbulence increase the thickness of the boundary layer, create fuller velocity profiles and alter the values of the longitudinal velocity fluctuations. Similar investigations done by KOMODA (1957) on the behaviour of a turbulent wake into a turbulent flow revealed an increase in the lateral spreading of the wake and the intensity of turbulence.

Both these investigations are related to the foundamental question dealing with the behaviour of two adjacent isotropic turbulences, as pointed out by CORRSIN and KISTLER (1955) and tentatively tested out by TOWNSEND (1956) and MOBBS (1968). Both intensity and scale of the external turbulence are therefore essential parameters which must be dealt with. The boundary layer case may be more avantageous than the wake case because in absence of external perturbations the turbulent level in the outer part is low. Another fundamental question arises from the mean velocity gradient and its subsequent mass entrainment process. An anisotropic external turbulence could therefore act differently from an isotropic one. The Reynole stresses existing in the external turbulence, mainly $-\rho\, \overline{U_1 U_2}$, can also become a relevant parameter of the problem, both in positive and negative values.

In the present investigation we have limited our scope to the effect of a closely approaching isotropy external turbulence generated by grids. Various configurations have been made in order to control independently the intensity and the scale of the external turbulence.

2. EXPERIMENTAL SET UP

2.1. Fluid mechanical apparatus

The wind tunnel is of the open return type. Air is driven by a blower placed upstream. The settling chamber is equipped with dust filters. The test section, 2,5 m long, has a cross section of about $0.5 \times 0.5\ m^2$ (Fig. :).

Immediately upstream of the test section is the turbulence - promoting section. Biplane grids with square meshes are used. Their rods (horizontal and vertical, respectively) are round or rectangular, and a choice can be made about the spacing between the rods planes (Fig. 1). The solidity of the grids lies between 0,30 and 0,42. The grid can be located at varying distances from the leading edge of the test plate.

The flat plate is horizontal, 2 m long, 0,5 m wide and 0,018 m thick. It is made of hard and polished wood. It rests upon an independent base by means of four struts, and a mass loaded suspension which has a 2 Hz natural frequency. The leading edge of the plate is a slightly asymmetric wedge with a rounded nose (Fig. 1). An adjustable flap is located at the downstream end of the test section. It is used in experiments on laminar boundary layers to set the position of the stagnation point and it is actually horizontal.

2.2. Measuring equipment and procedure

All data were taken with platinum wire, 5μ in diameter, connected to a DISA 55 DOI constant temperature unit. A single wire set normal to the mean flow is used for axial velocity measurements. Transvaree components of the velocity were obtained by means of a X - meter · Sensitivities to U_1 and U_2 fluctuations are determined directly from the empirical curves of voltage versus velocity and angle. For X meters, weighted differences or sums of the output signals are performed by means of Burr-Brown operational amplifiers. The distance from the wires to the plate is optically determined, within an accuracy of 0.02 mm.

Transverse integral scales $L_{11,2}$ are obtained from the curves giving the two-points velocity correlation. The band width of the electronic circuitry is 5 Hz-20 KHz.

Wall-shear stress measurements are performed by means of a Preston tube (outer diameter 4 mm).

3. EXPERIMENTAL CONDITIONS

3.1. External flow

All measurements are taken at a mean speed U_1^o of 10 m/sec. The top wall of the test section is set slightly divergent in such way that no measureble axial mean velocity gradient occurs.

Without grid in the tunnel the turbulence level $\widetilde{U_1^2}/U_1^o$ is about 0.3 % on the tunnel axis.

In the first part of the investigation we established, at a given cross section X_1 , a turbulence of 6 different levels and approximatively of the same integral length scale. To achieve our second aim all the grids had equal meshes and were placed at the

same distance ℓ upstream from the leading edge of the plate. To attain the various levels, the geometry of the rods and the spacing of the two planes of rods were modified. Fig. 2 shows the obtained characteristics.

In the second part we adjusted, at a given cross section X_1, approximately the same turbulence level and two different integral length scales. Therefore we used grids whose meshes were different. However each grid is set at the same number of meshes upstream from the cross section X_1. For more systematic tests this kind of experiment was repeated at four different turbulence levels (Fig. 3).

3.2. Boundary layer

Baceuse of the plate being rather short, the turbulent boundary layer is simply obtained by allowing the separation to occur at the very beginning of the plate.

Without external turbulence, we have verified that the existing main characteristics (U_1 , $\widetilde{U}_1$, $\widetilde{U}_2$, $\overline{U_1 U_2}$) of this boundary layer show self-preserved profiles for $X_1 >$ 50 cm. Also a satisfactory two-dimensionality was identified, and at the downstream end of the plate the useful width was down to 25 cm. The boundary layer Reynolds number $U_1^o \delta / \gamma$ is about 20 000.

For the different external flow conditions, the virtual origins of the boundary layer are about 25 $\pm$ 5 cm upstream of the leading edge.

4. EFFECTS OF THE EXTERNAL TURBULENCE LEVEL

4.1. Thickness rate

Fig. 4 illustrates the strong increase of the thickness rate of the boundary layer with the external turbulence level $\widetilde{U}_1^o / U_1^o$. For instance the ratio of the thickness rates $[(d\delta/dX_1)_{\overline{U_1}} / (d\delta/dX_1)_{\overline{U_1} > 0}]_{X_1}$ with and without the grid creating the external turbulence, can reach about 1.5 for $\widetilde{U}_1^o / U_1^o$ = 5 % at X_1 = 0.5 m. In these results the accuracy is limited to $\pm$ 4 % because of the difficulty to locate the boundary layer edge.

4.2. Wall shear stress

At a given boundary layer Reynolds number $U_1^o \delta / \gamma$, we observe a systematic increase of the friction factor C_f with $\widetilde{U}_1^o / U_1^o$ (Fig. 5). For instance, the range 0.0037 to 0.0044 is covered when $\widetilde{U}_1^o / U_1^o$ varies from 0,3 % to 5 %. A $\pm$ 4 % accuracy is expected on these results.

4.3. Mean velocity profiles

The effect of $\widetilde{U}_1^o / U_1^o$ on the dimensionless representations of U_1 / U_1^o versus X_2 / δ is shown in Fig. 6, X_1 being kept constant. We can observe that at a same X_2 / δ the value of U_1 / U_1^o noticeably increases with $\widetilde{U}_1^o / U_1^o$. To provide an order of magnitude of this effect the power law $U_1 / U_1^o = (X_2 / \delta)^{1/m}$ can be used. Then the exponent m is found to increase from 5.3 to 8.2 when $\widetilde{U}_1^o / U_1^o$ varies from 0.3 to 5 % (Fig. 7). Another result is the lack of self preservation in the mean velocity profiles at different X_1 , for a given grid creating the external turbulence.

In the law of the wall representation U_1 / U_f versus $X_2^+ \equiv X_2 U_f / \gamma$ (Fig. 8) the investigated $\widetilde{U}_1^o / U_1^o$ levels inflect the curves beyond $X_2^+ = 300$ and do not seem to affect the profile for $X_2^+ <$ 300. In the defect law representation $(U_1^o - U_1)/U_f$ versus X_2 / δ this result appears more clearly (Fig. 9).

4.4. Turbulence level in the boundary layer

In the outer part of the boundary layer the turbulence levels $\widetilde{U}_1 / U_1$ are strongly increased by the external turbulence (Fig. 10). But in the proximity of the wall they remain almost unaltered. Analogous results are also obtained on the $\widetilde{U}_2 / U_1$ and $\widetilde{U}_3 / U_1$ values, for the outer part of the boundary layer.

4.5. Reynolds stress

The $\overline{U_1 U_2} / U_f^2$ profiles are likewise altered (Fig. 11), mainly in the outer region $0.8 < X_2 / \delta < 1.2$. There, in spite of the nearly isotropic state of the external turbulence, $\overline{U_1 U_2} / U_f^2$ increases by about 150 % when $\widetilde{U}_1^o / U_1^o$ varies from 0.3 to 5 %. Subsequently the main term of the turbulent kinetic energy production $\dfrac{\overline{U_1 U_2}}{U_f^2} \cdot \dfrac{d(U_1 / U_1^o)}{d(X_2 / \delta)}$ is increased despite the decrease present in $\partial U_1 / \partial X_2$.

4.6. Integral length scales

The distribution of $L_{11,2} / \delta$ across the boundary layer does not seem to depend upon the external turbulent fields which have different levels and a fixed integral

scale (Fig. 12, curve I). However the obtained distribution is different from the one corresponding to the boundary layer evolving in an almost perturbations free external flow (Fig. 12, curve II).

5. EFFECT OF THE EXTERNAL INTEGRAL LENGTH SCALE

Due to the scattering of the experimental results, no relationship between the established integral length scales of the external flow end the mean velocity profiles could be discerned. These profiles have been plotted in the three different ways as mentioned in section IV. Likewise no definite affect has been observed neither for the turbulence levels (both $\widetilde{U_1}/U_1^c$ and $\widetilde{U_2}/U_1^c$) nor for the wall shear stress, despite a slight increase of the boundary layer thickness rate with the external integral scale.

On the other hand the integral scales $L_{11,2}$ in the outer part of the boundary layer (Fig. 13) are strongly depending on the corresponding scales of the external flow.

6. CONCLUSION

The above experimental results show that a boundary layer is affected by an external quasi isotropic turbulence, this turbulence being more efficient by its level than by its integral length scale.

One of the most significant result seems to be the increase of the Reynolds stress $-\rho\,\overline{U_1.U_2}$ with $\widetilde{U^0}/U_1^c$. Actually a tentative interpretation (proposed by one of us, J.M.) could be based on the fact that an initially isotropic turbulence, submitted to a mean shear, later becomes anisotropic. (CRAYA 1958, ROSE 1966, CHAMPAGNE, HARRIS and CORRSIN 1970). Particularly the Reynolds stress $-\rho\overline{U_1 U_2}$ which appears depends on the initial turbulence level and on the atraining process. In our investigation an external "blob" of isotropic turbulence may acquire a $-\rho\,\overline{U_1 U_2}$ stress after its entrainment into the boundary layer, because of the mean velocity gradient existing there. As e consequence the distinct defect velocity profiles of Fig. 9 can be brought together (Fig. 14) by using the representation

$$\frac{U_1^0 - U_1}{U_f - \alpha\widetilde{U^0}} = f(\frac{X_2}{\delta})$$

where the quantity $\alpha.\widetilde{U^0}$ which takes into account the rearrangement of the external turbulence has been substracted from the friction velocity   .

To enlarge this work some additional experimental investigations are possible :

(i) - an analysis of the turbulent kinetic energy balance with a special focus on the convective term $\partial\,\overline{U_1(U_1^2+U_2^2+U_3^2)}/\partial X_2$ due the turbulent motion.

(ii) - a detection of the boundary layer edge, enu by means of a conditional sampling system (KOVASZNAY, KIBENS end BLACKWELDER, 1970) obtain properties of the only turbulence of the boundary layer.

(iii) - an extension of the experiments towards higher turbulence levels, probably obtained by means of "blowing" grids (MATHIEU et ALCARAZ, 1965).

(IV i) - finally, the investigation of an additional uniform mean shear in the external flow, this shear being "favorable" or "adverse" to the one existing in a boundary layer.

REFERENCES

- CHAMPAGNE F.H., HARRIS V.G. and CORRSIN S. (1970) - Experiments on nearly homogeneous turbulent shear flow, J. Fl. Mech. 41, 81-139.

- CORRSIN S. and KISTLER A. (1955) - Free stream boundaries of turbulent flow, N.A.C.A., T.R. 1244.

- CRAYA A. (1958) - Contribution à l'analyse de la turbulence associée à des vitesses moyennes, Publ. Sc. Tech. Min. Air, Paris, n° 345.

- KLINE S.J., LISIN A.V. and WAITMAN B.A. (1960) - Preliminary experimental investigation of effect of free stream turbulence on turbulent boundary layer growth, N.A.C.A., T.N. D-368.

- KOMODA H. (1957) - On the effect of free-stream turbulence on the structure of turbulent wake, J. Japan Soc. Aero. Eng., 274-279.

- KOVASZNAY L.S.G., KIBENS V., and BLACKWELDER R.F. (1970) - Large-scale motion in the intermittent region of a turbulent boundary layer, 41, 283-325.

- MATHIEU J., ALCARAZ E. (1965) - Réelisation d'une soufflerie à haut niveau de turbulence, C.R. Acad. Sc. Paris, 2435-2438.

- MOBBS F.R. (1968) - Spreading and contraction st the boundaries of free turbulent flows, J. Fl. Mech. 33, 227-239.

- ROSE W.G. (1966) - Results of an attempt to generate a homogeneous turbulent shear flow, J. Fl. Mech. 25, 57-120.
- SUGAWARA S., SATO T., KOMATSU H. and OSAKA H. (1958) - The effect of free-stream turbulence on heat transfer from a flat plate, N.A.C.A. Tech. Memorandum 1441.
- TOWNSEND (1956) - The structure of turbulent shear flow, Cambridge Univ. Press.

ACKNOWLEDGMENTS

*   Assistant à l'Université de Lyon - Enseignant à l'Ecole Centrale de Lyon
** Professeur à l'Université de Lyon - Enseignant à l'Ecole Centrale de Lyon
*** Professeur à l'Université de Lyon - Enseignant à l'Ecole Centrale de Lyon

Lyon, le 30 juin 1971

CAPTIONS FOR THE FIGURES

1. Sketch of wind-tunnel test section.
2. Turbulence levels and integral length scales generated by grids of fixed mesh.
3. Turbulence levels and integral length scales generated by grids of different meshes.
4. Thickness rate of the boundary layer versus $\widetilde{u_1^o}/U_1^o$
5. Friction factor C_f versus R_δ , for different $\widetilde{u_1^o}/U_1^o$
6. Mean velocity profiles.
7. Power law coefficient m versus $\widetilde{u_1^o}/U_1^o$
8. Logarithm representation of mean velocity profiles.
9. Defect law representation of mean velocity profiles.
10. Turbulence level profiles (longitudinal component)
11. Reynolds stress profiles
12. Transverse integral length scale profiles for different $\widetilde{u_1^o}/U_1^o$ and fixed M.
13. Transverse integral length scale profiles for different M and fixed $\widetilde{u_1^o}/U_1^o$
14. Rescaling of the defect velocity profiles.

Fig. 1 Sketch of wind-tunnel test section.
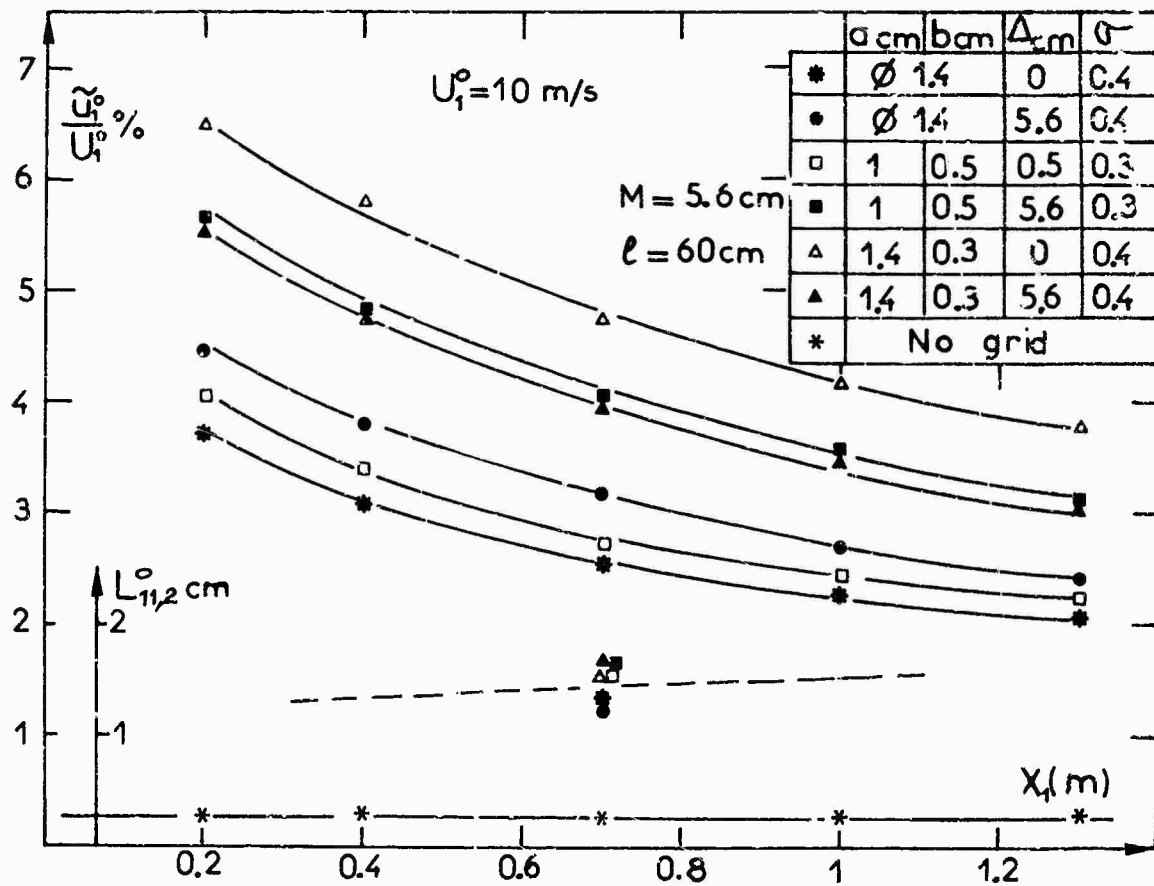
27.6

$U_1^o = 10$ m/s

$\dfrac{\tilde{u}_1^o}{U_1^o}\%$

$M = 5.6$ cm

$\ell = 60$ cm

$L_{11,2}^o$ cm

$X_1(m)$

	a cm	b cm	Δ cm	σ
✶	Ø 1.4		0	0.4
●	Ø 1.4		5.6	0.4
□	1	0.5	0.5	0.3
■	1	0.5	5.6	0.3
△	1.4	0.3	0	0.4
▲	1.4	0.3	5.6	0.4
✳	No grid			

Fig. 2 Turbulence levels and integral length scales generated by grids of fixed mesh.

Δ = 0

$\dfrac{\tilde{u}_1^o}{U_1^o}\%$

$X_1(m)$

$L_{11,2}^o$ (cm)

$X_1 = 0.7$ m

$\dfrac{\tilde{u}_1^o}{U_1^o}\%$

	a cm	b cm	l cm	M cm	σ
○	Ø=0.5		20	2	0.42
●	Ø=1.4		170	5.6	0.40
✳	0.5	1	25	2.5	0.34
✴	1	0.5	130	5	0.32
△	1	0.5	40	5	0.32
▲	2	0.5	160	10	0.30
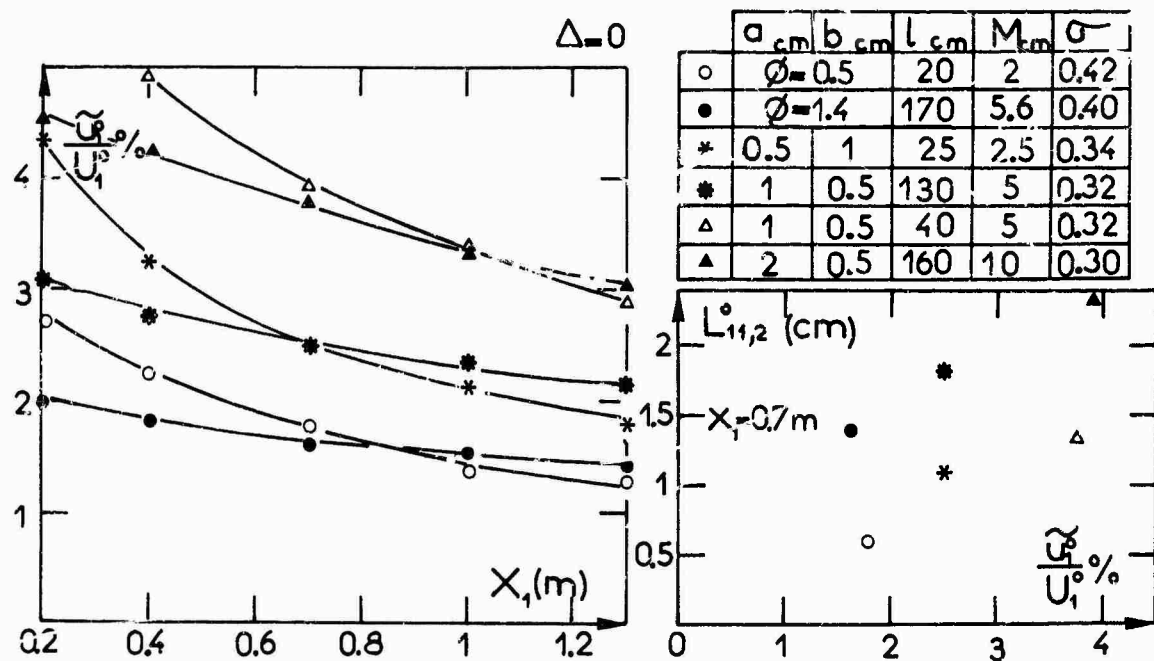
Fig. 3 Turbulence levels and integral length scales generated by grids of different meshes
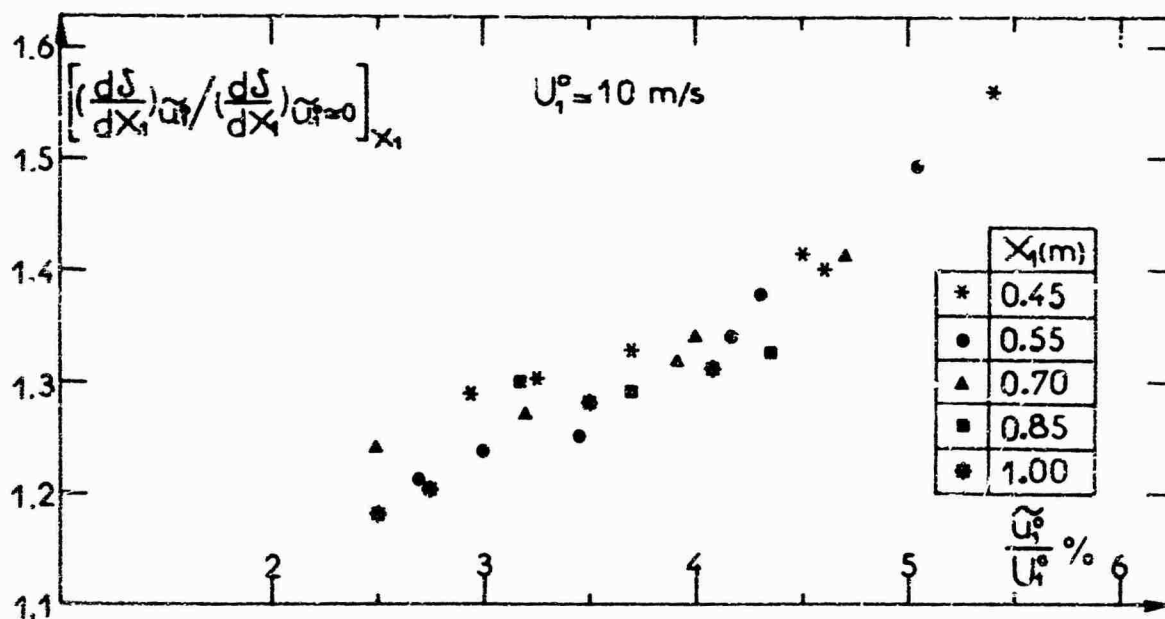
Fig. 4 Thickness rate of the boundary layer versus $\tilde{u}_1^o/U_1^o$.
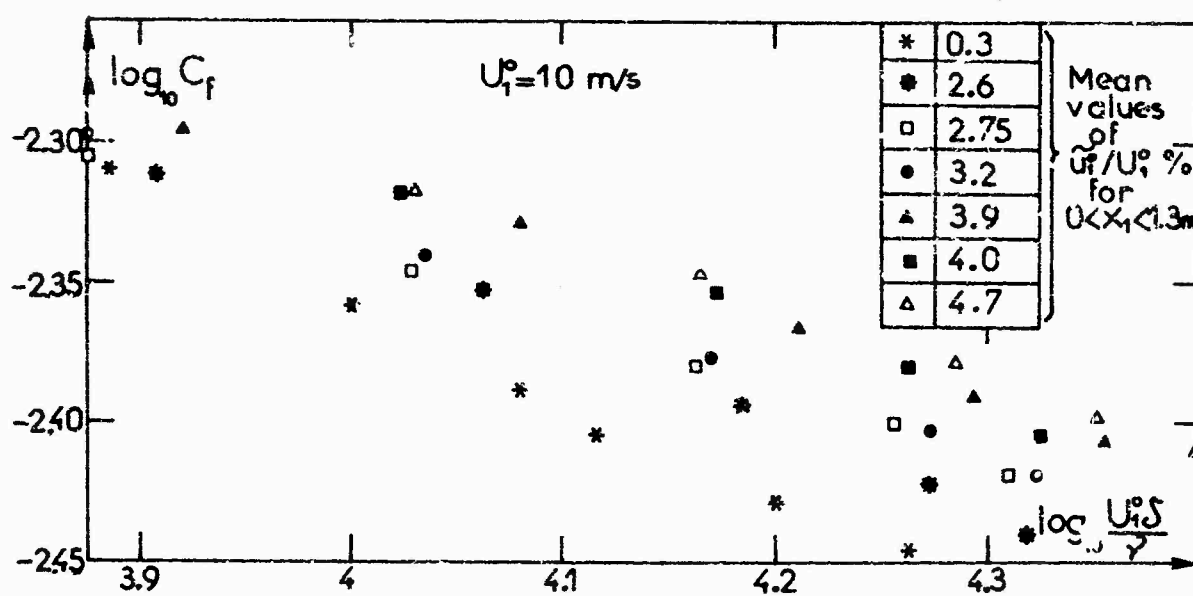
Fig. 5 Friction factor C_f versus R_δ, for different $\tilde{u}_1^o/U_1^o$.
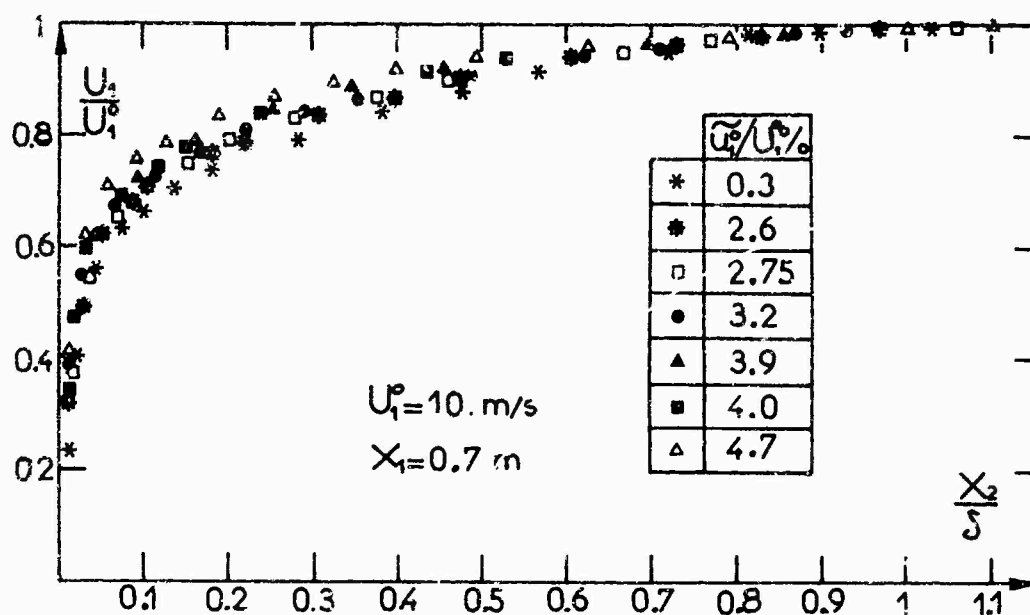
Fig. 6 Mean velocity profiles.
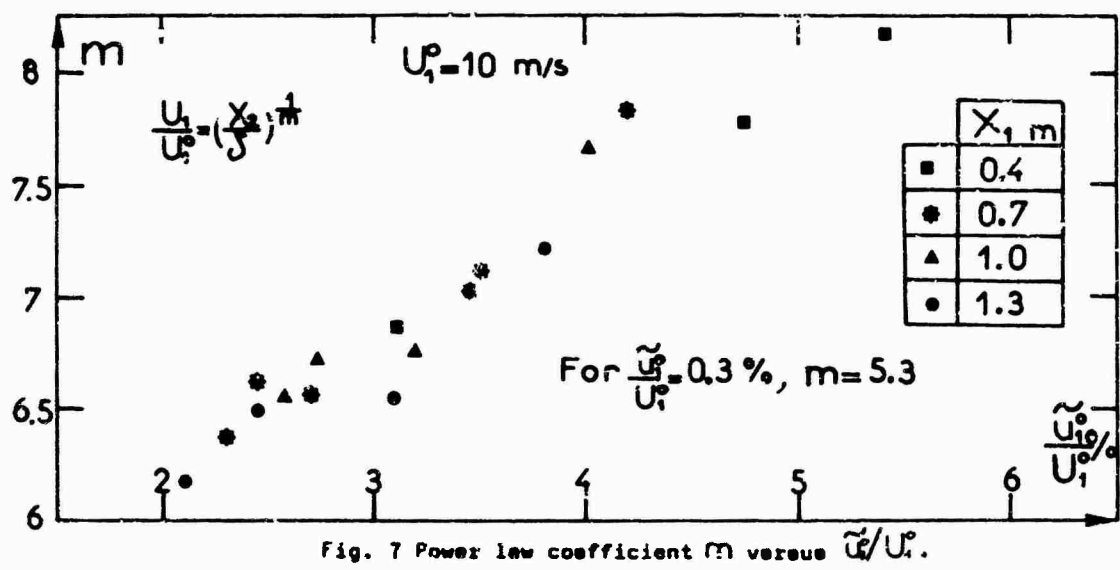
Fig. 7 Power law coefficient m versus $\tilde{u}_0^\infty/U_1^\infty$.
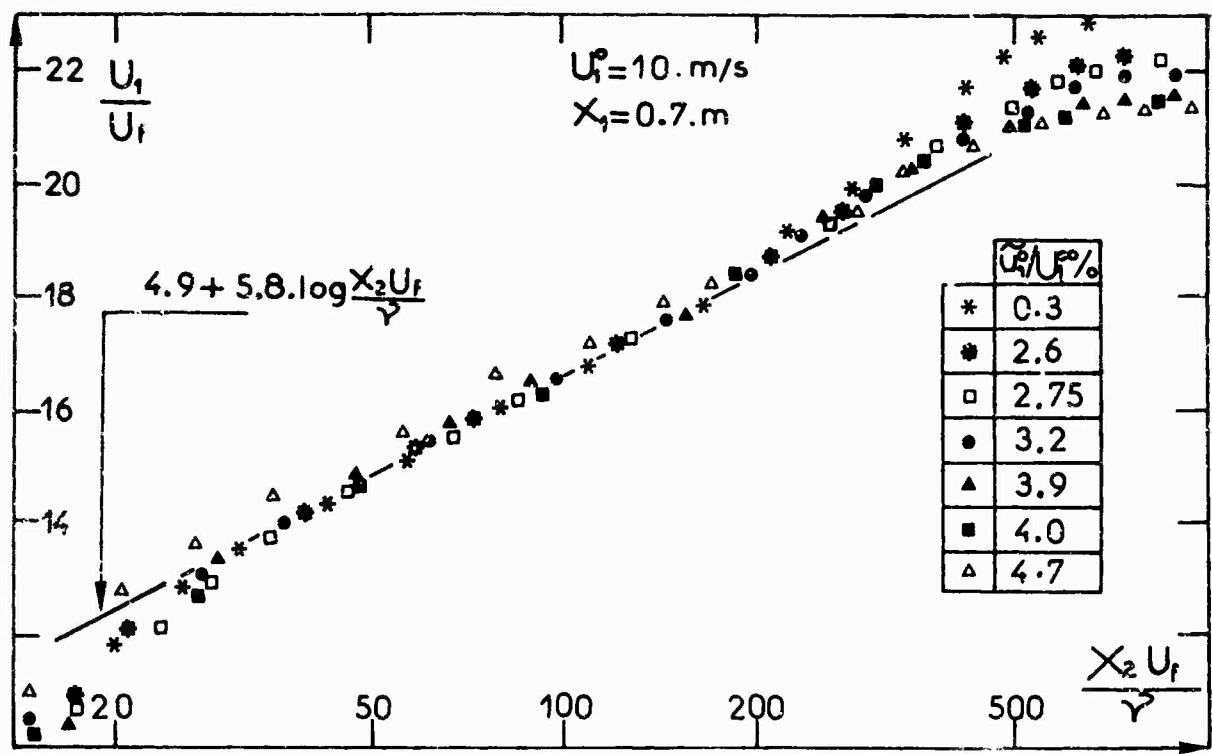
Fig. 8 Logarithm representation of mean velocity profiles.
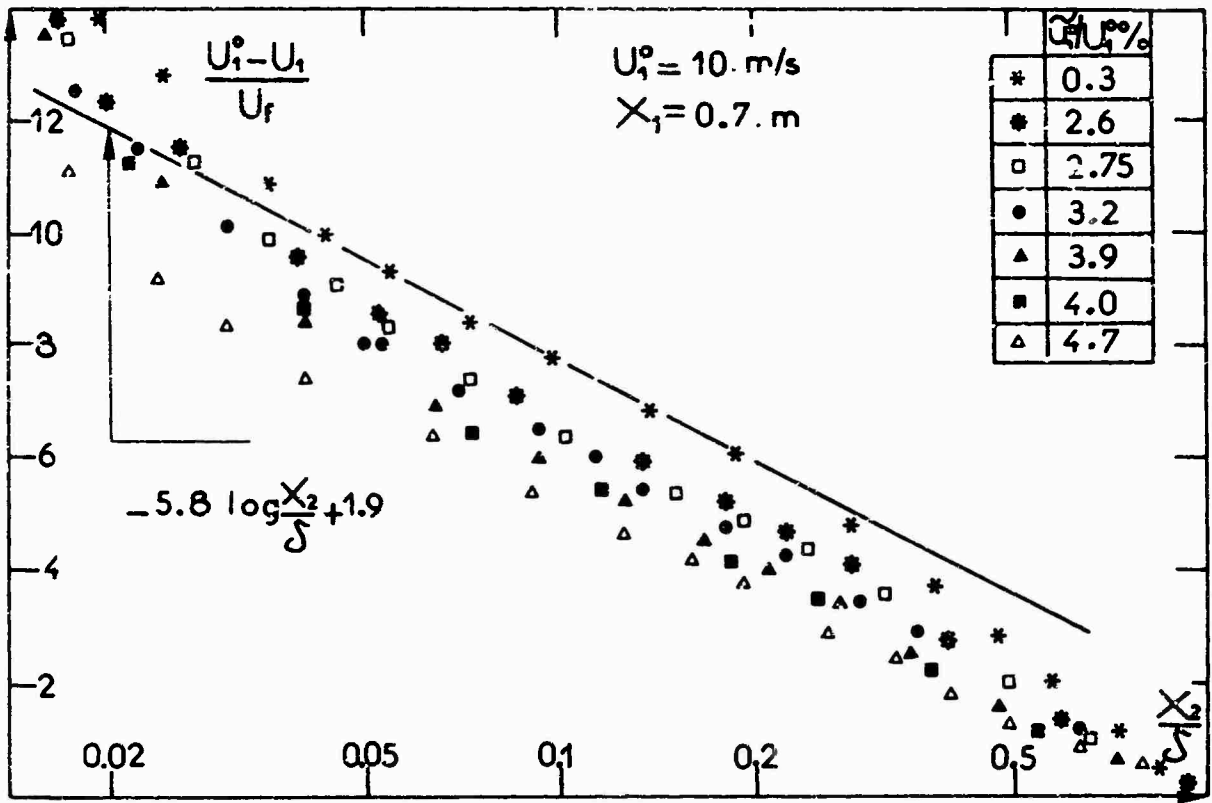
Fig. 9 Defect law representation of mean velocity profiles.
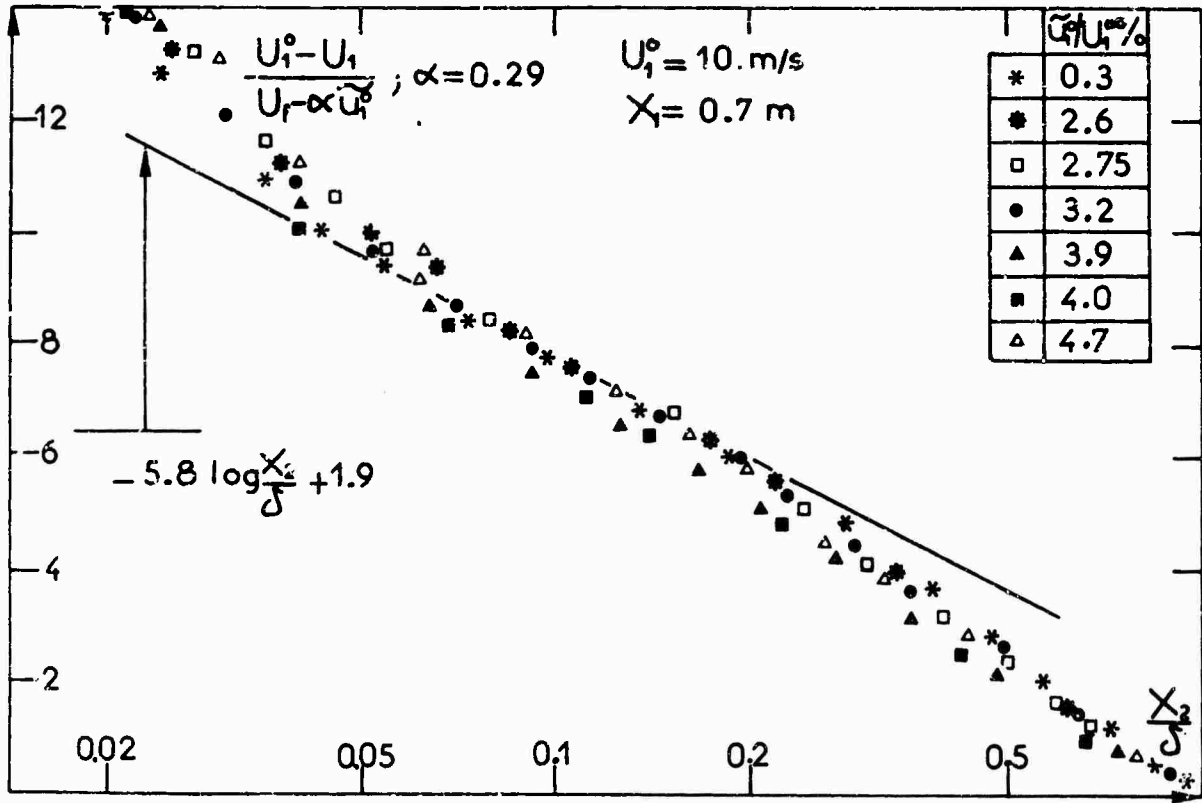
Fig 14 Rescaling of the defect velocity profiles.
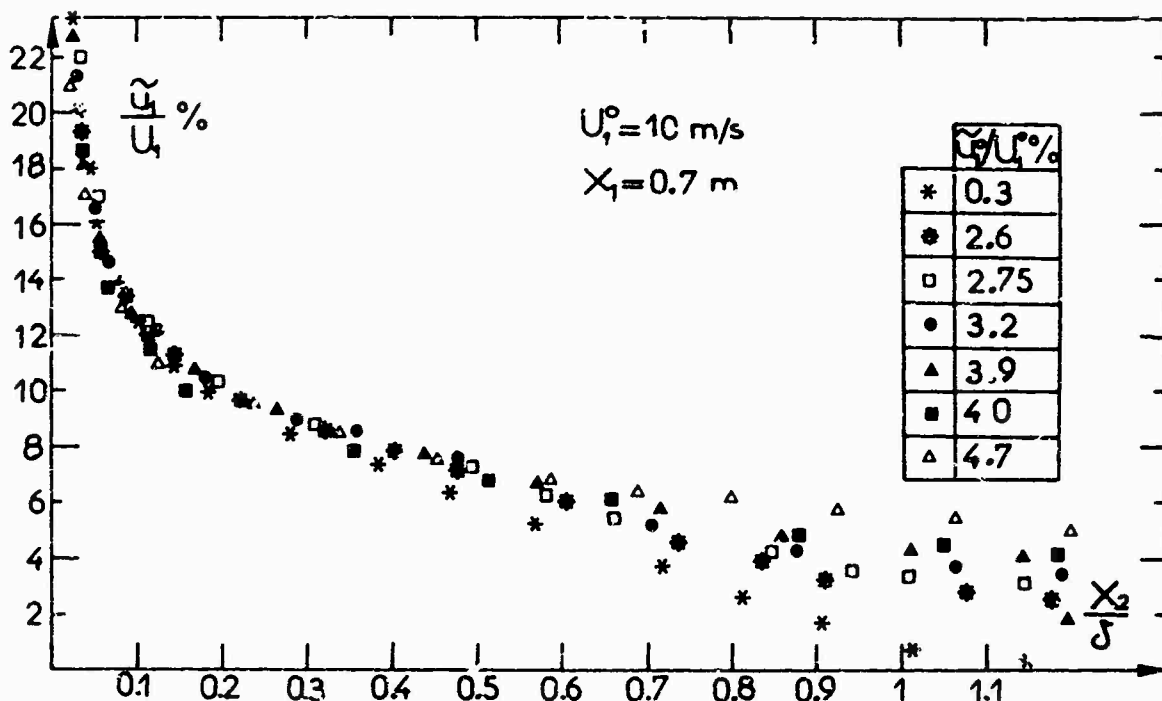
$\dfrac{\tilde{u}}{U}$ %

$U_1^o = 10$ m/s

$X_1 = 0.7$ m

	$\tilde{U}_2^o/U_1$%
*	0.3
✳	2.6
□	2.75
●	3.2
▲	3.9
■	4 0
△	4.7

$\dfrac{X_2}{\delta}$

fig. 10 Turbulence level profiles (longitudinal component).

$\overline{\dfrac{u_1 . u_2}{U_f^2}}$

	$\tilde{U}_2^o/U_1$%
*	0.3
✳	2.6
□	2.75
▲	3.9
■	4.0
△	4.7

$U_1^o = 10$ m/s

$X_1 = 0.7$ m

$\dfrac{X_2}{\delta}$

Fig. i1 Reynolds stress profiles.

$\dfrac{L_{11,2}}{\delta}$

$X_1 \, 07$ m

curve I

curve II

U_2^o%	$L_{11,2}^o$ cm
2.7	1.5
3.9	1.7
4.0	1.6

$\dfrac{X_2}{\delta}$

Fig. 12 Transverse integral length scale profiles for different U_2^o/U_1^o and fixed M.

$\dfrac{L_{11,2}}{\delta}$

$X_1 = 0.7$ m

U_2^o%	$L_{11,2}^o$ cm
○	1.55	0.60
●	1.30	1.35
*	2.50	1.05
✳	2.50	1.85
△	3.9	1.30
▲	3.8	2.20

$\dfrac{X_2}{\delta}$
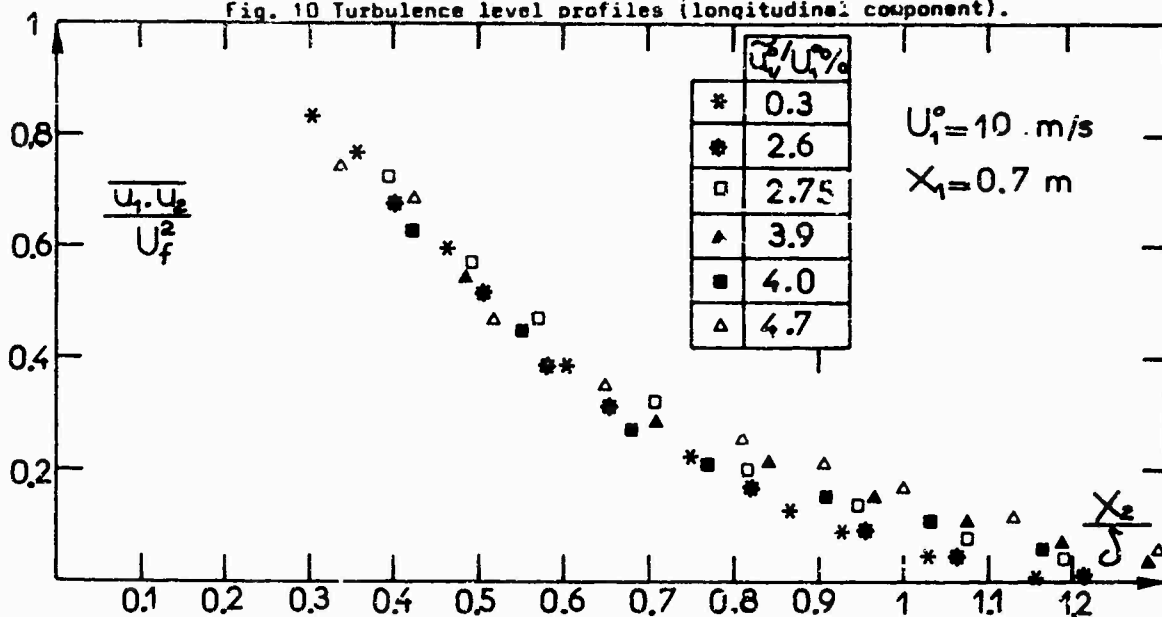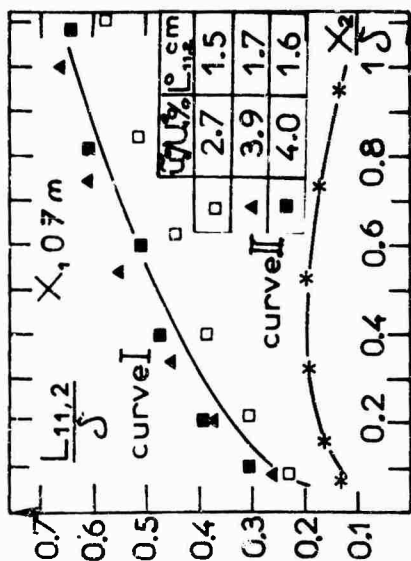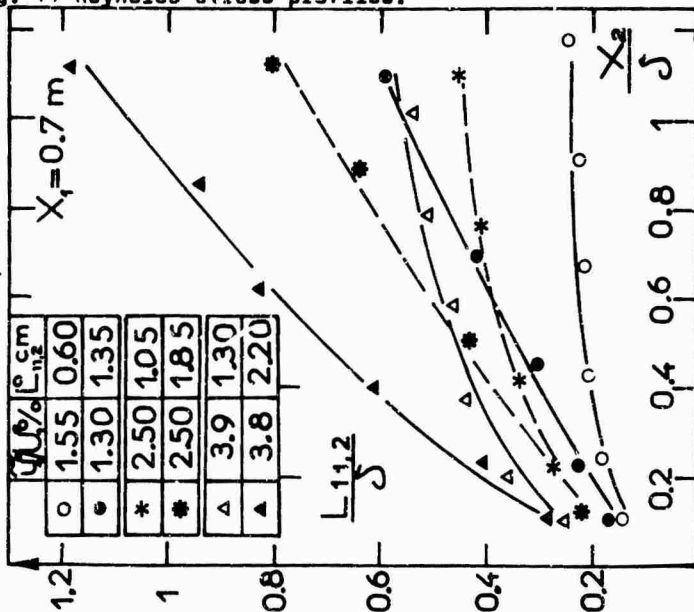
Fig. 13 Transverse integral length scale profiles for different M and fixed U_2^o/U_1^o.

SOME MEASUREMENTS OF THE DISTORTION OF TURBULENCE
APPROACHING A TWO-DIMENSIONAL BODY

P.W. Bearman[*]
Aeronautics Dept., Imperial College
London S.W.7.

SUMMARY

This paper describes an experimental study of the distortion of grid generated turbulence as it approaches the stagnation region of a two-dimensional body. When $L_x/D \gg 1$, where L_x is the scale of turbulence and D is a typical body dimension, along the mean stagnation streamline $\sqrt{u^2}$ attenuates like the mean flow. Whereas if $L_x/D \ll 1$ the turbulence is distorted by the mean flow field and $\sqrt{u^2}$ will amplify due to vortex stretching. When $L_x/D = O(1)$ there is found to be a combination of these effects with attenuation of energy at low wavenumbers and amplification at high wavenumbers. Measurements of the pressure fluctuations at the stagnation point show that at low wavenumbers the level of the pressure fluctuations can be predicted by assuming the turbulence to be irrotational.

1. INTRODUCTION

When a body is placed in a turbulent shear flow, for example a building in the Earth's boundary layer, there will be some complex interaction between the mean flow field around the body and the approaching stream turbulence. This interaction will influence the relationship between upstream velocity fluctuations and the resulting pressure fluctuations on the body surface. The aim of the research described in this paper was to study experimentally the passage of grid generated turbulence as it approaches the stagnation region of a two-dimensional body. Although this is a simpler problem than that posed above, it retains the important feature of turbulence distortion.

Hunt [1] has formulated a theory, based on the rapid distortion theory of Batchelor and Proudman [2], to analyse the distortion of turbulence in a flow sweeping past a body. The principal assumption made in the theory is that, in the time it takes for the turbulence to be swept past the body, the changes in the mean flow around the body and the effects of its boundaries distort the turbulence far more than its own internal viscous and non-linear inertial forces. The turbulence will be distorted by the stretching and rotating of vortex line filaments as they are convected past the body. The assumptions made in rapid distorting theory are firstly that the mean flow is irrotational and secondly that $\sqrt{u^2}/U \ll 1$ (where $\sqrt{u^2}$ is the root mean square value of the longitudinal component of the velocity fluctuations and U is mean velocity), so that the dominant contribution to the distortion comes from changes in the mean flow and not from the turbulence itself. The neglect of viscous effects is justified if the distortion takes place in such a short time that the viscous decay of energy is very small. Batchelor and Proudman [2] suggested the criterion

$$\iota - t' \ll \left(\frac{L_x}{\sqrt{u^2}}\right)_{t=t'}$$

where t' is the time at the beginning of the distortion and L_x is the integral scale of the longitudinal component of turbulence, say. For the flow past a body

$$t - t' = O\left(\frac{U_o}{D}\right)$$

where U_o is free stream velocity and D is a typical body dimension. This leads to the third condition that

$$\frac{\sqrt{u^2_o}}{U_o} \ll \frac{L_x}{D}$$

Using these three assumptions Hunt treated the problem of initially isotropic turbulence convected past a circular cylinder. Although the theory of Hunt will not be used directly the interpretation of the experimental results presented in this paper draws heavily on the basic ideas underlying this theory.

The flow was investigated along the stagnation streamline approaching a two-dimensional flat plate placed normal to the flow. The strain field along this line is described by the tensor

$$\alpha_{ij} = \frac{\partial U_i}{\partial x_j} = \left\{ \begin{array}{ccc} \frac{\partial U}{\partial x}, & 0, & 0 \\ 0, & -\frac{\partial U}{\partial x}, & 0 \\ 0, & 0, & 0 \end{array} \right\}$$

and the turbulence is only subjected to plane strain. Experimental work on uniform plane strain has been carried out by several investigators, including Townsend [3] and Tucker and Reynolds [4], in suitably shaped distorting ducts. These experiments are unsatisfactory in the sense that the condition $\sqrt{u^2}/U \ll L_x/D$ (where D is some duct dimension) is not met. Tucker and Reynolds, however, have made suitable allowance for viscous decay in the analysis of their results. In some respects the external flow around bodies is more suited to a rapid distortion treatment although there are regions of the flow, especially very close to the stagnation point, where the conditions of the theory are not satisfied. Along the stagnation streamline there is some balance between the distortion created by the modification to the vorticity field by the mean flow, which will increase $\sqrt{u^2}$, and the effect of the boundary

---

[*]formerly of National Physical Laboratory, Teddington, Middlesex, England.

condition, that there can be no velocity normal to the body surface, which will reduce $\overline{v_2}$.

The phenomenon of increased turbulence ahead of stagnation was first noted by Fiercy [5] in some measurements ahead of an aerofoil in a wind tunnel with a high background turbulence level. Work has been carried out by Sutera, Maeder and Kestin [6] and by Sutera [7] on the role of vorticity amplification in stagnation flow. They have examined theoretically a simple form of spatially varying, sinusoidal pattern of vorticity, favourably orientated to produce stretching, approaching a stagnation point. They find a neutral scale length for which amplification by stretching is exactly balanced by viscous dissipation. This theory has been extended by Sadeh, Sutera and Maeder [8, 9] to the outer flow field for a similar form of vorticity distribution. Their theory does not, however, allow for the important effect of the upstream influence of the condition that there can be no velocity normal to the surface. Their theory is only valid, therefore, at very high wavenumbers. They compare their theory with some measurements in a turbulent flow approaching e plate where $L_x/D \ll 1$.

The experiments described in this paper were made in the range where the scale of turbulence is of the same order as the size of the body. In addition to the investigation of the turbulent velocity field, measurements of pressure fluctuations at the stagnation point are presented. Marshall [10] has completed a similar programme of measurements on the turbulent flow approaching a disk normal to the flow. The general features of the flow are similar to those found in the two-dimensional case.

2. EXPERIMENTAL ARRANGEMENT

The experiments were conducted at the National Physical Laboratory in a wind tunnel with a 3 ft. (0.91 m) by 3 ft by 15 ft (4.57 m) long working section. The tunnel is of the closed-return type and has a free stream turbulence level of better than 0.07% and a maximum speed of about 150 ft/sec. Highly turbulent flow was generated by the installation of square mesh grids at the beginning of the working section. Details of the grids, which were constructed of bars of rectangular cross-section, are given in table 1.

Table 1

Grid	Mesh size, M cms	Bar size, b cms	Distance to stagnation point, $\frac{\overline{x}}{M}$
A	3·81	0·98	70·4
B	7·62	1·28	35·1
C	15·22	3·11	17·6
D	22·83	3·77	11·7

The wind tunnel was equipped with a fine pitch fan designed to operate unstalled with a high solidity grid in the working section.

The body used was a flat plate spanning the tunnel and mounted normal to the flow. The prime interest was the distortion of the approaching turbulence and in order to remove any unsteadiness in the flow, generated by vortex shedding in the wake of the plate, it was decided to fill in the wake along the theoretical free streamlines. The profile shape of the resulting body was designed according to Roshko's [11] notched hodograph method. Details of the design of the model are given in the appendix. The model cross-section is shown in figure 1 and the size of the equivalent flat plate, D, is 2.54 cms. The model side faces become parallel in a distance of just less than D and remain parallel for 10D. The body is terminated in a 6D streamlined tail fairing. Surface oil flow patterns showed there to be a region of separated flow situated towards the end of the curved portion of the 'free streamline'. Trip wires were fitted at about 0.5D from the 'edges' of the plate and they removed the unwanted separations.

Turbulence measurements were made with DISA constant-temperature linearised hot-wire anemometers. A traverse gear was embedded in the model and either normal wire or X-wire probes could be traversed out along the mean stagnation streamline. The hot-wire probe came out of the model through an air-tight seal. In addition to the velocity measurements, fluctuating pressure measurements on the stagnation line were made using a ½ in Brüel and Kjaer microphone. The microphone was connected to the surface hole by about 1.3 cms of 2 mm probe tubing. The frequency response of the microphone and probe tube was checked against a standard Brüel and Kjaer microphone. Some damping had to be added to the probe tube to suppress the lowest resonant frequency and with damping the frequency response was acceptably flat to 2 kHz. At low frequencies the level of power spectral densities was raised to allow for the fall in response at frequencies less than about 20 Hz. Fluctuating velocity and pressure signals were recorded on a tape recorder for later digitization and analysis on a computer.

3. EXPERIMENTAL RESULTS

3.1 Flow behind the turbulence producing grids

The turbulence structure behind the four grids was investigated on the centre line of the working section, in the absence of the model, at a distance from the grids corresponding to the distance to the stagnation point. The measurements of the intensity of the three components of the turbulence together with the integral scale of the along wind component, L_x, are presented in table 2. The measurements were made at a wind speed of about 18 m/sec and values of the grid Reynolds number, R_m, based on mesh size, are given in the table. In accordance with the results of other investigators, the turbulence components normal to the mean wind direction were found to be smaller than the along wind components. The values of scale were estimated from power spectral density measurements, assuming Taylor's hypothesis to hold.

Table 2

Grid	$\dfrac{\sqrt{\overline{u^2}}}{U} \times 10^2$	$\dfrac{\sqrt{\overline{v^2}}}{U} \times 10^2$	$\dfrac{\sqrt{\overline{w^2}}}{U} \times 10^2$	L_x cm	$\dfrac{L_x}{D}$	$R_{\theta} \times 10^{-4}$
A	2·09	1·63	1·66	3·05	1·2	4·7
B	2·83	2·2	2·34	4·57	1·8	9·5
C	5·71	4·4	4·81	6 54	2·57	18·9
D	6·40	4·95	5·31	6·05	2·38	28·4

The scale produced by the smaller mesh grid, grid C, is larger than that produced by grid D. This is because scale increases with distance from a grid and the measuring station was comparatively nearer to grid D.

Spectra measurements were made of the 'u' component of turbulence for the flow behind each of the grids. Figure 2 shows the spectra plotted in a normalised form. The power spectral density, F(n), is plotted in the non-dimensional form $(F(n)U_0)/(2\pi L_x U_0^2) = \theta_u$ against the frequency parameter $(2\pi n L_x)/U_0 = \tilde{n}$, where n is frequency. The results are shown compared with the spectrum calculated from von Kármán's interpolation formula (see Hinze [12]). This spectrum has the form

$\theta_u = (2/\pi)[1 + 1\cdot 8\,\tilde{n}^2]^{-5/6}$ and gives a good representation of the experimental results.

3.2 Velocity measurements ahead of the body

3.2.1 Mean velocity

The first measurements were made in smooth flow and the mean velocity profile along the stagnation streamline is shown in figure 3. The hot wire was traversed out to just over 4 plate widths ahead of the model. Within a distance of 0.1D from the surface the hot wire results were subject to a number of errors, the most serious of which was that the seal at the stagnation point could not be held when the wire was very close to the surface. Also the presence of the wire may have moved the stagnation point slightly. Either of these effects could have caused the small increase in velocity very close to the surface. As a check on the measuring technique the velocity distribution was compared with that predicted by Roshko's [11] hodograph method. Details of the computation of the velocity field are given in the appendix. The predicted profile is also shown in figure 3 and the agreement with experiment is seen to be good. In turbulent flow the mean velocity profile was measured in the flow behind each of the four grids and showed good agreement with the smooth flow result. Hiemenz's solution for the boundary layer at the stagnation point gives s thickness of just over 0.01D. All the measurements, therefore, were made well outside the region directly affected by viscosity.

3.2.2 Fluctuating velocities

Although not strictly part of this investigation, turbulence measurements with a normal wire were made in smooth flow ahead of the body and showed a number of unusual features. It is to be expected that the turbulence level based on local velocity might gradually rise as the model is approached. However, there were several local regions of increased turbulence level along the stagnation streamline, one as high as 1%, which appear to have been caused by the presence of the hot wire in the flow. The wire is situated in a region of strong adverse pressure gradient and it may well have had some disturbing effect on the flow. If the wire was moved slightly off the stagnation streamline the disturbance disappeared. Measurements in turbulent flow, on the other hand, showed no evidence of any interference by the hot-wire probe.

The intensity of all three components of turbulence were measured ahead of the body along the stagnation streamline. It is difficult to interpret their meaning if they are simply plotted as a variation of local turbulence intensity because the changes in intensity are dominated by the changes in the mean velocity. Instead the local root mean square value of the turbulence component has been divided by its value recorded at $x/D = 4.25$. Figure 4 shows the variation of $\sqrt{\overline{u^2}}/\sqrt{\overline{u_0^2}}$ ahead of stagnation for the four values of scale tested. The two smaller scales show an amplification of energy whereas the two larger scales show a continuous attenuation. At the surface, of course, the value of $\sqrt{\overline{u^2}}/\sqrt{\overline{u_0^2}}$ must drop to zero. There will be some natural decay of turbulence between $x/D = 4.25$ and zero. Without the model in position the turbulence was found to decay by only about 2 to 3% in this distance and no attempt has been made to correct the results.

Very near the stagnation point the hot wire can only give a rough indication of the level of the fluctuating velocities because of the very high local turbulence intensities. The hot-wire output was linearised but further errors are likely to arise at high levels of turbulence due to the non-linear yaw response. Table 3 shows the highest values of local intensity recorded and in all cases this occurred at $x/D = 0.1$. Grid A showed a nearly ninefold increase in the value of intensity.

The other component of turbulence in the plane containing the cross-section of the model, $\sqrt{\overline{v^2}}/\sqrt{\overline{v_0^2}}$, is shown in figure 5. The third component $\sqrt{\overline{w^2}}/\sqrt{\overline{w_0^2}}$, which is in a direction parallel to the stagnation line along the model, is plotted in figure 6. While $\sqrt{\overline{v^2}}/\sqrt{\overline{v_0^2}}$ shows generally an opposite effect to $\sqrt{\overline{u^2}}/\sqrt{\overline{u_0^2}}$, $\sqrt{\overline{w^2}}/\sqrt{\overline{w_0^2}}$ shows only amplification. Near the surface viscous effects will reduce these components to zero.

Table 3

Grid	Maximum $\sqrt{\bar{u}^2}/U$	Amplification of intensity
A	0.18	8.6
B	0.21	7.43
C	0.32	5.60
D	0.34	5.31

3.2.3 Power spectral density measurements of the longitudinal component

For each grid power spectral densities of the longitudinal component of turbulence were computed at $x/D = 3.025$, 0.624 and 0.183. The spectra measured at $x/D = 3.025$ showed no significant variation from those measured in the absence of the model. The spectra measured at $x/D = 0.624$ and 0.183 are shown in figures 7 and 8 respectively. Spectra are shown plotted as $(F(n)U_0)/(2\pi L_x \bar{u}_0^2) = \theta_u$ against $(2\pi L_x)/U_0 = \tilde{n}$ and the area beneath each spectrum is $\bar{u}^2/\bar{u}_0^2$, i.e. the square of the ratio shown in figure 4. As a comparison with the upstream spectra the curve obtained from the von Kármán interpolation formula is also shown.

Figure 7 shows that the power at low wavenumbers begins to decrease (or remain constant, grid A) and the largest attenuation occurs for the flow which had the largest scale, grid C. At higher wavenumbers the turbulence from all grids shows an increase in power. In figure 8 the apparent shift of energy from low wavenumbers to higher wavenumbers is more marked although at high wavenumbers the effects of viscous decay are more obvious. It is interesting to note that for grid A, the smallest scale, the turbulence amplified even at low wavenumbers.

3.3 Measurements of pressure fluctuations at the stagnation point

For each of the grids power spectral density measurements of the fluctuating pressure were made and the spectra for grids A and C, representing the smallest and largest values of L_x/D examined, are shown in figures 9 and 10. The power spectral density of the pressure, $F(p)(n)$, is presented in the non-dimensional form $(F(p)(n))/(2\pi L_x \rho^2 \bar{u}_0^2 U_0) = \theta_p$. The r.m.s. value of the fluctuating component of the pressure at the stagnation point, $\sqrt{\bar{p}^2}$, was measured for each of the grids. The results are shown plotted in figure 11 against the scale parameter D/L_x. The fluctuating pressure is presented in the non-dimensional form $\sqrt{\bar{p}^2}/(\rho U_0 \sqrt{\bar{u}_0^2})$ and the reason for this choice of parameter is left to the discussion. The values of $\sqrt{\bar{p}^2}$ were calculated from the spectra after they had been corrected for the effects of the variations in the frequency response of the transducer.

4. DISCUSSION OF RESULTS

The modification of the turbulence by the body is fundamentally different in the two extreme cases where $L_x \gg D$ and $L_x \ll D$.

4.1 $L_x \gg D$

When $L_x \gg D$ the flow approximates to a slow, quasi-steady variation of the direction and magnitude of the mean velocity. Hunt treats the flow around a circular cylinder and assumes the flow is inviscid and that $\sqrt{\bar{u}_0^2} = \sqrt{\bar{v}_0^2} = \sqrt{\bar{w}_0^2} = \tau U_0$ where τ is small. In the x direction the flow is similar to that caused by a slow variation of the longitudinal velocity and as the body is approached the fluctuating velocity will attenuate like the mean velocity.

$$\therefore \quad \frac{U_0 + u_0}{U_0} = \frac{\bar{U} + u}{\bar{U}}$$

$$\frac{\sqrt{\bar{u}_0^2}}{U_0} = \frac{\sqrt{\bar{u}^2}}{\bar{U}}$$

$$\text{and} \quad \therefore \quad \frac{\sqrt{\bar{u}^2}}{\sqrt{\bar{u}_0^2}} = \frac{\bar{U}}{\bar{U}_0} \tag{1}$$

In the y direction the effect of v_0 will be to alter the incidence of the flow and it can easily be shown by potential flow theory that, along the stagnation streamline

$$\frac{\sqrt{\bar{v}^2}}{\sqrt{\bar{v}_0}} = 2 - \frac{\bar{U}}{\bar{U}_0} \tag{2}$$

The component in the z direction is unaffected by the presence of the body and

$$\frac{\sqrt{\bar{v}^2}}{\sqrt{\bar{v}_o^2}} = 1 \qquad (3)$$

For a flat plate in potential flow there is no change in $\sqrt{\bar{v}^2}$ along the stagnation streamline although it would be unrealistic to use this result since in the real flow there is separation at the edges. For the free streamline model it is assumed that, for simplicity, at least away from the stagnation point itself, the flow is similar to that approaching a circular cylinder. This is a very idealised picture since if the scale of turbulence is infinite the v fluctuation will induce an alternating circulation on the body. For the model used in these experiments the length of the body was nearly an order of magnitude longer than the largest scale of turbulence and it seems reasonable, therefore, to treat the complete flow as inviscid and neglect the effect of any Kutta condition at the trailing edge. Equations (1), (2) and (3) are shown plotted in figures 4, 5 and 6 respectively.

4.2 $L_x \ll D$

If $L_x \ll D$ the distortion of the turbulence along the stagnation streamline approximates to that caused by uniform plane strain and the results of Batchelor and Proudman [2] can be used directly. The rapid distortion theory of Batchelor and Proudman predicts an amplification of $\sqrt{\bar{u}^2}$ and $\sqrt{\bar{w}^2}$ and an attenuation of $\sqrt{\bar{v}^2}$. Their results are also shown plotted in figures 4, 5 and 6.

4.3 $L_x = O(D)$

The experimental results are seen to fall between the two limiting curves with results for smaller scales generally tending towards the $L_x/D \rightarrow 0$ curve. The largest amplification of energy occurs for the w component although there is no rate of strain in this direction. Clearly close to the body the local intensity is rising to such a high value that the assumptions made in rapid distortion theory cannot hold and the non-linear terms in the vorticity equation will no longer be negligible.

Although vortex stretching amplifies $\sqrt{\bar{u}^2}$, close to the surface the effect of the wall on small scale eddies will be similar to its effect on larger scale eddies further away from the stagnation point, i.e. it attenuates the fluctuations. The turbulence is thus affected on the one hand by vortex stretching and rotation and on the other by the simple blocking of the flow by the body. At intermediate scale sizes it can be expected that low wavenumbers will exhibit some of the features of $L_x \gg D$ flows while high wavenumbers will be dominated by vortex stretching. This idea is well supported by the spectra measurements of the u component which show a large shift of energy to higher wavenumbers as the stagnation point is approached.

4.4 Pressure fluctuations

If $L_x \gg D$ it is possible to treat the velocity fluctuations in the vicinity of the plate as irrotational and to apply the unsteady version of Bernoulli's equation

$$\tfrac{1}{2}q^2 + \frac{P}{\rho} - \frac{\partial \varphi}{\partial t} + B = F(t) \qquad (4)$$

where q is the total velocity, ϕ is velocity potential, B is the body force potential and F(t) is constant throughout the flow at any instant of time. It can be shown that v and w produce no significant contribution to the fluctuating pressure at the stagnation point and the problem reduces to that of a flat plate in a flow of varying longitudinal velocity U(t). The velocity potential for a flat plate normal to a stream is

$$\phi(t) = U(t)\sqrt{x^2 + D^2/4}$$

and

$$B = x\frac{dU(t)}{dt}$$

Substituting in Eq (4)

$$\tfrac{1}{2}U(t)^2 + \frac{P}{\rho} - \frac{dU(t)}{dt}\sqrt{x^2 + D^2/4} + x\frac{dU(t)}{dt} = F(t) \qquad (5)$$

Away from the plate Eq (5) reduces to

$$\tfrac{1}{2}U(t)_o^2 + \frac{P(t)_o}{\rho} = F(t) \qquad (6)$$

where $P(t)_o$ is the pressure far from the plate. Batchelor [13] shows that in isotropic turbulence the fluctuating component of the static pressure is small and he obtains the relation

$$\frac{\sqrt{\bar{p}_o^2}}{\rho U_o \sqrt{\bar{u}_o^2}} \doteq 0.58\frac{\sqrt{\bar{u}_o^2}}{U_o}$$

The maximum value of $\sqrt{\bar{p}_o^2}/(\rho U_o \sqrt{\bar{u}_o^2})$ is 3.7×10^{-2} which occurs in the flow behind grid D. Since it can be shown that, at the stagnation point, $\sqrt{\bar{p}^2}/(\rho U_o \sqrt{\bar{u}_o^2})$ is of order unity neglecting the upstream fluctuating static pressure will introduce little error. Substituting Eq (6) in (5) and neglecting second order terms the relation for the fluctuating pressure at the stagnation point becomes

$$p = \rho\left(u_o U_o + \frac{D}{2}\frac{du_o}{dt}\right) \qquad (7)$$

Assuming that the record of the pressure fluctuations forms part of an infinite stationary random process it is possible to rewrite Eq (7) in terms of the power spectral densities of the pressure and the upstream velocity

$$F(p)(n) = \rho^2 F(n)\bar{U}_0^2 \left[1 + \frac{1}{4}\left(\frac{2\pi nD}{\bar{U}_0}\right)^2\right] \tag{8}$$

Expressing $F(n)$ in the non-dimensional form given earlier (by dividing by $(2\pi L_x \bar{u}_0^2)/\bar{U}_0)$) Eq (8) becomes

$$\frac{F(p)(n)}{2\pi\rho^2 U_0 L_x \bar{u}_0^2} = \frac{F(n)U_0}{2\pi L_x \bar{u}_0^2}\left[1 + \frac{1}{4}\left(\frac{2\pi nL_x}{\bar{U}_0}\right)^2\left(\frac{D}{L_x}\right)^2\right]$$

then

$$\theta_p = \theta_u\left[1 + \frac{\pi}{4}\left(\frac{D}{L_x}\right)^2\right] \tag{9}$$

If $D/L_x \to 0$, $\theta_p = \theta_u$ and the pressure and velocity spectra, non-dimensionalised as above, should be identical. The spectra of pressure and velocity are shown compared in figures 9 and 10 and it can be seen that they agree closely at low wavenumbers whereas at higher wavenumbers the pressure spectra fall away below the velocity spectra rather than show an increase according to Eq (9). At each scale size examined there was a definite break point where the pressure spectrum diverged from the velocity spectrum and with increasing values of L_x/D the break point moved to higher wavenumbers. At high wavenumbers the pressure spectra fell off at about 1.75 times as fast as the velocity spectra. These results, therefore, show that the assumption that the velocity fluctuations can be treated as irrotational fails before any acceleration effects are felt. The attenuation of the pressure spectra is a direct result of the rotational nature of the turbulence and the accompanying distortion of the vorticity field.

If $L_x/D = \infty$ then $\theta_p = \theta_u$ and $\sqrt{\bar{p}^2} = \rho \bar{U}_0\sqrt{\bar{u}_0^2}$ or $C_{Pr.m.s.} = 2\sqrt{\bar{u}_0^2}/\bar{U}_0$. The measurements of $\sqrt{\bar{p}^2}$ are shown non-dimensionalised by $\rho U_0\sqrt{\bar{u}_0^2}$ in figure 11 and it is to be expected that $\sqrt{\bar{p}^2}/(\rho \bar{U}_0\sqrt{\bar{u}_0^2}) = 1$ at $D/L_x = 0$. The results indicate that even when $D/L_x = 1$ the pressure fluctuations are still between 60 and 70% of $\rho\bar{U}_0\sqrt{\bar{u}_0^2}$. These findings are important when it comes to predicting the fluctuating loads induced on bodies in turbulent flow.

5. CONCLUSIONS

When $L_x/D \gg 1$ a quasi-steady type of approach can be used and, along the mean stagnation stream-line, $\sqrt{\bar{u}^2}$ will attenuate like the mean flow. Whereas if $L_x/D \ll 1$ the turbulence is distorted by the mean flow field and $\sqrt{\bar{u}^2}$ will amplify due to vortex stretching. In the experiments described here $L_x = 0(1)$ and there is found to be a combination of these effects with attenuation of energy at low wavenumbers and amplification at high wavenumbers. The other components of turbulence are found to behave in a consistent manner with the component parallel to the stagnation line on the body, which experiences no mean rate of strain, showing only amplification. Measurements of the pressure fluctuations at the stagnation point show that at low wavenumbers the level of pressure fluctuations can be predicted by assuming the turbulence to be irrotational. At higher wavenumbers the effect of the distorting field of the body is found to reduce the level of the pressure fluctuations.

6. REFERENCES

1. J.C.R. Hunt. A theory of flow over bodies. To be published.

2. G.K. Batchelor and 1. Proudman, Quart. J. Mech. and Applied Math. 7 (1954) p 83-103.

3. A.A. Townsend, Quart. J. Mech. and Applied Math. 7 (1954) p 104-127.

4. H.J. Tucker and A.J. Reynolds, J. Fluid Mech. 32 (1968) p 657-673.

5. N.A.V. Piercy, Aerodynamics, The English Universities Press Ltd., 1947.

6. S.P. Sutera, P.F. Maeder and J. Kestin, J. Fluid Mech. 16 (1963) p 497-520.

7. S.P. Sutera, J. Fluid Mech. 21 (1965) p 513-534.

8. W.Z. Sadeh, S.P. Sutera and P.F. Maeder, Z. angew. Math. Phys. 21 (1970) p 699-716.

9. W.Z. Sadeh, S.P. Sutera and P.F. Maeder, Z. angew. Math. Phys. 21 (1970) p 717-742.

10. R.D. Marshall. Pressure fluctuation correlations near an axisymmetric stagnation point. Ph.D. Thesis, Colorado State Univ., 1968.

11. A. Roshko, A new hodograph for free-streamline theory. NACA Tech. note 3168, 1954

12. J.O. Hinze. Turbulence, McGraw-Hill, 1959.

13. G.K. Batchelor, The theory of homogeneous turbulence, Cambridge University Press, 1953.

APPENDIX

Free streamline model

The profile shape of the flat plate model was designed according to Roshko's [11] notched hodograph method. His method requires a value to be assigned to the base pressure coefficient $(C_p)_b$. For this model $(C_p)_b$ was chosen to be -1 thus making $k = \sqrt{2}$ where $(C_p)_b = 1 - k^2$ and k is the ratio of the velocity along the free streamline near separation to the free stream velocity. Roshko's method maps the flat plate and its wake on to the positive half of the real axis of the complex w plane with the stagnation point at the origin. The free streamline model co-ordinates are given by

$$x_m = \frac{k^2 + 1}{2k} \left[\sqrt{w(w-1)} - \log(\sqrt{w} + \sqrt{w-1}) \right]$$

$$y_m = \frac{k^2 + 1}{2k} \left[\frac{\pi}{2} + \frac{1}{a} \sqrt{w(a^2 - w^2)} + a \tan^{-1} \sqrt{\frac{w}{a^2 - w}} \right]$$

for $\quad 1 \leqslant w \leqslant a^2$

where $\quad a = \dfrac{k^2 + 1}{k^2 - 1}$

The width of the flat p   s given by

$$D = \frac{k^2 + 1}{k} \left[\frac{\pi}{2} + \frac{1}{a} \sqrt{a^2 - 1} + a \tan^{-1} \sqrt{\frac{1}{a^2 - 1}} \right]$$

Beyond $w = a^2$ the body is parallel sided with thickness

$$H = \frac{k^2 + 1}{2k} \pi \left[1 + a \right]$$

The resulting profile shape is shown in figure 1.

Using the hodograph method it is possible to calculate the velocity profile along the stagnation streamline

$$\frac{U}{U_0} = \frac{2k^2}{k^2 + 1} \left(\left(\frac{1}{w} + \frac{1}{a^2} \right)^{1/2} + \left(\frac{1}{w} + 1 \right)^{1/2} \right)^{-1}$$

where

$$x = \frac{k^2 + 1}{2k} \left[\sqrt{w(1 + w)} + \log(\sqrt{1 + w} + \sqrt{w}) \right.$$
$$\left. + \frac{1}{a} \sqrt{w(a^2 + w)} + a \log \frac{\sqrt{a^2 + w} + \sqrt{w}}{a} \right]$$

and $\quad 0 \leqslant w \leqslant \infty$

The velocity profile is plotted in figure 3.
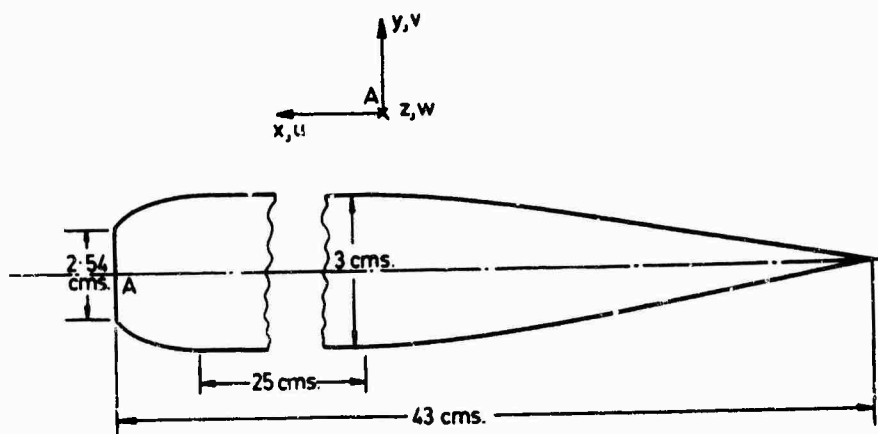
FIG. 1 FLAT PLATE FREE-STREAMLINE MODEL.
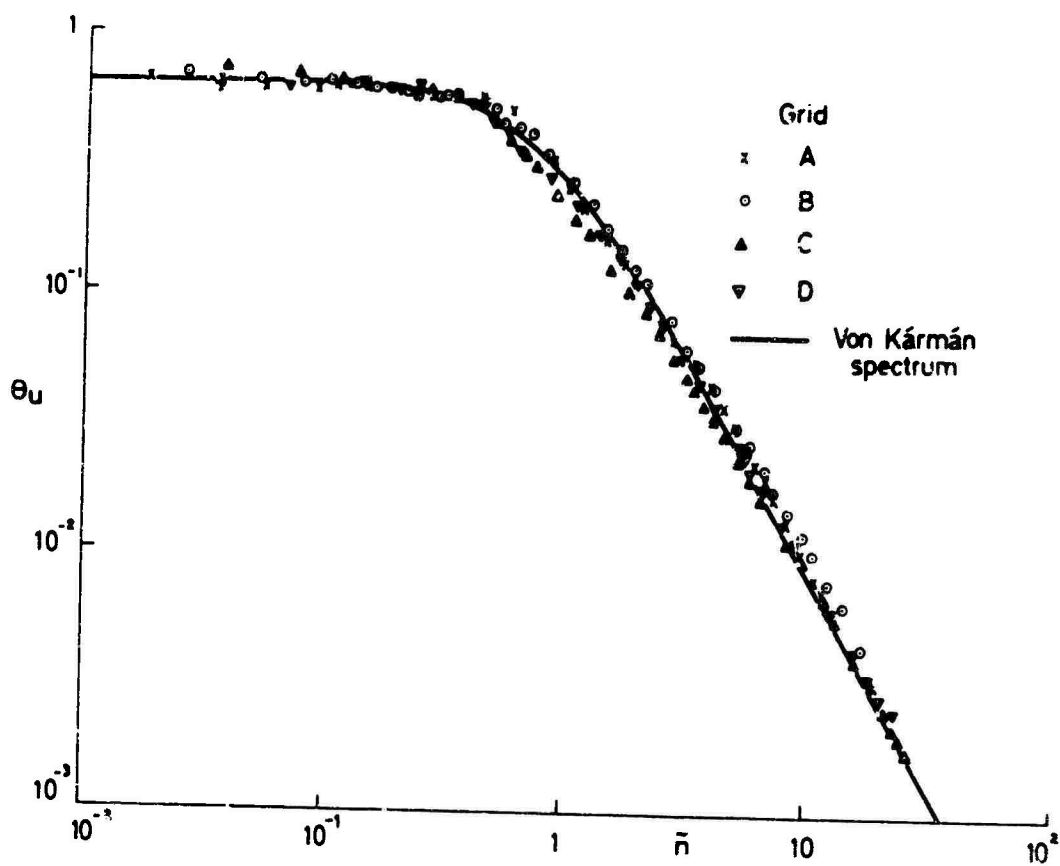
FIG. 2 SPECTRA OF u COMPONENT IN EMPTY TUNNEL.
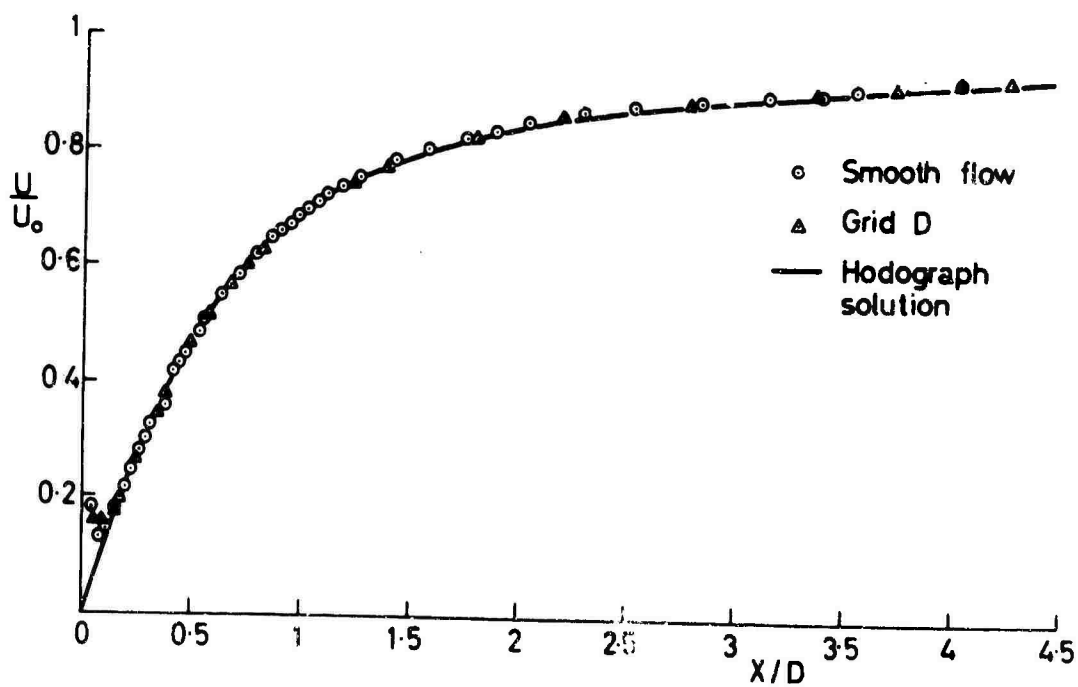
FIG. 3 MEAN VELOCITY APPROACHING STAGNATION.
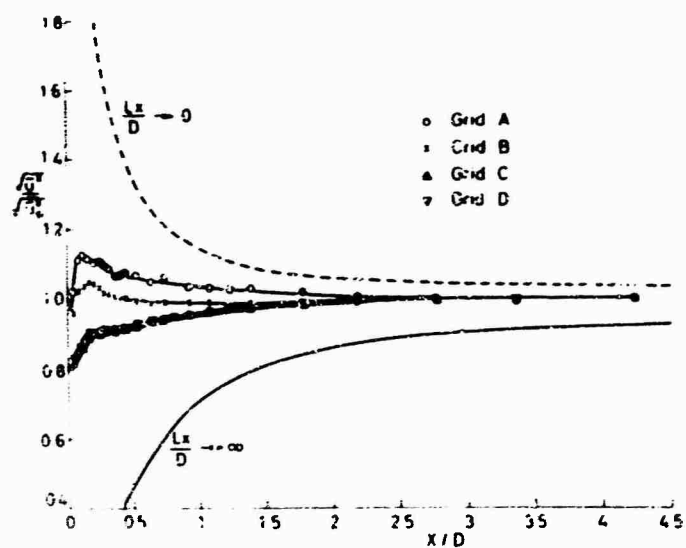
FIG 4 u COMPONENT APPROACHING STAGNATION
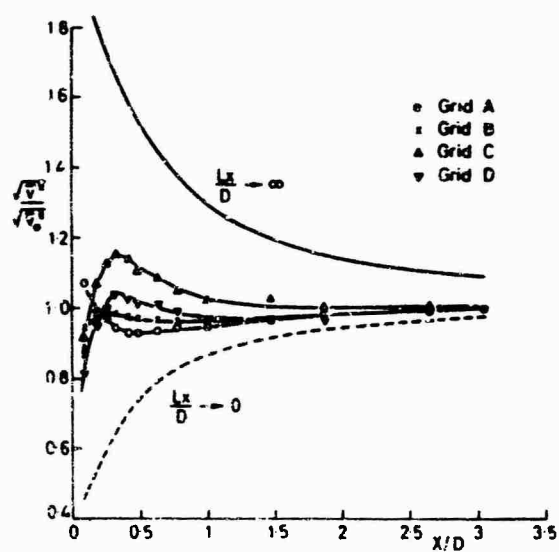
FIG 5 v COMPONENT APPROACHING STAGNATION
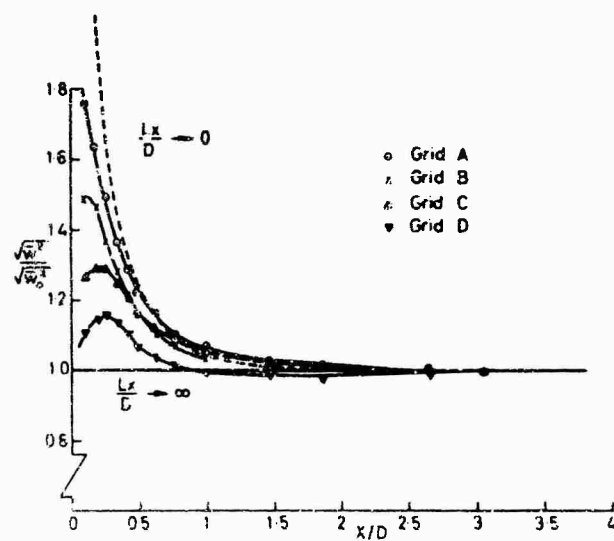
FIG 6 w COMPONENT APPROACHING STAGNATION
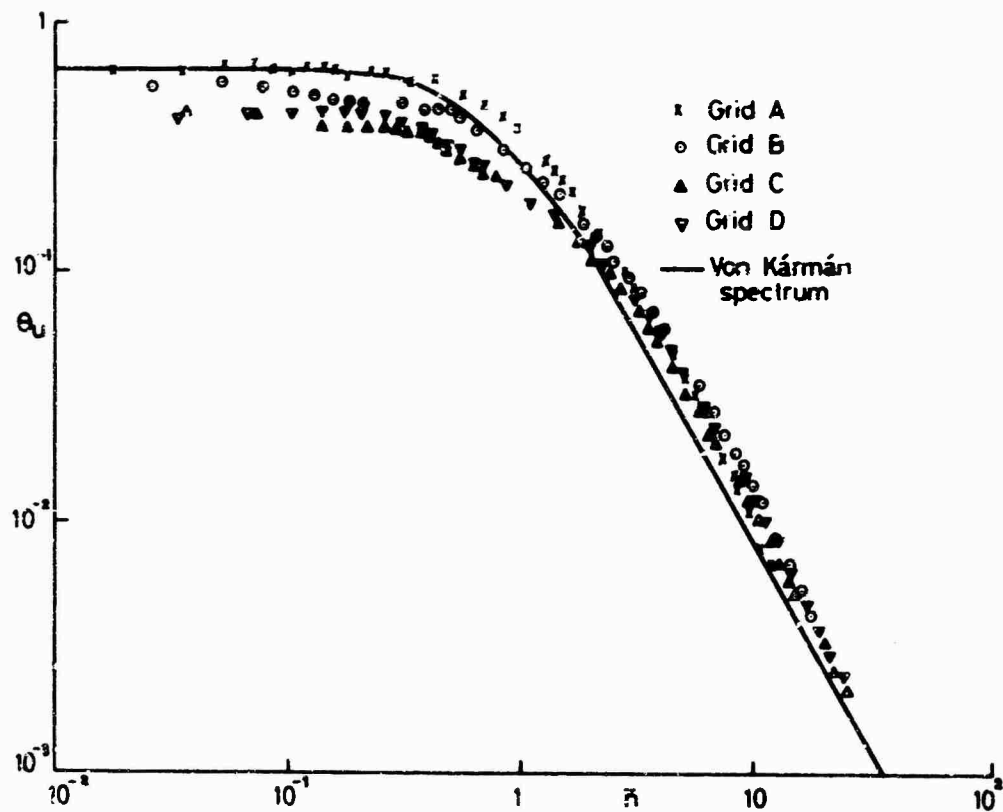
FIG. 7 SPECTRA OF THE u COMPONENT AT X/D = 0·624.
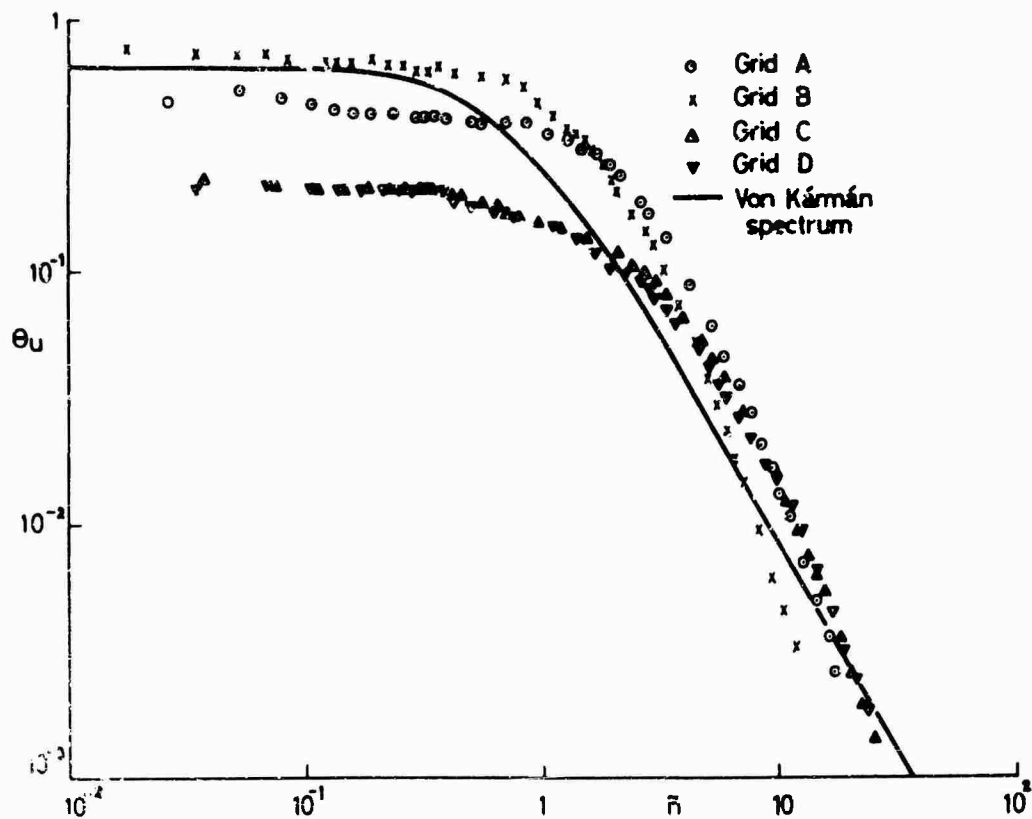
FIG 8 SPECTRA OF THE u COMPONENT AT X/D = 0·183.
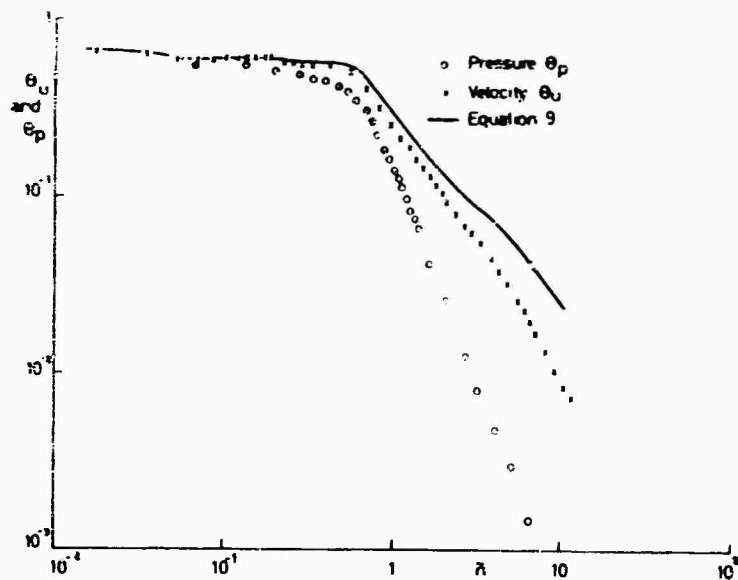
FIG 9 SPECTRUM OF PRESSURE FLUCTUATIONS AT THE STAGNATION
POINT, GRID A.
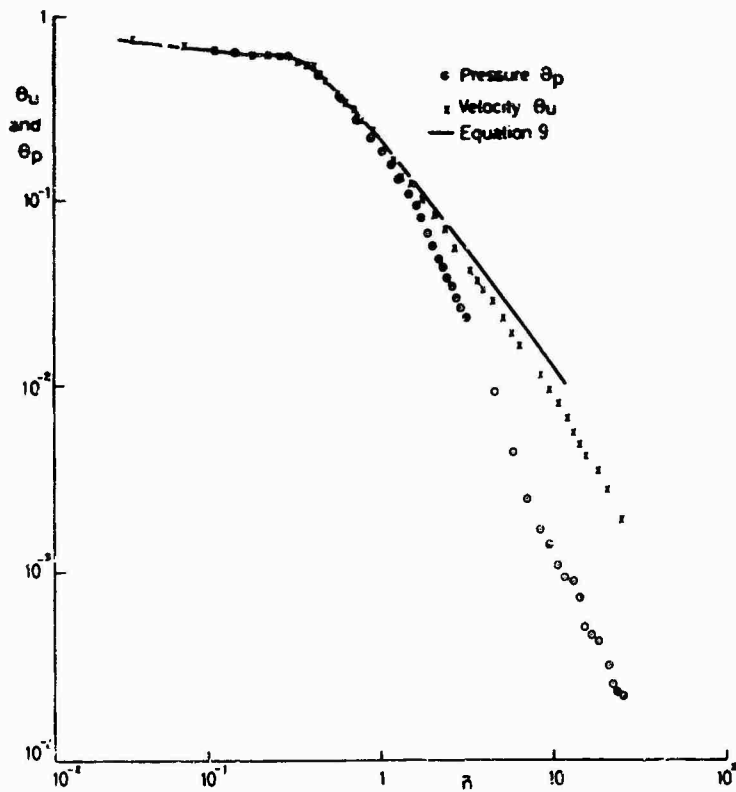
FIG 10 SPECTRUM OF PRESSURE FLUCTUATIONS AT THE STAGNATION
POINT, GRID C.
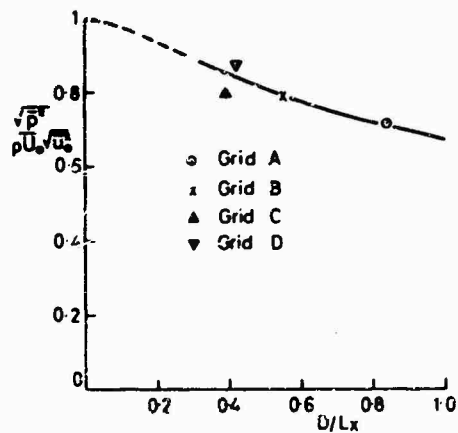
FIG. 11 ROOT MEAN SQUARE VALUE OF THE
PRESSURE FLUCTUATIONS AT THE
STAGNATION POINT.

APPENDIX A

DISCUSSIONS

following the presentation of papers at the
AGARD Fluid Dynamics Panel Specialists' Meeting on

TURBULENT SHEAR FLOWS

September 1971

London, England

This Appendix contains the discussions which followed the presentation
of the papers at the Specialists' Meeting on "Turbulent Shear Flows"
held at the Royal Zoological Society of London, England on 13–15
September 1971.

These discussions are transcribed from forms completed by the authors
and questioners during the meeting and are keyed (by reference number)
to the papers contained in this Conference Proceedings.

Le présent Appendice est un recueil des discussions qui ont suivi la
présentation des exposés à l'occasion de la Réunion des Experts tenue
à la Société Zoologique Royale de Londres, Angleterre, du 13 au 15
Septembre 1971 et consacrée au thème "Turbulent Shear Flows".

Le texte de ces discussions a été transcrit à partir de fiches remplies à
cet effet par les auteurs et par ceux ayant désiré poser des questions.
Les discussions sont numérotées suivant les numéros de référence des
exposés.

Discussion of Paper C
"Variations on a Theme of Prandtl"
presented by P.Bradshaw

L.S.G.Kovasznay: I have enjoyed Mr Bradshaw's Paper very much and I wish only to emphasize one point. In compressible flows or alternatively in heated turbulent flows, there is a strong fluctuation of temperature or entropy: correspondingly there is a large "buoyancy" effect that is a very strong source of new turbulence generation.

P.Bradshaw: Professor Kovasznay's comment is a very pertinent one. I hope that Morkovin's hypothesis (of the effective "incompressibility" of turbulence with Mach number fluctuations much less than unity) will keep us out of trouble in many cases: for instance it seems that the dear old mixing length formula, as re-licensed by Morkovin for $M < 5$, gives good results in the inner layer of compressible boundary layers. As I mentioned in the paper, strong compression or rarefaction may produce large effects on turbulence jus' like other strain rates: it may be this that produces the rather large differences between calculation methods and the measurements of Peake et al presented at this meeting.

A.D.Young: I would like to refer to a major point in Mr Bradshaw's lecture, namely that future experimentation should concentrate on the kind of data particularly needed by current calculation methods. Are there any comments on this point?

P.Bradshaw: I would not like to be any more specific than in the lecture: the general need is for more information about the exact transport equations for Reynolds stress; we know much less about them than about the turbulent energy equation. Most of all one would like measurements of the pressure-strain terms that govern the tendency to isotropy but, even in the atmosphere, pressure fluctuation measurements within the flow are not very reliable, as measurements in small-scale flow in the laboratory are extremely difficult. Perhaps the best advice one can give to experimenters is that they should bear in mind that the practical use of turbulence studies is to help engineers to predict turbulent flows.

D.J.Peake: In your presentation, the complexities of three-dimensional turbulent boundary layers were not especially emphasized in your remarks on "interacting flows". Would you please care to comment further on the importance of three-dimensionalities?

P.Bradshaw: As I am sure Mr Peake would agree, even true boundary layers (such as those far from a wing root or tip) are a difficult problem in three-dimensional flow, although one can get quite a long way by logical extension of "two-dimensional ideas". In three-dimensional interactions, the turbulence is usually strongly influenced by streamwise vorticity, whether produced by the inviscid secondary-flow mechanism or by the turbulence itself. We don't know much about what happens to turbulence when it is rotated about the flow direction. Since three-dimensional distortions and interactions are so important, we should encourage Mr Peake and his colleagues (and other workers) to investigate them further: the NAE flow-visualization work has already been very helpful in giving an overview of three-dimensional shear layers in real life.

C. du P.Donaldson: I would like to point out that an experiment that is easy to perform and is very useful to one who tries to construct models of turbulent shear flow is the dispersal of a passive scalar in any turbulent flow. The dispersion of a passive scalar does not in any way effect the primary flow yet the way it is dispersed by any turbulent flow yields information that can be extremely useful to one who tries to construct analytical models.

P.Bradshaw: I agree with Dr du P.Donaldson that passive scalar transport can illuminate one's ideas of momentum transport (as well as being important in its own right!).

W.Schönauer: The structure of the turbulent motion is mostly a nonequilibrium structure and by this fact many effects are superposed and the whole history affects the observed flows. I think we should go on with small steps and one of the first steps should be the study of equilibrium flows and to search for the definition of such equilibrium conditions. Then we should study the transition from one equilibrium flow to the other and go by this procedure to the nonequilibrium flows. In this way we can separate the different effects and may treat them by theory.

P.Bradshaw: I agree entirely with Dr Schönauer that equilibrium (i.e. self-preserving) flows are the simplest basis for studies of the different effects that control turbulence. In particular measurements of interactions and the effects of extra strain rates are much easier if the basic flow is an equilibrium one. However it seems that, to a good approximation, the turbulence is usually in *internal* equilibrium: even in nonequilibrium flows, structural parameters such as anisotropy ratios are almost universal. Therefore we may not *need* to investigate turbulence in situations of mean-flow equilibrium, but the experimental work will always be simpler in such situations because fewer readings are needed.

W.W.Willmarth: I think future experimental work in turbulence ought to be aimed at gaining an understanding of turbulent structure in simple flows in an effort to understand how the outer flow controls the generation of turbulence. For example, in a boundary layer near the wall, how is turbulent energy production controlled by pressure gradient or by polymer additives. Kovasznay's sampling techniques may be very useful in this respect. If understanding of turbulent structure is obtained, the computerized calculation of more complicated turbulent flows can then proceed more rapidly.

P.Bradshaw: I agree entirely.

J.J.D.Domingos: Don't you think that between the "inaccessible peak" of the Navier Stokes equations and the computational methods you referred to, which are for mean steady flows, there exists a promising alternative in the numerical computation of unsteady flows where you only need an apparent viscosity (or equivalent) to take account of the motion at scales smaller than the numerical mesh?

P.Bradshaw: Professor Domingos' point is a very good one, and I have been hoping that calculations like those of Deardoff (see the Boeing Symposium issue of J. Fluid Mech) will soon use a fine enough mesh to give useful estimates of unmeasurable quantities (such as the elusive pressure fluctuation). Given Illiac IV and money, results of direct use in calculation methods should appear in a year or two.

Discussion of Paper 3
"Structure of the Reynolds Stress Near the Wall"
presented by W.W.Willmarth

J.M.Wallace, Jr: I want to point out that Wallace, Eckelman, and Brodkey have measured the four quadrant contributions to the $\overline{u'v'}$ Reynolds stress term in MPI für Strömungsforschung Bericht 119, and are qualitatively in agreement with those of Professor Willmarth. We also measured scales and found that the two positive contributors are much larger in scale than the two negative contributors.

W.W.Willmarth: I believe the lower Reynolds number of your experiments may cause some quantitative difference in the four quadrant contributions to $u'v'$. Your observation that the negative contributions to $u'v'$ were of smaller scale than the positive ones is further evidence of the small scale of the bursting and sweep processes.

C.H.Gibson: Would you comment on the degree of convergence of your statistical parameters, especially since you emphasize the intermittency of the Reynolds stresses, and intermittency will increase the required sample sizes? The "four quadrant diagram" appears to be equivalent to estimating a joint probability distribution function with a four box joint histogram. Was this technique used to obtain convergence of your statistic with a limited sample size, or is there some other advantage of the "four quadrant diagram" over a joint histogram with better resolution?

W.W.Willmarth: I believe that the size of the samples used for the sampled Reynolds stress data of Figure 6 is adequate for Figure 6 b, c, d, e and the data become less accurate for extreme values of T.L. Figure 6 a, f, g. In regard to the effect of intermittency on required sample size, the data for extreme negative values of T.L. are affected as indicated by the time variation of $\widetilde{uv}/\overline{uv}$ when only 38 samples were obtained at T.L. $= -2.15u'_w$ (see Fig. 6 a).

The same comments apply to the data shown in the "four quadrant diagram". In the end, one's optimum statistical accuracy is set by the use one intends for the data. We have not analysed our accuracy in detail but I believe our data is accurate enough to show that large bursts contribute generously to the Reynolds stress. The average (in some as yet undefined sense) of a burst is an interesting question for further investigation.

Discussion of Paper 4
"Spectral Distributions of Thermal Fluctuations in a Turbulent Boundary Layer"
presented by L.Fulachier

C.A.Friehe: I would like to ask: 1. How was the temperature measured? 2. What was the spatial separation between the temperature and velocity probes, in terms of the wave number k_1, shown on the slides of the various spectra?

L.Fulachier:

1. Les fluctuations de température ont été mesurées par la méthode des diagrammes de fluctuations de Morkovin-Kovasznay appliquée par E.Verollet (voir référence 1) aux écoulements subsoniques (confert page 4-3). Les spectres de température ont été obtenus en appliquant cette méthode aux signaux filtrés en fréquence. Cependant, étant donné le longueur et la difficulté de ce genre de mesure, certains spectres de température ont été mesurés avec un fil chaud unique pur chauffé et corrigés de la contamination due à la fluctuation de vitesse u' (confert page 4-3). En fait, sur les figures 1 à 6 les points expérimentaux des spectres de température présentés n'ont pas été corrigés. La correction améliore la comparaison des spectres $F_{\theta\theta}$ et Q.

2. Les spectres de θ', u' et $\overline{\theta'u'}$ ont été mesurés avec un seul fil chaud (voir réponse 1). En ce qui concerne les spectres de v', w', et les cospectres de $\overline{u'v'}$ et $\overline{\theta'v'}$ nous avons utilisé deux fils chauds croisés en X et la méthode des diagrammes de fluctuations (confert page 4-3). La distance entre les deux fils était de 0,4 mm ce qui correspond à un nombre d'onde de 2500 m^{-1}.

Discussion of Paper 5
"Intermittent Structures in Boundary Layers"
presented by R.E.Kaplan

L.S.G.Kovasznay: I would like to comment on your last slide. Can you interpret your data in the light of Corino and Brodkey's terminology concerning the "sweep" of slow fluid?

R.E.Kaplan: Our results are in accord with the descriptions of Corino and Brodkey. In fact, they show in some greater quantitative detail the suddenness and the scope of their "sweep". We also show that this "sweep" is preceded by an "inflexional" velocity profile and can determine this profile quantitatively.

W.W.Willmarth: I wish to suggest that, in trying to compare your data (for example that of Figs. 6 and 7) to spatial models or flow visualization pictures, one might obtain a first approximation to the actual flow field at one instant in time by assuming that the data you obtain in Figures 6 and 7 is produced by a flow pattern that is convected past your hot wire array with unchanging configuration.

R.E.Kaplan: Our measurements shed no light on whether the suggestion is a valid first approximation. Since we present only u perturbations, that would suggest that u(x) resembles Figure 7. But there is strong evidence that the vertical velocities are quite small, hence continuity will be violated unless there is a corresponding strong flow in the crosswise direction. We expect to resolve this point in the near future.

J.M.Wallace: I want to ask if Professor Kaplan has measured v'(t) velocities simultaneously with his observation of the deceleration and rapid acceleration of the u'(t) velocity.

R.E.Kaplan: The measurements of v' and Reynolds stresses will be done in the near future.

C. du P.Donaldson: I am unfamiliar with a diagram such as your last slide. From your talk I take it that this in some way represents the time history of a disturbance which arises at the wall. Am I mistaken? If it does represent a record of a disturbance, should not the disturbance propagate downstream?

R.E.Kaplan: The last slide represents positions displaced normally from the surface. A striking feature is that the acceleration and the preceding deceleration experience a very small time delay as one proceeds outward from the wall. Of course, one should realize that the displacement of each trace is very small compared to distances downstream.

C. du P.Donaldson: I still do not understand. A disturbance originating at the wall should propagate downstream. Perhaps what I see is the record of a disturbance that has moved into the area from upstream.

R.E.Kaplan: The accelerated regions for large y/δ and negative delay times are more a reflection of the velocity profile indicated in slide 5 than the accelerated velocity following zero time for the lower two curves of the slide (Fig. 7). To repeat, we believe that these measurements show the formation first of a velocity profile, followed for small values of y/δ by a rapid acceleration of the flow. The local fluctuation level is highest immediately before the acceleration, and the acceleration occurs so rapidly that on the scales of structures even in the sublayer, it appears to be discontinuous.

W.W.Willmarth: In your results of Figure 7 a sudden jump (in time) of the streamwise velocity occurs near the wall at $y/\delta = 0.025$, 0.035 and 0.070. I believe this represents the passage of a shear layer between $y/\delta = 0.035$ and 0.070. The shear layer would have beneath it a low speed fluid parcel which will then erupt in the manner described by Corino and Brodkey.

R.E.Kaplan: That is an acceptable interpretation which more measurements can verify.

W.Schönauer: In isotropic turbulence, there is only "downwards cascading": the transformation of turbulence energy from large eddies to small eddies. But the large eddies must be created somehow by an "upwards cascading" and this can only take place in the presence of a shear layer. It seems to me that the intermittency and the turbulence bursts in the region between sublayer and turbulent layer are the sources for the upwards cascading. The turbulence energy created here then diffuses outwards and is then destroyed by the downwards cascading. In this sense I want to give an interpretation of the hydraulic diameter d_h · it is proportional to the ratio of the flow volume to the wetted surface (the zone of downwards cascading to the zone of upwards cascading). And many flows with the same d_h show identically the same behaviour, so the structure and the mechanism of cascading must be the same in such flows.

Discussion of Paper 19
"An Integral Method for Approximate Calculation of Compressible Turbulent Boundary Layers with Streamwise Pressure Gradient"
presented by H.J.Kuster

R.L.P.Voisinet: I wish to make a comment concerning the comparison of your theory to the H_{12} data of Lee, Yanta and Leonas. The discrepancy in the correlation appears to be due to an upstream cooling effect on the nozzle wall boundary layer flow. Upstream cooling affects downstream temperature profiles which in turn affect H_{12}. Refer to Paper No. 9 for an illustration of this effect.

H.J.Kuster: Thank you for your comment.

I think you may be right.

Indeed history effects are only accounted for in the velocity field by means of the FELSCH-dissipation law. An additional correction for temperature history effects seems to be necessary now.

Discussion of Paper 29
"An Eddy Viscosity Based on the Second Principal Invariant of the Deformation Tensor"
presented by W.Schönauer

O.O.Mojola:

1. In your Equation 2.7 you have uniquely related the stress tensor to the rate of deformation tensor via an eddy viscosity. But it is known that the stress does not necessarily vanish where the rate of deformation vanishes. What is your comment on this?

2. May I ask whether your type of analysis is valid for general complex flows in which there is considerable time lag between the rate of stress tensor and the rate of deformation tensor?

W.Schönauer:

1. There is no stress in my model, if there is no rate of strain, but it will surely be possible to change the constitutive equation such that it is valid for such extreme cases, too. I think that we should at first try to handle the simplest cases and then ameliorate the stress strain relation, if we then know its limitations. I believe the assumption of isotropy to be the most severe restriction, but here, too, we must at first see how far the simple relation describes the physical model before we give up isotropy and get those coefficients, which depend on the choice of the coordinate system.

2. The answer is the same as to question 1: we could provide for these effects especially with relaxation equations, but at first we should handle the simplest cases.

Discussion of Paper 21
"Effects of Strong Axial Pressure Gradients on Turbulent
Boundary Layer Flows"
presented by C.H.Lewis

D.J.Peake:

1. What are the essential differences between your two-layer calculation method and the (Douglas) method of Cebeci and Smith?

2. Why does the density profile for the AEDC Hotshot Nozzle Flow deviate sharply (as $y/\delta \to 0$) from the other calculations shown on your Figure 6 in the written version of your paper?

C.H.Lewis:

1. The fluid mechanical model is essentially identical to Cebeci and Smith if one uses their eddy viscosity law. The numerical method is different and the application, such as testing for convergence is unlike theirs. Also the method is easily extended to an arbitrary number of parabolic partial differential equations.

2. The small step size normal to the wall used in the present calculations permitted a detailed density profile to be computed near this highly cooled wall. The integral method results did not permit such to occur.

J.L.Stollery: Have similar calculations been made for the case of strong adverse pressure gradients and, if so, are your conclusions modified in any way?

C.H.Lewis: Yes, similar calculations have been made for adverse pressure gradients. Comparisons were made with experimental skin friction, velocity and total temperature profile distributions. The measurements were made on a flat plate with various curved ramps above the plate used to generate the adverse pressure gradient fields. We found good agreement with the data for "moderately" adverse pressure gradients: that is, for conditions not too near separation. The wall shear stress was measured with a floating-element gage and should be a good test of the numerical results. In general, the method seems adequate without modification, if one uses the eddy viscosity laws with the pressure gradient term included.

P.A.Libby: Could you tell us why you think the failure of your numerical analysis for cases of heated walls and favourable pressure gradient was due to the density transformation of the normal coordinate rather than, as I would guess off-hand, to a failure of the models for eddy-viscosity or Prandtl number? After all, if the flow were laminar, I presume you could compute these cases in terms of your transformed normal coordinate.

C.H.Lewis: The failure may be caused by the eddy viscosity models since we did not investigate laminar solutions for these heated wall conditions. We will investigate this suggestion since we did several numerical experiments such as varying the step sizes and convergence tests without significantly affecting the results.

A.D.Young: Am I right in thinking that you assumed the pressure as constant along a normal to the nozzle wall and if so, might not this account for the breakdown of the method that you encountered?

C.H.Lewis: We did assume that $dp/dy = 0$, consistent with boundary-layer theory, in all calculations. I do not think this could cause the failure of the numerical calculations. We did several numerical experiments such as varying the step sizes in both x and y directions without affecting the results. We did not include higher order boundary-layer effects such as longitudinal or transverse curvature and so we are unable to comment on their effects.

Discussion of Paper 30
"Mach Number Effects in Turbulent Flows"
presented by J.J.D.Domingos

W.Schönauer: Does your "fundamental equation" reduce to the Navier Stokes equations for the case of an atomic gas? I believe that all generalizations of flow equations should do this, because this is one of the rare cases where we need not make a phenomenological theory, but have a consistent theory from the micro motion (molecular motion described by the Boltzmann equation) to the laminar (macro) motion.

J.J.D.Domingos: I think you are referring to a dilute monatomic gas (Maxwell gas) because only in this asymptotic case has a complete deduction been made of the macroscopic equations starting from microscopic assumptions, although the usual point of view is to consider the microscopic approach as valid because it agrees with the phenomenological theory . . . May I point out that no such theory exists for dense gases or liquids? And also that it is questionable whether classical microscopic theories apply to turbulent flows?

Regarding now the contents of your question, it makes not much sense if you read, even quickly, my paper. In fact what I called the fundamental equation (I should have said a first order approximation) started from the Navier Stokes equations after the existence of a velocity potential had been proved.

Probably, a confusion arose in your mind because my reasoning was quite unfamiliar. We have not taken either a pure phenomological approach nor a pure microscopic one. Instead we have combined both. If both theories are consistent, as generally agreed. my approach is correct and simplifies considerably the continuum theories because it reduces the number of possible forms for the constitutive equations (see references in the paper). If my approach proves to be wrong, the two classical lines of thought (microscopic-continuum) are inconsistent: this would be in itself an important result. To summarize: microscopic concepts were only used to prove that a velocity potential exists. Once this is proved, we proceed in the usual way of continuum mechanics, through the postulation of constitutive relations. These are simpler, in their most general form, than the classical ones because they only involve tensors of zero order (scalars), not higher, because the constitutive equation concerns scalars instead of tensors of higher order.

Discussion of Paper 6
"A Two-Layer Model for High Speed, Three-Dimensional Turbulent Boundary Layers
and Supercritical Boundary Layer-Inviscid Flow Interactions"
presented by B.L.Reeves

L.C.Squire: You say the flow only relaxes to equilibrium values if C_{f_0} is not too small or too large. Can you say more about this?

B.L.Reeves: As stated in the paper on page 6-12 and as we have shown in Figures 2 and 6, the flow always relaxes back to the equilibrium C_f versus Re_θ variation if the initial value of the skin friction (C_{f_0}) lies above or below the equilibrium curve.

I think, perhaps, you have confused these results for relaxing flows with remarks made earlier in the paper concerning the "threshold" levels (upper and lower) of the turbulence production integral over the outer layer and the stability of the system of equations. The tacit assumption contained in this flow model is that the inner and outer layers are more or less distinct at any given station, but that as the flow proceeds downstream they are free to interact with one another. By treating the turbulent boundary layer as an inner and outer layer interaction problem. the results are expected to reveal certain consequences of that interaction which do not appear explicitly in other methods. Among these is the result that if in a flow the two-layer structure is maintained, that is, the wall layer does not swallow the outer layer or the outer layer does not swallow the inner one, the integral of the turbulence production over the outer layer has rather narrow bounds.

In other words, the production integral must be evaluated rather accurately or the interaction of the two layers will become unstable as the system is integrated downstream.

Consequently, the interaction between the inner and outer layers can be used to estimate, quite closely, the production integral in the outer layer. Such results would be quite useful because this integral has buried in it such effects as intermittency and long "memory" of large eddies.

Discussion of Paper 7
"Application d'un Schema Ameliore de Longueur de Melange à l'Etude des Couches
Limites Turbulentes Tri-Dimensionnelles"
presented by J.Cousteix

D.J.Peake: Do your calculated C_f values compare well with the experimental C_f values measured by East and Hoxey, in their protuberance experiment?

J.Cousteix: La comparaison des β_0 se fait comme suit: à partir des valeurs expérimentales de H et $R_{\theta_{11}}$ on détermine C_{fx} par la loi logarithmique C_{fx} (H, $R_{\theta_{11}}$). On obtcint alors la valeur de

$$G = \frac{H - 1}{H\sqrt{C_{fx}/2}} .$$

Ensuite on a besoin des valeurs expérimentales de δ_2 et K_2 pour former T. On peut alors calculer tg β_0 à partir de la fonction de C_{fx}, G et T.

Dans ces conditions, l'accord pour C_{fx} et tg β_0 a été satisfaisant.

Discussion of Paper 8
"A Calculation Method for Three-Dimensional Incompressible
Turbulent Boundary Layers"
presented by P.Wesseling

J.P.Johnston: Recent results obtained at Stanford University by Wheeler and Johnston (report MD-30, Thermosciences Division, Mechanical Engineering Department) are in agreement with the primary results of this paper. Of particular significance is the importance of accurate knowledge of free-stream pressure gradients.

P.Wesseling: I am glad to hear this. The agreement between your results and ours is encouraging.

D.J.Peake: Are you satisfied that the limiting streamlines (see your Figure 15 in the written paper) from the NLR experiment were not influenced by "end-wall" effects?

P.Wesseling: Yes. No correction was applied to the pressure distribution; the pressure distribution used in the calculation was taken directly from the measurements. Great care was taken in the experiment to eliminate "end-wall" effects. One of the measures which was taken was the use of curved side-walls. The absence of spanwise variations was thoroughly checked by means of pressure measurements and oil-flow pictures — see Figure 14. This experiment was a preliminary exercise for an experiment with a similar but larger model, to be carried out at NLR by Messrs B. van den Berg and A.Elsenaar in the near future.

Discussion of Paper B
"Calculation of Turbulent Shear Flows for Atmospheric and Vortex Motions"
presented by C. du P.Donaldson

L.S.G.Kovasznay: I have two questions. Firstly, were the comparisons with experiments computed assuming similarity solutions?

Secondly, what do you do in the presence of solid walls?

C. du P.Donaldson:

1. No. The comparisons were made using a forward marching procedure. The computations were carried far enough so that the flows were essentially similar. The viscous terms were retained in the equations.

2. In a previous paper on the boundary layer we have tried to treat the presence of a solid surface by the inclusion of a boundary condition, on Λ_1, derived from the nature of the model equations near the wall. At present, I believe it is not clear just how much complexity must be built into any model near a surface. Hopefully, we may be able to retain a very simple model that will be adequate.

C.H.Gibson: Regarding the question of whether or not free jets are isotropic on the centerline, I would like to comment that our recent measurements of the skewness of the streamwise derivative of temperature on the axis of a heated jet give values of about minus one; clearly not zero as required by isotropy.

It would seem fortuitous for the large scale structure of the velocity field to be isotropic if the small scale structure of a convected scalar field is not.

C. du P.Donaldson: Good I am glad to hear that your experiments tend to support non-isotropy on the jet centre-line. It would be very difficult to get a good invariant model if one were required to produce centre-line isotropy for the case of the axially symmetric free jet.

P.A.Libby: I have two comments as follows:

1. I am somewhat discouraged to learn that you now believe it necessary to alter your original formulation which involves three parameters, Λ, a and b, to incorporate three length scales, Λ_1, Λ_2, Λ_3, so that we now face the need to select five parameters. In view of the paucity of high quality data even with crucial, basic flows, I am afraid we shall not be able to select rationally these five parameters. I wonder whether we should accept some inaccuracies in these few basic flows in compensation for simplicity and hopefully generality.

2. I have been using your original formulation on the two-dimensional mixing layer. Although I have gotten some solutions of limited accuracy, my present point is that your $\overline{p'u_k'}$ modeling is not even in qualitative agreement with the recent measurements of Spencer and Jones. However I find that a modelling $\overline{p'u_k'} \propto -e \, \overline{u_1} \, \overline{u_1'u_k'}$ is at least qualitatively correct but then I need another parameter!

C. du P.Donaldson:

1. It was only with great reluctance that I abandoned the use of a single capital Λ. It was, however, absolutely necessary. I am still hopeful that only four parameters will prove adequate (that is taking $\Lambda_2 = \Lambda_3$) but only time and comparison with experimental data can answer this question.

2. (No comment was made on this part of the question.)

B.E.Launder: There is quite a lot of experimental evidence which indicates that the approximation of the pressure-strain correlation used here is not generally adequate in flows where there are appreciable mean rates of strain. For example, it leads to incorrect predictions of the relative stress levels in the plane homogeneous shear layer of Champagne, Harno and Corssin (1970) (an interesting flow, this, because convective and diffusive transports are very small). What seems to be needed, in addition to Rotta's "return-to-isotropy" proposal adopted by Dr Donaldson are terms involving products of the Reynolds stresses, and the mean rate of strain Rotta's early work (1951)

shows that such a form is suggested by the exact equation for $p \dfrac{\overline{\partial u_i}}{\partial x_j}$. It may be of interest to mention that

specific proposals of this type have recently been proposed and tested by Reynolds (1970) and by Launder and Hanjalic (1971).

References

1. Champagne, F.H., Harris, V.G. and Corssin, S. (1970) "Experiments on nearly homogeneous turbulent shear flow" Jl. Fluid Mech., Vol. 41, p.31.

2. Hanjalic, K. and Launder, B.E. (1971) "A Reynolds stress model of turbulence and its application to asymmetric boundary layers", Imperial College, Mech. Eng. Dept Rept, TM/TN A/8.

3. Reynolds, W.C. (1970) "Turbulent boundary layer computation state of the art 1970" Thermosciences Division Report.

4. Rotta, J. (1951) "Statistische Theorie Nichthomogener Turbulenz" Zeitsch. für Physik, Vol. 129, pp.547-572.

C. du P.Donaldson: I agree with Dr Launder's remarks completely. I am well aware of the shortcomings of the tendency to isotropy model and have given some thoughts to alternative models, but as yet have not tried computations with any of these.

Discussion of Paper 1
"A Re-evaluation of Zero Pressure Gradient Compressible Turbulent
Boundary Layer Measurements"
presented by J.E.Danberg

F.M.White: Is there any systematic effect of Mach number on the wake constant π_u ? I would expect π_u to decrease with M_δ . (Hypersonic data by Fiore (adiabatic) and by Kemp (heat transfer) show that π_u approaches zero).

J.E.Danberg: Plots have been prepared similar to those shown in Figure 5 of the paper with Mach number as the variable instead of Reynolds number and there was no systematic variation with Mach number. This was confirmed by statistical analysis which indicated no significant correlation with Reynolds number or Mach number. One point to consider is that the use of a reduced velocity as a compressibility transformation has an effect on the magnitude of the wake constant, as compared with the wake constant calculated without this transformation.

Discussion of Paper 2
"Some Boundary Layers Measurements on a Flat Plate at Mach Numbers from
2.5 to 4.5"
presented by D.G.Mabey

D.J.Peake: Do you know the turbulence level in the settling chamber or free stream and could they have influenced these measurements?

D.G.Mabey: We know the turbulence level in the settling chamber was very low $u'/u = 0.5\%$ and thus unlikely to influence the measurements. This level in the settling chamber was achieved by extensive modifications to the tunnel and corresponding reductions in flow fluctuations were obtained in the working section. These modifications, and the corresponding turbulence measurements are fully described in Reference 5.

J.P.Hartzuiker: Does the roughness band alter the velocity profiles?

D.G.Mabey: Apparently not, because at least at $M = 4.0$, our values of wake component (transition fixed) agree quite well with those obtained by Hastings and Sawyer (transition free) at the same Reynolds numbers based on boundary layer momentum thickness.

S.M.Bogdonoff: Your plots showed some considerable variation of wall recovery factor at high Mach number – large increases at the most downstream station. Might this be some indication that the boundary layer is not completely turbulent (equilibrium) and this may be due to the transition strip you used?

D.G.Mabey: The state of the boundary layer was monitored during the tests by surface hot films (Ref. 4). The character of the hot film signal, even at the forward station, the highest Mach number and the lowest unit Reynolds number, was laminar. All the velocity profiles measured were turbulent in character and I think it unlikely that "non-equilibrium" flow could be responsible for the high temperatures at the end of the plate.

R.K.Lobb: What recovery factor correction did you apply to Dr Meier's temperature probe, particularly near the wall?

D.G.Mabey: The recovery factor of the total temperature probe was assumed to be a unique function of the mass flow through it, as for other probes of this type (Meier, Ref. 3). Typical recovery factors were 0.99 in the free stream and 0.96 close to the wall. The relationship between recovery factor and mass flow was determined from tests in the free stream, varying the mass flow by varying the unit Reynolds number at constant Mach number with the orifice used for the boundary layer traverses. The free stream total temperature was measured with a much larger Meier probe. The free stream total temperature was uniform across the working section and within $0.5°C$ of the settling chamber total temperature. The settling chamber total temperature was also uniform to about $0.5°C$ over a large area.

The most serious uncertainty is thus introduced by the assumption that the free stream calibration was applicable throughout the boundary layer.

Discussion of Paper 11
"Comparisons between some High Reynolds Number Turbulent Boundary Layer
Experiments and Various Recent Calculation Procedures at Mach 4"
presented by D.J.Peake

S.M.Bogdonoff: First, a question of clarification; did you say that the Mach number went up and the pressure
went down for the adverse pressure gradient case?

D.J.Peake: I referred to the possibility of the existence of a small static pressure gradient normal to the test wall
in the region of the streamwise pressure increase (that is, roughly between $X = 12$ and $\ldots$ inches). The particular
boundary layer traverses under discussion were at $X = 16.62$ and $X = 20.62$ inches . We postulated that
because of the slightly concave displacement surface (and hence because of the nature of the additional compression
disturbances generated there), in addition to the reflections of the incoming waves (from the region of the test wall),
that there was the possibility of a normal pressure gradient existing such that the static pressure reduced marginally
with increasing distance from the wall towards the boundary layer edge. Such behaviour had indeed been measured
by Michel (see ONERA Publication No.102 (1961), for instance) in experiments with a concave test wall. If such a
reducing static pressure across the boundary layer were admissible, then the new found boundary layer edge
conditions yield skin friction coefficients from the Preston tube correlations that are in line with the predictions
from the various boundary layer calculation methods. I don't wish to place too much emphasis on this conjecture,
for as we pointed out, we did not measure the static pressure distribution across the boundary layer to prove or
disprove such a hypothesis. It is, moreover, the reason for the stressing of the word "tentative" in Conclusion No.3
in the written text.

S.M.Bogdonoff: I don't believe that this can be true physically. The incoming compression waves affect the outer
edge of the boundary layer first, resulting in higher pressures and lower Mach numbers than indicated by the
surface pressure. For about 4-5 boundary layer thicknesses, the wall static pressure is less than the pressure at the
outer edge. This physical picture (method of characteristics) makes it almost impossible to directly compare surveys
normal to the wall with the theoretical predictions.

D.J.Peake: What you say about the incoming compression waves in the initial region of streamwise adverse pressure
gradient is true, but at the positions in the flow that are under discussion (that is, at the second and third experi-
mental boundary layer traverses) the outgoing waves from the test boundary layer should be stronger than the
incoming waves, leading to the hypothesis advanced above.

J.E.Green: Taking Professor Bogdonoff's comment a little further, the region in which only incoming waves cross
the boundary layer will be of limited extent, say 4δ at $M = 4$. There will then be a region of similar extent
through which the leading wave, reflected at the wall, traverses out through the boundary layer. Thus there will
be a region of extent roughly 8δ , in which the incoming wave system predominates, pressure is higher at the
edge of the boundary layer than at the wall, and the boundary layer approximation $\partial p/\partial y = 0$ is not too well
satisfied. Downstream of this region, incoming and outgoing wave systems will cross each other and the pressure
difference across the boundary layer will be rather closer to zero. Given this flow structure, it is interesting that
the discrepancies between the skin-friction predictions of the finite difference methods and the measurements of
the surface tube starts some distance downstream of the onset of the adverse pressure gradient.

Following this comment, could I ask what static pressure was assumed in reducing the data to obtain the
velocity profiles which you have presented?

D.J.Peake: Yes, the pressure difference that we have assumed across the boundary layer during the streamwise
pressure rise, is small.

Answering your last point, the experimental velocity profiles displayed on the figures were calculated assuming
a constant static pressure across the boundary layer equal to the value at the wall. For plotting purposes, however,
if one views Tables 6.2.1 and 6.2.2 for traverse T2 with and without an assumed normal pressure gradient, one
will note that the plot would show a discernible but quite small difference for the effect of normal pressure gradient
on the velocity profile.

The discrepancy between the theoretical skin-friction results and the Preston tube measurements (assuming

constant static pressure across the boundary layer, equal to p_w) begins where the value of $\dfrac{dP}{dx}$, having reached

its maximum value, then begins to decrease (i.e. at $X \doteq 14$ inches). Where this occurs, the Preston tube pressure
itself, P_p , still continues to increase at its former rate, however, thereby leading to a sudden reversal in behaviour
of the experimental C_F distribution (that is based on Preston tube pressure coefficient – see Figure 10).

C.H.Lewis: Experiments and calculations have recently been made at $M = 2.4$ for similar adverse pressure
gradient turbulent boundary layer flows in which normal static pressure profiles were measured. Small normal

static pressure gradients were measured. Calculations assuming zero normal pressure gradients and using the "wall" conditions showed good agreement with measured skin-friction, velocity and total temperature profiles for adverse pressure gradients not near separation.

D.J.Peake: One will note from Figure 9a in the written paper that the experimental C_F values obtained during the streamwise pressure increase, either by means of an intermediate temperature hypothesis, or by using an adiabatic wall temperature, both yield the same trend in experimental results. In this case, therefore, the use of wall values would not seem to improve the comparison between experiment and calculation.

Discussion of Paper D
"The Structure of Turbulence in Shear Flows"
presented by L.S.G.Kovasznay

P.O.A.L.Davies: Dr Fisher, one of my colleagues at Southampton, has similar convincing evidence of deterministic structure in the circular jet. Does Professor Kovasznay feel that the high velocity peaks, i.e. those noted by Professor Kaplan yesterday, are traces of high velocity fluid drawn in from outside the boundary layer? The high velocity peaks we have observed in the jet flow appear to be induced high velocity fluid from the core of the jet.

J.M.Wallace, Jr: Would you comment on the similarity between the "bursting" phenomena and the transition phenomena?

L.S.G.Kovasznay: It is difficult to relate the laminar instability to the bursting because the outer flow is highly turbulent and it can "drive" the events in the sublayer.

W.Schönauer: I am very glad to see your results because they help my arguments that the turbulent motion should be described by equilibrium flows and relaxation times for transition from one equilibrium to another. It is well known from random motion that if the scale of the random motion is of the same order as the macro motion scale, then the random motion has a large memory (it reacts very slowly to changing the macroscopic conditions) and relaxation plays an important rôle. The example of the acceleration in the pipe is here a good example. If we describe the turbulence structure in dimensionless coefficients, these coefficients do not change in a short acceleration part (even if there are very strong changes in the flow conditions); this is well shown by your experiment.

J.A.B.Wills: In the question of the energy content of the large eddies, (you claimed that extrapolating back the tail of the velocity space-time correlation to the origin gave a large-scale contribution of about 0.5 of the total energy) I think that some boundary-layer experiments of Peter Bradshaw's gave values of at least 0.25 for the large-eddy contribution.

Secondly, if you assume that the bulges in the outer motion cause the sublayer bursts, how do you reconcile this with the classical separation of the boundary layer into independent inner and outer layers?

L.S.G.Kovasznay: The separation into inner and outer layers is a concept that originated from mean flow measurements, not from fluctuations. The fluctuations *do not* scale with distance from the wall and local mean velocity, even in the so-called logarithmic region. The "feed-back" mechanism has not been clarified, but it must be through the pressure fluctuations that cause a response in the viscous sublayer.

R.E.Kronauer: Near the end of your talk you suggested that spectral methods were to be avoided. The picture of randomly occurring spatially organized events is as equally well represented in wave number variables as in terms of correlations, and much of the data you have shown here, such as the exponential decay or the correlation plots with positive and negative regimes, are more efficiently presented in spectral terms.

L.S.G.Kovasznay: I believe it is a civil right of anyone to Fourier transform any data he wishes. It is a matter of taste.

Discussion of Paper 15
"Velocity and Density Measurements in a Free Jet"
presented by O.H.Wehrmann

W.W.Willmarth: This appears to be the first workable scheme for measuring small pressure fluctuations without disturbing the flow when the fluctuations are known to be isentropic. Have you estimated the signal to noise ratio for your measurements in which the sensitivity is $\Delta_{e/e} \approx 10^{-5}$? Also, in your measurements have you considered the influence of the size of the region in which density fluctuations are correlated on the strength of the signal from the detector?

O.H.Wehrmann: The signal to noise ratio depends on the noise level of the laser to be used (plasma instabilities, hum and random frequency variations). To reduce the hum, the laser was operated with a separate stabilized high voltage power supply. The noise level was reduced by an additional R.F. unit to reduce plasma instabilities. The spatial resolution of the signal depends on the correlation of the fluctuations in the area of the focal point. A general analysis will be given in the paper (Ref. 2) under preparation.

P.O.A.L.Davies: An alternative system is laser Schlieren which is simpler and cheaper to set up but suffers from the disadvantage that one integrates along the beam. Though crossed beams help here one still has an interpretation problem. My colleague at Southampton, Dr Fisher, has measurements of fluctuating density gradients we must compare with the measurements reported here.

J.E.Green: Could you say what the spatial resolution of your technique is, particularly along the beam axis?

O.H.Wehrmann: The resolution is approximately of the order of 1 mm.

M.A.S.Ross: Was the laser used in continuous running or intermittent?

O.H.Wehrmann: The laser was operated in a continuous mode.

Discussion of Paper 16
"An Experimental Investigation of Curved Two-Dimensional Turbulent Jets"
presented by C.Schwartzbach

L.S.G.Kovasznay: Did you try to vent the recirculating region in order to control the position of the stagnation point?

C.Schwartzbach: The influence on the reattachment point position due to venting the recirculating region was investigated by blowing secondary air through distributed perforations of the wall. Qualitatively the result was that the reattachment point moves downstream as the secondary volume flow increases. The secondary volume flow rate needed to prevent reattachment is of about the same size as the nozzle volume flow rate.

C. du P.Donaldson: May I ask how the reattachment point was determined?

C.Schwartzbach: The reattachment point was located by traversing a hot wire probe along and very close to the wall. The probe signal cannot be interpreted very close to the reattachment point, but the mean velocity variations at some distance from the reattachment point can easily be linked together, and thereby give the location of the point of zero mean velocity, which is the reattachment point.

Discussion of Paper 23
"The Effect of Density Non-Uniformity on the Turbulent Mixing Layer"
presented by G.Brown

R.C.Maydew: How did you determine the effective starting length, XO ?

G.Brown: We determined the origin by calculating on a profile integral at each X and then, on a plot of the value of the integral against X , we extrapolate a straight line through the points back to the origin.

J.L.Stollery: What was the thickness of the splitter plate in terms of the boundary layer thickness on either side, and was the geometry varied in any way?

G.Brown: The thickness of the splitter plate at the trailing edge is about 0.002" and the momentum thickness of the boundary layer at this edge is about 0.001" at high pressure and typical values of velocity on the high speed side. For the measurements the geometry was not varied but we did take some shadowgraph pictures with a trip wire at the trailing edge and this did not noticeably change the features of the large structure some distance downstream of the trip.

H.E.Fiedler: I should like to report on some observations I made in a similar flow configuration i.e. a two-dimensional shear layer between a heated stream of air and the ambient fluid at rest:

1. The temperature behaviour as a function of time exhibits a very distinct saw-tooth on which small scale turbulent fluctuations are superimposed. This is indirect evidence of the large scale you observed!

2. The mean temperature profile shows a distinct tendency towards having a small "platform" approximately in the half velocity plane, which again points towards a large scale transport mechanism.

Question: Have such profiles also been observed by the author?

G.Brown: Yes we do find density profiles which have a gentle bump on the low density side in cases where the low density is on the high speed side. This is most noticeable for the results that we have in which e^u is the same in both streams. I think it is consistent with the large structure.

D.K.Lezius: In the later scenes of your film the flow appeared, at least to me, to consist of spirals rolling up. How can you be sure that the flow is truly two-dimensional under these conditions of high shear?

G.Brown: The correlation between the outputs of two hot wires 2" apart and 2" downstream where the layer is only ½" thick is, I think, evidence that the structure is not that of spirals rolling up. Looking at the film frame by frame gives one a stronger impression of a "two-dimensional" flow. The film is a shadowgraph so that the result is an integration of variations along the light path. Since this path is 4" through the layer it is hard to see how one would see a spiral if the layer were a series of spirals. Some experiments on the two-dimensionality of the flow are being done at present.

P.A.Libby: To get my thinking straight, could I ask if I am to understand that the turbulent structures in boundary layers and shear layers, both of which are two-dimensional in the mean, are entirely different, three-dimensional in the former and two-dimensional in the latter?

G.Brown: Yes. Boundary layer experiments indicate that the motion near the wall is highly correlated in the stream direction and no doubt this gives the boundary layer its three-dimensional character. The free shear layer has no such wall region, the mean velocity profile is unstable except at Reynolds numbers of order 1 and I think it not unreasonable to expect a different large-scale structure. That this is the case is perhaps evident from the fact that the entrainment rate non-dimensionalized by, say, the turbulence energy is much greater for free shear layers than for boundary layers.

L.S.G.Kovasznay: The difference between a free shear layer and a wall layer is great. In the case of a free shear layer there is always inviscid instability due to the inflection in the profile, while in boundary layers one must go to much higher Reynolds numbers before bursts will occur.

P.O.A.L.Davies: (Comments to Professor P.A.Libby) If one has a jet with a laminar initial condition one finds a good circumferential coherence. In the turbulent jet, the boundary layer disturbances provide a spacially incoherent initial condition at the jet lip and circumferential coherence is lost. Again some 25 years ago in experiments on a two-dimensional water jet when the boundary layer was laminar, I had a shear layer that developed two-dimensional instabilities. With a turbulent boundary layer this coherence was largely lost.

J.E.Green: Do you have any difficulty reconciling, in your own mind, the clearly intermittent flow structure, where the rotational and irrotational flows are separated by a thin boundary and the diffusivity in the irrotational flow is presumably negligible, with the much greater spread of the density profile compared with that of the velocity profile?

G.Brown: Yes, to some extent I do. I have no explanation except the qualitative notion that it is easy to decelerate helium. I guess by your question you expect the turbulent Schmidt number to be near 1, but I don't know what is the basis for expecting that. We find a Schmidt number of 0.3 gives a reasonable agreement with the measured profiles.

Discussion of Paper 14
"Measurements of the Instantaneous Spatial Distribution of a Passive Scalar in an Axisymmetric Turbulent Wake"
presented by A.M.Schneiderman

C.A.Friehe: How was the value of ψ determined in the calculation of β ?

A.M.Schneiderman: The method used is described in the text of the paper. Essentially, I used Taylor's Hypothesis to approximate $\frac{d}{dt}(\sigma^2)$ in terms of a power law form for σ^2 versus z. I chose the exponent on the basis of the mean flow data.

Discussion of Paper A
"Recent Attempts to Develop a Generally Applicable Calculation Method for Turbulent Shear Flow Layers"
presented by J.C.Rotta

P.Bradshaw: I would like to congratulate Dr Rotta both on his lecture and on the 20th anniversary of the publication of his Zeitschrift für Physik papers, on which we still rely so much.

I have one comment and one question.

Dr Rotta mentioned that the assumption we made for boundary layers, that shear stress is proportional to turbulent energy, is not suitable for flows in which the shear stress changes sign. This viewpoint seems to be winning some acceptance. We did not make it clear enough in the original paper that this is simply an approximation to experimental data in boundary layers. In other flows one would use some other *empirical* relation between shear stress and energy. Calculations have already been made in ducts (as mentioned in my paper at this meeting) and in jets and wakes. I apologize to Dr Rotta for using his casual remark as an excuse for setting the record straight.

Has Dr Rotta made any calculations in a duct taking account of turbulent transport ("diffusion") of length scale?

J.C.Rotta: For plane channel flow, some calculations have been made using a collocation method to solve the ordinary differential equations. The results agree better with experiments than the solutions with the diffusion terms neglected. But a different set of coefficients was used for these early calculations. The collocation method was not used any longer.

B.E.Launder: Our experience at Imperial College with the length scale equation conforms with Dr Rotta's remarks concerning the variation of L near a wall: namely, that one does not predict a length scale which increases linearly with distance from the wall unless one introduces an extra generation-like term. We have found, however, that the difficulty is circumvented through the use of a transport equation for ϵ, the energy dissipation rate (in the manner of Chou, Davidov and Harlow and his colleagues at the Los Alamos Scientific Laboratories).

Our view is that the differences in behaviour of these two equations are traceable to the diffusion terms in the respective equations; for, while the diffusion term is not the dominant one, it is nonetheless of significance in the length-scale-determining equation near a wall. Current modelling practices usually entail the approximation of the diffusion process by a gradient-type closure. It turns out, however, as one of those unpalatable facts of life that the length scale (on q^2L) just does not diffuse at a rate proportional to its spatial gradient. It was precisely for this reason that Ng and Spalding (1970) had to add empirically an extra term to their q^2L equation to secure a linearly increasing length scale in near-wall shearflows.

In contrast, in one equation for the transport of energy-dissipation rate a gradient hypothesis for the diffusion of ϵ leads, without further tampering with the equation, to satisfactory predictions of the length scale (which may be taken as q^3/ϵ) in plane flows both near to and remote from walls. A recent paper by Dr Hanjalić and me has provided some theoretical support for representing the rate of diffusion of dissipation by a gradient flux approximation, at any rate for the boundary-layer flows which are here in question.

References

Ng, K-H. and Spalding, D.B. "Prediction of 2-Dimensional boundary layers on smooth walls with a 2-equation model of turbulence" Imperial College, Mech. Eng. Dept Rep. BL/TN/A/25, January 1970.

Hanjalić, K. and Launder, B.E. "A Reynolds stress model of turbulence and its application to asymmetric boundary layers" Imperial College Mech. Eng. Dept Rep. TM/TN/A/8. March 1971.

J.C.Rotta: The recent work of Dr Launder, Professor Spalding and other members of this group of imperial College provides a great amount of valuable experience. Further investigations will certainly benefit by this work. it was interesting to learn that the experiences of these investigators with the length scale equation conform to my own findings, although different ways have been tried to overcome the difficulties.

L.S.G-Kovasznay: Your theory is asymptotic in Reynolds number Does this mean that it cannot show dependence of results on Reynolds number?

A.Rotta: Theory predicts no Reynolds number effect for free shear flow cases. For flows with solid boundaries a Reynolds number effect appears as a consequence of matching the solution with the law of the wall.

K.Gersten: You mentioned the fact that the constant a_p was too small to fit the experiments properly. Since you have five different constants to be adjusted, how can you be sure that just the constant a_p is responsible for certain discrepancies between theory and experiment?

J.A.Rotta: To answer this question, it may be kept in mind that the law of the wall constraint requires the coefficient of the dissipative term of the shear stress equation, k_p, to be proportional to a_p. Consequently, with a small value, $a_p = 0.09$, both terms, production and dissipation, are weak. Since mean velocity gradient and shear stress have opposite signs in the central region, when saddle shaped profiles occur, the shear stress production and dissipation have the same sign. They are balanced mainly by the shear stress convection. On the other hand, with a high value of a_p (and k_p), the dissipative term is strong and is compensated by a strong production of opposite sign. Thus, mean velocity gradient and shear stress have the same sign everywhere. The shear convection has only a weak effect in this case. Calculations based on a value of $a_p = 0.25$ indicate no saddle shaped mean velocity profiles, even though the diffusion coefficients, k_q and k_{qr}, are varied in a wide range.

.

Discussion of Paper 9
"An Experimental Study of the Compressible Turbulent Boundary Layer
with an Adverse Pressure Gradient"
presented by R.P.L.Voisinet

J.E.Green: Did you make any checks on the streamwise integral balances of momentum and heat transfer? And, if so, are you able to identify the source of the appreciable energy defect which you have measured in your "adiabatic" boundary layer?

R.P.L.Voisinet: A streamwise momentum balance was made and is discussed in the report, however, an energy balance was not made. The energy defect in the adiabatic data appears to be due to the fact that the "adiabatic" condition could not be maintained precisely in the throat region. And, as was pointed out in the paper, slight variations in the wall temperature at the throat cause large variations in the downstream temperature profiles.

F.M.White: For the plots of $\dfrac{T_t - T_w}{T_{te} - T_w}$ versus $\dfrac{U}{U_e}$, is T_{te} the *measured* value? If so, is it *varying*

downstream from the throat and a function of nozzle cooling? If so, there is nothing anomalous about your plots, since the "lost heat" is merely being convected across the outer layer by the vertical velocity component. In general, I believe there is little to be gained of a fundamental character from such T_t plots. Both Crocco and Walz are wrong for *fundamental physical reasons*, e.g. $P_r \neq 1$, so we get nothing but confusion and arguments from displaying the data in this manner.

My personal thanks for announcing to the world that nozzle cooling *has no effect on the skin-friction*, since this is one of the basic assumptions of my little theory.

R.P.L.Voisinet: The value of T_{te} is a locally measured property of the flow and was not observed to change with streamwise distance or throat cooling.

Discussion of Paper 10
"The Supersonic Turbulent Boundary Layer in Adverse Pressure Gradient –
Experiment and Data Analysis"
presented by W.B.Sturek

A.D.Young With regard to the difficulty of determining integral quantities due to the ambiguity in defining the boundary layer edge, have you considered doing the integration along the isobars, or lines coinciding with the isobars near the boundary layer edge? In that case there should be no ambiguity.

W.B.Sturek: No attempt has been made to evaluate the integral thicknesses along isobars; however, isobars have been plotted for the flow over the ramp model. These isobars deviated sufficiently from simple straight line extensions of Mach lines from the outer flow to discourage their use as a path of integration.

I.S.Donaldson: How confident is the author that a transverse measurement of static pressure is a measure of two-dimensionality of the flow?

W.B.Sturek: I don't consider the transverse static pressure measurements to indicate absolute two-dimensionality, but rather to provide an indication of the magnitude of the departure from two-dimensionality for the conditions of this test.

J.E.Green: In your slide on fluctuating quantities, is the scaling quantity e_0 based on a local or a reference quantity; i.e. does the slide indicate an absolute or only a relative increase in the fluctuation levels in the adverse pressure gradient?

W.B.Sturek: The reference value was 0.005 Volt and was the same for all data points shown.

Discussion of Paper 31
"Turbulent Boundary Layers at Supersonic and Hypersonic Speeds"
presented by G.T.Coleman

R.N.Cox: Figure 14 of your paper draws an important conclusion that the flap angle in for separation levels out as the Mach number increases. There must be some doubt about the two-dimensionality of the experiments as the plate has a small aspect ratio, the boundary layer is thick, and much of the flap even lies within the tip vortex region. How sure are you that this levelling out does really occur?

G.T.Coleman: The data on Figure 14 represent a "slice" through the data of Figure 12 at a Reynolds number of 4×10^6 – this was chosen because it included a lot of data especially our new data scaled to the condition. However a similar cross-section taken at a higher Reynolds number has shown a similar tread.

J.L.Stollery: (Comments only) To add to Mr Coleman's reply, we are of course aware that no experiment is absolutely two-dimensional. We would however expect that α_i reached a level since, at a flap angle of $46°$, the oblique shock will detach and form a normal one.

L.C.Squire: In your paper you deduce values of R_θ via a Reynolds analogy. How do these values agree with those found from your traverse?

G.T.Coleman: We have not done this, as yet. However, it will be carried out but it should be remembered that an assumed temperature distribution was used in the derivation of the velocity profiles.

Discussion of Paper 12
"An Experimental Investigation of the Turbulent Boundary Layer
Along a Streamwise Corner"
presented by A.D.Young

S.M.Bogdonoff: I was most interested in the secondary flow phenomena you described. Is it possible to answer the question as to whether the secondary flow is due purely to the laminar character or is it possible that it is due to geometry or physical set up?

A..D.Young: I do not think that the secondary flow observed in the laminar case is just a peculiarity of our experiments, although I accept the possibility. It was evident in a wide range of circumstances and pressure distributions. However, I think that the question remains as to whether it is an essential feature of laminar flow, or whether it is a manifestation of instability and is therefore presumably dependent on Reynolds number. We were not able to get down to a low enough Reynolds number to see any essential change in the development of the secondary flow; nevertheless, i am inclined to favour the instability hypothesis because of the way the mean flow velocity profiles change with distance downstream from the leading edge.

Prof. K.Gersten: How does the work reported compare with results obtained by Rubin et al.?

A.D.Young: I recall seeing a paper a few years ago by Rubin and his colleagues setting out the analysis and resulting equations for the laminar flow in a corner, and the paper indicated that work was proceeding on some solutions of those equations. I have not, however, seen any results of such calculations as yet and so I cannot say how they compare with our measurements. Perhaps Mr Mojola may have more up-to-date information on Rubin's work.

R.H.Korkegi: It may be well to point out that the Brooklyn Polytechnic team have developed two analyses:

(1) One by Bloom and co-workers on the corner boundary layer at low speeds and later

(2) A merged layer analysis by Rubin which holds for relatively low Reynolds numbers and, I believe, high Mach numbers, and represents the flow fields all the way from the wall to the shock wave.

Dr Gersten was alluding to the former study, I believe.

O.O.Mojola: The work of Rubin and his co-workers has been published in a recent issue of the Quarterly of Applied Mathematics. Their recent work indicates a secondary flow which is directed inwards along the walls and outwards roughly along the corner bisector. But as far as I can make out, their calculated contours of the streamwise mean velocity do not reflect the experimental observed (Zamir and Young, 1970, Ref. 24) distortion of the streamwise velocity.

P.Bradshaw: Were the static pressure measurements corrected for the effect of turbulence on the probe?

O.O.Mojola: The answer is NO, because we don't know HOW!

Discussion of Paper 24
"Etude d'une Couche Limite Turbulente Avec Injection a la Paroi d'un Meme
Gaz ou d'un Gaz Etranger"
presented by R.Michel

H.McDonald: Do you have any comment on the fact that some people, for instance Abeci et al., find it necessary to include an effect of blowing on the damping constant A^+ in order to improve the agreement between theory and experiment?

R.Michel: Notre hypothèse fondamentale est que la correction de la longueur de mélange proposée par Van Driest est valable dans le cas général à condition de retenir comme paramètre d'influence le rapport τ_t/τ_e du frottement turbulent ou frottement laminaire. Dans le cas de l'injection, ceci conduit quand on exprime la correction en fonction de y^+, à prendre pour la "damping constant"

$$A^+ = 26(1 + v_w^+ u^+)^{-1/2} .$$

La modification nous apparait donc comme logiquement nécessaire; il nous semble intéressant d'avoir pu la faire apparaitre par le seul concept d'influence de τ_t/τ_e valable très généralement.

Discussion of Paper 25
"A Survey of Data for Turbulent Boundary Layers with Mass Transfer"
presented by D.Coles

F.M.White: If Stevenson's law is used to prepare curves similar to your Figure 2, what discrepancies occur, e.g. are the slopes (κ) variable or the wake heights erratic, as in your Figure 11? Is Simpson's law "immensely" better, "much" better, "somewhat" better, or "slightly" better?

L.C.Squire: I have done a similar analysis for Simpson's and McQuaid's data but I get a different result in that I support Stevenson's proposal for the law of the wall. This is basically due to the differences in skin-friction results. I have re-analysed Simpson's data and get different skin-friction values so that his profiles agree with Stevenson's law.

D.Coles: (Answers to both F.M.White and L.C.Squire) In all of my data processing so far, three different analyses have been carried out in parallel. Two of these are discussed at length in my paper. The third is a mixing-length analysis based on Stevenson's condition for the intercept in the logarithmic formula. I have not studied the results very carefully, because I consider the values obtained for C_f to be much too low (for moderate or large blowing) compared to values recommended by the experimenters. The latter should of course be verified, and I have not yet done so. At the moment, I consider Simpson's law to be "much" better than Stevenson's. An exchange of information seems to be in order.

Discussion of Paper 26
"The Suppression of Shear Layer Turbulence with Mass Transfer"
presented by J.P.Johnston

P.Bradshaw: In Figures 7b and 7c the effect of increasing rotation number at given Richardson number is apparently to *reduce* the mixing length. Granted that this is stretching the data rather far the trend seems fairly well established. Have you any comments on this rather surprising trend?

J.P.Johnston: The trend noted is clear in Figure 7b, but not in Figure 7c. If one accepts the accuracy of the data to be better than $\pm 10\%$, the data at $Ro = 0.056$ in Figure 7c is not consistent with the idea of a reduction of mixing length as suggested. However, if the trend is indeed real, it suggests that the parameter β is itself a function of rotation number. No specific claims are currently made for the absolute accuracy of the data, but it is felt that the trend at least of Figure 7b is real and deserves some comments. First, on the stable side of the channel, the flow will become laminar at sufficiently high Ro. When laminar, the mixing length ratio for the condition of our experiments will be of the order of 0.1 and it will be independent of Richardson number. The transition rotation number for $Re = 3.5 \times 10^4$ is close to $Ro \doteq 0.2$, roughly twice the maximum rotation number of the data in Figure 7b. Since the transition process is not sudden, it appears logical that as Ro approaches the magnitude necessary for transition back to laminar flow, the mixing length ratio should reflect the apparent fact that the real flow may be intermittently laminar and turbulent as transition spots sweep by a fixed point. At this time, I am not prepared to quantify this point however.

B.E.Launder: In order to calculate the mixing-length distributions in your flow you would have had to calculate the shear stress distribution across the channel. Could you mention briefly how you determined this, please?

J.P.Johnston: [Dr Johnston replied to the effect that the flow was considered fully developed and the wall stresses were found by way of Preston tube.]

B.E.Launder: Would it be fair to say that, by using surface impact devices to determine the surface stress, you have used a device which relies, for its accuracy, on the universality of the mixing length near the wall, in order to measure non-universal features in the mixing-length profile?

J.P.Johnston: As pointed out, the flow was close to fully-developed and thus the shear stress distribution was linear. Its absolute value could hence be determined by measurement of the wall shear stress. The Preston tube was used only when the wall-layer flow was turbulent. In the original study, Reference 1, experiments were conducted to determine the effects of rotation and tube diameter, d, on the Preston tube results in terms of the parameter $\Omega d^2/\nu$. No effects were noted. Our limited study was conducted to confirm the results of earlier work (Hill and Moon, M.I.T., Gas Turbine Lab. Rept No. 69, June 1962) in which $\Omega d^2/\nu$ was varied by an order of magnitude at fixed Re and Ro, without effect on the wall shear indicated by the tubes.

Discussion of Paper 27
"Développement d'une Couche Limite Turbulente dans un Ecoulement
Exterieur Turbulent"
presented by G.Charnay

L.S.G.Kovasznay:

1. Les auteurs doivent être félicités pour cette contribution interessante. J'aimerais poser les questions suivantes: Quelle est la définition exacte de l'épaisseur de la couche limite? Comment est-elle définie?

2. Est-ce que les tensions de Reynolds étaient nulles à l'épaisseur $y = \delta$ ou restaient-elles ..e valeurs finies dans le cas de pre turbulence forte?

G.Charnay:

1. Pour une section droite, l'épaisseur de la couche limite est égale à la distance entre la paroi et le point où la vitesse moyenne atteint 99% de la vitesse extérieure. A cause de l'incertitude qui existe sur la détermination de cette distance. chacune des épaisseurs rapportée ici est en fait une moyenne des résultats obtenus lors de plusieur essais.

2. Les mesures comparatives que nous avons effectuées montrent que pour $y = \delta$, les tensions de Reynolds ne sont pas nulles et ce d'autant moins que le niveau de turbulence extérieur est plus élevé. A partir des seuls résultats présentés ici, il est difficile de faire le point des différents phénomènes qui contribuent à l'accroissement de ces tensions de Reynolds. car aucun échantillonnage n'a été encore utilisé.

W.Schönauer: In my paper (Ref. No. 29) I gave boundary layer equations, which contain a term $\hat{c}_0$. This term is responsible for the eddy viscosity at the edge of the boundary layer. If in the outside motion there is turbulence, the value of $\hat{c}_0$ increases and this causes a flattening of the velocity profile at the outer edge (the boundary layer is enlarged) and an increase of the friction coefficient. This $\hat{c}_0$ term does not appear, when in the Prandtl boundary layer equations an eddy viscosity is introduced instead of the laminar viscosity. But this term just dominates the flow at the outer edge of the boundary layer, and explains theoretically the effects which you found by your measurements.

G.Charnay: Votre article se rattache au concept du coefficient de viscosité. Nous pensons que les phénomènes qui se passent au bord de la couche limite perturbée sont, dans leur mécanisme, beaucoup plus complexes.

J.M.R.Graham: I recently measured the turbulent energy balance in a boundary layer in a similar situation and found that the turbulence diffusion (obtained by difference) was largely suppressed in the outer region of the boundary layer. This I assume to be due to entrainment of the freestream turbulence into the boundary layer in the "gaps" between the large eddies. This inward diffusion of turbulence opposes, in the mean, the outward diffusion of boundary layer turbulence in the large eddies of the boundary layer.

G.Charnay: Oui, vos résultats paraissent bien corroborer notre opinion sur l'origine des modifications observées à savoir qu'elles ne sont probablement pas dues à une augmentation du processus diffusif de l'intérieur vers l'extérieur de la couche limite.

Discussion of Paper 28
"Some Measurements of the Distortion of Turbulence Approaching
a Two-Dimensional Body"
presented by P.W.Bearman

R.N.Cox: Your argument that filling the wake by a free streamline body would avoid pressure fluctuations coming from downstream of the body presumably only applies to the case of $L_x/D \ll 1$. For $L_x/D \gg 1$, would one not expect such fluctuations due to variation of the equivalent free streamlines, lift effects etc? Did you measure pressure fluctuations on the body surface?

P.W.Bearman: Professor Cox is right to point out that when $L_x/D \ll 1$ the v-component of turbulence could induce circulation changes about the complete body. The cross-section of the model looks somewhat like a blunt-nosed aerofoil section. However the length of the body was nearly an order of magnitude greater than the largest scale of turbulence, and it should be valid to treat the complete flow as inviscid and neglect the effect of any Kutta condition at the trailing edge. When stating the condition $L_x \gg D$ this should be accompanied by the further condition $L_x \ll c$, where c is the model chord. The measurements of pressure fluctuations at the stagnation point suggested that these were related directly to the approaching turbulence.

APPENDIX B

MEETING SUMMARY SESSION

Professor Bogdonoff

The next two speakers will be Dr Küchemann from England and Prof. Libby from the U.S. My instructions to them were to tell us what they thought was important or what they thought was not important, or tell us something about the scale of confusion that reigned in the last three days. This was a most difficult assignment to make, but I thought it might be appropriate in this field of turbulence to end off perhaps still in a very turbulent state.

MEETING SUMMARY SESSION

Dr Küchemann:

Mr Chairman, Ladies and Gentlemen, I can tell you what the specification was in my case. I am the outsider, someone who is really not concerned either with preparing this meeting nor with the work that is being done in this field. I look at it as someone who knows nothing about it, and I can promise you that I shall leave you confused. I should also say that I did get permission from the Chairman to say outrageous things. Now, as to my impression, I must say that I am quite impressed by what I heard. So impressed, in fact, that I am almost flat, almost two-dimensional. Seriously, as an outsider, who hears about what is going on only occasionally, mainly at such conferences, one is really impressed how alive the subject is and how much progress is really made. Things are moving, there is no doubt about it, but, on the other hand, I would also say that the end is not yet in sight. That is the impression that I got. I also think that there was a very large proportion of very substantial contributions, really solid papers, and that progress was reported both on the theoretical side and in experiments. By theory, I mean methods for calculating things as well as numerical methods using computational aids. It is really amazing what can now be done in both fields. Another impression I got was that the emphasis in recent years in the work reported here was to firm up on the fundamentals. It seems that many people want to get down to it and find out more about the fundamentals. Now, that had several consequences. One, I think, was that people did tend to concentrate on two-dimensional flows. This was rather in contrast to Bradshaw's introduction, where he showed us "complex flows" and "awkward cases". Actually, very little of that did come up at the meeting. There were very few papers concerned with any of these more complex flows, and very little on three-dimensional flows. Also, whereas previously in order to be respectable you had to prove that your method would predict separation, there was almost utter silence about the phenomenon of separation at this meeting. Nobody seemed to want to know about that. I think that, in this respect, there was very little progress to report on, and I think in all the cases that Bradshaw mentioned, which are quite important cases from the practical point of view, we are really a very long way behind. I think we find it all very difficult even to visualize what the large-scale structure of these flows really is. In this respect we are poor. Another possible consequence of concentrating on the fundamentals was the apparent emphasis on flows where an equilibrium structure had been achieved. This was described in various ways: self-similar flows, self-preserving flows, and some people talked about relaxed flows. I'm not sure what the professionals mean by that, but it conjures up visions in my mind of a tired boundary layer coming home after a hectic day, putting its feet up and just burbling along a little. If you look at it from the practical point of view, then we are a very long way away from these rather select boundary layers. Just to mention one typical case some of us are concerned with, the flow over a supercritical wing. There, the boundary layer comes out of a very confusing transition process, it hardly knows what instability criteria it should obey. Then it is subjected to incoming compression waves because people want shockless compressions. These waves must affect at least the turbulence structure in the outer part of the boundary layer, I would have thought. After that, we put a strong shockwave on it, which usually comes so suddenly that it has to separate. When, luckily, it will re-attach, it has to settle down to some other kind of turbulence structure. But we hardly leave it   time for a rest and subject it to the strongest possible adverse pressure gradient, nearly up to the point of separa   on. Then we bend the whole thing round near the trailing edge and let it join up with another lot which had an entirely different history. In the process, there is still some circulation left in the near wake, and all the time the poor boundary layer is kicked sideways, this way and that way, on these three-dimensional wings. This is not a relaxed life, and these are the boundary layers some of us are really interested in.   That is what I mean by saying that we have a long way to go.

For this reason, I got a bit frightened by the apparent complexity of what has been described here, even in the simple case of two-dimensional flows. The theories get very complex, and the experimental methods get equally complex. In the theory, I think we seem to get up to 9 differential equations. On the experimental side, I got the impression that even the conditional samplers find it difficult to understand each other. How can one then predict practical situations? The only comfort there was expressed by Mr Peake with some undisguised glee, when he said that he found no increase in accuracy or prediction with the complexity of method. Even the simple methods gave adequate answers, in his opinion. This was not resolved during the meeting. When he said it, there was very little reaction. I thought there would be some outbursts, but nothing much happened.

There is another matter which to my mind was not resolved at the meeting. Bradshaw suggested that future experiments should concentrate on measuring quantities that appear in the calculation, and Young, as the Chairman, then questioned this, and also asked whether Bradshaw's statement that the theory was now realistic enough could be accepted. But there was no answer to these questions. These are important points, and it is rather a pity that we did not discuss them further. If you ask me, I am inclined to answer No to Professor Young's questions. For one thing, I have the feeling our theories are not yet realistic enough. It may well be that at least some of the bars over every term will have to come off before we get a theory which is physically realistic. To explain what I mean by that, I'd like to introduce two more variations on a theme of Prandtl. Bradshaw started with it, so I might as well end the meeting with it. The first variation is a sort of adagio in 6/8 time: waves in a supersonic flow with a compressible boundary layer underneath. This was some work that Prandtl made me do over 30 years ago. He wanted to know what are the interactions between these waves and the compressible boundary layer. It is a problem that is still with us. Well, at that time I had to take account of the pressure field and vary the pressure right into the boundary layer. I had to take rotation into account, as there was shear in the boundary layer, but I was allowed to leave the whole flow inviscid. I treated an inviscid boundary layer and actually got some answers about the interaction. Maybe, we could play this variation again sometime and include the pressure field induced by whatever disturbances we have and in some places even leave viscosity out. I'm not sure whether Professor Domingos would approve of this.

My second variation comes from Prandtl's paper of 1904, the one we all live on and play tunes on. There are actually only a couple of pages on boundary layer theory in that paper, the rest is concerned with flow separations and its consequences, especially with free shear layers. These he regarded to be surfaces of discontinuity, and what he conjectured then was actually demonstrated to us at this meeting by Dr Brown in a paper by Brown and Roshko. I think that was one of the highlights of the meeting. A really beautifully carried-out and thought-out experiment, where one could see what was going on. I have a feeling that the main features of that flow can probably be explained by a model of an inviscid flow involving only surfaces of discontinuity. I do not think that this is a stability problem. There are vortex cores present all the time. We have an array of vortex cores growing in time as they move, which fits well with the observations. It is a regular array of double-branched vortex cores which are swept downstream. They induce a certain far field and that, in the first place, can explain the gradual transition from one velocity level to another. The near field, if you happen to go through one of the cores, will explain for you the velocity jumps. This may be worth working out in more detail. It would be a model which involves no shear stress, no eddy viscosity, none of that; only large lumps of vorticity tumbling along. If there is anything in that model, one thing that it would demonstrate is that whatever one observes depends very much on how one observes it. An instantaneous, infinitely fast, traverse would pick up the features I just described. A slow traverse would show something quite different. Of course, it must be very difficult then to make any sense of it at all and to analyse such results. That is what I mean: if you put bars over what you measure, you might in fact obscure what is a perfectly regular motion. This kind of model, I think, is getting fairly close to Kovasznay's notion of large-scale organized motion inside the boundary layer. With the presence of a wall, it must be more complicated, and that is why he said organized motion but "occurring at random". What I described would be perfectly regular, no randomness in it at all.

Altogether, I think we are now catching sight of some of the real physical occurrences. That was one of the outcomes of this meeting, one of the impressions I got. We are getting to grips with physical reality, and I really am hopeful that the enormous improvements in the experimental techniques will help us to see better what is going on. We had some most impressive reports on experimental work; Kovasznay himself, Willmarth, Wehrmann, Kaplan and Laufer are looking into what is going on. So there is some real hope for the future, and I can only say, carry on, please, we might get there one day. Or perhaps, I should address this to our masters and ask them, please let us go on.

Professor Paul A.Libby:

Mr Chairman, Ladies and Gentlemen. When Professor Bogdonoff called me a few weeks ago and asked me to make some remarks at the close of this meeting, I quickly said yes. That is an example of a phenomenon which perhaps others of you have experienced, namely, if you are invited to do something two weeks ahead, then that is infinite, you forget about saying no, and you just go ahead and say yes. That is in fact what I did, but as this moment approached, I became more and more uneasy about presenting an Olympian view of this meeting. Perhaps that is due to the fact that I do not want to think of myself as old enough to put forth Olympian views. So what I can do is give you some personal impressions, for what they may be worth, of this meeting and what we heard.

I think it is perhaps convenient to divide just roughly the papers up into those which concern predictive methods and those which provide experimental data. Then further, of course, the predictive methods can be divided into the more or less classical methods involving eddy-viscosity and mixing length concepts, that is those methods which close the equations we have to deal with at the very first level. I must say, as an academic person, it is very discouraging to find how well those methods do, even for relatively complicated flows. We had several papers involving three-dimensionality, we had integral methods doing very complicated flows with re-attachment and things of that sort, and by and large, they predict very well many of the things that an engineer wants to know, like skin-friction and heat transfer.

However, these methods do have their troubles. If you try to apply them to a slot flow, I think you will get into difficulty. You will get into difficulty in general when things are changing relatively rapidly with x, that is, still slowly enough with x, so that we can think in terms of a boundary layer theory, but changing relatively rapidly with x as far as the turbulence is concerned. In addition, there is always, it seems to me, a large class of problems where we may want to know more than just skin-friction and mean velocity profile. There are problems where we want to know what the turbulent kinetic energy is for example. Dr Donaldson pointed out the very interesting fact that, if we want to treat in a more serious way, chemically reacting turbulent flows, we are going to have to do something about those second and third order correlations, which we have been disregarding, not because we knew that they were negligible, but because we did not know what to do with them. For these reasons, it seems to me the second group of predictive methods that we heard about, that is those which involve closure at a lower level, are certainly worthy of great attention. They are in my view rather exciting. I must say, however, that as somebody who has been working very close to the Donaldson model, in fact, simply applying Donaldson's modelling to a very simple flow, namely the two-dimensional mixing flow, I am somewhat discouraged. I certainly was not further encouraged by Professor Rotta's talk this morning. It seems to me that when we start worrying about selecting 5, 8 or 9 parameters, even though some of them may be constrained by things that we know, as Professor Rotta told us this morning, we will soon run into the fact that the amount of high quality data available to make that selection forms a zero set.

I have had the discouraging experience recently of taking what I thought to be perfectly reliable data on two-dimensional mixing flow, not being able to predict anything very well, and then deciding to back off somewhat in what I was trying to do. I took the view that the mean velocity profile is well-known and is given by an elementary function. From that you can compute the shear, that is, you make a prediction about what the shear must be. I did that and compared it with the so-called measured shear. It was off by a factor of 1.5! Now, it is too difficult to ask a predictive method to be applied to that sort of situation. Certainly, you are not going to be able to predict 5 or 8 parameters from data of that quality. Furthermore, if you do somehow or other rationalize the selection of that many parameters in these new methods for simple flows, I am afraid we are not going to have any confidence that those parameters are invariant when we go to a more complex flow. If you wanted to predict, as Dr Donaldson said, the two-dimensional mixing problem just to get the mean velocity profile, you certainly would not use these methods, but these methods had better be able to predict that flow a priori, or else you certainly are not going to make predictions with confidence in some of the more exotic flows that we are really interested in. As to the experimental data, it seems to me that they can be also divided into two sets; those which involve mean flow measurements in more or less practical flows, not of the complexity that Dr Küchemann described to us, but they are high speed, with mass transfer, with pressure gradient, approaching separation, etc., and, of course, the more detailed measurements involving conditioned sampling, hot wire anemometry and the like.

With respect to the former flows, I was very impressed and pleased, I must say, that several research workers actually compared their data with a variety of predictive methods. I think that is very important, because one of the things I have found disturbing over the years is the following: there are many predictive methods, the literature is cluttered with them, but they never compare, or make a prediction about the same flow. You know, Researcher A compares with one set of data, and Researcher B, who has a different method, compares with another set of data. I defy anyone, without a lot of work, to make an assessment of which of those predictive methods has some general applicability.

A few years aog, I tried to convince the NASA Fluid Mechanics Advisory Committee that in the case of turbulent compressible boundary layers, it should select a few model situations with the notion that a Committee of that sort would be able to impose a moral obligation on the various generators of predictive methods to calculate those model flows, so that you and I can tell how well they do on those particular flows. Well, they thought that it was a great idea, but they told me to go home and arrange it. I must say that that was not what I had in mind.

We realize now that the great contribution of the Stanford meeting was that it took a particular class of turbulent flows and did just as I have indicated should be done for other flows, namely, they set up some model cases and people who had methods were asked to compare their predictions for those flows. That, of course, was very illuminating. I can guarantee that sometime in the future somebody will do just that for the compressible turbulent boundary layer. I can also guarantee that when it is done, the predictions will simply scatter all over the map for a few iterations, and then some parameters will be adjusted and things will perhaps settle down.

With respect to the second class of experimental data, that is those concerned with spectra and conditioned sampling, these certainly are useful in elucidating our notions of turbulence. I would like to remind you of that charming observation of Professor Kovasznay, in which he divided the turbulent community into those who had predictive methods without much turbulence, and those with turbulent experimental data who did not wish to predict anything. There is perhaps a third set, which Dr Küchemann really suggested, namely, those engineers who have to make a prediction about skin-friction or heat transfer. They do not care about either one of the former groups of people.

I do have the definite impression, it may be wrong, that spectral data and conditioned sampling have had almost zero impact on predictive methods. Accordingly I was pleased to see that Professor Kovasznay at least

indicated in the last paragraph of his paper, that he is thinking along the lines of how some of our notions of turbuient shear flows, which come from conditioned sampling, would fit into a predictive method.

Considering the fact that this is an AGARD meeting, I want to remind you that it has been six years since we had a meeting of this sort. The last one was in 1965 in Naples, I believe. If I would compare where we stand now with what I recall of that meeting, I have the impression that the predictive methods have definitely improved in power and generality. The catalogue of mean flow data that we have at our disposal has expanded. Our fundamental notions of turbulence seem to have improved. But I also want to tell you that I have the impression that we are sort of fighting our way into a thicket, and that it will be a long time before we come out the other side, if at all. *That*, of course, reminds me of the distinguished scientist who was quoted as saying that when he faced the good Lord on Judgement Day, he was going to ask him to explain two matters, namely, the fundamental meaning of quantum mechanics and secondly, the nature of turbulence.

In closing, I think we all must thank the Program Committee for arranging this excellent meeting and must urge them in five or six years from now to have a corresponding meeting. I think we must also thank our United Kingdom colleagues for their fine hospitality in this wonderful city. Finally, we must all go home and do some more work on turbulent shear flows.

APPENDIX C

A SELECTION OF
AGARD PUBLICATIONS IN RECENT YEARS

A SELECTION OF
AGARD PUBLICATIONS iN RECENT YEARS

CATEGORY I — PUBLISHED BY TECHNIVISION SERVICES AND
PURCHASABLE FROM BOOKSELLERS OR FROM:—

Technical Press Ltd
112 Westbourne Grove
London W.2
England

Hans Heinrich Petersen
Postfach 265
Borsteler Chausee 85
2000 Hamburg 61
West Germany

Circa Publications Inc.
415 Fifth Avenue
Pelham
New York 10803, USA

Diffusione Edizioni Anglo-Americaine
Via Lima
00198 Rome
Italy

1969

AGARDograph 120   Supersonic turbo-jet propulsion systems and components
Edited by J.Chauvin, August 1969.

1970

AGARDograph 115   Wind effects on launch vehicles
By E.D.Geissler, February 1970.

AGARDograph 130   Measurement techniques in heat transfer
By E.R.G.Eckert and R.J.Goldstein, November 1970.

Conference   New experimental techniques in propulsion and energetics research
Proceedings 38   Edited by D.Andrews and J.Surugue, October 1970.

CATEGORY II — NOT ON COMMERCIAL SALE — FOR
AVAILABILITY SEE BACK COVER

1965

Report 514   The production of intense shear layers by vortex stretching and convection
By J.T.Stuart, May 1965. (Report prepared for the AGARD Specialists' Meeting on
"Recent developments in boundary layer research", May 1965.)

AGARDograph 91   The theory of high speed guns
By A.E.Seigel, May 1965.

AGARDograph 97   Recent developments in boundary layer research
(in four parts)   AGARD Specialists' Meeting, Naples, May 1965.

AGARDograph 102   Supersonic inlets
By Ione D.V.Faro, May 1965.

AGARDograph 103   Aerodynamics of power plant installation
AGARD Specialists' Meeting, Tullahoma, October 1965.

1966

Report 525   The pitot probe in low-density hypersonic flow
By S.A.Schaaf, January 1966.

Report 526   Laminar incompressible leading and trailing edge flows and the near wake rear stagnation point
By Sheldon Weinbaum, May 1966.

Report 539   Changes in the flow at the base of a bluff body due to a disturbance in its wake
By R.Hawkins and E.G.Trevett, May 1966.

Report 542   Transonic stability of fin and drag stabilized projectiles
By B.Cheers, May 1966.

Report 548   Separated flows
(Round Table Discussion), Edited by J.J.Ginoux, May 1966.

Report 550   A new special solution to the complete problem of the internal ballistics of guns
By C.K.Thornhill, 1966.

Report 551   A review of some recent progress in understanding catastrophic yaw
By J.D.Nicolaides, 1966.

AGARDograph 109   Subsonic wind tunnel wall corrections
By Gardner, Acum and Maskell, 1966.

AGARDograph 112   Molecular beams for rarefied gasdynamic research
By J.B.French, 1966.

AGARDograph 113   Freeflight testing in high speed wind tunnels
By B.Dayman, Jr, 1966.

Conference   Separated flows
Proceedings 4   Specialists' Meeting, Rhode-Saint-Genèse (VKI), May 1966.
(two parts and one supplement)

Conference   The fluid dynamic aspects of ballistics
Proceedings 10   Specialists' Meeting, Mulhouse, September 1966.

Conference   Recent advances in aerothermochemistry
Proceedings 12   7th AGARD Colloquium sponsored by PEP and FDP, Oslo, May 1966.
(in two parts)

1967

Report 558   Experimental methods in wind tunnels and water tunnels, with special emphasis on the hot-wire anemometer
By K.Wieghardt and J.Kux, 1967.

Advisory Report 13   Aspects of V/STOL aircraft development
(This report consists of three papers presented during the joint session of the AGARD FDP and FMP held in Göttingen, September 1967.)

AGARDograph 98   Graphical methods in aerothermodynamics
By O.Lutz and G.Stoffers, November 1967.

AGARDograph 117   Behaviour of supercritical nozzles under three-dimensional oscillatory conditions
By L.Crocco and W.A.Sirignano, 1967.

AGARDograph 119   Thermo-molecular pressure effects in tubes and at orifices
By M.Kinslow and G.D.Arney, Jr, 1967.

AGARDograph 121   Techniques for measurement of dynamic stability derivatives in ground test facilities
By C.J.Schueler, L.K.Ward and A.E.Hodapp, Jr, 1967.

AGARDograph 124   Nonequilibrium effects in supersonic-nozzle flows
By J.Gordon Hall and C.E.Treanor, 1967.

Conference   Fluid physics of hypersonic wakes
Proceedings 19   Specialists' Meeting, Fort Collins, Colorado, May 1967.
(in two parts)

Conference   Fluid dynamics of rotor and fan supported aircraft at subsonic speeds
Proceedings 22   Specialists' Meeting, Göttingen, September 1967.

Conference   As above — with supplement
Proceedings 22 – S 4

1968

AGARDograph 132   The electron beam fluorescence technique
By E.P.Muntz, 1968.

Conference   Hypersonic boundary layers and flow fields
Proceedings 30   Specialists' Meeting, London, May 1968.

Conference   Supplement to the above.
Proceedings 30 Suppl.

Conference   Transonic aerodynamics
Proceedings 35   Specialists' Meeting, Paris, September 1968.

Conference   Supplement to the above.
Proceedings 35 Suppl.

1969

Advisory Report 17   Technical Evaluation Report on AGARD Specialists' Meeting on Transonic aerodynamics
By D.Küchemann, April 1969.

AGARDograph 134   A portfolio of stability characteristics of incompressible boundary layers
By H.J.Obremski, M.V.Morkovin and M.Landahl, 1969.

AGARDograph 135   Fluidic controls systems for aerospace propulsion
Edited by R.J.Reilly, September 1969.

AGARDograph 137   Tables of inviscid supersonic flow about circular cones at incidence $\gamma = 1,4$
(in two parts)   By D.J.Jones, November 1969.

Conference   Aircraft engine noise and sonic boom
Proceedings 42   Joint Meeting of the Fluid Dynamics and Propulsion and Energetics Panels, held in
Saint-Louis, France, May 1969.

Conference   The aerodynamics of atmospheric shear flow
Proceedings 48   Specialists' Meeting, Munich, September 1969.

1970

Report 575   Test cases for numerical methods in transonic flows
By R.C.Lock, 1970.

Advisory Report 22   Aircraft engine noise and sonic boom*
By W.R.Sears. (Technical Evaluation Report on AGARD FDP and PEP Joint Meeting
on "Aircraft engine noise and sonic boom".) January 1970.

---

*See also Advisory Report 26 by J.O.Powers and M.Pianko, June 1970. AR26 has the same title as AR22 but was produced by
the Propulsion and Energetics Panel of AGARD and deals primarily with engine noise.